

Recent Results in Cancer Research

Series Editors: Alwin Krämer · Jiade J. Lu

Otmar Schober

Fabian Kiessling

Jürgen Debus *Editors*

Molecular Imaging in Oncology

Second Edition

Indexed in PubMed/Medline

 Springer

Recent Results in Cancer Research

Volume 216

Series Editors

Alwin Krämer, German Cancer Research Center, Heidelberg, Germany

Jiade J. Lu, Shanghai Proton and Heavy Ion Center, Shanghai, China

More information about this series at <http://www.springer.com/series/392>

Otmar Schober • Fabian Kiessling •
Jürgen Debus
Editors

Molecular Imaging in Oncology

Second Edition

 Springer

Editors

Otmar Schober
Department of Nuclear Medicine
University of Münster
Münster, Germany

Jürgen Debus
Department of Radiation Oncology
Ruprecht Karl University
Heidelberg, Germany

Fabian Kiessling
Institute for Experimental Molecular
Imaging
University Hospital, RWTH Aachen
University
Aachen, Germany

ISSN 0080-0015

ISSN 2197-6767 (electronic)

Recent Results in Cancer Research

ISBN 978-3-030-42617-0

ISBN 978-3-030-42618-7 (eBook)

<https://doi.org/10.1007/978-3-030-42618-7>

1st edition: © Springer-Verlag Berlin Heidelberg 2013

2nd edition: © Springer Nature Switzerland AG 2020

This work is subject to copyright. All rights are reserved by the Publisher, whether the whole or part of the material is concerned, specifically the rights of translation, reprinting, reuse of illustrations, recitation, broadcasting, reproduction on microfilms or in any other physical way, and transmission or information storage and retrieval, electronic adaptation, computer software, or by similar or dissimilar methodology now known or hereafter developed.

The use of general descriptive names, registered names, trademarks, service marks, etc. in this publication does not imply, even in the absence of a specific statement, that such names are exempt from the relevant protective laws and regulations and therefore free for general use.

The publisher, the authors and the editors are safe to assume that the advice and information in this book are believed to be true and accurate at the date of publication. Neither the publisher nor the authors or the editors give a warranty, express or implied, with respect to the material contained herein or for any errors or omissions that may have been made. The publisher remains neutral with regard to jurisdictional claims in published maps and institutional affiliations.

This Springer imprint is published by the registered company Springer Nature Switzerland AG
The registered company address is: Gewerbestrasse 11, 6330 Cham, Switzerland

Preface

What does “molecular imaging” mean? There are several definitions in the literature. The term “molecular imaging” was formed in the early twenty-first century as a discipline at the intersection of molecular biology and *in vivo* imaging. It is defined as the visualization, characterization, and quantification of biologic processes at the cellular and molecular levels in living organisms. With the help of molecular imaging, cellular and molecular pathways and mechanisms of disease can be studied longitudinally in their own physiologically authentic environment in order to elucidate their molecular abnormalities that form the basis of disease.

This is an innovative conception, which is in deep contrast to the classical form of diagnostic imaging where documented findings show the end effects of molecular alterations, which are typically verified by well-established methods of pathology. We have to keep in mind, that the present era of precision medicine sees “cancer” as a consequence of molecular derangements occurring at the commencement of the disease process, with morphological changes happening much later in the process of tumorigenesis [7].

The application of principles of engineering and physics has shaped molecular imaging together with contributions to all aspects of cancer biology, from quantitative understanding of tumour growth and progression to improved detection and treatment of cancer [6]. Molecular imaging includes diagnostic methods along with various different strategies to yield imaging signals. Radiolabeled molecules (tracers) are preclinically and clinically established in molecular imaging to produce signals. Alternative methods can lead to images via means of x-rays (CT), sound (ultrasound), magnetism (MR), or light (OI, optical techniques of bioluminescence and fluorescence). Furthermore, hybrid imaging modalities have been developed enabling to assess different complementary information simultaneously and to bring tissue morphology and function into context with its molecular regulation. In this context, probe design is playing a crucial role in the development of molecular imaging applications.

These molecular imaging procedures can be considered important enablers of precision medicine in many fields including cancer, neurological and cardiovascular diseases. This is particularly true if molecular imaging is integrated in radiomic analyses, where multiple quantitative imaging features are extracted from the

images and analyzed alone or in conjunction with other omics and clinical data using machine learning [4].

Out of the increasing number of publications, comprising all fields of molecular imaging, this handbook focuses on the increasing impact of molecular imaging in the diagnostic and even the therapeutic field of oncology. The development of molecular imaging in the twenty-first century will and has to go ahead to multimodality imaging. Therefore, hybrid devices, which can cover the whole spectrum of preclinical and clinical imaging, will become more and more relevant. The prospects and challenges of these innovative techniques will be presented in detail in this handbook. In addition, optical tomographic hybrid approaches such as fluorescence molecular tomography–X-ray computer tomography (FMT–XCT) systems or multi-spectral optoacoustic tomography (MSOT) systems offer unprecedented levels of performance [3] and are increasingly applied in image-guided surgery [1].

The second edition of this book has further been expanded by chapters about molecular ultrasound imaging [5], spectral and phase contrast x-ray computed tomography, and radiomics [4] and covers emerging methods bridging between *ex vivo* and *in vivo* imaging such as RAMAN spectroscopy [2] and advanced microscopy.

Molecular imaging plays an important role in therapy decisions. Results of molecular imaging may serve as biomarker for response and prognosis of cancer patients. Moreover, molecular imaging plays a crucial role to visualize and define the target volume in radiation oncology. Recent studies demonstrating the strength of this approach are discussed in three new chapters of this book.

The development of all previously mentioned innovative multimodality imaging approaches require the competence and accreditation of scientists from different disciplines. Therefore, molecular imaging in oncology in the twenty-first century is not possible without close interdisciplinary and interfaculty collaborations.

This handbook highlights the immense potential this reintegration of different disciplines will offer in the future. It provides updated information about molecular imaging in oncology for nuclear physicians as well as radiologists, oncologists, chemists, mathematicians, computer scientists, and physicists. A careful selection of experts in the different fields of molecular imaging was made to outline the major trends and challenges in molecular imaging in oncology bridging the gap between basic research and clinical applications in a unique way. With respect to the distinct profiles of expertise, each chapter is self-contained.

In view of this background, the handbook was structured according to the single steps in the development and implementation of molecular imaging applications, i.e. from device and probe design to preclinical and then to clinical application. Accordingly, the following sections were defined:

- Technology and Probe Design
- Preclinical Studies
- Clinical Applications and
- Future Challenges

We are grateful that the first edition of the handbook has been accepted by the scientific community. This edition again assembles exceptionally comprehensive and stimulating contributions from outstanding stakeholders in molecular imaging

in oncology from America and Europe. Paradigmatically they cover the disciplines radiology, nuclear medicine, and radiotherapy/radiooncology on one clinical challenge and bring them together.

Münster, Germany
Aachen (Aix-la-Chapelle), Germany
Heidelberg, Germany

Otmar Schober
Fabian Kiessling
Jürgen Debus

References

1. de Boer E, Harlaar NJ, Taruttis A, Nagengast WB, Rosenthal EL, Ntziachristos V, van Dam GM (2015) Optical innovations in surgery. *Br J Surg* 102(2):56–72
2. Cialla-May D, Zheng XS, Weber K, Popp J (2017) Recent progress in surface-enhanced Raman spectroscopy for biological and biomedical applications: from cells to clinics. *Chem Soc Rev* 46(13):3945–3961
3. Condeelis J, Weissleder R (2010) In vivo imaging in cancer. *Cold Spring Harb Perspect Biol* 2: a003848
4. Gillies RJ, Kinahan PE, Hricak H (2015) Radiomics: images are more than pictures, *They Are Data*. *Radiology* 278(2):563–577
5. Kiessling F, Fokong S, Bzyl J, Lederle W, Palmowski M, Lammers T (2014) Recent advances in molecular, multimodal and theranostic ultrasound imaging. *Adv Drug Deliv Rev* 72:15–27
6. Mitchell MJ, Jain RK, Langer R (2017) Engineering and physical sciences in oncology: challenges and opportunities. *Nat Rev Cancer* (11):659–675. Review. Erratum in: *Nat Rev Cancer*. 2018 (11):720
7. Vaidya T, Agrawal A, Mahajan S, Thakur MH, Mahajan A (2019) The continuing evolution of molecular functional imaging in clinical oncology: the road to precision medicine and radiogenomics (Part I/II). *Mol Diagn Ther* (1):1–26; 27–51. Review

Contents

Part I Technology and Probe Design

1	Advanced X-ray Imaging Technology	3
	Daniela Pfeiffer, Franz Pfeiffer, and Ernst Rummeny	
2	Computed Tomography and Magnetic Resonance Imaging	31
	Monique R. Bernsen, Marcel van Straten, Gyula Kotek, Esther A. H. Warnert, Joost C. Haeck, Alessandro Ruggiero, Piotr A. Wielopolski, and Gabriel P. Krestin	
3	(Hybrid) SPECT and PET Technologies	111
	Teresa Nolte, Nicolas Gross-Weege, and Volkmar Schulz	
4	Ultrasound Imaging	135
	Georg Schmitz and Stefanie Dencks	
5	Optical and Optoacoustic Imaging	155
	Daniel Razansky and Vasilis Ntziachristos	
6	Multifunctional Magnetic Resonance Imaging Probes	189
	Philipp Biegger, Mark E. Ladd, and Dorde Komljenovic	
7	Single Photon Emission Computed Tomography Tracer	227
	Hans-Jürgen Pietzsch, Constantin Mamat, Cristina Müller, and Roger Schibli	
8	¹⁸F-Labeled Small-Molecule and Low-Molecular-Weight PET Tracers for the Noninvasive Detection of Cancer	283
	Christopher M. Waldmann, Klaus Kopka, and Stefan Wagner	
9	Ultrasound Molecular Imaging of Cancer: Design and Formulation Strategies of Targeted Contrast Agents	319
	Alexander L. Klibanov	
10	Optical and Optoacoustic Imaging Probes	337
	Michel Eisenblätter and Moritz Wildgruber	

Part II Preclinical Studies

- | | | |
|-----------|---|-----|
| 11 | Preclinical SPECT and SPECT-CT in Oncology | 359 |
| | Benjamin L. Franc, Youngho Seo, Robert Flavell,
and Carina Mari Aparici | |
| 12 | Preclinical Applications of Magnetic Resonance Imaging
in Oncology | 405 |
| | Wilfried Reichardt and Dominik von Elverfeldt | |
| 13 | Optical and Optoacoustic Imaging | 439 |
| | Joanna Napp, Andrea Markus, and Frauke Alves | |
| 14 | Applications of Small Animal PET | 493 |
| | Sonja Schelhaas | |
| 15 | Molecular Ultrasound Imaging | 509 |
| | Jasmin Baier, Anne Rix, and Fabian Kiessling | |
| 16 | Molecular Imaging in Oncology: Advanced Microscopy
Techniques | 533 |
| | Dimitrios Kapsokalyvas and Marc A. M. J. van Zandvoort | |

Part III Clinical Applications

- | | | |
|-----------|--|-----|
| 17 | Quantitative SPECT/CT—Technique and Clinical
Applications | 565 |
| | Philipp Ritt and Torsten Kuwert | |
| 18 | Fluorescence Imaging of Breast Tumors and Gastrointestinal
Cancer | 591 |
| | Dirk Grosenick and Christoph Bremer | |
| 19 | FDG PET Hybrid Imaging | 625 |
| | Juliane Becker, Sarah M. Schwarzenböck, and Bernd J. Krause | |
| 20 | Non-FDG PET/CT | 669 |
| | Egesta Lopci and Stefano Fanti | |
| 21 | Clinical MR Biomarkers | 719 |
| | Daniel Paech and Heinz-Peter Schlemmer | |
| 22 | Clinical PET/MR | 747 |
| | Wolfgang Weber | |
| 23 | Advanced Ultrasound Imaging for Patients in Oncology:
DCE-US | 765 |
| | Nathalie Lassau | |

24	Image-Guided Radiooncology: The Potential of Radiomics in Clinical Application	773
	Jan C. Peeken, Benedikt Wiestler, and Stephanie E. Combs	
25	Non-invasive Imaging Techniques: From Histology to In Vivo Imaging	795
	Thomas Bocklitz, Anja Silge, Hyeonsoo Bae, Marko Rodewald, Fisseha Bekele Legesse, Tobias Meyer, and Jürgen Popp	
26	Image-Guided Brain Surgery	813
	Stephanie Schipmann-Miletić and Walter Stummer	
Part IV Image Guided Radiooncology		
27	Molecular Imaging in Photon Radiotherapy	845
	Jamina Tara Fennell, Eleni Gkika, and Anca L. Grosu	
28	Molecular Imaging for Particle Therapy: Current Approach and Future Directions	865
	Katharina Seidensaal, Semi Ben Harrabi, and Jürgen Debus	
29	Internal Radiation Therapy	881
	Uwe Haberkorn, Clemens Kratochwil, and Frederik Giesel	
Part V Future Challenges		
30	Future Challenges of Multimodality Imaging	905
	Diego Alfonso López-Mora, Luis Alarcón Lagos, Montserrat Estorch, and Ignasi Carrio	

Part I
Technology and Probe Design



Advanced X-ray Imaging Technology

1

Daniela Pfeiffer, Franz Pfeiffer, and Ernst Rummeny

Contents

1.1	Introduction.....	4
1.2	Dual-Energy and Spectral CT.....	6
1.2.1	Basic Principles.....	6
1.2.2	State of the Art in Dual-Energy CT.....	8
1.2.3	Benchmarking Quantitative and Material-Specific CT Imaging.....	8
1.2.4	Clinical Implications for Oncological Imaging.....	11
1.3	Application Examples in Oncology.....	12
1.3.1	Improved Lesion CNR in Iodine Material Density CT Images.....	13
1.3.2	Quantification of Iodine Material Density CT Imaging.....	14
1.4	Future: Spectral Photon-Counting CT.....	14
1.5	Phase-Contrast and Dark-field X-ray Imaging.....	18
1.5.1	Basic Principles and Milestones.....	18
1.5.2	Early Years of Phase-Contrast Imaging.....	18
1.5.3	Milestones in Grating-Based Imaging.....	19
1.6	Image Formation and Preclinical Results.....	19
1.6.1	From 2D to 3D: Multi-contrast X-ray CT.....	22
1.7	Application Examples in Oncology.....	25

D. Pfeiffer · F. Pfeiffer (✉) · E. Rummeny
Department of Diagnostic and Interventional Radiology, Klinikum rechts der Isar,
Technical University of Munich, 81675 München, Germany
e-mail: franz.pfeiffer@tum.de

F. Pfeiffer
Department of Physics, Munich School of BioEngineering, Technical University of Munich,
85748 Garching, Germany

1.8 Present Stage of Clinical Translation.....	28
References	28

Abbreviations

CT	Computed Tomography
DECT	Dual-Energy CT
DFC	Dark-field Contrast
DLCT	Dual-Layer CT
DPC	Differential Phase-Contrast
DSCT	Dual-Source CT
IMD	Iodine Material Density
KVSCT	Rapid kVp Switching CT
MRI	Magnetic Resonance Imaging
SPCCT	Spectral Photon-Counting CT
VME	Virtual Mono-Energetic
VNC	Virtual Non-Contrast

1.1 Introduction

Since their discovery by Wilhelm Conrad Röntgen in 1895, X-rays have become the most widely available, typically fastest, and usually most cost-effective medical imaging modality today. From the early radiographic approaches using X-ray films as detectors, the portfolio of medical X-ray imaging devices developed into a large range of dedicated instrumentation for various applications. Today, we have dedicated devices for mammography screening, angiographic interventions, fluoroscopy, general digital radiography, and 3D-computed tomography as major workhorses in diagnostic imaging. In addition to technological developments towards better detectors, X-ray generators, and more precise machinery in general, a wealth of dedicated software solutions for image post-processing, automated diagnosis, visualization, or quantitative extraction of biomarkers has been developed.

While X-ray imaging has come a long way, there are some physical properties of X-rays, which have not yet been fully exploited, and which may offer quite some room for further enhancements of current X-ray imaging equipment.

Firstly, X-ray imaging today is mainly black and white, despite the fact that X-ray generators actually create a full spectrum of X-ray energies, and that the interactions of X-rays that occur within the human body are not the same for all energies and every material (see Fig. 1.1a). Exploiting these spectral dependencies allows to not only obtain black and white CT images, but also to obtain more molecularly specific information, which is relevant particularly in oncological precision radiology. This first aspect is detailed more in section two of this chapter.

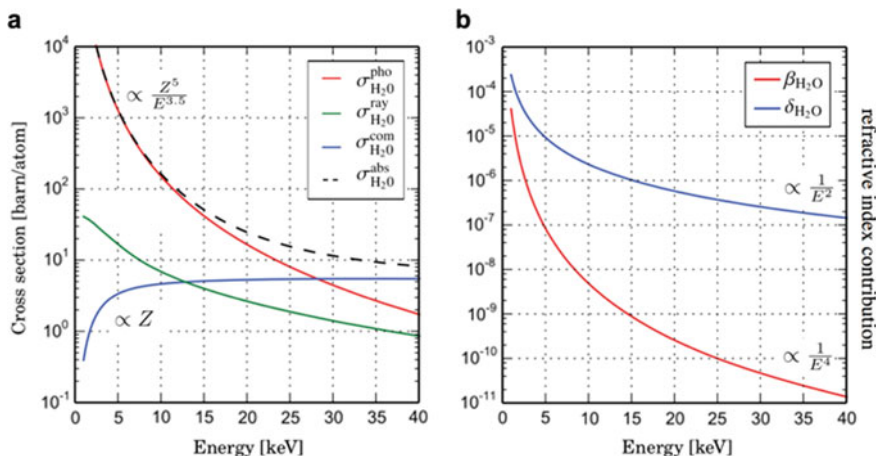


Fig. 1.1 X-ray attenuation and phase-shift characteristics as a function of energy (for water). **a** Three interaction processes, namely the photoelectric absorption (σ_{pho}), Compton scattering (σ_{com}), and Rayleigh scattering (σ_{ray}) contribute to the overall cross section for X-ray attenuation. They all have different dependencies on energy. While the photo-effect dominates at lower energies, and quickly drops off towards higher energies, the Compton effect remains the dominating interaction at higher energies. Rayleigh scattering only has a weak contribution to the attenuation effect. **b** When interpreting X-rays as waves, the interaction of the material is described by a refractive index $n = 1 - \delta + i\beta$. The decrement δ is related to the phase shift that X-rays undergo when traversing matter, and the imaginary part β reflects the attenuation of the amplitude of the X-ray wave. Note that δ exceeds β by up to four orders of magnitude, and that δ only decreases with $1/E^2$ towards higher energies, whereas β decreases more rapidly, with around $1/E^4$. Pfeiffer D./TUM

The second aspect, as so far in radiology mainly neglected and unused property of X-rays, is the physical fact that X-ray can also be interpreted in the wave picture, and not only as presently been done in the particle picture. If interpreted as waves, X-rays—just like visible light—experience a phase shift in matter, and this—if exploited correctly—can produce a new class of X-ray images, which then depict the wave interactions of X-rays with matter, rather than only the attenuating properties, as done until now. In that case, one typically describes the interaction of X-rays with the material by a refractive index $n = 1 - \delta + i\beta$. The decrement δ is related to the phase shift that X-rays undergo when traversing matter, and the imaginary part β reflects the attenuation of the amplitude of the X-ray wave. As can be seen in Fig. 1.1, the wave interaction, as described by δ typically exceeds β by up to four orders of magnitude, and one also observes that δ only decreases with $1/E^2$ towards higher energies, whereas β decreases more rapidly, with around $1/E^4$. This second aspect, which has an enormous potential for changing and enhancing X-ray imaging with a new contrast modality, is described further in section three of this chapter.

1.2 Dual-Energy and Spectral CT

1.2.1 Basic Principles

Dual-Energy CT (DECT) is based on the fact that the interactions of X-rays that occur within the human body are not the same for all energies and every material. Exploiting these spectral dependencies allows to not only obtain a black and white CT image, but also obtain more molecularly specific information, which is relevant particularly in oncological precision radiology.

So far, mainly three different technological approaches have been developed for obtaining dual-energy data (see Fig. 1.2). Dual-Source CT (DSCT) was the first technology to be implemented in medical CT imaging [12, 15]. In DSCT, two X-ray tubes as well as two detectors are integrated into one scanner. These two sets of source and detector can then be independently operated at two different acceleration voltages. Rapid kVp Switching CT (KVSCT) [16] followed a little later, and utilizes only one single set of X-ray generator and detector. It achieves to obtain

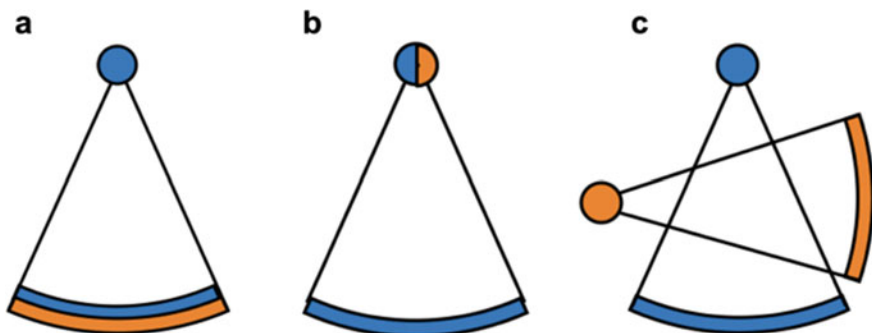


Fig. 1.2 The three presently most widely used Dual-Energy CT (DECT) system configurations. **a** The most recently introduced concept uses a single X-ray generator and dual-layer scintillator detector. This Dual-Layer CT (DLCT) concept achieves spectral separation at the detector by detecting the lower energy photons predominantly in the thin upper layer, and the remaining high-energy X-ray photons in the thick layer below. The main advantages of DLCT are a perfect temporal and spatial registration, very low correlated noise in the two energy bins, and the fact that dual-energy information is always available. **b** The Rapid kVp Switching CT (KVSCT) design also utilizes only one single set of X-ray generator and detector, but achieves dual-energy information by switching between two tube voltages in very short time intervals. The main advantage of KVSCT is that it is technologically relatively straightforward to implement. The main disadvantage is the large spectral overlap, and thus correspondingly large noise levels in the separated material basis images. **c** Dual-source CT (DSCT) was the first technology to be implemented in medical CT imaging. In DSCT, two X-ray tubes as well as two detectors are integrated into one scanner. As the main advantage, the very good spectral separation is usually named. The main disadvantages are a reduced field of view (as one of the two detectors is smaller and does not cover the entire patient body) and the relatively high noise level due to cross Compton scatter. Pfeiffer D./TUM

dual-energy information by switching between two tube voltages in very short time intervals. The most recently developed technique for DECT is a scanner equipped with a spectral detector, which uses a Dual-Layer CT (DLCT) detector design [3]. DLCT provides spectral information by using a single X-ray tube and two predefined detector layers that resolve the X-ray beam into low- and high-energy photons. Besides these mainly used concepts, other—less-efficient concepts—exist, such as the twin-beam DECT where the X-ray beam is divided into a low- and high-energy part along the scan axis by inserting different filter materials or a DECT system, which uses two separate and sequential scans at different kVp settings.

For abdominal CT, especially for oncological applications, DECT has shown a high value for diagnostic imaging and therapy planning. The benefits are based on a variety of additional and complementary imaging information that becomes available with DECT. This is shown in Fig. 1.3, which displays the typical imaging portfolio, as generated by present dual-energy spectral CT scanners (in this case: Philips IQon spectral CT). Here, a scan for a contrast-enhanced (portal venous phase) abdominal CT scan is shown. Instead of one conventional CT image only (Fig. 1.3a), and additional Virtual Non-Contrast (VNC) CT image (Fig. 1.3b), and an Iodine Material Density (IMD) image (Fig. 1.3c) is produced. These are

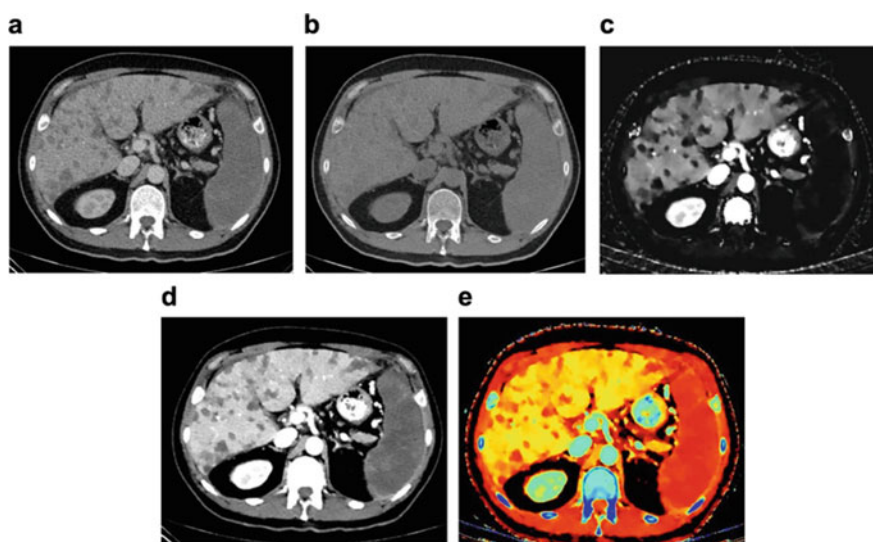


Fig. 1.3 Typical imaging portfolio, as generated by present dual-energy spectral CT scanners (in this case: Philips IQon Spectral CT), here a contrast-enhanced (portal venous phase) abdominal CT scan. **a** Conventional CT image. **b** Virtual Non-Contrast (VNC) CT image. **c** Iodine Material Density (IMD) image. These are obtained by post-processing the dual-energy information into a new set of basis material images (here VNC and IMD). **d** Virtual Mono-Energetic (VME) CT image (here at 40 keV), obtained by interpolating and fusion of the previously separated photo-effect and Compton-basis images at the desired energy. **e** Z-effective map, which displays the average atomic number of the material, from red (low-Z) to blue (high-Z). Pfeiffer D./TUM

obtained by post-processing the dual-energy information into a new set of basis material images (here VNC and IMD). Furthermore, so-called Virtual Mono-Energy (VME) CT images (typically between 40 and 200 keV) can be obtained by interpolating and fusion of the previously separated photo-effect and Compton-basis images at the desired energy (Fig. 1.3d). Finally, a Z-effective CT map (Fig. 1.3e) can be computed. It displays molecular imaging information, by plotting the average atomic number of the material, typically in a colour map from red (low-Z) to blue (high-Z).

1.2.2 State of the Art in Dual-Energy CT

In order to compare the different technological DECT concepts and evaluate their performance for specific clinical applications, several studies have been performed in the recent past. This includes studies focusing on renal [1], cardiac (Chandarana et al. 2011) or radiation therapy applications [2]. In the following, we review a more recently published study [34], which is particularly relevant for oncological precision radiology, as it discusses the precision quantification of iodine maps, and also the noise levels in VME images. Both are considered to be of high clinical relevance for oncological precision radiology and tumour therapy monitoring and follow-up.

1.2.3 Benchmarking Quantitative and Material-Specific CT Imaging

To evaluate different DECT platforms, typically semi-anthropomorphic abdomen phantoms (QRM-Abdomen-Phantom, QRM GmbH, Möhrendorf, Germany) with different extension rings (Fig. 1.4) to mimic different patient sizes are used. Such phantoms can be equipped with tissue-simulating inserts (\varnothing 2 cm), which include surrogates for the following various tissue types, e.g. water, adipose, muscle, liver, and bone-like material. Furthermore, a range of iodine concentrations (0.5, 0.75, 1.0, 2.0, 5.0, 10.0, and 15.0 mg/ml) can be used to assess specifically the quantitative performance with respect to quantitative iodine CT imaging.

In the study by Sellerer et al. [34], the following DECT systems were evaluated: DLCT (IQon Spectral CT, Philips Healthcare, Best, the Netherlands), first-generation KVSCT (Discovery CT750 HD, GE Healthcare, Chicago, IL, USA), and third-generation DSCT (SOMATOM Definition Force, Siemens Healthcare GmbH, Erlangen, Germany). Care has to be taken in such studies where acquisition parameters are similar for all systems, and therefore one typically uses the same imaging protocols. Here, an abdominal imaging protocol was used in this case. Furthermore, the radiation dose is typically fixed to specific values (CTDIvol: 10, 20, and 30 mGy).

As one example of the evaluated quantitative imaging performance, Fig. 1.5 shows measured and true VME-HU values of the used tissue-simulating inserts. Except for the KVSCT system, which shows small deviations for VMEs lower than

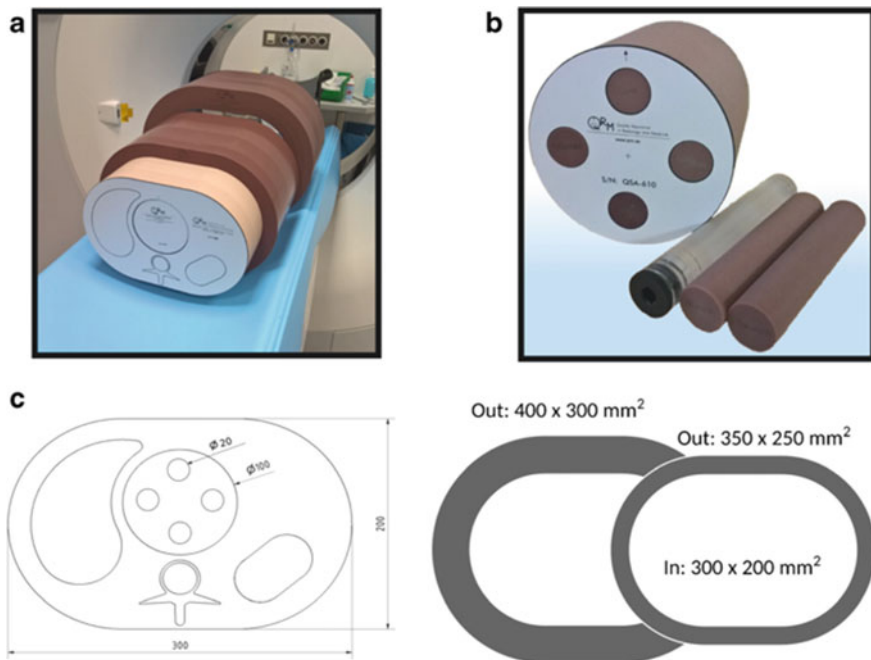


Fig. 1.4 Abdominal CT phantom, with precision inserts for quantifying DECT imaging performances relevant for oncology. **a** Abdomen phantom (semi-anthropomorphic) with extension rings to mimic larger patient diameters. **b** Inserts with calibrated rods of specific materials (e.g. different iodine concentrations, bone-, and adipose-tissue equivalent materials of varying density). **c** Size of abdomen phantom, inserts, and extension rings (units in mm). Adapted from Sellerer et al. [34]

60 keV, all three scanners exhibit a high accuracy for soft tissue-like materials over the complete energy range.

Figure 1.6 shows typical results for the quantitative VME CT image noise performance as a function of the different keV levels at a radiation dose of 20 mGy, and for three different patient sizes. For every system, the image noise is the smallest for the highest possible VME value and exhibits a plateau above 100 keV. The image noise rises for lower keV values and reaches its maximum at 40 keV for all systems. Generally, the noise levels increase towards lower VMEs for all systems, but for KVSCT and DSCT it is more pronounced, while the increase in noise is rather low in the case of DLCT. The better noise characteristics in the DLCT system is mainly due to the fact that anti-correlated noise in the two layers of the detector can be corrected more efficiently than uncorrelated noise (KVSCT and DSCT) or cross-scatter (DSCT).

In Fig. 1.7, the performance with respect to quantitative iodine concentration imaging is shown. As discussed before, this is of high relevance for oncological imaging. Generally speaking, the measured (Fig. 1.7a, open circles) follow the true

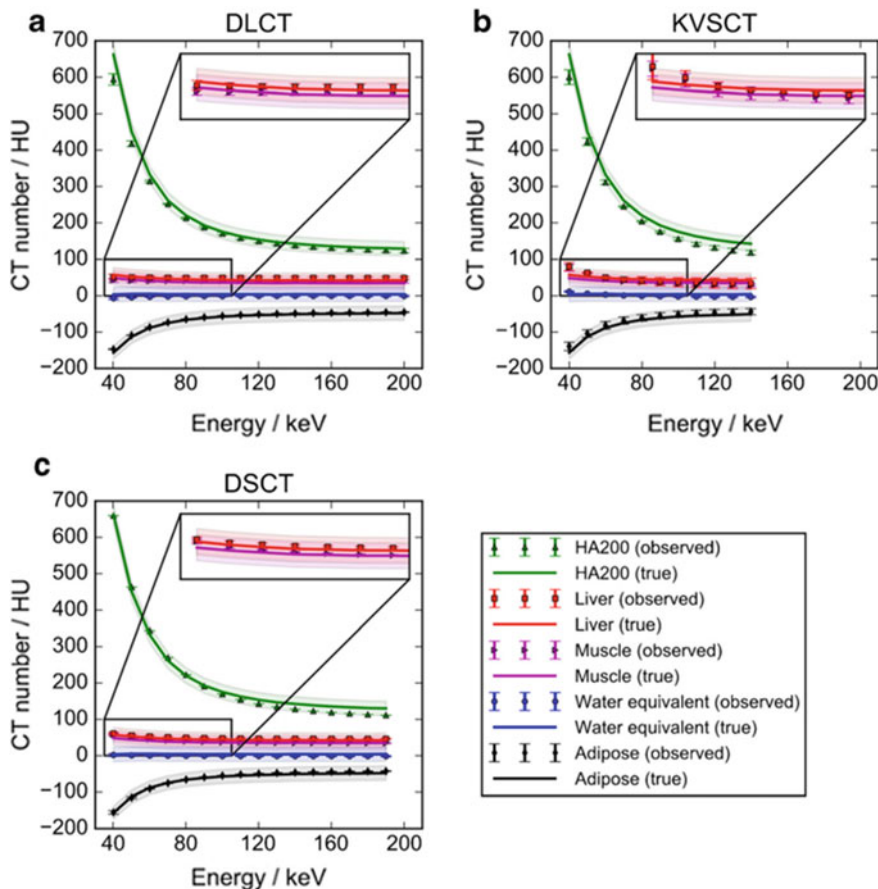


Fig. 1.5 Quantitative Virtual Mono-Energetic (VME) CT imaging performance for a medium-sized phantom at 20 mGy across different DECT platforms. **a** Dual-Layer CT (DLCT). **b** Rapid kVp Switching CT (KVSCT). **c** Dual-Source CT (DSCT). Errors reflect the threefold standard deviation between repeated scans. Adapted from Sellerer et al. [34]

(Fig. 1.7a, line) iodine concentrations for all systems evaluated, i.e. the DLCT, KVSCT, and DSCT system. However, when the absolute deviation from the real values is considered, there are differences observed for the three systems. These are shown in the Bland–Altman plots in Fig. 1.7b (here for a medium patient size and 20 mGy radiation dose). It can be seen that DLCT delivers the smallest absolute errors of measured iodine concentration, followed by the KVSCT system. The mean errors observed in DSCT are significantly larger. It can also be seen that the absolute iodine quantification error increases with iodine concentration for all scanner types. In this study, DLCT tends to slightly underestimate the iodine

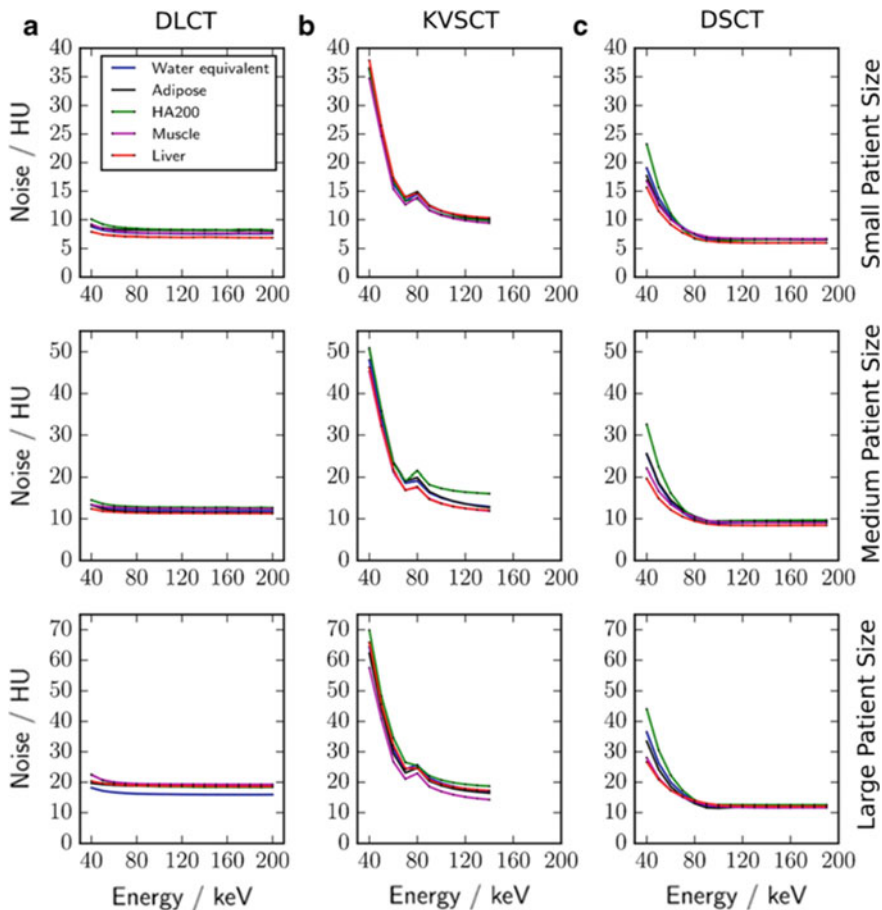


Fig. 1.6 Noise performance (standard deviation) in the quantitative Virtual Mono-Energetic (VME) CT images for all DECT platforms and small, medium, and large patient size. **a** Dual-Layer CT (DLCT). **b** Rapid kVp Switching CT (KVSCT). **c** Dual-Source CT (DSCT). The noise values are given in Hounsfield units (standard deviation) at 20 mGy CTDIvol and for each CT system. Adapted from Sellerer et al. [34]

content, while DSCT overestimates the iodine content at the same patient size and radiation dose.

1.2.4 Clinical Implications for Oncological Imaging

In summary, it can be noted that the presently available high-end DECT scanners already allow quantitative image assessment in both the Virtual Mono-Energetic (VME) and Iodine Material Density (IMD) CT images. All evaluated DECT

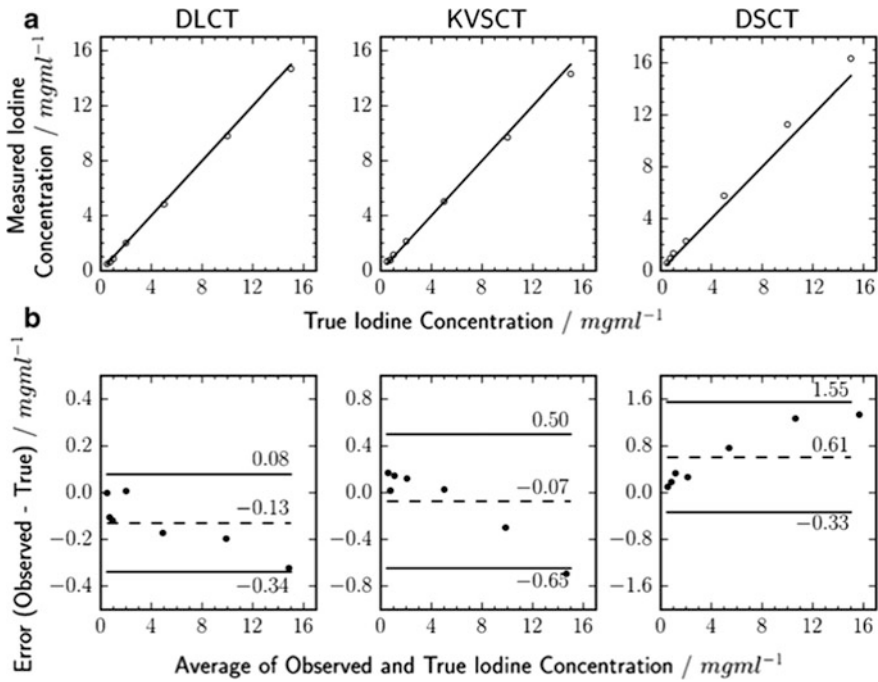


Fig. 1.7 Measured iodine concentrations and absolute errors. **a** Measured (open circles) and true (line) iodine concentrations for the Dual-Layer CT (DLCT), Rapid kVp Switching CT (KVSCT), and Dual-Source CT (DSCT) system. **b** Bland–Altman plots of the mean signed deviation between observed and true concentrations. All values are given for a medium-sized phantom and 20 mGy CTDIvol. Adapted from Sellerer et al. [34]

platforms can be used in clinical day-to-day routine, but noticeable differences in imaging performance exist between the platforms. When considering in particular the image noise levels in the VME images and quantitative iodine concentration accuracy, the most recently introduced system, namely the DLCT concept, produces the best performance.

1.3 Application Examples in Oncology

For oncological precision radiology, mainly the Virtual Non-Contrast (VNC), Virtual Mono-Energetic (VME), and material-specific Iodine Material Density (IMD) CT images are useful. Particularly, the IMD CT images enable the quantitative differentiation of hypo-dense tumours from hypo- or hyper-attenuating cysts and facilitate detection of iso-attenuating and hyper-dense lesions [1, 9, 27].

1.3.1 Improved Lesion CNR in Iodine Material Density CT Images

As one potential application of the beneficial use of quantitative IMD CT images derived from DECT in oncology, the following example shall be given. It shows the arterial phase hyper-enhancement and portal venous washout associated with HCC. In this recent study by Pfeiffer D. et al. [27], the performance of IMD-based imaging has been compared to mono-energetic 65 keV images and benchmarked to the currently clinically established standard of magnetic resonance imaging (MRI).

Figure 1.8 shows axial IMD CT and MR images of a 72-year-old male patient with hepatocellular carcinoma (HCC) in segment VI. The CT scans were obtained on a single-source dual-energy 64-channel CT scanner with fast kVp switching (80/140 kVp, GE Discovery CT 750 HD scanner, GE Healthcare, Milwaukee, WI, USA), and acquired in arterial and portal venous phase. Before the scan, contrast agent was given intravenously (Isovue, 370 mg of iodine per mL; 1.2 mL per KG body weight; Bracco Diagnostics, Princeton, NJ, USA) at an injection rate of 3 mL/s followed by a 40-mL saline chaser at the same rate. The arterial phase was acquired 10–15 s after the attenuation threshold was reached at the supraceliac abdominal aorta, and the portal venous phase images were obtained 70 s following contrast injection.

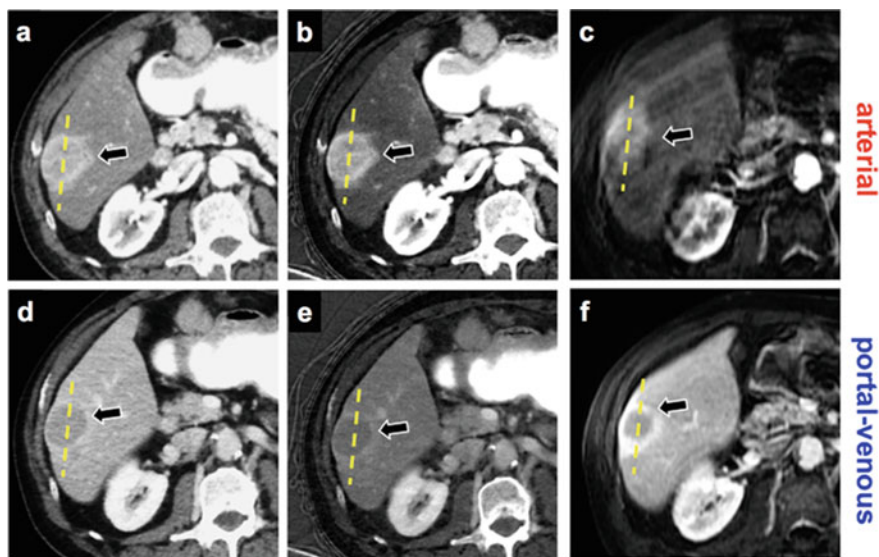


Fig. 1.8 Axial DECT and MR images of a 72-year-old male patient with hepatocellular carcinoma (HCC) in segment VI. **a–c** Arterial phase. **d–f** Portal venous phase. **a, d** Virtual Mono-Energetic (VME) CT image (65 keV). **b, e** Quantitative Iodine Material Density (IMD) CT image. **c, f** MR image of the same patient. In (**b, e**) one observes an increased contrast between HCC and non-tumour liver. Adapted from Pfeiffer D. et al. [27]

As can be seen in Fig. 1.8, the contrast between HCC and the background liver is clearly increased in the IMD images (Fig. 1.8b, e) compared to the VME images in Fig. 1.8a, d, and MRI (Fig. 1.8c, f), respectively. When evaluated quantitatively, on the basis of a CNR analysis, one finds that the CNR is significantly higher in the IMD images in both the arterial (81.87 ± 40.42) and the portal venous phase images (33.31 ± 27.86), compared to the VME images (6.34 ± 4.23 and 1.89 ± 1.87) and MRI (30.48 ± 25.52 and 8.27 ± 8.36), respectively.

In summary, this specific example shows that IMD CT images, as derived from DECT scans, can provide significantly improved detection of cancer lesions, as shown here for a hepatocellular carcinoma (HCC).

1.3.2 Quantification of Iodine Material Density CT Imaging

Iodine Material Density CT images can not only be used to improve CNR for lesion detection, as has been shown above, but they can also be used to draw more information from the images. One such example is that it has been found that quantitative IMD values can help to differentiate metastases depending on different primary malignancies.

In a recent study, for example, by Deniffel et al. [10], pulmonary metastases of 130 patients (77 men and 53 women, mean age 63, range 22–87) were evaluated with respect to their primary origin. These were primary bone (OS), breast, colorectal (CRC), head and neck, kidney (RCC), lung, pancreato-biliary (PBC), prostate, soft tissue, skin, and urinary tract malignancies.

Figure 1.9 shows some exemplary results of the quantitative evaluation of the IMD values found in the metastases as a function of the different origins. Significant differences can be noted for pulmonary metastases from RCC (IC: 2.83 mg/ml) versus breast cancer (IC: 1.47 mg/ml), CRC (IC: 1.23 mg/ml), HNC (IC: 1.54 mg/ml), OS (IC: 2.36 mg/ml), PBC (IC: 2.16 mg/ml), and urinary tract carcinoma (IC: 2.21 mg/ml). Based on these findings, one can conclude that quantitative IMD assessment in DECT images can be used to differentiate pulmonary metastases from OS, HNC, and RCC from other pulmonary metastases (area under ROC curve, 0.69–0.79).

Figure 1.10 shows how well this discrimination performs by considering the receiver operating characteristic (ROC) curves.

1.4 Future: Spectral Photon-Counting CT

Photon-Counting Spectral CT (PCCT) takes the concept of dual-energy spectral CT one step further, and can perform real “colour” X-ray detection, in a way that it can discriminate the energy of individual X-ray quanta. By sorting these X-ray photons in three or more energy bins, it is possible to obtain more information about the elemental composition of an object, than what is presently possible with

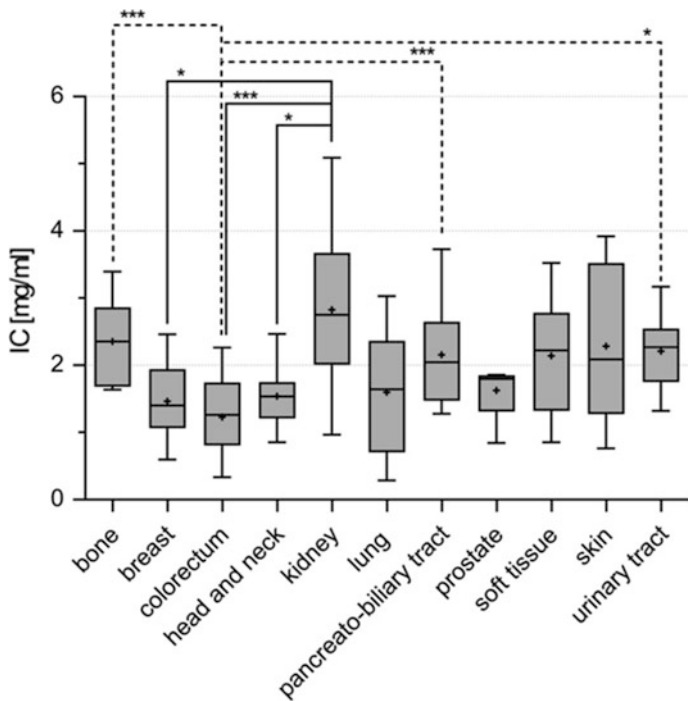


Fig. 1.9 Quantitative Iodine Material Density (IMD) values for intrapulmonary metastases from different primary tumours. Based on this quantitative evaluation, significant differences can be noted for pulmonary metastases from RCC (IC: 2.83 mg/ml) versus breast cancer (IC: 1.47 mg/ml), CRC (IC: 1.23 mg/ml), HNC (IC: 1.54 mg/ml), OS (IC: 2.36 mg/ml), PBC (IC: 2.16 mg/ml), and urinary tract carcinoma (IC: 2.21 mg/ml). Adapted from [10]

dual-energy CT systems. Over the last years, the effort to translate Spectral Photon-Counting Detector concepts into the clinical routine has accelerated with the installation of several preclinical CT systems.

With respect to oncological imaging, Photon-Counting Spectral CT may provide several new options for improving the present state of the art. One such example could be the usage of PCCT for advancing screening for colorectal cancer, as suggested by Muenzel et al. [24, 25]. This is described in the following.

Computed Tomographic (CT) colonography can be used as a screening method for non-invasive evaluation of the colon [18]. Its diagnostic performance for the detection of colon polyps is similar to that of conventional colonoscopy [8]. Unfortunately, both methods, conventional as well as CT-based colonography, require a cathartic preparation of the bowel. And this procedure exhibits lower acceptance by the patients, especially for elderly patients and those with multiple morbidities.

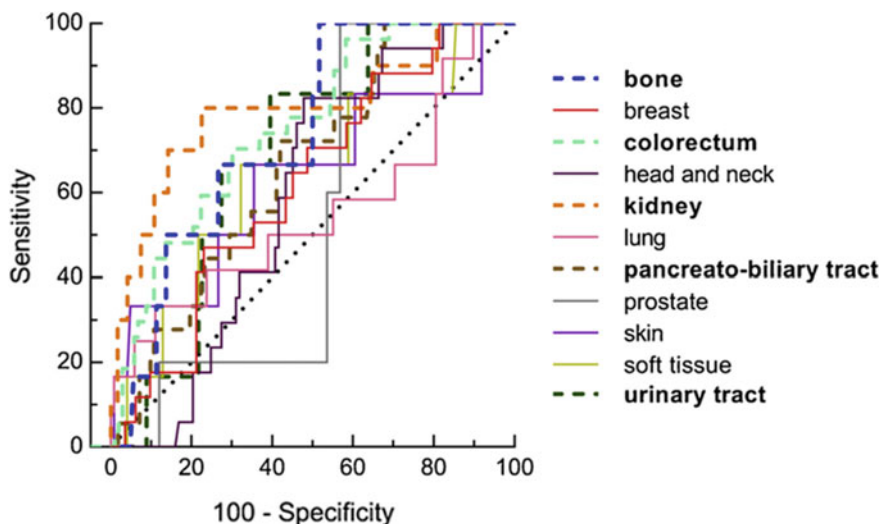


Fig. 1.10 Receiver operating characteristic (ROC) curves for diagnostic performance of the Iodine Material Density (IMD) CT values. The ROC curves discriminate pulmonary metastases from a specific primary tumour versus metastases from other malignancies. Bold dashed lines represent diagnostic tests that can distinguish between the two groups. Adapted from [10]

So-called laxative-free colonography uses barium or iodine for tagging of the faeces, and can, in principle, be done without cathartic cleansing of the bowel. It is typically performed in combination with oral ingestion of a water-soluble iodinated contrast agent and enables contrast enhancement of the faecal material and residual fluid in the bowel. After the CT scan, a software algorithm is used to virtually remove the contrast-enhanced faecal material from the CT images (“electronic cleansing”).

Although this novel CT colonographic method may increase patient acceptance of the procedure, it has some limitations. From a clinical point of view, it would be very important to not only find polyps, but also discriminate them according to their behaviour in terms of, i.e. contrast agent uptake. This, however, is not possible in conventional CT, as a contrast agent is already used for tagging the faeces.

Spectral Photon-Counting CT (SPCCT) may provide an alternative route, as it could enable the radiologist to differentiate between two contrast agents in a single CT acquisition. In the present case of colonography, for example, one contrast agent could be injected intravenously for enhancement of polyps and a second contrast agent could be given orally for tagging of the faecal material and residual fluid in the bowel.

Figures 1.11 and 1.12 show a dedicated phantom and preclinical results obtained in a recent study [24, 25] on a prototype SPCCT system, which demonstrates the feasibility of the approach described further above.

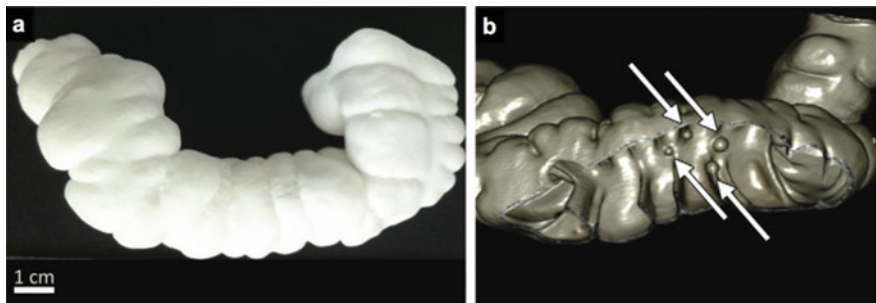


Fig. 1.11 Colon phantom created by 3D printing. **a** Picture of the colon phantom. **b** 3D iso-surface rendering (from CT data). Arrows indicate polyps added to phantom before production. Adapted from Muenzel et al. [27, 28]

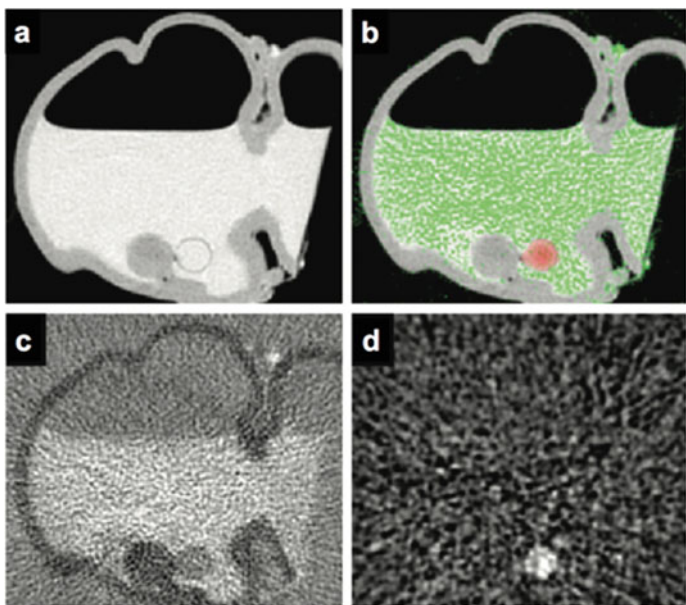


Fig. 1.12 Single Photon-Counting CT (SPCCT) scan of colon phantom. **a** Conventional CT image. **b** Same (conventional CT image) with an overlay of iodine (green) and gadolinium (red) material density image. **c** Iodine material density image. **d** Gadolinium material density image. Both material density images are obtained from a decomposition algorithm and are visually and quantitatively distinguishable. Therefore, SPCCT enables a separation between gadolinium-enhanced polyp tissue and iodine-tagged fluids and faeces in colon. Adapted from Muenzel et al. [27, 28]

To mimic a realistic case, rapid-prototyping can be used to fabricate a colon phantom (Fig. 1.11). Based on a digital model of a real patient, the colon was modified by inserting non-enhancing polyps (filled with a polymer mixture similar to the colon wall). Additionally, a gadolinium-filled capsule representing an enhanced polyp was placed on the colon wall, and the interior was filled with conventional iodine contrast agent as used in CT.

Figure 1.12 shows the results after SPCCT-based material separation. The different panels show the conventional CT image (Fig. 1.12a), the conventional CT image with an overlay of iodine (green) and gadolinium (pink) (Fig. 1.12b), the Iodine Material Density image (Fig. 1.12c), and the gadolinium material density image (Fig. 1.12d). Both, the iodine and gadolinium maps are generated from the post-processing algorithm and can clearly be differentiated. Thus the idea of using Spectral Photon-Counting CT in combination with two contrast agents (one intravenously injected, and one upon oral ingestion) has the potential to improve CT-based colonography, including a differential diagnosis for enhancing and non-enhancing polyps.

More recently, several other preclinical SPCCT studies have been carried out, which use two contrast agents also for simultaneous acquisition of multiphase CT scans [7, 24, 25, 37] or use the natural occurring difference between the energy-dependent attenuation behaviour of different materials [32].

1.5 Phase-Contrast and Dark-field X-ray Imaging

1.5.1 Basic Principles and Milestones

In conventional X-ray imaging, the image contrast is formed by X-ray attenuation, and reflects the physical interactions of photoelectric absorption and Compton scattering. Both of these interaction processes are modelled conveniently by interpreting X-rays as photonic particles. If, in contrary, X-rays are described as electromagnetic waves, other, wave-optical interaction effects occur, and result in diffraction, refraction, phase shift, and small-angle scattering. Dark-field contrast in this context means that particularly the small-angle scattering effect is used as an imaging signal.

1.5.2 Early Years of Phase-Contrast Imaging

To exploit wave-optical interactions of X-rays with matter, several methods have been investigated already in the last century. They can be classified into interferometric methods, techniques using an analyser, and free-space propagation methods. These methods differ in the nature of the signal recorded, the experimental setup, and the requirements on the illuminating radiation. Because of the use of crystal optics, crystal interferometric and analyser-based methods typically rely on a

highly parallel and monochromatic X-ray beam. Propagation-based methods can overcome the stringent requirements on the temporal coherence, but still require typically microfocus X-ray sources (with correspondingly low power) or highly brilliant synchrotrons. This is why these methods are not easily applicable to medical X-ray tubes, which do not provide the required brilliance.

1.5.3 Milestones in Grating-Based Imaging

Grating-based imaging presents an alternative phase-contrast imaging method, which can be used with standard medical imaging equipment and also provides the dark-field signal. It was first reported at a synchrotron source by Momose et al. [20], and the first tomographic grating-based phase-contrast results were then reported by Weitkamp et al. [41] and Momose et al. [21]. The transition from highly brilliant synchrotron sources to incoherent lab-based X-ray tubes was achieved by Pfeiffer F. et al. in [28], followed shortly by the first quantitative phase-contrast CT imaging performed at X-ray tubes in 2007 [29]. Dark-field or scattering imaging was discovered by Pfeiffer F. et al. [30], and extended to quantitative dark-field scattering CT by Bech et al. [5].

The more recent progress in grating-based X-ray imaging includes the development of advanced phase-stepping or data analysis schemes (reported by Zhu et al. [45], Qi et al. [31], Modregger et al. or Zanette et al. [19, 44]), the development of fast phase-stepping and tomography procedures (reported by Momose et al. [22]).

With respect to biomedical applications, several preclinical investigations have also been performed until now. These include a first preclinical CT scan of a human hand (reported by Donath et al. [11]), a comprehensive study of the potential of grating-based imaging for mammography (reported by Stampanoni et al. [35]), or the application of grating-based imaging for enhanced cartilage visualization (reported by Stutman et al. [36]).

1.6 Image Formation and Preclinical Results

Figure 1.13 shows the basic experimental arrangement for grating-based X-ray imaging [Pfeiffer et al. 2016]. It consists of a source grating G0, a phase grating G1, and an analyser grating G2. The source grating (G0), typically placed close to the X-ray tube, is an aperture mask with transmitting slits. It creates an array of periodically repeating line sources and effectively enables the use of relatively large, that is, square-millimetre-sized X-ray sources, without compromising the coherence requirements of the arrangement formed by G1 and G2. The image contrast itself is formed via the combined effect of the two gratings G1 and G2. The second grating (G1) acts as a phase mask, and imprints a periodic phase modulation onto the incoming wave field.

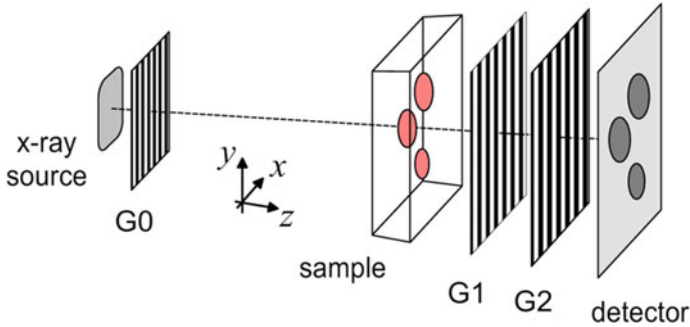


Fig. 1.13 Basic setup for grating-based X-ray imaging. The arrangement for grating-based X-ray imaging (a so-called Talbot-Lau interferometer) consists of a source grating G0, a phase grating G1, and an analyser grating G2. The source grating (G0) is typically placed close to the X-ray tube, whereas G1 and G2 are placed close to the detector, behind the sample. Pfeiffer F./TUM

Through the Talbot effect, the phase modulation is transformed into an intensity modulation in the plane of G2, forming a linear periodic fringe pattern perpendicular to the optical axis and parallel to the lines of G1 (see Fig. 1.14a). The third grating (G2), with absorbing lines and the same periodicity and orientation as the fringes created by G1, is placed in the detection plane, in front of the detector. When one of the gratings is scanned along the transverse direction, the intensity signal in each pixel in the detector plane oscillates as a function of the grating transverse position (Fig. 1.14b).

In order to retrieve the three different image signals (conventional attenuation, phase-contrast, and dark-field contrast), a so-called phase-stepping scan is performed with the interferometer, in which several exposures (typically 3 or 4) are acquired while one grating is stepped sideways in the direction perpendicular to the grating lines [Pfeiffer et al. 2016]. Subsequently, Fourier processing of the recorded frames is used to extract the three image signals. A typical result of such a procedure is shown in Fig. 1.15 for a simple test sample [5].

Figure 1.16 shows some exemplary images from a small animal (mouse), in vivo [6]. As can be seen, the information gained from each of the three contrast mechanisms is of complementary nature. The conventional X-ray image (Fig. 1.16a) shows very good contrast between bones and soft tissue, mainly due to the increased X-ray attenuation of calcium compared to the lighter soft tissue. The differential phase-contrast image (Fig. 1.16b) enhances details in the soft tissue. In particular the interfaces of air-filled regions are clearly shown, such as the trachea (marked by an arrow) or the lungs. Finally, the dark-field image (Fig. 1.16c) enhances features containing sub-pixel-sized microstructures. Particularly the lungs exhibit a strong signal, as their main morphological structures—the alveoli—have a typical size of a few tens of micrometres.

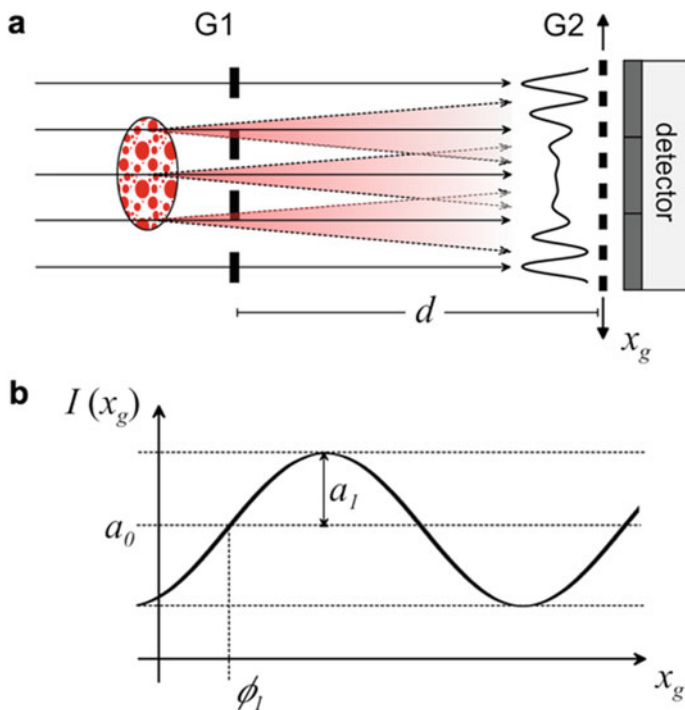


Fig. 1.14 Contrast generation and data processing in grating-based X-ray imaging. **a** In order to detect the dark-field (small-angle scattering) signal created by an object, the periodic fringe pattern created by G1 is analysed in the plane of G2. A sample with a significant scattering contribution diffuses the beam and yields a locally reduced fringe visibility. **b** The signal is obtained by analysing the intensity oscillations in every detector pixel as a function of the grating position G2. Pfeiffer F./TUM

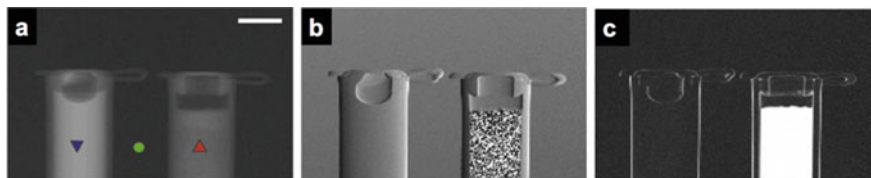


Fig. 1.15 Multi-contrast X-ray images of a test sample containing two plastic containers filled with a liquid (water, left, A) and a powder (sugar, right, B). **a** Conventional X-ray transmission image. **b** Differential phase-contrast image. **c** Dark-field image of the same sample. Adapted from [6]

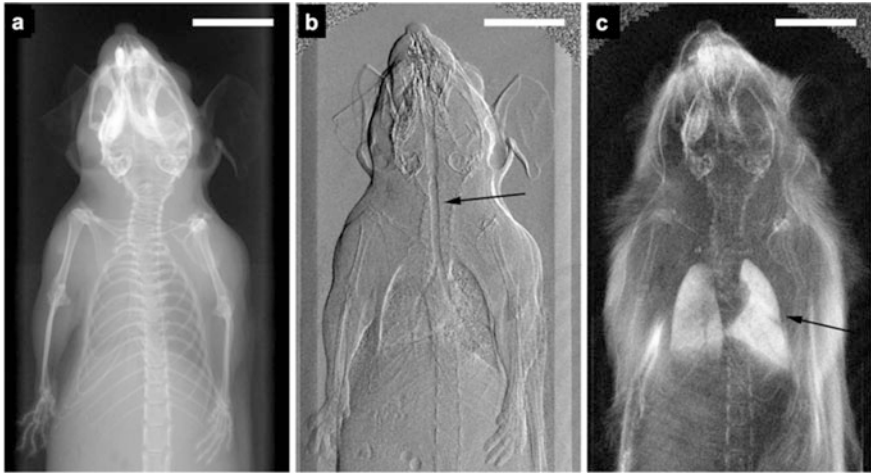


Fig. 1.16 First in-vivo multi-contrast X-ray images of a mouse. Data processing of the raw phase-stepping scans yields three separated and complementary X-ray images. **a** Conventional X-ray attenuation image. **b** Differential phase-contrast image based on X-ray refraction. **c** Dark-field image based on X-ray small-angle scattering. All three images are intrinsically registered as they are extracted from the same data. Examples of regions of enhanced contrast compared to the attenuation image are marked with arrows, showing the refraction of the trachea (**b**) and the small-angle scattering of the lung (**c**). The total dose for these images was 3.5 mGy. Adapted from [6]

1.6.1 From 2D to 3D: Multi-contrast X-ray CT

Grating-based phase- and dark-field imaging can not only be done in radiographic mode, but is also fully compatible with quantitative CT reconstruction (Pfeiffer et al. 2017).

Figure 1.17 shows the first preclinical prototype CT scanner, which was developed in 2012 [39]. It consists of a standard rotating CT gantry with X-ray source, specimen opening, and a flat-panel detector. It comprises additionally a three-grating Talbot-Lau interferometer to extract multi-contrast X-ray projection images. This allows the system to deliver conventional transmission images, differential phase-contrast images, and dark-field images. In the first step of the development, the compact gantry was built and operated stand-alone in rotating sample mode. In its present configuration, the gantry is now implemented into a typical preclinical CT scanner housing, featuring an animal bed, animal monitoring, gas anaesthesia, and a flat-panel imaging detector.

As an exemplary application, Fig. 1.18 shows some in vivo X-ray dark-field CT scans of mice. Here thoracic tomographic data were acquired of a healthy control mouse, a mouse with pulmonary emphysema, and a mouse with pulmonary fibrosis. The scope of this study [40] was to highlight the feasibility and to demonstrate the potential diagnostic benefit of the novel contrast modality in 3D imaging.

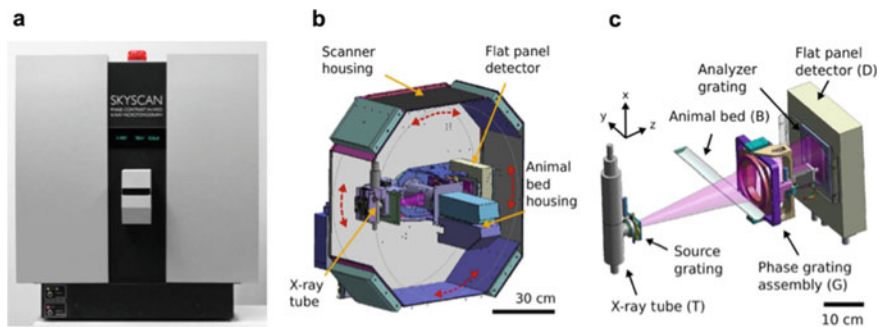


Fig. 1.17 Small-animal phase- and dark-field CT scanner. **a** Photograph of the previously developed rotating-gantry CT scanner. **b** Schematics of the scanner housing with rotating gantry (gantry movement indicated by red arrows). The gantry is oriented horizontally in the displayed view. The housing dimensions are approximately 95 cm in width, 100 cm in height, and 85 cm in depth. **c** Grating interferometer implementation, which is contained within the gantry. Adapted from Tapfer et al. [39]

Comparing the conventional CT scan of the emphysematous mouse (Fig. 1.18b, e) with the control (Fig. 1.18a, d), only subtle differences towards darker grey values in peripheral lung tissue in the emphysematous case can be observed. The resolution of the imaging system does not allow a direct depiction of the alveolar wall structure. In the corresponding CT slices of the dark-field channel (Fig. 1.18g, j for control, h, k for emphysema), the strong difference in signal allows for striking discernibility between control and diseased case. The destruction of alveolar walls and resulting enlargement of air spaces cause significantly reduced small-angle X-ray scattering.

In the case of lung fibrosis (Fig. 1.18c, f for attenuation, i, l for dark-field) the replacement of the functional alveolar network by solid scar tissue is clearly apparent in both modalities, since the presented case is at an advanced stage. The dark-field image reveals areas with the remaining functional alveolar structure.

For a better three-dimensional visualization, Fig. 1.18s, t provide views of volume renderings of the acquired datasets. Bones were segmented from the attenuation signal, whereas lung tissue was extracted from the dark-field CTs and represented by a semi-transparent hot colour map to enhance inter- and intra-pulmonary structural variations. The 3D views confirm the earlier findings from the 2D slices: The control lung exhibits a strong homogeneous scattering pattern all over its volume, whereas the fibrotic lung lacks scattering areas in the central, peribronchial regions.

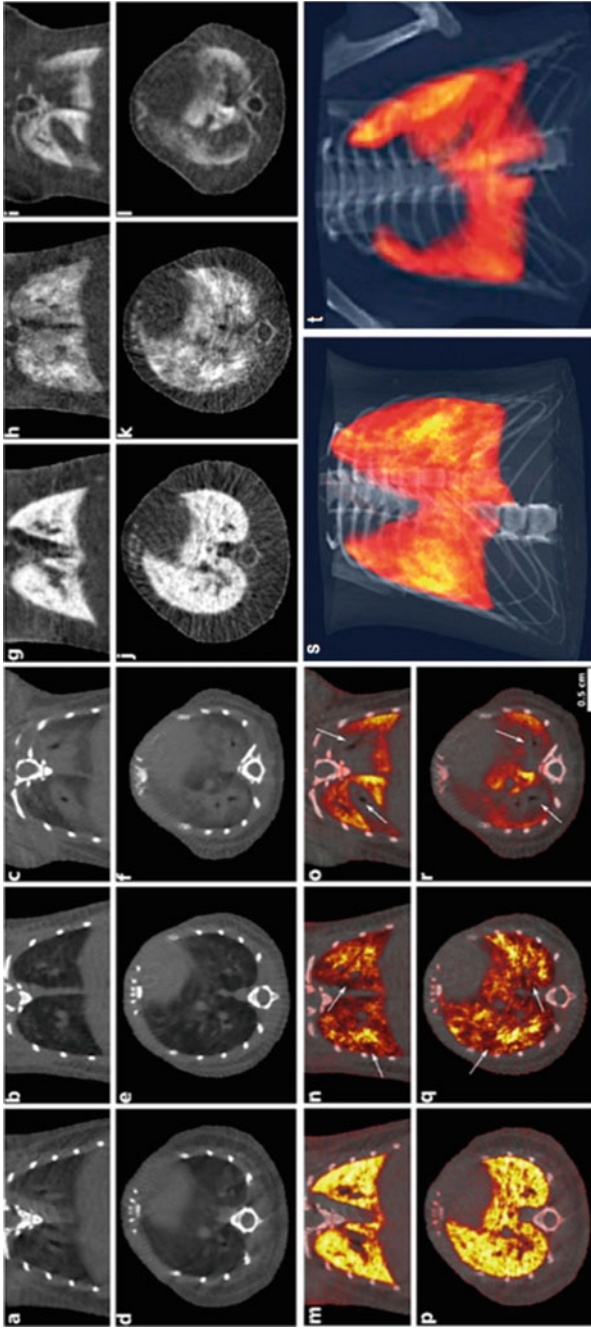


Fig. 1.18 Attenuation and dark-field CT slices, their fused representation, and volume renderings of lungs of three *in vivo* mice. Pathophysiological changes are subtle in the attenuation-based, but striking in dark-field images. Grey-value windows for single-modality slices were chosen for best visual appearance, but consistent within the same modality, respectively. **a, d, g, j, m, p, s** Control mouse. **b, e, h, k, n, q** Emphysematous mouse. **c, f, i, l, o, r, t** Fibrotic mouse. **a–c** Coronal slices of attenuation CT. **d–f** Axial slices of attenuation CT. **g–i** Coronal slices of dark-field CT. **j–l** Axial slices of dark-field CT. **m–o**: Coronal slices of fused CT. **p–r** Axial slices of fused CT. **s, t** Volume renderings of **s** emphysematous, and **t** a fibrotic case. The skeletal structure was segmented from attenuation CT, whereas the lung tissue was extracted from dark-field CT and represented by a semi-transparent hot colour map. Adapted from Velroyen et al. [40]

1.7 Application Examples in Oncology

Lung cancer is one of the leading causes of cancer-induced deaths worldwide, with around 1.5 million deaths a year worldwide. It is mostly diagnosed at an advanced stage with poor prognosis, and the average 5-year survival rate is very low, on the order of 15%. Conventional chest X-rays are typically used as a starting point in clinical diagnostic routine, but the sensitivity of detecting small nodules is very low [13]. This is why conventional X-ray chest radiography is not as efficient as a screening program for lung cancer.

Low-dose CT (LDCT) is presently discussed as a screening alternative, and is actually recommended in the US for high-risk groups (heavy smokers). While the sensitivity of detecting lung cancer in LDCT is indeed very high, the application to population-wide screening is still not possible, because also LDCT (a few mSv) presents a radiation dose about hundred times higher than a conventional chest X-ray image (a few ten micro-Sv).

X-ray dark-field radiography can potentially overcome this shortcoming, and provide a screening modality with high sensitivity than conventional chest X-rays, but yet at a dose that is much lower than LDCT.

This has been evaluated in a recent study by Scherer et al. [33], which demonstrated in an *in vivo* small-animal lung cancer model (Fig. 1.19) that X-ray dark-field contrast is also highly suitable for the detection of small tumour nodules, which could be overlooked at the corresponding conventional image. The improved detection rates in dark-field imaging essentially result from the distortion of the

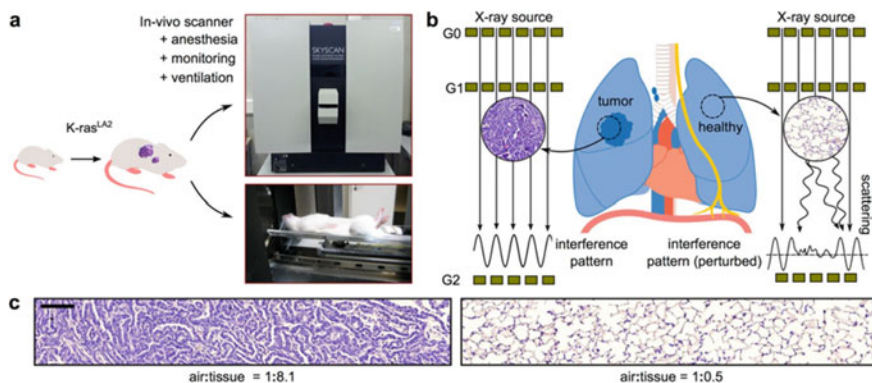


Fig. 1.19 Conceptual designs of dark-field imaging study on small-animal lung tumour mice models and the effect of reduced dark-field imaging signal from lung tumours. **a** In-vivo dark-field imaging was achieved using a preclinical phase-contrast small-animal scanner and K-rasLA2 mice. **b** X-ray dark-field imaging is highly sensitive to changes in the natural lung micro-anatomy. Cancerous tissue, with a smaller air:tissue ratio reduces the dark-field signal significantly compared to healthy tissue, which exhibits a larger air:tissue ratio. **c** Histological sections of typical tumour tissue (left) versus healthy tissue (right). Adapted from Scherer et al. [33]

generally overall high signal that healthy lungs provide, and the lack of overlying anatomical background (e.g. bones).

Figure 1.20 shows qualitative radiographic investigation assessment of the detection of lung cancer using X-ray dark-field radiography, compared to conventional attenuation imaging. Here, a transgenic animal model with spontaneous K-ras oncogene-driven growth of lung tumours, which closely resembles human lung tumour development, was used. Due to overlaying structures, e.g. ribcage, heart shadow, and the diaphragm, it is difficult to detect lung lesions on the transmission radiograms. Additionally, small tumour lesions only lead to minor variations to the overall optical density with respect to the surrounding healthy tissue, and therefore detection of small nodules is extremely challenging. In comparison, the impact of overlaying structures in dark-field images is much less present, since signal arising from the lung—more precisely the alveoli—is dominant in the thoracic region. This advantage enhances the assessment of lung lesions, since distortions in the homogeneous (strongly scattering) lung pattern are more easily perceived by the radiologist.

Compared to the conventional chest X-rays, significantly more lung lesions (especially small nodules) are visible as (poorly scattering) black voids in the dark-field projections (as indicated by red arrows). Furthermore, the size and

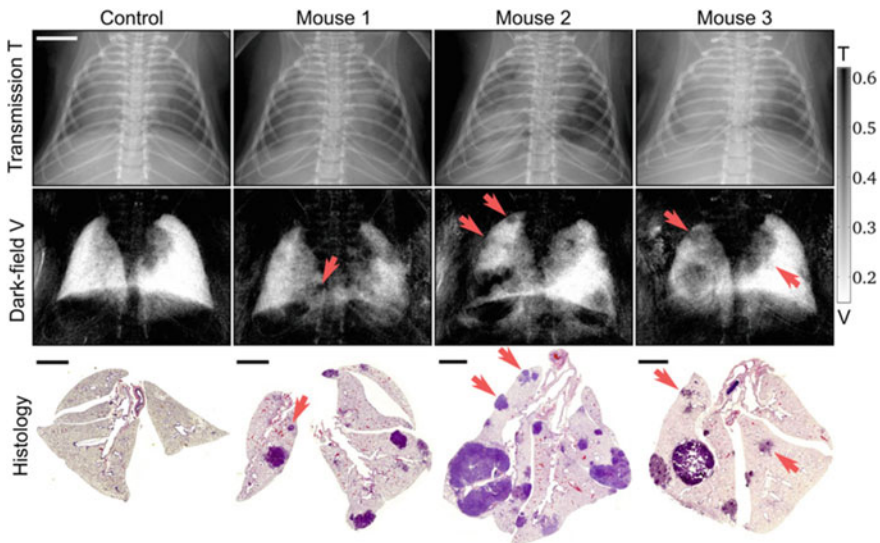


Fig. 1.20 Conventional and dark-field X-ray images and histologies of the investigated mice. Small cancer nodules are much easier to detect within the dark-field image (red arrows) than in the attenuation channel. This is mainly due to less anatomical overlay (e.g. of the ribs or other soft tissue) and the generally very strong and dominant dark-field signal of the lung within the thorax. The scale bars correspond to 5 mm and 2.5 mm on the radiograms and histological sections, respectively. Adapted from Scherer et al. [33]

location of the tumours can be more clearly identified and were found to be in agreement with the histopathological workup (Fig. 1.20c).

Figure 1.21 displays the results of a subsequent quantitative reader study with three experienced radiologists. The radiologists were blinded and both transmission and dark-field radiograms were presented separately, with the option of scaling data sets freely. In this study a total of 16 murine lungs were considered. The number of detected tumours (true-positives) on conventional and dark-field images demonstrates that dark-field imaging significantly outperforms transmission imaging with respect to the assessment of lung nodules. This was verified by histology as a method of reference. In comparison to the transmission radiographs, an increase in tumour detection rates ranging from at least 92% up to a maximum of 267%, was found, when the dark-field images are used. Furthermore, this study also yielded that dark-field-based diagnostics increases the diagnostic specificity of lung tumour assessment, by reducing the number of false-positives within the control group of healthy mice from an overall of 6 to 4 incidences.

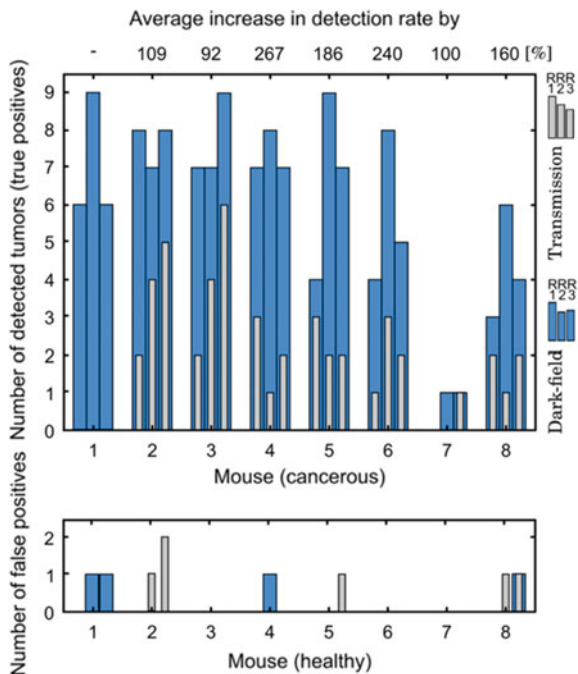


Fig. 1.21 Results of a reader study, aiming at the detection of lesions in dark-field versus conventional attenuation X-ray images. A significant improvement in the detection rate (true-positives) was observed, when using dark-field images. This improvement ranged from an average increase of 92% up to a maximum increase of 267%. Moreover, dark-field radiography additionally enhances diagnostic specificity, by reducing the number of false-positives from an overall of 6 to 4 incidences. Adapted from Scherer et al. [33]

1.8 Present Stage of Clinical Translation

Meanwhile, dark-field imaging has been taken up by more than two dozen research groups worldwide. So far, the method has been implemented in several prototypical preclinical demonstrator systems focusing on mammography [26, 42]; Garret et al. 2014; [4, 17], musculoskeletal applications [23, 38], and chest X-rays [14, 43].

It is expected that in the next 2–3 years these efforts will lead to the first patient studies, which will verify the high potential of phase- and dark-field-contrast imaging in routine medical imaging applications.

References

1. Agrawal MD et al (2014) Oncologic applications of dual-energy CT in the Abdomen. *RadioGraphics* 34:589–612
2. Almeida IP et al (2017) Dual-energy CT quantitative imaging: a comparison study between twin-beam and dual-source CT scanners. *Med Phys* 44:171–179
3. Altman A, Carmi R (2009) TU-E-210A-03: A double-layer detector, dual-energy CT—principles. *Advan Appl Med Phys* 36:2750–2750
4. Arboleda C et al (2017) Sensitivity-based optimization for the design of a grating interferometer for clinical X-ray phase contrast mammography. *Opt Express* 25:6349–6364
5. Bech M et al (2010) Quantitative x-ray dark-field computed tomography. *Phys Med Biol* 55:5529–5539
6. Bech M et al (2013) In-vivo dark-field and phase-contrast x-ray imaging. *Scientif Reports* 3:3209
7. Cormode DP et al (2017) Multicolor spectral photon-counting computed tomography: in vivo dual contrast imaging with a high count rate scanner. *Scientific Reports* 7:4784
8. Cotton PB et al (2004) Computed Tomographic Colonography (Virtual Colonoscopy): A Multicenter Comparison With Standard Colonoscopy for Detection of Colorectal Neoplasia. *JAMA* 291:1713–1719
9. Deniffel D et al (2018) Computed Tomography Perfusion Measurements in Renal Lesions Obtained by Bayesian Estimation, Advanced Singular-Value Decomposition Deconvolution, Maximum Slope, and Patlak Models: Intermodel Agreement and Diagnostic Accuracy of Tumor Classification. *Invest Radiol* 53:477–485
10. Deniffel D et al (2019) Differentiating intrapulmonary metastases from different primary tumors via quantitative dual-energy CT based iodine concentration and conventional CT attenuation. *Eur J Radiol* 111:6–13
11. Donath T et al (2010) Toward clinical X-ray phase-contrast CT: demonstration of enhanced soft-tissue contrast in human specimen. *Invest Radiol* 45:445–452
12. Flohr TG et al (2006) First performance evaluation of a dual-source CT (DSCT) system. *Eur Radiol* 16:256–268
13. Freedman MT, Lo S-CB, Seibel JC, Bromley CM (2011) Lung nodules: improved detection with software that suppresses the rib and clavicle on chest radiographs. *Radiology* 260:265–273
14. Gromann LB et al (2017) In-vivo X-ray Dark-Field Chest Radiography of a Pig. *Scientific Reports* 7:4807
15. Johnson TRC et al (2006) Dual-source CT cardiac imaging: initial experience. *Eur Radiol* 16:1409–1415
16. Karçaaltıncaba M, Aktaş A (2011) Dual-energy CT revisited with multidetector CT: review of principles and clinical applications. *Diagn Interv Radiol* 17:181–194

17. Koehler T et al (2015) Slit-scanning differential x-ray phase-contrast mammography: Proof-of-concept experimental studies. *Med Phys* 42:1959–1965
18. Levin, B. *et al.* Screening and Surveillance for the Early Detection of Colorectal Cancer and Adenomatous Polyps, 2008: A Joint Guideline from the American Cancer Society, the US Multi-Society Task Force on Colorectal Cancer, and the American College of Radiology*†. *CA: A Cancer Journal for Clinicians* **58**, 130–160 (2008)
19. Modregger P et al (2012) Imaging the Ultrasmall-Angle X-Ray Scattering Distribution with Grating Interferometry. *Phys Rev Lett* 108:048101
20. Momose A et al (2003) Demonstration of X-Ray Talbot Interferometry. *Jpn J Appl Phys* 42: L866–L868
21. Momose A (2005) Recent Advances in X-ray Phase Imaging. *Jpn J Appl Phys* 44:6355–6367
22. Momose A, Kuwabara H, Harasse S, Yashiro W (2011) Four-dimensional X-ray phase tomography with Talbot interferometry and white synchrotron radiation: dynamic observation of a living worm. *Opt Express* 19:8423–8432
23. Momose A et al (2014) X-ray phase imaging: from synchrotron to hospital. *Philosophical Transactions of the Royal Society A: Mathematical, Physical and Engineering Sciences* 372:20130023–20130023
24. Muenzel D et al (2017) Spectral Photon-counting CT: Initial Experience with Dual-Contrast Agent K-Edge Colonography. *Radiology* 283:723–728
25. Muenzel D et al (2017) Simultaneous dual-contrast multi-phase liver imaging using spectral photon-counting computed tomography: a proof-of-concept study. *Eur Radiol Exp* 1:25
26. Olivo A et al (2013) Low-dose phase contrast mammography with conventional x-ray sources. *Med Phys* 40:090701
27. Pfeiffer D et al (2018) Iodine material density images in dual-energy CT: quantification of contrast uptake and washout in HCC. *Abdom Radiol (NY)* 43:3317–3323
28. Pfeiffer F, Weitkamp T, Bunk O, David C (2006) Phase retrieval and differential phase-contrast imaging with low-brilliance X-ray sources. *Nat Phys* 2:258–261
29. Pfeiffer F, Kottler C, Bunk O, David C (2007) Hard X-Ray Phase Tomography with Low-Brilliance Sources. *Phys Rev Lett* 98:108105
30. Pfeiffer F et al (2008) Hard-X-ray dark-field imaging using a grating interferometer. *Nat Mater* 7:134–137
31. Qi Z, Zambelli J, Bevins N, Chen GH (2010) Quantitative imaging of electron density and effective atomic number using phase contrast CT. *Phys Med Biol* 55:2669–2677
32. Riederer I et al (2019) Differentiation between blood and iodine in a bovine brain-Initial experience with Spectral Photon-Counting Computed Tomography (SPCCT). *PLoS ONE* 14: e0212679
33. Scherer K et al (2017) X-ray Dark-field Radiography—In-Vivo Diagnosis of Lung Cancer in Mice. *Scientific Reports* 7:402
34. Sellerer T et al (2018) Dual-energy CT: a phantom comparison of different platforms for abdominal imaging. *Eur Radiol* 28:2745–2755
35. Stampanoni M et al (2011) The First Analysis and Clinical Evaluation of Native Breast Tissue Using Differential Phase-Contrast Mammography. *Invest Radiol* 46:801–806
36. Stutman, D., Beck, T. J., *Medicine, J. C. P.* I.2011. Talbot phase-contrast x-ray imaging for the small joints of the hand. *iopscience.iop.org*
37. Symons R et al (2017) Photon-counting CT for simultaneous imaging of multiple contrast agents in the abdomen: An in vivo study. *Med Phys* 44:5120–5127
38. Tanaka J et al (2013) Cadaveric and in vivo human joint imaging based on differential phase contrast by X-ray Talbot-Lau interferometry. *Zeitschrift für Medizinische Physik* 23:222–227
39. Tapfer A et al (2012) Experimental results from a preclinical X-ray phase-contrast CT scanner. *Proc Natl Acad Sci USA* 109:15691–15696
40. Velroyen A et al (2015) Grating-based X-ray Dark-field Computed Tomography of Living Mice. *EBIOM* 2:1500–1506

41. Weitkamp T et al (2005) X-ray phase imaging with a grating interferometer. *Opt Express* 13:6296–6304
42. Wen H et al (2013) Subnanoradian X-ray phase-contrast imaging using a far-field interferometer of nanometric phase gratings. *Nature Communications* 4:2659
43. Willer K et al (2018) X-ray dark-field imaging of the human lung—A feasibility study on a deceased body. *PLoS ONE* 13:e0204565
44. Zanette I et al (2012) Trimodal low-dose X-ray tomography. *Proc Natl Acad Sci USA* 109:10199–10204
45. Zhu P et al (2010) Low-dose, simple, and fast grating-based X-ray phase-contrast imaging. *Proc Natl Acad Sci USA* 107:13576–13581



Computed Tomography and Magnetic Resonance Imaging

2

Monique R. Bernsen, Marcel van Straten, Gyula Kotek,
Esther A. H. Warnert, Joost C. Haeck, Alessandro Ruggiero,
Piotr A. Wielopolski, and Gabriel P. Krestin

Contents

2.1	Imaging Targets in Cancer	32
2.1.1	Introduction	32
2.1.2	Physiological Imaging Targets	34
2.1.3	Molecular Targets	34
2.1.4	Cellular Targets	35
2.1.5	Image-Guided Drug Delivery	36
2.2	Recent Technological Developments in X-Ray Computed Tomography of Cancer	36
2.2.1	Basics of Multi-slice Spiral Computed Tomography	36
2.2.2	Multi-energy Computed Tomography	41
2.2.3	Preclinical Computed Tomography	42
2.2.4	Dedicated Imaging Systems and New Developments	43
2.2.5	Multimodality Imaging with CT	44
2.3	Recent Technological Developments in Magnetic Resonance Imaging of Cancer	45
2.3.1	Magnetic Resonance Imaging: Introduction	45
2.3.2	MRI Signal Formation and Contrast	46
2.3.3	Magnetic Field Strength and Signal Sensitivity	49
2.3.4	Imaging Gradients, Signal Encoding, and Signal Reception Chain	50
2.3.5	MRI Pulse Sequences, Parametric Mapping	52
2.3.6	Compressed Sensing	54
2.3.7	Contrast-Enhanced MRI	56
2.3.8	Multimodality Imaging with MRI	56

M. R. Bernsen (✉) · A. Ruggiero
Department of Radiology, Royal Papworth Hospital NHS Foundation Trust, Papworth Road,
Cambridge Biomedical Campus, Cambridge CB2 0AY, UK
e-mail: m.bernsen@erasmusmc.nl

M. van Straten · G. Kotek ·
Esther A. H. Warnert · J. C. Haeck · P. A. Wielopolski · G. P. Krestin
Department of Radiology & Nuclear Medicine, Erasmus MC-University Medical Center
Rotterdam, PO Box 2040, 3000 Rotterdam, The Netherlands

2.4	Imaging Biomarkers in Cancer	59
2.4.1	Imaging Biomarkers: X-Ray Computed Tomography	59
2.4.2	Imaging Biomarkers: Magnetic Resonance Imaging	60
2.5	Magnetic Resonance Imaging Probes in Cancer	71
2.5.1	Introduction	71
2.5.2	Non-Targeted Probes	72
2.5.3	Targeted Probes	82
2.5.4	Responsive Probes	84
2.5.5	Reporter Genes	85
2.6	Future Perspectives	93
	References	93

2.1 Imaging Targets in Cancer

2.1.1 Introduction

Classically, imaging is used in clinical response assessment of anticancer therapies through measurements of tumor size from cross-sectional anatomical images obtained by CT or MRI [84, 298, 346]. While these measurements can be readily and widely performed, they suffer from a number of limitations. Quantification is fairly crude and not suitable for diffuse and/or multiple tumor lesions and changes in tumor size do not always accurately reflect the response to treatment [329]. Therefore, significant effort is put into the development and validation of new imaging techniques and imaging biomarkers [29, 230]. These include techniques aimed at the quantitative visualization of metabolic processes and of cellular and molecular interactions. Such approaches are not only valuable for monitoring treatment responses, but also offer opportunities in studies regarding elucidation of mechanisms involved in cancer pathophysiology, identification of (new) targets for treatment, in drug development, for selection of patients likely to respond to the treatment at hand, and for monitoring of drug delivery efficacy.

In this respect, it is important to consider that the view on tumor formation and tumor progression has changed considerably over the past two decades. Until the realization that the microenvironment of tumors plays a crucial role in a variety of oncogenic processes [123], cancer was considered to be a disease mainly arising from transformed cells that, through successive oncogenic mutations, acquire autonomous resistance to cell death and enhanced proliferative and invasive capacities [261]. Instead of this cancer cell-focused view, it is now recognized that the tumor stroma plays a crucial role in oncogenesis. Tumor stroma consists of a variety of nonmalignant cells and extracellular matrix (Fig. 2.1). The various cell types within the tumor stroma comprise fibroblasts, immune cells, and endothelial cells; they are in principle nonmalignant but they do have an altered phenotype and function when compared to normal tissue. Through cell–cell interactions and the production of cytokines these tumor stroma cells actively contribute to tumor formation, progression, and metastasis and resistance to treatment [167, 267, 290].

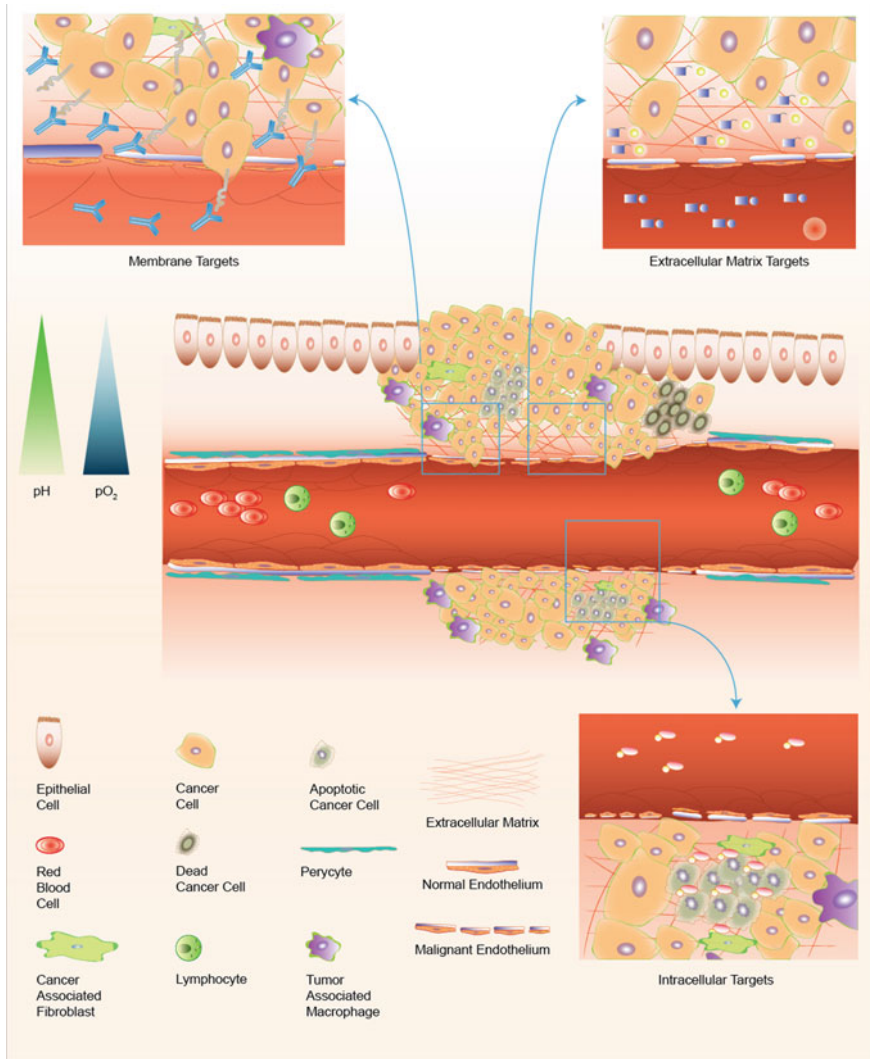


Fig. 2.1 Schematic representation of the complex composition of a tumor. Various cellular and stromal components can function as targets for therapy and imaging

This paradigm shift has led to the realization that for successful control of cancer, treatment strategies should not only be directed at the tumor cells but also targeted at the tumor microenvironment, for which an understanding of the complex molecular and cellular interactions in cancer tissue is paramount. Therefore, imaging techniques are becoming increasingly important in the development, design, and monitoring of cancer drugs and treatment strategies.

2.1.2 Physiological Imaging Targets

Tumors are known to have an aberrant vascular network and microcirculation. Tumor vasculature is typically highly disorganized with many structural and functional irregularities such as: incomplete endothelial lining, endothelial fenestrations, arteriovenous shunts, absence of flow regulation, increased vascular permeability, aberrant flow conditions, and inadequate lymphatic drainage. In addition, interstitial fibrosis is often also a hallmark of tumors. These irregularities are responsible for various pathophysiological conditions within tumors such as interstitial hypertension, hypoxia, and acidosis that contribute to the malignant phenotype and resistance to various treatments [318–326]. Plasma flow aberrations and high interstitial fluid pressure in tumors can severely hamper drug delivery efficiency through inadequate perfusion and convection within the tumor; hypoxic conditions negatively affect the radiation and cytostatic drug efficacy through reduced production of free radicals and altered cell cycle kinetics. Tumor blood volume, tumor perfusion, tumor oxygenation levels, interstitial acidosis, and fibrosis are, therefore, valuable imaging biomarkers in oncology. They can be used as either prognostic/predictive indicators or as treatment response parameters [58, 66, 75, 171, 318–326, 362]. Within this pathophysiological environment, tumor cells also display altered energy metabolism as reflected in increased glucose uptake and shifted balances in metabolic products. Metabolic fingerprinting of tumors by imaging techniques is, therefore, also a widely pursued approach in cancer management [11, 28, 27, 42, 122, 243].

Another aspect of tumor physiology considered to be of value as a quantifiable imaging target is tissue cellularity. Depending on the type of tissue, tissue cellularity can be higher or lower in malignant tumors compared to normal tissue. For instance, in edematous tumors, cellularity is typically lower compared to normal tissue. In contrast, in breast tumors cellularity is often higher compared to normal tissue that typically has a high-fat content [3, 343]. Cellularity can be determined by imaging based on water diffusion kinetics and in pretreatment situations used for staging and as a prognostic indicator. Cellularity measurements can also be used as an early marker in treatment response assessment [226].

2.1.3 Molecular Targets

Imaging of molecular targets commonly comprises the assessment of the presence and/or activity of a specific molecule. Various strategies can be employed, including the use of: imaging probes functionalized by a specific ligand, imaging probes that contain a substrate specific for the molecular function of the target molecule, or reporter gene technology. Imaging probes functionalized by conjugation to a ligand (e.g., antibody, peptide, aptamer, amino acid, or lectine) are generally aimed at molecules expressed on the cell surface such as somatostatin receptors [189], HER-2 [287], VEGF-receptors [37] and integrins [344]. These surface molecules can be involved in tumor cell proliferation, migration, drug

resistance and can thus be used as an imaging biomarker in diagnostics, prognostics, and treatment response assessment.

Imaging probes that contain a substrate specific for the molecular function of the target molecule are often referred to as “smart probes”, “activatable probes”, or “responsive probes”. Characteristic for these probes is that they are largely undetectable in their native state, but following interaction with their target undergo a physiochemical change creating a detectable signal. Typical targets for these imaging probes are enzymes such as MMPs [336], Cathepsins [227], lipases [133], and peroxidases [309]. However, responsive probes are more and more also being designed to interrogate physicochemical conditions such as pH, temperature, oxygen pressure, and redox potential in the tumor microenvironment in vivo [6, 103, 163, 253].

Reporter gene imaging is based on the introduction of a specific gene construct into the cells of interest whereby the reporter gene encodes for a receptor, a transporter, or an enzyme resulting in the binding, accumulation, or physicochemical modulation of an injectable probe or a naturally occurring substrate with inherent signal properties such as iron. Reporter gene technology can be used to interrogate the activity of specific signaling pathways, for monitoring of gene therapy, and to track migration and fate of specific cells in vivo (see also below) [155, 278].

2.1.4 Cellular Targets

Cellular imaging has applications in diagnosis, prognosis and treatment monitoring in oncology. Main goals in such approaches are directed at the assessment of the presence, distribution or fate of a specific cell population. Generally, this involves the incorporation of an imaging probe by the cells of interest, either by labeling the cells with exogenous probes or by reporter gene technology. Examples of cellular imaging applications that can serve diagnostic, prognostic as well as response monitoring purposes can be found in liver and lymph node imaging with intravascularly injected imaging probes. In these applications, the selective uptake characteristics of imaging probes by liver parenchymal cells or cells of the reticuloendothelial system are exploited by which presence of tumor (metastatic) lesions can be monitored [177, 186, 348]. A cellular imaging application that has elicited a wide interest in the past decade is in the field of cell-based therapies. Cell-based therapies are considered to offer unique benefits in cancer treatment. Cells as drug or drug carriers offer potentially favorable targeting and biocompatibility properties, e.g., crossing of the blood–brain barrier, compared to many synthetic drugs (carriers). In vivo cell tracking techniques by which the fate and function of transplanted cells can be monitored are of major importance in developing and improving such treatment strategies [29, 30, 132, 135, 161, 245, 295, 306]. Cellular imaging techniques are also widely used for cancer cell imaging to follow tumor development, tumor cell migration, and metastatic activity in vivo m[223, 281, 306, 368].

2.1.5 Image-Guided Drug Delivery

The many developments in imaging techniques have also created exciting possibilities for image-guided drug delivery. In pharmaceutical research, drug development is a slow, high risk, and costly process. Despite that the specifics and duration of each step depend on the drug class and target indication, overall the introduction of a new drug into clinical development generally takes 10 years [342].

Molecular imaging guidance plays an increasing role in many aspects of pharmaceutical research, providing important advantages over conventional readouts. High spatial and temporal resolution of imaging approaches allows for quantitative, uniform, and potentially high-throughput studies on the same living subject at different time points, increasing the statistical power and reducing the number of animals and relative costs. Especially in the early stages of drug research and development imaging allows for rapid, noninvasive longitudinal assessment of a drug's pharmacokinetics and pharmacodynamics [69] aiding the selection of lead successful candidates and excluding or deprioritizing others. Therefore, image-guided approaches have the potential to expedite the research and clinical approval of novel imaging and therapeutics probes [143].

By far, the oncology field benefited most of the recent advancements in molecular imaging. Several targeting moieties (antibodies, peptides, aptamers) specifically directed to molecular targets on malignant cells are currently available. These allow the design of specific probes suitable for the early detection of molecular events that precede the macroscopic development of a disease. Similarly, probes can be designed to perform a therapeutic effect (chemotherapy or radiotherapy) or to be activated in the specific site of interest (ph, thermal, enzymatic activation).

2.2 Recent Technological Developments in X-Ray Computed Tomography of Cancer

2.2.1 Basics of Multi-slice Spiral Computed Tomography

2.2.1.1 Brief History

The history of multi-slice spiral computed tomography (CT) starts in Germany in 1895 when Wilhelm Conrad Röntgen (1845–1923) discovered a new type of radiation, which he called X-rays. This type of electromagnetic radiation, which has a shorter wavelength than visible light and the ability to penetrate matter, was immediately used to image the inner human body. The images thus obtained showed a two-dimensional (2D) projection of the inner structures. The contrast in the images was based on the differences in X-ray attenuation coefficients and in the thickness of the various tissues. For decades, the principle of observing the inner human body by looking at projection images in the form of photographs (“X-rays”)

or fluoroscopic images did not really change. In these images, the depth information was lost and details were obscured by overprojection of other structures. Several attempts were made to image only a certain plane of the inner human body, a technique that became known as tomography.

After initial work by Allan M. Cormack (1924–1998), the principle of reconstructing cross sections was introduced into the medical world by the British engineer Godfrey Newbold Hounsfield (1919–2004). In 1972, he presented the first full-scale CT scanner (EMI Mark I, EMI Ltd., London, United Kingdom) and the first picture of a patient's head [13, 136]. This image represented a cross section with a thickness of 13 mm and consisted of a matrix of 80 by 80 pixels, which showed the anatomical structure of the brain. Compared to a plain X-ray image, the CT image showed a remarkable contrast between tissues with small differences in the X-ray attenuation coefficient. A survey of American physicians showed that the invention of CT, together with magnetic resonance imaging (MRI), is seen as the most important medical innovation in the past three decades of the twentieth century [99].

After the introduction in 1972, CT scanners and reconstruction algorithms were improved greatly. The time to obtain the information for reconstructing a cross section was reduced to the order of one second, and the spatial resolution was improved substantially. Most CT scanners utilized the fan-beam geometry, in which the X-ray tube rotates around the patient and attenuation measurements are obtained with an array of detectors, which also rotates. After data are acquired for one rotation of the X-ray tube, the scanner table is moved and the next slice is scanned. For nearly two decades this scanning technique, which is called the sequential technique, basically remained the same.

Based on new ideas and technical improvements, the German physicist Willi A. Kalender (1949) developed the spiral CT technique and reported the first clinical examinations with spiral CT at the 1998 annual meeting of the Radiological Society of North America. With spiral CT, the patient is moved through the CT scanner, with simultaneous acquisition of projection data of the continuously rotating X-ray source and detector array.

The performance of the spiral CT scanner was further improved by the introduction of scanners which measured multiple fans simultaneously. With multi-slice spiral CT, multiple *fan* measurements are made and an arbitrary number of *slices* can be reconstructed. In literature, a number of alternative terms can be found, like multisection, multichannel, and volumetric CT. In 1998 most CT manufacturers introduced a CT system that was able to acquire four fans simultaneously. This innovation reduced the time that was needed for a CT scan, without necessarily decreasing the spatial resolution. Since then, the technical developments in multi-slice spiral CT were primarily focused on increasing the number of fans. Currently, CT scanners are available which acquire up to 320 fans simultaneously.

The overview given above of the history of multi-slice spiral CT is of course far from complete. For a more extensive overview, the reader is referred to a book on CT by Kalender [154].

2.2.1.2 Data Acquisition

A CT scanner basically consists of a patient table and a gantry. The patient, who lies on the table, can be moved through the gantry. The table moves in a direction parallel to the z-axis. The gantry accommodates an X-ray tube and a detector array, which rotates around the patient (Fig. 2.2).

The width of the detectors in the axial plane influences the spatial resolution in the x, y-direction. This width, which generally cannot be chosen by the user, is in the order of 0.25–0.7 mm when scaled to the center of the field-of-view, depending on the CT scanner used. The width of the detector array in the z-direction influences the z-resolution or effective slice thickness. The width of the detector array generally can be varied between 0.5 and 10 mm, scaled to the center of the gantry.

For one complete rotation, the projection data are acquired for approximately 1000 X-ray tube angles. At sequential CT, the data are acquired while the patient table does not move. These data can be used to reconstruct cross-sectional images in the region covered by the X-ray (cone) beam. After data acquisition, the patient can be translated in the z-direction for the next region to be covered. State-of-the-art multi-slice CT scanners with 256 or more detector arrays can cover the complete region of interest within a single rotation without movement of the patient at all.

At spiral CT, the projection data are acquired while the patient is moved through the scanner gantry. The ratio of the table translation or table feed per 360° rotation of the X-ray tube and the total width of the detector arrays, is called the pitch value of a spiral scan. The quality of the sampling varies with the pitch. Low pitch spiral scans provide better image quality at the cost of longer scan time.

Motion of the patient during data acquisition, other than the enforced translation in the z-direction, may lead to inconsistencies in the projection data and to artifacts in the reconstructed images. Therefore, the patient is instructed to lie still and normally to hold his or her breath during data acquisition. This limits the scan time

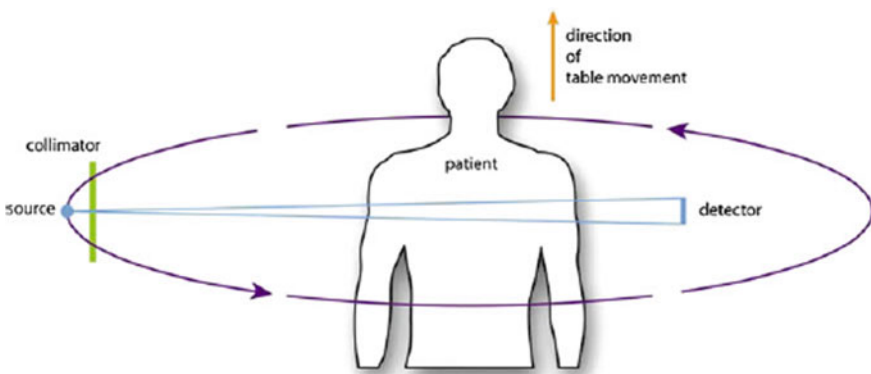


Fig. 2.2 Schematic drawing of a clinical fan-beam CT scanner. The gantry accommodates an X-ray source, beam collimator, and detector array, which rotate around the patient. The patient lies on a table which can be moved through the gantry during data acquisition

to approximately 30 s. Other motions, for example, due to heartbeat and vessel pulsation, cannot be suppressed. The influence of these motions can be reduced by using only projection measurements that are made during a particular part of the cardiac cycle in which the motion is minimal [150]. For this purpose, the electrocardiogram (ECG) can be recorded during data acquisition. The temporal resolution of a CT scanner can be defined by the width of the part of the cardiac cycle used for reconstruction. This width is—at the iso-center of the axial plane—equal to half the rotation time. Nowadays, scanners are available with two X-ray tubes instead of one. Each tube acquires half of the data needed for image reconstruction. This way, the temporal resolution is improved by a factor of two for these dual-source CT scanners [93].

Normally, there is virtually no difference in attenuation coefficient between blood and surrounding tissue. Consequently, blood vessels are not visible on CT images. When the vessels have to be visualized, a contrast agent, which increases the attenuation coefficient of blood, is administered intravenously. Most contrast agents contain iodine which has a relatively high atomic number compared to soft tissue and blood.

2.2.1.3 Image Reconstruction

In CT, the attenuation coefficient μ is reconstructed with the aid of the measured intensity of the attenuated X-rays along lines through the human body. Cross-sectional images are primarily reconstructed analytically with the filtered backprojection technique [152]. Reconstructions are made at a large number of (equidistant) z-positions to obtain a volumetric data set. With the introduction of multi-slice CT, the scanning geometry is transformed from fan-beam geometries to cone-beam geometries. The reconstruction algorithms used in fan-beam geometries were not suited for cone-beam geometries. In nonclinical CT, the cone-beam geometry was already more common (Fig. 2.3) and accompanying reconstruction techniques were developed as well [238]. These techniques appeared to be useful in preclinical CT (see below) and later on in multi-slice cone-beam CT as well.

The spatial resolution is primarily determined by the size of the focal spot of the X-ray tube, the dimensions of the detectors, the sampling distance, and the reconstruction kernel used in the filtered backprojection. The choice of this kernel determines the trade-off between the in-plane spatial resolution and the noise level. The relatively sharp filters are mostly used for special purposes, for instance when the detail in bony structures is required. They enhance, however, the noise level and may emphasize reconstruction artifacts.

The analytical filtered backprojection technique has the advantage that it can be implemented robustly at a low computational cost. It has the disadvantage that sparse data and irregular sampling of X-ray tube positions are difficult to take into account. More importantly, the well-known photon-counting statistics and the physics of image acquisition are virtually ignored when solving the reconstruction problem analytically. Model-based, iterative reconstruction techniques are more suitable methods for this purpose albeit at a much higher computational cost. Thanks to the exponentially grown computational capacities easily available

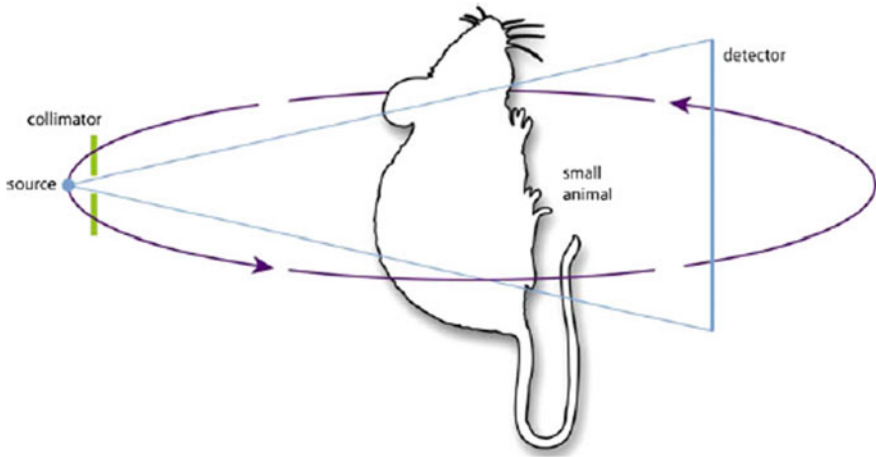


Fig. 2.3 Schematic drawing of a preclinical cone-beam CT scanner. The gantry accommodates an X-ray source, beam collimator, and detector array, which rotate around the small animal. The cone-beam geometry allows for imaging a relatively large volume without moving the animal during data acquisition

nowadays, the use of iterative techniques in daily practice has become feasible. All modern CT scanners have now implemented these techniques in one way or the other, claiming better image quality, i.e., lower noise levels, less artifacts, or higher spatial resolution at lower radiation dose levels [25].

The linear attenuation coefficient μ is not used directly in CT imaging. A value, which represents the attenuation coefficient relative to the attenuation coefficient of water, is used instead. In honor of the inventor of CT this value is specified in Hounsfield units (HU). By definition the CT value of water is 0 HU, and that of air virtually—1000 HU. The maximum CT value on a scanner can be in the order of a few thousand HU. A transfer function is used to convert these CT values to different shades of gray on a screen. The human observer can only discern a limited number of gray levels. Therefore, usually a reduced range of CT values is displayed, which depicts only a part of the complete information available in the image. CT values below and above this range are represented by black and white, respectively. The user-defined range is specified by the CT values of the level (center of the range) and window (width of the range).

2.2.1.4 Radiation Dose

Ionizing radiation, including X-rays, is potentially harmful to the human body. To reduce the risk of a CT examination the radiation dose should, therefore, be “as low as reasonably achievable” (ALARA principle). The possible damage of radiation to the human tissue is in the first place related to the absorbed dose in that tissue. The absorbed dose, in Gray (Gy), is by definition the absorbed energy in Joule (J) per unit of mass (kg). Above a certain threshold for the absorbed dose, ionizing

radiation may induce so-called deterministic effects, for example, induction of erythema or cataract. In general, the absorbed dose due to clinical CT examinations is far below this threshold.

Besides deterministic effects, the exposure to X-rays may induce stochastic effects, i.e., the induction of cancer, or genetic damage when the reproductive organs are exposed. It is generally assumed that—for a CT examination of a certain part of the human body—the danger of X-rays is proportional to the total amount of energy absorbed in that part of the body. This absorbed dose is not the same for all organs and tissues when a CT scan is made. Organ dose levels depend on which part of the human body is scanned, on the design of the CT scanner, and on the scanning parameters. Moreover, the risk for a given absorbed dose is not equal for all organs and tissues. Therefore an additional quantity, the effective dose, in Sievert (Sv), has been introduced to take these aspects into account. This quantity is a measure of the total damage due to radiation for an average member of a reference population.

The effective dose of an examination can be translated to an estimated risk to induce cancer. This risk depends on the age of the individual and the part of the human body that is scanned. It is assumed that the absorption of even a small amount of radiation will increase the risk of inducing cancer and genetic defects. It is estimated that an effective dose of 1 mSv corresponds to a risk of the induction of fatal cancer for an average patient of 1:20,000. Generally, the advantages of the information obtained with a CT scan are much greater than the estimated risks, especially for elderly patients.

2.2.2 Multi-energy Computed Tomography

CT provides information on the attenuation coefficient μ of a tissue or material via the CT number in Hounsfield Units. Tissue characterization and differentiation are based on differences in the attenuation coefficient. Unfortunately, some tissues have virtually the same attenuation coefficient and cannot be easily discerned. This is, for example, the case for iodinated blood vessels and bone tissue. The attenuation coefficient depends on the tissue type, tissue density but also on the energy of the X-rays.

In multi-energy CT, the energy dependence of the attenuation coefficient is used to discriminate between different tissue types. For this purpose, the X-ray attenuation measurements are performed at different X-ray energies. The measurements should be obtained preferably simultaneously in order to avoid discrepancies between the measurements due to patient or animal movement. Several measurement setups are currently available in clinical practice for multi-energy CT [209]. These setups include CT scanners with two X-ray sources operating at different tube voltages [145], CT scanners with an X-ray tube capable of rapidly switching the tube voltage during data acquisition [153], and CT scanners with energy discriminating sandwich detectors [45].

In the literature, several (potential) clinical applications of dual-source, dual-energy CT are described. These include the differentiation between iodine and bone in CT angiography [335], virtual CT colonoscopy approaches [156] and for differential diagnosis of adrenal nodules [121]. In a preclinical setting, Anderson and colleagues have produced images of mice with the aid of energy discriminating, photon-counting detectors that allowed distinguishing between calcium, iodine, and barium [15]. They make use of the fact that these materials show a well-defined, up to 10-fold, sharp increase of the attenuation coefficient. This sharp edge in the attenuation profile is called the K-edge and K-edge imaging or K-edge subtraction is one of the advantages of multi-energy imaging.

The possibility of multi-energy CT to better quantify the density of given materials, contrast agents, and possibly tracers is a valuable contribution to the conventional single-energy CT systems. For example, several studies showed promising results for lung tumor characterization with multi-energy CT-based iodine mapping [272, 363]. It may also enable assessment of changes in the perfusion or radiation toxicity, in patients treated for lung cancer [316]. Since it is a single-shot technique lacking dynamic information, there are many practical factors that influence the outcome measure based on the observed iodine density only, including scan delay, total amount of contrast agent, injection rate. Therefore, multi-energy CT is unable to grasp the full characteristics of blood perfusion in lung tissue.

2.2.3 Preclinical Computed Tomography

After the introduction of clinical CT in the 70s, dedicated imaging of small specimen and animals with CT was introduced in the 80s [262, 268]. The principle of preclinical CT is the same as clinical CT (Fig. 2.3). The most important difference is the higher spatial resolution required for preclinical CT. Therefore, preclinical CT is often also referred to as micro-CT or μ CT. The required high resolution has consequences for several components of the scanner. First of all, the X-ray focal spot and the detector elements need to be smaller than that of a clinical CT scanner and the scanner geometry has to be adjusted accordingly. The focal spot size of an X-ray tube in preclinical CT is 1–100 μm , while the focal spot size in clinical CT is typically 300 μm or more. A smaller focal spot size means a better spatial resolution, but it limits the X-ray power that can be applied. With a limited X-ray power, the scanning times can increase considerably to obtain the required image quality, i.e. image noise level. In state-of-the-art clinical CT, the volume of interest can be scanned within a fraction of a second, while in preclinical CT the scanning time can be reduced to the fraction of a minute, but is, in general, several minutes long. Preclinical CT scanners with two X-ray tubes are available, which improve the temporal resolution and scan speed by a factor of two like in clinical cardiac CT systems.

The use of ionizing radiation is of concern in preclinical CT as well. In clinical CT, the main focus is on lowering the dose to avoid the long term, stochastic

effects. In preclinical CT, the radiation dose is higher. Doses of an imaging series can be in the order of the lethal dose of the animal. Particularly, when one animal is scanned multiple times before being killed, it is important to reduce the dose and assure that the ionizing radiation does not affect the biological processes under investigation [220].

Because the size of the animals is much smaller than the patients in clinical CT, the attenuation of the X-rays is much lower. This allows the use of relatively low energies in preclinical CT which has the advantage of a better image contrast when using contrast agents with a high atomic number.

Contrast agents used in clinical CT are less suitable for preclinical CT because in small laboratory animals the contrast agent is largely removed from the blood by the kidneys before the data acquisition can be finished. Therefore, new contrast agents have been developed which act as a blood pool agent with a higher blood pool half-life and allow for longer acquisition times. Iodinated liposomes proved to be suitable for this purpose. Liposomes are spherical vesicles with a diameter of 100–400 nm (see also further below and Fig. 2.15). This size limits the passage of the liposomes across the vascular walls. The aqueous core of the liposome can be filled with iodine. Montet et al., for example, have shown that iodinated liposomes are a suitable contrast agent for improved visualization of vessels and hepatic tumors in micro-CT [220].

2.2.4 Dedicated Imaging Systems and New Developments

High-resolution or micro-CT imaging systems are mainly used in preclinical research. Although in clinical applications this high resolution is desired as well, it is not generally available because the radiation dose needed for diagnostic image quality at high spatial resolutions would be too high. Moreover, practical considerations like scan time limitations and larger focal spot sizes needed to penetrate the patient play a role. Nevertheless, dedicated high-resolution systems are being developed for specific imaging purposes. A good example is the development of a dedicated breast CT scanner. For a breast CT examination, the patients are laid prone with the breast pendant through the table aperture. Each breast is scanned individually and without compression during a breath hold. The X-ray source and the flat-panel detector rotate in the horizontal plane 360° around the patient's breast. High-resolution breast CT imaging is expected to improve the sensitivity and specificity of breast cancer screening and diagnosis because it provides the radiologist with 3D cross-sectional images whereas conventional 2D mammograms of the breast suffer from overprojecting tissue, especially in dense breasts [194]. In radionuclide imaging, improved breast cancer-specific probes are being actively developed. Therefore, this field is likely to expand with selective targeting probes that are overexpressed in particular types of breast cancer cells. Since high-resolution breast CT is now available, the development of micro-CT probes that target specific molecular changes associated with breast cancer formation is an opportunity for clinical success as well.

As an alternative for multi-energy CT, dynamic contrast-enhanced CT is emerging as a valuable tool to quantitatively measure vascular parameters such as perfusion, vascular permeability, blood volume, and mean transit time in tumors and normal tissue. Dynamic imaging may have prognostic and predictive value for the response of certain cancers to chemo and radiation therapy. To our knowledge, it has not been qualified as an endpoint for radiation therapy assessment or for treatment modification in any prospective phase III clinical trial for any tumor site. It was observed that in particular technical validation steps are needed to further enhance such advanced CT perfusion techniques [54].

As an alternative for the energy-integrating X-ray detectors, which are currently used in the vast majority of CT imaging systems, are photon-counting detectors. Photon-counting CT is an emerging technology with the potential to dramatically change clinical CT, including the feasibility of molecular imaging [341]. This technology uses new energy-resolving X-ray detectors, with mechanisms that differ substantially from those of conventional detectors. It results in better image quality. In particular, image noise due to electronic detector noise can be avoided; paving the way for improved spatial resolution. Moreover, energy discrimination is much better than with the techniques described above for the application of multi-energy CT. Photon-counting CT combined with advanced iterative reconstruction techniques creates opportunities for high resolution, quantitative imaging. Clinical photon-counting CT scanners are not yet commercially available, however, the first clinical results with scanner prototypes are published [341].

Apart from the K-edge subtraction technique mentioned above, other contrast-enhancing mechanisms are currently investigated that might result in the development of new molecular imaging techniques using ionizing radiation. These mechanisms include X-ray phase delay, X-ray scatter, X-ray diffraction, and X-ray fluorescence [262]. One should realize that imaging techniques based on these mechanisms have been investigated yet in very controlled experimental situations only and that much technological development is needed to make these techniques available for preclinical and clinical CT.

2.2.5 Multimodality Imaging with CT

X-ray CT by itself is not yet used as a molecular imaging technique in routine clinical practice. It is, however, routinely combined with molecular imaging techniques like single-photon emission computed tomography (SPECT) and positron emission tomography (PET), which are covered in detail in subsequent chapters. The integration of an X-ray CT scanner with a SPECT or PET scanner allows for a virtually simultaneous acquisition of detailed anatomical and functional information [305]. Moreover, the 3D distribution of the attenuation coefficient μ obtained with CT can be used in the reconstruction of the SPECT and PET images for the correction of the attenuation of the gamma rays originating from the radioactive tracer inside the patient or animal. Still, in experimental or developmental stages, the use of hybrid systems combining optical imaging techniques with CT are also being explored [352].

2.3 Recent Technological Developments in Magnetic Resonance Imaging of Cancer

2.3.1 Magnetic Resonance Imaging: Introduction

The ability to view deep within the body without actually cutting it open is a tool of immense importance in medical and biological research. Techniques such as confocal and multi-photon fluorescent microscopy, which allow the researcher to locate fluorescent molecules up to several millimeters deep, have greatly increased our knowledge in a multitude of scientific fields. Yet these techniques only enable the researcher to see labels, not the surrounding structures.

Nuclear Magnetic Resonance, abbreviated NMR, was observed and characterized independently by the groups led by the two Nobel Prize recipients Bloch and Purcell in 1946 [38, 249]. Since then, NMR has been used extensively as an analytical tool in Physics and Chemistry for spectral analysis (magnetic resonance spectroscopy, MRS) and the characterization of chemical compounds. NMR techniques have also been exploited to monitor metabolic reactions and have been widely used to elucidate the complex structure of organic molecules.

NMR was introduced in the medical field in the late 1970s, under the name Magnetic Resonance Imaging (MRI). Since then, MRI has provided one of the most exciting imaging techniques and research tools for studying the anatomy and physiology of living tissue.

MRI is based on the imaging of hydrogen atoms. Given the natural abundance of water in the body (approximately 70% of total body weight), it is possible to obtain morphological images with high spatial resolution and with exquisite contrast difference using the diverse magnetization properties of the imaged tissues (intrinsic or modified by the use of contrast agents). On the other hand, MRI can look at more than just the water signal: all nuclei that have an odd number of protons in its core have the properties of magnetic resonance. Therefore, MRI can be tuned to obtain the distribution of other nuclei that are relevant for molecular imaging cancer research such as sodium (^{23}Na) and phosphorus (^{31}P) [112].

In the past decade, MRI has grown exponentially in the clinical field with a large installation base worldwide. The present generation of MRI systems, while allowing noninvasive, non-harmful examinations, offers the combination of near-cellular (5–40 μm) resolutions and whole-body imaging capabilities to obtain information regarding tissue anatomy and relevant functional information (e.g., perfusion, diffusion, tracer uptake/clearance, and neuronal activation). Some of the basic principles and technological innovations of MRI are highlighted in the following sections.

2.3.2 MRI Signal Formation and Contrast

The strength of the NMR signal (the magnetization, M_0) is dependent on the polarizing main magnetic field B_0 (Fig. 2.4). Under the influence of a magnetic field, the nuclear moments of atomic nuclei align themselves along the magnetic field. To generate an NMR signal from the polarized nuclei it is necessary to irradiate or provide energy in the form of a radio-frequency excitation (RF) tuned at the precise frequency of the atomic nucleus of interest. This frequency ω_0 , the resonance frequency, bears a linear relation with the magnetic field applied (B_0) and the gyromagnetic ratio (γ) of the imaged nuclei (Table 2.1). The resonance frequency, better known as the Larmor frequency, is given by the relation $\omega_0 = \gamma B_0$.

After cessation of RF excitation, the disturbed magnetization of the excited nuclei returns to its equilibrium condition (Fig. 2.5). Interactions between the protons and the surrounding media (lattice) and between protons themselves (spins) cause the absorbed energy to be dissipated in the lattice.

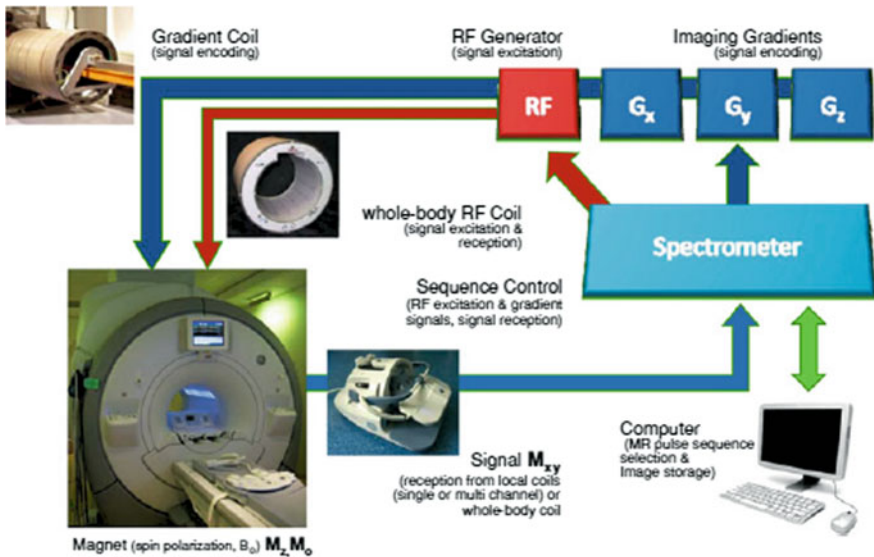


Fig. 2.4 Diagram of an MRI scanner. The magnet at a field strength B_0 provides the spin polarization M_0 (or M_z) of protons in the sample. The computer, storing all the MR sequence pulse programs instructs the spectrometer to command the radio-frequency excitation (RF) and the imaging gradients for signal selection and image encoding, respectively. A whole-body coil (surrounding the sample) is used for RF excitation (or signal reception, in some cases) to produce the transverse magnetization signal (M_{xy}) that will be encoded by the same coil or by a local (single or multichannel coil). The imaging gradient coils (G_x , G_y , G_z), surrounding the sample, provides the magnetic field gradients necessary to provide the spatial encoding of the signal. The computer reconstructs and displays the images after the MR pulse sequence finalizes the measurement

Table 2.1 Larmor frequency at different magnetic field strengths for hydrogen nuclei

Magnet strength B_0 (Tesla, T)	Resonance frequency at various magnetic field strengths for hydrogen nuclei
	Resonance frequency (MHz)
	$\omega_0 = \gamma B_0$ $\gamma = 42.58 \text{ MHz/T}$
1.5	63.87
3.0	127.74
7.0	298.06
9.4	383.22

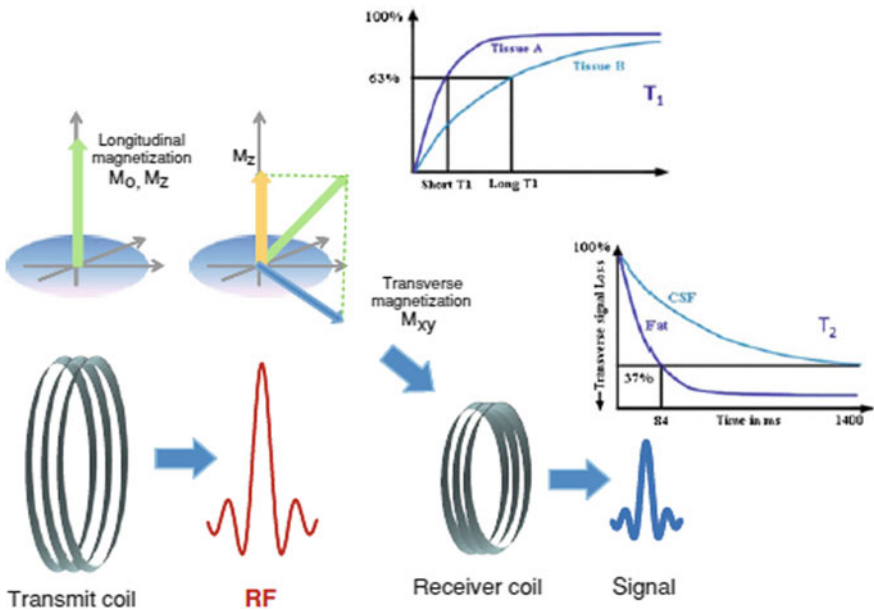


Fig. 2.5 A transmit coil produces an RF excitation that tilts the magnetization M_0 from its equilibrium condition. Part of this magnetization, M_{xy} , the one that can be picked up by a receiver coil is the signal that encodes the final image. After the RF excitation, the signal M_{xy} decays according to the T_2 relaxation constant. In the meanwhile, the magnetization M_z recovers to its equilibrium condition M_0 with a time constant T_1

The rate at which energy is dissipated in the lattice is characterized by the T_1 or spin–lattice relaxation time while T_2 , or spin–spin relaxation time, governs the disappearance of the transverse magnetization. This emitted energy is the signal that is received by the MRI equipment using a signal receive coil tuned at the Larmor frequency.

The contrast capabilities of MRI are mainly defined by the proton density and two relaxation times T_1 and T_2 , of the imaged tissues (Figs. 2.6 and 2.7). Through MRI pulse sequences contrast characteristics, based on these parameters, can be controlled by changing the timing between the RF irradiation and the time the NMR signal is read during an MRI experiment. Many other mechanisms can provide contrast in biological tissues such as water diffusion, flow or motion, magnetic field inhomogeneities, and magnetization transfer contrast to better differentiate various tissue types. When magnetic field inhomogeneities are present the decay of the NMR signal is modified, shortening the T_2 relaxation time. In these cases, an effective relaxation T_2^* then dominates the image contrast. This mechanism has been exploited intensively in MRI for molecular imaging applications to provide hypointense signals for cells and tissues.

In the ambit of molecular imaging, in order to fully use the capabilities of MRI, it is necessary to have molecular probes and imaging reporter genes that use paramagnetic and superparamagnetic agents (Gd or iron oxide-based constructs) that can dramatically change the T_1 and T_2 relaxation times of the NMR signal when activated selectively or in response to specific biological events. These types

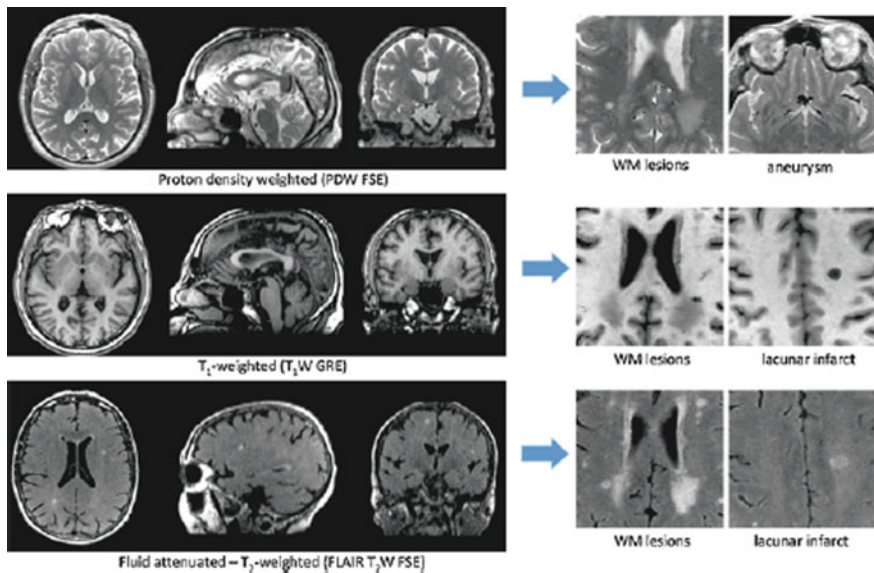


Fig. 2.6 Contrast capabilities of MRI. Using mainly the proton density and the T_1 and T_2 relaxation times of tissues, it is possible to define an optimal contrast for tissue differentiation. This figure illustrates the volumetric capabilities of MRI and some of the contrast possibilities in the brain of patients with degenerative brain diseases (e.g., dementia, white matter disease). The three panels demonstrate a proton density weighted (PDW), a T_1 -weighted and a fluid-attenuated T_2 -weighted acquisition. On the right side, it is possible to appreciate the different contrasts achieved for white matter (WM) lesion differentiation from healthy WM). FSE refers to fast spin echo and GRE to gradient recalled echo MR pulse sequences used for the acquisition

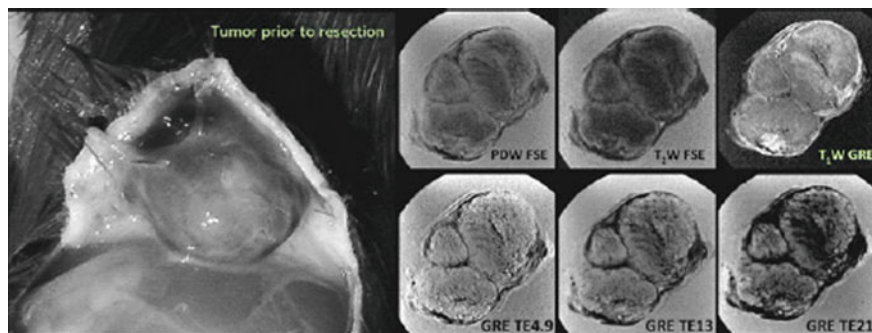


Fig. 2.7 For cancer research, it is useful to count on a combination of MR pulse sequences and imaging parameters to study different compartments in tumors. The panels show different acquisitions performed on a tumor implanted in a rat limb: a proton density weighted (PDW) fast spin echo (FSE), a more T_2 -weighted (T_2W) version, a T_1 -weighted (T_1W) gradient recalled acquisition (GRE). To enhance the magnetic susceptibility effects of blood components, it is possible to use a GRE scan with variations in the echo time (TE) to provide more or less weighting (darker structures visualized). The brighter spots in the T_1W GRE scan are correlated with methemoglobin (hemorrhage, blood denaturalization)

of probes are currently being developed and are becoming commercially available in an ever-increasing variety (see further in this chapter).

2.3.3 Magnetic Field Strength and Signal Sensitivity

Nuclei polarize under any magnetic field strength to provide an effective magnetization in the direction of the applied magnetic field. However, the spatial resolution that can be achieved in a specific measurement time for MRI or MRS depends on the strength of the magnetization achieved. Usually, it is assumed that the strength of the signal received has a linear dependence on the magnetic field strength applied. Table 2.2 illustrates a comparison of how spatial resolution or imaging times are influenced by the choice of the magnetic field strength, given that the same reception hardware is utilized.

Table 2.2 Comparison of the output of MRI systems of various magnetic field strengths

A comparison of the output of MRI systems of various magnetic field strengths		
Magnet strength (T, Tesla)	Resolution at a fixed scan time	Scan time at a fixed resolution
1.5	100 $\mu\text{m} \times 100 \mu\text{m}$	3 h
3.0	70 $\mu\text{m} \times 70 \mu\text{m}$	45 min
9.4	40 $\mu\text{m} \times 40 \mu\text{m}$	5 min

For MRS, not only the spatial resolution but also the spectral resolution of MRS increases with the strength of the magnet. At present, the sensitivity of MRI at molecular levels is less than that of techniques based on radioactive tracers and optical luminescence. Nonetheless, its versatility, the numerous contrast mechanisms, and the possibilities for future signal amplification strategies are enormous in comparison, making it possible to build an integrated spectrum of information regarding a particular disease process.

2.3.4 Imaging Gradients, Signal Encoding, and Signal Reception Chain

The linearity of the Larmor equation has been used extensively to enable spatial encoding of the NMR signal. Spatial encoding is performed by using changing magnetic field gradients (known as imaging gradients) that are superimposed over the main magnetic field B_0 in order to produce a frequency dispersion that translates into a different resonance frequency at each location in an object, through which the origin of a received signal can be identified (Fig. 2.4). The larger the frequency dispersion created, the higher the spatial resolution that can be achieved. These imaging gradients are used in what is known as the MRI pulse sequence and are executed in a specific order during the RF excitation and during the readout to encode the spatial distribution of protons in the imaging volume.

Developments in MRI hardware, specifically the performance of the imaging gradients and receiver hardware, have made it possible to dramatically improve the quality of two-dimensional (2D) and three-dimensional (3D) MRI for molecular imaging protocols. The enhancement in the strength and speed of the imaging gradients provides faster encoding with improved spatial resolution. By today's standards, the imaging gradient subsystem can be regarded as the most influential component of an MRI scanner to produce images with high spatial resolution and large volume coverage. Contemporary clinical MRI units have been equipped with imaging gradients with stronger peak gradient amplitudes (>30 mT/m) and faster rise times (100–200 mT/m/ms) that enable high-quality images. More so, for translational research where molecular imaging protocols in conjunction with MR sensitive probes are developed in animals, newer imaging gradients (e.g., 300 mT/m with rise times >1000 mT/m/ms) can provide resolutions that are adequate for near-cellular resolution and beyond. Accordingly, the higher resolution is accompanied by large numbers of reception channels to provide higher SNR and decreased acquisition speed. On the signal reception hardware side, the incorporation of increasing numbers of signal reception channels (coils combined in a phased-array configuration) has provided a several-fold improvement in signal-to-noise ratio (SNR) with large field-of-view (FOV) capabilities [129]. Both features combined make it possible to reduce imaging time dramatically for highly resolved morphological imaging.

The long-standing standard for volume acquisitions in MRI experiments has been a volume coil resonator to provide homogeneous signal reception in the

volume of interest. Therefore, at high spatial resolution, the only remedy in the past to provide good image quality was to use a stronger main magnetic field B_0 (a costly solution) or to make use of multiple excitations (averaging), translating into longer imaging times and more data corruption from physiologic effects. Multichannel receiver coils have provided a valuable alternative, promoting the use of many MRI sequences to produce different contrasts and encouraging the use of T1, T2, and T2* parametric mapping to produce more quantitative data in more reasonable scanning times.

Parallel imaging can shorten the acquisition speeds by encoding the signal with less RF excitations and using the spatial distribution of the coils in the phased-array configuration to reconstruct the missing data; however generally at the cost of SNR [36, 72, 130, 180]. This has been used extensively in clinical MRI in the past few years but its incorporation into animal MRI scanners has been more recent providing increased benefits for new imaging scenarios for molecular imaging and translational research. In the same way, imaging speed can be improved dramatically by sampling less data necessary to encode images with virtually no loss in image resolution using a newer technology referred to as Compressed Sensing (CS) [1, 107]. Compressed sensing (CS) comprises several methodologies for accelerated MR data acquisition that uses a pseudo-random, incomplete sampling of the base raw data (referred to as k-space). Images are then reconstructed using specially designed iterative optimization processes depending on the type of data scanned and using a priori knowledge of the imaging process (anatomical and physiologic information) creating intermediate images that do not use the typical Fourier transformation prior to producing the final results. Despite being in the early development stages, CS methodology has proved promising in the realms of fast magnetic resonance angiography (MRA), including both 3D time-of-flight (TOF) variants and time and multi-axis velocity encoded phase contrast MRI (4Dflow), dynamic contrast-enhanced (DCE) studies for even faster temporal resolution with high-resolution isotropic voxels, diffusion-weighted imaging (including tensor and multi-shell) and cardiac MR imaging applications [24, 170, 182]. More so, considerable improvements in SNR may be possible and the possibilities of even faster scanning with lower MRI field strengths (such as in newer combined SPECT/MRI and PET/MRI systems using magnetic field strengths of 1.0 T or less [100, 115, 178, 224] using special filtering algorithms and the possible image quality improvements possible nascent deep learning (DL) and artificial intelligence (AI) technologies [63, 206, 205, 366]. This would enable the use of contrast agents for cancer research that have been designed specifically for human applications with higher relaxivity at clinical field strengths precisely at lower magnetic field strengths. DL and AI can provide even higher gains in the realm of faster MR image acquisitions by providing greater image fidelity with virtually higher reductions of raw data collection (with an ever smarter data undersampling schemes). Additionally DL and AI altogether may produce cleaner images despite any remnant artifacts or data corruption that may be induced by possible MR scanner hardware instabilities, subject and sample induced motion, and reconstruction inconsistencies

and increased imaging noise with parallel imaging or compress sensing higher speeding acceleration factors.

2.3.5 MRI Pulse Sequences, Parametric Mapping

A receiver coil acquires the MR signal (transverse magnetization) after the protons in tissue are perturbed by an RF excitation. This transverse magnetization can be read either in the form of a spin echo (SE) or a gradient-echo (GE). For a simple SE readout, a 90° RF excitation converts all the available magnetization aligned along the main magnetic field (the longitudinal magnetization) to transverse magnetization and is immediately followed by a 180° RF refocusing pulse to produce a spin echo that is read by a signal reception coil (Fig. 2.8a). A gradient-echo readout can collect the MR signal after the application of the 90° RF excitation but it requires that a bipolar readout imaging gradient be applied to dephase and consequently rephase the transverse magnetization to form an echo (Fig. 2.8b). SE or GE readouts provide the basis for all the different MRI pulse sequences available. The choice for a particular readout depends on the required contrast and the sensitivity to magnetic field inhomogeneities (e.g., using T2*-weighted with GE scans).

In conventional SE imaging, proton density, T1- and T2-weighted images are acquired by setting a specific repetition time (TR) and echo time (TE). Proton-density weighting may be acquired by using long TR and short TE. T2 weighting is adjusted by lengthening TE. Intermediate values of TR with short TE produce T1-weighted images. Imaging techniques using GE readouts can modify the RF excitation or flip angle ($\leq 90^\circ$, partial flip angle imaging) to produce optimal signal strength for a specific tissue at a fixed TR value. The flexibility of GE techniques to use partial flip angles provides the possibility to acquire proton density-, T1-, T2-, T2*-, and T1/T2-weighted images with short TR settings for faster acquisitions. SE readout variants, referred to as fast SE, make them competitive to GE scans for faster scanning yet with excellent SNR and devoid of magnetic susceptibility weighting. Fast SE techniques make use of multiple refocusing 180° RF pulses after the initial 90° RF excitation to read the signal, making the acquisition more compact and efficient.

New scanning strategies to produce even more robust scanning scenarios for high-resolution small animal imaging in regions that contain tumors and plagued by constant physiologic motion (from respiratory, cardiac, or bowel movements) have been devised using GE or SE techniques or a clever combination of both. MR data acquisition is usually triggered by synchronizing the MR signal detection with the motion that is taking place. Nonetheless, this can cause an extensive lengthening of the data collection time that may not be compatible with the anatomical and physiologic signature that is to be addressed and with the experimental setup. The use of the dynamic passage of a contrast agents injection for tumor detection, angiography, and angiogenesis or even perfusion may not be at all possible at high resolution despite the higher imaging gradients that are present in a high-end MRI animal scanner and especially with 3D imaging protocols and despite the use of

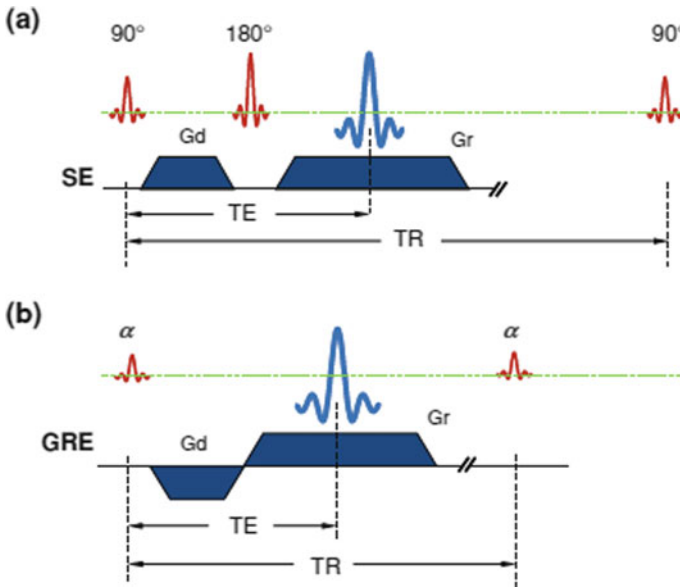


Fig. 2.8 Proton-density, T_1 -, and T_2 - (and T_2^* -) weighted images are acquired by setting a specific repetition time (TR), echo time (TE), RF flip angle α , and the imaging encoding technique: spin echo (SE) or gradient recalled echo (GRE) readouts. For an SE readout, a 90° RF excitation tips the magnetization M_z to transverse magnetization M_{xy} and is immediately followed by a 180° RF refocusing pulse to produce a spin echo. A positive dephaser gradient (G_d) is applied prior to a 180° RF refocusing pulse and subsequently, a positive rephaser (G_r) is used to spatially encode the signal received. GRE readouts can modify the RF excitation or flip angle ($\leq 90^\circ$, partial flip angle imaging α and no refocusing 180° RF pulse) to produce optimal signal strength for a specific tissue at a fixed TR value. The signal is produced with opposite polarities of G_d and G_r and no refocusing 180° RF pulse. The flexibility of GRE techniques to use partial flip angles provides the possibility to acquire proton density-, T_1 -, T_2 -, T_2^* -, and T_1/T_2 -weighted images with short TR settings for faster acquisitions. SE readout variants, referred to as fast SE (FSE), make them competitive to GRE scans for faster scanning yet devoid of magnetic susceptibility weighting. Fast SE techniques make use of multiple refocusing 180° RF pulses after the initial 90° RF excitation to read the signal, making the acquisition more compact and efficient

parallel imaging (PI), compressed sensing (CS), and deep learning/artificial intelligence (DL/AI) (as addressed in the previous section). The correct scanning scenario may not be at all possible without motion artifacts and with the desired imaging speed. Clever MR raw data sampling scenarios and data sharing techniques have been devised using a form of radial sampling similar to what is commonplace in computed tomography. Radial sampling (both in the form of spokes or blades) have increased the utility and image quality in clinical MRI and have been successfully applied in small animal imaging [34, 235, 296, 327]. Using this enhanced acquisition methodology, the tracking and correct timing of the passage of an injected contrast agent can be devised while monitoring inherently physiologic

motion thus producing adequate and non-artifacted high-resolution angiographic and perfusion maps for many small animal research scenarios in this problematic motion prone regions. Likewise, silent 3D MRI technology has been devised using a similar radial acquisition pattern with fast RF switching and acquisition during constant imaging gradient readouts that reduce to a whisper the high noise typically produced by the strong imaging gradients with standard MRI pulse sequences [9, 181]. These 3D silent acquisitions also benefit from similar motion robustness—nearly artifact-free imaging. Silent 3D MRI makes it also possible to use minimal sedation for scanning animals thus reducing the detrimental effects that sedatives may have during animal monitoring and disturb minimally the animal physiology.

Molecular imaging can benefit immensely from using parametric mapping by providing a more quantitative evaluation of tissue properties, e.g., in the relaxation times, especially for longitudinal studies [23, 308, 353]. Parametric mapping can provide better accuracy in the evaluation of changes as a result of treatment or quantify density parameters of imaging labels that have been incorporated in tissues or cells (e.g., tracking cell density of iron-oxide labeled cells through T2 and T2* effects). Parametric mapping can eliminate the need for coil sensitivity corrections and also the a priori knowledge of the relaxivity effect that contrast material will induce on tissues. Once tissue properties are determined accurately, it is possible to reconstruct synthetically an image with the best contrast possibilities to permit greater tissue differentiation [70, 71, 333, 334]. In the simplest form of mapping, proton density, T1, and T2 information can be computed directly by acquiring several imaging experiments with changes in TR and TE using SE cans. For T2* mapping, TE is changed using GE techniques.

In cancer research, the combination of more functional parameters besides mapping the inherent T1 and T2 relaxation times, such as maps derived from MRS imaging, diffusion-weighted imaging (DWI), and contrast-enhanced MRI (CE MRI), especially at higher field strengths, can provide a more precise assessment of the tumor environment and [173].

2.3.6 Compressed Sensing

Compressed Sensing (CS) recently became available in the field of clinical MR Imaging. The area of its application is constantly growing. The technique made its entry into a research MRI in 2008. Imaging technique products (sequences) using CS received FDA approval in 2017.

CS is a remarkable breakthrough in image acquisition. The original concept was proposed in 2004 by Candes et al. [53]. Its application in MR Imaging was proposed in 2006 [201]. The concept behind the technique is not specific to MR image acquisition. It is applicable also for data compression and transmission. Its current application can be found in data compression such as MPEG for sound and JPEG 2000 for images. The core of the concept exploits the properties of the data. Image and sound data are compressible without compromising important details, meaning the data can be represented by far less parameters than thought before. Classically,

the Nyquist criterion set the lower bound for data sampling in data acquisition that allows the reproduction of the signal without distortion (aliasing). Intuitively though one can propose that not all voice (or image) recordings have the same amount of information content even if they have the same length and frequency bandwidth. The energy of the information content may be comprised in a very limited set of parameters; the data appears to be sparse. If the parameter space is well chosen such sparsity becomes obvious and the relevant part (highest in energy) can be selected and the rest discarded, yet sufficient details can be preserved. For example for a single-frequency sound, it is wasteful to store several minutes with high bandwidth, it is more efficient to store only one single parameter (the frequency). The parameter space transformation in this example would be time-to-frequency (Fourier transform). In CS applications this transform is playing an important role, it is the sparsity transformation. Its goal is to compress the energy of the data to a few parameters. Since the best transformation is not necessarily known, an acceptable invertible transformation is usually chosen (such as the Fourier, discrete cosine, or wavelet transform). The number of parameters is not reduced yet at this point. In order to reduce the data size, a subsampling follows as the next logical step. One can naturally propose to follow a truncation in energy and keep the high-value components (similar as in Principal Component Analysis or Singular Value Decomposition methods). Candes et al. showed that incoherent sampling would suffice to maintain most of the features of the data set. Surprisingly the incoherent subsampling breaks the limit set by the Nyquist criterion, previously considered as a hard limit. This allows a very high rate of compression. It is natural to suggest that only limited data should be collected and stored.

In MR Imaging, the data collection happens in k-space (Fourier transform of spatial representation of images). The data collection is performed in a sequential manner where only a certain part of the k-space is acquired. The sparsity transformation is naturally provided. Compressed sensing in MR Imaging targets shortening the total acquisition time by acquiring a sufficient subset of data as described above. In MR Imaging, the incoherent data sampling is not following a rigorously random distribution in k-space due to hardware limitations. Also, it usually follows the distribution of the signal energy in k-space that is not uniform.

The main application area of CS in MR Imaging is in the acceleration of acquisition. The time gained by CS can be traded for higher Signal-to-Noise Ratio (noise can be truncated as incoherent and low energy signal), higher resolution (more samples in k-space) or removing artifacts (CS in combination with Parallel Imaging). In dynamic MR (e.g., dynamic contrast enhancement) or high temporal resolution application as functional MR Imaging (fMRI) gain in acquisition time is the direct goal. These applications may use different subsampling strategies, but the concept is mostly the same.

CS is often found in applications combined with other techniques. A combination with acceleration with Parallel Imaging is applied in multi-coil acquisitions yielding an acceleration factor of 8–10. In dynamic MR Imaging, CS is used for taking advantage of spatial similarities along the temporal evolution (k-t CS). Spatial similarities of images along the temporal evolution due to periodic motions

are exploited by CS in cardiac and 4D flow MR Imaging. Deep Learning in combination with CS has been recently demonstrated as a novel image reconstruction strategy with the potential to remove noise and artifacts [366].

The literature and the online resources of CS-related applications in MR Imaging is growing steadily. The authors encourage the reader to consult the original papers for the concept and mathematical details of Compressed Sensing [21, 53], and on the broader mathematical framework [80]. For additional references on the applicability of CS to MR Imaging, we refer to papers by Lustig et al. [201, 202], and reviews by Rani et al. and Sandilya et al. [257, 266].

2.3.7 Contrast-Enhanced MRI

In addition to the contrast mechanisms described in the previous sections, tissue contrast can be further manipulated through the use of MRI contrast agents. Based on their contrast effects, MRI contrast agents can be subdivided into so-called T1 and T2 contrast agents. T1 contrast agents are agents that predominantly shorten T1 and T2 contrast agents predominantly shorten T2. With most pulse sequences shortening of T1 results in increases in signal intensity, while shortening of T2 results in reduction of signal intensity, therefore T1 and T2 contrast agents are often also referred to as positive contrast agents and negative contrast agents, respectively. The most prominent examples of T1-agents are paramagnetic gadolinium and manganese-based contrast agents and superparamagnetic iron oxide particles are the most prominent examples of T2 contrast agents. Some more detailed descriptions of MRI contrast agents and recent developments in the use of MRI contrast agents can be found further in this chapter.

2.3.8 Multimodality Imaging with MRI

2.3.8.1 PET/MRI

Combined PET and MRI (PET-MRI) scanners can acquire PET and MR images simultaneously. Small animal PET-MRI has been available since 1995. The first clinical integrated scanners were launched in 2011. As of today in 2019, there are two healthcare manufacturers producing clinical whole-body integrated PET-MRI scanners. Overcoming the major technical hurdles in producing clinically available scanners took about 15 years. For these details, we refer the readers to the review paper of Stefaan Vandenberghe and Paul K. Marsden [323]. The major breakthrough was made possible by the small size MR compatible PET detectors. The hardware of the clinical scanners is based on 3.0 T wide-bore clinical MR scanners with a PET detector insert.

The evolution of the integrated systems was driven by technological advancement rather than urgent clinical demand, despite the obvious advantages of an integrated system. The value of multimodal imaging is obvious, PET and MR Imaging is based on an entirely different source of signal. PET relies on

extraneously administered positron-emitting agents while MR relies on naturally abundant water in tissues. The algorithms of image formation from the detected signals are also completely different; PET builds on detection of the position of positron annihilation events while MR is based on radiofrequency excitation response with Fourier or backprojection methods. The temporal and spatial resolution of these modalities are set apart. In PET-MRI scanners, the two image acquisitions are performed independently. PET image reconstruction may rely on MRI data in attenuation correction and motion correction (similarly to CT images in integrated PET-CT scanners). With an integrated PET and MR scanner, there is no need for separate scan sessions (two appointments for patients, transfer for animals). The simultaneous scanning largely reduces the need for co-registration of images from the two modalities.

The current technical development and challenges in PET-MRI can be understood by the comparison with the competing multimodal PET-CT imaging and by the demands of the current clinical applications. The advantage of PET-MRI to PET-CT are: improved sensitivity of soft tissue lesions due to rich contrast capabilities of MR, no excess radiation exposure by MR, motion correction by MR images for PET image reconstruction without increased radiation exposure. There are also disadvantages. MR Imaging is problematic in low signal areas like bone and lung parenchyma. The differentiation of signal void due to short relaxation time in bone and signal void due to a low abundance of water (e.g., lung parenchyma) is quite problematic. The development of ultrashort echo time MR scans (Zero TE, UTE) is addressing this issue [367]. Another challenge—specific to MR—is image distortion due to susceptibility artifacts at air–tissue interfaces (cavities in the head and neck region or around bowels in the pelvic region) or around bones in musculoskeletal imaging (tissue heterogeneities in shoulder and hip). A more fundamental issue that is strongly related to oncological imaging is the lack of a direct relationship between MR signal and electron density. CT provides direct information about the Hounsfield units that are used in radiation treatment planning. Current developments in pseudo-CT (MR images producing CT like information) are aimed to answer the latter two challenges [83, 147]. The field of view of MR imaging is smaller than that of PET or CT, due to magnetic field inhomogeneity and gradient field accuracy. In case of need for whole-body imaging (e.g., lymph node scanning) this poses a technical challenge. With the recent development of advanced image reconstruction technique and better gradients, this problem can be mitigated.

Despite these challenges, current studies indicate that PET-MRI is technically and clinically a viable alternative to PET-CT and exceeds it in certain oncological imaging areas. In oncological imaging PET-MRI is used in the following regions: intracranial, head and neck, thorax, pelvic (liver and prostate) and musculoskeletal [264]. Where oncological PET-MRI excels (as of the time of this writing) is prostate cancer imaging (T2 and diffusion-weighted MR images in combination with PSMA specific PET tracers). The clinical indication for PET-MRI is for high-risk prostate cancer and biochemical recurrence (increased PSMA after treatment) [242]. It also proved to be superior in search for the primary tumor in the

head and neck region [294]. In general, the increased sensitivity of MRI in soft tissues provides the advantage.

A field yet in the clinical research stage promises a bright future. Quantitative techniques in MR in combination with quantitative PET techniques provide multi-parametric multi-modal data [106]. MR can produce physiological data with techniques such as dynamic contrast enhancement (intravenously administered contrast agent), diffusion (Apparent Diffusion Coefficient), flow, micro-vascularization, oxygenation (BOLD imaging). Further quantitative, MR specific parameters that are in relation to cellularity and tissue types are T1, T2, and T2* relaxation times. PET produces quantitative parameters related to biochemical processes, and also kinetic parameters in dynamic PET [77, 254], or direct measurement of oxygenation. PET-MRI has the potential to provide a vast amount of information facilitating to establish the links between these biomarkers and pathologies. It can provide a quantitative asset for treatment planning, treatment efficiency monitoring, phenotyping, monitoring progression. Artificial Intelligence and Deep Learning have been proposed to establish these links [106, 196]. The main role of PET-MRI in the immediate near future might very well be in clinical research aimed at establishing a stronger and more accurate connection between parameters derived from imaging and development of pathologies.

The technical challenges are very different in the different anatomies and pathologies: field of view (in whole-body scanning), temporal and spatial resolution (dynamic scans), image distortion (MR), signal void (artifacts in MR or misregistration in PET), attenuation correction (MR based), motion correction (small nodes in PET). The interplay of the modalities will continue in bringing different research areas together from basic sciences to imaging technologies, from technical to clinical sciences.

2.3.8.2 SPECT/MRI

SPECT imaging remains a powerful tool in the diagnostic and prognostic evaluation in many pathologies, as will be detailed in later chapters in this book. MRI has the capability of supplying both accurate anatomical reference and add complementary (functional) information on the disease status as is highlighted in the current chapter. Preclinical studies have already shown to benefit from acquiring complementary imaging information using both SPECT and MRI separately [35, 43].

The design of current SPECT cameras uses the principle of detectors on a rotating gantry. Simply adding an MRI to the existing SPECT hardware is sub-optimal due to the magnetic field influence on the detectors and SPECT electronics, in addition to the SPECT hardware influencing the magnetic field of the MRI. Preclinically a commercial system was achieved through a combination of a permanent 1T MRI and a multi-detector gantry SPECT camera in the NanoScan system (Mediso, Budapest, Hungary). The 1T permanent magnet setup enables sufficient RF shielding from the surrounding SPECT equipment, and the magnetic field distortions on the SPECT hardware are compensated for through local shielding and software correction. Clinically, fully integrated solutions are

exclusively explored as sequential imaging is considered too time consuming for patient applications and with simultaneous imaging motion-related artifacts can be avoided. SPECT inserts have been designed for preclinical systems and are under construction for clinical applications [113, 315]. An insert limits the bore size and thus requires specific configurations for specific applications. The brain is currently an organ of interest due to the imaging possibilities using a SPECT insert. The first prototypes are in the testing phase [139].

Various hardware and software challenges are in the process of being addressed for SPECT/MRI imaging. Several safety and compatibility issues are identical to the PET/MRI systems and are discussed in that section. These issues are being addressed and the current developments in the PET/MRI field are beneficial to the introduction of SPECT/MR in clinical use [323]. Regarding the use of an insert, the paper of Hutton et al. describes the solutions to the problems regarding magnet inhomogeneity and gradient interference in great lengths.

2.4 Imaging Biomarkers in Cancer

2.4.1 Imaging Biomarkers: X-Ray Computed Tomography

The main application of X-ray CT is the detailed depiction of anatomical structures in 3D. In cancer diagnostics, location, size, and specific attenuation values of a lesion before and after contrast are used as diagnostic and prognostic indicators [76, 95, 188]. Apart from these structural biomarkers, functional biomarkers are available. The enhancement of a lesion after administration of a contrast agent as a function of time is such a functional biomarker. The corresponding perfusion parameters such as relative blood volume provide physiological correlates for the microscopic changes that occur with tumor angiogenesis [214]. The measurements can be used to assess the tumor response to drug therapy or to discriminate benign and malignant lesions [215].

The biomarkers mentioned above, do not depict processes on a molecular or cellular level. The iodinated contrast agent used in clinical CT contains molecules that are nonspecifically targeted since they cannot be conjugated to most biological components or cancer markers. Moreover, they allow only very short imaging times due to rapid clearance by the kidneys. In preclinical CT, this problem has been solved by the introduction of contrast agents with a higher blood-pool half-life.

First results of molecular imaging biomarkers are presented in the literature for preclinical CT. Wyss et al. showed that the use of a specific molecular contrast agent is able to detect specific molecular markers on activated vessel walls in vivo [349]. The contrast agent used consisted of liposomes filled with iodine. Into the membrane of the liposomes, a specific targeting moiety was inserted to detect activated endothelial cells with micro-CT. It has been demonstrated in an in vitro study that targeted gold nanoparticles enable molecular CT imaging of head and neck cancer cells [246]. As gold has a higher atomic number and electron density

than iodine, the attenuation coefficient of gold-labeled tracers can be higher than that of iodine-labeled tracers. A higher attenuation coefficient of the label will improve its detectability for a given concentration of the imaging probe.

The major challenge of molecular imaging with CT is to make it more sensitive to small differences in image probe concentrations. This might be achieved by the development of new, highly attenuating imaging probes or by the development of new X-ray imaging techniques that are not based on the differences in linear attenuation coefficient for the generation of image contrast.

In the future, improved sensitivity of X-ray CT and the development of new imaging tracers might result in a more pronounced and independent role of CT in molecular imaging in oncology.

2.4.2 Imaging Biomarkers: Magnetic Resonance Imaging

Given the wide spectra of questions that may be tackled with MRI, many answers can be found that provide a more complete understanding of the biological processes of interest. In the scope of oncological studies, noninvasive imaging using MRI can promote a greater understanding and provide a unique opportunity to explore a wide variety of scientific questions from macro to molecular levels. To study the tumor microenvironment (TME) and its response to therapy, it is possible to use several biomarkers that can be measured effectively using MRI. These include the following:

- Angiogenesis and vascular distribution (high-resolution MR angiography, MRA, and vessel architecture MRI).
- Perfusion and vascular permeability (dynamic contrast enhancement studies, DCE MRI, dynamic susceptibility contrast imaging, DSC, and arterial spin labeling, ASL).
- Oxygen-level dependent and hypoxia imaging (susceptibility-weighted imaging, SWI, blood-oxygen-level dependent, BOLD, imaging, asymmetric spin echo, ASE).
- Diffusion imaging (restriction of movement of water molecules in the extracellular matrix; diffusion-weighted imaging, DWI, and intravoxel incoherent motion, IVIM, imaging).
- Extracellular pH.
- Intracellular pH and protein content (chemical exchange saturation transfer, CEST, imaging).
- Sodium (intracellular and extracellular concentrations).
- Metabolite concentration (using MRS, e.g., quantifying ratios between choline and citrate concentrations in tumors).
- Multiparametric MRI, in which several MRI biomarkers are combined to measure tissue structure and physiology.

Likewise, tumor monitoring (progression and treatment) can be performed by noninvasively tracking the movement of stromal cells (fibroblasts, immune cells, stem cells or endothelial progenitor cells in tumors) that have been adequately labeled with an MRI-sensitive contrast agent.

2.4.2.1 Angiogenesis and Vessel Architecture

Studies on vascular development and its stimulation or inhibition have become a major field of research in the diagnosis and treatment of cancer. Manipulation of the pathophysiology of a tumor (its vasculature), the inhibition of new vessel formation and the destruction of the tumor-associated vasculature can be studied effectively with high-resolution vascular MRI (magnetic resonance angiography, MRA) [321]. To provide consistent image quality, contrast agents can be injected to produce a contrast-enhanced MRA (CE MRA; Figs. 2.9 and 2.10). The contrast typically used is Gd-based to provide shortening of T1-relaxation times and generate high positive contrast between blood vessels and surrounding tissues, and therefore T1-weighted MR sequences are used for acquiring the data. With the rise of ultra-high field MRI (7 T) more detailed images of tumor vasculature can be made and research about quantification of tumor vascular morphology based on MRA is advancing [252]. Vessel architecture measurements can also be done with dynamic susceptibility

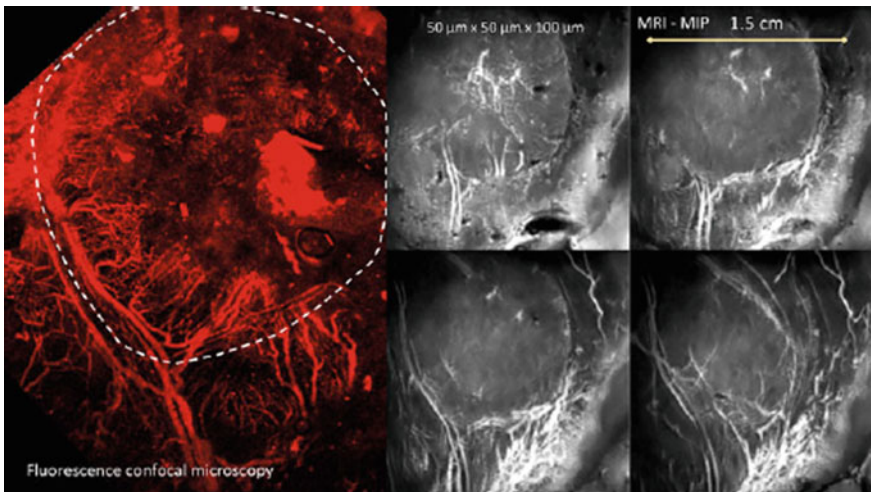


Fig. 2.9 Magnetic resonance angiography (MRA). A folded skin window model with a BN tumor implanted on a rat was imaged at 8 days post tumor implantation using fluorescence confocal microscopy and MRI. To visualize in vivo the tumor vascular network using MRI, an intravascular contrast agent was used. The MRI panels show thin slice maximum intensity projections (MIP) at four different positions to illustrate the three dimensionality of the acquisition and the spatial resolution that can be achieved (voxel size of $50\ \mu\text{m} \times 50\ \mu\text{m} \times 100\ \mu\text{m}$) that makes it suitable for comparison to the microscopy image. Acquisition performed at 3.0 T using a 3D T₁-weighted GRE technique and a 10 mm surface receiver loop

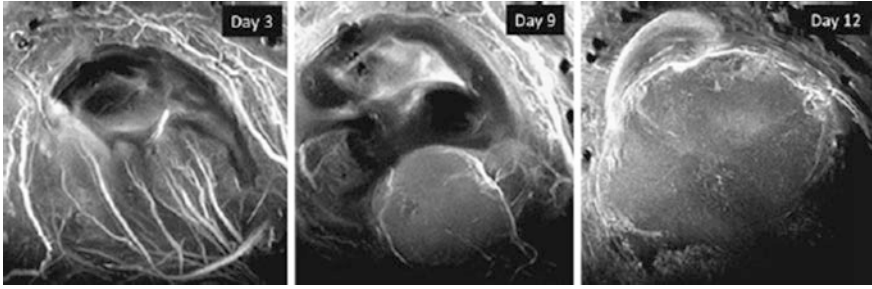


Fig. 2.10 Another folded skin window model example showing the noninvasive, in vitro longitudinal tracking possibilities with MRI/MRA. The BN tumor vascular network evolution was visualized for several days after tumor implantation. The panels show a MIP from acquisitions performed at days 3, 9, and 12 (voxel size of $80\ \mu\text{m} \times 80\ \mu\text{m} \times 100\ \mu\text{m}$). Acquisition performed at 3.0 T using an intravascular contrast agent and a 3D T_1 -weighted GRE technique and a 20 mm surface receiver loop

contrast (DSC) imaging, in which the circulation of a bolus of Gd-based contrast agent is followed as it moves through the tumor's vasculature. In this case, DSC needs to be done with simultaneous gradient and spin echo image acquisitions such that T_2 - and T_2^* -weighted images are acquired. The MR signal perturbations caused by the passage of Gd-based contrast agent can be modeled such that quantitative parameters such as vessel size and microvascular density can be calculated [162]. Recent histological validation of these measurements in human tissue is moving these measurements toward widespread application [157].

2.4.2.2 Perfusion and Vascular Permeability

Several MRI techniques exist that allow for the measurement of perfusion and/or perfusion-related biomarkers of tissues. Notably, there are techniques that use intravenously injected contrast agent (mostly Gd-based): DSC and dynamic contrast-enhanced (DCE) MRI. However, in light of the recent finding of Gd deposits in the brain, the completely noninvasive technique for measurement of perfusion of Arterial Spin Labelling (ASL), which is done without CA injection, is finding its way to clinical application.

Firstly, DCE is an imaging technique in which sequential T_1 -weighted imaging is done, while a Gd-contrast agent is injected and it is mainly the leakage of this CA through the permeable tumor vasculature that is assessed. More detailed and quantitative approaches to dynamic contrast-enhanced (DCE) MRI have been increasingly used to examine tumor perfusion and capillary permeability as an indicator of tumor angiogenesis (Fig. 2.11). DCE MRI is based on changes in signal intensity in the tumor due to leakage of contrast material through leaky vessel walls. Functional parameters, such as vessel permeability (K_{trans}) and the volume fraction of contrast material per tissue compartment (V_e) are the main biomarkers calculated in DCE MRI. Since antiangiogenic and antivascular agents affect tumor

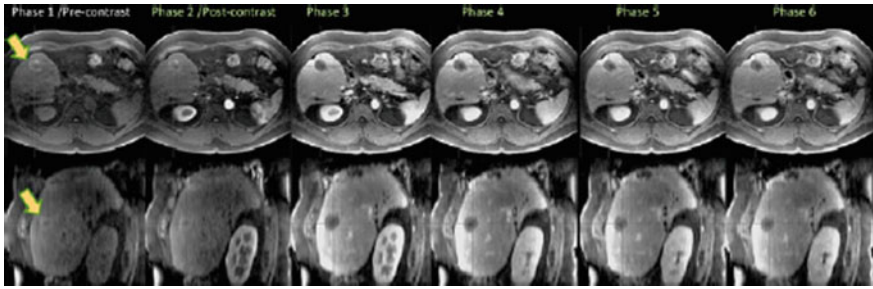


Fig. 2.11 Contrast-enhanced (CE) MRI. Tissue perfusion can be performed using repeatedly a 3D fat-suppressed T_1 -weighted GRE technique after the injection of Gd-DTPA as the enhancement medium. The panels demonstrate both the original axial and the reformatted sagittal views from the MRI perfusion study (phase 1, pre-contrast, phase 2–6 post-contrast) of a patient that had an intrahepatic cholangiocarcinoma (*arrows*) successfully removed with an RF ablation procedure. Acquisition performed at 1.5 T with breath-hold acquisitions of 15 s over a 2 min period and an 8-channel torso coil

blood vessels, DCE MRI has been employed in numerous trials to monitor the efficacy of these agents [231]. DCE MRI has also been used for the therapeutic evaluation of radiotherapy [360] as tumor perfusion and oxygenation status influence the efficacy of radiotherapy. DCE MRI-derived parameters are also being studied for their ability to predict the delivery of anticancer agents in the interstitium of the tumor [18, 318]. On a voxel-based level, a significant correlation between the presence of MRI contrast agent and drug delivery was found [18]. Correlation with histopathology showed the ability of DCE MRI parameters to monitor treatment response by identifying areas of residual viable tumor tissue in, for example, osteosarcoma [82] and soft tissue sarcoma [319].

Different methods are used to quantify DCE MRI scans. Per region of interest, the enhancement of the MR signal over time is quantified. The curves can be described by empirical semiquantitative parameters, such as the maximal enhancement or the amount of time required for maximal enhancement, or the initial area under the curve. It has been shown that these empirical parameters to some extent correlate with malignancy [86, 151, 195]. These parameters are relatively simple to calculate. Their clinical value, however, may be limited by the lack of calibration procedures. The value of these parameters depends on the MRI sequence and the scanner used [232]. Therefore, results obtained with different scanners or scanning protocols cannot be compared unless a reliable calibration procedure is used. A further disadvantage of such heuristic parameters is that their correlation with underlying tumor physiology and contrast agent kinetics is not clear.

To overcome these problems, pharmacokinetic models have been introduced in order to quantify the underlying (patho-) physiologic parameters. Different models are described, but generally a two-compartment model, consisting of a vascular and an extracellular/extravascular compartment, is used. The transfer rates of contrast

agent between the two compartments, K_{trans} , and the volumes of the compartments, V_e , are the key parameters of these models [49, 232, 302].

Due to the more rapid T2- or T2*-weighted imaging with which DSC imaging is performed the first (and often second) pass of the contrast agent through the tumor vasculature is assessed, from which relative blood volume and perfusion can be calculated. DSC imaging can be done with gradient echo (T2*-weighted) or spin echo (T2-weighted) imaging. (When gradient and spin echo acquisitions are combined quantitative vessel size imaging can be done, see the previous section). Gradient echo DSC MRI has a higher CNR and SNR to detect rCBV than spin echo DSC, which is due to the greater changes in T2* than in T2 due to the Gd-based contrast agent [291]. However, gradient echo DSC is also more susceptible to magnetic field inhomogeneities, causing signal drop-out in regions close to air/tissue interfaces in the body. Tumors located near such interfaces may be better visualized with spin echo DSC imaging.

The key parameter calculated with DSC imaging is relative blood volume (relative cerebral blood volume, rCBV, when applied to the brain), which is calculated via measurement of the area under the curve of the first passage of the bolus of contrast agent, compared to the first pass in a control region with a large vessel (arterial input function). In brain tumors, rCBV can be used to do grading [288], as well as differentiation of tumor progression and radiation necrosis after treatment [48]. Although traditionally mostly applied in brain tumors, novel applications of DSC imaging are emerging in the literature suggesting DSC MRI can be used to differentiate rectal cancers with and without lymph node metastases [118] or to differentiate malignant from benign parotid tumors [2].

ASL MRI is finding widespread clinical application to assess cerebral blood flow (CBF) or perfusion in brain tumors. In ASL, water protons in arterial blood are magnetically labeled and used as an intrinsic kinetic tracer omitting the need for an injection of an external contrast agent. In general, water protons will be labeled as they flow through the major brain feeding arteries (i.e., internal carotid and vertebral arteries). Imaging of the brain is done after a 1–2 s delay after labeling when the labeled protons will have perfused the brain tissue, since water is a freely diffusible tracer. Because the labeling decays with the T1 relaxation time of water, the SNR of ASL increases with increasing magnetic field strength.

Several variations of ASL exist in which the magnetic labeling of arterial blood is done in different manners. These different techniques initially hampered the translation of ASL to clinical settings, as specialized staff was necessary to carry out ASL procedures. However, since the international consensus paper on the use of ASL [12] a recommended imaging and CBF quantification protocol now exists and is also implemented on scanners of all major MRI vendors.

Moderate to high correlations are found between ASL-CBF and DSC MRI cerebrovascular markers [160] indicating the use of CBF for grading tumors [251], as well as follow-up of tumors throughout the disease course [52]. For the measurement of tumor perfusion in regions of the body other than the brain technical developments are emerging that either allow for magnetic labeling of blood in other major feeding arteries, such as the liver [146], or techniques in which blood is

labeled based on its velocity (velocity selective ASL; [120]) which omits the need for a major artery being present and opens up the possibility of perfusion imaging of tumors in other regions of the body.

2.4.2.3 Oxygenation and Hypoxia Imaging

Aggressive tumors tend to have rapidly growing, which often results in irregular and leaky vessels. As a consequence, perfusion of tumor tissue is insufficient which leads to the presence of hypoxia (decreased oxygen tension) and microhemorrhages. MRI techniques exist that are sensitive to oxygenation, in which the primary source of contrast is endogenous, paramagnetic deoxyhemoglobin which decreases the MR transverse relaxation time ($T2^*$) of water in the blood and surrounding tissues. However, it is also possible to use MRI techniques to assess the changes in $T1$ relaxation times caused by changes in oxygen tension.

Susceptibility-weighted imaging (SWI) is a technique in which $T2^*$ -weighted imaging is done that sensitizes contrast to blood products and allows for the detection of hemorrhage independent of contrast agents. It is a technique with which phase, rather than magnitude, information from the image acquisition is used to measure magnetic field perturbations caused by deoxygenated blood and blood products. It can detect changes in tissue properties due to the vasculature before vessels become leaky, which means that with SWI techniques occult tumors can be detected that do not show on a $T1$ -weighted Gd-DTPA post-contrast scan [219]. An additional property of SWI is that it is sensitive to calcium deposits, and can, therefore, also be used to detect calcifications in the brain tumors and prostate cancer [4].

Blood-oxygenation-level-dependent MRI is sensitive to oxygen partial pressure (pO_2) in tissues adjacent to perfused vessels, due to $T2^*$ shortening caused by the presence of paramagnetic deoxyhemoglobin. BOLD imaging is done by using the magnitude information of $T2^*$ -weighted, gradient echo imaging, which allows for rapid image acquisition. It has been used in revascularization studies in the heart, kidney, and brain, and in tumor hypoxia studies of resistance to treatment [233, 234]. More recently, measurement of $R2^*$ (the inverse of $T2^*$) is used to detect hypoxia in tumors in the breast [292, 332] and prostate [203]. Additionally, steps are being made to validate the use of BOLD MRI for hypoxia imaging in brain tumors via comparison of BOLD MRI with PET measurements of hypoxia [247].

To measure the oxygen partial pressure pO_2 it is also feasible to use exogenous sensing molecules that exhibit sensitivity to oxygen concentration levels. Probes that cause a change in $T1$ relaxation times have been developed for in vivo measurement of pO_2 for both 1H and ^{19}F MRI and MRS [165, 364]. In the case of ^{19}F , it has been shown that local oxygen tension can be performed using hexafluorobenzene as a reporter molecule [364].

2.4.2.4 Diffusion-Weighted Imaging

In order to develop and optimize a treatment strategy for cancer therapy, quantitative, reproducible, and noninvasive functional parameter determination for the modes of action of specific therapy scenarios are required. New technological

developments in Molecular Imaging, such as the characterization of diffusion in tissues allow for the assessment of the microenvironment of a tumor. These techniques are based on an assessment of the motility or diffusion of water molecules in intra- and extracellular spaces through the use of diffusion-weighted imaging (DWI). DWI has long been identified as a potential and completely noninvasive and fast MRI methodology for the detection and staging of tumors and the evaluation of therapy. Additionally, Intravoxel Incoherent Motion (IVIM) is emerging as a DWI-based technique that can assess the cellular as well as the microvascular environment of tumors.

Water mobility is dependent on both the relative volume of intra- and extracellular spaces and cellular membrane integrity and permeability [185]. In tumors, quantitative diffusion values are strongly affected by tissue cellularity and extracellular volume (Fig. 2.12). Recently, DWI has been used as an early response parameter in cancer treatment: Treatment-induced loss of tumor cell integrity will result in a local increase in water diffusion, which can be quantified by DWI. Such effects probably occur before macroscopic changes in mass, size, or morphology as removal of cellular debris occurs relatively slowly. Indeed, in preclinical studies, treatment responses could be qualitatively assessed with DWI as early as 2 days post-therapy [102, 128, 159]. In competition with nuclear medicine (PET and SPECT imaging), a recent concept has received a lot of attention in the medical community: whole-body diffusion imaging for diagnosis and therapy follow-up. Without the need for radioactive tracers and with better spatial resolution and coregistration with high-resolution morphological imaging, it is possible to provide a high degree of detection sensitivity for tumors and metastatic processes [91, 193].

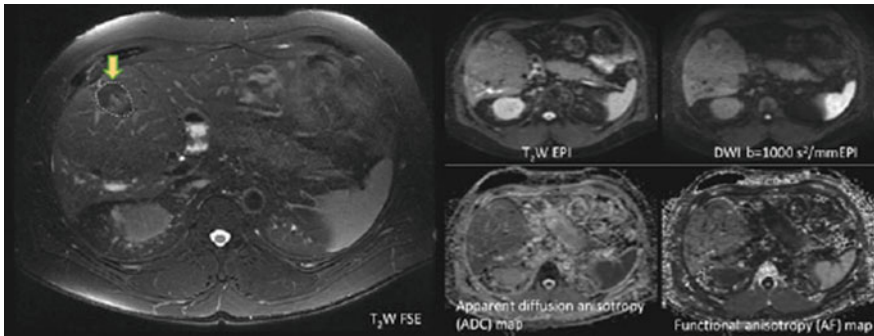


Fig. 2.12 Diffusion-weighted (DWI) MRI. The same patient as in Fig. 2.11 with an RF-ablated intrahepatic cholangiocarcinoma was imaged with a diffusion-weighted b-factor of $600 \text{ mm}^2/\text{s}$. The left panel shows a respiratory-gated 2D T_2 -weighted fat-suppressed FSE acquisition. The right panels demonstrate a respiratory-gated T_2 -weighted echo-planar imaging (EPI) acquisition ($b = 0 \text{ mm}^2/\text{s}$) and corresponding isotropic $b = 600 \text{ mm}^2/\text{s}$ measurement. The panels below illustrate both the apparent diffusion coefficient (ADC) and the fractional anisotropy (FA) maps. The diffusion values in the ablated tumor show successful elimination of tumorous tissue. Acquisition performed at 1.5 T using an 8-channel torso coil

IVIM as a technique was introduced by Le Bihan et al. [184], and is based on the varying sensitivity of diffusion-weighted signal to protons diffusing at different velocities; with DWI with low b -values being sensitive to rapidly moving protons in the microvasculature while at high b -values DWI is sensitive to slowly moving protons with which cellularity can be probed (as described above). Therefore, by applying a range of b -values (typically from 0 to 2000 mm²/s), a diffusion model is fitted to the DWI data that accounts for the varying compartments within a voxel that contains moving protons. This model includes quantification of the diffusion coefficient (D), the pseudo-diffusion or diffusion-weighted perfusion coefficient (D^*), and the microvascular volume fraction within the voxel (f).

Research studies are emerging that show good correlation with IVIM-based perfusion measurements and those assessed with either DSC or ASL [280, 345]. As a consequence, IVIM is a promising technique that allows for novel biomarkers for identification and follow-up of tumors, in particular in regions where DSC or ASL is not (yet) feasible or difficult. Examples of emerging applications are tumors in the head and neck region [131], in the prostate [33], and liver [190].

2.4.2.5 Intracellular and Extracellular Sodium Concentrations

Cancer cells have unusually high sodium content. Similarly to mapping ¹H diffusion values in tumors, sodium concentration mapping determined by ²³Na MRI, can provide dynamic and spatial changes after therapeutic intervention in tumors and could be considered a complementary technique, potentially even more sensitive to subtle changes in tumors [270]. For some time, it was difficult to differentiate intracellular from extracellular sodium unless specific shift reagents were used that remained exclusively extracellular but nonetheless toxic. The Triple Quantum Filtered (TQF) ²³Na MRI technique has been proposed as a potential way to monitor the alteration of intracellular sodium without the use of shift reagents [271].

²³Na has much lower spatial resolution than ¹H DWI imaging mainly related to the difference in abundance between sodium and proton ions in the body. Nonetheless, clinical systems with higher field strengths (≥ 3 T) are providing encouraging results with shorter acquisition times and good spatial resolution [39, 250] (Fig. 2.13). ²³Na measurements are quantitatively more robust in the presence of motion thus giving better access to monitoring therapy in regions affected by cardiac and/or respiratory motion, regions where DWI usually fails. Improved sequences and processing techniques have been developed with better SNR that could provide potentially better resolution with reduced scanning times [50, 92, 269, 301].

2.4.2.6 Cancer Metabolism and Metabolite Concentration Using MRS

Magnetic Resonance Spectroscopy (MRS), a technique that has progressed in the domain of cancer research for decades allows analysis of functional and metabolic parameters of cells located deep within the living body, again, without resorting to invasive techniques. MRS can categorize specific chemical signatures and measures the regional concentrations of biochemical species. The addition of MRS to obtain

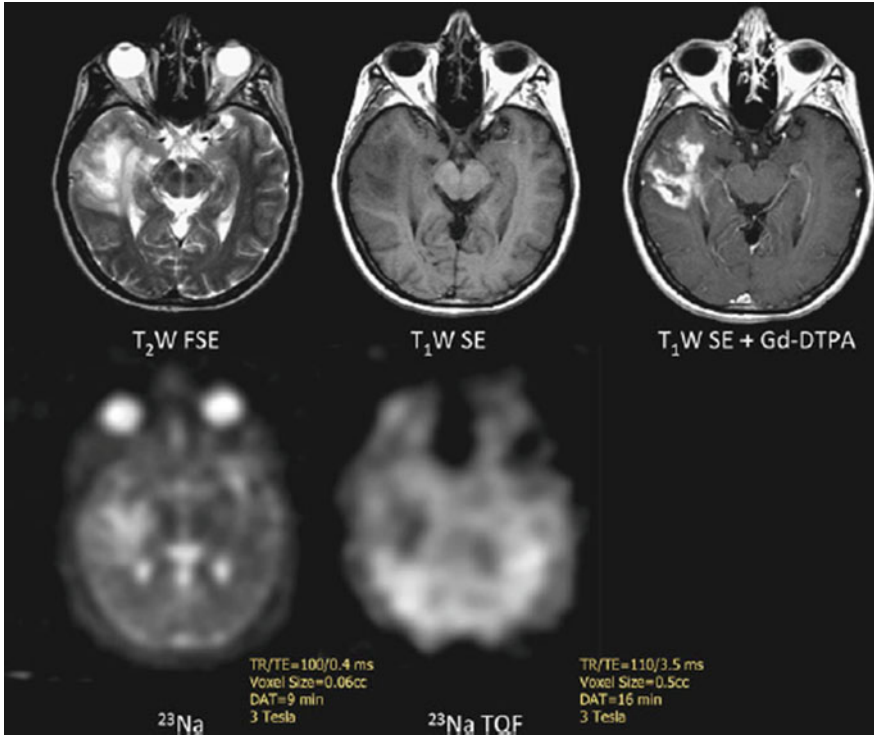


Fig. 2.13 Sodium (^{23}Na) MRI. ^{23}Na MRI can provide similar dynamic and spatial changes after therapeutic intervention in tumors. Here, a patient with a tumor on the left side of the brain was imaged with a T_2 -weighted FSE and pre- and post-contrast acquisition of a T_1 -weighted SE scan (enhancement only happens in regions where there is a disruption of the brain–blood barrier, thus showing more clearly the tumor). The triple quantum filtered (TQF) ^{23}Na acquisition permits to monitor the intracellular Na concentration but at much lower resolution (larger voxels) as compared to a ^{23}Na image (which looks similar to a T_2 -weighted scan). Acquisition performed at 3.0 T using a double-tuned proton-sodium head coil. Image courtesy of Dr. Fernando Boada (University of Pittsburgh, USA)

metabolic images (spectra) based on the relative concentrations of cellular biochemicals can help to determine more subtle differences in tissue constitution that leads to better diagnostics of cancer [175, 174, 236]. Differences in the behavior of metabolites such as choline, creatine, and citrate between healthy tissues and tumor can provide a measure of cancer aggressiveness [176]. Studies monitoring the changes in local metabolites after therapy, have indicated that MRS could be effective as an early indicator of cancer response [28, 27, 211, 255].

MRS has a significantly lower spatial resolution in comparison to MRI. The use of higher magnetic field strengths and MRS pulse sequence developments have promoted 3D measurements of metabolite concentrations with an acceptable voxel resolution of 1 cm or less [44]. One of MRS imaging's main limitations, the low

sensitivity of the technique, has more recently been addressed by the use of hyperpolarized probes. Most commonly, ^{13}C -labeled biomolecules are used to interrogate glucose metabolism in tumors [79, 172] (Fig. 2.14), however, other nuclei with the ability to absorb and emit radio-frequency energy such as ^{129}Xe , ^{15}N , and ^{31}P can be used [101, 172]. The use of hyperpolarized ^{13}C nuclei has allowed for increase in the signal-to-noise ratio and detection sensitivity with up to 10,000-fold enhancement compared to conventional MRI. The potential and current challenges in developing MRI with hyperpolarized probes into a technique suitable for routine clinical practice have recently been discussed in a white paper by Kurhanewicz et al. [172].

2.4.2.7 Extracellular pH

In order for cells, healthy or cancerous, to live and reproduce it is required that a pH range in the surrounding environment stays between 6.5 and 7.5. While healthy cells maintain a pH around 7.35, cancer cells are more acidic in nature. The

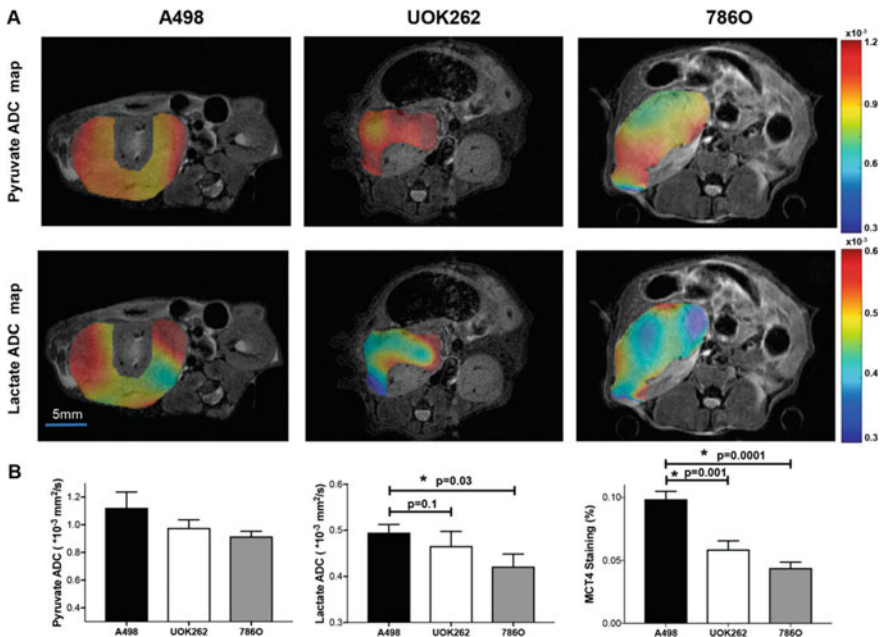


Fig. 2.14 Hyperpolarized (HP) ^{13}C pyruvate MRI showing differences in lactate production and compartmentalization of orthotopic renal cell carcinoma tumors. **a** ^{13}C pyruvate and ^{13}C lactate ADC maps from diffusion-weighted HP ^{13}C MRI overlaid on the T2-weighted anatomic images. **b** The ^{13}C pyruvate, ^{13}C lactate, and monocarboxylate transporter 4 (MCT4). The levels of lactate appear to correspond to the different levels of MCT4 which mediates lactate export out of tumor cells. Reprinted with permission under the Creative Commons Attribution License from Sriram et al., Non-Invasive Assessment of Lactate Production and Compartmentalization in Renal Cell Carcinomas Using Hyperpolarized ^{13}C Pyruvate MRI, *Cancers* 10(9), pp 13 (2018)

extracellular pH is lower in tumors as compared to healthy tissues, degrading the nearby extracellular matrix and facilitating tumor development and invasiveness [105]. It has been shown that pH values influence dramatically tumor progression and the efficiency of treatment and can be used as an effective biomarker for MRI and MRS in order to understand better tumor dynamics [237]. Nonetheless, this is only possible with the use of specific probes. The introduction of exogenous probes that remain in the extracellular environment, such as imidazol-1-yl-3-ethoxycarbonylpropionic acid, produce chemical shifts which are pH sensitive and can be seen on ^1H spectra and mapped with spectroscopic imaging [237]. ^{31}P and fluorine ^{19}F have also been developed that are sensitive to pH. ^{19}F provides a strong NMR signal with minimal background interference and has extreme sensitivity to changes in the tumor microenvironment that can be exploited with varied reporter molecules [358].

To measure effectively the oxygen partial pressure pO_2 , it is necessary to use sensing molecules that exhibit sensitivity to oxygen concentration levels. Probes that cause a change in T1 relaxation times have been developed for in vivo measurement of pO_2 for both ^1H and ^{19}F MRI and MRS [165, 364]. In the case of ^{19}F , it has been shown that local oxygen tension can be performed using hexafluorobenzene as a reporter molecule [364].

CEST contrast agents are being applied in several different disease models, some of which could be useful in oncological applications. Amide proton chemical exchange saturation transfer (acidoCEST) is a measure of extracellular pH. Using the clinically approved iodinated CT contrast agent iopromide, containing two amide protons for CEST saturation, in a mammary carcinoma model, it was possible to monitor the change in pH after bicarbonate alkalization treatment [59] and a decrease in pH following metformin treatment in a xenograft model of human pancreatic adenocarcinoma after iopamidol injection using acidoCEST (Goldenberg et al. *Mol Imaging Biol*, 2018).

2.4.2.8 Intracellular Protein Content and pH (CEST MRI)

Chemical Exchange Saturation Transfer (CEST) imaging is a novel MRI technique with great potential for measuring molecular biomarkers within tumors. In comparison to ^1H MRS, CEST MRI shows increased SNR, which allows for images to be acquired at higher resolution and with greater coverage. This technique allows for interrogating tissues where exchangeable protons on molecules in the solute pool exchange with the free-water pool. These include protons in amide and amine side-groups in mobile metabolites, proteins, and enzymes that have specific off-resonance frequencies different from the on-resonance frequency of protons in the free-water pool. Recent preclinical studies have highlighted that CEST can be used to inform on physiological processes within tumors including cell proliferation [265] and glutamate metabolism [125], which make this technique an excellent candidate for early detection of physiological changes that herald tumor growth.

CEST MRI is based on the indirect saturation of the free-water pool via saturation of exchangeable protons bound to mobile proteins within tissue [322]. The

contrast that can be generated, therefore, not only depends on the amount of protons available (which is proportional to the amount of metabolites, proteins, and enzymes present), but also on the exchange rate of these protons. This exchange rate is highly dependent on the local pH, which means that in turn CEST contrasts are also sensitive to local pH levels. Note that it is assumed that most of the CEST contrast is generated intracellularly, due to the abundance of mobile proteins within the cells compared to outside the cells.

Although the first steps for CEST to be applied in clinical practice have recently been made [365], there are still several issues that need to be overcome before this technique is ready for clinical use. The main issue is that most CEST MRI is done at high (>3 T) field strength, and the sensitivity of CEST MRI at 3 or 1.5 T is low. In addition, the validation of the origin of CEST signal, i.e., either mobile protein build-up or changes in pH in human tumors is still under investigation [351]. Despite these shortcomings, CEST MRI is a promising technique for tumor grading and follow-up. Additionally, CEST MRI with exogenous contrast agents can be used that probe specific molecular processes and that therefore may be used as novel targets of or markers to follow new therapies [124].

2.4.2.9 Multiparametric MRI

With the plethora of MRI biomarkers of physiology of tumors as described above, it may not come as a surprise that recent advances in MRI imaging of tumors have led to multiparametric MRI models. In such models, several of structural, vascular, perfusion, diffusion, and CEST imaging parameters are measured and in post-processing techniques combined to characterize the different types of tissues present within tumors. As examples, these techniques are emerging to characterize heterogeneity within a tumor [89] and can even be linked to cellularity [57], but also to improve grading and differentiation of different pathophysiology in treatment [19, 78]. However, because of the endless possibilities that exist with the combination of all these MRI techniques consensus of how to do multiparametric MRI is still far from being reached, despite the building evidence that multiparametric MRI improves tissue characterization.

2.5 Magnetic Resonance Imaging Probes in Cancer

2.5.1 Introduction

Probes for MR application can be divided according to their biodistribution and consequent applications of contrast-enhanced MRI that they allow. Nonspecific probes are those that do not interact with any specific type of cells, and include low molecular weight (MW) agents that equilibrate rapidly between the intravascular and interstitial space and undergo a fast kidney clearance and high-molecular weight agents, that stay within the intravascular space and are slowly excreted by kidneys and/or the liver. Specific probes are considered those that are passively

directed to a particular cell type or those that are actively directed with a targeting moiety to a specific target molecule on the cell. There are also responsive, smart, or activatable agents, whose contrast is modulated upon activation in the presence of specific targets in the tissue of interest.

2.5.2 Non-Targeted Probes

Although the ultimate goal of molecular imaging is providing tools for the visualization and measurement of specific molecular targets in the living organism, the pathophysiological characteristics of tumor microenvironment allow the design of macromolecules or nanoparticles capable to accumulate within the tumor compartment without any specific targeting agent. In the process of tumor formation, when tumor cells multiply and form aggregates of 2–3 mm, upon the release of pro-angiogenic factors the development of a tumoral blood supply commences [94]. Malignant neovasculature differs greatly from that in normal tissue. Newly formed vessels are abnormal in form and architecture, lack a smooth muscle layer and have no effective lymphatic drainage. Endothelial cells are poorly aligned, with wide fenestrations (in most peripheral human tumors ranges from 200 to 600 nm in diameter) [359]. All these factors lead to abnormal molecular and fluid transport dynamics, resulting in extensive leakage of circulating macromolecules into the tumor tissue. Furthermore, a defective venous and lymphatic system ensures a longer retention of extravasated components within the tumor interstitium. This effect, defined EPR (Enhanced Permeability Effect) known for almost two decades, represents the physiological basis for tumor accumulation of macromolecular drugs within solid tumors [204]. It accounts for the accumulation of untargeted macromolecules and nanoparticles 10–50-fold higher concentrations than in normal tissue within 1–2 days [141]. Importantly, the EPR does apply only to high molecular size (larger than 40 kDa, above kidney clearance threshold) macromolecules, since low molecular weight substances (described below for the sake of completeness) undergo a faster clearance through a renal route. While large size is a prerequisite for the EPR effect to occur, it is not the only determining factor. Biocompatibility and surface charge of the biomolecules are also of major influence. Chemical modification of large molecules such as α 2-microglobulin and albumin can cause blood clearance of these molecules within minutes [204].

2.5.2.1 Low-Molecular Weight Agents

Low-molecular weight agents pioneered the improvement of MR contrast. These comprise largely Gd^{3+} chelates of linear or macrocyclic polyaminocarboxylate ligands and are the most important class of MR contrast agents commercially available, e.g., Magnevist®, Dotarem®, Omniscan®, and Prohance®. After being intravenously injected, these agents clear rapidly from the intravascular space through capillaries into the interstitial space with a distribution half-life of about 5 min. Noteworthy, they do not cross the intact blood–brain barrier, and are eliminated through the renal route (half-life: 1.5 h) with no detectable

biotransformation, decomposition, or serum protein binding [26]. They can be used for MR angiography (MRA) and provide increased enhancement and visualization of malignant lesions, due to altered permeability. Due to the extravasation to the interstitial space and the rapid elimination from the circulation, the timing for studies is restricted. Due to recent concerns regarding the toxicity of Ga-based contrast agents and prolonged accumulation of Gd in tissue after repeated administration [256], studies using low molecular weight iron chelates as alternative contrast agents for T1-weighted contrast-enhanced MRI [40].

2.5.2.2 High Molecular Weight Agents

Macromolecular metal-chelate complexes, known also as blood pool agents are larger compounds with MW higher than 40 kDa. Their size prevents extravasation through healthy vascular endothelium, prolongs intravascular half-life and favors the EPR effect in leaky malignant vasculature. Furthermore, because of increased steric hindrance, they have higher relaxivity than low molecular weight agents such as Dotarem or Magnevist. Slower molecular tumbling increases rotational correlation time, τ_r , resulting in more enhancement per unit dose of paramagnetic ion [328]. Moreover, the possibility to append multiple paramagnetic moieties into a macromolecular platform, increases the enhancement and reduces the dose of agent administered. These agents can be divided into: (a) protein-based MR agents, (b) systems based on liposomes (c) system based on polymers, and (d) systems based on superparamagnetic agents.

2.5.2.3 Protein-Based MR Agents

In order to increase circulation time and signal enhancement, the approach of using albumin, the most abundant protein in plasma, as a carrier of paramagnetic agents received a lot of attention in the past few years. Albumin-Gd³⁺-DTPA was first synthesized in 1987 by Ogan et al. In a typical synthesis of paramagnetically labeled albumin 25–35 molecules of Gd³⁺-DTPA are covalently bound to each albumin molecule, resulting in a molecular weight of 92 kDa with a diameter of 6 nm [22]. Prolonged accumulation within neoplastic tissues (>2 h) was shown to reflect abnormal capillary permeability for macromolecules, associated with neovascularity [340]. Moreover, quantitative assays of tumor microvascular characteristics based on albumin-Gd³⁺-DTPA dynamic MR imaging was shown to correlate with the histopathologic grade in mammary [65] and prostate [116] tumors, and with radiation-induced changes in tumor capillary permeability [276]. Despite some successes also several drawbacks were recognized. With plasma half-life of several hours, clearance from the body is slow and incomplete with retention for more than a week. The potential immunogenicity of albumin constitutes another limitation to the clinical translation of albumin-based contrast agents [22].

To overcome these limitations, Gd-complexes that can reversely bind to serum albumin have been generated. The supramolecular complexes that are formed in this way have beneficial effects on blood circulation time and enhancement of T1 relaxation [183, 199]. It contains a lipophilic chemical group (diphenylcyclohexyl)

that mediates binding to serum albumin. A few preclinical studies have been performed on cancer imaging. In rats bearing chemically induced breast cancer, no significant correlation was found between MS-325-enhanced microvascular assays with either tumor grade or with microvascular density (MVD as opposed to albumin-GD³⁺-DTPA [304–312]. This was probably due to the use of a rodent model. In primates and rabbits, the elimination of MS-325 is relatively long (2–3 h), whereas in rats it is shorter (25 min) and the volume of distribution is twofold higher compared to humans [304–312]. New formulations with more preferable pharmacokinetics in rodents may be more useful for studying tumor vessel characteristics in rodent tumor models [199].

2.5.2.4 Lipid-Based Nanoparticles

A wide variety of lipid-based nanoparticles has been proposed and used as candidates for MR contrast agents since the 1980s [56]. Lipids are naturally occurring amphiphilic molecules that contain a hydrophilic head and a hydrophobic tail. Due to the hydrophobic associative interactions of the tails and the repulsive interactions between the hydrophilic head groups they aggregate and self-assemble in water into well-defined structures such as micelles, liposomes, and microemulsions. Possible structures are illustrated in Fig. 2.15. Micelles can be formed from lipids with a relatively large head group, such as lipids with a single fatty acyl chain that constitute the core with their hydrophobic part and the corona with their hydrophilic component. Liposomes are nanosized vesicles used extensively in the biomedical field for many years, both as model system for studying the properties of biological membranes and as drug carriers. They are created from bilayer forming lipids, which are usually comprised of a polar head group and two fatty acyl chains, entrapping an aqueous core. Molecules can be captured in the aqueous core, integrated into the lipid shell or covalently linked to the surface.

The ability of liposomes to generate MR signal enhancement depends and the structure and composition of the lipidic bilayer and also on the specific location of the paramagnetic agent (either in the aqueous lumen or in the lipid bilayer). The first type of liposomes described were liposomes entrapping paramagnetic agents. Agents, such as MnCl₂, Gd-DTPA, Mn-DTPA, Gd-DTPA-BMA, and Gd-HP-DO3A in the aqueous core [56, 74, 96, 166]. Early studies demonstrated the feasibility of the use of these molecules in mouse models of liver cancer [313] and metastasis [314]. However, the main limitation of the loading of paramagnetic agents within the aqueous lumen is the reduced relaxivity, due to the limited exchange of bulk water with the paramagnetic agent. The major role in this exchange is played by liposome permeability, which depends on the lipidic composition and can be altered by incorporating cholesterol [114]. Unfortunately, there is a balance between permeability and liposome stability, resulting in more permeable liposomes to be less stable compared to those with a more rigid bilayer. This property has been used to design activatable liposomes to monitor drug/imaging agent release depending on temperature [97] or pH [198]. In another class of liposomal contrast agents, by using lipophilic chelate such as DTPA-stearate [275], DTPA-phosphatidylethanolamine [307] or DTPA attached to

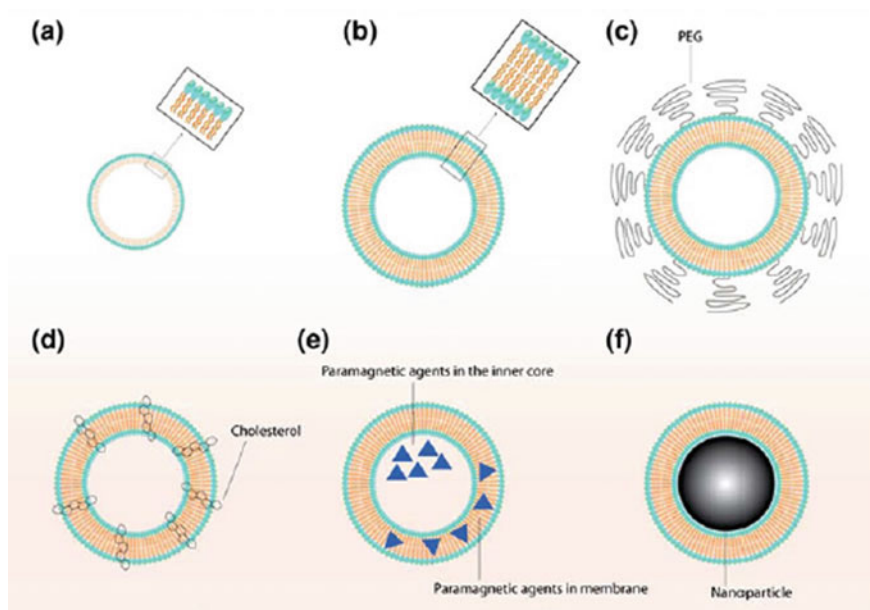


Fig. 2.15 Illustration of various structures of liposome-based contrast agents

alkyl chains via amide linkers [32, 149], the paramagnetic component can be integrated into the lipidic bilayer (Fig. 2.16). Higher exchange rate between the contrast agent and the bulk water is obtained with this approach, therefore improved ionic relaxivity of the metal. Liposomes were initially developed for selective imaging of liver and spleen due to their preferential uptake within the Kupffer cells and the reticuloendothelial system (RES), respectively. By coating liposomes with polyethylene glycol (PEG), the RES uptake is greatly reduced, blood circulation and passive tumor targeting are improved (“stealth” liposome).

More recently a new approach of liposome-based imaging has been reported, taking advantage of the chemical exchange saturation transfer (CEST), a method of generating MR contrast that relies on the saturation transfer that occurs between the bulk water protons and exchangeable protons on mobile proteins. By selectively applying a saturation RF pulse at a specific proton frequency (associated with a particular molecule or CEST agent) that is in exchange with surrounding water molecules, the MR signal from the surrounding bulk water molecules is also attenuated. Images obtained with and without the RF saturating pulse reveal the location of the CEST agent. Aime et al. reported the first example of LipoCEST comprised of a Tm^{3+} complex encapsulated within a liposome [7]. The detection of two different water resonances was reported: intense signal corresponding to the bulk solvent and a less intense peak corresponding to the intraliposomal water in slow exchange with the bulk water through the liposomal bilayer.

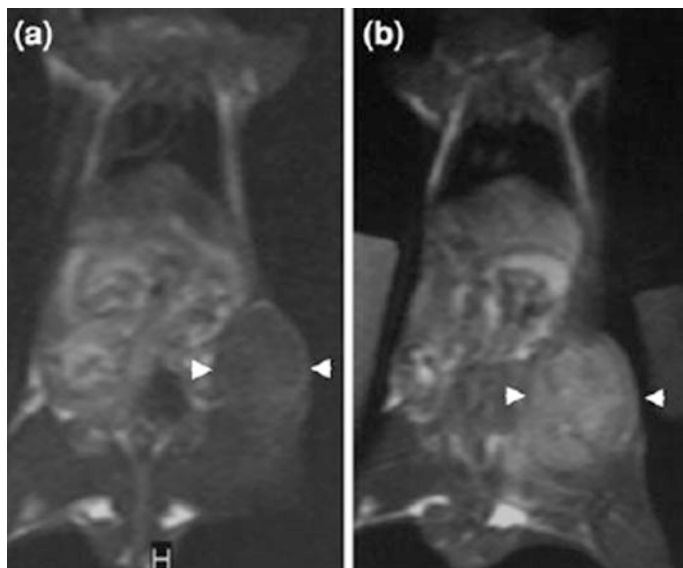


Fig. 2.16 T1-weighted images of a mouse **a** before and **b** 20 h after the injection of PEG-stabilized paramagnetic liposomes containing Gd-DMPE-DTPA (Reprinted with permission from John Wiley and Sons: [32])

A further development of this approach has been reported by using liposomes entrapping the compound Gd^{3+} -HPDO3A. After osmotic induction of liposome shrinking from spheres to oblate vesicles increased relaxivity and shift of the intraliposomal water from the bulk by 7 ppm was reported [5]. Temperature-sensitive liposome has been used as a lipoCEST agent. By entrapping both Tm^{3+} chelate, as CEST reporter, and NH_4PF_6 , as ^{19}F MRS probe Langereis et al. monitored the “activation” (melting) of the liposome. Below the melting temperature the liposome structure is intact and the CEST, effect due to Tm^{3+} , is observed. Above the melting temperature, the liposome content leaks out thus switching off the CEST effect and turning on the ^{19}F resonance [179] (Fig. 2.17).

To overcome some limitations in the use of lipoCest agents, more recent studies have introduced adaptations in lipoCest formulations including: alterations in shape of the lipid vesicles, variations in liposome size, composition of lipid membrane, and use of amphiphilic shift reagents [114]. Further developments in lipoCest reagents are focused on their use as theranostic agents using targeting vectors and physiology responsive elements [90, 207].

2.5.2.5 Dendrimers

Dendrimers (dendron in greek, meaning tree) are highly branched synthetically produced polymers, used for the first time as MR contrast agent in 1994 [339]. They have a globular architecture comprising a central core, an interior, and a surface.

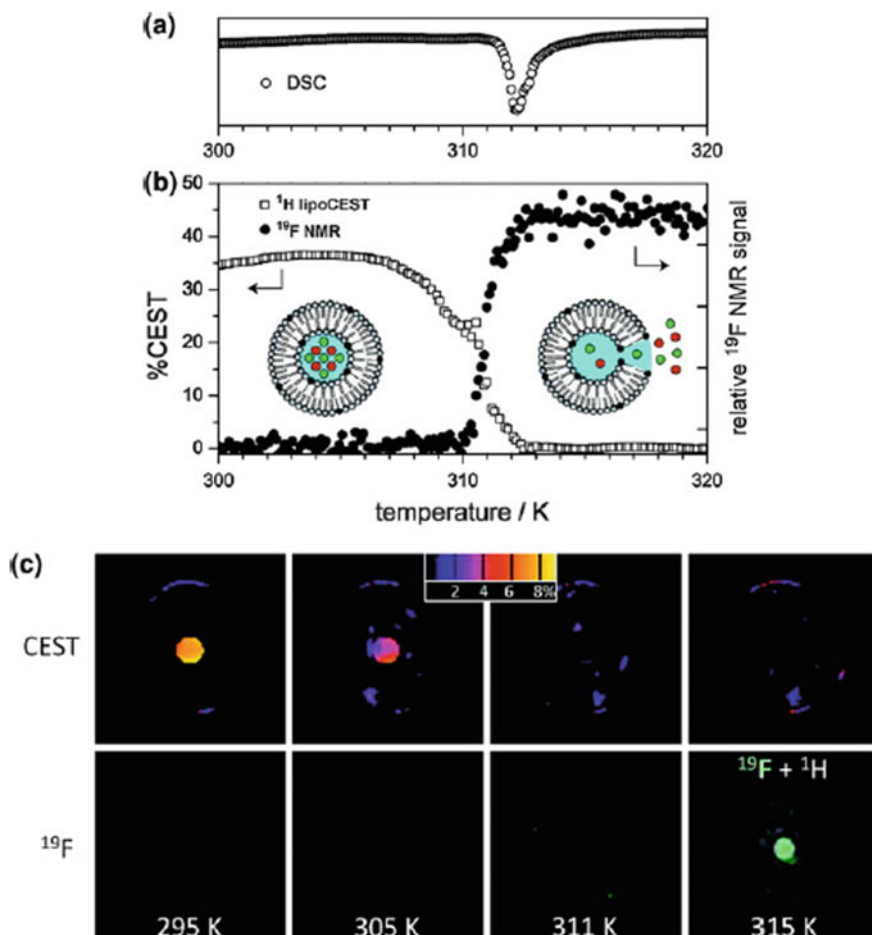


Fig. 2.17 A temperature-sensitive liposomal ^1H CEST and ^{19}F contrast agent. **a** DSC thermogram showing the melting temperature of the lipid membrane. **b** The ^1H CEST effect and the ^{19}F NMR signal intensity of liposomes containing [Tm(HPDO3A)(H₂O)] and NH₄PF₆ as a function of temperature. **c** MRI images of the liposomal agent. The CEST signal (color scale in percent) vanished at $T \geq 311$ K while the fluorine signal appeared at 315 K (overlay with the ^1H image for colocalization and clarity) (Reprinted with permission from American Chemical Society: [179])

Dendrimers are synthesized in steps similar to solid-phase peptide synthesis using building blocks like polyamidoamine (PAMAM) and poly(propylene imine) (PPI), poly-L-lysine (PLL), 2,2-bis-methylolpropionic acid (bis-MPA), phenoxymethyl (methylhydrazone) (PMMH).

Two types of commercially available dendrimers have been studied extensively: polyamidoamine (PAMAM) and poly(propylene imine) (PPI), the former having an

amide functional group core component and the latter a pure aliphatic polyamine core. The synthetic chemistry used permits the production of monodisperse products of a specific physical size with high consistency and reproducibility. Different “generation” molecules can be synthesized according to their size and molecular weight. Lower generation (second and third generation) rapidly leak from the vasculature into surrounding tissues. Medium-sized dendrimers (fifth and sixth generation) with a diameter less than 8 nm are able to selectively extravasate through hyperpermeable tumor vessels. Dendrimers with a diameter higher than 9 nm (6th generation and above) demonstrate good vascular enhancement, but only minimal leakage from the circulation even in the tumors. While dendrimers smaller than 7 nm (fifth generation and below) are excreted via the renal route, ninth and tenth generation are generally excreted through the liver, as they are trapped by RES. Linkage to other groups, such as PEG, dramatically alters the biodistribution and pharmacokinetic profiles of these constructs. Dendrimer-enhanced MRI has been used to image tumors in mouse models. It has been shown that eighth-generation PAMAM-Gd enhanced tumor vasculature, whereas the analogous smaller sixth-generation (10 nm) agent provided better delineation of tumor tissue [356]. PAMAM generation 8 has also been used to evaluate malignant permeability after selective irradiation [164] (Fig. 2.18).

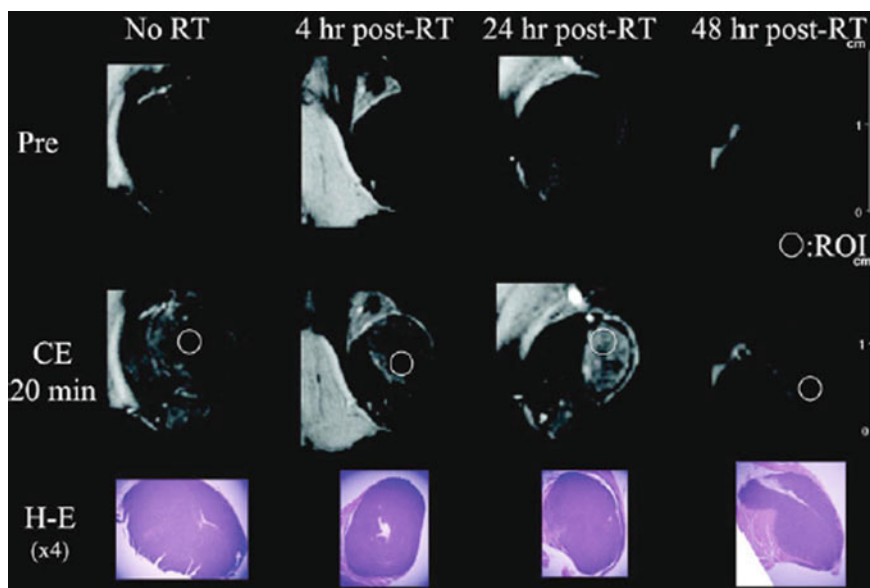


Fig. 2.18 Representative pre- and postenhanced magnetic resonance images. Magnetic resonance images of the SCCVII tumor are shown at selected time points pre- and postirradiation (15 Gy). Corresponding micrographs of the H&E staining are presented for histologic comparison of the effects on the xenografts (Reprinted by permission from American Association for Cancer Research, Inc: [164])

Gadomers, developed by Schering, are a class of polylysine dendrimers. Their internal structure comprises aromatic rings, and are simpler and smaller in size compared to PAMAM or PII. Clearance through glomerular filtration and no long-term accumulation or retention of the nonmetabolized agent in tissues make them promising as blood pool agents. Gadomer-17 (Bayer Schering Pharma, Berlin, Germany) approximates the size of third-generation dendrimers and are being successfully used for MR lymphography [216] and myocardial perfusion imaging [109]. Despite extensive characterization in preclinical studies, gadomers are not clinically available. More recent developments in dendrimer chemistry have explored their use as a backbone for other paramagnetic and superparamagnetic contrast agents or CEST imaging as recently reviewed by McMahon et al. [210]. A major line of research currently focuses on using the versatility of dendrimers as theranostic agents and multimodality probes [87, 138, 259].

2.5.2.6 Linear Polymers (Polylysine, PEG and Polysaccharide Complexes)

The wide commercial availability and easy synthesis of monomers and resulting polymers allowed their evaluation as a potential contrast agent in MRI. Poly-L-lysine is available in a broad range of molecular weights and is the most studied and used linear polymer. The conjugation to DTPA takes place on the ϵ -amino group of the lysine. For the macromolecular compound Gd-DTPA-polylysine, relaxivity was three times higher than that of Gd-DTPAGd³⁺ [274] independently of the polymer chain length [289]. Pharmacokinetic studies showed good tolerance in vivo and complete elimination mainly through the renal route within 1 day in rat and rabbit. Gd-DTPA-polylysine resulted in higher and sustained enhancement of tumor tissue in rat models of breast and liver cancer compared to Gd-DTPA [117, 229]. Polyethylene glycol (PEG) is a nontoxic, biocompatible hydrophilic polymer and it has been the most likely candidate for use as a macromolecular MR contrast agent. The advantage of using such polymers resides in the ability to manipulate the size and its virtual non-immunogenicity. GD-DTPA-PEG constructs with MW higher than 20 kDa have been shown to provide good blood pool enhancement dynamic and efficient and sustained tumor enhancement in rabbits [73]. In an attempt to reduce the immunogenicity and improve the solubility of polylysine a new class of PEG-polylysine MR macromolecular agent has been designed and tested, by introducing two diverging polylysine cascade amplifiers at each end of a polyethylene glycol (PEG) backbone, followed by substitution of terminal lysine amino groups with Gd-DTPA chelates. These constructs exhibited high water solubility, narrow size polydispersity, and relaxivities threefold higher than Gd-DTPA [98]. MRI assays of vascular endothelial leakiness after injection of these agents demonstrated the ability to visualize and differentiate normal and malignant microvessels in a breast cancer model [64]. Polysaccharides, such as dextran, have been used as a plasma expander for more than 50 years. The well-known pharmacokinetic and pharmacodynamic profiles, together with their low immunogenic effect and their degradation into small subunits cleared through glomerular filtration raised the interest to use them as a platform for MR contrast agents.

Gd-DTPA-dextran compounds have been synthesized and higher (>twofold) relaxivities compared to the monomeric chelate have been reported. Their use as blood pool agents for vascular and tumor imaging in rabbits, demonstrated improved vascular residence time than a conventional Gd-chelate and increased tumor rim enhancement.

2.5.2.7 Iron Oxides

Superparamagnetic iron oxide (SPIO) nanoparticles are a class of contrast agents having a large magnetic moment. They function by acting as magnetic inhomogeneities, locally disturbing the magnetic field. This leads to enhanced dephasing of protons, resulting in decreased signal intensity on T2-weighted and T2*-weighted images. These nanoparticles often consist of a core of iron oxide (magnetite and/or maghemite) or mixed ferrites with a polymeric or polysaccharide coating such as dextran and PEG. They are considered to be biocompatible, have a limited effect on cell function and can be synthesized to be biodegradable [299, 331].

According to their size, these particles can be classified as monocrystalline iron oxide particles (MION, also called USPIO, ultrasmall superparamagnetic particles 10–30 nm), superparamagnetic iron oxide (SPIO; 60–150 nm), and micron-sized iron oxide particles (MPIO, 0.7–1.6 μm). The pharmacokinetics and biodistribution of SPIO depends on the size and the physicochemical composition of the coating; however, they are mainly cleared through liver, spleen, and lymph nodes and subsequent incorporation into the body's iron pool.

Ferucarbotran (Resovist) and ferumoxides (Endorem and Feridex) are iron oxide nanoparticles approved by FDA for contrast-enhanced MRI imaging of liver tumors [277] and metastatic involvement of lymph nodes. In a normal lymph node with preserved architecture and function, macrophages take up a substantial amount of iron oxides, shortening T2 and T2* relaxation times, therefore, resulting in a decreased signal. Conversely, in malignant lymph nodes, macrophages are replaced by malignant cells, and therefore the high signal intensity is retained and a heterogeneous signal is displayed [126].

USPIO has been used in dynamic contrast enhancement studies to demonstrate angiogenesis in a murine model of breast cancer; a significant correlation has been reported between the dynamic contrast enhancement and microvascular density [304–312]. Similarly, USPIO uptake has been correlated to tumor grade [304–312].

In molecular imaging, SPIOs are a prevalent means of labeling cells and to perform cell tracking by MRI. Cell uptake is mediated through the size and electrostatic charge conditions of the SPIO [300]. Further, loading can be augmented through the addition of cell-penetrating peptides, electroporation, or transfection agents [31, 208]. Conventionally, the nanoparticles are believed to have little effect on cell functionality and differentiation [88, 137]. The ability of stem cells to specifically home to tumors has suggested their use as delivery for cancer imaging and therapy. The mechanism underlying this process is not completely understood, although it is thought to involve the release of chemokines and other inflammatory chemoattractants in the tumor pathophysiological environment. Anderson et al. demonstrated the ability to monitor angiogenesis in a glioma model using labeled

stem cells injected intravenously. Bone marrow-derived stem cells (Sca+) with phenotypic characteristics of both hematopoietic and endothelial progenitors, were shown to migrate toward the tumor and incorporate in the tumor vasculature, attracted by angiogenic stimuli [16]. In another study, SPIO labeled mesenchymal stem cells have been demonstrated to specifically home to lung metastasis as monitored in vivo by MRI and confirmed by histology [197]. A major issue regarding the use of SPIO for cell labeling involves the contrast specificity to the presence of cells. Namely, the hypointense indication is maintained at a site regardless of transplanted cell survival. At longer time points, SPIO were found present not necessarily within implanted stem cells, but rather in phagocytosing monocytes following cell death [14]. These disadvantages of using SPIO as cell label are mitigated by a novel imaging technique called magnetic particle imaging. In MPI, there is no background signal in tissue, only in areas where SPIO are present a signal can be generated by magnetic gradient field changes [51]. With the increasing appreciation of the crucial role of macrophages in tumor biology, and the fact that nanoparticles preferentially accumulate in macrophages following intravenous administration, the use of SPIO and other nanoparticles for imaging of tumor-associated macrophages (TAM) has been explored [279]. In a study by Daldrup-Link et al., it was shown that the presence of TAM in breast cancer tumor models could be visualized following the systemic administration of SPIO. Shin et al. used Fluorine-19 containing nanoparticles to study the relationship between the presence of TAMs and tumor aggressiveness as assessed by ^{18}F -FDG PET [282]. They found that ^{19}F -MRI signal intensities were inversely correlated with ^{18}F -FDG uptake while being positively correlated with tumor growth. In addition to these findings, recent studies have also indicated that the functional state of TAM may be altered following nanoparticle uptake [260]. The functional change depends on both the original state of the TAM and the type of nanoparticle used. Further studies are needed to fully understand these effects and for potential use in cancer treatment strategies.

2.5.2.8 Gadofullerenes and Gadonanotubes

Fullerenes are molecules composed entirely of carbon with their atoms arranged in the form of a closed, endohedral cage, also called buckyballs or in a cylindrical form called carbon nanotubes. Endohedral gadofullerenes were initially attractive as a potential contrast agent for two reasons: the fullerene acts as a perfect chelate, preventing Gd^{3+} leakage in vivo and they demonstrate enhanced relaxivity compared to traditional MR contrast agent (20 times higher than Gd^{3+} -DTPA at 1T) [46, 213]. The anionic $\text{Gd}@C_{60}[\text{COOH}]$ has been used for labeling mammalian cells close to 100% efficiency. Gadofullerene-labeled cells have been reported to show a 250% increase of the T1 signal intensity of labeled cells versus unlabeled cells, suggesting its potential as a probe for in vivo tracking of cells by MRI [285]. However, low yields and difficult purification steps during synthesis together with high costs of synthesis reduced the practical applicability of gadofullerenes. Another class of carbon structures, defined gadonanotubes outperformed endohedral gadofullerenes and have been suggested as a new platform for molecular

imaging [218, 286]. Gd-³⁺-nanotubes are ultrashort carbon structures with an average length of 40 nm, obtained from fluorination and pyrolysis of full-length single-wall carbon nanotubes. These gadonanotubes have been found to have relaxivities nearly 40 times higher than those of current contrast agents measured at clinical field strength (20–60 MHz) [286]. Moreover, their relaxivity has been found to be pH dependent, exhibiting a dramatic increase when the pH changes from 7.4 to 7.0 suggesting their use as a probe to detect the lower pH environment of malignancies [127]. While these properties are beneficial for increasing detection sensitivity, broad application and clinical of these structures has been hampered by the issues regarding purification and standardization.

2.5.3 Targeted Probes

In targeted imaging, various strategies can be employed which can be subdivided into passive targeting strategies and active targeting strategies. Passive targeting strategies include the use of the enhanced permeability and retention (EPR) effect, already described in the previous section, and the selective uptake of nanoparticles by phagocytic cells, such as macrophages and Kupffer cells. Active targeting involves the use of a specific targeting ligand conjugated to the signaling probe. The targeting ligands can consist of antibodies [228], antibody fragments [347], proteins [55], peptides [187], peptidomimetics [47], aptamers [140], sugars [317], and small molecules [10] and may offer specific advantages or limitations regarding specificity, affinity, availability, immunogenicity, and stability. Various strategies have been used to target surface molecules on tumor cells as well as stromal cells. Examples of successful targeted imaging of such targets by MRI *in vivo* are listed in Table 2.3 and may offer specific advantages or limitations regarding specificity, affinity, availability, immunogenicity, and stability.

The most direct way to create a targeted imaging probe is by direct conjugation of the ligand to the signaling moiety. For monovalent complexes, several limitations are encountered for targeted MRI probes, *i.e.*, limited sensitivity, rapid clearance from the circulation, and low avidity. Strategies to circumvent these limitations involve the use of macromolecular contrast agents and nanoparticles (see also previous sections). Through these approaches higher payloads of the signaling part [222], longer circulation times [320] and improved target-binding capabilities [273] can be achieved. Recent technological advances in nanotechnology have even further widened the versatility of targeted imaging probes. The use of nanoparticle platforms do not only offer the earlier mentioned advantages but are now also being developed for the combination of signaling components suitable for imaging with different modalities [60] and/or the capability to simultaneously function as a carrier for therapeutics, thus combining targeted imaging with targeted drug delivery; an approach referred to as theranostics (or theragnostics) [283] as already referred to in previous sections and addressed in other chapters of this book.

Table 2.3 Examples of targeted imaging applications in oncology

Target	Ligand/probe	References
Breast cancer: HER2/neu	Anti-HER2 antibody (Herceptin®)/ Iron oxide nanoparticle	[59]
Somatostatin receptor	Somatostatin peptidomimetic (Octreotide)/Iron oxide nanoparticle	Li et al. [191]
Gastrin-releasing peptide receptors	DSPION-BBN/dextran-coated spin conjugated with bombesin	[142]
Carcinoma: folate receptor	Folate/Gd-dendrimer	Swanson et al. (2008)
Prostate cancer: Gastrin-releasing peptide receptor	Bombesin peptide/Iron oxide containing nanoparticle	[187]
Prostate-specific membrane antigen	ProCA32.PSMA/protein Gd(3+) contrast agent	[248]
Gliosarcoma: transferrin receptor	Transferrin protein/Iron oxide nanoparticle	Högemann-Savellano et al. [134]
Pancreatic cancer: epidermal growth factor receptor	Anti-EGFR antibody fragment/Iron oxide nanoparticle	[352]
Glioma:	Anti-iNOS antibody	Towner et al. [304]
Inducible nitric oxide synthase	Albumin-Gd-DTPA	
Lung cancer/endothelial cells:	Arginine–glycine–aspartic acid (RGD) peptide	Jiang et al. [144]
Alphavbeta3 integrin	Iron oxide nanoparticle	[350]
Folate receptor (FR)	FR-targeted perfluorocarbon nanoparticles	
Tumor-associated macrophages	Poly-L-glutamic acid/Gd-DTPA conjugated nanoparticle	Melancon et al. [212]
Endothelial cells (Glioma):	Anti-VEGFR2 antibody	Towner et al. [303]
Vascular endothelial growth factor receptor	Iron oxide nanoparticle	
Colorectal cancer: epithelial cell adhesion molecule	Anti-EpCAM-Gd-DTPA/single-chain variable antibody fragment	[158]

While the various strategies in targeted imaging show great promise in improving cancer diagnostics, prognostics, and treatment, significant hurdles in the application and clinical translation are still faced. Especially regarding issues on sensitivity, reproducibility, and regulatory requirements.

2.5.4 Responsive Probes

Increasing interest is directed at the development of so-called smart, responsive, or activatable probes in molecular imaging of cancer. Due to the importance of microenvironmental conditions in tumor development and response to treatment, there is a need to non-invasively assess these conditions. Responsive probes are designed to elicit a detectable change in signal upon the enzymatic activity or in response to specific biophysical conditions. Typical conditions to which responsive agents can be sensitive to are: pH, temperature, oxygen pressure, enzymatic activity, redox potential, and concentration of a specific ion. Due to the underlying mechanisms by which paramagnetic contrast agents exert their signaling properties, they are extremely suitable for generating responsive agents. We will only describe the basic concepts of these mechanisms by which agents can be made “responsive”. For more detailed explanations of these mechanisms, the reader is referred to specific textbooks or manuscripts on these subjects.

Paramagnetic agents exert their contrast effect by the exchange of water molecules. Water molecules linked to a paramagnetic molecule undergo efficient relaxation. Due to the fast exchange of linked molecules with surrounding bulk water molecules (millions per second), paramagnetic agents shorten the relaxation time of their surroundings. The efficiency by which a paramagnetic molecule increases the relaxation speed of their surroundings (relaxivity) is dependent on the molecular structure of the agent. The main molecular characteristics that influence the relaxation properties of paramagnetic agents are: the number of exchangeable water molecules linked to the agent, the speed by which these molecules can be exchanged and the motion dynamics of the molecule (molecular tumbling rate). Thus by manipulation of the molecular characteristics of paramagnetic agents, their relaxivity can be altered and thus probes can be made responsive to their physiological environment [354].

The majority of the studies on synthesizing such agents are still limited to concepts or in vitro studies. However, proof of principle has already been obtained in in vivo studies. Garcia-Martin et al. demonstrated the ability to create a pH map in a rat glioma tumor using a Gd-based pH-responsive agent [104]. For temperature-responsive probes, liposome-based paramagnetic nanoparticles seem to offer major benefits [179, 244]. Liposome composition can be adapted such that water exchange and molecular diffusion over the liposome membrane can be made temperature dependent. Through these techniques, hyperthermia-mediated drug delivery can be monitored.

Another application of responsive MRI probes that have shown significant progress is the design of enzyme-responsive agents. Various mechanisms can be employed whereby through enzymatic activity either the number or the exchange rate of exchangeable water molecules is manipulated or through manipulation of the tumbling rate of the paramagnetic agent. Moats et al. generated a Gd-based responsive agent sensitive to the activity of. In this approach, the Gd-ion is “caged” in a sugar moiety preventing water access to the Gd-ions. Upon cleavage of this sugar moiety by β -galactosidase, water exchange is restored and the relaxivity of

the agent increases [200, 217]. An alternative approach to a β -galactosidase responsive probe was published by Avena et al. using a Gd-based responsive probe that upon exposure to β -galactosidase formed Gd-Dota melanin oligomers and polymers with consequently increased proton relaxation effects [17]. Bogdanov et al. synthesized a peroxidase activatable monomer consisting of a Gd-chelate linked to benzene-1,2-diol. In the presence of peroxide, the monomers are oligomerized, yielding a threefold increase in relaxivity due to an increase in molecular tumbling rate [41]. This principle was used in vivo to monitor myeloperoxidase activity in animal models of aneurism and atherosclerotic plaques [67, 263]. Also bioresponsive T2-weighted probes have been explored. These approaches involve strategies to promote the clustering of iron oxide particles resulting in enhanced T2 relaxation. Due to the fact that the resulting effect is signal loss, this approach is very challenging to apply in vivo [241]. More recent approaches in the development of MRI bioresponsive probes involve the use of CEST-based agents [258, 284].

Some other examples of studies using MRI responsive agents for monitoring enzyme activity include: proteases [124], transglutaminase activity [297], β -glucuronidase [81], caspase-3 [355] glutamic acid decarboxylase [225], glutathione [192]. Many of the presented principles are reported to be adaptable to interrogate the activity of other enzymes.

In recognition of the needs for imaging probes that can report on specific tissue environmental conditions, various groups dedicate their entire research to the development and testing of responsive and molecular targeting MRI probes. A major challenge that is faced with responsive probes however, is the need for pre- and post-injection MRI scans to generate subtraction images and activity maps. Interpretation of data can be hampered by issues associated with image registration and alterations in tumor geometry over time.

2.5.5 Reporter Genes

The convergence of advancements in imaging technology and molecular/cell biology resulted in the mid-1990s in the development of reporter gene techniques for in vivo application. The capability to noninvasively reveal insights into molecular-genetic processes in vivo, the potential use in cell tracking (stem cells, targeted lymphocytes, etc.) and monitoring of gene therapy are areas of major benefit with this approach. Reporter gene approaches have been widely used for in vivo application in bioluminescence imaging (e.g., luciferase), but have also been developed for nuclear medicine (e.g., HSV1-tk), and magnetic resonance imaging (MRI) applications.

The reporter gene paradigm requires the appropriate combination of a reporter transgene and a reporter probe, such that the reporter gene product has to interact with an exogenous/endogenous imaging probe (optical, nuclear, magnetic) and following this interaction, detection of the signal with the corresponding imaging modality. The first step is to generate a reporter system in the cells. Here, the cDNA

expression cassette containing the reporter gene is introduced into the cell of interest through transfection mediated by a vector. While there is a variety of choices for vectors and transfection agents (retrovirus, adenovirus, lentivirus, liposomes, etc.) it should be noted that the ability to image transgene expression is largely independent of the method.

Currently, MR reporter genes can be chosen to encode for (a) proteins that are expressed on the cell surface to allow or increase probe uptake (e.g., transferrin receptor); (b) proteins that bind and thus accumulate the probe (e.g., ferritin); (c) enzymes that biochemically activate/modify the probe (e.g., β -galactosidase, tyrosinase); (d) genes that encode for proteins that can be detected directly with imaging techniques (e.g., MagA) (Fig. 2.19).

2.5.5.1 Transferrin Receptor Reporter Gene

In the bloodstream, iron is bound to the plasma protein transferrin (Tf) and enters the cells through interaction with the transferrin receptor (TfR). Upon binding, the TfR-Tf complex is internalized, dissociated in acidic endosomes and iron is released. One of the first attempts to use human TfR as a reporter gene was described by Koretsky et al., in this work transfected fibroblasts overexpressing TfR exhibited a threefold increase in iron levels, therefore a 20% reduced MR signal intensity in T2-weighted images [169]. To amplify the MR signal, the overexpression of an engineered TfR, lacking the feedback down-regulation of receptor expression in response to iron uptake, has been combined with the administration of transferrin covalently conjugated with monocrystalline iron oxide (Tf-MION) as an exogenous probe. In tumors grown from tumor cells transfected with the engineered TfR, a significant increase in iron accumulation was obtained. Importantly, the MR signal correlated to the cellular Tf-MION concentrations and the TfR expression

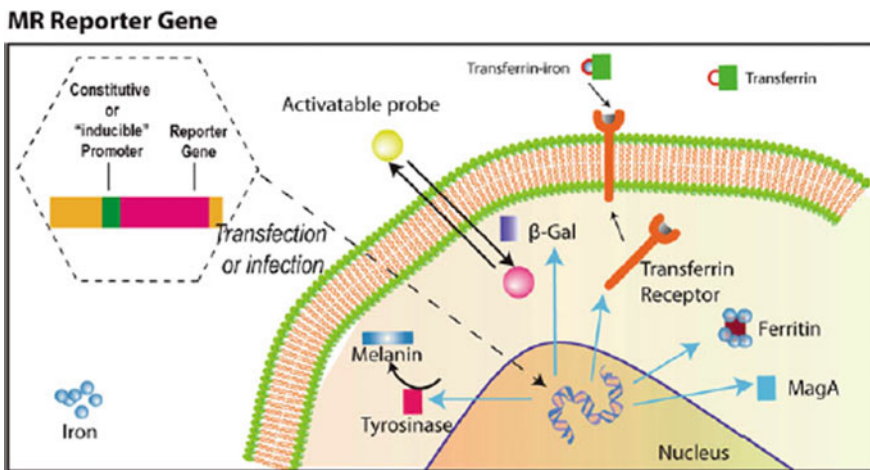


Fig. 2.19 Illustration of the most common reporter gene for MR and their corresponding probe

[221, 337]. Due to the low efficiency of the TfR as signal reporter and concerns regarding effects on cells iron homeostasis has limited use of this technology [239].

2.5.5.2 Ferritin Reporter Gene

Ferritin, the major intracellular iron-binding protein that serves as the body's iron depot, has been used as a candidate MRI reporter gene. Ferritin comprises 24 subunits that are heavy (H-ferritin) and light chains (L-Ferritin) and can sequester up to 4000 Fe^{3+} atoms. The feasibility of this approach has been tested in C6 rat glioma [61] by overexpressing H-ferritin under a conditional tetracycline promoter (*tet-hfer*), allowing the expression of the reporter gene to be switched "on" and "off" upon the administration of tetracycline (Fig. 2.20). H-ferritin overexpression resulted in the up-regulation of the transferrin receptor, increased iron uptake, and therefore shortening of T1 and T2 relaxation times. Recently, the generation of a *tet-hfer* transgenic mice in which the overexpression of hemagglutinin-tagged ferritin and EGFP is under tetracycline regulation has been reported [62]. These animals, lacking the tetracycline transactivator (tTA) do not express the transgene, however, when mated with mice expressing tTA driven by a promoter of interest, the progeny expresses the reporter gene in those cells in which the promoter is active. By crossing the *tet-hfer* mice with mice expressing tTA under regulation of VE-cadherin or liver-associated proteins, overexpression of H-ferritin was detected with MRI in sparse endothelial cells or hepatocytes, respectively [62]. Genove et al. reported the use of a replication-defective adenovirus to deliver in vivo the ferritin transgenes (both heavy and light chains). Following the focal inoculation of the viral vector into the mouse brain, the reporter activity was measured by time-lapse MRI. Robust contrast in virus-transduced neurons and glia was observed for several weeks [108] (Fig. 2.21). Thereafter, a combined reporter system of TfR overexpression and H-ferritin in a mouse neural stem cell line increased iron accumulation in the supplemented iron environment and signal loss on T2-weighted and T2*-weighted images [68]. Ferritin-based reporter imaging is still used in studies for tracking transplanted stem cells, although issues regarding sensitivity, toxicity, and specificity of the signal limit widespread application [361].

2.5.5.3 Tyrosinase MR Reporter Gene

Melanotic melanomas, unlike the majority of tumors, appear hyperintense on T1-weighted images. This effect is related to the high affinity and binding capacity of melanin, a polymeric pigment, for metal ions [85]. Overexpression of tyrosinase has been considered as a potential approach to increase the cellular accumulation of iron to generate contrast for MRI application. Tyrosinase catalyzes the hydroxylation of tyrosine to dioxyphenylalanine (DOPA) and its subsequent oxidation to DOPAquinone. DOPAquinone is then converted to melanin.

The transfection of mouse fibroblast and human embryonic kidney with a vector encoding for constitutive expression of human tyrosinase gave elevated levels of tyrosinase mRNA, higher melanin production and higher metal-binding capacity, therefore enhanced MR signal intensity [338].

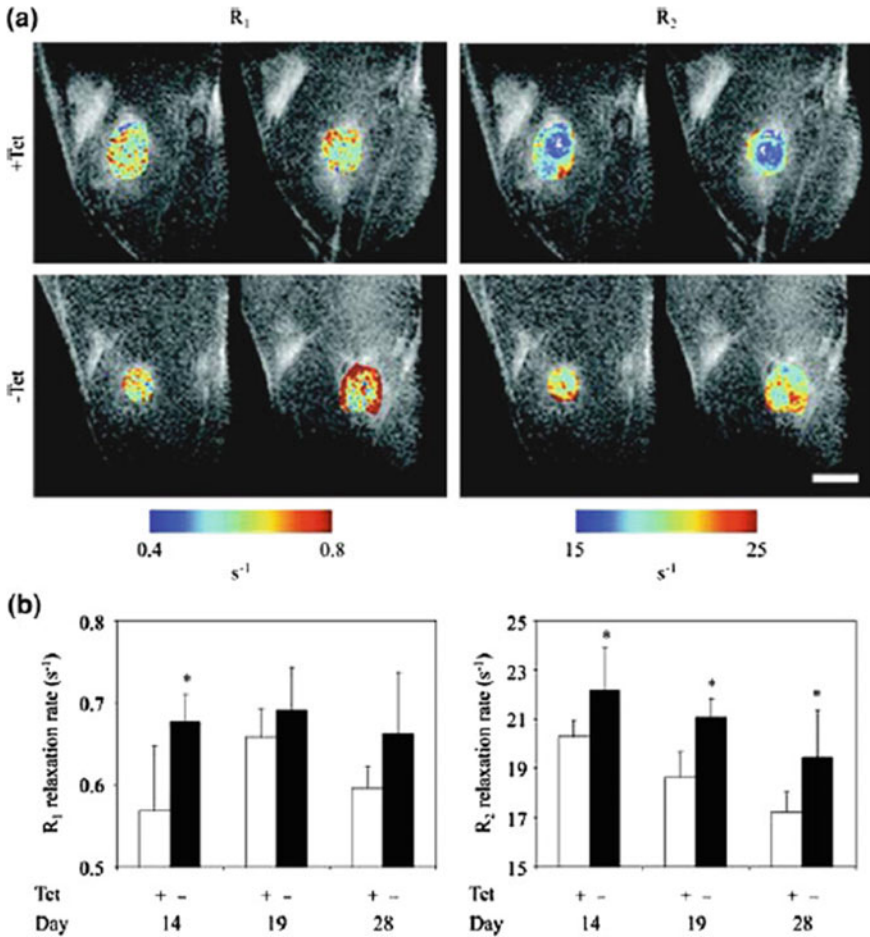


Fig. 2.20 In vivo detection of ferritin in C6 cells transfected with the “inducible” reporter gene TET-EGFP-ferritin implanted in the hind limb of a nude mice. **a** R₁ and R₂ maps of tumor regions overlaid on the MR images are shown for two representative mice from each group. **b** R₁ and R₂ values (mean ± SD) at the tumor region in the presence (ferritin off) or absence (ferritin on) of TET in drinking water at 14, 19, and 28 days after tumor inoculation (Reprinted by permission from Neoplasia: [61])

This approach was further explored in breast cancer cells transfected with a human tyrosinase reporter gene under control of the tetracycline response element which allowed the suppression of gene expression by adding doxycycline to the medium. Cells cultured with doxycycline showed no background expression of the human tyrosinase gene, whereas withdrawal of doxycycline resulted in detectable tyrosinase messenger RNA expression. Induction of tyrosinase expression resulted in T1 shortening in vitro after culture in the iron-enriched medium. Since melanin is

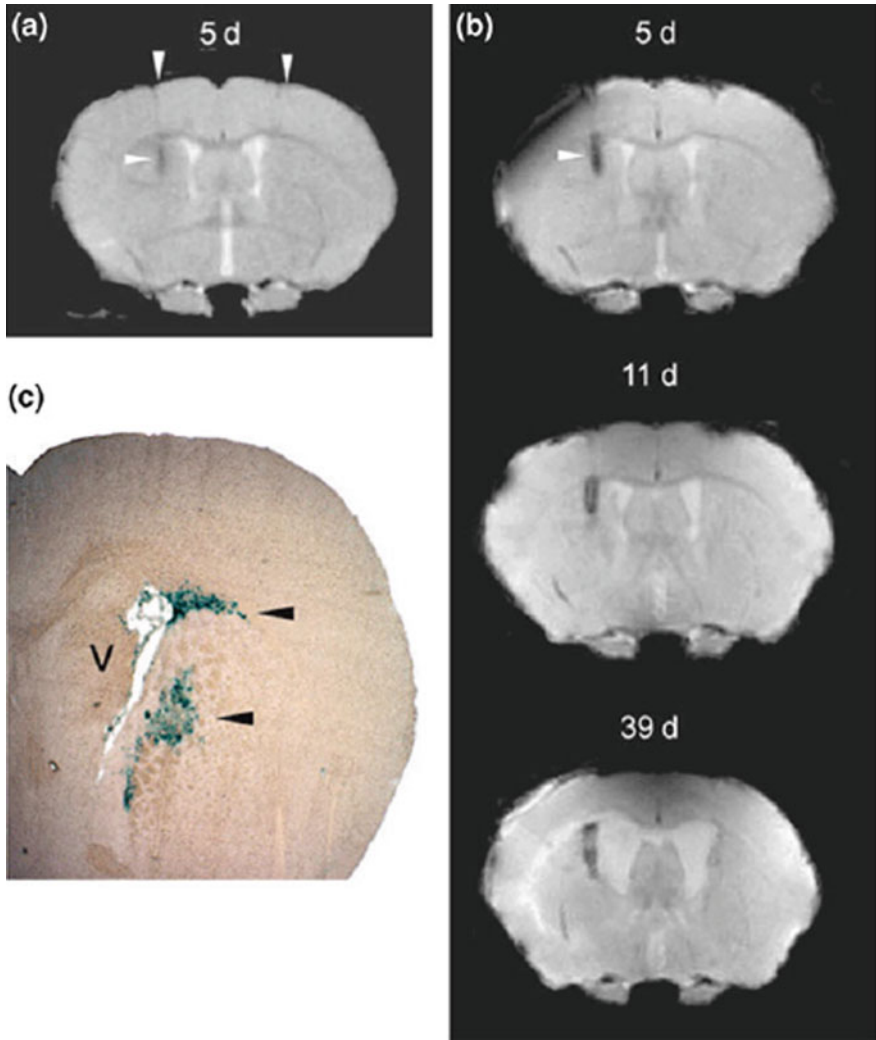


Fig. 2.21 MRI detection of in vivo delivery of ferritin transgene by using a replication-defective adenovirus. **a** T2-w image 5 days after injection showing the inoculated sites (*left arrows*, MRI reporter; *right arrow*, AdV-lacZ control). **b** X-gal-stained AdV-LacZ transduction pattern at 5 d after inoculation (Reprinted by permission from Macmillan Publishers Ltd.: [108])

a highly stable molecule, MR contrast is preserved for a considerable time interval after switching off tyrosinase expression [8]. However, since melanin and its precursors in catalyzing and binding iron produce reactive oxygen species, this approach may exhibit significant toxic effects and thus limit its application [110, 111].

2.5.5.4 β -Galactosidase and MagA Reporter Gene

Another enzyme explored for MR imaging is β -galactosidase (β -gal), the LacZ gene product of *Escherichia coli* [148] responsible for the hydrolysis of lactose and other β -galactosides to monosaccharides. B-gal possesses broad substrate specificity and several colored or fluorescent products are candidates for cleavage, therefore it is a marker frequently used in molecular biology assays and microscopy. The use of β -gal as an MR reporter gene was demonstrated by designing “activatable” gadolinium-based MR contrast agents, such as (1-(2-(β -Galactopyranosyloxy)propyl)-4,7,10-tris(carboxymethyl)-1,4,7,10 tetraazacyclododecane) gadolinium(III) (abbreviated as EGadMe) a modified sugar substrate containing a gadolinium chelate [200]. It consists of a (1) high-affinity chelator that occupies eight of the nine coordination sites on Gd^{3+} and (2) a galactopyranose residue positioned to block the remaining coordination site on Gd^{3+} from water access. In the absence of β -Gal, EGadMe is uncleaved and Gd^{3+} is in a water-inaccessible conformation; its T1 relaxivity is low because the primary contribution is only from the outer sphere water. In the presence of β -gal, the galactopyranose is enzymatically cleaved from EGadMe, freeing one coordination site, leading to water’s proton increased access to Gd^{3+} , resulting in inner sphere relaxation enhancement and therefore an increase in the T1 relaxivity (higher MR contrast in T1-weighted images). This change in T1 relaxivity can be used for measuring the activity of β -Gal by MRI. The main limitation of this approach is the low cleavage rate of EGadMe and its rapid renal clearance. Alternative approaches using other paramagnetic complexes may overcome this limitation [119, 357].

A set of gram-negative bacteria, defined as magnetotactic, exhibit motility thought to be directed by the earth’s magnetic field. They naturally synthesize intracellular structures, known as magnetosomes, tiny magnets that can affect the MR signal, similarly to SPIO nanoparticles. It is likely that multiple genes are involved in the production of these magnetosomes. Recently, *magA*, a gene from *Magnetospirillum Magneticum* known to be involved with iron transport, has been transfected and expressed in a ^{293}FT human cell line, resulting in the production of magnetic, iron oxide nanoparticles and increased transverse relaxivity. This work showed that magnetic particles can be formed in vivo utilizing endogenous iron and can be used to visualize cells positive for *magA*. This approach generates readily detectable MR contrast, and it has been used as a MR reporter in vitro and in vivo [369] (Fig. 2.22). While initially received with enthusiasm, *magA* reporter gene technology has also been associated with cellular toxicity limiting broad applicability [240].

2.5.5.5 Alternate Approaches

Also, alternate approaches from the ones listed above have been explored. These include reporter genes using contrast mechanisms based on chemical exchange saturation transfer (CEST) and magnetic resonance spectroscopy (MRS).

CEST contrast relies on the magnetization transfer that occurs between the bulk water protons and macromolecular protons. The contrast produced by CEST-agents can be switched on and off by selectively irradiating (saturating) at the

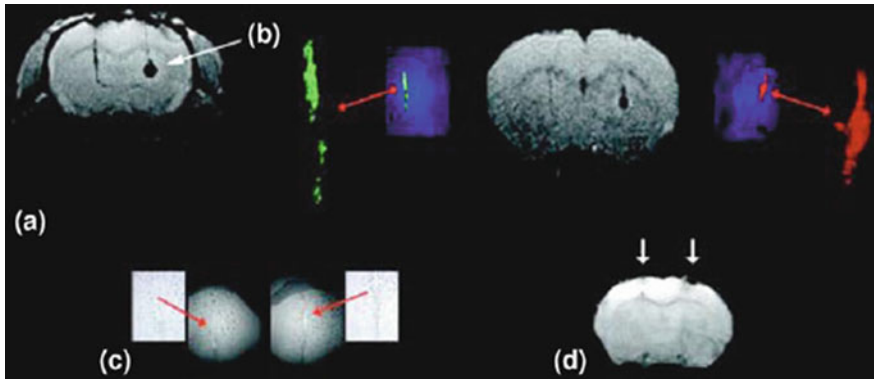


Fig. 2.22 Detection of the gene MagA in a mouse brain. **a** T2*-weighted image of mouse brain with transplanted magA cells (white arrow) (right) and GFP control cells (left) after 5 d of induction. **a** T2-w image of the same mouse brain showing, although with lower sensitivity, the presence of cells. Histology confirms the presence of control (green) and magA positive cells (red) (Reprinted by permission from John Wiley and Sons: [369])

exchangeable proton-resonance frequency of the target molecule. Images obtained with and without the RF saturating pulse reveal the location of the specific molecule or CEST agent. Gilad et al. tested the possibility to create a nonmetallic biodegradable reporter by constructing a gene encoding for an artificial lysine-rich protein (LRP). The lysine-rich protein functions as a “natural” in vivo CEST reporter, and was shown to provide excitation frequency dependent contrast in LRP-expressing xenografts in mouse brain [110, 111]. This approach is of particular interest since the contrast properties are switchable and tunable, resulting in the elimination of background signals the potential for “multicolor” imaging through the use of reporter gene products having different proton frequencies.

MRS can provide useful information regarding the metabolic state, viability, and also cell localization by using a dedicated MRS reporter gene. Creatine kinase (CK) and arginine kinase (AK) are a family of enzymes that catalyze the exchange of phosphate between ATP and creatine (Cr) and arginine (Arg), and therefore are detectable with ^{31}P MRS. In 1989, a reporter gene was investigated for MRS for the first time. CK activity was measured by ^{31}P MRS in *Escherichia coli* [168] and subsequently in the liver of a transgenic mouse [168].

High concentrations of phosphocreatine were detectable in the NMR spectra compared to controls. Subsequent studies used these approaches to monitor viral gene transfer by ^{31}P MRS using CK [20] or AK [330] constructs as reporter genes. For AK special benefits were suggested since AK is not naturally present in vertebrate cells thus PArg accumulates only in cells where the transgenic gene is located, therefore no background is detected and there is no need for an external probe.

Another potential use of the MRS reporter is based on the in vivo monitoring of the catalytic conversion of a pro-drug into an “active” drug. Stegman et al.

demonstrated the *in vivo* quantification of yeast cytosine deaminase (yCD) expression in HT29 colon carcinoma xenografts based on the catalyzed conversion of the nontoxic 5-fluorocytosine (5-FC) pro-drug into the chemotherapeutic agent 5-Fluorouracil (5-FU), as measured by ^{19}F MRS [293].

A brief overview of the various reporter gene approaches and their basic principles and limitations is given in the Table 2.4.

Table 2.4 Overview of various MRI reporter gene strategies

Reporter Gene	Probe	Contrast	Advantages	Disadvantages
Transferrin receptor	Transferrin conjugated with monocrystalline iron oxide (Tf-MION)	T2/T2*	High sensitivity	Aspecific uptake of the probe
Ferritin	Endogenous or exogenous iron	T2/T2*	High sensitivity	MR signal depends on iron loading factor. Persistence of signal void after cell death, until ferritin-based nanoparticles are degraded in lysosomes and further metabolized
MagA	Endogenous or exogenous iron	T2/T2*	High sensitivity	Potential immunogenicity
β -Gal	Exogenous probe (such as EgadMe)	T1	Increased signal	Background signal due to aspecific activation of the probe
Tyrosinase	Endogenous or exogenous iron	T1; T2/T2*	Since melanin is a highly stable molecule, MR contrast is preserved for a considerable time	Melanin and its precursor catalyzing and binding iron produce reactive oxygen species that may exhibit significant toxic effects
LRP	None	MRS	Signal switchable and simultaneous imaging of multiple targets (multicolor)	Low sensitivity with current techniques
CK	ATP	^{31}P MRS	No background	Low resolution (spectroscopy)
yCD	5-FC	^{19}F X MRS	No background	Low resolution (spectroscopy)

2.6 Future Perspectives

Because of their high-resolution deep tissue imaging capabilities and currently rapid advances are being made in transforming CT and MRI/MRS remain interesting modalities for molecular imaging applications. The classic limitations regarding detection sensitivity and monospectral (visualization of one single probe within the same object) capabilities are still hurdles to overcome in some applications. Concurrent developments in hardware, software, and innovative imaging probes keep improving the possibilities and applications. Also the implementation of the innovative (concepts of) imaging probes still face specific challenges in getting to an agent in which optimized characteristics regarding specificity, sensitivity, biocompatibility and biodistribution, and larger scale production are all fulfilled. This will require combined efforts from different platforms in academics, industry, and legislative and regulatory bodies.

References

1. Abascal JF, Montesinos P, Marinetto E et al (2014) Comparison of total variation with a motion estimation based sensing approach for self-gated cardiac cine MRI in small animal studies. *PLoS ONE* 9(10):e110594
2. Abdel Razeq AA, Gaballa G, Ashamalla G et al (2015) Dynamic susceptibility contrast perfusion-weighted magnetic resonance imaging and diffusion-weighted magnetic resonance imaging in differentiating recurrent head and neck cancer from postradiation changes. *J Comput Assist Tomogr* 39(6):849–854
3. Abdel Razeq AA, Gaballa G, Denewer A et al (2010) Diffusion weighted MR imaging of the breast. *Acad Radiol* 17(3):382–386
4. Adams LC, Bressemer K, Boker SM et al (2017) Diagnostic performance of susceptibility-weighted magnetic resonance imaging for the detection of calcifications: a systematic review and meta-analysis. *Sci Rep* 7(1):15506
5. Aime S, Delli Castelli D, Lawson D et al (2007) Gd-loaded liposomes as T1, susceptibility, and CEST agents, all in one. *J Am Chem Soc* 129(9):2430–2431
6. Aime S, Botta M, Gianolio E et al (2000) A p(O₂)-responsive MRI contrast agent based on the redox switch of manganese(ii/iii)—porphyrin complexes. *Angewandte Chemie (International ed)* 39(4):747–750
7. Aime S, Delli Castelli D, Terreno E (2005) Highly sensitive mri chemical exchange saturation transfer agents using liposomes. *Angewandte Chemie (International ed)* 44(34):5513–5515
8. Alfke H, Stoppler H, Nocken F et al (2003) In vitro MR imaging of regulated gene expression. *Radiology* 228(2):488–492
9. Alibek S, Vogel M, Sun W et al (2014) Acoustic noise reduction in MRI using silent scan: an initial experience. *Diagn Interv Radiol*. 20(4):360–363
10. Allen MJ, Meade TJ (2003) Synthesis and visualization of a membrane-permeable MRI contrast agent. *J Biol Inorg Chem* 8(7):746–750
11. Allen-Auerbach M, Weber WA (2009) Measuring response with FDG-pet: methodological aspects. *Oncologist* 14(4):369–377
12. Alsop DC, Detre JA, Golay X et al (2015) Recommended implementation of arterial spin-labeled perfusion MRI for clinical applications: a consensus of the ISMRM perfusion study group and the European consortium for ASL in dementia. *Magn Reson Med* 73(1):102–116

13. Ambrose J, Hounsfield G (1973) Computerized transverse axial tomography. *Br J Radiol* 46 (542):148–149
14. Amsalem Y, Mardor Y, Feinberg MS et al (2007) Iron-oxide labeling and outcome of transplanted mesenchymal stem cells in the infarcted myocardium. *Circulation* 116(11 Suppl):I38–I45
15. Anderson NG, Butler AP, Scott NJ et al (2010) Spectroscopic (multi-energy) CT distinguishes iodine and barium contrast material in mice. *Eur Radiol* 20(9):2126–2134
16. Anderson SA, Glod J, Arbab AS et al (2005) Noninvasive MR imaging of magnetically labeled stem cells to directly identify neovasculature in a glioma model. *Blood* 105(1):420–425
17. Arena F, Singh JB, Gianolio E et al (2011) Beta-gal gene expression MRI reporter in melanoma tumor cells. Design, synthesis, and in vitro and in vivo testing of a Gd(III) containing probe forming a high relaxivity, melanin-like structure upon beta-gal enzymatic activation. *Bioconjug Chem* 22(12):2625–2635
18. Artemov D, Solaiyappan M, Bhujwala ZM (2001) Magnetic resonance pharmacangiography to detect and predict chemotherapy delivery to solid tumors. *Can Res* 61(7):3039–3044
19. Artzi M, Bokstein F, Blumenthal DT et al (2014) Differentiation between vasogenic-edema versus tumor-infiltrative area in patients with glioblastoma during bevacizumab therapy: a longitudinal MRI study. *Eur J Radiol* 83(7):1250–1256
20. Auricchio A, Zhou R, Wilson JM et al (2001) In vivo detection of gene expression in liver by ³¹P nuclear magnetic resonance spectroscopy employing creatine kinase as a marker gene. *Proc Natl Acad Sci USA* 98(9):5205–5210
21. Baraniuk RG (2007) Compressive sensing [lecture notes]. *IEEE Signal Process Mag* 24 (4):118–121
22. Barrett T, Kobayashi H, Brechbiel M et al (2006) Macromolecular MRI contrast agents for imaging tumor angiogenesis. *Eur J Radiol* 60(3):353–366
23. Baudrexel S, Nurnberger L, Rub U et al (2010) Quantitative mapping of T1 and T2* discloses nigral and brainstem pathology in early Parkinson's disease. *NeuroImage* 51 (2):512–520
24. Bauman G, Johnson KM, Bell LC et al (2015) Three-dimensional pulmonary perfusion MRI with radial ultrashort echo time and spatial-temporal constrained reconstruction. *Magn Reson Med* 73(2):555–564
25. Beister M, Kolditz D, Kalender WA (2012) Iterative reconstruction methods in x-ray CT. *Phys Med* 28(2):94–108
26. Bellin MF (2006) MR contrast agents, the old and the new. *Eur J Radiol* 60(3):314–323
27. Belouche-Babari M, Chung YL, Al-Saffar NM et al (2010) Metabolic assessment of the action of targeted cancer therapeutics using magnetic resonance spectroscopy. *Br J Cancer* 102(1):1–7
28. Belouche-Babari M, Chung YL, Al-Saffar NM et al (2010) Metabolic assessment of the action of targeted cancer therapeutics using magnetic resonance spectroscopy. *Br J Cancer* 102(1):1–7
29. Bernsen MR, Guenoun J, van Tiel ST et al (2015) Nanoparticles and clinically applicable cell tracking. *Br J Radiol* 88(1054):20150375
30. Bernsen MR, Kooiman K, Segbers M et al (2015) Biomarkers in preclinical cancer imaging. *Eur J Nucl Med Mol Imaging* 42(4):579–596
31. Bernsen MR, Moelker AD, Wielopolski PA et al (2010) Labelling of mammalian cells for visualisation by MRI. *Eur Radiol* 20(2):255–274
32. Bertini I, Bianchini F, Calorini L et al (2004) Persistent contrast enhancement by sterically stabilized paramagnetic liposomes in murine melanoma. *Magn Reson Med* 52(3):669–672
33. Beyhan M, Sade R, Koc E et al (2018) The evaluation of prostate lesions with IVIM DWI and MR perfusion parameters at 3T MRI. *Radiol Med*

34. Bianchi A, Lux F, Tillement O et al (2013) Contrast enhanced lung MRI in mice using ultra-short echo time radial imaging and intratracheally administrated Gd-dota-based nanoparticles. *Magn Reson Med* 70(5):1419–1426
35. Bison SM, Haeck JC, Bol K et al (2015) Optimization of combined temozolomide and peptide receptor radionuclide therapy (PRRT) in mice after multimodality molecular imaging studies. *EJNMMI Res* 5(1):62
36. Blaimer M, Breuer F, Mueller M et al (2004) Smash, sense, pils, grappa: how to choose the optimal method. *Top Magn Reson Imaging* 15(4):223–236
37. Blankenberg FG, Levashova Z, Sarkar SK et al (2010) Noninvasive assessment of tumor VEGF receptors in response to treatment with pazopanib: a molecular imaging study. *Transl Oncol* 3(1):56–64
38. Bloch FHWPEM (1946) Nuclear induction. *Phys Rev* 69:460–474
39. Boada FE, Tanase C, Davis D et al (2004) Non-invasive assessment of tumor proliferation using triple quantum filtered ^{23}Na mri: technical challenges and solutions. *Conf Proc IEEE Eng Med Biol Soc.* 7:5238–5241
40. Boehm-Sturm P, Haeckel A, Hauptmann R et al (2018) Low-molecular-weight iron chelates may be an alternative to gadolinium-based contrast agents for T1-weighted contrast-enhanced mr imaging. *Radiology* 286(2):537–546
41. Bogdanov A Jr, Matuszewski L, Bremer C et al (2002) Oligomerization of paramagnetic substrates result in signal amplification and can be used for mr imaging of molecular targets. *Mol Imaging* 1(1):16–23
42. Bohndiek SE, Brindle KM (2010) Imaging and ‘omic’ methods for the molecular diagnosis of cancer. *Expert Rev Mol Diagn* 10(4):417–434
43. Bol K, Haeck JC, Groen HC et al (2013) Can DCE-MRI explain the heterogeneity in radioligand uptake imaged by SPECT in a pancreatic neuroendocrine tumor model? *PLoS ONE* 8(10):e77076
44. Bolan PJ, Nelson MT, Yee D et al (2005) Imaging in breast cancer: magnetic resonance spectroscopy. *Breast Cancer Res* 7(4):149–152
45. Boll DT, Merkle EM, Paulson EK et al (2008) Calcified vascular plaque specimens: assessment with cardiac dual-energy multidetector ct in anthropomorphically moving heart phantom. *Radiology* 249(1):119–126
46. Bolskar RD, Benedetto AF, Husebo LO et al (2003) First soluble M@C60 derivatives provide enhanced access to metallofullerenes and permit in vivo evaluation of Gd@C60[C(COOH) $_2$] $_{10}$ as a MRI contrast agent. *J Am Chem Soc* 125(18):5471–5478
47. Boutry S, Burtea C, Laurent S et al (2005) Magnetic resonance imaging of inflammation with a specific selectin-targeted contrast agent. *Magn Reson Med* 53(4):800–807
48. Boxerman JL, Ellingson BM, Jeyapalan S et al (2017) Longitudinal DSC-MRI for distinguishing tumor recurrence from pseudoprogression in patients with a high-grade glioma. *Am J Clin Oncol* 40(3):228–234
49. Brix G, Semmler W, Port R et al (1991) Pharmacokinetic parameters in CNS Gd-DTPA enhanced mr imaging. *J Comput Assist Tomogr* 15(4):621–628
50. Broeke NC, Peterson J, Lee J et al (2018) Characterization of clinical human prostate cancer lesions using 3.0-T sodium MRI registered to gleason-graded whole-mount histopathology. *J Magn Reson Imaging*
51. Bulte JWM (2018) Superparamagnetic iron oxides as MPI tracers: a primer and review of early applications. *Adv Drug Deliv Rev*
52. Calmon R, Puget S, Varlet P et al (2018) Cerebral blood flow changes after radiation therapy identifies pseudoprogression in diffuse intrinsic pontine gliomas. *Neuro Oncol* 20(7):994–1002
53. Candes EJ, Romberg J, Tao T (2006) Robust uncertainty principles: exact signal reconstruction from highly incomplete frequency information. *IEEE Trans Inf Theory* 52(2):489–509

54. Cao Y (2011) The promise of dynamic contrast-enhanced imaging in radiation therapy. *Semin Radiat Oncol* 21(2):147–156
55. Caravan P (2009) Protein-targeted gadolinium-based magnetic resonance imaging (MRI) contrast agents: design and mechanism of action. *Acc Chem Res* 42(7):851–862
56. Caride VJ, Sostman HD, Winchell RJ et al (1984) Relaxation enhancement using liposomes carrying paramagnetic species. *Magn Reson Imaging* 2(2):107–112
57. Chang PD, Malone HR, Bowden SG et al (2017) A multiparametric model for mapping cellularity in glioblastoma using radiographically localized biopsies. *AJNR Am J Neuro-radiol* 38(5):890–898
58. Charnley N, Donaldson S, Price P (2009) Imaging angiogenesis. *Methods Mol Biol (Clifton, NJ)* 467:25–51
59. Chen LQ, Howison CM, Jeffery JJ et al (2014) Evaluations of extracellular pH within in vivo tumors using acidocestr mri. *Magn Reson Med* 72(5):1408–1417
60. Cheon J, Lee JH (2008) Synergistically integrated nanoparticles as multimodal probes for nanobiotechnology. *Acc Chem Res* 41(12):1630–1640
61. Cohen B, Dafni H, Meir G et al (2005) Ferritin as an endogenous MRI reporter for noninvasive imaging of gene expression in C6 glioma tumors. *Neoplasia* 7(2):109–117
62. Cohen B, Ziv K, Plaks V et al (2007) MRI detection of transcriptional regulation of gene expression in transgenic mice. *Nat Med* 13(4):498–503
63. Coupe P, Yger P, Prima S et al (2008) An optimized blockwise nonlocal means denoising filter for 3-D magnetic resonance images. *IEEE Trans Med Imaging* 27(4):425–441
64. Cyran CC, Fu Y, Raatschen HJ et al (2008) New macromolecular polymeric MRI contrast agents for application in the differentiation of cancer from benign soft tissues. *J Magn Reson Imaging* 27(3):581–589
65. Daldrup H, Shames DM, Wendland M et al (1998) Correlation of dynamic contrast-enhanced mr imaging with histologic tumor grade: comparison of macromolecular and small-molecular contrast media. *AJR Am J Roentgenol* 171(4):941–949
66. DeClerck K, Elble RC (2010) The role of hypoxia and acidosis in promoting metastasis and resistance to chemotherapy. *Front Biosci* 15:213–225
67. DeLeo MJ 3rd, Gounis MJ, Hong B et al (2009) Carotid artery brain aneurysm model: in vivo molecular enzyme-specific mr imaging of active inflammation in a pilot study. *Radiology* 252(3):696–703
68. Deans AE, Wadghiri YZ, Bernas LM et al (2006) Cellular MRI contrast via coexpression of transferrin receptor and ferritin. *Magn Reson Med* 56(1):51–59
69. Deng CX, Exner A (2010) Image-guided therapeutics. *Mol Pharm* 7(1):1–2
70. Deoni SC, Peters TM, Rutt BK (2005) High-resolution T1 and T2 mapping of the brain in a clinically acceptable time with DESPOT1 and DESPOT2. *Magn Reson Med* 53(1):237–241
71. Deoni SC, Williams SC, Jezzard P et al (2008) Standardized structural magnetic resonance imaging in multicentre studies using quantitative T1 and T2 imaging at 1.5 T. *NeuroImage* 40(2):662–671
72. Deshmane A, Gulani V, Griswold MA et al (2012) Parallel MR imaging. *J Magn Reson Imaging* 36(1):55–72
73. Desser TS, Rubin DL, Muller HH et al (1994) Dynamics of tumor imaging with Gd-DTPA-polyethylene glycol polymers: dependence on molecular weight. *J Magn Reson Imaging* 4(3):467–472
74. Devoisselle JM, Vion-Dury J, Galons JP et al (1988) Entrapment of gadolinium-DTPA in liposomes. Characterization of vesicles by P-31 NMR spectroscopy. *Invest Radiol* 23(10):719–724
75. Dhermain F, Saliou G, Parker F et al (2010) Microvascular leakage and contrast enhancement as prognostic factors for recurrence in unfavorable low-grade gliomas. *J Neurooncol* 97(1):81–88
76. Dighe M, Chaturvedi A, Lee JH et al (2008) Staging of gynecologic malignancies. *Ultrasound Q* 24(3):181–194

77. Dimitrakopoulou-Strauss A, Pan L, Strauss LG (2012) Quantitative approaches of dynamic FDG-pet and pet/CT studies (DPET/CT) for the evaluation of oncological patients. *Cancer Imaging* 12:283–289
78. Dinis Fernandes C, van Houdt PJ, Heijmink S et al (2018) Quantitative 3T multiparametric MRI of benign and malignant prostatic tissue in patients with and without local recurrent prostate cancer after external-beam radiation therapy. *J Magn Reson Imaging*
79. Dong Y, Eskandari R, Ray C et al (2019) Hyperpolarized MRI visualizes warburg effects and predicts treatment response to MTOR inhibitors in patient-derived CCRCC xenograft models. *Can Res* 79(1):242–250
80. Donoho DL (2006) Compressed sensing. *IEEE Inf Theory Soc* 52(4):1289–1306
81. Duimstra JA, Femia FJ, Meade TJ (2005) A gadolinium chelate for detection of beta-glucuronidase: a self-immolative approach. *J Am Chem Soc* 127(37):12847–12855
82. Dyke JP, Panicek DM, Healey JH et al (2003) Osteogenic and Ewing sarcomas: estimation of necrotic fraction during induction chemotherapy with dynamic contrast-enhanced mr imaging. *Radiology* 228(1):271–278
83. Edmund JM, Nyholm T (2017) A review of substitute ct generation for MRI-only radiation therapy. *Radiat Oncol* 12(1):28
84. Eisenhauer EA, Therasse P, Bogaerts J et al (2009) New response evaluation criteria in solid tumours: revised RECIST guideline (version 1.1). *Eur J Cancer* 45(2):228–247
85. Enochs WS, Petherick P, Bogdanova A et al (1997) Paramagnetic metal scavenging by melanin: MR imaging. *Radiology* 204(2):417–423
86. Erlemann R, Sciuk J, Bosse A et al (1990) Response of osteosarcoma and Ewing sarcoma to preoperative chemotherapy: assessment with dynamic and static MR imaging and skeletal scintigraphy. *Radiology* 175(3):791–796
87. Esmaeili E, Khalili M, Sohi AN et al (2018) Dendrimer functionalized magnetic nanoparticles as a promising platform for localized hyperthermia and magnetic resonance imaging diagnosis. *J Cell Physiol*
88. Farrell E, Wielopolski P, Pavljasevic P et al (2009) Cell labelling with superparamagnetic iron oxide has no effect on chondrocyte behaviour. *Osteoarthritis Cartilage* 17(7):961–967
89. Fathi Kazerooni A, Nabil M, Zeinali Zadeh M et al (2018) Characterization of active and infiltrative tumorous subregions from normal tissue in brain gliomas using multiparametric MRI. *J Magn Reson Imaging* 48(4):938–950
90. Ferrauto G, Di Gregorio E, Ruzza M et al (2017) Enzyme-responsive lipocest agents: assessment of MMP-2 activity by measuring the intra-liposomal water (1) h NMR shift. *Angewandte Chemie (International ed)* 56(40):12170–12173
91. Fischer MA, Nanz D, Hany T et al (2010) Diagnostic accuracy of whole-body MRI/DWI image fusion for detection of malignant tumours: a comparison with PET/CT. *Eur Radiol*
92. Fleysher L, Oesingmann N, Inglese M (2010) B(0) inhomogeneity-insensitive triple-quantum-filtered sodium imaging using a 12-step phase-cycling scheme. *NMR Biomed*
93. Flohr TG, McCollough CH, Bruder H et al (2006) First performance evaluation of a dual-source ct (DSCT) system. *Eur Radiol* 16(2):256–268
94. Folkman J (1995) Angiogenesis in cancer, vascular, rheumatoid and other disease. *Nat Med* 1(1):27–31
95. Forstner R (2007) Radiological staging of ovarian cancer: imaging findings and contribution of CT and MRI. *Eur Radiol* 17(12):3223–3235
96. Fossheim SL, Fahlvik AK, Klaveness J et al (1999) Paramagnetic liposomes as MRI contrast agents: influence of liposomal physicochemical properties on the in vitro relaxivity. *Magn Reson Imaging* 17(1):83–89
97. Frich L, Bjornerud A, Fossheim S et al (2004) Experimental application of thermosensitive paramagnetic liposomes for monitoring magnetic resonance imaging guided thermal ablation. *Magn Reson Med* 52(6):1302–1309

98. Fu Y, Raatschen HJ, Nitecki DE et al (2007) Cascade polymeric MRI contrast media derived from poly(ethylene glycol) cores: Initial syntheses and characterizations. *Biomacromol* 8 (5):1519–1529
99. Fuchs VR, Sox HC Jr (2001) Physicians' views of the relative importance of thirty medical innovations. *Health Aff (Millwood)* 20(5):30–42
100. Fulop A, Szijarto A, Harsanyi L et al (2014) Demonstration of metabolic and cellular effects of portal vein ligation using multi-modal PET/MRI measurements in healthy rat liver. *PLoS ONE* 9(3):e90760
101. Gabellieri C, Reynolds S, Lavie A et al (2008) Therapeutic target metabolism observed using hyperpolarized ¹⁵n choline. *J Am Chem Soc* 130(14):4598–4599
102. Galban S, Brisset JC, Rehemtulla A et al (2010) Diffusion-weighted MRI for assessment of early cancer treatment response. *Curr Pharm Biotechnol* 11(6):701–708
103. Gao GH, Im GH, Kim MS et al (2010) Magnetite-nanoparticle-encapsulated ph-responsive polymeric micelle as an MRI probe for detecting acidic pathologic areas. *Small* 6(11):1201–1204
104. Garcia-Martin ML, Martinez GV, Raghunand N et al (2006) High resolution ph(e) imaging of rat glioma using ph-dependent relaxivity. *Magn Reson Med* 55(2):309–315
105. Gatenby RA, Gillies RJ (2004) Why do cancers have high aerobic glycolysis? *Nat Rev Cancer* 4(11):891–899
106. Gatidis S, Scharpf M, Martirosian P et al (2015) Combined unsupervised-supervised classification of multiparametric PET/MRI data: application to prostate cancer. *NMR Biomed* 28(7):914–922
107. Geethanath S, Reddy R, Konar AS et al (2013) Compressed sensing mri: a review. *Crit Rev Biomed Eng* 41(3):183–204
108. Genove G, DeMarco U, Xu H et al (2005) A new transgene reporter for in vivo magnetic resonance imaging. *Nat Med* 11(4):450–454
109. Gerber BL, Bluemke DA, Chin BB et al (2002) Single-vessel coronary artery stenosis: Myocardial perfusion imaging with gadomer-17 first-pass MR imaging in a swine model of comparison with gadopentetate dimeglumine. *Radiology* 225(1):104–112
110. Gilad AA, McMahon MT, Walczak P et al (2007) Artificial reporter gene providing MRI contrast based on proton exchange. *Nat Biotechnol* 25(2):217–219
111. Gilad AA, Winnard PT Jr, van Zijl PC et al (2007) Developing MR reporter genes: promises and pitfalls. *NMR Biomed* 20(3):275–290
112. Gillies RJ, Morse DL (2005) In vivo magnetic resonance spectroscopy in cancer. *Annu Rev Biomed Eng* 7:287–326
113. Gjestebly L, Cong W, Yang Q et al (2018) Simultaneous emission-transmission tomography in an MRI hardware framework. *IEEE Trans Radiat Plasma Med Sci.* 2(4):326–336
114. Glogard C, Stensrud G, Hovland R et al (2002) Liposomes as carriers of amphiphilic gadolinium chelates: the effect of membrane composition on incorporation efficacy and in vitro relaxivity. *Int J Pharm* 233(1–2):131–140
115. Goetz C, Breton E, Choquet P et al (2008) Spect low-field MRI system for small-animal imaging. *J Nucl Med* 49(1):88–93
116. Gossman A, Okuhata Y, Shames DM et al (1999) Prostate cancer tumor grade differentiation with dynamic contrast-enhanced mr imaging in the rat: comparison of macromolecular and small-molecular contrast media—preliminary experience. *Radiology* 213 (1):265–272
117. Grandin C, Van Beers BE, Demeure R et al (1995) Comparison of gadolinium-DTPA and polylysine-gadolinium-DTPA-enhanced magnetic resonance imaging of hepatocarcinoma in the rat. *Invest Radiol* 30(10):572–581
118. Grovik E, Redalen KR, Storås TH et al (2017) Dynamic multi-echo DCE- and DSC-MRI in rectal cancer: low primary tumor k(trans) and delta²* peak are significantly associated with lymph node metastasis. *J Magn Reson Imaging* 46(1):194–206

119. Gulaka PK, Yu JX, Liu L et al (2013) Novel s-Gal(r) analogs as (1)h MRI reporters for in vivo detection of beta-galactosidase. *Magn Reson Imaging* 31(6):1006–1011
120. Guo J, Wong EC (2015) Increased snr efficiency in velocity selective arterial spin labeling using multiple velocity selective saturation modules (mm-VSASL). *Magn Reson Med* 74(3):694–705
121. Gupta RT, Ho LM, Marin D et al (2010) Dual-energy ct for characterization of adrenal nodules: initial experience. *AJR Am J Roentgenol* 194(6):1479–1483
122. Haberkorn U, Altmann A, Mier W et al (2007) Molecular imaging of tumor metabolism and apoptosis. *Ernst Schering Foundation Symposium Proceedings* 4:125–152
123. Hanahan D, Weinberg RA (2000) The hallmarks of cancer. *Cell* 100(1):57–70
124. Haris M, Singh A, Mohammed I et al (2014) In vivo magnetic resonance imaging of tumor protease activity. *Sci Rep* 4:6081
125. Haris M, Yadav SK, Rizwan A et al (2015) Molecular magnetic resonance imaging in cancer. *J Transl Med* 13:313
126. Harisinghani MG, Barentsz J, Hahn PF et al (2003) Noninvasive detection of clinically occult lymph-node metastases in prostate cancer. *N Engl J Med* 348(25):2491–2499
127. Hartman KB, Laus S, Bolskar RD et al (2008) Gadonanotubes as ultrasensitive pH-smart probes for magnetic resonance imaging. *Nano Lett* 8(2):415–419
128. Hayashida Y, Yakushiji T, Awai K et al (2006) Monitoring therapeutic responses of primary bone tumors by diffusion-weighted image: initial results. *Eur Radiol* 16(12):2637–2643
129. Hayes CE, Hattes N, Roemer PB (1991) Volume imaging with MR phased arrays. *Magn Reson Med* 18(2):309–319
130. Heidemann RM, Ozsarlak O, Parizel PM et al (2003) A brief review of parallel magnetic resonance imaging. *Eur Radiol* 13(10):2323–2337
131. Hejduk B, Bobek-Billewicz B, Rutkowski T et al (2017) Application of intravoxel incoherent motion (IVIM) model for differentiation between metastatic and non-metastatic head and neck lymph nodes. *Pol J Radiol* 82:506–510
132. Helfer BM, Balducci A, Nelson AD et al (2010) Functional assessment of human dendritic cells labeled for in vivo (19)f magnetic resonance imaging cell tracking. *Cytherapy* 12(2):238–250
133. Himmelreich U, Aime S, Hieronymus T et al (2006) A responsive mri contrast agent to monitor functional cell status. *NeuroImage* 32(3):1142–1149
134. Högemann-Savellano D, Bos E, Blondet C et al (2003) The transferrin receptor: a potential molecular imaging marker for human cancer. *Neoplasia* 5(6):495–506
135. Hong H, Yang Y, Zhang Y et al (2010) Non-invasive cell tracking in cancer and cancer therapy. *Curr Top Med Chem* 10(12):1237–1248
136. Hounsfield GN (1973) Computerized transverse axial scanning (tomography). 1. Description of system. *Br J Radio* 46(552):1016–1022
137. Hsiao JK, Chu HH, Wang YH et al (2008) Macrophage physiological function after superparamagnetic iron oxide labeling. *NMR Biomed* 21(8):820–829
138. Hu J, Hu K, Cheng Y (2016) Tailoring the dendrimer core for efficient gene delivery. *Acta Biomater* 35:1–11
139. Hutton BF, Occhipinti M, Kuehne A et al (2018) Development of clinical simultaneous SPECT/MRI. *Br J Radiol* 91(1081):20160690
140. Hwang do W, Ko HY, Lee JH et al (2010) A nucleolin-targeted multimodal nanoparticle imaging probe for tracking cancer cells using an aptamer. *J Nucl Med* 51(1):98–105
141. Iyer AK, Khaled G, Fang J et al (2006) Exploiting the enhanced permeability and retention effect for tumor targeting. *Drug Discov Today* 11(17–18):812–818
142. Jafari A, Salouti M, Shayesteh SF et al (2015) Synthesis and characterization of bombesin-superparamagnetic iron oxide nanoparticles as a targeted contrast agent for imaging of breast cancer using MRI. *Nanotechnology* 26(7):075101
143. Jardim DL, Schwaederle M, Hong DS et al (2016) An appraisal of drug development timelines in the era of precision oncology. *Oncotarget* 7(33):53037–53046

144. Jiang T, Zhang C, Zheng X (2009) Noninvasively characterizing the different alphavbeta3 expression patterns in lung cancers with RGD-USPIO using a clinical 3.0T MR scanner. *Int J Nanomedicine* 4:241–249
145. Johnson TR, Krauss B, Sedlmair M et al (2007) Material differentiation by dual energy CT: initial experience. *Eur Radiol* 17(6):1510–1517
146. Johnson SP, Ramasawmy R, Campbell-Washburn AE et al (2016) Acute changes in liver tumour perfusion measured non-invasively with arterial spin labelling. *Br J Cancer* 114(8):897–904
147. Johnstone E, Wyatt JJ, Henry AM et al (2018) Systematic review of synthetic computed tomography generation methodologies for use in magnetic resonance imaging-only radiation therapy. *Int J Radiat Oncol Biol Phys* 100(1):199–217
148. Juers DH, Jacobson RH, Wigley D et al (2000) High resolution refinement of beta-galactosidase in a new crystal form reveals multiple metal-binding sites and provides a structural basis for alpha-complementation. *Protein Sci* 9(9):1685–1699
149. Kabalka GW, Davis MA, Moss TH et al (1991) Gadolinium-labeled liposomes containing various amphiphilic Gd-DTPA derivatives: targeted MRI contrast enhancement agents for the liver. *Magn Reson Med* 19(2):406–415
150. Kachelriess M, Ulzheimer S, Kalender WA (2000) Ecg-correlated image reconstruction from subsecond multi-slice spiral CT scans of the heart. *Med Phys* 27(8):1881–1902
151. Kaiser WA, Zeitler E (1989) Mr imaging of the breast: Fast imaging sequences with and without Gd-DTPA. Preliminary observations. *Radiology* 170(3 Pt 1):681–686
152. Kak ACaS M (1988) Principles of computerized tomographic imaging. IEEE Press
153. Kalender WA, Perman WH, Vetter JR et al (1986) Evaluation of a prototype dual-energy computed tomographic apparatus. I. Phantom studies. *Med Phys* 13(3):334–339
154. Kalender WA (2005) Computed tomography. Fundamentals, system technology, image quality, applications, 2nd edn. Publicis Corporate Publishing, Erlangen
155. Kang JH, Chung JK (2008) Molecular-genetic imaging based on reporter gene expression. *J Nucl Med* 49(Suppl 2):S164–S179
156. Karcaaltincaba M, Karaosmanoglu D, Akata D et al (2009) Dual energy virtual ct colonoscopy with dual source computed tomography: initial experience. *Rofo*. 181(9):859–862
157. Kellner E, Breyer T, Gall P et al (2015) Mr evaluation of vessel size imaging of human gliomas: validation by histopathology. *J Magn Reson Imaging* 42(4):1117–1125
158. Khantaspun K, Saiviroonporn P, Jarussophon S et al (2018) Anti-epcam scfv gadolinium chelate: a novel targeted MRI contrast agent for imaging of colorectal cancer. *MAGMA* 31(5):633–644
159. Kharuzhyk SA, Petrovskaya NA, Vosmitel MA (2010) Diffusion-weighted magnetic resonance imaging in non-invasive monitoring of antiangiogenic therapy in experimental tumor model. *Exp Oncol* 32(2):104–106
160. Khashbat MdD, Abe MdT, Ganbold MdM et al (2016) Correlation of 3D arterial spin labeling and multi-parametric dynamic susceptibility contrast perfusion mri in brain tumors. *J Med Invest* 63(3–4):175–181
161. Kim J, Chhour P, Hsu J et al (2017) Use of nanoparticle contrast agents for cell tracking with computed tomography. *Bioconjug Chem* 28(6):1581–1597
162. Kiselev VG, Strecker R, Ziyeh S et al (2005) Vessel size imaging in humans. *Magn Reson Med* 53(3):553–563
163. Kobayashi H, Nishikawa M, Sakamoto C et al (2009) Dual temperature-and pH-responsive fluorescence molecular probe for cellular imaging utilizing a pnipaam-fluorescein copolymer. *Anal Sci* 25(8):1043–1047
164. Kobayashi H, Reijnders K, English S et al (2004) Application of a macromolecular contrast agent for detection of alterations of tumor vessel permeability induced by radiation. *Clin Cancer Res* 10(22):7712–7720
165. Kodibagkar VD, Cui W, Merritt ME et al (2006) Novel 1 h NMR approach to quantitative tissue oximetry using hexamethyldisiloxane. *Magn Reson Med* 55(4):743–748

166. Koenig SH, Brown RD 3rd, Kurland R et al (1988) Relaxivity and binding of Mn²⁺ ions in solutions of phosphatidylserine vesicles. *Magn Reson Med* 7(2):133–142
167. Komohara Y, Takeya M (2017) Cafs and tams: maestros of the tumour microenvironment. *J Pathol* 241(3):313–315
168. Koretsky AP, Brosnan MJ, Chen LH et al (1990) Nmr detection of creatine kinase expressed in liver of transgenic mice: determination of free adp levels. *Proc Natl Acad Sci USA* 87(8):3112–3116
169. Koretsky AP, Lin Y-J, Schorle H, Jaenisch R (1996) Genetic control of MRI contrast by expression of the transferrin receptor. *Proc Int Soc Magn Reson Med* 4:69
170. Kramer M, Motaal AG, Herrmann KH et al (2017) Cardiac 4D phase-contrast CMR at 9.4 T using self-gated ultra-short echo time (UTE) imaging. *J Cardiovasc Magn Reson* 19(1):39
171. Krohn KA, Link JM, Mason RP (2008) Molecular imaging of hypoxia. *J Nucl Med* 49(Suppl 2):S129–S148
172. Kurhanewicz J, Vigneron DB, Ardenkjaer-Larsen JH et al (2019) Hyperpolarized (13)C MRI: path to clinical translation in oncology. *Neoplasia* 21(1):1–16
173. Kurhanewicz J, Vigneron D, Carroll P et al (2008) Multiparametric magnetic resonance imaging in prostate cancer: present and future. *Curr Opin Urol* 18(1):71–77
174. Kurhanewicz J, Vigneron DB, Hricak H et al (1996) Prostate cancer: metabolic response to cryosurgery as detected with 3D h-1 MR spectroscopic imaging. *Radiology* 200(2):489–496
175. Kurhanewicz J, Vigneron DB, Hricak H et al (1996) Three-dimensional h-1 MR spectroscopic imaging of the in situ human prostate with high (0.24–0.7-cm³) spatial resolution. *Radiology* 198(3):795–805
176. Kurhanewicz J, Vigneron DB, Males RG et al (2000) The prostate: MR imaging and spectroscopy. Present and future. *Radiol Clin North Am* 38(1):115–138, viii–ix
177. Kweon S, Lee HJ, Hyung WJ et al (2010) Liposomes coloaded with iopamidol/lipiodol as a res-targeted contrast agent for computed tomography imaging. *Pharm Res* 27(7):1408–1415
178. Lamb J, Holland JP (2018) Advanced methods for radiolabeling multimodality nanomedicines for SPECT/MRI and PET/MRI. *J Nucl Med* 59(3):382–389
179. Langeris S, Keupp J, van Velthoven JL et al (2009) A temperature-sensitive liposomal 1 h CEST and 19F contrast agent for mr image-guided drug delivery. *J Am Chem Soc* 131(4):1380–1381
180. Larkman DJ, Nunes RG (2007) Parallel magnetic resonance imaging. *Phys Med Biol* 52(7):R15–R55
181. Larson PE, Han M, Krug R et al (2016) Ultrashort echo time and zero echo time MRI at 7T. *MAGMA* 29(3):359–370
182. Laslett LJ, Sabin A (1989) Wearing of caps and masks not necessary during cardiac catheterization. *Cathet Cardiovasc Diagn* 17(3):158–160
183. Lauffer RB, Parmelee DJ, Ouellet HS et al (1996) Ms-325: a small-molecule vascular imaging agent for magnetic resonance imaging. *Acad Radiol* 3(Suppl 2):S356–S358
184. Le Bihan D, Breton E, Lallemand D et al (1988) Separation of diffusion and perfusion in intravoxel incoherent motion mr imaging. *Radiology* 168(2):497–505
185. Lee KC, Hamstra DA, Bhojani MS et al (2007) Noninvasive molecular imaging sheds light on the synergy between 5-fluorouracil and TRAIL/APO21 for cancer therapy. *Clin Cancer Res* 13(6):1839–1846
186. Lee CM, Jeong HJ, Kim EM et al (2009) Superparamagnetic iron oxide nanoparticles as a dual imaging probe for targeting hepatocytes in vivo. *Magn Reson Med* 62(6):1440–1446
187. Lee S, Xie J, Chen X (2010) Peptide-based probes for targeted molecular imaging. *Biochemistry* 49(7):1364–1376
188. Lee JW, Yoon DY, Choi CS et al (2008) Anaplastic thyroid carcinoma: computed tomographic differentiation from other thyroid masses. *Acta Radiol* 49(3):321–327
189. Lewis JS, Lewis MR, Srinivasan A et al (1999) Comparison of four 64Cu-labeled somatostatin analogues in vitro and in a tumor-bearing rat model: evaluation of new derivatives for positron emission tomography imaging and targeted radiotherapy. *J Med Chem* 42(8):1341–1347

190. Li YT, Cercueil JP, Yuan J et al (2017) Liver intravoxel incoherent motion (ivim) magnetic resonance imaging: a comprehensive review of published data on normal values and applications for fibrosis and tumor evaluation. *Quant Imaging Med Surg* 7(1):59–78
191. Li X, Du X, Huo T, Liu X et al (2009) Specific targeting of breast tumor by octreotide-conjugated ultrasmall superparamagnetic iron oxide particles using a clinical 3.0-Tesla magnetic resonance scanner. *Acta Radiol* 50(6):583–594
192. Li J, Wang S, Wu C et al (2016) Activatable molecular mri nanoprobe for tumor cell imaging based on gadolinium oxide and iron oxide nanoparticle. *Biosens Bioelectron* 86:1047–1053
193. Lin C, Luciani A, Itti E et al (2010) Whole-body diffusion-weighted magnetic resonance imaging with apparent diffusion coefficient mapping for staging patients with diffuse large B-cell lymphoma. *Eur Radiol* 20(8):2027–2038
194. Lindfors KK, Boone JM, Nelson TR et al (2008) Dedicated breast CT: initial clinical experience. *Radiology* 246(3):725–733
195. Liu PF, Debatin JF, Caduff RF et al (1998) Improved diagnostic accuracy in dynamic contrast enhanced MRI of the breast by combined quantitative and qualitative analysis. *Br J Radiol* 71(845):501–509
196. Liu S, Zheng H, Feng Y et al (2017) Prostate cancer diagnosis using deep learning with 3D multiparametric MRI. SPIE Medical Imaging, Orlando, Florida, United States
197. Loebinger MR, Kyrtatos PG, Turmaine M et al (2009) Magnetic resonance imaging of mesenchymal stem cells homing to pulmonary metastases using biocompatible magnetic nanoparticles. *Can Res* 69(23):8862–8867
198. Lokling KE, Fossheim SL, Skurtveit R et al (2001) Ph-sensitive paramagnetic liposomes as MRI contrast agents: in vitro feasibility studies. *Magn Reson Imaging* 19(5):731–738
199. Longo DL, Arena F, Consolino L et al (2016) Gd-aazta-madec, an improved blood pool agent for DCE-MRI studies on mice on 1 T scanners. *Biomaterials* 75:47–57
200. Louie AY, Huber MM, Ahrens ET et al (2000) In vivo visualization of gene expression using magnetic resonance imaging. *Nat Biotechnol* 18(3):321–325
201. Lustig M, Donoho D, Pauly JM (2007) Sparse MRI: the application of compressed sensing for rapid MR imaging. *Magn Reson Med* 58(6):1182–1195
202. Lustig M, Donoho D, Santos JM et al (2008) Compressed sensing MRI. *IEEE Signal Process Soc* 25(2):72–82
203. Luttje MP, van Buuren LD, Luijten PR et al (2017) Towards intrinsic R2* imaging in the prostate at 3 and 7 Tesla. *Magn Reson Imaging* 42:16–21
204. Maeda H, Nakamura H, Fang J (2013) The epr effect for macromolecular drug delivery to solid tumors: improvement of tumor uptake, lowering of systemic toxicity, and distinct tumor imaging in vivo. *Adv Drug Deliv Rev* 65(1):71–79
205. Manjon JV, Coupe P, Buades A et al (2012) New methods for mri denoising based on sparseness and self-similarity. *Med Image Anal* 16(1):18–27
206. Manjon JV, Coupe P, Marti-Bonmati L et al (2010) Adaptive non-local means denoising of MR images with spatially varying noise levels. *J Magn Reson Imaging* 31(1):192–203
207. Maruyama S, Ueda J, Kimura A et al (2016) Development and characterization of novel lipocest agents based on thermosensitive liposomes. *Magn Reson Med Sci* 15(3):324–334
208. Matuszewski L, Persigehl T, Wall A et al (2005) Cell tagging with clinically approved iron oxides: feasibility and effect of lipofection, particle size, and surface coating on labeling efficiency. *Radiology* 235(1):155–161
209. McCollough CH, Leng S, Yu L et al (2015) Dual- and multi-energy CT: principles, technical approaches, and clinical applications. *Radiology* 276(3):637–653
210. McMahon MT, Bulte JWM (2018) Two decades of dendrimers as versatile MRI agents: a tale with and without metals. *Wiley Interdiscip Rev Nanomed Nanobiotechnol* 10(3):e1496
211. Meisamy S, Bolan PJ, Baker EH et al (2004) Neoadjuvant chemotherapy of locally advanced breast cancer: predicting response with in vivo (1)h MR spectroscopy—a pilot study at 4 t. *Radiology* 233(2):424–431

212. Melancon MP, Lu W, Huang Q et al (2010) Targeted imaging of tumor-associated M2 macrophages using a macromolecular contrast agent PG-Gd-NIR813. *Biomaterials* 31 (25):6567–6573
213. Mikawa M, Kato H, Okumura M et al (2001) Paramagnetic water-soluble metallofullerenes having the highest relaxivity for MRI contrast agents. *Bioconjug Chem* 12(4):510–514
214. Miles KA (2002) Functional computed tomography in oncology. *Eur J Cancer* 38(16):2079–2084
215. Miles KA (2006) Perfusion imaging with computed tomography: brain and beyond. *Eur Radiol* 16(Suppl 7):M37–M43
216. Misselwitz B, Schmitt-Willich H, Michaelis M et al (2002) Interstitial magnetic resonance lymphography using a polymeric t1 contrast agent: initial experience with gadomer-17. *Invest Radiol* 37(3):146–151
217. Moats R, Ma LQ, Wajed R et al (2000) Magnetic resonance imaging for the evaluation of a novel metastatic orthotopic model of human neuroblastoma in immunodeficient mice. *Clin Exp Metas* 18(6):455–461
218. Moghaddam SE, Hernandez-Rivera M, Zaibaq NG et al (2018) A new high-performance gadonanotube-polymer hybrid material for stem cell labeling and tracking by mri. *Contrast Media Mol Imaging* 2018:2853736
219. Mohammed W, Xunning H, Haibin S et al (2013) Clinical applications of susceptibility-weighted imaging in detecting and grading intracranial gliomas: a review. *Cancer Imaging* 13:186–195
220. Montet X, Pastor CM, Vallee JP et al (2007) Improved visualization of vessels and hepatic tumors by micro-computed tomography (CT) using iodinated liposomes. *Invest Radiol* 42 (9):652–658
221. Moore A, Josephson L, Bhorade RM et al (2001) Human transferrin receptor gene as a marker gene for MR imaging. *Radiology* 221(1):244–250
222. Morawski AM, Winter PM, Crowder KC et al (2004) Targeted nanoparticles for quantitative imaging of sparse molecular epitopes with MRI. *Magn Reson Med* 51(3):480–486
223. Murrell DH, Zarghami N, Jensen MD et al (2017) MRI surveillance of cancer cell fate in a brain metastasis model after early radiotherapy. *Magn Reson Med* 78(4):1506–1512
224. Nagy K, Toth M, Major P et al (2013) Performance evaluation of the small-animal nanoscan PET/MRI system. *J Nucl Med* 54(10):1825–1832
225. Napolitano R, Pariani G, Fedeli F et al (2013) Synthesis and relaxometric characterization of a MRI Gd-based probe responsive to glutamic acid decarboxylase enzymatic activity. *J Med Chem* 56(6):2466–2477
226. Nilsen L, Fangberget A, Geier O et al (2010) Diffusion-weighted magnetic resonance imaging for pretreatment prediction and monitoring of treatment response of patients with locally advanced breast cancer undergoing neoadjuvant chemotherapy. *Acta Oncol (Stockholm, Sweden)* 49(3):354–360
227. Ntziachristos V, Bremer C, Tung C et al (2002) Imaging cathepsin b up-regulation in ht-1080 tumor models using fluorescence-mediated molecular tomography (FMT). *Acad Radiol* 9(Suppl 2):S323–S325
228. Olafsen T, Wu AM (2010) Antibody vectors for imaging. *Semin Nucl Med* 40(3):167–181
229. Opsahl LR, Uzgiris EE, Vera DR (1995) Tumor imaging with a macromolecular paramagnetic contrast agent: Gadopentetate dimeglumine-polylysine. *Acad Radiol* 2(9):762–767
230. O'Connor JP, Aboagye EO, Adams JE et al (2017) Imaging biomarker roadmap for cancer studies. *Nat Rev Clin Oncol* 14(3):169–186
231. O'Connor JP, Jackson A, Parker GJ et al (2007) DCE-MRI biomarkers in the clinical evaluation of antiangiogenic and vascular disrupting agents. *Br J Cancer* 96(2):189–195
232. Padhani AR (2002) Dynamic contrast-enhanced MRI in clinical oncology: current status and future directions. *J Magn Reson Imaging* 16(4):407–422
233. Padhani AR (2005) Where are we with imaging oxygenation in human tumours? *Cancer Imaging* 5:128–130

234. Padhani AR, Krohn KA, Lewis JS et al (2007) Imaging oxygenation of human tumours. *Eur Radiol* 17(4):861–872
235. Pandit P, Qi Y, Story J et al (2010) Multishot propeller for high-field preclinical MRI. *Magn Reson Med* 64(1):47–53
236. Parivar F, Hricak H, Shinohara K et al (1996) Detection of locally recurrent prostate cancer after cryosurgery: evaluation by transrectal ultrasound, magnetic resonance imaging, and three-dimensional proton magnetic resonance spectroscopy. *Urology* 48(4):594–599
237. Pathak AP, Gimi B, Glunde K et al (2004) Molecular and functional imaging of cancer: advances in MRI and MRS. *Methods Enzymol* 386:3–60
238. Paulus MJ, Gleason SS, Kennel SJ et al (2000) High resolution X-ray computed tomography: an emerging tool for small animal cancer research. *Neoplasia* 2(1–2):62–70
239. Pereira SM, Moss D, Williams SR et al (2015) Overexpression of the mri reporter genes ferritin and transferrin receptor affect iron homeostasis and produce limited contrast in mesenchymal stem cells. *Int J Mol Sci* 16(7):15481–15496
240. Pereira SM, Williams SR, Murray P et al (2016) Ms-1 maga: revisiting its efficacy as a reporter gene for MRI. *Mol Imaging* 15
241. Perez JM, Josephson L, O’Loughlin T et al (2002) Magnetic relaxation switches capable of sensing molecular interactions. *Nat Biotechnol* 20(8):816–820
242. Piert M, Montgomery J, Kunju LP et al (2016) 18f-choline PET/MRI: the additional value of pet for MRI-guided transrectal prostate biopsies. *J Nucl Med* 57(7):1065–1070
243. Plathow C, Weber WA (2008) Tumor cell metabolism imaging. *J Nucl Med* 49(Suppl 2):43S–63S
244. Ponce AM, Viglianti BL, Yu D et al (2007) Magnetic resonance imaging of temperature-sensitive liposome release: drug dose painting and antitumor effects. *J Natl Cancer Inst* 99(1):53–63
245. Ponomarev V (2009) Nuclear imaging of cancer cell therapies. *J Nucl Med* 50(7):1013–1016
246. Popovtzer R, Agrawal A, Kotov NA et al (2008) Targeted gold nanoparticles enable molecular CT imaging of cancer. *Nano Lett* 8(12):4593–4596
247. Preibisch C, Shi K, Kluge A et al (2017) Characterizing hypoxia in human glioma: a simultaneous multimodal MRI and PET study. *NMR Biomed* 30(11)
248. Pu F, Salarian M, Xue S et al (2016) Prostate-specific membrane antigen targeted protein contrast agents for molecular imaging of prostate cancer by MRI. *Nanoscale* 8(25):12668–12682
249. Purcell EMT HC, Pound RV (1946) Resonance absorption by nuclear magnetic moment in a solid. *Phys Rev* 69:37
250. Qian Y, Stenger VA, Boada FE (2009) Parallel imaging with 3D TPI trajectory: SNR and acceleration benefits. *Magn Reson Imaging* 27(5):656–663
251. Qiao XJ, Kim HG, Wang DJJ et al (2017) Application of arterial spin labeling perfusion MRI to differentiate benign from malignant intracranial meningiomas. *Eur J Radiol* 97:31–36
252. Radbruch A, Eidel O, Wiestler B et al (2014) Quantification of tumor vessels in glioblastoma patients using time-of-flight angiography at 7 tesla: a feasibility study. *PLoS ONE* 9(11): e110727
253. Raghunand N, Jagadish B, Trouard TP et al (2006) Redox-sensitive contrast agents for mri based on reversible binding of thiols to serum albumin. *Magn Reson Med* 55(6):1272–1280
254. Rahmim A, Lodge MA, Karakatsanis NA et al (2019) Dynamic whole-body pet imaging: principles, potentials and applications. *Eur J Nucl Med Mol Imaging* 46(2):501–518
255. Rajeshkumar NV, Dutta P, Yabuuchi S et al (2015) Therapeutic targeting of the warburg effect in pancreatic cancer relies on an absence of p53 function. *Can Res* 75(16):3355–3364
256. Ranga A, Agarwal Y, Garg KJ (2017) Gadolinium based contrast agents in current practice: risks of accumulation and toxicity in patients with normal renal function. *Indian J Radiol Imaging* 27(2):141–147

257. Rani M, Dhok SB, Deshmukh RB (2018) A systematic review of compressive sensing: concepts, implementations and applications. *IEEE Access* 6:4875–4894
258. Ratnakar SJ, Soesbe TC, Lumata LL et al (2013) Modulation of cest images in vivo by t1 relaxation: a new approach in the design of responsive paracest agents. *J Am Chem Soc* 135 (40):14904–14907
259. Ray S, Li Z, Hsu CH et al (2018) Dendrimer- and copolymer-based nanoparticles for magnetic resonance cancer theranostics. *Theranostics* 8(22):6322–6349
260. Reichel D, Tripathi M, Perez JM (2019) Biological effects of nanoparticles on macrophage polarization in the tumor microenvironment. *Nanotheranostics* 3(1):66–88
261. Renan MJ (1993) How many mutations are required for tumorigenesis? Implications from human cancer data. *Mol Carcinog* 7(3):139–146
262. Ritman EL (2002) Molecular imaging in small animals—roles for micro-ct. *J Cell Biochem Suppl* 39:116–124
263. Ronald JA, Chen JW, Chen Y et al (2009) Enzyme-sensitive magnetic resonance imaging targeting myeloperoxidase identifies active inflammation in experimental rabbit atherosclerotic plaques. *Circulation* 120(7):592–599
264. Rosenkrantz AB, Friedman K, Chandarana H et al (2016) Current status of hybrid PET/MRI in oncologic imaging. *AJR Am J Roentgenol* 206(1):162–172
265. Sagiyama K, Mashimo T, Togao O et al (2014) In vivo chemical exchange saturation transfer imaging allows early detection of a therapeutic response in glioblastoma. *Proc Natl Acad Sci USA* 111(12):4542–4547
266. Sandilya M, Nirmala SR (2017) Compressed sensing trends in magnetic resonance imaging. *Eng Sci Technol Int J* 20(4):1342–1352
267. Santi A, Kugeratski FG, Zanivan S (2018) Cancer associated fibroblasts: the architects of stroma remodeling. *Proteomics* 18(5–6):e1700167
268. Schambach SJ, Bag S, Schilling L et al (2010) Application of micro-CT in small animal imaging. *Methods* 50(1):2–13
269. Schepkin VD (2016) Sodium MRI of glioma in animal models at ultrahigh magnetic fields. *NMR Biomed* 29(2):175–186
270. Schepkin VD, Chenevert TL, Kuszpit K et al (2006) Sodium and proton diffusion MRI as biomarkers for early therapeutic response in subcutaneous tumors. *Magn Reson Imaging* 24 (3):273–278
271. Schepkin VD, Choy IO, Budinger TF et al (1998) Sodium TQF NMR and intracellular sodium in isolated crystalloid perfused rat heart. *Magn Reson Med* 39(4):557–563
272. Schmid-Bindert G, Henzler T, Chu TQ et al (2012) Functional imaging of lung cancer using dual energy CT: how does iodine related attenuation correlate with standardized uptake value of 18FDG-PET-CT? *Eur Radiol* 22(1):93–103
273. Schottelius M, Laufer B, Kessler H et al (2009) Ligands for mapping $\alpha_v\beta_3$ -integrin expression in vivo. *Acc Chem Res* 42(7):969–980
274. Schuhmann-Giampieri G, Schmitt-Willich H, Frenzel T et al (1991) In vivo and in vitro evaluation of Gd-DTPA-polylysine as a macromolecular contrast agent for magnetic resonance imaging. *Invest Radiol* 26(11):969–974
275. Schwendener RA, Wuthrich R, Duewell S et al (1990) A pharmacokinetic and MRI study of unilamellar gadolinium-, manganese-, and iron-DTPA-stearate liposomes as organ-specific contrast agents. *Invest Radiol* 25(8):922–932
276. Schwickert HC, Stiskal M, Roberts TP et al (1996) Contrast-enhanced mr imaging assessment of tumor capillary permeability: effect of irradiation on delivery of chemotherapy. *Radiology* 198(3):893–898
277. Semelka RC, Helmlinger TK (2001) Contrast agents for mr imaging of the liver. *Radiology* 218(1):27–38
278. Serganova I, Mayer-Kukuck P, Huang R et al (2008) Molecular imaging: reporter gene imaging. *Handbook Exp Pharmacol* (185 Pt 2):167–223

279. Serkova NJ (2017) Nanoparticle-based magnetic resonance imaging on tumor-associated macrophages and inflammation. *Front Immunol* 8:590
280. Shen N, Zhao L, Jiang J et al (2016) Intravoxel incoherent motion diffusion-weighted imaging analysis of diffusion and microperfusion in grading gliomas and comparison with arterial spin labeling for evaluation of tumor perfusion. *J Magn Reson Imaging* 44(3):620–632
281. Shimokawa M, Ohta Y, Nishikori S et al (2017) Visualization and targeting of Igr5(+) human colon cancer stem cells. *Nature* 545(7653):187–192
282. Shin SH, Park SH, Kang SH et al (2017) Fluorine-19 magnetic resonance imaging and positron emission tomography of tumor-associated macrophages and tumor metabolism. *Contrast Media Mol Imaging* 2017:4896310
283. Shubayev VI, Pisanic TR 2nd, Jin S (2009) Magnetic nanoparticles for theragnostics. *Adv Drug Deliv Rev* 61(6):467–477
284. Sinharay S, Randtke EA, Howison CM et al (2018) Detection of enzyme activity and inhibition during studies in solution, in vitro and in vivo with catalycest MRI. *Mol Imaging Biol.* 20(2):240–248
285. Sitharaman B, Tran LA, Pham QP et al (2007) Gadofullerenes as nanoscale magnetic labels for cellular MRI. *Contrast Media Mol Imaging* 2(3):139–146
286. Sitharaman B, Wilson LJ (2006) Gadonanotubes as new high-performance MRI contrast agents. *Int J Nanomed* 1(3):291–295
287. Smith TA (2010) Towards detecting the her-2 receptor and metabolic changes induced by her-2-targeted therapies using medical imaging. *Br J Radiol* 83(992):638–644
288. Soliman RK, Gamal SA, Essa AA et al (2018) Preoperative grading of glioma using dynamic susceptibility contrast MRI: relative cerebral blood volume analysis of intra-tumoural and peri-tumoural tissue. *Clin Neurol Neurosurg* 167:86–92
289. Spanoghe M, Lanens D, Dommissie R et al (1992) Proton relaxation enhancement by means of serum albumin and poly-l-lysine labeled with DTPA-Gd3+ : relaxivities as a function of molecular weight and conjugation efficiency. *Magn Reson Imaging* 10(6):913–917
290. Spaw M, Anant S, Thomas SM (2017) Stromal contributions to the carcinogenic process. *Mol Carcinog* 56(4):1199–1213
291. Speck O, Chang O, DeSilva NM et al (2000) Perfusion MRI of the human brain with dynamic susceptibility contrast: gradient-echo versus spin-echo techniques. *J Magn Reson Imaging* 12(3):381–387
292. Stadlbauer A, Zimmermann M, Bennani-Baiti B et al (2018) Development of a non-invasive assessment of hypoxia and neovascularization with magnetic resonance imaging in benign and malignant breast tumors: initial results. *Mol Imaging Biol*
293. Stegman LD, Rehemtulla A, Beattie B et al (1999) Noninvasive quantitation of cytosine deaminase transgene expression in human tumor xenografts with in vivo magnetic resonance spectroscopy. *Proc Natl Acad Sci USA* 96(17):9821–9826
294. Szyszko TA, Cook GJR (2018) PET/CT and PET/MRI in head and neck malignancy. *Clin Radiol* 73(1):60–69
295. Tang C, Russell PJ, Martiniello-Wilks R et al (2010) Nanoparticles and cellular carriers— allies in cancer imaging and cellular gene therapy? *Stem cells*. Dayton, Ohio
296. Teh I, Golay X, Larkman DJ (2010) Propeller for motion-robust imaging of in vivo mouse abdomen at 9.4 T. *NMR Biomed* 23(9):1077–1086
297. Tei L, Mazooz G, Shellef Y et al (2010) Novel MRI and fluorescent probes responsive to the factor xiii transglutaminase activity. *Contrast Media Mol Imaging* 5(4):213–222
298. Therasse P, Arbuck SG, Eisenhauer EA et al (2000) New guidelines to evaluate the response to treatment in solid tumors. European organization for research and treatment of cancer, national cancer institute of the United States, national cancer institute of Canada. *J Natl Cancer Inst* 92(3):205–16
299. Thorek DL, Chen AK, Czupryna J et al (2006) Superparamagnetic iron oxide nanoparticle probes for molecular imaging. *Ann Biomed Eng* 34(1):23–38

300. Thorek DL, Tsourkas A (2008) Size, charge and concentration dependent uptake of iron oxide particles by non-phagocytic cells. *Biomaterials* 29(26):3583–3590
301. Thulborn KR, Lu A, Atkinson IC et al (2018) Residual tumor volume, cell volume fraction, and tumor cell kill during fractionated chemoradiation therapy of human glioblastoma using quantitative sodium MR imaging. *Clin Cancer Res*
302. Tofts PS, Brix G, Buckley DL et al (1999) Estimating kinetic parameters from dynamic contrast-enhanced T(1)-weighted MRI of a diffusible tracer: standardized quantities and symbols. *J Magn Reson Imaging* 10(3):223–232
303. Towner RA, Smith N, Doblaz S et al (2010) In vivo detection of inducible nitric oxide synthase in rodent gliomas. *Free Radic Biol Med* 48(5):691–703
304. Towner RA, Smith N, Asano Y et al (2010) Molecular magnetic resonance imaging approaches used to aid in the understanding of angiogenesis in vivo: implications for tissue engineering. *Tissue Eng Part A* 16(2):357–364
305. Townsend DW (2008) Dual-modality imaging: combining anatomy and function. *J Nucl Med* 49(6):938–955
306. Tremblay ML, Davis C, Bowen CV et al (2018) Using MRI cell tracking to monitor immune cell recruitment in response to a peptide-based cancer vaccine. *Magn Reson Med* 80(1):304–316
307. Trubetskoy VS, Cannillo JA, Milshtein A et al (1995) Controlled delivery of Gd-containing liposomes to lymph nodes: surface modification may enhance MRI contrast properties. *Magn Reson Imaging* 13(1):31–37
308. Tsien C, Galban CJ, Chenevert TL et al (2010) Parametric response map as an imaging biomarker to distinguish progression from pseudoprogression in high-grade glioma. *J Clin Oncol* 28(13):2293–2299
309. Tsourkas A, Newton G, Perez JM et al (2005) Detection of peroxidase/H₂O₂-mediated oxidation with enhanced yellow fluorescent protein. *Anal Chem* 77(9):2862–2867
310. Turetschek K, Floyd E, Helbich T et al (2001) MRI assessment of microvascular characteristics in experimental breast tumors using a new blood pool contrast agent (MS-325) with correlations to histopathology. *J Magn Reson Imaging* 14(3):237–242
311. Turetschek K, Huber S, Floyd E et al (2001) Mr imaging characterization of microvessels in experimental breast tumors by using a particulate contrast agent with histopathologic correlation. *Radiology* 218(2):562–569
312. Turetschek K, Roberts TP, Floyd E et al (2001) Tumor microvascular characterization using ultrasmall superparamagnetic iron oxide particles (USPIO) in an experimental breast cancer model. *J Magn Reson Imaging* 13(6):882–888
313. Unger EC, MacDougall P, Cullis P et al (1989) Liposomal Gd-DTPA: effect of encapsulation on enhancement of hepatoma model by MRI. *Magn Reson Imaging* 7(4):417–423
314. Unger EC, Winokur T, MacDougall P et al (1989) Hepatic metastases: liposomal Gd-DTPA-enhanced MR imaging. *Radiology* 171(1):81–85
315. Van Audenhaege K, Van Holen R, Vanhove C et al (2015) Collimator design for a multipinhole brain SPECT insert for mri. *Med Phys* 42(11):667989
316. Van Elmpt W, Zegers CM, Das M et al (2014) Imaging techniques for tumour delineation and heterogeneity quantification of lung cancer: overview of current possibilities. *J Thorac Dis* 6(4):319–327
317. Van Kasteren SI, Campbell SJ, Serres S et al (2009) Glyconanoparticles allow pre-symptomatic in vivo imaging of brain disease. *Proc Natl Acad Sci USA* 106(1):18–23
318. Van Laarhoven HW, Klomp DW, Rijpkema M et al (2007) Prediction of chemotherapeutic response of colorectal liver metastases with dynamic gadolinium-DTPA-enhanced MRI and localized ¹⁹F mrs pharmacokinetic studies of 5-fluorouracil. *NMR Biomed* 20(2):128–140
319. Van Rijswijk CS, Geirnaerd MJ, Hogendoorn PC et al (2003) Dynamic contrast-enhanced MR imaging in monitoring response to isolated limb perfusion in high-grade soft tissue sarcoma: initial results. *Eur Radiol* 13(8):1849–1858

320. Van Tilborg GA, Strijkers GJ, Pouget EM et al (2008) Kinetics of avidin-induced clearance of biotinylated bimodal liposomes for improved mr molecular imaging. *Magn Reson Med* 60(6):1444–1456
321. Van Vliet M, van Dijke CF, Wielopolski PA et al (2005) MR angiography of tumor-related vasculature: from the clinic to the micro-environment. *Radiographics* 25 Suppl 1:S85–S97 (discussion S-8)
322. Van Zijl PCM, Lam WW, Xu J et al (2018) Magnetization transfer contrast and chemical exchange saturation transfer MRI. Features and analysis of the field-dependent saturation spectrum. *NeuroImage* 168:222–241
323. Vandenberghe S, Marsden PK (2015) PET-MRI: a review of challenges and solutions in the development of integrated multimodality imaging. *Phys Med Biol* 60(4):R115–R154
324. Vaupel P (2009) Prognostic potential of the pre-therapeutic tumor oxygenation status. *Adv Exp Med Biol* 645:241–246
325. Vaupel P (2009) Physiological mechanisms of treatment resistance. In: Molls M, Vaupel P, Nieder C et al (eds) *The impact of tumor biology on cancer treatment and multidisciplinary strategies*. Springer, Heidelberg, pp 273–290
326. Vaupel P (2009) Pathophysiology of solid tumors. In: Molls M, Vaupel P, Nieder C et al (eds) *The impact of tumor biology on cancer treatment and multidisciplinary strategies*. Springer, Heidelberg, pp 51–92
327. Vautier J, Heilmann M, Walczak C et al (2010) 2D and 3D radial multi-gradient-echo DCE MRI in murine tumor models with dynamic R*2-corrected R1 mapping. *Magn Reson Med* 64(1):313–318
328. Villaraza AJ, Bumb A, Brechbiel MW (2010) Macromolecules, dendrimers, and nanomaterials in magnetic resonance imaging: the interplay between size, function, and pharmacokinetics. *Chem Rev* 110(5):2921–2959
329. Wahl RL, Jacene H, Kasamon Y et al (2009) From recist to perclist: evolving considerations for pet response criteria in solid tumors. *J Nucl Med* 50(Suppl 1):S122–S150
330. Walter G, Barton ER, Sweeney HL (2000) Noninvasive measurement of gene expression in skeletal muscle. *Proc Natl Acad Sci USA* 97(10):5151–5155
331. Wang YX, Hussain SM, Krestin GP (2001) Superparamagnetic iron oxide contrast agents: physicochemical characteristics and applications in MR imaging. *Eur Radiol* 11(11):2319–2331
332. Wang Y, Liu M, Jin ML (2017) Blood oxygenation level-dependent magnetic resonance imaging of breast cancer: Correlation with carbonic anhydrase ix and vascular endothelial growth factor. *Chin Med J (Engl)* 130(1):71–76
333. Warntjes JB, Dahlqvist O, Lundberg P (2007) Novel method for rapid, simultaneous T1, T*2, and proton density quantification. *Magn Reson Med* 57(3):528–537
334. Warntjes JB, Leinhard OD, West J et al (2008) Rapid magnetic resonance quantification on the brain: optimization for clinical usage. *Magn Reson Med* 60(2):320–329
335. Watanabe Y, Uotani K, Nakazawa T et al (2009) Dual-energy direct bone removal CT angiography for evaluation of intracranial aneurysm or stenosis: comparison with conventional digital subtraction angiography. *Eur Radiol* 19(4):1019–1024
336. Watkins GA, Jones EF, Scott Shell M et al (2009) Development of an optimized activatable MMP-14 targeted SPECT imaging probe. *Bioorg Med Chem* 17(2):653–659
337. Weissleder R, Moore A, Mahmood U et al (2000) In vivo magnetic resonance imaging of transgene expression. *Nat Med* 6(3):351–355
338. Weissleder R, Simonova M, Bogdanova A et al (1997) Mr imaging and scintigraphy of gene expression through melanin induction. *Radiology* 204(2):425–429
339. Wiener EC, Brechbiel MW, Brothers H et al (1994) Dendrimer-based metal chelates: a new class of magnetic resonance imaging contrast agents. *Magn Reson Med* 31(1):1–8
340. Wikstrom MG, Moseley ME, White DL et al (1989) Contrast-enhanced MRI of tumors. Comparison of Gd-DTPA and a macromolecular agent. *Invest Radiol* 24(8):609–615

341. Willemink MJ, Persson M, Pourmorteza A et al (2018) Photon-counting CT: technical principles and clinical prospects. *Radiology* 289(2):293–312
342. Willmann JK, van Bruggen N, Dinkelborg LM et al (2008) Molecular imaging in drug development. *Nat Rev* 7(7):591–607
343. Wilson CB, Lammertsma AA, McKenzie CG et al (1992) Measurements of blood flow and exchanging water space in breast tumors using positron emission tomography: a rapid and noninvasive dynamic method. *Can Res* 52(6):1592–1597
344. Winter PM, Caruthers SD, Allen JS et al (2010) Molecular imaging of angiogenic therapy in peripheral vascular disease with $\alpha_v\beta_3$ -integrin-targeted nanoparticles. *Magn Reson Med* 64(2):369–376
345. Wirestam R, Borg M, Brockstedt S et al (2001) Perfusion-related parameters in intravoxel incoherent motion mr imaging compared with CBV and CBF measured by dynamic susceptibility-contrast MR technique. *Acta Radiol* 42(2):123–128
346. World Health Organisation (1979) Who handbook for reporting results of cancer treatment. WHO
347. Wu AM, Yazaki PJ (2000) Designer genes: recombinant antibody fragments for biological imaging. *Q J Nucl Med* 44(3):268–283
348. Wu L, Cao Y, Liao C et al (2010) Diagnostic performance of USPIO-enhanced MRI for lymph-node metastases in different body regions: a meta-analysis. *Eur J Radiol*
349. Wyss C, Schaefer SC, Juillerat-Jeanneret L et al (2009) Molecular imaging by micro-CT: specific e-selectin imaging. *Eur Radiol* 19(10):2487–2494
350. Xu X, Yan Y, Liu F et al (2018) Folate receptor-targeted (19) F MR molecular imaging and proliferation evaluation of lung cancer. *J Magn Reson Imaging* 48(6):1617–1625
351. Yan K, Fu Z, Yang C et al (2015) Assessing amide proton transfer (apt) MRI contrast origins in 9 l gliosarcoma in the rat brain using proteomic analysis. *Mol Imaging Biol* 17(4):479–487
352. Yang X, Gong H, Quan G et al (2010) Combined system of fluorescence diffuse optical tomography and microcomputed tomography for small animal imaging. *Rev Sci Instrum* 81(5):054304
353. Yao W, Qu N, Lu Z et al (2009) The application of T1 and T2 relaxation time and magnetization transfer ratios to the early diagnosis of patellar cartilage osteoarthritis. *Skeletal Radiol* 38(11):1055–1062
354. Yoo B, Pagel MD (2008) An overview of responsive MRI contrast agents for molecular imaging. *Front Biosci* 13:1733–1752
355. Yoo B, Raam MS, Rosenblum RM et al (2007) Enzyme-responsive paracet MRI contrast agents: a new biomedical imaging approach for studies of the proteasome. *Contrast Media Mol Imaging* 2(4):189–198
356. Yordanov AT, Kobayashi H, English SJ et al (2003) Gadolinium-labeled dendrimers as biometric nanoprobe to detect vascular permeability. *J Mater Chem* 13(7):1523–1525
357. Yu JX, Gulaka PK, Liu L et al (2012) Novel Fe(3 +)-based (1h) MRI beta-galactosidase reporter molecules. *ChemPlusChem* 7(5):370–378
358. Yu JX, Kodibagkar VD, Cui W et al (2005) 19F: a versatile reporter for non-invasive physiology and pharmacology using magnetic resonance. *Curr Med Chem* 12(7):819–848
359. Yuan F, Dellian M, Fukumura D et al (1995) Vascular permeability in a human tumor xenograft: molecular size dependence and cutoff size. *Can Res* 55(17):3752–3756
360. Zahra MA, Hollingsworth KG, Sala E et al (2007) Dynamic contrast-enhanced MRI as a predictor of tumour response to radiotherapy. *Lancet Oncol* 8(1):63–74
361. Zhang F, Duan X, Lu L et al (2017) In vivo long-term tracking of neural stem cells transplanted into an acute ischemic stroke model with reporter gene-based bimodal mr and optical imaging. *Cell Transplant* 26(10):1648–1662
362. Zhang X, Lin Y, Gillies RJ (2010) Tumor pH and its measurement. *J Nucl Med* 51(8):1167–1170
363. Zhang LJ, Yang GF, Wu SY et al (2013) Dual-energy CT imaging of thoracic malignancies. *Cancer Imaging* 13:81–91

364. Zhao D, Ran S, Constantinescu A et al (2003) Tumor oxygen dynamics: correlation of in vivo MRI with histological findings. *Neoplasia* 5(4):308–318
365. Zhao X, Wen Z, Li C et al (2015) Quantitative amide proton transfer imaging with reduced interferences from magnetization transfer asymmetry for human brain tumors at 3T. *Magn Reson Med* 74(1):208–216
366. Zhu B, Liu JZ, Cauley SF et al (2018) Image reconstruction by domain-transform manifold learning. *Nature* 555(7697):487–492
367. Zucker EJ, Cheng JY, Haldipur A et al (2018) Free-breathing pediatric chest MRI: performance of self-navigated golden-angle ordered conical ultrashort echo time acquisition. *J Magn Reson Imaging* 47(1):200–209
368. Zumsteg A, Strittmatter K, Klewe-Nebenius D et al (2010) A bioluminescent mouse model of pancreatic β -cell carcinogenesis. *Carcinogenesis* 31(8):1465–1474
369. Zurkiya O, Chan AW, Hu X (2008) Maga is sufficient for producing magnetic nanoparticles in mammalian cells, making it an MRI reporter. *Magn Reson Med* 59(6):1225–1231



(Hybrid) SPECT and PET Technologies

3

Teresa Nolte, Nicolas Gross-Weege, and Volkmar Schulz

Contents

3.1	Introduction.....	112
3.2	SPECT and PET Technology	112
3.2.1	Basic SPECT and PET Physics	112
3.2.2	Image Reconstruction	117
3.2.3	SPECT and PET Detector Technology.....	118
3.2.3.1	Requirements	118
3.2.3.2	Detection Principle	118
3.2.3.3	Detector Designs.....	121
3.3	Hybridizing SPECT and PET	123
3.3.1	Motivation for Hybrid Imaging.....	123
3.3.2	Challenges with Respect to MR Compatibility	124
3.4	State-of-the-Art Hybrid Systems.....	125
3.4.1	PET-CT	125
3.4.2	SPECT-CT.....	127
3.4.3	PET-MRI	127
3.4.4	SPECT-MRI.....	128
3.5	Conclusion.....	128
	References.....	129

T. Nolte · N. Gross-Weege · V. Schulz (✉)
Physics of Molecular Imaging Systems, Experimental Molecular Imaging,
RWTH Aachen University, Aachen, Germany
e-mail: volkmar.schulz@pmi.rwth-aachen.de

V. Schulz
Hyperion Hybrid Imaging Systems GmbH, Aachen, Germany
Fraunhofer Institute for Digital Medicine MEVIS, Bremen, Germany

© Springer Nature Switzerland AG 2020
O. Schober et al. (eds.), *Molecular Imaging in Oncology*,
Recent Results in Cancer Research 216,
https://doi.org/10.1007/978-3-030-42618-7_3

3.1 Introduction

Nuclear medicine imaging (NMI) methods, such as Positron Emission Tomography (PET) and Single Photon Emission Computed Tomography (SPECT), belong to the tracer-based medical imaging modalities. The tracers are unstable radioactive isotopes, which offer three-dimensional localization of specific molecular processes. In contrast to optical imaging, SPECT and PET are based on the detection of high-energy photons. This allows the measurement of tracer distributions within larger objects, which supports the translational character of NMI technologies. Thus, PET and SPECT are intensively used in clinical as well as preclinical applications. While SPECT uses tracers that directly emit single high-energy photons, PET is based on the detection of photon pairs resulting from an annihilation process of positrons and electrons. The detection concepts used make PET about 10–100 times more sensitive than SPECT. This sensitivity advantage of PET over SPECT leads to clinical PET images with higher spatial resolution.

In order to localize the tracer distribution, PET and SPECT are usually combined with imaging modalities that offer anatomical information with high spatial resolution, such as Computed Tomography (CT) and Magnetic Resonance Imaging (MRI). These so-called hybrid-imaging modalities are nowadays standard. Actually, PET or SPECT are hardly sold as standalone device anymore, neither for preclinical nor for clinical applications. Anatomical information that may be seen in SPECT or PET images alone originates mostly from unspecifically bound or non-metabolized tracer background. Besides the aspect of tracer localization, CT and MRI are also used to improve the quantification of PET and SPECT, as the emitted photons are being absorbed and scattered within the objects.

This chapter is giving an overview of NMI technologies and their hybridization with MRI and CT, written for people who want to understand the basic principles of NMI. Subchapter two concentrates on the basic idea and fundamental physics of PET and SPECT, covering aspects from detection up to image reconstruction. The third subchapter is about the already mentioned step of hybridizing the functional and anatomical imaging methods, including the challenges that come with it. In the last subchapter, we describe the current hybrid systems and give an overview of the recent developments in the field.

3.2 SPECT and PET Technology

3.2.1 Basic SPECT and PET Physics

SPECT and PET belong to the tomographic imaging modalities, which mean that they allow for a slice-wise representation of data from inside a three-dimensional object. More specifically, both SPECT and PET permit to reconstruct the spatial distribution of a radiotracer inside the body, i.e., of a molecule labeled with an isotope that undergoes radioactive decay. As the radiotracer distribution in the body

Table 3.1 Overview over radionuclides and their half-life times [3, 6, 7]

Radionuclide	Modality	Half-life time
^{99m}Tc	SPECT	6.0 h
^{201}Tl	SPECT	73.1 h
^{67}Ga	SPECT	3.3 d
^{123}I	SPECT	0.55 d
^{11}C	PET	20.3 min
^{13}N	PET	9.97 min
^{15}O	PET	2.03 min
^{18}F	PET	110 min
^{64}Cu	PET	12.7 h
^{89}Zr	PET	3.3 d

correlates with regions of high metabolic activity, SPECT and PET are counted among the functional imaging methods. Thereby, they provide important diagnostic information for oncology, cardiology, and neurology [1].

SPECT and PET both detect gamma photons that are emitted from locations of radioactive tracer accumulation. However, both modalities differ in their setup and, consequently, on the radiotracers that may be utilized. Table 3.1 summarizes commonly employed radionuclides in SPECT and PET imaging. Radiotracers usually used for SPECT are based on gamma emitters with a long half-life time $\tau_{1/2}$ of several hours to days [2] and with gamma photon energies of $E = 100\text{--}150$ keV [3]. Upon nuclear de-excitation, they emit a single gamma photon, of which the energy depends on the radionuclide. ^{99m}Tc with $\tau_{1/2} = 6.0$ h and $E_\gamma = 140$ keV is the most commonly used SPECT radiotracer [3]. Radiotracers employed in PET are β^+ emitters with shorter $\tau_{1/2}$ of minutes to a few hours [2]. During a β^+ decay, a proton within the atomic nucleus is converted into a neutron under the emission of a positron and an electron neutrino. After traveling a finite length in the surrounding tissue, the so-called positron range, the emitted positron may encounter an electron. This leads to the annihilation of both particles under the emission of two 511 keV - photons in opposite directions. The positron range varies between a few tenths of a mm and several mm, depending on the radionuclide and the kinetic energy of the positron as well as on the tissue type [4, 5]. The most widely employed isotope in PET, primarily because of its use in the radiotracer molecule FDG, is ^{18}F . ^{18}F has a half-life time of $\tau_{1/2} = 110$ min [3]. In general, a short $\tau_{1/2}$ limits the radiation dose needed per study and facilitates waste disposal. However, the production of such radionuclides needs to take place on-site or close to the hospital, which limits their availability.

The working principle of SPECT and PET systems is shown in Fig. 3.1. For SPECT imaging, one or more gamma photon detectors, also referred to as gamma cameras, rotate slowly around the patient as sketched in Fig. 3.1a. Single gamma photons originating from the body of the patient need to pass by a collimator before hitting the detector plane. Figure 3.2 sketches different collimator designs. Prevalent in most clinical SPECT systems, the parallel-hole collimator is

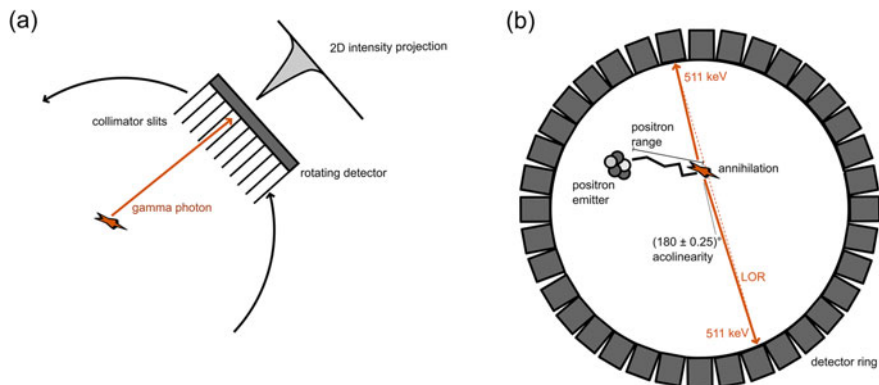


Fig. 3.1 Different setup of **a** SPECT and **b** PET imaging systems. For SPECT imaging, the gamma photon detector is rotated around the FOV, thereby recording several two-dimensional intensity projections of the radionuclide distribution. For PET imaging, two detectors register the back-to-back emission of two 511 keV gamma photons. The two incidence points define the line of response (LOR), indicated as a dashed orange line, along which the annihilation event is assumed to have taken place. The finite positron range and acollinearity effect pose fundamental limits to the resolution of PET scanners

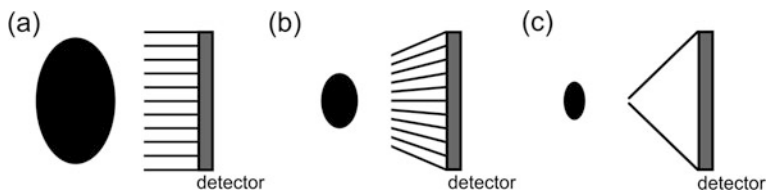


Fig. 3.2 Different collimator designs. **a** Parallel-hole collimator. **b** Converging hole collimator. **c** Pinhole collimator

constituted by a honeycomb pattern of parallel openings [8], cf. Figure 3.2a. Its geometry restricts the spatial origin of gamma photons to lines that are parallel or close-to-parallel to the collimation direction, enabling the gamma camera to record a two-dimensional projection of the object of interest. When measuring projections under several angles, a three-dimensional image can be reconstructed from the data. Spatial resolution is improved by decreasing the diameter of the holes or by increasing the collimator length, i.e., decreasing the angle under which a gamma photon may reach the detector. Yet, this simple approach restricts the number of detected photons per time and thus the sensitivity of a SPECT scanner. One means of counterbalancing low sensitivity is to let more than one gamma camera rotate around the field of view. Besides the parallel-hole collimator, a number of other SPECT collimator designs have been proposed [8]. Figure 3.2b shows a converging

hole collimator, which can either be realized in a fan beam or a cone beam design. The openings of a fan beam collimator converge towards a focal line parallel to the rotation axis of the SPECT system, whereas the openings of a cone beam collimator converge towards a focal point. If the object to be imaged is smaller than the surface of the gamma camera, converging hole collimators make more optimal use of the detector surface than a parallel-hole collimator. An example application area for converging hole collimators is brain SPECT imaging [8]. Figure 3.2c shows a pinhole collimator with a single pinhole. Pinhole collimators provide a magnifying property and thus high spatial resolution, albeit being of low sensitivity. They are particularly useful in small animal imaging, where submillimeter resolution is desirable. Multiple pinhole collimator designs combine high resolution and sensitivity and are thus advantageous for dynamic studies [9]. For more advanced collimator designs such as coded aperture or slit-slat collimators, the interested reader is referred to the article of Audenhaege et al. [8].

A PET scanner, as sketched in Fig. 3.1b, consists of a ring of gamma photon detectors positioned around the field of view. Each time two gamma photons are emitted back-to-back after the annihilation of an electron–positron pair, two detectors will register an event simultaneously, which is thus also termed coincidence event. The two detectors define a line of response (LOR) along which the event must have taken place. PET is from a geometrical point of view more sensitive than SPECT imaging because it does not need any collimators in front of the detectors, which reject most (approximately 99.99%) of all incident photons [9]. This higher sensitivity of PET reduces the required imaging time to obtain equal image quality. In contrast to SPECT, PET bears two intrinsic resolution limits, which are not of technological, but of physical nature: The first one is due to the above-mentioned positron range, i.e., the finite distance that a positron travels in the tissue before annihilation. The second one is the acollinearity effect: As both positron and electron may possess some momentum before they annihilate, the back-to-back emission of two gamma photons takes place under an angle which is characterized by a Gaussian distribution around 180° with an FWHM of 0.25° . This angular uncertainty results in image blurring, scaling up proportionally with the radius of the PET detector ring [9].

Due to the electronic coincidence measurement in PET, no collimators are needed in front of the detectors. However, when measuring coincidences, a careful distinction needs to be made between true coincidences and undesired scatter and random coincidences. A true coincidence originates from the annihilation of the radioactive tracer somewhere along the LOR and is sketched in Fig. 3.3a. If even very small differences in arrival time of the gamma photons are analyzed, one speaks of time-of-flight PET (TOF-PET). The small-time difference between the two detected gamma photons helps to narrow down the position along the LOR at which the annihilation event occurred, resulting in a higher sensitivity and contrast-to-background ratio. Opposite to true coincidences, scattered and random coincidences may add false information to the reconstructed PET images. A gamma photon undergoing one or more Compton scatter events before its detection as shown in Fig. 3.3b loses variable amounts of both energy and momentum to the

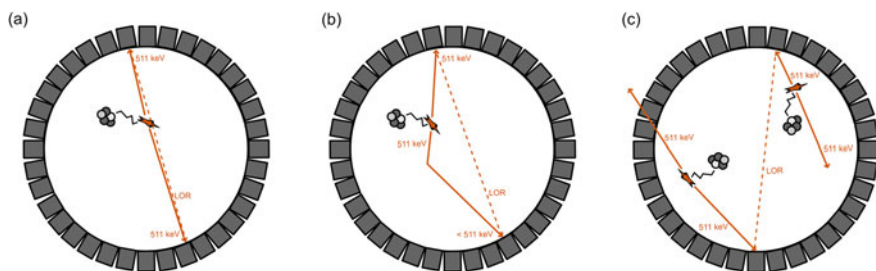


Fig. 3.3 Types of coincidences encountered in PET imaging. **a** True coincidence, **b** scattered coincidence and **c** random coincidence. Only for true coincidences, the assumed LOR corresponds to the actual path of the photon pair

tissue or the scintillator material. As a result, the assumed LOR does not actually describe the true photon path, which contains at least one change of direction. Such inelastic scatter events may be discarded prior to image reconstruction by imposing an energy window around 511 keV on the energy spectrum of each detection event. Random coincidences, as sketched in Fig. 3.3c, are caused by two gamma photons being detected in coincidence, however, originating from two different radioactive nuclei. Their respective annihilation partners may have escaped detection either due to absorption in tissue, scattering out of the scanner FOV or because they were simply not absorbed by the detector material. Unlike the scattered coincidences, random coincidences cannot be discarded during postprocessing; however, allowing only a short time window for the coincidence measurement reduces the possibility to measure them. Moreover, the rate of random coincidences may be estimated from the measured data, e.g., by the delayed coincidence method [10], and deducted from the overall measured activity.

Scattering within the tissue furthermore leads to another phenomenon called attenuation, which occurs both in PET and SPECT measurements. At the origin of attenuation are those scatter events that deflect the gamma photon outside of the detector ring and which thereby reduce the number of detected photons from a location of activity [11]. As the attenuation probability depends on the types of tissue along the photon path and their respective linear attenuation coefficients, the attenuation effect influences the reconstructed activity distribution. Bone tissue has a high linear attenuation coefficient ($\mu = 0.172 \text{ cm}^{-1}$), whereas values of $\mu = 0.09 \text{ cm}^{-1}$ and $\mu = 0.1 \text{ cm}^{-1}$ were reported for adipose and soft tissue, respectively [12]. In air, there is a neglectable attenuation, i.e., $\mu = 0 \text{ cm}^{-1}$. In PET imaging, attenuation can be corrected for, as each pair of photons travels along the whole line of response, independently of where exactly their annihilation took place. For such a correction, a map of the tissue distribution is needed. It is typically provided by a second, anatomical imaging modality. In SPECT imaging, the distance of gamma photon emission from the detector and thus the path to be taken

into account for attenuation correction is a priori not known. Therefore, SPECT presents a lower quantitative accuracy than PET [11].

3.2.2 Image Reconstruction

Image reconstruction comprises the conversion of measured coincidences into the spatial distribution of radiotracer activity. The measured data is either stored in a histogram format, i.e., count numbers are accumulated per location of detection, or in a so-called list-mode format, i.e., counts are sequentially stored under indication of the corresponding location and time-stamp [13].

Prior to reconstruction, the data is commonly reorganized into projections [14]. In the case of SPECT, a projection comprises all data acquired under a single detector angle (c.f. Fig. 3.1a), whereas in the case of PET, a projection is defined as a set of parallel LORs, which equally correspond to a rotation angle. A sinogram is a common representation of this projection data, depicting the projections depending on the rotation angle for an angular range of $[0, 2\pi)$. A number of reconstruction algorithms exists that work directly on list-mode data, providing the opportunity to reconstruct dynamic processes [13]. At this stage, the above-mentioned attenuation correction of the data is typically incorporated.

2D (or 2D multi-slice) PET imaging exclusively utilizes coincidence data originating from transversal slices, i.e., slices perpendicular to the scanner axis. For fully 3D PET imaging, additional data from oblique planes is acquired and processed, adding complexity to the reconstruction task [14].

Reconstruction methods for PET and SPECT can be divided into analytic and iterative reconstruction methods. Filtered Back Projection (FBP) commonly uses a 2D analytical reconstruction technique [15, 16]. During the back projection step, the projection intensity is equally redistributed along the corresponding LORs before obtaining the back projected image from superposing all LORs. The preceding filtering step corrects for the fact that the superposition of LORs adds more intensity to the center of the field of view than to the edges, but results in object blurring [15]. FBP is straightforward to implement and of low computation time; however, it does neither take any degrading factors, nor the stochastic nature of the detection process [14] nor system-specific properties into account. Iterative methods, on the contrary, are able to incorporate such effects, albeit demanding for more computational power. Projections are computed based on an initial estimate of the radiotracer distribution and subsequently compared to the measured projections. Based on the observed differences, the estimated image is updated. Maximum-likelihood expectation maximization (MLEM) and ordered-subsets expectation maximization (OSEM) are two commonly used iterative reconstruction methods [15, 16], the latter one providing accelerated convergence. For more details, the interested reader referred to [16] for SPECT and [14] for PET.

3.2.3 SPECT and PET Detector Technology

3.2.3.1 Requirements

A detector for nuclear imaging, i.e., both for SPECT and PET, needs to convert gamma photon incidences into electrically measurable signals. These signals convey information about the location, time-stamp, and energy spectrum of any detected gamma photon. In order to measure these parameters as accurately as possible, an optimal gamma photon detector should, therefore, among a number of other technical requirements, provide a high spatial, energy and timing resolution.

Spatial Resolution

The overall spatial resolution of a PET and SPECT system, meaning, the minimum distance above which two features are still distinguishable, depends on several factors such as the scanner geometry, the positron range, and the used reconstruction method. When speaking of the spatial resolution of a detector, one usually refers to its intrinsic spatial resolution, which is given by the accuracy of the detector to determine the position of the impinging gamma photon. Experimentally, it can be determined from the full-width half maximum of the measured light distribution of an event [15, 17].

Energy Resolution

To measure the energy of an incident gamma photon, one basic requirement needs to be met: The output signal of the detector should be proportional to the energy of the incident gamma photon. As described above, knowledge about the gamma photon energy permits to discard all scattered photons with energies lower than the expected photon energy. It is, generally speaking, favorable if the detector provides intrinsic amplification of the gamma photon signal. The ratio between the output signal strength and the initially measured signal strength of the detector is also called gain. Ideally, the gain should be stable over time and show a few variations with temperature [18, 19].

Time Resolution

The time resolution of the detector should be high to allow accurate coincidence measurements. This is especially important if one is interested in the exact arrival time of the gamma photons, as it is the case for TOF-PET capable detectors. Moreover, after being triggered, the detector should be quickly available to detect the next gamma photon incidence. This is in particular important for high count rate applications in the preclinical regime [20].

A last requirement concerns uniquely hybrid PET-MRI applications, for which the detector should be capable of working in strong magnetic fields [19].

3.2.3.2 Detection Principle

The majority of gamma photon detectors consist of two main building blocks, namely, a scintillator coupled to a photodetector. As sketched in Fig. 3.4, the scintillator first converts an incident gamma photon into a number of optical

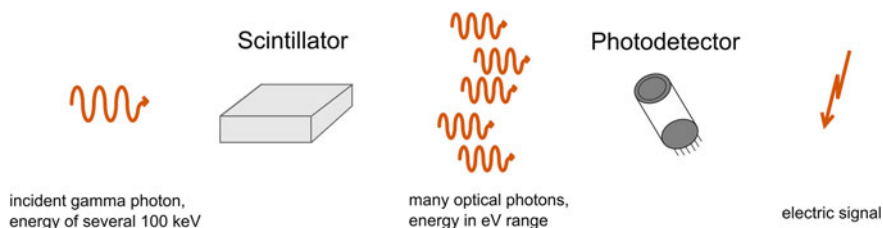


Fig. 3.4 Detection principle of a gamma detector for nuclear imaging. Scintillator and photodetector are the two building blocks of the detector: the gamma photon is transformed into an electrical signal via a conversion step into optical photons

photons. Subsequently, the photodetector transforms the optical photons into electric signals. The functioning of both components will be described in detail below. Though out of scope of this chapter, a note should be made on solid-state, direct detector types, as for example made of CdTe or CdZnTe. These types of gamma photon detectors omit the conversion into optical photons and emerge as a promising alternative especially for small animal SPECT and PET systems [21].

Scintillators

Most scintillators for PET and SPECT detectors consist of inorganic single-crystal materials. The ability of these materials to produce visible light is rooted in their electronic band structure. Within the bandgap of a few eV, separating the conduction from the valence band, additional activator states can be found. These activator states originate either from intrinsic or dopant impurities [22]. The activator states provide fast energetic transitions in the visible range, of which the transition wavelength should match with the next detection stage, namely, the photodetector. An incident gamma photon in the SPECT and PET energy range transfers its energy to the crystal in two possible ways: either completely by the generation of a photoelectron or partially by Compton scattering. These two interaction processes depend on the atomic number with Z^4 to Z^5 and Z , respectively [22]. In both cases, the generated electron excites many electron-hole pairs that recombine at the activator sites [23]. Table 3.2 summarizes the properties of prominent scintillator materials for nuclear imaging. A high effective atomic number (Z_{eff}) and a high density facilitate the deposition of the total gamma photon energy in the scintillator [24]. The probability of absorption for a gamma photon in tissue is described by the (energy-dependent) attenuation length. After having traveled this length through matter, the gamma photon's probability of not being absorbed drops to $1/e$. Other important characteristic properties of a scintillator material are the scintillation light yield, i.e., the number of photons generated per deposited energy of the incident gamma photon, and the scintillation decay time, i.e., the time needed for the scintillation pulse to decrease again after an incidence of a gamma photon.

Table 3.2 Properties of some different crystalline scintillator materials (adapted from (1) Lecomte [25]; (2) Lecoq [26]; (3) Melcher [24]; (4) Grupen [27]; (5) Northrup [28])

Property	NaI	CsI	BGO	GSO	LSO	LYSO
Effective atomic number Z_{eff}	50 (1) 51 (3)	54 (3)	75 (3)	58 (1) 59 (3)	65 (1,3)	64 (1)
Density/g/cm ³	3.67 (1, 3)	4.51 (3)	7.13 (1, 3)	6.71 (1, 3)	7.35 (1) 7.40 (3)	7.19 (1)
Attenuation length @ 511 keV/cm	2.9 (3) (4) 2.6 (1)	2.3 (4)	1.1 (1)	1.5 (1)	1.2 (1)	1.3 (1)
Attenuation length @ 140 keV/cm	0.4 (5)	0.3 (5)				
Light yield/photons/MeV	38,000 (2) 41,000 (1, 4, 5)	54,000 (2) 56,000 (5) 66,000 (4)	9000 (1,4)	8000 (1,4)	23,000 (5) 27,000 (2) 30,000 (1, 4)	30,000 (1)
Decay time/ns	230/~10000 (3)	1000 (3)	300/60 (1) 300 (3)	60/600 (3)	40 (1, 3)	40 (1) 30–35 (2)

Numbers may show variation depending on exact atomic composition and dopant concentrations. *NaI* thallium-doped sodium iodide (NaI:Tl), *CsI* thallium-doped cesium iodide, *BGO* bismuth germanate (Bi₄Ge₃O₁₂), *GSO* cerium-doped gadolinium orthosilicate (Gd₂SiO₅:Ce), *LSO* cerium-doped lutetium orthosilicate (Lu₂SiO₅:Ce), *LYSO* cerium-doped lutetium–yttrium oxyorthosilicate (Lu_{1.9}Y_{0.1}SiO₅:Ce)

Scintillators for SPECT detectors are almost exclusively consisting of Thallium-doped NaI, a scintillator material characterized by a high light yield [24], with CsI as a possible alternative [22]. Since the detection efficiency of NaI at higher gamma photon energies is fairly low, PET applications demand scintillator materials of higher stopping power (namely, of higher density, higher Z_{eff} , and thus shorter attenuation length) such BGO, GSO, LSO, and LYSO. Among these, LSO and LYSO combine a high light yield with a short scintillation decay time, which makes them, moreover, attractive for applications in TOF-PET capable scanners [24].

Alternatives to crystalline scintillator materials with a potential for nuclear imaging are condensed noble gases such as liquid xenon [29] or plastic scintillators [30].

Photodetectors

Photodetector devices comprise three main groups: photomultiplier tubes (PMT), avalanche photodiodes (APD), and silicon photomultipliers (SiPM). Table 3.3 compares their characteristics. PMTs continue to equip most clinical PET and SPECT systems; yet, solid-state technology and especially SiPMs emerged as an alternative, combining many of the advantages of PMTs with compactness and insensitivity to magnetic fields. Notably, they are the technology of choice in PET imaging applications for which space is limited, such as small animal imaging, or for MRI-based hybrid-imaging devices [31].

A photomultiplier tube (PMT) is a vacuum glass tube consisting of a photocathode layer, a chain of dynodes, and an anode. At the photocathode, an incident optical photon is converted into an electron by the photoelectric effect. An electric potential

in the kV range accelerates the electron from dynode to dynode towards the anode. At the dynodes, each incident electron produces several secondary electrons, thereby amplifying the electric signal exponentially by a factor of about 10^6 . Importantly, the number of secondary electrons is proportional to the number of incident photons. Moreover, PMTs have a low dependency on temperature, which is less than 1% per °C. Conventional PMTs exhibit a sensitive area in the cm^2 range (they are thus quite bulky), cannot be operated in magnetic fields and require high bias voltages [20]. An important development in the PMT area are multi-anode position-sensitive PMTs. They provide an improved intrinsic spatial resolution, which made their integration into preclinical imaging systems possible [33].

An avalanche photodiode (APD) is a solid-state photodetector, thus made of a semiconductor material such as silicon. An APD is formed by a semiconductor layer structure that is operated under reverse bias, but below its breakdown voltage (i.e., below a threshold above which the structure would become conductive again). This so-called p-i-p-n layer structure consists of a positively (p) doped layer, an intrinsic (i) layer without any additional doping, another p-layer and last of a negatively doped (n) layer, which leads to the formation of a distinct electric field profile across the structure. After absorption of an optical photon in the intrinsic layer, an electron-hole pair is created and attracted towards the contacts. At the p-n interface, a steep electric field gradient leads to a multiplication of charge carriers by impact ionization. Thereby, the APD achieves an intrinsic signal amplification of about 10^2 – 10^3 , while the electric signal strength stays proportional to the number of incident photons [32]. APDs are magnetic field compatible and small, with a sensitive area in the mm^2 range. As a drawback, they require an additional amplification stage due to their lower intrinsic gain and exhibit a higher temperature dependency than PMTs of about 3% per °C [20].

A single photon APD (SPAD) or Geiger-mode APD is an APD operated beyond the breakdown voltage. Each incident optical photon develops into a self-sustaining avalanche that is only stopped when the voltage exceeds the resistance of a quenching resistor being coupled in series with the SPAD. The detection principle is thus binary, and the energy of the electric pulse is no longer proportional to the photon energy. During an avalanche discharge, the SPAD cannot detect other photons. Hence, measuring more than one scintillation photon requires several SPADs. This leads to the development of SiPMs, which are two-dimensional assemblies of 100–10,000 individual microcells per mm^2 , namely, of Geiger-mode APDs with their quenching resistors, with a geometric extension of a few $100 \mu\text{m}^2$ [32]. After a scintillation pulse, a number of microcells trigger and generate a signal. Thus, the output signal of the whole SiPM, i.e., the integral of the signal of the microcells, is proportional to the energy of the scintillation pulse as long as each microcell is not triggered by more than one photon. The SiPM, therefore, possesses quasi-analog signal characteristics.

3.2.3.3 Detector Designs

There are two basic detector designs, which distinguish themselves by employing either a continuous scintillation crystal or pixelated scintillator arrays. The concepts,

Table 3.3 Comparison of different photodetector types for SPECT and PET applications [20, 32]

Detector type	Proportionality	Gain [32]	Temperature stability [20] (%/°C)	Rise time [20] (ns)	Sensitive area [20]	Magnetic field compatibility
PMT	Yes	10^6	<1	~1	cm ²	No
APD	Yes	10^2 – 10^3	~3	~5	mm ²	Yes
SiPM	Yes	10^5 – 10^7	~1–8	~1	mm ²	Yes

originally described as the Anger camera and the Block detector, respectively, continue to form the basis for virtually all modern SPECT and PET detectors designs.

In 1952, Hal Anger proposed a NaI:Tl based scintillation detector design [34], which nowadays still prevails in most SPECT systems. It consists of a large-area scintillation crystal that is coupled to an array of PMTs, which are arranged in a hexagonal fashion. A light guide material between crystal and PMTs is used for refractive index matching and light distribution. In front of the scintillator, the collimator is located. When a gamma photon traverses the collimator and causes a scintillation event, optical photons are emitted isotropically from the location of interaction. In consequence, the individual PMTs behind the scintillator detect varying fractions of scintillation light. Behind the PMTs, electronic circuits determine the position and energy of the gamma photon incidence. While the position is derived from the center of gravity of the signal amplitudes, the energy of the gamma photon is determined by summing over the PMT signals. This readout scheme is also referred to as Anger logic. A typical Anger camera achieves about 10% FWHM in energy resolution for ^{99m}Tc and 2–4 mm FWHM for a camera size of 21" × 28" (about 53 cm × 71 cm) [18].

The first PET detectors, on the contrary, were implemented as pixelated detectors based on a one-to-one coupling scheme, i.e., one individual crystal needle was mounted per PMT. The individual crystal diameter thus determined the intrinsic, i.e., minimal achievable spatial resolution of such a detector design. Moreover, the resolution was limited by the packing density of the PMT array due to the non-negligible thickness of the PMT glass envelopes. Other limitations of this design included cost and a high number of channels to be read out by the processing electronics [32].

In 1986, Casey and Nutt proposed the Block detector design for PET detectors [35], which permitted to reduce the number of PMTs that are required to read out a pixelated array of crystals. In this design, either an array of individual scintillators or one larger crystal with saw cuts is mounted onto a small number of PMTs—for example, 6 × 6 crystals may be found on top of 2 × 2 PMTs. Inserting a reflective layer between the individual crystals reduces crosstalk between these. The position of the gamma photon incidence can be derived from the horizontal and vertical PMT signal ratios, while the energy is derived as sum over the PMTs similar to the above-described Anger logic [32].

For PET imaging, special detector designs can be adapted that allow to additionally obtain depth-of-interaction (DOI) information [36]. Locating the depth of a scintillation event within the crystals permits to reduce the so-called parallax error in PET, which leads to increased image blurring, especially for small PET rings with long scintillation crystals. For pixelated detectors, discrete DOI information can be obtained by using a multi-layer detector design, where the depth resolution is determined by the thickness of one detection layer. If several layers of crystals are stacked onto a single layer of photodetectors, the crystal layers may be distinguished by pulse shape discrimination, by relative offsets between the crystal layers or by combinations thereof. For pulse shape discrimination, the layers need to consist of scintillators with different timing characteristics, whereas stacking two layers with half a crystal pitch offset works for the same scintillating material. It is equally possible to stack whole detector blocks, i.e., scintillator and photodetector, on top of each other. A continuous DOI measurement can be achieved by a dual-ended readout of the scintillator. For detectors based on monolithic crystals (back to the Anger camera approach!), the DOI can be traced back from the width of the light dispersion. One challenge that arises for monoliths is related to edge effects such as reflections, which distort the light dispersion and thereby hamper the 3D-positioning of the event. Remedies may be of physical nature, such as reducing surface reflections by roughening or black paint, or be found in the postprocessing step, for which maximum-likelihood positioning algorithms [37, 38] and supervised machine learning methods such as gradient boosted decision trees [39, 40] prove to improve upon the classical positioning approach.

3.3 Hybridizing SPECT and PET

3.3.1 Motivation for Hybrid Imaging

Since PET- and SPECT-only visualize the distribution of the tracer, i.e., the functional information, the exact information about the position of the tracer in the body, i.e., the anatomical information, is missing. Therefore, it is of added diagnostic value to combine PET and SPECT with an image modality delivering anatomical information, such as CT or MRI. CT measures the attenuation of X-rays, with an energy of about 80–140 keV. The attenuation of the X-rays in tissue is dominated by the tissue density. Since the density of different soft tissues is very similar, CT shows poor soft-tissue contrast. However, bone tissue can be visualized with high spatial resolution. Besides the benefit of gaining the anatomical information, a gamma photon attenuation map can be measured with CT, which can be used in the SPECT/PET image reconstruction for attenuation correction (c.f. Sect. 3.2.1 and [41]). One technical restriction of the hybrid-imaging modality is the sequential image acquisition of the SPECT/PET and the CT image, i.e., both images are acquired after each other. Simultaneous acquisition is not possible since SPECT/PET and CT detectors absorb gamma particles within a similar energy

range. However, in higher integrated systems, the SPECT/PET and CT systems are built directly next to each other around the same patient bed and both images can be acquired directly after each other.

SPECT/PET can also be combined with MRI to gain anatomical information. In contrast to CT, MRI offers high soft-tissue contrast without using ionizing radiation. Furthermore, MRI allows visualizing many different contrasts. MR can measure spectroscopic information, diffusion (DWI) or brain activity (fMRI) and many more, such as Magnetic Resonance Angiography [42], Chemical Exchange Saturation Transfer (CEST) [43] and Dynamic Contrast Enhancement MRI (DCE MRI) [44]. Hybrid SPECT/PET-MRI systems can be differentiated by their level of integration. In lowly integrated systems, the SPECT/PET scanner and MRI scanner are separated but share the same patient bed. The SPECT/PET image is acquired separately just as in SPECT/PET-CT systems. In highly integrated systems, the SPECT/PET scanner is implemented inside the MRI scanner allowing for simultaneous acquisition of the SPECT/PET and MRI image. Simultaneous acquisition of both images provides many advantages:

- Reduced space requirements, since both modalities are integrated into one device
- Reduced scan time, since the SPECT/PET and MRI measurement time is in the same order of magnitude for typical examinations; this does not apply for SPECT/PET-CT because CT is much faster
- Better temporal and spatial registration especially in dynamic studies, since sequential scans come with a temporal and very likely with a spatial offset
- Many techniques for motion compensation are enabled [45]
- Higher spatial resolution of PET, since the strong magnetic field of the MR system deflects the positrons and thus decreases the positron range [46].

3.3.2 Challenges with Respect to MR Compatibility

Combining a SPECT/PET scanner with an MRI scanner for simultaneous imaging is technically challenging. On the one hand, MRI uses strong and high-frequency magnetic fields, creating a harsh environment for the electronic of the SPECT/PET scanner. Therefore, also common pacemakers and magnetic implants are not allowed to be brought into an MRI. On the other hand, an MRI scanner is a very sensitive device, which can be easily distorted by electronic devices, such as the SPECT/PET scanner. An MRI system can be divided into three different subsystems: a strong static magnetic field B_0 in the order of magnitude of a few Tesla, a radio-frequency (RF) field B_1 with a strength of several μT and frequencies in the MHz range depending on the B_0 and the excited nucleus, and a so-called gradient magnetic field, which can be switched in each of the three spatial directions to modify B_0 linearly in space with a strength and slew rate of a few 10 and 100 mT/m/ms for typical clinical MRI systems. The distortion of the SPECT/PET

scanner by the MRI scanner is usually investigated for each of the MRI subsystems since all three can have a different effect on the PET system and vice versa. Figure 3.5 summarizes the mutual distortion effects between the MRI subsystems and the SPECT/PET scanner.

The strong static magnetic B_0 field is shielded passively in common MRI systems. Therefore, the magnetic field strongly increases from outside to the inside of the MRI isocenter. This strong gradient causes a force on materials with high magnetic susceptibility resulting in high mechanical stress. On the SPECT/PET side, many electrical components do not work properly inside the MRI system, such as electronic components based on ferrite materials. Furthermore, the Lorentz force acts on moving electrons, which can cause malfunctions of electronic components [47]. For this reason, photomultiplier tubes cannot be used inside the MRI.

On the MRI side, materials with a high magnetic susceptibility distort the B_0 field causing image artifacts. Especially, sequences that rely on high spectroscopic resolution degrade with poor B_0 field homogeneity.

The RF field B_1 can induce voltages up to several Volts in conducting paths, which can distort [48, 49] or even damage the electronic components of the SPECT/PET detectors. Otherwise, the SPECT/PET detectors can emit RF signals, which may couple into the MRI measurement chain. The spurious signals result in a decrease of the signal-to-noise ratio [50–52] and/or zipper artifacts [53, 54] in the MRI data. To prevent the RF interferences between the SPECT/PET and MRI system, the SPECT/PET detectors are commonly equipped with RF shields.

The gradient magnetic field can induce eddy currents in all conductive components of the SPECT/PET detectors. On the SPECT/PET side, the eddy currents can distort the SPECT/PET detector signals [55–57] and cause vibrations of the conductive components. On the MRI side, the eddy currents can produce superimposing magnetic fields, which distort the gradient magnetic fields causing image artifacts [58–60]. As the frequency of the switching gradient magnetic field is only in the kHz range, shielding is not feasible and the SPECT/PET system should have high gradient transparency. High gradient transparency can be realized by minimizing the conductance of all components of the SPECT/PET system, i.e., reducing the size of the components and the conductivity of the materials used [60].

3.4 State-of-the-Art Hybrid Systems

3.4.1 PET-CT

PET-CT is an established clinical hybrid-imaging modality, employing state-of-the-art, i.e., multi-slice and high resolution, CT technology. The first commercial PET-CT scanners appeared in 2001 and rapidly took over the market from PET-only devices [61].

Important developments in clinical PET-CT technology concern the incorporation of TOF-PET capability into clinical systems, which started in 2006 [62]. The

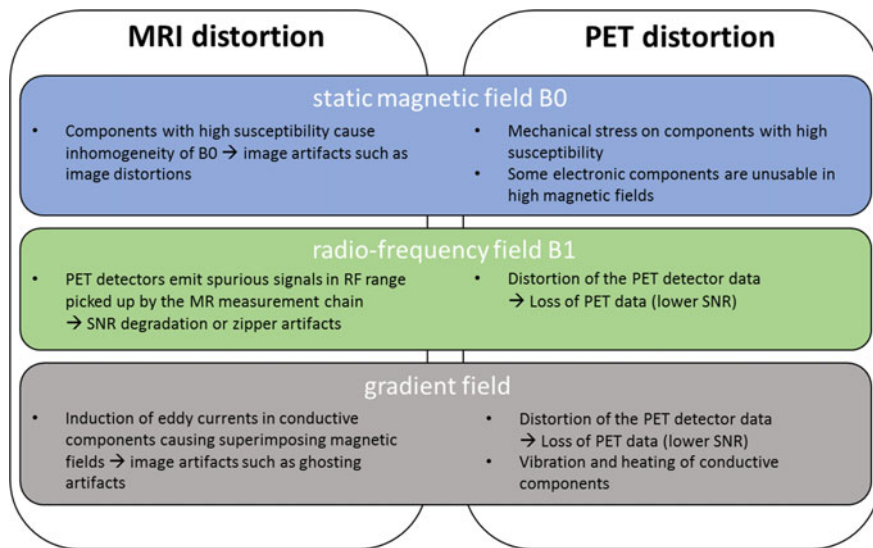


Fig. 3.5 Mutual influences of simultaneous PET-MRI

specifications of five recent clinical PET/CT systems (Philips Ingenuity TF, Philips Vereos, GE Discovery 710, GE Discovery IQ, Siemens Biograph mCT Flow (True V)) are summarized in the review of [63]. Most of the compared systems exhibit a spatial PET resolution of 4–5 mm, employ LYSO crystals as scintillator materials and base on analog PMTs for the optical signal readout. Four out of the five reviewed systems have TOF-PET capability. Here, the Philips Vereos system, employing digital SiPMs and a 1:1 coupling scheme, distinguishes itself by a significantly lower timing resolution of about 350 ps as compared to about 550 ps in the other systems, yielding an improved localization of the annihilation event along the LOR (within a distance of about 5 cm compared to 8–9 cm). The term “digital SiPM” refers to a digital readout logic, which counts and digitizes the photons on-chip. Another recent digital PET/CT system, the Biograph Vision (Siemens Healthineers), has been evaluated in [64] and is reported to have an even lower timing resolution of 215 ps.

Modern PET/CT scanners acquire PET data in a three-dimensional fashion, meaning, several parallel PET rings are used to not only detect coincidences within the individual 2D slices but also between different rings [63]. A whole-body scan is then conventionally acquired in a “step and shoot” approach, i.e., stitched together from several discrete, overlapping bed positions. The mCT Flow technology by Siemens uses continuous bed motion to acquire a whole-body scan in a single volume [61]. Future efforts may comprise the development of so-called total-body PET [65], extending the PET field of view over the entire length of the body. This approach will increase the sensitivity for total-body examinations; however, it comes with considerably higher production cost, which might hamper widespread commercial usage.

Preclinical commercial PET-CT systems have PET spatial resolutions below 1–1.5 mm [66, 15]. Some examples for commercially available systems are G8 PET/CT by Perkin Elmer [67], nanoScan PET/CT by Mediso [15], Inveon PET/CT by Siemens [68], U-PET+ with VECT by MiLabs [66], Super Argus PET/CT by Sedecal [66], or the Albira PET/SPECT/CT platform by Bruker [69].

3.4.2 SPECT-CT

All major vendors offer clinical SPECT/CT systems. The Siemens Healthineers Symbia T-Series [70] and Symbia Intevo [71] systems combine diagnostic, fast rotation and multi-slice CT imaging with two gamma camera head arranged in opposite orientation in front of the CT gantry. The GE Discovery NM/CT 670 systems equally offer multi-slice CT (8 or 16 slices) with two gamma cameras arranged in front of the CT gantry in 90° orientation [72, 73]. Mediso's trimodal AnyScan SPECT/PET/CT system builds upon the same concept [74]. Philips chose an alternative approach with the Brightview XCT: two gamma cameras as well as a flat-panel X-ray detector are arranged in a co-planar fashion, which eliminates the need for table movement at the cost of lower rotation speeds [75, 73].

Preclinical SPECT-CT systems reach submillimeter SPECT resolutions [76], a few commercial examples are the Bruker Albira [69], Bioscan nanoSPECT/CT [77], MiLabs Vector [78], and Siemens Inveon [68].

A recent trend is given by equipping SPECT devices with CZT (Cd-Zn-Te) detector technology. The pixelated, solid-state CZT detectors directly convert the emitted or scattered gamma photons into electrical signals, without the need for an additional photomultiplier stage (c.f. Sect. 3.2.3). This results in more compact gamma cameras with improved higher intrinsic spatial resolution and higher count rates, albeit also in higher purchase cost. Next to CZT-based SPECT-only devices, GE's Discovery NM/CT 670 ZCT is the only clinical SPECT/CT system equipped with this technology on the market [79].

3.4.3 PET-MRI

The first commercial simultaneous PET-MRI systems for clinical applications have been available for about 5 years: Siemens Healthineers Biograph mMR (<https://www.healthcare.siemens.com/magnetic-resonance-imaging/mr-pet-scanner/biograph-mmr>, [80]) and GE Healthcare SIGNA™ PET/MR (<https://www.gehealthcare.com/en/products/magnetic-resonance-imaging/3-0t/signa-pet-mr>, [81]). Furthermore, commercial simultaneous PET-MRI systems for preclinical applications are offered by the following vendors: Bruker PET/MR 3T (<https://www.bruker.com/products/preclinical-imaging/nuclear-molecular-imaging/petmr-3t/overview.html>), MR Solutions PET INSERT Simultaneous PET/MR (<http://www.mrsolutions.com/products/imaging-systems/pet-insert-simultaneous-petmr/>) and Aspect Imaging SimPET

(<https://www.aspectimaging.com/pre-clinical-mri/simpet-simultaneous-pet-mri-complete-solution/>). Besides the commercial systems, many research devices were developed for clinical or preclinical applications [82–84]. A widely applied approach is the integration of so-called PET inserts into existing MRI systems. For the first PET insert, the scintillation crystals inside the MRI system were attached to optical fibers, which transmit the optical photons outside the MRI system to the MRI-incompatible photomultiplier tubes [85]. However, the light loss due to the long optical fibers strongly limited the PET performance. Advances in the solid-state photodetectors, such as APDs and SiPMs, enabled to implement the complete gamma detectors inside the MRI system. In the past years, the research was based on further increasing the level of integration, for example, by using battery-operated PET detectors enabling electrically floating PET systems [53] or by integrating an optical transparent RF shield as the light sharing element of the PET detector [86]. Furthermore, PET inserts are developed for clinical applications that focus on one organ [87, 88, <http://www.hypmed.eu/>]. Compared to the commercial total-body PET-MRI systems, organ-specific devices are closer to the organ of interest and therefore, have following benefits: higher sensitivity because of the possibility to cover a larger solid angle and the potential lower attenuation through the body; higher spatial resolution because of a lower acollinearity effect.

3.4.4 SPECT-MRI

The progress in the development of SPECT-MRI system is very limited and commercial simultaneous SPECT-MRI systems are not available, yet [89]. Only two commercial sequential SPECT-MRI systems for preclinical applications are distributed (MEDISO and MR Solutions).

Some research SPECT-MRI systems were developed in the past years, however, only one simultaneous SPECT insert for brain SPECT-MRI is under development [90, 49]. Additionally, research simultaneous SPECT-MRI systems for preclinical applications were developed and characterized [91–94].

3.5 Conclusion

Hybrid imaging has proven its value in the clinical as well as the preclinical domain. The high level of integration of current hybrid-imaging devices offers a simplified workflow with respect to measurement time and animal or patient handling. While the combination of PET and SPECT with CT offers a nearly push-button usage, the combination with MRI still holds a few challenges. The major challenges are the stability and accuracy of the quantitative corrections from MRI and the complexity of use of PET or SPECT in combination with MRI devices. Nevertheless, technical innovations will most probably overcome both aspects in

the next years and the overall complexity of hybrid imaging will be hidden by smart software interfaces.

Even though SPECT and PET are appreciated for their high sensitivity, the need for dose reduction and higher spatial resolution in the clinical domain are the main drivers for future developments. Research on new concepts such as long axial FOV PET scanners and systems with coincidence timing resolution below 100 ps will drive the field. These developments will result in clinical scanners with 10–100 times higher sensitivity than nowadays, allowing for substantially higher spatial resolution and lower doses.

In the preclinical domain, the push for higher spatial resolution, which goes hand in hand with higher sensitivity, will be the main driver for future developments. Solid-state detectors will become the state-of-the-art for all kinds of NMI systems. Interestingly, the past has shown us that the development of preclinical devices is mostly driven by new technical innovations from developments in the clinical domain. This is an unfortunate side-effect of the combination of development costs and market sizes in the preclinical domain.

Besides all these technical developments, the preclinical and clinical domain will substantially benefit from new image reconstruction methods based on machine learning, which will likely offer nearly real-time imaging at high quantitative accuracy. Furthermore, also triggered by the development of clinical scanners with long axial FOV, highly sensitive preclinical systems allowing for dynamic PET reconstruction could become state-of-the-art in the near future.

References

1. Czernin J, Israel O, Herrmann K et al (2017) Clinical applications of PET/CT and SPECT/CT imaging. In: Dahlbohm M (ed) *Physics of PET/CT and SPECT/CT*. CRC Press, Boca Raton
2. Lu F, Yuan Z (2015) PET/SPECT molecular imaging in clinical neuroscience: recent advances in the investigation of CNS diseases. *Quant Imaging Med Surg* 5(3):433–447
3. Ruth T (2009) The uses of radiotracers in the life sciences. *Rep Prog Phys* 72:016701
4. Conti M, Eriksson L (2004) Physics of pure and non-pure positron emitters for PET: a review and a discussion. *Appl Radiat Isot* 60:301–305
5. Sanchez-Crespo A, Andreo P, Larsson S (2004) Positron flight in human tissues and its influence on PET image spatial resolution. *Eur J Nucl Med Mol Imaging* 31:44–51
6. Da Silva M, de Almeida M, da Silva C et al (2004) Use of the reference source method to determine the half-lives of radionuclides of importance in nuclear medicine. *Appl Radiat Isot* 60:301–305
7. Severin GW, Engle JW, Nickles RJ, Barnhart TE (2011) ^{89}Zr radiochemistry for PET. *Med Chem* 7(5):389–394
8. Audenhaege K, Holen R, Vandenberghe S et al. (2015) Review of SPECT collimator selection, optimization, and fabrication for clinical and preclinical imaging. *Med Phys* 42(8)
9. Rahmim A, Zaidi H (2008) PET versus SPECT: strengths, limitations and challenges. *Nucl Med Commun* 29:193–207
10. Brasse D, Kinahan PE, Lartizien C et al (2005) Correction methods for random coincidences in fully 3D whole-body PET: impact on data and image quality. *J Nucl Med* 46:859–867
11. Ollinger J, Fessler J (1997) Positron emission tomography. *IEEE Signal Process Mag* 43–55

12. Berker Y, Franke J, Salomon A et al (2012) MRI-based attenuation correction for hybrid PET/MRI systems: a 4-class tissue segmentation technique using a combined ultrashort-echo-time/Dixon MRI sequence. *J Nucl Med* 53(5)
13. Lewitt R, Matej S (2003) Overview of methods for image reconstruction from projections in emission computed tomography. *Proc IEEE* 91(10)
14. Tong S, Alessio AM, Kinahan PE (2010) Image reconstruction for PET/CT scanners: past achievements and future challenges. *Imaging Med* 2(5):529–545
15. Saha GB (2016) Basics of PET imaging: physics, chemistry, and regulations, 3rd edn. Springer International Publishing Switzerland
16. Bruyant P (2002) Analytic and iterative reconstruction algorithms in SPECT. *J Nucl Med* 43(10)
17. Moses WW (2011) Fundamental limits of spatial resolution in PET. *Nucl Instrum Methods Phys Res A* 648(Supplement 1):S236–S240
18. Peterson TE, Furenlid LR (2011) SPECT detectors: the anger camera and beyond. *Phys Med Biol* 56(17):R145–R182
19. Moses WW (2009) Photodetectors for nuclear medical imaging. *Nucl Instrum Methods Phys Res A* 610(1):11–15
20. Spanoudaki VC, Levin CS (2010) Photo-detectors for time of flight positron emission tomography (ToF-PET). *Sensors* 10:10484–10505
21. Russo P, Del Guerra A (2014) Solid-state detectors for small-animal imaging. In: Zaidi H (ed), *Molecular imaging of small animals: instrumentation and applications*. Springer Science + Business Media, New York
22. Lecoq P, Gektin A, Korzhik M (2017) *Inorganic scintillators for detector systems: physical principles and crystal engineering*, 2nd edn. Springer Publishing International Edition, Switzerland
23. Weber MJ (2002) Inorganic scintillators: today and tomorrow. *J Lumin* 100:35–45
24. Melcher CL (2000) Scintillation crystals for PET. *J Nucl Med* 41:6
25. Lecomte R (2009) Novel detector technology for clinical PET. *Eur J Nucl Med Mol Imaging* 36(Suppl 1):S69–S85
26. Lecoq P (2016) Development of new scintillators for medical applications. *Nucl Instrum. Methods Phys Res A*(809):130–139
27. Grupen C, Buvat I (eds) (2012) *Handbook of particle detection and imaging*. Springer, Berlin-Heidelberg
28. Northrup RB (2002) *Noninvasive instrumentation and measurement in medical diagnosis*. CRC Press, Boca Raton
29. Ferrario (2018) Liquid xenon in nuclear medicine: state-of-the-art and the PETALO approach. *JINST* 13 C01044
30. Moskal P, Bednarski T, Białas P (2012) TOF-PET detector concept based on organic scintillators. *Nucl Med Rev* 15(suppl. C):C81–C84
31. Dahlbohm M (ed) (2017) *Physics of PET/CT and SPECT/CT*. CRC Press, Boca Raton
32. Wellen TK (2008) Recent developments in PET detector technology. *Phys Med Biol* 53(17):R287–R317
33. Bisogni MG, Del Guerra A, Belcari M (2018) *Med Appl Silicon Photomultipl*. <https://doi.org/10.1016/j.nima.2018.10.175>
34. Anger HO (1958) Scintillation camera. *Rev Sci Instrum* 29:27
35. Casey ME, Nutt R (1986) A multicrystal two dimensional BGO detector system for positron emission tomography. *IEEE Trans Nucl Sci* 33(1):460–463
36. Ito M, Hong SJ, Lee JS (2011) Positron emission tomography (PET) Detectors with depth-of-interaction (DOI) capability. *Biomed Eng Lett* 1:70–81
37. Hunter WCJ, Barrett HH, Furenlid L (2009) Calibration method for ml estimation of 3D interaction position in a thick gamma-ray detector. *IEEE Trans Nucl Sci* 56(3):725

38. Gross-Weege N, Schug D, Hallen P, Schulz V (2016). Maximum likelihood positioning algorithm for high-resolution PET scanners. *Med Phys* 43(6Part1):3049–3061
39. Mueller F, Schug D, Hallen P et al (2018) A novel DOI positioning algorithm for monolithic scintillator crystals in PET based on gradient tree boosting. <https://doi.org/10.1109/TRPMS.2018.2884320>
40. Müller F, Schug D, Hallen P, Grahe J, Schulz V (2018) Gradient tree boosting-based positioning method for monolithic scintillator crystals in positron emission tomography. *IEEE Trans Radiat Plasma Med Sci* 2(5):411–421
41. Kinahan PE et al (1998) Attenuation correction for a combined 3D PET/CT scanner. *Med Phys* 25(10):2046–2053
42. Dumoulin CL et al (1989) Three-dimensional phase contrast angiography. *Magn Reson Med* 9(1):139–149
43. Walker-Samuel S et al (2013) In vivo imaging of glucose uptake and metabolism in tumors. *Nat Med* 19(8):1067
44. Jackson A, Buckley DL (2005) Dynamic contrast-enhanced magnetic resonance imaging in oncology. Ed. Geoffrey JM Parker. Springer, Berlin
45. Catana C (2015) Motion correction options in PET/MRI. In: *Seminars in nuclear medicine*, vol 45, no 3. WB Saunders
46. Levin CS, Hoffman EJ (1999) Calculation of positron range and its effect on the fundamental limit of positron emission tomography system spatial resolution. *Phys Med Biol* 44(3):781
47. Weissler B (2016) Digital PET/MRI for preclinical applications. Diss. PhD thesis, dissertation, RWTH Aachen
48. Maramraju SH et al (2012) Electromagnetic interactions in a shielded PET/MRI system for simultaneous PET/MR imaging in 9.4 T: evaluation and results. *IEEE Trans Nucl Sci* 59(5):1892–1899
49. Occhipinti M et al (2018) Characterization of the detection module of the INSERT SPECT/MRI clinical system. *IEEE Trans Rad Plasma Med Sci* 2(6):554–563
50. Yamamoto S et al (2011) Interference between PET and MRI sub-systems in a silicon-photomultiplier-based PET/MRI system. *Phys Med Biol* 56(13):4147
51. Gebhardt P et al (2015) RESCUE-reduction of MRI SNR degradation by using an MR-synchronous low-interference PET acquisition technique. *IEEE Trans Nucl Sci* 62(3):634–643
52. Gebhardt P et al (2016) FPGA-based RF interference reduction techniques for simultaneous PET–MRI. *Phys Med Biol* 61(9):3500
53. Lee, BJ et al (2018) MR performance in the presence of a radio frequency-penetrable positron emission tomography (PET) insert for simultaneous PET/MRI. *IEEE Trans on Med Imaging* 37(9):2060–2069
54. Gross-Weege N et al (2018) Characterization methods for comprehensive evaluations of shielding materials used in an MRI. *Med phys* 45(4):1415–1424
55. Wehner J et al (2015) MR-compatibility assessment of the first preclinical PET-MRI insert equipped with digital silicon photomultipliers. *Phys Med Biol* 60(6) 2231
56. Weirich C et al (2012) Analysis and correction of count rate reduction during simultaneous MR-PET measurements with the BrainPET scanner. *IEEE Trans Med Imaging* 31(7):1372–1380
57. Omidvari, N et al (2018) MR-compatibility assessment of MADPET4: a study of interferences between an SiPM-based PET insert and a 7 T MRI system. *Phys Med Biol* 63(9):095002
58. Jezzard P, Barnett AS, Pierpaoli C (1998) Characterization of and correction for eddy current artifacts in echo planar diffusion imaging. *Magn Reson Med* 39(5):801–812
59. Weissler B et al (2015) A digital preclinical PET/MRI insert and initial results. *IEEE Trans Med Imaging* 34(11):2258–2270
60. Gross-Weege N, Nolte T, Schulz V (2018) MR image corrections for PET-induced gradient distortions. *Phys Med Biol*

61. Jones D, Townsend D (2017) History and future technical innovation in positron emission tomography. *J Med Imag* 4(1):011013
62. Vandenberghe S, Mikhaylova E, D'Hoe E (2016) Recent developments in time-of-flight PET. *EJNMMI Phys* 3:3
63. Slomka PJ, Pan T, Germano G (2016) Recent advances and future progress in PET instrumentation. *Semin Nucl Med* 46:5–19
64. Sluis J, Jong J, Schaar J (2019) Performance characteristics of the digital biograph vision PET/CT system. *J Nucl Med*. <https://doi.org/10.2967/jnumed.118.215418>
65. Cherry SR, Jones T, Karp JS (2018) Total-body PET: maximizing sensitivity to create new opportunities for clinical research and patient care. *J Nucl Med* 59:3–12
66. Kagadis GC, Ford NL, Karnabatidis DN (eds) (2018) Handbook of small animal imaging: preclinical imaging, therapy, and applications. CRC Press
67. Gu Z, Taschereau R, Vu NT et al (2018) Performance evaluation of G8, a high sensitivity benchtop preclinical PET/CT tomograph. <https://doi.org/10.2967/jnumed.118.208827>
68. Magota K, Kubo N, Yuji K (2011) Performance characterization of the Inveon preclinical small-animal PET/SPECT/CT system for multimodality imaging. *Eur J Nucl Med Mol Imaging* 38(4):742–752
69. Sanchez F, Orero A, Soriano A, et al (2013) ALBIRA: a small animal PET/SPECT/CT imaging system. *Med Phys* 40(5)
70. Siemens (2013) Symbia t-series system specifications. <https://3.imimg.com/data3/AC/PC/MY-13438971/gamma-camera.pdf>. Accessed 6th April 2019
71. Siemens Healthineers (2017) Symbia Intevo Series https://static.healthcare.siemens.com/siemens_hwem-hwem_sxxa_websites-context-root/wcm/idc/groups/public/@global/@imaging/@molecular/documents/download/mda4/mjyz/~edisp/symbia_intevo_brochure-05353616.pdf. Accessed 6th April 2019
72. GE Discovery NM/CT 670 Pro Data Sheet (2014) <https://mind.net.au/wp-content/uploads/2017/01/Discovery-NMCT-670-Pro-Data-Sheet.pdf>. Accessed 6th April 2019
73. Ritt P, Sanders J, Kuwert T (2014) SPECT/CT technology. *Clin Transl Imaging* (2014) 2:445–457
74. Mediso (2015) AnyScan https://www.mediso.de/media/Brochure%20AnyScan%20Mediso%20English_0915_web.pdf. Accessed 6th April 2019
75. Philips (2012) Brightview X and XCT specifications http://incenter.medical.philips.com/doclib/enc/6281414/BrightView_X_and_XCT_Technical_Specifications_Data_Sheet.pdf%3ffunc%3ddoc.Fetch%26nodeid%3d6281414. Accessed 6th April 2019
76. Khalil MM, Tremoleda JL, Bayomy TB, et al (2011) Molecular SPECT imaging: an overview. *Int J Mol Imaging*. Article ID 796025
77. Gupta A, Kim KY, Hwang D et al (2018) Performance evaluation and quantitative accuracy of multipinhole nanoSPECT/CT scanner for theranostic Lu-177 imaging. *J Korean Phys Soc* 72(11):1379–1386
78. Goorden MC, van der Have F, Kreuger R (2013) VECTor: a preclinical imaging system for simultaneous submillimeter SPECT and PET. *J Nucl Med* 54:1–7
79. Ljungberg M, Pretorius PH (2018) SPECT/CT: an update on technological developments and clinical applications. *Br J Radiol* 90:20160402
80. Delso G et al (2011) Performance measurements of the Siemens mMR integrated whole-body PET/MR scanner. *J Nucl Med* 52.12 (2011):1914–1922
81. Grant AM et al (2016) NEMA NU 2-2012 performance studies for the SiPM-based ToF-PET component of the GE SIGNA PET/MR system. *Med phys* 43(5):2334–2343
82. Disselhorst JA et al (2016) Principles of PET/MR imaging. *J Nucl Med* jnumed-113
83. Vandenberghe S, Marsden PK (2015) PET-MRI: a review of challenges and solutions in the development of integrated multimodality imaging. *Phys Med Biol* 60(4):R115
84. Zaidi H, Del Guerra A (2011) An outlook on future design of hybrid PET/MRI systems. *Med Phys* 38(10):5667–5689

85. Shao Y et al (1965) Simultaneous PET and MR imaging. *Phys Med Biol* 42.10:1965
86. Parl C et al (2017) A novel optically transparent RF shielding for fully integrated PET/MRI systems. *Phys Med Biol* 62(18):7357
87. González AJ et al (2016) The MINDView brain PET detector, feasibility study based on SiPM arrays. *Nucl Instrum Methods Phys Res Sect A: Accel, Spect, Detect Assoc Equip* 818:82–90
88. Benlloch JM et al (2018) The MINDVIEW project: first results. *Eur Psychiatry* 50:21–27
89. Hutton BF, Erlandsson K, Thielemanns K (2018) Advances in clinical molecular imaging instrumentation. *Clin Transl Imaging* 6:31–45
90. Hutton BF et al (2018) Development of clinical simultaneous SPECT/MRI. *Brit J Radiol* 91 (1081):20160690
91. Van Holen R, Vandenberghe S (2013) Optimization of a stationary small animal SPECT system for simultaneous SPECT/MRI. In: 2013 IEEE nuclear science symposium and medical imaging conference (2013 NSS/MIC). IEEE
92. Meier D et al (2011) A SPECT camera for combined MRI and SPECT for small animals. *Nucl Instrum Methods Phys Res, Sect A* 652(1):731–734
93. Hamamura MJ et al (2010) Development of an MR-compatible SPECT system (MRSPECT) for simultaneous data acquisition. *Phys Med Biol* 556:1563
94. Cai L et al (2014) MRC-SPECT: A sub-500 μm resolution MR-compatible SPECT system for simultaneous dual-modality study of small animals. *Nucl Instrum Methods Phys Res Sect A: Accel, Spectrometers, Detect Assoc Equip* 734:147–151



Ultrasound Imaging

4

Georg Schmitz and Stefanie Dencks

Contents

4.1 Introduction.....	136
4.2 Ultrasound Image Formation.....	137
4.2.1 Spatial and Temporal Resolution.....	137
4.2.2 Ultrasonic Signals and Speckle Noise.....	138
4.2.3 Attenuation.....	139
4.2.4 Image Contrast.....	140
4.3 Imaging Techniques.....	141
4.3.1 Line-Oriented Image Acquisition.....	141
4.3.2 Ultrafast Imaging Techniques.....	143
4.3.3 Harmonic Imaging.....	144
4.4 Ultrasound Bioeffects.....	145
4.4.1 Thermal Effects.....	145
4.4.2 Mechanical Effects.....	145
4.5 Contrast-Enhanced Ultrasound Imaging (CEUS).....	146
4.5.1 Contrast Agents.....	146
4.5.2 Contrast Specific Imaging.....	147
4.5.3 Super-Resolution Vascular Imaging by Microbubble Localization.....	149
References.....	151

G. Schmitz (✉) · S. Dencks
Bochum, Germany
e-mail: Georg.Schmitz@ruhr-uni-bochum.de

S. Dencks
e-mail: Stefanie.Dencks@ruhr-uni-bochum.de

© Springer Nature Switzerland AG 2020
O. Schober et al. (eds.), *Molecular Imaging in Oncology*,
Recent Results in Cancer Research 216,
https://doi.org/10.1007/978-3-030-42618-7_4

4.1 Introduction

Ultrasound imaging was introduced around 1950 as a two-dimensional real-time imaging modality by Wild and Reid [51]. Acoustic waves at ultrasonic frequencies are transmitted into the body and the scattered and reflected echo-signals are processed to reconstruct an image. Since then, ultrasound imaging is often the first imaging method applied and is valued for its point-of-care nonionizing real-time imaging capabilities. The image quality has increased significantly since the beginning and was driven by miniaturized transducers and electronics in combination with Moore's law, which enabled real-time capability for increasingly advanced image reconstruction and processing algorithms. On the downside, the user-dependency and lack of reproducibility must be mentioned. However, these drawbacks may be overcome using three-dimensional imaging in more application areas and novel machine learning algorithms (Deep Learning).

For about five decades the recording and reconstruction methods followed the same line-based approach as proposed by Wild and Reid: The sound wave is focused along a line at a certain depth and the echo strength is represented as brightness on the screen. Using line-by-line scanning an image is recorded. The line position was first changed mechanically within a two-dimensional plane by transducer movement, later by electronic beamforming with piezoelectric transducer arrays with hundreds of elements. When the first electronically steered volumetric scans became possible with two-dimensional transducer arrays [43, 49] and up to thousands of elements, the conventional line-by-line scanning had to be abandoned to achieve volumetric real-time imaging because the limiting factor for three-dimensional line-by-line scanning is the speed of sound of about 1540 m/s in soft tissues. This physical limitation makes the sequential acquisition of lines for a complete volume too slow. Therefore, new methods for image formation from weakly focused wide transmit beams with multi-line receive beamforming were proposed first [43]. Alternatively, algorithms for reconstructions from the echoes of a plane or diverging transmit waves were developed allowing the frame and volume rates up to the kilohertz-range ("ultrafast imaging"), see, e.g., [25, 29, 33]. At the same time, the availability of faster computers with graphics processing units (GPUs) enabled completely software-programmable image reconstruction on general-purpose systems, which makes shorter innovation cycles possible.

Besides this paradigm change in image reconstruction, several innovations extended the capabilities of ultrasound imaging over the years: Flow analysis by Doppler imaging [23] was added to the modality in the 1980s. To overcome the low echogenicity of blood, ultrasound contrast agents made of encapsulated gas microbubbles were introduced in the 1990s [4]. Then, dedicated harmonic imaging techniques enabled their sensitive, nearly background-free imaging. Consequently, attaching specific ligands to these bubbles enabled ultrasound molecular imaging [7, 27, 28]. Around the same time, elastography was introduced by Ophir et al. [36]: The deformation of tissue is measured in the ultrasound images (strain imaging). From this, elastic tissue parameters can be reconstructed. This static elastographic

approach was further developed by vibro-acoustography [13], acoustic-radiation-force imaging (ARFI) [34], and shear wave elastography [39]. A review of elastographic methods can be found in Gennisson et al. [17]. A more recent innovation in contrast-enhanced imaging is ultrasound localization microscopy, which exploits the high spatial accuracy of the localization of isolated microbubbles for super-resolution imaging [6, 42].

In the following, this chapter will be focused on the technical aspects of the methods that are important in molecular imaging. Therefore, some important topics for general clinical ultrasound like Doppler imaging are left out here. For an in-depth technical description of all aspects of ultrasound imaging, the textbook by Szabo is recommended [46].

4.2 Ultrasound Image Formation

4.2.1 Spatial and Temporal Resolution

Ultrasound images are formed by transmitting a mechanical wave at ultrasonic frequencies from the transducer into the tissue. The reflected and scattered waves are recorded with the same transducer and the image is reconstructed from the received data. The frequencies are typically in the range of 1.5–15 MHz in clinical imaging and up to 50 MHz for preclinical systems. The average speed of sound waves in soft tissue is about 1540 m/s, which results in wavelengths in the range of 1 mm–0.1 mm for typical clinical imaging and down to around 30 μm for preclinical applications. The wavelengths already give the order of magnitude of the spatial resolution that can be achieved in the best case although the actual resolution depends on the specific design of the imaging system. The theoretical diffraction limit is given by half the wavelength, which often is not achieved in practice. However, using contrast agents for ultrasound localization microscopy, imaging of vasculature beyond the diffraction limit is feasible and will be discussed in a separate section.

In line-oriented scanning, the axial resolution (resolution in the direction of sound propagation) is determined mainly by the frequency bandwidth of the ultrasound pulse. The lateral resolution (the resolution in the image plane perpendicular to the sound propagation direction) is determined by the transmit and receive focusing, which is characterized by the ratio of the imaging depth to the aperture size (F-number) of the active transducer. Typically, the lateral resolution is not as good as the axial resolution, which is in the order of a wavelength. In two-dimensional imaging, the resolution in the third dimension, i.e., the slice thickness or elevational focusing, is often not taken into account although it is the least effective focusing. Many clinical ultrasound systems use a fixed focus acoustic lens in front of the transducer, which has only a small aperture in the elevation direction. This results in a relatively large F-number (ratio of the focus distance to the transducer width perpendicular to the imaging plane) with the corresponding

weak focusing. Information about this fixed focus is usually not shown on screen and is often unknown to the investigator.

The temporal resolution of ultrasound imaging is limited by the speed of sound and depends on the imaging depth. For a typical clinical imaging depth of 7.5 cm, the sound wave must travel to this depth and back, resulting in 15 cm with a travel time of 0.1 ms. Therefore, with novel ultrafast plane wave imaging systems a maximum frame rate of 10 kHz is achieved. These systems acquire a whole image with only one transmit/receive cycle. The high temporal resolution allows, for example, real-time volumetric imaging of the heart. However, standard clinical two-dimensional ultrasound imaging techniques acquire data in a sequential line-by-line fashion, which reduces frame rates to a few 10 Hz for one line per transmit/receive cycle or in the 100 Hz range for systems with parallel multi-line acquisitions.

4.2.2 Ultrasonic Signals and Speckle Noise

Ultrasound images show a characteristic spatial noise pattern which is termed “speckle” and arises from the interference of the echoes from small scatterers that cannot be resolved. Figure 4.1a shows a typical ultrasound pulse that is transmitted into tissue and a corresponding raw echo signal (Fig. 4.1b), for which often the term *A-scan* (Amplitude scan) is used. In ultrasound images, only the signal strength of the echoes is presented as brightness. Therefore, the envelope of the signal as shown in Fig. 4.1b in red is extracted by amplitude demodulation and logarithmically transformed to stretch the lower signal amplitudes and compress the bright echoes. This is also the origin of the term *B-mode* (Brightness-mode), which is used for ultrasound images in contrast to the raw or radio-frequency-signals (*RF-signals*). A usual dynamic range of ultrasound images on a logarithmic

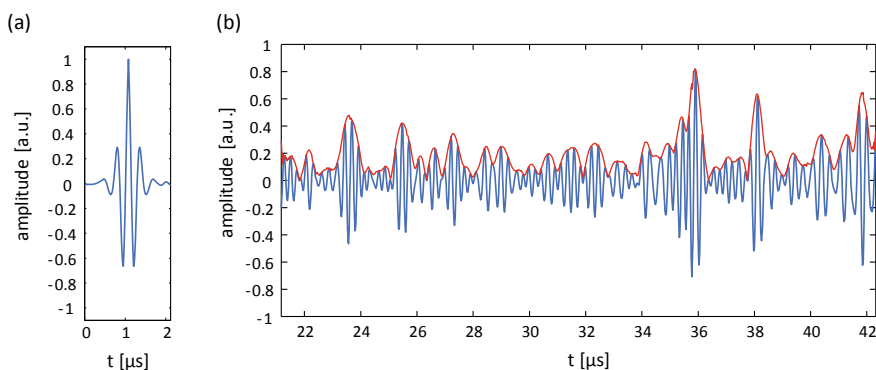


Fig. 4.1 **a** Ultrasound transmit pulse and **b** radio-frequency (rf) echo from soft tissue (“A-scan”, blue) and demodulated envelope signal (red) which is used as brightness in *B-mode* images after logarithmic transformation

brightness scale is close to 60 dB, which represents a ratio of 1:1000 between the darkest and the brightest gray value.

When the oscillating echoes of many small sub-resolution scatterers in the tissue add up in the ultrasound transducer, the result has a random fluctuation because the oscillating signals may interfere constructively or destructively depending on the distances of the scatterers to the transducer. The sum of signals in two pixels of the image gives statistically independent results when their locations are further apart than the image resolution. Therefore, a spatially varying random variation of the intensity is observed with a typical feature size that corresponds to the image resolution. This pattern can be modeled as multiplicative spatial noise. As the noise is spatially but not temporally varying, temporal filtering cannot remove this pattern. The most effective method to reduce the speckle pattern is to overlay image acquisitions from different angles, for which the speckle pattern varies (compound imaging). Compound imaging modes are realized in many commercial systems in various ways. For example, only the receive beams can be angled to the same point from different directions. However, it is more effective to vary the transmit directions as well. Additional image processing can be used to further reduce speckle.

4.2.3 Attenuation

The spatial resolution and penetration depth of ultrasound imaging are coupled because of the frequency-dependent attenuation in soft tissues. A rough estimation for the attenuation assumes a linear frequency dependence of the attenuation coefficient α , which is around 0.6 dB/(MHz cm) in soft tissues but with considerable variations depending on tissue type [11]. The ratio of the transmitted pressure p_0 and the received pressure p after distance z at frequency f is then given by

$$\frac{P}{p_0} = 10^{-\frac{\alpha}{20\text{dB}}fz}. \quad (4.1)$$

For example, for an imaging depth of 5 cm, i.e., $d = 10$ cm to the target and back, the attenuation at $f = 1$ MHz is $\alpha fz = -6$ dB, which is equivalent to a factor of 0.5, while the attenuation at $f = 10$ MHz is $\alpha fz = -60$ dB, which gives a factor of 0.001.

Summarizing, the spatial resolution increases linearly with increasing frequency, the echo signal strength and—together with it—the penetration depth decay exponentially. For this reason, the spatial resolution and penetration depth of ultrasound imaging cannot be scaled down completely from clinical to preclinical imaging.

It is a physical principle derived from causality that frequency-dependent attenuation is coupled to a frequency-dependent speed of sound (dispersion). This is known as the Kramers-Kronig relations and holds for ultrasound waves in soft tissues [50]. However, the deviation over the relevant frequency bandwidth is only a few m/s and typically can be neglected.

4.2.4 Image Contrast

As ultrasound is a mechanical wave, it is reflected and scattered at changes in the mechanical properties of the medium. The mechanical properties determining the wave propagation are the mass density ρ and the compressibility κ of the medium. They both determine the propagation speed $c = 1/\sqrt{\rho\kappa}$ of the wave. In biological soft tissues the mass density varies less than the compressibility. The principal soft tissue components contributing to scattering are water, fat, and collagen [41]. Their spatial organization and contrast determine the average signal strength from a tissue. The usual ultrasound imaging techniques, which use linear reconstruction schemes, cannot reconstruct the absolute material parameters but only show when the material parameters change. Thus, blood—as a relatively homogeneous medium—only shows weak scattering in clinical ultrasound and appears dark in images. When reflection at a surface occurs, the acoustic impedance $Z = \sqrt{\rho/\kappa} = \rho c$ of the materials can be used to calculate the pressure reflection coefficient. For normal incidence of the wave with amplitude p_0 the reflected wave amplitude p is given by

$$\frac{p}{p_0} = \frac{Z_2 - Z_1}{Z_2 + Z_1} \quad (4.2)$$

where Z_1 is the acoustic impedance of the medium the wave is passing through before it is reflected at the border to the medium with Z_2 . Because of the comparatively low contrast in material parameters a significant amount of energy can penetrate deeper into tissue. However, ultrasound echoes from larger depths are very weak, also because of the additional effect of attenuation. To cope with this, an ultrasound system needs a dynamic range of up to 150 dB between the strongest and weakest echoes it can receive.

In Table 4.1, values for the speed of sound and acoustical impedance for some typical tissues, air, and water at 37 °C are listed. The soft-tissue average of the speed of sound is $c = 1540$ m/s. It is used to calculate the distance z of a target from the target's echo time t by $z = ct/2$. This setting may be adapted in some systems

Table 4.1 Speed of sound and acoustic impedance. For tissues, mid-range values are given [11]. All values at 37 °C

Material	Speed of sound in m/s	Acoustical impedance in MRayls = 10^6 kg/(m ² s)
Air	330	0.0004
Water	1524	1.48
Fat	1450	1.38
Liver	1570	1.65
Muscle	1580	1.70
Bone	3500	7.80
Soft tissue average	1540	1.63

by tissue-specific presets or adaptive algorithms. The strong impedance mismatch between air and soft tissue leads to the complete reflection at air interfaces and explains the need for coupling media (ultrasound gels) between the transducer and the skin surface.

Consequently, in ultrasonic molecular imaging, processes at the molecular level can only be imaged without using contrast agents when they lead to a change in the bulk tissue properties, e.g., by a change of the tissue's water content. However, to realize sensitive molecular imaging, contrast media with ligands attached to them are needed as molecular probes.

4.3 Imaging Techniques

4.3.1 Line-Oriented Image Acquisition

Ultrasound imaging was developed as line-oriented pulse-echo image acquisition. This is still true for many systems but extensions to fast multi-line acquisitions, plane wave or diverging-wave imaging are already available in commercial systems and will be discussed in the next section.

Figure 4.2 shows a linear transducer array as it is often used in high-frequency applications and preclinical scanners. The transducer array consists of hundreds of piezoelectric transducers with regular spacing in the order of the wavelength λ . An active group of elements around the image line is connected to the system's electronic channels. To focus at a given focal depth on the line, all transmitted signals

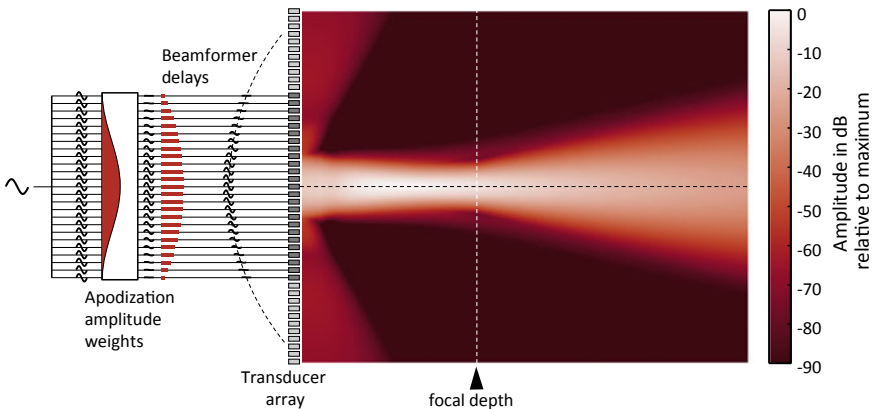


Fig. 4.2 Schematic diagram of linear array beamforming. By weighting and delaying the signals in transmit and receive the sound beam is focused at the focal depth and the sound energy is restricted around a line at the transmit position. The image shows the normalized maximum pressure amplitude for pulse excitation of the field

must arrive at this depth at the same time. Therefore, elements further away from the focus must be pulsed earlier than elements in the center of the transducer, which have the closest distance to the focus. The necessary delays can be calculated easily from geometric considerations. Additionally, the signals can be amplitude weighted over the aperture (apodised) which results in a smoother lateral profile of the beam. In Fig. 4.2 the normalized maximum pressure recorded when a pulse travels through the homogenous medium is shown for a transducer with an element spacing of λ . This sound field was simulated with Field II for MATLAB [24, 26]. The pressure distribution is well centered along the image line. The lateral extent determines the lateral resolution. Behind the focus the beam widens, and objects will be imaged with lower lateral resolution. Therefore, often several transmit foci are placed at different depths, typically marked by arrows on the scanner's display. The displayed images are reconstructed by blending over between acquisitions with different focal depths. The more foci are selected, the lower the image frame rate will become because more acquisitions per line are needed.

After the acquisition of one line, the centerline is shifted to the next position. In the simplest case this is done by moving the active group by one element, but also shifts smaller than the element size can be realized by shifting and resampling the apodization weight function to record lines between elements.

Alternatively, for phased arrays, the line position is changed by steering the beam under different angles. In this case, all lines start at the same point on the aperture and the active group of elements remains the same, often all elements. The focus is put on different positions on a circle around this point with a focal depth radius. Delays are again calculated from the geometric distances of the elements from the focal point. By this, a sector scan around the center of the array is generated. Linear array transducers with extended field of view use a combination of linear shifting in the center of the image and beam steering at the borders resulting in a trapezoid field of view.

The element spacing together with the channel count has significant impact on the achievable image quality and the cost of the system. The array is used to synthesize transmit sound fields and to sample the echo sound fields. Ideally, the array spacing would be as small as half the wavelength ($\lambda/2$) at the highest frequency of the used bandwidth. In practice, often larger distances between array elements are realized due to a limited number of channels for a fixed transducer size. In line beamforming these compromises lead to grating lobes, i.e., the transducer transmits and receives not only under the main line but shows grating sidelobes. This reduces the overall image contrast by clutter signals from the sidelobe reception. For a linear array with spacing s the first grating lobes occur at $\varphi = \sin^{-1}(\lambda/s)$ measured from the scan line. The field in Fig. 4.2 was simulated for the typical linear array spacing $s = \lambda$, which puts the grating lobes at $\pm 90^\circ$. Parts of the sidelobes can be seen in the image as the triangular shaped fields in front of the transducer. If the beam is steered, these sidelobes will also be steered into the image and the spacing should be reduced further for phased array imaging.

In receive mode, the same delays can be applied to shift echoes coming from a certain depth back to the same time and then add all channels constructively. This technique is termed delay-and-sum (DAS) beamforming. In contrast to the fixed transmit focus, the receive focus can be adapted dynamically to the depth from which the echoes are received by continuously changing the beamformer delays. Additionally, often the aperture size is adapted to the depth to achieve a constant F-number and lateral resolution over imaging depth. State-of-the-art high-end systems additionally use retrospective beamforming techniques [16], which use the acquisitions of several neighboring lines and process them to achieve better lateral resolution. It has to be noted that the image in Fig. 4.2 shows the pressure amplitude in the field. The sensitivity in receive has the same shape and the resulting pulse-echo sensitivity is the product of both and will result in a better focus than observed in Fig. 4.2.

Because the time for one pulse-echo acquisition at maximum depth is determined by the speed of sound, the frame rate of the imaging process is determined by the number of acquired lines, the number of foci per line, and the imaging depth. This results in frame rates of about 10–50 Hz for 2D line-by-line imaging. To speed-up image acquisition, several transmit beams that are spatially well separated can be excited simultaneously. Receive beamforming must run in parallel for this number of beams and thus needs sufficient computing power. To keep the beams separated only a few parallel beams can be used and the speed-up is only directly proportional to the number of beams. Therefore, very high frame rates in the kilohertz-range can only be achieved with unfocused or less focused transmit beams.

4.3.2 Ultrafast Imaging Techniques

To increase the frame rate, unfocused transmissions are used, and complete frames are reconstructed in parallel. This can be achieved, e.g., by plane wave-imaging (PWI). Here, all elements of the transducer are fired at the same time to send a quasi-plane wave into the tissue. Again, for each point in the field, the travel time of the wave can be calculated, as well as the time back to any receiving transducer element. For each image position, this results in unique delays at each channel. These are considered by the DAS-beamformer to generate the image pixel at this point. The resulting images have reduced focusing and less contrast because of the missing transmit focus but can be acquired at frame rates of several kilohertz. These ultrafast acquisitions enabled new imaging modalities like shear wave elastography [39] and functional ultrasound imaging [30]. Furthermore, it was also demonstrated that the transmission of plane waves at different angles and the addition of beamforming results allowed to flexibly exchange frame rate for image quality. Interestingly, the same image quality as a line-by-line acquisition could be realized at much higher frame rates [33]. This is demonstrated in Fig. 4.3: Here, different numbers of plane wave acquisitions were compounded for retrospective transmit focusing using a Verasonics Vantage 256 research scanner with an L12-3v linear array transducer (ca. 8 MHz center frequency) and parallel receive beamforming on

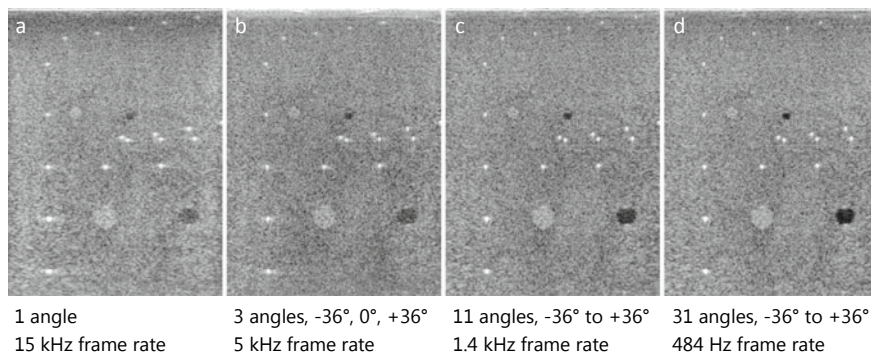


Fig. 4.3 Plane wave acquisitions of an ultrasound test phantom (CIRS model 040) with retrospective beamforming: Frame rate can be traded for image quality. The number of acquired angles is **a** 1, **b** 3, **c** 11, and **d** 31 from -36° to $+36^\circ$. Image size is $38.2 \text{ mm} \times 51.3 \text{ mm}$. The image quality difference is best seen for the contrast of the echo-free cyst in the lower right of the image and the resolution of the point targets

192 lines. Figure 4.3a shows a single plane wave acquisition under 0° . In Fig. 4.3b–d the angle was varied from -36° to $+36^\circ$ in 3, 11, and 31 equal steps, respectively.

The maximum achievable frame rates for the acquisitions can be calculated from the image depth of 5.13 cm and are 15 kHz, 5 kHz, 1.4 kHz, and 484 Hz, respectively. A line-by-line acquisition of 192 lines would have a maximum frame rate of 78 Hz and comparable quality as Fig. 4.3d. It is demonstrated that frame rates can be traded for image quality. With an increasing number of angles, the frame rate decreases while the lateral resolution and the dynamic range of the image significantly improves.

4.3.3 Harmonic Imaging

Most clinical standard imaging with line-oriented methods is done using the tissue harmonic imaging (THI) mode that was introduced in 1997 [2]. This mode exploits the nonlinear transmission behavior of soft tissues: For large pressure amplitudes in the ultrasound wave the speed of sound increases. For the case that a monofrequent sine wave is transmitted, it will be deformed thus generating higher harmonics. The deeper the wave travels, the more energy is shifted to the higher harmonics. Because of the limited bandwidth of ultrasound transducers mainly the second harmonic at double the original frequency can be used for imaging. Since the high frequencies are generated within the tissue, they are not attenuated on the path to the depth where they are generated.

For harmonic imaging, the image is formed only by the higher harmonics using dedicated pulse sequences similar to those used for contrast media imaging and

discussed in that section. The main advantage of harmonic imaging is not so much an increase in resolution due to the high frequencies but a considerable reduction in reverberation and clutter signals, which improves the overall image contrast. The grating lobes of the transmit and the receive beam occur at different angles, so that the clutter signals, which improves sidelobes are attenuated. Additionally, reverberations in superficial tissue layers that are received at the same time as the echoes from deeper structures do not develop the same level of harmonics because they lose the necessary pressure amplitude during the multiple reflections. Therefore, these artifacts are efficiently suppressed. Unfortunately, THI does not work well with unfocused transmissions because the amplitudes of plane wave excitation are much lower than those for line excitation.

4.4 Ultrasound Bioeffects

4.4.1 Thermal Effects

The absorption of ultrasound in the tissue leads to an increase in temperature, which depends on the temporal average intensity of the sound field. To give the investigator an estimate of the expected temperature increase in tissue, diagnostic ultrasound scanners must display the thermal index (TI) as part of the Output Display Standard (ODS) on the screen. The thermal index is the ratio of the system's power to the power needed to increase the temperature at the hottest point of a model tissue by one degree. If the TI is less than 0.4, it does not need to be displayed. There are various thermal index calculations, e.g., for soft tissue (TIS), bone (TIB), and skull (TIC) as model tissues. They all assume worst-case scenarios and may not match the actual scanning situation. Thus, the thermal index is not a measure of the actual temperature increase, but an indication of the risk of such an increase.

4.4.2 Mechanical Effects

The tissue can also be damaged by direct mechanical effects known as cavitation, which occur in the underpressure phase of the wave. Cavitation is more likely to occur when cavitation nuclei, such as gas microbubbles are present in the tissue. The effect is frequency-dependent and occurs at lower pressure amplitudes for lower frequencies. The mechanical index (MI) is displayed as an indication of the risk of cavitation:

$$MI = \frac{p_{-\max}}{\sqrt{f}} \frac{\sqrt{\text{MHz}}}{\text{MPa}}. \quad (4.3)$$

In this, $p_{-\max}$ is the peak negative pressure and f the frequency. The units in the equation make the MI dimensionless: It must be displayed for values larger than 0.4

and the Food and Drug Administration (FDA) limits it to a maximum of 1.9. Cavitation can destroy cells and especially in the presence of microbubbles that are cavitation nuclei, bioeffects like capillary rupture have been observed [32].

4.5 Contrast-Enhanced Ultrasound Imaging (CEUS)

4.5.1 Contrast Agents

In some applications, the low echogenicity of blood is problematic. Therefore, contrast media were applied already in 1968 to visualize the aortic root: Gramiak and Shah used small air bubbles they generated by shaking a saline solution before injection [18]. From the very small acoustic impedance of air, it is expected that scatterers made of gas have the best contrast of all possible materials. However, microbubbles with a radius of less than ten micrometers, which are small enough to pass through the lung and all capillaries, dissolve quickly without encapsulation. For this reason, commercial contrast agents, which came to the market in the 1990s, are microbubbles that are encapsulated by a shell. The agents with wide clinical use typically have soft shells made of phospholipid monolayers. Alternatively, hard-shelled bubbles can be used and recently have been applied mainly in pre-clinical imaging. One example of these use polymer shells made from poly n-butyl cyanoacrylate (PBCA) [15]. While first-generation contrast media were filled with air, current contrast media use gas with low solubility, e.g., sulfur hexafluoride (SF₆), see the overview in Table 4.2. These bubbles are stable for several minutes, stay in the vascular system, and will eventually be phagocytosed in the liver and spleen.

The oscillation of free gas bubbles is nonlinear and was already investigated by Lord Rayleigh [38]. The additional effect of the shell has been accounted for by various model extensions of which the Marmottant-model [31] was a milestone for modeling the nonlinear behavior of the shell considering effects like the buckling of the shell's phospholipids. A comprehensive overview of the physical properties of lipid-encapsulated microbubbles can be found in the review by Helfield [19].

Table 4.2 Examples of clinically approved lipid-shelled microbubbles, data from FDA clinical approval, prescription information, and [45]

Agent	Gas	Ø (µm)	Manufacturer
Imagent	Perflhexane	<3 (78.8%) <10 (99.8%)	Alliance Pharmaceuticals Inc.
Definity	Octafluoropropane	1.1–3.3 <10 (98%)	Lantheus Medical Imaging
Sonazoid	Perfluorobutan	2.1 <7 (99.9%)	GE Healthcare
SonoVue/Lumason	Sulfurhexafluoride	1.5–2.5 <10 (99%)	Bracco Diagnostics Inc.

All the nonlinear models have in common that for higher pressure amplitudes the expansion of the bubble in the underpressure phase of the sound wave behaves differently from the compression of the bubble in the overpressure phase. Depending on the frequency, amplitude, and bubble properties the oscillations are more compression dominated (“compression-only” oscillations) or expansion dominated. For the excitation with a monofrequent sine wave, this results in an asymmetric oscillation and a periodic non-sinusoidal scattered signal containing higher harmonics of the driving fundamental frequency. Additionally, subharmonics below the fundamental frequency can be generated. These harmonics and subharmonics can be exploited to sensitively and specifically detect microbubbles [40]. Dedicated sequences for contrast harmonic imaging are available on commercial scanners. When the pressure amplitude is increased over a certain threshold, the bubbles will be destroyed in the compression phase, i.e., they are split into several smaller bubbles. Because their scattering cross section is much smaller, they will not be imaged anymore. For microbubble imaging, the mechanical index (MI) should be below ca. 0.4 to reduce bubble destruction. However, microbubble destruction can also be exploited for contrast specific imaging: When the microbubbles are destroyed, they emit a broadband acoustic wave that is termed stimulated acoustic emission (SAE) [3]. Additionally, the bubble destruction can be observed in Doppler imaging as a short flash [47]. Due to the sudden loss of correlation, the destruction is misinterpreted by the system as motion.

4.5.2 Contrast Specific Imaging

To detect the microbubbles sensitively and to suppress the tissue background signals, their nonlinear oscillation is exploited by imaging only the higher harmonics. However, this cannot be solved satisfactorily by bandpass filters for these harmonics, because the frequency bands of the fundamental and the harmonics overlap. This is caused by the short broadband ultrasound pulses used for imaging, that—for optimal resolution—use the full frequency band of the transducer. For harmonic imaging a smaller frequency band can be used, however, the second harmonic band is double as wide as the fundamental and still overlaps with it. Higher order harmonics are mostly not within the frequency band of the transducer anymore, and therefore, cannot contribute to the imaging.

For these reasons, contrast specific imaging works with multi-pulse acquisitions that are combined to achieve harmonic separation. The simplest version of this concept is pulse inversion imaging (also called phase-inversion) [21, 22] illustrated in Fig. 4.4: Here, the first acquisition with an ultrasound pulse (Fig. 4.4a) is repeated with a negative replica of the same pulse (Fig. 4.4b). A linear scatterer will respond to the second pulse also with a negative replica of the echo of the first acquisition. Adding the two acquisitions (Fig. 4.4c, d) will cancel the signal from linear scatterers (Fig. 4.4e). However, for a nonlinear scatterer, the response to the positive and negative pulse (Fig. 4.4f, g) will look different and the harmonic signals from nonlinear scatterers will remain (Fig. 4.4h) after adding the

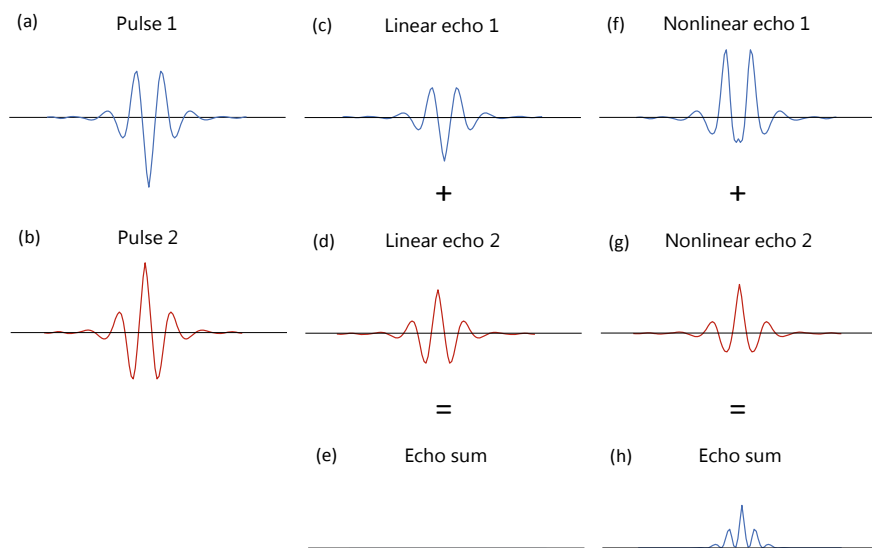


Fig. 4.4 Pulse inversion imaging: two sequential acquisitions with the pulse in **a** and its negative replica in **b** are acquired. Adding the echoes of a linear scatterer **c** and **d** results in no signal **e** while adding together the echoes **f** and **g** from a nonlinear scatterer results in a harmonic signal (**h**)

acquisitions. Besides pulse inversion with two acquisitions, also other amplitude modulations of several pulse acquisitions are used to acquire the harmonic content, e.g., “Contrast Pulse Sequencing” (CPS) with three acquisitions with a pulse weighting of -0.5 , 1.0 , and -0.5 [37]. The advantage of this sequence is that the nonlinearity also generates fundamental frequency components that are not canceled in contrast to the fundamental frequency components from linear scatterers.

The tissue background cannot be suppressed completely with these sequences because of the nonlinear propagation of sound in tissue. When the first contrast-specific sequences were applied, it was realized that the nonlinear propagation in tissue also generates harmonic signal contents. Now, this is also used to improve image quality by tissue harmonic imaging.

While contrast-specific sequences work well for soft-shelled microbubbles like Sonovue around the resonance frequencies at the lower MHz range, they may not work well for hard-shelled bubbles in preclinical imaging at 40 MHz (for example, PBCA microbubbles [15]). In general, in preclinical imaging at high frequencies, the strong backscatter from microbubbles is more important than the nonlinearity to sensitively detect microbubbles and contrast imaging concepts may not translate easily from small animal studies to clinical applications.

4.5.3 Super-Resolution Vascular Imaging by Microbubble Localization

A new method of super-resolution vascular imaging using microbubbles was presented first in 2011 independently by Couture et al. [6] and Siepmann et al. [42]. It is based on the idea that the position of an isolated microbubble can be localized with a precision much higher than the resolution of the imaging system. This can be achieved by detecting single microbubbles in the image and correlating their signals with the expected microbubble response or by determining the centroid of a microbubble signal. The measured position can be marked in the image as a point with an arbitrarily small extent. However, it is reasonable to use a size that represents the uncertainty of localization. By pinpointing the microbubbles passing through the vessels over time, the vascular system is reconstructed in high resolution. As a common name for this technique, *Ultrasound Localization Microscopy (ULM)* has been established. In most of its applications, the microbubbles are also tracked from frame to frame over time to fill the vascular system also between their localizations and to determine functional parameters like flow velocity and direction [1, 5, 12]. For this, the bubble localizations in different frames are associated with tracks. In Fig. 4.5 the general idea and the resolution improvement is schematically visualized. In (a), the microbubble responses for consecutive frames are shown. In (b), the localized microbubble positions (marked with crosses) of frame 1 are assigned to the positions determined in frame 2 and the flow velocities are derived

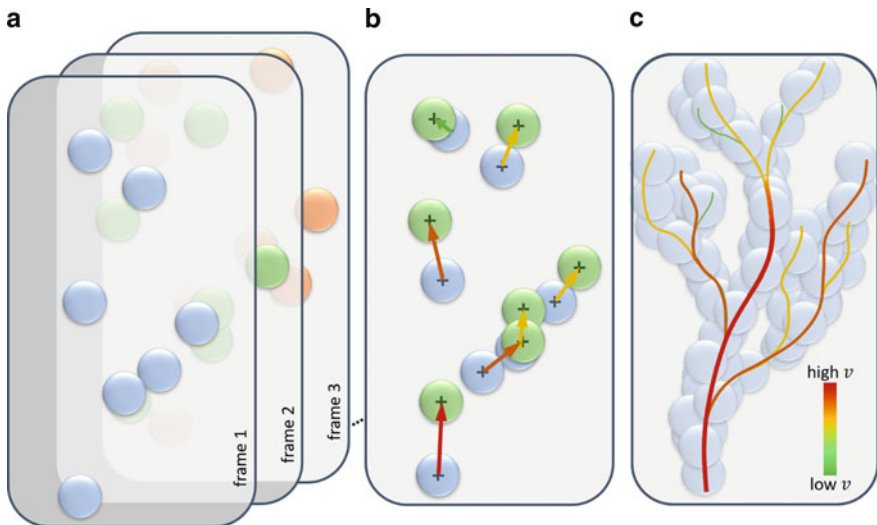


Fig. 4.5 **a** Microbubbles are isolated from the background in several frames by image processing. **b** A tracking algorithm connects the bubble positions of probable tracks. **c** After observing bubbles in many frames over time (shown in the background), high-resolution images of the tracks reveal the vasculature together with velocity information

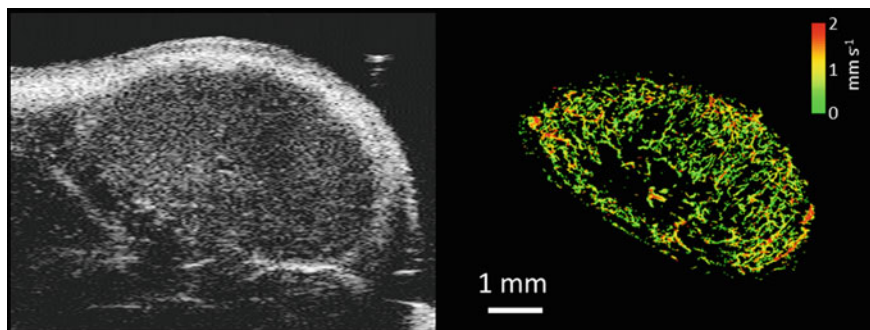


Fig. 4.6 A431 tumor (murine xenograft) imaged with hard-shelled PBCA microbubbles at 40 MHz center frequency with a VisualSonics Vevo 2100 preclinical ultrasound scanner (left panel) and the vasculature from the ULM method. The color scale indicates the number of microbubbles observed in the vessel. Details on the image acquisition and processing can be found in Opacic [35]. The data presented here were prepared from the same tracking data as the figures published in Opacic [35] under the creative commons license BY4.0

from the covered distances. The vasculature reconstructed from several frames is shown in (c). The resolution improvement compared to the simple overlay of the microbubble responses (white bubbles) is clearly noticeable. Larger vessels of higher flow velocities are typically passed by more microbubbles leading to more localizations within the extent of the vessel. If a certain number of microbubbles is detected within a vessel, also the flow profile can be derived. Based on the flow profiles of two very close vessels that can be still separated, the resolution of the *ULM* image can be estimated. Two very close vessels can also be easily separated in case of opposite flow directions (Fig. 4.6).

The reliability of the tracking—and thus the reconstruction of the vasculature—depends on several parameters. In case of very high frame rates (e.g. 500 Hz) the distances covered by the microbubbles between consecutive frames are very small, and in combination with low densities, the assignment of bubble localizations to tracks in consecutive frames is unambiguous and can be easily accomplished with the nearest neighbor tracking [5, 12]. In the case of low frame rates and higher localization densities, the unique associations can get lost and more advanced tracking algorithms are needed to ascertain the reliable assignment of tracks [8]. This also holds for very complex vasculatures if the fine net of vessels in conjunction with the poor elevational focus leads to many apparent crossings of vessels in the image plane.

The potential of *ULM* has been proven for a wide range of preclinical applications [5, 12, 14, 35, 44] leading to resolutions down to approximately a tenth of the wavelength. Also, the feasibility of a clinical application with a pixel size of 10 μm has already been shown [10, 35]. However, still, some advances must be made for its translation into clinical practice. One of the most critical issues to be mentioned is the tissue motion estimation, because the advantage of a precise

bubble localization in each frame gets lost in case of poorly registered frames: The reconstructed vasculature gets blurred and details will get lost [20].

Another important aspect is the determination of suitable microbubble concentrations because the quality of reconstruction highly depends on the number of detected microbubbles. The higher the number of localizations the more detailed information can be derived. To decrease examination times, a high concentration of microbubbles would be desirable. Nevertheless, very high concentrations lead to more and closer overlapping microbubble responses in each frame, thus, hindering the precise detection. Therefore, the enhancement of detection algorithms is one focus of research [48]. But, as discussed earlier, higher concentrations also increase the ambiguity of track assignments, so a good compromise has to be found. Generally, the number of localizations in a limited acquisition time can also be increased by high frame rates. However, the number of passing microbubbles is not increased. This can be relevant especially for microvasculatures whose capillaries are infrequently flown through by microbubbles. Therefore, the optimal parameter settings might depend on the applications.

For the recognition and characterization of pathologic vascularization, the definition and relevance of new structural and functional parameters and their optimal combination will be one objective of future research. In clinical practice, it is to be expected that only a certain degree of the vasculature can be reconstructed within the acquisition time [8, 9]. Therefore, it will also be necessary to estimate the degree of reconstruction to standardize the derived structural and functional parameters.

The translation of *ULM* from 2D to 3D offers several advantages. By increasing the elevational resolution, the track assignments become less ambiguous. Additionally, the complexity of the microvasculature can be revealed better in a volume instead of an imaging plane. Furthermore, flow velocities can be correctly estimated (for 2D, only the flow velocities projected onto the imaging plane are calculated). But, most importantly, the out-of-plane motion could be better handled leading to better motion corrections.

References

1. Ackermann D, Schmitz G (2016) Detection and tracking of multiple microbubbles in ultrasound B-Mode images. *IEEE Trans Ultrason Ferroelectr Freq Control* 63(1):72–82
2. Averkiou MA, Roundhill DN, Powers JE (1997) A new imaging technique based on the nonlinear properties of tissues. In: An international symposium on 1997 IEEE ultrasonics symposium proceedings (Cat. No.97CH36118)
3. Bauer A, Schlieff R, Zomack M, Urbank A, Niendorf HP (1997) Acoustically stimulated microbubbles in diagnostic ultrasound: properties and implications for diagnostic use. *Advances in Echo Imaging Using Contrast Enhancement*. N. C. Nanda, R. Schlieff and B. B. Goldberg. Dordrecht, Springer Netherlands, pp 669–684
4. Burns PN, Hilpert P, Goldberg BB (1990) Intravenous contrast agent for ultrasound Doppler: in vivo measurement of small tumor vessel dose-response. In: Proceedings of the twelfth annual international conference of the IEEE engineering in medicine and biology society, vol 12(1), pp 322–324

5. Christensen-Jeffries K, Browning RJ, Tang MX, Dunsby C, Eckersley RJ (2015) In vivo acoustic super-resolution and super-resolved velocity mapping using microbubbles. *IEEE Trans Med Imaging* 34(2):433–440
6. Couture O, Besson B, Montaldo G, Fink M, Tanter M (2011) Microbubble ultrasound super-localization imaging (MUSLI). *IEEE Int Ultrasonics Symposium 2011*:1285–1287
7. Dayton PA, Ferrara KW (2002) Targeted imaging using ultrasound. *J Magn Reson Imaging* 16:362–377
8. Dencks S, Ackermann D, Schmitz G (2016) Evaluation of bubble tracking algorithms for super-resolution imaging of microvessels. In: 2016 IEEE international ultrasonics symposium (IUS). <https://doi.org/10.1109/ultsym.2016.7728500>
9. Dencks S, Piepenbrock M, Schmitz G, Opacic T, Kiessling F (2017). Determination of adequate measurement times for super-resolution characterization of tumor vascularization. 2017 IEEE International Ultrasonics Symposium (IUS)
10. Dencks S, Piepenbrock M, Opacic T, Krauspe B, Stickeler E, Kiessling F, Schmitz G (2019) clinical pilot application of super-resolution US imaging in breast cancer. *IEEE Trans Ultrason Ferroelectr Freq Control* 66(3):517–526
11. Duck FA (1990) *Physical Properties of Tissue*. Academic Press, New York
12. Errico C, Pierre J, Pezet S, Desailly Y, Lenkei Z, Couture O, Tanter M (2015) Ultrafast ultrasound localization microscopy for deep super-resolution vascular imaging. *Nature* 527(7579):499–502
13. Fatemi M, Greenleaf JF (1998) Ultrasound-stimulated vibro-acoustic spectrography. *Science* 280(5360):82–85
14. Foiret J, Zhang H, Ilovitsh T, Mahakian L, Tam S, Ferrara KW (2017) Ultrasound localization microscopy to image and assess microvasculature in a rat kidney. *Scientif Reports* 7(1):13662
15. Fokong S, Siepmann M, Liu Z, Schmitz G, Kiessling F, Gätjens J (2011) Advanced characterization and refinement of poly n-Butyl cyanoacrylate microbubbles for ultrasound imaging. *Ultrasound Med Biol* 37(10):1622–1634
16. Freeman S, Li PC, O'Donnell M (1995) Retrospective dynamic transmit focusing
17. Gennisson JL, Deffieux T, Fink M, Tanter M (2013) Ultrasound elastography: principles and techniques. *Diagnostic Intervent Imaging* 94(5):487–495
18. Gramiak R, Shah PM (1968) Echocardiography of the aortic root. *Invest Radiol* 3:356–366
19. Helfield B (2019) A review of phospholipid encapsulated ultrasound contrast agent microbubble physics. *Ultrasound Med Biol* 45(2):282–300
20. Hingot V, Errico C, Tanter M, Couture O (2017) Subwavelength motion-correction for ultrafast ultrasound localization microscopy. *Ultrasonics* 77:17–21
21. Hope Simpson D, Burns PN, Averkiou MA (2001) Techniques for perfusion imaging with microbubble contrast agents. *IEEE Trans Ultrason Ferroelectr Freq Control* 48(6):1483–1494
22. Simpson DH, Chin CT, Burns PN (1999) Pulse inversion Doppler: a new method for detecting nonlinear echoes from microbubble contrast agents. *IEEE Trans. Ultrason., Ferroelectr Freq Contr* 46(2), 372–382
23. Jensen JA (1996) Estimation of blood velocities using ultrasound: a signal processing approach. Cambridge University Press, New York
24. Jensen JA (1996) Field: a program for simulating ultrasound systems. In: 10th Nordic-Baltic conference on biomedical imaging published in *medical & biological engineering & computing* 34, 351–353
25. Jensen JA, Holm O, Jensen LJ, Bendtsen H, Nikolov SI, Tomov BG, Munk P, Hansen M, Salomonsen K, Hansen J, Gormsen K, Pedersen HM, Gammelmark KL (2005) Ultrasound research scanner for real-time synthetic aperture data acquisition. *IEEE Trans Ultrason Ferroelectr Freq Control* 52(5):881–891
26. Jensen JA, Svendsen NB (1992) Calculation of pressure fields from arbitrarily shaped, apodized, and excited ultrasound transducers. *IEEE Trans Ultrason Ferroelectr Freq Control* 39(2):262–267

27. Lindner JR (2004) Microbubbles in medical imaging: current applications and future directions. *Nat Rev Drug Discovery* 3:527–532
28. Lindner JR, Song J, Xu F, Klibanov AL, Singbartl K, Ley K, Kaul S (2000) Noninvasive ultrasound imaging of inflammation using microbubbles targeted to activated Leukocytes. *Circulation* 102(22):2745–2750
29. Lu JY (1998) Experimental study of high frame rate imaging with limited diffraction beams. *IEEE Trans Ultrason Ferroelectr Freq Control* 45(1):84–97
30. Mace E, Montaldo G, Cohen I, Baulac M, Fink M, Tanter M (2011) Functional ultrasound imaging of the brain. *Nat Methods* 8(8):662–664
31. Marmottant P, van der Meer S, Emmer M, Versluis M, de Jong N, Hilgenfeldt S, Lohse D (2005) A model for large amplitude oscillations of coated bubbles accounting for buckling and rupture. *J Acoustical Soc Am* 118(6):3499–3505
32. Miller DL, Quddus J (2000) Diagnostic ultrasound activation of contrast agent gas bodies induces capillary rupture in mice. *PNAS* 97(18):10179–10184
33. Montaldo G, Tanter M, Bercoff J, Benech N, Fink M (2009) Coherent plane-wave compounding for very high frame rate ultrasonography and transient elastography. *IEEE Trans Ultrason Ferroelectr Freq Control* 56(3):489–506
34. Nightingale KR, Palmeri ML, Nightingale RW, Trahey GE (2001) On the feasibility of remote palpation using acoustic radiation force. *J Acoustical Soc Am* 110(1):625–634
35. Opacic T, Dencks S, Theek B, Piepenbrock M, Ackermann D, Rix A, Lammers T, Stickeler E, Delorme S, Schmitz G, Kiessling F (2018) Motion model ultrasound localization microscopy for preclinical and clinical multiparametric tumor characterization. *Nat Commun* 9(1):1527
36. Ophir J, Céspedes I, Ponnekanti H, Yazdi Y, Li X (1991) Elastography: a quantitative method for imaging the elasticity of biological tissues. *Ultrason Imaging* 13(2):111–134
37. Phillips P (2001) Contrast pulse sequences (CPS): imaging nonlinear microbubbles. In: *Proc. IEEE ultrasonics symposium*, pp 1739–1745
38. Rayleigh L (1917) On the pressure development in a liquid during the collapse of a spherical cavity. *Philos. Mag* 32(S. 8):94–98
39. Sandrin L, Tanter M, Catheline S, Fink M (2002) Shear modulus imaging with 2-D transient elastography. *IEEE Trans Ultrason Ferroelectr Freq Control* 49(4):426–435
40. Schrope BA, Newhouse VL (1993) Second harmonic ultrasonic blood perfusion measurement. *Ultrasound Med Biol* 19(7):567–579
41. Sehgal CM (1993) Quantitative relationship between tissue composition and scattering of ultrasound. *J Acoust Soc Am* 94(4):1944–1951
42. Siepmann M, Bzyl J, Palmowski M, Kiessling F, Schmitz G (2011) Imaging tumor vascularity by tracing single microbubbles. *IEEE International Ultrasonics Symposium*. Orlando, Florida, pp 1906–1909
43. Smith SW, Pavy HR, von Ramm OT (1991) High-speed ultrasound volumetric imaging system. I. Transducer design and beam steering. *IEEE Trans Ultrason Ferroelectr Freq Control* 38(2):100–108
44. Song P, Trzasko JD, Manduca A, Huang R, Kadirvel R, Kallmes DF, Chen S (2018) Improved super-resolution ultrasound microvessel imaging with spatiotemporal nonlocal means filtering and bipartite graph-based microbubble tracking. *IEEE Trans Ultrason Ferroelectr Freq Control* 65(2):149–167
45. Sontum PC (2008) Physicochemical characteristics of Sonazoid™, a new contrast agent for ultrasound imaging. *Ultrasound Med Biol* 34(5):824–833
46. Szabo TL (2014) *Diagnostic ultrasound imaging: inside out*. Boston, Academic Press
47. Tiemann K, Pohl C, Schlosser T, Goenechea J, Bruce M, Veltmann C, Kuntz S, Bangard M, Becher H (2000) Stimulated acoustic emission: pseudo-Doppler shifts seen during the destruction of nonmoving microbubbles. *Ultrasound Med Biol* 26(7):1161

48. Van Sloun RJ, Solomon O, Eldar YC, Wijkstra H, Mischi M (2017) Sparsity-driven super-resolution in clinical contrast-enhanced ultrasound. In: IEEE international ultrasonics symposium
49. von Ramm OT, Smith SW, Pavy HR (1991) High-speed ultrasound volumetric imaging system. II. Parallel processing and image display. *IEEE Trans Ultrason Ferroelectr Freq Control* 38(2):109–115
50. Waters KR, Mobley J, Miller JG (2005) Causality-imposed (Kramers-Kronig) relationships between attenuation and dispersion. *IEEE Trans Ultrason Ferroelectr Freq Control* 52(5):822–823
51. Wild JJ, Reid JM (1952) Application of echo-ranging techniques to the determination of structure of biological tissues. *Science* 115(2983):226–230



Optical and Optoacoustic Imaging

5

Daniel Razansky and Vasilis Ntziachristos

Contents

5.1 Surgical Vision Through Fluorescence.....	156
5.2 Selection of Fluorescence Agent.....	158
5.3 Need for Standardization in Clinical Fluorescence Imaging.....	161
5.4 Multispectral Optoacoustic Tomography (MSOT).....	171
5.5 MSOT Imaging of Endogenous Absorption Contrast.....	174
5.6 Molecular Sensing with MSOT.....	175
5.7 Clinical Translation of Optoacoustic Imaging.....	177
5.8 The Future of Fluorescence and MSOT Imaging.....	180
References.....	181

Human vision has been used for disease detection since the beginning of medicine. Using both morphological and spectral features, the visual observation remains a major detection method in many clinical segments today, including general examinations or surgical and endoscopic procedures. Even today, surgeons and endoscopists are guided by what they see with their own eyes either directly or through optical systems that produce photographic and video representations of tissue, such as the color videos viewed during laparoscopy on a computer screen.

D. Razansky

Faculty of Medicine and Institute of Pharmacology and Toxicology, University of Zurich, Zurich, Switzerland

Department of Information Technology and Electrical Engineering, Institute for Biomedical Engineering, ETH Zurich, Zurich, Switzerland

V. Ntziachristos (✉)

Institute of Biological and Medical Imaging, Helmholtz Zentrum München, Neuherberg, Germany

e-mail: v.ntziachristos@tum.de

Technical University of Munich, Ismaningerstr. 22, 81675 Munich, Germany

Therefore, even when using advanced methods such as high-definition white-light imaging [1] or stereoscopic imaging [2], detection in many surgical and endoscopic procedures depends on human vision in ways that resemble those from the beginning of medicine.

More sophisticated forms of “vision” exist in medicine, but are impractical or impossible to bring into the surgical suite [3, 4]. X-ray imaging and magnetic resonance imaging systems, for example, cannot fit into typical operating rooms or allow surgical teams to come close enough to the patient. In addition, X-ray imaging lacks the contrast or resolution to image cancer borders or detect lymph node metastases. Tomography scanners are far too expensive to become routine tools during surgery, and in fact they lack the resolution and contrast needed to guide surgeons effectively during procedures. Gamma scanners can be used in the surgical suite, such as for identifying lymph nodes, but they offer low resolution and require radioactivity. Ultrasonography offers limited contrast, it must be performed with the probe in direct contact with the tissue, which increases risk of contamination, and it cannot survey areas as large as wide-field optical methods.

5.1 Surgical Vision Through Fluorescence

Fluorescence imaging can surpass limitations of human vision to image cancerous or otherwise diseased tissue that would be invisible or indistinguishable from healthy tissue, as first demonstrated 70 years ago [5, 6]. It can illuminate tissues lying several millimeters below the surface, or deeper, especially when near-infrared dyes are used, without the need for dangerous or fast-decomposing radioactive contrast from isotopes. Fluorescence imaging systems are generally of small form factors and can be seamlessly integrated into surgical and endoscopic suites or miniaturized as parts of endoscopes, making them well suited as surgical and endoscopic tools. Fluorescence imaging now promises to become fully integrated into the surgical suite within a decade.

Fluorescence contrast can be engineered by utilizing agents that reveal specific aspects of morphology, function or cellular and molecular features associated with disease and/or tissue differentiation. For instance, cancer can be identified in the context of functional contrast, such as when an agent that outlines abnormal permeability is utilized. Lymph nodes can be visualized by injecting appropriate fluorescence dyes into the lymphatic drainage. Alternatively, a fluorescent agent with targeting ability to specific cellular moieties can identify receptors, enzymes, or other cellular expression and function associated with features of the disease of interest. Targeted fluorescent agents that recognize specific disease biomarkers support so-called fluorescence molecular imaging (FMI), which offers high sensitivity and imaging below the surface [7–9]. For example, a fluorescence dye that can target the folate receptor on ovarian cancer cells may improve detection of ovarian cancer [9, 10]. Fluorescently labeled Cetuximab may improve precision in

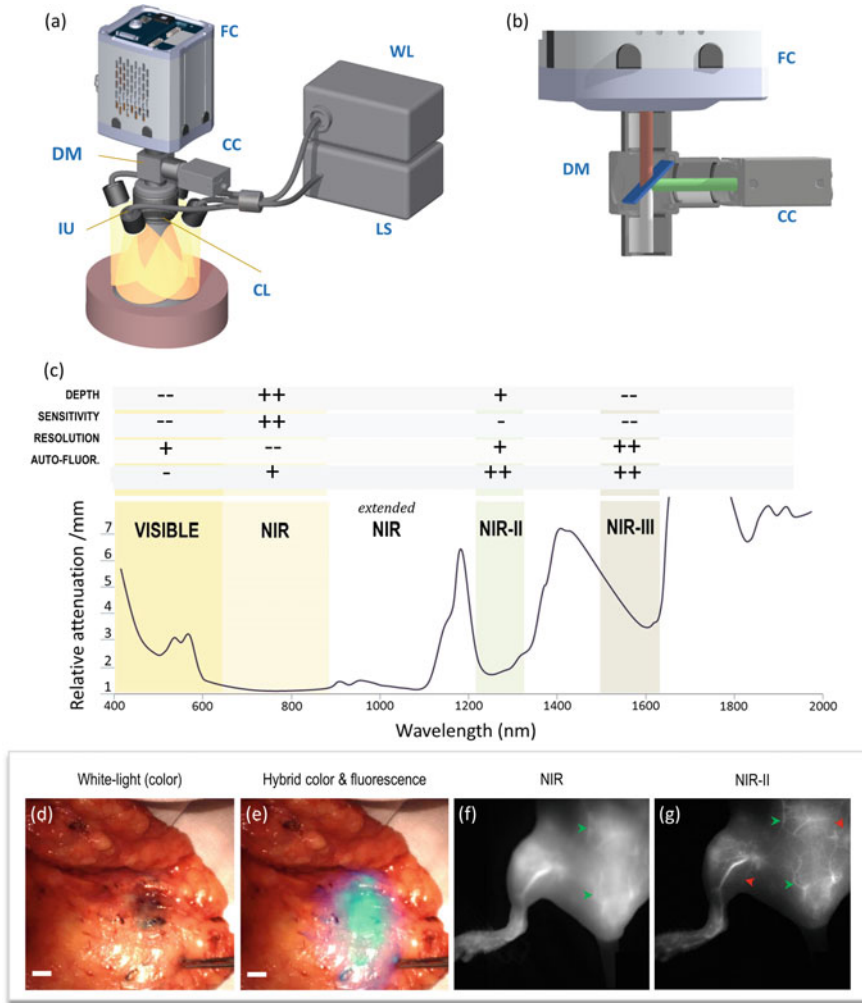


Fig. 5.1 Intraoperative fluorescence imaging. **a** Composite camera system using a highly sensitive fluorescence camera (FC) to collect fluorescence images and a color camera (CC) to collect white-light images through a dichroic mirror (DM) and common lens (CL). Different sources may be used for white-light excitation (WL) and fluorescence excitation using a laser source (LS) and common illumination unit (IU). **b** Optical paths collected through the dichroic mirror. Visible light (green path) is directed to the color camera and near-infrared light (brown path) is directed to the fluorescence camera. **c** Absorption spectrum of tissue obtained by optoacoustic spectroscopy from mouse skin *in vivo*. The spectrum shows the different spectral ranges typically used in FMI. The “+” and “-” symbols indicate advantages and disadvantages of each range. **d** Color image collected intraoperatively from breast tissue of a breast cancer patient. **e** Superposition of the color image in panel (d) onto a fluorescence image in pseudo-cyan/green, identifying breast cancer below the surface. The fluorescence image was obtained after systemic administration of bevacizumab labeled with the NIR fluorescence dye CW800 (Licor). **f** Image of a mouse hind limb in the NIR region. **g** Image corresponding to panel (f) but obtained in the NIR-II region. Resolution is better in the NIR-II region because of less scatter. Figure 5.1f, g Adapted from [17] under the terms of the Creative Commons Attribution License; © 2017 Starosolski et al. Figure 5.1 adapted from reference [18]; copyright belongs to author

surgery to excise oral tumors [11]. Fluorescent dyes have been developed to target sarcoma, colonic dysplasia, and Crohn's disease [12–14].

FMI relies on a camera sensitive to fluorescence photons (Fig. 5.1a), which is fitted with high-pass or band-pass filters that block photons at the excitation wavelength and instead allow only photons exiting the tissue surface at the emission wavelengths to pass through the camera's detector. Different spectral bands are considered for fluorescence imaging, typically over a range that could span a region of the 400–1,700 nm range (Fig. 5.1c). Different cameras are required for different parts of this range, using photon detection technology that is sensitive to the visible ($\sim 400\text{--}650$ nm), near-infrared (NIR: $\sim 650\text{--}950$ nm) and short-wavelength infrared (SWIR: $\sim 950\text{--}1700$ nm) ranges. The fluorescence camera is often combined with a color camera (Fig. 5.1b), which provides a morphological reference that allows registration of the two types of images (Fig. 5.1e). A preferred method to superimpose the fluorescence image onto the color image is to render pixels transparent if their fluorescence intensity is low; in this case, strong fluorescence signals appear in pseudocolor, while weak fluorescence signals are invisible [15]. The fluorescence camera, alone or combined with a color camera, can be used as a stand-alone device operating above the operating table, in handheld modes or it can be combined with flexible endoscopes [16].

Corresponding to the camera technology used, fluorescent agents for FMI have been described covering a broad spectral range, covering the visible, NIR and SWIR. Each spectral range comes with different detection characteristics, due to the variation of tissue optical properties with wavelength. In particular, imaging in the visible may showcase images with low photon diffusion (good resolution) but at superficial depths, due to the high absorption of visible photons by tissue. In the NIR, FMI can achieve greater imaging depth, because tissue (in particular hemoglobin) absorbs NIR photons much less than visible photons. Conversely, due to this lower absorption, the effects of photon scattering in tissue are more visible, leading to images that appear low resolution due to photon diffusion effects. Finally, imaging in the extended NIR (950–1,100 nm) or even more so in the NIR-II (1,100–1,700 nm) benefits for the reduced photon scattering with increasing wavelength. However, in these ranges water and lipids absorb significantly, which also weights the image toward more superficial depths compared to the NIR range. Nevertheless, imaging at longer wavelengths may balance the effects of absorption and scattering and offers an interesting range for FMI as well, whereby imaging deeper than in the visible is possible but with reduced scattering (photon diffusion) compared to the NIR (Fig. 5.1f, g) [17, 19].

5.2 Selection of Fluorescence Agent

An advantage of FMI is that the contrast offered can be engineered and tuned to specific applications through the development and selection of particular fluorescence agents. Nonspecific fluorescent dyes can reveal morphological and functional

features of tissue to guide medical research and various types of surgeries, as we have highlighted elsewhere [7]. Since the 1950s, indocyanine green (ICG) has been used to study hepatic clearance [20], cardiac output [21], and retinal vasculature [22]. More recently, it has been used in the technique called ICG video-angiography to analyze tissue perfusion in many contexts. Since ICG remains mostly within the vascular system, it allows visualization of vascular flow in real time to assess perfusion in organ transplantation [23], plastic surgery [24–27], cardiac surgery [28] and neurosurgery [29]. The technique has been used to monitor perfusion following colorectal anastomosis in order to detect leakage [30], which can cause severe and potentially deadly complications. It can assess whether transplanted tissue is adequately perfused during mastectomy and reconstructive surgery; if not, the resulting ischemia and necrosis can cause severe complications [31].

ICG has also proven extremely useful for localizing sentinel lymph nodes, which are often embedded deep within adipose tissue (Fig. 5.2). In many types of cancer, these lymph nodes are extracted and analyzed for the presence of metastatic cancer [32, 33], which is critical for accurate staging and treatment planning. ICG is more effective than methylene blue for identifying deep-seated lymph nodes because it fluoresces in the NIR range. ICG also avoids the need for radioactivity, in contrast to gamma sensor-based detection of lymph nodes [34]. The power of ICG-based detection of lymph nodes has been demonstrated for numerous types of cancer [35–44]. In fact, ICG can aid the identification of nearly all lymph nodes into which the tumor drains, not only sentinel lymph nodes [45]. In this case, longitudinal monitoring of ICG distribution can identify the first draining node.

For certain types of surgery involving cancer or other diseases, targeted fluorescent agents rather than ICG are used. One key application is in aiding identification of tumor margins. When using visual inspection, it is not generally possible to know whether surgeons have completely resected a tumor until after postoperative histopathology, which can take several hours or even days. If excision is incomplete, then secondary procedures may be needed, which increase patient stress, risk of complications, and healthcare costs. On the other hand, excessive resection can mean removal of too much healthy tissue around the tumor, increasing risk of irreversible damage (e.g., nerve damage) and postoperative complications. Several targeted fluorescent agents show potential for use during tumor resection, such as a FITC-conjugated ligand of the folate receptor- α [9], fluorescently labeled versions of clinically approved anti-cancer therapeutic antibodies [11, 48], and even agents that induce fluorogenic reactions within tumors [49–53]. It may also be possible to use specific fluorescence agents to identify tumor metastasis in lymph nodes without the need to remove them from the body or analyze them postoperatively [7].

Clinical fluorescence imaging must offer sensitivity adequate to help surgeons make critical decisions in real time. Nonspecific vascular dyes such as ICG are often injected in doses of up to 25 mg when given systemically, or in doses of approximately 1 mg when given intratumorally [7]. The final concentration in tissue is usually several-hundred nanomolar to several micromolar. Targeted agents

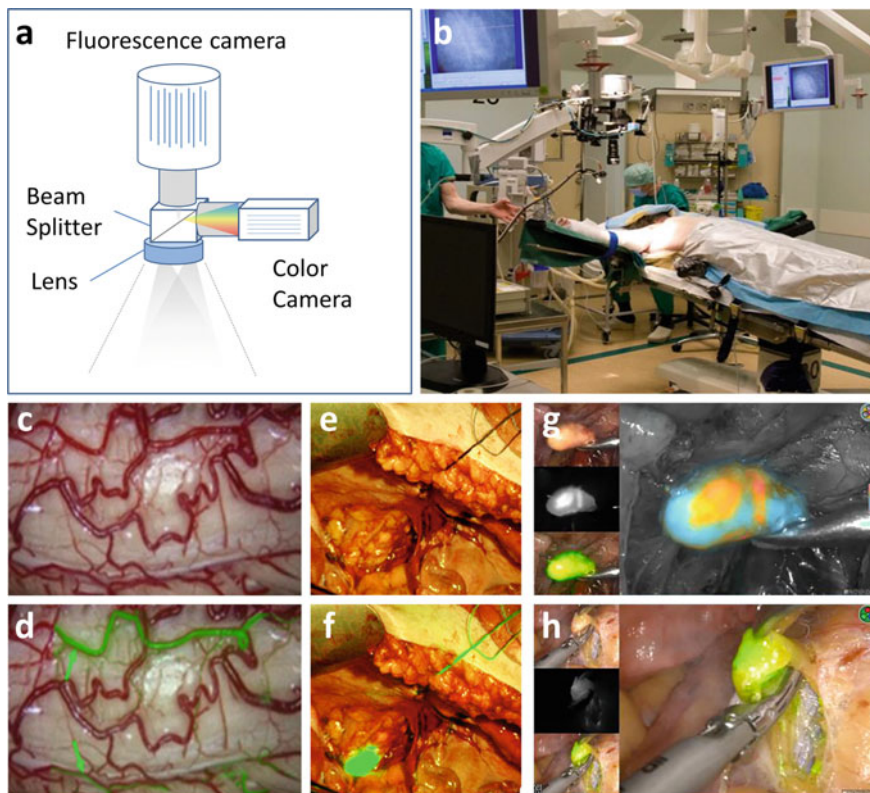


Fig. 5.2 Indocyanine green (ICG)-enhanced interventional imaging. **a** Intraoperative fluorescence imaging system using simultaneous image collection from a fluorescence and white-light (color) camera visualizing the same field of view through a shared optical system (beam splitter and lens). An endoscope system can be connected instead of a lens. **b** Photograph of a camera in the operating room. The camera is placed above the patient; white-light, fluorescence, and overlay images can be projected on monitors in the operating room. The camera is typically wrapped in sterile drapes (not shown). Figure 5.1b Adapted from [9]; copyright belongs to author. **c–d** Color reflection image (**c**) and ICG-based video-angiography (**d**) of the spinal cord. The fluorescence signal was overlaid on the color reflection image. The image was rendered by alpha-blending the fluorescence values after spatial anatomical landmark registration. ICG-angiography visualized the microvascular flow and anatomical orientation, necessary to ensure safe and precise resection of spinal intramedullary tumors. The image shows an early stage soon after ICG injection and highlights the posterior spinal arteries on both sides. Figure 5.1c, d adapted from [46] under the terms of the Creative Commons Attribution License; © 2013 Takami T. **e–f** White-light reflection image (**e**) overlaid with a fluorescence image (**f**) revealing a lymph node in early-stage cervical cancer surgery. The lymph node cannot be identified by human vision on the white-light image as it is located under the tissue surface. Figure 5.1e, f adapted from [41]; copyright belongs to author. **g–h** Endoscopic sentinel lymph node (SLN) mapping in multiple imaging modes after ICG injection in patients at high-risk for endometrial cancer. **g** Color map indicating areas of high (red) and low (gray) ICG uptake. **h** Fluorescence overlay on white-light image of SLN. Figure 5.2g, h adapted from [47] under the terms of the Creative Commons Attribution 4.0 International License

are used at much lower concentrations [7, 48, 54] because most of the dye is ultimately cleared from the body. Targeted agents may be present in the desired tissue at concentrations 5–6 orders of magnitude lower than ICG [7, 55].

5.3 Need for Standardization in Clinical Fluorescence Imaging

To realize the full potential FMI in particular, and fluorescence imaging more broadly, universal standards are needed that define appropriate fluorescence performance. Such standards already exist for radiology, but they have yet to be formulated for fluorescence imaging. FMI standardization is complicated by the existence of a broad range of commercially available imaging systems featuring diverse cameras, illumination sources, and data processing software. This means that different FMI systems can differ in their sensitivity and specificity when analyzing the same disease using the same fluorescent agent. This problem can be avoided by defining minimum standard performance parameters that can be applied across fluorescence imaging systems and medical centers. Developing uniform standards is always challenging, but it is even more so in the case of clinical fluorescence imaging because available dyes cover such a broad spectral range from the visible to NIR-II and even longer wavelengths [19, 56–58]. Uniform standards are essential for achieving what we term high-fidelity fluorescence imaging (HiFFI), as we have described in greater depth elsewhere [18]. Analogous to the use of “high fidelity” in audio systems, we refer to high fidelity in fluorescence imaging as the accurate reproduction of fluorescence signal with minimal distortions, leading to accurate visualization of the biodistribution of the dye in tissue, independently of the imaging system and processing algorithms used, the tissue analyzed, or the surgical conditions.

Separation of FMI measurements from the particular imaging setup and data processing used is important for comparing results obtained for different patients within the same medical center or at different medical centers. This may facilitate the definition of consensus guidelines for disease diagnosis, staging, and treatment; it may also facilitate large, multisite clinical studies. It may allow a change in the current practice of regulatory authorities of licensing the combination of fluorescent agents and a specific FMI camera. With the establishment of HiFFI, fluorescent agents could be licensed on their own.

Several parameters need to be taken into account in order to develop uniform standards. One set of parameters can be considered invariable. They are defined by the hardware and overall design of the FMI system and therefore do not change during measurements (Table 5.1, *upper section*). One invariable parameter is sensitivity: FMI should be able to detect fluorescent dye concentrations from sub-nanomolar to 0.1-micromolar [7]. The requirement for sensitivity becomes particularly acute in video-rate FMI, where the typical 24 frames-per-second video means that each frame is captured during only approximately 42 ms. This highlights the importance of highly sensitive cameras (Fig. 5.3a–c). Other parameters

Table 5.1 Parameters affecting FMI performance. Adapted from reference [18]

Parameter	Typical range	Effect on FMI performance	Calibration	Remedy
<i>Invariable parameters</i>				
Camera Sensitivity Electrical/read noise	nM–pM $2e^-$ to $20e^-$ per read operation	<ul style="list-style-type: none"> • Dose of agent required • Frame rate achieved • Minimum fluorescence activity detected • Phase 0/Microdosing operation • Sensitivity and specificity of clinical findings 	Measure (calibrate) sensitivity with standard (FIS)	Use highly sensitive CCD/CMOS/InGaAs technology, current amplification methods, low-noise electronics, and cooling technology to reduce noise
Resolution	10–500 μm	<ul style="list-style-type: none"> • Minimum lesion size visible on white-light images 	Register white-light and apparent diffusive resolution with standard	Match the number of pixels and field of view to the desired resolution
Dynamic range and dark current	10^4 – 10^6	<ul style="list-style-type: none"> • Ability to differentiate between different amounts of distributed agent • Saturation effects 	Measure with standard	Select sensors with high full well capacity
Frame capture speed	1–100 Hz	<ul style="list-style-type: none"> • Quality of video 	N/A	Select camera with fast read-electronics and data transfer
Spectral coverage	400–1700 nm	<ul style="list-style-type: none"> • Resolution achieved • Sensitivity achieved • Depth achieved 	Use fluorochromes (quantum dots) whose spectral responses are known	Select sensor technology with sufficient sensitivity in spectral range covered
Filters, cross-talk & ambient light	0.1–50% of excitation light	<ul style="list-style-type: none"> • Reduction of sensitivity • Increase background noise • Increase image artefacts 	Measure cross-talk and ambient light under control conditions	Select proper filters; condition light source; subtract reference light/time-share measurement

(continued)

Table 5.1 (continued)

Parameter	Typical range	Effect on FMI performance	Calibration	Remedy
Illumination intensity & spectral profile	1–200 mW/m ² upper value may be regulated by ANSI limits	<ul style="list-style-type: none"> • Same as in “Camera sensitivity” 	Measure (calibrate) intensity with a standard (FIS), power meter and/or spectrometer	Employ illumination close to the ANSI limit and sources of optimal spectral response
Illumination homogeneity	Varies with system design	<ul style="list-style-type: none"> • Shadowing effects on the images collected • Accuracy (quantification) variations of different lesions • Sensitivity and specificity of clinical findings 	Measure the illumination pattern (see also Box 5.1)	Multi-angle illumination; normalize image with captured illumination pattern
<i>Variable parameters</i>				
Camera-tissue distance and field of view	15–100 cm	<ul style="list-style-type: none"> • Variations in fluorescence intensity recorded • Changes in focus • Sensitivity 	Record changes in field of view and distance	Real-time distance and FOV sensors or estimators
Depth of focus	1–10 cm	Reduced resolution with changes in tissue elevation and camera-tissue distance	Record iris and depth of focus settings	Use high depth of focus to avoid out-of-focus images; use an autofocus mechanism
Variation of optical properties	Scatter: 30 cm ⁻¹ Absorption: 0.05–0.5 cm ⁻¹	<ul style="list-style-type: none"> • Variations in fluorescence signal intensity • Variations in apparent fluorescence distribution • Variations in resolution and diffusion on the image 	Record system performance as a function of optical property changes	Record variations in tissue absorption and scattering in real time

(continued)

Table 5.1 (continued)

Parameter	Typical range	Effect on FMI performance	Calibration	Remedy
Auto-fluorescence	Varies with spectral region (see Fig. 5.1c)	<ul style="list-style-type: none"> • Reduces detection sensitivity • May lead to false positives 	Record system performance as a function of background fluorescence	Use spectral differentiation of target fluorescence over background fluorescence
Lesion depth	0–2 cm	<ul style="list-style-type: none"> • Attenuation of fluorescence intensity • Variable diffusion and loss of resolution • Spectral changes 	Record system performance as a function of fluorescence depth	Tomography; depth reconstruction based on spectral changes

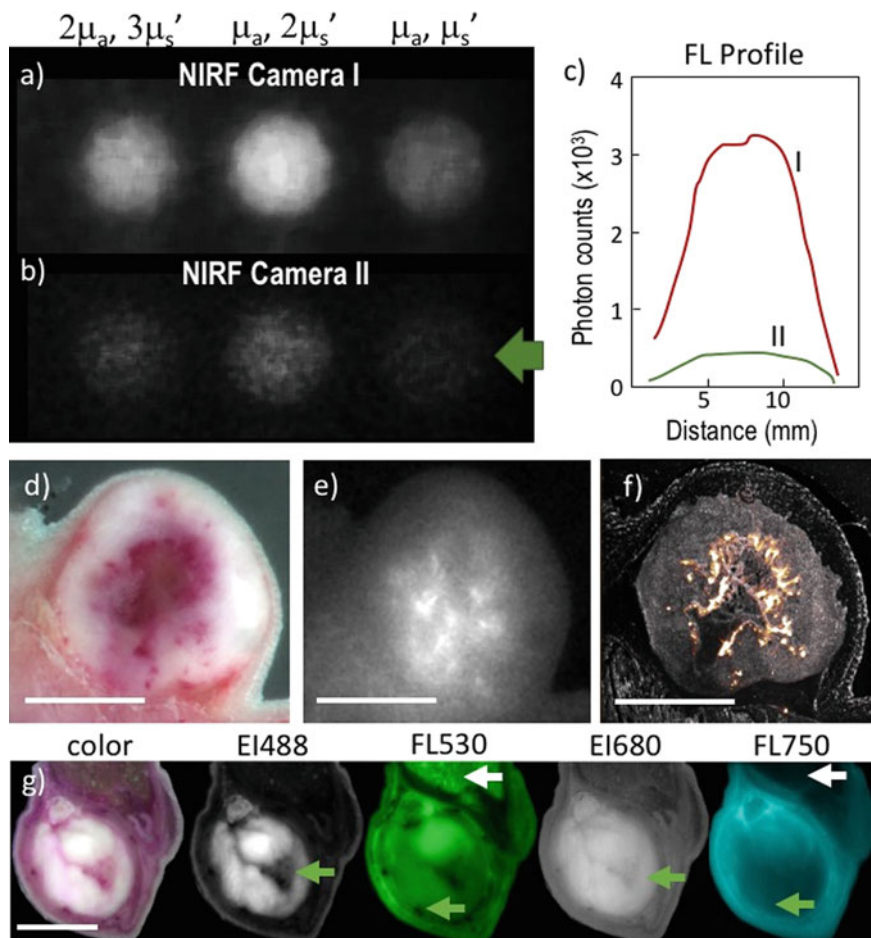
affecting FMI sensitivity include the intensity and spectral response of the fluorochrome excitation, and the ability to block excitation light and other light from entering the fluorescence channel (cross-talk). More sensitive detection means that lower concentrations of dye can be used, which reduces risk to the patient and costs of preparing or purchasing the dye.

ANSI, American National Standards Institute; CCD, charge-coupled device; CMOS, complementary metal–oxide–semiconductor; FIS, fluorescence imaging standard; FOV, field of view; InGaAs, indium-gallium-arsenide; N/A, not applicable.

The ability to detect agents with high sensitivity can make possible “micro-dosing” studies, in which the agent is administered at doses orders of magnitude lower than the likely therapeutic dose in order to analyze the body’s response to the drug while minimizing the risk of serious adverse events [48]. Researchers succeeded in carrying out such studies with bevacizumab, a recombinant humanized monoclonal antibody effective against various cancers [59]. In that work, signal-to-noise ratios of approximately 12 dB were achieved using cooled cameras capable of detecting a few electrons. Whether the FMI system can support video-rate imaging, preferred for intraoperative uses, also depends on the camera’s maximum frame rate and sensitivity.

Several other invariable parameters may affect image performance. Dynamic range, defined as the distance between the largest and smallest signals that can be recorded by a camera, determines how well the camera captures strong and weak fluorescence signals. Spatial resolution defines the smallest fluorescence source that can be recorded accurately, or how close can two sources be so that they can be reliably separated. How uniformly the illumination energy excites the field of view is also important, because spatial variations in this energy can cause changes in fluorescence intensity unrelated to agent concentration. Moreover, tissue elevations and curved surfaces can give rise to “shadowing” effects, therefore another aspect of illumination is the angle distribution by which it illuminates tissue. The range of fluorescent agents that can be imaged adequately depends on the spectral range covered by the camera.

The second set of parameters to take into account when developing uniform standards can be considered variable, because they can differ from one measurement to the next or even during a single measurement (Table 5.1, *lower section*). Such parameters include camera focus, zoom, and distance from the tissue; all these factors influence the fluorescence intensity that is recorded, the field of view that is observed, and the minimum field of view that can be resolved. Several variable parameters relate to the optical properties of the tissue being imaged [60–62]. This is because fluorescence photons are generated inside the tissue, not on the tissue surface. These photons are isotropically emitted within tissue and most are scattered multiple times before detection, so the optical properties of the surrounding tissue affect their behavior and therefore the resulting fluorescence image (Fig. 5.3e–g). For example, images collected with excitation in the NIR-II range appear to have higher resolution than images collected with NIR illumination because NIR-II wavelengths are scattered less. NIR wavelengths, in turn, can interrogate deeper in tissues than visible or NIR-II illumination because of lower light absorption by tissue



in these wavelengths. Finally, contrast in the NIR and NIR-II regions is generally better than in the visible, due to strong autofluorescence from components such as collagen and nicotinamide adenine dinucleotide in visible wavelengths (Fig. 5.3g).

The strong dependence of fluorescence images on optical properties of the tissue under study has at least three important implications for analyzing and optimizing FMI and for defining appropriate standards. Fluorescence images do not report the true biodistribution of fluorescent agents but rather a composite signal that depends on the concentration of the agent and the optical properties of the tissue. Second, the diffusive behavior of fluorescence photons within the tissue blurs edges and borders, which makes it more difficult to differentiate healthy and diseased tissue. Third, the fluorescence signal measured by the camera depends strongly and non-linearly on the depth of the fluorescence source. As a result, the same type or size of lesion may appear quite differently on fluorescence images depending on experimental parameters.

◀ **Fig. 5.3** Challenges in fluorescence imaging. These examples illustrate the effects of system and tissue parameters on fluorescence images. **a–b** Three fluorescent wells in the upper right quadrant of the composite phantom described in Box 5.1 were imaged using near-infrared fluorescence (NIRF) cameras with the same filters and illumination parameters. Camera I (iXon, Andor) offers 10-fold higher sensitivity than camera II (Luca, Andor). Camera II nearly fails to detect a well (green arrow) that camera I resolves. All wells contained the same amount of fluorophore; intensity variations are attributed to variation in optical properties. **c** Fluorescence profiles through the rightmost well imaged by the two cameras illustrate the marked detection difference between them. **d–e** Color image (**d**) obtained by cryo-slicing through a 4T1 tumor subcutaneously grown on a nude mouse, and corresponding image at 750 nm (**e**) after administration of liposomal ICG (24 h before euthanasia). **f** Fluorescence image of a 100- μ slide obtained from panel (e) reveals a more detailed pattern of fluorescence distribution not prone to photon diffusion. Such images may contain cross-talk from the excitation channel (see Table 5.1), which can be eliminated using calibration. **g** Effects of optical properties and spectral region on the fluorescence image. A mouse bearing an intramuscular 4T1 tumor was injected intravenously with equal amounts of AF488 and AF750 fluorescent dyes, then imaged in epi-illumination mode using white-light (color) illumination. Excitation wavelengths were 488 and 680 nm (EI488, EI680); fluorescence was imaged at approximately 530 and 750 nm (FL530; FL750). Arrows indicate regions of special interest: white arrows indicate an area of strong autofluorescence in the visible range, which disappears in the NIR range; green arrows indicate regions of high absorption that also disappear in the NIR region. Scale bars, 5 mm. Figure 5.3 Adapted from reference [18]; copyright belongs to author

The range of invariable and variable parameters can affect fluorescence imaging, and the resulting range in FMI performance between medical centers and even within the same medical center, between commercially available devices and even for the same device used on different patients or by different operators. These factors make clear the need for consensus standards on what system performance is adequate to make diagnostic decisions or guide surgeries. For example, no standards exist on the minimal acceptable sensitivity in clinical fluorescence imaging. This lack of standardization is hindering broader clinical implementation of FMI, which is unfortunate given the technique's potential for real-time, patient-specific guidance on procedures. The benefits of FMI become all the more important as medical care moves toward minimally invasive and robot-assisted surgery [63].

For standardization purposes, we have recently proposed a phantom (Box 5.1) [18, 64] that integrates different experimental conditions and can measure for multiple camera parameters simultaneously. Such phantom could lead to system quality control and calibration, or more generally in system standardization. Measurements performed with standardized systems can facilitate comparisons of data obtained using different imaging systems, such as those obtained at different medical centers in a multisite clinical study, which may improve reproducibility of procedures and treatments and facilitate benchmarking of FMI systems against one another. It can also alert operators to a decrease in performance by their system, perhaps indicating the need to replace or upgrade components or adjust their measurement procedure to take into account features of particular patients or disease situations. FMI characterization using a calibrated phantom standard could serve as a quantitation of the reliability of FMI analysis in applications for regulatory approval of a novel treatment or intervention.

Box 5.1. Phantoms

Imaging phantoms, i.e., objects that contain features simulating tissue features with predetermined shapes and contrast, are common in radiological imaging for evaluating, confirming or measuring the performance of a device or method. Phantoms are generally employed in medical imaging for quality control and quality assurance. For optical imaging standardization, phantoms should meet three basic requirements, i.e.,

- (i) allow the implementation of desired optical properties (absorption, scattering, fluorescence),
- (ii) provide long-term photostability in diverse environmental conditions, and
- (iii) assume a fixed shape (termed a “solid phantom”) that suffers no mechanical deformation over time.

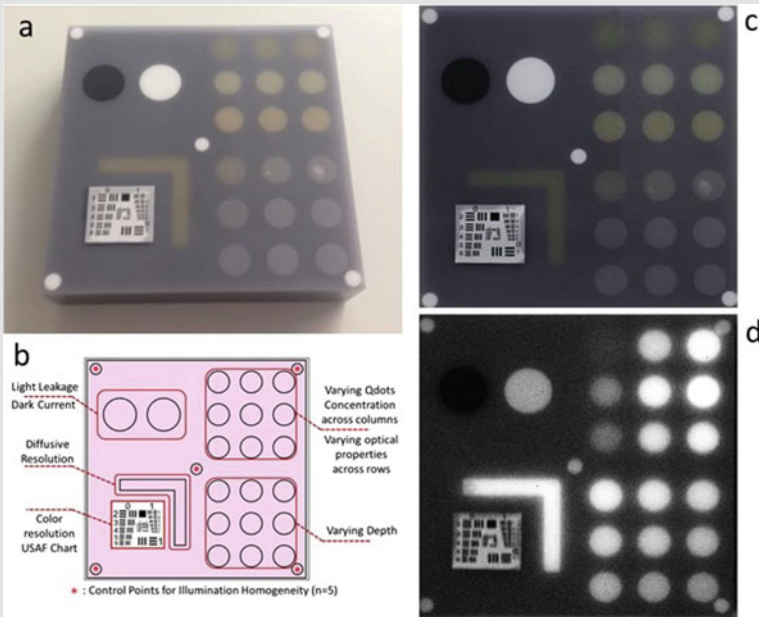
To meet these requirements, optical phantoms typically use epoxy, polyester resin, or polyurethane as base material. When cured, these materials can be machined into different shapes and volumes. Optical properties can be flexibly manipulated by adding absorbers, scatterers, and fluorophores prior to curing. Typically, absorption properties are based on the addition of absorbing dyes (e.g., India ink, nigrosin) and scattering properties are based on the addition of TiO₂ particles into the base material. Homogeneous distribution can be ensured with sonication. Quantum dots are typically preferred for fluorescence emission. Unlike organic fluorophores, which suffer from fast photo-bleaching, quantum dots provide better photostability, which is required in applications involving long-term imaging [65–68].

Several phantoms have been considered for fluorescence imaging studies. A typical parameter addressed is sensitivity, using different titrations of a known fluorochrome [69]. Other parameters have been considered, such as the effects of depth [70] or the cross-talk between excitation and emission channels [69]. However, a limitation of current phantoms is that they address only one or a few of the specifications in Table 5.1 [69, 71, 72].

HiFFI standardization and reversion require the measurement and calibration of a large number of parameters (Table 5.1). Fortunately, modern cameras used for FMI contain more than 10⁶ pixels, and the high pixel density means that each photograph may contain more than 1 million independent measurements. The actual number of independent features that an FMI camera captures is probably less given the presence of diffusion, the need for a minimum signal-to-noise ratio and other practical considerations; nevertheless, this number of features is sufficient to retrieve all invariable and variable parameters in Table 5.1. Consequently, we have recently introduced the concept of *composite phantoms*, i.e., phantoms that enable the characterization of the parameters in Table 5.1 in a single snapshot (photograph). A first composite phantom (**inset**) was constructed out of polyurethane and employed

multiple targets, each exploring a different camera performance parameter. The construction of the phantom and its application has been described in detail elsewhere [64, 73]. In brief, the background material and the different targets introduced are made of different mixtures of TiO_2 particles, photon-absorbing dyes, and quantum dots. The phantom uses nigrosin as a generic absorber with a flat absorption spectrum, as well as hemin, an iron-containing porphyrin with a hemoglobin-like absorption spectrum that simulates the absorption of blood. This composite phantom enables the implementation of multiple features, including the measurement of sensitivity, cross-talk, illumination homogeneity, dark current, resolution and the effects of depth and optical properties (see legend to **inset**).

Composite phantoms could be employed as fluorescence imaging standards (FIS) for different standardization operations, as discussed in the main text, and for examining the performance of reversion methods. Preferably phantoms should be relatively straightforward and inexpensive to manufacture. An ideal phantom should balance imaging features against manufacturing complexity. It is therefore possible that simpler or more complex features could be introduced, depending on the particular application. The preliminary phantom in the inset is not a comprehensive phantom for all parameters in Table 5.1; for example, it does not contain features for spectral measurements or calibrations. Next-generation phantoms can contain a larger number of wells that more accurately report on camera performance over a wider dynamic and spectral range. 3D printing techniques may significantly simplify manufacturing of complex phantoms for FMI standardization.



Inset. Composite Phantom for FMI Standardization in the Visible Range. (a) Color photograph of the phantom, which has outer dimensions of $10 \times 10 \times 2.2 \text{ cm}^3$. (b) Schematic explaining the function of the different parts of the phantom. (c) Reflectance image of the phantom obtained with the color camera of a hybrid FMI system. (d) Fluorescence image of the phantom. Background absorption was set to $\sim 2.2 \text{ cm}^{-1}$ by adding nigrosin dissolved in alcohol (Sigma Aldrich, St. Louis, USA) to the base material, while the reduced scattering coefficient was set to $\sim 10 \text{ cm}^{-1}$ by adding 1 mg/g TiO_2 particles [titanium(IV) oxide; Sigma Aldrich, St. Louis, USA]. The upper right quadrant of the phantom contains an array of nine fluorescent wells (10 mm diameter) that interrogates the sensitivity and fluorescence intensity variation as a function of optical properties. The wells contain a mix of cured polyurethane with organic quantum dots at varying concentrations (1, 5 and 10 nM) across the columns and varying hemin concentration (20, 20 and 40 $\mu\text{g/g}$) and TiO_2 amount (0.33, 0.66 and 1 mg/g) across the rows. The bottom right quadrant contains nine fluorescence wells embedded within the phantom at increasing depths below the phantom surface (0.2, 0.4, 0.6, 0.8, 1, 1.33, 1.66, 2 and 3 mm). The upper left quadrant examines camera dark-current offset and camera cross-talk, i.e., excitation light leakage into the fluorescence channel. The lower left quadrant assesses the resolution of the fluorescence and visible images. Five identical reflective circular areas (5 mm diameter), made of 10 mg/g titanium oxide in polyurethane, sample the homogeneity of the light illumination employed by the camera system. Four circular areas lie at the corners of the phantom, and one area lies in the center. Adapted from reference [18]; copyright belongs to the author.

Standardized measurements can also permit the conversion of measurements into absolute concentrations of fluorophores. Currently, FMI focuses on reporting relative measures [62, 74, 75], such as the intensity of fluorescence signal in one area over background intensity (Fig. 5.3g) or calculating other ratios. HiFFI aims to go one step further by enabling the use of absolute metrics. This requires correcting or “reverting” [18, 60] experimental measurements to take into account the effects of the parameters in Table 5.1.

Another objective of such standards is to validate methods that minimize FMI sensitivity to experimental parameters and achieve what we have defined as HiFFI: the accurate representation of fluorochrome biodistribution in tissue, independent of the FMI system or environmental conditions during the measurement. In HiFFI, the clinical results do not change when the parameters in Table 5.1 are modified. One key to developing such FMI performance is to develop methods that obtain detailed information about the experimental parameters of an FMI acquisition at any point in time, such as based on measurements of a calibrated phantom and possibly also from tissue, in real time. Overall, correcting for the effects of invariable parameters is relatively straightforward. For example, the cross-talk coefficient relating different channels can be quantitated using a calibration phantom such as in Box 5.1, and the excitation image can be multiplied by this coefficient and then subtracted

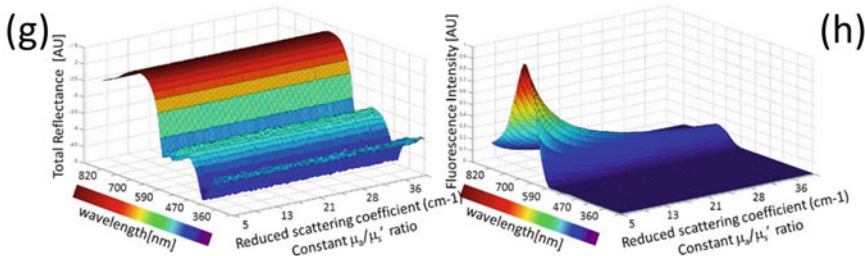
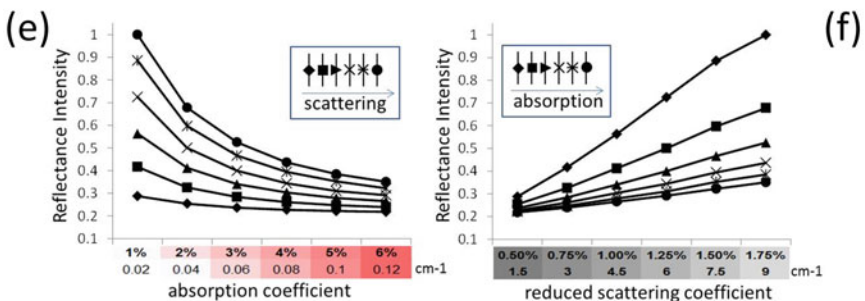
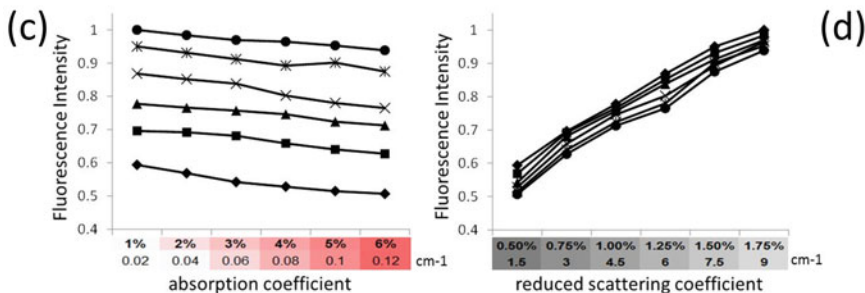
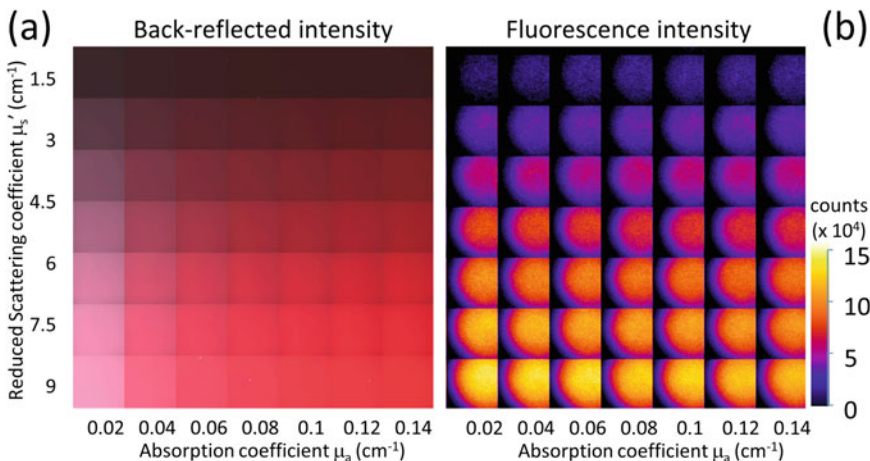
from the fluorescence image. The effects of ambient light can also be quantitated through calibration and then controlled through improvements in hardware and data processing techniques [76, 77]. More complex is correcting for variable parameters, which typically requires dedicated hardware that collects additional information about the environment and the tissue measured. For example, it is possible to record tissue properties with another camera, so that the variation of optical properties in the tissue imaged is collected (Fig. 5.4e, f). It has been shown that imaging of light reflected from tissue depends on the ratio of the absorption coefficient to the reduced scattering coefficient (μ_a/m_s) [78, 79]. An additional complication therefore in FMI occurs because when this ratio is uniform across the image, then the reflectance image collected will show spatially uniform intensity, even if the absolute optical properties and the fluorescence signal collected may vary. Correcting for optical properties using reflectance images remains a challenge because simple reflectance measurements cannot independently separate absorption from scattering [80, 81]. Collection methods and data processing schemes are currently under research to record data that allow for separation of absorption from scatter and the accurate correction of fluorescence images [60].

In addition to methods that explicitly resolve optical properties, ratiometric approaches are being used to report relative measures in FMI. For example, ratios can be measured using at least two fluorescence images obtained in different spectral regions in order to minimize the effects of autofluorescence and scatter [62, 82]. In a study involving a mouse model of pulmonary inflammation, animals were injected with a protease-sensitive fluorescent agent that emits at 780 nm and a fluorescent agent with similar biodistribution that emits at 695 nm. Normalization of images at 780 nm with those at 695 nm minimized the effects of agent distribution and depth, improving quantitation of inflammation [83]. This normalization approach has also proved effective in a study quantitating expression of epidermal growth factor receptor in a mouse model of metastatic breast cancer [84].

5.4 Multispectral Optoacoustic Tomography (MSOT)

Optoacoustic interrogation of biological tissues has been considered since the early 1970s [85–87] and offers a powerful methodology for molecular imaging investigations. In vivo imaging of cellular and sub-cellular markers can be achieved by multispectral optoacoustic tomography (MSOT), an emerging field in the imaging sciences. MSOT overcomes the major limitations of conventional optical imaging while it retains many of the advantages of photonic methods.

The MSOT principle of operation is shown in Fig. 5.5. Short laser pulses in the nano-second range illuminate the tissue of interest at multiple wavelengths. Absorption of the fast laser pulses by tissue photo-absorbers, such as oxy- and deoxy-hemoglobin, melanin, or extrinsically administered probes and agents create a transient temperature increase which in turn leads to a thermo-elastic expansion. This process creates ultra-wideband acoustic waves in the 0.1–100 MHz range,



◀ **Fig. 5.4** Effects of tissue optical properties on the fluorescence and back-reflected intensity. **a** Phantom containing wells showing different levels of absorption (x-axis) and scatter (y-axis). All wells contain 1 mM Alexa 750 fluorochrome. **b** Fluorescence intensity measured in wells shown in panel (a). Signal variation across the wells is due to inhomogeneous illumination. **c** Fluorescence intensity recorded from the wells in panel (b) as a function of absorption coefficient. The symbols are defined in panel (e). **d** Fluorescence intensity recorded from wells in panel (b) as a function of reduced scattering coefficient. The symbols are defined in panel (f). **e** Reflectance intensity recorded from the wells in panel (b) as a function of absorption coefficient. Symbols are organized with scatter increasing toward the right. **f** Reflectance intensity recorded from the wells in panel (b) as a function of reduced scattering coefficient. Symbols are organized with absorption increasing toward the right. **g** Reflectance intensity spectra generated by Monte Carlo simulations as scattering and absorption coefficients increase, but their ratio remains constant. **h** Fluorescence intensity spectra generated by Monte Carlo simulations as scattering and absorption coefficients increase, but their ratio remains constant. Measurements in panels (g–h) have been experimentally confirmed (data not shown). Adapted from reference [18]

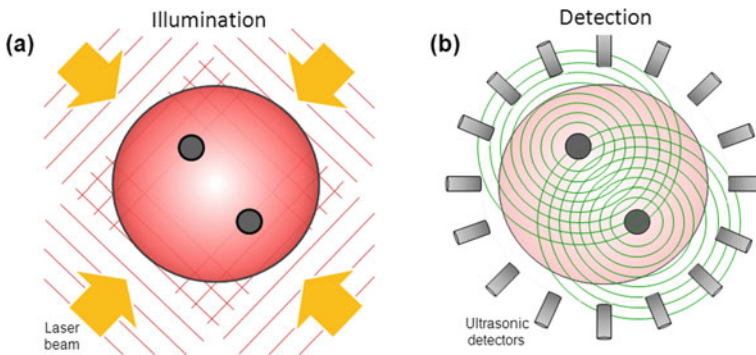


Fig. 5.5 Principle of MSOT operation. **a** Pulsed light of time-shared multiple wavelengths illuminates the tissue of interest and establishes transient photon fields in tissue. **b** In response to the fast absorption transients by tissue elements, acoustic responses are generated via the thermo-acoustic phenomenon, which are then detected with acoustic detectors. By modeling photon and acoustic propagation in tissues and using inversion (tomographic) methods images can then be generated and spectrally unimixed to yield the biodistribution of reporter molecules and tissue biomarkers. Adapted with permission from [91]; Copyright 2010 American Chemical Society

which can then be detected with multiple ultrasound elements placed around the illuminated area. By combining the ultrasonic measurements in the mathematical data inversion scheme, high-resolution images of tissue can be produced. The amplitude of the generated broadband ultrasound waves reflects local optical absorption properties. As a result, MSOT reports on the versatile optical absorption contrast but relative to other optical methods provides a sort of “super-vision” by exploiting the low scattering of ultrasound to break through the barriers imposed by optical diffusion. The spatial resolution of the method is therefore solely determined by the diffraction limit of ultrasound waves or the available bandwidth of the ultrasonic detector.

MSOT further employs spectral identification of known reporter molecules, such as common fluorochromes or other chromophores, dyes and photo-absorbing nanoparticles. Molecules with spectra that are different than the ones of background tissue can be accurately resolved by MSOT with high specificity [88]. However, in practice, MSOT images obtained from tissues represent a mixed contribution of photon energy delivered in each volume element imaged and the total absorption contribution from the volume element. Consequently, significant measures are taken to decompose the resulting image from the effects of inhomogeneous light attenuation in the tissue of interest [89, 90].

5.5 MSOT Imaging of Endogenous Absorption Contrast

Biological tissues contain a variety of endogenous chromophores with distinct absorption spectra that can be exploited for label-free structural and functional imaging with MSOT [92]. In the visible and NIR ranges, light is mainly absorbed in living mammalian tissues by hemoglobin, melanin, lipids, and water (Fig. 5.6). Differences in the absorption spectrum of hemoglobin associated to oxygen binding encode important information related to physiological activity. Since many diseases undergo structural changes at time scales ranging from days to weeks and months, imaging can be used to visualize and quantify these changes. For example, vascular structures can be mapped for depths of millimeters to centimeters within mammalian tissues [93] and accurate estimation of oxygen saturation is possible with proper models of light attenuation [94]. Due to the strong intrinsic hemoglobin

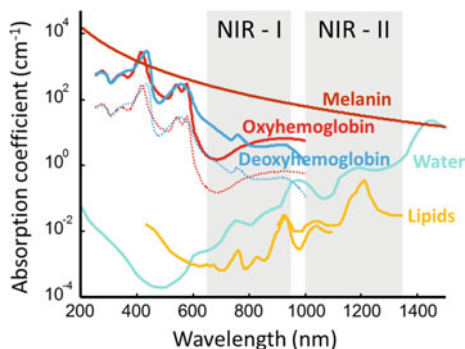


Fig. 5.6 Optical absorption spectra of major endogenous chromophores at typical concentrations occurring in living mammalian tissues. Melanin spectrum (brown) is shown for typical concentrations in the skin [106]; hemoglobin (red—oxygenated, blue—deoxygenated) for typical concentrations in whole blood (150 g/l—continuous lines) and average soft tissues (15 g/l—dashed lines) (<http://omic.org/spectra>); water (cyan) for a typical concentration of 80% by volume in soft tissues [107]; lipids (yellow) for a concentration of 20% by volume [108, 109]. The first (NIR—I) and second (NIR—II) windows [110], where optical absorption is minimized, are indicated

contrast, MSOT represents a valuable tool to study the evolution of important hallmarks of cancer such as angiogenesis [95, 96] and hypermetabolism [97, 98]. Imaging the vascular fat deposition in atherosclerotic plaques is also possible at infrared wavelengths [99, 100], while the strong absorption of melanin can be exploited to characterize skin melanomas [101] and metastatic melanoma cells [102]. Measurable endogenous changes may also occur on significantly shorter time scales. Changes in blood oxygen saturation, total hemoglobin, blood volume, oxygenized, and deoxygenized forms of hemoglobin can be readily monitored with optoacoustic systems operating at sub-second or even millisecond-scale temporal resolution [103–105].

Background absorption of light by intrinsic tissue chromophores along with optical scattering is also responsible for the strong attenuation of light in biological tissues. Optical attenuation is significantly stronger as compared with acoustic attenuation for frequencies below 20–30 MHz, thus it represents the main limiting factor for deep tissue imaging [111]. Light penetration is maximized in the so-called near-infrared (NIR) window between 650 and 1350 nm [110], while it is significantly aggravated by strong absorption of blood at shorter wavelengths and water at longer wavelengths (Fig. 5.6). For deep tissue imaging purposes, excitation optical wavelengths within this range are therefore commonly selected, where MSOT imaging with centimeter-scale penetration is possible [112, 113]. The wavelength dependence of optical attenuation further contributes to the distortion (spectral coloring) of the MSOT signals originating from deep locations [114]. Thereby, the performance of the particularly employed unmixing approach, rather than the signal-to-noise performance of the imaging system, generally determines the minimum detectable concentration of extrinsically administered contrast agents.

5.6 Molecular Sensing with MSOT

The presence of strong endogenous (background) contrast may in fact hinder detection of useful signals when attempting to enhance the contrast extrinsically, e.g., in targeted molecular imaging applications. With a typical 2 mM concentration of hemoglobin in blood [115], vascular structures may conceal, e.g., signals from genetically-expressed labels that can typically attain concentrations on the micromolar level in vivo [116]. Thereby, signal amplification approaches based on spectral unmixing or dynamic contrast enhancement become essential in order to efficiently map the distribution of relatively low concentrations of contrast agents [117, 118].

To this end, various molecular sensors have been used to probe tumor microenvironments and monitor treatments with MSOT. A temperature-sensitive nanoswitch probe was synthesized by intercalation of light-harvesting porphyrins within thermoresponsive nanovesicles [119]. The probe functions by absorbing light at two distinct wavelengths (680 and 824 nm) while its spectral features can be reversibly switched by exceeding a temperature threshold. Using this thermochromic

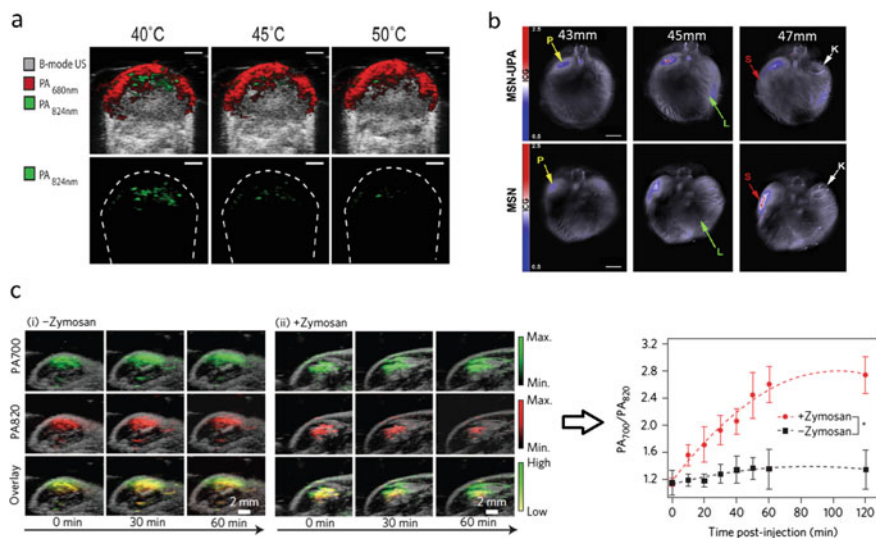


Fig. 5.7 Optoacoustic molecular imaging and sensing. **a** Temperature threshold sensing in tumor xenografts injected with J-aggregating bacteriophagephorbide α -lipid nanoparticles JPN16 by comparison of cross-sectional optoacoustic images at two different wavelengths. Figure is adapted from [119] with permission under the License from Standard ACS Authors' Choice Usage Agreement; Copyright © 2014 American Chemical Society. A 1 mm scale bar was added and image identification was altered. **b** Multispectral optoacoustic tomography (MSOT) images of a mouse implanted with S2VP10 pancreatic cancer cells after injection of mesoporous silica nanoparticles (MSN) with chitosan and urokinase plasminogen activator (MSN-UPA) (top) or untargeted MSN (bottom). Scale bar—5 mm. Adapted with permission from [120]; © 2015 Elsevier. **c** Optoacoustic sensing of reactive oxygen species (ROS) by comparison of cross-sectional optoacoustic images for saline-treated (left) and zymosan-treated (middle) regions in a mouse and the time profiles of the optoacoustic amplitude ratios for two wavelengths (right) after injection of ratiometric semiconducting polymer nanoparticles (RSPN). Adapted with permission from [121]; © 2014 Macmillan Publishers Ltd.

property, localized temperature changes within tumor xenografts were determined *in vivo* and noninvasively (Fig. 5.7a).

Similar strategies may be applied to detect other stimuli such as pH and enzymatic activity. Due to their high metabolic rate, malignant tumors are commonly characterized by lower than normal pH levels. A theranostic nanovehicle for targeting pancreatic cancer was designed based on mesoporous silica nanoparticles (MSN) that encapsulate Indocyanine Green for enhancing MSOT contrast [120]. The tumor specificity was improved with the addition of both chitosan, targeting acidic pH, and urokinase plasminogen activator (UPA), targeting UPAR. Accordingly, the signal increase due to acidic pH conditions resulted in a 20-fold stronger optoacoustic response. *In vivo*, MSN-UPA particles demonstrated orthotopic pancreatic tumor specific accumulation compared to liver or kidney, as identified using real-time MSOT. By tracking *in vivo* nanoparticle biodistribution with MSOT, it

was further confirmed that pH-responsive, ligand-targeted MSNs preferentially bind to pancreatic tumors for payload delivery (Fig. 5.7b).

MSOT imaging has also been found capable of imaging oedema, whose different variants include cerebral, pulmonary, macular, or lymphatic fluid build-ups within the body. One suitable probe for this is a nanoparticle based on semiconducting polymer particles (SPN1) [121]. It exhibits preferential narrowband absorption in the NIR and is resilient against photodegradation and oxidation. Most important is its ability to ratiometrically detect reactive oxygen species (ROS) at 700 and 820 nm (Fig. 5.7c). In fact, the increase in ROS has also been shown as a marker of apoptosis. In the same study, using a mouse model of acute oedema and Zymosan to simulate ROS generation, SPN1 was successfully used to monitor the ROS regulation process intra-muscularly.

Another promising application of dynamic molecular sensing with MSOT is the monitoring of thyroid-related disorders. The thyroid gland regulates many of the most important functions of the body, from metabolism to breathing. Thyroid cancer is rare but benign nodules on the gland are common. Follicular thyroid carcinomas are very similar to benign nodules yet differ in terms of environmental conditions. One noticeable difference is the activity and presence of the matrix metalloproteinases (MMPs) and two members of this family (MMP-2 & MMP-9) were determined as biomarkers of malignant thyroid lesions. An MMP-activatable optoacoustic probe based on Alexa-Fluor 750 was successfully used to image FTC133 thyroid tumors subcutaneously implanted in nude mice *in vivo* [122]. Both MMP-2 and MMP-9 cleave the protein in a non-reversible fashion, which increases its optoacoustic and fluorescent signal.

5.7 Clinical Translation of Optoacoustic Imaging

The great potential of optoacoustic imaging showcased in preclinical research has encouraged the translation of this technology into the clinics with multiple applications envisioned, from intraoperative diagnostics to ophthalmology, dermatology, and endoscopic imaging. One of the key advantages of optoacoustic imaging is its intrinsic potential to deliver complete volumetric tomographic datasets from the imaged object with a single interrogating laser pulse, a possibility that does not exist in other clinical imaging modalities. This capacity also comes with important clinical advantages, such as the ability to dynamically visualize the biodistribution of contrast agents in 3D and reduce out-of-plane and motion artefacts, thus facilitating clinical observations.

Dedicated handheld optoacoustic probes have recently been introduced for high performance imaging of human subjects. Those come with real-time tomographic imaging capacities in 2D [123, 124] and 3D [125] as well as integrated pulse-echo ultrasonography capabilities [126]. One promising application is the assessment of the metastatic status of sentinel lymph nodes in human melanoma. In the first-in-human study, cross-sectional and volumetric MSOT were used to image

SLNs *ex vivo* and *in vivo* in patients with melanoma [102]. In comparison with the conventional protocols for analysis of excised SLNs, it was possible to significantly improve the tumor metastasis detection rate from 214 melanoma patients using MSOT. When combining non-invasive MSOT imaging with subcutaneous injection of the ICG contrast agent, visualization of the SLNs *in vivo* in 20 patients was further performed with up to 5-cm effective imaging depth (Fig. 5.8a). MSOT identified cancer-free SLNs *in vivo* and *ex vivo* without a single false negative (189 total lymph nodes), with 100% sensitivity and 48–62% specificity. The handheld MSOT imaging technology was also used in a feasibility study assessing peripheral blood supply and vascular disease in human feet. Such diagnosis is important in the context of peripheral arterial diseases, diabetic foot, and (autoimmune) vasculitis [127]. In this study, MSOT imaging has been shown to be superior to conventional imaging methods (e.g., duplex ultrasonography) in terms of resolution (capillaries as small as 100 μm in diameter were resolved) and its intrinsic spectroscopic capacity to differentiate between arteries and veins. Also, due to its imaging speed, MSOT imaging allowed to identify pulsation in arteries.

One potential valuable application of MSOT is the diagnosis of breast lesions. It is a favored application due to the generally low light attenuation in the breast as compared with other tissues [115], which allows penetrating the entire human breast [129]. Indeed, breast cancer diagnosis was aimed with the very first implementations of optoacoustic tomography scanners [130, 131], which was recently followed by several designs optimized for deeper imaging and better detection sensitivity [132]. Several clinical breast imaging studies are ongoing and the method has shown potential for non-invasive detection of malignant lesions. In a clinical study on infiltrating ductal carcinoma, distinct optoacoustic patterns could be classified as mass-like, non-mass like, and ring-shaped [133]. In another pilot clinical study, real-time handheld MSOT scanner was used to identify high-resolution patterns of lesions in 10 patients of ages 48–81 years with malignant nonspecific breast cancer or invasive lobular carcinoma [128] (Fig. 5.8a–e). MSOT data acquisitions were guided by ultrasonography and X-ray mammography or MRI. The extended spectral range in the 700–970 nm window allowed the computation of oxygenated hemoglobin (HbO_2), deoxygenated hemoglobin (HB), total blood volume (TBV), lipid, and water contributions, allowing first insights into *in vivo* high-resolution breast tissue MSOT cancer patterns. TBV and Hb/ HbO_2 images resolved marked differences between cancer and control tissue, manifested as a vessel-rich tumor periphery with highly heterogeneous spatial appearance compared with healthy tissue. Significant TBV variations between different tumors and between tumors over healthy tissues were reported. Water and fat lipid layers further appeared disrupted in cancer versus healthy tissue.

In the field of dermatology, new non-invasive skin imaging tools are essential to aid real-time diagnosis of skin tumors, chronic inflammation, alopecia, scarring, burns, etc., thus minimizing the need for invasive skin biopsy. MSOT offers the unique capacity for high-resolution 3D optical mapping of tissue by further delivering highly specific optical contrast from a depth of several millimeters to centimeters in living tissues. A recent study performed on human volunteers, has

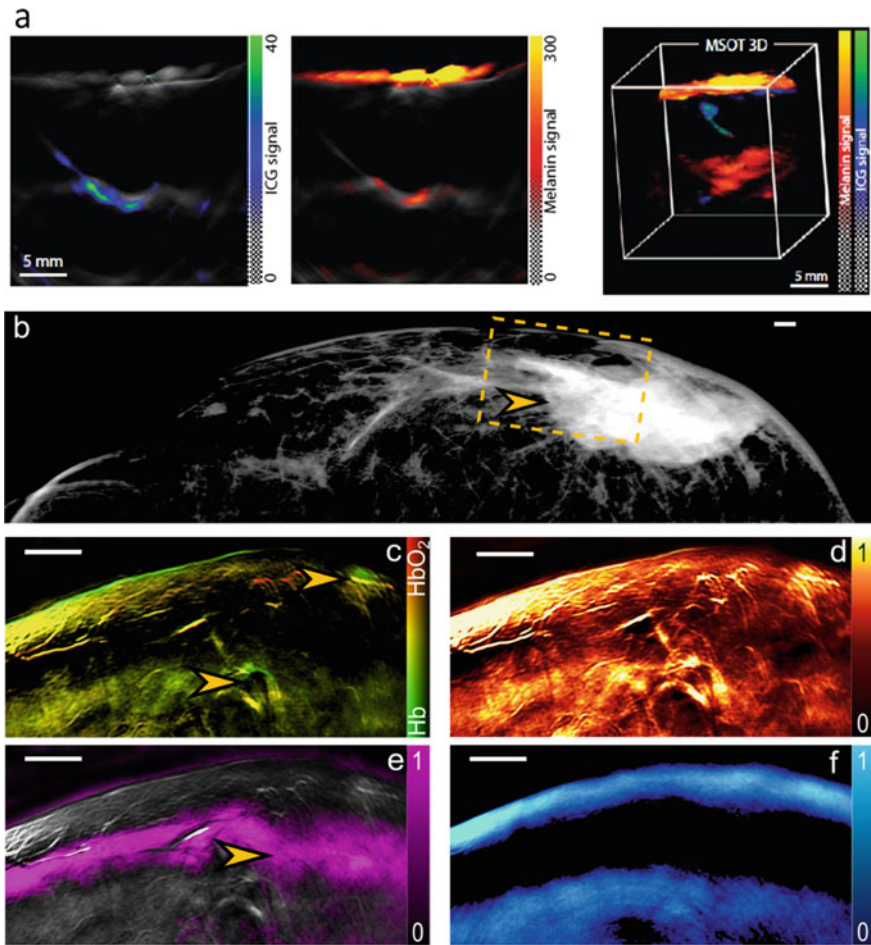


Fig. 5.8 Examples of clinical multispectral optoacoustic tomography (MSOT) studies in oncology. **a** Metastatic status of sentinel lymph nodes in melanoma patients determined noninvasively with MSOT. Preoperative non-invasive assessment of ICG (green scale) and melanin (orange) distribution in suspected metastatic sentinel lymph nodes using handheld cross-sectional and volumetric MSOT scanners. Penetration of up to 5 cm was claimed with 100% sensitivity and 48–62% lesion detection specificity. Adapted with permission from [102]; © 2015 American Association for the Advancement of Science **b** X-ray mammography image revealing a >4 cm, subcutaneous, nonspecific breast tumor. **c** MSOT image of Hb and HbO₂ obtained from the field of view labeled in panel (b); arrows point to areas of increased blood volume. **d** MSOT image of TBV showing constitutive hyperemia through an extended area of the tumor. **e** MSOT image of lipid showing disruption of the fat layer (arrow) at the area of the tumor mass. **f** MSOT image of water. Adapted from [128]; © 2017 American Association for Cancer Research

shown capacity for non-invasive structural and functional analysis of intact hair follicles and pilosebaceous units by volumetric handheld MSOT [134]. On-the-fly assessment of key morphometric parameters of follicles and lipid content as well as functional oxygenation parameters of the associated capillary bed was demonstrated with high spatial resolution below 70 μm . Precision assessment of label-free psoriasis biomarkers in the human skin has been demonstrated with a high-resolution version of MSOT termed ultra-broadband optoacoustic mesoscopy [135]. In particular, skin morphology and vascular patterns in the dermis and sub-dermis of psoriasis patients have been visualized, enabling quantification of inflammation and other biomarkers of psoriasis without the need for contrast agents. The label-free biomarkers detected by the handheld imaging scanner correlated well with the clinical score.

One major limitation for clinical translation remains the lack of clinically approved probes for contrast-enhanced optoacoustic imaging. ICG has been approved for human use since the 1960s. However, there are currently no other approved compounds that absorb light in the near-infrared, which is essential for deep tissue imaging with MSOT. In addition, successful completion of multicenter trials in a number of key clinical applications is crucial in order to facilitate the transition of MSOT from a highly potent research platform to an accepted clinical imaging modality.

5.8 The Future of Fluorescence and MSOT Imaging

FMI is expected to augment interventional procedures in surgery suites for guiding procedures but could play a key role in early detection of disease in endoscopic procedures such as colonoscopy or esophageal and gastric inspection. We expect that significant attention will be given to research and translation of targeted fluorescence agents for further improving tumor visualization, margin identification, or early cancer detection compared to the current state-of-the-art fluorescence imaging agents. Agents that identify other tissue structures such as nerves can also play a major role in interventional procedures. We further anticipate that the fluorescent agents will play a role in other medical fields, such as interventional cardiology, for example, in identifying biological parameters associated with atheroma and stent condition [136].

On the technology front, we expect that attention will shift from camera developments to advanced measurement schemes and data processing methods that account for the effects of the parameters in Table 5.1. Phantoms such as the one described in Box 5.1 can play a key role in validating these methods and in quality control and standardization processes. Such quality control is necessary to develop FMI as a reliable tool for clinical propagation and for ensuring accurate studies as required for regulatory approval of clinical systems and agents.

The great potential of MSOT imaging showcased in preclinical research has encouraged the translation of this technology into the clinics with multiple applications envisioned, from intraoperative diagnostics to ophthalmology, dermatology, cardiovascular, and endoscopic imaging. One of the key advantages of MSOT is its intrinsic potential to deliver complete volumetric tomographic datasets from the imaged object with a single interrogating laser pulse, a possibility that does not exist in other clinical imaging modalities. This capacity enables dynamic visualization of contrast agent biodistribution in 3D with high spatial resolution, thus reducing image blurring and motion artefacts and facilitating quantified depth-resolved observations.

Given the current progress in nanoparticle research and the versatility of MSOT contrast mechanisms, it is anticipated that future developments in light-absorbing agents would bring the contrast enhancement approaches to a new level of performance. Novel smart agents that selectively change their absorption-based contrast with environmental changes or theranostic agents releasing drugs at specific targets may all lead to paradigm shifts in biomedical research. Ideally, agents need to be optimized for more efficient optoacoustic signal generation, both in terms of the overall generated signal strength and spectral response. In this regard, development of novel dyes and genetic labels with preferential absorption in the far-red or NIR ranges for deep tissue MSOT imaging represents a highly promising research direction. To this end, most novel MSOT contrast agents have only been tested at a proof-of-principle level or early stages of exploration, thus further validations for biocompatibility, toxicity, and targeting efficiency are necessary to establish in vivo applicability.

Acknowledgments The work of DR is supported by the European Research Council Grant *ERC-2015-CoG-682379*, National Institute of Health grant UF1-NS107680, Human Frontier Science Program (HFSP) Grant RGY0070/2016 and the German research Foundation Grant RA1848/5-1. The work of VN is supported by the European Union's Horizon 2020 research and innovation programme under grant agreement 687866 (INNODERM) and from the German Research Foundation (Gottfried Wilhelm Leibnitz Prize 2013; NT 3/10-1).

Conflicts of Interest VN and DR have equity in iThera Medical GmbH. VN also serves as a consultant to SurgVision BV.

References

1. Galloro G (2012) High technology imaging in digestive endoscopy. *World J Gastrointest Endosc* 4:22–27
2. Freschi C et al (2013) Technical review of the da Vinci surgical telemanipulator. *Int J Med Robot* 9:396–406
3. Roberts DW, Hartov A, Kennedy FE, Miga MI, Paulsen KD (1998) Intraoperative brain shift and deformation: a quantitative analysis of cortical displacement in 28 cases. *Neurosurgery* 43:749–758
4. Labadie RF, Davis BM, Fitzpatrick JM (2005) Image-guided surgery: what is the accuracy? *Curr Opin Otolaryngol Head Neck Surg* 13:27–31

5. Moore GE, Hunter SW, Hubbard TB (1949) Clinical and experimental studies of fluorescein dyes with special reference to their use for the diagnosis of central nervous system tumors. *Ann Surg* 130:637–642
6. Novotny HR, Alvis D (1960) A method of photographing fluorescence in circulating blood of the human eye. *Tech Doc Rep SAMTDR USAF Sch Aerosp Med* 60–82:1–4
7. Koch M, Ntziachristos V (2016) Advancing surgical vision with fluorescence imaging. *Annu Rev Med* 67:153–164
8. Zhang RR et al (2017) Beyond the margins: real-time detection of cancer using targeted fluorophores. *Nat Rev Clin Oncol* 14:347–364
9. van Dam GM et al (2011) Intraoperative tumor-specific fluorescence imaging in ovarian cancer by folate receptor-alpha targeting: first in-human results. *Nat Med* 17:1315–1319
10. Tummers QRJG et al (2016) Intraoperative imaging of folate receptor alpha positive ovarian and breast cancer using the tumor specific agent EC17. *Oncotarget* 7:32144–32155
11. Rosenthal EL et al (2015) Safety and tumor specificity of cetuximab-IRDye800 for surgical navigation in head and neck cancer. *Clin Cancer Res* 21:3658–3666
12. Whitley MJ et al (2016) A mouse-human phase I co-clinical trial of a protease-activated fluorescent probe for imaging cancer. *Sci Transl Med* 8:320ra324
13. Hsiung PL et al (2008) Detection of colonic dysplasia in vivo using a targeted heptapeptide and confocal microendoscopy. *Nat Med* 14:454–458
14. Atreya R et al (2014) In vivo imaging using fluorescent antibodies to tumor necrosis factor predicts therapeutic response in Crohn's disease. *Nat Med* 20:313–318
15. Glatz J, Symvoulidis P, Garcia-Allende PB, Ntziachristos V (2014) Robust overlay schemes for the fusion of fluorescence and color channels in biological imaging. *J Biomed Opt* 19:040501
16. Glatz J et al (2013) Concurrent video-rate color and near-infrared fluorescence laparoscopy. *J Biomed Opt* 18:101302
17. Starosolski Z et al (2017) Indocyanine green fluorescence in second near-infrared (NIR-II) window. *PLoS ONE* 12:e0187563
18. Koch M, Symvoulidis P, Ntziachristos V (2018) Tackling standardization in fluorescence molecular imaging. *Nat Photonics* 12:505–515
19. Hong G et al (2014) Through-skull fluorescence imaging of the brain in a new near-infrared window. *Nat Photonics* 8:723–730
20. Leevy CM (1967) Indocyanine green clearance as a test for hepatic function. *JAMA* 200:236–240
21. Rowell LB, Marx HJ, Bruce RA, Conn RD, Kusumi F (1966) Reductions in cardiac output, central blood volume, and stroke volume with thermal stress in normal men during exercise. *J Clin Invest* 45:1801–1816
22. Craandijk A, Van Beek CA (1976) Indocyanine green fluorescence angiography of the choroid. *Br J Ophthalmol* 60:377–385
23. Sekijima M et al (2004) An intraoperative fluorescent imaging system in organ transplantation. *Transplant Proc* 36:2188–2190
24. Jonsson K et al (1991) Tissue oxygenation, anemia, and perfusion in relation to wound healing in surgical patients. *Ann Surg* 214:605–613
25. Azuma R et al (2008) Detection of skin perforators by indocyanine green fluorescence nearly infrared angiography. *Plast Reconstr Surg* 122:1062–1067
26. Liu DZ, Mathes DW, Zenn MR, Neligan PC (2011) The application of indocyanine green fluorescence angiography in plastic surgery. *J Reconstr Microsurg* 27:355–364
27. Holm C et al (2002) Intraoperative evaluation of skin-flap viability using laser-induced fluorescence of indocyanine green. *Br J Plast Surg* 55:635–644
28. Detter C et al (2002) Near-infrared fluorescence coronary angiography: a new noninvasive technology for intraoperative graft patency control. *Heart Surg Forum* 5:364–369

29. Ferroli P, Nakaji P, Acerbi F, Albanese E, Broggi G (2011) Indocyanine green (ICG) temporary clipping test to assess collateral circulation before venous sacrifice. *World Neurosurg* 75:122–125
30. Sherwinter DA (2012) Transanal near-infrared imaging of colorectal anastomotic perfusion. *Surg Laparosc Endosc Percutan Tech* 22:433–436
31. Yamaguchi S et al (2004) The “perfusion map” of the unipedicled TRAM flap to reduce postoperative partial necrosis. *Ann Plast Surg* 53:205–209
32. Lyman GH et al (2014) Sentinel lymph node biopsy for patients with early-stage breast cancer: American society of clinical oncology clinical practice guideline update. *J Clin Oncol* 32:1365–1383
33. Yared MA et al (2002) Recommendations for sentinel lymph node processing in breast cancer. *Am J Surg Pathol* 26:377–382
34. Cox CE et al (1998) Guidelines for sentinel node biopsy and lymphatic mapping of patients with breast cancer. *Ann Surg* 227:645–651
35. Mieog JS et al (2011) Toward optimization of imaging system and lymphatic tracer for near-infrared fluorescent sentinel lymph node mapping in breast cancer. *Ann Surg Oncol* 18:2483–2491
36. Wishart GC, Loh SW, Jones L, Benson JR (2012) A feasibility study (ICG-10) of indocyanine green (ICG) fluorescence mapping for sentinel lymph node detection in early breast cancer. *Eur J Surg Oncol* 38:651–656
37. Verbeek FP et al (2014) Near-infrared fluorescence sentinel lymph node mapping in breast cancer: a multicenter experience. *Breast Cancer Res Treat* 143:333–342
38. Fujiwara M, Mizukami T, Suzuki A, Fukamizu H (2009) Sentinel lymph node detection in skin cancer patients using real-time fluorescence navigation with indocyanine green: preliminary experience. *J Plast Reconstr Aes* 62:e373–378
39. van den Berg NS et al (2012) Concomitant radio- and fluorescence-guided sentinel lymph node biopsy in squamous cell carcinoma of the oral cavity using ICG-(99 m)Tc-nanocolloid. *Eur J Nucl Med Mol Imaging* 39:1128–1136
40. Crane LM et al (2011) Intraoperative near-infrared fluorescence imaging for sentinel lymph node detection in vulvar cancer: first clinical results. *Gynecol Oncol* 120:291–295
41. Crane LM et al (2011) Intraoperative multispectral fluorescence imaging for the detection of the sentinel lymph node in cervical cancer: a novel concept. *Mol Imaging Biol* 13:1043–1049
42. Misiak M, Rzepka JK, Zalewski K, Kopczyński J, Gozdz S (2014) Fluorescence-guided lymph node mapping with indocyanine green for endometrial cancer: a feasibility study. *Clin J Oncol (Meet Abstr)* 32:e16549
43. Yamashita S et al (2012) Sentinel node navigation surgery by thoracoscopic fluorescence imaging system and molecular examination in non-small cell lung cancer. *Ann Surg Oncol* 19:728–733
44. Abu-Rustum NR (2014) Sentinel lymph node mapping for endometrial cancer: a modern approach to surgical staging. *J Natl Compr Cancer Netw* 12:288–297
45. Rasmussen JC, Tan IC, Marshall MV, Fife CE, Sevick-Muraca EM (2009) Lymphatic imaging in humans with near-infrared fluorescence. *Curr Opin Biotechnol* 20:74–82
46. Takami T, Yamagata T, Naito K, Arima H, Ohata K (2013) Intraoperative assessment of spinal vascular flow in the surgery of spinal intramedullary tumors using indocyanine green videoangiography. *Surg Neurol Int* 4:135
47. Wang T, Hu YJ, He Y, Sun PS, Guo ZC (2019) A retrospective validation study of sentinel lymph node mapping for high-risk endometrial cancer. *Arch Gynecol Obstet* 299:1429–1435
48. Scheuer W, van Dam GM, Dobosz M, Schwaiger M, Ntzichristos V (2012) Drug-based optical agents: infiltrating clinics at lower risk. *Sci Transl Med* 4:134ps111
49. Harada K et al (2013) Detection of lymph node metastases in human colorectal cancer by using 5-aminolevulinic acid-induced protoporphyrin IX fluorescence with spectral unmixing. *Int J Mol Sci* 14:23140–23152

50. Kamp MA et al (2012) 5-aminolevulinic acid (5-ALA)-induced fluorescence in intracerebral metastases: a retrospective study. *Acta Neurochir* 154:223–228
51. Kishi K et al (2012) Staging laparoscopy using ALA-mediated photodynamic diagnosis improves the detection of peritoneal metastases in advanced gastric cancer. *J Surg Oncol* 106:294–298
52. Stummer W et al (2000) Fluorescence-guided resection of glioblastoma multiforme by using 5-aminolevulinic acid-induced porphyrins: a prospective study in 52 consecutive patients. *J Neurosurg* 93:1003–1013
53. Stummer W et al (2006) Fluorescence-guided surgery with 5-aminolevulinic acid for resection of malignant glioma: a randomised controlled multicentre phase III trial. *Lancet Oncol* 7:392–401
54. DSouza AV, Lin H, Henderson ER, Samkoe KS, Pogue BW (2016) Review of fluorescence guided surgery systems: identification of key performance capabilities beyond indocyanine green imaging. *J Biomed Opt* 21:80901
55. Marshall MV et al (2010) Near-infrared fluorescence imaging in humans with indocyanine green: a review and update. *Open Surg Oncol J* 2:12–25
56. Hong GS et al (2012) Multifunctional in vivo vascular imaging using near-infrared II fluorescence. *Nat Med* 18:1841
57. Ghosh D et al (2014) Deep, noninvasive imaging and surgical guidance of submillimeter tumors using targeted M13-stabilized single-walled carbon nanotubes. *Proc Natl Acad Sci USA* 111:13948–13953
58. Carr JA et al (2018) Shortwave infrared fluorescence imaging with the clinically approved near-infrared dye indocyanine green. *Proc Natl Acad Sci USA* 115:4465–4470
59. Medicine, U. N. L. o (2012) VEGF-targeted fluorescent tracer imaging in breast cancer. <https://clinicaltrials.gov/ct2/show/NCT01508572>
60. Bradley RS, Thorniley MS (2006) A review of attenuation correction techniques for tissue fluorescence. *J R Soc Interface* 3:1–13
61. Themelis G, Yoo JS, Soh KS, Schulz R, Ntziachristos V (2009) Real-time intraoperative fluorescence imaging system using light-absorption correction. *J Biomed Opt* 14:064012
62. Moriyama EH, Kim A, Bogaards A, Lilje L, Wilson BC (2008) A ratiometric fluorescence imaging system for surgical guidance. *Adv Opt Technol* 2008:1–10
63. Barbash GI, Glied SA (2010) New technology and health care costs—the case of robot-assisted surgery. *N Engl J Med* 363:701–704
64. Gorpas D, Koch M, Anastasopoulou M, Klemm U, Ntziachristos V (2017) Benchmarking of fluorescence cameras through the use of a composite phantom. *J Biomed Opt* 22:16009
65. Niedre MJ et al (2008) Early photon tomography allows fluorescence detection of lung carcinomas and disease progression in mice in vivo. *Proc Natl Acad Sci USA* 105:19126–19131
66. Resch-Genger U, Grabolle M, Cavaliere-Jaricot S, Nitschke R, Nann T (2008) Quantum dots versus organic dyes as fluorescent labels. *Nat Methods* 5:763–775
67. Gao X et al (2005) In vivo molecular and cellular imaging with quantum dots. *Curr Opin Biotechnol* 16:63–72
68. Alivisatos AP, Gu W, Larabell C (2005) Quantum dots as cellular probes. *Annu Rev Biomed Eng* 7:55–76
69. Zhu B, Tan IC, Rasmussen JC, Sevick-Muraca EM (2012) Validating the sensitivity and performance of near-infrared fluorescence imaging and tomography devices using a novel solid phantom and measurement approach. *Technol Cancer Res Treat* 11:95–104
70. Roy M, Kim A, Dadani F, Wilson BC (2011) Homogenized tissue phantoms for quantitative evaluation of subsurface fluorescence contrast. *J Biomed Opt* 16:016013
71. Zhu B, Rasmussen JC, Sevick-Muraca EM (2014) A matter of collection and detection for intraoperative and noninvasive near-infrared fluorescence molecular imaging: to see or not to see? *Med Phys* 41:022105

72. Moffitt T, Chen YC, Prahla SA (2006) Preparation and characterization of polyurethane optical phantoms. *J Biomed Opt* 11:041103
73. Anastasopoulou M et al (2016) Comprehensive phantom for interventional fluorescence molecular imaging. *J Biomed Opt* 21:091309
74. Ntziachristos V et al (2005) Planar fluorescence imaging using normalized data. *J Biomed Opt* 10:064007
75. Valdes PA et al (2012) Quantitative, spectrally-resolved intraoperative fluorescence imaging. *Sci Rep* 2:798
76. Zhu B, Rasmussen JC, Sevick-Muraca EM (2014) Non-invasive fluorescence imaging under ambient light conditions using a modulated ICCD and laser diode. *Biomed Opt Express* 5:562–572
77. Sexton K et al (2013) Pulsed-light imaging for fluorescence guided surgery under normal room lighting. *Opt Lett* 38:3249–3252
78. Zonios G, Dimou A (2006) Modeling diffuse reflectance from semi-infinite turbid media: application to the study of skin optical properties. *Opt Express* 14:8661–8674
79. Garcia-Allende PB et al (2016) Uniqueness in multispectral constant-wave epi-illumination imaging. *Opt Lett* 41:3098–3101
80. Saager RB, Cuccia DJ, Saggese S, Kelly KM, Durkin AJ (2011) Quantitative fluorescence imaging of protoporphyrin IX through determination of tissue optical properties in the spatial frequency domain. *J Biomed Opt* 16:126013
81. Yang B, Tunnell JW (2014) Real-time absorption reduced surface fluorescence imaging. *J Biomed Opt* 19:90505
82. Bogaards A, Sterenborg HJ, Wilson BC (2007) In vivo quantification of fluorescent molecular markers in real-time: a review to evaluate the performance of five existing methods. *Photodiagnosis Photodyn Ther* 4:170–178
83. Haller J et al (2008) Visualization of pulmonary inflammation using noninvasive fluorescence molecular imaging. *J Appl Physiol* 104:795–802
84. Tichauer KM et al (2014) Microscopic lymph node tumor burden quantified by macroscopic dual-tracer molecular imaging. *Nat Med* 20:1348–1353
85. Rosencwaig A (1973) Photoacoustic spectroscopy of biological materials. *Science* 181:657–658
86. Bowen T (1982) Radiation-induced thermoacoustic soft-tissue imaging. *IEEE Trans Sonics Ultrasonics* 29:187
87. Oraevsky A, Steven J, Esenaliev R, Tittel F (1994) Laser-based optoacoustic imaging in biological tissues. *Proc SPIE* 2134:122
88. Razansky D, Vinegoni C, Ntziachristos V (2007) Multispectral photoacoustic imaging of fluorochromes in small animals. *Opt Lett* 32:2891–2893
89. Rosenthal A, Razansky D, Ntziachristos V (2009) Quantitative optoacoustic signal extraction using sparse signal representation. *IEEE Trans Med Imaging* 28:1997–2006
90. Rosenthal A, Razansky D, Ntziachristos V (2010) Fast semi-analytical model-based acoustic inversion for quantitative optoacoustic tomography. *IEEE Trans Med Imaging* 29:1275–1285
91. Ntziachristos V, Razansky D (2010) Molecular imaging by means of multispectral optoacoustic tomography (MSOT). *Chem Rev* 110:2783–2794
92. Dean-Ben XL, Gottschalk S, Mc Larney B, Shoham S, Razansky D (2017) Advanced optoacoustic methods for multiscale imaging of in vivo dynamics. *Chem Soc Rev* 46:2158–2198
93. Wang LV, Hu S (2012) Photoacoustic tomography: in vivo imaging from organelles to organs. *Science* 335:1458–1462
94. Tzoumas S et al (2016) Eigenspectra optoacoustic tomography achieves quantitative blood oxygenation imaging deep in tissues. *Nat Commun* 7:12121
95. Laufer J et al (2012) In vivo preclinical photoacoustic imaging of tumor vasculature development and therapy. *J Biomed Opt* 17:056016

96. Omar M, Schwarz M, Soliman D, Symvoulidis P, Ntziachristos V (2015) Pushing the optical imaging limits of cancer with multi-frequency-band raster-scan optoacoustic mesoscopy (RSOM). *Neoplasia* 17:208–214
97. Herzog E et al (2012) Optical imaging of cancer heterogeneity with multispectral optoacoustic tomography. *Radiology* 263:461–468
98. Yao J, Maslov KI, Wang LV (2012) In vivo photoacoustic tomography of total blood flow and potential imaging of cancer angiogenesis and hypermetabolism. *Technol Cancer Res Treat* 11:301–307
99. Wang B et al (2010) Detection of lipid in atherosclerotic vessels using ultrasound-guided spectroscopic intravascular photoacoustic imaging. *Opt Express* 18:4889–4897
100. Jansen K, van der Steen AF, van Beusekom HM, Oosterhuis JW, van Soest G (2011) Intravascular photoacoustic imaging of human coronary atherosclerosis. *Opt Lett* 36:597–599
101. Zhang HF, Maslov K, Stoica G, Wang LV (2006) Functional photoacoustic microscopy for high-resolution and noninvasive in vivo imaging. *Nat Biotechnol* 24:848–851
102. Stoffels I et al (2015) Metastatic status of sentinel lymph nodes in melanoma determined noninvasively with multispectral optoacoustic imaging. *Sci Transl Med* 7:317ra199
103. Gottschalk S, Fehm TF, Dean-Ben XL, Razansky D (2015) Noninvasive real-time visualization of multiple cerebral hemodynamic parameters in whole mouse brains using five-dimensional optoacoustic tomography. *J Cereb Blood Flow Metab* 35:531–535
104. Hu S (2016) Listening to the brain with photoacoustics. *IEEE J Sel Top Quant* 22:6800610
105. Nasirivanaki M et al (2014) High-resolution photoacoustic tomography of resting-state functional connectivity in the mouse brain. *Proc Natl Acad Sci USA* 111:21–26
106. Jacques SL, Glickman RD, Schwartz JA (1996) Internal absorption coefficient and threshold for pulsed laser disruption of melanosomes isolated from retinal pigment epithelium. In: *Proceedings of the SPIE* 2681, Laser-Tissue Interaction VII
107. Hale GM, Querry MR (1973) Optical constants of water in the 200-nm to 200- μ m wavelength region. *Appl Opt* 12:555–563
108. van Veen RLP et al (2005) Determination of visible near-IR absorption coefficients of mammalian fat using time- and spatially resolved diffuse reflectance and transmission spectroscopy. *J Biomed Opt* 10:054004
109. Tsai C-L, Chen J-C, Wang W-J (2001) Near-infrared absorption property of biological soft tissue constituents. *J Med Biol Eng* 21:7–14
110. Smith AM, Mancini MC, Nie S (2009) Bioimaging: second window for in vivo imaging. *Nat Nanotechnol* 4:710–711
111. Dean-Ben XL, Razansky D, Ntziachristos V (2011) The effects of acoustic attenuation in optoacoustic signals. *Phys Med Biol* 56:6129–6148
112. Ku G, Wang LV (2005) Deeply penetrating photoacoustic tomography in biological tissues enhanced with an optical contrast agent. *Opt Lett* 30:507–509
113. Dean-Ben XL, Fehm TF, Gostic M, Razansky D (2016) Volumetric hand-held optoacoustic angiography as a tool for real-time screening of dense breast. *J Biophotonics* 9:253–259
114. Cox B, Laufer JG, Arridge SR, Beard PC (2012) Quantitative spectroscopic photoacoustic imaging: a review. *J Biomed Opt* 17:061202
115. Jacques SL (2013) Optical properties of biological tissues: a review. *Phys Med Biol* 58:R37–61
116. Krumholz A, Shcherbakova DM, Xia J, Wang LV, Verkhusha VV (2014) Multicontrast photoacoustic in vivo imaging using near-infrared fluorescent proteins. *Sci Rep* 4:3939
117. Stiel AC et al (2015) High-contrast imaging of reversibly switchable fluorescent proteins via temporally unmixed multispectral optoacoustic tomography. *Opt Lett* 40:367–370
118. Tzoumas S, Deliolanis N, Morscher S, Ntziachristos V (2014) Unmixing molecular agents from absorbing tissue in multispectral optoacoustic tomography. *IEEE Trans Med Imaging* 33:48–60

119. Ng KK et al (2014) Stimuli-responsive photoacoustic nanoswitch for in vivo sensing applications. *ACS Nano* 8:8363–8373
120. Gurka MK et al (2016) Identification of pancreatic tumors in vivo with ligand-targeted, pH responsive mesoporous silica nanoparticles by multispectral optoacoustic tomography. *J Control Release* 231:60–67
121. Pu K et al (2014) Semiconducting polymer nanoparticles as photoacoustic molecular imaging probes in living mice. *Nat Nanotechnol* 9:233–239
122. Levi J et al (2013) Molecular photoacoustic imaging of follicular thyroid carcinoma. *Clin Cancer Res* 19:1494–1502
123. Dima A, Ntziachristos V (2012) Non-invasive carotid imaging using optoacoustic tomography. *Opt Express* 20:25044–25057
124. Buehler A, Dean-Ben XL, Claussen J, Ntziachristos V, Razansky D (2012) Three-dimensional optoacoustic tomography at video rate. *Opt Express* 20:22712–22719
125. Dean-Ben XL, Razansky D (2013) Functional optoacoustic human angiography with handheld video rate three dimensional scanner. *Photoacoustics* 1:68–73
126. Fehm TF, Dean-Ben XL, Razansky D (2014) Four dimensional hybrid ultrasound and optoacoustic imaging via passive element optical excitation in a hand-held probe. *Appl Phys Lett* 105:173505
127. Taruttis A et al (2016) Optoacoustic imaging of human vasculature: feasibility by using a handheld probe. *Radiology* 281:256–263
128. Diot G et al (2017) Multispectral optoacoustic tomography (MSOT) of human breast cancer. *Clin Cancer Res* 23:6912–6922
129. Kruger RA, Lam RB, Reinecke DR, Del Rio SP, Doyle RP (2010) Photoacoustic angiography of the breast. *Med Phys* 37:6096–6100
130. Manohar S, Kharine A, van Hespden JC, Steenbergen W, van Leeuwen TG (2004) Photoacoustic mammography laboratory prototype: imaging of breast tissue phantoms. *J Biomed Opt* 9:1172–1181
131. Ermilov SA et al (2009) Laser optoacoustic imaging system for detection of breast cancer. *J Biomed Opt* 14:024007
132. Valluru KS, Wilson KE, Willmann JK (2016) Photoacoustic imaging in oncology: translational preclinical and early clinical experience. *Radiology* 280:332–349
133. Heijblom M et al (2015) Photoacoustic image patterns of breast carcinoma and comparisons with magnetic resonance imaging and vascular stained histopathology. *Sci Rep* 5:11778
134. Ford SJ et al (2016) Structural and functional analysis of intact hair follicles and pilosebaceous units by volumetric multispectral optoacoustic tomography. *J Invest Dermatol* 136:753–761
135. Aguirre J et al (2017) Precision assessment of label-free psoriasis biomarkers with ultra-broadband optoacoustic mesoscopy. *Nat Biomed Eng* 1:0068
136. Jaffer FA et al (2011) Two-dimensional intravascular near-infrared fluorescence molecular imaging of inflammation in atherosclerosis and stent-induced vascular injury. *J Am Coll Cardiol* 57:2516–2526



Multifunctional Magnetic Resonance Imaging Probes

6

Philipp Biegger, Mark E. Ladd, and Dorde Komljenovic

Contents

6.1	The Role of Non-invasive Imaging Methods in Oncology.....	190
6.2	Magnetic Resonance Imaging of Cancer—Imaging Techniques and Contrast Agents.....	190
6.2.1	Intrinsic Contrasts in MR Imaging— $T_1/T_2/T_2^*$	191
6.2.2	Contrast Agents in MRI.....	192
6.2.3	CEST MRI.....	193
6.3	Multifunctional Imaging Probes.....	194
6.3.1	Inorganic Nanoparticles.....	194
6.3.2	Other Materials for Imaging Probe Design.....	210
6.3.3	Multifunctional Probes for ^{19}F MRI.....	211
6.3.4	CEST Probes.....	213
6.4	Theranostics.....	215
6.5	Novel Imaging Approaches.....	217
6.5.1	Magnetic Particle Imaging (MPI).....	217
6.5.2	Hyperpolarized Multifunctional MRI Probes.....	219
6.6	Outlook.....	220
	References.....	221

P. Biegger · M. E. Ladd · D. Komljenovic (✉)
Medical Physics in Radiology, German Cancer Research Center (DKFZ), Heidelberg, Germany
e-mail: d.komljenovic@dkfz.de

M. E. Ladd
Faculty of Medicine, University of Heidelberg, Heidelberg, Germany
Faculty of Physics and Astronomy, University of Heidelberg, Heidelberg, Germany

6.1 The Role of Non-invasive Imaging Methods in Oncology

Early diagnosis is crucial for the management of cancer patients. Refinement of existing therapeutic options and the rapid development and translation of novel options in clinical oncology has in recent years favorably led to the prolonged median survival time in patients suffering from different cancer entities, including some of those most prevalent such as breast and lung cancer. These treatment options include surgery, chemotherapy, radiation therapy, immunotherapy, hormone therapy, or targeted radionuclide therapy and which treatment option will be used is dependent on many factors, including the stage of the disease at the time of diagnosis. Imaging is among the most important tools, if not *the* most important, in the management of cancer and improvement of the quality of life of cancer patients. It enables, for example, the selection and commencement of the therapy most suitable for the current stage of the disease. The portfolio of imaging techniques in clinical settings nowadays includes MR imaging, ultrasonography (US), computed tomography (CT), and X-ray radiography as well as the nuclear medicine functional imaging methods positron emission tomography (PET) and single-photon emission computed tomography (SPECT). Multimodal imaging aims to benefit from the synergistic information available from combined multiple modalities. Such a complementary approach unifies modalities that enable excellent anatomical details with those offering superb sensitivity for the detection of minute quantities of cancerous material. In preclinical settings, an abundance of probes has been suggested that provide sophisticated platforms to not only unify different imaging tags but also enable drug delivery. Clinical transfer of such platforms is often challenged by insufficiently resolved biocompatibility concerns or the lack of capability to target structures of interest at a level that enables the acquisition of an adequate imaging signal. The following sections will be focused on MR as one of the methods at the forefront of biomedical imaging as well as on possibilities to add functionalities to probes applicable in MR imaging.

6.2 Magnetic Resonance Imaging of Cancer—Imaging Techniques and Contrast Agents

The imaging techniques nowadays applied in clinical settings differ not only in their basic physical principles but also in sensitivity, capability to assess tissue morphology, overall costs, or exposition of patients to harmful noxae such as ionizing radiation. How does MR imaging compare to the other most common imaging modalities? MR imaging is a tomographic technique enabling excellent soft-tissue contrast and detailed anatomical and physiological/functional readouts devoid of ionizing radiation but bound with considerable costs [85]. On the other hand, the sensitivity achievable by MR imaging is inferior to PET in depicting minute tracer quantities. In recent years, changes in the regulation of some broadly applied and

well-researched gadolinium-based MR contrast agents have been witnessed, resulting in recommendations for either the replacement of such agents or narrowing of their indication windows. Nevertheless, the significance of MR imaging in patient care is reflected by the rapid and steady increase in the number of MR scanners worldwide. Since the first commercial MR imaging system was introduced in the early 1980s [22] recent reports point to more than 30,000 installed MR scanners worldwide [33].

6.2.1 Intrinsic Contrasts in MR Imaging— $T_1/T_2/T_2^*$

Many nuclei in the human body possess a magnetic moment including ^1H , ^{17}O , ^{19}F , or ^{23}Na ; however, the vast majority of MR imaging applications nowadays are based on the signal coming from the nuclei of hydrogen atoms (^1H), which have a high natural abundance. In a strong external magnetic field (B_0), slightly more magnetic moments align parallel to B_0 (as this state of alignment requires the least energy), thus producing net macroscopic longitudinal magnetization [17]. In B_0 , magnetic moments not only align with the field but also undergo precession about the field at a speed proportional to the strength of the applied strong external magnetic field (Larmor or precessional frequency). When a radiofrequency (RF) pulse of the same frequency as the Larmor frequency is introduced into a spin system, the absorption of energy and accordingly the excitation of the spin system occur. If the RF pulse is strong enough, it tips the magnetization vector by 90° causing the longitudinal magnetization to rotate to become transverse magnetization [107].

When the RF is shut off, the spin system returns to a lower energy state by emitting an amount of energy equal to the amount of energy absorbed. This return is referred to as relaxation. During relaxation, recovery of the longitudinal magnetization occurs exponentially, the rate of which is defined by the time constant T_1 , whereby T_1 is the time needed to recover 63% of the longitudinal magnetization. Simultaneously, transverse component magnetization relaxation occurs, governed by the time constant T_2 , which is the time taken for 63% of the transverse component magnetization to diminish [55]. T_2^* relaxation describes the effects resulting from the combination of T_2 relaxation and the de-phasing that results from inhomogeneity in B_0 ; thus, $T_2^* \leq T_2$.

Different molecules exhibit different efficiency at T_1 relaxation, e.g., free water has relatively long T_1 relaxation times. The T_1 value of bound or structured water is less than free water (ca. 400–800 vs. 4000 ms). Short T_1 values are characteristic of fat tissue, partly because of carbon bonds at the ends of the fatty acids having frequencies near the Larmor frequency, which allows effective energy transfer [17]. Free water such as cerebrospinal fluid is also characterized by longer T_2 values (appearing brighter on T_2 -weighted images) compared with water-based tissues with larger macromolecular content, such as grey matter.

6.2.2 Contrast Agents in MRI

Contrast achievable by MR imaging can be significantly improved by the application of extrinsic agents. Contrary to, e.g., computed tomography or ultrasound, extrinsic MR imaging agents are not directly visualized—the signal rather comes from the magnetic effect of such agents on the MR-active nuclei in the tissue of interest. Uptake of the given contrast agent can differ largely between diseased and healthy tissues, also due to changes in the metabolic parameters on the cellular level. The majority of applied MR contrast agents change the relaxation times of surrounding protons. Positive contrast agents predominantly shorten the T_1 , negative agents the T_2 relaxation time. Since the early 1980s, there has been rapid development of novel MRI contrast agents. This has resulted in various agent classifications that are based on different properties including magnetic behavior or chemical structure, e.g., paramagnetic/superparamagnetic agents.

6.2.2.1 Gadolinium Agents

Gadolinium is a rare earth metal with seven unpaired electrons in the 4f subshell, making it applicable as a paramagnetic agent. Gadolinium may not be applied as a free ion due to its toxicity and accumulation in organs such as the liver and thus requires the use of a chelating agent (chelated complex substances). Chelates must fulfill numerous stability and safety requirements in order to limit the release of free gadolinium ions to the very minimum. Studies published in recent years report the increased signal intensity on T_1 -weighted images after serial application of the linear gadolinium-based contrast agent gadopentetate dimeglumine in the human body, e.g., in the nucleus dentatus and globus pallidus of the brain [75]. Although the clinical implications of these notions remain unclear, the responsible regulatory body at the EU level, the European Medicines Agency (EMA), recommended in 2017 restrictions and suspensions for certain intravenous linear agents in order to prevent any potential health risks. In summary, the intravenous linear agents gadoxetic acid and gadobenic acid can continue to be used for liver imaging because they are taken up in the liver and meet an important diagnostic need; likewise, gadopentetic acid can continue to be used for joint scans utilizing the intra-articular route, which are distinguished by the very low dose of gadolinium used. EU-wide suspension of all other intravenously applied linear compounds (gadodiamide, gadopentetic acid, and gadoversetamide) was recommended. Macrocyclic gadolinium-containing agents (gadobutrol, gadoteric acid, and gadoteridol) are currently considered to have a lower propensity to release gadolinium than linear agents and can continue to be used for their current indications; however, they should be utilized in the lowest doses that sufficiently enhance images and only when unenhanced scans are not sufficient [23].

6.2.2.2 Iron Oxide Particles

For the use of iron oxide (IO) nanoparticles in a variety of biomedical applications, biocompatibility and a sufficiently large magnetic moment are necessary [89]. IO nanoparticles are often classified as ultra-small superparamagnetic IO (USPIO);

average diameter <50 nm), superparamagnetic IO (SPIO; average diameter between 50 nm and 1 μm), or MPIO (micron-sized particles of iron oxide, average diameter >1 μm). Iron oxide-containing superparamagnetic agents come in the form of colloids made up of particles (5–200 nm) in suspension that are composed of small crystallites (1–10 nm) containing several thousand magnetic ions [27]. These induce strong magnetic field inhomogeneities and significantly decrease T_2 relaxation times, enabling the visualization of a small number of cells. For in vivo applications, usually magnetite Fe_3O_4 and maghemite $\gamma\text{-Fe}_2\text{O}_3$ are used due to their stability and favorable toxicity profile [24]. However, due to naturally occurring aggregation, iron oxide particles need to be stabilized before in vivo application, e.g., by employing a polymer coating such as dextran or polyethylenglycol. Apart from the signal alteration in T_2 -weighted images, iron oxide particles are also used for hyperthermia applications and magnet-mediated drug delivery. Thermoresponsive, polymer-coated $\gamma\text{-Fe}_2\text{O}_3$ particles loaded with the anti-cancer drug doxorubicin were shown to successfully release the drug under magnetic hyperthermia conditions in vitro [74].

6.2.2.3 Manganese-Based Contrast Agents

The non-lanthanide metal manganese carries in its bivalent state five unpaired electrons and is applicable as a paramagnetic contrast material in MR imaging. Similar to other paramagnetic ions (e.g., Gd^{3+} or Cu^{2+}), manganese ions (Mn^{2+}) shorten the T_1 relaxation time of water protons, which results in a hyperintense signal on T_1 -weighted images [70] (also see Sect. 6.3.1.2). Although possessing good properties for use as imaging contrast agents, the applicability of manganese ion-based compounds as such is still linked to substantial risks due to the fact that manganese ions play an important role in biological processes, e.g., in the metabolism of lipids or proteins. These ions are known to be transported anterogradely in axonal tracts and may influence synaptic transmission, rendering them potentially harmful for eventual in vivo applications, as unwanted effects on biological processes cannot be excluded [26].

6.2.3 CEST MRI

The concept of Chemical Exchange Saturation Transfer (CEST) [105] is an emerging tool within the molecular imaging community well suited for the detection of low-concentration probes based on the rapid exchange between protons in the probes and bulk water. Solute protons on either an exogenous agent or endogenous molecule are saturated at their specific resonance frequency in the proton spectrum, and this saturation is transferred to water through chemical exchange of the excited metabolite protons with non-excited water protons. This leads to a decrease in the water signal that is detectable by standard MR acquisition methods, providing an indirect measure of the concentration of the substance of interest [64, 108]. The preceding decade was marked by a rapid development of endogenous and exogenous probes that contain suitable protons (see Sect. 6.3.4).

6.3 Multifunctional Imaging Probes

The development of new imaging probes is crucial for the improvement of cancer diagnosis, treatment planning, and therapy monitoring. Combining different functionalities within one probe allows their application in several imaging techniques and enables, therefore, a more precise diagnosis by giving insights in different regions of interest. In principle, there are two different possibilities for the construction of multifunctional probes, namely inorganic-based materials such as metal or metal compounds, amorphous silica, or carbogenic graphene, or they can be composed of organic materials such as polymeric nanospheres or nanocapsules, dendrimers, or lipids forming liposomes or micelles (Fig. 6.1). Obviously, there are also hybrid materials combining different types of materials in all kinds of architecture. All of these structures allow conjugation of the components by covalent binding or by physical encapsulation. While covalent binding does not allow burst release, it shows poor loading efficiency as well as inhomogeneous distribution within the nanoparticle matrix. In contrast, physical encapsulation shows the exact opposite: high loading capacity and homogeneous matrix distribution but potential risk of burst release [86]. A more detailed picture will be given in the next sections, where recent advances in the field of multifunctional imaging probes are described.

6.3.1 Inorganic Nanoparticles

Most of the recent developments in multifunctional imaging probes are based on inorganic nanoparticles due to their specific physical and chemical properties, which can be controlled through their nanoscale size [39]. In addition, easy surface functionalization enables modification with a broad range of different molecules,

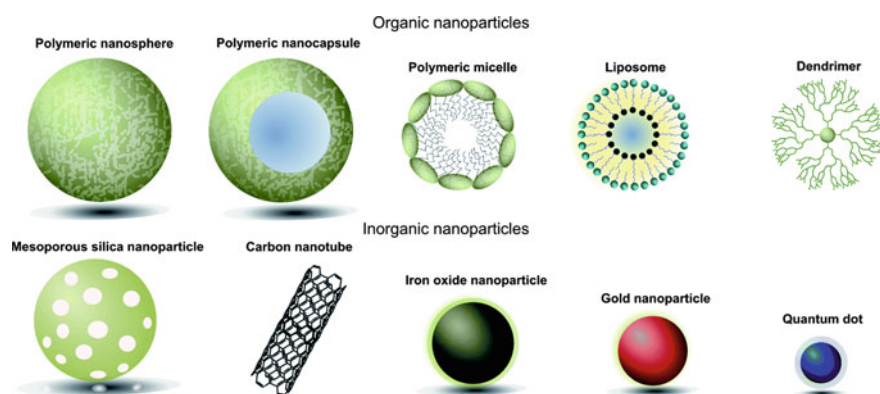


Fig. 6.1 Structural designs of different types of nanoparticles on the basis of organic or inorganic materials. Reprinted with permission from [78]. Published by The Royal Society of Chemistry

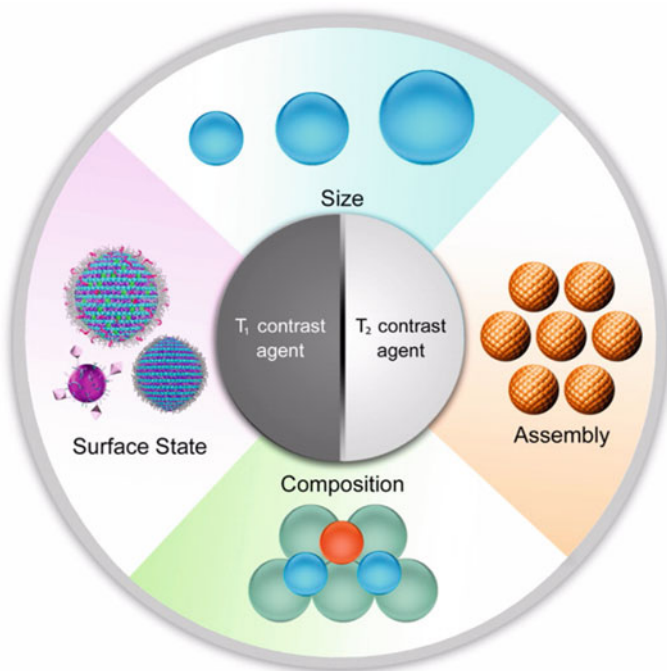


Fig. 6.2 Structure of magnetic nanoparticles. The molecular structure of magnetic nanoparticles determines their MR contrast properties. Reprinted with permission from [49]. Copyright 2015 American Chemical Society

allowing the combination of several functionalities in one probe. These constructs also show longer blood circulation times and more specific biodistribution compared to small molecule-based contrast agents currently used in clinics [41]. Especially iron oxide-based nanoparticles have attracted the interest of the scientific community since they show great diversity in tuning their size-dependent magnetic properties from nearly paramagnetic to ferromagnetic [39], opening a wide spectrum of applications either as positive T_1 or negative T_2 contrast agents (Fig. 6.2).

Also lanthanide-based nanostructures are of high interest due to their paramagnetic properties, leading to strong contrast enhancement effects. Additionally, their magnetization does not saturate with field strengths above 1.5 T. This is particularly interesting, as new instruments operating at fields of 7 T and higher are currently being investigated in preclinical research [6]. To circumvent potential toxic side effects of the imaging probes, silica-based nanospheres are often used due to their chemical stability and lower cytotoxicity, thus exhibiting high biocompatibility. In addition, their surfaces can be easily functionalized with various functional groups [58]. Therefore, this material is mainly applied in hybrid nanocomposite engineering as a protecting agent for the combined compounds [98].

With their intrinsic multifunctional optical and magnetic properties, semi-conducting carbon nanotubes (CNTs) and other related graphene structures have also been the subject of current research. However, potential long-term toxic effects of these materials still remain unclear [28]. Only CNTs with proper surface coating such as PEGylation have been shown to be excreted through biliary and renal pathways [44, 60].

In the next sections, more detail will be presented on the recent literature about the development and application of iron oxide-based nanostructural imaging probes, lanthanide and other metal-based nanomaterials, silica-based nanoparticles, and nanostructures on the basis of graphitic carbon.

6.3.1.1 (Ultrasmall) Superparamagnetic Iron Oxide (U)SPIO Nanoparticles

Most of the recent literature related to multifunctional imaging probes describes the synthesis of (ultrasmall) superparamagnetic iron oxide (U)SPIO-based nanoconstructs and their use in multimodal imaging applications. However, this fact is not surprising, as iron oxide nanoparticles show higher intrinsic signal sensitivity compared to macrocyclic gadolinium complexes, as well as good biocompatibility due to the biological role of iron in living organisms [62, 104]. Typically, these probes are composed of an iron oxide nanoparticle core of magnetite Fe_3O_4 and/or maghemite $\gamma\text{-Fe}_2\text{O}_3$ coated with a hydrophilic coating facilitating water solubility [92].

Often these coatings are polymeric, which can either embed small molecules such as organic dyes or be easily functionalized through covalent bonding with a large variety of (bio)molecules, generating multifunctionality regarding imaging as well as therapeutic and targeting applications (Fig. 6.3). Yang et al. developed such magnetic nanoparticles coated with biocompatible and biodegradable folate bearing a poly(succinimide) cross-linkable graft copolymer showing high *in vivo* stability [112]. The polymer coating was covalently functionalized with standard Cy5.5 fluorescent dyes to enable dual optical/magnetic resonance imaging. These probes showed high T_2 relaxivity coefficients (r_2) and were accumulated abundantly in folate receptor-positive KB cells in mouse models. Another approach was reported by Zhu et al. using a polymer-SPIO core coated with polymerized europium complexes for magnetic resonance and optical imaging [125]. Zhang et al. extended this strategy and combined two lanthanide (Gd^{3+} and Eu^{3+}) complexes for surface polymerization of the SPIO core nanoparticles [121]. These magnetic microspheres showed signal enhancement in both T_1 - and T_2 -weighted MRI through a combination of positive contrast gadolinium and negative contrast iron ions as well as fluorescence luminescence from Eu^{3+} suitable for optical imaging. Utilizing the physical properties of different metal ions was also achieved through the encapsulation of SPIO nanoparticles together with infrared emitting lead(II) sulfide (PbS) quantum dots in an FDA-approved polymeric poly(lactic-co-glycolic-acid) (PLGA) matrix [69]. This magnetic-fluorescent hybrid nanostructure could overcome the classical tissue penetration limits of optical imaging due to the luminescence of PbS being located in the second biological window [83] (1000–1350 nm), enabling subcutaneous imaging studies via OI as shown *in vivo* in living mice in combination with MRI (Fig. 6.4).

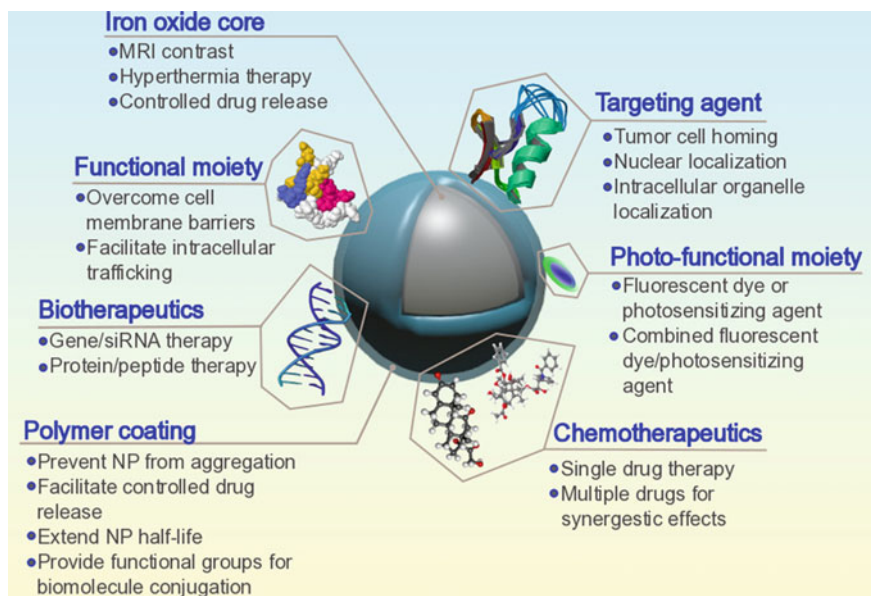


Fig. 6.3 General architecture of multifunctional iron oxide-based nanoprobes. Surface functionalization allows incorporation of additional functionalities into MRI probes such as therapeutics, targeting agents, or contrast agents for other modalities. Reprinted with permission from [77]. Copyright 2015. Published by Elsevier Ltd

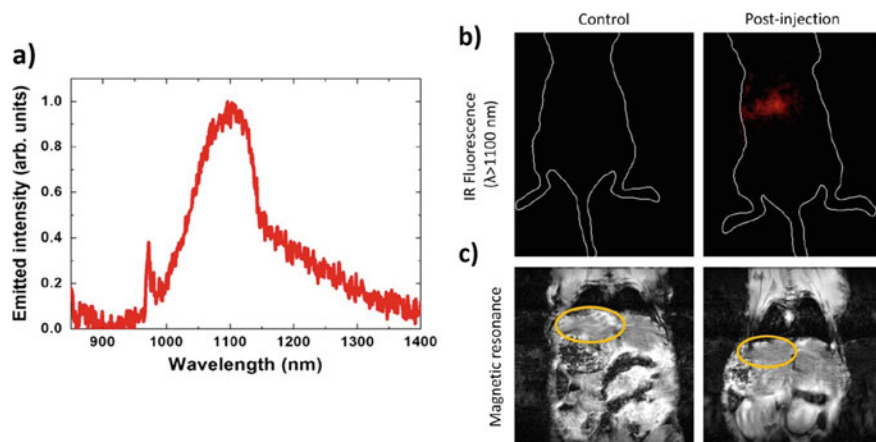


Fig. 6.4 Development of SPIO/PbS quantum dot hybrid nanostructure (HNS) for dual-modal OI/MRI. **a** Emission spectrum of the HNS lying in the second biological window. **b** In vivo IR imaging before (Control/left) and after injection (right) of the HNS. Auto-fluorescence was removed using a long-pass filter with a cut-off at 1100 nm. **c** Coronal spin-echo MRI of the same mouse before and after injection. The yellow selections highlight the liver area where fluorescence signal was detected. A darkening of this area demonstrates the capability to utilize HNS for bimodal imaging. Adapted with permission from [69]. Copyright 2016 American Chemical Society

Embedding iron oxide nanoparticles into a dielectric polymer matrix within the core structure protects them from aggregation and likewise enables control of their size and physical properties. The modification of the core polymer surface with biomolecules such as chitosan before further deposition of a gold shell structure prevents direct contact between the SPIO nanoparticles and the Au layer while retaining the magnetic field strength. By using biocompatible and biodegradable materials, these composites show low cytotoxic and hemolytic behavior [103]. Chitosan was not only found to reduce the toxicity of SPIO nanoparticles, it also protects encapsulated cadmium(II) sulfide (CdS) quantum dots in multifunctional magneto-fluorescent hybrid nanocomposite materials from photobleaching [99].

Also, the incorporation of targeting ligands has been reported. Surface functionalization of poly(ethyleneimine)-stabilized SPIO nanoparticles with hyaluronic acid has led to CD44 receptor overexpressing HeLa cells targeting bimodal imaging probes using the iron core as the MRI component and covalently bound fluorescein as the OI probe [51]. Folate receptor targeting SPIO nanoparticles with a fluorescent amphiphilic oligo(*p*-phenyleneethynylene)-PEG coating were synthesized via a facile hydrophobic encapsulation process [115]. In vitro and in vivo experiments demonstrated their suitability as targeted MRI and two-photon optical imaging probes. Another approach made use of alendronic acid (Aln), a bone-targeting bisphosphonate drug that is used in osteoporosis [110]. PLGA-embedded USPIO nanoparticles functionalized with an NIR (near-infrared) dye were postmodified with Aln. These particles showed up to 10-fold higher affinity for synthetic and biogenic hydroxyapatite compared to premodified structures. RGD peptide-functionalized SPIO nanoparticles labeled with ^{125}I have been developed to target integrin $\alpha_v\beta_3$ protein [102]. In vivo studies in a U87MG glioblastoma xenograft model revealed high binding affinity as shown by MR and SPECT imaging. In addition, these nanoparticles could also be used in photothermal therapy, showing good therapeutic efficacy as a theranostic agent. Tea polyphenol as an environmentally friendly ligand was used for the synthesis of multifunctional metal-doped (Mn, Zn) fluorescent SPIO nanoparticles, showing excellent hydrophilicity and protein adsorption resistance due to the catechol-metal coordination interaction [34]. The addition of different metal ions such as manganese and zinc, in this case, qualifies these probes for applications in dual-modal fluorescent/MR imaging.

Lanthanides can be used for the development of intrinsic fluorescent nanoparticles. Multifunctional terbium-doped CeF_3 -coated SPIO nanoparticles showed high water solubility and good biocompatibility [61]. Their surface modification with citric acid allowed covalent bonding of the carboxyl functionalities with folic acid as the targeting ligand. The efficiency of these targeted probes in simultaneous fluorescence imaging/MRI has been shown in vitro in HeLa cells with overexpressed folate receptors. In general, metal-based core/shell structures can be synthesized rather simply by depositing a shell around a core structure. This method has also been applied by Tian et al., who synthesized copper sulfide-coated SPIO nanoparticles that can be used for photothermal therapy as well as dual-modal IR thermal/MR imaging [93]. In vitro and in vivo experiments demonstrated that variation of the copper content allows control of the intensity of the photothermal

effect. The inverse strategy was applied in another approach for the synthesis of dual-functional nanoparticle conjugates targeting human epithelial growth factor receptor 2 (HER2) to deliver oxaliplatin into the target cells [56]. Here, iron pentacarbonyl was decomposed on the surface of gold nanoparticles in the presence of oleic acid and oleylamine, followed by PEGylation of the resulting nanoparticles and conjugation of the anti-HER2 antibody Herceptin (trastuzumab) and oxaliplatin. Active targeting against human gastric cancer cells SC-7901 was verified in cell culture and in subcutaneous xenograft mouse models, where drug release was triggered by pH variation, allowing simultaneous magnetic tracing and HER2-targeted chemotherapy. A third method has been described fusing distinct nanocrystals via solid-state interfaces, where iron oxide nanoparticles have been connected to gold nanoparticles through a platinum spacer (Fig. 6.5), resulting in hybrid heteronanostructures [15]. These multifunctional nanoparticle-based probes were suitable for dual T_1 - and T_2 -weighted MRI combining both positive contrast gadolinium-chelate-coated gold nanoparticles and negative contrast iron oxide particles. In addition, ^{64}Cu labeling of the gold surface was successful, enabling a small-animal PET imaging study.

The development of SPIO/carbon hybrid structures opens up further possibilities for surface functionalization by functional groups such as $-\text{OH}$ or $\text{C}=\text{O}$ or by generating new intrinsic physical properties [95]. Core/shell structures of magnetite/carbon colloidal nanoparticles [100] have been further modified with a silver nanosphere surface and covalent bonding of doxorubicin, creating a bimodal two-photon fluorescence/MR imaging probe in combination with NIR light-triggered drug release [12]. These hybrid nanoparticles have been synthesized through the deposition of silver via the reduction of AgNO_3 with glucose, followed by NIR-induced coupling of doxorubicin to carboxylic groups on the carbogenic surface. Such amorphous graphitic carbon-coated SPIO nanoparticles have also been used as intrinsic multifunctional magnetic and fluorescent core/shell nanoparticles for OI/MRI [95]. These structures can be synthesized in a one-step method and they are non-toxic, highly optically active, and photostable, providing unique excitation-dependent multicolor emission. A multifunctional graphene-based material with various encapsulated particles was reported by Chen et al. [14]. A facile physical approach allowed the one-step synthesis of these hybrid nanomaterials via aerosol-phase graphene encapsulation of unifunctional nanoparticles. The mechanism of this process is assumed to be based on colloidal interactions within the drying microdroplets, showing improved yields at higher pH. Furthermore, a polymer coating was required for slow cargo release of the graphene nanocarriers. A reduced graphene oxide/Au/SPIO hybrid nanomaterial exemplarily showed good contrast enhancement in both MRI and CT.

Silica coating of SPIO nanoparticles is generally recognized as a suitable method to improve their biocompatibility and their stability towards biodegradation since no toxic effects could be shown in many biological systems. In addition, silica can be easily synthesized in various shapes and sizes with mesoporous or dense structures, leading to a wide variety of different properties, together with easily functionalizable high surface areas and large pore volumes [3]. The incorporation of

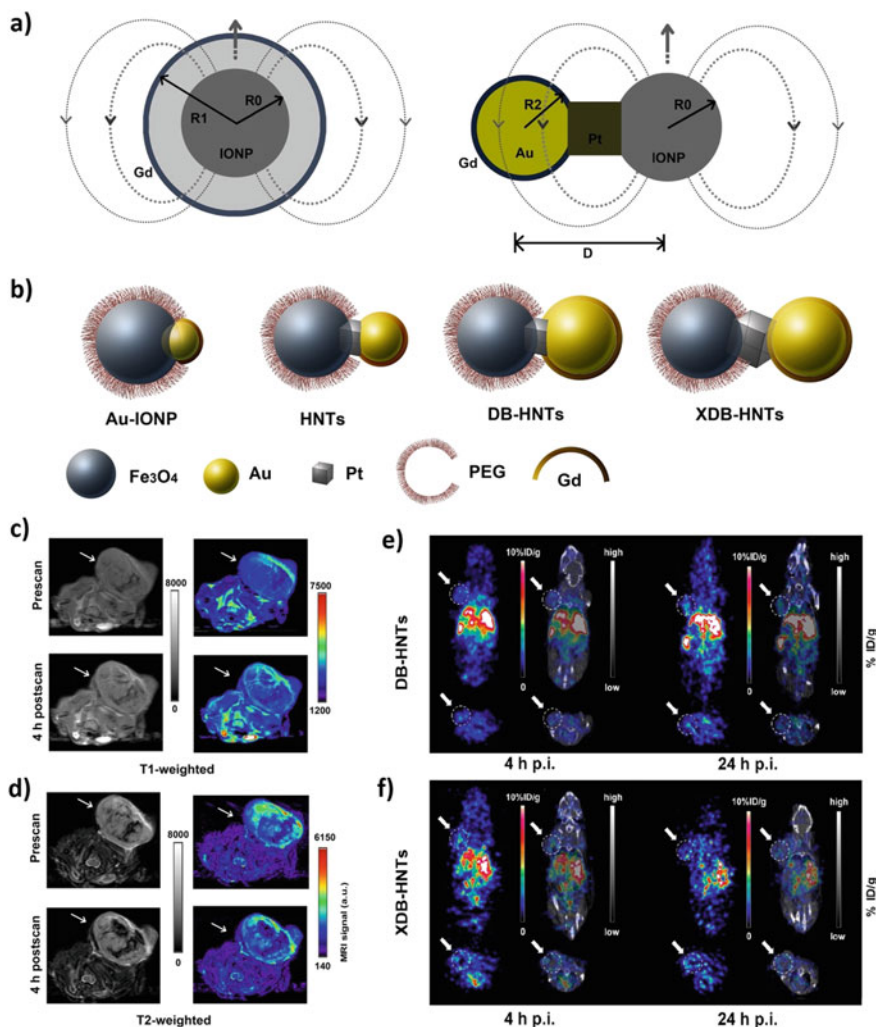


Fig. 6.5 (Extra-large) dumbbell hybrid nanotrimers ((X)DB-HNTs) for T_1/T_2 dual-weighted MRI. **a** Schematic illustration of heterogeneous (left) core/shell nanostructures and (right) dumbbell structures. Engineering of the magnetic coupling of the components is achieved by different architectures. R_0 is the radius of the T_2 contrast agent (iron oxide nanoparticle IONP), R_1 is the radius of the T_1 contrast agent Gd, R_2 is the radius of the gold nanoparticles, and D is the center-to-center distance between the gold and IONP. **b** Four different architectures of the developed dumbbell(-like) heteronanostructures. In vivo **c** T_1 - and **d** T_2 -weighted MRI of a HT-29 tumor-bearing mouse before and 4 h after intravenous injection of Gd-DB-HNTs into the tail-vein with (left) grey-scale and (right) colored images. In vivo small-animal (left) PET and (right) PET/CT images of HT-29 tumor-bearing mouse 4 and 24 h after tail-vein injection of ^{64}Cu -labeled Cu-DB-HNTs (instead of Gd labeling). The arrows indicate the tumor region. Adapted with permission from [15]. Copyright 2014 American Chemical Society. Further permissions related to this material should be directed to the ACS

fluorescein isothiocyanate (FITC) into mesoporous silica-coated SPIO nanoparticles led to fluorescent high-performance MRI probes with a clear core/shell structure that showed improved cell labeling efficiency for neural progenitor cells compared to fluorescent dense silica-coated SPIO nanoparticles [122]. These probes were used for tracking cell migration in vivo with MRI, as mesoporous silica has been shown to improve cellular uptake [57] and thus possesses great potential for future cell imaging contrast agents. Further coating of the mesoporous silica surface with positively charged poly(allylamine hydrochloride) enhanced cellular uptake through electrostatic interactions with the negatively charged surface of cancer cells [52]. These indocyanine green (ICG)-loaded fluorescent mesoporous silica-coated SPIO nanoparticles were suitable for bimodal NIR/MR imaging and showed additional NIR photothermal therapy effects. Cancer cell targeting could also be achieved by covalent surface functionalization of fluorescent mesoporous silica-coated SPIO nanoparticles with biomolecules such as aptamers [106] or peptides [35]. These targeted nanomaterials exhibit good biocompatibility and low cytotoxicity and can be used for simultaneous fluorescence/MR imaging, as shown both in vitro and in vivo.

By using a covalently bound MMP-2 enzyme-responsive peptide as surface coating, the commercially available anti-cancer drug doxorubicin could be encapsulated within the cavities of a mesoporous silica-coated SPIO nanoparticle and delivered to the tumor site through magnet-guided nanocarrier accumulation by applying an external magnetic field (Fig. 6.6) [50]. The enzyme-responsive particles showed high specificity for controlled drug release in cancer cell lines with high MMP-2 enzyme expression as shown both in vitro and in vivo, qualifying these nanoagents for application in MRI-guided cancer chemotherapy. A combined chemo-photothermal treatment platform was achieved through the development of a hybrid nanocarrier system containing a SPIO core and a mesoporous silica shell embedded with carbon dots and the chemotherapeutic agent paclitaxel interacting through supramolecular π -stacking and covered by another silica layer [101]. The SPIO core therein served as the MRI probe, whereas the carbon dots operated both as confocal and two-photon fluorescence imaging probes. Local heating of the carbon dots under NIR irradiation could be used for photothermal therapy and additionally led to the release of paclitaxel to generate a synergistic therapeutic effect.

While most of the SPIO-based multifunctional imaging probes consist of an iron oxide core structure and a functional shell material, there have also been reports about the development of inverse architectures with SPIO nanoparticles located on the outer shell structure. In situ formation of SPIO nanoparticles on the surface of preformed polypyrrole nanoparticles produced multifunctional polypyrrole@Fe₃O₄ nanoparticles, where Fe³⁺ ions are used as oxidizing agents for polymer formation [94]. In vitro and in vivo studies revealed their functionality as contrast agents for MRI, infrared thermal imaging as well as photothermal therapy (PTT). Bimodal superparamagnetic persistent luminescence nanohybrids have been synthesized with a luminescent chromium-doped zinc gallate oxide core suitable for real-time optical imaging and USPIO nanoparticles embedded in a mesoporous silica shell to

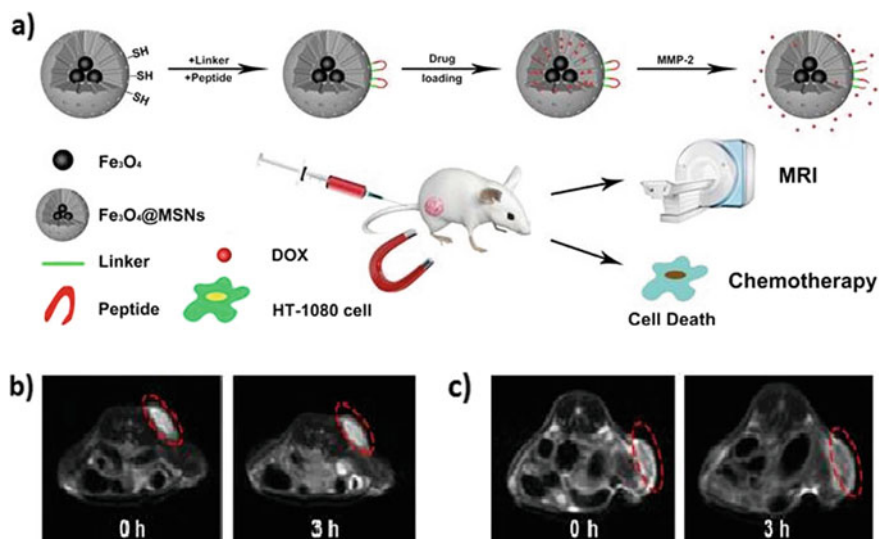


Fig. 6.6 Multifunctional SPIO-encapsulating mesoporous silica nanoparticles, peptide-Fe₃O₄@MSNs/DOX, for enzyme-responsive drug delivery and MRI-guided chemotherapy. **a** Schematic illustration of the probe structure. MSN = mesoporous silica-based nanoplateforms. Peptide = Gly-Gly-Pro-Leu-Gly-Val-Arg-Gly-Lys. DOX = doxorubicin. In vivo T_2 -weighted MRI images of the tumor region in a mouse **b** treated with peptide-Fe₃O₄@MSNs/DOX taken at 0 h and 3 h after injection and **c** treated with peptide-Fe₃O₄@MSNs/DOX and magnet taken at 0 h after injection and after 3 h magnet treatment at the tumor site. The selections show a decrease in signal intensity in the tumor region treated with a magnet for 3 h. Adapted with permission from [50]. Copyright 2018 Ivyspring International Publisher

enable in vivo MRI with high spatial resolution [90]. Additionally, these particles can be maneuvered with an external magnetic field, qualifying them for MRI tracking. Another inverse architecture approach has been achieved through the development of multifunctional polymer-shelled magnetic air-filled microbubbles, where SPIO nanoparticles were either physically or chemically integrated into a poly(vinyl alcohol) shell, generating a dual-modal ultrasound/MRI probe [73]. Neither the physical nor chemical approaches altered the diameter or shell thickness, but embedding the SPIO nanoparticles into the polymeric shell led to reinforcement of the microbubble shell, while covalent bonding caused the loss of connections within the shell structure, leading to softening of the shell. An even more multifunctional synergistic microcarrier platform was described by Zhang et al. consisting of a multicomponent magnetic polymer yolk/shell particle structure, where SPIO nanoparticles are embedded in the outer poly- ϵ -caprolactone shell layer, comprising an interfacing oil layer and a polymeric core [120]. In addition, three fluorescent dyes (Nile blue, acridine yellow, and Sudan red G) with varying hydrophobicities were co-encapsulated (Fig. 6.7). Although this complex structure seems to require a sophisticated synthetic strategy, it could be synthesized via a

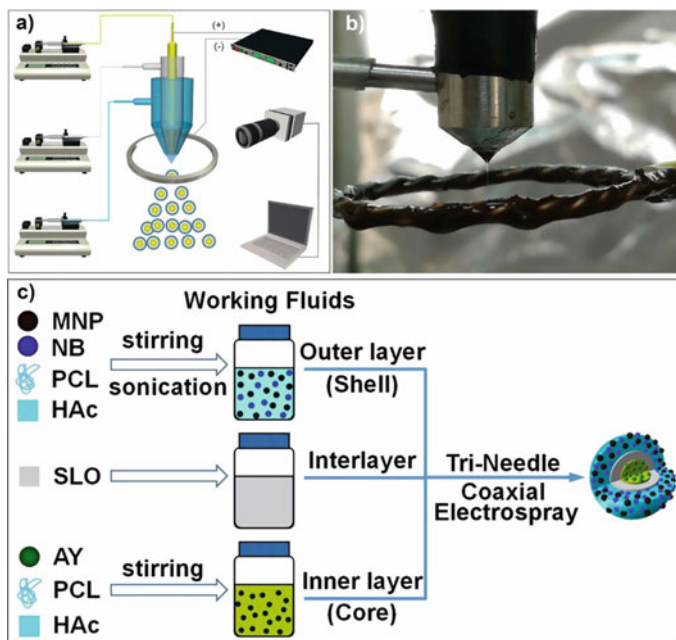


Fig. 6.7 Synthesis of magnetic yolk/shell particles (YSPs) for dual-modal ultrasound/MRI and external auxiliary magnetic field (AMF)-enhanced drug release. **a** Schematic illustration of the applied tri-needle coaxial electrospaying system. **b** Digital image of the tri-needle nozzle assembly showing stable jetting behavior. **c** Schematic illustration of the synthetic procedure for the fabrication of YSPs. MNP = magnetic nanoparticle, NB = Nile Blue, PCL = poly-ε-caprolactone, HAc = glacial acetic acid, SLO = silicone oil, AY = acridine yellow. Adapted with permission from [120]. Copyright 2017 American Chemical Society

facile tri-needle coaxial electrospaying process. In vitro dual-modal ultrasound/MRI and external auxiliary magnetic field (AMF)-enhanced drug release demonstrated its functionality as a theranostic agent.

6.3.1.2 Other Metal-Oxygen Compounds

Besides iron, there are also other metals forming oxides that are potentially interesting as imaging contrast agents. Manganese-based nanoparticles represent another class of probes for MRI with positive contrast properties by increasing the signal intensity of T_1 -weighted MR images. Manganese has a high spin number in its bivalent state due to five unpaired electrons, leading to a mechanism for contrast enhancement similar to other paramagnetic ions such as Gd^{3+} [70]. Synthetic approaches towards manganese oxides resemble those of SPIO nanoparticles. Functionalized magnetic Mn_3O_4 nanoparticles suitable for MRI could be synthesized by thermal decomposition of metal-organic precursors, also applicable for Fe_3O_4 nanoparticles [31]. This method also allowed combination of both manganese and iron ions for the synthesis of $MnFe_2O_4$ nanoparticles. Multifunctional

probes thereof could be generated via conjugation of fluorescent rhodamine B dye and folic acid-targeting folate receptor overexpressing cells onto the amino-functionalized surface. Inclusion of biomolecules can enhance the biocompatibility of such compounds, as was demonstrated in the synthesis of multifunctional polydopamine-coated manganese oxide core/shell nanoparticles [18]. These nanotheranostic agents functionalized with folic acid and loaded with doxorubicin allowed MRI-guided synergetic chemo-/photothermal therapy (PTT) by simultaneous induction of PTT and drug release via NIR laser irradiation, resulting in a synergistic combined treatment effect with higher therapeutic efficacy as demonstrated in both *in vitro* and *in vivo* experiments. The integration of other metal ions was achieved by intrinsic labeling of PEGylated manganese oxide nanoparticles with ^{89}Zr , enabling *in vivo* dual-modality PET/MR imaging and lymph node mapping [119]. Tetravalent manganese was used to develop an intelligent multimodal diagnostic nanoagent modulating the tumor cellular defense mechanism [7]. Cu_{2-x}S was grown on PEGylated MnO_2 nanosheets followed by siRNA modification. After cellular uptake, Mn^{4+} was reduced to Mn^{2+} under acidic conditions in the tumor microenvironment, triggering decomposition of H_2O_2 into O_2 and enhancing the MRI signal, whereas Cu_{2-x}S functioned as a photoacoustic and photothermal imaging agent.

As already mentioned, another very important ion for MRI is the highly paramagnetic Gd^{3+} . Commonly used in single-molecule chelates due to its toxicity as a free ion, gadolinium can also be integrated into inorganic nanoparticulate forms. This was demonstrated by the high-temperature solvothermal synthesis of europium-doped Gd_2O_3 nanoplates [81]. Subsequent surface functionalization with a polyacrylate coating followed by controlled conjugation of folic acid and drug loading with daunorubicin and curcumin led to multimodal fluorescent magnetic nanostructures suitable for efficient targeted and pH-responsive drug delivery with high cytotoxic effects. In addition, hybrid nanostructures have been developed on the basis of gadolinium oxide. Multifunctional $\text{Gd}_2\text{O}_3/\text{Au}$ nanoprobles were synthesized via a mild one-step biomineralization approach using bovine serum albumin as a template structure [87]. The resulting hybrid nanostructures were further functionalized as tumor-targeting probes using RGD peptide and showed good biocompatibility as well as intense NIR fluorescence and satisfactory MRI sensitivity in *in vivo* experiments. Nucleolin-targeting multimodal OI/MRI nanocomposites were synthesized using PEGylated ultra-small Gd_2O_3 conjugated to aptamer AS1411-Ag nanoclusters [53]. Enhanced signal intensity on fluorescence and MR imaging could be achieved with optimized ratios of both components. High yields of ^{89}Zr -labeled chelator-free metal oxide nanostructures could be achieved through strong interaction of oxyphilic $^{89}\text{Zr}^{4+}$ ions with the oxygen atoms on the surface of ten different PEG-coated metal oxide platforms M_xO_y ($\text{M} = \text{Gd}, \text{Ti}, \text{Te}, \text{Eu}, \text{Ta}, \text{Er}, \text{Y}, \text{Yb}, \text{Ce}, \text{or Mo}; x = 1-2; y = 2-5$) [16]. The resulting PET-suitable nanomaterials showed good serum stabilities. Gadolinium oxide-based materials suitable for MRI enabled dual-modal imaging. *In vivo* lymph node mapping was shown to be superior to application of free ^{89}Zr (Fig. 6.8).

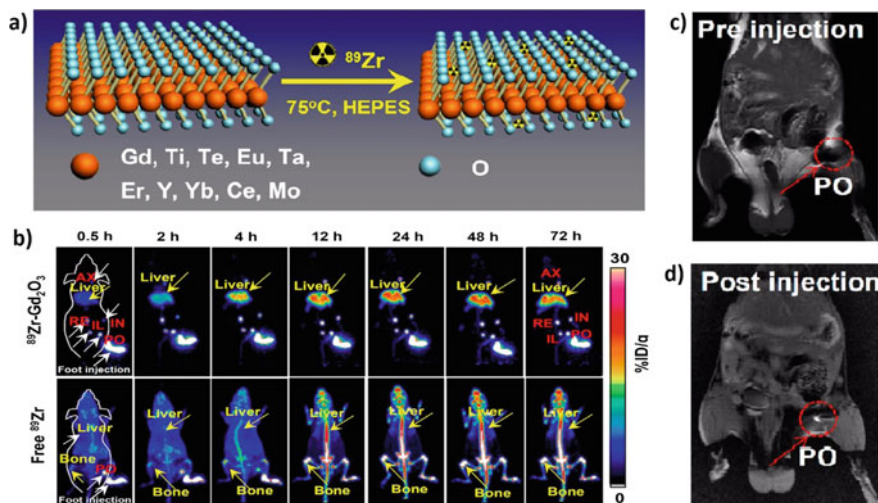


Fig. 6.8 Chelator-free labeling of metal oxide platforms with ^{89}Zr for PET imaging. **a** Schematic illustration of the synthetic procedure. **b** In vivo lymph node (LN) mapping after local injection of ^{89}Zr - Gd_2O_3 -PEG nanorods and free ^{89}Zr imaged with PET. AX = axillary LN, RE = renal LN, IL = iliac LN, IN = inguinal LN, PO = popliteal LN. In vivo LN mapping with T_1 -weighted MRI **c** before and **d** after injection of Gd_2O_3 -PEG nanorods. Adapted with permission from [16]. Copyright 2017 American Chemical Society

Besides gadolinium oxide, gadolinium vanadates GdVO_4 have also been used in MRI applications. The synthetic approaches resemble those of the previously described inorganic nanoparticles, such as simple solvothermal synthesis, accompanied by Eu^{3+} -dotation [68]. It was found that the europium doping level affects luminescence properties, with an optimum at 10%. To enable further conjugation of biologically active molecules, amino-dextran polymer and poly(acrylic acid) were used to modify the surface with either amino or carboxylate functionalities, resulting in different colloidal stabilities. These nanoparticles are also suitable for combined OI/MRI. Other surface functionalization such as amino acids has been shown to result in effective metabolizability and high biocompatibility of $\text{GdVO}_4:\text{Eu}$ [19]. Additionally, these nanophosphors were well suited for trimodal imaging comprising luminescence imaging, MRI, and CT. Abdesselam et al. reported another possible application of the multifunctional $\text{GdVO}_4:\text{Eu}$ nanoparticles as oxidant sensors [1]. Superficial Eu^{3+} is photo-reduced to Eu^{2+} and re-oxidized by oxidants such as H_2O_2 , modulating the luminescence emission. It was further demonstrated that two different synthetic pathways (the so-called “normal” and “citrate” methods) led to particles with varying contrast performances in MRI and reactive oxygen species (ROS) detection. A very important point that has to be thoroughly investigated is the toxicity of both free Gd^{3+} ions as well as VO_4^{3-} ions. As already mentioned, Gd^{3+} is highly toxic, which is due to its ionic radius being similar to that of Ca^{2+} . But also vanadate has been reported to show carcinogenicity with a similar

diameter as phosphate, thus binding to phosphate binding sites for example in signaling pathways [5]. This issue has been taken into account in some designs, and negligible leaching of Gd^{3+} and VO_4^{3-} as shown by complexometric titrations could be demonstrated [1]. Inverse architectural structures have been developed by another synthetic approach using monodisperse $\text{Gd}(\text{OH})\text{CO}_3:\text{Yb}^{3+}/\text{Er}^{3+}$ particles for templated outward growth of lanthanide-doped $\text{GdVO}_4:\text{Ln}$ hollow spheres, which were subsequently filled with poly(acrylic acid) via photo-induced polymerization, followed by loading of the anti-cancer drug doxorubicin [38]. Different lanthanides ($\text{Ln} = \text{Yb}/\text{Er}, \text{Yb}/\text{Ho}, \text{Yb}/\text{Tm}$) were used as dopants, tuning the upconversion cell imaging properties of the spheres by changing the dopant compositions. In addition, the spheres are suitable for MRI as well as pH-dependent drug release of doxorubicin, making use of the lower pH in cancer cells to affect the pH-sensitive polymer core. The utilization of multifunctional poly(L-lysine)-coated europium-doped $\text{NaGd}(\text{MoO}_4)_2$ nanoparticles only required 5% doping level of europium for a maximum luminescence efficiency of dual-modal OI/MRI contrast agents [45]. Interestingly, surface functionalization with poly(L-lysine) caused a significant increase in the magnetic relaxivity value ratio r_2/r_1 , thereby changing the nanoparticles from positive to negative MRI contrast agents. Effective signal enhancement for both MRI and OI was also reported for surface coating of bifunctional europium-doped GdPO_4 nanorods using the biocompatible silk fibroin peptide [20].

6.3.1.3 Other Metal Compounds

Lanthanide doping of transparent Gd^{3+} -based nanoparticles with fluoride as a counter-ion leads to luminescent multimodal upconverting nanoparticles (UCNPs) that combine optical and magnetic properties. They can be used for multimodal upconversion luminescence (UCL) imaging, MRI, and CT due to the highly paramagnetic gadolinium ions and strong X-ray attenuation properties of lanthanides [10]. This trimodal approach has been demonstrated with surface functionalized $\text{BaGdF}_5:\text{Yb}/\text{Tm}$ -based nanoparticles that exhibit a specific core/shell structure for increased UCL intensity [111]. Additionally, a therapeutic component was introduced with a pH-triggered drug carrier module consisting of hydrazine-conjugated doxorubicin that was cleavable in the acidic environment of tumor cells.

Enhancement of the upconversion efficiency could be achieved via incorporation of an intermediate CaF_2 layer functioning as an internal barrier between the core and shell structure of citrate-coated $\text{NaYbF}_4:\text{Tm}@/\text{CaF}_2@/\text{NaDyF}_4$ nanocomposites to reduce cross-relaxation and surface quenching effects [54]. These nanoparticles were used for imaging lymphatic nodes in vivo via trimodal UCL, MRI, and CT. A tetramodal imaging probe was reported by Sun et al., who described citrate-coated lanthanide-based upconversion nanophosphors for tumor angiogenesis imaging [88]. The core structure consisting of $\text{NaLuF}_4:\text{Yb},\text{Tm}$ was surrounded by a ^{153}Sm -doped NaGdF_4 shell suitable for UCL, CT, MRI, and SPECT as demonstrated by in vivo experiments providing detailed information about contrast agent distribution, tumor angiogenesis, and localization as well as 3D anatomical data (Fig. 6.9).

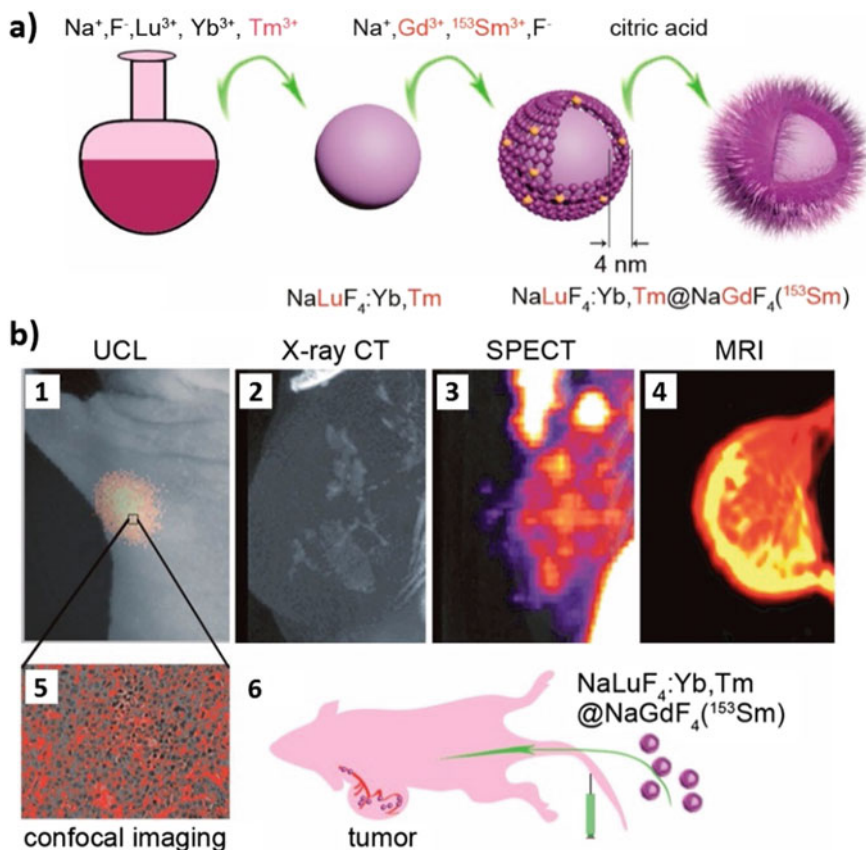


Fig. 6.9 Development of core/shell $\text{NaLuF}_4:\text{Yb}, \text{Tm}@ \text{NaGdF}_4({}^{153}\text{Sm})$ nanocomposites for UCL, CT, SPECT, and MRI. **a** Schematic illustration of the synthetic procedure. **b** In vivo tetramodal imaging of tumor angiogenesis using UCL (1), CT (2), SPECT (3), and MRI (4) one hour after intravenous injection as well as confocal image of the paraffin section of the tumor (5). (6) shows a schematic illustration of the set-up. Adapted with permission from [88]. Copyright 2013 American Chemical Society

Interestingly, UCNP s such as PEG-coated $\text{NaGdF}_4:\text{Dy}$ were also described as high-performance T_1/T_2 dual-weighted MRI and CT imaging probes [36]. This fact was investigated by Yi et al. in more detail for hybrid lanthanide nanoparticles on the basis of BaGdF_5 hosts [114]. It was shown that adjusting the r_1/r_2 value can be achieved by doping the host nanoparticles with Yb^{3+} , Er^{3+} , or Dy^{3+} (Fig. 6.10). Through this method, the T_1 -weighted agent BaGdF_5 can be changed into a dual-weighted T_1/T_2 contrast agent and eventually a single-weighted T_2 contrast agent. For example, $\text{BaGdF}_5:50\% \text{Er}$ was used as a dual-weighted MRI contrast agent in vivo.

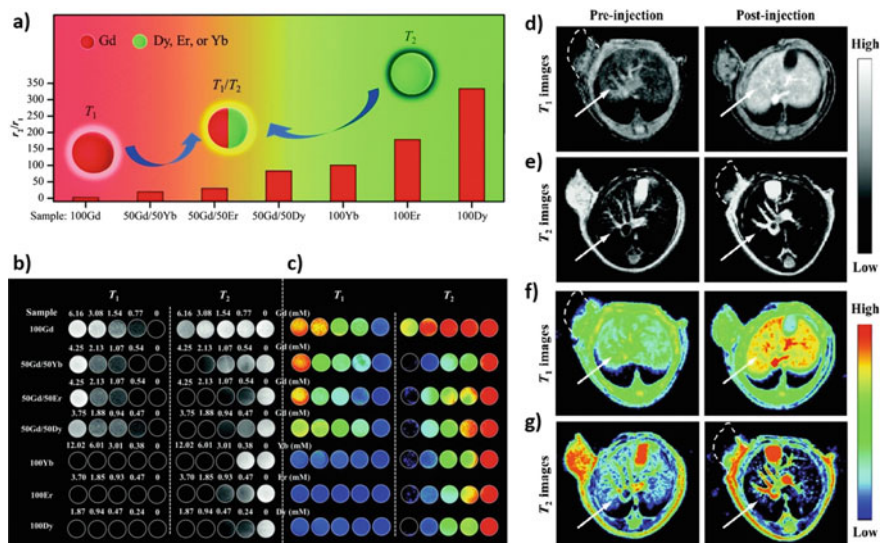


Fig. 6.10 Hybrid lanthanide-based nanoparticles with BaGdF₅ as host for in vivo T_1/T_2 dual-weighted MRI. **a** Variation of dopants (Dy³⁺, Er³⁺ or Yb³⁺) and doping levels result in a change in r_2/r_1 values. **b** In vitro T_1 and T_2 phantom images and **c** their corresponding color images. All phantom images were acquired on a 1.5 T MRI scanner. **d** T_1 - and **e** T_2 -weighted in vivo transverse MRI images of a HeLa cell tumor-bearing mouse before and 3 h after intravenous injection of BaGdF₅:50% Er³⁺ nanoparticles into the tail-vein and **f**, **g** the corresponding color images. The arrows point to the liver region and the dashed circles highlight the tumor area, both showing high contrast effects. All in vivo images were acquired on a 1.0 T MRI scanner. Adapted from [114] with permission from The Royal Society of Chemistry

Glioblastoma-targeting UCNP were developed using lactoferrin and chlorotoxin-functionalized multifunctional SiO₂-coated core/shell NaGdF₄:Yb,Er, Li@NaGdF₄ nanocomposites, suitable for dual-modal imaging [113]. These biocompatible nanoparticles permeated the blood–brain barrier via receptor-mediated transcytosis and bound to glioma, showing strong upconversion luminescence and MRI contrast as demonstrated in rat glioma xenograft model. Taking advantage of the non-toxic properties of silica, mesoporous silica nanoparticles were used as a pH-sensitive drug delivery platform, where doxorubicin was loaded into the pores, which were then locked by ultra-small lanthanide-based NaGdF₄:Yb/Tm@NaGdF₄ UCNP via acid-labile acetal conjugation on the silica surface [13]. In vitro and in vivo experiments showed high efficiency for drug release, and passive accumulation of the probes in the tumor region through the enhanced permeability and retention (EPR) effect was verified with MRI.

Other approaches using various types of iron compounds have been described. Ultra-small bovine serum albumin-coated gallic acid-Fe(III) nanoparticles were self-assembled by means of paclitaxel via the hydrophobic effect, enhancing the MRI performance and tumor accumulation in comparison to the individual

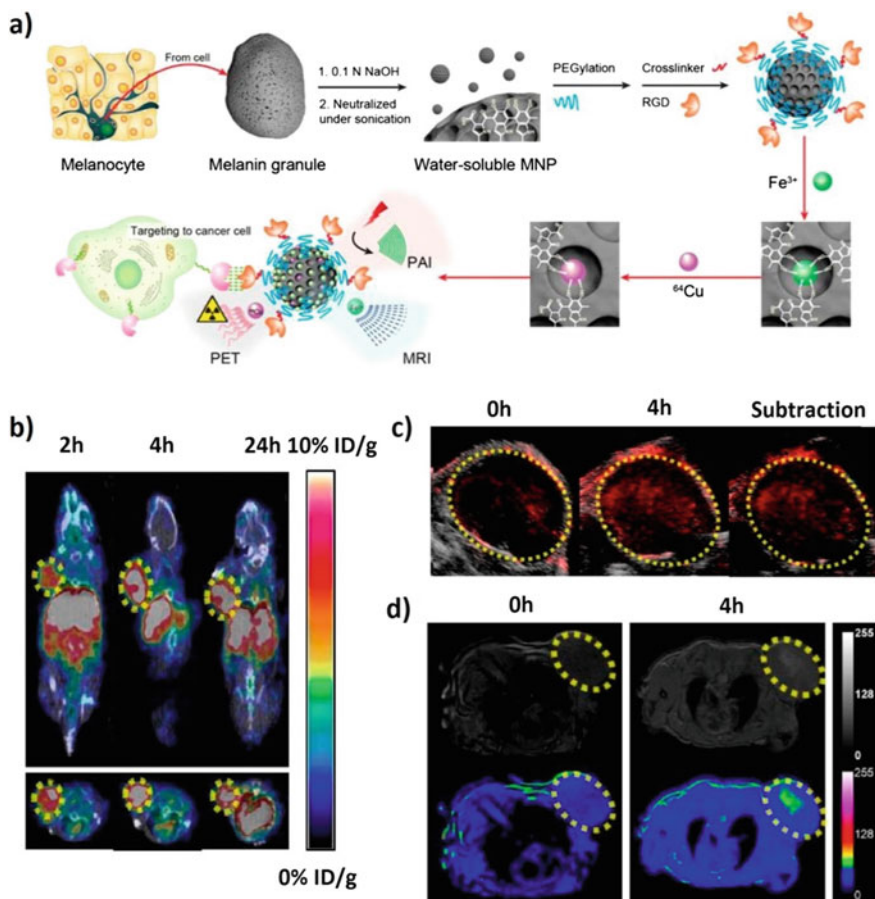


Fig. 6.11 Development of functionalized melanin nanoparticles (MNPs) for PET/PAI/MRI multimodal imaging. **a** Schematic illustration of the synthetic procedure of ^{64}Cu -Fe-RGD-PEG-MNP. In vivo imaging of U87MG tumor-bearing mice with **b** ultrasound (grey) and PAI (red) before (0 h) and 4 h after tail-vein injection of ^{64}Cu -Fe-RGD-PEG-MNP as well as the corresponding subtraction image. **c** Combined small-animal CT (grey) and PET (color) imaging of coronal (top) and transaxial (bottom) cross-section 2, 4, and 24 h after tail-vein injection of ^{64}Cu -Fe-RGD-PEG-MNP and Fe-RGD-PEG-MNP. **d** Grey-scale (top) and corresponding color-scale (bottom) MRI images before and 4 h after tail-vein injection of ^{64}Cu -Fe-RGD-PEG-MNP and Fe-RGD-PEG-MNP. The yellow circle highlights the tumor area. Adapted with permission from [25]. Copyright 2014 American Chemical Society. Further permissions related to this material should be directed to the ACS

nanoparticles [2]. In addition, the particles allowed combined chemo- and photothermal therapy for improved therapeutic efficiency. Another targeted platform for MRI- and photoacoustic imaging (PAI)-guided PTT was reported using Hägg iron carbide Fe_5C_2 nanoparticles as magnetic core structures and carbon coating for NIR absorbance and conversion, thereby enabling PAI and PTT [116]. These probes were functionalized with the targeted affibody $Z_{\text{HER2}:342}$, generating multifunctional theranostic agents.

6.3.2 Other Materials for Imaging Probe Design

Due to their high surface functionality and good biocompatibility [3, 40], amorphous silica is often used as a coating material to reduce the toxicity of nanoparticles and enable further modification [58, 98]. Silica nanoparticles can thus function as a platform for surface functionalization, generating multifunctional probes by combining different entities. For example, nonporous silica nanoparticles have been coated with gadolinium complexes, fluorescein or Cy5.5 fluorophores, and cell-penetrating peptides to generate multifunctional OI/MRI probes [37]. Interestingly, *in vitro* experiments revealed fast cellular uptake of the particles, but also the formation of large extracellular agglomerates in biological environments, hindering internalization by cultured cells *in vivo* and leading to persistent accumulation in the lung, the liver, and to a lesser extent in the spleen. Only very few reports about the use of such small-molecule-based gadolinium-chelating MRI contrast agents have been published in recent years. This is probably due to the fact that gadolinium deposition in the human body has been associated with the administration of such gadolinium-based contrast agents [79], provoking intense discussions about the usage of these contrast agents and leading to some FDA- and EMA-approved contrast agents being restricted. While commercially available gadolinium-based contrast agent chelators mainly consist of ethylene-bridged amines functionalized with acetic acids, the fluorescent macrocycle porphyrine was used by Yuzhakova et al. to chelate Gd^{3+} to combine optical and magnetic properties in one molecule, thereby allowing MR/fluorescence imaging [117]. Furthermore, the aromatic macrocycle can be used as a photosensitizer for photodynamic therapy (PDT). Selective accumulation in the tumor area was demonstrated by *in vivo* imaging measurements that showed higher fluorescence signal and MRI contrast enhancement compared to the surrounding tissue.

The use of biomolecules as a platform for the development of functional materials offers several advantages such as biocompatibility, bioregenerativity, and biodegradability. Natural melanin-based nanoparticles were used as the basis of multimodal imaging probes [25]. The melanin nanoparticles showed native photoacoustic signals and strong binding affinity to metal ions such as $^{64}\text{Cu}^{2+}$ and Fe^{3+} , enabling combined PET and MRI (Fig. 6.11). Here, iron was used instead of gadolinium due to the high toxicity of the latter. Further modification with $\alpha_v\beta_3$ integrin-binding cyclic RGD peptide allowed selective tumor targeting as shown by *in vivo* experiments.

Another approach made use of pepino mosaic virus, which was functionalized at the cysteine side chains via Michael addition and reaction of thiol-selective probes [48]. Gd-DOTA was conjugated to lysine side chains, and fluorescent Oregon green 288 dyes as well as biotin tags were coupled to cysteines. The resulting nanofilament was suitable for OI/MRI and showed significantly enhanced MRI contrast and good fluorescence signals.

6.3.3 Multifunctional Probes for ^{19}F MRI

A promising alternative to conventional ^1H MRI is the emerging field of ^{19}F MRI. The only existing natural isotope fluorine-19 has a very low biological background concentration, thus providing good signal-to-noise ratio and high sensitivity for exogenous contrast agents, which might be useful to overcome sensitivity problems of conventional MRI techniques [47, 97]. Perfluorocarbons (PFCs) are often used as ^{19}F MRI contrast agents, which are chemically and metabolically stable due to their inertness. Because of their low solubility in aqueous solutions, which decreases with increasing number of fluorine atoms, PFCs need to be encapsulated within a lipid shell to form a micelle [96]. PFC nanoemulsions allow a wide variety of possible applications enabled through functionalization of the lipid surface with different entities such as MRI probes, fluorophores, radionuclides, or drugs. Additionally, these contrast agents can also be designed to target molecular processes on tumor cells.

A simple encapsulation process yielded ICG/perfluoro-15-crown-5-ether (PFCE) nanoemulsions formed by a PEGylated phosphatidylcholine cholesterol lipid capsule [4]. This bimodal PFC-based contrast agent exhibited less aggregation of the cyanine dye, thus leading to increased fluorescence intensity and higher in vitro and in vivo as well as physicochemical stability compared to free aqueous ICG. The suitability of this probe was efficiently demonstrated through in vivo sentinel lymph node mapping using simultaneous NIR OI and ^{19}F MRI (Fig. 6.12).

A new methodology to build up ^{19}F MRI probes has been described by Matsushita et al. that allows more facile surface modification [63]. Core/shell silica nanoparticles consisting of a centered micelle formed by phospholipids and filled with liquid PFCE and a robust surrounding silica shell showed good biocompatibility, sufficient in vivo stability, and high sensitivity in ^{19}F MRI. To enable the structuring of the silica shell, a novel surfactant was developed, which consists of a lipophilic alkyl part interacting with the phospholipid layer and a basic pyridinyl group to initiate the sol-gel process of silica polymerization. In addition, the surface could be easily modified with rhodamine B dye and PEG, allowing fluorescence imaging and tumor tissue detection in living mice.

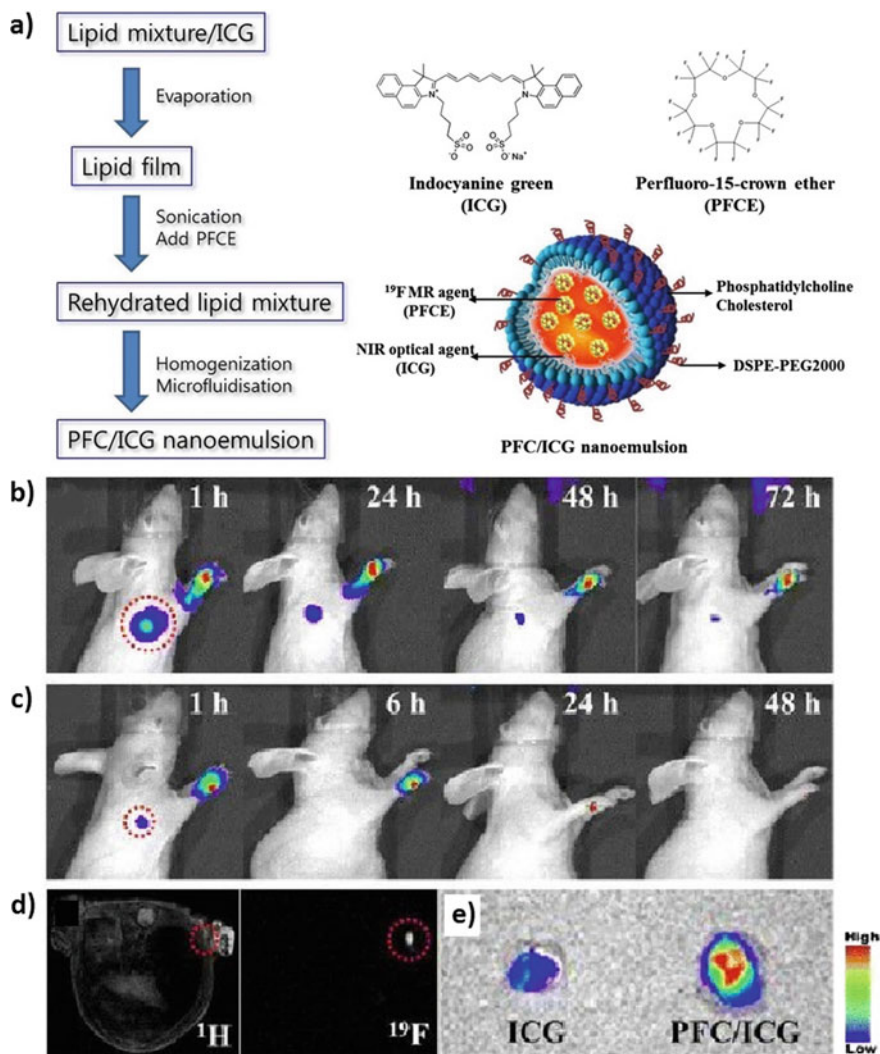


Fig. 6.12 PFC/ICG nanoemulsions for bimodal NIR OI/MRI. **a** Schematic illustration of the synthetic procedure (left) and structure of ICG, PFCE, and the PFC/ICG nanoemulsion (right). In vivo sentinel lymph node mapping using NIR fluorescence imaging at the indicated time after intradermal injection of **b** PGC/ICG nanoemulsions and **c** free ICG solutions into the right paw of a mouse. The signal intensity of the nanoemulsions was significantly prolonged compared to the free ICG solution. **d** In vivo ¹H (left) and ¹⁹F MRI (right) after intradermal injection of PFC/ICG nanoemulsions into the right paw of a mouse. The red circle highlights the sentinel lymph node. **e** Ex vivo NIR fluorescence imaging of the dissected lymph nodes 1 h after injection of the free ICG solution (left) and the PFC/ICG nanoemulsion (right), confirming the in vivo imaging results. Adapted with permission from [4]. Copyright 2014 Springer

Encapsulation of the organic dye 4,4',4'',4'''-(ethene-1,1,2,2-tetrayl)tetraaniline (ETTA) within an oleylamine-functionalized polysuccinimide- and 1H,1H,2H,2H-perfluorodecyltriethoxysilane-based micelle structure generated multifunctional ^{19}F -loaded nanocomposites with a fluorescent core for bimodal fluorescence/ ^{19}F MR imaging [29]. ETTA was used in this case to take advantage of its aggregation-induced emission properties, leading to significantly increased fluorescence emission after formation of the agglomerated dye core structure. The conjugation of the cell-targeting RGD peptide afforded tumor-targeting capability as demonstrated with both *in vitro* and *in vivo* experiments. A completely different approach described the one-pot synthesis of $\text{Cu}_{1.75}\text{S}$ nanoparticles with high ^{19}F loading through encapsulation of PFCE into a silica-coated oleylamine-functionalized polysuccinimide layer on the particles [11]. These nanoprobe showed good molecular mobility resulting from the relatively small particle size (~ 20 nm) compared to micelle-based ^{19}F MRI probes [96] and the ultrathin polymer coating. *In vivo* experiments demonstrated multifunctional applicability including simultaneous ^{19}F MRI with strong signal intensity, photothermal imaging, and PTT.

6.3.4 CEST Probes

CEST applications in the biomedical field focus both on metabolites that naturally occur in the human body and on extrinsic substances suitable for administration as contrast agents. Different classifications of CEST agents exist. The agents are often grouped based on their chemical shifts including diamagnetic, these being mostly endogenous not involving metallic ions (e.g., D-glucose, creatine, glutamate, L-arginine, salicylic acid, or thymidine), and paramagnetic substances, mostly exogenous and characterized by the presence of a metallic ion (e.g., paramagnetic lanthanide, iron, cobalt, and nickel) [64]. To non-invasively image the viability of encapsulated cells, Chan et al. used L-arginine as a pH-sensitive CEST contrast agent. In this study, L-arginine-filled liposomes were incorporated inside the capsule and protamine sulfate in the alginate capsule coating as an arginine-rich cross-linker. As the CEST contrast decreased upon cell death overtime, the capsules were shown to have potential as an indirect local marker for cell viability (Fig. 6.13) [8].

In another study employing diamagnetic CEST probes, lipid-based nanocarriers were co-loaded with barbituric acid (BA) as the contrast agent and the chemotherapeutic agent doxorubicin (DOX). BA is a heterocyclic pyrimidinetrione with excellent contrast properties at a frequency of 5 ppm away from water [9]. After intravenous administration of lipid-based nanocarriers in mice bearing experimental colorectal adenocarcinoma, *in vivo* CEST imaging was performed. Tumors in mice co-treated with a proinflammatory cytokine $\text{TNF-}\alpha$, known to increase the tumor vascular permeability, have shown enhanced accumulation of

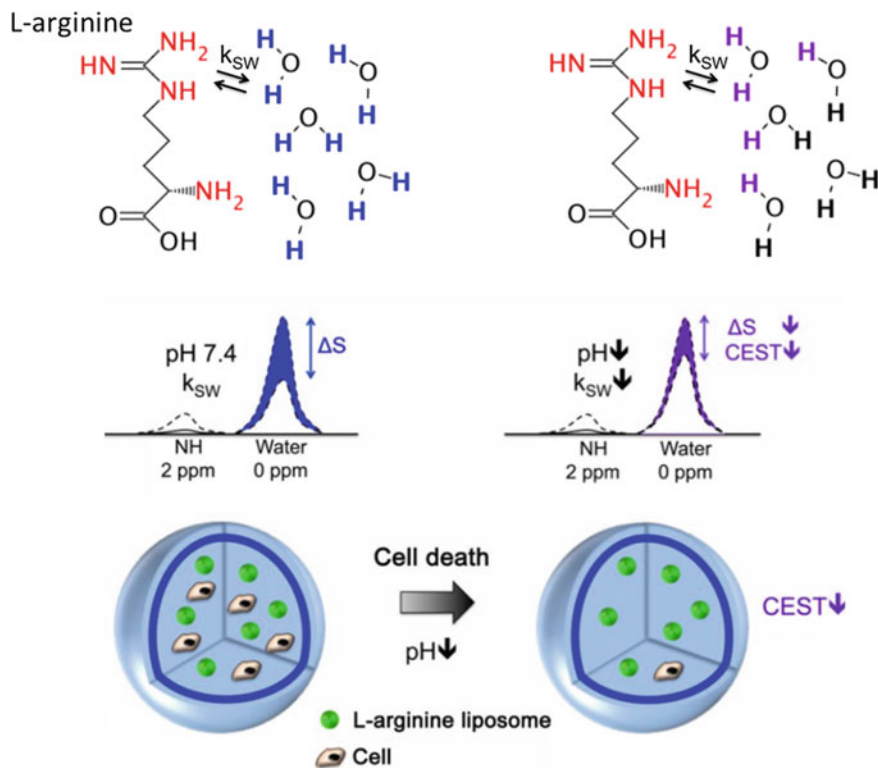


Fig. 6.13 After a selective saturation of the NH protons in L-arginine at 2 ppm, a decrease in the signal intensity of water (ΔS) can be seen enabling the measurement of the CEST contrast. The L-arginine protons inside the capsules exchange (k_{SW}) with the surrounding water protons. When the pH decreases, k_{SW} is reduced for NH protons in L-arginine, which causes a significant decrease in CEST contrast. Adapted with permission from [8]. Copyright 2013 Springer Nature

liposomes in tumors and increased CEST contrast (Fig. 6.14). Significant enhancement in pH sensitivity in physiologically relevant conditions using paramagnetic CEST probes was described in a recent study. The authors employed an amine-functionalized dicobalt CEST probe featuring an ancillary amine-substituted bisphosphonate ligand and exhibiting enhanced pH sensitivity by utilizing the different pH dependencies of the amine and amide CEST peak intensities [91].

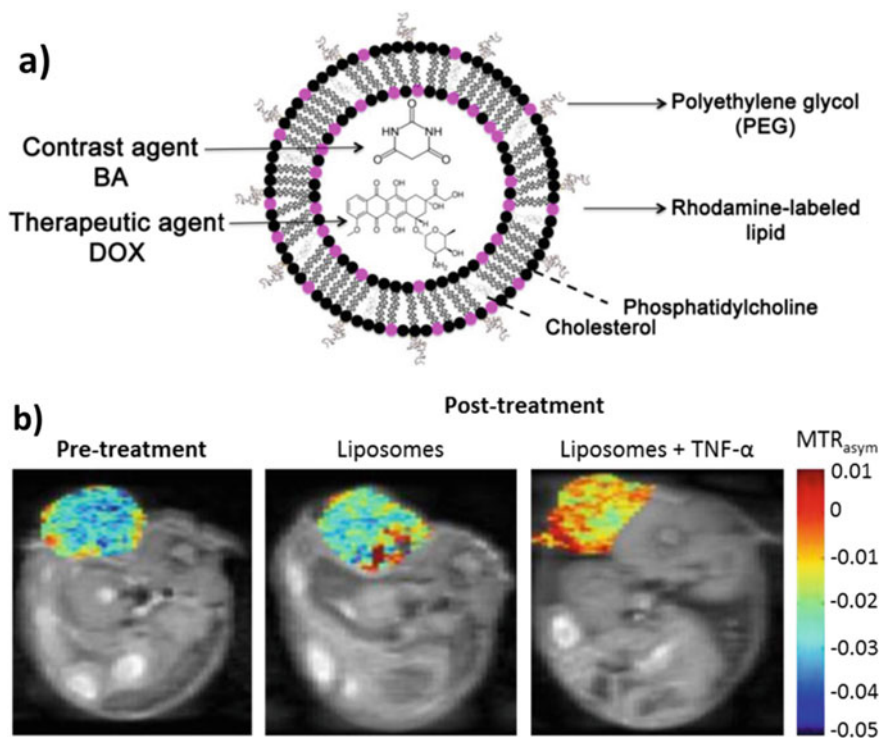


Fig. 6.14 MRI-traceable diamagnetic CEST liposomes co-loaded with barbituric acid (BA) as the contrast agent and the chemotherapeutic agent doxorubicin (DOX). **a** Architecture of BA/DOX co-loaded diamagnetic CEST liposomes. **b** CEST contrast MTR_{asym} (asymmetry in the magnetization transfer ratio) maps at 5 ppm for representative animals before and after treatment with $TNF-\alpha$. Adapted with permission from [9]. Copyright 2014. Published by Elsevier B.V

6.4 Theranostics

Based on pharmacogenetics, proteomics, metabolomics, and biomarker profiling, theranostics is emerging as a platform for the management of a disease at a molecular, personalized, patient-specific level. Advanced nanotheranostic systems are multicomponent individual particles, composed of organic and/or inorganic materials and often functionalized with biocompatible materials, suitable for both diagnostic and therapeutic use [82]. Nanotheranostic systems aim at customized, patient-specific action in terms of diagnosis and treatment in a single platform. Such an approach enables not only complementary imaging readouts from diseased tissues but also targeted drug delivery and controlled drug release in close proximity to the tumor, aiming to reduce the profound unwanted effects on the entire organism that systemically applied chemotherapeutic anti-cancer drugs regularly exhibit.

Synthesis of theranostic compounds is limited by many factors, including high safety standards and difficulties in obtaining favorable pharmacokinetics and pharmacodynamics and stability under physiological conditions as well as in achieving surface charge and ligation chemistry solutions compatible with blood environment, lung passage, and body temperature. Primarily described in the field of multifunctional gold-based nanoparticles (GNP) and in general applicable for other theranostic systems, Dykman and colleagues classified the main routes for the fabrication of multifunctional theranostic nanocomposites into three main groups: composite/hybrid nanoparticles (enabling diagnostic and therapeutic actions); nanoparticles functionalized with a set of different molecules using smart bioconjugation techniques; and, finally, the combination of these two routes, i.e., additional functionalization of a composite/hybrid nanoparticle with molecules that possess different properties, resulting in multifunctionalized composite nanoparticles [21].

In a study by Song and colleagues, bioconjugated plasmonic vesicles assembled from surface-enhanced Raman scattering (SERS)-active amphiphilic GNP intended for cancer-targeted drug delivery were described. These vesicles are detectable by plasmonic imaging and Raman spectroscopy. Here, pH-responsive disassembly of the plasmonic vesicle was used to achieve the triggering of intracellular drug release [84]. This approach excellently illustrates the use of external stimuli such as pH to put disease-specific physiological conditions to use for localized therapy, namely an acidic extracellular tumor environment and acidic intracellular endocytic compartments.

A quintuple-modality theranostic nanoprobe based on gold nanostars was reported in another study, comprising the following functionalities: SERS, MRI, CT, two-photon luminescence (TPL) imaging, and PTT [59]. The multifunctionality of such an approach enables preoperative tumor scanning with MR imaging and CT, intra-operative tumor detection with SERS and two-photon luminescence, as well as post-operative PTT.

Design of multifunctional nanotheranostic Fe_3O_4 -MTX@HBc core/shell nanoparticles was described in a recent study by Zhang et al. Here, methotrexate was chemically conjugated to Fe_3O_4 nanoparticles and embedded into a shell of hepatitis B virus core protein (HBc) virus-like particles. The authors showed the feasibility of this approach for MRI-guided photothermal chemotherapy of cancer. In vivo analyses revealed well-defined morphology and good biocompatibility/biodegradation, with the HBc virus-like particle shell providing a protective effect to the Fe_3O_4 -MTX nanoparticles against the reticuloendothelial system, as well as favorable properties as an MRI contrast agent and strong NIR absorption features, which were shown to be accompanied by enhanced stability and biocompatibility of the nanodrugs [123].

6.5 Novel Imaging Approaches

6.5.1 Magnetic Particle Imaging (MPI)

Introduced in 2005, MPI is a promising imaging modality that enables the depiction of tracers based on magnetic nanoparticles with only limited background contamination. As is the case for other imaging techniques, it has revealed at this early evaluation stage many beneficial qualities in preclinical settings but also some challenges. The method does not require ionizing radiation and the expectations regarding its very high temporal resolution have been fulfilled; however, its sensitivity is inferior to nuclear medicine functional imaging techniques and its currently reported spatial resolution in the range of 1–5 mm is still seen as one of the challenges of this technique. Importantly, this method is suitable for the acquisition of quantitative data, as the strength of the MPI signal is proportional to the concentration of the tracer in the field of view [71].

Tracers commonly used are iron oxide-based magnetic nanoparticles (MNP). MPI tracers usually contain a magnetic core and suitable coating (e.g., dextran or PEG) that renders them biocompatible and prevents *in vivo* agglomeration of particles [42]. Signal generation in MPI is dependent on the response of superparamagnetic iron oxide nanoparticles to magnetic fields generated by a unique coil topology in the MPI scanner. The magnetization response changes upon variation in the strength and/or direction of the external field. The resulting dynamic evolution in the magnetic moments of the tracer is summed up and used as the basis for the three-dimensional visualization of the spatial distribution of the tracer [42, 71].

As a methodology, MPI is currently being scaled up for possible use in humans. Preliminary studies completed so far in small animals have indicated the applicability of MPI in vascular, oncology, and inflammation imaging as well as in cell tracking [109]. As a tracer-dependent imaging modality, the fate of MPI will certainly remain closely connected to the safety profile of the nanoparticles intended for human use. Due to the need for complementary anatomical information and co-registration of MPI readouts with CT or MR imaging, hybrid systems will be desirable.

In a study published by Zheng and colleagues, MPI was employed to monitor the delivery of mesenchymal stem cells (MSCs) *in vivo*. MSCs show promising results in the treatment of various diseases including cardiovascular and neurologic. Targeted delivery of MSCs to specific tissues is desirable, yet intravenously administered MSCs commonly end up being entrapped in lung microvessels. In this study, rats were injected with Resovist-labeled human MSCs (hMSCs) and the authors noted initial entrapment of hMSCs in the lungs followed by clearance to the liver, whereas injection of control iron oxide resulted in immediate hepatic and splenic uptake (Fig. 6.15) [124]. Results acquired using MPI/CT were corroborated by control optical (fluorescent) and MR imaging.

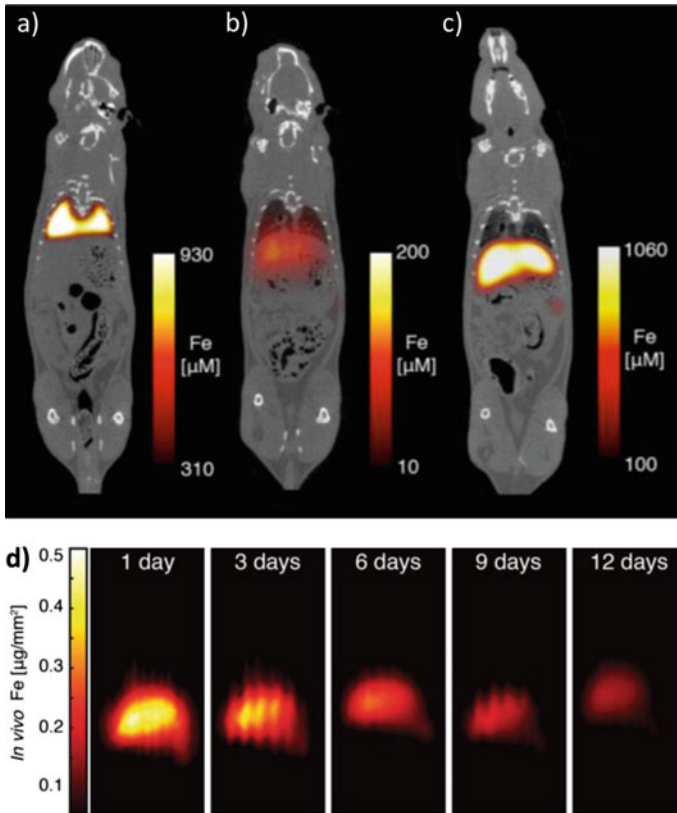


Fig. 6.15 MPI/CT coronal reconstructions in rats after intravenous injection of labeled hMSCs (**a**, **b**, **d**) or Resovist-only (**c**). Entrapment of labeled hMSCs in lungs **a** one hour and **b** 12 days post-injection as visualized by MPI. **c** Resovist-only read-out one hour after intravenous injection as seen by MPI, indicating immediate hepatic and splenic uptake. **d** Coronal summed intensity projections of gradual clearance of iron oxide from liver (day 1 to day 12 post-hMSC injection) using in vivo MPI. Adapted with permission from [124]. Copyright 2016 Ivyspring International Publisher

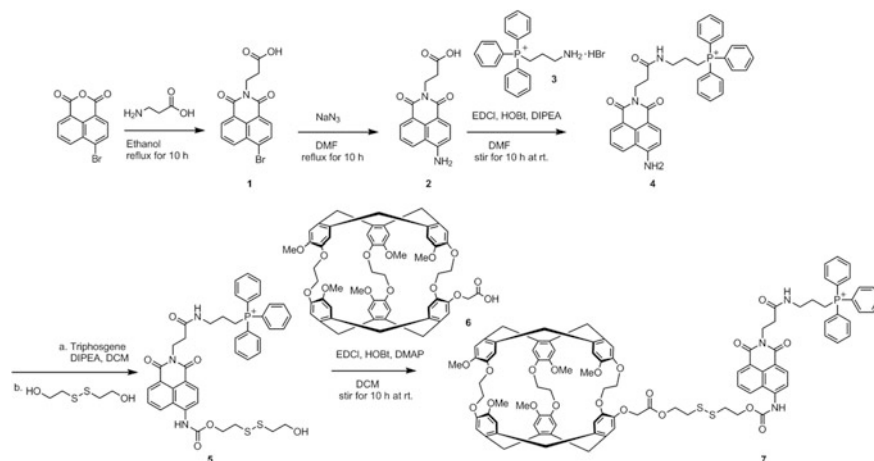
In a recent study, the potential of MPI was tested for in vivo detection of stem cell transplants employing clinically translatable ferumoxytol. Ferumoxytol is an iron oxide nanoparticle compound consisting of an iron oxide core and a carboxymethyl-dextran coat, currently approved by the FDA for the treatment of iron deficiency anemia [67]. Ferumoxytol-labeled mesenchymal stem cells transplanted in calvarial defects of mice showed higher MPI signal and higher calculated iron content than unlabeled MSCs, indicating the possible perspective of MPI for clinical translation.

6.5.2 Hyperpolarized Multifunctional MRI Probes

An emerging field in the clinical application of MR spectroscopy (MRS) is the use of hyperpolarization [43, 66, 72, 80]. With this relatively new technique, several thousandfold sensitivity enhancement is achieved to overcome the limitations of conventional MRS. While initially hyperpolarization was used only with gases such as ^3He and ^{129}Xe exhibiting long T_1 values, the application to other nuclei like ^{13}C or ^{15}N has become the subject of many investigations in the recent decade. Mostly, ^{13}C -labeled biogenically occurring substrates such as pyruvate have been subjected to hyperpolarization, monitoring the metabolic pathway of the downstream products after *in vivo* injection. These are small molecules that are generated only for the purpose of MR imaging, and the incorporation of additional functionalities appears to be challenging considering their short-lived hyperpolarized state and their susceptible stability. Thus, it is not surprising that only very few reports on the development of multifunctional hyperpolarized probes for MRI have been published. Multimodal approaches using hyperpolarized ^{13}C -labeled metabolites have only been reported in combination with other modalities applying individual probes successively. A convenient approach is provided by the combination of ^{18}F -FDG-PET and ^{13}C -pyruvate MRI as demonstrated in various *in vivo* studies [30, 32, 65, 76].

Due to the relatively short T_1 values of hyperpolarized nuclei, hyperpolarized probes need to be prepared directly before *in vivo* application and image acquisition. Thus, the preparation of hyperpolarized probes generally requires well-conceived set-ups. For example, Lakshmanan et al. described the development of biogenic hyperpolarized ^{129}Xe gas-filled protein nanostructures for ultrasound and hyperpolarized ^{129}Xe MRI [46]. The applied gas vesicles were isolated from native and heterologous host organisms, followed by purification and functionalization with fluorescent and targeting moieties. The sophisticated procedure for probe preparation and use involved generation of hyperpolarized ^{129}Xe gas through a xenon hyperpolarizer, introduction of the Xe gas into a solution of the gas vesicles, and subsequent image acquisition. These multifunctional imaging probes have been applied in *in vitro* experiments using chemical exchange saturation transfer (Hyper-CEST MRI) between vesicle-bound and dissolved xenon.

Zeng et al. reported the development of a mitochondria-targeting fluorescence/ ^{129}Xe -NMR multimodal biosensor for detection of intracellular biothiol levels [118]. This sensor consisted of a cryptophane A cage host molecule loaded with ^{129}Xe , a thiol-specific cleavable disulfide bond linker, a fluorescent naphthalimide group, and a mitochondria-targeting triphenylphosphonium moiety, likewise increasing the hydrophilic character of the molecule (Scheme 6.1). Non-invasive detection of abnormal cellular biothiol levels was achieved through cleavage of disulfide bonds caused by the intracellular biothiols, leading in turn to enhanced fluorescence signal intensity via intramolecular cyclization and release of the naphthalimide group as well as a change in the chemical shift of ^{129}Xe . The behavior of the biosensor was demonstrated *in vitro* as well as in live cells using Hyper-CEST NMR, showing good targeting ability to the mitochondria.



Scheme 6.1 Synthetic route of a mitochondria-targeting fluorescence/ ^{129}Xe -NMR multimodal biosensor. Starting with 4-bromonaphthalic anhydride, a fluorescent naphthalimide was synthesized and a cryptophane A cage (^{129}Xe host) as well as a triphenylphosphonium moiety (hydrophilic mitochondria-targeting group) was coupled. Reprinted with permission from [118]. Copyright 2017 American Chemical Society

Although these examples show interesting results of *in vitro* experiments with multifunctional hyperpolarized MRI probes, further advances towards *in vivo* applications still remain challenging.

6.6 Outlook

MR imaging is one of the fastest expanding imaging modalities in both preclinical and clinical settings due to its good safety profile, unsurpassed soft tissue discrimination, and the possibility for non-invasive functional/physiological characterization of diseased tissues. Although inferior to nuclear medicine methods with regards to imaging sensitivity, current research in the field of multifunctional imaging probes is significantly pushing MR imaging forward also in this regard. Efforts in the development of hybrid imaging methodologies also give constant rise to numerous extrinsic compounds that yield complementary imaging readouts. The addition of compounds with therapeutic effects to diagnostic probes, a field nowadays widely referred to as theranostics, enables local delivery and/or controlled release of the therapeutic. The need for ever-improving solutions for ligation chemistry during the synthesis of these probes remains one of the core issues to be resolved. Safety profiles of extrinsically applied agents are often the limiting factor for intended clinical translation. Largely due to this issue, the extensive research in this field has not been paralleled by significantly broadened clinical application of

multifunctional MR imaging probes. An optimal multifunctional probe in oncology will have to fulfill the increasingly stringent criteria for safe use under physiological conditions in humans, meet expectations for temporal and spatial resolution under in vivo imaging conditions, and reach sensitivity and specificity sufficient for lesion detection and characterization before obvious morphological changes. The focus of the multimodal imaging and multifunctional imaging probes research communities in the coming years will most certainly remain the linking of morphological methods like MRI/CT and high sensitivity methods, such as nuclear medicine. Multidisciplinarity at the forefront of preclinical and clinical research, especially for bridging the interface between a tissue or a cell on the one side and clinical diagnostic platforms on the other, is no longer a matter of choice but a *conditio sine qua non*.

References

1. Abdesselam M et al (2014) Multifunctional rare-Earth vanadate nanoparticles: luminescent labels, oxidant sensors, and MRI contrast agents. *ACS Nano* 8(11):11126–11137
2. An L et al (2018) Paclitaxel-induced ultrasmall gallic Acid-Fe@BSA Self-assembly with enhanced MRI performance and tumor accumulation for cancer theranostics. *ACS Appl Mater Interfaces* 10(34):28483–28493
3. Asefa T, Tao Z (2012) Biocompatibility of mesoporous silica nanoparticles. *Chem Res Toxicol* 25(11):2265–2284
4. Bae PK et al (2014) Highly enhanced optical properties of indocyanine green/perfluorocarbon nanoemulsions for efficient lymph node mapping using near-infrared and magnetic resonance imaging. *Nano Converg* 1(1):6
5. Beyersmann D, Hartwig A (2008) Carcinogenic metal compounds: recent insight into molecular and cellular mechanisms. *Arch Toxicol* 82(8):493
6. Biju S, Parac-Vogt T (2018) Recent advances in lanthanide based nano-architectures as probes for ultra high-field magnetic resonance imaging. *Curr Med Chem* 25:1–9
7. Cao Y et al (2018) Intelligent MnO₂/Cu₂-xS for multimode imaging diagnostic and advanced single-laser irradiated photothermal/photodynamic therapy. *ACS Appl Mater Interfaces* 10(21):17732–17741
8. Chan KW et al (2013) MRI-detectable pH nanosensors incorporated into hydrogels for in vivo sensing of transplanted-cell viability. *Nat Mater* 12(3):268–275
9. Chan KW et al (2014) A diaCEST MRI approach for monitoring liposomal accumulation in tumors. *J Control Release* 180:51–59
10. Chen C et al (2016) Current advances in lanthanide-doped upconversion nanostructures for detection and bioapplication. *Adv Sci* 3(10):1600029
11. Chen H et al (2016) Ultrahigh (19)F Loaded Cu_{1.75}S nanoprobe for simultaneous (19)F magnetic resonance imaging and photothermal therapy. *ACS Nano* 10(1):1355–1362
12. Chen J et al (2013) Multifunctional Fe₃O₄@C@Ag hybrid nanoparticles as dual modal imaging probes and near-infrared light-responsive drug delivery platform. *Biomaterials* 34(2):571–581
13. Chen Y et al (2015) Multifunctional envelope-type mesoporous silica nanoparticles for pH-responsive drug delivery and magnetic resonance imaging. *Biomaterials* 60:111–120
14. Chen Y et al (2013) Encapsulation of particle ensembles in graphene nanosacks as a new route to multifunctional materials. *ACS Nano* 7(5):3744–3753
15. Cheng K et al (2014) Hybrid nanotrimers for dual T₁ and T₂-weighted magnetic resonance imaging. *ACS Nano* 8(10):9884–9896

16. Cheng L et al (2017) Chelator-free labeling of metal oxide nanostructures with zirconium-89 for positron emission tomography imaging. *ACS Nano* 11(12):12193–12201
17. Currie S et al (2013) Understanding MRI: basic MR physics for physicians. *Postgrad Med J* 89(1050):209–223
18. Ding X et al (2016) Polydopamine coated manganese oxide nanoparticles with ultrahigh relaxivity as nanotheranostic agents for magnetic resonance imaging guided synergetic chemo-/photothermal therapy. *Chem Sci* 7(11):6695–6700
19. Dong K et al (2014) Ultrasmall biomolecule-anchored hybrid GdVO₄ nanophosphors as a metabolizable multimodal bioimaging contrast agent. *Nanoscale* 6(20):12042–12049
20. Du Q et al (2015) Facile preparation and bifunctional imaging of Eu-doped GdPO₄ nanorods with MRI and cellular luminescence. *Dalton Trans* 44(9):3934–3940
21. Dykman LA, Khlebtsov NG (2016) Multifunctional gold-based nanocomposites for theranostics. *Biomaterials* 108:13–34
22. Edelman RR (2014) The history of MR imaging as seen through the pages of radiology. *Radiology* 273(2 Suppl):S181–S200
23. EMA (2017) European Medicines Agency, EMA/625317/2017. <https://www.ema.europa.eu/en/medicines/human/referrals/gadolinium-containing-contrast-agents>. Accessed 2 April 2020.
24. Estelrich J et al (2015) Nanoparticles in magnetic resonance imaging: from simple to dual contrast agents. *Int J Nanomedicine* 10:1727–1741
25. Fan Q et al (2014) Transferring biomarker into molecular probe: melanin nanoparticle as a naturally active platform for multimodality imaging. *J Am Chem Soc* 136(43):15185–15194
26. Garcia-Hevia L et al (2019) Recent progress on manganese-based nanostructures as responsive MRI contrast agents. *Chem Eur J* 25(2):431–441
27. Geraldès CF, Laurent S (2009) Classification and basic properties of contrast agents for magnetic resonance imaging. *Contrast Media Mol Imaging* 4(1):1–23
28. Gong H et al (2013) Carbon nanotubes for biomedical imaging: the recent advances. *Adv Drug Deliv Rev* 65(15):1951–1963
29. Guo C et al (2017) Multifunctional nanoprobe for both fluorescence and ¹⁹F magnetic resonance imaging. *Nanoscale* 9(21):7163–7168
30. Gutte H et al (2015) Simultaneous hyperpolarized ¹³C-Pyruvate MRI and ¹⁸F-FDG PET (HyperPET) in 10 dogs with cancer. *J Nucl Med* 56(11):1786–1792
31. Hu H et al (2014) General protocol for the synthesis of functionalized magnetic nanoparticles for magnetic resonance imaging from protected metal-organic precursors. *Chem Eur J* 20(23):7160–7167
32. Hundshammer C et al (2018) Simultaneous characterization of tumor cellularity and the Warburg effect with PET, MRI and hyperpolarized (¹³C)-MRSI. *Theranostics* 8(17):4765–4780
33. IMV (2019) <https://imvinfo.com/?sec=mri&sub=dis&itemid=200085>. Accessed 24 Jan 2019
34. Jiang W et al (2014) “Green” functionalization of magnetic nanoparticles via tea polyphenol for magnetic resonance/fluorescent dual-imaging. *Nanoscale* 6(3):1305–1310
35. Jiang Y et al (2017) Magnetic mesoporous nanospheres anchored with LyP-1 as an efficient pancreatic cancer probe. *Biomaterials* 115:9–18
36. Jin X et al (2015) An ultrasmall and metabolizable PEGylated NaGdF₄: Dy nanoprobe for high-performance T(1)/T(2)-weighted MR and CT multimodal imaging. *Nanoscale* 7(38):15680–15688
37. Joshi R et al (2013) Multifunctional silica nanoparticles for optical and magnetic resonance imaging. *Biol Chem* 394(1):125–135
38. Kang X et al (2013) Poly(acrylic acid) modified lanthanide-doped GdVO₄ hollow spheres for up-conversion cell imaging, MRI and pH-dependent drug release. *Nanoscale* 5(1):253–261
39. Kim D et al (2018) Recent development of inorganic nanoparticles for biomedical imaging. *ACS Cent Sci* 4(3):324–336

40. Kim IY et al (2015) Toxicity of silica nanoparticles depends on size, dose, and cell type. *Nanomedicine* 11(6):1407–1416
41. Kim J et al (2009) Multifunctional nanostructured materials for multimodal imaging, and simultaneous imaging and therapy. *Chem Soc Rev* 38(2):372–390
42. Knopp T et al (2017) Magnetic particle imaging: from proof of principle to preclinical applications. *Phys Med Biol* 62(14):R124–R178
43. Kurhanewicz J et al (2008) Current and potential applications of clinical ^{13}C MR spectroscopy. *J Nucl Med* 49(3):341–344
44. Lacerda L et al (2008) Carbon-nanotube shape and individualization critical for renal excretion. *Small* 4(8):1130–1132
45. Laguna M et al (2016) Multifunctional Eu-doped $\text{NaGd}(\text{MoO}_4)_2$ nanoparticles functionalized with poly(L-lysine) for optical and MRI imaging. *Dalton Trans* 45(41):16354–16365
46. Lakshmanan A et al (2017) Preparation of biogenic gas vesicle nanostructures for use as contrast agents for ultrasound and MRI. *Nat Protoc* 12(10):2050–2080
47. Lanza GM et al (2005) $^1\text{H}/^{19}\text{F}$ magnetic resonance molecular imaging with perfluorocarbon nanoparticles. *Curr Top Dev Biol* 70:57–76
48. Le DHT et al (2017) Chemical addressability of potato virus X for its applications in bio/nanotechnology. *J Struct Biol* 200(3):360–368
49. Lee N et al (2015) Iron oxide based nanoparticles for multimodal imaging and magnetoresponsive therapy. *Chem Rev* 115(19):10637–10689
50. Li E et al (2018) Multifunctional magnetic mesoporous silica nanoagents for in vivo enzyme-responsive drug delivery and mr imaging. *Nanotheranostics* 2(3):233–242
51. Li J et al (2014) Hyaluronic acid-modified hydrothermally synthesized iron oxide nanoparticles for targeted tumor MR imaging. *Biomaterials* 35(11):3666–3677
52. Li J et al (2013) Multifunctional uniform core-shell $\text{Fe}_3\text{O}_4@\text{mSiO}_2$ mesoporous nanoparticles for bimodal imaging and photothermal therapy. *Chem Asian J* 8(2):385–391
53. Li J et al (2014) Gadolinium oxide nanoparticles and aptamer-functionalized silver nanoclusters-based multimodal molecular imaging nanoprobe for optical/magnetic resonance cancer cell imaging. *Anal Chem* 86(22):11306–11311
54. Li Y et al (2016) Core-Shell-Shell $\text{NaYbF}_4:\text{Tm}@\text{CaF}_2@\text{NaDyF}_4$ Nanocomposites for Upconversion/ T_2 -Weighted MRI/Computed Tomography Lymphatic Imaging. *ACS Appl Mater Interfaces* 8(30):19208–19216
55. Lipton ML (2008) *Totally accessible MRI*. Springer, New York
56. Liu D et al (2018) Target-specific delivery of oxaliplatin to HER2-positive gastric cancer cells in vivo using oxaliplatin-au- fe_3o_4 -herceptin nanoparticles. *Oncol Lett* 15(5):8079–8087
57. Liu H-M et al (2008) Mesoporous silica nanoparticles improve magnetic labeling efficiency in human stem cells. *Small* 4(5):619–626
58. Liu JN et al (2015) Silica coated upconversion nanoparticles: a versatile platform for the development of efficient theranostics. *Acc Chem Res* 48(7):1797–1805
59. Liu Y et al (2013) Quintuple-modality (SERS-MRI-CT-TPL-PTT) plasmonic nanoprobe for theranostics. *Nanoscale* 5(24):12126–12131
60. Liu Z et al (2008) Circulation and long-term fate of functionalized, biocompatible single-walled carbon nanotubes in mice probed by Raman spectroscopy. *Proc Natl Acad Sci USA* 105(5):1410–1415
61. Ma ZY et al (2015) Folic acid-targeted magnetic Tb-doped CeF_3 fluorescent nanoparticles as bimodal probes for cellular fluorescence and magnetic resonance imaging. *Dalton Trans* 44(37):16304–16312
62. Mao X et al (2016) Functional nanoparticles for magnetic resonance imaging. *Wiley Interdiscip Rev Nanomed Nanobiotechnol* 8(6):814–841
63. Matsushita H et al (2014) Multifunctional core-shell silica nanoparticles for highly sensitive (^{19}F) magnetic resonance imaging. *Angew Chem Int Ed* 53(4):1008–1011

64. McMahon MT, Chan KW (2014) Developing MR probes for molecular imaging. *Adv Cancer Res* 124:297–327
65. Menzel MI et al (2013) Multimodal assessment of in vivo metabolism with hyperpolarized [^{13}C]MR spectroscopy and ^{18}F -FDG PET imaging in hepatocellular carcinoma tumor-bearing rats. *J Nucl Med* 54(7):1113–1119
66. Miloushev VZ et al (2016) Hyperpolarization MRI: preclinical models and potential applications in neuroradiology. *Top Magn Reson Imaging* 25(1):31–37
67. Nejadnik H et al (2018) Ferumoxytol can be used for quantitative magnetic particle imaging of transplanted stem cells. *Mol Imaging Biol*
68. Nunez NO et al (2013) Surface modified Eu:GdVO₄ nanocrystals for optical and MRI imaging. *Dalton Trans* 42(30):10725–10734
69. Ortgies DH et al (2016) In vivo deep tissue fluorescence and magnetic imaging employing hybrid nanostructures. *ACS Appl Mater Interfaces* 8(2):1406–1414
70. Pan D et al (2011) Manganese-based MRI contrast agents: past, present and future. *Tetrahedron* 67(44):8431–8444
71. Panagiotopoulos N et al (2015) Magnetic particle imaging: current developments and future directions. *Int J Nanomedicine* 10:3097–3114
72. Penet MF et al (2013) MR—eyes for cancer: looking within an impenetrable disease. *NMR Biomed* 26(7):745–755
73. Poehlmann M et al (2014) On the interplay of shell structure with low- and high-frequency mechanics of multifunctional magnetic microbubbles. *Soft Matter* 10(1):214–226
74. Purushotham S et al (2009) Thermoresponsive core-shell magnetic nanoparticles for combined modalities of cancer therapy. *Nanotechnology* 20(30):305101
75. Radbruch A et al (2015) Gadolinium retention in the dentate nucleus and globus pallidus is dependent on the class of contrast agent. *Radiology* 275(3):783–791
76. Ravoori MK et al (2017) in vivo assessment of ovarian tumor response to Tyrosine Kinase inhibitor pazopanib by using hyperpolarized ^{13}C -Pyruvate MR spectroscopy and ^{18}F -FDG PET/ct imaging in a mouse model. *Radiology* 285(3):830–838
77. Revia RA, Zhang M (2016) Magnetite nanoparticles for cancer diagnosis, treatment, and treatment monitoring: recent advances. *Mater Today* 19(3):157–168
78. Richards DA et al (2017) Antibody fragments as nanoparticle targeting ligands: a step in the right direction. *Chem Sci* 8(1):63–77
79. Rogosnitzky M, Branch S (2016) Gadolinium-based contrast agent toxicity: a review of known and proposed mechanisms. *Biometals* 29(3):365–376
80. Roos JE et al (2015) Hyperpolarized Gas MR imaging: technique and applications. *Magn Reson Imaging Clin N Am* 23(2):217–229
81. Saha A et al (2017) Surface-engineered multifunctional Eu:Gd₂O₃ nanoplates for targeted and pH-responsive drug delivery and imaging applications. *ACS Appl Mater Interfaces* 9(4):4126–4141
82. Silva CO et al (2019) Current trends in cancer nanotheranostics: metallic, polymeric, and lipid-based systems. *Pharmaceutics* 11(1)
83. Smith AM et al (2009) Second window for in vivo imaging. *Nat Nanotechnol* 4:710
84. Song J et al (2012) Self-assembled plasmonic vesicles of SERS-encoded amphiphilic gold nanoparticles for cancer cell targeting and traceable intracellular drug delivery. *J Am Chem Soc* 134(32):13458–13469
85. Sosnovik DE, Weissleder R (2007) Emerging concepts in molecular MRI. *Curr Opin Biotechnol* 18(1):4–10
86. Srikar R et al (2014) Polymeric nanoparticles for molecular imaging. *Wiley Interdiscip Rev Nanomed Nanobiotechnol* 6(3):245–267
87. Sun SK et al (2013) Fabrication of multifunctional Gd₂O₃/Au hybrid nanoprobe via a one-step approach for near-infrared fluorescence and magnetic resonance multimodal imaging in vivo. *Anal Chem* 85(17):8436–8441

88. Sun Y et al (2013) Core-shell lanthanide upconversion nanophosphors as four-modal probes for tumor angiogenesis imaging. *ACS Nano* 7(12):11290–11300
89. Sutens B et al (2016) Tunability of size and magnetic moment of iron oxide nanoparticles synthesized by forced hydrolysis. *Materials* 9(7):E554
90. Teston E et al (2015) Design, properties, and in vivo behavior of super-paramagnetic persistent luminescence nanohybrids. *Small* 11(22):2696–2704
91. Thorarinsdottir AE, Harris TD (2019) Dramatic enhancement in pH sensitivity and signal intensity through ligand modification of a dicobalt PARACEST probe. *Chem Commun (Camb)* 55(6):794–797
92. Thorek DL et al (2006) Superparamagnetic iron oxide nanoparticle probes for molecular imaging. *Ann Biomed Eng* 34(1):23–38
93. Tian Q et al (2013) Sub-10 nm Fe₃O₄@Cu(2-x)S core-shell nanoparticles for dual-modal imaging and photothermal therapy. *J Am Chem Soc* 135(23):8571–8577
94. Tian Q et al (2014) Multifunctional polypyrrole@Fe(3)O(4) nanoparticles for dual-modal imaging and in vivo photothermal cancer therapy. *Small* 10(6):1063–1068
95. Tiwari A et al (2018) Carbon coated core-shell multifunctional fluorescent SPIONs. *Nanoscale* 10(22):10389–10394
96. Tran TD et al (2007) Clinical applications of perfluorocarbon nanoparticles for molecular imaging and targeted therapeutics. *Int J Nanomed* 2(4):515–526
97. Wahsner J et al (2019) Chemistry of MRI contrast agents: current challenges and new frontiers. *Chem Rev* 119(2):957–1057
98. Walia S, Acharya A (2015) Silica micro/nanospheres for theranostics: from bimodal MRI and fluorescent imaging probes to cancer therapy. *Beilstein J Nanotechnol* 6:546–558
99. Walia S et al (2016) A bimodal molecular imaging probe based on chitosan encapsulated magneto-fluorescent nanocomposite offers biocompatibility, visualization of specific cancer cells in vitro and lung tissues in vivo. *Int J Pharm* 498(1–2):110–118
100. Wang H et al (2010) Synthesis of carbon-encapsulated superparamagnetic colloidal nanoparticles with magnetic-responsive photonic crystal property. *Dalton Trans* 39(40):9565–9569
101. Wang H et al (2016) Preloading of hydrophobic anticancer drug into multifunctional nanocarrier for multimodal imaging, NIR-responsive drug release, and synergistic therapy. *Small* 12(46):6388–6397
102. Wang J et al (2016) MR/SPECT imaging guided photothermal therapy of tumor-targeting Fe@Fe₃O₄ nanoparticles in vivo with low mononuclear phagocyte uptake. *ACS Appl Mater Interfaces* 8(31):19872–19882
103. Wang X et al (2013) Multifunctional Fe₃O₄@P(St/MAA)@chitosan@Au core/shell nanoparticles for dual imaging and photothermal therapy. *ACS Appl Mater Interfaces* 5(11):4966–4971
104. Wang Y-X et al (2013) Recent advances in superparamagnetic iron oxide nanoparticles for cellular imaging and targeted therapy research. *Curr Pharm Des* 19(37):6575–6593
105. Ward KM et al (2000) A new class of contrast agents for MRI based on proton chemical exchange dependent saturation transfer (CEST). *J Magn Reson* 143(1):79–87
106. Wei Z et al (2016) Multifunctional nanoprobe for cancer cell targeting and simultaneous fluorescence/magnetic resonance imaging. *Anal Chim Acta* 938:156–164
107. Weishaupt D et al (2006) How does MRI work?. Springer, Berlin Heidelberg
108. Wu B et al (2016) An overview of CEST MRI for non-MR physicists. *EJNMMI Phys* 3(1):19
109. Wu LC et al (2019) A review of magnetic particle imaging and perspectives on neuroimaging. *AJNR Am J Neuroradiol* 40(2):206–212
110. Wyss PP et al (2016) Nanoprobes for multimodal visualization of bone mineral phase in magnetic resonance and near-infrared optical imaging. *ACS Omega* 1(2):182–192
111. Yang D et al (2014) Ultra-small BaGdF₅-based upconversion nanoparticles as drug carriers and multimodal imaging probes. *Biomaterials* 35(6):2011–2023

112. Yang H-M et al (2018) Cross-linked magnetic nanoparticles with a biocompatible amide bond for cancer-targeted dual optical/magnetic resonance imaging. *Colloids Surf B Biointerfaces* 161:183–191
113. Yang L et al (2016) Multifunctional upconversion nanoparticles for targeted dual-modal imaging in rat glioma xenograft. *J Biomater Appl* 31(3):400–410
114. Yi Z et al (2016) Hybrid lanthanide nanoparticles as a new class of binary contrast agents for in vivo T1/T2 dual-weighted MRI and synergistic tumor diagnosis. *J Mater Chem B* 4(15):2715–2722
115. Yin C et al (2015) Fluorescent oligo(p-phenyleneethynylene) contained amphiphiles-encapsulated magnetic nanoparticles for targeted magnetic resonance and two-photon optical imaging in vitro and in vivo. *Nanoscale* 7(19):8907–8919
116. Yu J et al (2014) Multifunctional Fe₅C₂ nanoparticles: a targeted theranostic platform for magnetic resonance imaging and photoacoustic tomography-guided photothermal therapy. *Adv Mater* 26(24):4114–4120
117. Yuzhakova DV et al (2017) In vivo multimodal tumor imaging and photodynamic therapy with novel theranostic agents based on the porphyrazine framework-chelated gadolinium (III) cation. *Biochim Biophys Acta Gen Subj* 1861(12):3120–3130
118. Zeng Q et al (2017) Mitochondria targeted and intracellular biothiols triggered hyperpolarized (¹²⁹Xe) magnetofluorescent biosensor. *Anal Chem* 89(4):2288–2295
119. Zhan Y et al (2018) Intrinsically zirconium-89-labeled manganese oxide nanoparticles for in vivo dual-modality positron emission tomography and magnetic resonance imaging. *J Biomed Nanotechnol* 14(5):900–909
120. Zhang C et al (2017) Tri-needle coaxial electrospray engineering of magnetic polymer yolk-shell particles possessing dual-imaging modality, multiagent compartments, and trigger release potential. *ACS Appl Mater Interfaces* 9(25):21485–21495
121. Zhang L et al (2016) Facile preparation of multifunctional uniform magnetic microspheres for T1-T2 dual modal magnetic resonance and optical imaging. *Colloids Surf B Biointerfaces* 144:344–354
122. Zhang L et al (2013) High MRI performance fluorescent mesoporous silica-coated magnetic nanoparticles for tracking neural progenitor cells in an ischemic mouse model. *Nanoscale* 5(10):4506–4516
123. Zhang Q et al (2018) Construction of multifunctional Fe₃O₄-MTX@HBc nanoparticles for MR imaging and photothermal therapy/chemotherapy. *Nanotheranostics* 2(1):87–95
124. Zheng B et al (2016) Quantitative magnetic particle imaging monitors the transplantation, biodistribution, and clearance of stem cells in vivo. *Theranostics* 6(3):291–301
125. Zhu H et al (2013) Magnetic, fluorescent, and thermo-responsive Fe₃O₄/rare earth incorporated poly(*St*-NIPAM) core-shell colloidal nanoparticles in multimodal optical/magnetic resonance imaging probes. *Biomaterials* 34(9):2296–2306



Single Photon Emission Computed Tomography Tracer

7

Hans-Jürgen Pietzsch, Constantin Mamat, Cristina Müller,
and Roger Schibli

Contents

7.1	Introduction.....	228
7.2	General Aspects for the Design of SPECT Tracers	231
7.3	Peptide-Receptor Radionuclide Imaging.....	235
7.3.1	Somatostatin Analogs.....	235
7.3.2	Bombesin Analogs.....	239
7.3.3	Neurotensin Analogs	242
7.3.4	Other Peptide-Based Radiotracers.....	243
7.4	Antibodies and Antibody Fragments	245
7.4.1	Targeting Fibronectin Extra-Domain B: Antiangiogenic Antibody Fragment L19.....	247
7.5	Vitamin-Based Radiotracers	247
7.5.1	Folic Acid Conjugates.....	248
7.5.2	Vitamin B ₁₂ Conjugates	251
7.5.3	Other Vitamin Targeting Agents—Pretargeting	253

H.-J. Pietzsch (✉) · C. Mamat
Helmholtz-Zentrum Dresden-Rossendorf (HZDR), Institute of Radiopharmaceutical
Cancer Research, Dresden, Germany
e-mail: h.j.pietzsch@hzdr.de

C. Mamat
e-mail: c.mamat@hzdr.de

C. Müller · R. Schibli
Center for Radiopharmaceutical Sciences ETH-PSI-USZ, Paul Scherrer Institute, 5232,
Villigen-PSI, Zürich, Switzerland
e-mail: cristina.mueller@psi.ch

R. Schibli
e-mail: roger.schibli@psi.ch

R. Schibli
Department of Chemistry and Applied Biosciences, ETH Zurich, 8093 Zurich, Switzerland

7.6	Intracellular Targets.....	256
7.6.1	^{99m} Tc-Carbohydrate Complexes.....	256
7.6.2	Radiolabeled Nucleoside Analogs for Targeting Human Thymidine Kinase...	258
7.6.3	Radioiodinated meta-Iodobenzylguanidine (MIBG).....	260
7.7	Glutamate-Ureido-Based Inhibitors of Prostate-Specific Membrane Antigen (PSMA).....	261
7.7.1	¹²³ I- and ¹³¹ I-Labeled PSMA Radioligands	262
7.7.2	^{99m} Tc-Labeled PSMA Radioligands	263
7.8	Sentinel Lymph Node (SNL) Localization	264
7.9	Optimization of SPECT Tracer Design and Potential Reasons for Failure.....	266
7.10	Summary and Conclusion	266
	References.....	268

7.1 Introduction

Single photon emission computed tomography (SPECT) and positron emission tomography (PET) are valuable molecular imaging modalities as both are capable of detecting minute amounts of radioactive tracer [232, 272]. Clinical PET is currently about 2–3 orders of magnitude more sensitive than SPECT, has a better spatial resolution, and offers superior quantification. Nowadays, many nuclear imaging centers possess PET or PET/CT scanners. However, the large infrastructure that is needed for the production of β^+ -emitting radioisotopes (e.g., ¹⁸F, ¹¹C, ⁶⁴Cu, ⁶⁸Ga, ⁴⁴Sc) makes PET an expensive technology. At the moment, an approved clinical grade generator for PET radioisotopes is only available for ⁶⁸Ga. Hence, for routine application SPECT is still the state-of-the-art nuclear imaging modality because it is less expensive and can make use of a broader array of suitable and available radionuclides (Table 7.1). Importantly, SPECT imaging is a useful technology for monitoring targeted radionuclide therapy employing radioisotopes that emit—concomitantly with the therapeutic radiation— γ -rays of suitable energies for SPECT (e.g., ¹⁷⁷Lu, ^{188/186}Re, ⁶⁷Cu, ¹³¹I, ²¹³Bi) [10].

Generally, SPECT radiopharmaceuticals can be classified according to their biodistribution characteristics. There are those whose tissue distribution is determined exclusively by their chemical and physical properties and those whose distribution and accumulation are determined by their specific interaction with a biological target that is expressed at the site of interest (e.g., tumor-associated receptor) [24, 157]. Herein we focus on the development and (pre) clinical application of target-specific radiotracers. A target-specific SPECT radiopharmaceutical can be divided into two main parts: a targeting biomolecule and a γ -radiation-emitting radionuclide [157]. In the case of using radiometals as the radiation source, a bifunctional chelator is needed as an additional component of the radiopharmaceutical. Thus, a metallic radioisotope is coordinated by a suitable chelating agent that is conjugated to the targeting agent via a linker entity (Fig. 7.1). In a rational design of a SPECT tracer, the single components have to be critically

Table 7.1 Selection of radioisotopes for SPECT imaging (and therapy)

SPECT isotopes	Half-life	γ -Energy [keV]	
^{99m}Tc	6.02 h	141 (89%)	
^{111}In	2.80 d	171 (91%), 245 (94%)	
^{67}Ga	3.26 d	93 (39%), 185 (21%), 300 (17%), 394 (5%)	
^{123}I	13.22 h	159 (83%)	
^{125}I	59.41 d	35.5 (93%)	
^{155}Tb	5.32 d	87 (32%), 105 (25%)	
^{197m}Hg	23.8 h	134 (34%)	
^{197}Hg	64.1 h	77 (19%), 279 (6%)	
Therapy/SPECT isotopes	Half-life	β^- -Energy _{average} [keV]	γ -Energy [keV]
^{177}Lu	6.65 d	134 (100%)	113 (10%), 208 (10%)
^{186}Re	3.72 d	347 (93%)	137 (9.5%)
^{188}Re	17.0 h	763 (100%)	155 (16%)
^{67}Cu	2.58 d	141 (100%)	185 (49%)
^{131}I	8.03 d	182 (100%)	365 (82%)

evaluated in order to achieve a balance among the demands of an adequate target binding and a rapid excretion.

The majority of diagnostic radiopharmaceuticals currently available in nuclear medicine make use of metallic radioisotopes. For SPECT imaging, technetium-99m is the most widely applied radioisotope because of its ideal physical decay properties and easy availability by a generator system (Table 7.1). Indium-111 is another SPECT radioisotope frequently used in the clinics where it is often employed as a surrogate for yttrium-90 analogs since ^{90}Y that is used for therapeutic purposes is a pure β^- -emitter. In contrast, clinical application of gallium-67 is relatively rare. Non-metallic radionuclides used for SPECT are basically the isotopes of iodine. Iodine-123 is the preferred isotope for imaging purposes (Table 7.1) due to its dosimetry and imaging characteristics that are superior to iodine-131 and iodine-125.

A targeting biomolecule serves as a “carrier” for specific delivery of the radionuclide to the target-expressing cells of interest. Such biomolecules could be biomacromolecules like specific antibodies (or antibody fragments) or small-molecular-weight molecules (e.g., peptides, vitamins, nucleosides). Each class of targeting agents has its pros and cons for its use in diagnostic nuclear medicine and for a potential translation to therapeutic applications. Peptide-based radiopharmaceuticals represent by far the largest group of tumor-targeted nuclear imaging agents currently in use.

During tracer development, the first steps are based on chemistry and molecular biology methods such as peptide syntheses, conventional or combinatorial chemistry, and phage display techniques for preparation, identification, and isolation of high-affinity binders to a particular receptor. Determination of the tumor-targeted radiotracer’s stability *in vitro* and its ability to bind with high affinity to the target

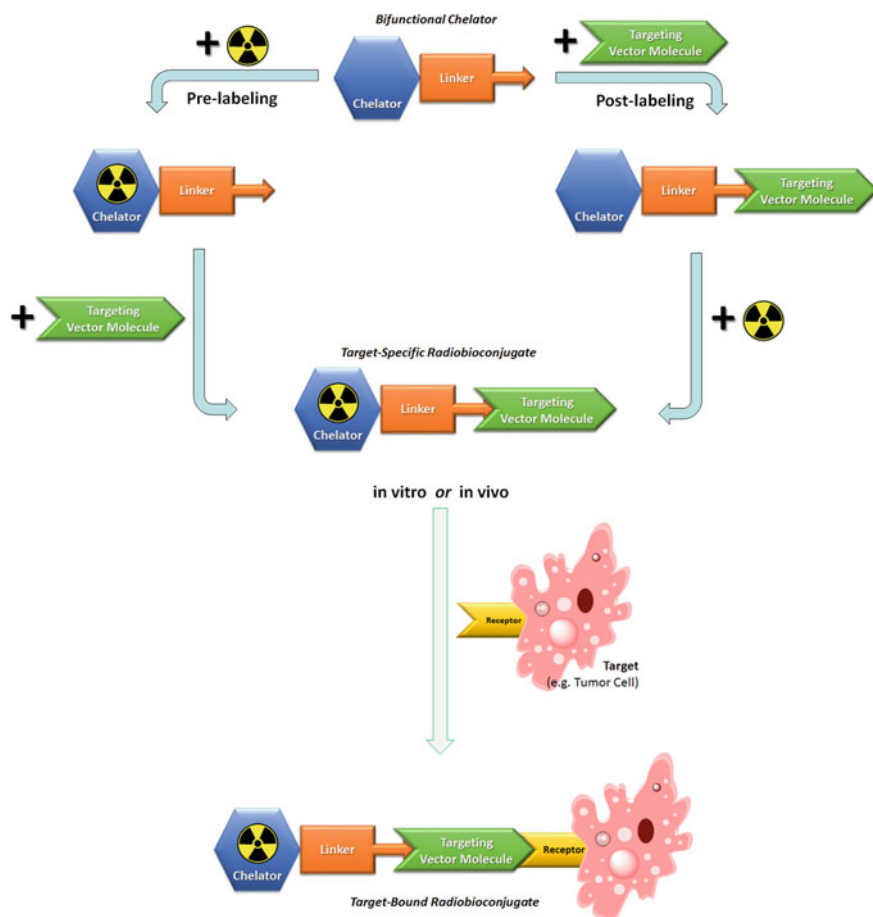


Fig. 7.1 Schematic representation of a biomolecule (targeting vector molecule) that is conjugated to a radiometal. The bifunctional chelator that is conjugated to the target-specific biomolecule is necessary for coordination of the radiometal. Two strategies are possible to conjugate the biomolecules to the chelator and the radionuclide: pre-labeling and post-labeling. After radiolabeling, the target-specific radiobioconjugate was intravenously administered, binds to the tumor cell surface-associated target (e.g., receptor) and allows visualization of target-expressing malignant lesions via SPECT

structure on cultured cancer cells are the first requirements in this early development stage. The *in vitro* evaluation is followed by investigations *in vivo* using an adequate animal model, typically tumor-bearing small rodents. It is important to recognize that radiolabeled tumor imaging agents display different biodistributions and pharmacokinetics in animal models compared to humans due to a different metabolism, differences in the volume of distribution, and potential cross-reactivity of the targeting entity with normal tissues expressing the target receptor or antigen

in humans [42]. Significant variability in the tissue distribution of radiotracers might occur among different animal models (e.g., mice vs. rats) or different animal strains (e.g., nude mice vs. normal mice). However, small rodents have emerged as generally the most useful and cost-effective animal models for developing and evaluating radiotracers and to test new experimental approaches to increase their localization in tumors. Postmortem biodistribution studies allow the detection and quantification of a cumulated activity portion in targeted and non-targeted tissues, and thus the determination of the radiotracer's pharmacokinetic profile. Collection of blood and tissue samples for identification of metabolites at different time points after radiotracer application provides information about the radiotracer's circulation time and its *in vivo* stability. By increasing the availability of small-animal SPECT and SPECT/CT scanners in recent years, the process of radiotracer development has been significantly improved and accelerated while the number of test animals required has been reduced. Thus, a wide variety of targeted SPECT radiotracers are currently being developed and preclinically tested for imaging of various tumor types expressing one or more of the most relevant receptor types [247].

The focus of this chapter is to present general aspects for the design of SPECT tracers followed by specific examples of recent SPECT imaging agents based on biomacromolecules like antibodies, antibody fragments, proteins as well as other small-molecular-weight biomolecules such as peptides, vitamins, or nucleosides referred to as vector molecules. The examples demonstrate possibilities for optimization of the tracer design by tuning single components of these imaging agents. Finally, potential causes for failures in SPECT tracer design are discussed.

7.2 General Aspects for the Design of SPECT Tracers

The ideal SPECT tracer exhibits excellent tissue penetration, high affinity to the target structure, specific uptake and retention in the target cells, and rapid clearance from non-targeted tissues and organs. In addition, it is highly stable *in vivo*, easy to prepare, and safe for human application. These aspects are crucial because injected radiotracers that are not stable, not bound to the target, or not rapidly excreted create high background signals resulting in low tumor-to-background contrast, false positive results, and unnecessary radiation dose burden to the patient [10].

In the case of metallic radioisotopes, a bifunctional chelator is needed that is covalently linked to a biomolecule [157]. Since the stability of the radiometal complex is a critical aspect for the success of a radiopharmaceutical, it is important to choose an ideal chelating system that allows the formation of radiometal complexes of high thermodynamic stability and kinetic inertness [24]. Among the SPECT isotopes currently in use, technetium-99m is still the workhorse of diagnostic nuclear medicine. It is used in the majority of diagnostic scans conducted each year in hospitals worldwide. The preferred use of ^{99m}Tc -radiopharmaceuticals reflects the ideal nuclear properties of the isotope and, until recently, the convenient availability from commercial $^{99}\text{Mo}/^{99m}\text{Tc}$ -generators.

Technetium is a transition metal that presents a major challenge with respect to designing radiopharmaceuticals with favorable in vivo properties. In order to link the radionuclide to a targeting molecule, [^{99m}Tc]pertechnetate with Tc in the oxidation state +VII that is eluted from the $^{99}\text{Mo}/^{99m}\text{Tc}$ -generator must be reduced to build a complex with an appropriate bifunctional chelating system, most commonly in the oxidation state +I, +III or +V. The $^{99m}\text{Tc(V)}$ -oxo and $^{99m}\text{Tc(V)}$ -organohydrazino cores are most extensively studied (Fig. 7.2). The $^{99m}\text{Tc(V)}$ -oxo-core generally adopts a square-pyramidal geometry with the π -bonding oxo-group in the apical position. The core is stabilized by σ - and π -donating groups where amino, amido, and thiolate ligands as well as tetradentate ligands of the N_xS_{4-x} -class have been investigated [24, 157, 211]. A prominent example of a tetradentate chelator is the peptide-based chelator mercapto-acetylglycylglycylglycine (H_5MAG_3) [150].

An alternative approach is the use of the $^{99m}\text{Tc(V)}$ -organohydrazino nicotinamide (HYNIC) core that was first introduced by Abrams et al. 20 years ago [1, 250]. The advantages of this system are the facile functionalization of targeting entities via amide linkage. It has therefore been used for ^{99m}Tc -labeling of a variety of high, medium, and small-molecular weight biomolecules [65, 66, 83, 107, 161, 235, 274, 279, 296]. Since the HYNIC chelator can only occupy one or two coordination sites on the metal center, co-ligands such as tricine are needed to complete the coordination sphere of ^{99m}Tc [74, 160, 219]. The possibility for selection of appropriate co-ligands is advantageous for an easy modulation of the hydrophilicity and pharmacokinetics of the ^{99m}Tc -HYNIC-derivatized biomolecules. However, the presence of multiple species in solution due to different bonding modalities of the HYNIC moiety and co-ligands might be problematic for a commercial development, because of the increasing regulatory hurdles and the requirements of fully characterized products.

Another, less frequently employed approach is the use of a $^{99m}\text{Tc(V)}$ -dioxo-core coordinated by nitrogen ligands that form octahedral complexes with the oxygens *trans* to each other [129]. The group of Nock and Maina made successful use of a tetraamine chelator for ^{99m}Tc -radiolabeling of several peptide-based biomolecules forming monocationic polar complexes with the $^{99m}\text{Tc(V)}$ -dioxo core [171, 205, 207]. The advantages of this radiolabeling strategy include its easy formation at

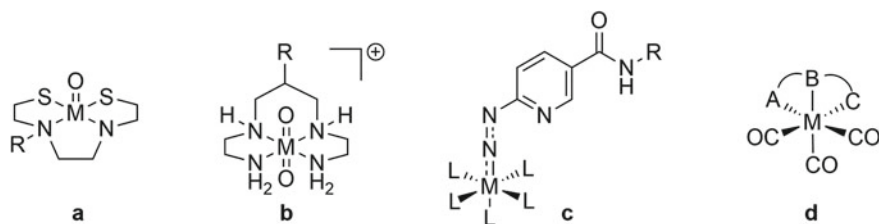


Fig. 7.2 The most frequently used ^{99m}Tc -complexes for radiobioconjugates. **a** $^{99m}\text{Tc(V)}$ oxo core, **b** $^{99m}\text{Tc(V)}$ dioxo core, **c** $^{99m}\text{Tc(V)}$ organohydrazino nicotinamide (HYNIC) core, and **d** $^{99m}\text{Tc(I)}$ -tricarbonyl core. M = ^{99m}Tc , L = co-ligands

ambient temperature, its high stability in the biological milieu, and considerable hydrophilicity.

A completely different ^{99m}Tc -radiolabeling strategy has been introduced by the development of the tricarbonyl technique which offered new opportunities for the design of $^{99m}\text{Tc}(\text{I})$ -radiotracers [6–9, 75, 76, 240, 241]. The water-soluble $^{99m}\text{Tc}(\text{I})$ -tricarbonyl precursor's aqua ligands are readily exchanged allowing the coordination of preferentially tridentate chelators that can be modified to provide complexes with cationic, neutral, or anionic overall charge [92, 174, 194, 216, 240, 251]. In addition, the tricarbonyl radiolabeling strategy is also accessible for the preparation of stable radiometal complexes using β -particle-emitting rhenium isotopes ($^{186/188}\text{Re}$, Table 7.1). Hence, the production of isostructural compounds with the "matched pair" $^{99m}\text{Tc}/^{188/186}\text{Re}$ for diagnostic and therapeutic purposes has become feasible thanks to the tricarbonyl strategy, a feature which is often not fulfilled with $\text{Re}(\text{V})$ complexes [195].

Radiolanthanides (e.g., ^{177}Lu) and lanthanide-like isotopes as well as indium and gallium are used in the oxidation state +III. They can generally be coordinated by polyaminopolycarboxy chelating systems. Coordination numbers of lanthanides are typically between seven and ten whereas coordination numbers of eight or nine are most common in $\text{Ln}(\text{III})$ complexes with polydentate chelators. The 1,4,7,10-tetraazacyclododecane-1,4,7,10-tetraacetic acid (DOTA) chelator emerged as particularly useful for lanthanide coordination of therapeutic radiopharmaceuticals because of the formation of metal complexes of extremely high thermodynamic stability and kinetic inertness (Fig. 7.3). In addition, the hydrophilic acetate chelating arms of DOTA favor a fast clearance of radiotracers from the blood and non-targeted organs and tissues. Despite the similarities of the SPECT radioisotopes gallium-67 and indium-111 they are different in size, coordination number, and charge density. Ga^{3+} has a small ionic radius (0.65 Å) and the coordination number is six whereas the ionic radius of In^{3+} is larger (0.92 Å) and it is seven- or eight-coordinated in its complexes. The structural differences among Ga and In complexes might have an influence on the overall tissue distribution of one and the same bioconjugate as recently exemplified with a somatostatin analog [114]. A higher tumor uptake and a lower kidney retention have been reported for ^{67}Ga -DOTATOC compared to that of ^{111}In -DOTATOC. Whereas DOTA appears to be an ideal chelator for coordination of lanthanide (radio)isotopes like Lu^{3+} or In^{3+} , its coordination cavity is not ideal for Ga^{3+} as it is too large. On the other hand, there is a perfect fit between the size of Ga^{3+} and the coordination cavity formed by the N_3O_3 donor atoms of the macrocyclic 1,4,7-triazacyclononane-1,4,7-triacetic acid (NOTA) chelator [157]. Consequently, a higher thermodynamic stability constant has been found for Ga-NOTA complexes compared to those of Ga-DOTA-complexes [67]. In some cases, open chelating systems are more favorable than macrocycles because they are capable to form radiometal complexes at ambient temperature which is particularly important for temperature-sensitive targeting agents. Examples are variable versions of diethylenetriamine pentaacetic acid (DTPA, CHX-A"-DTPA, etc., Fig. 7.3). DTPA is one of the most commonly employed acyclic ligands in radiochemistry useful for coordination of ^{111}In , ^{67}Ga ,

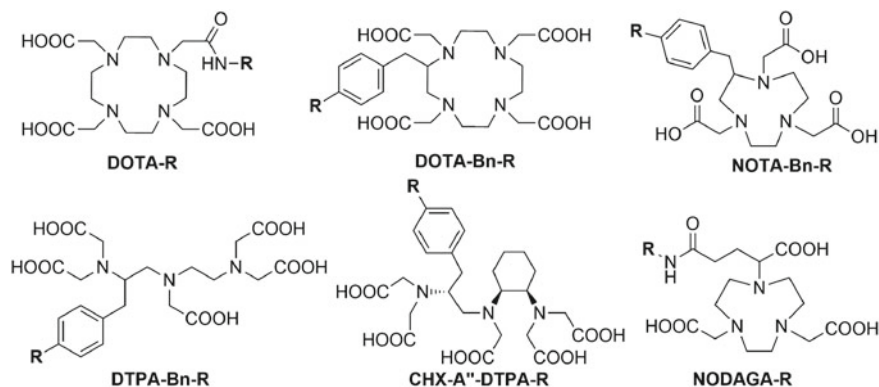


Fig. 7.3 The most frequently used macrocyclic (DOTA, NOTA) and acyclic (DTPA) chelators for complexation of radioisotopes for SPECT imaging (e.g., ^{111}In , ^{67}Ga) and combined therapy/SPECT imaging (e.g., ^{177}Lu)

and radiolanthanides. For ^{111}In -complexation DTPA emerged as the ideal chelating agent [173].

In addition to the bifunctional chelator's function for stable coordination of the radiometal, the linker entity is important for conjugation with the biomolecule and might influence the overall pharmacokinetics of the radiopharmaceutical. By affecting the biomolecule's lipophilic or hydrophilic characteristics the linker system can serve for controlling its in vivo behavior. Thus, the nature of a bifunctional chelator in terms of geometry, lipophilicity, and overall charge plays a crucial role in determining the biodistribution of (tumor-) targeted radiopharmaceuticals [24].

Functionalization of amino acid side chains (e.g., lysine, cysteine) with chemically reactive probes of bifunctional chelators is a largely uncontrolled random process that results in a heterogeneous mixture of conjugates modified at variable sites. A considerable advantage of small-molecular weight biomolecules (e.g., peptides and vitamins) is the fact that derivatization with a bifunctional chelating agent can be governed by specific chemical reactions that yield a single, clearly defined species. In contrast, loss of binding affinity is of concern during the process of antibody derivatization because modification of the Fab region (antigen-binding site) can possibly have deleterious effects on the target binding of the protein. Both loss of binding activity to the target and overlabeling effects are highly undesired processes because they result in unwanted background radiation and unspecific accumulation of the antibody radioconjugates in the liver. For this reason, recent endeavors were undertaken for the development of site-specific derivatization via enzymatic reactions that are selective for a particular amino acid [128, 185] or sugar residue [34] at a specified site of the antibody.

Since small-molecular-weight molecules are usually stable at a broad range of temperatures and pH values, the radiolabeling procedure is mostly smooth and quantitative. In contrast, proteins are generally sensitive to elevated temperatures.

Thus, commonly applied methods for radiometal-labeling of proteins are time-consuming due to the low reaction temperature applicable. To overcome this drawback, pre-labeling strategies have been proposed allowing the preparation of radioimmunoconjugates within a shorter period of time while preventing the risk of affecting the antibody's scaffold under possibly harsh conditions needed for direct radiolabeling strategies [153, 302].

7.3 Peptide-Receptor Radionuclide Imaging

Since receptors for regulatory peptides are overexpressed in a variety of human cancers, it is a prominent strategy to use radiolabeled analogs of these physiologically occurring peptides for tumor-targeted nuclear imaging. Advantages of using peptides are their good tissue penetration, a fast clearance, and minimal immunogenicity [247]. Small peptides of usually less than 40 amino acid residues are easily accessible through solid-phase peptide synthesis. Their tolerance toward bulky modification and resistance toward harsh chemical conditions that are sometimes inevitable during radiolabeling procedures are further advantages. Importantly, a formulation of a radiolabeled peptide consists of identical molecules with a well-defined structure. Clearly, the most outstanding example of success in the field of peptide-based diagnostic and therapeutic nuclear medicine has been the use of somatostatin analogs for targeting the somatostatin receptor [144]. Somatostatin-derived tracers designed to image somatostatin receptor subtype 2 (sst2)-expressing tumors have enjoyed almost two decades of successful preclinical development and extensive clinical application. This example has paved the path for further exploration of radiolabeled peptides targeting other tumor-associated receptors such as gastrin-releasing peptide receptors, neurotensin receptors, or cholecystinin receptors [29, 225].

7.3.1 Somatostatin Analogs

The prototypes of radiolabeled peptides for SPECT imaging are the somatostatin analogs commonly labeled with ^{111}In or $^{99\text{m}}\text{Tc}$. Somatostatin receptors are overexpressed on neuroendocrine tumors including pituitary adenomas, pheochromocytomas, paragangliomas, neuroblastomas, and medullary thyroid cancers. From the five subtypes of somatostatin receptors belonging to the G-protein coupled receptors, subtype 2 is the most widely overexpressed form in neuroendocrine tumors. In the beginning of their development, somatostatin analogs suffered from rapid degradation *in vivo*. Such limitations have been overcome by stabilization strategies through the development of synthetic peptides. Peptides of high chemical stability became accessible by introduction of D-amino acids or other unnatural amino acids at known cleavage sites, cyclization, or modification of C- and N-termini via amidation, reduction, alkylation, or acylation [247]. The clinically

approved ^{111}In -labeled DTPA⁰-octreotide (OctreoScan) has proven to be a successful and versatile molecular imaging agent (Figs. 7.4 and 7.5). The most frequently used DOTA-coupled, somatostatin-based peptides are [DOTA⁰, Tyr³]-octreotide and [DOTA⁰, Tyr³, Thr⁸]-octreotate usually referred as DOTATOC and DOTATATE (Fig. 7.4). These analogs have also been successfully employed for therapeutic purposes when radiolabeled with particle-emitting radioisotopes (e.g., ^{177}Lu , ^{90}Y). Several sst2-binding somatostatin analogs are currently used in the clinic. Further research projects are focusing on the development of new and improved somatostatin analogs with a broader receptor subtype affinity profile. Such compounds would extend the range of targeted cancer candidates and increase the net tumor uptake when several receptor subtypes are expressed on the same tumor cell [112, 184].

Although [^{111}In]In-DTPA-(D-Phe¹)-octreotide proved to be reliable for the detection of neuroendocrine tumors (NET), the potential clinical advantage of $^{99\text{m}}\text{Tc}$ -labeling in comparison to radiolabeling with ^{111}In led to the development of $^{99\text{m}}\text{Tc}$ -labeled somatostatin analogs. [$^{99\text{m}}\text{Tc}$]Tc-EDDA-HYNIC-TOC ($^{99\text{m}}\text{Tc}$ -Tektrotyd) is a radiopharmaceutical indicated for diagnosis of tumors with overexpression of SSTR, especially subtype 2 (SSTR2) [15, 90, 143, 285].

The complex formation requires the use of a coligand such as tricine or ethylenediamine diacetic acid (EDDA). The coordination mode of HYNIC with $^{99\text{m}}\text{Tc}$ is not known exactly. Usually, a monodentate “end-on”-N=N- coordination is proposed (Fig. 7.4).

The generally high kidney uptake of radiometallated peptides due to their reabsorption in the renal proximal tubules is a drawback for peptide-based tumor targeting as it may lead to reduced contrast and quality of diagnostic imaging and damage radiosensitive kidneys if applied for therapeutic purposes [104]. Thus, several strategies to reduce tubular reabsorption of peptidic radiotracers have been investigated. One strategy relies on the chemical modification of the peptide with entities or overall charges that would potentially reduce renal uptake. A successful example of such modification is given by the work of Schwaiger and co-workers who developed ^{125}I -somatostatin analogs modified with carbohydrate entities [248, 305]. Glycation modified the physicochemical behavior of the radiotracers in that pharmacokinetics were significantly improved as shown by reduced hepatic uptake and biliary excretion and a rapid clearance from the circulation via the kidneys without increasing renal accumulation of radioactivity. Another approach is based on the administration of additional substances for potential inhibition of peptide reabsorption. In this respect the co-infusion of the cationic amino acids lysine and arginine is the most prominent example since this combination successfully reduced renal accumulation of radiolabeled somatostatin analogs in preclinical studies [31, 61, 294] and in patients [111, 229].

Originally, it was proposed that peptide agonists that are efficiently internalized into receptor-expressing cancer cells would be the best candidates for tumor imaging [48]. However, the two somatostatin analogs ^{111}In -DOTA-sst2-ANT and ^{111}In -DOTA-sst3-ODN-8 showed extremely high tumor accumulation despite being receptor antagonists [100]. It could be shown in vitro that a more than 15-fold

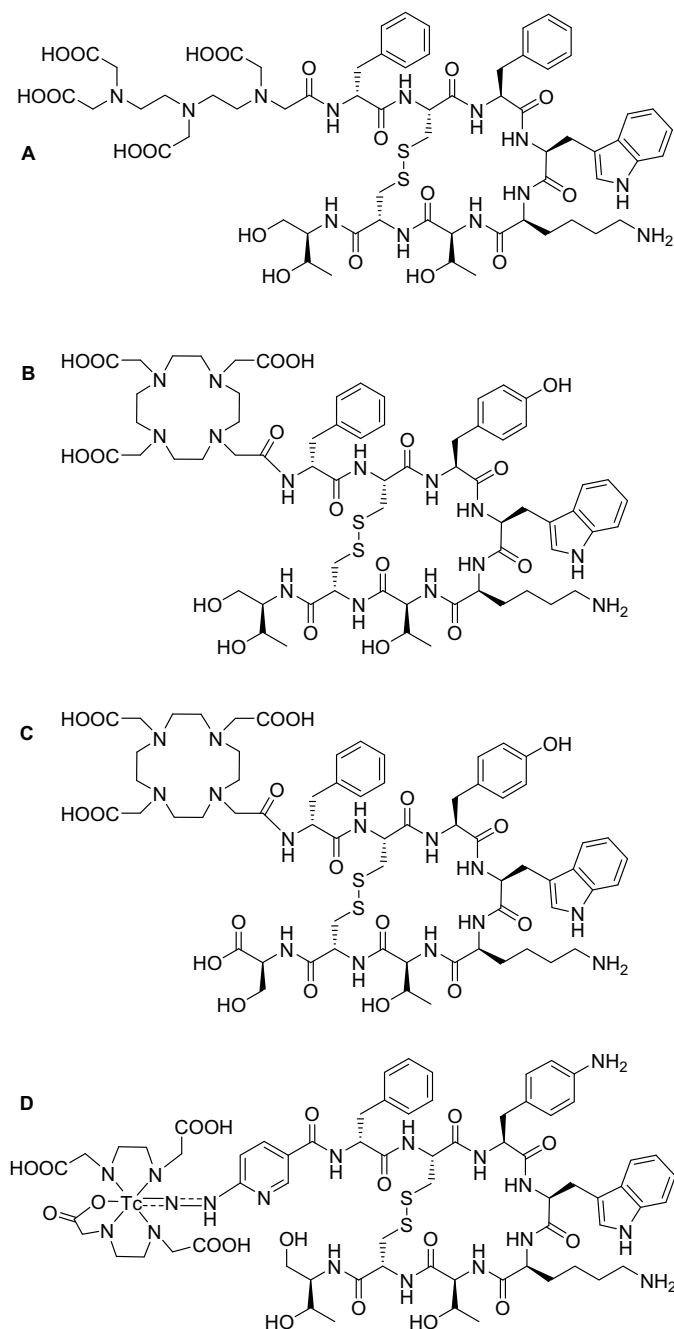


Fig. 7.4 Chemical structures of DTPA- and DOTA-modified somatostatin analogs for targeted diagnosis and therapy of somatostatin receptor-positive cancer diseases. **a** DTPA⁰-octreotide, **b** DOTA⁰-Tyr³-octreotide (DOTATOC), **c** DOTA⁰-Tyr³-Thr⁸-octreotide (DOTATATE), **d** [^{99m}Tc] Tc-EDDA-HYNIC-TOC (^{99m}Tc-Tektrotyd)

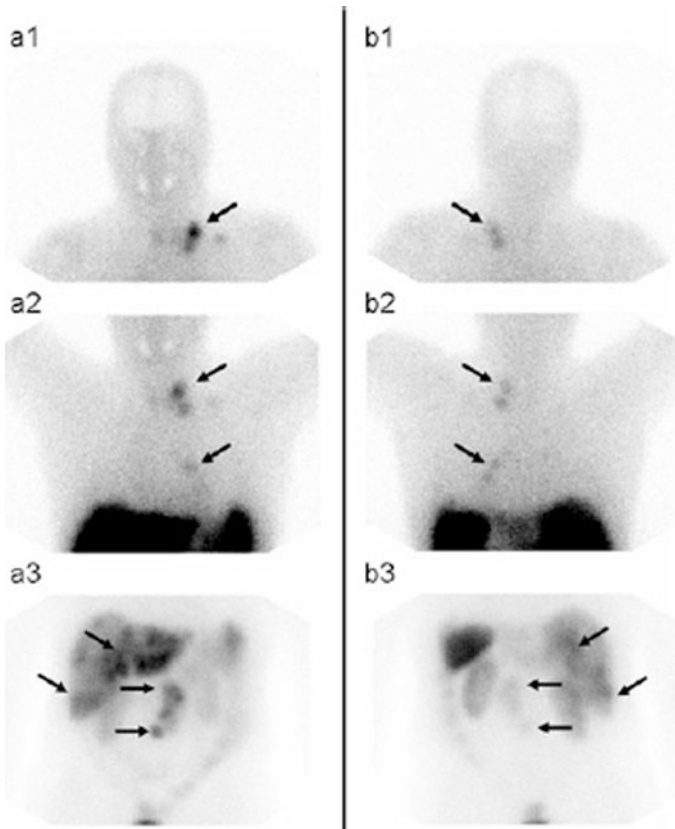


Fig. 7.5 Scintigraphy [multiple planar spot views, anterior **a** and posterior **b** of the head/neck (1), thorax (2), and abdomen (3)] performed 24 h after injection of ^{111}In -octreotide (OctreoScan; Covidien, Petten, the Netherlands) in a patient diagnosed with a well-differentiated endocrine carcinoma (carcinoid) with lymphogenic spread in the abdomen and supraclavicular and multiple metastatic lesions in the liver and lungs. The images have been kindly provided by J.J.M. Teunissen (MD, Ph.D.), Erasmus Medical Center, Rotterdam, The Netherlands

increased number of binding sites per cell were accessible for antagonists compared to their agonist analogs and in addition slow ligand dissociation from the receptor was determined. These findings attracted the attention of many research groups and led to the development of further *sst2*-binding somatostatin-based antagonists. The studies confirmed that high-affinity somatostatin receptor antagonists that poorly internalize in tumor cells exhibit improved tumor-targeting characteristics than corresponding agonists. The fact that this phenomenon was found not only for *sst2*-selective compounds but also for *sst3*-selective compounds suggests that this phenomenon is valid for more than just one particular receptor [47].

7.3.2 Bombesin Analogs

The bombesin receptor family comprises four receptor subtypes whereof the gastrin-releasing peptide (GRP) receptor or bombesin receptor subtype 2 (BB2) has been studied most thoroughly [268, 269]. The impetus for targeting the GRP receptor is based on the fact that a variety of human tumors overexpress GRP receptors including prostate, breast, and small cell lung cancers [106, 177, 187, 256]. The development of ^{99m}Tc - and ^{111}In -bombesin analogs has been the focus in recent years in many research laboratories (Table 7.2) [20, 206, 288]. De Barros and colleagues presented a BBN-kit using HYNIC and EDDA as chelating source for ^{99m}Tc [59]. A detailed summary was published by Moreno et al. in 2016 [188]. The tricarbonyl technique, which was developed in view of the opportunity to use ^{99m}Tc and ^{188}Re as matched pair for diagnosis and therapy [6, 242], has been employed most extensively for radiolabeling of bombesin analogs [85, 86, 91–93, 145, 226, 230, 251, 266, 267, 317]. A drawback of this strategy is, however, the fact that the most $^{99m}\text{Tc}/^{188}\text{Re}$ -tricarbonyl-based bombesin derivatives are predominantly cleared via the hepatobiliary excretion pathway because of the tricarbonyl's inherent lipophilicity [64]. Increasing the hydrophilicity of radiolabeled GRP-targeting peptide conjugates is necessary because accumulation of radioactivity in the liver and intestinal tract would compromise their capacity to effectively image solid tumors and metastatic lesions in the abdomen. This has been accomplished, for example, by introduction of “innocent” peptide sequences such as polylysine, polyglycine, or polyaspartic acid residues [159]. Additionally, it was shown that the introduction of a polar serylserylserine spacer into ^{99m}Tc -tricarbonyl pyrazolyl bombesin analogs resulted in a longer retention time of the radiotracer in the tumor tissue compared to analogs with more lipophilic linker entities consisting of β -alanine or triglycine [12]. Based on the promising results experienced with somatostatin analogs conjugated to carbohydrates [230, 248, 305], glycation of bombesin tracers was approached with the aim to increase their overall hydrophilicity [251]. In this respect Garcia et al. tested three different bombesin analogs in vitro and in vivo. One of the derivatives was modified with a linker bearing a lysine that was coupled to the glycomimetic shikimic acid at the ϵ -amino group. Another bombesin derivative was glycated via an Amadori rearrangement and the third compound was a bombesin analog derivatized with an azido-glucose that was connected to an alkyne-functionalized linker entity via the Cu-catalyzed click reaction (Table 7.2). The introduction of polar carbohydrates had no negative effects on the in vitro stability and the internalization or efflux profile of the radiotracers in cultured tumor cells. In contrast, these modifications led to a significant reduction in abdominal radiotracer accumulation, a clearly higher tumor uptake, and thus improved tumor-to-background ratios in vivo. The best results were obtained with the bombesin analog modified via a “click” reaction that contained a triazole-coupled glucose entity. The tissue distribution could be clearly ameliorated as demonstrated via SPECT/CT imaging studies where the tumor uptake was shown to be increased (Fig. 7.6).

Table 7.2 Sequence of various bombesin analogs

Analog	Chelator	Linker	1-6	7-13	14
Bombesin			pGlu-Gln-Arg-Leu-Gly-Asn-	-Gln-Trp-Ala-Val-Gly-His-Leu-	-Met-NH ₂
Demobesin-1	N4	-BzDig-	-DPhe-	-Gln-Trp-Ala-Val-Gly-His-Leu-	-Met-NH ₂
KBBN ₅₀	HYNIC	-βAla-		-Gln-Trp-Ala-Val-Gly-His-Leu-	
BBS-1	(N ⁹ His)Ac-	-βAla-βAla-		-Gln-Trp-Ala-Val-Gly-His-Leu-	
BBS-2	(N ⁹ His)Ac-	Lys(sha)-βAla-βAla-		-Gln-Trp-Ala-Val-Gly-His-Leu-	
BBS-3	(N ⁹ His)Ac-	Lys(Amd)-βAla-βAla-		-Gln-Trp-Ala-Val-Gly-His-Leu-	
BBS-4	(N ⁹ His)Ac-	-Ala(^N TG)-βAla-βAla-		-Gln-Trp-Ala-Val-Gly-His-Leu-	
MP2653	DTPA		-aCmpip-Tha-	-Gln-Trp-Ala-Val-βAla-His-Tha-	-Nle-NH₂
MP2346	DOTA		-Pro-Gln-Arg-Tyr-Gly-Asn-	-Gln-Trp-Ala-Val-Gly-His-Leu-	-Met-NH ₂
Pesin	DOTA	-dPEG ₄ -		-Gln-Trp-Ala-Val-Gly-His-Leu-	-Met-NH ₂
AMBA	DOTA	-CH ₂ CO-Gly-(4-aminobenzoyl)-		-Gln-Trp-Ala-Val-Gly-His-Leu-	-Met-NH ₂
RM 1	DOTA	-CH ₂ CO-Gly-(4-aminobenzoyl)-	-Phe-	-Gln-Trp-Ala-Val-Gly-His-Leu-	-Leu-NH₂

Lys(sha) = lysine-coupled shikimic acid, Lys(Amd) = Amadori Product; Ala(^NTG) = triazole-coupled glucose, Sta = statyl (3S,4S-4-amino-3-hydroxy-6-methylheptanoyl)

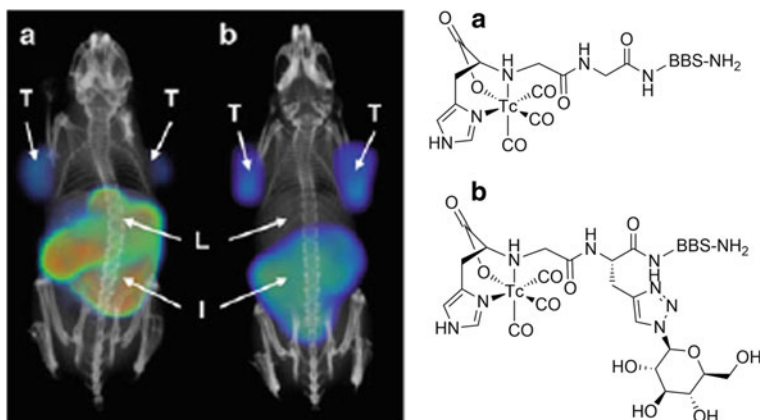


Fig. 7.6 SPECT/CT images of PC-3 tumor-bearing mice 1.5 h after injection of **a** $^{99m}\text{Tc}(\text{CO})_3\text{-(N}^2\text{His)Ac-}\beta\text{Ala-}\beta\text{Ala-}[\text{Cha}^{13},\text{Nle}^{14}]\text{BBS(7-14)-NH}_2$ (control compound) and **b** $^{99m}\text{Tc}(\text{CO})_3\text{-(N}^2\text{His)Ac-Ala}(\text{NTG})\text{-}\beta\text{Ala-}\beta\text{Ala-}[\text{Cha}^{13},\text{Nle}^{14}]\text{BBS(7-14)-NH}_2$, (NTG = N-linked triazole-linked glucose). T = tumor, L = liver, I = intestines [251]

On the other hand accumulation in the liver was significantly reduced. Despite the higher kidney uptake found for the carbohydrate bombesin analogs at early time points after injection, this decreased rapidly with time indicating that the radiotracers were not trapped in the renal tissues. By this example, the strategy of radiotracer glycation has been demonstrated as a potent method to increase the overall hydrophilicity of a tracer and thus to improve the tissue distribution.

Based on the advantages of using trivalent radiometals for preparation of site-directed diagnostic/therapeutic radiopharmaceuticals [98, 268], interest has been sparked into the synthesis and biological evaluation of trivalent radiometalated bombesin derivatives using radioisotopes such as ^{111}In or ^{177}Lu (Table 7.2) [37, 62, 121, 127, 265]. One such example is the bombesin analog referred to as DOTA-AMBA useful for both diagnostic and therapeutic purposes [119, 146, 168]. Also, a so-called pan-bombesin analog has been designed with the special characteristic of displaying high affinity to all three bombesin receptor subtypes possibly allowing a broader field of application [320].

The majority of research efforts into the design of bombesin-based radiotracers have been performed by using GRP receptor agonists. Such bombesin analogs undergo receptor-mediated endocytosis enabling residualization of the attached radiometal within the targeted tumor cell. However, ^{99m}Tc -demobesin-1 is a potent antagonist, which clearly exhibited high affinity to the GRP receptor even though significant internalization into PC-3 prostate tumor cells was not observed. This radiotracer allowed imaging of PC-3 tumors in mice with higher tumor-to-background contrast compared to the best available agonist analog [178, 205]. Furthermore, an improved quantification of the beta cell mass after pancreas visualization was accomplished with ^{99m}Tc -demobesin-4 combined with a beta cell

imaging with ^{111}In -exendin-3 in rodents [289]. Thus, endeavors were directed also toward the development of bombesin antagonists. Recently, superior imaging properties of the ^{111}In -radiolabeled bombesin antagonist RM1 over the agonist ^{111}In -DOTA-AMBA have been demonstrated [172]. Whether or not bombesin antagonists are also favorable over agonists for therapeutic purposes remains to be investigated.

Dual receptor-targeted probes based on BBN and RGD-peptides combining an integrin $\alpha_v\beta_3$ and GRPR-targeting peptide were developed, e.g., for breast cancer imaging as alternative to ultra sound [49, 125, 126]. They found that this imaging technic is a useful alternative to US but cannot replace US. Furthermore, a $^{99\text{m}}\text{Tc}$ -labeled RGD-BBN peptide was used to image lung carcinoma (Lewis lung carcinoma (LLC), U87MG human glioma, and PC-3 human prostate cancer cells) in a small-animal model. It was possible to detect subcutaneous and pulmonary metastatic Lewis lung carcinomas and to distinguish tumor from inflammation using $^{99\text{m}}\text{Tc}$ -RGD-BBN [164]. Other attempts dealt with the connection of shepherdin (79–87) to BBN as an inhibitor of the survivin-Hsp90 interaction and Hsp90 ATPase activity [86]. To use the therapeutic impact, $^{99\text{m}}\text{Tc}$ has to be located at the nucleus of the cells. For this purpose, BBN was connected to the TAT (49–57) peptide and radiolabeled with $^{99\text{m}}\text{Tc}$ with N_2S_2 as chelating moiety [237]. Cell binding and proliferation were tested showing an efficient internalization to PC-3, MDA-MB231, and MCF7 cells with a significant reduction in the cell proliferation.

7.3.3 Neurotensin Analogs

Neurotensin (NT) is a linear tridecapeptide that can be found in the central nervous system and in peripheral tissues. Among the three NT receptors (NTR), NTR1 has been found in several neuroendocrine tumor types. Of special interest are exocrine pancreatic carcinomas that overexpress NTR1 with an incidence of 75–88% [224]. Thus, several studies focused on the development of NT analogs for radiolabeling with SPECT radionuclides such as $^{99\text{m}}\text{Tc}$ [94, 95, 170] and ^{111}In [11, 63]. Similar to other small neuropeptides, neurotensin is rapidly metabolized in plasma by endogenous peptidases. Thus, neurotensin analogs which are stabilized at one or more of the three potential cleavage sites were developed. In this respect, the research group of Maina and Nock developed several $^{99\text{m}}\text{Tc}(\text{V})$ -neurotensin analogs, referred to as $^{99\text{m}}\text{Tc}$ -demotensin, employing amino acid substitutions and/or reduction in the amide bond $\text{Arg}^8/\text{Lys}^8\text{-Arg}^9$ to the corresponding amine [170, 207]. Garcia and co-workers reported the biological evaluation of neurotensin analogs in which two of the three cleavage sites have been stabilized [39, 95, 169]. These interventions allowed the preparation of neurotensin analogs of high plasma stability, affinity to the NTR1 in the nanomolar range, and significant tumor uptake in preclinical and clinical studies. A promising candidate is the $^{99\text{m}}\text{Tc}$ radiolabeled peptide ($\text{N}^Z\text{-His}$)Ac-Arg-(N- CH_3)-Arg-Pro-Tyr-Tle-Leu ($^{99\text{m}}\text{Tc}$ -NT-XII), which has been stabilized at the cleavage sites 8–9 and 11–12. Other than in the case of bombesin derivatives (see Sect. 7.3.2), the introduction of a glycomimetic entity

(shikimic acid) coupled to the side chain of an additional lysine residue did not result in an improved tissue distribution of the radiotracer. Although the expected lower kidney and liver uptake could be achieved, both the receptor affinity and the tumor uptake were unfavorably reduced. Recently, the group of Garcia reported the evaluation of a $^{99m}\text{Tc}(\text{CO})_3$ -neurotensin analog, ^{99m}Tc -NT-XIX, modified at all three cleavage sites [94, 95]. Despite a slight decrease in receptor affinity and a lower rate of internalization, the in vitro and in vivo stability of this novel radiopeptide has been significantly increased (Table 7.3).

This example of a triple-stabilized neurotensin analog demonstrates the importance of the radiotracer's metabolic stability to increase its accumulation in the tumor tissue which was—in the case of ^{99m}Tc -NT-XIX—even able to compensate a slightly lower receptor-binding affinity. The clearly improved tumor-to-background contrast of ^{99m}Tc -NT-XIX over ^{99m}Tc -NT-XII could be visualized by SPECT/CT imaging (Fig. 7.7). Thus, the development of neurotensin ^{99m}Tc -radiotracers, where single-amino acids have been substituted for peptide stabilization, is an example for optimization of a radiotracer's tissue distribution by increasing its in vivo stability.

7.3.4 Other Peptide-Based Radiotracers

Beyond somatostatin and GRP receptor targeting with bombesin and neurotensin analogs, many other regulatory peptide receptors are overexpressed on a variety of tumor types. Thus, peptide analogs in various stages of preclinical or clinical development include derivatives of cholecystokinin-2 (CCK-2) [60], glucagon-like peptide-1 (GLP-1) [138], neuropeptide Y (NPY) [322], and Arg-Gly-Asp (RGD) peptides [246] among others. CCK-2 receptors are expressed in medullary thyroid cancers. Initial gastrin-ligands for CCK-2 receptor targeting comprising a DTPA-DGlu-chelator showed unfavorable tumor-to-kidney ratios of radioactivity accumulation and were therefore not developed further. New gastrin derivatives lacking the glutamate-moiety showed excellent CCK-2 receptor affinity and lower renal retention in a rat AR42J tumor model [103]. Recently, it was found that

Table 7.3 Stability and affinity of different radiolabeled NT analogs [94]

Analog	Amino acid sequence	In vitro stability		In vivo stability	Affinity K_d (nM)
		Plasma	HT-29	Blood	
^{99m}Tc -NT-II	(N^α -His) Ac-Arg-Arg-Pro-Tyr-Ile-Leu	5.6 min	n.d.	<1 min	0.3 ± 0.2
^{99m}Tc -NT-XII	(N^α -His)Ac-Arg-(N-CH₃) Arg-Pro-Tyr- Tle -Leu	21 d	6.5 h	0.75 h	2.0 ± 1.6
^{99m}Tc -NT-XIX	(N^α -His)Ac-Arg-(N-CH₃) Arg-Pro- Dmt - Tle -Leu	28 d	2.4 d	1.40 h	15.0 ± 9.2

The modifications in the binding sequence are marked in *bold*

(N^α His)Ac Retro[N^α -carboxymethyl-histidine], *Tle* tertiary-leucine, *Dmt* dimethyltyrosine, *n.d.* not determined

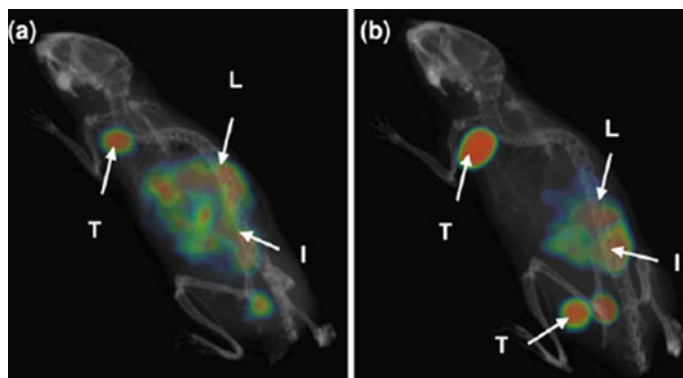


Fig. 7.7 SPECT/CT images of HT-29 tumor-bearing mice 1.5 h after injection of **a** ^{99m}Tc -NT-XII and **b** ^{99m}Tc -NT-XIX. T = tumor, L = liver, I = intestines [94]

GLP-1 receptors are highly overexpressed in virtually all insulinomas and gastrinomas [138]. Metabolically more stable GLP-1 congeners referred to as exendin-3 and exendin-4 have been derivatized with a DTPA or DOTA chelating system for radiolabeling with ^{111}In or lanthanide radioisotopes. Remarkable tumor targeting was found in a human patient while employing ^{111}In -DOTA-exendin-4 [51]. NPY analogs are of interest because of the frequent overexpression of NPY receptors in a variety of tumor types including breast cancer. A recent article reports on the synthesis and evaluation of a large number of NPY analogs where a DOTA-derivatized compound radiolabeled with ^{111}In performed as a potent radiotracer [322]. However, the *in vivo* studies with this tracer showed only a low tumor uptake whereas radioactivity retention in the kidneys was extremely high. RGD peptides that do not belong to the group of regulatory peptides are of particular interest for targeting integrin receptors such as the $\alpha_v\beta_3$ integrin. This integrin subtype is strongly expressed on activated and proliferating endothelial cells during tumor angiogenesis and metastasis but is not readily detectable in resting endothelial cells and most normal organs. Thus, a variety of RGD-peptide analogs for targeting $\alpha_v\beta_3$ integrins have been developed and the promising potential of RGD-based radiotracers for SPECT radio imaging has been shown [246]. To enhance binding affinity for the $\alpha_v\beta_3$ integrin, various multivalent cyclic RGD-based peptides have been developed. All oligomeric peptide probes bound more strongly to the target cells than the monomeric RGD peptide in an integrin $\alpha_v\beta_3$ -positive U87MG xenograft mouse model (Fig. 7.8) [260, 299].

Through RGD peptides the advantage of multivalent tumor-targeting agents over monovalent agents has been demonstrated. Most likely, the employment of the multimer-strategy also improves tumor-targeting properties of non-RGD-based peptides. Accordingly, investigations of divalent and multivalent peptides are ongoing for targeting of many of the tumor-associated receptors mentioned above, among those imaging agents for targeting the CCK-2 receptor [271] and somatostatin

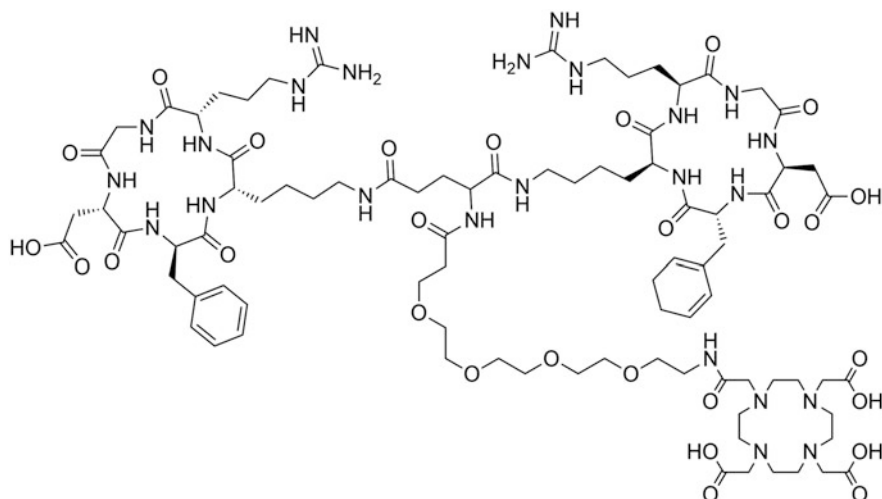


Fig. 7.8 Chemical structure of DOTA-3PEG₄-RGD dimer [158, 259]

receptor [312]. Also, the strategy of using dual tumor-targeting agents that combine targeting ligands for two different receptors (e.g., integrin and GRP receptor) might improve the radiotracer's diagnostic utility and applicability [162, 163].

7.4 Antibodies and Antibody Fragments

Another approach of nuclear imaging is the use of radiolabeled antibodies that target-specific cell surface antigens. Radioimmunoimaging has been traditionally developed in parallel with radioimmunotherapy for the evaluation of the antibodies' targeting properties and for dosimetry. Common tumor-associated targets for radioimmunoimaging (and -therapy) are epidermal growth factor receptors (EGFR) [281, 309], the carcinoembryonic antigen (CEA) [123], the prostate-specific membrane antigen (PSMA) [152], cluster of differentiation antigens (e.g., CD20), the pancarcinoma antigen (TAG-72), and the HER2 receptor among others. In addition, a number of angiogenesis markers—protein antigens expressed either on blood vessels or in the adjacent matrix of vessels—have been characterized as targets for selective delivery of antibodies to the tumor neovasculature [36]. Examples are the fibronectin extra-domain B (EDB) [204], the integrin $\alpha_v\beta_3$ [217], the vascular endothelial growth factor (VEGF) [38], and annexin A1 [209].

Potential concerns for radioimmunodiagnosis and strategies for optimization have been summarized in several review articles [41, 42, 293]. The main disadvantage of antibodies, namely their immunogenicity, could be largely overcome by the application of humanized antibodies that evade the immune system and are

resistant to degradation. However, the slow vascular clearance (days to weeks) of antibodies as a consequence of their high-molecular-weight (IgG antibodies: ~ 150 kDa) and the low tissue penetration are generally disadvantageous for radioimaging because of the resulting low target-to-non-target contrast at early time points after administration. Although it is generally accepted that antibodies are not the preferred biomolecules for nuclear imaging, the application of antibody fragments for SPECT has been successfully exemplified. Similar to peptides, antibody fragments are rapidly cleared from the blood and from non-targeted tissues. The results thereof are higher tumor-to-background ratios compared with intact antibodies and a lower radiation absorbed dose in non-targeted tissues and organs. A reduced percentage of injected doses of radioactivity in the tumor tissue and higher radiation doses in the kidneys are also consequences of the reduced size of antibody fragments [42].

Efforts have been directed toward the development of antibody fragments such as $F(ab')_2$, $F(ab')$ and single-chain Fv (scFv) fragments to achieve faster clearance from the blood and in addition a better tumor penetration [313, 314]. Application of high-affinity scFv resulted in a relatively high tumor uptake combined with a rapid blood clearance and hence favorable targeting ratios [27]. Multimers of antibody fragments may result in improved tumor localization compared with monomeric species as a result of higher affinity and slower blood clearance [134].

Another approach to achieve improved pharmacokinetics is the pretargeting strategy. Pretargeting involves an initial targeting agent, which itself can be bound by secondarily injected agents. Secondary agents are either quickly clearing radiotracers that bind the initial agent with high affinity [102, 151, 213, 249, 273] or “chase” reagents that clear an unbound radiolabeled antibody in circulation [135]. The pretargeting approach is, however, not commonly applied for SPECT. In contrast, this strategy is much more favorable for radioimmunotherapy in order to reduce the radioactive dose burden to the bone marrow and thus to avoid potential hemotoxicity of long circulating antibodies labeled with particle-emitting radioisotopes.

Radioimmunodiagnosis is of particular interest to evaluate a potential application of antibodies for targeted radionuclide therapy by interchanging a diagnostic with a therapeutic radioisotope of similar chemical characteristics (e.g., ^{111}In and ^{90}Y) or using a therapeutic radionuclide that emits concomitantly with therapeutic radiation also diagnostic γ -rays of a suitable energy for SPECT (e.g., ^{177}Lu , Table 7.1). The most prominent example of an antibody employed for radioimmunotherapy is ibritumomab tiuxetan (Zevalin), a ^{90}Y -radiolabeled monoclonal anti-CD20 antibody for the treatment of non-Hodgkins lymphoma. Its ^{111}In -radiolabeled counterpart is usually administered prior to therapy for detection of receptor-positive malignant tissue via SPECT imaging and for dosimetry.

7.4.1 Targeting Fibronectin Extra-Domain B: Antiangiogenic Antibody Fragment L19

Angiogenesis is an underlying process in many human diseases, including cancer. An established target in this respect is the extra-domain B of fibronectin (EDB), a domain of 91 amino acids, which is typically inserted in fibronectin molecules at sites of tissue remodeling but not in fibronectin molecules under normal conditions. Thus, the expression of EDB has been shown in malignant tumors but not in healthy tissues [315]. The Neri group has isolated a number of human monoclonal antibodies to EDB [43, 204, 215]. The human antibody fragment, scFv(L19) displayed subnanomolar affinity to EDB and has been shown to efficiently localize on tumoral neovasculature in animal models [68]. Importantly, the ^{123}I -labeled dimeric L19 antibody fragment L19(scFv)_2 has been evaluated for targeting primary tumors and metastatic lesions in cancer patients through immunoscintigraphy [236]. This clinical study was performed with 20 patients whereof the majority had colorectal or lung cancer. It could be demonstrated that the antibody $^{123}\text{I-L19(scFv)}_2$ selectively accumulated in malignancies and allowed distinguishing among actively growing and quiescent lesions. Another Phase I/II clinical immunoscintigraphy study used $^{123}\text{I-L19(scFv)}_2$ in patients with head and neck squamous cell carcinoma [32]. It was observed that for head and neck scintigraphy, iodinated antibodies have severe disadvantages. Although the thyroid gland was protected by competitive application of non-radioactive iodide, there were substantial artifacts in this area in all cases as a result of the uptake of liberated free iodide that was always present to a certain degree. Since dehalogenases are present in the salivary glands, free iodide also gave a high background in the 4 h postinjection scintigraphy in the parotid and submandibular glands as well as in the minor salivary glands of the oral and nasal mucosa. Although the $^{123}\text{I-L19(scFv)}_2$ is probably less suited as a diagnostic imaging modality for head and neck cancer, L19(scFv)_2 offers a general potential to be used as a tumor-targeting agent for both diagnostic and therapeutic purposes. Because neovasculature and tissue remodeling are required for the growth of all aggressive solid tumors, imaging approaches that use angiogenesis markers can be used for different types of cancer. An advantage of this strategy might be the fact that noninvasive imaging of angiogenesis via EDB fibronectin targeting allows the discrimination between quiescent and actively growing lesions.

7.5 Vitamin-Based Radiotracers

The use of small-molecular-weight targeting compounds is favorable to surmount the drawbacks of long circulation times and thus poor tumor-to-background contrast as well as possible immunogenicity encountered with antibodies. In this respect the application of vitamins as targeting agents provides several advantages: vitamins are small in size, inexpensive, relatively easily amenable for chemical modification, and non-immunogenic. Rapidly dividing cancer cells have an

increased demand for certain vitamins such as folates, vitamin B12 (cobalamin), biotin, and riboflavin. These B-group vitamins are required for cell survival and proliferation because they act as co-enzymes of biochemical reactions that are essential for the synthesis of amino acids and for nucleotide bases [233]. The most thoroughly investigated vitamin to be used as tumor-targeting agent is folic acid. The utility of folic acid conjugates has been widely exemplified in a variety of (pre)clinical studies for targeting the folate receptor (FR) that is overexpressed on a wide variety of cancer types [165]. Also, it has been demonstrated that vitamin B₁₂ has the potential to be used as cancer-targeting agent whereas only few studies have focused on the applicability of biotin for direct tumor targeting [233]. Since vitamins are indispensable for sustaining life, it is unlikely that a mutational arrest of vitamin uptake would occur with concomitant failure of vitamin-mediated diagnosis or therapy. This is a distinct feature of vitamins and an advantage for their application as tumor-targeting agents. Thus, using vitamin-based imaging agents is attractive and the strategy holds promise to also be used for therapeutic purposes.

7.5.1 Folic Acid Conjugates

Folic acid and folates (reduced forms) are water-soluble vitamins of the B-complex group. Humans cannot synthesize folates and hence must necessarily obtain them from food. Although only small quantities of folates are required, these vitamins are vital for various biochemical reactions including those for the synthesis of RNA and DNA, amino acid metabolism, and gene regulation. Cellular uptake of folates is accomplished by either carrier systems or the high-affinity folate receptor (FR). The FR is a glucosylphosphatidylinositol (GPI)-anchored protein that is frequently overexpressed in a variety of tumor types including cancers of the breast, ovaries, cervix, endometrium, lungs, kidneys, colon, and brain [13, 212]. In normal organs and tissues, FR-expression is highly restricted to only a few sites where it is located on the apical side of polarized epithelia in the lung, the placenta, and the choroid plexus of the brain and in the proximal tubule cells of the kidneys [13, 212, 304]. Thus, folic acid can be used as a molecular “Trojan horse” for selective delivery of attached probes to FR-positive cancer cells [165]. During the last decades, a variety of folic acid conjugates of radioisotopes useful not only for SPECT imaging (^{99m}Tc, ¹¹¹In, ⁶⁷Ga) has been developed and evaluated (Fig. 7.9) [16, 79, 130, 131, 196–198, 264]. Biodistribution studies of radiofolates in mice showed a specific uptake in FR-positive tumor (xeno)grafts, whereas unspecific radioactivity in background tissues was rapidly cleared in particular if the derivatives displayed hydrophilic properties. In the kidneys, however, high radioactivity retention was observed as a consequence of the specific binding of radiofolates to FRs expressed in the proximal tubule cells. This process results in unfavorably low tumor-to-kidney ratios of radiofolates in general. Clinical application of the two most promising candidates, ¹¹¹In-DTPA-folate [179, 261, 300] and ^{99m}Tc-EC20 [87, 149, 223], also known as ^{99m}Tc-etarfolatide or FolateScan, revealed the same phenomenon in humans that was previously found in tumor-bearing mice [181]. ^{99m}Tc-EC20 is currently

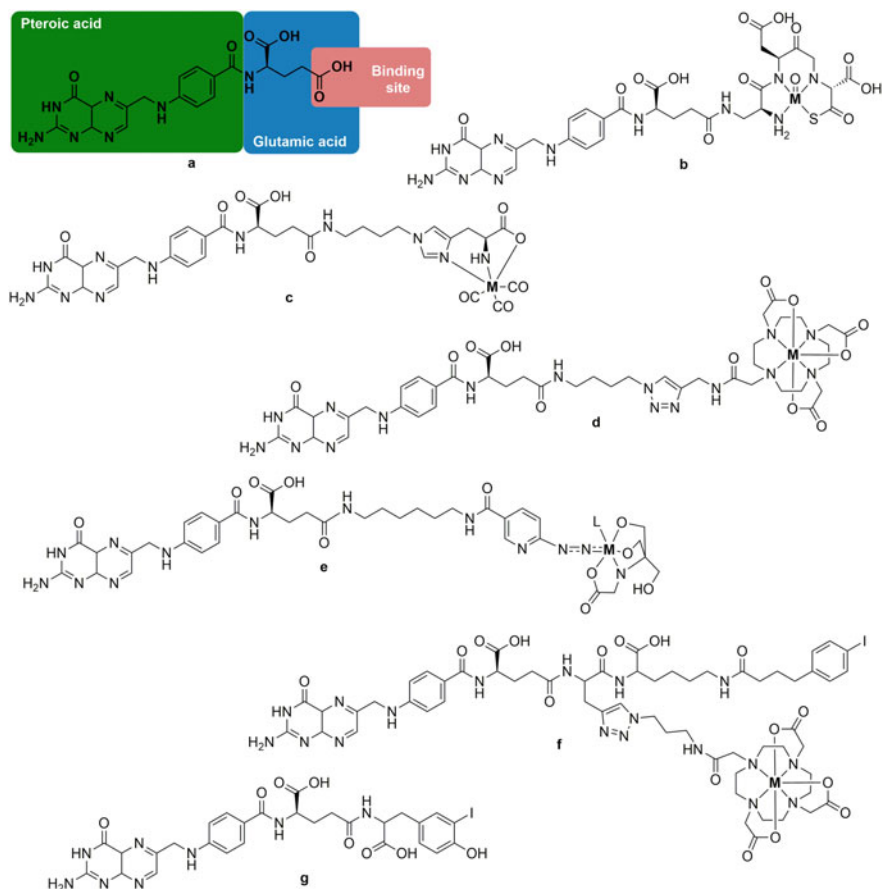


Fig. 7.9 Chemical Structures of the vitamin folic acid. **a** EC20 ($M = {}^{99m}\text{Tc}$). **b** His-folate ($M = {}^{99m}\text{Tc}$, ${}^{188}\text{Re}$). **c** DOTA-folate ($M = {}^{111}\text{In}$, ${}^{177}\text{Lu}$). **d** ${}^{99m}\text{Tc}$ -HYNIC-folate. **e** DOTA-folate with albumin-binding entity ($M = {}^{161}\text{Tb}$, ${}^{177}\text{Lu}$) **f** and ${}^{125}\text{I}$ -folate (**g**)

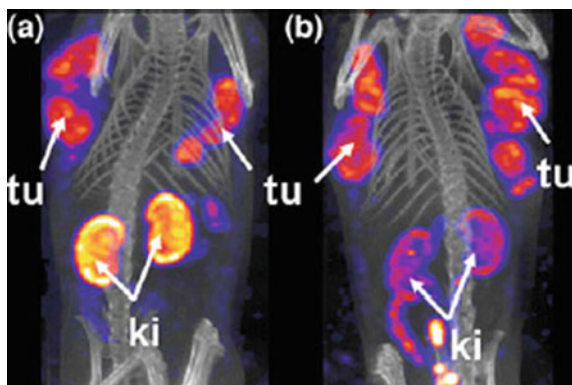
undergoing Phase 1 and 2 clinical trials in several institutions within the US and Europe. Mostly, renal cell carcinomas, pituitary adenomas, ovarian, and breast carcinomas were investigated. While imaging of malignant tissue could be successfully achieved, high radioactivity uptake was found in the kidneys of patients where the FR is expressed to approximately the same level as in mouse kidneys [212]. Healthy volunteers were enrolled in another phase I clinical study to assess the pharmacokinetics in terms of safety and radiation dosimetry. The activity of ${}^{99m}\text{Tc}$ -EC20 at 5 min postinjection was largest in the bone marrow, followed by the liver and kidneys, and decreased in all organs/tissues within 1 day without appreciable retention [310]. In a phase II multicenter study, 43 patients with advanced ovarian cancer were imaged with ${}^{99m}\text{Tc}$ -EC20 for lesion detection before

treatment with vintafolide [189]. In a 2009-reported clinical study, ^{99m}Tc -EC20 was used to determine inflammatory diseases like rheumatoid arthritis in comparison with healthy humans. It could be illustrated that imaging with ^{99m}Tc -EC20 is more sensitive for these diseases compared to physical examinations [180].

In an attempt to improve the low tumor-to-kidney ratio of radiofolates, it was hypothesized that application of antifolates (e.g., pemetrexed) could increase the “appetite” of the tumor cells for folates and thus lead to an increased accumulation of folic acid conjugates. This hypothesis was confirmed *in vitro* [190]. However, in mice that were treated with antifolates, radiofolate uptake in tumor xenografts was not increased. While approaching this hypothesis, injection of pemetrexed was accomplished at different time points prior to the radiotracer. None of the experiments revealed an increased tumor accumulation of radioactivity, however, surprisingly administration of pemetrexed short before the radiofolate resulted in a significant reduction in kidney uptake [190]. The result was a tremendous increase in the tumor-to-kidney ratio of radioactivity. This effect could be reproduced with a variety of folic acid conjugates radiolabeled with various radionuclides (^{99m}Tc , ^{188}Re , ^{111}In , ^{125}I , ^{146}Tb , ^{177}Lu) and in mouse models bearing different tumor (xeno)grafts (KB, IGROV-1, SKOV-3; M109) [191–193, 195, 199–201, 222]. The clearly superior SPECT imaging quality of mice that received pre-dosed pemetrexed could be impressively demonstrated while using ^{111}In -radiolabeled DTPA-folate (Fig. 7.10). This example demonstrates a pharmacological intervention by a non-radioactive substance that results in an improved tissue distribution of the radiotracer compared to the results obtained after radiotracer administration alone.

Another approach to reduce the kidney uptake deals with the modification of the backbone of the folate conjugate. For this purpose, an albumin-binding entity was connected to enhance the circulation time of the radioconjugate in the blood associated with an increase in the tumor-to-kidney ratio. In this regard, other radionuclides for imaging (^{44}Sc , ^{64}Cu , and ^{68}Ga for PET) and therapy (^{177}Lu , ^{47}Sc) were applied to survey the therapeutic eligibility [78, 197, 200, 264]. Other approaches dealing with the combination of bombesin (1–14) with a DOTA-FA as theragnostic

Fig. 7.10 SPECT/CT of mice injected with **a** ^{111}In -DTPA-folate only and **b** in combination with pre-dosed pemetrexed



agent labeled with ^{177}Lu for breast cancer showed a higher tumor uptake as the DOTA-FA alone in T47D-tumor-bearing mice combined with a high renal clearance [14]. HYNIC is known to bind Tc efficiently. Thus, approaches with FA-HYNIC conjugates [167] using a click chemistry approach for the linkage of the Tc-core and FA [108] and a multimerization of FA [109] were presented. However, the best tumor-to-organ ratio was found with the PEGylated monomer using KB tumor-bearing mice. Nanocarriers like PAMAM were extensively studied as well. A PAMAM-DTPA-conjugate was presented showing a high tumor accumulation (13.34%ID) combined with an uptake in the liver (9.48%ID) and the heart (6.88%ID/g) after 3 h pi in KB-bearing mice [321]. The PAMAM-HYNIC-conjugate showed a substantial accumulation in the tumor (10.61%ID/g), but the uptake in liver with 69.34%ID/g and spleen with 14.43%ID/g combined with a blood content of 7.68%ID/g was high after 3 h pi in BALB/c mice with 4T1-breast cancer [203]. Other nanocarriers based on poly(ethylene glycol)-poly(lactic-co-glycolic acid) were used with a particle size of 104–128 nm mean showing a high tumor uptake (21.3%ID/g), but also a high uptake in liver, kidneys, spleen, and blood of > 13%ID after 3 h pi in SKOV-3-bearing tumor mice. Efforts to develop nanoprobe as $^{99\text{m}}\text{Tc}$ -imaging agents were made by the use of nanographene oxide (nGO). Thus, nGO was modified with PEG and further functionalized with FA ready for labeling with $^{99\text{m}}\text{TcO}_4^-$ and SnCl_2 . A biodistribution study using mice demonstrated a long residence time in the blood; a high accumulation in liver, spleen, lung, and kidneys; and a comparatively low uptake in the tumor [77].

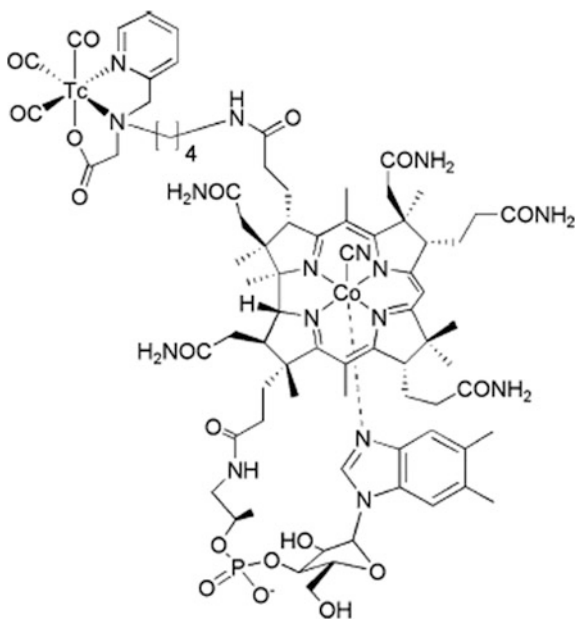
Humanized IgG1 antibodies like farletuzumab that specifically recognizes the folate receptor alpha ($\text{FR}\alpha$) were radiolabeled with ^{111}In and additionally with a fluorescent dye to use this radiopharmaceutical for the intraoperative detection of ovarian cancer lesions. ^{111}In -farletuzumab-IRDye800CW showed optimal tumor-to-blood ratios of 3.4–3.7 at protein doses up to 30 μg in mice with intraperitoneal IGROV-1 tumors and can be blocked by coinjection of an excess of unlabeled farletuzumab [113].

7.5.2 Vitamin B₁₂ Conjugates

The earliest studies of radiolabeled vitamin B₁₂ (cobalamin) using cobalt radioisotopes (^{57}Co , ^{58}Co , ^{60}Co) showed radioactivity accumulation in peripheral, actively growing tumors with highest accumulation in sarcomas [33, 88, 89]. Other studies used radioiodinated arylstannylcobalamin conjugates showing enhanced uptake into renal carcinomas in nude mice when compared with other healthy tissues and organs [307]. Collins et al. developed ^{111}In -DTPA-analogs of cobalamin (DTPA cobalamin analogs = DACs) and tested them in preliminary biodistribution experiments in mice with CCL8 sarcomas and in pigs [53]. The overall biodistribution of DACs showed tumor uptake and high radioactivity accumulation in healthy organs that were almost identical to previous studies performed with $^{57/60}\text{Co}$ -radiolabeled vitamin B₁₂. The same group reported the first patient study performed with ^{111}In -DTPA-adenosylcobalamin for cancer imaging [54].

^{111}In -DTPA-adenosylcobalamin was found to be effective for detection of high-grade aggressive tumors in humans with the most successful results in patients with breast cancer and high-grade lung, colon, thyroid, and sarcomatous malignancies [55]. However, the most significant uptake of these cobalamin derivatives was found in the liver, kidneys, and spleen followed by radioactivity accumulation in several glands. Vitamin B_{12} is bound to soluble transport proteins in circulation, namely, transcobalamin I (TCI), intrinsic factor (IF), and transcobalamin II (TCII) whereof the latter is the principle vitamin B_{12} binding protein [252–254]. TCII-cobalamin binds to TCII-receptors that are ubiquitously expressed in cells for effective acquisition of this important vitamin. Originally, vitamin B_{12} -mediated tumor targeting was thought to be dependent on undisturbed interaction of cobalamin with these main transport systems and tumor uptake were believed to be mediated via up-regulated TCII-receptors [25, 233]. Later, it was hypothesized that selective TCII non-binders would lead to improved tissue distribution. Various cobalamin derivatives comprising a (pyridine-2-ylmethylamino)acetic acid (PAMA) chelator for coordination of the $^{99\text{m}}\text{Tc}$ -tricarbonyl core were developed with different spacer lengths [C-2 to C-6, i.e., $(-\text{CH}_2)_n$, $n = 2-6$]. $^{99\text{m}}\text{Tc}(\text{CO})_3$ -PAMA-cobalamin derivatives with a spacer length of C-5 or longer displayed TCII binding affinity whereas those with shorter spacer lengths (C-2 to C-4, Fig. 7.11) were identified as TCII non-binders, but displayed retained interaction with IF and TCI [298]. The results of biodistribution studies in tumor-bearing mice performed

Fig. 7.11 Chemical Structure of $^{99\text{m}}\text{Tc}$ -PAMA-C4-cobalamin, a TCII non-binder vitamin B_{12} derivative



with $^{99m}\text{Tc}(\text{CO})_3\text{-PAMA-C5-cobalamin}$ and $^{99m}\text{Tc}(\text{CO})_3\text{-PAMA-C6-cobalamin}$ were similar to previously evaluated $^{111}\text{In-DTPA-adenosylcobalamin}$ tracers [298]. In contrast, data of $^{99m}\text{Tc}(\text{CO})_3\text{-PAMA-cobalamin}$ derivatives with spacer lengths shorter than C-5 showed a significantly improved tumor-to-blood and tumor-to-kidney ratio of radioactivity. Thus, abolished interaction of the radiolabeled cobalamin tracer with TCII resulted in decreased accumulation of the radiotracer in the blood and in organs and tissues that would otherwise be predestined to have high cobalamin uptake such as kidneys and diverse glands (Fig. 7.12).

$^{99m}\text{Tc}(\text{CO})_3\text{-PAMA-C4-cobalamin}$ (Fig. 7.11) was selected as the most favorable candidate because it displayed the highest tumor-to-blood and tumor-to-kidney ratios in animal experiments. These findings suggest that the transport of cobalamin derivatives into malignant tissue is not dependent on the transport protein TCII but rather mediated via TCI. By this example, it could be demonstrated that variation of the radiotracer's linker length could have a tremendous impact on the overall tissue distribution of a radiotracer and thus, on its successful application. Excellent results achieved in preclinical studies paved the path toward a clinical application of cobalamin-targeted radioimaging in patients using the TCI-selective organometallic ^{99m}Tc -vitamin B₁₂ derivative.

7.5.3 Other Vitamin Targeting Agents—Pretargeting

It is likely that carriers and receptors of vitamins other than folates and vitamin B₁₂ could be used for tumor-targeted nuclear imaging purposes. Among the vitamins of the B-group, it was suggested that cancer cells also overexpress a biotin receptor that could, however, not yet be identified [186, 233, 311]. Additionally, a possible reason for the generally little interest in biotin as a direct tumor-targeting agent could be the fact that renal filtration and reabsorption of biotin and its conjugates

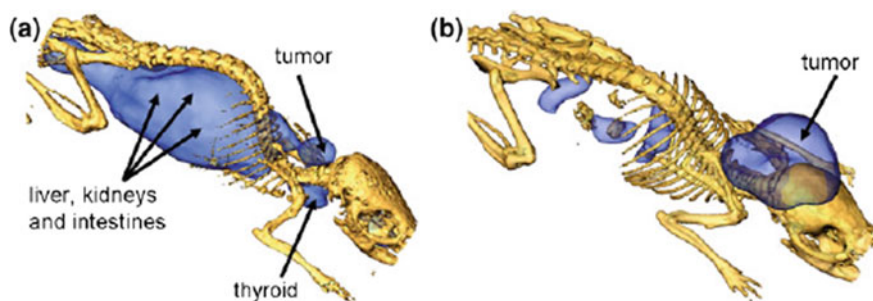


Fig. 7.12 Whole-body SPECT/CT scans of B16F10 tumor-bearing mice, 24 h after injection of **a** $^{99m}\text{Tc}(\text{CO})_3\text{-PAMA-C6-cobalamin}$ (TCII binder) and **b** $^{99m}\text{Tc}(\text{CO})_3\text{-PAMA-C4-cobalamin}$ (TCII non-binder)

lead to high renal uptake of radioactivity in the kidneys. Recently, it was shown that vitamin C (ascorbate) conjugated nanoparticles could be delivered into the brain presumably via the sodium-dependent ascorbic acid transporter SVCT2 whose RNA was found in the choroid plexus epithelium [234]. The SVCT2 carrier was found on rat glioma cells (C6 and F98) and on mouse fibroblasts (NIH/3T3). This study introduced the perspective of using the SVCT2 transporter for brain targeting through the choroid plexus where it is selectively expressed. There might also be a potential to use this vitamin C transporter for nuclear imaging purposes of cancer diseases in the future.

Efforts have been done to use biotin as component in the (strept)avidin–biotin-pretargeting system as their strong affinities ($K_d = 10^{-15}$ M) allow the *in vivo* radiolabeling of high-molecular-weight compounds like proteins, antibody fragments, or antibodies for imaging and radiotherapy [257]. The problems of slow distribution kinetics of these compounds in association with insufficient tumor-to-organ ratios combined with a slow blood clearance should be avoided with this system in contrast to the application of directly radiolabeled biomacromolecules. For this purpose, the biomacromolecule (e.g., antibody) was connected to the (strept)avidin and the radionuclide was connected to the biotin or in the opposite way (Fig. 7.13).

In general, the pretargeting system consists of three steps [35]. First, a non-radiolabeled but avidin-functionalized antibody was administered intravenously allowing a slow distribution and the binding to the target site over 2 to 3 days *in vivo*. Afterward in the second step, a clearing agent was given that helps to remove the remaining unbound antibody from the body whereas the antibody reaches the highest uptake in the targeted tissue. In the third step, a radiolabeled conjugate was administered, which consists of the biotin bearing the radiolabel. This radioconjugate binds with a high affinity to the (strept)avidin-functionalized antibody given previously and exhibits fast distribution properties *in vivo*. Due to the fast blood clearance of the biotin-radioconjugate through the kidneys, a high tumor-to-background ratio will be achieved combined with a protection of the liver. Importantly, the antibody itself has to be located at the surface of the cell during the time of the radioconjugate injection. It should not be internalized.

The first approach to use the avidin–biotin-system for radiolabeling purposes was accomplished by Hnatowich and co-workers [118]. A biotin-conjugated antibody and a DTPA-coupled avidin were used and the radiolabeling was done with ^{111}In . They showed that the target/non-target radioactivity ratios were significantly improved with respect to the conventional radiolabeling procedures. Later, Rosebrough discovered the pharmacokinetics and biodistribution of radiolabeled avidin, streptavidin, and biotin [231] using rabbits and dogs. He found that both ^{111}In -DTPA-biotin and ^{111}In -DTPA-biotin–avidin have a high excretion rate (<5% circulation in the blood after 1 h) in contrast to the ^{111}In -labeled DTPA-biotin–streptavidin-conjugate (>30% after 6 h). In this regard, ~80% of the dose of ^{111}In -DTPA-biotin–avidin was found in the liver after 6 h. In contrast,

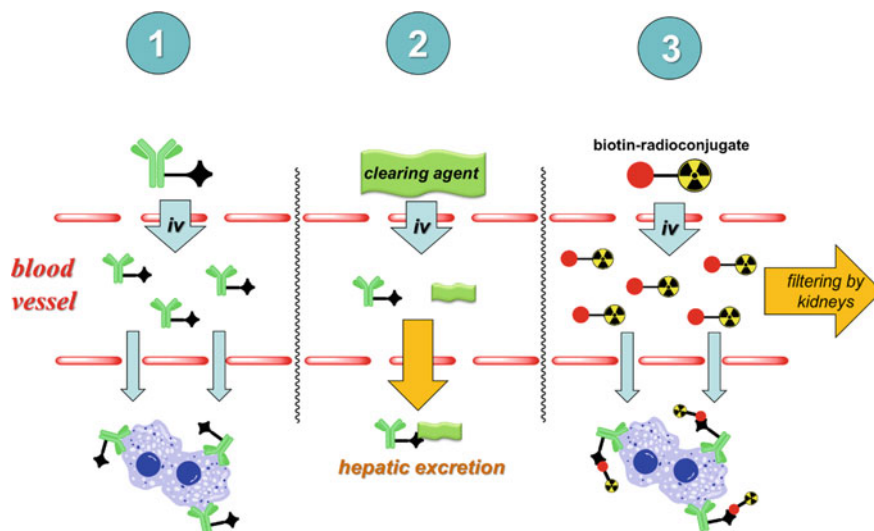


Fig. 7.13 Pretargeting concept using a radiolabeled biotin-conjugate and a (strept)avidin-functionalized antibody. Step 1: distribution of the functionalized antibody to the target (tumor cells); Step 2: clearance of the unbound antibody from the blood; Step 3: administration of the biotin-radioconjugate and binding to the antibody (remaining biotin-radioconjugate will be excreted rapidly)

^{111}In -DTPA-biotin–streptavidin had only $\sim 5\%$ liver accumulation 6 h after injection. They and others stated that the blood clearance of the radiolabeled streptavidin and avidin differed markedly due to the difference in net charge exhibited at physiological pH [124]. Based on these facts, attempts were done to decrease the uptake of streptavidin in the liver [110, 308].

A multitude of biotin–chelator-conjugates not only for $^{99\text{m}}\text{Tc}$ [136, 148] but also for ^{111}In [18] and ^{68}Ga [280] or dual modality imaging probes [70] as well as for pretargeted radioimmunotherapy with ^{90}Y , ^{67}Ga , ^{177}Lu , and other therapeutic radionuclides were developed [155, 183]. Additionally, biotin conjugates for biorthogonal click chemistry were designed (see, e.g., [139, 218]); examples are shown in Fig. 7.14. A phase II study with 25 patients bearing a metastatic colon cancer using ^{90}Y -DOTA-biotin-conjugate and a NR-LU-10 antibody/streptavidin-conjugate showed relatively disappointing results in terms of therapeutic efficacy and toxicity, but beneficial information was obtained concerning normal tissue tolerance to low-dose-rate irradiation [140]. A deeper insight to the pretargeting concept in general is published by Liu [156].

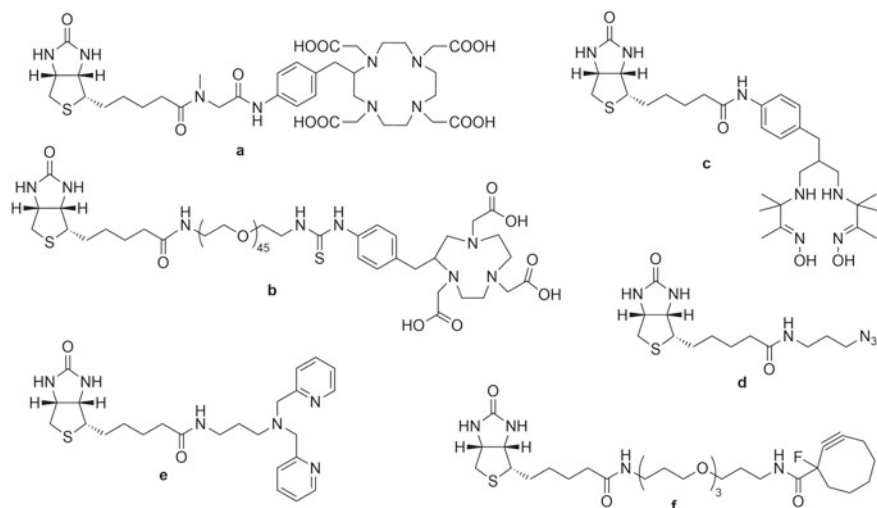


Fig. 7.14 Selected radioconjugates with biotin skeleton containing chelating systems based on macrocycles (a) and (b); for ^{99m}Tc -labeling (c) and (d); for bioorthogonal click reactions (e) and (f)

7.6 Intracellular Targets

7.6.1 ^{99m}Tc -Carbohydrate Complexes

The most frequently used radiotracer for nuclear imaging purposes is currently the glucose analog 2- ^{18}F fluoro-deoxy glucose (^{18}F FDG). This PET tracer is taken up by tumor cells mainly by facile diffusion through the glucose transport protein 1 (Glut1). In the cell interior ^{18}F FDG is phosphorylated by the enzyme hexokinase yielding ^{18}F FDG-6-phosphate which cannot escape the cell anymore. Thus, this trapping mechanism results in accumulation of radioactivity in metabolically active (cancer) cells [270]. The clinical relevance of ^{18}F FDG promoted the development of inexpensive and readily available ^{99m}Tc -labeled glucose analogs.

Most of the derivatives reported in the literature were $^{99m}\text{Tc(V)}$ -glucose complexes [56, 58, 154, 210, 227, 282, 301, 319]. However, these ^{99m}Tc -tracers did not match the criteria and features of ^{18}F FDG, such as active transport via Glut1 and phosphorylation via hexokinase. Later, Dapuetto and colleagues could show a higher uptake of $^{99m}\text{Tc-IDAG}$ and $^{99m}\text{Tc-AADG}$ into the tumor of melanoma bearing C57BL/6 mice with tumor-to-muscle ratios of 12.1 ± 3.73 and 2.88 ± 1.40 [57].

Endeavors have been undertaken by the group of Schibli and others to design organometallic glucose and glucosamine analogs using the matched pair $^{99m}\text{Tc}/^{186/188}\text{Re}$ [26, 71, 214, 239]. Later, Lin et al., Zeltchan et al. and Khan et al. reported new ^{99m}Tc -labeled glucose derivatives bearing a $^{99m}\text{Tc}(\text{CO})_3$ core [132,

318]. Both tracers were subjected to cell studies either with Chinese hamster ovary cells CHO, human breast adenocarcinoma MCF-7 cells, and murine sarcoma S180 cells. Following animal studies revealed a substantial uptake into the tumor tissue, but also in excretion organs like liver and kidneys. In addition, the ^{99m}Tc -thio-glucose derivative prepared by Zeltchan et al. accumulates in the brain.

Biological characterization has been reported from a variety of organometallic $^{99m}\text{Tc}(\text{CO})_3$ -glucose complexes, derivatized at the C-1, C-2, C-3, and C-6 positions with various chelating systems. These compounds were tested for their ability to be internalized into Glut1 expressing cancer cells, HT29, and in addition, it was investigated on whether or not they would be phosphorylated via the hexokinase reaction. Unfortunately, all of the complexes tested appeared not to be recognized and transported via Glut1. The authors stated the likeliness of $^{99m}\text{Tc}(\text{CO})_3$ -glucose complexes being sterically too demanding for recognition at the extracellular binding site and/or transportation via Glut1. Also, other than [^{18}F]FDG, the organometallic glucose derivatives were not phosphorylated by hexokinase. Orvig and his collaborators reported several new approaches of organometallic carbohydrate complexes. Among others, they synthesized *N*-hydroxybenzylamino-deoxyglucose derivatives (Fig. 7.15) and carbohydrate-appended hydroxypyridone derivatives [26, 80–82, 275]. However, most of these compounds revealed neither to be hexokinase substrates nor inhibitors. Although basic cell data of these carbohydrate radiometal complexes is lacking, it is likely that they are not taken up via the Glut1 transporter or other specific transport mechanisms and thus would fail to accumulate in cancer cells in vivo.

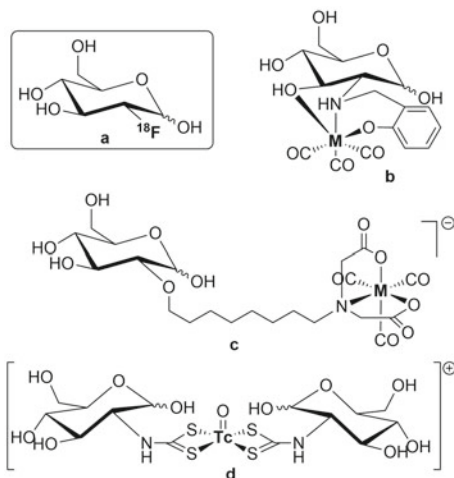


Fig. 7.15 [^{18}F]FDG **a** two C-2 functionalized glucose derivatives of a *N*-(2'-hydroxybenzyl)-amino-chelating system [26] **b** and an imino diacetic acid chelator [239] **c** radiolabeled with ^{99m}Tc -tricarbonyl ($M = ^{99m}\text{Tc}$) and a ^{99m}Tc -tracer based on deoxyglucose dithiocarbamate **d** [154]

7.6.2 Radiolabeled Nucleoside Analogs for Targeting Human Thymidine Kinase

In mammalian cells, salvage pathway phosphorylation of thymidine is catalyzed by two different thymidine kinases (TK): the cell-cycle regulated cytoplasmic TK1 and the constitutively expressed mitochondrial TK2. The human TK1 (hTK1) activity is known to fluctuate with cellular DNA synthesis, the activity being high in proliferating and malignant cells and low or absent in quiescent cells, whereas TK2 activity is low in both dividing and quiescent cells [202]. Since the activity of hTK1 is often dramatically increased in cancer cells, interest has been sparked in targeting this enzyme by radioactive thymidine analogs for selective imaging of proliferating cancer cells. In the cell interior nucleosides are rapidly phosphorylated to nucleotides, which renders them unable to penetrate biological membranes and thus they are “trapped” inside the cells. Thymidine and thymidine analogs labeled with PET radioisotopes such as [^{11}C]methyl-thymidine, 5- ^{76}Br]bromo-2'-fluoro-2'-deoxyuridine, and 3'- ^{18}F]fluoro-3'-deoxythymidine (^{18}F]FLT) are either under development or already in use as proliferation marker [40, 96]. However, due to the high costs for the production of PET radioisotopes and the unfavorably short half-lives of PET isotopes, the use of SPECT radioisotopes $^{99\text{m}}\text{Tc}$ or ^{111}In would be more advantageous. Schmid et al. focused on the preparation of radiometal labeled thymidine complexes functionalized at position N3 with a DO3A-chelator suitable for radiolabeling with ^{111}In or lanthanide radioisotopes [243]. However, cellular uptake of the thymidine metal complexes in DoHH2 and HL60 cells failed. Clearly, there is an interest to develop thymidine derivatives suitable for radiolabeling with $^{99\text{m}}\text{Tc}$. Celen et al. reported the preparation and evaluation of a $^{99\text{m}}\text{Tc(V)}$ -MAMA-propyl-thymidine complex as a potential probe for in vivo visualization of tumor cell proliferation via SPECT [46]. However, this ligand could not be phosphorylated because it was too bulky. The group of Schibli focused on the development of thymidine analogs labeled with the organometallic $^{99\text{m}}\text{Tc}$ -tricarbonyl-core (Fig. 7.16) [69, 276, 277]. The design of organometallic $^{99\text{m}}\text{Tc}$ -derivatives could be favorable as these complexes were sterically less demanding than previously prepared thymidine radiometal complexes. Those organometallic thymidine derivatives were systematically evaluated regarding the influence of the spacer length between the thymidine and the chelating system, the overall charge of the complex after radiometal coordination and the uptake in human neuroblastoma SKNMC cells. From these studies, it was concluded that neutral and anionic complexes are more readily accepted as substrates than cationic complexes.

Moreover, modeling experiments suggested that the flexibility of a longer spacer between the thymidine molecule and the organometallic core further improves the ability of the complex to be accommodated in the binding site of the enzyme. Cellular uptake was higher for complexes with log P values greater than one but still about 6-fold lower than for the ^3H -thymidine control compound. Although some of the organometallic thymidine complexes were identified as enzyme substrates, the low and often almost absent permeability of the thymidine metal complexes through the cellular membrane remains a major hurdle for these compounds.

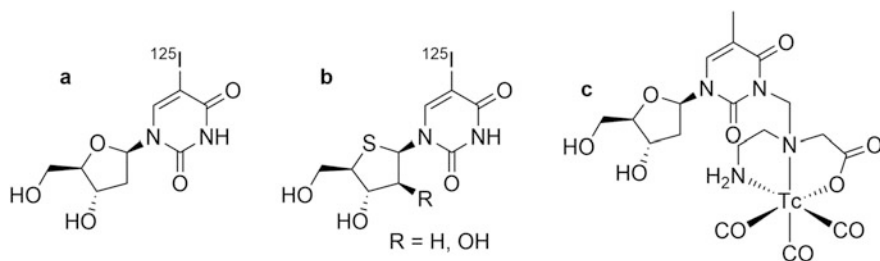


Fig. 7.16 Chemical structures of nucleoside-based SPECT tracers. **a** 5- ^{125}I iodo-2'-deoxyuridine (^{125}I IdUrd) [72, 255], **b** 5- ^{125}I iodo-4'-thio-2'-deoxyuridine (^{125}I ITdU, R = H) and 5- ^{125}I iodo-1-(4'-thio- β -arabinofuranosyl)-uracil (^{125}I ITAU, R = OH) [283] and **c** $^{99\text{m}}\text{Tc}(\text{CO})_3$ -thymidine derivatives ($n = 2, 3, 5$ or 10) [69]

Iodinated thymidine analogs (e.g., 5-iodo-2'-deoxyuridine (IdUrd)) were used in another strategy as cell proliferation markers for nuclear imaging purposes and potential therapeutic application. However, the imaging quality was found to be impaired by the tracer's rapid *in vivo* degradation. Pre-application of 5-fluoro-2'-deoxyuridine (FdUrd) was tested with the aim to block thymidine synthesis and thus trigger the tumor uptake of ^{125}I IdUrd [72]. Indeed, as a result of FdUrd pre-dosing ^{125}I IdUrd incorporation into glioblastoma cells and tumors was increased and thus, the tumor-to-background contrast slightly improved. The same research group reported a beneficial effect of combining the administration of ^{125}I IdUrd with unlabeled IdUrd to increase the rate of DNA incorporation of ^{125}I IdUrd in malignant gliomas [73]. Apparently, the C–N-glycosidic bond of IdUrd is too labile *in vivo* which leads to metabolites that display reduced tumor affinity. In an attempt to increase the radiotracer's *in vivo* stability the tracer has been chemically modified by fluorination of the sugar moiety at different positions (3' or 2'-substitution). However, the preparation of fluorine-stabilized iodinated thymidine analogs with retained cellular uptake, cytosolic phosphorylation, and selectivity for hTK1, appears to be quite challenging [97, 182]. A strategy for stabilizing the C–N-glycosidic bond without interfering with the cytosolic thymidine kinase has been carried out by the replacement of the furanose ring oxygen with sulfur for preparation of 5- ^{125}I iodo-4'-thio-2'-deoxyuridine (^{125}I ITdU) and 5- ^{125}I iodo-1-(4'-thio- β -D-arabinofuranosyl)uracil (^{125}I ITAU) (Fig. 7.16) [283]. ITdU exhibited high resistance to the glycosidic bond cleavage reaction provoked by thymidine phosphorylase, while maintaining affinity to nucleoside kinases. Also, the increased *in vivo* radioiodination stability and rapid DNA incorporation of ITdU resulted in a preferential uptake of radioactivity in the proliferating organs making this tracer a promising tumor-imaging agent. A comparative study of six 5-iodonucleosides revealed that the *in vivo* proliferation-imaging potential of nucleosides might be estimated by their *in vitro* affinity for TK1 and their C–N-glycosidic bond stability [284]. However, since these iodonucleosides have not been examined with regard to the important step of the nucleoside transport activity, further investigations would be necessary to allow a clear statement which radiotracer would be the most suitable for imaging of tumor cell proliferation.

By the examples of nucleoside derivatives and conjugates of carbohydrates, it was demonstrated that the development of radiotracers for intracellular targets might be problematic if bulky metal chelates are employed since cellular uptake of these radiotracers via transmembrane-spanning carriers or passive diffusion could be hindered.

7.6.3 Radioiodinated meta-Iodobenzylguanidine (MIBG)

Finally, we would like to highlight a long-serving but still frequently used tumor-imaging agent with an intracellular target. Meta-Iodobenzylguanidine (MIBG), a catecholamine analog, is suitable for radiolabeling with radioactive iodine (e.g., ^{123}I) for the purpose of SPECT imaging of neuroendocrine and carcinoid tumors, a subtype of neuroendocrine tumors [133]. Radiolabeled MIBG was first synthesized at the University of Michigan as early as 1980 [306]. It localizes through the physiologic nor-epinephrine reuptake mechanisms with uptake into catecholamine storage vesicles of adrenergic nerve ending and the cells of the adrenal medulla. Carcinoid tumor cells share the common characteristic of a sodium-dependent ATP/Mg^{2+} neuronal pump mechanism in their cell membranes that allows the accumulation of nor-epinephrine and MIBG where MIBG is not significantly metabolized. Initially, ^{131}I -labeled MIBG was used for the detection of neuroendocrine tumors such as pheochromocytomas, but later its application has been extended also to scintigraphic visualization of neuroblastoma and carcinoid tumors [44, 45, 52, 105, 258, 297].

Although both [^{123}I]MIBG and [^{131}I]MIBG can be used for the purpose of radionuclide imaging, ^{123}I has dosimetry and imaging characteristics superior to ^{131}I and thus, it is the preferred radionuclide for SPECT imaging (Fig. 7.17). In contrast, ^{131}I is preferred for therapy due to the emission of β -particles and dosimetric considerations [120].

To develop an MIBG analog with improved uptake in tumors, no-carrier-added [^{131}I]MIBG has been developed. The methodology for producing high specific activity (no-carrier-added) [^{131}I]MIBG was originally described in 1993, but only recently it has been developed for clinical application. With this method, nearly every molecule of MIBG contains an ^{131}I -radiolabel, whereas prior methods provided a mixture of the ^{131}I -tracer and the non-radioactive compound (with ^{127}I), wherein only 1 of 2,000 molecules of MIBG contained radioactive iodine. As a result of the high specific activity achieved by the no-carrier-added radiolabeling method, the mass of the MIBG administered can be reduced and thus undesired side-effects caused by the non-radioactive MIBG, such as hypertension during infusion could be minimized. The only concern of the no-carrier-added [^{131}I]MIBG has been that normal tissues and organs with relatively low levels of nor-epinephrine uptake might absorb more radioactivity because of the lack of competitive inhibition of radiotracer uptake by the non-radioactive MIBG.

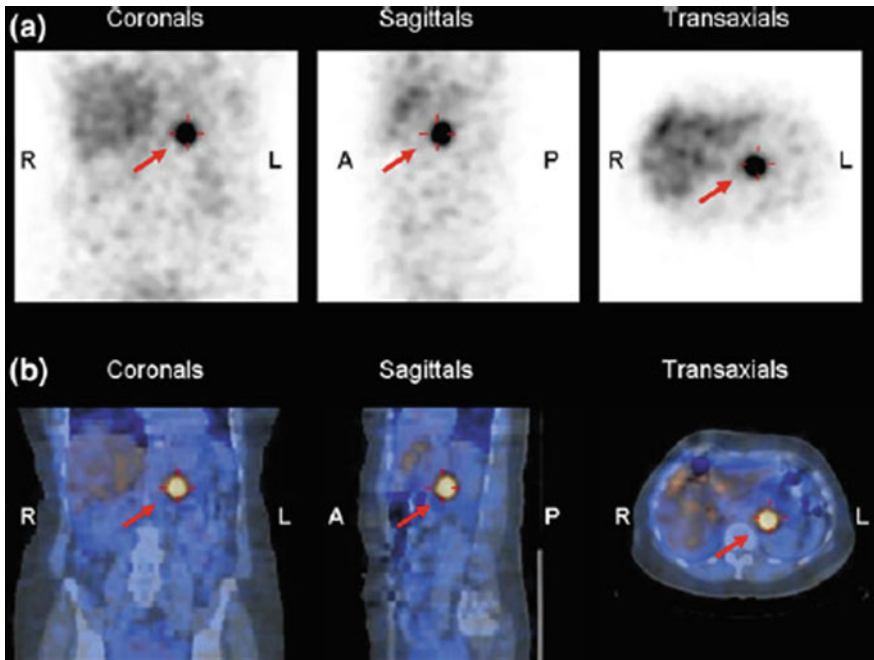


Fig. 7.17 SPECT images **a** and SPECT/CT overlay **b** of a patient with a neuroendocrine tumor (pheochromocytoma) in the upper thorax. Accumulation of [^{123}I]MIBG in the malignant tissue is indicated with red arrows. The images have been kindly provided by N. Schäfer, (MD, Ph.D.), University Hospital, Zurich, Switzerland

7.7 Glutamate-Ureido-Based Inhibitors of Prostate-Specific Membrane Antigen (PSMA)

Prostate-specific membrane antigen (PSMA) is a metallopeptidase expressed in epithelial cells of the prostate and highly overexpressed in 95% of advanced prostate cancers. PSMA is also known as glutamate carboxypeptidase II (GCPII), folate hydrolase 1 (FOLH1), and *N*-acetyl-L-aspartyl-L-glutamate peptidase I (NAALADase). PSMA undergoes constitutive internalization, has no known ligand, is not specific to the prostate gland, and is expressed in other normal (e.g., salivary glands, duodenal mucosa, proximal renal tubular cells, and neuroendocrine cells in the colonic crypts) and neoplastic (e.g., transitional cell carcinoma, renal cell carcinoma, colon carcinoma, and endothelial cells of neovasculature) tissues [262].

PSMA can be selectively targeted using radiolabeled ligands based on urea-linked dipeptides, e.g., Glu-urea-Lys. These small-molecules binding the PSMA can be radiolabeled with γ -emitters like ^{99m}Tc and $^{123/131}\text{I}$ or positron emitters like ^{68}Ga [3, 5, 22] and ^{18}F for diagnosis [99] as well as with their theranostic counterparts such as ^{177}Lu (γ - and β -emitter) or ^{225}Ac (α -emitter) for therapy [4, 122, 141, 221, 245]. Reviews summarizing the theranostic role of PSMA ligands for molecular imaging and targeted molecular radiotherapy have been published recently [2, 17, 137, 142, 220]. Here, the discussion is focused on the appropriate glutamate-ureido-based tracers labeled with ^{123}I or ^{99m}Tc .

7.7.1 ^{123}I - and ^{131}I -Labeled PSMA Radioligands

The use of low-molecular-weight PSMA ligands both for diagnosis and therapy began with the development of the ^{123}I - and ^{131}I -labeled PSMA inhibitors MIP-1072 and MIP-1095 [115, 116, 174]. Both tracers have very similar structures (Fig. 7.18) and comparable pharmacokinetics [50].

MIP-1095 can be used for SPECT imaging (^{123}I -MIP-1095), PET imaging (^{124}I -MIP-1095), and endoradionuclide therapy PSMA(^{131}I -MIP-1095-RLT). The first evaluation of ^{123}I -MIP-1095 for SPECT imaging in patients was described by Barrett et al. in 2013 [23]. Zechmann et al. reported dosimetry and therapy results using matched pair ^{124}I -MIP-1095 PET imaging and ^{131}I -MIP-1095 PSMA-RLT [316]. Afshar-Oromieh et al. evaluated toxicity and antitumor activity after single and repeated PSMA-targeting radioligand therapy of metastatic prostate cancer with ^{131}I -MIP-1095 [3, 5].

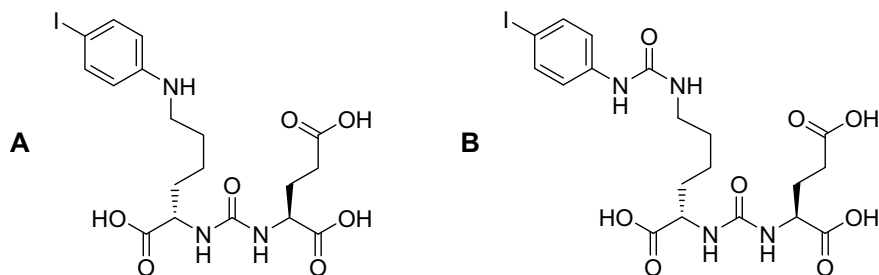


Fig. 7.18 Chemical structures of MIP-1072 (a) and MIP-1095 (b)

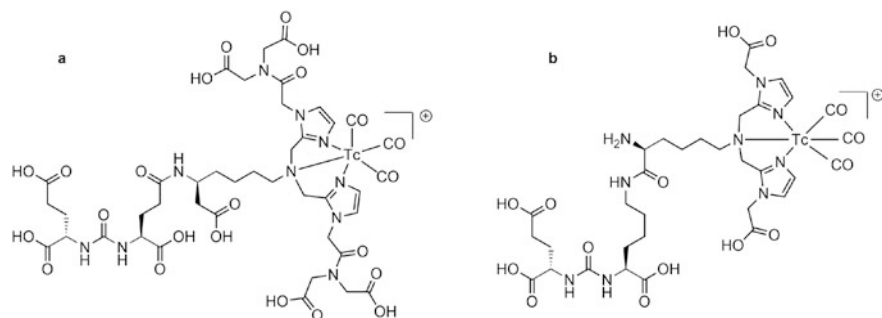


Fig. 7.19 Chemical structures of [^{99m}Tc]Tc-MIP-1404 (a) and [^{99m}Tc]Tc-MIP-1405 (b)

7.7.2 ^{99m}Tc -Labeled PSMA Radioligands

Several studies have been published dealing with the preclinical development of ^{99m}Tc -labeled PSMA radiotracers [166, 287]. The most promising agents among all ^{99m}Tc -labeled PSMA radiotracers are [^{99m}Tc]Tc-MIP-1404, also known as Trofolastat, and [^{99m}Tc]Tc-MIP-1405 (Fig. 7.19). Both compounds have been developed by Molecular Insight Pharmaceuticals (MIP) [117, 175]. The MIP structures contain single-amino-acid chelators (SAACs). Functionalized polar imidazole rings have been introduced in order to reduce lipophilicity and hepatobiliary excretion. ^{99m}Tc labeling follows the technetium tricarbonyl approach.

In preclinical studies [^{99m}Tc]Tc-MIP-1404 showed a fast clearance from the kidneys and non-target tissues while retained to the LNCaP tumor over 4 h. Furthermore, [^{99m}Tc]Tc-MIP-1404 also displayed the highest tumor-to-blood and tumor-to-skeletal muscle ratios [101, 117, 175]. [^{99m}Tc]Tc-MIP-1404 (Trofolastat) is the first PSMA imaging low-molecular-weight molecule that has been used in a phase-III clinical trials for noninvasive imaging of prostate cancer (European Union Trials Register EudraCT 2012-001864-30; ClinicalTrials.gov NCT02615067 [proSPECT-AS]).

A clinical database search from April 2013 to May 2017 yielding 93 patients with histologically confirmed cancer in whom SPECT/CT with [^{99m}Tc]Tc-MIP-1404 had been performed for primary whole-body staging before therapy [244, 245]. The authors claimed that imaging with this tracer has a high accuracy and low interobserver variability in the diagnosis of PC and allows detection of lymph node and bone metastases in a significant proportion of as yet untreated PC patients.

Recently two additional radiotracers have been introduced, [^{99m}Tc]Tc-PSMA-I&S [228, 303] and [^{99m}Tc]Tc-EDDA/HYNIC-iPSMA, where iPSMA stands for Lys(Nal)-Urea-Glu [84, 238]. The chemical structures are shown in Fig. 7.20. In a comparative analysis Lawal et al. evaluated the diagnostic sensitivity of SPECT/CT versus PET/CT in prostate carcinoma imaging using [^{99m}Tc]Tc-EDDA/HYNIC-iPSMA in comparison with [^{68}Ga]Ga-PSMA-11 [147].

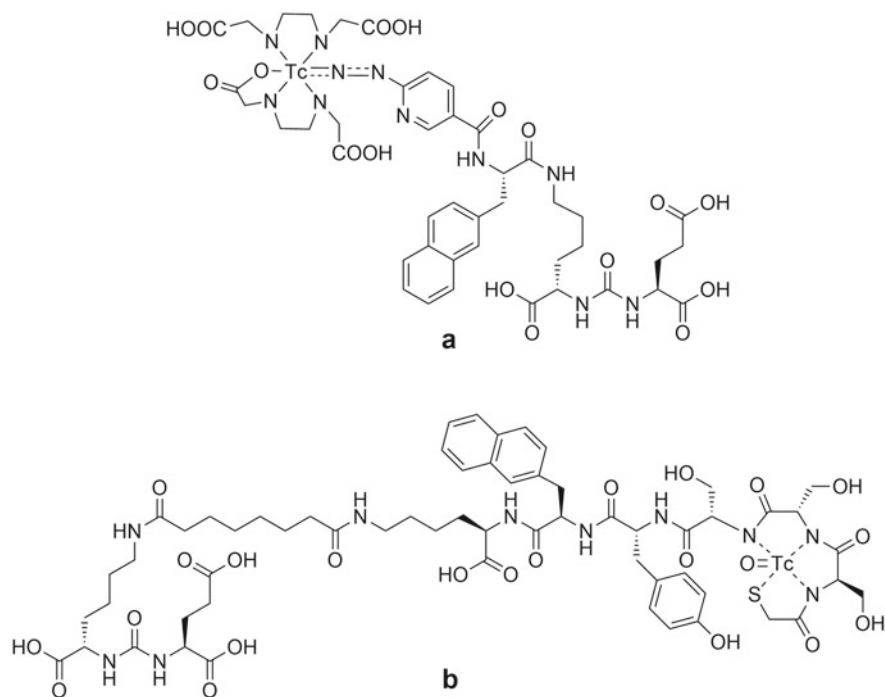


Fig. 7.20 Chemical structures of $[^{99m}\text{Tc}]\text{Tc-EDDA/HYNIC-iPSMA}$ (a) and $[^{99m}\text{Tc}]\text{Tc-PSMA-I\&S}$ (b)

7.8 Sentinel Lymph Node (SNL) Localization

Detection of the sentinel lymph node (SNL), the first node to receive lymphatic flow as well as metastatic cells from the primary tumor site, is currently employed for planning the therapeutic treatment of cancers such as breast cancer and skin melanoma. Commonly, ^{99m}Tc -labeled colloids in combination with blue dyes are used to detect the sentinel lymph node. The labeled colloids are injected beneath the skin surrounding the primary tumor or alternatively directly into the tumor. After entering the lymphatic vessels, colloids use the same drainage pathway as potential metastatic cancer cells and are eventually retained in the first draining lymph node (sentinel node) by phagocytosis or mechanical trapping. However, colloidal radiopharmaceuticals such as ^{99m}Tc -sulfur colloid, ^{99m}Tc -antimony trisulfide, and ^{99m}Tc -labeled albumin microcolloids have disadvantages, like slow elimination rates from the injection site and migration to secondary nodes [208]. Thus, non-colloidal particles have been developed as alternatives such as ^{99m}Tc -labeled human serum albumin and ^{99m}Tc -labeled dextran.

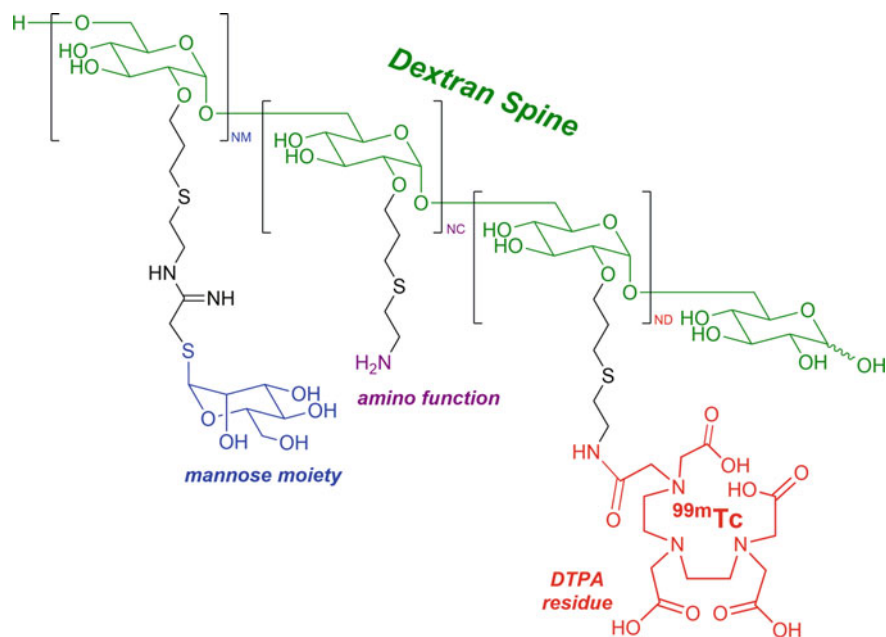


Fig. 7.21 Schematic representation of ^{99m}Tc -Tilmanocept for lymphatic mapping and Sentinel Lymph Node (SNL) localization. The unlabeled DTPA-mannosyl-dextran has a molecular weight of 35,800 g/mol and a molecular diameter of 7.1 nm. The final amino (NC), mannose (NM), and DTPA (ND) densities were 23, 55, and 8 mol per dextran [292]

A fluorescence-labeled ^{99m}Tc -HSA derivative (indocyanine green ICG- ^{99m}Tc -NanoColl) was used to improve the surgical accuracy of laparoscopic lymph node (LN) dissection by integration of molecular imaging and intraoperative image guidance [290]. The authors could demonstrate that multimodal ICG- ^{99m}Tc -NanoColloid, in combination with a laparoscopic fluorescence laparoscope, can be used to facilitate and optimize dissection of SLNs during robot-assisted laparoscopic prostatectomy.

^{99m}Tc -Tilmanocept (Lymphoseek), a tailor-made ^{99m}Tc -radiopharmaceutical for SLN diagnosis based on dextran has been approved by the FDA in 2013 [19, 21, 263, 278, 286, 292, 295]. It is a macromolecule (18 kDa, 7 nm size) composed of a dextran backbone and multiple subunits of DTPA and mannose (Fig. 7.21). ^{99m}Tc -Tilmanocept belongs to the class of receptor-binding radiopharmaceuticals. The mannose residues serve as ligands for receptors expressed on myeloid cells for recognition and binding. ^{99m}Tc -labeling of the macromolecule is performed via diethylenetriamine pentaacetic acid (DTPA). The structure of the Tc chelate is not exactly known.

Extending the diagnostic use of Tilmanocept an ^{111}In -labeled derivative was described to target mannose receptor expression on macrophages in atherosclerotic plaques of apolipoprotein E-knockout mice [291].

7.9 Optimization of SPECT Tracer Design and Potential Reasons for Failure

The design and development of a nuclear imaging probe independent of PET or SPECT comprises an appropriate biomolecule as targeting vector, a site for conjugation that does not interfere with the biomolecule's binding affinity to the tumor-associated target, a suitable linker length, and a radioisotope that matches with an appropriate biomolecule. For stable coordination of metallic radioisotopes, the choice of a suitable chelator is crucial. There are several possible strategies to optimize SPECT tracers with regard to their specificity to and selectivity for the targeted malignant tissue while minimizing their uptake in healthy tissues and organs. Variation of the radionuclide, modification of the bifunctional chelator, introduction of linker entities of variable spacer length for stabilization or modulation of the overall tracer characteristics, alteration of the radiolabeling technique and manipulation of the radiotracer's blood, and normal tissue clearance by variation of the biomolecule's overall size (e.g., antibodies versus antibody fragments or peptides). Finally, optimization of the tissue distribution of radiotracers might also be accomplished by a combination with non-radioactive substances whereof the most prominent example is the application of positively charged amino acids (e.g., lysine) that blocks renal uptake of radiolabeled Fab fragments of antibodies [28, 30] and peptides [61, 229, 294].

During the course of about two decades of (pre)clinical research with tumor-targeted SPECT tracers several reasons for potential failures of SPECT imaging agents could be identified (Table 7.4). Based on the data obtained with nuclear imaging agents that initially failed, new strategies to optimize the design and utility of SPECT tracers are currently being developed.

7.10 Summary and Conclusion

A variety of approaches for the design and improvement of SPECT tracers have been discussed herein. Each class of targeting agents, antibodies, peptides, and non-peptide-based small-molecules such as vitamins has its pros and cons for application in diagnostic nuclear medicine. In principle, it would be ideal to use SPECT tracers that accumulate specifically in malignancies and that are rapidly cleared via kidneys allowing high tumor-to-background contrast of radioactivity already short after administration. Such optimal characteristics are, however, not always easy to achieve.

The recent observation that somatostatin and bombesin analog antagonists provide superior characteristics over agonists with regard to their tumor accumulation is an unexpected finding that is not yet completely understood. Using oligomeric ligands to improve binding and targeting properties of radiolabeled peptides over their monomeric counterparts appears to be a more rational design that could be successfully proven, for example, with RGD-based analogs. Recently,

Table 7.4 Potential reasons for failure of tumor-targeted nuclear imaging

Possibilities for failure	Consequences	Examples
Expression of the target structure in normal tissues and organs	Radiotracer accumulation in normal tissues and organs	<ul style="list-style-type: none"> – Bombesin receptor (pancreas) – Somatostatin receptor (adrenals) – Folate receptor (kidneys)
Long circulation time	High background radiation in the blood—dose burden to healthy tissues (bone marrow)	– Monoclonal antibodies
Short circulation time	Low tumor accumulation	– Small-molecular-weight targeting agents (e.g., folic acid)
Rapid enzymatic metabolism	Low tumor accumulation of metabolites in kidneys and liver	– Non-stabilized neurotensin analogs
Binding to physiological transport proteins	High background radiation in the blood	– Vitamin B ₁₂ /transcobalamin II
Intracellular targets	Cellular uptake via carrier systems or passive diffusion hindered by bulky radiometal complexes	<ul style="list-style-type: none"> – ^{99m}Tc-glucose analogs – ^{99m}Tc-thymidine analogs
Lipophilic character	Unspecific accumulation of the radiotracer in the bile, liver, and intestinal tract	<ul style="list-style-type: none"> – ^{99m}Tc(CO)₃-moiety – Alkyl chain-spacers
Low-specific activity	Low tumor uptake undesired side-effects as a result of substantial amount of injected “cold” tracer	– [¹³¹ I]MIBG

vitamin-based radio imaging agents have been developed that are selectively accumulated in tumor cells. In the case of vitamin B₁₂, analogs with abolished binding to the ubiquitous protein transcobalamin II showed a reduced uptake in non-targeted tissues. In the case of FR-targeting, it was the combined application with the antifolate pemetrexed that led to an improved tumor selectivity of folic acid-based radioconjugates while undesired uptake in FR-positive kidneys could be reduced. Targeting of intracellular tumor markers such as the enzymes hexokinase or human thymidine kinase 1 turned out to be a more problematic strategy for SPECT tracers, particularly those that are based on radiometals, compared to the targeting of cell surface-exposed tumor markers. The necessity of the targeting agent to permeate cancer cell membranes via carrier systems or passive diffusion to reach intracellular targets could be a hindrance for a proper function of the targeting system in particular if the radioconjugate is composed of a bulky radiometal complex.

Finally, it has to be critically acknowledged that only a small selection of examples for tracer designs could be included in this chapter. The immense opportunities for the design of radiopharmaceuticals and the enormous potential it

provides for future development of new and improved SPECT tracers holds great promise for early clinical application of novel imaging agents in oncology.

References

1. Abrams MJ, Juweid M et al (1990) Technetium-99m-human polyclonal IgG radiolabeled via the hydrazino nicotinamide derivative for imaging focal sites of infection in rats. *J Nucl Med* 31:2022–2028
2. Afshar-Oromieh A, Babich JW et al (2016) The rise of PSMA ligands for diagnosis and therapy of prostate cancer. *J Nucl Med* 57(S3):79S–89S
3. Afshar-Oromieh A, Haberkorn U et al (2017) Repeated PSMA-targeting radioligand therapy of metastatic prostate cancer with ^{131}I -MIP-1095. *Eur J Nucl Med Mol Imaging* 44:950–959
4. Afshar-Oromieh A, Hetzheim H et al (2015) The theranostic PSMA Ligand PSMA-617 in the diagnosis of prostate cancer by PET/CT: biodistribution in humans, radiation dosimetry, and first evaluation of tumor lesions. *J Nucl Med* 56:1697–1705
5. Afshar-Oromieh A, Holland-Letz T et al (2017) Diagnostic performance of ^{68}Ga -PSMA-11 (HBED-CC) PET/CT in patients with recurrent prostate cancer: evaluation in 1007 patients. *Eur J Nucl Med Mol Imaging* 44:1258–1268
6. Alberto R, Ortner K et al (2001) Synthesis and properties of boranocarbonate: a convenient in situ CO source for the aqueous preparation of $[\text{}^{99\text{m}}\text{Tc}(\text{OH}_2)_3(\text{CO})_3]^+$. *J Am Chem Soc* 123:3135–3136
7. Alberto R, Schibli R et al (1998) A novel organometallic aqua complex of technetium for the labeling of biomolecules: synthesis of $[\text{}^{99\text{m}}\text{Tc}(\text{OH}_2)_3(\text{CO})_3]^+$ from $[\text{}^{99\text{m}}\text{TcO}_4]^-$ in aqueous solution and its reaction with a bifunctional ligand. *J Am Chem Soc* 120:7987–7988
8. Alberto R, Schibli R et al (1999) First application of *fac*- $[\text{}^{99\text{m}}\text{Tc}(\text{OH}_2)_3(\text{CO})_3]^+$ in bioorganometallic chemistry: design, structure, and in vitro affinity of a 5-HT1A receptor ligand labeled with $^{99\text{m}}\text{Tc}$. *J Am Chem Soc* 121:6076–6077
9. Alberto R, Schibli R et al (1999) Basic aqueous chemistry of $[\text{M}(\text{OH}_2)_3(\text{CO})_3]^+$ (M = Re, Tc) directed towards radiopharmaceutical application. *Coord Chem Rev* 192:901–919
10. Alford R, Ogawa M et al (2009) Molecular probes for the in vivo imaging of cancer. *Mol Biosyst* 5:1279–1291
11. Alshoukr F, Rosant C et al (2009) Novel neurotensin analogues for radioisotope targeting to neurotensin receptor-positive tumors. *Bioconj Chem* 20:1602–1610
12. Alves S, Correia JD et al (2006) Pyrazolyl conjugates of bombesin: a new tridentate ligand framework for the stabilization of *fac*- $[\text{M}(\text{CO})_3]^+$ moiety. *Nucl Med Biol* 33:625–634
13. Antony AC (1996) Folate receptors. *Ann Rev Nutr* 16:501–521
14. Aranda-Lara L, Ferro-Flores G et al (2016) Synthesis and evaluation of Lys1(α , γ -Folate) Lys3(^{177}Lu -DOTA)-Bombesin(1–14) as a potential theranostic radiopharmaceutical for breast cancer. *Appl Radiat Isot* 107:214–219
15. Artiko V, Afgan A et al (2016) Evaluation of neuroendocrine tumors with $^{99\text{m}}\text{Tc}$ -EDDA/HYNIC TOC. *Nucl Med Rev* 19:99–103
16. Assaraf YG, Leamon CP et al (2014) The folate receptor as a rational therapeutic target for personalized cancer treatment. *Drug Resist Updates* 17:89–95
17. Awang ZH, Essler M et al (2018) Radioligand therapy of metastatic castration-resistant prostate cancer: current approaches. *Radiat Oncol* 13:98
18. Axworthy DB, Reno JM et al (2000) Cure of human carcinoma xenografts by a single dose of pretargeted yttrium-90 with negligible toxicity. *Proc Natl Acad Sci USA* 97:1802–1807
19. Azad AK, Rajaram MVS et al (2015) Tilmanocept, a new radiopharmaceutical tracer for cancer sentinel lymph nodes, binds to the mannose receptor (CD206). *J Immunol* 195:2019–2029

20. Baidoo KE, Lin KS et al (1998) Design, synthesis, and initial evaluation of high-affinity technetium bombesin analogues. *Bioconjug Chem* 9:218–225
21. Baker JL, Pu M et al (2015) Comparison of [^{99m}Tc]Tilmanocept and filtered [^{99m}Tc]Sulfur colloid for identification of SLNs in breast cancer patients. *Ann Surg Oncol* 22:40–45
22. Baranski AC, Schäfer M et al (2017) Improving the imaging contrast of ⁶⁸Ga-PSMA-11 by targeted linker design: charged spacer moieties enhance the pharmacokinetic properties. *Bioconjugate Chem* 28:2485–2492
23. Barrett JA, Coleman RE et al (2013) First-in-man evaluation of 2 high-affinity PSMA-avid small molecules for imaging prostate cancer. *J Nucl Med* 54:380–387
24. Bartholoma MD, Louie AS et al (2010) Technetium and gallium derived radiopharmaceuticals: comparing and contrasting the chemistry of two important radiometals for the molecular imaging era. *Chem Rev* 110:2903–2920
25. Bauer JA, Morrison BH et al (2002) Effects of interferon beta on transcobalamin II-receptor expression and antitumor activity of nitrosylcobalamin. *J Natl Cancer Inst* 94:1010–1019
26. Bayly SR, Fisher CL et al (2004) Carbohydrate conjugates for molecular imaging and radiotherapy: ^{99m}Tc(I) and ¹⁸⁶Re(I) tricarbonyl complexes of N-(2'-hydroxybenzyl)-2-amino-2-deoxy-D-glucose. *Bioconjug Chem* 15:923–926
27. Begent RH, Verhaar MJ et al (1996) Clinical evidence of efficient tumor targeting based on single-chain Fv antibody selected from a combinatorial library. *Nat Med* 2:979–984
28. Behr TM, Becker WS et al (1996) Reduction of renal uptake of monoclonal antibody fragments by amino acid infusion. *J Nucl Med* 37:829–833
29. Behr TM, Gotthardt M et al (2001) Imaging tumors with peptide-based radioligands. *Q J Nucl Med* 45:189–200
30. Behr TM, Sharkey RM et al (1995) Reduction of the renal uptake of radiolabeled monoclonal antibody fragments by cationic amino acids and their derivatives. *Cancer Res* 55:3825–3834
31. Bernard BF, Krenning EP et al (1997) D-lysine reduction of indium-111 octreotide and yttrium-90 octreotide renal uptake. *J Nucl Med* 38:1929–1933
32. Birchler MT, Thuerl C et al (2007) Immunoscintigraphy of patients with head and neck carcinomas, with an anti-angiogenetic antibody fragment. *Otolaryngol Head Neck Surg* 136:543–548
33. Blomquist L, Flodh H et al (1969) Uptake of labelled vitamin B12 and 4-iodophenylalanine in some tumors of mice. *Experientia* 25:294–296
34. Boeggeman E, Ramakrishnan B et al (2009) Site specific conjugation of fluoroprobes to the remodeled Fc N-glycans of monoclonal antibodies using mutant glycosyltransferases: application for cell surface antigen detection. *Bioconjug Chem* 20:1228–1236
35. Boerman OC, van Schaijk FG et al (2003) Pretargeted radioimmunotherapy of cancer: progress step by step. *J Nucl Med* 44:400–411
36. Brack SS, Dinkelborg LM et al (2004) Molecular targeting of angiogenesis for imaging and therapy. *Eur J Nucl Med Mol Imaging* 31:1327–1341
37. Breeman WA, de Jong M et al (2002) Preclinical comparison of ¹¹¹In-labeled DTPA- or DOTA-bombesin analogs for receptor-targeted scintigraphy and radionuclide therapy. *J Nucl Med* 43:1650–1656
38. Brekken RA, Huang X et al (1998) Vascular endothelial growth factor as a marker of tumor endothelium. *Cancer Res* 58:1952–1959
39. Bruhlmeier M, Garayoa EG et al (2002) Stabilization of neurotensin analogues: effect on peptide catabolism, biodistribution and tumor binding. *Nucl Med Biol* 29:321–327
40. Buchmann I, Vogg AT et al (2003) [¹⁸F]5-fluoro-2-deoxyuridine-PET for imaging of malignant tumors and for measuring tissue proliferation. *Cancer Biother Radiopharm* 18:327–337
41. Buchsbaum DJ (1995) Experimental approaches to increase radiolabeled antibody localization in tumors. *Cancer Res* 55:5729s–5732s

42. Buchsbaum DJ (1997) Experimental tumor targeting with radiolabeled ligands. *Cancer* 80:2371–2377
43. Carnemolla B, Neri D et al (1996) Phage antibodies with pan-species recognition of the oncofoetal angiogenesis marker fibronectin ED-B domain. *Int J Cancer* 68:397–405
44. Carrasquillo JA, Pandit-Taskar N et al (2016) I-131-metaiodobenzylguanidine therapy of pheochromocytoma and paraganglioma. *Semin Nucl Med* 46:203–214
45. Carrasquillo JA, Pandit-Taskar et al (2012) Radionuclide therapy of adrenal tumors. *J Surg Oncol* 06:632–642
46. Celen S, de Groot T et al (2007) Synthesis and evaluation of a ^{99m}Tc -MAMA-propyl-thymidine complex as a potential probe for in vivo visualization of tumor cell proliferation with SPECT. *Nucl Med Biol* 34:283–291
47. Cescato R, Erchegyi J et al (2008) Design and in vitro characterization of highly sst2-selective somatostatin antagonists suitable for radiotargeting. *J Med Chem* 51:4030–4037
48. Cescato R, Schulz S et al (2006) Internalization of sst2, sst3, and sst5 receptors: effects of somatostatin agonists and antagonists. *J Nucl Med* 47:502–511
49. Chen Q, Ma Q et al (2015) An exploratory study on ^{99m}Tc -RGDBBN peptide scintimammography in the assessment of breast malignant lesions compared to ^{99m}Tc -3P4-RGD2. *PLoS ONE* 10:e0123401
50. Chopra A (2009) ^{123}I -Labeled (S)-2-(3-((S)-1-carboxy-5-(4-iodobenzylamino)-pentyl)ureido)-pentanedoic acid. In: *Molecular imaging and contrast agent database (MICAD)* [Internet]. Bethesda (MD): national center for biotechnology information (US); 2004–2013
51. Christ E, Wild D et al (2009) Glucagon-like peptide-1 receptor imaging for localization of insulinomas. *J Clin Endocrinol Metab* 94:4398–4405
52. Cistaro A, Quartuccio N et al (2015) ^{124}I -MIBG: a new promising positron-emitting radiopharmaceutical for the evaluation of neuroblastoma. *Nucl Med Rev* 18:102–106
53. Collins DA, Hogenkamp HP (1997) Transcobalamin II receptor imaging via radiolabeled diethylene-triaminepentaacetate cobalamin analogs. *J Nucl Med* 38:717–723
54. Collins DA, Hogenkamp HP et al (1999) Tumor imaging via indium-111-labeled DTPA-adenosylcobalamin. *Mayo Clin Proc* 74:687–691
55. Collins DA, Hogenkamp HP et al (2000) Biodistribution of radiolabeled adenosylcobalamin in patients diagnosed with various malignancies. *Mayo Clin Proc* 75:568–580
56. Dapuelto R, Castelli R et al (2011) Biological evaluation of glucose and deoxyglucose derivatives radiolabeled with [$^{99m}\text{Tc}(\text{CO})_3(\text{H}_2\text{O})_3$] $^+$ core as potential melanoma imaging agents. *Bioorg Med Chem Lett* 21:7102–7106
57. Dapuelto R, Aguiar RB et al (2015) Technetium glucose complexes as potential cancer imaging agents. *Bioorg Med Chem Lett* 25:4254–4259
58. de Barros ALB, Cardoso VN et al (2010) Synthesis and biodistribution studies of carbohydrate derivatives radiolabeled with technetium-99m. *Bioorg Med Chem Lett* 20:315–317
59. de Barros ALB, das Gracas Mota L et al (2012) Kit formulation for ^{99m}Tc -labeling of HYNIC- β Ala-Bombesin(7–14). *Appl Radiat Isot* 70:2440–2445
60. de Jong M, Bakker WH et al (1999) Preclinical and initial clinical evaluation of ^{111}In -labeled nonsulfated CCK8 analog: a peptide for CCK-B receptor-targeted scintigraphy and radionuclide therapy. *J Nucl Med* 40:2081–2087
61. de Jong M, Rolleman EJ et al (1996) Inhibition of renal uptake of indium-111-DTPA-octreotide in vivo. *J Nucl Med* 37:1388–1392
62. de Visser M, Bernard HF et al (2007) Novel ^{111}In -labelled bombesin analogues for molecular imaging of prostate tumours. *Eur J Nucl Med Mol Imaging* 34:1228–1238
63. de Visser M, Janssen PJ et al (2003) Stabilised ^{111}In -labelled DTPA- and DOTA-conjugated neurotensin analogues for imaging and therapy of exocrine pancreatic cancer. *Eur J Nucl Med Mol Imaging* 30:1134–1139

64. Decristoforo C, Mather SJ (2002) The influence of chelator on the pharmacokinetics of ^{99m}Tc -labelled peptides. *Q J Nucl Med* 46:195–205
65. Decristoforo C, Mather SJ et al (2000) ^{99m}Tc -EDDA/HYNIC-TOC: a new ^{99m}Tc -labelled radiopharmaceutical for imaging somatostatin receptor-positive tumours; first clinical results and intra-patient comparison with ^{111}In -labelled octreotide derivatives. *Eur J Nucl Med* 27:1318–1325
66. Decristoforo C, Melendez-Alafort L et al (2000) ^{99m}Tc -HYNIC-[Tyr³]-octreotide for imaging somatostatin-receptor-positive tumors: preclinical evaluation and comparison with ^{111}In -octreotide. *J Nucl Med* 41:1114–1119
67. Delgado R, da Silva JJ (1982) Metal complexes of cyclic tetra-azatetra-acetic acids. *Talanta* 29:815–822
68. Demartis S, Tarli L et al (2001) Selective targeting of tumour neovasculature by a radiohalogenated human antibody fragment specific for the ED-B domain of fibronectin. *Eur J Nucl Med* 28:534–539
69. Desbouis D, Struthers H et al (2008) Synthesis, in vitro, and in silico evaluation of organometallic technetium and rhenium thymidine complexes with retained substrate activity toward human thymidine kinase type I. *J Med Chem* 51:6689–6698
70. Dong C, Yang S et al (2016) SPECT/NIRF dual modality imaging for detection of intraperitoneal colon tumor with an avidin/biotin pretargeting system. *Sci Rep* 6:18905
71. Dumas C, Schibli R et al (2003) Versatile routes to C-2- and C-6-functionalized glucose derivatives of iminodiacetic acid. *J Org Chem* 68:512–518
72. Dupertuis YM, Vazquez M et al (2001) Fluorodeoxyuridine improves imaging of human glioblastoma xenografts with radiolabeled iododeoxyuridine. *Cancer Res* 61:7971–7977
73. Dupertuis YM, Xiao WH et al (2002) Unlabelled iododeoxyuridine increases the rate of uptake of [^{125}I]iododeoxyuridine in human xenografted glioblastomas. *Eur J Nucl Med Mol Imaging* 29:499–505
74. Edwards DS, Liu S et al (1997) New and versatile ternary ligand system for technetium radiopharmaceuticals: water soluble phosphines and tricine as coligands in labeling a hydrazinonicotinamide-modified cyclic glycoprotein IIb/IIIa receptor antagonist with ^{99m}Tc . *Bioconjug Chem* 8:146–154
75. Egli A, Alberto R et al (1999) Organometallic ^{99m}Tc -aquaion labels peptide to an unprecedented high specific activity. *J Nucl Med* 40:1913–1917
76. Egli A, Hegetschweiler K et al (1997) Hydrolysis of the organometallic aqua ion *fac*-triaquatriscarbonylrhenium(I). Mechanism, $\text{p}K_{\text{a}}$, and formation constants of the polynuclear hydrolysis products. *Organometallics* 16:1833–1840
77. Fan G, Wan R et al (2018) The distribution and imaging of ^{99m}Tc -nGO-PEG-FA in human Patu8988 tumor-bearing nude mice. *Cancer Biother Radiopharm* 33:445–459
78. Farkas R, Siwowska et al (2016) ^{64}Cu - and ^{68}Ga -based PET imaging of folate receptor-positive tumors: development and evaluation of an albumin-binding. *Mol Pharm* 13:1979–1987
79. Fernández M, Javaid F, Chudasama (2018) Advances in targeting the folate receptor in the treatment/imaging of cancers. *Chem Sci* 9:790–810
80. Ferreira CL, Bayly SR et al (2006) Carbohydrate-appended 3-hydroxy-4-pyridinone complexes of the $[\text{M}(\text{CO})_3]^+$ core (M = Re, ^{99m}Tc , ^{186}Re). *Bioconjug Chem* 17:1321–1329
81. Ferreira CL, Ewart CB et al (2006) Glucosamine conjugates of tricarbonylcyclopentadienyl rhenium(I) and technetium(I) cores. *Inorg Chem* 45:6979–6987
82. Ferreira CL, Marques FL et al (2010) Cationic technetium and rhenium complexes with pendant carbohydrates. *Appl Radiat Isot* 68:1087–1093
83. Ferro-Flores G, Arteaga de Murphy C et al (2006) Preparation and evaluation of ^{99m}Tc -EDDA/HYNIC-[Lys³]-bombesin for imaging gastrin-releasing peptide receptor-positive tumours. *Nucl Med Commun* 27:371–376
84. Ferro-Flores G, Luna-Gutiérrez M et al (2017) Clinical translation of a PSMA inhibitor for ^{99m}Tc -based SPECT. *Nucl Med Biol* 48:36–44

85. Ferro-Flores G, Rivero IA et al (2010) Click chemistry for [$^{99m}\text{Tc}(\text{CO})_3$] labeling of Lys³-bombesin. *Appl Radiat Isot* 68:2274–2278
86. Fischer CA, Vomstein S, Mindt TL (2014) A bombesin-shepherdin radioconjugate designed for combined extra- and intracellular targeting. *Pharmaceuticals* 7:662–675
87. Fisher RE, Siegel BA et al (2008) Exploratory study of ^{99m}Tc -EC20 imaging for identifying patients with folate receptor-positive solid tumors. *J Nucl Med* 49:899–906
88. Flodh H (1968) Autoradiographic studies on distribution of radiocobalt chloride in pregnant mice. *Acta Radiol Ther Phys Biol* 7:121–128
89. Flodh H, Ullberg S (1968) Accumulation of labelled vitamin B₁₂ in some transplanted tumours. *Int J Cancer* 3:694–699
90. Garai I, Barna S et al (2016) Limitations and pitfalls of ^{99m}Tc -EDDA/HYNIC-TOC (Tektrotyd) scintigraphy. *Nucl Med Rev* 19:93–98
91. Garcia Garayoa E, Ruegg D et al (2007) Chemical and biological characterization of new Re($\text{CO})_3$ [^{99m}Tc]($\text{CO})_3$ bombesin analogues. *Nucl Med Biol* 34:17–28
92. Garcia Garayoa E, Schweinsberg C et al (2007) New [^{99m}Tc]bombesin analogues with improved biodistribution for targeting gastrin releasing-peptide receptor-positive tumors. *Q J Nucl Med Mol Imaging* 51:42–50
93. Garcia Garayoa E, Schweinsberg C et al (2008) Influence of the molecular charge on the biodistribution of bombesin analogues labeled with the [$^{99m}\text{Tc}(\text{CO})_3$]-core. *Bioconjug Chem* 19:2409–2416
94. Garcia-Garayoa E, Blauenstein P et al (2009) A stable neurotensin-based radiopharmaceutical for targeted imaging and therapy of neurotensin receptor-positive tumours. *Eur J Nucl Med Mol Imaging* 36:37–47
95. Garcia-Garayoa E, Maes V et al (2006) Double-stabilized neurotensin analogues as potential radiopharmaceuticals for NTR-positive tumors. *Nucl Med Biol* 33:495–503
96. Gardelle O, Roelcke U et al (2001) [^{78}Br]Bromodeoxyuridine PET in tumor-bearing animals. *Nucl Med Biol* 28:51–57
97. Gati WP, Misra HK et al (1984) Structural modifications at the 2'- and 3'-positions of some pyrimidine nucleosides as determinants of their interaction with the mouse erythrocyte nucleoside transporter. *Biochem Pharmacol* 33:3325–3331
98. Giblin MF, Veerendra B et al (2005) Radiometallation of receptor-specific peptides for diagnosis and treatment of human cancer. *Vivo* 19:9–29
99. Giesel FL, Will L et al (2018) Biochemical recurrence of prostate cancer: initial results with [^{18}F]PSMA-1007 PET/CT. *J Nucl Med* 59(4):632–635
100. Ginj M, Zhang H et al (2006) Radiolabeled somatostatin receptor antagonists are preferable to agonists for in vivo peptide receptor targeting of tumors. *Proc Natl Acad Sci USA* 103:16436–16441
101. Goffin KE, Joniau S et al (2017) Phase 2 Study of ^{99m}Tc -Trofolostat SPECT/CT to identify and localize prostate cancer in intermediate- and high-risk patients undergoing radical prostatectomy and extended pelvic LN dissection. *J Nucl Med* 58:1408–1413
102. Goldenberg DM, Rossi EA et al (2008) Multifunctional antibodies by the dock-and-lock method for improved cancer imaging and therapy by pretargeting. *J Nucl Med* 49:158–163
103. Good S, Walter MA et al (2008) Macrocyclic chelator-coupled gastrin-based radiopharmaceuticals for targeting of gastrin receptor-expressing tumours. *Eur J Nucl Med Mol Imaging* 35:1868–1877
104. Gotthardt M, van Eerd-Vismale J et al (2007) Indication for different mechanisms of kidney uptake of radiolabeled peptides. *J Nucl Med* 48:596–601
105. Grünwald F, Ezziddin S (2010) ^{131}I -metaiodobenzylguanidine therapy of neuroblastoma and other neuroendocrine tumors. *Semin Nucl Med* 40:153–163
106. Gugger M, Reubi JC (1999) Gastrin-releasing peptide receptors in non-neoplastic and neoplastic human breast. *Am J Pathol* 155:2067–2076

107. Guo W, Hinkle GH et al (1999) ^{99m}Tc -HYNIC-folate: a novel receptor-based targeted radiopharmaceutical for tumor imaging. *J Nucl Med* 40:1563–1569
108. Guo Z, Zhang P et al (2014) Synthesis and preliminary evaluation of novel ^{99m}Tc -labeled folate derivative via click reaction for SPECT imaging. *Appl Radiat Isot* 91:24–30
109. Guo Z, You L et al (2017) Development of a new FR-targeting Agent ^{99m}Tc -HYNFA with improved imaging contrast and comparison of multimerization and/or PEGylation strategies for radio-folate modification. *Mol Pharm* 14:3780–3788
110. Hamblett KJ, Press OW et al (2005) Role of biotin-binding affinity in streptavidin-based pretargeted radioimmunotherapy of lymphoma. *Bioconjug Chem* 16:131–138
111. Hammond PJ, Wade AF et al (1993) Amino acid infusion blocks renal tubular uptake of an indium-labelled somatostatin analogue. *Br J Cancer* 67:1437–1439
112. Hankus J, Tomaszewska R (2016) Neuroendocrine neoplasms and somatostatin receptor subtypes expression. *Nucl Med Rev* 19:111–117
113. Hekman MCH, Boerman OC et al (2017) Improved intraoperative detection of ovarian cancer by folate receptor alpha targeted dual-modality imaging. *Mol Pharm* 14:3457–3463
114. Heppeler A, Froidevaux S et al (1999) Radiometal-labelled macrocyclic chelator-derivatised somatostatin analogue with superb tumour-targeting properties and potential for receptor-mediated internal radiotherapy. *Chem-Eur J* 5:1974–1981
115. Hillier SM, Kern AM et al (2011) ^{123}I -MIP-1072, a small-molecule inhibitor of prostate-specific membrane antigen, is effective at monitoring tumor response to taxane therapy. *J Nucl Med* 52:1087–1093
116. Hillier SM, Maresca KP et al (2009) Preclinical evaluation of novel glutamate-urea-lysine analogues that target prostate-specific membrane antigen as molecular imaging pharmaceuticals for prostate cancer. *Can Res* 69:6932–6940
117. Hillier SM, Maresca KP et al (2013) ^{99m}Tc -labeled small-molecule inhibitors of prostate-specific membrane antigen for molecular imaging of prostate cancer. *J Nucl Med* 54:1369–1376
118. Hnatowich DJ, Virzi F (1987) Investigations of avidin and biotin for imaging applications. *J Nucl Med* 28:1294–1302
119. Ho C-L, Liu I-H et al (2011) Molecular imaging, pharmacokinetics, and dosimetry of ^{111}In -AMBA in human prostate tumor-bearing mice. *J Biomed Biotechnol* 2011:Article ID 101497. <https://doi.org/10.1155/2011/101497>
120. Hoefnagel CA, den Hartog Jager FC et al (1987) The role of ^{131}I -MIBG in the diagnosis and therapy of carcinoids. *Eur J Nucl Med* 13:187–191
121. Hoffman TJ, Gali H et al (2003) Novel series of ^{111}In -labeled bombesin analogs as potential radiopharmaceuticals for specific targeting of gastrin-releasing peptide receptors expressed on human prostate cancer cells. *J Nucl Med* 44:823–831
122. Hofman MS, Violet J et al (2018) [^{177}Lu]-PSMA-617 radionuclide treatment in patients with metastatic castration-resistant prostate cancer (LuPSMA trial): a single-centre, single-arm, phase 2 study. *Lancet Oncol* 19:825–833
123. Hong H, Sun J et al (2008) Radionuclide-based cancer imaging targeting the carcinoembryonic antigen. *Biomark Insights* 3:435–451
124. Jeong JM, Kinuya S et al (1994) Application of high affinity binding concept to radiolabel avidin with Tc-99m labeled biotin and the effect of pI on biodistribution. *Nucl Med Biol* 21:935–940
125. Ji T, Sun Y et al (2015) The diagnostic role of ^{99m}Tc -dual receptor targeted probe and targeted peptide bombesin (RGD-BBN) SPET/CT in the detection of malignant and benign breast tumors and axillary lymph nodes compared to ultrasound. *Hell J Nucl Med* 18:108–113
126. Ji T, Gao S (2016) ^{99m}Tc -Glu-c(RGDyK)-bombesin SPECT can reduce unnecessary biopsy of masses that are BI-RADS category 4 on ultrasonography. *J Nucl Med* 57:1196–1200

127. Johnson CV, Shelton T et al (2006) Evaluation of combined ^{177}Lu -DOTA-8-AOC-BBN (7-14) NH_2 GRP receptor-targeted radiotherapy and chemotherapy in PC-3 human prostate tumor cell xenografted SCID mice. *Cancer Biother Radiopharm* 21:155–166
128. Josten A, Haalck L et al (2000) Use of microbial transglutaminase for the enzymatic biotinylation of antibodies. *J Immunol Methods* 240:47–54
129. Kastner ME, Lindsay MJ et al (1982) Synthesis and structure of trans- $[\text{O}_2(\text{en})_2\text{Tc}^{\text{V}}]^+$. *Inorg Chem* 21:2037–2040
130. Ke CY, Mathias CJ et al (2003) The folate receptor as a molecular target for tumor-selective radionuclide delivery. *Nucl Med Biol* 30:811–817
131. Ke CY, Mathias CJ et al (2004) Folate-receptor-targeted radionuclide imaging agents. *Adv Drug Deliv Rev* 56:1143–1160
132. Khan IU, Shahid A et al (2016) Development and bioevaluation of $^{99\text{m}}\text{Tc}(\text{CO})_3$ -labeled (1-azido-1-deoxy- β -D-glucopyranoside) complex as a potential tumor-seeking agent. *Pak J Pharm Sci* 29:213–219
133. Khan MU, Morse M et al (2008) Radioiodinated metaiodobenzylguanidine in the diagnosis and therapy of carcinoid tumors. *Q J Nucl Med Mol Imaging* 52:441–454
134. King DJ, Turner A et al (1994) Improved tumor targeting with chemically cross-linked recombinant antibody fragments. *Cancer Res* 54:6176–6185
135. Kobayashi H, Sakahara H et al (1994) Improved clearance of radiolabeled biotinylated monoclonal antibody following the infusion of avidin as a “chase” without decreased accumulation in the target tumor. *J Nucl Med* 35:1677–1684
136. Koch P, Mäcke HR (1992) $^{99\text{m}}\text{Tc}$ Labeled Biotin Conjugate in a Tumor “Pretargeting” Approach with Monoclonal Antibodies. *Angew Chem Int Ed* 31:1507–1509
137. Kopka K, Benešová M et al (2017) Glu-ureido-based inhibitors of prostate-specific membrane antigen: lessons learned during the development of a novel class of low-molecular-weight theranostic radiotracers. *J Nucl Med* 58(Suppl 2):17S–26S
138. Körner M, Stockli M et al (2007) GLP-1 receptor expression in human tumors and human normal tissues: potential for in vivo targeting. *J Nucl Med* 48:736–743
139. Knight JC, Cornelissen B (2014) Bioorthogonal chemistry: implications for pretargeted nuclear (PET/SPECT) imaging and therapy. *Am J Nucl Med Mol Imaging* 4:96–113
140. Knox SJ, Goris ML et al (2000) Phase II trial of yttrium-90-DOTA-biotin pretargeted by NR-LU-10 antibody/streptavidin in patients with metastatic colon cancer. *Clin Cancer Res* 6:406–414
141. Kratochwil C, Bruchertseifer F et al (2016) ^{225}Ac -PSMA-617 for PSMA-targeted α -radiation therapy of metastatic castration-resistant prostate cancer. *J Nucl Med* 57(12):1941–1944
142. Kulkarni HR, Singh A et al (2018) Theranostics of prostate cancer: from molecular imaging to precision molecular radiotherapy targeting the prostate specific membrane antigen. *Brit J Radiol* 91:20180308
143. Kunikowska JI, Lewington V et al (2017) Optimizing somatostatin receptor imaging in patients with neuroendocrine tumors: the impact of $^{99\text{m}}\text{Tc}$ -HYNICTOC SPECT/SPECT/CT versus ^{68}Ga -DOTATATE PET/CT upon clinical management. *Clin Nucl Med* 42(12):905–911
144. Kwekkeboom D, Krenning EP et al (2000) Peptide receptor imaging and therapy. *J Nucl Med* 41:1704–1713
145. La Bella R, Garcia-Garayoa E et al (2002) A $^{99\text{m}}\text{Tc}(\text{I})$ -postlabeled high affinity bombesin analogue as a potential tumor imaging agent. *Bioconjug Chem* 13:599–604
146. Lantry LE, Cappelletti E et al (2006) ^{177}Lu -AMBA: synthesis and characterization of a selective ^{177}Lu -labeled GRP-R agonist for systemic radiotherapy of prostate cancer. *J Nucl Med* 47:1144–1152
147. Lawal IO, Ankrah AO et al (2017) Diagnostic sensitivity of Tc-99m HYNIC PSMA SPECT/CT in prostate carcinoma: a comparative analysis with Ga-68 PSMA PET/CT. *Prostate* 77:1205–1212

148. Lazarova L, Causey PW et al (2011) The synthesis, magnetic purification and evaluation of ^{99m}Tc -labeled microbubbles. *Nucl Med Biol* 38:1111–1118
149. Leamon CP, Parker MA et al (2002) Synthesis and biological evaluation of EC20: a new folate-derived, ^{99m}Tc -based radiopharmaceutical. *Bioconjug Chem* 13:1200–1210
150. Lei K, Rusckowski M et al (1996) Technetium-99m antibodies labeled with MAG_3 and SHNH: an in vitro and animal in vivo comparison. *Nucl Med Biol* 23:917–922
151. Leonidova A, Foerster C et al (2015) In vivo demonstration of an active tumor pretargeting approach with peptide nucleic acid bioconjugates as complementary system. *Chem Sci* 6:5601–5616
152. Leyton JV, Olafsen T et al (2008) Humanized radioiodinated minibody for imaging of prostate stem cell antigen-expressing tumors. *Clin Cancer Res* 14:7488–7496
153. Li M, Meares CF et al (1995) Prelabeling of chimeric monoclonal antibody L6 with $^{90}\text{yttrium}$ - and $^{111}\text{indium}$ -1,4,7,10-tetraazacyclododecane-N, N', N'', N'''-tetraacetic acid (DOTA) chelates for radioimmunodiagnosis and therapy. *Cancer Res* 55:5726s–5728s
154. Lin X, Jin Z et al (2012) Synthesis and biodistribution of a New ^{99m}Tc -oxo complex with deoxyglucose dithiocarbamate for tumor imaging. *Chem Biol Drug Des* 79:239–245
155. Lindegren S, Frost SH (2011) Pretargeted radioimmunotherapy with α -particle emitting radionuclides. *Curr Radiopharm* 4:248–260
156. Liu G (2018) A revisit to the pretargeting concept—A target conversion. *Front Pharmacol* 9:1476
157. Liu S (2008) Bifunctional coupling agents for radiolabeling of biomolecules and target-specific delivery of metallic radionuclides. *Adv Drug Deliv Rev* 60:1347–1370
158. Liu S (2009) Radiolabeled cyclic RGD peptides as integrin $\alpha(v)\beta(3)$ -targeted radiotracers: maximizing binding affinity via bivalency. *Bioconjug Chem* 20:2199–2213
159. Liu S, Edwards DS (1999) ^{99m}Tc -Labeled small peptides as diagnostic radiopharmaceuticals. *Chem Rev* 99:2235–2268
160. Liu S, Edwards DS et al (1998) A novel ternary ligand system for ^{99m}Tc -labeling of hydrazino nicotinamide-modified biologically active molecules using imine-N-containing heterocycles as coligands. *Bioconjug Chem* 9:583–595
161. Liu S, Kim YS et al (2008) Coligand effects on the solution stability, biodistribution and metabolism of the ^{99m}Tc -labeled cyclic RGDfK tetramer. *Nucl Med Biol* 35:111–121
162. Liu Z, Li ZB et al (2009) Small-animal PET of tumors with ^{64}Cu -labeled RGD-bombesin heterodimer. *J Nucl Med* 50:1168–1177
163. Liu Z, Niu G et al (2009) ^{68}Ga -labeled NOTA-RGD-BBN peptide for dual integrin and GRPR-targeted tumor imaging. *Eur J Nucl Med Mol Imaging* 36:1483–1494
164. Liu Z, Huang J et al (2012) ^{99m}Tc -labeled RGD-BBN peptide for small-animal SPECT/CT of lung carcinoma. *Mol Pharm* 9:1409–1417
165. Low PS, Henne WA et al (2008) Discovery and development of folic-acid-based receptor targeting for imaging and therapy of cancer and inflammatory diseases. *Acc Chem Res* 41:120–129
166. Lu G, Maresca KP et al (2013) Synthesis and SAR of $^{99m}\text{Tc}/\text{Re}$ -labeled small molecule prostate specific membrane antigen inhibitors with novel polar chelates. *Bioorg Med Chem Lett* 23:1557–1563
167. Lu J, Pang Y et al (2011) Synthesis and in vitro/in vivo evaluation of ^{99m}Tc -labeled folate conjugates for folate receptor imaging. *Nucl Med Biol* 38:557–565
168. Maddalena ME, Fox J et al (2009) ^{177}Lu -AMBA biodistribution, radiotherapeutic efficacy, imaging, and autoradiography in prostate cancer models with low GRP-R expression. *J Nucl Med* 50:2017–2024
169. Maes V, Garcia-Garayoa E et al (2006) Novel ^{99m}Tc -labeled neurotensin analogues with optimized biodistribution properties. *J Med Chem* 49:1833–1836
170. Maina T, Nikolopoulou A et al (2007) [^{99m}Tc]Demotensin 5 and 6 in the NTS1-R-targeted imaging of tumours: synthesis and preclinical results. *Eur J Nucl Med Mol Imaging* 34:1804–1814

171. Maina T, Nock B et al (2002) [^{99m}Tc]Demotate, a new ^{99m}Tc-based [Tyr³]octreotate analogue for the detection of somatostatin receptor-positive tumours: synthesis and preclinical results. *Eur J Nucl Med Mol Imaging* 29:742–753
172. Mansi R, Wang X et al (2009) Evaluation of a 1,4,7,10-tetraazacyclododecane-1,4,7,10-tetraacetic acid-conjugated bombesin-based radioantagonist for the labeling with single-photon emission computed tomography, positron emission tomography, and therapeutic radionuclides. *Clin Cancer Res* 15:5240–5249
173. Mardirossian G, Wu C et al (1993) The stability in liver homogenates of indium-111 and yttrium-90 attached to antibody via two popular chelators. *Nucl Med Biol* 20:65–74
174. Maresca KP, Hillier SM et al (2009) Comprehensive radiolabeling, stability, and tissue distribution studies of technetium-99m single amino acid chelates (SAAC). *Bioconjug Chem* 20:1625–1633
175. Maresca KP, Hillier SM et al (2012) Small molecule inhibitors of PSMA incorporating technetium-99m for imaging prostate cancer: effects of chelate design on pharmacokinetics. *Inorg Chim Acta* 389:168–175
176. Maresca KP, Hillier SM et al (2009) A series of halogenated heterodimeric inhibitors of prostate specific membrane antigen (PSMA) as radiolabeled probes for targeting prostate cancer. *J Med Chem* 52(2):347–357
177. Markwalder R, Reubi JC (1999) Gastrin-releasing peptide receptors in the human prostate: relation to neoplastic transformation. *Cancer Res* 59:1152–1159
178. Mather SJ, Nock BA et al (2014) GRP receptor imaging of prostate cancer using [^{99m}Tc] Demobesin 4: a first-in-man study. *Mol Imaging Biol* 16:888–895
179. Mathias CJ, Wang S et al (1998) Indium-111-DTPA-folate as a potential folate-receptor-targeted radiopharmaceutical. *J Nucl Med* 39:1579–1585
180. Matteson EL, Lowe VJ et al (2009) Assessment of disease activity in rheumatoid arthritis using a novel folate targeted radiopharmaceutical folatescan. *Clin Exp Rheumatol* 27:253–259
181. Maurer AH, Elsinga P et al (2014) Imaging the folate receptor on cancer cells with ^{99m}Tc-etarfolatide: properties, clinical use, and future potential of folate receptor imaging. *J Nucl Med* 55:701–704
182. Mercer JR, Xu LH et al (1989) Synthesis and tumor uptake of 5-⁸²Br- and 5-¹³¹I-labeled 5-halo-1-(2-fluoro-2-deoxy-beta-D-ribofuranosyl)uracils. *J Med Chem* 32:1289–1294
183. Meredith RF, Buchsbaum DJ (2006) Pretargeted radioimmunotherapy. *Int J Radiat Oncol Biol Phys* 66:S57–S59
184. Mikołajczak R, Maecke HR (2016) Radiopharmaceuticals for somatostatin receptor imaging. *Nucl Med Rev* 19(2):126–132
185. Mindt TL, Jungi V et al (2008) Modification of different IgG1 antibodies via glutamine and lysine using bacterial and human tissue transglutaminase. *Bioconjug Chem* 19:271–278
186. Minko T, Paranjpe PV et al (2002) Enhancing the anticancer efficacy of camptothecin using biotinylated poly (ethylene glycol) conjugates in sensitive and multidrug-resistant human ovarian carcinoma cells. *Cancer Chemother Pharmacol* 50:143–150
187. Moody TW, Russell EK et al (1983) Bombesin-like peptides in small cell lung cancer: biochemical characterization and secretion from a cell line. *Life Sci* 32:487–493
188. Moreno P, Ramos-Álvarez I et al (2016) Bombesin related peptides/receptors and their promising therapeutic roles in cancer imaging, targeting and treatment. *Expert Opin Ther Targets* 20:1055–1073
189. Morris RT, Joyrich RN et al (2014) Phase II study of treatment of advanced ovarian cancer with folate-receptor-targeted therapeutic (vintafolide) and companion SPECT-based imaging agent (^{99m}Tc-etarfolatide). *Ann Oncol* 25:852–858
190. Müller C, Brühlmeier M et al (2006) Effects of antifolate drugs on the cellular uptake of radiofolates in vitro and in vivo. *J Nucl Med* 47:2057–2064

191. Müller C, Mindt TL et al (2009) Evaluation of a novel radiofolate in tumour-bearing mice: promising prospects for folate-based radionuclide therapy. *Eur J Nucl Med Mol Imaging* 36:938–946
192. Müller C, Reddy JA et al (2010) Effects of the antifolates pemetrexed and CB3717 on the tissue distribution of ^{99m}Tc -EC20 in xenografted and syngeneic tumor-bearing mice. *Mol Pharm* 7:597–604
193. Müller C, Schibli R et al (2008) Pemetrexed improves tumor selectivity of ^{111}In -DTPA-folate in mice with folate receptor-positive ovarian cancer. *J Nucl Med* 49:623–629
194. Müller C, Schubiger PA et al (2006) Synthesis and in vitro/in vivo evaluation of novel ^{99m}Tc (CO)₃-folates. *Bioconjug Chem* 17:797–806
195. Müller C, Schubiger PA et al (2007) Isostructural folate conjugates radiolabeled with the matched pair $^{99m}\text{Tc}/^{188}\text{Re}$: a potential strategy for diagnosis and therapy of folate receptor-positive tumors. *Nucl Med Biol* 34:595–601
196. Müller C, Schibli R (2013) Prospects in folate receptor-targeted radionuclide therapy. *Front Oncol* 3:249
197. Müller C, Struthers H et al (2013) DOTA conjugate with an albumin-binding entity enables the first folic acid-targeted ^{177}Lu -radionuclide tumor therapy in mice. *J Nucl Med* 54:124–131
198. Müller C (2013) Folate-based radiotracers for PET imaging-update and perspectives. *Molecules* 18:5005–5031
199. Müller C, Bunka M et al (2014) Promising prospects for $^{44}\text{Sc}/^{47}\text{Sc}$ -based theragnostics: application of ^{47}Sc for radionuclide tumor therapy in mice. *J Nucl Med* 55:1658–1664
200. Müller C, Reber J et al (2014) Direct in vitro and in vivo comparison of ^{161}Tb and ^{177}Lu using a tumour-targeting folate conjugate. *Eur J Nucl Med Mol Imaging* 41:476–485
201. Müller C, Reber J et al (2014) Folate receptor targeted alpha-therapy using terbium-149. *Pharmaceuticals* 7:353–365
202. Munch-Petersen B, Cloos L et al (1995) Human thymidine kinase 1. regulation in normal and malignant cells. *Adv Enzyme Regul* 35:69–89
203. Narmani A, Yavari K et al (2017) Imaging, biodistribution and in vitro study of smart ^{99m}Tc -PAMAM G4 dendrimer as novel nano-complex. *Coll Surf B* 159:232–240
204. Neri D, Carnemolla B et al (1997) Targeting by affinity-matured recombinant antibody fragments of an angiogenesis associated fibronectin isoform. *Nat Biotechnol* 15:1271–1275
205. Nock B, Nikolopoulou A et al (2003) [^{99m}Tc]Demobesin 1, a novel potent bombesin analogue for GRP receptor-targeted tumour imaging. *Eur J Nucl Med Mol Imaging* 30:247–258
206. Nock BA, Nikolopoulou A et al (2005) Potent bombesin-like peptides for GRP-receptor targeting of tumors with ^{99m}Tc : a preclinical study. *J Med Chem* 48:100–110
207. Nock BA, Nikolopoulou A et al (2006) Toward stable N4-modified neurotensins for NTS1-receptor-targeted tumor imaging with ^{99m}Tc . *J Med Chem* 49:4767–4776
208. Núñez EG, Faintuch BL et al (2009) Influence of colloid particle profile on sentinel lymph node uptake. *Nucl Med Biol* 36:741–747
209. Oh P, Li Y et al (2004) Subtractive proteomic mapping of the endothelial surface in lung and solid tumours for tissue-specific therapy. *Nature* 429:629–635
210. Ozker K, Collier BD et al (1999) Biodistribution of ^{99m}Tc -labelled 5-thio-D-glucose. *Nucl Med Commun* 20:1055–1058
211. Papagiannopoulou D (2017) Technetium-99m radiochemistry for pharmaceutical applications. *J Label Comp Radiopharm* 60:502–520
212. Parker N, Turk MJ et al (2005) Folate receptor expression in carcinomas and normal tissues determined by a quantitative radioligand binding assay. *Anal Biochem* 338:284–293
213. Patra M, Zarschler K et al (2016) New insights into the pretargeting approach to image and treat tumours. *Chem Soc Rev* 45:6415–6431

214. Petrig J, Schibli R et al (2001) Derivatization of glucose and 2-deoxyglucose for transition metal complexation: substitution reactions with organometallic ^{99m}Tc and Re precursors and fundamental NMR investigations. *Chemistry* 7:1868–1873
215. Pini A, Viti F et al (1998) Design and use of a phage display library. human antibodies with subnanomolar affinity against a marker of angiogenesis eluted from a two-dimensional gel. *J Biol Chem* 273:21769–21776
216. Piramoon M, Hosseinimehr SJ (2016) The past, current studies and future of organometallic $^{99m}\text{Tc}(\text{CO})_3$ labeled peptides and proteins. *Curr Pharm Des* 22:4854–4867
217. Posey JA, Khzaeli MB et al (2001) A pilot trial of vitaxin, a humanized anti-tronectin receptor (anti alpha v beta 3) antibody in patients with metastatic cancer. *Cancer Biother Radiopharm* 16:125–132
218. Pretze M, Wuest F et al (2010) The traceless Staudinger ligation with fluorine-18: a novel and versatile labeling technique for the synthesis of PET-radiotracers. *Tetrahedron Lett* 51:6410–6414
219. Purohit A, Liu S et al (2003) Phosphine-containing HYNIC derivatives as potential bifunctional chelators for ^{99m}Tc -labeling of small biomolecules. *Bioconjug Chem* 14:720–727
220. Rahbar K, Afshar-Oromieh A et al (2018) PSMA theranostics: current status and future directions. *Mol Imaging* 17:1536012118776068
221. Rahbar K, Ahmadzadehfar H et al (2017) German multicenter study investigating ^{177}Lu -PSMA-617 radioligand therapy in advanced prostate cancer patients. *J Nucl Med* 58:85–90
222. Reber J, Struthers H et al (2012) Radioiodinated folic acid conjugates: evaluation of a valuable concept to improve tumor-to-background contrast. *Mol Pharm* 9:1213–1221
223. Reddy JA, Xu LC et al (2004) Preclinical evaluation of ^{99m}Tc -EC20 for imaging folate receptor-positive tumors. *J Nucl Med* 45:857–866
224. Reubi JC, Waser B et al (1998) Neurotensin receptors: a new marker for human ductal pancreatic adenocarcinoma. *Gut* 42:546–550
225. Rezazadeh F, Sadeghzadeh N (2018) Tumor targeting with ^{99m}Tc radiolabeled peptides: clinical application and recent development. *Chem Biol Drug Design*. <https://doi.org/10.1111/cbdd.13413>
226. Retzlaff L, Heinzke L et al (2010) Evaluation of [^{99m}Tc -(CO) $_3$ -X-Y-Bombesin(7-14)NH $_2$] conjugates for targeting gastrin-releasing peptide receptors overexpressed on breast carcinoma. *Anticancer Res* 30:19–30
227. Risch VR, Honda T et al (1977) Distribution of ^{99m}Tc -1-thiogluconate in rats: effect of administration route on pancreatic specificity. *Radiology* 124:837–838
228. Robu S, Schottelius M et al (2017) Preclinical evaluation and first patient application of ^{99m}Tc -PSMA-I&S for SPECT imaging and radioguided surgery in prostate cancer. *J Nucl Med* 58(2):235–242
229. Rolleman EJ, Valkema R et al (2003) Safe and effective inhibition of renal uptake of radiolabelled octreotide by a combination of lysine and arginine. *Eur J Nucl Med Mol Imaging* 30:9–15
230. Römhild K, Fischer CA, Mindt TL (2017) Glycated ^{99m}Tc -tricarboxyl-labeled peptide conjugates for tumor targeting by “Click-to-Chelate”. *ChemMedChem* 12:66–74
231. Rosebrough SF (1993) Pharmacokinetics and biodistribution of radiolabeled avidin, streptavidin and biotin. *Nucl Med Biol* 20:663–668
232. Rowland DJ, Cherry SR (2008) Small-animal preclinical nuclear medicine instrumentation and methodology. *Semin Nucl Med* 38:209–222
233. Russell-Jones G, McTavish K et al (2004) Vitamin-mediated targeting as a potential mechanism to increase drug uptake by tumours. *J Inorg Biochem* 98:1625–1633
234. Salmaso S, Pappalardo JS et al (2009) Targeting glioma cells in vitro with ascorbate-conjugated pharmaceutical nanocarriers. *Bioconjug Chem* 20:2348–2355
235. Salouti M, Rajabi H et al (2008) Breast tumor targeting with ^{99m}Tc -HYNIC-PR81 complex as a new biologic radiopharmaceutical. *Nucl Med Biol* 35:763–768

236. Santimaria M, Moscatelli G et al (2003) Immunoscintigraphic detection of the ED-B domain of fibronectin, a marker of angiogenesis, in patients with cancer. *Clin Cancer Res* 9:571–579
237. Santos-Cuevas CL, Ferro-Flores G et al (2011) ^{99m}Tc -N₂S₂-Tat(49-57)-bombesin internalized in nuclei of prostate and breast cancer cells: kinetics, dosimetry and effect on cellular proliferation. *Nucl Med Commun* 32:303–313
238. Santos-Cuevas C, Davanzo J et al (2017) ^{99m}Tc -labeled PSMA inhibitor: biokinetics and radiation dosimetry in healthy subjects and imaging of prostate cancer tumors in patients. *Nucl Med Biol* 52:1–6
239. Schibli R, Dumas C et al (2005) Synthesis and in vitro characterization of organometallic rhenium and technetium glucose complexes against Glut 1 and hexokinase. *Bioconjug Chem* 16:105–112
240. Schibli R, La Bella R et al (2000) Influence of the denticity of ligand systems on the in vitro and in vivo behavior of ^{99m}Tc (I)-tricarbonyl complexes: a hint for the future functionalization of biomolecules. *Bioconjug Chem* 11:345–351
241. Schibli R, Schubiger PA (2002) Current use and future potential of organometallic radiopharmaceuticals. *Eur J Nucl Med Mol Imaging* 29:1529–1542
242. Schibli R, Schwarzbach R et al (2002) Steps toward high specific activity labeling of biomolecules for therapeutic application: preparation of precursor [$^{188}\text{Re}(\text{H}_2\text{O})_3(\text{CO})_3$]⁺ and synthesis of tailor-made bifunctional ligand systems. *Bioconjug Chem* 13:750–756
243. Schmid M, Neumaier B et al (2006) Synthesis and evaluation of a radiometal-labeled macrocyclic chelator-derivatised thymidine analog. *Nucl Med Biol* 33:359–366
244. Schmidkonz C, Cordes M et al (2018) SPECT/CT with the PSMA ligand ^{99m}Tc -MIP-1404 for whole-body primary staging of patients with prostate cancer. *Clin Nucl Med* 43:225–231
245. Schmidkonz C, Hollweg C et al (2018) ^{99m}Tc -MIP-1404-SPECT/CT for the detection of PSMA-positive lesions in 225 patients with biochemical recurrence of prostate cancer. *Prostate* 78:54–63
246. Schottelius M, Laufer B et al (2009) Ligands for mapping alphavbeta3-integrin expression in vivo. *Acc Chem Res* 42:969–980
247. Schottelius M, Wester HJ (2009) Molecular imaging targeting peptide receptors. *Methods* 48:161–177
248. Schottelius M, Wester HJ et al (2002) Improvement of pharmacokinetics of radioiodinated Tyr³-octreotide by conjugation with carbohydrates. *Bioconjug Chem* 13:1021–1030
249. Schubert M, Foerster C et al (2017) A novel tumor pretargeting system based on complementary L-configured oligonucleotides. *Biocon Chem* 28:1176–1188
250. Schwartz DA, Abrams MJ et al (1991) Preparation of hydrazino-modified proteins and their use for the synthesis of ^{99m}Tc -protein conjugates. *Bioconjug Chem* 2:333–336
251. Schweinsberg C, Maes V et al (2008) Novel glycosylated [$^{99m}\text{Tc}(\text{CO})_3$]-labeled bombesin analogues for improved targeting of gastrin-releasing peptide receptor-positive tumors. *Bioconjug Chem* 19:2432–2439
252. Seetharam B (1999) Receptor-mediated endocytosis of cobalamin (vitamin B₁₂). *Annu Rev Nutr* 19:173–195
253. Seetharam B, Li N (2000) Transcobalamin II and its cell surface receptor. *Vitam Horm* 59:337–366
254. Seetharam B, Yammani RR (2003) Cobalamin transport proteins and their cell-surface receptors. *Expert Rev Mol Med* 5:1–18
255. Semnani ES, Wang K et al (2005) 5-[$^{123}\text{I}/^{125}\text{I}$]iodo-2'-deoxyuridine in metastatic lung cancer: radiopharmaceutical formulation affects targeting. *J Nucl Med* 46:800–806
256. Shariati F, Aryana K et al (2014) Diagnostic value of ^{99m}Tc -bombesin scintigraphy for differentiation of malignant from benign breast lesions. *Nucl Med Commun* 35:620–625
257. Sharkey RM, Karacay H et al (2005) Improving the delivery of radionuclides for imaging and therapy of cancer using pretargeting methods. *Clin Cancer Res* 11:7109s
258. Sharp SE, Trout AT et al (2016) MIBG in neuroblastoma diagnostic imaging and therapy. *RadioGraphics* 36:258–278

259. Shi J, Kim YS et al (2009) Improving tumor uptake and pharmacokinetics of ^{64}Cu -labeled cyclic RGD peptide dimers with Gly(3) and PEG(4) linkers. *Bioconjug Chem* 20:750–759
260. Shi J, Wang L et al (2008) Improving tumor uptake and excretion kinetics of $^{99\text{m}}\text{Tc}$ -labeled cyclic arginine-glycine-aspartic (RGD) dimers with triglycine linkers. *J Med Chem* 51:7980–7990
261. Siegel BA, Dehdashti F et al (2003) Evaluation of ^{111}In -DTPA-folate as a receptor-targeted diagnostic agent for ovarian cancer: initial clinical results. *J Nucl Med* 44:700–707
262. Silver DA, Pellicer I et al (1997) Prostatespecific membrane antigen expression in normal and malignant human tissues. *Clin Cancer Res* 3:81–85
263. Silvestri C, Christopher A et al (2019) Consecutive case series of melanoma sentinel node biopsy for lymphoseek compared to sulfur colloids. *J Surg Res* 233:149–153
264. Siwowska K, Müller C (2015) Preclinical development of small-molecular-weight folate-based radioconjugates: a pharmacological perspective. *Quart J Nucl Med Mol Imaging* 59:269–286
265. Smith CJ, Gali H et al (2003) Radiochemical investigations of ^{177}Lu -DOTA-8-Aoc-BBN [7-14]NH₂: an in vitro/in vivo assessment of the targeting ability of this new radiopharmaceutical for PC-3 human prostate cancer cells. *Nucl Med Biol* 30:101–109
266. Smith CJ, Sieckman GL et al (2003) Radiochemical investigations of gastrin-releasing peptide receptor-specific [$^{99\text{m}}\text{Tc}(\text{X})(\text{CO})_3$ -Dpr-Ser-Ser-Ser-Gln-Trp-Ala-Val-Gly-His-Leu-Met-(NH₂)] in PC-3, tumor-bearing, rodent models: syntheses, radiolabeling, and in vitro/in vivo studies where Dpr = 2,3-diaminopropionic acid and X = H₂O or P(CH₂OH)₃. *Ca Cancer Res* 63:4082–4088
267. Smith CJ, Sieckman GL et al (2003) Radiochemical investigations of [$^{188}\text{Re}(\text{H}_2\text{O})(\text{CO})_3$ -diaminopropionic acid-SSS-bombesin(7-14)NH₂]: syntheses, radiolabeling and in vitro/in vivo GRP receptor targeting studies. *Anticancer Res* 23:63–70
268. Smith CJ, Volkert WA et al (2003) Gastrin releasing peptide (GRP) receptor targeted radiopharmaceuticals: a concise update. *Nucl Med Biol* 30:861–868
269. Smith CJ, Volkert WA et al (2005) Radiolabeled peptide conjugates for targeting of the bombesin receptor superfamily subtypes. *Nucl Med Biol* 32:733–740
270. Smith TAD (2001) The rate-limiting step for tumor [^{18}F]fluoro-2-deoxy-D-glucose (FDG) incorporation. *Nucl Med Biol* 28:1–4
271. Sosabowski JK, Matzow T et al (2009) Targeting of CCK-2 receptor-expressing tumors using a radiolabeled divalent gastrin peptide. *J Nucl Med* 50:2082–2089
272. Spanoudaki VC, Ziegler SI (2008) PET and SPECT instrumentation. *Handb Exp Pharmacol* 185:53–74
273. Steen EJJ, Edem PE et al (2018) Pretargeting in nuclear imaging and radionuclide therapy: improving efficacy of theranostics and nanomedicines. *Biomaterials* 179:209–245
274. Steffens MG, Oosterwijk E et al (1999) In vivo and in vitro characterizations of three $^{99\text{m}}\text{Tc}$ -labeled monoclonal antibody G250 preparations. *J Nucl Med* 40:829–836
275. Storr T, Fisher CL et al (2005) A glucosamine-dipicolylamine conjugate of $^{99\text{m}}\text{Tc}(\text{I})$ and $^{186}\text{Re}(\text{I})$ for use in imaging and therapy. *Dalton Trans* 21(4):654–655
276. Struthers H, Hagenbach A et al (2009) Organometallic [$\text{Re}(\text{CO})_3$]⁺ and [$\text{Re}(\text{CO})_2(\text{NO})$]²⁺ labeled substrates for human thymidine kinase 1. *Inorg Chem* 48:5154–5163
277. Struthers H, Spingler B et al (2008) “Click-to-chelate”: design and incorporation of triazole-containing metal-chelating systems into biomolecules of diagnostic and therapeutic interest. *Chemistry* 14:6173–6183
278. Surasi DS, O’Malley J et al (2015) $^{99\text{m}}\text{Tc}$ -Tilmanocept: a novel molecular agent for lymphatic mapping and sentinel lymph node localization. *J Nucl Med Technol* 43:87–91
279. Tang Y, Scollard D et al (2005) Imaging of HER2/neu expression in BT-474 human breast cancer xenografts in athymic mice using [$^{99\text{m}}\text{Tc}$]-HYNIC-trastuzumab (Herceptin) Fab fragments. *Nucl Med Commun* 26:427–432
280. Tienken L, Drude N et al (2018) Evaluation of a pretargeting strategy for molecular imaging of the prostate stem cell antigen with a single chain antibody. *Sci Rep* 8:3755

281. Tolmachev V, Friedman M et al (2009) Affibody molecules for epidermal growth factor receptor targeting in vivo: aspects of dimerization and labeling chemistry. *J Nucl Med* 50:274–283
282. Torizuka T, Tamaki N et al (1995) In vivo assessment of glucose metabolism in hepatocellular carcinoma with FDG-PET. *J Nucl Med* 36:1811–1817
283. Toyohara J, Hayashi A et al (2002) Rationale of 5-¹²⁵I-iodo-4'-thio-2'-deoxyuridine as a potential iodinated proliferation marker. *J Nucl Med* 43:1218–1226
284. Toyohara J, Hayashi A et al (2003) Development of radioiodinated nucleoside analogs for imaging tissue proliferation: comparisons of six 5-iodonucleosides. *Nucl Med Biol* 30:687–696
285. Trogrlic M, Tezak S (2016) ^{99m}Tc-EDDA/HYNIC-TOC in management of patients with head and neck somatostatin receptor positive tumors. *Nucl Med Rev* 19:74–80
286. Unkart JT, Wallace AM (2017) Use of ^{99m}Tc-tilmanocept as a single agent for sentinel lymph node identification in breast cancer: a retrospective pilot study. *J Nucl Med Technol* 45:181–184
287. Vallabhajosula S, Nikolopoulou A et al (2014) ^{99m}Tc-labeled small-molecule inhibitors of prostate-specific membrane antigen: pharmacokinetics and biodistribution studies in healthy subjects and patients with metastatic prostate cancer. *J Nucl Med* 55:1791–1798
288. Van de Wiele C, Dumont F et al (2000) Technetium-99m RP527, a GRP analogue for visualisation of GRP receptor-expressing malignancies: a feasibility study. *Eur J Nucl Med* 27:1694–1699
289. van der Kroon I, Joosten L et al (2016) Improved quantification of the beta cell mass after pancreas visualization with ^{99m}Tc-demobesin-4 and beta cell imaging with ¹¹¹In-exendin-3 in rodents. *Mol Pharm* 13:3478–3483
290. van der Poel HG, Buckle T et al (2011) Intraoperative laparoscopic fluorescence guidance to the sentinel lymph node in prostate cancer patients: clinical proof of concept of an integrated functional imaging approach using a multimodal tracer. *Eur Urol* 60:826–833
291. Varasteh Z, Hyafil F et al (2017) Targeting mannose receptor expression on macrophages in atherosclerotic plaques of apolipoprotein E-knockout mice using ¹¹¹In-tilmanocept. *EJNMMI Res* 7:40
292. Vera DR, Wallace AM et al (2001) A synthetic macromolecule for sentinel node detection: ^{99m}Tc-DTPA-Mannosyl-dextran. *J Nucl Med* 42:951–959
293. Verhaar-Langereis MJ, Zonnenberg BA et al (2000) Radioimmunodiagnosis and therapy. *Cancer Treat Rev* 26:3–10
294. Verwijnen SM, Krenning EP et al (2005) Oral versus intravenous administration of lysine: equal effectiveness in reduction of renal uptake of [¹¹¹In-DTPA]octreotide. *J Nucl Med* 46:2057–2060
295. Vidal-Sicart S, Vera DR et al (2018) Next generation of radiotracers for sentinel lymph node biopsy: What is still necessary to establish new imaging paradigms? *Rev Esp Med Nucl Imagen Mol* 37:373–379
296. von Guggenberg E, Dietrich H et al (2007) ^{99m}Tc-labelled HYNIC-minigastrin with reduced kidney uptake for targeting of CCK-2 receptor-positive tumours. *Eur J Nucl Med Mol Imaging* 34:1209–1218
297. Vöö S, Bucerius J et al (2011) I-131-MIBG therapies. *Methods* 55(3):238–245
298. Waibel R, Treichler H et al (2008) New derivatives of vitamin B₁₂ show preferential targeting of tumors. *Cancer Res* 68:2904–2911
299. Wang L, Shi J et al (2009) Improving tumor-targeting capability and pharmacokinetics of ^{99m}Tc-labeled cyclic RGD dimers with PEG(4) linkers. *Mol Pharm* 6:231–245
300. Wang S, Luo J et al (1997) Design and synthesis of [¹¹¹In]DTPA-folate for use as a tumor-targeted radiopharmaceutical. *Bioconj Chem* 8:673–679
301. Wang Y, Zhu J et al (2014) Synthesis and evaluation of ^{99m}Tc-2-[(3-carboxy-1-oxopropyl)amino]-2-deoxy-D-glucose as a potential tumor imaging agent. *Bioorg Med Chem Lett* 24:3882–3885

302. Wängler C, Schirmacher R et al (2009) Simple and convenient radiolabeling of proteins using a prelabeling-approach with thiol-DOTA. *Bioorg Med Chem Lett* 19:1926–1929
303. Weineisen M, Šimeček J et al (2014) Synthesis and preclinical evaluation of DOTAGA-conjugated PSMA ligands for functional imaging and endoradiotherapy of prostate cancer. *EJNMMI Res* 4:63
304. Weitman SD, Lark RH et al (1992) Distribution of the folate receptor GP38 in normal and malignant cell lines and tissues. *Cancer Res* 52:3396–3401
305. Wester HJ, Schottelius M et al (2002) Comparison of radioiodinated TOC, TOCA and Mtr-TOCA: the effect of carbohydrate on the pharmacokinetics. *Eur J Nucl Med Mol Imaging* 29:28–38
306. Wieland DM, Wu J et al (1980) Radiolabeled adrenergi neuron-blocking agents: adrenomedullary imaging with [¹³¹I]iodobenzylguanidine. *J Nucl Med* 21:349–353
307. Wilbur DS, Hamlin DK et al (1996) Synthesis and nca-radioiodination of arylstannyl-cobalamin conjugates. evaluation of arylido-cobalamin conjugate binding to transcobalamin II and biodistribution in mice. *Bioconjug Chem* 7:461–474
308. Wilbur DS, Hamlin DK et al (1998) Synthesis and evaluation of ^{99m}Tc/⁹⁹Tc-MAG₃-biotin conjugates for antibody pretargeting strategies. *Nucl Med Biol* 25:611–619
309. Xu N, Cai G et al (2009) Molecular imaging application of radioiodinated anti-EGFR human Fab to EGFR-overexpressing tumor xenografts. *Anticancer Res* 29:4005–4011
310. Yamada Y, Nakatani H et al (2015) Phase I clinical trial of ^{99m}Tc-etarfolatide, an imaging agent for folate receptor in healthy Japanese adults. *Ann Nucl Med* 29:792–798
311. Yang W, Cheng Y et al (2009) Targeting cancer cells with biotin-dendrimer conjugates. *Eur J Med Chem* 44:862–868
312. Yim CB, Boerman OC et al (2009) Versatile conjugation of octreotide to dendrimers by cycloaddition (“click”) chemistry to yield high-affinity multivalent cyclic peptide dendrimers. *Bioconjug Chem* 20:1323–1331
313. Yokota T, Milenic DE et al (1992) Rapid tumor penetration of a single-chain Fv and comparison with other immunoglobulin forms. *Cancer Res* 52:3402–3408
314. Yokota T, Milenic DE et al (1993) Microautoradiographic analysis of the normal organ distribution of radioiodinated single-chain Fv and other immunoglobulin forms. *Cancer Res* 53:3776–3783
315. Zardi L, Carnemolla B et al (1987) Transformed human cells produce a new fibronectin isoform by preferential alternative splicing of a previously unobserved exon. *EMBO J* 6:2337–2342
316. Zechmann CM, Afshar-Oromieh A et al (2014) Radiation dosimetry and first therapy results with a ¹²⁴I/¹³¹I-labeled small molecule (MIP-1095) targeting PSMA for prostate cancer therapy. *Eur J Nucl Med Mol Imaging* 41:1280–1292
317. Zelenka K, Lubor Borsig L, Alberto R (2011) Trifunctional ^{99m}Tc based radiopharmaceuticals: metal-mediated conjugation of a peptide with a nucleus targeting intercalator. *Org Biomol Chem* 9:1071–1078
318. Zeltchan R, Medvedeva A et al (2016) Experimental study of radiopharmaceuticals based on technetium-99m labeled derivative of glucose for tumor diagnosis. *IOP Conf Ser: Mater Sci Eng* 135:012054
319. Zhang J, Ren J (2009) Synthesis and biological evaluation of a novel ^{99m}Tc nitrido radiopharmaceutical with deoxyglucose dithiocarbamate, showing tumor uptake. *Bioorg Med Chem Lett* 19:2752–2754
320. Zhang H, Chen J et al (2004) Synthesis and evaluation of bombesin derivatives on the basis of pan-bombesin peptides labeled with indium-111, lutetium-177, and yttrium-90 for targeting bombesin receptor-expressing tumors. *Cancer Res* 64:6707–6715
321. Zhang Y, Sun Y et al (2010) Radiosynthesis and micro-SPECT imaging of ^{99m}Tc-dendrimer poly(amido)-amine folic acid conjugate. *Bioorg Med Chem Lett* 20:927–931
322. Zwanziger D, Khan IU et al (2008) Novel chemically modified analogues of neuropeptide Y for tumor targeting. *Bioconjug Chem* 19:1430–1438



^{18}F -Labeled Small-Molecule and Low-Molecular-Weight PET Tracers for the Noninvasive Detection of Cancer

Christopher M. Waldmann, Klaus Kopka, and Stefan Wagner

Contents

8.1	Introduction.....	284
8.2	2-Deoxy-2- ^{18}F Fluoro-D-Glucose (^{18}F FDG) for Imaging Glucose Metabolism	285
8.3	^{18}F -Labeled Amino Acids for Imaging Amino Acid Transport and Protein Synthesis	287
8.3.1	<i>O</i> -(2- ^{18}F Fluoroethyl)-L-Tyrosine (^{18}F FET).....	287
8.3.2	6- ^{18}F Fluoro-3,4-Dihydroxy-L-Phenylalanine (^{18}F FDOPA).....	288
8.3.3	<i>Anti</i> -1-Amino-3- ^{18}F Fluorocyclobutane-1-Carboxylic Acid (^{18}F Flu- clovine, ^{18}F FACBC).....	291
8.4	^{18}F -Labeled Choline Derivatives for Imaging Membrane Lipid Synthesis	292
8.4.1	Dimethyl- ^{18}F Fluoromethyl-2-Hydroxyethylammonium (^{18}F Fluoromethyl- choline, ^{18}F FCH)	292
8.4.2	Dimethyl-2- ^{18}F Fluoroethyl-2-Hydroxyethylammonium (^{18}F Fluoroethyl- choline, ^{18}F FECH).....	293
8.5	^{18}F -Labeled Nucleoside Derivatives for Imaging Cell Proliferation.....	295
8.5.1	3'-Deoxy-3'- ^{18}F Fluorothymidine (^{18}F FLT).....	295
8.5.2	1-(2'-Deoxy-2'- ^{18}F Fluoro- β -D-Arabinofuranosyl)-5-Methyluracil (^{18}F FMAU)	296
8.6	^{18}F -Labeled Nitroimidazole Derivatives for Imaging of Tumor Hypoxia.....	298

C. M. Waldmann (✉)

Department of Nuclear Medicine, University Medical Center Mainz, Langenbeckstr. 1,
55131 Mainz, Germany

e-mail: christopher.waldmann@unimedizin-mainz.de

K. Kopka

Institute of Radiopharmaceutical Cancer Research, Helmholtz-Zentrum Dresden-Rossendorf
(HZDR), Bautzner Landstr. 400, 01328 Dresden, Germany

S. Wagner

Department of Nuclear Medicine, University Hospital Münster, Albert-Schweitzer-Campus 1,
Building A1, 48149 Münster, Germany

© Springer Nature Switzerland AG 2020

O. Schober et al. (eds.), *Molecular Imaging in Oncology*,

Recent Results in Cancer Research 216,

https://doi.org/10.1007/978-3-030-42618-7_8

8.6.1	1 <i>H</i> -1-(3-[¹⁸ F]Fluoro-2-Hydroxypropyl)-2-Nitroimidazole ([¹⁸ F]Fluoromisonidazole, [¹⁸ F]FMISO)	298
8.6.2	1-(5-Deoxy-5-[¹⁸ F]Fluoro- α -D-Arabinofuranosyl)-2-Nitroimidazole ([¹⁸ F]FAZA).....	299
8.7	16 α -[¹⁸ F]Fluoro-17 β -Estradiol ([¹⁸ F]FES) for Imaging Estrogen Receptor Status.....	300
8.8	¹⁸ F-Labeled Glu-Ureido-Based Inhibitors for Imaging Prostate-Specific Membrane Antigen (PSMA).....	301
8.8.1	(3 <i>S</i> ,10 <i>S</i> ,14 <i>S</i>)-1-(4-(((<i>S</i>)-4-Carboxy-2-((<i>S</i>)-4-Carboxy-2-(6-[¹⁸ F]Fluoronicotinamido)Butanamido)Butanamido)Methyl)Phenyl)-3-(Naphthalen-2-Ylmethyl)-1,4,12-Trioxo-2,5,11,13-Tetraazahexadecane-10,14,16-Tricarboxylic Acid ([¹⁸ F]PSMA-1007).....	301
8.8.2	2-(3-(1-Carboxy-5-[(6-[¹⁸ F]Fluoro-Pyridine-3-Carbonyl)-Amino]-Pentyl)-Ureido)-Pentanedioic Acid ([¹⁸ F]DCFPyL)	302
8.9	Sodium [¹⁸ F]Fluoride (Na[¹⁸ F]F) for Imaging Bone Mineralization	304
8.10	Conclusion	305
	References	305

8.1 Introduction

Molecular imaging *in vivo* involves the visualization, characterization, and measurement of biological processes at the molecular and cellular level [208]. In nuclear medicine, the scintigraphic techniques single-photon emission computed tomography (SPECT) and positron emission tomography (PET) are used for the molecular imaging of disease. These techniques rely on radiolabeled compounds, referred to as tracers or radiopharmaceuticals, that detect disease-specific biological targets or biochemical processes. SPECT and PET cameras include capabilities for computer tomography (CT), resulting in high-end hybrid tomographic imaging devices referred to as SPECT/CT or PET/CT. In addition, PET is combined with magnetic resonance imaging (PET/MRI). All these techniques combine high-resolution morphological imaging with highly sensitive molecular imaging and are known to significantly improve diagnostic capabilities in a variety of clinical disciplines. In an oncological setting, the hybrid imaging devices mentioned above are routinely used to differentiate malignant from benign diseases, to localize and stage a given disease, to grade tumors, and to detect the primary tumor and its metastases in patients. Furthermore, the identification of residual disease after treatment, the detection and localization of recurrences, the investigation of response to therapies, and the planning of radiation therapies is possible with the aforementioned imaging techniques [180].

The availability of disease-specific radiotracers for oncological imaging is critical to ensure patient care. For this purpose, the field of radiopharmaceutical chemistry has established the availability of various radiotracers for a wide array of applications. During radiosynthesis, tailor-made precursor compounds are labeled with a radionuclide yielding the corresponding radiotracer. For PET diagnostic purposes, neutron-deficient positron emitters such as fluorine-18 are used.

Fluorine-18 is the most frequently used PET-radionuclide in both preclinical research and routine clinical applications. Its physical half-life ($t_{1/2} = 109.8$ min, 97% β^+ decay) is long enough to allow for moderately complex syntheses while its comparably low positron energy (maximum β^+ energy = 635 keV) allows for imaging with high spatial resolution. Although the labeling of some PET tracers historically relied on the use of carrier-added, electrophilic $[^{18}\text{F}]\text{F}_2$, it is nowadays preferred to utilize non-carrier-added, nucleophilic $[^{18}\text{F}]\text{fluoride}$. $[^{18}\text{F}]\text{Fluoride}$ with high molar activities (A_m) is typically produced with a cyclotron under no-carrier-added conditions by the $^{18}\text{O}(\text{p},\text{n})^{18}\text{F}$ nuclear reaction using $[^{18}\text{O}]\text{H}_2\text{O}$ as the target material. The produced positron emitter fluorine-18 is then introduced into organic compounds like small molecules, peptides, peptidomimetics, and proteins using automated radiochemistry systems that are installed in lead shielded hotcells [209]. Before release, the formulated radiopharmaceuticals in injectable form must pass a series of quality control (QC) tests in accordance with applicable regulatory requirements. Common QC parameters for PET-radiopharmaceuticals are visual appearance of the solution, pH-value, osmolality, radiochemical identity, (radio-)chemical purity as well as radionuclide purity. Details about QC parameters are described in the corresponding monographs of the respective pharmacopoeias such as the European Pharmacopoeia (Ph. Eur.) and the United States Pharmacopoeia (USP).

The following sections describe the clinical applications of the most commonly used small-molecule and low-molecular-weight ^{18}F -labeled radiopharmaceuticals in oncological PET imaging. Besides the discussion of tracer accumulation mechanisms, the synthetic strategies used in clinical routine production are emphasized.

8.2 2-Deoxy-2- $[^{18}\text{F}]\text{Fluoro-D-Glucose}$ ($[^{18}\text{F}]\text{FDG}$) for Imaging Glucose Metabolism

Since the metabolic tracer 2-deoxy-2- $[^{18}\text{F}]\text{fluoro-D-glucose}$ ($[^{18}\text{F}]\text{FDG}$) was evaluated for the first time in the 1970s, it has developed into the most important radiopharmaceutical in clinical PET imaging [4, 53, 79, 167]. The radiotracer is predominantly used for tumor imaging, particularly for the estimation of enhanced glucose utilization in malignant lesions [70, 126, 154, 206].

The intracellular uptake mechanism of $[^{18}\text{F}]\text{FDG}$ is similar to that of D-glucose. Both compounds differ chemically in the formal replacement of a hydroxy moiety by fluorine-18 at the C-2 position. The glucose transport proteins GLUT-1–GLUT-7 and GLUT-10–GLUT-12 are responsible for the active and stereospecific transport of $[^{18}\text{F}]\text{FDG}$ into the cells. Following cell uptake, $[^{18}\text{F}]\text{FDG}$ is phosphorylated immediately by hexokinase isozymes I–IV to form $[^{18}\text{F}]\text{FDG-6-phosphate}$ ($[^{18}\text{F}]\text{FDG-6-P}$) [189]. Transport protein GLUT-1 and hexokinase II are the best-understood subtypes in the context of glucose metabolism in tumor cells [117]. Unlike with D-glucose, further catalytic metabolization of $[^{18}\text{F}]\text{FDG-6-P}$ by phosphoglucose-isomerase is hindered with ^{18}F -fluorine in the

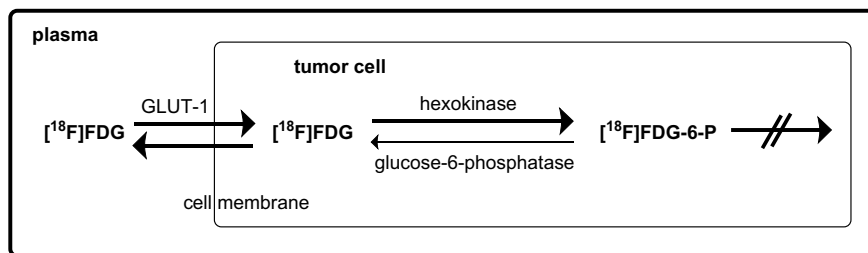


Fig. 8.1 Cellular [^{18}F]FDG accumulation by metabolic trapping

C-2-position. [^{18}F]FDG-6-P has a low membrane permeability and therefore accumulates intracellularly with the rate of accumulation proportional to glucose utilization. This mechanism is referred to as metabolic trapping [20] (Fig. 8.1). [^{18}F]FDG is not specific for cancer and accumulates in all areas with high levels of metabolism and glycolysis. Accumulation of the tracer may, for example, occur in inflamed tissue, sites of tissue repair as well as muscular or nervous hyperactivity.

^{19}F NMR spectroscopic investigations with macroscopic (millimolar) amounts of nonradioactive FDG *in vivo* demonstrated that FDG-6-P can be metabolized into 2-deoxy-2-fluoro-D-mannose-6-phosphate in specific organs, such as the brain and heart [20]. Furthermore, it is shown that glucose-6-phosphatase that is activated in defined organs is able to dephosphorylate [^{18}F]FDG-6-P and as a result decreases the metabolic trapping of [^{18}F]FDG. [^{18}F]FDG uptake is therefore increased in organs that are characterized by less intracellular amounts of glucose-6-phosphatase (e.g., brain and heart). In contrast, high enterohepatic glucose-6-phosphatase concentrations result in low [^{18}F]FDG uptake, e.g., in liver and intestines [190].

The production procedure of [^{18}F]FDG is well established and often carried out in high activity amounts (typically 37–370 GBq) by radiopharmacies that distribute the radiotracer to the sites of imaging. The handling of high activity amounts requires remotely controlled automated radiosynthesizers that perform the radiosynthesis in a shielded environment. The key synthetic step in the radiolabeling procedure is the replacement of a trifluoromethanesulfonate group (TfO) in the precursor molecule **1** with [^{18}F]fluoride in a bimolecular nucleophilic substitution ($\text{S}_{\text{N}}2$) reaction (Fig. 8.2). Before this step, cyclotron produced [^{18}F]fluoride has to be activated to allow the reaction to occur. For this, [^{18}F]fluoride is trapped

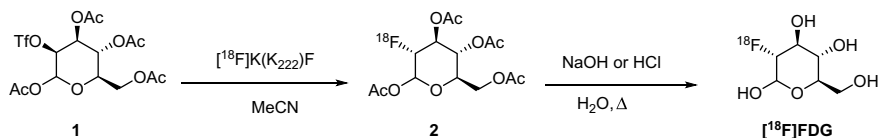


Fig. 8.2 Radiosynthesis of [^{18}F]FDG. Abbr.: OTf = trifluoromethanesulfonate; OAc = acetoxy

on an anion exchange resin and the bulk of [^{18}O]water is removed. The activity is released from the resin with basic solutions of large cations such as tetrabutylammonium or potassium-aminopolyether (Cryptand 222/ $\text{K}(\text{K}_{222})^+$). Water is then removed by azeotropic evaporation in the presence of acetonitrile (MeCN). Without the solvating water and in the presence of large counter-cations, the nucleophilicity of [^{18}F]fluoride is sufficient to carry out the $\text{S}_{\text{N}}2$ reaction upon heating. After the ^{18}F -labeling step, the acetyl (Ac) protection groups are removed by either acidic or basic hydrolysis to yield [^{18}F]FDG [51, 67]. [^{18}F]FDG is isolated from the reaction mixture by solid-phase extraction (SPE) procedures and formulated in physiological buffer. QC requirements are defined in the Eur. Ph. Monograph 9.0/1325 Fludeoxyglucose (^{18}F) injection.

8.3 ^{18}F -Labeled Amino Acids for Imaging Amino Acid Transport and Protein Synthesis

8.3.1 O -(2-[^{18}F]Fluoroethyl)- L -Tyrosine ([^{18}F]FET)

The ^{18}F -fluorinated tyrosine derivative O -(2-[^{18}F]fluoroethyl)- L -tyrosine ([^{18}F]FET) is a widely used tracer for the imaging of amino acid transport in tumor growth. The tracer has proven useful in diagnosing glioblastomas [33–37, 41, 199, 207]. Compared to [^{18}F]FDG, uptake in physiological brain structures is low and accumulation in inflammatory tissue is minor—both of which contribute to the superior sensitivity of [^{18}F]FET in brain tumor imaging.

The accumulation of [^{18}F]FET in tumor tissue has been shown to be dominated by active transport processes [21, 81, 86]. The incorporation of the unnatural amino acid [^{18}F]FET into proteins via protein synthesis, however, does not play a significant role in the tumor retention of the tracer [73, 210].

Three different synthetic strategies were established for the routine clinical production of [^{18}F]FET. In the most frequently used procedure, the precursor O -(2-tosyloxyethyl)- N -trityl- L -tyrosine *tert*-butylester (**3**) is labeled with [^{18}F]fluoride in the presence of potassium carbonate and Cryptand 222, followed by hydrolysis using 2 N HCl (Approach A, Fig. 8.3). HPLC purification and final formulation yields injectable [^{18}F]FET. The automated procedure using a commercial radiosynthesizer yields the radiopharmaceutical with a radiochemical yield (RCY) of 55%. The radiosynthesis time is 63 min and A_{m} is greater than 90 GBq/ μmol [17].

In the original approach, [^{18}F]FET is prepared via the prosthetic group 1-[^{18}F]fluoro-2-(tosyloxy)ethane (**6**) [210]. A toluenesulfonyl group in the labeling precursor ethylene glycol di-*p*-tosylate (**5**) is replaced with [^{18}F]fluoride in a $\text{S}_{\text{N}}2$ reaction and the resulting prosthetic group **6** is used for the O -alkylation of the di-sodium salt of L -tyrosine. After HPLC purification and final formulation, [^{18}F]FET is obtained with a RCY of 40% and a radiochemical purity (RCP) of 97–99% in approximately 60 min. HPLC purification was successfully replaced by a cartridge purification methodology reducing the total synthesis time by 10 min [134].

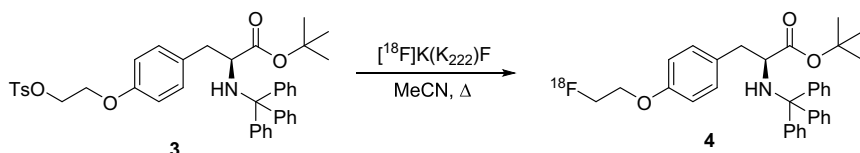
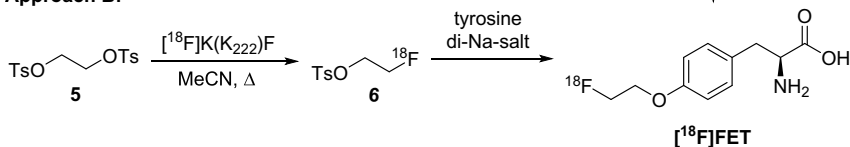
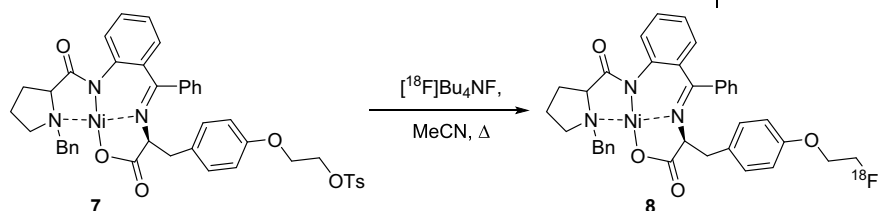
Approach A:**Approach B:****Approach C:**

Fig. 8.3 Synthetic strategies toward the radiosynthesis of $[^{18}\text{F}]\text{FET}$. Approach A [17]; Approach B [210]; Approach C [47]. Abbr.: OTs = tosylate; Ph = phenyl; Bn = benzyl

Instead of prosthetic group **6**, 1-bromo-2- $[^{18}\text{F}]\text{fluoroethane}$ can be used as well. Using this approach, the preparation time is shortened to 35 min and the RCY is increased to 45% (not decay corrected) [218].

The third approach utilizes the chiral labeling precursor **7**. The precursor structure comprises of a Ni(II) complex of (S)-[N-2-(N'-benzylpropyl)amino]benzophenone (BPB) and the O-alkylated L-tyrosine Schiff base. The procedure involves $\text{S}_{\text{N}}2$ -substitution of the toluenesulfonyl group with $[^{18}\text{F}]\text{fluoride}$, cleavage of the Ni(II) complex, SPE purification and formulation. $[^{18}\text{F}]\text{FET}$ was obtained in 35% RCY in 45 min and an enantiomeric purity of >95% [47]. QC requirements are defined in the Eur. Ph. Monograph 9.3/2466 Fluoroethyl-L-tyrosine (^{18}F) injection.

8.3.2 6- $[^{18}\text{F}]\text{Fluoro-3,4-Dihydroxy-L-Phenylalanine}$ ($[^{18}\text{F}]\text{FDOPA}$)

The tracer 6- $[^{18}\text{F}]\text{fluoro-3,4-dihydroxy-L-phenylalanine}$ ($[^{18}\text{F}]\text{FDOPA}$) has proven useful for imaging of neurological and oncological diseases. Notably, $[^{18}\text{F}]\text{FDOPA}$ was used in investigations of the dopaminergic system [44, 45], of

neurodegenerative disorders such as Parkinson's disease (PD) [54, 104, 113], Alzheimer's disease (AD) [82], as well as behavioral disorders such as schizophrenia [147]. Similar to other ¹⁸F-labeled amino acid tracers, [¹⁸F]FDOPA also represents a useful PET tracer for the in vivo visualization of cancers. Important applications are the imaging of pheochromocytomas [77, 80, 128], medullary thyroid carcinomas [11, 61, 76, 91], gliomas [127], and neuroendocrine tumors [19, 84, 90, 178].

[¹⁸F]FDOPA, an ¹⁸F-labeled precursor to 6-[¹⁸F]fluorodopamin, was developed to help evaluate the transport of the neurotransmitter dopamine from the blood into the central nervous system (CNS) and to investigate the storage, degradation as well as turnover of intracerebral dopamine [55, 56]. The biosynthesis of the neurotransmitter dopamine starts with the hydroxylation of L-tyrosine to yield 3,4-dihydroxy-L-phenylalanine (L-DOPA). L-DOPA crosses the intact blood–brain barrier and enters the CNS via a neutral amino acid carrier (L type). The subsequent decarboxylation of L-DOPA by either L-DOPA decarboxylase or aromatic amino acid decarboxylase (AAAD) yields dopamine [148]. In a similar manner, [¹⁸F]FDOPA can cross the blood–brain barrier where it is metabolized in several ways: *O*-methylation catalyzed by the catechol-*O*-methyl transferase (COMT) results in 6-[¹⁸F]fluoro-4-hydroxy-3-methoxy-L-phenylalanine ([¹⁸F]FHMP). Decarboxylation by AAAD yields 6-[¹⁸F]fluorodopamine ([¹⁸F]FDA), which is metabolized to 6-[¹⁸F]fluoro-3,4-dihydroxy-phenylacetic acid ([¹⁸F]FDPA) by monoamine oxidase. Subsequent transfer of a methyl group by COMT produces the metabolite 6-[¹⁸F]fluoro-4-hydroxy-3-methoxy-phenylacetic acid ([¹⁸F]FHMPA). To reduce the release of metabolites in blood as well as the decarboxylase activity, and to increase the amount of the unmetabolized [¹⁸F]FDOPA parent compound during the PET investigation, the decarboxylase inhibitor carbidopa can be applied [114, 123].

The preparation of [¹⁸F]FDOPA is realized via either electrophilic or nucleophilic fluorination methods. The electrophilic approach is based on the aromatic substitution of *N*-formyl-3,4-di-*tert*-butoxycarbonyloxy-6-(trimethylstannyl)-L-phenylalanine ethyl ester (**9**) with [¹⁸F]F₂-gas or ¹⁸F-labeled acetylhypofluoride ([¹⁸F]AcOF) (Approach A, Fig. 8.4) [40, 135]. The electrophilic aromatic substitution of the trimethylstannyl group with [¹⁸F]F₂-gas was initially performed in chlorotrifluoromethane (CF₃Cl), but it has been shown that this environmentally hazardous solvent can be replaced with deuteriochloroform (CDCl₃) [52]. Acidic cleavage of the *tert*-butyloxycarbonyl and formyl protecting groups as well as ester hydrolysis yields [¹⁸F]FDOPA. After HPLC purification and formulation, the tracer is obtained in an RCY of 8–26% in 45–60 min and an RCP > 99%. A procedure that meets the standards of the USP was also reported [89].

Although well established and reliable, the electrophilic method requires inconvenient gas targetry, the need for a dedicated synthesis setup, and the tracer is produced in low A_m of around 37 MBq/μmol. Therefore, nucleophilic methods utilizing [¹⁸F]fluoride have emerged. [¹⁸F]Fluoride is routinely obtained from a cyclotron in high activity amounts and high A_m. Excellent reviews of both electrophilic and nucleophilic ¹⁸F-labeling of aromatic compounds and [¹⁸F]FDOPA are available [43, 157, 159].

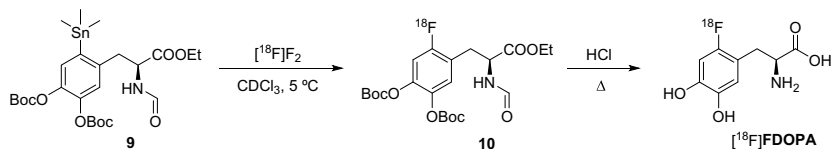
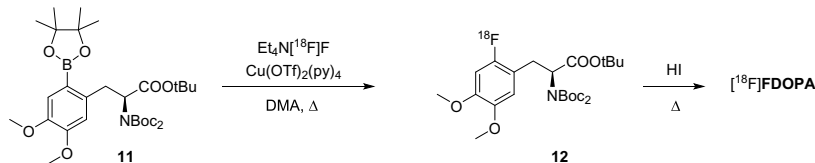
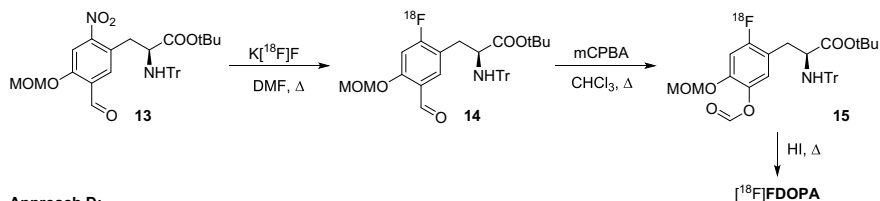
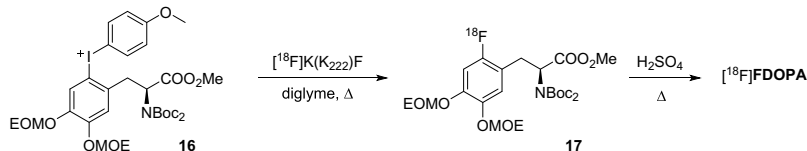
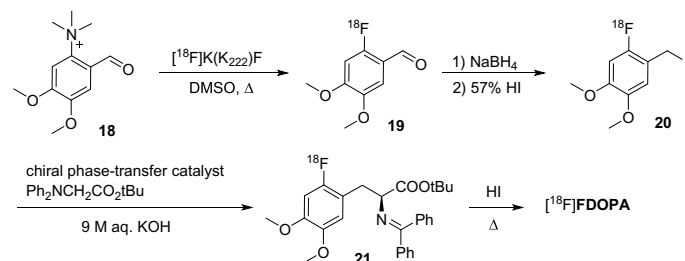
Approach A:**Approach B:****Approach C:****Approach D:****Approach E:**

Fig. 8.4 Different synthetic routes toward $[^{18}\text{F}]\text{FDOPA}$. Approach A [52]; Approach B [200]; Approach C [78, 121, 158]; Approach D [103]; Approach E [109]. Abbr.: Boc = *tert*-butoxycarbonyl; tBu = *tert*-butyl; MOM = methoxymethyl; Tr = triphenylmethyl; EOM = ethoxymethyl; Ph = phenyl

A copper-mediated ^{18}F -fluorination strategy starting from aryl boronic ester precursor **11** was developed by Tredwell et al. (Approach B, Fig. 8.4) [200]. Other groups expanded on the method, thereby proving its large substrate scope and overall usefulness in the preparation of ^{18}F -labeled aromatic moieties [130, 156, 217]. By using this strategy, the automated production of $[^{18}\text{F}]\text{FDOPA}$ yields the

tracer in an RCY of 22% within 146 min. An activity yield of 2.2 GBq from 25.0 GBq of ^{18}F fluoride was reported. The procedure was not optimized for routine clinical production and the presence of an UV-impurity in the final formulation prevented determination of A_m .

Höpping et al. developed a method based on the nucleophilic radiofluorination of a commercially available chiral precursor **13**, followed by a Baeyer–Villiger oxidation reaction and finally a deprotection reaction to form ^{18}F FDOPA (Approach C, Fig. 8.4) [78, 121]. Pretze et al. further adapted the conditions using a radiosynthesizer and reported an RCY of 19% with a radiosynthesis time of 114 min, RCP of >98% and A_m up to 2.2 GBq/ μmol [158].

The method developed by Kuik et al. involves the nucleophilic ^{18}F -fluorination of a diaryliodonium salt precursor **16** followed by deprotection to give ^{18}F FDOPA (Approach D, Fig. 8.4) [103]. The RCY of the manual synthesis was reported to be 14% within 117 min and a RCP of >95%. An automated synthesis using this method was reported and produced the tracer with an RCY of 4.5% within 71 min and A_m in a range of 30–33 GBq/ μmol [32].

Lemaire et al. have developed a multistep synthesis, which utilizes a chiral phase-transfer catalyzed alkylation step (Approach E, Fig. 8.4) [109, 110]. After formation of the intermediate 2- ^{18}F fluoro-4,5-dimethoxybenzyl iodide (**20**) in three steps (radiofluorination of **18**, reduction of the benzylic aldehyde **19**, and iodination), an enantioselective carbon-carbon bond formation and subsequent deprotection generates the desired tracer. Automation of the procedure on a cassette-based radiosynthesizer yielded ^{18}F FDOPA in high enantiomeric excess of $\sim 97\%$. The RCY is reported to be 36% within 63 min, and A_m is ≥ 753 GBq/ μmol . High activity yields (AY) of >45 GBq starting from 185 GBq of ^{18}F F $^-$ render this approach useful to produce multiple patient doses. QC requirements of ^{18}F FDOPA, that is prepared by the electrophilic strategy, are defined in the Eur. Ph. Monograph 9.0/1918.

8.3.3 *Anti*-1-Amino-3- ^{18}F Fluorocyclobutane-1-Carboxylic Acid (^{18}F Fluciclovine, ^{18}F FACBC)

Anti-1-Amino-3- ^{18}F fluorocyclobutane-1-carboxylic acid (^{18}F Fluciclovine, ^{18}F FACBC) is a radiofluorinated, synthetic leucine derivative. Like other ^{18}F -labeled amino acid tracers, ^{18}F FACBC accumulates in a manner that reflects amino acid transport in tissues [141]. ^{18}F FACBC has been evaluated in several studies in patients with prostate cancer and the U.S. Food and Drug Administration (U.S. FDA) approved the tracer for detection of suspected recurrent prostate cancer in 2016 [85, 136, 137, 181]. Furthermore, the tracer shows promising results in the diagnostic imaging of brain tumors such as gliomas [98, 202, 205].

The uptake of ^{18}F FACBC in prostate cancer is likely mediated via sodium-dependent (ASC) and sodium-independent (L type) amino acid transporters [142, 143]. The tracer is not metabolized in vivo and urinary excretion is comparably low. Preclinical studies have indicated that ^{18}F FACBC is taken up by brain

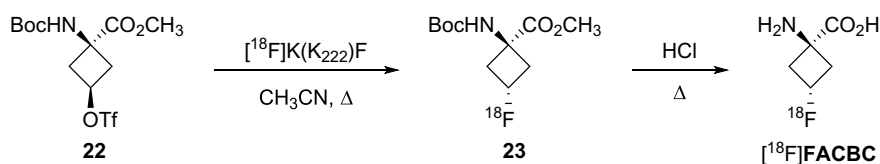


Fig. 8.5 Synthesis of [^{18}F]FACBC [186]. Abbr.: Boc = *tert*-butyloxycarbonyl

tumors through amino acid transporters and that its accumulation is dependent on the proliferation of tumors [144, 175, 215].

The radiosynthesis of [^{18}F]FACBC was first reported by Shoup et al. and resembles that of [^{18}F]FDG [186]. The triflate group in the precursor 1-*tert*-butyl carbamate-3-trifluoromethanesulfonyloxy-1-cyclobutane-1-carboxylic acid methyl ester (**22**) is substituted with [^{18}F]fluoride in the first step (Fig. 8.5). After removal of the protecting groups, [^{18}F]FACBC is purified by SPE. Using an automated procedure with optimized conditions, [^{18}F]FACBC was obtained in an RCY of 24% within 70 min and RCP > 99% [122]. A cassette-based synthesis was reported delivering the probe in RCYs up to 63% within 43 min [193].

8.4 ^{18}F -Labeled Choline Derivatives for Imaging Membrane Lipid Synthesis

8.4.1 Dimethyl- [^{18}F]Fluoromethyl-2-Hydroxyethylammonium ([^{18}F]Fluoromethylcholine, [^{18}F]FCH)

The choline analog dimethyl- [^{18}F]fluoromethyl-2-hydroxyethylammonium ([^{18}F]fluoromethylcholine, [^{18}F]FCH) was developed as a tumor imaging agent and initially evaluated in PC-3 human prostate cancer cells, PC-3 human prostate cancer xenografts, as well as human prostate and brain tumor patients [31]. The biodistribution of [^{18}F]FCH in the murine PC-3 human prostate cancer xenograft model proved to be comparable to that of [^{14}C]choline [34]. Similar to [^{11}C]choline, [^{18}F]FCH proved to be a promising agent for prostate cancer imaging but with the advantage of a longer physical half-life and increased spatial resolution [8, 12, 16, 25].

Choline is a vitamin-like essential nutrient and represents an important component of cell membrane phospholipids. Malignant tumors are characterized by an increased proliferation rate and, therefore, an increased metabolism of cell membrane components including choline and its metabolites. The cellular metabolism of choline includes phosphorylation by choline kinase yielding phosphorylcholine followed by subsequent incorporation into phospholipids such as phosphatidylserine [153]. Choline is also the metabolic precursor of betaine, which is formed from choline in a two-step, enzyme-catalyzed oxidation. Furthermore, the

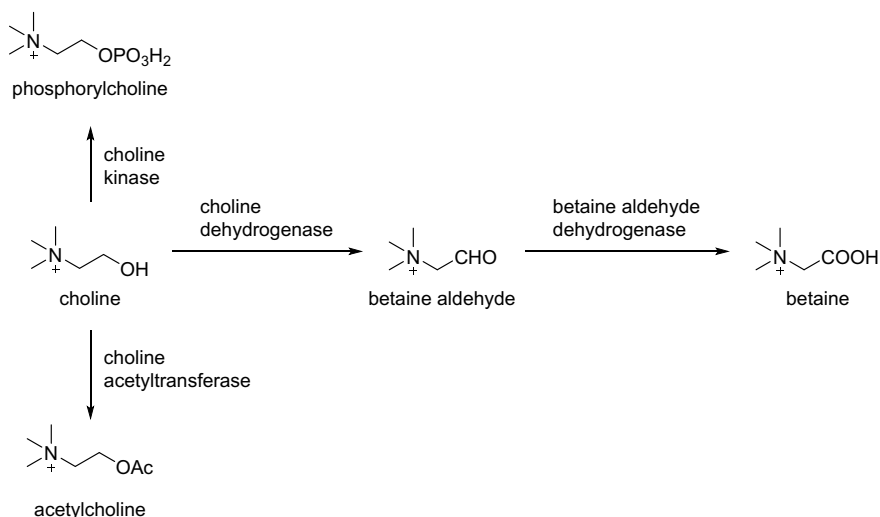


Fig. 8.6 Schematic of the choline metabolism

neurotransmitter acetylcholine is formed from choline by acetylation with choline acetyltransferase [169]. The metabolism of choline is outlined in Fig. 8.6.

The radiosynthesis of [^{18}F]FCH is achieved by ^{18}F -fluoroalkylation of *N,N*-dimethylaminoethanol (**25**) with bromo- ^{18}F -fluoromethane (**27**) ([^{18}F]BFM) [34, 35] or [^{18}F]fluoromethyl triflate (**28**) ([^{18}F]FCH₂OTf) [83] (Fig. 8.7). Both synthetic pathways start with the labeling of dibromomethane (**26**) to yield [^{18}F]BFM. [^{18}F]BFM is either directly used for the alkylation, or it is further transformed into the labeling synthon [^{18}F]FCH₂OTf (**28**). Fully automated [^{18}F]FCH synthesis procedures using commercially available radiosynthesizers were published [102, 183]. The procedures yield the target compound in RCYs of 15–25% (not decay corrected) with RCP of >99% and $A_m > 37$ GBq/ μmol . Synthesis times are reported to be <35 min. QC requirements of [^{18}F]FCH are defined in the Eur. Ph. Monograph 9.0/2793.

8.4.2 Dimethyl-2- ^{18}F Fluoroethyl-2-Hydroxyethylammonium ([^{18}F] Fluoroethylcholine, [^{18}F]FECH)

The tracer dimethyl-2- ^{18}F fluoroethyl-2-hydroxyethylammonium ([^{18}F]fluoroethylcholine, [^{18}F]FECH) differs from [^{18}F]FCH only in the additional methylene group within the ^{18}F -labeled side chain. Studies of the choline transport system suggest that only two methyl groups of the ammonium moiety in choline derivatives are essential for their transport characteristics, whereas the third methyl group can safely be

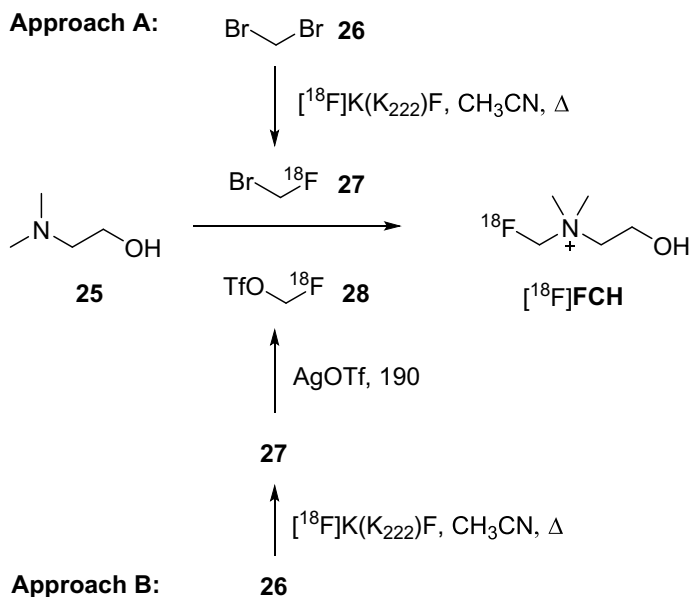


Fig. 8.7 Different synthetic routes toward [^{18}F]FCH. Approach A [102]; Approach B [83]

replaced with a prolonged alkyl chain [38]. Moreover, investigations into the substrate specificity of choline kinase for synthetic choline analogs also show that the replacement of one out of three methyl groups with another alkyl chain is tolerated [30]. Consequently, the in vivo biodistribution and diagnostic accuracy of those structurally similar tracers were shown to be comparable throughout the published literature [22]. Hara et al. suggested [^{18}F]FECH as a potential oncological PET tracer and demonstrated its usefulness in the imaging of prostate cancer in patients [69]. Simultaneous [^{18}F]FECH PET/MRI was used for the imaging of astrocytic tumors in children during therapy [50]. In prostate cancer imaging, [^{18}F]FCH is increasingly being replaced by [^{18}F]FACBC (see Sect. 3.3) and the ^{18}F -labeled PSMA radioligands [^{18}F]DCFPyL and [^{18}F]PSMA-1007 (see Chap. 8).

Similar to [^{18}F]FCH, two main strategies are applied in the reported radiosyntheses of [^{18}F]FECH. In the more common approach, 1- ^{18}F fluoro-2-(tosyloxy) ethane (**6**) is used to alkylate *N,N*-dimethylaminoethanol (**25**) (Approach A, Fig. 8.8) [7, 69, 146, 151]. Using this approach, an RCY of up to 48% (not decay corrected) within 55 min and an RCP > 99% was reported. An alternative approach uses the intermediate 1-bromo-2- ^{18}F fluoroethane (**29**) (^{18}F]BFE), which is generated by ^{18}F -labeling of 2-bromoethyltriflate (**30**) and requires purification by distillation. Using this strategy, [^{18}F]FECH is synthesized with a RCY of 47% (not decay corrected) within 40 min (Approach B, Fig. 8.8) [219].

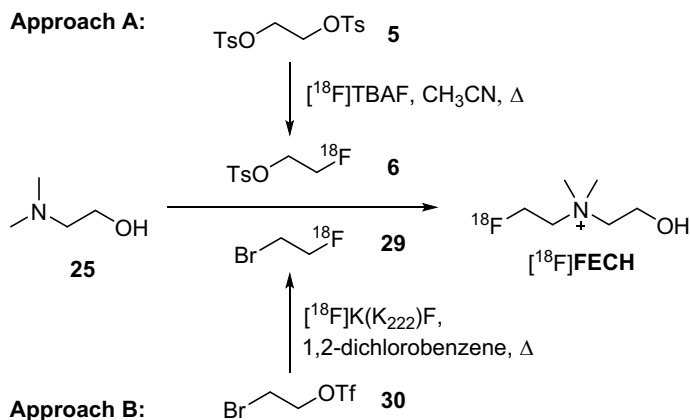


Fig. 8.8 Two synthetic strategies toward $[\text{}^{18}\text{F}]\text{FECH}$. Approach A [7]; Approach B [219]

8.5 ^{18}F -Labeled Nucleoside Derivatives for Imaging Cell Proliferation

8.5.1 3'-Deoxy-3'- $[\text{}^{18}\text{F}]\text{Fluorothymidine}$ ($[\text{}^{18}\text{F}]\text{FLT}$)

The radiotracer 3'-deoxy-3'- $[\text{}^{18}\text{F}]\text{fluorothymidine}$ ($[\text{}^{18}\text{F}]\text{FLT}$) was developed to measure the proliferation rate of tumors [185]. Studies evaluated the benefit of $[\text{}^{18}\text{F}]\text{FLT}$ imaging in colorectal cancer [132, 212], hepatocellular carcinoma [42], and gastric cancer [87, 88]. $[\text{}^{18}\text{F}]\text{FLT}$ has also been used to monitor tumor response to treatment [74, 107].

DNA synthesis is a measure of proliferation and an increased level of cellular proliferation is a hallmark of cancer [68]. DNA synthesis and cell proliferation are, therefore, an attractive target in oncological molecular imaging and radiolabeled DNA building blocks were developed for tumor imaging [125, 184]. Similar to natural DNA building blocks, $[\text{}^{18}\text{F}]\text{FLT}$ enters the cells via diffusion and nucleoside transporter proteins [13]. The tracer is phosphorylated by thymidine kinase 1 to form $[\text{}^{18}\text{F}]\text{FLT}$ -5'-phosphate which is metabolically stable and trapped intracellularly [9, 163]. Because of fluorine-18 in the 3'-position of the sugar moiety, $[\text{}^{18}\text{F}]\text{FLT}$ acts as a terminator of the growing DNA chain and only small amounts of tracer are actually accumulated in DNA. Similar to $[\text{}^{18}\text{F}]\text{FDG}$, the compound reflects accumulation by transport as well as activation in the utilization pathways resulting in metabolic trapping. A direct relationship of $[\text{}^{18}\text{F}]\text{FLT}$ accumulation and cell proliferation has been questioned [177].

The most commonly applied synthetic strategy in the preparation of $[\text{}^{18}\text{F}]\text{FLT}$ starts with the precursor molecule 5'-O-(4,4'-dimethoxytriphenylmethyl)-l-(2'-deoxy-3'-O-nosyl- β -D-threo-pentofuranosyl)-3-N-Boc-thymine (**31**) (Fig. 8.9,

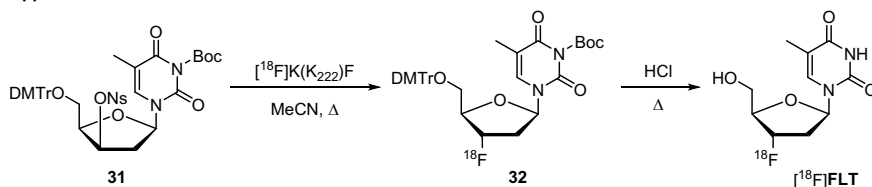
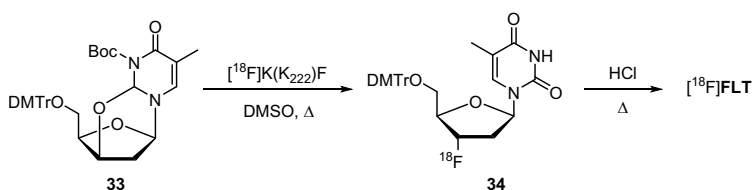
Approach A:**Approach B:**

Fig. 8.9 Different routes toward the radiosynthesis of [^{18}F]FLT. Approach A [216]; Approach B [116]. Abbr.: DMTr = 4,4-dimethoxytrityl; Boc = *tert*-butyloxycarbonyl; Ns = 4-nitrobenzylsulfonfyl (nosyl)

Approach A) [216]. After nucleophilic substitution of the nosyl-group with [^{18}F] fluoride, the protecting groups are removed under acidic conditions and [^{18}F]FLT is purified by semi-preparative HPLC. A fully automated synthesis was reported yielding [^{18}F]FLT in an RCY of 49% when starting with 37 GBq of [^{18}F]fluoride [140]. Tang et al. developed a purification procedure based on solid-phase extraction cartridges instead of HPLC, thereby reducing the synthesis time to 35 min [196]. A fully automated synthesis that allows the reduction of the amount of precursor while retaining RCY was reported by Marchand et al. [120]. The alternative approach toward the synthesis of [^{18}F]FLT uses the precursor 5'-*O*-(4,4'-dimethoxytriphenylmethyl)-2,3'-anhydrothymidine (**33**). After nucleophilic ring opening with [^{18}F]fluoride, hydrolysis of the protecting group and HPLC purification, [^{18}F]FLT was synthesized with an RCY of 14% within 90 min (Fig. 8.9, Approach B) [116]. QC requirements of [^{18}F]FLT are defined in the Eur. Ph. Monograph 9.0/2460.

8.5.2 1-(2'-Deoxy-2'-[^{18}F]Fluoro- β -D-Arabinofuranosyl)-5-Methyluracil ([^{18}F]FMAU)

Similar to [^{18}F]FLT, the ^{18}F -labeled nucleoside analog 1-(2'-deoxy-2'-[^{18}F]fluoro- β -D-arabinofuranosyl)-5-methyluracil ([^{18}F]FMAU) binds to thymidine kinase and represents a tracer for measuring proliferation [2]. In contrast to [^{18}F]FLT, [^{18}F]FMAU is selectively taken up and incorporated into the DNA of proliferating cells [101]. In a series of initial studies, patients with brain, prostate, colorectal, lung and breast cancers were imaged with [^{18}F]FMAU PET [191, 197]. It was shown that

^{18}F FMAU-imaging in the abdominal region is limited due to its physiological uptake in the liver and the kidneys. A pilot study of ^{18}F FMAU PET in breast cancer patients was reported where the images revealed the primary breast tumors as well as metastatic lesions [33].

The commonly used synthetic route toward ^{18}F FMAU is a multistep procedure that is difficult to automate (Fig. 8.10, Approach A) [3, 118]. The protected triflate precursor **35** is reacted with ^{18}F fluoride to perform a nucleophilic substitution reaction. Subsequent bromination, substitution of bromine by a thymine silyl ether derivative and cleavage of the benzoyl protecting groups yields ^{18}F FMAU, which is purified by semi-preparative HPLC. Using this strategy, ^{18}F FMAU is produced in RCYs of 25–45%, RCPs > 98% and A_m of 85–111 GBq/ μmol within 3–4 h. The challenging automation of this sophisticated radiosynthesis route was reported by several groups [5, 32, 145]. A simplified approach (Fig. 8.10, Approach B) that starts with THP-protected precursor **35** and facilitates the radiosynthesis in one reaction vessel results in low RCYs. Values of 2% were reported by Turkman et al. (Fig. 8.10, Approach B) [203].

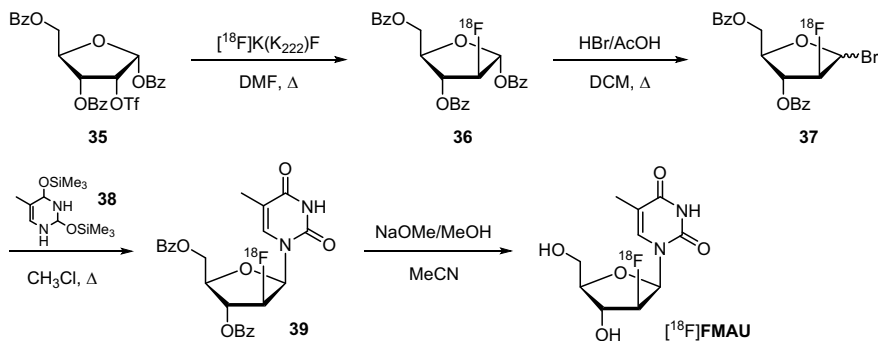
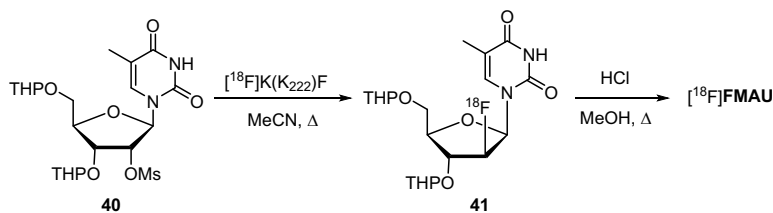
Approach A:**Approach B:**

Fig. 8.10 Radiosynthesis of ^{18}F FMAU. Approach A [3, 118]; Approach B [203]. Abbr.: Bz = benzyl; OTf = triflate; THP = 2-tetrahydropyranyl; OMs = mesylate

8.6 ^{18}F -Labeled Nitroimidazole Derivatives for Imaging of Tumor Hypoxia

8.6.1 1*H*-1-(3- ^{18}F Fluoro-2-Hydroxypropyl)-2-Nitroimidazole ([^{18}F]Fluoromisonidazole, [^{18}F]FMISO)

In 1987, 1*H*-1-(3- ^{18}F fluoro-2-hydroxypropyl)-2-nitroimidazole ([^{18}F]Fluoromisonidazole, [^{18}F]FMISO) was proposed by Rasey et al. as a hypoxia imaging agent for imaging of tumor hypoxia with PET [164]. The tracer is widely used to guide chemotherapy or radiotherapy in patients suffering from cancers such as head and neck cancer [65, 95, 108, 115], glioblastoma [57, 93, 194], non-small cell lung carcinoma [204], breast cancer [6], and rectal cancer [160, 168].

A means to estimate the oxygenation in tumors is of utmost clinical interest since it allows predicting tumor response to radiotherapy, chemotherapy and radiochemotherapy [49, 63, 131]. Well-oxygenated cancer cells (normoxia) are more sensitive toward the radiotoxic effects of ionizing radiation than poorly oxygenated ones (hypoxia) [133]. Radiolabeled nitroimidazoles were suggested as markers of hypoxia and, therefore, as a tool to evaluate the tumor response to radiation therapy [27]. After passive diffusion into the cells, nitroimidazole derivatives are reduced to their corresponding nitro radical anions by a single electron transfer mechanism (Fig. 8.11). In the presence of oxygen, the radical anions are re-oxidized to form oxygen superoxide anions, which can diffuse out of the cell. Under hypoxic conditions, the re-oxidation does not occur and subsequent reductions form reactive intermediates of nitroimidazole such as hydroxylamines and amines. These reduced intermediates bind to intracellular components such as macromolecules (e.g., proteins and DNA) and accumulate in the cells [97].

Two synthetic routes toward the clinical preparation of [^{18}F]FMISO are described. The first strategy entails the nucleophilic fluorination of (2*R*)-glycidyl tosylate (**42**) with [^{18}F]fluoride to yield [^{18}F]epifluorohydrin (**43**) (Fig. 8.12, Approach A). The subsequent nucleophilic ring opening with 2-nitroimidazole forms [^{18}F]FMISO, which is purified by HPLC to obtain a final formulation with RCYs of 40% in 140–180 min, RCPs of 99%, and A_m of 37 GBq/ μmol [64, 106]. The second strategy uses the precursor 1-(2'-nitro-1'-imidazolyl)-2-*O*-tetrahydropyranyl-3-*O*-toluenesulfonyl-propanediol (**44**) (Fig. 8.12, Approach B). Nucleophilic substitution of the tosylate leaving group with [^{18}F]fluoride and subsequent cleavage of the protecting group under acidic conditions yields [^{18}F]

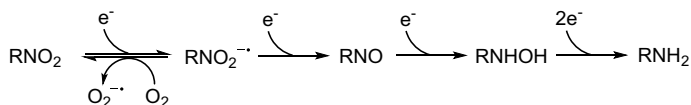


Fig. 8.11 Oxygen-dependent metabolism of nitroimidazoles. Abbr.: R = rest [97]

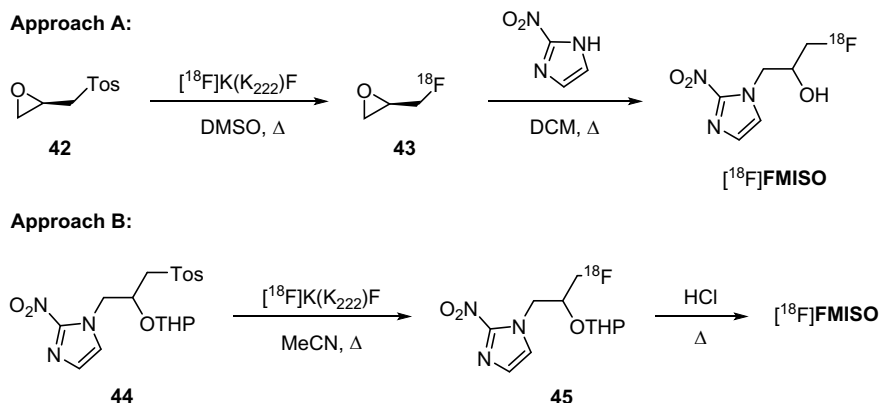


Fig. 8.12 Different routes toward the radiosynthesis of [^{18}F]FMISO. Abbr.: Tos = tosylate; THP = 2-tetrahydropyranyl

FMISO. After purification with HPLC and/or SPE, RCYs of 55–80% in 50 min, RCPs of >99%, and A_m of >22 GBq/ μmol can be achieved [29, 106, 111, 139]. QC requirements are described in the Eur. Ph. Monograph 9.0/2459.

8.6.2 1-(5-Deoxy-5- ^{18}F Fluoro- α -D-Arabinofuranosyl)-2-Nitroimidazole ([^{18}F]FAZA)

The compound 1-(5-deoxy-5- ^{18}F fluoro- α -D-arabinofuranosyl)-2-nitroimidazole ([^{18}F]FAZA) is a second generation hypoxia PET tracer. Compared to [^{18}F]FMISO, this nitroimidazole derivative is more hydrophilic and, therefore, shows a more rapid clearance from blood and non-target tissues. This results in increased tumor-to-background ratios [152]. Initial studies demonstrate that [^{18}F]FAZA-PET can be used for hypoxia imaging in patients with head and neck cancer [66], squamous cell carcinoma of the head and neck [174, 182], non-small-cell lung cancer [96, 176], pancreatic cancer [124], and gliomas [155].

The radiosynthesis of [^{18}F]FAZA is based on a nucleophilic substitution of the tosylate moiety in precursor **46** with [^{18}F]fluoride and subsequent hydrolysis of the acetyl protecting groups (Fig. 8.13). After HPLC purification, [^{18}F]FAZA is

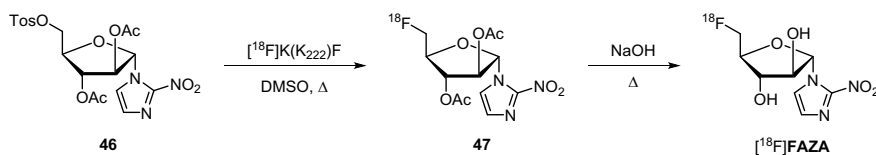


Fig. 8.13 Radiosynthesis of [^{18}F]FAZA

obtained with RCYs of 21% (not decay corrected) in 50 min [166]. An automated procedure yielded [^{18}F]FAZA with RCYs of 52% in 51 min [72].

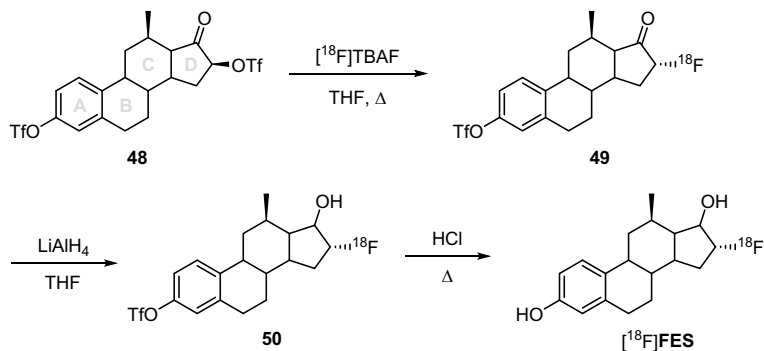
8.7 16α -[^{18}F]Fluoro- 17β -Estradiol ([^{18}F]FES) for Imaging Estrogen Receptor Status

Estrogen receptor-positive (ER+) tumors possess a slower rate of growth and are likely to respond to endocrine therapy [48, 170]. Therefore, an approach for the noninvasive assessment of the ER status of breast tumors in vivo is clinically desirable [112]. Among the several developed radiolabeled ER ligands, 16α -[^{18}F] fluoro- 17β -estradiol ([^{18}F]FES) represents the most intensively investigated and promising option [94]. [^{18}F]FES was evaluated in patients with ovarian cancer [214], uterine tumors [201, 213], and breast cancer [62, 149, 150, 192].

Similar to the steroid hormone estradiol, [^{18}F]FES circulates in the bloodstream where it binds to sex hormone-binding proteins (SBP) and albumin [198]. The fraction of [^{18}F]FES that binds to SBP is protected against liver metabolism, thereby enabling the transport of the parent compound to the target tissue [211]. Free [^{18}F]FES, however, is rapidly metabolized in vivo and the formation of glucuronidated and sulfated radiometabolites that are not accumulated by ER+ tumors contribute to a high background activity complicating the quantitative interpretation of [^{18}F]FES PET images [119].

Two strategies toward the synthesis of [^{18}F]FES were reported. An early approach was developed by Kiesewetter et al. (Fig. 8.14, Approach A) [94]. The first step consists of nucleophilic replacement of a triflate leaving group on the 5-membered D Ring in precursor **48** with [^{18}F]fluoride. Reduction of the ketone and subsequent hydrolysis of the triflate group on the aromatic A ring constitutes the target compound. After HPLC purification, the tracer is obtained in a RCY of 43% in 75–90 min, RCP > 99% and A_m in a range of 7–10 GBq/ μmol . The more common approach starts with the precursor 3-*O*-methoxymethyl-16,17-*O*-sulfuryl-16-epi-estradiol (**51**) (Fig. 8.14, Approach B) [111]. Nucleophilic ring opening of the cyclic sulfate with [^{18}F]fluoride and subsequent acidic hydrolysis of the methoxymethyl- and sulfate groups yields [^{18}F]FES. Several groups automated this approach on commercially available radiosynthesizers [39, 105, 173]. Syntheses based on disposable cassettes were reported yielding the tracer in RCYs of up to 45% in 76–88 min. RCPs were reported to be >99% and A_m was observed in a range of 58–111 GBq/ μmol [129, 138].

Approach A:



Approach B:

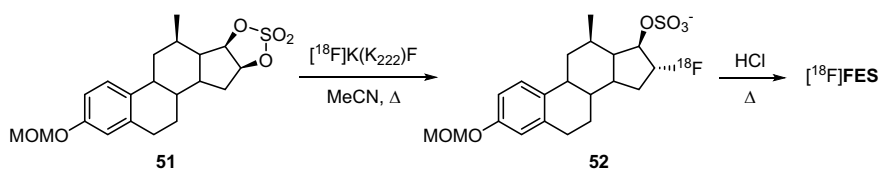


Fig. 8.14 Two routes toward the radiosynthesis of $[^{18}\text{F}]\text{FES}$. Approach A [94]; Approach B [111]. Abbr.: TfO = triflate, MOM = methoxymethyl

8.8 ^{18}F -Labeled Glu-Ureido-Based Inhibitors for Imaging Prostate-Specific Membrane Antigen (PSMA)

8.8.1 (3*S*,10*S*,14*S*)-1-(4-(((*S*)-4-Carboxy-2-((*S*)-4-Carboxy-2-(6- $[^{18}\text{F}]\text{Fluoronicotinamido})\text{Butanamido})\text{Butanamido})\text{Methyl})\text{Phenyl})-3-(\text{Naphthalen-2-ylmethyl})-1,4,12\text{-Trioxy-2,5,11,13-Tetraazahexadecane-10,14,16-Tricarboxylic Acid ($[^{18}\text{F}]\text{PSMA-1007}$)$

Radioligands targeting the prostate-specific membrane antigen (PSMA) are a new class of radiopharmaceuticals for diagnostics and treatment of prostate cancer [99]. On the diagnostic side, the field is currently dominated by the ^{68}Ga -labeled PET tracer $[^{68}\text{Ga}]\text{Ga-PSMA-11}$ [1]. Caused by the limited production capacity for this $^{68}\text{Ge}/^{68}\text{Ga}$ -generator-dependent PET tracer (1–3 patient doses per production run), ^{18}F -labeled PSMA ligands were developed and introduced into the clinic. The tracer (3*S*,10*S*,14*S*)-1-(4-(((*S*)-4-carboxy-2-((*S*)-4-carboxy-2-(6- $[^{18}\text{F}]\text{fluoronicotinamido})\text{butanamido})\text{butanamido})\text{methyl})\text{phenyl})-3-(\text{naphthalen-2-ylmethyl})-1,4,12\text{-trioxy-2,5,11,13-tetraazahexadecane-10,14,16-tricarboxylic acid ($[^{18}\text{F}]\text{PSMA-1007}$) was introduced in 2017 [24]. In contrast to $[^{68}\text{Ga}]\text{Ga-PSMA-11}$,$

[¹⁸F]PSMA-1007 can be produced in high activity yields allowing the examination and imaging of multiple patients from a single production run. From an imaging perspective, **[¹⁸F]PSMA-1007** has the advantage that tracer-associated activity-accumulation in the urinary bladder is low, which can be advantageous with regard to delineation of the primary tumor and local recurrence, as well as pelvic lymph node metastasis in various patients [60]. The tracer shows very promising results in imaging patients with biochemical recurrent prostate cancer [58, 59, 161].

Like other peptidomimetic Glu-ureido-based PSMA inhibitors, **[¹⁸F]PSMA-1007** binds to PSMA which is a binuclear membrane-bound zinc protease, called glutamate carboxypeptidase II (GCP II), that is highly upregulated in all stages of prostate cancer with very low expression in healthy tissues [15, 188]. Moreover, there is a significant correlation between the level of expression of PSMA and the progression of the disease. After the binding of the ligand to its membrane-anchored target, internalization occurs resulting in an effective transportation of the bound molecule into the cells [162]. Internalization leads to enhanced tumor uptake and retention, resulting in high-image quality for diagnostic procedures and a high local dose for therapeutic applications when therapeutic ligands such as PSMA-617 are used [75, 100].

Two synthetic approaches toward the radiosynthesis of **[¹⁸F]PSMA-1007** were reported. The initial approach utilizes a two-step synthesis strategy (Fig. 8.15, Approach A) [23, 24]. The first step involves the formation of the prosthetic group 6-**[¹⁸F]fluoronicotinic acid 2,3,5,6-tetrafluorophenyl ester (54)** with subsequent SPE purification. In the second step, the free amino group in the PSMA inhibitor moiety **55** reacts with the activated ester of prosthetic group **54**. After HPLC purification, **[¹⁸F]PSMA-1007** is obtained in RCYs of 2–6% (not decay corrected) within a total synthesis time of 45 min (without **[¹⁸F]fluoride** activation and formulation steps).

In clinical routine service, the two-step approach has been replaced with an efficient one-step radiosynthesis in which the unprotected PSMA inhibitor moiety **56** is radiolabeled directly and HPLC purification is not required [23]. **[¹⁸F]PSMA-1007** is produced in RCYs ranging from 25 to 80% within 55 min. With starting activities of up to 90 GBq, activity yields of up to 49 GBq can be achieved using any commercially available radiosynthesizer.

8.8.2 2-(3-(1-Carboxy-5-[(6-¹⁸F]Fluoro-Pyridine-3-Carbonyl)-Amino]-Pentyl)-Ureido)-Pentanedioic Acid (**[¹⁸F]DCFPyL**)

Beside **[¹⁸F]PSMA-1007**, the tracer 2-(3-(1-carboxy-5-[(6-¹⁸F]fluoro-pyridine-3-carbonyl)-amino]-pentyl)-ureido)-pentanedioic acid (**[¹⁸F]DCFPyL**) is another promising radiofluorinated PSMA inhibitor for the imaging of prostate cancer. **[¹⁸F]DCFPyL** was introduced by Chen et al. in 2011 and its biodistribution and safety were investigated in a first-in-human study later on [28, 195]. The tracer demonstrates promising results in imaging patients with suspected prostate cancer

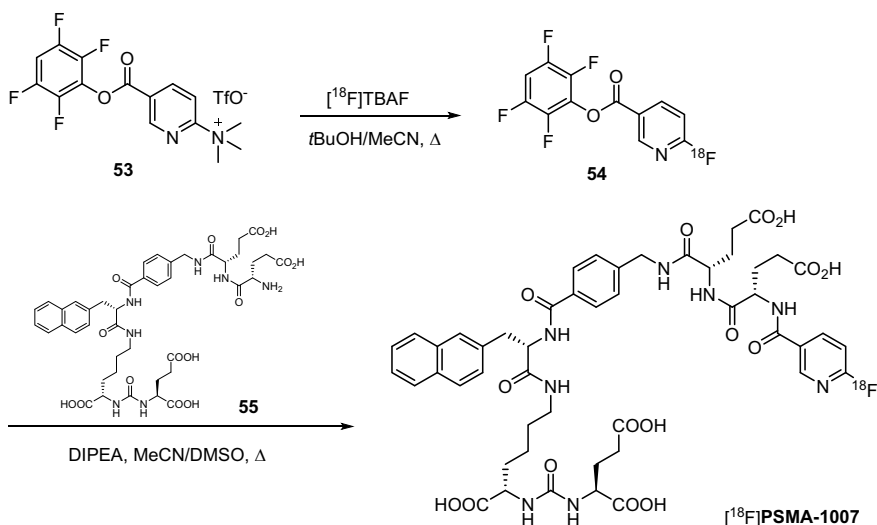
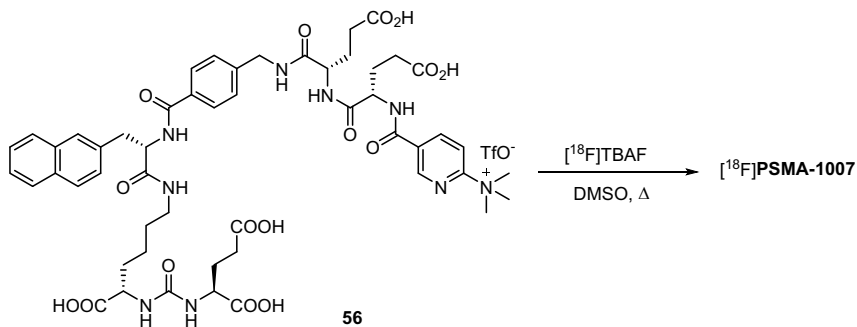
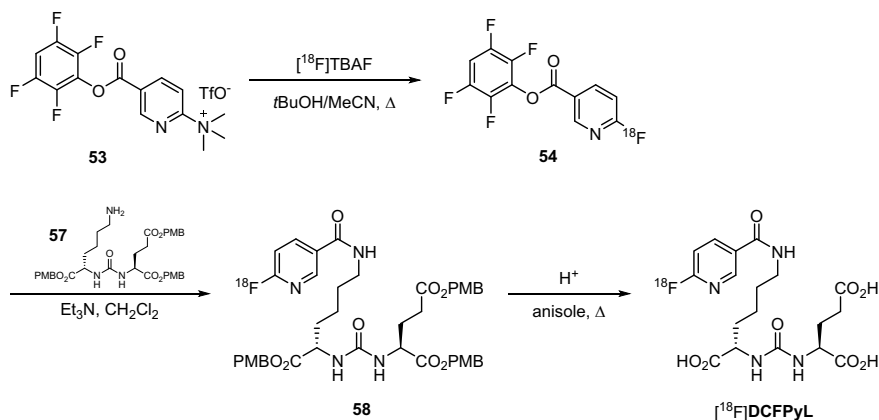
Approach A:**Approach B:**

Fig. 8.15 Two synthetic strategies toward the synthesis of $[^{18}\text{F}]\text{PSMA-1007}$. Initial Approach A [24]; Approach B is used in clinical routine service [23]. Abbr.: TBAF = tetrabutylammonium fluoride; DIPEA = diisopropylethylamine; DMSO = dimethyl sulfoxide

recurrence [171]. In contrast to $[^{18}\text{F}]\text{PSMA-1007}$, $[^{18}\text{F}]\text{DCFPyL}$ shows a lower hepatic background which might be favorable for imaging patients in late stages of the disease when rare cases of liver metastases can occur [60].

Similar to $[^{18}\text{F}]\text{PSMA-1007}$, two strategies toward the synthesis of $[^{18}\text{F}]\text{DCFPyL}$ have been reported (Fig. 8.16). One strategy utilizes prosthetic groups, whereas the other consists of a direct-labeling procedure. The first reported radiosynthesis uses the prosthetic group 6- $[^{18}\text{F}]\text{fluoronicotinic acid 2,3,5,6-tetrafluorophenyl ester (54)}$ which is reacted with the amino group in the PSMA inhibitor moiety **57** (Fig. 8.16, Approach A) [28]. After removal of the protecting groups and subsequent HPLC

Approach A:



Approach B:

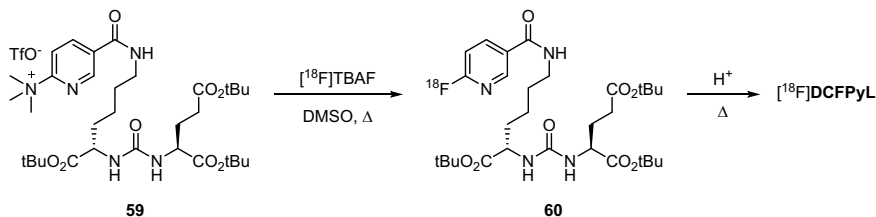


Fig. 8.16 Two synthetic strategies toward the synthesis of [¹⁸F]DCFPyL. Approach A [28]; Approach B [18, 165]. Abbr.: TfO⁻ = triflate; TBAF = tetrabutylammonium fluoride; PMB = *para*-methoxybenzyl; tBu = *tert*-butyl

purification, [¹⁸F]DCFPyL is obtained in RCYs ranging from 36 to 53% within 128 min. Independently, two strategies where the PSMA inhibitor moiety is directly labeled were developed in the same year [18, 165]. Both approaches start with the nucleophilic substitution of a trimethylammonium moiety in precursor **59** with [¹⁸F] fluoride (Fig. 8.16, Approach B). Removal of the protecting groups and HPLC purification yielded [¹⁸F]DCFPyL in RCYs ranging from 23 to 31% within synthesis times between 55 and 66 min.

8.9 Sodium [¹⁸F]Fluoride (Na[¹⁸F]F) for Imaging Bone Mineralization

[¹⁸F]Fluoride (Na[¹⁸F]F) was suggested as a potential tracer for bone scintigraphy in 1962 [14]. Since then, the radiofluorinated ion pair has been evaluated in multiple clinical studies concerning the imaging of bone and joint disorders [10].

Multitudes of primary neoplasms, such as breast-, prostate-, thyroid-, renal-, and lung tumors, are likely to metastasize to bone [172]. Na^{18}F -PET is a highly sensitive and specific imaging method for the detection of skeletal metastases in patients with prostate cancer [46, 92], breast cancer [92, 179] [92], and urinary bladder carcinoma [26].

In the bloodstream, Na^{18}F dissociates into sodium cations (Na^+) and ^{18}F fluoride anions. Bone uptake of ^{18}F fluoride occurs through ion exchange with hydroxide ions (OH^-) in the bone mineral hydroxylapatite ($\text{Ca}_5(\text{PO}_4)_3\text{OH}$) thereby forming ^{18}F fluoroapatite ($\text{Ca}_5(\text{PO}_4)_3^{18}\text{F}$) [71]. Increased ^{18}F fluoride uptake reflects an increase in regional blood flow and bone turnover as observed in malignant bone lesions.

^{18}F fluoride is produced directly in the cyclotron target system by irradiation of ^{18}O water in the nuclear $^{18}\text{O}(\text{p},\text{n})^{18}\text{F}$ reaction. Subsequent removal from the irradiated ^{18}O water by adsorption on anion exchange resins and desorption of ^{18}F fluoride from the resin with isotonic NaCl solution yields sodium ^{18}F fluoride in physiological solution. QC requirements are specified in the Ph. Eur. Monograph 9.0/2390.

8.10 Conclusion

The clinically relevant small-molecule and low-molecular-weight ^{18}F -labeled PET tracers presented here can sustainably support clinical management of patients suffering from early and progressive cancer. Small-molecule and low-molecular-weight radiotracers for the detection of glucose utilization, amino acid transport, protein synthesis, membrane lipid synthesis, cell proliferation, cell death, hypoxia, estrogen receptor status, PSMA expression, and bone mineralization of tumors are introduced. Due to the tremendous dynamics of PET tracer development, this list cannot be exhaustive and additional ^{18}F -labeled tracers that are not listed here might be introduced into the clinic in the future.

References

1. Afshar-Oromieh A, Haberkorn U, Eder M, Eisenhut M, Zechmann C (2012) ^{68}Ga Gallium-labelled PSMA ligand as superior PET tracer for the diagnosis of prostate cancer: comparison with ^{18}F -FECH. *Eur J Nucl Med Mol Imaging* 39(6):1085–1086
2. Alauddin MM (2018) Journey of 2'-deoxy-2'-fluoro-5-methyl-1-beta-D-arabinofuranosyluracil (FMAU): from antiviral drug to PET imaging agent. *Curr Med Chem* 25 (16):1867–1878
3. Alauddin MM, Conti PS, Fissekis JD (2003) A general synthesis of 2'-deoxy-2'- ^{18}F fluoro-1- β -D-arabinofuranosyluracil and its 5-substituted nucleosides. *J Label Compd Rad* 46(4):285–289
4. Alavi A, Dann R, Chawluk J, Alavi J, Kushner M, Reivich M (1986) Positron emission tomography imaging of regional cerebral glucose metabolism. *Semin Nucl Med* 16(1):2–34

5. Amaraesekera B, Marchis PD, Bobinski KP, Radu CG, Czernin J, Barrio JR, Michael van Dam R (2013) High-pressure, compact, modular radiosynthesizer for production of positron emitting biomarkers. *Appl Radiat Isot* 78:88–101
6. Asano A, Ueda S, Kuji I, Yamane T, Takeuchi H, Hirokawa E, Sugitani I, Shimada H, Hasebe T, Osaki A, Saeki T (2018) Intracellular hypoxia measured by ^{18}F -fluoromisonidazole positron emission tomography has prognostic impact in patients with estrogen receptor-positive breast cancer. *Breast Cancer Res* 20(1):78
7. Asti M, Farioli D, Iori M, Guidotti C, Versari A, Salvo D (2010) Efficient automated one-step synthesis of 2- ^{18}F]fluoroethylcholine for clinical imaging: optimized reaction conditions and improved quality controls of different synthetic approaches. *Nucl Med Biol* 37(3):309–315
8. Bauman G, Belhocine T, Kovacs M, Ward A, Beheshti M, Rachinsky I (2012) ^{18}F -fluorocholine for prostate cancer imaging: a systematic review of the literature. *Prostate Cancer Prostatic Dis* 15(1):45–55
9. Been LB, Suurmeijer AJ, Cobben DC, Jager PL, Hoekstra HJ, Elsinga PH (2004) ^{18}F]FLT-PET in oncology: current status and opportunities. *Eur J Nucl Med Mol Imaging* 31(12):1659–1672
10. Beheshti M (2018) ^{18}F -sodium fluoride PET/CT and PET/MR imaging of bone and joint disorders. *PET Clin* 13(4):477–490
11. Beheshti M, Pöcher S, Vali R, Waldenberger P, Broinger G, Nader M, Kohlfürst S, Pirich C, Dralle H, Langsteger W (2009) The value of ^{18}F -DOPA PET-CT in patients with medullary thyroid carcinoma: comparison with ^{18}F -FDG PET-CT. *Eur Radiol* 19(6):1425–1434
12. Beheshti M, Vali R, Waldenberger P, Fitz F, Nader M, Loidl W, Broinger G, Stoiber F, Foglman I, Langsteger W (2008) Detection of bone metastases in patients with prostate cancer by ^{18}F fluorocholine and ^{18}F fluoride PET-CT: a comparative study. *Eur J Nucl Med Mol Imaging* 35(10):1766–1774
13. Belt JA, Marina NM, Phelps DA, Crawford CR (1993) Nucleoside transport in normal and neoplastic cells. *Adv Enzyme Regul* 33:235–252
14. Blau M, Nagler W, Bender MA (1962) Fluorine-18: a new isotope for bone scanning. *J Nucl Med* 3:332–334
15. Bostwick DG, Pacelli A, Blute M, Roche P, Murphy GP (1998) Prostate specific membrane antigen expression in prostatic intraepithelial neoplasia and adenocarcinoma: a study of 184 cases. *Cancer Metastasis Rev* 82(11):2256–2261
16. Bouchelouche K, Oehr P (2008) Positron emission tomography and positron emission tomography/computerized tomography of urological malignancies: an update review. *J Urol* 179(1):34–45
17. Bourdier T, Greguric I, Roselt P, Jackson T, Faragalla J, Katsifis A (2011) Fully automated one-pot radiosynthesis of *O*-(2- ^{18}F]fluoroethyl)-L-tyrosine on the TracerLab FX(FN) module. *Nucl Med Biol* 38(5):645–651
18. Bouvet V, Wüst M, Jans H-S, Janzen N, Genady AR, Valliant JF, Benard F, Wüst F (2016) Automated synthesis of ^{18}F]DCFPyL via direct radiofluorination and validation in preclinical prostate cancer models. *EJNMMI Res* 6(1):40
19. Bozkurt MF, Virgolini I, Balogova S, Beheshti M, Rubello D, Decristoforo C, Ambrosini V, Kjaer A, Delgado-Bolton R, Kunikowska J, Oyen WJG, Chiti A, Giammarile F, Sundin A, Fanti S (2017) Guideline for PET/CT imaging of neuroendocrine neoplasms with ^{68}Ga -DOTA-conjugated somatostatin receptor targeting peptides and ^{18}F -DOPA. *Eur J Nucl Med Mol Imaging* 44(9):1588–1601
20. Brock CS, Meikle SR, Price P (1997) Does fluorine-18 fluorodeoxyglucose metabolic imaging of tumours benefit oncology? *Eur J Nucl Med* 24(6):691–705
21. Busch H, Davis JR, Honig GR, Anderson DC, Nair PV, Nyhan WL (1959) The uptake of a variety of amino acids into nuclear proteins of tumors and other tissues. *Cancer Res* 19:1030–1039

22. Calabria F, Gallo G, Schillaci O, Cascini GL (2015) Bio-Distribution, imaging protocols and diagnostic accuracy of PET with tracers of lipogenesis in imaging prostate cancer: a comparison between ¹¹C-choline, ¹⁸F-fluoroethylcholine and ¹⁸F-methylcholine. *Curr Pharm Des* 21(32):4738–4747
23. Cardinale J, Martin R, Remde Y, Schäfer M, Hienzsch A, Hübner S, Zerges A-M, Marx H, Hesse R, Weber K (2017) Procedures for the GMP-compliant production and quality control of [¹⁸F]PSMA-1007: a next generation radiofluorinated tracer for the detection of prostate cancer. *Pharmaceuticals* 10(4):77
24. Cardinale J, Schäfer M, Benešová M, Bauder-Wüst U, Leotta K, Eder M, Neels OC, Haberkorn U, Giesel FL, Kopka K (2017) Preclinical evaluation of ¹⁸F-PSMA-1007, a new prostate-specific membrane antigen ligand for prostate cancer imaging. *J Nucl Med* 58(3):425–431
25. Caroli P, De Giorgi U, Scarpi E, Fantini L, Moretti A, Galassi R, Celli M, Conteduca V, Rossi L, Bianchi E, Paganelli G, Matteucci F (2018) Prognostic value of ¹⁸F-choline PET/CT metabolic parameters in patients with metastatic castration-resistant prostate cancer treated with abiraterone or enzalutamide. *Eur J Nucl Med Mol Imaging* 45(3):348–354
26. Chakraborty D, Bhattacharya A, Mete UK, Mittal BR (2013) Comparison of ¹⁸F fluoride PET/CT and ^{99m}Tc-MDP bone scan in the detection of skeletal metastases in urinary bladder carcinoma. *Clin Nucl Med* 38(8):616–621
27. Chapman JD, Franko AJ, Sharplin J (1981) A marker for hypoxic cells in tumours with potential clinical applicability. *Br J Cancer* 43(4):546–550
28. Chen Y, Pullambhatla M, Foss CA, Byun Y, Nimmagadda S, Senthamizhchelvan S, Sgouros G, Mease RC, Pomper MG (2011) 2-(3-{1-Carboxy-5-[(6-[¹⁸F]Fluoro-Pyridine-3-Carbonyl)-Amino]-Pentyl}-Ureido)-pentanedioic acid, [¹⁸F]DCFPyL, a PSMA-based PET imaging agent for prostate cancer. *Clin Cancer Res* 17(24):7645
29. Cherif A, Yang DJ, Tansey W, Kim EE, Wallace S (1994) Rapid synthesis of 3-[¹⁸F]Fluoro-1-(2'-Nitro-1'-Imidazolyl)-2-Propanol ([¹⁸F]Fluoromisonidazole). *Pharm Res* 11(3):466–469
30. Clary GL, Tsai CF, Guynn RW (1987) Substrate specificity of choline kinase. *Arch Biochem Biophys* 254(1):214–221
31. Coleman R, DeGrado T, Wang S, Baldwin S, Orr M, Reiman R, Price D (2000) Preliminary evaluation of F-18 Fluorocholine (FCH) as a PET tumor imaging agent. *Clin Positron Imaging* 3(4):147
32. Collins J, Waldmann CM, Drake C, Slavik R, Ha NS, Sergeev M, Lazari M, Shen B, Chin FT, Moore M, Sadeghi S, Phelps ME, Murphy JM, van Dam RM (2017) Production of diverse PET probes with limited resources: 24 ¹⁸F-labeled compounds prepared with a single radiosynthesizer. *Proc Natl Acad Sci USA* 114(43):11309–11314
33. Conti P, Chen K, Tripathy D, Jadvar H (2015) [¹⁸F]FMAU for PET imaging in breast cancer patients. *J Clin Oncol* 33(15_suppl):11056–11056
34. DeGrado TR, Baldwin SW, Wang S, Orr MD, Liao RP, Friedman HS, Reiman R, Price DT, Coleman RE (2001) Synthesis and evaluation of ¹⁸F-labeled choline analogs as oncologic PET tracers. *J Nucl Med* 42(12):1805–1814
35. DeGrado TR, Coleman RE, Wang S, Baldwin SW, Orr MD, Robertson CN, Polascik TJ, Price DT (2001) Synthesis and evaluation of ¹⁸F-labeled choline as an oncologic tracer for positron emission tomography: initial findings in prostate cancer. *Cancer Res* 61(1):110–117
36. Debus C, Afshar-Oromieh A, Floca R, Ingrisich M, Knoll M, Debus J, Haberkorn U, Abdollahi A (2018) Feasibility and robustness of dynamic ¹⁸F-FET PET based tracer kinetic models applied to patients with recurrent high-grade glioma prior to carbon ion irradiation. *Sci Rep* 8(1):14760
37. Debus C, Waltenberger M, Floca R, Afshar-Oromieh A, Bougatf N, Adeberg S, Heiland S, Bendszus M, Wick W, Rieken S, Haberkorn U, Debus J, Knoll M, Abdollahi A (2018) Impact of ¹⁸F-FET PET on target volume definition and tumor progression of recurrent high grade glioma treated with carbon-ion radiotherapy. *Sci Rep* 8(1):7201

38. Deves R, Krupka RM (1979) The binding and translocation steps in transport as related to substrate structure. a study of the choline carrier of erythrocytes. *Biochim Biophys Acta* 557(2):469–485
39. Dixit M, Shi J, Wei L, Afari G, Bhattacharyya S (2013) Synthesis of clinical-grade [^{18}F]-fluoroestradiol as a surrogate PET biomarker for the evaluation of estrogen receptor-targeting therapeutic drug. *Int J Mol Imaging* 2013:10
40. Dolle F, Demphel S, Hinnen F, Fournier D, Vaufrey F, Crouzel C (1998) 6- ^{18}F Fluoro-L-DOPA by radiofluorodestannylation: a short and simple synthesis of a new labelling precursor. *J Label Compd Rad* 41(2):105–114
41. Dunet V, Rossier C, Buck A, Stupp R, Prior JO (2012) Performance of ^{18}F -fluoro-ethyl-tyrosine (^{18}F -FET) PET for the differential diagnosis of primary brain tumor: a systematic review and Metaanalysis. *J Nucl Med* 53(2):207–214
42. Eckel F, Herrmann K, Schmidt S, Hillerer C, Wieder HA, Krause BJ, Schuster T, Langer R, Wester HJ, Schmid RM, Schwaiger M, Buck AK (2009) Imaging of proliferation in hepatocellular carcinoma with the in vivo marker ^{18}F -fluorothymidine. *J Nucl Med* 50(9):1441–1447
43. Edwards R, Wirth T (2015) [^{18}F]6-fluoro-3,4-dihydroxy-L-phenylalanine—recent modern syntheses for an elusive radiotracer. *J Label Compd Rad* 58(5):183–187
44. Egerton A, Demjaha A, McGuire P, Mehta MA, Howes OD (2010) The test-retest reliability of ^{18}F -DOPA PET in assessing striatal and extrastriatal presynaptic dopaminergic function. *NeuroImage* 50(2):524–531
45. Elsinga PH, Hatano K, Ishiwata K (2006) PET tracers for imaging of the dopaminergic system. *Curr Med Chem* 13(18):2139–2153
46. Even-Sapir E, Metser U, Mishani E, Lievshitz G, Lerman H, Leibovitch I (2006) The detection of bone metastases in patients with high-risk prostate cancer: $^{99\text{m}}\text{Tc}$ -MDP planar bone scintigraphy, single- and multi-field-of-view SPECT, ^{18}F -fluoride PET, and ^{18}F -fluoride PET/CT. *J Nucl Med* 47(2):287–297
47. Fedorova O, Kuznetsova O, Stepanova M, Maleev V, Belokon Y, Wester H-J, Krasikova R (2014) A facile direct nucleophilic synthesis of *O*-(2- ^{18}F)-fluoroethyl)-l-tyrosine (^{18}F]-FET) without HPLC purification. *J Radioanal Nucl Chem* 301(2):505–512
48. Fisher B, Costantino J, Redmond C, Poisson R, Bowman D, Couture J, Dimitrov NV, Wolmark N, Wickerham DL, Fisher ER, Margolese R, Robidoux A, Shibata H, Terz J, Paterson AHG, Feldman MI, Farrar W, Evans J, Lickley HL, Ketner M (1989) A randomized clinical trial evaluating tamoxifen in the treatment of patients with node-negative breast cancer who have estrogen-receptor–positive tumors. *N Engl J Med* 320(8):479–484
49. Foo SS, Abbott DF, Lawrentschuk N, Scott AM (2004) Functional imaging of intratumoral hypoxia. *Mol Imaging Biol* 6(5):291–305
50. Fraioli F, Shankar A, Hargrave D, Hyare H, Gaze MN, Groves AM, Alongi P, Stoneham S, Michopoulou S, Syed R, Bomanji JB (2015) ^{18}F -fluoroethylcholine (^{18}F -Cho) PET/MRI functional parameters in pediatric astrocytic brain tumors. *Clin Nucl Med* 40(1):e40–e45
51. Füchtner F, Steinbach J, Mäding P, Johannsen B (1996) Basic hydrolysis of 2- ^{18}F]-fluoro-1, 3, 4, 6-tetra-*O*-acetyl-glucose in the preparation of 2- ^{18}F]-fluoro-2-deoxy-D-glucose. *Appl Radiat Isot* 47(1):61–66
52. Füchtner F, Zessin J, Mäding P, Wüst F (2008) Aspects of 6- ^{18}F]-fluoro-L-DOPA preparation. *Nuklearmedizin* 47(01):62–64
53. Gallagher BM, Fowler JS, Gutterson NI, MacGregor RR, Wan CN, Wolf AP (1978) Metabolic trapping as a principle of radiopharmaceutical design: some factors responsible for the biodistribution of [^{18}F] 2-deoxy-2-fluoro-D-glucose. *J Nucl Med* 19(10):1154–1161
54. Gallagher CL, Johnson SC, Bendlin BB, Chung MK, Holden JE, Oakes TR, Brooks BR, Konopacki RA, Dogan S, Abbs JH, Xu G, Nickles RJ, Pyzalski RW, DeJesus OT, Brown WD (2011) A longitudinal study of motor performance and striatal [^{18}F]-fluorodopa uptake in Parkinson’s disease. *Brain Imaging Behav* 5(3):203–211

55. Garnett E, Firnau G, Chan P, Sood S, Belbeck L (1978) [¹⁸F]Fluoro-dopa, an analogue of dopa, and its use in direct external measurements of storage, degradation, and turnover of intracerebral dopamine. *Proc Nat Acad Sci USA* 75(1):464–467
56. Garnett E, Firnau G, Nahmias C (1983) Dopamine visualized in the basal ganglia of living man. *Nature* 305(5930):137
57. Gerstner ER, Zhang Z, Fink JR, Muzi M, Hanna L, Greco E, Prah M, Schmainda KM, Mintz A, Kostakoglu L, Eikman EA, Ellingson BM, Ratai EM, Sorensen AG, Barboriak DP, Mankoff DA, Group AT (2016) ACRIN 6684: assessment of tumor hypoxia in newly diagnosed glioblastoma using ¹⁸F-FMISO PET and MRI. *Clin Cancer Res* 22(20):5079–5086
58. Giesel FL, Hadaschik B, Cardinale J, Radtke J, Vinsensia M, Lehnert W, Kesch C, Tolstov Y, Singer S, Grabe N, Duensing S, Schäfer M, Neels OC, Mier W, Haberkorn U, Kopka K, Kratochwil C (2017) F-18 labelled PSMA-1007: biodistribution, radiation dosimetry and histopathological validation of tumor lesions in prostate cancer patients. *Eur J Nucl Med Mol Imaging* 44(4):678–688
59. Giesel FL, Knorr K, Spohn F, Will L, Maurer T, Flechsig P, Neels O, Schiller K, Amaral H, Weber W, Schwaiger M, Hohenfellner M, Kratochwil C, Debus J, Haberkorn U, Choyke P, Kramer V, Kopka K, Eiber M (2018) Detection efficacy of [¹⁸F]PSMA-1007 PET/CT in 251 patients with biochemical recurrence after radical prostatectomy. *J Nucl Med*. <https://doi.org/10.2967/jnumed.118.212233>
60. Giesel FL, Will L, Lawal I, Lengana T, Kratochwil C, Vorster M, Neels O, Reyneke F, Haberkorn U, Kopka K, Sathekge M (2018) Intraindividual Comparison of ¹⁸F-PSMA-1007 and ¹⁸F-DCFpyL PET/CT in the prospective evaluation of patients with newly diagnosed prostate carcinoma: a pilot study. *J Nucl Med* 59(7):1076–1080
61. Golubic AT, Pasini Nemir E, Zovic M, Mutvar A, Kusacic Kuna S, Despot M, Samardzic T, Huic D (2017) The value of ¹⁸F-DOPA PET/CT in patients with medullary thyroid carcinoma and increased calcitonin values. *Nucl Med Commun* 38(7):636–641
62. Gong C, Yang Z, Sun Y, Zhang J, Zheng C, Wang L, Zhang Y, Xue J, Yao Z, Pan H, Wang B, Zhang Y (2017) A preliminary study of ¹⁸F-FES PET/CT in predicting metastatic breast cancer in patients receiving docetaxel or fulvestrant with docetaxel. *Sci Rep* 7(1):6584
63. Gray LH, Conger AD, Ebert M, Hornsey S, Scott OC (1953) The concentration of oxygen dissolved in tissues at the time of irradiation as a factor in radiotherapy. *Br J Radiol* 26(312):638–648
64. Grierson JR, Link JM, Mathis CA, Rasey JS, Krohn KA (1989) A radiosynthesis of fluorine-18 fluoromisonidazole. *J Nucl Med* 30(3):343–350
65. Grkovski M, Schöder H, Lee NY, Carlin SD, Beattie BJ, Riaz N, Leeman JE, O'Donoghue JA, Humm JL (2017) Multiparametric imaging of tumor hypoxia and perfusion with ¹⁸F-fluoromisonidazole dynamic PET in head and neck cancer. *J Nucl Med* 58(7):1072–1080
66. Grosu A-L, Souvatzoglou M, Röper B, Dobritz M, Wiedenmann N, Jacob V, Wester H-J, Reischl G, Machulla H-J, Schwaiger M, Molls M, Piert M (2007) Hypoxia imaging with FAZA-PET and theoretical considerations with regard to dose painting for individualization of radiotherapy in patients with head and neck cancer. *Int J Radiat Oncol Biol Phys* 69(2):541–551
67. Hamacher K, Coenen HH, Stöcklin G (1986) Efficient stereospecific synthesis of no-carrier-added 2-[¹⁸F]-fluoro-2-deoxy-D-glucose using aminopolyether supported nucleophilic substitution. *J Nucl Med* 27(2):235–238
68. Hanahan D, Weinberg RA (2000) The hallmarks of cancer. *Cell* 100(1):57–70
69. Hara T, Kosaka N, Kishi H (2002) Development of ¹⁸F-fluoroethylcholine for cancer imaging with PET: synthesis, biochemistry, and prostate cancer imaging. *J Nucl Med* 43(2):187–199
70. Hatt M, Majdoub M, Vallieres M, Tixier F, Le Rest CC, Groheux D, Hindie E, Martineau A, Pradier O, Hustinx R, Perdriset R, Guillemin R, El Naqa I, Visvikis D (2015) ¹⁸F-FDG PET

- uptake characterization through texture analysis: investigating the complementary nature of heterogeneity and functional tumor volume in a multi-cancer site patient cohort. *J Nucl Med* 56(1):38–44
71. Hawkins RA, Choi Y, Huang S-C, Hoh CK, Dahlbom M, Schiepers C, Satyamurthy N, Barrio JR, Phelps ME (1992) Evaluation of the skeletal kinetics of fluorine-18-fluoride ion with PET. *J Nucl Med* 33(5):633–642
 72. Hayashi K, Furutsuka K, Takei M, Muto M, Nakao R, Aki H, Suzuki K, Fukumura T (2011) High-yield automated synthesis of [¹⁸F]fluoroazomycin arabinoside ([¹⁸F]FAZA) for hypoxia-specific tumor imaging. *Appl Radiat Isot* 69(7):1007–1013
 73. Heiss P, Mayer S, Herz M, Wester HJ, Schwaiger M, Senekowitsch-Schmidtke R (1999) Investigation of transport mechanism and uptake kinetics of O-(2-[¹⁸F]fluoroethyl)-L-tyrosine in vitro and in vivo. *J Nucl Med* 40(8):1367–1373
 74. Herrmann K, Buck AK, Schuster T, Junger A, Wieder HA, Graf N, Ringshausen I, Rudelius M, Wester HJ, Schwaiger M, Keller U, Dechow T (2011) Predictive value of initial ¹⁸F-FLT uptake in patients with aggressive non-Hodgkin lymphoma receiving R-CHOP treatment. *J Nucl Med* 52(5):690–696
 75. Hofman MS, Violet J, Hicks RJ, Ferdinandus J, Thang SP, Akhurst T, Irvani A, Kong G, Ravi Kumar A, Murphy DG, Eu P, Jackson P, Scalzo M, Williams SG, Sandhu S (2018) [¹⁷⁷Lu]-PSMA-617 radionuclide treatment in patients with metastatic castration-resistant prostate cancer (LuPSMA trial): a single-centre, single-arm, phase 2 study. *Lancet Oncol* 19(6):825–833
 76. Högerle S, Althöfer C, Ghanem N, Brink I, Moser E, Nitzsche E (2001) ¹⁸F-DOPA positron emission tomography for tumour detection in patients with medullary thyroid carcinoma and elevated calcitonin levels. *Eur J Nucl Med* 28(1):64–71
 77. Högerle S, Nitzsche E, Althöfer C, Ghanem N, Manz T, Brink I, Reincke M, Moser E, Neumann HP (2002) Pheochromocytomas: detection with ¹⁸F DOPA whole-body PET—initial results. *Radiology* 222(2):507–512
 78. Höpping A, Müller M, Smits R, Mollitor J, Clausnitzer A, Baumgart D (2014) Precursors and process for the production of ¹⁸F-labelled amino acids. Google Patents
 79. Ido T, Wan CN, Casella V, Fowler J, Wolf A, Reivich M, Kuhl D (1978) Labeled 2-deoxy-D-glucose analogs. ¹⁸F-labeled 2-deoxy-2-fluoro-D-glucose, 2-deoxy-2-fluoro-D-mannose and ¹⁴C-2-deoxy-2-fluoro-D-glucose. *J Label Compd Rad* 14(2):175–183
 80. Imani F, Agopian VG, Auerbach MS, Walter MA, Imani F, Benz MR, Dumont RA, Lai CK, Czernin JG, Yeh MW (2009) ¹⁸F-FDOPA PET and PET/CT accurately localize pheochromocytomas. *J Nucl Med* 50(4):513–519
 81. Isselbacher KJ (1972) Sugar and amino acid transport by cells in culture—differences between normal and malignant cells. *N Engl J Med* 286(17):929–933
 82. Itoh M, Meguro K, Fujiwara T, Hatazawa J, Iwata R, Ishiwata K, Takahashi T, Ido T, Sasaki H (1994) Assessment of dopamine metabolism in brain of patients with dementia by means of ¹⁸F-fluorodopa and PET. *Ann Nucl Med* 8(4):245–251
 83. Iwata R, Pascali C, Bogni A, Furumoto S, Terasaki K, Yanai K (2002) [¹⁸F]fluoromethyl triflate, a novel and reactive [¹⁸F]fluoromethylating agent: preparation and application to the on-column preparation of [¹⁸F]fluorocholeline. *Appl Radiat Isot* 57(3):347–352
 84. Jager PL, Chirakal R, Marriott CJ, Brouwers AH, Koopmans KP, Gulenchyn KY (2008) 6-L-¹⁸F-fluorodihydroxyphenylalanine PET in neuroendocrine tumors: basic aspects and emerging clinical applications. *J Nucl Med* 49(4):573
 85. Jambor I, Kuisma A, Kähkönen E, Kemppainen J, Merisaari H, Eskola O, Teuvo J, Perez IM, Pesola M, Aronen HJ, Boström PJ, Taimen P, Minn H (2018) Prospective evaluation of ¹⁸F-FACBC PET/CT and PET/MRI versus multiparametric MRI in intermediate- to high-risk prostate cancer patients (FLUCIPRO trial). *Eur J Nucl Med* 45(3):355–364
 86. Johnstone RM, Scholefield PG (1965) Amino acid transport in tumor cells. *Adv Cancer Res* 9:143–226

87. Kameyama R, Yamamoto Y, Izuishi K, Sano T, Nishiyama Y (2011) Correlation of ^{18}F -FLT uptake with equilibrative nucleoside transporter-1 and thymidine kinase-1 expressions in gastrointestinal cancer. *Nucl Med Commun* 32(6):460–465
88. Kameyama R, Yamamoto Y, Izuishi K, Takebayashi R, Hagiike M, Murota M, Kaji M, Haba R, Nishiyama Y (2009) Detection of gastric cancer using ^{18}F -FLT PET: comparison with ^{18}F -FDG PET. *Eur J Nucl Med Mol Imaging* 36(3):382–388
89. Kao C-HK, Hsu W-L, Xie H-L, Lin M-C, Lan W-C, Chao H-Y (2011) GMP production of [^{18}F]FDOPA and issues concerning its quality analyses as in USP “Fluorodopa F18 Injection”. *Ann Nucl Med* 25(5):309–316
90. Kauhanen S, Seppänen M, Ovaska J, Minn H, Bergman J, Korsoff P, Salmela P, Saltevo J, Sane T, Välimäki M (2009) The clinical value of [^{18}F]fluoro-dihydroxyphenylalanine positron emission tomography in primary diagnosis, staging, and restaging of neuroendocrine tumors. *Endocr Relat Cancer* 16(1):255–265
91. Kauhanen S, Schalin-Jääntti C, Seppänen M, Kajander S, Virtanen S, Schildt J, Lisinen I, Ahonen A, Heiskanen I, Väisänen M (2011) Complementary roles of ^{18}F -DOPA PET/CT and ^{18}F -FDG PET/CT in medullary thyroid cancer. *J Nucl Med* 52(12):1855
92. Kawaguchi M, Tateishi U, Shizukuishi K, Suzuki A, Inoue T (2010) ^{18}F -fluoride uptake in bone metastasis: morphologic and metabolic analysis on integrated PET/CT. *Ann Nucl Med* 24(4):241–247
93. Kawai N, Maeda Y, Kudomi N, Miyake K, Okada M, Yamamoto Y, Nishiyama Y, Tamiya T (2011) Correlation of biological aggressiveness assessed by ^{11}C -methionine PET and hypoxic burden assessed by ^{18}F -fluoromisonidazole PET in newly diagnosed glioblastoma. *Eur J Nucl Med Mol Imaging* 38(3):441–450
94. Kiesewetter DO, Kilbourn MR, Landvatter SW, Heimann DF, Katzenellenbogen JA, Welch MJ (1984) Preparation of four fluorine-18-labeled estrogens and their selective uptakes in target tissues of immature rats. *J Nucl Med* 25(11):1212–1221
95. Kikuchi M, Yamane T, Shinohara S, Fujiwara K, Hori SY, Tona Y, Yamazaki H, Naito Y, Senda M (2011) ^{18}F -fluoromisonidazole positron emission tomography before treatment is a predictor of radiotherapy outcome and survival prognosis in patients with head and neck squamous cell carcinoma. *Ann Nucl Med* 25(9):625–633
96. Kinoshita T, Fujii H, Hayashi Y, Kamiyama I, Ohtsuka T, Asamura H (2016) Prognostic significance of hypoxic PET using ^{18}F -FAZA and ^{62}Cu -ATSM in non-small-cell lung cancer. *Lung Cancer* 91:56–66
97. Kizaka-Kondoh S, Konse-Nagasawa H (2009) Significance of nitroimidazole compounds and hypoxia-inducible factor-1 for imaging tumor hypoxia. *Cancer Sci* 100(8):1366–1373
98. Kondo A, Ishii H, Aoki S, Suzuki M, Nagasawa H, Kubota K, Minamimoto R, Arakawa A, Tominaga M, Arai H (2016) Phase IIa clinical study of [^{18}F]fluciclovine: efficacy and safety of a new PET tracer for brain tumors. *Ann Nucl Med* 30(9):608–618
99. Kopka K, Benešová M, Bařinka C, Haberkorn U, Babich J (2017) Glu-ureido–based inhibitors of prostate-specific membrane antigen: lessons learned during the development of a novel class of low-molecular-weight theranostic radiotracers. *J Nucl Med* 58(Supplement 2):17S–26S
100. Kratochwil C, Bruchertseifer F, Giesel FL, Weis M, Verburg FA, Mottaghy F, Kopka K, Apostolidis C, Haberkorn U, Morgenstern A (2016) ^{225}Ac -PSMA-617 for PSMA-targeted α -radiation therapy of metastatic castration-resistant prostate cancer. *J Nucl Med* 57(12):1941–1944
101. Krohn KA, Mankoff DA, Eary JF (2001) Imaging cellular proliferation as a measure of response to therapy. *J Clin Pharmacol* 41(S7):96S–103S
102. Kryza D, Tadino V, Filannino MA, Villeret G, Lemoucheux L (2008) Fully automated [^{18}F] fluorocholine synthesis in the TracerLab MX FDG coincidence synthesizer. *Nucl Med Biol* 35(2):255–260
103. Kuik W-J, Kema IP, Brouwers AH, Zijlma R, Neumann KD, Dierckx RAJO, DiMaggio SG, Elsinga PH (2015) In vivo biodistribution of no-carrier-added 6- ^{18}F -fluoro-3,4-dihydroxy-l-

- phenylalanine (^{18}F -DOPA), produced by a new nucleophilic substitution approach, compared with carrier-added ^{18}F -DOPA, prepared by conventional electrophilic substitution. *J Nucl Med* 56(1):106–112
104. Kumakura Y, Danielsen EH, Gjedde A, Vernaleken I, Buchholz H-G, Heinz A, Gründer G, Bartenstein P, Cumming P (2010) Elevated [^{18}F]FDOPA utilization in the periaqueductal gray and medial nucleus accumbens of patients with early Parkinson's disease. *NeuroImage* 49(4):2933–2939
 105. Kumar P, Mercer J, Doerkson C, Tonkin K, McEwan AJ (2007) Clinical production, stability studies and PET imaging with 16- α -[^{18}F]fluoroestradiol ([^{18}F]FES) in ER positive breast cancer patients. *J Pharm Pharm Sci* 10(2):256s–265s
 106. Kämäräinen E-L, Kyllönen T, Nihtilä O, Björk H, Solin O (2004) Preparation of fluorine-18-labelled fluoromisonidazole using two different synthesis methods. *J Label Compd Rad* 47(1):37–45
 107. Lee H, Kim SK, Kim YI, Kim TS, Kang SH, Park WS, Yun T, Eom HS (2014) Early determination of prognosis by interim 3'-deoxy-3'- ^{18}F -fluorothymidine PET in patients with non-Hodgkin lymphoma. *J Nucl Med* 55(2):216–222
 108. Lee N, Nehmeh S, Schoder H, Fury M, Chan K, Ling CC, Humm J (2009) Prospective trial incorporating pre-/mid-treatment [^{18}F]-misonidazole positron emission tomography for head-and-neck cancer patients undergoing concurrent chemoradiotherapy. *Int J Radiat Oncol Biol Phys* 75(1):101–108
 109. Lemaire C, Gillet S, Guillouet S, Plenevaux A, Aerts J, Luxen A (2004) Highly enantioselective synthesis of no-carrier-added 6-[^{18}F]fluoro-L-dopa by chiral phase-transfer alkylation. *Eur J Org Chem* 2004(13):2899–2904
 110. Libert LC, Franci X, Plenevaux AR, Ooi T, Maruoka K, Luxen AJ, Lemaire CF (2013) Production at the curie level of no-carrier-added 6- ^{18}F -fluoro-l-dopa. *J Nucl Med* 54(7):1154–1161
 111. Lim J-L, Berridge MS (1993) An efficient radiosynthesis of [^{18}F]fluoromisonidazole. *Appl Radiat Isot* 44(8):1085–1091
 112. Linden HM, Peterson LM, Fowler AM (2018) Clinical potential of estrogen and progesterone receptor imaging. *PET Clin* 13(3):415–422
 113. Loane C, Politis M (2011) Positron emission tomography neuroimaging in Parkinson's disease. *Am J Transl Res* 3(4):323–341
 114. Luxen A, Guillaume M, Melega W, Pike VW, Solin O, Wagner R (1992) Production of 6-[^{18}F] fluoro-L-dopa and its metabolism in vivo—a critical review. *Int J Rad Appl Instrum B* 19(2):149–158
 115. Löck S, Perrin R, Seidlitz A, Bandurska-Luque A, Zschaek S, Zöphel K, Krause M, Steinbach J, Kotzerke J, Zips D, Troost EGC, Baumann M (2017) Residual tumour hypoxia in head-and-neck cancer patients undergoing primary radiochemotherapy, final results of a prospective trial on repeat FMISO-PET imaging. *Radiother Oncol* 124(3):533–540
 116. Machulla H-J, Blocher A, Kuntzsch M, Piert M, Wei R, Grierson JR (2000) Simplified Labeling Approach for Synthesizing 3'-Deoxy-3'-[^{18}F]fluorothymidine ([^{18}F]FLT). *J Radioanal Nucl Chem* 243(3):843–846
 117. Mamede M, Higashi T, Kitaichi M, Ishizu K, Ishimori T, Nakamoto Y, Yanagihara K, Li M, Tanaka F, Wada H, Manabe T, Saga T (2005) [^{18}F]FDG uptake and PCNA, Glut-1, and Hexokinase-II expressions in cancers and inflammatory lesions of the lung. *Neoplasia* 7(4):369–379
 118. Mangner TJ, Klecker RW, Anderson L, Shields AF (2003) Synthesis of 2'-deoxy-2'-[^{18}F] fluoro-beta-D-arabinofuranosyl nucleosides, [^{18}F]FAU, [^{18}F]FMAU, [^{18}F]FBAU and [^{18}F] FIAU, as potential PET agents for imaging cellular proliferation. synthesis of [^{18}F]labelled FAU, FMAU, FBAU, FIAU. *Nucl Med Biol* 30(3):215–224
 119. Mankoff DA, Tewson TJ, Eary JF (1997) Analysis of blood clearance and labeled metabolites for the estrogen receptor tracer [F-18]-16 alpha-fluoroestradiol (FES). *Nucl Med Biol* 24(4):341–348

120. Marchand P, Ouadi A, Pelliccioli M, Schuler J, Laquerriere P, Boisson F, Brasse D (2016) Automated and efficient radiosynthesis of [¹⁸F]FLT using a low amount of precursor. *Nucl Med Biol* 43(8):520–527
121. Martin R, Baumgart D, Hübner S, Juttler S, Saul S, Clausnitzer A, Mollitor J, Smits R, Höpping A, Müller M (2013) Automated nucleophilic one-pot synthesis of ¹⁸F-L-DOPA with high specific activity using the GE TRACERlab MXFDG. *J Label Compd Rad* 56(S1): S126
122. McConathy J, Voll RJ, Yu W, Crowe RJ, Goodman MM (2003) Improved synthesis of anti-[¹⁸F]FACBC: improved preparation of labeling precursor and automated radiosynthesis. *Appl Radiat Isot* 58(6):657–666
123. Melega WP, Hoffman JM, Luxen A, Nissenson CH, Phelps ME, Barrio JR (1990) The effects of carbidopa on the metabolism of 6-[¹⁸F]fluoro-L-dopa in rats, monkeys and humans. *Life Sci* 47(2):149–157
124. Metran-Nascente C, Yeung I, Vines DC, Metser U, Dhani NC, Green D, Milosevic M, Jaffray D, Hedley DW (2016) Measurement of tumor hypoxia in patients with advanced pancreatic cancer based on ¹⁸F-fluoroazomyin arabinoside uptake. *J Nucl Med* 57(3):361–366
125. Meyer JP, Probst KC, Westwell AD (2014) Radiochemical synthesis of 2'-[¹⁸F]-labelled and 3'-[¹⁸F]-labelled nucleosides for positron emission tomography imaging. *J Label Compd Rad* 57(5):333–337
126. Mitra E, Quon A (2009) Positron emission tomography/computed tomography: the current technology and applications. *Radiol Clin N Am* 47(1):147–160
127. Morana G, Puntoni M, Garre ML, Massollo M, Lopci E, Naseri M, Severino M, Tortora D, Rossi A, Piccardo A (2016) Ability of ¹⁸F-DOPA PET/CT and fused ¹⁸F-DOPA PET/MRI to assess striatal involvement in paediatric glioma. *Eur J Nucl Med Mol Imaging* 43(9):1664–1672
128. Moreau A, Giraudet AL, Kryza D, Borson-Chazot F, Bournaud C, Mognetti T, Lifante J-C, Combemale P, Giammarile F, Houzard C (2017) Quantitative analysis of normal and pathologic adrenal glands with ¹⁸F-FDOPA PET/CT: focus on pheochromocytomas. *Nucl Med Commu* 38(9):771–779
129. Mori T, Kasamatsu S, Mosdzianowski C, Welch MJ, Yonekura Y, Fujibayashi Y (2006) Automatic synthesis of 16 α -[¹⁸F]fluoro-17 β -estradiol using a cassette-type [¹⁸F] fluorodeoxyglucose synthesizer. *Nucl Med Biol* 33(2):281–286
130. Mossine AV, Brooks AF, Makaravage KJ, Miller JM, Ichiishi N, Sanford MS, Scott PJH (2015) Synthesis of [¹⁸F]arenes via the copper-mediated [¹⁸F]fluorination of boronic acids. *Org Lett* 17(23):5780–5783
131. Moulder JE, Rockwell S (1987) Tumor hypoxia: its impact on cancer therapy. *Cancer Metastasis Rev* 5(4):313–341
132. Muijs CT, Beukema JC, Widder J, van den Bergh AC, Havenga K, Pruim J, Langendijk JA (2011) ¹⁸F-FLT-PET for detection of rectal cancer. *Radiother Oncol* 98(3):357–359
133. Muz B, de la Puente P, Azab F, Azab AK (2015) The role of hypoxia in cancer progression, angiogenesis, metastasis, and resistance to therapy. *Hypoxia (Auckl)* 3:83–92
134. Müller D, Klette I, Kalb F, Baum RP (2011) Synthesis of *O*-(2-[¹⁸F]fluoroethyl)-L-tyrosine based on a cartridge purification method. *Nucl Med Biol* 38(5):653–658
135. Namavari M, Bishop A, Satyamurthy N, Bida G, Barrio JR (1992) Regioselective radiofluorodestannylation with [¹⁸F]F₂, and [¹⁸F]CH₃COOF: a high yield synthesis of 6-[¹⁸F]fluoro-L-dopa. *Appl Radiat Isot* 43(8):989–996
136. Nanni C, Zannoni L, Pultrone C, Schiavina R, Brunocilla E, Lodi F, Malizia C, Ferrari M, Rigatti P, Fonti C, Martorana G, Fanti S (2016) ¹⁸F-FACBC (anti1-amino-3-¹⁸F-fluorocyclobutane-1-carboxylic acid) versus ¹¹C-choline PET/CT in prostate cancer relapse: results of a prospective trial. *Eur J Nucl Med Mol Imaging* 43(9):1601–1610
137. Odewole OA, Tade FI, Nieh PT, Savir-Baruch B, Jani AB, Master VA, Rossi PJ, Halkar RK, Osunkoya AO, Akin-Akintayo O, Zhang C, Chen Z, Goodman MM, Schuster DM (2016)

- Recurrent prostate cancer detection with anti-3- ^{18}F FACBC PET/CT: comparison with CT. *Eur J Nucl Med Mol Imaging* 43(10):1773–1783
138. Oh SJ, Chi DY, Mosdzianowski C, Kil HS, Ryu JS, Moon DH (2007) The automatic production of 16α - ^{18}F fluoroestradiol using a conventional ^{18}F FDG module with a disposable cassette system. *Appl Radiat Isot* 65(6):676–681
 139. Oh SJ, Chi DY, Mosdzianowski C, Kim JY, Gil HS, Kang SH, Ryu JS, Moon DH (2005) Fully automated synthesis of ^{18}F fluoromisonidazole using a conventional ^{18}F FDG module. *Nucl Med Biol* 32(8):899–905
 140. Oh SJ, Mosdzianowski C, Chi DY, Kim JY, Kang SH, Ryu JS, Yeo JS, Moon DH (2004) Fully automated synthesis system of 3'-deoxy-3'- ^{18}F fluorothymidine. *Nucl Med Biol* 31(6):803–809
 141. Oka S, Okudaira H, Ono M, Schuster DM, Goodman MM, Kawai K, Shirakami Y (2014) Differences in transport mechanisms of trans-1-amino-3- ^{18}F fluorocyclobutanecarboxylic acid in inflammation, prostate cancer, and glioma cells: comparison with 1-[Methyl- ^{11}C]methionine and 2-deoxy-2- ^{18}F fluoro-d-glucose. *Mol Imaging Biol* 16(3):322–329
 142. Oka S, Okudaira H, Yoshida Y, Schuster DM, Goodman MM, Shirakami Y (2012) Transport mechanisms of trans-1-amino-3-fluoro[1- ^{14}C]cyclobutanecarboxylic acid in prostate cancer cells. *Nucl Med Biol* 39(1):109–119
 143. Okudaira H, Shikano N, Nishii R, Miyagi T, Yoshimoto M, Kobayashi M, Ohe K, Nakanishi T, Tamai I, Namiki M, Kawai K (2011) Putative transport mechanism and intracellular fate of trans-1-amino-3- ^{18}F fluorocyclobutanecarboxylic acid in human prostate cancer. *J Nucl Med* 52(5):822–829
 144. Ono M, Oka S, Okudaira H, Schuster DM, Goodman MM, Kawai K, Shirakami Y (2013) Comparative evaluation of transport mechanisms of trans-1-amino-3- ^{18}F fluorocyclobutanecarboxylic acid and L-[methyl- ^{11}C] methionine in human glioma cell lines. *Brain Res* 1535:24–37
 145. Paolillo V, Riese S, Gelovani JG, Alauddin MM (2009) A fully automated synthesis of ^{18}F -FEAU and ^{18}F -FMAU using a novel dual reactor radiosynthesis module. *J Label Compd Radiopharm* 52(13):553–558
 146. Pascali G, D'Antonio L, Bovone P, Gerundini P, August T (2009) Optimization of automated large-scale production of ^{18}F fluoroethylcholine for PET prostate cancer imaging. *Nucl Med Biol* 36(5):569–574
 147. Patel NH, Vyas NS, Puri BK, Nijran KS, Al-Nahas A (2010) Positron emission tomography in schizophrenia: a new perspective. *J Nucl Med* 51(4):511–520
 148. Patrick GL (2013) An introduction to medicinal chemistry. Oxford University Press, Oxford
 149. Peterson LM, Kurland BF, Link JM, Schubert EK, Stekhova S, Linden HM, Mankoff DA (2011) Factors influencing the uptake of ^{18}F -fluoroestradiol in patients with estrogen receptor positive breast cancer. *Nucl Med Biol* 38(7):969–978
 150. Peterson LM, Mankoff DA, Lawton T, Yagle K, Schubert EK, Stekhova S, Gown A, Link JM, Tewson T, Krohn KA (2008) Quantitative imaging of estrogen receptor expression in breast cancer with PET and ^{18}F -fluoroestradiol. *J Nucl Med* 49(3):367–374
 151. Piel M, Bauman A, Baum RP, Hohnemann S, Klette I, Wortmann R, Rösch F (2007) Improved automated synthesis of ^{18}F fluoroethylcholine as a radiotracer for cancer imaging. *Bioorg Med Chem* 15(9):3171–3175
 152. Piert M, Machulla HJ, Picchio M, Reischl G, Ziegler S, Kumar P, Wester HJ, Beck R, McEwan AJ, Wiebe LI, Schwaiger M (2005) Hypoxia-specific tumor imaging with ^{18}F -fluoroazomycin arabinoside. *J Nucl Med* 46(1):106–113
 153. Podo F (1999) Tumour phospholipid metabolism. *NMR Biomed* 12(7):413–439
 154. Poeppel TD, Krause BJ, Heusner TA, Boy C, Bockisch A, Antoch G (2009) PET/CT for the staging and follow-up of patients with malignancies. *Eur J Radiol* 70(3):382–392
 155. Postema EJ, McEwan AJ, Riauka TA, Kumar P, Richmond DA, Abrams DN, Wiebe LI (2009) Initial results of hypoxia imaging using 1-alpha-D: -(5-deoxy-5- ^{18}F -fluoroarabino-furanosyl)-2-nitroimidazole (^{18}F -FAZA). *Eur J Nucl Med Mol Imaging* 36(10):1565–1573

156. Preshlock S, Calderwood S, Verhoog S, Tredwell M, Huiban M, Hienzsch A, Gruber S, Wilson TC, Taylor NJ, Cailly T, Schedler M, Collier TL, Passchier J, Smits R, Mollitor J, Hoeppling A, Mueller M, Genicot C, Mercier J, Gouverneur V (2016) Enhanced copper-mediated ¹⁸F-fluorination of aryl boronic esters provides eight radiotracers for PET applications. *Chem Commun (Camb)* 52(54):8361–8364
157. Preshlock S, Tredwell M, Gouverneur V (2016) ¹⁸F-labeling of arenes and heteroarenes for applications in positron emission tomography. *Chem Rev* 116(2):719–766
158. Pretze M, Franck D, Kunkel F, Föb̈hag E, Wängler C, Wängler B (2017) Evaluation of two nucleophilic syntheses routes for the automated synthesis of 6-[¹⁸F]fluoro-L-DOPA. *Nucl Med Biol* 45:35–42
159. Pretze M, Wängler C, Wängler B (2014) 6-[¹⁸F]fluoro-L-DOPA: a well-established neurotracer with expanding application spectrum and strongly improved radiosyntheses. *Biomed Res Int* 2014:674063
160. Puri T, Greenhalgh TA, Wilson JM, Franklin J, Wang LM, Strauss V, Cunningham C, Partridge M, Maughan T (2017) [¹⁸F]fluoromisonidazole PET in rectal cancer. *EJNMMI Res* 7(1):78
161. Rahbar K, Afshar-Oromieh A, Seifert R, Wagner S, Schäfers M, Bögemann M, Weckesser M (2018) Diagnostic performance of ¹⁸F-PSMA-1007 PET/CT in patients with biochemical recurrent prostate cancer. *Eur J Nucl Med Mol Imaging* 45(12):2055–2061
162. Rajasekaran SA, Anilkumar G, Oshima E, Bowie JU, Liu H, Heston W, Bander NH, Rajasekaran AK (2003) A novel cytoplasmic tail MXXXL motif mediates the internalization of prostate-specific membrane antigen. *Mol Biol Cell* 14(12):4835–4845
163. Rasey JS, Grierson JR, Wiens LW, Kolb PD, Schwartz JL (2002) Validation of FLT uptake as a measure of thymidine kinase-1 activity in A549 carcinoma cells. *J Nucl Med* 43(9):1210–1217
164. Rasey JS, Grunbaum Z, Magee S, Nelson NJ, Olive PL, Durand RE, Krohn KA (1987) Characterization of radiolabeled fluoromisonidazole as a probe for hypoxic cells. *Radiat Res* 111(2):292–304
165. Ravert HT, Holt DP, Chen Y, Mease RC, Fan H, Pomper MG, Dannals RF (2016) An improved synthesis of the radiolabeled prostate-specific membrane antigen inhibitor, [¹⁸F]DCFPyL. *J Label Compd Rad* 59(11):439–450
166. Reischl G, Ehrlichmann W, Bieg C, Solbach C, Kumar P, Wiebe LI, Machulla HJ (2005) Preparation of the hypoxia imaging PET tracer [¹⁸F]FAZA: reaction parameters and automation. *Appl Radiat Isot* 62(6):897–901
167. Reivich M, Kuhl D, Wolf A, Greenberg J, Ma Phelps, Ido T, Casella V, Fowler J, Hoffman E, Alavi A (1979) The [¹⁸F]fluorodeoxyglucose method for the measurement of local cerebral glucose utilization in man. *Circ Res* 44(1):127–137
168. Roels S, Slagmolen P, Nuyts J, Lee JA, Loeckx D, Maes F, Stroobants S, Penninckx F, Haustermans K (2008) Biological image-guided radiotherapy in rectal cancer: is there a role for FMISO or FLT, next to FDG? *Acta Oncol* 47(7):1237–1248
169. Roivainen A, Forsback S, Gronroos T, Lehtikoinen P, Kahkonen M, Sutinen E, Minn H (2000) Blood metabolism of [methyl-¹¹C]choline; implications for in vivo imaging with positron emission tomography. *Eur J Nucl Med* 27(1):25–32
170. Rose C, Andersen K, Mouridsen H, Thorpe S, Pedersen B, Blichert-Toft M, Rasmussen B (1985) Beneficial effect of adjuvant tamoxifen therapy in primary breast cancer patients with high oestrogen receptor values. *Lancet* 325(8419):16–19
171. Rowe SP, Macura KJ, Mena E, Blackford AL, Nadal R, Antonarakis ES, Eisenberger M, Carducci M, Fan H, Dannals RF (2016) PSMA-based [¹⁸F]DCFPyL PET/CT is superior to conventional imaging for lesion detection in patients with metastatic prostate cancer. *Mol Imaging Biol* 18(3):411–419
172. Rubens RD, Mundy GR (2000) Cancer and the skeleton
173. Römer J, Füchtner F, Steinbach J, Johannsen B (1999) Automated production of 16 α -[¹⁸F]fluoroestradiol for breast cancer imaging. *Nucl Med Biol* 26(4):473–479

174. Saga T, Inubushi M, Koizumi M, Yoshikawa K, Zhang MR, Obata T, Tanimoto K, Harada R, Uno T, Fujibayashi Y (2016) Prognostic value of PET/CT with ^{18}F -fluoroazomycin arabinoside for patients with head and neck squamous cell carcinomas receiving chemoradiotherapy. *Ann Nucl Med* 30(3):217–224
175. Sasajima T, Ono T, Shimada N, Doi Y, Oka S, Kanagawa M, Baden A, Mizoi K (2013) Trans-1-amino-3- ^{18}F -fluorocyclobutanecarboxylic acid (anti- ^{18}F -FACBC) is a feasible alternative to ^{11}C -methyl-L-methionine and magnetic resonance imaging for monitoring treatment response in gliomas. *Nucl Med Biol* 40(6):808–815
176. Savi A, Incerti E, Fallanca F, Bettinardi V, Rossetti F, Monterisi C, Compierchio A, Negri G, Zannini P, Gianolli L, Picchio M (2017) First evaluation of PET-based human biodistribution and dosimetry of ^{18}F -FAZA, a tracer for imaging tumor hypoxia. *J Nucl Med* 58(8):1224–1229
177. Schelhaas S, Wachsmuth L, Viel T, Honess DJ, Heinzmann K, Smith DM, Hermann S, Wagner S, Kuhlmann MT, Müller-Tidow C, Kopka K, Schober O, Schäfers M, Schneider R, Aboagye EO, Griffiths J, Faber C, Jacobs AH (2014) Variability of proliferation and diffusion in different lung cancer models as measured by 3'-Deoxy-3'- ^{18}F -fluorothymidine PET and diffusion-weighted MR imaging. *J Nucl Med* 55(6):983–988
178. Schiesser M, Veit-Haibach P, Müller M, Weber M, Bauerfeind P, Hany T, Clavien PA (2010) Value of combined 6-[^{18}F]fluorodihydroxyphenylalanine PET/CT for imaging of neuroendocrine tumours. *Br J Surg* 97(5):691–697
179. Schirrmester H, Guhlmann A, Kotzerke J, Santjohanser C, Kuhn T, Kreienberg R, Messer P, Nussle K, Elsner K, Glatting G (1999) Early detection and accurate description of extent of metastatic bone disease in breast cancer with fluoride ion and positron emission tomography. *J Clin Oncol* 17(8):2381–2389
180. Schober O, Heindel W (2008) PET-CT. Georg Thieme Verlag, Stuttgart
181. Schuster DM, Taleghani PA, Nieh PT, Master VA, Amzat R, Savir-Baruch B, Halkar RK, Fox T, Osunkoya AO, Moreno CS (2013) Characterization of primary prostate carcinoma by anti-1-amino-2-[^{18}F]-fluorocyclobutane-1-carboxylic acid (anti-3-[^{18}F]FACBC) uptake. *Am J Nucl Med Mol Imaging* 3(1):85
182. Servagi-Vernat S, Differding S, Hanin FX, Labar D, Bol A, Lee JA, Gregoire V (2014) A prospective clinical study of ^{18}F -FAZA PET-CT hypoxia imaging in head and neck squamous cell carcinoma before and during radiation therapy. *Eur J Nucl Med Mol Imaging* 41(8):1544–1552
183. Shao X, Hoareau R, Hockley BG, Tluczek LJM, Henderson BD, Padgett HC, Scott PJH (2011) Highlighting the versatility of the tracerlab synthesis modules. Part 1: fully automated production of [^{18}F]labelled radiopharmaceuticals using a Tracerlab FXFN. *J Label Compd Rad* 54(6):292–307
184. Shields AF (2003) PET imaging with ^{18}F -FLT and thymidine analogs: promise and pitfalls. *J Nucl Med* 44(9):1432–1434
185. Shields AF, Grierson JR, Dohmen BM, Machulla HJ, Stayanoff JC, Lawhorn-Crews JM, Obradovich JE, Muzik O, Mangner TJ (1998) Imaging proliferation in vivo with [^{18}F]FLT and positron emission tomography. *Nat Med* 4(11):1334–1336
186. Shoup TM, Olson J, Hoffman JM, Votaw J, Eshima D, Eshima L, Camp VM, Stabin M, Votaw D, Goodman MM (1999) Synthesis and evaluation of [^{18}F]1-amino-3-fluorocyclobutane-1-carboxylic acid to image brain tumors. *J Nucl Med* 40(2):331–338
187. da Silva NA, Lohmann P, Fairney J, Magill AW, Oros Peusquens AM, Choi CH, Stirnberg R, Stoffels G, Galldiks N, Golay X, Langen KJ, Jon Shah N (2018) Hybrid MR-PET of brain tumours using amino acid PET and chemical exchange saturation transfer MRI. *Eur J Nucl Med Mol Imaging* 45(6):1031–1040
188. Silver DA, Pellicer I, Fair WR, Heston W, Cordon-Cardo C (1997) Prostate-specific membrane antigen expression in normal and malignant human tissues. *Clin Cancer Res* 3(1):81–85

189. Smith TA (2000) Mammalian hexokinases and their abnormal expression in cancer. *Br J Biomed Sci* 57(2):170–178
190. Southworth R, Dearling JL, Medina RA, Flynn AA, Pedley RB, Garlick PB (2002) Dissociation of glucose tracer uptake and glucose transporter distribution in the regionally ischaemic isolated rat heart: application of a new autoradiographic technique. *Eur J Nucl Med Mol Imaging* 29(10):1334–1341
191. Sun H, Sloan A, Mangner TJ, Vaishampayan U, Muzik O, Collins JM, Douglas K, Shields AF (2005) Imaging DNA synthesis with [¹⁸F]FMAU and positron emission tomography in patients with cancer. *Eur J Nucl Med Mol Imaging* 32(1):15–22
192. Sun Y, Yang Z, Zhang Y, Xue J, Wang M, Shi W, Zhu B, Hu S, Yao Z, Pan H, Zhang Y (2015) The preliminary study of 16 α -[¹⁸F]fluoroestradiol PET/CT in assisting the individualized treatment decisions of breast cancer patients. *PLoS ONE* 10(1):e0116341
193. Svadberg A, Wickstrøm T, Hjelstuen OK (2012) Degradation of acetonitrile in eluent solutions for [¹⁸F]fluoride PET chemistry: impact on radiosynthesis of [¹⁸F]FACBC and [¹⁸F]FDG. *J Label Compd Rad* 55(3):97–102
194. Swanson KR, Chakraborty G, Wang CH, Rockne R, Harpold HL, Muzi M, Adamsen TC, Krohn KA, Spence AM (2009) Complementary but distinct roles for MRI and ¹⁸F-fluoromisonidazole PET in the assessment of human glioblastomas. *J Nucl Med* 50(1):36–44
195. Szabo Z, Mena E, Rowe SP, Plyku D, Nidal R, Eisenberger MA, Antonarakis ES, Fan H, Dannals RF, Chen Y (2015) Initial evaluation of [¹⁸F]DCFPyL for prostate-specific membrane antigen (PSMA)-targeted PET imaging of prostate cancer. *Mol Imaging Biol* 17(4):565–574
196. Tang G, Tang X, Wen F, Wang M, Li B (2010) A facile and rapid automated synthesis of 3'-deoxy-3'-[¹⁸F]fluorothymidine. *Appl Radiat Isot* 68(9):1734–1739
197. Tehrani OS, Muzik O, Heilbrun LK, Douglas KA, Lawhorn-Crews JM, Sun H, Mangner TJ, Shields AF (2007) Tumor imaging using 1-(2'-deoxy-2'-¹⁸F-fluoro-beta-D-arabinofuranosyl) thymine and PET. *J Nucl Med* 48(9):1436–1441
198. Tewson TJ, Mankoff DA, Peterson LM, Woo I, Petra P (1999) Interactions of 16 α -[¹⁸F]-fluoroestradiol (FES) with sex steroid binding protein (SBP). *Nucl Med Biol* 26(8):905–913
199. Thiele F, Ehmer J, Piroth MD, Eble MJ, Coenen HH, Kaiser HJ, Schaefer WM, Buell U, Boy C (2009) The quantification of dynamic FET PET imaging and correlation with the clinical outcome in patients with glioblastoma. *Phys Med Biol* 54(18):5525–5539
200. Tredwell M, Preshlock SM, Taylor NJ, Gruber S, Huiban M, Passchier J, Mercier J, Genicot C, Gouverneur V (2014) A general copper-mediated nucleophilic ¹⁸F fluorination of arenes. *Angew Chem Int Ed Engl* 53(30):7751–7755
201. Tsujikawa T, Yoshida Y, Mori T, Kurokawa T, Fujibayashi Y, Kotsuji F, Okazawa H (2008) Uterine tumors: pathophysiologic imaging with 16 α -[¹⁸F]fluoro-17 β -estradiol and ¹⁸F fluorodeoxyglucose PET—Initial experience. *Radiology* 248(2):599–605
202. Tsuyuguchi N, Terakawa Y, Uda T, Nakajo K, Kanemura Y (2017) Diagnosis of brain tumors using amino acid transport PET imaging with ¹⁸F-fluciclovine: a comparative study with L-methyl-¹⁴C-methionine PET imaging. *Asia Ocean J Nucl Med Biol* 5(2):85–94
203. Turkman N, Gelovani JG, Alauddin MM (2010) A novel method for stereospecific fluorination at the 2'-arabino-position of pyrimidine nucleoside: synthesis of [¹⁸F]-FMAU. *J Label Compd Rad* 53(13):782–786
204. Vera P, Thureau S, Chaumet-Riffaud P, Modzelewski R, Bohn P, Vermandel M, Hapdey S, Pallardy A, Mahe MA, Lacombe M, Boisselier P, Guillemard S, Olivier P, Beckendorf V, Salem N, Charrier N, Chajon E, Devillers A, Aide N, Danhier S, Denis F, Muratet JP, Martin E, Riedinger AB, Kolesnikov-Gauthier H, Dansin E, Massabeau C, Courbon F, Farcy Jacquet MP, Kotzki PO, Houzard C, Mornex F, Vervueren L, Paumier A, Fernandez P, Salaun M, Dubray B (2017) Phase II study of a radiotherapy total dose increase in hypoxic lesions identified by ¹⁸F-misonidazole PET/CT in patients with non-small cell lung carcinoma (RTEP5 Study). *J Nucl Med* 58(7):1045–1053

205. Wakabayashi T, Iuchi T, Tsuyuguchi N, Nishikawa R, Arakawa Y, Sasayama T, Miyake K, Nariai T, Narita Y, Hashimoto N, Okuda O, Matsuda H, Kubota K, Ito K, Nakazato Y, Kubomura K (2017) Diagnostic performance and safety of positron emission tomography using ^{18}F -fluciclovine in patients with clinically suspected high- or low-grade gliomas: a multicenter phase IIb trial. *Asia Ocean J Nucl Med Biol* 5(1):10–21
206. Warburg O, Posener K, Negelein E (1924) VIII. The metabolism of cancer cells. *Biochem Zeitschr* 152:129–169
207. Weckesser M, Langen KJ, Rickert CH, Kloska S, Straeter R, Hamacher K, Kurlemann G, Wassmann H, Coenen HH, Schober O (2005) *O*-(2- ^{18}F]fluoroethyl)-L-tyrosine PET in the clinical evaluation of primary brain tumours. *Eur J Nucl Med Mol Imaging* 32(4):422–429
208. Weissleder R, Mahmood U (2001) Molecular imaging. *Radiology* 219(2):316–333
209. Welch MJ, Redvanly CS (2003) Handbook of radiopharmaceuticals: radiochemistry and applications. Wiley, London
210. Wester HJ, Herz M, Weber W, Heiss P, Senekowitsch-Schmidtke R, Schwaiger M, Stocklin G (1999) Synthesis and radiopharmacology of *O*-(2- ^{18}F]fluoroethyl)-L-tyrosine for tumor imaging. *J Nucl Med* 40(1):205–212
211. Van de Wiele C, De Vos F, Slegers G, Van Belle S, Dierckx RA (2000) Radiolabeled estradiol derivatives to predict response to hormonal treatment in breast cancer: a review. *Eur J Nucl Med* 27(9):1421–1433
212. Yamamoto Y, Kameyama R, Izuishi K, Takebayashi R, Hagiike M, Asakura M, Haba R, Nishiyama Y (2009) Detection of colorectal cancer using ^{18}F -FLT PET: comparison with ^{18}F -FDG PET. *Nucl Med Commun* 30(11):841–845
213. Yamamoto M, Tsujikawa T, Yamada S, Kurokawa T, Shinagawa A, Chino Y, Mori T, Kiyono Y, Okazawa H, Yoshida Y (2017) ^{18}F -FDG/ ^{18}F -FES standardized uptake value ratio determined using PET predicts prognosis in uterine sarcoma. *Oncotarget* 8(14):22581–22589
214. Yoshida Y, Kurokawa T, Tsujikawa T, Okazawa H, Kotsuji F (2009) Positron emission tomography in ovarian cancer: ^{18}F -deoxy-glucose and 16α - ^{18}F -fluoro-17 β -estradiol PET. *J Ovarian Res* 2(1):7
215. Yu W, Williams L, Camp VM, Olson JJ, Goodman MM (2010) Synthesis and biological evaluation of anti-1-amino-2- ^{18}F] fluoro-cyclobutyl-1-carboxylic acid (anti-2- ^{18}F] FACBC) in rat 9L gliosarcoma. *Bioorg Med Chem Let* 20(7):2140–2143
216. Yun M, Oh SJ, Ha HJ, Ryu JS, Moon DH (2003) High radiochemical yield synthesis of 3'-deoxy-3'- ^{18}F]fluorothymidine using (5'-O-dimethoxytrityl-2'-deoxy-3'-O-nosyl-beta-D-threo pentofuranosyl)thymine and its 3-N-BOC-protected analogue as a labeling precursor. *Nucl Med Biol* 30(2):151–157
217. Zischler J, Kolks N, Modemann D, Neumaier B, Zlatopolskiy BD (2017) Alcohol-enhanced Cu-mediated radiofluorination. *Chem Eur J* 23(14):3251–3256
218. Zuhayra M, Alfteimi A, Forstner CV, Lutzen U, Meller B, Henze E (2009) New approach for the synthesis of ^{18}F]fluoroethyltyrosine for cancer imaging: simple, fast, and high yielding automated synthesis. *Bioorg Med Chem* 17(21):7441–7448
219. Zuhayra M, Alfteimi A, Papp L, Lutzen U, Lutzen A, Von Forstner C, Meller B, Henze E (2008) Simplified fast and high yielding automated synthesis of ^{18}F]fluoroethylcholine for prostate cancer imaging. *Bioorg Med Chem* 16(20):9121–9126



Ultrasound Molecular Imaging of Cancer: Design and Formulation Strategies of Targeted Contrast Agents

9

Alexander L. Klibanov

Contents

9.1	Introduction.....	319
9.2	Bubbles and Their Interaction with Ultrasound: The Basis for Ultrasound Contrast Physics	320
9.3	Microbubbles In Vivo: How and When Molecular Imaging Could Happen	322
9.4	Preparation of Ultrasound Contrast Particles.....	324
9.5	Microbubble Shell Design.....	326
9.6	Targeting Ligand Attachment to Microbubble Shell.....	327
9.7	Bubble Targeting Tumors In Vivo: Microbubbles in Animal Models.....	329
9.8	Nanobubbles: A Smaller-Size Approach to Molecular Ultrasound Imaging.....	330
9.9	Targeted Ultrasound Contrast in Clinic and Clinical Trials.....	331
9.10	Conclusion	332
	References	333

9.1 Introduction

Ultrasound imaging is the most widespread imaging modality, and it is rapidly becoming even more popular, with millions of exams per year in the US alone, far exceeding imaging performed with PET/SPECT and MRI. For the decade between 2000 and 2011, globally, the number of ultrasound imaging examinations has increased by an order of magnitude; for other imaging modalities it had just about doubled [47]. Ultrasound equipment does not require the use of ionizing radiation; it is considered so safe, that imaging in pregnancy is widespread, and considered

A. L. Klibanov (✉)

Cardiovascular Division (Department of Medicine), Robert M Berne Cardiovascular Research Center, University of Virginia, Charlottesville, VA 22908, USA
e-mail: sklib1@gmail.com

standard of care. Ultrasound equipment is portable. Just a decade ago, ultrasound system was a cart of several hundred pounds. Lately, it is a laptop system, or a small handheld unit that may even use a smartphone as a screen. So, ultrasound is usable in the environments well beyond the hospital or doctor's office, including remote geographies or battlefield.

Ultrasound provides the ability to image anatomy and guide interventional procedures in real time; Doppler ultrasound allows imaging blood flow in large vessels. Ultrasound contrast, in the form of microbubbles, has already reached clinical practice, and gradually gains acceptance (and procedure cost reimbursement in most countries) as a blood pool agent, both in radiology and cardiology use. It provides enhancement of Doppler ultrasound signal, as well as the ability to monitor and assess blood flow in the tissue, including microvasculature, where non-contrast Doppler is not sufficiently sensitive. Tissue perfusion information may provide an added benefit in cancer imaging, for instance, in monitoring tumor response to therapy (traditional CT or MRI do not provide tissue viability information, and perfusion does).

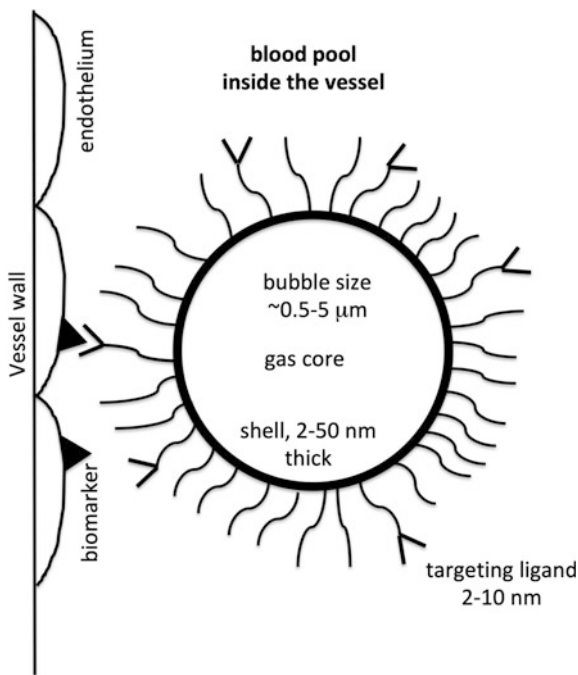
Ultrasound imaging per se does not provide specific molecular information on the status of the tissue without a specific contrast agent (likewise, most other in vivo imaging modalities will require labeled targeting ligands or metabolites carrying a fluorescent dye, MRI contrast, or a radioisotope). That is where ultrasound contrast materials can help, and combine the stated advantages of ultrasound (cost, portability, and ease of use) with the ability to perform molecular imaging, with substantial penetration depth (many cm) without the use of ionizing radiation. The basis for molecular imaging with ultrasound contrast is a gas-filled bubble structure, which is coated with a thin stabilizer shell that carries targeting ligands on its surface, so that the contrast particle would specifically bind and adhere to the tumor-related biomarker molecules (Fig. 9.1 presents a cartoon version of a targeted microbubble).

In this review we will discuss general directions of the design and implementation of ultrasound contrast agents for targeted molecular imaging in cancer. For the past two decades, this field had advanced from the early idea stage toward clinical use. We will look into the advantages and complications of this technology, provide examples of the most successful applications, target selection, and proper contrast agent preparation strategies.

9.2 Bubbles and Their Interaction with Ultrasound: The Basis for Ultrasound Contrast Physics

The use of gas-filled bubbles as ultrasound contrast materials for imaging and therapy is based on the drastic difference in compressibility of water-based biological tissues and gases [27]. Water and soft tissues (with their high water content) are not compressible; so ultrasound pressure wave passes through the tissue with only minor attenuation and energy loss. During the passage of ultrasound waves

Fig. 9.1 Cartoon presentation of a targeted microbubble (drawn not to scale). A thin shell stabilizes the gas core. Microparticle is coated with a lipid/protein/polymer shell, which is additionally decorated with a grafted PEG brush. Targeting ligand is attached to an extended spacer to avoid steric hindrance. Receptor surface density lower than 100 molecules per μm^2 of the target vessel wall surface can assure efficient adhesion and microbubble retention



through the tissue, respective cycles of compression and rarefaction occur. If a gas bubble is present in the tissue, and its movement is not constrained by a thick shell, effect of the ultrasound field on the bubble results in the sequential compression and expansion of gas. Medical ultrasound is operated at MHz frequency; in its diagnostic imaging mode it may exceed MPa pressure levels, i.e., 10 bar, generated in the tissue, for sub-microsecond time intervals. So during compression portion of the cycle, bubble volume should decrease by an order of magnitude, and during the rarefaction period, bubble is drastically expanded. The interface between the gas and the aqueous phase (e.g., blood) becomes a miniature “speaker membrane” that generates secondary ultrasound waves, which can be detected by the ultrasound imaging equipment. The increase of the size of the gas bubble implies stronger ultrasound scattering (Rayleigh scattering is proportional to sixth power of particle radius). Therefore, larger microbubbles would be preferred, but they cannot exceed several micrometers in diameter (the upper limit should be smaller than the size of red blood cells) if intravascular administration is intended. We would want to prevent these particles from lodging in the capillaries and blocking the blood flow.

Modern ultrasound devices are capable of monitoring acoustic signal at multiple frequencies. They allow multi-pulse imaging sequences for rapid suppression of relatively linear tissue backscatter signal, and highly non-linear signal from microbubbles [2]. Therefore, the detection of individual microbubbles by ultrasound imaging has become possible and common in many clinical scanners. Figure 9.2 presents images of individual microbubbles dispersed in an aqueous

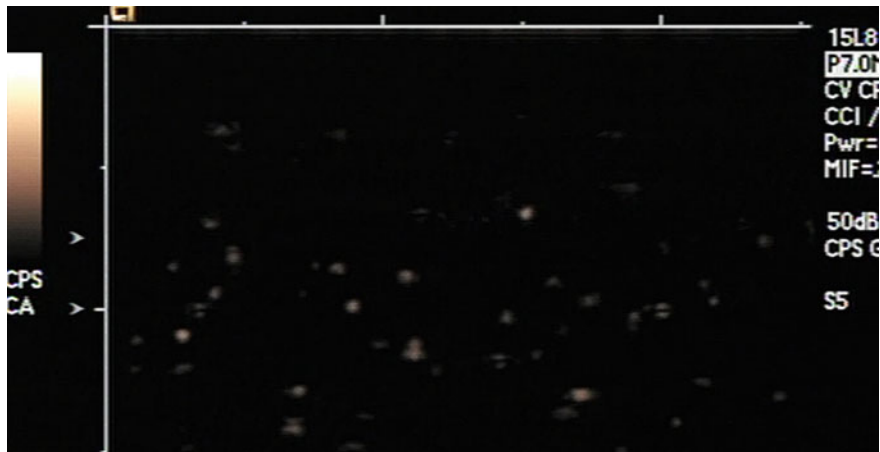


Fig. 9.2 Diluted dispersion of individual microbubbles at high dilution, suspended in deionized water. Each bright speckle on a dark background represents a point-spread function generated by a single microbubble $\sim 1\text{--}3$ μm in diameter and sub-picogram mass. Acuson Sequoia 512 with 15L8 probe, Cadence Contrast Pulse Sequencing imaging mode, image width 2.5 cm, 7 MHz, non-destructive mode (MI 0.2). Imaging is most efficient close to focal zone

medium at low density. For targeted/molecular imaging purposes it means that an individual microbubble, with micrometer-size range, that is coated with a lipid monolayer shell that comprises ~ 20 million molecules of lipid (and has sub-pg mass) and carries e.g., $\sim 10^4\text{--}10^5$ molecules of a targeting ligand attached to the shell, can be detected by ultrasound imaging with clinical equipment, at multi-cm levels of tissue depth [51]. What is observed on the ultrasound system screen is not the bubble itself (typically, 2–3 μm in diameter) but the point-spread function of the equipment. Imaging resolution typically matches the wavelength of ultrasound applied for imaging. Lately, additional mathematical treatment of the point-spread function image makes it possible to break the wavelength barrier, as it was done earlier for light microscopy [3]: imaging of vessels down to tens of micrometers in diameter has become possible [9].

9.3 Microbubbles In Vivo: How and When Molecular Imaging Could Happen

Microbubbles, due to their relatively large particle size (generally, several micrometers), have to be used as the intravascular contrast agents. Therefore, the target for molecular imaging has to be available to the vessel lumen. Such biomarkers, specific to the vasculature in the tumors, for instance, VEGF Receptors [31], are well known and overexpressed on vascular endothelium. Targeting ligands

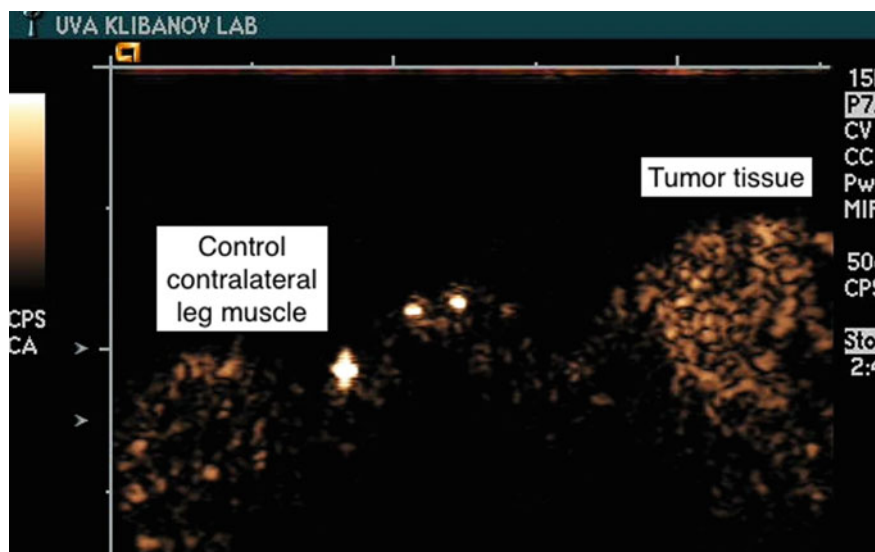


Fig. 9.3 Molecular ultrasound imaging in a murine tumor model. Microbubbles decorated with anti-VCAM-1 antibody were injected intravenously; image taken 5 min later. Tumor (right side), control contralateral muscle (left side). Acuson Sequoia CPS, 15L8 probe, 7 MHz, non-destructive low power imaging (MI 0.2). Image width, 2.5 cm

with high specificity to these materials are available, e.g., VEGF itself. So microbubbles decorated with such targeting ligands can be applied for specific binding and imaging. Microbubbles should possess a strong enough shell that would not tear off in the flow when ligand on the bubble shell adheres to the receptor on the target surface; the anchor that is used for the ligand attachment should also not pull out from the shell.

Following intravenous injection, microbubbles rapidly distribute within the bloodstream, reaching peak contrast intensity there at ~ 30 s. Bubbles recirculate through the vasculature; while they circulate, they have the opportunity to touch and adhere to endothelium, where ligand-receptor pair formation is efficient. In the areas where the tumor biomarker molecule density on endothelium is high enough, the microbubble adherence would occur. Bubbles will become immobilized in that area, and delineate the target tumor. Figure 9.3 demonstrates an example of targeted ultrasound contrast image of a tumor and control contralateral muscle, 5 min after intravenous bolus administration, with a moderate amount of microbubbles still present in the bloodstream, yet significant amount of material accumulated and retained in the tumor (right side of image frame). Circulating bubbles are gradually cleared from the bloodstream. In a small animal model it usually takes about ten minutes [1], and in humans it may take up to half hour [52].

Circulating microbubbles lifetime in the bloodstream is a basic yet critical factor in the success of contrast ultrasound imaging; bubbles have to recirculate for the period long enough, for the sufficient amount of bubbles to travel through the target site and adhere. Early generation microbubbles had air used as the gas core (e.g., Albunex and Levovist). These bubbles also possess a thin shell, which is not a very good barrier for gas transfer, and deflate out of existence very quickly, losing entrapped gas and ultrasound scattering capability. In order to improve circulation time, a “second-generation” version of microbubbles was formulated, which contained perfluorocarbon gas core instead of air: perfluoropropane, sulfur hexafluoride, and, especially, perfluorobutane, are orders of magnitude less soluble in water (and in blood) than oxygen and nitrogen of air. Therefore, gas loss from these bubbles is slowed down greatly, and at 10–30 min after intravenous injection there is still enough non-deflated bubbles present as adherent to tumor vasculature, so they could be detected by contrast ultrasound imaging. One can hypothesize that circulating bubbles rapidly moving with the flow of blood at high shear and repeatedly passing through the lungs, lose their gas much faster than the bubbles that are adherent in the slow-flow capillaries or the post-capillary venules in the tumor tissue—this effect may be partially responsible for the improvement of target-to-blood and target-to-control tissue ratio, that is routinely observed for molecular ultrasound imaging.

9.4 Preparation of Ultrasound Contrast Particles

Microbubbles used as blood pool contrast agents have been approved by FDA and by other regulatory agencies and are already in widespread clinical use, worldwide, therefore, the methods of microbubble preparation have been well developed and described. For molecular imaging these microbubble particles are decorated with targeting ligands that are attached onto the microbubble shell (that process will be discussed in a separate section below).

There are generally three major approaches to microbubble making and handling that have reached clinical use. The first approach, as applied for the ultrasound contrast formulation that had obtained clinical approval status in the US first [23], is to make microbubbles in bulk (e.g., by sparging gas phase through the aqueous medium during sonication). Immediately after formation, gas–water interface is stabilized by the shell material that is present in the aqueous phase. Stabilizer can be a protein, polymer, lipid, surfactant, micelles, or even nanoparticles. Sometimes, additional stabilization of the shell is performed, e.g., by polymerization [12]. Resulting bubbles are stable on storage, and can be aseptically packaged in sterile vials as the aqueous dispersion. Microbubbles float upwards, to the top of the aqueous medium, and create a thick “cake” structure at the interface between the vial gas headspace and aqueous medium. During storage, the stabilizer shell serves as a barrier to prevent fusion of adjacent bubbles that form the cake. When bubble

use is planned, a vial is placed on a slow rotator mixer, and cake gently dissociates back to the original individual bubbles within minutes.

The second approach is based on matrix dissolution; this type of bubbles was first approved in Europe [43]. A water-soluble matrix material, e.g., carbohydrate or PEG, is intermixed with lipids: palmitic acid [43] or phospholipids [37], and placed in the sterile vials (either directly, as dry material, or following lyophilization). This dry matrix approach may demonstrate remarkable storage stability, several years at room temperature (but not to exceed 40 °C for the phospholipid material). Gas space in the vial may be a poorly soluble fluorinated gas (instead of air), to improve the lifetime of microbubbles *in vivo*. When it is time to administer the bubble for the contrast study, sterile water is added to the vial through the septum, rapidly dissolving the matrix and leaving behind gas bubble “pockets” suspended in the aqueous medium; lipid shell components stabilize the gas–liquid interface. Resulting microbubbles, such as Sonovue/BR1/Lumason [37], Perflhexane/Imagent [6] and Sonazoid [21] should be used soon after the preparation, typically within several hours.

The third approach is based on amalgamation, i.e., the use of a specialized version of a dental shaker to prepare microbubbles in a sterile sealed vial, without opening it, at the hospital site, up to several hours prior to use [14]. Definity microbubbles (with Luminity name in Europe) are manufactured this way [34]. The vial contains an aqueous medium with lipids and co-surfactants, such as propylene glycol; the vial is sealed, with perfluorocarbon gas headspace. In an amalgamator the vial is forcefully vibrated, for several thousand cycles, at high shear, for less than a minute. Gas is mixed with aqueous medium; lipids and surfactants immediately stabilize the newly formed gas–water interface. This results in the rapid formation of bubbles of the desired size distribution. At higher concentration of lipids in the media the efficacy of bubble generation is improved [48]. Likewise, at higher concentrations of co-surfactant and shell-forming lipid material, most of the lipid is transferred from the aqueous medium to the bubble coating. This approach has two other advantages: it does not require harsh conditions of sonication, and the aqueous lipid medium that is used for microbubble preparation can be sterile-filtered and aseptically filled into vials prior to amalgamation, making production and clinical translation much easier. Vial temperature conditions during amalgamation process should be kept reproducible, to manufacture microbubbles of the desirable acoustic behavior and reproducible size: even a moderate variation of vial temperature during amalgamation (refrigerated, room temperature, or 37 °C) results in a significant size distribution change, which results in drastic acoustic backscatter response differences [18].

9.5 Microbubble Shell Design

Design of the microbubble shell is based on a compromise between two conflicting requirements. First, the shell should be thick and robust, to minimize gas loss from the core, and stabilize the bubble structure during storage as well as *in vivo*. Second, bubble shell should be elastic and not restrict compression and expansion of the gas core when it is subjected to the very significant pressure variations of the ultrasound field. “Solid” shell can be made of biocompatible polymer (as is approved for manufacturing of bioresorbable sutures), such as polylactide [39, 45], or a surgical glue, such as a cyanoacrylate polymer [12, 17]. The trick here is to find a good balance between the bubble stability and lifetime in the bloodstream, and the level of the acoustic pressure that is needed to “crack” the bubble shell, so it could provide strong acoustic backscatter at moderate ultrasound energies [7, 28]. As of now, polymer bubbles described in the literature have shell thickness of tens of nanometers. They have not yet made it into practical clinical use as perfusion agents [39], even following clinical trials. Advantage of polymer bubbles is in their robustness and stability. It is easy to handle these particles for the attachment of a wide variety of targeting ligands, either by covalent [32] and/or noncovalent [25] coupling schemes. These bubbles can be subjected to repeated flotations in the aqueous medium, then dried, and stored as dry powders, to be reconstituted in the aqueous medium prior to injection.

On the other side of the spectrum is the lipid bubble formulation. Lipid base microbubbles are in widespread clinical practice, and are currently the most popular formulation approach. A bubble consists of a lipid monolayer shell [6, 21, 37], often supplemented with a brush of grafted polymer, such as Definity [34] to minimize potential side effects, *i.e.*, nonspecific adhesion in the vasculature, or complement activation [11]. Longer-chain lipids with fully saturated fatty acid chains are preferred [16], as they provide better particle stability and longer circulation time. Although the shell of these particles is based on a monomolecular lipid layer, ~ 2 nm thick, they can provide reasonable stability (up to several months of refrigerated storage after preparation for some formulations, in sealed vials under fluorocarbon gas atmosphere). They offer bloodstream lifetime of several minutes, which is sufficient for molecular imaging studies in preclinical research, and in clinical trials. Synthesis of targeting ligand-lipid conjugates is well described in the liposome research literature of the last century, and it can be applied directly to the preparation of microbubbles that are decorated with targeting ligands (see below).

Protein-based microbubbles are also possible: microbubble shell is based on human albumin, which is a natural fully biocompatible material, which has widespread use in clinical practice in large volumes. Albumin bubbles are approved as Albunex and Optison, respectively, as the first- and second-generation microbubble contrast agents, with Optison containing octafluoropropane gas instead of air. They are prepared by sonication of albumin solutions in the aqueous medium: upon sonication, albumin molecules located at the gas–water interface are “melted” and

irreversibly denatured, exposing the inner hydrophobic core of the protein molecule. Shell is immediately formed; albumin bubble coat is thicker than lipid, ~10–15 nm range. This assures year-long refrigerated storage stability. Albumin shell bubbles demonstrate circulation time in the bloodstream that is similar to lipid bubbles, and have an excellent safety profile. While decorating these bubbles with antibodies or other targeting ligands can be accomplished, there is some level of concern that covalently modified albumin might get considered by the body as a foreign protein, leading to a hapten-like immune response.

9.6 Targeting Ligand Attachment to Microbubble Shell

There are two options to prepare microbubbles that are decorated with targeting ligands: (a) to formulate the bubbles with the standard shell components, of which one carries a ligand molecule, or (b) make the bubbles first (as described in the previous section) and attach targeting ligand to them later.

The first targeted microbubble preparation was performed for a model ligand-receptor pair, biotin-avidin. Biotin was first attached to the shell component covalently, and bubbles were then prepared by sonication [24]. These bubbles effectively adhered to avidin-coated surface, providing the proof that targeted ultrasound contrast is feasible. As biotin is a small molecule, it easily tolerates harsh conditions associated with a sonication procedure. This preparation approach is only feasible with smaller, robust targeting ligands, such as peptides, for example cyclic RGD derivatives, carbohydrates, such as sialyl Lewis derivatives [50], peptide mimetics [20], or aptamers. A significant disadvantage of the sonication procedure is in the relatively low efficacy of transfer of shell components from the aqueous medium to the bubble shell: for ligand-lipid it may not exceed 25%, [48]. Wasting most of the expensive lipid-conjugated ligand material used in the preparation is difficult to justify (although one might suggest recycling of the shell material that is left behind in the aqueous medium). So the alternative tools of bubble manufacturing without sonication should be considered.

Another significant disadvantage of sonication is the use of harsh preparation conditions—therefore, there is a significant risk of denaturation and loss of binding affinity of certain targeting ligands (e.g., antibodies or other proteins). Therefore, it is necessary to prepare microbubbles first, and attach protein targeting ligands to them later. The first published example of this approach was in a model system *in vitro*, with anti-ICAM-1 antibody that adhered to activated endothelial cells in culture [49]. A carboxy-PEG-lipid-carrying microbubbles were used in that study. Overall covalent coupling procedure consisted of several steps. First, as sonicated bubbles were in a media with large excess of free lipid micelles, not incorporated into the bubble shell, the latter had to be removed, because it would compete with the bubbles for covalent coupling of the antibody. Purification was accomplished with a slow-speed centrifugal wash in a degassed buffer. Next, carboxy group of the lipid associated with the microbubble shell was activated with the standard

carbodiimide/hydroxysulfosuccinimide chemistry, as was described for liposomes earlier [4], and antibody was coupled via a primary aminogroup. Unfortunately, concentration of carboxy groups, and the antibody in the reaction mixture was low for microbubbles (unlike for liposomes), so the reaction rate was reduced drastically, and in order to get to $\sim 10^5$ antibody molecules per one liposome level, large excess of expensive antibody had to be added and most of it was wasted. One of the reasons for the low coupling efficacy is a side reaction, hydrolysis of the active ester of the carboxy group: at low concentration of amino- and carboxy-components, hydrolysis of the active ester becomes dominant. A better approach had to be found: it was the use of noncovalent coupling of targeting ligands to the microbubble shell, that is traditional in modern biotechnology: the use of streptavidin. Biotinylated bubbles, prepared by sonication as described earlier [24], are stable during refrigerated storage for many months. They can be washed in a low-speed centrifuge to remove unincorporated lipid micelles, then incubated with streptavidin, and after a short wash incubated with biotinylated antibody [29]. Targeted microbubbles to be used for proof of principle research in vitro and animal models, as prepared by this technique, had dominated the preclinical research field for many years, with dozens of published manuscripts. However, the use of a foreign protein, such as streptavidin, makes it difficult to consider approval for clinical use in humans. Therefore, more efficient covalent coupling options have to be used; such chemistries are also widely available. One example is maleimide coupling chemistry, where maleimide-carrying-microbubbles are incubated in oxygen-free environment with thiolated targeting ligand, e.g., VEGF, a protein that naturally binds to VEGF receptors [1]. In this case, a genetically engineered version of single-chain VEGF dimer, that carries a thiol on the adapter outside of the VEGFR binding site, was used for coupling. Clinical translation of this approach may also be feasible with antibodies and antibody fragments [55].

The most modern and efficient technique for covalent bioconjugation is known as click chemistry [30, 41], also called bioorthogonal chemistry [58, 59]. This novel approach is highly selective and efficient; it allows not just attaching targeting peptides to the shell of existing microbubbles in vitro [41]: it can also be used for “pretargeting,” which becomes in vivo covalent targeting. In particular [58], an anti-VEGFR2 antibody modified with tetracycloctene was injected intravenously into tumor-bearing mice expressing the receptor. Next, tetrazine-decorated microbubbles were administered, and formed a covalent bond via Diels–Alder reaction only with the antibody in vivo. Click chemistry reactions are fast, highly specific, and can offer high-yield coupling with minimal loss of expensive targeting ligands.

All covalent chemistries listed above can be used for the attachment of targeting ligands to the shell of pre-formulated microbubbles. As an alternative, ligand-lipid conjugates (usually in the form of ligand-PEG-lipid) can be prepared first, and added to the shell-forming lipid mixture prior to the bubble-making step. Advantage of this approach is the ability to perform coupling in the optimal conditions,

and assure pure form of ligand-PEG-lipid, for any ligand, such as small molecules, peptides, and larger proteins, such as antibodies and scFv.

Unlike sonication, amalgamation procedure use for the preparation of microbubbles assures that most of the added ligand-PEG-lipid will be associated with the bubble shell [48]. Blood pool microbubbles prepared by matrix dissolution have most of the lipid on the shell of the bubbles, and not left behind in the surrounding aqueous medium [38]. We can expect that protein-PEG-lipid derivatives will follow the same trend, with efficient transfer of the conjugate from the aqueous medium to the microbubble shell. Obviously, sonication protocol for bubble preparation does not seem to be applicable for the targeted microbubble formulations where the protein-PEG-lipid conjugate is prepared first: sonication conditions imply high temperature, which will likely denature and inactivate the protein.

9.7 Bubble Targeting Tumors In Vivo: Microbubbles in Animal Models

The question of the ability of targeted ultrasound contrast imaging to delineate molecular patterns in tumor vasculature begins with the questions of detection sensitivity, common to all imaging modalities, and the administered dose of contrast material. The lower the required dose, the smaller would be the amount of expensive materials that needs to go into manufacturing of contrast agent, and the chance of any undesirable side effects, however minor they might be, would also be lowered. If we expect tumor blood flow to be e.g., ~ 0.3 ml/g/min [22], then a 1 g tumor will have about 1 ml of blood pass through the tumor in about 3 min time. This is about half of the total blood volume of a typical mouse. Therefore, if we inject intravenously, e.g., $\sim 10^7$ microbubbles, as a bolus, and assume only limited signal loss due to deflation during ~ 3 min circulation time, it would imply that well over a million bubbles are expected to pass through the tumor vasculature. Some contrast particles in the bloodstream might have no chance to touch the target endothelium, or might be carried away with the flow of blood due to inefficient adherence. Poor adhesion may happen due to slow adhesion kinetics for ligand-receptor pair, or because of the insufficient ligand or receptor concentrations to obtain stable adhesion. So far, we did not find a published report that would compare the amount of microbubbles passing through the tumor with the amount of bubbles that actually adhered. For simplicity, for a very conservative assumption of 1% bubble target adhesion efficacy, it may be expected that at least 10^4 microbubbles per ml could be adherent, i.e., every mm^3 of target tumor tissue may have ten microbubbles accumulated in it. This implies at least one bubble per one voxel, as a very conservative estimate, and should be sufficient for imaging, which is indeed the case: we will discuss specific examples of molecular ultrasound imaging of tumors in a separate section below.

The first example of delineating tumor vasculature biomarkers with targeted contrast ultrasound imaging in animal model was provided by [8], where bubbles targeted to $\alpha_v\beta_3$ were selectively adherent. In those early studies, bubble detection capabilities of ultrasound systems were not as good as desirable; in order to image targeted bubbles, they had to be destroyed by a high-power imaging pulse. Later, the ultrasound imaging equipment has advanced, reaching the ability to detect and monitor individual microbubbles in the tissues, nondestructively, with high bubble-to-tissue signal ratio, and in real time. This helped expand the testing of microbubble targeting to a wider variety of ligand and receptor pairs, from RGD-based peptides [46] and proteins [8] to VEGFR2-binding antibodies [36] and peptides [35], neuropilin-binding peptides such as ATWLPPR [57], knottin [53], E-selectin-binding peptide [44] and anti-VCAM-1 nanobodies [19]. There are numerous tumor endothelium-specific molecular biomarkers that are continuously being discovered. These new molecules could potentially serve as targets for ultrasound molecular imaging, to delineate the tumors, assess potency and status of vasculature prior to and in response to therapeutic interventions, or serve as an imaging guide for biopsy and ablation.

9.8 Nanobubbles: A Smaller-Size Approach to Molecular Ultrasound Imaging

So far we have discussed targeting of microbubbles toward the markers of tumor endothelium. However, lately there are discussions on the possibilities to attempt targeting biomarkers that are present on the surface of tumor cells [59]: the receptor in that study, prostate-specific membrane antigen, (PSMA), is available on human tumor xenograft cells, so anti-human PSMA antibodies need to be replaced with anti-(murine + human) PSMA antibody to improve targeting efficacy, perhaps via murine PSMA on tumor endothelium. Generally, only a small fraction of tumor cells is exposed to the vessel lumen [5], where microbubbles are restricted to circulate, due to their micrometer size. It remains to be confirmed if such mosaic cancer cells can serve as a target for molecular imaging with microbubbles. Meanwhile, another concept had appeared and moved forward significantly by the efforts of Exner et al. and others: the nanobubble formulation of ultrasound contrast agents [26]. Nanobubbles are prepared by the same methods as microbubbles, and then centrifugal flotation is used to remove larger particles, leaving behind the nanoparticles filled with gas.

While acoustic backscatter of gas bubbles is much stronger for larger particles, existence and reasonable stability of submicron gas formulations had been proven [54]. It is also known that tumor vasculature is leaky, and particles as large as several hundred nanometers can leave the bloodstream [56], at least in subcutaneous tumors in murine models. Therefore, targeted nanobubble particles would have an opportunity to extravasate and adhere to the tumor cell surface biomarkers in the interstitial space. This concept had been successfully proven in a murine

model in a number of recent studies, where ligand-decorated nanobubbles (targeted to PSMA, folate, or CA-125 receptors) accumulated in a tumor that had high expression levels of the receptor on tumor cell membrane, but not in control [10, 15, 33, 40]. The number of nanobubbles ($\sim 200\text{--}600$ nm diameter) had to be significantly higher than the number of microbubbles required for imaging, because acoustic response of nanobubbles is orders of magnitude less than in micrometer-size particles. Even despite this limitation, significant accumulation of nanobubbles in the target tumor was observed by ultrasound imaging. As nanobubbles were no longer in the bloodstream after extravasation, due to the significant reduction of convection levels in the tumor interstitial space, gas loss from nanobubbles was also reduced, as compared with the gas loss in the bloodstream. It remains to be seen if nanobubble targeting approach will be applicable beyond murine tumor models: in larger animals and humans, in slowly growing naturally developed tumors, vasculature defects might not always be large enough to allow passage of submicron particles into the interstitial space, for extravascular delivery and selective targeting.

9.9 Targeted Ultrasound Contrast in Clinic and Clinical Trials

There are currently two contrast agents that may be considered as targeted ultrasound imaging agents in cancer setting: a clinically approved Sonazoid (which has received marketing authorization in Norway, Japan, and Korea) and BR55 (which is at Phase II clinical trials stage).

The principle of action of Sonazoid (earlier known as NC100100 from Nycomed) is based on the fact that it is rapidly taken up by phagocytic cells, such as Kupffer cells in the parenchyma of normal liver tissue [13]. The shell of Sonazoid microbubbles is made just of phosphatidylserine (PS), which is a known biological signal for rapid phagocytosis. So the shell lipid material itself serves as a targeting ligand. Therefore, PS bubbles are rapidly taken up by Kupffer cells, and unlike circulating bubbles, which clear from the bloodstream within several minutes, normal liver parenchyma maintains contrast ultrasound signal for longer time, sufficient for all of the liver tissue to be examined in good detail even with 2D ultrasound. Tumor tissue does not possess Kupffer cells at the same level as normal liver, so negative imaging of tumor node location becomes possible, as dark masses on white background. Targeted contrast ultrasound imaging with PS microbubbles can be used relatively frequently as an inexpensive scouting survey technique that does not involve ionizing radiation (versus PET or CT). Another alternative to Sonazoid survey scanning is MRI, which is expensive and not always immediately available. So targeted contrast ultrasound with PS bubbles finds its clinical use for higher-risk population groups, such as patients with hepatitis C, or cirrhosis, a frequent consequence of fatty liver disease and the modern epidemic of obesity and alcoholism.

BR55, a lipid-PEG microbubble targeted to VEGFR2 via a heterodimeric peptide [35], an agent for molecular ultrasound imaging of tumor neovasculature, has already successfully completed early-stage clinical trials, (NCT01253213 and 02142608). Successful visualization of tumor sites has been achieved and was corroborated by immunohistology, in prostate cancer [42], as well as ovarian and breast cancer settings [52]. Enhancement of ultrasound signal in the tumor tissue was observed up to 30 min following intravenous bolus injection. Additional clinical trials are listed as ongoing (NCT03493464 and 03486327), including a trial for imaging VEGFR2 in pancreatic ductal adenocarcinoma, with the doses of contrast agent up to 0.08 ml/kg. For a 100 kg patient this would imply intravenous bolus administration of 8 ml of aqueous dispersion of BR55, which contains e.g., 16.10^9 microbubbles, to be distributed in ~ 7 L of blood volume. If we repeat the same approximate calculation as for a mouse scenario, as described in a section above, the following numbers can be generated. Over the course of several minutes, assuming ~ 0.3 ml/g/min blood flow, we can roughly estimate passage of ~ 2 million bubbles through the vasculature of a 1-cm tumor. Even if 1% of the circulating bubbles is adhered and retained on the target surface, this will be quite sufficient for selective imaging and delineation of the tumor area by the acoustic backscatter provided by these microbubbles. For the exploratory requirement of this test, targeting peptide dose is limited to <0.1 mg dose per patient. Lesion enhancement contrast ultrasound images of VEGFR2-targeted bubbles provided in [52] and online supplement therein clearly demonstrate selective accumulation, very likely sufficient for diagnostics and biopsy guidance. As BR55 is the first clinical example of neovasculature-targeted microbubbles in oncology, this contrast agent demonstrates the feasibility of the approach and will serve as a justification for additional studies in clinical translation with this and other molecular biomarker targets.

9.10 Conclusion

Microbubbles decorated with targeting ligands have been studied as molecular ultrasound contrast imaging agents in vitro and in animal models. Early-stage clinical trials seem to support the concept of molecular ultrasound imaging. Many key prior patents in the area of bubble formulation either have expired or will be expiring shortly, giving freedom to operate to all interested. With the widest level of availability of ultrasound imaging equipment, and expanding need for molecular-level information, targeted microbubbles may help improve rapid diagnostics and assist in the guidance of biopsy and therapeutic procedures.

Acknowledgments A.L. Klibanov is supported in part via NIH R01 EB023055, awarded by the National Institute of Biomedical Imaging and Bioengineering of the National Institutes of Health. The content of this publication is solely the responsibility of the author and does not necessarily represent the official views of the National Institutes of Health.

References

1. Anderson CR, Rychak JJ, Backer M, Backer J, Ley K, Klibanov AL (2010) scVEGF microbubble ultrasound contrast agents: a novel probe for ultrasound molecular imaging of tumor angiogenesis. *Invest Radiol* 45(10):579–585. <https://doi.org/10.1097/RLI.0b013e3181efd581>
2. Averkiou M, Powers J, Skyba D, Bruce M, Jensen S (2003) Ultrasound contrast imaging research. *Ultrasound Q* 19(1):27–37
3. Betzig E, Patterson GH, Sougrat R, Lindwasser OW, Olenych S, Bonifacino JS, Davidson MW, Lippincott-Schwartz J, Hess HF (2006) Imaging intracellular fluorescent proteins at nanometer resolution. *Science* 313(5793):1642–1645. <https://doi.org/10.1126/science.1127344>
4. Bogdanov AA Jr, Klibanov AL, Torchilin VP (1988) Protein immobilization on the surface of liposomes via carbodiimide activation in the presence of N-hydroxysulfosuccinimide. *FEBS Lett* 231(2):381–384
5. Chang YS, di Tomaso E, McDonald DM, Jones R, Jain RK, Munn LL (2000) Mosaic blood vessels in tumors: frequency of cancer cells in contact with flowing blood. *Proc Natl Acad Sci USA* 97(26):14608–14613. <https://doi.org/10.1073/pnas.97.26.14608>
6. Cheng KT (2004) Perflerane-lipid microspheres. In: *Molecular imaging and contrast agent database (MICAD)*. Bethesda, MD
7. Chlon C, Guedon C, Verhaagen B, Shi WT, Hall CS, Lub J, Bohmer MR (2009) Effect of molecular weight, crystallinity, and hydrophobicity on the acoustic activation of polymer-shelled ultrasound contrast agents. *Biomacromol* 10(5):1025–1031. <https://doi.org/10.1021/bm801243u>
8. Ellegala DB, Leong-Poi H, Carpenter JE, Klibanov AL, Kaul S, Shaffrey ME, Sklenar J, Lindner JR (2003) Imaging tumor angiogenesis with contrast ultrasound and microbubbles targeted to alpha(v)beta3. *Circulation* 108(3):336–341. <https://doi.org/10.1161/01.CIR.0000080326.15367.0C>
9. Errico C, Pierre J, Pezet S, Desailly Y, Lenkei Z, Couture O, Tanter M (2015) Ultrafast ultrasound localization microscopy for deep super-resolution vascular imaging. *Nature* 527(7579):499–502. <https://doi.org/10.1038/nature16066>
10. Fan X, Wang L, Guo Y, Tu Z, Li L, Tong H, Xu Y, Li R, Fang K (2015) Ultrasonic nanobubbles carrying anti-PSMA nanobody: construction and application in prostate cancer-targeted imaging. *PLoS One* 10(6):e0127419. <https://doi.org/10.1371/journal.pone.0127419>
11. Fisher NG, Christiansen JP, Klibanov A, Taylor RP, Kaul S, Lindner JR (2002) Influence of microbubble surface charge on capillary transit and myocardial contrast enhancement. *J Am Coll Cardiol* 40(4):811–819
12. Fokong S, Theek B, Wu Z, Koczera P, Appold L, Jorge S, Resch-Genger U, van Zandvoort M, Storm G, Kiessling F, Lammers T (2012) Image-guided, targeted and triggered drug delivery to tumors using polymer-based microbubbles. *J Control Release* 163(1):75–81. <https://doi.org/10.1016/j.jconrel.2012.05.007>
13. Forsberg F, Piccoli CW, Liu JB, Rawool NM, Merton DA, Mitchell DG, Goldberg BB (2002) Hepatic tumor detection: MR imaging and conventional US versus pulse-inversion harmonic US of NC100100 during its reticuloendothelial system-specific phase. *Radiology* 222(3):824–829. <https://doi.org/10.1148/radiol.2223001786>
14. Fritz TA, Unger EC, Sutherland G, Sahn D (1997) Phase I clinical trials of MRX-115. A new ultrasound contrast agent. *Invest Radiol* 32(12):735–740
15. Gao Y, Hernandez C, Yuan HX, Lilly J, Kota P, Zhou H, Wu H, Exner AA (2017) Ultrasound molecular imaging of ovarian cancer with CA-125 targeted nanobubble contrast agents. *Nanomedicine* 13(7):2159–2168. <https://doi.org/10.1016/j.nano.2017.06.001>

16. Garg S, Thomas AA, Borden MA (2013) The effect of lipid monolayer in-plane rigidity on in vivo microbubble circulation persistence. *Biomaterials* 34(28):6862–6870. <https://doi.org/10.1016/j.biomaterials.2013.05.053>
17. Hauff P, Fritzsche T, Reinhardt M, Weitschies W, Luders F, Uhlendorf V, Heldmann D (1997) Delineation of experimental liver tumors in rabbits by a new ultrasound contrast agent and stimulated acoustic emission. *Invest Radiol* 32(2):94–99
18. Helfield BL, Huo X, Williams R, Goertz DE (2012) The effect of preactivation via temperature on the acoustic properties of definity. *Ultrasound Med Biol* 38(7):1298–1305. <https://doi.org/10.1016/j.ultrasmedbio.2012.03.005>
19. Hernot S, Unnikrishnan S, Du Z, Shevchenko T, Cosyns B, Broisat A, Toczek J, Caveliers V, Muyldermans S, Lahoutte T, Klibanov AL, Devoogdt N (2012) Nanobody-coupled microbubbles as novel molecular tracer. *J Control Release* 158(2):346–353. <https://doi.org/10.1016/j.jconrel.2011.12.007>
20. Hughes MS, McCarthy JE, Marsh JN, Arbeit JM, Neumann RG, Fuhrhop RW, Wallace KD, Znidarsic DR, Maurizi BN, Baldwin SL, Lanza GM, Wickline SA (2007) Properties of an entropy-based signal receiver with an application to ultrasonic molecular imaging. *J Acoust Soc Am* 121(6):3542–3557. <https://doi.org/10.1121/1.2722050>
21. Hvattum E, Uran S, Sandbaek AG, Karlsson AA, Skotland T (2006) Quantification of phosphatidylserine, phosphatidic acid and free fatty acids in an ultrasound contrast agent by normal-phase high-performance liquid chromatography with evaporative light scattering detection. *J Pharm Biomed Anal* 42(4):506–512. <https://doi.org/10.1016/j.jpba.2006.04.027>
22. Kallinowski F, Schlenger KH, Runkel S, Kloes M, Stohrer M, Okunieff P, Vaupel P (1989) Blood flow, metabolism, cellular microenvironment, and growth rate of human tumor xenografts. *Cancer Res* 49(14):3759–3764
23. Keller MW, Glasheen W, Kaul S (1989) Albutex: a safe and effective commercially produced agent for myocardial contrast echocardiography. *J Am Soc Echocardiogr* 2(1):48–52
24. Klibanov AL, Hughes MS, Marsh JN, Hall CS, Miller JG, Wible JH, Brandenburger GH (1997) Targeting of ultrasound contrast material. An in vitro feasibility study. *Acta Radiol Suppl* 412:113–120
25. Koczera P, Appold L, Shi Y, Liu M, Dasgupta A, Pathak V, Ojha T, Fokong S, Wu Z, van Zandvoort M, Iranzo O, Kuehne AJC, Pich A, Kiessling F, Lammers T (2017) PBCA-based polymeric microbubbles for molecular imaging and drug delivery. *J Control Release* 259:128–135. <https://doi.org/10.1016/j.jconrel.2017.03.006>
26. Krupka TM, Solorio L, Wilson RE, Wu H, Azar N, Exner AA (2010) Formulation and characterization of echogenic lipid-pluronic nanobubbles. *Mol Pharm* 7(1):49–59. <https://doi.org/10.1021/mp9001816>
27. Leighton TG (1994) *The acoustic bubble*. Academic Press, London
28. Leong-Poi H, Song J, Rim SJ, Christiansen J, Kaul S, Lindner JR (2002) Influence of microbubble shell properties on ultrasound signal: implications for low-power perfusion imaging. *J Am Soc Echocardiogr* 15(10 Pt 2):1269–1276
29. Lindner JR, Song J, Christiansen J, Klibanov AL, Xu F, Ley K (2001) Ultrasound assessment of inflammation and renal tissue injury with microbubbles targeted to P-selectin. *Circulation* 104(17):2107–2112
30. Liu X, Gong P, Song P, Xie F, Miller Li AL, Chen S, Lu L (2018) Fast functionalization of ultrasound microbubbles using strain promoted click chemistry. *Biomater Sci* 6(3):623–632. <https://doi.org/10.1039/c8bm00004b>
31. Lu E, Wagner WR, Schellenberger U, Abraham JA, Klibanov AL, Woulfe SR, Csikari MM, Fischer D, Schreiner GF, Brandenburger GH, Villanueva FS (2003) Targeted in vivo labeling of receptors for vascular endothelial growth factor: approach to identification of ischemic tissue. *Circulation* 108(1):97–103. <https://doi.org/10.1161/01.CIR.0000079100.38176.83>
32. Palmowski M, Morgenstern B, Hauff P, Reinhardt M, Huppert J, Maurer M, Woenne EC, Doerk S, Ladewig G, Jenne JW, Delorme S, Grenacher L, Hallscheidt P, Kauffmann GW, Semmler W, Kiessling F (2008) Pharmacodynamics of streptavidin-coated cyanoacrylate

- microbubbles designed for molecular ultrasound imaging. *Invest Radiol* 43(3):162–169. <https://doi.org/10.1097/RLI.0b013e31815a251b>
33. Perera R, de Leon A, Wang X, Wang Y, Ramamurthy G, Peiris P, Abenojar E, Basilion JP, Exner AA (2019) Real time ultrasound molecular imaging of prostate cancer with PSMA-targeted nanobubbles. *bioRxiv*. <https://doi.org/10.1101/634444>
 34. Perflutren (2001) <http://www.definityimaging.com>. Accessed 05 June 2019
 35. Pochon S, Tardy I, Bussat P, Bettinger T, Brochot J, von Wronski M, Passantino L, Schneider M (2010) BR55: a lipopeptide-based VEGFR2-targeted ultrasound contrast agent for molecular imaging of angiogenesis. *Invest Radiol* 45(2):89–95. <https://doi.org/10.1097/RLI.0b013e3181c5927c>
 36. Rychak JJ, Graba J, Cheung AM, Mystry BS, Lindner JR, Kerbel RS, Foster FS (2007) Microultrasound molecular imaging of vascular endothelial growth factor receptor 2 in a mouse model of tumor angiogenesis. *Mol Imaging* 6(5):289–296
 37. Schneider M, Arditì M, Barrau MB, Brochot J, Broillet A, Ventrone R, Yan F (1995) BR1: a new ultrasonographic contrast agent based on sulfur hexafluoride-filled microbubbles. *Invest Radiol* 30(8):451–457
 38. Schneider M, Brochot J, Puginier J, Yan F (1993) Stable microbubble suspensions comprising saturated phospholipids for ultrasound echography. USA Patent US5686060A
 39. Senior R, Monaghan M, Main ML, Zamorano JL, Tiemann K, Agati L, Weissman NJ, Klein AL, Marwick TH, Ahmad M, DeMaria AN, Zabalgaitia M, Becher H, Kaul S, Udelson JE, Wackers FJ, Walovitch RC, Picard MH, Ramp-1 and Ramp-2 Investigators (2009) Detection of coronary artery disease with perfusion stress echocardiography using a novel ultrasound imaging agent: two Phase 3 international trials in comparison with radionuclide perfusion imaging. *Eur J Echocardiogr* 10(1):26–35. <https://doi.org/10.1093/ejehocard/jen321>
 40. Shen Y, Lv W, Yang H, Cai W, Zhao P, Zhang L, Zhang J, Yuan L, Duan Y (2019) FA-NBs-IR780: Novel multifunctional nanobubbles as molecule-targeted ultrasound contrast agents for accurate diagnosis and photothermal therapy of cancer. *Cancer Lett* 455:14–25. <https://doi.org/10.1016/j.canlet.2019.04.023>
 41. Slagle CJ, Thamm DH, Randall EK, Borden MA (2018) Click conjugation of cloaked peptide ligands to microbubbles. *Bioconjug Chem* 29(5):1534–1543. <https://doi.org/10.1021/acs.bioconjchem.8b00084>
 42. Smeenge M, Tranquart F, Mannaerts CK, de Reijke TM, van de Vijver MJ, Laguna MP, Pochon S, de la Rosette J, Wijkstra H (2017) First-in-human ultrasound molecular imaging with a VEGFR2-specific ultrasound molecular contrast agent (BR55) in prostate cancer: a safety and feasibility pilot study. *Invest Radiol* 52(7):419–427. <https://doi.org/10.1097/RLI.0000000000000362>
 43. Smith MD, Elion JL, McClure RR, Kwan OL, DeMaria AN (1989) Left heart opacification with peripheral venous injection of a new saccharide echo contrast agent in dogs. *J Am Coll Cardiol* 13(7):1622–1628
 44. Spivak I, Rix A, Schmitz G, Fokong S, Iranzo O, Lederle W, Kiessling F (2016) Low-dose molecular ultrasound imaging with E-selectin-targeted PBCA microbubbles. *Mol Imaging Biol* 18(2):180–190. <https://doi.org/10.1007/s11307-015-0894-9>
 45. Straub JA, Chickering DE, Church CC, Shah B, Hanlon T, Bernstein H (2005) Porous PLGA microparticles: AI-700, an intravenously administered ultrasound contrast agent for use in echocardiography. *J Control Release* 108(1):21–32. <https://doi.org/10.1016/j.jconrel.2005.07.020>
 46. Streeter JE, Gessner RC, Tsuruta J, Feingold S, Dayton PA (2011) Assessment of molecular imaging of angiogenesis with three-dimensional ultrasonography. *Mol Imaging* 10(6):460–468
 47. Szabo TL (2014) *Diagnostic ultrasound imaging: inside out*, 2nd edn. Academic Press, Oxford, p 25

48. Unnikrishnan S, Du Z, Diakova G, Klibanov AL (2018) Formation of microbubbles for targeted ultrasound contrast imaging: practical translation considerations. *Langmuir*. <https://doi.org/10.1021/acs.langmuir.8b03551>
49. Villanueva FS, Jankowski RJ, Klibanov S, Pina ML, Alber SM, Watkins SC, Brandenburger GH, Wagner WR (1998) Microbubbles targeted to intercellular adhesion molecule-1 bind to activated coronary artery endothelial cells. *Circulation* 98(1):1–5
50. Villanueva FS, Lu E, Bowry S, Kilic S, Tom E, Wang J, Gretton J, Pacella JJ, Wagner WR (2007) Myocardial ischemic memory imaging with molecular echocardiography. *Circulation* 115(3):345–352. <https://doi.org/10.1161/CIRCULATIONAHA.106.633917>
51. Wang S, Herbst EB, Mauldin FW Jr, Diakova GB, Klibanov AL, Hossack JA (2016) Ultra-low-dose ultrasound molecular imaging for the detection of angiogenesis in a mouse murine tumor model: how little can we see? *Invest Radiol* 51(12):758–766. <https://doi.org/10.1097/RLI.0000000000000310>
52. Willmann JK, Bonomo L, Testa AC, Rinaldi P, Rindi G, Valluru KS, Petrone G, Martini M, Lutz AM, Gambhir SS (2017) Ultrasound molecular imaging with BR55 in patients with breast and ovarian lesions: first-in-human results. *J Clin Oncol* 35(19):2133–2140. <https://doi.org/10.1200/JCO.2016.70.8594>
53. Willmann JK, Kimura RH, Deshpande N, Lutz AM, Cochran JR, Gambhir SS (2010) Targeted contrast-enhanced ultrasound imaging of tumor angiogenesis with contrast microbubbles conjugated to integrin-binding knottin peptides. *J Nucl Med* 51(3):433–440. <https://doi.org/10.2967/jnumed.109.068007>
54. Wu H, Rognin NG, Krupka TM, Solorio L, Yoshiara H, Guenette G, Sanders C, Kamiyama N, Exner AA (2013) Acoustic characterization and pharmacokinetic analyses of new nanobubble ultrasound contrast agents. *Ultrasound Med Biol* 39(11):2137–2146. <https://doi.org/10.1016/j.ultrasmedbio.2013.05.007>
55. Yeh JS, Sennoga CA, McConnell E, Eckersley R, Tang MX, Nourshargh S, Seddon JM, Haskard DO, Nihoyannopoulos P (2015) A targeting microbubble for ultrasound molecular imaging. *PLoS One* 10(7):e0129681. <https://doi.org/10.1371/journal.pone.0129681>
56. Yuan F, Dellian M, Fukumura D, Leunig M, Berk DA, Torchilin VP, Jain RK (1995) Vascular permeability in a human tumor xenograft: molecular size dependence and cutoff size. *Cancer Res* 55(17):3752–3756
57. Zhang H, Tam S, Ingham ES, Mahakian LM, Lai CY, Tumbale SK, Teesalu T, Hubbard NE, Borowsky AD, Ferrara KW (2015) Ultrasound molecular imaging of tumor angiogenesis with a neuropilin-1-targeted microbubble. *Biomaterials* 56:104–113. <https://doi.org/10.1016/j.biomaterials.2015.03.043>
58. Zlitni A, Janzen N, Foster FS, Valliant JF (2014) Catching bubbles: targeting ultrasound microbubbles using bioorthogonal inverse-electron-demand Diels-Alder reactions. *Angew Chem Int Ed Engl* 53(25):6459–6463. <https://doi.org/10.1002/anie.201402473>
59. Zlitni A, Yin M, Janzen N, Chatterjee S, Lisok A, Gabrielson KL, Nimmagadda S, Pomper MG, Foster FS, Valliant JF (2017) Development of prostate specific membrane antigen targeted ultrasound microbubbles using bioorthogonal chemistry. *PLoS One* 12(5):e0176958. <https://doi.org/10.1371/journal.pone.0176958>



Optical and Optoacoustic Imaging Probes

10

Michel Eisenblätter and Moritz Wildgruber

Contents

10.1	Unspecific, Perfusion-Type Optical Probes	339
10.2	Targeted Contrast Agents.....	340
10.2.1	Binding Moieties	342
10.2.2	Signalling Molecules	346
10.2.3	Linkers/Spacers.....	350
10.3	Smart Probes.....	351
10.4	Summary.....	351
	References	352

Tissue has characteristic properties when it comes to light absorption and scattering. For optical (OI) and optoacoustic imaging (OAI) these properties can be utilised to visualise biological tissue characteristics, as, for example, the oxygenation state of haemoglobin alters the optical and optoacoustic properties of the molecule.

Substances of particular build-up have the ability to absorb light. Upon energy absorption, molecules subtly expand, creating a shear wave in the immediate environment and, after a distinct time, emit energy again. Mostly in the form of thermal energy, in part in the form of light of—as compared to the absorbed light—lower energy/wavelength.

This emission can be measured and can be used for creation of images.

The physiological components of tissue differ regarding light absorption, and do exhibit a slight autofluorescence in the blue range of the spectrum for specific

M. Eisenblätter (✉)

Department of Diagnostic and Interventional Radiology, University Medical Center Freiburg, Freiburg im Breisgau, Germany
e-mail: eisenblaetter@uni-muenster.de; michel.eisenblaetter@uniklinik-freiburg.de

M. Wildgruber

Department of Radiology, Ludwig Maximilians-University of Munich, Munich, Germany

imaging applications, however, extrinsic contrast agents are essentially required, mostly operating in the red range of the spectrum.

Absorption-based imaging can be enhanced by using very strong absorbers but would, in principle, not essentially rely on such. Recently, the photodynamic effect—the resulting shear wave in tissue following absorption of light in specifically equipped molecules—has been explored for imaging as well and substances with a particularly strong photodynamic effect, such as gold, have been assessed as contrast material.

In summary, the basic principles of optical imaging—absorption imaging including photoacoustic imaging on the one hand and fluorescence imaging on the other hand—leaves us with two different groups of contrast agents: strong absorbers, creating a negative contrast in most imaging modalities and/or a strong photodynamic signal and fluorescent substances that, from absorbed light, create a lower energy light signal and thermal energy. The efficacy of fluorescent substances is expressed as photon yield—the amount of light energy, emitted in relation to the excitation energy.

In addition to these two groups of contrast agents for optical imaging, bioluminescence and fluorescence proteins do play a relevant role, mainly in preclinical research. For both approaches, cells of interest are equipped with genes, encoding proteins that either act as a fluorescent dye or enable for processing of specific substrates, resulting in luminescent dyes.

Imaging of tissue characteristics beyond the features that directly influence light absorption, scattering and autofluorescence essentially requires the use of probes or contrast agents.

These can be various in design and abilities, differ regarding the biological imaging potential, pharmacodynamic and signalling properties.

Simple probes are unspecific and distribute following their physical properties and consecutively most frequently reflect perfusion and/or diffusion, depending on their size and chemical makeup [1].

More complex probes are target-specific. These probes typically consist of a targeting moiety with affinity for a specific molecule and a signalling moiety for optical or photoacoustic imaging, mostly linked by a more or less complex spacer.

These probes can differ in all three components—the target-specific site, the signalling molecule and the potential chemical linker. All components can influence the *in vivo* behaviour and performance of the probe and need to be considered [2].

Further developments are so-called smart probes. Smart probes do offer an even more refined contrast as compared to targeted probes [3]. These complex compounds alter their signal characteristics upon interaction with a target molecule, usually switching from no contrast to a high detectable signal. Only a few target structures qualify for activation of a smart probe and therefore, only few, properly established examples can be shown for this class of tracers [4].

10.1 Unspecific, Perfusion-Type Optical Probes

Perfusion-type contrast agents do not have a specific, target-binding aspect *in vivo* and distribute with the blood flow or, where and if possible, leave the vasculature and diffuse through the interstitial space.

In the very close definition, they would therefore not qualify as tracers but rather be counted as contrast agents. They can indicate perfusion, vascularisation and vascular integrity and in this context provide highly relevant information for the estimation of cancer biology *in vivo* albeit not exactly molecular information [5].

Due to the enhanced permeability of tumour vasculature and the properties of tumour interstitium, promoting retention of extravascular components in the context of the enhanced permeability and retention effect (EPR), the passive accumulation of perfusion-type contrast agents can still provide useful diagnostic information and is—if not tumour-specific, at least indicative of cancer-associated changes of vascularity and therefore representative of disease and can, in the absence of other mitigating factors, guide surgery or aid diagnostics [6].

Although research-wise not as strongly represented as the other two classes of optical tracers, perfusion-type contrast agents have an undisputed impact as they are by far the most abundant in clinical practice.

Fluorescein isothiocyanate (FITC) was among the first fluorescent dyes to get approval by the US Food and Drug Administration (FDA) for diagnostic application in humans.

After intravenous (iv) application, FITC enabled the detection of malignant lesions in the bowel by endoscopy, based on the elevated perfusion [7]. However, the absorption/emission characteristics of FITC with maxima close to haemoglobin limit the imaging depth and the achievable contrast. The intense photobleaching of FITC moreover limits the longitudinal use, e.g. during complex interventions.

Indocyanine green (ICG), also one of the first clinically approved fluorescent dyes has spectral characteristics, virtually ideal for in human use—absorption/excitation and emission maxima are in the range of 800 nm, well beyond the physiological autofluorescence background. ICG itself is small but quickly binds serum albumin, forming complexes of 5–10 nm that are eliminated via the hepatobiliary route [8].

Initially used for optical angiography of the eye [9], ICG quickly developed into a tool for cystoscopic and endoscopic applications as well. The imaging equipment was adapted and ICG has now been used for endoscopic imaging of organ perfusion [10], mapping of locoregional draining lymph nodes [11] as well as grading of arthritis [12]. Moreover, surgery can be guided by intraoperative ICG imaging [13–15].

ICG has been used successfully for both, OI and OAI [16, 17].

5-Aminolevulinic acid (5-ALA) is not the typical unspecific probe and certainly not a perfusion-type contrast agent. It is a non-proteinogenic amino acid and part of the pathway to porphyrin synthesis. Not fluorescent *per se*, downstream products of 5-ALA metabolism during porphyrin and heme synthesis are highly fluorescent

with emission maxima around 640 nm. Vital, metabolically active tumour cells are supposed to prefer 5-ALA for heme synthesis [18, 19] but uptake in non-malignant cells has also been reported. The resulting specificity is moderate and not necessarily a diagnostic criterion for malignancy.

In addition to the described dyes and organic compounds, OAI can also be driven by other substances that exhibit a photoelastic expansion upon absorption of light.

Exclusively suitable for OAI, gold can serve as a potent signalling molecule for targeted contrast agents (see below) and as stand alone contrast material without specific binding capacity [20].

The photoelastic expansion of gold, driving the optoacoustic effect, peaks for light of around 500 nm but can be tuned in larger compounds in the range of 650–1100 nm, depending on the desired application.

Gold is in this context either used to coat nano-sized tubes or spheres to create a layer of gold ions, resonating with light, the principle is called surface plasmon resonance, or packed in a particle shell that can subsequently be coated to improve or tune the biodistribution, compatibility and availability [21–23].

In this context, coating of a particle with polyethylene glycol (PEG) increases the circulation time from several minutes to several hours while at the same time reducing cell toxicity and immunogenicity [24, 25].

Especially the prolonged availability in serum is attributed to the PEG coating's almost immediate attraction of serum proteins and the consecutive increase of the effective particle size.

10.2 Targeted Contrast Agents

The next step in development of imaging specificity towards visualisation of molecular processes in disease constitutes targeted contrast agents.

These probes are constructed of a binding motif and a signalling molecule, often joined by a linker to enhance specific chemical properties. All three components of the probe can vary and determine the chemical, physical and biological behaviour of the probe.

Depending on the target and the desired application, variation on each of the probe components can be performed for an optimal imaging result.

The accumulated probe size, the charge, the balance between hydrophilicity, lipophilicity, etc., are all determined, to different degrees, by all three probe components.

The initial and most important step in the development of a targeted imaging agent would still be the selection of an appropriate target. This target structure should be easily available to the probe, therefore, either be located intravascular, e.g. on the endothelium or within the area around the vasculature that can realistically be reached by probes via diffusion. A target in the very centre of a tumour lesion has, in this context, reduced potential for attracting a specific imaging agent as compared to a target structure, located in the immediate vicinity of a vessel,

considering that even the supply of oxygen and other, small nutrients to the tumour centre frequently fails. Intact endothelium has pores of around 5 nm diameter. Smaller probes would easily leave the vessel and rapidly reach a relevant concentration in the extravascular space with access to the target structure, larger probes would need much longer or not reach an equilibrium between intravascular and extravascular space [26].

Moreover, the target structure needs to be overexpressed on the tumour and/or other target cell as compared to healthy background tissue [27, 28]. For targeted therapy and imaging approaches alike, a threefold overexpression is generally considered appropriate to achieve a high enough contrast to allow for differentiation of the signal relative to the unspecific background [29]. In addition to the relative expression level, the absolute expression of the target and the consecutive absolute amount of tracer that can consecutively accumulate in the target area are important factors for consideration of a specific target. With a view to the imaging approach, at least picomolar (optical) to micromolar (magnetic resonance tomography) amounts of the signalling molecule are required for safe detection. Moreover, as outlined in accompanying chapters in this book, even between different optical imaging modalities, the sensitivity varies significantly. To a certain degree, low absolute expression levels of a target structure can be compensated for by highly sensitive imaging approaches or very effective labelling of the tracer.

Upon selection of an appropriate target, several factors for probe design need to be considered. These factors include size, charge and lipophilicity/hydrophilicity.

Depending on their size, probes are eliminated from the blood either quickly via the kidneys or rather slowly via liver and bile. The threshold generally given for renal elimination is a size of about 60 kDa or 5 nm effective molecule size, depending, e.g. on binding of plasma proteins or hydration [30]. With primarily renal elimination, the overall circulation half-life of a probe is limited to a couple of hours at most, more likely to a time span of up to one hour. This is further determined by the sum charge of the probe [31] with a cationic sum charge promoting rapid elimination and an anionic charge delaying it due to a more intensive interaction at the glomerular capillary wall [32].

Large probes are eliminated from the blood via the reticuloendothelial system and/or Kupffer cells and the bile. For complete elimination, this process can take days to weeks [33].

The circulation time influences the optimal imaging time point. A quick decrease of free probe in the blood reduces the unspecific background around the specifically bound tracer in the tumour lesion and therefore enables earlier imaging after tracer administration.

At the same time, smaller probes should, in theory, have easier access to deep tissue, further away from the vasculature.

Large probes may be able to leave the vasculature but might not diffuse further into the interstitium—access to target structures can thus be obviated.

On the other hand, the exposure time of the target structures to the probe is higher for long-circulating, larger probes which are therefore more likely to bind targets with only little absolute expression.

Hydrophilicity promotes rapid elimination, lipophilicity leads to binding of probe and serum proteins, resulting in an artificially large compound with an increased circulation time and delayed elimination.

The perfect probe balances all these properties in a way, ideal for the individual, desired application.

10.2.1 Binding Moieties

Every binding moiety can—in theory—serve as the basis for a targeted tracer.

Most often, the largest and most complex component of a targeted probe, development of the binding moiety is arguably the most challenging part of tracer development.

The model basis for binding moieties of targeted probes has in this context been provided by nature itself: antibodies offer high specificity, biocompatibility and—usually—a size that allows for chemical alteration, e.g. equipment for imaging, without interference with the target-binding site [34].

From there, further development led to fragments of antibodies, smaller peptidic probes and non-peptidic small molecules [35].

The challenge in design and development of a binding moiety is to balance specificity with high target affinity and chemical properties with an influence on tracer distribution.

10.2.1.1 Antibodies and Antibody Fragments

Full-length antibodies have a size of around 150 kDa in case of human/primate IgG and comprise four peptide chains, two identical heavy chains and two identical light chains. The neighbouring ends of both, heavy and light chains combined feature the antigen-binding Fv portion, part of the Fab fragment of light chain and immediately linked heavy chain parts, the other end of the heavy chains forms the backbone of the antibody, the Fc part that is conserved across the antibody class.

More primitive antibodies as found in sharks or camelids comprise heavy chains only, resulting in a size of 80–100 kDa.

While the Fab part determines the specific binding affinity, the Fc part has a strong influence on unspecific antibody distribution and accumulation [36]. Some cells, especially immune cells even have Fc receptors for antibody binding and consecutive endocytosis. The Fc part of an antibody can trigger immunogenicity and build-up of immune complexes, especially if used in a syngeneic setting in the source species [37]. Antibody complexes distribute differently than single antibodies and can further hamper *in vivo* performance of antibody-based probes.

Antibodies are relatively stable in serum and have a half-life of several days to weeks before slowly clearing hepatically or being eliminated via cellular ingestion and lysis or recycling [38].

The relatively big size of antibodies allows for easy, random labelling with virtually all commercially available signalling molecules via an active ester–cysteine binding. Even though a certain amount of the antibody solution would lose

binding affinity because of dye in the active binding centre, the loss of affinity after labelling is generally regarded to be negligible. More demanding is the treatment, antibodies require during the labelling process—they are highly sensitive to changes of pH and temperature and some amendments to the generally most effective labelling protocols had to be made to enable conjugation of antibodies with dyes or chelators, in order not to interfere with integrity and function of the antibody [39, 40].

Antibodies can intertwine and form immune complexes, triggering phagocytosis of antigens that have been recognised and labelled that way. For tracers, this formation of immune complexes can, however, hamper the imaging performance, leading to a further delay in elimination and interference with target binding [41].

Antibodies are specific for species. An antibody, generated in rat, mouse or rabbit can elicit an immune reaction in other species, especially in humans, following repeated application. Conversely, immune complexes form within one species only with Fc receptor mediated, unspecific binding significantly reducing the amount of tracer that is actively contributing to the target-specific imaging signal [42, 43].

The generation of antibodies can follow the natural route by immunisation of an animal with the desired antigen, isolation of the antibody from serum and purification. The result is a polyclonal antibody, a mixture of multiple antibodies of different Fab/Fv makeup.

Especially for random labelling approaches, the resulting heterogeneity has the tremendous advantage that the probability to lose binding affinity of the tracer due to dye in the active, target-binding region is lower—even if some antibody should exhibit dye binding in the active region, this region is unlikely to be present in the other antibody clones which would therefore likely remain active.

Monoclonal antibodies are produced in bacterial cell culture following genetic fusion of immunised splenic cells and bacteria. They are easier to produce in large amounts and procedures, driven by these antibodies are easier to standardise. However, monoclonal antibodies are more prone to lose affinity upon random labelling: if a prominent site for conjugation is present in the target-binding region, it is present in all antibodies.

A huge number of antibody-based tracers have been established over the past couple of years due to the number of antibodies, available and characterised for *in vitro* applications [35] or therapy [44]. A transfer for *in vivo* imaging is technically easy. For successful transfer, the target availability needs to be verified and tested *in vivo*—the relatively large size of antibodies favours targets with intravascular availability or abundance in close proximity of the vasculature.

The size hampers imaging early after tracer administration. Systematic assessment of tracer accumulation in target tissue and subsequent optimisation of imaging procedures mostly results in imaging at least 24 h, sometimes 48 h after tracer injection [45].

Rapidly repeated measurements are obviated or at least limited by the long tracer half-life.

Consecutively, isolation of fragments from whole IgG antibodies or primitive variants has been established and by now widely commercialised in the form of kits for fragmentation of IgG.

It is, e.g. possible to abate the Fc part of IgG, leaving the two Fab fragments, linked at the common basis, a bivalent compound of about 110 kDa. The isolated single Fab fragments, dissected from IgG for further processing via Papain-mediated cleavage, is a compound of about 50 kDa (see Fig. 10.1). Depending on the label, the resulting tracer maybe just above or just below the renal elimination threshold.

Fab fragments constitute the binding ability of an IgG and in theory, the affinity should be conserved in isolated fragments, however, numerous studies showed Fab, especially Fab of polyclonal antibodies, to significantly lose target-binding capacity as compared to the full-length IgG.

To overcome this limitation, fusion compounds of multiple Fab fragments or further isolated Fv domains even in the form of single-chain Fv domains [46], diabodies of two fragments and other combination compounds have been created [47]. These compounds are meant to compensate for the loss of affinity by combination of multiple target-binding units.









Format	Composition	Valency	Approx. MW (kDa)	Typical Serum $t_{1/2}$	Clearance Route	
	Intact IgG	$(V_H + V_L)_2$	Bivalent	150-160	1-3 weeks	Hepatic
	$F(ab')_2$	$(V_H C_H1 + V_L + C_L)_2$	Bivalent	110	8-10 h	Hepatic
	Minibody	$(scFv + C_H1)_2$	Bivalent	75	5-10 h	Hepatic
	Fab	$V_H C_H1 + V_L + C_L$	Monovalent	50-55	12-20 h	Renal
	Diabody	$(scFv)_2$	Bivalent	50	3-5 h	Renal
	scFv	$V_H + V_L$	Monovalent	28	2-4 h	Renal
	Nanobody	$V_H H$ (Camelid)	Monovalent	12-15	30-60 m	Renal
	Affibody	Z domain of protein A (<i>S. aureus</i>)	Monovalent	7	30-60 m	Renal

Fig. 10.1 Features of full-length antibodies, antibody fragments and compounds, generated from antibody fragments, relevant in preclinical and clinical imaging applications (Modified from Freise AC, Wu AM; In vivo imaging with antibodies and engineered fragments. Mol Immunol. 2015; 67(2 Pt A):142–52. <https://doi.org/10.1016/j.molimm.2015.04.001>. Epub 2015 Apr 28.)

Nanobodies are generally regarded the smallest antibody fragment with specific binding capacity. The size varies between 12 and 15 kDa, accounted for mostly by the variable domains of heavy chain only antibodies, such as camelids [48].

The serum half-life of these compounds ranges from 12 to 20 h for Fab fragments in their mono- or bivalent presentation down to under 1 h for nanobodies.

While full-length IgG can reliably be labelled randomly using ester–cysteine reactions, smaller fragments frequently require site-specific labelling approaches so that the label does not interfere with the binding capacity of the compound [49]. This requires sequencing and recombinant production in cell culture after genetic modification of the fragment/compound by adding a tag for site-specific labelling. More complex regarding the set-up, this approach guarantees high volume production of a tracer backbone that can be labelled reliably.

Figure 10.1 summarises the characteristics and features of antibodies, antibody fragments and compounds, generated from fragments.

10.2.1.2 Peptides

Constructs of less than 100 amino acids (full-length IgG comprises more than 1000) are called (poly) peptides; less than 10 amino acids constitute an oligopeptides.

Some peptides do have a binding capacity and can therefore serve as a binding moiety in tracers.

Rather recent work demonstrated the potential of phage display for the identification of oligopeptides for tracer synthesis [50].

The strength of the small compounds—usually less than 10 kDa—is the potential for chemical modification enabling site-specific labelling and recombinant, high volume production.

Even production in pharmaceutical quality, ready for use in humans, can be established.

The size renders rapid clearance after tracer administration and enables early subsequent imaging.

A specific subgroup of polypeptides are affibodies, which are based on *Staphylococcus aureus* protein A and usually comprise 50–60 amino acids. The high antigen affinity, easy producibility and small size (6 kDa) favour them over antibodies in many ways [51]. Moreover, a high tolerance for pH changes and temperature make the handling of an affibody during labelling easier and the compound more versatile.

10.2.1.3 Small Molecules

Non-peptidic molecules with binding affinity for specific target structures can also serve as a backbone for target-specific tracers and frequently result in the smallest tracers. The molecular weight of small molecules is very low, the size consecutively small.

The variation across the heterogeneous group of small molecules is huge. Relevant examples include targeted drugs [52, 53] or labelled substrates of cellular metabolism [54].

In this context, folate, binding folate receptor alpha and overexpressed in various malignant diseases including ovarian cancer, has been used for cancer imaging. Small molecules even easily cross cell membranes, if the engineering and sum charge of the compound allow for it. This enables imaging of intracellular targets such as gene loci and intracellular enzymes.

10.2.2 Signalling Molecules

Depending on the imaging application, a variety of labels would enable detection of the targeted probe by OI or OAI.

In both scenarios, OI and OAI, the signalling molecule absorbs light of a distinct wavelength, retains the energy for a short while (fluorescence lifetime), emitting thermal energy and light of longer wavelength, reflecting lower energy. This process is called fluorescence.

While for OAI, the ultrasound wave, induced by the slight expansion of the signalling molecule upon light absorption and thermal increase is used to generate image information, OI relies on the emitted fluorescence light.

For both applications, the required excitation light essentially influences imaging performance.

It has been stated earlier that light of longer wavelength, e.g. light of the near-infrared range of the spectrum penetrates deeper into tissue due to lower absorption and scattering and is therefore better suited for the deep tissue *in vivo* imaging.

The energy transfer, needed to create OAI signals would albeit be higher for short-wavelength light of higher energy.

Even normal tissue and molecules, regularly present in tissue have an albeit low still measurable ability for fluorescence. In the light spectrum range between 270 nm (collagen) [55] and 400 nm (melanin) [56], different tissue components do absorb heavily, producing autofluorescence around 500–600 nm, limiting the achievable contrast for probes, operating in this spectral range. On the other end of the so-called optical window, the absorption maximum of water at around 1000 nm wavelength limits tissue penetration dramatically.

The currently established signalling molecules aim for absorption and emission in this optical window with some experimental exemptions.

Signalling molecules need to fulfil some criteria for optimal performance and these criteria differ, depending on the desired application: for an optimal use in OI, the quantum yield should be as high as possible—the energy loss by thermal energy should be as low as possible so that as much light as possible is emitted and detectable. For OAI, this emission is negligible and higher thermal energy, inducing the measurable ultrasound wave in tissue leads to stronger imaging signals per signalling molecule.

The size and the charge of the molecule are relevant during the labelling process as they determine how much influence the molecule will have on the biodistribution of the tracer compound and whether or not a linker is required to separate binding moiety and signalling molecule.

Most signalling molecules are by now commercially available in some variety, mostly regarding the excitation and emission characteristics and the active conjugation motif, enabling fusion with the binding moiety and/or required linkers.

The ideal signalling molecule can be conjugated to the binding moiety quickly and under physiological conditions, resulting in a stable compound with reproducible, highly efficient labelling at constant ratios between target-specific binding moiety and label, to enable qualified signal interpretation.

Especially the latter favours site-specific labelling approaches over random labelling. While considerably easy with no further processing of the targeting moiety required, random labelling results in a heterogeneous product, potentially even reducing immunoreactivity of at least a fraction of the antibody solution.

Site-specific labelling results in a homogenous, standardised product, enabling easier quantification of imaging results. The downside is that engineering of the antibody or antibody fragment is essentially required.

Table 10.1 compares features and performance parameters of organic cyanine dyes and quantum dots.

Table 10.1 Comparison of cyanine dyes and quantum dots regarding imaging relevant characteristics and performance parameters

Property	Organic dye	Quantum dot
Absorption spectra	Discrete bands, FWHM 35 nm to 80–100 nm	Steady increase towards UV wavelengths starting from absorption onset; enables free selection of excitation wavelength
Molar absorption coefficient	2.5×10^4 – $2.5 \times 10^5 \text{ M}^{-1} \text{ cm}^{-1}$ (at long-wavelength absorption maximum)	10^5 – $10^6 \text{ M}^{-1} \text{ cm}^{-1}$ at first excitonic absorption peak, increasing towards UV wavelengths; larger (longer wavelength) QDs generally have higher absorption
Emission spectra	Asymmetric, often tailing to long-wavelength side; FWHM, 35 nm to 70–100 nm	Symmetric, Gaussian profile; FWHM, 30–90 nm
Stokes shift	Normally <50 nm, up to >150 nm	Typically <50 nm for visible wavelength-emitting QDs
Quantum yield	0.5–1.0 (visible), 0.05–0.25 (NIR)	0.1–0.8 (visible), 0.2–0.7 (NIR)
Fluorescence lifetimes	1–10 ns, mono-exponential decay	10–100 ns, typically multi-exponential decay
Solubility or dispersibility	Control by substitution pattern	Control via surface chemistry (ligands)
Binding to biomolecules	Via functional groups following established protocols Often several dyes bind to a single biomolecule Labelling-induced effects on spectroscopic properties of reporter studied for many common dyes	Via ligand chemistry; few protocols available Several biomolecules bind to a single QD Very little information available on labelling-induced effects

(continued)

Table 10.1 (continued)

Property	Organic dye	Quantum dot
Size	~0.5 nm; molecule	6–60 nm (hydrodynamic diameter); colloid
Thermal stability	Dependent on dye class; can be critical for NIR-wavelength dyes	High; depends on shell or ligands
Photochemical stability	Sufficient for many applications (visible wavelength), but can be insufficient for high-light flux applications; often problematic for NIR-wavelength dyes	High (visible and NIR wavelengths); orders of magnitude higher than that of organic dyes; can reveal photobrightening
Toxicity	From very low to high; dependent on dye	Little known yet (heavy metal leakage must be prevented, potential nanotoxicity)
Reproducibility of labels (optical, chemical properties)	Good, owing to defined molecular structure and established methods of characterisation; available from commercial sources	Limited by complex structure and surface chemistry; limited data available; few commercial systems available
Spectral multiplexing	Possible, 3 colours (MegaStokes dyes), 4 colours (energy-transfer cassettes)	Ideal for multicolour experiments; up to 5 colours demonstrated

Modified from Resch-Genger U1, Grabolle M, Cavaliere-Jaricot S, Nitschke R, Nann T.; Quantum dots versus organic dyes as fluorescent labels. *Nat Methods*. 2008 Sep; 5(9):763–75. <https://doi.org/10.1038/nmeth.1248>

10.2.2.1 Blue Dyes

The majority of fluorescent dyes with absorption below 720 nm are blue dyes. The absorption maximum in a range, close to the absorption of tissue, haemoglobin, etc., renders a use in deep tissue impossible.

However, especially OI and OAI application in subcutaneous settings or endoscopic scenarios is possible and well established.

Some of the most prominent blue dyes, in part established in histology, feature in this category and even have FDA approval for use in humans.

Evans Blue and Methylene Blue as well as Coomassie Blue all have similar absorption features, are visible to the naked eye if used in appropriate concentration [57, 58].

All blue dyes have a strong potential for OAI and induce rather strong photoacoustic signals, however, the absorption overlap with endogenous OAI contrast limits the applicability for highly specific imaging.

10.2.2.2 Cyanine Dyes

Cyanine dyes are by far the largest group of commercially available fluorescent contrast agents for OI. Most of the cyanine scaffold-based dyes exhibit absorption at or above 700 nm with consecutively less scattering or absorption by surrounding tissue.

ICG follows the basic structure of cyanine dyes as do IR 870 Iodine, IRDye or ALEXA Fluor 750.

All these dyes feature the same basic structure, amended for side chains or sites for possible conjugation, such as a single chlorine atom at the central benzoyl structure in IR870 [59].

Rather recent advances in cyanine dye design include the encapsulation of the dye to enhance the solubility in water [59] and the creation of chemosensitive probes, based on the cyanine scaffold. Conformational changes of these probes, e.g. upon pH variation, change the photophysical properties of the dye, therefore enabling *in vivo* pH monitoring [60].

Cyanine dyes generally promote lipophilicity and polarity of the tracer compound and therefore extend serum half-life and shift from renal elimination of the probe towards hepatic/biliary elimination [61]. It has moreover been demonstrated that cyanine dyes such as ICG as well as cyanine dye-labelled compounds are actively taken up by hepatocytes, mediated through binding the organic anion transport protein (OATP) [62, 63]. This further alters the biodistribution and bioavailability and potentially limits sensitivity and specificity for imaging of liver processes.

10.2.2.3 Quenchers in OAI

For OI, a high quantum yield is most desirable; in OAI, the emitted fluorescence is merely an unwanted side effect. A low quantum yield—an only low fluorescence, following a specific excitation could even lead to a higher OAI signal as more energy can be converted into thermal energy and the consecutive US wave.

So-called dark quenchers fulfil this criterion: the excitation energy is almost exclusively converted into thermal energy and only very little fluorescence [64]. Commercially available dark quenchers are being used in FRET assays or to probe protease activity [65, 66].

The chemical structure of quenchers resembles cyanine dyes and specific engineering of the molecules provides solutions for site-specific labelling.

10.2.2.4 Quantum Dots

Artificial colloidal nanocrystals are called quantum dots (QD).

Comparable to cyanine dyes and other signalling molecules, QD can absorb light, usually broadly, and emit light of a very narrow wavelength spectrum in response.

The excitation and emission characteristics are determined by size and composition of the QD and thus tuneable according to the desired application [67].

Around a specific core, QD feature a shell or coating. The components of QD usually stem from the alkaline earth metals, the scandium, vanadium and/or chromium group [68].

Being built from some hundred to thousand single atoms, QD reach a size around 5 nm. Larger QD are hence eliminated via the reticuloendothelial system, smaller QD can still be cleared via the kidneys [69].

A major hurdle for QD when it comes to in vivo applications and specifically to use in humans is the inherent toxicity of the QD components such as the frequently present cadmium.

Moreover, QD and QD residues have been observed in specimen as long as two years after application and initial in vivo imaging.

10.2.2.5 Nanoparticles

Similar to QD, nanoparticles, nanoshells or nanotubes are optically tuneable based on their size and composition. They feature a dielectric core and a thin shell, in biomedical imaging applications most often gold [70]. Further content of nanoparticles is highly variable. They can be used for imaging as well as for photodynamic therapy, depending on the excitation light [71]. Moreover, nanoparticles can serve as carriers for drugs and additional contrast agents, e.g. for MRI.

The particles can be engineered with several binding and further signalling molecules [72]. Polar surface coating enables solubility in water/serum even though nanoparticles are quite large (between 1 and 100 nm).

10.2.3 Linkers/Spacers

Not actually an entity in its own right, clearly not one that gets a lot of attention of the uninitiated, spacers are crucial for tracer optimisation.

Especially small binding moieties lose binding capacity if labelled directly with a rather large signalling molecule.

The addition of a spacer at a site of the binding moiety that does not interfere with the crucial activity circumvents this issue.

Spacers can simply be long histone tags.

Length and structure of the tag can be used for tuning tracer characteristics, e.g. the circulation time or the lipo-/hydrophilicity. Tags can also promote temporary serum protein binding to increase the intravascular availability of the tracer even further.

In this context, the addition of a polyethylene glycol (PEG) to antibody fragments can alter liver uptake and aid imaging of liver lesions [73].

The size and the structure of the spacer can also influence the tracer signal intensity. Several fluorescent molecules in close proximity quench each others' signal. Especially probes that bear more than one signalling molecule therefore need carefully designed spacers.

10.3 Smart Probes

While perfusion-type contrast agents offer only limited contrast in target lesions, purely depending on the differences in perfusion/vascularisation and/or vascular integrity between tumour and healthy tissue and the signal of targeted probes at least competes against unbound tracer in the blood pool, smart probes do virtually not have any unspecific background signal to compete with—the signal and contrast to noise ratio is far higher than for the other two classes of contrast agents.

The price is a more complex chemistry that enables a change of signal characteristics upon interaction with the target and in this context a target that can interact and change a tracer molecule.

Among the first smart probe approaches was the imaging of protease activity [4]. The activity of proteases—cleaving of long-chain proteins—was used to activate fluorescence by separating cyanine dyes, linked to a long PEG chain and thereby quenched in the naïve state.

The resulting fluorescence was directly reflective of local protease activity and correlated with the infiltrative and overall malignant lesion potential.

Further developments of this paradigm have led to protease-specific probes for OAI [74].

To a similar extend, pH sensitive probes, changing conformation upon interaction with the subcellular environment have been used in cancer imaging experimentally [75, 76].

10.4 Summary

In the different classes of contrast agents for OI and OAI, particularly suited probes can be found or created for virtually every application in clinical or preclinical scenarios.

While unspecific contrast agents reflecting perfusion or vascularity (ICG) or cell metabolism (5-ALA) are already established clinical tools for diagnostics and image-guided therapy, the vast amount of targeted probes, tested and presented in preclinical studies, has still to prove usability and impact for patient care, and even for biological research. In this context, one could argue that OI or OAI are more suited for preclinical testing and optimisation of probes and methodology for further transfer to radionuclide-driven imaging for translation. In any case, identification of the appropriate target, the optimal, specific binding partner and the most effective label with regards to bioavailability of the tracer need to be considered and thoughtfully combined.

Smart probes have a very complex chemistry and are limited to few applications, defined by read-out parameters that can influence on tracer structure and consecutive performance. Initial clinical trials have not yet led to a broader application of smart probes and it is doubtful, they will in the near future.

Probe design requires a clear idea of the biological/pathological process, the imaging is desired to reflect and a plan for in vivo applications.

The model system, the availability of a potential target, the imaging modality and the expected kinetics and planned imaging time points should influence the choice of probe/tracer and label.

Further refinement in the chemistry of targeting moieties on the one hand and methodological sensitivity on the other will certainly foster and expand the potential use of OI and OAI for both, preclinical and clinical applications.

References

1. Towle EL, Richards LM, Kazmi SM, Fox DJ, Dunn AK (2012) Comparison of indocyanine green angiography and laser speckle contrast imaging for the assessment of vasculature perfusion. *Neurosurgery* 71:1023–1030; discussion 1030–1021
2. Joshi BP, Wang TD (2018) Targeted optical imaging agents in cancer: focus on clinical applications. *Contrast Media Mol Imaging* 2018:2015237
3. Ntziachristos V, Bremer C, Weissleder R (2003) Fluorescence imaging with near-infrared light: new technological advances that enable in vivo molecular imaging. *Eur Radiol* 13:195–208
4. Bremer C et al (2005) Optical imaging of spontaneous breast tumors using protease sensing ‘smart’ optical probes. *Invest Radiol* 40:321–327
5. Wall A et al (2008) Differentiation of angiogenic burden in human cancer xenografts using a perfusion-type optical contrast agent (SIDAG). *Breast Cancer Res* 10:R23
6. Tummers QR et al (2015) The value of intraoperative near-infrared fluorescence imaging based on enhanced permeability and retention of indocyanine green: feasibility and false-positives in ovarian cancer. *PLoS ONE* 10:e0129766
7. Wallace MB et al (2010) The safety of intravenous fluorescein for confocal laser endomicroscopy in the gastrointestinal tract. *Aliment Pharmacol Ther* 31:548–552
8. Schwarz C et al (2019) The value of indocyanine green clearance assessment to predict postoperative liver dysfunction in patients undergoing liver resection. *Sci Rep* 9:8421
9. Feenstra DJ et al (2019) Indocyanine green molecular angiography of choroidal neovascularization. *Exp Eye Res* 180:122–128
10. Handgraaf HJM et al (2018) Staging laparoscopy with ultrasound and near-infrared fluorescence imaging to detect occult metastases of pancreatic and periampullary cancer. *PLoS ONE* 13:e0205960
11. Schaafsma BE et al (2014) Optimization of sentinel lymph node mapping in bladder cancer using near-infrared fluorescence imaging. *J Surg Oncol* 110:845–850
12. Beck MC et al (2017) Fluorescence optical imaging in pediatric patients with inflammatory and non-inflammatory joint diseases: a comparative study with ultrasonography. *Arthritis Res Ther* 19:233
13. Al-TaHER M et al (2018) Intraoperative enhanced imaging for detection of endometriosis: a systematic review of the literature. *Eur J Obstet Gynecol Reprod Biol* 224:108–116
14. Nakaseko Y, Ishizawa T, Saiura A (2018) Fluorescence-guided surgery for liver tumors. *J Surg Oncol* 118:324–331
15. Skubleny D et al (2018) Diagnostic evaluation of sentinel lymph node biopsy using indocyanine green and infrared or fluorescent imaging in gastric cancer: a systematic review and meta-analysis. *Surg Endosc* 32:2620–2631
16. Capozza M et al (2018) Photoacoustic imaging of integrin-overexpressing tumors using a novel ICG-based contrast agent in mice. *Photoacoustics* 11:36–45

17. Chen Z, Dean-Ben XL, Gottschalk S, Razansky D (2018) Performance of optoacoustic and fluorescence imaging in detecting deep-seated fluorescent agents. *Biomed Opt Express* 9:2229–2239
18. Fukuda H, Casas A, Batlle A (2005) Aminolevulinic acid: from its unique biological function to its star role in photodynamic therapy. *Int J Biochem Cell Biol* 37:272–276
19. Wei L, Roberts DW, Sanai N, Liu JTC (2019) Visualization technologies for 5-ALA-based fluorescence-guided surgeries. *J Neurooncol* 141:495–505
20. Copland JA et al (2004) Bioconjugated gold nanoparticles as a molecular based contrast agent: implications for imaging of deep tumors using optoacoustic tomography. *Mol Imaging Biol* 6:341–349
21. Liopo A et al (2012) Biocompatible gold nanorod conjugates for preclinical biomedical research. *J Nanomed Nanotechnol* S2
22. Lozano N et al (2012) Liposome-gold nanorod hybrids for high-resolution visualization deep in tissues. *J Am Chem Soc* 134:13256–13258
23. Manohar S, Ungureanu C, Van Leeuwen TG (2011) Gold nanorods as molecular contrast agents in photoacoustic imaging: the promises and the caveats. *Contrast Media Mol Imaging* 6:389–400
24. Lankveld DP et al (2011) Blood clearance and tissue distribution of PEGylated and non-PEGylated gold nanorods after intravenous administration in rats. *Nanomedicine (Lond)* 6:339–349
25. Rayavarapu RG et al (2010) In vitro toxicity studies of polymer-coated gold nanorods. *Nanotechnology* 21:145101
26. Longmire M, Choyke PL, Kobayashi H (2008) Clearance properties of nano-sized particles and molecules as imaging agents: considerations and caveats. *Nanomedicine (Lond)* 3:703–717
27. Rhodes DR et al (2004) ONCOMINE: a cancer microarray database and integrated data-mining platform. *Neoplasia* 6:1–6
28. Shin G et al (2011) GENT: gene expression database of normal and tumor tissues. *Cancer Inform* 10:149–157
29. Srinivasarao M, Galliford CV, Low PS (2015) Principles in the design of ligand-targeted cancer therapeutics and imaging agents. *Nat Rev Drug Discov* 14:203–219
30. Choi HS et al (2007) Renal clearance of quantum dots. *Nat Biotechnol* 25:1165–1170
31. Deen WM, Lazzara MJ, Myers BD (2001) Structural determinants of glomerular permeability. *Am J Physiol Renal Physiol* 281:F579–F596
32. Ohlson M, Sorensson J, Haraldsson B (2001) A gel-membrane model of glomerular charge and size selectivity in series. *Am J Physiol Renal Physiol* 280:F396–F405
33. Kelloff GJ et al (2005) The progress and promise of molecular imaging probes in oncologic drug development. *Clin Cancer Res* 11:7967–7985
34. Kaur S et al (2012) Recent trends in antibody-based oncologic imaging. *Cancer Lett* 315:97–111
35. Freise AC, Wu AM (2015) In vivo imaging with antibodies and engineered fragments. *Mol Immunol* 67:142–152
36. Knowles SM, Wu AM (2012) Advances in immuno-positron emission tomography: antibodies for molecular imaging in oncology. *J Clin Oncol* 30:3884–3892
37. Strasser J et al (2019) Unraveling the macromolecular pathways of IgG oligomerization and complement activation on antigenic surfaces. *Nano Lett*
38. Wu AM (2014) Engineered antibodies for molecular imaging of cancer. *Methods* 65:139–147
39. Cooper MS, Sabbah E, Mather SJ (2006) Conjugation of chelating agents to proteins and radiolabeling with trivalent metallic isotopes. *Nat Protoc* 1:314–317
40. Kaden TA (2006) Labelling monoclonal antibodies with macrocyclic radiometal complexes. A challenge for coordination chemists. *Dalton Trans* 3617–3623
41. Lobo ED, Hansen RJ, Balthasar JP (2004) Antibody pharmacokinetics and pharmacodynamics. *J Pharm Sci* 93:2645–2668

42. Vugmeyster Y et al (2008) Preclinical pharmacokinetics, interspecies scaling, and tissue distribution of humanized monoclonal anti-IL-13 antibodies with different IL-13 neutralization mechanisms. *Int Immunopharmacol* 8:477–483
43. Wang W, Wang EQ, Balthasar JP (2008) Monoclonal antibody pharmacokinetics and pharmacodynamics. *Clin Pharmacol Ther* 84:548–558
44. Chiu ML, Gilliland GL (2016) Engineering antibody therapeutics. *Curr Opin Struct Biol* 38:163–173
45. Vogl T et al (2014) Alarmin S100A8/S100A9 as a biomarker for molecular imaging of local inflammatory activity. *Nat Commun* 5:4593
46. Chester KA et al (2000) Clinical applications of phage-derived sFvs and sFv fusion proteins. *Dis Markers* 16:53–62
47. Smolarek D, Bertrand O, Czerwinski M (2012) Variable fragments of heavy chain antibodies (VHHs): a new magic bullet molecule of medicine? *Postepy Hig Med Dosw (Online)* 66:348–358
48. Salvador JP, Vilaplana L, Marco MP (2019) Nanobody: outstanding features for diagnostic and therapeutic applications. *Anal Bioanal Chem* 411:1703–1713
49. Massa S, Xavier C, Muyldermans S, Devoogdt N (2016) Emerging site-specific bioconjugation strategies for radioimmunotracer development. *Expert Opin Drug Deliv* 13:1149–1163
50. Peng L et al (2018) Phage display-derived peptide-based dual-modality imaging probe for bladder cancer diagnosis and resection postinstillation: a preclinical study. *Mol Cancer Ther* 17:2100–2111
51. Eder M et al (2019) Bicyclic peptides as a new modality for imaging and targeting of proteins overexpressed by tumors. *Cancer Res* 79:841–852
52. Faust A et al (2015) Development and evaluation of a non-peptidic ligand for the molecular imaging of inflammatory processes using S100A9 (MRP14) as a novel target. *Chem Commun (Camb)* 51:15637–15640
53. Voller T et al (2018) A non-peptidic S100A9 specific ligand for optical imaging of phagocyte activity in vivo. *Mol Imaging Biol* 20:407–416
54. Keating JJ et al (2017) Intraoperative near-infrared fluorescence imaging targeting folate receptors identifies lung cancer in a large-animal model. *Cancer* 123:1051–1060
55. Georgakoudi I et al (2002) NAD(P)H and collagen as in vivo quantitative fluorescent biomarkers of epithelial precancerous changes. *Cancer Res* 62:682–687
56. Fernandes B, Matama T, Guimaraes D, Gomes A, Cavaco-Paulo A (2016) Fluorescent quantification of melanin. *Pigment Cell Melanoma Res* 29:707–712
57. Slooter MD, Janssen A, Bemelman WA, Tanis PJ, Hompes R (2019) Currently available and experimental dyes for intraoperative near-infrared fluorescence imaging of the ureters: a systematic review. *Tech Coloproctol* 23:305–313
58. van Manen L et al (2018) A practical guide for the use of indocyanine green and methylene blue in fluorescence-guided abdominal surgery. *J Surg Oncol* 118:283–300
59. Ptaszek M (2013) Rational design of fluorophores for in vivo applications. *Prog Mol Biol Transl Sci* 113:59–108
60. Ni Y, Wu J (2014) Far-red and near infrared BODIPY dyes: synthesis and applications for fluorescent pH probes and bio-imaging. *Org Biomol Chem* 12:3774–3791
61. Sato K et al (2016) Effect of charge localization on the in vivo optical imaging properties of near-infrared cyanine dye/monoclonal antibody conjugates. *Mol BioSyst* 12:3046–3056
62. Hage C et al (2018) Comparison of the accuracy of FMT/CT and PET/MRI for the assessment of antibody biodistribution in squamous cell carcinoma xenografts. *J Nucl Med* 59:44–50
63. Ho CM et al (2012) Use of indocyanine green for functional assessment of human hepatocytes for transplantation. *Asian J Surg* 35:9–15
64. Laramie MD, Smith MK, Marmarchi F, McNally LR, Henary M (2018) Small molecule optoacoustic contrast agents: an unexplored avenue for enhancing in vivo imaging. *Molecules* 23

65. Matayoshi ED, Wang GT, Krafft GA, Erickson J (1990) Novel fluorogenic substrates for assaying retroviral proteases by resonance energy transfer. *Science* 247:954–958
66. Swan DC, Tucker RA, Holloway BP, Icenogle JP (1997) A sensitive, type-specific, fluorogenic probe assay for detection of human papillomavirus DNA. *J Clin Microbiol* 35:886–891
67. Chinnathambi S, Shirahata N (2019) Recent advances on fluorescent biomarkers of near-infrared quantum dots for in vitro and in vivo imaging. *Sci Technol Adv Mater* 20:337–355
68. Himmelstoss SF, Hirsch T (2019) A critical comparison of lanthanide based upconversion nanoparticles to fluorescent proteins, semiconductor quantum dots, and carbon dots for use in optical sensing and imaging. *Methods Appl Fluoresc* 7:022002
69. Sukhanova A et al (2018) Dependence of nanoparticle toxicity on their physical and chemical properties. *Nanoscale Res Lett* 13:44
70. Padmanabhan P, Kumar A, Kumar S, Chaudhary RK, Gulyas B (2016) Nanoparticles in practice for molecular-imaging applications: an overview. *Acta Biomater* 41:1–16
71. Sarcan ET, Silindir-Gunay M, Ozer AY (2018) Theranostic polymeric nanoparticles for NIR imaging and photodynamic therapy. *Int J Pharm* 551:329–338
72. Wang K et al (2019) Small fluorescent albumin nanoparticles for targeted photothermal therapy via albumin-binding protein pathways. *Colloids Surf B Biointerfaces* 181:696–704
73. Maawy AA et al (2014) Specific tumor labeling enhanced by polyethylene glycol linkage of near infrared dyes conjugated to a chimeric anti-carcinoembryonic antigen antibody in a nude mouse model of human pancreatic cancer. *J Biomed Opt* 19:101504
74. Liu C et al (2018) Multispectral photoacoustic imaging of tumor protease activity with a gold nanocage-based activatable probe. *Mol Imaging Biol* 20:919–929
75. Shi H et al (2019) A simple, pH-activatable fluorescent aptamer probe with ultralow background for bi-specific tumor imaging. *Anal Chem*
76. Tang Y et al (2019) pH-Activatable tumor-targeting gold nanoprobe for near-infrared fluorescence/CT dual-modal imaging in vivo. *Colloids Surf B Biointerfaces* 179:56–65

Part II

Preclinical Studies



Preclinical SPECT and SPECT-CT in Oncology

11

Benjamin L. Franc, Youngho Seo, Robert Flavell,
and Carina Mari Aparici

Contents

11.1	Introduction.....	360
11.2	Part I: Evaluating the Potential Role of SPECT-CT Imaging in a Preclinical Oncology Research Application.....	361
11.2.1	Choice and Implications of Various Small Animal Models of Cancer.....	361
11.2.2	Choice of Imaging Modality.....	363
11.2.3	SPECT Versus SPECT-CT.....	365
11.2.4	SPECT-MRI.....	366
11.3	Part II: Technical Considerations When Implementing SPECT-CT in Preclinical Oncology Research.....	367
11.3.1	Anesthesia and Animal Handling.....	367
11.3.2	Availability of Radiopharmaceuticals and Evaluation of Their Biodistribution Characteristics.....	368
11.3.3	Injection of the Radiopharmaceutical.....	370
11.3.4	Injection of Contrast Agents.....	370
11.3.5	Radiation Exposure.....	370
11.4	Part III: State of the Art of Preclinical SPECT-CT Systems.....	372
11.4.1	SPECT-CT System Design.....	372
11.4.2	Radiation Detector.....	372
11.4.3	Collimator.....	373
11.4.4	Image Reconstruction Techniques.....	375
11.4.5	Quantitative SPECT-CT.....	376
11.4.6	Quality Assurance.....	377
11.4.7	A Sampling of Available Small Animal SPECT and SPECT-CT Systems ...	377

B. L. Franc (✉) · C. M. Aparici
Department of Radiology, Stanford University School of Medicine, 300 Pasteur Drive, H2232,
MC 5281, Stanford, CA 94305-5105, USA
e-mail: benster@stanford.edu

Y. Seo · R. Flavell
Department of Radiology and Biomedical Imaging, University of California, San Francisco,
USA

11.5	Part IV: SPECT-CT as Applied in the Preclinical Oncology Setting.....	379
11.5.1	Cancer Detection	379
11.5.2	Characterizing Tumorigenesis and Malignant Spread.....	379
11.5.3	Imaging the Targeting Abilities of Molecules in the Development of Potential Therapeutics and Molecular Imaging Agents.....	380
11.5.4	Small Molecules	382
11.5.5	Theranostics	383
11.5.6	Predicting Therapeutic Response and Monitoring Response to Therapy	383
11.5.7	Imaging Cell Trafficking	384
11.5.8	Imaging Gene Transfer and Expression.....	384
11.5.9	Imaging Drug Delivery and Using SPECT in Drug Design.....	386
11.5.10	Imaging Other Pathologic Processes Associated with Cancer or Cancer Therapies.....	388
11.6	Part V: Areas of Rapid Advancement of the Science of Molecular Imaging with SPECT-CT.....	388
11.6.1	Next-Generation Imaging Systems.....	388
11.6.2	Imaging Immune Activation	389
11.6.3	Multimodality Probes	389
11.6.4	Radiomics and Computational Advances	389
11.7	Conclusion	390
	References	390

11.1 Introduction

Cancer is a dynamic molecular process. Its understanding requires the study of the multiple interactions of complex biologic systems. This is performed initially in animals (preferably small mammals) in a way that spatially and temporally recapitulates that seen in humans.

Traditional methods employing single-tissue culture or tissue sectioning in small animal models of disease no longer appear sufficient to address the complex, highly intertwined, and heavily dynamic cancerous processes. Molecular imaging of small animal models on the other hand enables the study of real-time molecular interactions in a living system. Single-photon emission computed tomography (SPECT) imaging of gamma-emitting radionuclides offers a powerful method of observing processes in vivo with many advantages over other modalities. One of the main advantages could be the ability of obtaining several metabolic images of the same process at the same point in time by administering several radiopharmaceuticals simultaneously. With the appropriate window selection or list mode acquisition, a metabolic image of every single radiopharmaceutical could be obtained.

By incorporating anatomic data from CT (computer tomography), SPECT-CT provides enhanced tissue-specific radiopharmaceutical localization, as well as the opportunity to improve imaging by correcting the SPECT data for such physical processes as attenuation of the gamma photons by soft tissue, photon scatter, and collimator blurring. In fact, many small-animal SPECT and SPECT-CT systems

enable nowadays exquisite sub-millimeter resolution of images of targeted biochemical processes in vivo.

As SPECT radiopharmaceuticals and multimodality imaging have been progressively adopted in the clinic, the development of new models of studying the course and therapeutic response of various cancers using multimodal approaches in small animals have accelerated [175]. SPECT-based quantitative imaging also continues to advance secondary to innovations in detector and collimator hardware, image reconstruction methodologies, computational capabilities, and software. SPECT-CT can be an extremely powerful tool in the hands of an oncology investigator who understands the underlying physics of image acquisition, reconstruction, and quantification, as well as the limitations of the specific animal model utilized and the targeting method(s) of the radiopharmaceutical agent employed in the study. Generally, a successful oncology SPECT-CT program includes a team of individuals with expertise in pathophysiology, biology, physics, and chemistry.

Certainly, this chapter cannot exhaustively address each of the important components of preclinical SPECT. It is meant to provide, however, a place to begin in the implementation of SPECT and SPECT-CT in preclinical oncology work. The chapter is presented in five parts: Part I focuses on various considerations when choosing SPECT-CT in preclinical oncology applications; Part II focuses on considerations when implementing SPECT-CT; Part III describes the “state of the art” in small animal SPECT-CT device and reconstruction technology; Part IV provides some examples of the types of preclinical questions and molecular processes that SPECT-CT is suited to address; and Part V explores those areas that are pushing the boundaries of current preclinical SPECT and SPECT-CT.

11.2 Part I: Evaluating the Potential Role of SPECT-CT Imaging in a Preclinical Oncology Research Application

11.2.1 Choice and Implications of Various Small Animal Models of Cancer

Preclinical small animal models abound [192], but mouse models are popular given the mouse genome is 95% identical to the human genome. Mouse models include induction of tumors in syngeneic mice, human xenografts grown in immunodeficient mice, and spontaneous tumors in genetically engineered mice [45].

Syngeneic mouse models are generated using primary induction of a tumor in a mouse via chemical or surgical means (mouse A) with subsequent orthotopic or subcutaneous implantation of tumor cells from this primary tumor to a naïve animal of the same species (mouse B). Orthotopic models attempt to recapitulate the natural environment of a tumor type but require surgical technical skills and a more sophisticated surgical setup than simple subcutaneous implantation. While offering a logistically easy and reproducible approach to generating the tumor model in

immunocompetent mice, the mapping of biochemical processes from tumors derived from mice to those derived from humans is often not clear and many such models are not representative of the human form of the cancer being modeled. Generally, this risks the development of models of biochemical pathways that are mouse-specific or developing therapeutic agents that treat the mouse form of the disease, but not the form seen in humans, although notable exceptions exist [118]. From an imaging perspective, these models are quite straightforward to study, as they are immunocompetent and therefore do not require the level of sterile conditions as other models. In addition, tumors are in a pre-assigned location, usually optimal based on the biodistribution of the SPECT radiopharmaceutical, allowing targeting the imaging field of view of a primary site with SPECT or SPECT-CT. Although theoretically, given these characteristics, the syngeneic mouse models should allow a method of easily performing serial SPECT imaging of a process or tumor response to therapy, logistics of the local small animal resource center or geographic relationship between the institution's animal care center and SPECT imaging facilities may prevent this type of serial imaging, and investigators must take significant care in planning their experiments in light of these potential logistical hurdles. Some institutions may allow temporary holding of a small group of animals in the imaging facility itself to enable such long-term studies with limits based upon the total amount of radioactivity emitted from the animals stored at any one time.

Xenografts and allografts utilize human-derived cell lines or explants that are then implanted in subcutaneous or orthotopic locations in immune-deficient mice (e.g., athymic (nu/nu) mice or mice with severe combined immunodeficiency (SCID)). Specific human cell lines of a cancer may be chosen because they express a specific molecular marker that can be targeted for imaging or therapy, or are derived from malignant cells within a particular phase of a cancers' metastatic progression. For example, just in prostate cancer alone, more than 30 cell lines developed over the past century showing differing levels of expression of androgen receptor (AR) and prostate-specific antigen (PSA) (two of the key molecular targets in clinical prostate cancer imaging and therapy) [198]. Alternatively, naïve cell lines can be genetically engineered to express such a specific molecular marker. The mouse environment may or may not accurately reflect the human environment for a specific tumor type, and xenograft models have shown correlation between pre-clinical and clinical efficacy only in specific cell types and under specific conditions [206]. Despite this, xenograft models have remained the most widely utilized *in vivo* tumor models and are particularly valuable in testing hypotheses about tumor growth and differentiation when those questions are reasonably separable from the tumor environment, or in the development and evaluation of therapies that require immune response or that target specific components of blood vessels or the extracellular matrix [29, 178]. SPECT imaging studies with these types of models can be challenging given the higher degree of sterility demanded by immunosuppressed animals and the inherent logistical hurdles of serial studies. Short-term serial studies (over a period of a few days to 2 weeks) may be accomplished using a temporary holding facility in the imaging suite. Alternatively, both

institution-specific and commercial efforts have been made to provide solutions to the transport of small animals between the imaging device and the sterile barrier.

The availability of *genetically engineered* mouse strains has improved significantly over the past decade due, in part, to multi-institutional collaborative efforts such as the National Cancer Institute's Mouse Models of Human Cancer Consortium in the United States. Genetically engineered spontaneous mouse models of cancer offer the ability to study the genesis of a malignancy from its initial development through its course of progression to local and eventual distant metastasis in an immunocompetent mouse system [58, 145]. Broadly, spontaneous mouse models can be separated into "knock-in" models, where the endogenous sequence of a gene is exchanged for one that mimics carcinogenesis in the human, and "knock out" models, where the function or expression of an endogenous gene is suppressed. Although these models utilize syngeneic mice, the genetic, molecular, and histologic characteristics of spontaneous tumors in these models often closely reflect those of the human form of the malignancy and have been integral in the elucidation of the molecular mechanisms behind various forms of carcinogenesis [14, 53, 122, 145]. The background in which the tumor arises, for instance, in BRCA-null murine breast cancer models, may also more closely mimic the clinical patient for whom a drug is being developed [59]. The ability to study the tumor and its interactions with the molecular environment is invaluable. Drawbacks of these models are the high cost of developing and maintaining such mouse lines and the high degree of expertise required for maintenance of such strains, underscoring the advantage of collaborating with a mouse model group.

Within each of these general classifications of mouse tumor models, further refinement of the specific model chosen for study depends on whether primary or metastatic malignancy (e.g., metastatic disease to bone, lung, or brain) is being studied [164, 174, 233]. If *in vivo* characterization of an oncologic process is to be addressed using *in vivo* imaging, including SPECT, the level of robustness of the animal to withstanding multiple manipulations and the logistics of studying the tumor using *in vivo* imaging must be considered to ensure the success of the study. The idea of *in vivo* imaging is to image processes in a *live* animal. An overview of the advantages and disadvantages of various tumor models is provided in a recently published set of guidelines for the use of animals in cancer research [215].

11.2.2 Choice of Imaging Modality

Traditional methods of monitoring molecular processes, tumor growth, and tumor response to therapy in small animals are still often accomplished using tissue sectioning and pathology (or in the case of radionuclide-based assays, well-counting, and autoradiography), after euthanasia. These traditional methods provide relatively inexpensive and the vast majority of molecular markers that can only be assayed using histological methods. However, they are temporally very static since they only provide information at a single time point; therefore, it usually requires large cohorts of animals to gather temporal and developmental information.

Molecular imaging modalities on the other hand have certainly assumed a critical role in monitoring a single animal over serial time points. Obviously, it behooves the researcher to thoroughly plan the imaging portion of any research project before even initiating growth of the first tumor in the first animal model as the research questions, required measurements, chosen animal model, and available imaging modalities must all be in sync spatially and temporally to ensure valid data. Thoroughly planned, molecular imaging studies may not only provide unique, *in vivo*, real-time information of multiple processes happening at the same time, but significantly reduced the number of animals required to gather the so needed information.

Questions of anatomical growth of a spontaneous tumor are best answered using high-resolution anatomical imaging methods, such as MR or CT. Questions related to viable mass of implanted tumor may be most easily addressed with bioluminescence. Perfusion may be studied with MR, fast-acquisition CT, SPECT, or PET. Studies of physiologic processes involving major organic molecules or studies requiring absolute quantification may be addressed with SPECT and PET. SPECT is useful at identifying ligand–receptor relationships, monitoring the locations of administered radiolabeled molecules (over a short time course), and *in vivo* molecular characterization of tumors. Newer imaging systems incorporating SPECT in tandem with higher resolution CT and/or MRI obviously offer the potential to answer questions about both tumor growth and molecular expression in a single imaging study.

In vivo gamma imaging (including SPECT) is most applicable to studying deep tissues and is therefore particularly suited for orthotopic tumor models with/without potential for metastasis (for example, LNCaP orthotopic prostate cancer model [210]) or spontaneous tumor models (for example, pancreatic neuroendocrine tumors in transgenic models [76]). Structures at or just below the skin's surface/subcutaneous tissues and tissues able to be accessed via endoscopic means may be more amenable to optical imaging (bioluminescence versus fluorescence), a group of techniques that are relatively inexpensive, utilize stable imaging agents, and do not subject the animal or tumor to ionizing radiation. PET imaging offers equal or higher sensitivity than SPECT and allows for absolute quantification, an area where significant progress has been made in SPECT in only the past decade. However, PET may require a close by cyclotron and other sophisticated infrastructure.

Thus, gamma imaging/SPECT is uniquely suited for studying the presence of specific molecular markers or processes in small animal cancer models when a radiolabeled ligand is able to be produced. SPECT is also capable of providing images of multiple probes labeled with different isotopes that emit different energy levels of gamma emission, enabling simultaneous study of multiple molecular or cellular events. SPECT is capable of resolving very small primary tumors or their metastases (on the order of 0.5–2 mm), and therefore is a viable method for evaluating all types of mouse models of cancer, including spontaneous models where the primary or metastatic sites may be unknown and can be quite small.

11.2.3 SPECT Versus SPECT-CT

The integration of SPECT-CT in a single small animal imaging device has been accomplished by mounting both CT and gamma camera components on a single gantry in an “in-line” configuration. The CT portion of these systems typically comprised of a microfocus X-ray tube source and X-ray detector (e.g., a charge-coupled device or a complementary metaloxide semiconductor with pixels on the order of 50 μm), achieving reconstructed resolutions of $<100\mu\text{m}$. Contrast may also be used to enhance delineation of soft tissues, although this proves to be quite challenging.

When utilizing small animal tumor models in which small tumors are growing in deep tissues, the co-registration of SPECT images with CT can be invaluable as physiologic excretion of the tracer or focal tracer collection in the blood pool can be differentiated from a small soft tissue tumor due to anatomical localization on the CT. In humans, the CT portion of the SPECT-CT often provides near-diagnostic quality images that clearly elucidate the anatomic abnormality associated with the abnormality or lesion identified on SPECT and can greatly assist in the diagnosis. In practice, the CT portion of the SPECT-CT for small animals has, in the past, been more limited in its contribution, secondary, in part, to (1) the difficulty in administering the volumes of contrast necessary through the tiny veins of a mouse in any time period in which images could be acquired, (2) the difficulty in timing administration of oral contrasts in feeds with anesthesia and imaging, (3) the compact nature of the organs in lab animals as compared to the typical patient, whose slower metabolism allows for the accumulation of a significant amount of fat that separates organs and other anatomic structures, and (4) the relatively low levels of radiation used in small animal CT systems and the limitation on signal-to-noise ratios imposed by small voxel sizes. It is not common for small tumors within organs to be able to be seen discretely on the CT portion of small animal SPECT-CT. Realistically, the correlation of focal radiopharmaceutical uptake on SPECT just within a specific organ location (e.g., the pancreatic head), within a discrete soft tissue structure (e.g., localization within nodule surrounded by fat rather than localization within adjacent muscle), or simply in relation to the skeleton is considered a successful contribution of CT in small animal SPECT-CT.

A more substantial contribution of CT in SPECT-CT may be its use to assemble an attenuation map and to provide structural data for incorporation into the reconstruction algorithm (CT for attenuation correction and anatomic localization or CTAC). By providing correction of the SPECT image for attenuation and potentially scatter, these types of reconstruction algorithms will undoubtedly play a large role in the future of SPECT-CT’s use in small animal imaging as there is an ever-increasing demand for quantitatively accurate imaging of radiopharmaceutical distribution.

The remainder of this chapter will focus on SPECT-CT as a single dual-modality imaging method for preclinical oncology studies.

11.2.4 SPECT-MRI

The concept of additional hybrid combinations, including SPECT-MRI, offers potential advantages over SPECT-CT. Compared with CT, MRI has superior soft tissue contrast. While this does not matter for the commonly used subcutaneous xenograft models, this offers particular advantages for orthotopic or genetically engineered spontaneous tumor models, in which the tumor is either implanted or spontaneously grows in another region of the body. For example, brain tumors, and abdominal and pelvic tumors such as prostate, renal cell, or pancreatic cancer, are far easier to delineate on MRI compared against non-contrast CT. Improved soft tissue contrast would therefore enable improved delineation of regions of interest in these models, and therefore more accurate interpretation of the SPECT data. Devices have been reported combining SPECT with MRI [67, 74, 75, 140, 187].

MR, however, tends to be quite expensive to implement, usually focuses on a narrow field of view, and provides access to interrogation of a limited number of processes unless spectroscopic or other advanced time-intensive techniques are employed. There has been continued interest, nevertheless, in the development of contrast agents for MR imaging [160]. An alternative approach is to fuse MRI images with SPECT/CT images in a post hoc fashion after acquisition [52]. These preliminary systems have also spawned interest in the synthesis and initial evaluation of combined SPECT and MRI probes, for example, by combining superparamagnetic iron oxide nanoparticles (SPIO) with radiolabeled antibodies [149]. However, owing to various technical limitations, and increased utilization of PET versus SPECT imaging, there has not yet been a SPECT/MRI system reported [24, 89].

Specific applications amenable to SPECT-MRI might include nanoparticle-based contrast agents, or combination of one or several simultaneous SPECT agents (to provide localization) with advanced magnetic resonance imaging techniques to enable detailed metabolic analysis. One such technique is hyperpolarized ^{13}C magnetic resonance imaging (HP-MRI), in which the signal-to-noise ratio of administered ^{13}C labeled probes can be markedly increased by the process of dynamic nuclear polarization. This method, most commonly utilized with ^{13}C pyruvate, has been applied in preclinical models [3], and more recently, in patients [158]. Recently, this technology has been combined with ^{18}F -FDG PET, with the intriguing finding of similar metabolic profiles between ^{18}F -FDG and ^{13}C lactate production [72]. These intriguing results suggest that HP-MRI could be combined with SPECT in future studies.

11.3 Part II: Technical Considerations When Implementing SPECT-CT in Preclinical Oncology Research

11.3.1 Anesthesia and Animal Handling

SPECT-CT imaging typically captures a snapshot of a biochemical/ molecular process at a specific time point. With current systems, anesthesia is required to avoid deterioration of image quality from animal motion and to ensure high spatial resolution and accurate co-registration of the SPECT and CT portions of the exam. Experimental conditions before, during, and after imaging must remain consistent across the population of animal studies and should minimize stress to the animal. The same animal strain and sex should be used throughout a study to avoid altered baseline pharmacokinetics and physiology. The timing of imaging experiments should take the circadian cycle into account to enable reproducibility [85]. Body temperature before, during, and after anesthesia can be controlled using a combination of circulating water pads and/or heated stages combined with physiologic monitoring built into many commercially available imaging systems [209]. Even throughout the imaging period, anesthetized animals require constant attention. Although rodents have very rapid heart and respiratory rates, equipment is available for monitoring the physiology of small animals. In vivo studies can go very badly very quickly, and ex vivo imaging is usually not the primary goal in SPECT-CT.

Anesthetics commonly employed to restrain small animals during imaging include injected drugs, such as barbiturates and ketamine, and inhaled anesthetics such as isoflurane. Highly lipid-soluble barbiturates, such as pentobarbital, are short- or ultrashort acting, typically resulting in anesthesia times of <1 h and total sleep times <2–3 h. Side effects that could affect image acquisition approach include respiratory depression and reduced cardiovascular output. Ketamine, another injectable (i.v. or i.p.) drug that is commonly employed along with other anesthetics, lacks a significant effect on respiration or cardiac output. Obviously, if a SPECT imaging agent targets adrenergic receptors or other points along the sympathetic nervous response, ketamine would potentially interfere with the study. There is also evidence of other potential changes in tracer biodistribution that depends on the anesthetic agent used, particularly when targeting processes in the brain. In intracranial applications, a mouse conscious restraint system may be preferred over anesthesia. Ketamine is commonly administered with a muscle relaxant/sedative (e.g., xylazine) and, as such, can provide anesthesia for <30 min and total sleep times <1–2 h. Importantly, potential side effects of the ketamine/xylazine combination include respiratory depression, hypotension, bradycardia, hypothermia, and hypoglycemia [85]. The experimental setup must take into account these potential side effects. For example, an i.v. catheter may need to be maintained during the imaging study in case hydrating fluids or glucose needs to be administered. Likewise, all setups should include a heat lamp to avoid hypothermia. Inhalation anesthetics offer significantly improved control of anesthesia than injectable anesthetics and possess less potential for impaired cardiac function as

well as more rapid recovery times. However, special preparations and space requirements may be needed to implement inhaled anesthesia in the imaging suite before and during the acquiring of the SPECT-CT images. This will depend on the configuration of the SPECT-CT imaging system and the space available. Dead space in the anesthesia circuit should be minimized [40].

In general, the stress of anesthesia, and in particular, multiple sequential episodes of anesthesia, must be considered and minimized when designing experiments. In most instances, including serial imaging studies of animals with more advanced tumor burden, inhaled anesthetics, such as isoflurane or sevoflurane, are preferred over injected anesthetics, such as ketamine/xylazine or avertin. When using inhaled anesthetics, the dose of anesthetic can be titrated and rapidly reversed [209]. Complications of anesthesia include hypothermia, pulmonary atelectasis, hypercapnia, acidosis, hypoxia, hepatic toxicity, and tracheal irritation from repeated intubations [40]. Not only can these causes significantly alter the biodistribution of the radiopharmaceutical, but they can be life-threatening to the animal research subject. Simple strategies, such as employing multiple animal cohorts with imaging time points that partially overlap, can be useful in reducing the risk of losing critical amounts of data secondary to imaging-related complications.

Because anesthesia and animal handling can both influence molecular processes systemically, they can potentially have non-negligible effects on the biodistribution of radioactively labeled tracers. More extended anesthesia and special imaging chamber setups may be necessary if the researcher also wants to perform MR or image the distribution of a PET radiopharmaceutical with subsequent co-registration to SPECT-CT images [37]. When transferring an animal between imaging systems for a single experiment, pre-planning is critical such that anesthesia and supportive care is not interrupted. For example, if the animal is to transfer from a SPECT-CT system to MRI, or if SPECT-MRI is employed, MR-compatibility of anesthesia equipment, heat packs, physiologic monitoring, and other supportive equipment must be considered.

11.3.2 Availability of Radiopharmaceuticals and Evaluation of Their Biodistribution Characteristics

Several commercially available single-photon-emitting radiopharmaceuticals are available for clinical use and can also have applications in small animal imaging. These include In-111-labeled pentetrotide, a somatostatin analog that can image neuroendocrine tumors [18]; Tc-99m-sestamibi and Tc-99m tetrofosmin, two cardiac perfusion agents that have also been utilized in a number of oncologic applications such as in brain cancer, lung cancer, and lymphoma [179]; and In-111-labeled capromab pendetide (Prostascint) for tumors expressing prostate-specific antigen. In addition, other indirect tumor imaging agents, such as Tc-99m-methylene diphosphonate (MDP) that targets osteoblastic activity surrounding osseous metastatic disease, have proven useful in proving the validity of various mouse bone metastatic models using small animal SPECT [222].

In addition, relatively straightforward chemistry has also been developed to label molecules for specific applications in small animal SPECT. For example, radiolabeled antibodies (such as Tc-99m epidermal growth factor receptor (EGFR) [139]) and labeled peptides can be prepared using direct labeling of a moiety or via a linkage/chelator mechanism [68]. Some molecules that have been extensively studied, such as annexin V, have been labeled with a variety of gamma-emitting radionuclides, each with their own set of advantages and disadvantages [15]. In single-chain antibody fragment synthesis and peptide synthesis, there is greater flexibility in techniques as amino acids enabling direct labeling can be incorporated outside of the active targeting site [17, 203]. Manual or automated peptide synthesis can be used to produce targeting probes containing synthetic amino acids with sites for post-synthesis radiometal chelation [183]. Alternatively, disulfide bonds, strategies utilizing high-affinity streptavidin–biotin interactions, or other techniques can be used to link the targeting portion of the molecule to the radionuclide-containing residues [205]. Other small-molecule classes, such as nucleic acids, have also been radiolabeled with radionuclides capable of being imaged with SPECT [134, 135, 137].

Of paramount importance is optimizing the radiopharmaceutical for SPECT-CT imaging by optimizing its ratio of uptake in the tumor to that in background (T:B) through chemistry-mediated methods and timing, as well as optimization of its biodistribution. Selection of chemistry techniques and strategies can have significant ramifications on the biodistribution of the resulting radiopharmaceutical. For example, non-specific binding of Tc-99m to the amino group when labeling antibodies has been shown to occur in a significant fraction of the labeled molecules and can lead to increased hepatic uptake and resulting diminished uptake in the tumor itself [100]. One strategy to enhance target-to-background activity has been to image farther out from the time of radiopharmaceutical administration as the non-specific uptake in organs often dissipates over time. By maintaining targeted molecular imaging agents in circulation, modification with polyethylene glycol chains allows greater bioavailability for tumor uptake [108]. Coupling of antibody fragments with larger molecules, such as albumin, have also demonstrated increased tumor targeting, deposition, and retention, as well as high tumor to blood ratios [47].

Such techniques are especially useful in designing effective molecular radiopharmaceuticals for small animal SPECT applications because of the high metabolic rates of rodents and the resulting rapid extraction of agents from the blood by the liver and kidneys. When using conjugate linkers, stability of the chelate is a key factor in acquiring high-quality images and parameters of stability should be provided by the radiochemistry laboratory. Methods to improve stability, such as modifying peptide sequences to enable better coordination with chelator, can be useful [109].

11.3.3 Injection of the Radiopharmaceutical

As a rule of thumb, the maximum volume of an intravenous injection should not exceed 4–5% of the animal's blood volume. Thus, coordination between the animal imaging researcher and the radiochemistry laboratory is imperative. Increasing the time between radiochemistry preparation and purification results in decreasing the dose/volume injected and can result in decreased sensitivity for the detection of a specific molecular target. Potential for breakdown of the radiopharmaceutical must also be considered when planning for the time before dose administration as well as the pH, buffer capacity, and other characteristics of the solvent in which the radiopharmaceutical is administered. Some purified agents may be highly acidic or basic, and care must be taken to provide these to the animal in a form that does not damage the vein or adversely affect the animals' health. The specific activity (radioactivity per mass) will also decrease over time for any given radiopharmaceutical. As this occurs, for any administered dose, a larger number of molecules are injected. The relatively lower initial specific activity of many SPECT imaging probes in general and the requirements of high specific activity for increased spatial resolution equate into an elevated risk that a higher binding occupancy of receptors will be achieved, enabling a pharmacologic effect rather than simply providing labeling of a small number of receptors for imaging [85].

Of course, if more than a single imaging time point is planned prior to animal sacrifice, the injection must be made only following sterile preparation of the injection site. More complicated injection scenarios (such as under a biologics hood) may be required in the case of immunodeficient mice (e.g., SCID mice).

11.3.4 Injection of Contrast Agents

In small animal SPECT-CT, constant infusion of CT contrast agents is typically required for fast excreting IV iodinated contrast that is used, with exact volume rates depending on the concentration of iodine in the contrast agent. Thus, volumes of administered fluid may exceed those that can be handled by the circulatory system. Complications of CT contrast agents in mice include renal toxicity and hypersensitivity. This issue can be avoided when slow circulating contrast agent based on iodinated lipids or metal nanoparticles. However, these preclinical-only CT contrast agents also present other challenges in terms of much higher cost and requirement of well-controlled injection.

11.3.5 Radiation Exposure

One drawback to SPECT-CT is the added dose of ionizing radiation in forming the CT image over that of SPECT alone. Radiation doses to the small animal subject during SPECT during a single study are probably non-significant, with whole-body exposure estimates ranging from 6 to 90 cGy in mice and 1 to 27 cGy for rats [64].

Tissue activity concentrations in small animal studies are higher than in humans but the small size of rodents results in a higher fraction of gamma radiation escaping prior to interaction with the animals' soft tissues. Cumulative effects of radiation provided by multiple administrations of radiopharmaceuticals are not negligible. For instance, the kidneys retain circulating peptides for significant periods, and long-term nephrotoxic effects have been observed in mice administered In-111-labeled peptides (octreotide, exendin, octreotate, neurotensin, and mini-gastrin analogs) for imaging at 3–6-week intervals over a course of 16–20 weeks. Murine gene expression can be altered at doses of 20 cGy [141, 142, 5, 6] (Amundson et al. 2001b).

Radiation provided to the small animal during a single CT exam is probably also insignificant in most cases. Using thermoluminescent dosimeters (TLDs), Figueroa and colleagues showed that the average mouse organ received a radiation absorbed dose of 76.0 ± 5.0 mGy [61]. Others have reported radiation doses ranging from 35 to 300 mGy [19]. Direct measurement of absorbed dose of radiation from CT associated with small animal SPECT-CT studies suggests the potential for high dose levels, particularly in those animals undergoing serial scans [207].

Reference CT images can be produced without observable DNA damage or compromised image quality if low voltage, flux, and exposure times are implemented; however, the standard settings provided by the manufacturer tend to underestimate the actual absorbed dose. Care must be given to truly understand the parameters of the imaging system and not treat the system as ready to use “out of the box” [106]. Radiation-induced tumorigenesis is not generally a concern given the relatively short timeframes of any serial mouse imaging studies and the long-time frame of radiation-induced malignancy. However, multiple exposures to radiation from CT may have a positive or a negative effect on tumor growth. Using histomorphometry, a study evaluating the effect of weekly small animal CT studies over a course of 5 weeks on a mouse model of breast cancer metastatic to bone found a significant increase in tumor areas in the leg bones of mice that received weekly CT exposure when compared to mice without such exposure [43]. On the other hand, there is a theoretical possibility of some therapeutic effect of the radiation provided to tumors by CT over multiple serial imaging time points. Even over multiple studies, however, there is an ability to minimize CT radiation dose to a level that would be unlikely to have any such therapeutic effect by adjusting various acquisition parameters or utilizing a multidetector system that is capable of ultrafast CT [22]. These parameters will be discussed later in this chapter. In extreme cases, such as monitoring expression of a tumor receptor with SPECT-CT imaging on a near-daily basis over a prolonged period (e.g., over the course of several weeks), SPECT alone could be considered, but, for the foreseeable future, SPECT-CT will be the standard modality for *in vivo* gamma imaging in small animals.

11.4 Part III: State of the Art of Preclinical SPECT-CT Systems

In a limited number of cases, such as renal scintigraphy, organ-based functional analyses can be accomplished using clinical SPECT systems [181]. However, when the anatomy of the application is complex, such as in gastric motility studies [163], or the target of imaging is small, such as most tumors or their metastases [78], molecular oncologic imaging requires a dedicated system designed specifically for small animal imaging. An alternative to a dedicated small animal SPECT or SPECT-CT camera is the use of a clinical SPECT system in combination with a multipinhole collimator [50]. This may be the most efficient use of space for an imaging laboratory that performs studies in animals of a range of sizes (e.g., mice, rats, sheep, pigs, dogs, and/or horses).

11.4.1 SPECT-CT System Design

While it is unlikely that the small animal imaging researcher in oncology will have the opportunity to choose the exact model of SPECT-CT imaging system to be used in a particular study and will likely have to accommodate the one available at the given research institution, it is important to understand the general parameters governing the acquisition of quality SPECT images and the particular characteristics inherent to the system being utilized. The following summary of the key components of a preclinical SPECT-CT system points out the key attributes of the various design choices.

11.4.2 Radiation Detector

A critical step in the image-making process is acquisition of projection information of the radiopharmaceutical distribution by the detector. In order to enable eventual reconstruction of high-quality images, detectors must have a high intrinsic efficiency, good energy resolution, and good intrinsic spatial resolution (Madsen et al. 2007).

Detector technology has also advanced, moving from traditional scintillators to small compact detectors specifically designed for application in small animal SPECT. The earliest dedicated small animal SPECT systems employed traditional NaI(Tl) scintillators, largely because these crystals produce a large light output. Newer crystal technologies without hygroscopic characteristics are being evaluated for specific applications in small animal SPECT-CT [101]. Detectors composed of lutetium yttrium orthosilicate (LYSO) crystal have shown improved spatial resolution over that of a NaI(Tl) detector, though the low intrinsic activity in the energy window limits potential applications to those where energy resolution is less important [48]. Employing pixilation of newer crystal detectors in concert with

position-sensitive photomultiplier tubes has been evaluated. Position-sensitive photomultiplier tubes and segmented scintillation crystals allow more efficient use of detector area and enable greater magnification. For example, pixelated Ce-doped Gd₂SiO₅ (GSO) block detectors with high quantum efficiency position-sensitive photomultiplier tubes (PSPMTs) have shown the potential to improve imaging of low-energy gamma photons [221]. When utilizing cameras with position-sensitive photomultiplier tubes, it is important to pay close attention to calibration to achieve good spatial uniformity and to correct for pincushion distortion.

Semiconductor-based or solid-state detectors such as cadmium telluride (CdTe) [2, 71] and cadmium zinc telluride (CdZnTe, or CZT) allow excellent energy discrimination, important in dual-energy tracer applications [111, 168]. Solid-state materials directly convert the gamma-ray to an electrical signal and have proven to provide images with very high spatial resolution as well as both high- and low-energy resolutions [105]. Older CZT detector systems can be prone to minute impurities associated with low-energy spectral tailing, pixel dropout, hot spots, and nonuniform response [186]. Methods to correct pixel defects in CZT detectors have been developed [219]. Since CZT has been adopted for a few clinical SPECT systems, the quality and stability of CZT detectors have improved greatly.

11.4.3 Collimator

Parallel hole collimation is most relevant for planar imaging. When employed in SPECT applications, the parallel hole collimator trades high sensitivity for lower resolution [84]. Parallel hole collimators of various materials and hole sizes are available or can be machined, depending on the required functional parameters such as spatial resolution and sensitivity [166]. Applications requiring greater sensitivity may benefit from other collimator configurations, such as slit-hole collimator [133].

Most modern small animal SPECT and SPECT-CT systems employ single-pinhole or multiple-pinhole collimators that may be optimized for a number of applications. For example, given their difference in size, mice and rats may be optimally imaged using different collimators [16]. In design of pinhole collimators, there is a balance of material, geometry, and reconstruction approach [95]. The earliest pinhole systems were composed of a single scintillation camera with a single-pinhole collimator. Systems have evolved to include multiple detectors, each with multipinhole collimators, allowing a combination of high (millimeter or sub-millimeter) spatial resolution and rapid acquisition speed (Fig. 11.1). The multipinhole design can increase the system sensitivity by approximately a factor equal to the number of pinholes allowing better spatial resolution from the use of smaller pinholes without sacrificing counting statistics. When using a multipinhole collimator, an important distinction to make is whether the collimator design is non-overlapping or overlapping (multiplexing). Multiplexing can diminish the signal-to-noise ratio and may facilitate artifacts. Of course, the choice of collimators also depends on the application: small field-of-view acquisitions (e.g., of an intracranial malignancy) can benefit from pinhole collimation while parallel hole

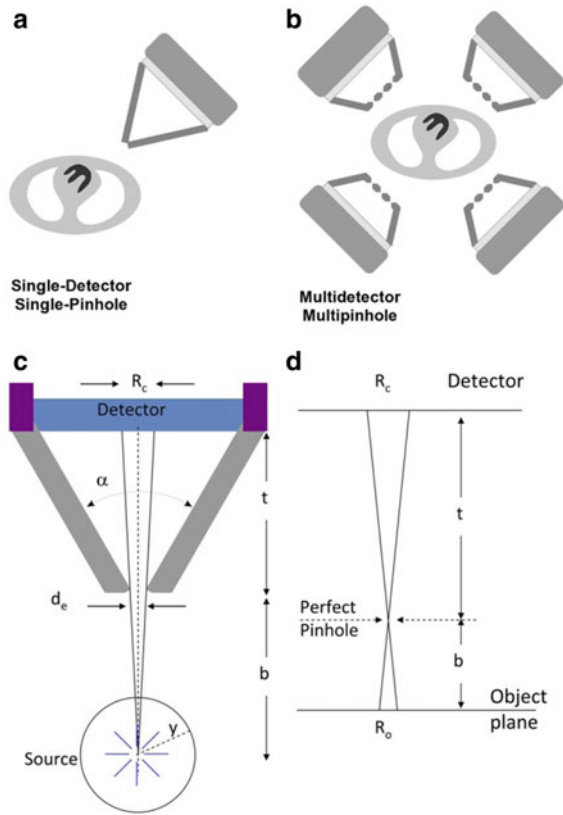


Fig. 11.1 Schematic diagrams of single- (a), multipinhole–multidetector (b) small animal SPECT systems. The image magnification is achieved by the source-to-pinhole-to-detector geometry (c and d). R_c = geometric resolution measured on detector plane; R_o = detector point spread function projected to object plane; d_e = pinhole aperture; α = angle between collimator walls, t = pinhole aperture-to-detector distance; b = pinhole aperture-to-object distance. Reprinted with permission from ref. [Franc et al. JNM 2008, 49(10):1651–1663]

collimation is required on traditional systems to achieve large FOV acquisitions (e.g., when imaging the whole animal to evaluate the extent of metastatic disease).

Iodine-131 (^{131}I) or I-131-labeled therapeutics with SPECT poses inherent challenges; photons emitted by I-131 have a high energy that enables them to penetrate the collimator wall and pinhole edges. Using a system with clustered multipinhole collimators (CMPs) designed to accommodate gamma photons of SPECT and PET energies, with each pinhole having a narrower open angle than would be typical of a dedicated SPECT system, Van der Have and colleagues demonstrated the ability to acquire quantitative sub-millimeter I-131 SPECT imaging in mice [77]. With the growing interest of utilizing ^{188}Re -labeled molecules for therapeutic applications, preclinical SPECT has also explored

requirements of imaging the lower energy gamma photons of ^{188}Re for therapy planning and dosimetry. As in the case of I-131, collimators designed for higher energies have provided superior images given the small percentage of gamma photons emitted concomitantly at very high energies [57].

At the other end of the spectrum are applications requiring high sensitivity because of low counts due to the presence of a low amount of radiotracer or secondary to the requirement for rapid dynamic imaging, and for which uncollimated imaging tactics [208] and multipinhole collimators with large numbers of pinholes have been designed [96]. As well as methods of reduced angular sampling in the imaging protocol [119] and analysis of reduced spatial volumes for calculations of input function [226].

Synthetic-collimator SPECT systems where a single detector or detectors of different materials are placed at different distances behind the multipinhole aperture [126], dual-resolution collimator tubes that provide both whole-body projections and more targeted projections centered on the target of interest [153], in-line X-ray optics [189], adaptive aperture approaches [25], and new innovations to coded aperture (CA) collimation [154] are other approaches being explored to overcome multiplexing and other challenges in using multipinhole collimation. A recent review of collimator selection, optimization, and fabrication addresses many important considerations in the application of SPECT to small animal imaging [195].

11.4.4 Image Reconstruction Techniques

A SPECT study essentially is composed of multiple planar images acquired at a number of angles, creating a set of projection data. An image dataset is then reconstructed from this projection data. The most basic of tomographic image reconstruction algorithms, filtered backprojection (FBP), takes the counts in the projections from thin “slices” of the imaged subject and redistributes them in a spatial distribution by “backprojecting” the data (with or without prior filtering) by smearing the projected data back along the same line as from where the photon was emitted. Obviously, this is an imperfect solution to the reconstruction problem that produces adequate images in many instances but is not amenable to quantitative applications.

Iterative reconstruction techniques, including maximum likelihood expectation maximization (MLEM) and ordered subsets expectation maximization (OSEM), essentially predict what the final image should look like, create a projected dataset from that predicted image, compare the acquired projected dataset to the projection data of the predicted image, and make some adjustments, repeating the process iteratively for a set number of iterations or until some stop condition is met. Iterative reconstruction methods have been developed for all configurations of SPECT imaging, including helical pinhole SPECT imaging [88]. Importantly, metrics of image quality can be significantly affected by parameters used during reconstruction, such as iteration or subset number [138].

Although iterative reconstruction techniques may be more susceptible to motion artifacts and artifacts induced from spurious noise, iterative reconstruction techniques allow for the introduction of various resolution-improving corrections during or after (post-) reconstruction and are therefore the basis of quantitative SPECT imaging reconstruction techniques. Corrections that may be introduced into the iterative reconstruction algorithm include resolution recovery based on measured or simulated collimator–detector response functions in the MLEM or OSEM image reconstruction algorithm [228], modeling of the point spread function (resolution recovery) [169], depth-of-interaction (DOI) modeling in the detector, and models of photon paths that go through multiple pinholes, in the case of multipinhole configurations [69]. Although computational memory capabilities have expanded rapidly over the past decades, additional strategies to deal with the computational burden of modern-day small animal SPECT-CT imaging systems have been developed [146, 147].

11.4.5 Quantitative SPECT-CT

The ability to achieve accurate and quantitative image data with SPECT is complicated by limitations in instrumentation and the imaging process. The imaging system possesses an intrinsic resolution, blurring the distribution of radioactivity and contributing to partial-volume effect. When traveling through tissue, photons may be scattered or absorbed. Photon attenuation and scatter play a much smaller role in small animal imaging than in human imaging. Attenuation of photons by soft tissue is estimated to be up to 50% when imaging I-125 and up to 25% when imaging Tc-99m in rodent-sized objects. In general, an estimated 20–25% of the total counts in the projected image dataset may be accounted for by scattered photons, although the number falls to 10% in the case of Tc-99m and the overall contribution to scatter effect to quantitative error turns out to be relatively small for numerous reasons including the pinhole or multiple structures rejecting a large portion of scattered photons [90, 91].

Photon attenuation can be accounted for in reconstruction or post-reconstruction processing and has been shown to improve absolute activity quantification estimates using simple calibration methods [66] and potentially improve the reproducibility of quantitative measurements over serial images due to fluctuations in the animal's mass over the course of therapy [185]. Various methods of attenuation correction in small animal SPECT-CT have been compared elsewhere [120]. The reconstructed image can be used to extract an animal boundary used in post-processing calculations. More accurately, an external radiation source (e.g., CT) can be used to map the attenuation distribution of the animal, making the advantage of dual-modality SPECT-CT obvious [105, 212]. Early work in the area of improving the quantitative abilities of small animal SPECT by utilizing data from the CT to provide specific attenuation maps was focused on cardiac applications [92]. More recently, using CT to provide attenuation maps for incorporation into iterative reconstruction of scatter- and attenuation-corrected pinhole SPECT

images, researchers have achieved quantitative measurements of activity concentrations in a mouse with an average error of $-7.9 \pm 10.4\%$ when compared to measurements from a dose calibrator [201]. Using body outline contours obtained with optical cameras, another group has implemented the post-reconstruction correction algorithm developed by Chang [26], a first-order attenuation correction algorithm, to correct data acquired with focusing pinhole SPECT for attenuation [12, 13].

Scatter correction [171], edge-preserving smoothing, and resolution recovery have also been applied to improve quantification of small animal SPECT images [199]. In combination with scatter correction, the method derived from the Chang attenuation correction algorithm produced images with average quantitative measurement error of 1.7% in phantoms and 2.1% in animal studies [216]. Other promising approaches to improving the quantitative accuracy of SPECT data have been designed for human clinical systems, and hopefully some of these same techniques will prove useful in small animal imaging [49].

In many applications of quantitative SPECT, it is necessary to understand the relationship between the uptake in various organs or the tumor with the arterial input function, the concentration gradient across the blood pool, and the tissue of interest. For greater quantitative accuracy and evaluation of radioactivity associated with blood metabolites of various SPECT tracers, a microfluidics-based lab-on-a-chip device has been developed [42].

Finally, once the best estimate of the activity distribution has been produced, automated image registration and segmentation methods for direct comparison of numerous datasets must be available [107].

11.4.6 Quality Assurance

In general, a rigorous quality assurance process should be implemented with regular evaluations of camera spatial resolution, spatial uniformity, energy resolution, and counting-rate response. SPECT-CT imaging systems are often shared by numerous laboratories, each of which may require different system configurations (in terms of collimators, etc.). The more users and changes made to the configuration; generally, the more often recalibration will be necessary. What may seem a mild misalignment or minimal change in calibration can have devastating effects on the quality of imaging data in longitudinal studies.

11.4.7 A Sampling of Available Small Animal SPECT and SPECT-CT Systems

Some of the first and most advanced systems are “one-of-a-kind” and are housed in specific research institutions [152, 176]. The preclinical SPECT-CT scanner built at the University of California, San Francisco, had an in-plane SPECT-CT configuration with single-pinhole collimation. Both the SPECT and CT components were

made of semiconductor materials (CdZnTe and gadolinium oxysulfide, respectively), and both have helical scan capability. A compact SPECT-CT system designed and built at the University of Arizona's Center for gamma-ray imaging had an in-plane SPECT-CT configuration and utilizes the CdZnTe detector materials as the SPECT camera [105]. However, it utilized a rotating stage (vertical animal holder), similar to that reported earlier from the University of Amsterdam [73] rather than the traditional rotating detector model. Collimation was high-resolution parallel hole with a matching pitch on detector pixels. A SPECT unit with a high degree of flexibility in the pinhole collimation configuration and magnification had also been developed by the same group [83]. There were two generations of the preclinical SPECT-CT development from the group from Jefferson Lab and University of Virginia in collaboration with Johns Hopkins University [184, 213]. These were notable for their use of position-sensitive photomultiplier tubes in the SPECT detector (NaI(Tl)-PSPMT). Either parallel hole or pinhole collimation was possible. This configuration of this imaging system allowed imaging unanesthetized mice using infrared tracking for animal motion [211]. In addition to dedicated SPECT-CT systems, some systems also incorporate additional modalities such as PET [151] and fluorescence imaging [130].

As researchers aim to broaden access to SPECT technology in small animal applications, there has been a strong interest, particularly among commercial manufacturers of small animal SPECT-CT systems, in decreasing the complexity and size of systems that were once essentially miniature versions of available clinical systems [196]. For example, stationary detectors have become a central tenet of many of the commercially available systems. eXplore speCZT (GE Healthcare, Milwaukee, WI, USA) was a dedicated preclinical SPECT system using a full ring of 10 stationary cadmium zinc telluride (CZT)-based detectors equipped with interchangeable rotating collimators. The system could be coupled with a micro-CT for SPECT-CT. Characterization of the system demonstrated that resolution recovery enabled sub-millimeter spatial resolution and improved uniformity for all the collimators tested [138]. NanoSPECT (Mediso, Budapest, Hungary), U-SPECT (MILabs, Utrecht, the Netherlands), and γ -CUBE (Molecubes, Ghent, Belgium) are all multipinhole SPECT systems that provide stationary acquisition modes and very high spatial resolution, offered as a docked or serial configuration combining two separate SPECT and CT modules. This configuration requires an animal bed that translates between the two imaging modalities or transportable to the other modality without removing the animal from the bed, a fact that needs to be taken into consideration when setting up the animal's anesthesia apparatus. One advantage of such a configuration, however, is the ability to acquire SPECT and CT images independently. This could be beneficial in the setting of serial imaging studies where the potential effect of CT dose on the tumor or animal may be non-negligible.

More recent generations of the U-SPECT/CT systems use multipinhole mouse collimators with sensitivities that span a range allowing sub-half-millimeter to sub-millimeter resolution levels, depending on the radionuclide dose. Characterization of these systems has shown discrimination between molecular concentrations

in adjacent volumes down to 0.015 mL [194, 97]. A platform combining a SPECT system such as U-SPECT with optical imaging (i.e., bioluminescence and fluorescence imaging) has also been developed [197].

The discussion of systems above is certainly not exhaustive and does not include all of the systems developed or being developed. However, many of the key features of all current systems have been included in the sampling of systems described above. Deleye and colleagues have published a direct comparison of the spatial resolution, image uniformity, point-source sensitivity and contrast recovery of the USPECT-II (MILabs), the NanoSPECT-NSO (BioScan), and the X-SPECT (GE) scanners equipped with multipinhole general-purpose and multipinhole high-resolution collimators [46].

11.5 Part IV: SPECT-CT as Applied in the Preclinical Oncology Setting

Small animal SPECT-CT has been applied to all facets of molecular imaging in oncology, from detecting malignancy to characterizing it, from determining the most appropriate pharmaceuticals for cancer management to evaluating response to therapy.

11.5.1 Cancer Detection

As models of tumorigenesis have evolved, SPECT imaging has enabled the evaluation of various strategies of early cancer detection. For example, a Technetium-99m (Tc-99m)-labeled antibody to CD11b, a molecule active in the innate immune response and expressed in myeloid-derived suppressor cells (MDSCs), has been shown to have potential to diagnose very early-stage colon cancer using SPECT-CT by detecting an inflammatory microenvironment around early tumors in an *in situ* mouse model of colon cancer [35]. Improvements in sentinel lymph node imaging and evaluations of new sentinel node agents have also utilized small animal SPECT-CT [191].

11.5.2 Characterizing Tumorigenesis and Malignant Spread

One of the most promising areas in the application of molecular imaging in oncology is the characterization of molecular processes underlying tumorigenesis and malignant spread in a spatial and temporal manner. The high resolution of small animal SPECT imaging systems enables inherent heterogeneities in tumor perfusion or in the distribution of other radiopharmaceuticals to be visualized [193].

Many novel molecules have been developed and radiolabeled with the specific purpose of providing *in vivo* characterization of processes of tumor genesis or

progression. For example, integrins, specifically the $\alpha(v)\beta(3)$ heterodimers, have been linked to tumor-induced angiogenesis and invasiveness, and radiolabeled ligand analogs to these receptors have been imaged with SPECT with the goal of mapping the distribution of receptors in tumors as well as the biodistribution of these molecular reporters [54, 51]. SPECT-CT of small organic ligands such as Tc-99m-labeled RGD peptide monomer has been used to monitor progression in a breast cancer lung metastasis model [234], and Tc-99m-labeled acetazolamide, a carbonic anhydrase ligand with high affinity for the tumor-associated isoform IX (CAIX) transmembrane transporter, has been used in CAIX-expressing renal cell carcinoma [114].

By using the sodium/iodide symporter (NIS) as a reporter gene constitutively expressed in a human colon cancer cell line coupled with $^{99m}\text{TcO}_4^-$ as the imaging agent, researchers have successfully imaged a spontaneously metastasizing orthotopic human colon cancer model in mice with SPECT, enabling *in vivo* monitoring of the burden of liver metastases [93]. A less specific but readily quantifiable means of assessing liver tumor burden consists of quantification of areas without radio-tracer uptake (“cold spot quantification”) with SPECT after the administration of Tc-99m macro-aggregated albumin particles ([Tc-99m]-MAA), normally taken up by normal liver cells [202].

As in human clinical applications, SPECT imaging with Tc-99m-methyl diphosphonate (Tc-99m-MDP) provides a highly sensitive means of detecting osseous involvement in malignancy, enabling earlier identification of involvement than possible with CT [4]. Thus, Tc-99m-MDP nuclear bone scintigraphy can be used to monitor for response to therapy or progression of osseous involvement in small animal cancer models, parallel to its clinical role in monitoring response to therapy in patients with cancers of the breast or prostate.

11.5.3 Imaging the Targeting Abilities of Molecules in the Development of Potential Therapeutics and Molecular Imaging Agents

Antibody (Ab)-based therapies have evolved to become important tools in cancer therapy, and several have shown efficacy in slowing progression of a malignancy and improving progression-free survival. The targeted nature of these therapies allows increased localization at the site of disease, affording less side effects from non-specific delivery of therapy to normal tissues and potentially increased efficacy.

Evaluation and honing of this targeting capacity in small animals is an important tool in the development of immune- and radioimmunotherapies. Therapeutic monoclonal Abs may be linked to a radionuclide for SPECT imaging for cancer diagnosis, staging, molecular characterization, and therapeutic response assessment. The biodistribution of antibody therapy, and whether a sufficient amount of antibody will ultimately reach its target, can often best be assessed with *in vivo* studies, and imaging a single animal serially can help to fully understand the

pharmacokinetics and elucidate and evaluate potential strategies to improve the targeting rate of the Ab.

Abs utilized in a number of cancer therapeutic targeting strategies have been successfully labeled for *in vivo* characterization with SPECT such as epidermal growth factor receptor 2 Ab (anti-HER2), epidermal growth factor receptor Ab (anti-EGFR) [180], folate receptor Ab (anti-FR), prostate-specific membrane antigen Ab (anti-PSMA), anti-CD20, program death-1 Ab (anti-PD-1), and program death ligand-1 Ab (anti-PD-L1) [41, 115, 123, 128, 188]. SPECT imaging of IGF-1R expression has been demonstrated using the radiolabeled antibody R1507 in a triple-negative breast cancer model [82].

In the case of xenografts implanted in the subcutaneous tissues of the small animal model, such as in a study evaluating the biodistribution and pharmacokinetics of a fully humanized anti-EGFR mAb using an In-111-labeled version of the Ab in multiple tumor cell lines, planar scintigraphy may provide sufficient imaging data if the targeted disease is easily separated from areas of physiologic tracer distribution. For instance, if the tumor is located in the flank or near the hind limb, it can be easily separated from the non-specific uptake in the kidneys and liver. The fine anatomic localization provided by CT in SPECT-CT would not have added much value in this set of experiments. Interestingly, the significant findings in this study were the differing pharmacokinetics of the antibody depending on the presence or absence of tumor in the animal [172]. In another xenograft-based study of Ab therapeutic efficacy, a Tc-99m-labeled mouse mAb that binds to the DR5 death receptor for tumor necrosis factor-related apoptosis-inducing ligand (TRAIL/Apo2L), TRA-8, was imaged with SPECT. The SPECT imaging data provided a significant piece of information by demonstrating comparable Tc-99m-TRA-8 delivery to all of the animals studied. This information helped to support the hypothesis that increased efficacy observed when TRA-8 was given in combination with CPT-11 was due to the combination of drugs rather than spurious improved delivery of TRA-8 in one particular animal [162].

Baranowska-Kortylewicz and colleagues used SPECT imaging of I-125-labeled tumor-specific antibody to provide evidence of increased antibody uptake in colon adenocarcinomas grown subcutaneously in SCID mice following administration of the tumor stroma-reactive STI571, a platelet-derived growth factor receptor-B (PDGFR-B) antagonist [10]. Similarly, imaging radiolabeled antibodies with SPECT has provided important information in targeting and dose optimization of several potential antibody-based therapies [86, 172]. Radionuclides with longer half-lives that better match the biological half-lives of larger tumor-targeting molecules, such as terbium-155 (Tb-155) [155] and samarium-153 (Sm-153) [217], are being explored for their *in vivo* SPECT imaging capabilities.

Significantly increased interest in peptides and other small molecules as cancer therapeutics has encouraged the design and use of radiolabeled forms of these molecules to develop more specific diagnostic tests [102] and better understand their pharmacokinetics and biodistributions in small animal models [148, 182, 232, 113]. For example, He and colleagues used SPECT-CT to evaluate the tumor-targeting capability and potential of an internalizing human single-chain

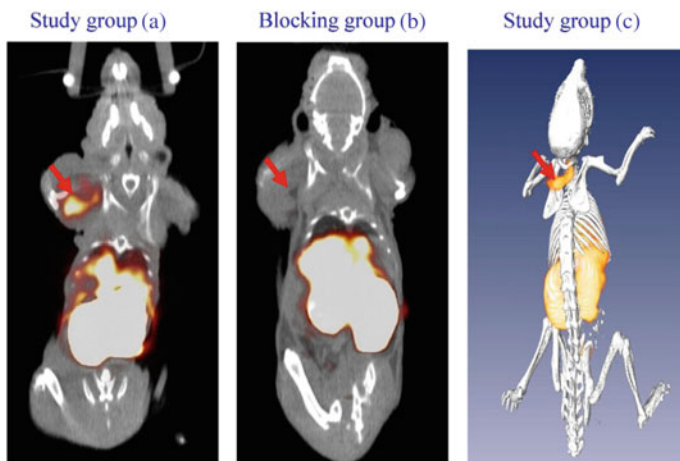


Fig. 11.2 Small animal SPECT/CT of nude mice bearing DU145 xenograft at front flank. **a** Image taken at 3 h after injection of ^{99m}Tc -UA20 scFv. **b** Image taken at 3 h after injection of ^{99m}Tc -labeled UA20 scFv. In this experiment, 10-fold excess of unlabeled UA20 scFv was injected 1 h before injection of ^{99m}Tc -UA20 scFv. **c** Representative image of three-dimensional rendering of tumor targeting by Tc-99m labeled UA20 scFv. Ref. [He, J et al. *JNM* 51(3):427–432] [79]

variable fragment (UA20 scFv) labeled with Tc-99m (Tc-99m-UA20) as a molecular imaging agent in a mouse model of human prostate carcinoma. SPECT-CT imaging of ^{99m}Tc -UA20 demonstrated rapid distribution and tumor visualization as early as 1 h after injection (Fig. 11.2) [79].

11.5.4 Small Molecules

Some of these peptide-based tracers are developed as companion imaging agents to therapeutics, such as a Tc-99m-labeled antagonist to chemokine receptor 4 (CXCR4), developed to identify tumors vulnerable to CXCR4-targeting therapeutic approaches [230]. Similarly, Tc-99m-3P-RGD₂ SPECT/CT of lung cancer xenografts in mice was developed as a means of *in vivo* quantification of integrin $\alpha_v\beta_3$ expression within tumors, ultimately for clinical translation to identify patients who may be candidates for $\alpha_v\beta_3$ -targeted therapies [62]. SPECT/CT of similar short peptides targeting $\alpha_v\beta_6$, another integrin associated with multiple poor prognostic cancers, has also been explored [235]. Other examples of SPECT-CT imaging of small molecules in their evaluation for potential use for therapy include imaging of radioiodinated androgen receptor ligands in ovarian adenocarcinoma [113].

11.5.5 Theranostics

Therapeutic radiopharmaceuticals often have companion versions incorporating an imaging agent, useful for understanding their targeting ability and for pre-therapy dosimetry calculations [117]. Some radionuclides, such as Re-188, can provide dual functionality, emitting particle radiation useful in therapeutic applications as well as gamma radiation for SPECT-CT imaging, enabling a single radiolabeled molecule to target a cancer for imaging or therapy [125].

Radioactive theranostic agents that have undergone preclinical study with SPECT or SPECT-CT include I-131-labeled benzamide for targeted radiotherapy of metastatic melanoma [103], I-131-labeled arginine-arginine-z peptide in nude mice bearing human prostate carcinoma [225], Re-188-(I)-tricarboxyl-labeled trastuzumab (Herceptin) in BT-474 human breast cancer xenografts [32], Lu-177-DOTA – panitumumab (Lu-177-Pan) and Lu-177-DOTA – cetuximab (Lu-177-Cet) in a preclinical head and neck cancer model [129], and Lu-177-labeled bombesin (BN)-like peptide in PC-3M prostate tumor-bearing mice [60, 124, 127]. In a study of a three-step pretargeted radioimmunotherapy in a mouse xenograft model of human colon cancer using a glycoprotein A33 (GPA33)-targeting bispecific antibody and a small-molecule radioactive hapten, a complex of Lu-177 and S-2-(4-aminobenzyl)-1,4,7,10-tetraazacyclododecane tetraacetic acid (Lu-177-DOTA-Bn), SPECT/CT imaging was used to monitor treatment response and calculate radiation absorbed doses to tumor [31]. An area where much future work will have to be performed is evaluating the dosimetry of many more of these agents, an application where SPECT-CT may provide a significant advantage [7].

11.5.6 Predicting Therapeutic Response and Monitoring Response to Therapy

The early detection of therapy-induced tumor cell death, whether by chemotherapy, other biologic therapies, or therapeutic radiopharmaceutical, has been a subject of investigation for decades. The most recent molecules targeting apoptosis are labeled with Tc-99m, enabling improved imaging characteristics over their earlier relatives which were labeled with other less amenable nuclides. Promising apoptotic imaging markers include [Tc-99m] annexin V, a large protein that binds to phosphatidylserine (PS), and [Tc-99m] duramycin, a shorter peptide that binds to phosphatidylethanolamine (PE) [55]. The temporal changes in apoptosis of numerous cancer types during therapy have been monitored qualitatively and quantitatively with SPECT using Tc-99m-hydrazinonicotinamide (HYNIC)-annexin V [200]. Other molecules developed specifically for tumor characterization, such as hypoxic agents, have been adapted for potential imaging with SPECT [28].

SPECT agents approved for use in humans, such as the perfusion agents Tc-99m-sestamibi (Tc-99m-MIBI) and Tc-99m-Tetrofosmin uptake (Tc-99m-TF),

have found new applications in evaluation of tumors for expression of P-glycoprotein (Pgp) and multidrug resistance-related protein-1 (MRP), potential factors in failure of tumors to respond to chemotherapy [65].

11.5.7 Imaging Cell Trafficking

Cell trafficking studies can help establish the stability of disease models and assess cellular migration. For example, in the development of orthotopic tumor models in mice, SPECT-CT imaging utilized to trace the location of injected lung tumor cells in the lung parenchyma via intratracheal instillation [21].

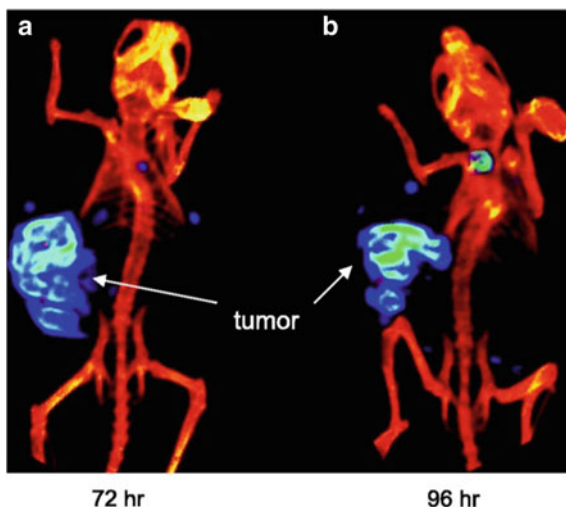
Another potential area where cell trafficking studies are important is in understanding the effects of disease processes or drugs on normal or pathologic cells, particularly those interacting with the immune system [11, 156]. For example, the ability of I-125 radiolabeled anti-CD206 antibody to identify tumor-associated macrophages (TAMs) that may contribute to drug resistance has been demonstrated using in a 4T1 mouse model of breast cancer [231].

With the advent of CAR-T cell therapy, there is renewed interest in monitoring the location of leukocytes in vivo. Various reporter genes can be introduced into the cells targeted for tracking, enabling imaging of their location with SPECT when a gamma-emitting substrate or ligand is introduced. For example, cells expressing the herpes simplex virus thymidine kinase (HSV-tk) concentrate on the substrate I-123-(1-(2'-deoxy-2'-fluoro-1- β -D-arabinofuranosyl)-5-iodouracil) (FIAU), enabling subsequent imaging with SPECT. Cells engineered to express human noradrenaline transporter (hNET) can be imaged after intravenous administration of the ligand ^{123}I -metaiodobenzylguanidine (MIBG) [56]. Stem cell-based therapies can also be monitored using these reporter gene strategies [104]. Human embryonic stem cell (hESC) engraftment and proliferation have been monitored with I-125-FIAU SPECT-CT in mice after transplantation of HSV1-TK-infected cells [170].

11.5.8 Imaging Gene Transfer and Expression

As gene therapies for cancer move into the clinic, there has been a significant interest in developing methods to monitor the activity of gene expression in a systemic manner without repeated tissue biopsy. Small imaging SPECT-CT of the products of reporter genes provides the means to evaluate strategies to track gene expression. When such imaging reporter genes are controlled by a promoter, the detection of the reporter protein using a radiolabeled imaging probe and SPECT is used to monitor the level of therapeutic gene expression, promoter activity, and protein-protein interaction in vivo [99, 224]. Several methods have shown promise. For example, using I-125-labeled radiolabeled 2'-fluoro-2'-deoxy-h-D-5-iodouracil-arabinofuranoside (FIAU) and SPECT-CT, Fu and colleagues demonstrated the ability to image chemotherapy (bortezomib)-induced thymidine kinase

Fig. 11.3 SPECT-CT images of [^{125}I]FIAU by an EBV(+) Burkitt's xenograft (Akata) at 72-h and 96-h time points. Reprinted with permission from ref. [Fu DX, et al. *Clinical cancer research* 2007;13(5): 1453–1458] [63]



(TK) expression indicating viral lytic induction in EBV(+) Burkitt's lymphoma xenografts in severe combined immunodeficient mice (Fig. 11.3) [63].

Investigators have monitored replication of an adenovirus encoding the Na/I symporter (hNIS) using SPECT-CT following $^{99\text{m}}\text{TcO}_4^-$ administration. Like iodine, $^{99\text{m}}\text{TcO}_4^-$ is taken up by cells expressing hNIS, thereby acting as a surrogate indicator of potential to concentrate iodine. hNIS can be used as a reporter gene with either $^{99\text{m}}\text{TcO}_4^-$ or I-125 or I-123 radioiodine administration for imaging viral biodistribution with SPECT-CT, enabling the ability to follow the selectivity and time course of a replicating adenovirus. Additionally, hNIS can be used in a therapeutic strategy in combination with I-131 administration [143, 144, 167]. SPECT-CT imaging of the hNIS reporter gene has also been utilized to monitor the biodistribution of gene transfer of polypropylenimine dendrimer PPIG3/DNA nanoparticles and prove the specific delivery and transgene expression of these agents in tumors grown subcutaneously in mice [36].

Similarly, the expression of an oncolytic engineered measles virus (MV) for pancreatic cancer therapy has been monitored in preclinical studies using a form of the virus expressing the sodium-iodide symporter gene (MV-NIS) in combination with I-123 SPECT-CT [23].

Chen and colleagues have incorporated two reporters into a single construct, allowing both optical and SPECT imaging of gene expression. SCC-9 human squamous cell carcinomas in mice were infected with adenovirus containing the investigators' somatostatin receptor-enhanced green fluorescent protein fusion construct (AdSSTR2-EGFP) and imaged *in vivo* with SPECT-CT after the administration of ^{111}In -DTPA-Tyr3-octreotate. The same tumors were also imaged with fluorescence [33]. In mouse studies, the ability to perform multimodality imaging is very advantageous as cells can be evaluated *in vivo* and *ex vivo* using one or both modalities. In addition, if frequent monitoring of a subcutaneous tumor

is required, some time points could potentially be evaluated with only optical imaging, minimizing the amount of radiation to the animal and tumor but also allowing occasional evaluations with a high spatial resolution combined with functional/anatomic imaging modality such as SPECT-CT.

By demonstrating a method of monitoring biodistribution and transgene expression in mice using SPECT-CT, these types of studies pave the way for direct translation of monitoring techniques when these therapies are introduced into humans.

11.5.9 Imaging Drug Delivery and Using SPECT in Drug Design

In drug development, small animal SPECT imaging can play a vital role in evaluating various compounds for their targeting potential, their potential for *in vivo* efficacy, pharmacokinetics, and pharmacodynamics, as well as their anticipated toxicities [131]. Given the expense to produce sophisticated small animal cancer models and a general desire to minimize the number utilized in research, SPECT imaging of radiolabeled versions of drug candidates enables serial use of the small animal models for characterization of multiple drug compound candidates [132]. Imaging of multiple small animals is possible in a single session; however, for those isotopes that emit a β particle with a kinetic energy greater than 219 keV, Cerenkov luminescence imaging may be a more convenient means to increase the rate of *in vivo* high throughput drug screening [190].

Nanoparticles and nanomolecules can serve as carriers of radiotracers or combined imaging/therapeutic agents [161]. Incorporation into nanocarriers accomplishes two goals: (1) enabling increased tumor targeting and resulting in increased therapeutic efficacy with reduced toxicity, and (2) allowing increased sensitivity of detection with SPECT-CT, enabling tracking of therapeutics *in vivo*. For example, in order to evaluate the tumor-targeting capability and biodistribution of Re-188-N, N-bis (2-mercaptoethyl)-N',N'-diethylethylenediamine (BMEDA)-labeled pegylated liposomal doxorubicin (DXR) (Re-188-DXR-liposome) in a C26 murine colon carcinoma solid tumor model, Chang and colleagues used small animal SPECT-CT imaging in tandem with pharmacokinetic studies. Once targeting had been proven with imaging, separate therapeutic efficacy studies were performed, showing a synergistic therapeutic effect of the combination radiochemotherapeutics [27]. Iyer and colleagues used SPECT imaging of In-111-labeled immunoliposome anchored by internalizing single-chain antibody fragment that targets all types of mesothelioma [98]. Marked uptake of this radioimmunoliposome was seen in M28 (epithelioid type) and VAMT-1 (sarcomatoid type) tumor xenografts in mice *in vivo* (Fig. 11.4). This imaging result presented a promising strategy for the development of enhanced targeting of liposomal drugs and targeted radionuclide therapy for malignant mesothelioma [98].

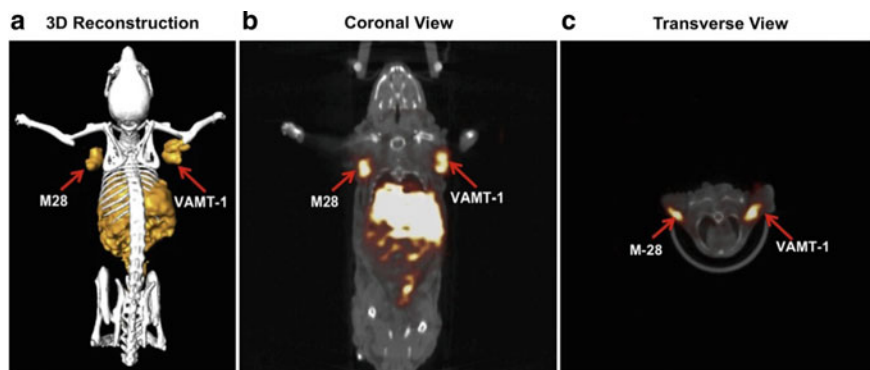


Fig. 11.4 SPECT-CT images of a mouse model with epithelioid (M28) and sarcomatoid (VAMT-1) mesothelioma tumors. 3D-rendered images of SPECT-CT (a), and two cross-sectional views to show the tumor uptake of In-111-labeled immunoliposome anchored by a single-chain antibody fragment, M1. Reprinted with permission from ref. [Iyer AK et al. Biomaterials 2011] [98]

Investigators have also used SPECT-CT to image the biodistribution and targeting efficacy of a number of carbon nanomaterial structures [229] as well as nanoparticles of other various compositions [214, 110]. Nanoparticle drug delivery systems also offer one means of designing tracers for dual-modality imaging, such as combined upconversion luminescence and SPECT imaging with $\text{NaLuF}_4\text{:}^{153}\text{Sm}$, Yb , Tm nanoparticles [223]. Multifunctional nanocarriers enable incorporation of multiple therapeutic and imaging agents into a single delivery system [41].

Other published reports of the use of SPECT and/or SPECT-CT in drug design include imaging the time of retention and biodistribution of subcutaneously injected polymers designed for drug delivery [112] and in vivo monitoring of small interfering RNA (siRNA)-based therapies [157], including a study by Chen and colleagues using a dual-modality approach of imaging siRNA radiolabeled with ^{131}I and conjugated to superparamagnetic iron oxide nanoparticles (SPIOs) with both SPECT and MRI [34]. With the aim of eventually administering selective doses of platinum-based therapies to cancer patients based upon the level of tumor uptake of the chemotherapy, researchers have characterized the ability of $^{195\text{m}}\text{Pt}$ to be imaged in small animal models with SPECT [1].

Imaging for radiation treatment planning, image-based dosimetry, and characterization of changes in biology over the course of radiotherapy, there has been an explosion of interest in preclinical models of radiotherapy and an interest in understanding the dynamics of biology occurring during radiation therapy in combination with various tumor-targeting drugs. Small animal image-guided precision radiotherapy platforms are increasingly used in tandem with small animal molecular imaging devices, such as SPECT-CT, to elucidate effects of therapy on the tumor and surrounding tissues [121] as well as to assist in planning radiation therapy [204].

By segmenting imaging data and combining data across imaging modalities, computational small animal imaging models have been constructed, aiding in treatment planning as well as dosimetry modeling to determine radiation doses delivered to tumors and surrounding normal structures [218].

11.5.10 Imaging Other Pathologic Processes Associated with Cancer or Cancer Therapies

Finally, small animal SPECT and SPECT-CT have found utility in the development of methods to detect complications associated with cancer or cancer therapies. To study hepatotoxicity of potential new therapeutics and potential drug–drug interactions, Tc-99m-labeled bile acid analogs have been developed and characterized in small animal models [159]. Non-alcoholic fatty liver disease (NAFLD) can contribute to chemotherapy toxicity. NAFLD has been studied in small animal models using SPECT combined with Tc-99m-2-methoxyisobutyl-isonitrile (Tc-99m-MIBI) [173]. Derivatives of Ga-67 deferoxamine (DFO) complexes have shown promise in *in vivo* SPECT imaging of infection in mouse models based upon uptake of the complex by bacteria that utilize the DFO siderophore to scavenge iron [94]. Cardiotoxicity, also a major consideration in studying the adverse effects of treatments such as chemotherapy or external beam radiotherapy, can be studied in small animals using similar techniques available in the clinic [38]. Markers of left ventricular function in small animal cardiac SPECT, including ejection function and end-diastolic volume, provide results comparable to 3D-echocardiography [81]. Renal failure associated with peptide receptor radionuclide therapy (PRRT) and methodologies to avoid the condition were studied in rats using Tc-99m mercaptoacetyltriglycine (MAG3) SPECT-CT following Lu-177-DOTA-Tyr3-octreotate therapy [141, 142].

11.6 Part V: Areas of Rapid Advancement of the Science of Molecular Imaging with SPECT-CT

11.6.1 Next-Generation Imaging Systems

The quality of images from current small animal SPECT-CT systems allows the study of innumerable processes both qualitatively and, in many instances, quantitatively. Bold concepts in imaging system design look beyond traditional concepts of imaging immobilized subjects one at a time. As the quest continues to image subjects in a more physiologic state over significant periods of time, methods are being developed to image non-anesthetized, free-moving animals [8, 9]. Other configurations for SPECT, including an open gantry desktop approach, have been explored using simulation [227]. Such designs may be aided by the application of artificial intelligence techniques.

11.6.2 Imaging Immune Activation

With the explosion in the use of immune-modulating therapeutics in oncology, imaging the activation of various components of the immune response is being explored as a means of identifying candidate patients and monitor the immune systems' ongoing response to these drugs. For example, imaging folate receptor expression can be used to identify activated macrophages [44]. In-111 labeled antibody to PD-L1 checkpoint inhibitor is being pursued to characterize the susceptibility of tumors to PD-L1 inhibition as a therapeutic strategy [30].

11.6.3 Multimodality Probes

One goal of multimodal detection of molecules is to enable study of pharmacokinetics and biodistribution over short (radionuclide-enabled) and more prolonged (CT- or MRI-enabled) periods. Doping of nanocrystals containing high-attenuating materials with radionuclides that are long-lived, such as in the case of poly(ethylene glycol)bis(carboxymethyl) ether (PEG) EuOF nanocrystals doped with $^{153}\text{Sm}^{3+}$ ions, allows dual-modality imaging with SPECT-CT [217]. Ultrasmall superparamagnetic iron oxide nanoparticles functionalized with c(RGDyC) peptides and labeled with Tc-99m can detect tumor angiogenesis using both SPECT and MRI [220]. Other groups have evaluated intrinsically radiolabeled magnetic nanoparticles to achieve a probe detectable by both MRI and SPECT. For example, [^{59}Fe]-superparamagnetic iron oxide nanoparticles ([^{59}Fe]-SPIONs) utilizes the long-lived radionuclide ^{59}Fe incorporated into the Fe_3O_4 nanoparticle crystal lattice to provide gamma photons capable of detection by a gamma-imaging system [87].

The ability to follow multiple independent molecular processes co-spatially and/or co-temporally opens up the possibility of understanding cell-cell interactions and signaling processes. As the theranostics field advances, more sophisticated therapeutic strategies, including immunomodulation and activation, are being coupled with multimodality imaging agents for SPECT, MRI, and fluorescence in single-nanocarrier platforms [39].

In clinical translational medicine, multimodality probes incorporating both radionuclides imaged with SPECT and fluorescing molecules capable of being imaged via optical means have the potential to bridge SPECT with surgical-based therapies [80, 177].

11.6.4 Radiomics and Computational Advances

As in clinically based radiomics and artificial intelligence efforts, a key driver of innovation in these areas in small animal SPECT and SPECT-CT is the availability of numerous datasets acquired in a standardized methodology [136]. Improvements in SPECT quantification are looking beyond region-of-interest analysis, including quantification methods operating on raw projection data [116].

Radiomics is a new way of image quantification, which is being applied to all types of images. With readily available tools, extraction of radiomic features such as texture, location, relation with surrounding tissue, shape, etc., and applying these features for image analysis has been actively studied. For images acquired from small animal SPECT and SPECT-CT, some studies already have utilized the power of radiomics [20].

Computational advances with relation to small animal SPECT and SPECT-CT imaging are basically twofold. Acceleration of SPECT reconstruction speed has been shown using graphics processing unit (GPU) [150, 165]. Machine learning and deep learning on images acquired from small animal SPECT and SPECT-CT can be certainly applied, and need more research into this as for many efforts are focused on using human equivalent data. Deep learning approaches can conceivably be utilized for improving SPECT reconstruction performance particularly when the noise and limited angular sampling are limitations [70].

11.7 Conclusion

In many ways, the radiopharmaceuticals with single-photon emitters make them specifically suitable for applications in the evaluation of molecular targeting agents. Their chemistry, decay characteristics, simultaneous acquisitions, and relative cost-efficiency allow wide use of these radionuclides. Continued advances in small animal SPECT and SPECT-CT imaging systems, imaging reconstruction algorithms, and radiochemistry have facilitated significant growth in the field of pre-clinical SPECT and have thus provided greater accessibility to these tools. The oncology researcher interested in preclinical SPECT/SPECT-CT needs to carefully plan experiments, keeping in mind the nuances that specific small animal models, imaging time points, or challenging radiochemistry may have in the overall research plan. Computational advances and ongoing developments in radiomics will require standardization of image acquisition protocols. Done with care, small animal SPECT and SPECT-CT can facilitate the rapid translation of molecular advances into clinical care.

References

1. Aalbersberg EA, de Wit-van der Veen BJ, Zwaagstra O, Codee-van der Schilden K, Vegt E, Vogel WV (2017) Preclinical imaging characteristics and quantification of platinum-195m SPECT. *Eur J Nucl Med Mol Imaging* 44:1347–1354
2. Abbaspour S, Mahmoudian B, Islamian JP (2017) Cadmium telluride semiconductor detector for improved spatial and energy resolution radioisotopic imaging. *World J Nucl Med* 16:101–107
3. Albers MJ, Bok R, Chen AP, Cunningham CH, Zierhut ML, Zhang VY, Kohler SJ, Tropp J, Hurd RE, Yen YF, Nelson SJ, Vigneron DB, Kurhanewicz J (2008) Hyperpolarized ^{13}C

- lactate, pyruvate, and alanine: noninvasive biomarkers for prostate cancer detection and grading. *Cancer Res* 68:8607–8615
4. Alves CRR, Faria DP, Carneiro CG, Garcez AT, Gutierrez VP, das Neves W, de Almeida NR, Cury Y, Chammass R, Brum PC (2018) (18)F-Fluoride PET/CT and (99m) Tc-MDP SPECT/CT can detect bone cancer at early stage in rodents. *Life Sci* 206:29–34
 5. Amundson SA, Bittner M, Meltzer P, Trent J, Fornace AJ Jr (2001) Biological indicators for the identification of ionizing radiation exposure in humans. *Expert Rev Mol Diagn* 1:211–219
 6. Amundson SA, Fornace AJ Jr (2001) Gene expression profiles for monitoring radiation exposure. *Radiat Prot Dosimetry* 97:11–16
 7. Andersson H, Cederkrantz E, Back T, Divgi C, Elgqvist J, Himmelman J, Horvath G, Jacobsson L, Jensen H, Lindegren S, Palm S, Hultborn R (2009) Intraperitoneal alpha-particle radioimmunotherapy of ovarian cancer patients: pharmacokinetics and dosimetry of (211)At-MX35 F(ab')₂—a phase I study. *J Nucl Med Off Publ Soc Nucl Med* 50:1153–1160
 8. Angelis GI, Ryder WJ, Bashar R, Fulton RR, Meikle SR (2014) Impact of extraneous mispositioned events on motion-corrected brain SPECT images of freely moving animals. *Med Phys* 41:092502
 9. Angelis GI, Ryder WJ, Gillam JE, Boisson F, Kyme AZ, Fulton RR, Meikle SR, Kench PL (2017) Rigid motion correction of dual opposed planar projections in single photon imaging. *Phys Med Biol* 62:3923–3943
 10. Baranowska-Kortylewicz J, Abe M, Pietras K, Kortylewicz ZP, Kurizaki T, Nearman J, Paulsson J, Mosley RL, Enke CA, Ostman A (2005) Effect of platelet-derived growth factor receptor-beta inhibition with STI571 on radioimmunotherapy. *Can Res* 65:7824–7831
 11. Beck BH, Kim HG, Kim H, Samuel S, Liu Z, Shrestha R, Haines H, Zinn K, Lopez RD (2010) Adoptively transferred ex vivo expanded gammadelta-T cells mediate in vivo antitumor activity in preclinical mouse models of breast cancer. *Breast Cancer Res Treat* 122:135–144
 12. Beekman FJ, van der Have F, Vastenhouw B, van der Linden AJ, van Rijk PP, Burbach JP, Smidt MP (2005) U-SPECT-I: a novel system for submillimeter-resolution tomography with radiolabeled molecules in mice. *J Nucl Med Off Publ Soc Nucl Med* 46:1194–1200
 13. Beekman FJ, Vastenhouw B (2004) Design and simulation of a high-resolution stationary SPECT system for small animals. *Phys Med Biol* 49:4579–4592
 14. Bergers G, Hanahan D, Coussens LM (1998) Angiogenesis and apoptosis are cellular parameters of neoplastic progression in transgenic mouse models of tumorigenesis. *Int J Dev Biol* 42:995–1002
 15. Boersma HH, Kietselaer BL, Stolk LM, Bennaghmouch A, Hofstra L, Narula J, Heidendal GA, Reutelingsperger CP (2005) Past, present, and future of annexin A5: from protein discovery to clinical applications. *J Nucl Med Off Publ Soc Nucl Med* 46:2035–2050
 16. Boisson F, Zahra D, Parmar A, Gregoire MC, Meikle SR, Hamse H, Reilhac A (2013) Imaging capabilities of the Inveon SPECT system using single-and multipinhole collimators. *J Nucl Med* 54:1833–1840
 17. Bolton AE, Hunter WM (1973) The labelling of proteins to high specific radioactivities by conjugation to a 125I-containing acylating agent. *Biochem J* 133:529–539
 18. Bombardieri E, Coliva A, Maccauro M, Seregini E, Orunesu E, Chiti A, Lucignani G (2010) Imaging of neuroendocrine tumours with gamma-emitting radiopharmaceuticals. *Q J Nucl Med Mol Imaging Off Publ Ital Assoc Nucl Med* 54:3–15
 19. Boone JM, Velazquez O, Cherry SR (2004) ‘Small-animal X-ray dose from micro-CT’, *Mol Imaging Off J Soc Mol Imaging* 3:149–158
 20. Branderhorst W, Blezer EL, Houtkamp M, Ramakers RM, van den Brakel JH, Witteveen H, van der Have F, Gratama van Andel HA, Vastenhouw B, Wu C, Walsum MS, van Dongen GA, Viergever MA, Bleeker WK, Beekman FJ (2014) Three-dimensional histologic validation of high-resolution SPECT of antibody distributions within xenografts. *J Nucl Med* 55:830–837

21. Buckle T, van Leeuwen FW (2010) Validation of intratracheal instillation of lung tumour cells in mice using single photon emission computed tomography/computed tomography imaging. *Lab Anim* 44:40–45
22. Carlson SK, Classic KL, Bender CE, Russell SJ (2007) Small animal absorbed radiation dose from serial micro-computed tomography imaging. *Mol Imaging Biol MIB Off Publ Acad Mol Imaging* 9:78–82
23. Carlson SK, Classic KL, Hadac EM, Dingli D, Bender CE, Kemp BJ, Russell SJ (2009) Quantitative molecular imaging of viral therapy for pancreatic cancer using an engineered measles virus expressing the sodium-iodide symporter reporter gene. *AJR Am J Roentgenol* 192:279–287
24. Carminati M, Montagnani GL, Occhipinti M, Kuehne A, Niendorf T, Nagy K, Nagy A, Czeller M, Fiorini C (2018) SPECT/MRI INSERT Compatibility: Assessment, Solutions, and Design Guidelines. *IEEE Trans Radiat Plasma Med Sci* 2
25. Chaix C, Kovalsky S, Kupinski MA, Barrett HH, Furenlid LR (2014) Fabrication of the pinhole aperture for AdaptiSPECT. *Proc SPIE Int Soc Opt Eng* 9214:921408
26. Chang LT (1978) A method for attenuation correction in radionuclide computed tomography. *IEEE Trans Nucl Sci* 25:638–643
27. Chang YJ, Chang CH, Yu CY, Chang TJ, Chen LC, Chen MH, Lee TW, Ting G (2010) Therapeutic efficacy and microSPECT/CT imaging of 188Re-DXR-liposome in a C26 murine colon carcinoma solid tumor model. *Nucl Med Biol* 37:95–104
28. Chapman JD, Coia LR, Stobbe CC, Engelhardt EL, Fenning MC, Schneider RF (1996) Prediction of tumour hypoxia and radioresistance with nuclear medicine markers. *Br J Cancer Suppl* 27:S204–S208
29. Charafe-Jauffret E, Ginestier C, Birnbaum D (2009) Breast cancer stem cells: tools and models to rely on. *BMC Cancer* 9:202
30. Chatterjee S, Lesniak WG, Gabrielson M, Lisok A, Wharram B, Sysa-Shah P, Azad BB, Pomper MG, Nimmagadda S (2016) A humanized antibody for imaging immune checkpoint ligand PD-L1 expression in tumors. *Oncotarget* 7:10215–10227
31. Cheal SM, Fung EK, Patel M, Xu H, Guo HF, Zanzonico PB, Monette S, Witttrup KD, Cheung NV, Larson SM (2017) Curative multicycle radioimmunotherapy monitored by quantitative SPECT/CT-based theranostics using bispecific antibody pretargeting strategy in colorectal cancer. *J Nucl Med* 58:1735–1742
32. Chen KT, Lee TW, Lo JM (2009) In vivo examination of (188)Re(I)-tricarboxyl-labeled trastuzumab to target HER2-overexpressing breast cancer. *Nucl Med Biol* 36:355–361
33. Chen R, Parry JJ, Akers WJ, Berezin MY, El Naqa IM, Achilefu S, Edwards WB, Rogers BE (2010) Multimodality imaging of gene transfer with a receptor-based reporter gene. *J Nucl Med Off Publ Soc Nucl Med* 51:1456–1463
34. Chen J, Zhu S, Tong L, Li J, Chen F, Han Y, Zhao M, Xiong W (2014) Superparamagnetic iron oxide nanoparticles mediated (131)I-hVEGF siRNA inhibits hepatocellular carcinoma tumor growth in nude mice. *BMC Cancer* 14:114
35. Cheng D, Zou W, Li X, Xiu Y, Tan H, Shi H, Yang X (2015) Preparation and evaluation of 99mTc-labeled anti-CD11b antibody targeting inflammatory microenvironment for colon cancer imaging. *Chem Biol Drug Des* 85:696–701
36. Chisholm EJ, Vassaux G, Martin-Duque P, Chevre R, Lambert O, Pitard B, Merron A, Weeks M, Burnet J, Peerlinck I, Dai MS, Alusi G, Mather SJ, Bolton K, Uchegbu IF, Schatzlein AG, Baril P (2009) Cancer-specific transgene expression mediated by systemic injection of nanoparticles. *Can Res* 69:2655–2662
37. Chow PL, Stout DB, Komisopoulou E, Chatziioannou AF (2006) A method of image registration for small animal, multi-modality imaging. *Phys Med Biol* 51:379–390
38. Cicone F, Viertl D, Quintela Pousa AM, Denoel T, Gnesin S, Scopinaro F, Vozenin MC, Prior JO (2017) Cardiac Radionuclide Imaging in Rodents: A Review of Methods, Results, and Factors at Play. *Front Med (Lausanne)* 4:35

39. Cobaleda-Siles M, Henriksen-Lacey M, Ruiz de Angulo A, Bernecker A, Gomez Vallejo V, Szczupak B, Llop J, Pastor G, Plaza-Garcia S, Jauregui-Osoro M, Meszaros LK, Mareque-Rivas JC (2014) An iron oxide nanocarrier for dsRNA to target lymph nodes and strongly activate cells of the immune system. *Small* 10:5054–5067
40. Colby LA, Morenko BJ (2004) Clinical considerations in rodent bioimaging. *Comp Med* 54:623–630
41. Colombo I, Overchuk M, Chen J, Reilly RM, Zheng G, Lheureux S (2017) Molecular imaging in drug development: Update and challenges for radiolabeled antibodies and nanotechnology. *Methods* 130:23–35
42. Convert L, Lebel R, Gascon S, Fontaine R, Pratte JF, Charette P, Aimez V, Lecomte R (2016) Real-Time Microfluidic Blood-Counting System for PET and SPECT Preclinical Pharmacokinetic Studies. *J Nucl Med* 57:1460–1466
43. Cowey S, Szafran AA, Kappes J, Zinn KR, Siegal GP, Desmond RA, Kim H, Evans L, Hardy RW (2007) Breast cancer metastasis to bone: evaluation of bioluminescent imaging and microSPECT/CT for detecting bone metastasis in immunodeficient mice. *Clin Exp Metastasis* 24(5):389–401
44. de Visser HM, Korthagen NM, Muller C, Ramakers RM, Krijger GC, Lafeber FPJG, Beekman FJ, Mastbergen SC, Weinans H (2018) Imaging of folate receptor expressing macrophages in the rat groove model of osteoarthritis: using a new DOTA-folate conjugate. *Cartilage* 9:183–191
45. de Jong M, Maina T (2010) Of mice and humans: are they the same?—Implications in cancer translational research. *J Nucl Med Off Publ Soc Nucl Med* 51:501–504
46. Deleye S, Van Holen R, Verhaeghe J, Vandenberghe S, Stroobants S, Staelens S (2013) Performance evaluation of small-animal multipinhole muSPECT scanners for mouse imaging. *Eur J Nucl Med Mol Imaging* 40:744–758
47. Dennis MS, Jin H, Dugger D, Yang R, McFarland L, Ogasawara A, Williams S, Cole MJ, Ross S, Schwall R (2007) Imaging tumors with an albumin-binding Fab, a novel tumor-targeting agent. *Can Res* 67:254–261
48. Deprez K, Van Holen R, Vandenberghe S (2014) A high resolution SPECT detector based on thin continuous LYSO. *Phys Med Biol* 59:153–171
49. Dewaraja YK, Koral KF, Fessler JA (2010) Regularized reconstruction in quantitative SPECT using CT side information from hybrid imaging. *Phys Med Biol* 55:2523–2529
50. Difilippo FP (2008) Design and performance of a multi-pinhole collimation device for small animal imaging with clinical SPECT and SPECT-CT scanners. *Phys Med Biol* 53:4185–4201
51. Dijkgraaf I, Beer AJ, Wester HJ (2009) Application of RGD-containing peptides as imaging probes for alphavbeta3 expression. *Front Biosci J Virtual Libr* 14:887–899
52. Dillenseger JP, Guillaud B, Goetz C, Sayeh A, Schimpf R, Constantinesco A, Choquet P (2013) Coregistration of datasets from a micro-SPECT/CT and a preclinical 1.5 T MRI. *Nucl Instrum Methods Phys Res Sect A* 702:144–147
53. Dimri G, Band H, Band V (2005) Mammary epithelial cell transformation: insights from cell culture and mouse models. *Breast Cancer Res*: BCR 7:171–179
54. Edwards WB, Akers WJ, Ye Y, Cheney PP, Bloch S, Xu B, Laforest R, Achilefu S (2009) Multimodal imaging of integrin receptor-positive tumors by bioluminescence, fluorescence, gamma scintigraphy, and single-photon emission computed tomography using a cyclic RGD peptide labeled with a near-infrared fluorescent dye and a radionuclide. *Mol Imaging: Off J Soc Mol Imaging* 8:101–110
55. Elvas F, Vangestel C, Rapic S, Verhaeghe J, Gray B, Pak K, Stroobants S, Staelens S, Wyffels L (2015) Characterization of [(99m)Tc]duramycin as a SPECT imaging agent for early assessment of tumor apoptosis. *Mol Imaging Biol* 17:838–847
56. Emami-Shahri N, Papa S (2016) Dynamic imaging for CAR-T-cell therapy. *Biochem Soc Trans* 44:386–390

57. Esquinas PL, Rodriguez-Rodriguez C, Carlos De La Vega J, Bokharaei M, Saatchi K, Shirmohammad M, Hafeli UO, Sossi V, Celler A (2017) (188)Re image performance assessment using small animal multi-pinhole SPECT/PET/CT system. *Phys Med* 33:26–37
58. Eyles J, Puaux AL, Wang X, Toh B, Prakash C, Hong M, Tan TG, Zheng L, Ong LC, Jin Y, Kato M, Prevost-Blondel A, Chow P, Yang H, Abastado JP (2010) Tumor cells disseminate early, but immunosurveillance limits metastatic outgrowth, in a mouse model of melanoma. *J Clin Investig* 120:2030–2039
59. Fasano J, Muggia F (2009) Breast cancer arising in a BRCA-mutated background: therapeutic implications from an animal model and drug development. *Ann Oncol Off J Eur Soc Med Oncol/ESMO* 20:609–614
60. Ferreira CA, Fuscaldi LL, Townsend DM, Rubello D, Barros ALB (2017) Radiolabeled bombesin derivatives for preclinical oncological imaging. *Biomed Pharmacother* 87:58–72
61. Figueroa SD, Winkelmann CT, Miller HW, Volkert WA, Hoffman TJ (2008) TLD assessment of mouse dosimetry during microCT imaging. *Med Phys* 35:3866–3874
62. Fu T, Qu W, Qiu F, Li Y, Shao G, Tian W, Hua Z, Zhang Y, Wang F (2014) (99m)Tc-3P-RGD2 micro-single-photon emission computed tomography/computed tomography provides a rational basis for integrin α v β 3-targeted therapy. *Cancer Biother Radiopharm* 29:351–358
63. Fu DX, Tanheco YC, Chen J, Foss CA, Fox JJ, Lemas V, Chong JM, Ambinder RF, Pomper MG (2007) Virus-associated tumor imaging by induction of viral gene expression. *Clin Cancer Res Off J Am Assoc Can Res* 13:1453–1458
64. Funk T, Sun M, Hasegawa BH (2004) Radiation dose estimate in small animal SPECT and PET. *Med Phys* 31:2680–2686
65. Fuster D, Vinolas N, Mallafre C, Pavia J, Martin F, Pons F (2003) Tetrofosmin as predictors of tumour response. *Q J Nucl Med Off Publ Ital Assoc Nucl Med* 47:58–62
66. Gerdekoohi SK, Vosoughi N, Tanha K, Assadi M, Ghafarian P, Rahmim A, Ay MR (2017) Implementation of absolute quantification in small-animal SPECT imaging: phantom and animal studies. *J Appl Clin Med Phys* 18:215–223
67. Goetz C, Breton E, Choquet P, Israel-Jost V, Constantinesco A (2008) SPECT low-field MRI system for small-animal imaging. *J Nucl Med* 49:88–93
68. Gooden CS, Snook DE, Maraveyas A, Rowlinson-Busza G, Peters AM, Epenetos AA (1995) Direct technetium-99m labeling of three anticancer monoclonal antibodies: stability, pharmacokinetics and imaging. *J Nucl Med* 36:842–849
69. Goorden MC, van Roosmalen J, van der Have F, Beekman FJ (2016) Optimizing modelling in iterative image reconstruction for preclinical pinhole PET. *Phys Med Biol* 61:3712–3733
70. Greenspan H, Ginneken BV, Summers RM (2016) Guest editorial: Deep learning in medical imaging: overview and future promise of an exciting new technique. *IEEE Trans Med Imag* 35:1153–1159
71. Groll A, Kim K, Bhatia H, Zhang JC, Wang JH, Shen ZM, Cai L, Dutta J, Li Q, Meng LJ (2017) Hybrid pixel-waveform (HPWF) enabled CdTe detectors for small animal gamma-ray imaging applications. *IEEE Trans Radiat Plasma Med Sci* 1:3–14
72. Gutte H, Hansen AE, Larsen MM, Rahbek S, Henriksen ST, Johannesen HH, Ardenkjaer-Larsen J, Kristensen AT, Hojgaard L, Kjaer A (2015) Simultaneous Hyperpolarized ^{13}C -Pyruvate MRI and ^{18}F -FDG PET (HyperPET) in 10 Dogs with Cancer. *J Nucl Med* 56:1786–1792
73. Habraken JB, de Bruin K, Shehata M, Booij J, Bennink R, van Eck Smit BL, Busemann Sokole E (2001) Evaluation of high-resolution pinhole SPECT using a small rotating animal. *J Nucl Med Off Publ Soc Nucl Med* 42:1863–1869
74. Hamamura MJ, Ha S, Roeck WW, Muftuler LT, Wagenaar DJ, Meier D, Patt BE, Nalcioglu O (2010) Development of an MR-compatible SPECT system (MRSPECT) for simultaneous data acquisition. *Phys Med Biol* 55:1563–1575

75. Hamamura MJ, Ha S, Roeck WW, Wagenaar DJ, Meier D, Patt BE, Nalcioglu O (2010) Initial Investigation of preclinical integrated SPECT and MR imaging. *Technol Cancer Res Treat* 9:21–28
76. Hanahan D (1989) Transgenic mice as probes into complex systems. *Science* 246:1265–1275
77. van der Have F, Ivashchenko O, Goorden MC, Ramakers RM, Beekman FJ (2016) High-resolution clustered pinhole (131)Iodine SPECT imaging in mice. *Nucl Med Biol* 43:506–511
78. Hayakawa T, Mutoh M, Imai T, Tsuta K, Yanaka A, Fujii H, Yoshimoto M (2013) SPECT/CT of lung nodules using ¹¹¹In-DOTA-c(RGDfK) in a mouse lung carcinogenesis model. *Ann Nucl Med* 27:640–647
79. He J, Wang Y, Feng J, Zhu X, Lan X, Iyer AK, Zhang N, Seo Y, VanBrocklin HF, Liu B (2010) Targeting prostate cancer cells in vivo using a rapidly internalizing novel human single-chain antibody fragment. *J Nucl Med Off Publ Soc Nucl Med* 51:427–432
80. Hekman MCH, Rijpkema M, Bos DL, Oosterwijk E, Goldenberg DM, Mulders PFA, Boerman OC (2017) Detection of micrometastases using SPECT/fluorescence dual-modality imaging in a CEA-expressing tumor model. *J Nucl Med* 58:706–710
81. Hendrikx G, Bauwens M, Wierits R, Mottaghy FM, Post MJ (2016) Left ventricular function measurements in a mouse myocardial infarction model. comparison between 3D-echocardiography and ECG-gated SPECT. *Nuklearmedizin* 55:115–122
82. Heskamp S, van Laarhoven HW, Molkenboer-Kueneen JD, Franssen GM, Versleijen-Jonkers YM, Oyen WJ, van der Graaf WT, Boerman OC (2010) ImmunoSPECT and immunoPET of IGF-1R expression with the radiolabeled antibody R1507 in a triple-negative breast cancer model. *J Nucl Med Off Publ Soc Nucl Med* 51:1565–1572
83. Hesterman JY, Kupinski MA, Furenlid LR, Wilson DW, Barrett HH (2007) The multi-module, multi-resolution system (M3R): a novel small-animal SPECT system. *Med Phys* 34:987–993
84. Higaki Y, Kobayashi M, Uehara T, Hanaoka H, Arano Y, Kawai K (2013) Appropriate collimators in a small animal SPECT scanner with CZT detector. *Ann Nucl Med* 27:271–278
85. Hildebrandt IJ, Su H, Weber WA (2008) Anesthesia and other considerations for in vivo imaging of small animals. *ILAR J/Natl Res Counc, Inst Lab Anim Resour* 49:17–26
86. Hoeben BA, Molkenboer-Kueneen J-D, Oyen WJ, Peeters WJ, Kaanders JH, Bussink J, Boerman OC (2010) Radiolabeled cetuximab: dose optimization for epidermal growth factor receptor imaging in a head-and-neck squamous cell carcinoma model. *Int J Cancer* 129(4):870–878
87. Hoffman D, Sun M, Yang L, McDonagh PR, Corwin F, Sundaresan G, Wang L, Vijayaragavan V, Thadigiri C, Lamichhane N, Zweit J (2014) Intrinsically radiolabelled [(59)Fe]-SPIONs for dual MRI/radionuclide detection. *Am J Nucl Med Mol Imaging* 4:548–560
88. Huang PC, Hsu CH (2015) Fast iterative reconstruction for helical pinhole SPECT imaging. *Biomed Mater Eng* 26(Suppl 1):S1371–S1380
89. Hutton BF, Occhipinti M, Kuehne A, Mathe D, Kovacs N, Waiczies H, Erlandsson K, Salvado D, Carminati M, Montagnani GL, Short SC, Ottobriani L, van Mullekom P, Piemonte C, Bukki T, Nyitrai Z, Papp Z, Nagy K, Niendorf T, deFrancesco I, Fiorini C (2018) Development of clinical simultaneous SPECT/MRI. *Br J Radiol* 91(1081):201606
90. Hwang AB, Franc BL, Gullberg GT, Hasegawa BH (2008) Assessment of the sources of error affecting the quantitative accuracy of SPECT imaging in small animals. *Phys Med Biol* 53:2233–2252
91. Hwang AB, Hasegawa BH (2005) Attenuation correction for small animal SPECT imaging using x-ray CT data. *Med Phys* 32:2799–2804
92. Hwang AB, Taylor CC, VanBrocklin HF, Dae MW, Hasegawa BH (2006) Attenuation correction of small animal SPECT images acquired with ¹²⁵I-iodorotone. *IEEE Trans Nucl Sci* 53

93. Inubushi M, Jin YN, Murai C, Hata H, Kitagawa Y, Saga T (2012) Single-photon emission computed tomography of spontaneous liver metastasis from orthotopically implanted human colon cancer cell line stably expressing human sodium/iodide symporter reporter gene. *EJNMMI Res* 2:46
94. Ioppolo JA, Caldwell D, Beiraghi O, Llano L, Blacker M, Valliant JF, Berti PJ (2017) (67) Ga-labeled deferoxamine derivatives for imaging bacterial infection: Preparation and screening of functionalized siderophore complexes. *Nucl Med Biol* 52:32–41
95. Islamian JP, Azazrm A, Mahmoudian B, Gharapapagh E (2015) Advances in pinhole and multi-pinhole collimators for single photon emission computed tomography imaging. *World J Nucl Med* 14:3–9
96. Ivashchenko O, van der Have F, Goorden MC, Ramakers RM, Beekman FJ (2015) Ultra-high-sensitivity submillimeter mouse SPECT. *J Nucl Med* 56:470–475
97. Ivashchenko, O., F. van der Have, J. L. Villena, H. C. Groen, R. M. Ramakers, H. H. Weinans, and F. J. Beekman. 2014. 'Quarter-millimeter-resolution molecular mouse imaging with U-SPECT(+)', *Mol Imaging*, 13
98. Iyer AK, Su Y, Feng J, Lan X, Zhu X, Liu Y, Gao D, Seo Y, Vanbrocklin HF, Courtney Broaddus V, Liu B, He J (2011) The effect of internalizing human single chain antibody fragment on liposome targeting to epithelioid and sarcomatoid mesothelioma. *Biomaterials* 32:2605–2613
99. Jiang ZK, Sato M, Wu L (2012) Chapter five–The development of transcription-regulated adenoviral vectors with high cancer-selective imaging capabilities. *Adv Cancer Res* 115:115–146
100. John E, Thakur ML, Wilder S, Alauddin MM, Epstein AL (1994) Technetium-99m-labeled monoclonal antibodies: influence of technetium-99m binding sites. *Journal of nuclear medicine: official publication, Society of Nuclear Medicine* 35:876–881
101. Johnson LC, Ovchinnikov O, Shokouhi S, Peterson TE (2015) Development of a Germanium Small-Animal SPECT System. *IEEE Trans Nucl Sci* 2015:2036–2042
102. Joosten L, Brom M, Schafer MKH, Boerman OC, Weihe E, Gotthardt M (2017) Preclinical evaluation of PAC1 targeting with radiolabeled Maxadilan. *Sci Rep* 7:1751
103. Joyal JL, Barrett JA, Marquis JC, Chen J, Hillier SM, Maresca KP, Boyd M, Gage K, Nimmagadda S, Kronauge JF, Friebe M, Dinkelborg L, Stubbs JB, Stabin MG, Mairs R, Pomper MG, Babich JW (2010) Preclinical evaluation of a 131I-labeled benzamide for targeted radiotherapy of metastatic melanoma. *Can Res* 70:4045–4053
104. Jurgielewicz P, Harmsen S, Wei E, Bachmann MH, Ting R, Aras O (2017) New imaging probes to track cell fate: reporter genes in stem cell research. *Cell Mol Life Sci* 74:4455–4469
105. Kastis GA, Furenlid LR, Wilson DW, Peterson TE, Barber HB, Barrett HH (2004) Compact CT/SPECT small-animal imaging system. *IEEE Trans Nucl Sci* 51:63–67
106. Kersemans V, Thompson J, Cornelissen B, Woodcock M, Allen PD, Buls N, Muschel RJ, Hill MA, Smart SC (2011) Micro-CT for anatomic referencing in PET and SPECT: radiation dose, biologic damage, and image quality. *J Nucl Med* 52(11):1827–1833
107. Khmelinskii A, Groen HC, Baiker M, de Jong M, Lelieveldt BP (2012) Segmentation and visual analysis of whole-body mouse skeleton microSPECT. *PLoS ONE* 7:e48976
108. Kim EM, Jeong HJ, Park IK, Cho CS, Bom HS, Kim CG (2004) Monitoring the effect of PEGylation on polyethylenimine in vivo using nuclear imaging technique. *Nucl Med Biol* 31:781–784
109. King R, Surfraz MB, Finucane C, Biagini SC, Blower PJ, Mather SJ (2009) 99mTc-HYNIC-Gastrin Peptides: Assisted Coordination of 99mTc by Amino Acid Side Chains Results in Improved Performance Both In Vitro and In Vivo. *Journal of nuclear medicine: official publication, Society of Nuclear Medicine* 50:591–598
110. Klippstein R, Wang JT, El-Gogary RI, Bai J, Mustafa F, Rubio N, Bansal S, Al-Jamal WT, Al-Jamal KT (2015) Passively Targeted Curcumin-Loaded PEGylated PLGA Nanocapsules for Colon Cancer Therapy In Vivo. *Small* 11:4704–4722

111. Kobayashi M, Matsunari I, Nishi K, Mizutani A, Miyazaki Y, Ogai K, Sugama J, Shiba K, Kawai K, Kinuya S (2016) Simultaneous acquisition of (99m)Tc- and (123)I-labeled radiotracers using a preclinical SPECT scanner with CZT detectors. *Ann Nucl Med* 30:263–271
112. Kojima C, Niki Y, Ogawa M, Magata Y (2014) Prolonged local retention of subcutaneously injected polymers monitored by noninvasive SPECT imaging. *Int J Pharm* 476:164–168
113. Kortylewicz ZP, Nearman J, Baranowska-Kortylewicz J (2009) Radiolabeled 5-iodo-3'-O-(17beta-succinyl-5alpha-androstan-3-one)-2'-deoxyuridine and its 5'-monophosphate for imaging and therapy of androgen receptor-positive cancers: synthesis and biological evaluation. *J Med Chem* 52:5124–5143
114. Krall N, Pretto F, Mattarella M, Muller C, Neri D (2016) A 99mTc-Labeled Ligand of Carbonic Anhydrase IX Selectively Targets Renal Cell Carcinoma In Vivo. *J Nucl Med* 57:943–949
115. Kruwel T, Nevoltris D, Bode J, Dullin C, Baty D, Chames P, Alves F (2016) In vivo detection of small tumour lesions by multi-pinhole SPECT applying a (99m)Tc-labelled nanobody targeting the Epidermal Growth Factor Receptor. *Sci Rep* 6:21834
116. Kupinski MK, Clarkson EW, Barrett HH (2013) Scanning linear estimation: improvements over region of interest (ROI) methods. *Phys Med Biol* 58:1283–1301
117. Laffon E, Thumerel M, Jougon J, Marthan R (2017) Cumulated Activity Comparison of (64)Cu-/(177)Lu-Labeled Anti-Epidermal Growth Factor Receptor Antibody in Esophageal Squamous Cell Carcinoma Model. *J Nucl Med* 58:888–890
118. Lanari C, Lamb CA, Fabris VT, Helguero LA, Soldati R, Bottino MC, Giulianelli S, Cerliani JP, Wargon V, Molinolo A (2009) The MPA mouse breast cancer model: evidence for a role of progesterone receptors in breast cancer. *Endocr Relat Cancer* 16:333–350
119. Lange C, Apostolova I, Lukas M, Huang KP, Hofheinz F, Gregor-Mamoudou B, Brenner W, Buchert R (2014) Performance evaluation of stationary and semi-stationary acquisition with a non-stationary small animal multi-pinhole SPECT system. *Mol Imaging Biol* 16:311–316
120. Lee HH, Chen JC (2013) Investigation of attenuation correction for small-animal single photon emission computed tomography. *Comput Math Methods Med* 2013:430276
121. Lee CL, Min H, Befera N, Clark D, Qi Y, Das S, Johnson GA, Badea CT, Kirsch DG (2014) Assessing cardiac injury in mice with dual energy-microCT, 4D-microCT, and microSPECT imaging after partial heart irradiation. *Int J Radiat Oncol Biol Phys* 88:686–693
122. Li Y, Welm B, Podsypanina K, Huang S, Chamorro M, Zhang X, Rowlands T, Egeblad M, Cowin P, Werb Z, Tan LK, Rosen JM, Varmus HE (2003) Evidence that transgenes encoding components of the Wnt signaling pathway preferentially induce mammary cancers from progenitor cells. *Proc Natl Acad Sci USA* 100:15853–15858
123. Li L, Wu Y, Wang Z, Jia B, Hu Z, Dong C, Wang F (2017) SPECT/CT Imaging of the Novel HER2-Targeted Peptide Probe (99m)Tc-HYNIC-H6F in Breast Cancer Mouse Models. *J Nucl Med* 58:821–826
124. Lim JC, Cho EH, Kim JJ, Choi SM, Lee SY, Nam SS, Park UJ, Park SH (2015) Preclinical pharmacokinetic, biodistribution, imaging and therapeutic efficacy of (177)Lu-Labeled glycosylated bombesin analogue for gastrin-releasing peptide receptor-positive prostate tumor targeting. *Nucl Med Biol* 42:234–241
125. Lin LT, Chang CH, Yu HL, Liu RS, Wang HE, Chiu SJ, Chen FD, Lee TW, Lee YJ (2014) Evaluation of the therapeutic and diagnostic effects of PEGylated liposome-embedded 188Re on human non-small cell lung cancer using an orthotopic small-animal model. *J Nucl Med* 55:1864–1870
126. Lin A, Kupinski MA, Peterson TE, Shokouhi S, Johnson LC (2018) Task-based design of a synthetic-collimator SPECT system used for small animal imaging. *Med Phys* 45:2952–2963
127. Liu IH, Chang CH, Ho CL, Chiu SP, Lee WC, Chang TJ, Chen LC, Wu YH, Chuang CH, Fu YK, Lee TW (2010) Multimodality imaging and preclinical evaluation of 177Lu-AMBA for human prostate tumours in a murine model. *Anticancer Res* 30:4039–4048

128. Liu X, Dong C, Shi J, Ma T, Jin Z, Jia B, Liu Z, Shen L, Wang F (2017) Radiolabeled novel mAb 4G1 for immunoSPECT imaging of EGFRvIII expression in preclinical glioblastoma xenografts. *Oncotarget* 8:6364–6375
129. Liu Z, Ma T, Liu H, Jin Z, Sun X, Zhao H, Shi J, Jia B, Li F, Wang F (2014) ¹⁷⁷Lu-labeled antibodies for EGFR-targeted SPECT/CT imaging and radioimmunotherapy in a preclinical head and neck carcinoma model. *Mol Pharm* 11:800–807
130. Lu Y, Yang K, Zhou K, Pang B, Wang G, Ding Y, Zhang Q, Han H, Tian J, Li C, Ren Q (2014) An integrated quad-modality molecular imaging system for small animals. *J Nucl Med* 55:1375–1379
131. Lutje S, Gerrits D, Molkenboer-Kueneen JD, Herrmann K, Fracasso G, Colombatti M, Boerman OC, Heskamp S (2018) Characterization of Site-Specifically Conjugated Monomethyl Auristatin E- and Duocarmycin-Based Anti-PSMA Antibody-Drug Conjugates for Treatment of PSMA-Expressing Tumors. *J Nucl Med* 59:494–501
132. Macholl S, Finucane CM, Hesterman J, Mather SJ, Pauplis R, Scully D, Sosabowski JK, Jouannot E (2017) High-throughput high-volume nuclear imaging for preclinical in vivo compound screening(section sign). *EJNMMI Res* 7:33
133. Mahani H, Raisali G, Kamali-Asl A, Ay MR (2017) Spinning slithole collimation for high-sensitivity small animal SPECT: Design and assessment using GATE simulation. *Phys Med* 40:42–50
134. Mamede M, Saga T, Ishimori T, Higashi T, Sato N, Kobayashi H, Brechbiel MW, Konishi J (2004) Hepatocyte targeting of ¹¹¹In-labeled oligo-DNA with avidin or avidin-dendrimer complex. *Journal of controlled release: official journal of the Controlled Release Society* 95:133–141
135. Mang'era KO, Liu G, Yi W, Zhang Y, Liu N, Gupta S, Rusckowski M, Hnatowich DJ (2001) Initial investigations of ^{99m}Tc-labeled morpholinos for radiopharmaceutical applications. *Eur J Nucl Med* 28:1682–1689
136. Mannheim JG, Kara F, Doorduyn J, Fuchs K, Reischl G, Liang S, Verhoye M, Gremse F, Mezzanotte L, Huisman MC (2018) Standardization of Small Animal Imaging-Current Status and Future Prospects. *Mol Imaging Biol* 20:716–731
137. Mardrossian G, Lei K, Rusckowski M, Chang F, Qu T, Egholm M, Hnatowich DJ (1997) In vivo hybridization of technetium-^{99m}-labeled peptide nucleic acid (PNA). *Journal of nuclear medicine: official publication, Society of Nuclear Medicine* 38:907–913
138. Matsunari I, Miyazaki Y, Kobayashi M, Nishi K, Mizutani A, Kawai K, Hayashi A, Komatsu R, Yonezawa S, Kinuya S (2014) Performance evaluation of the eXplore speCZT preclinical imaging system. *Ann Nucl Med* 28:484–497
139. Meenakshi A, Ganesh V, Suresh Kumar R, Siva Kumar N (2003) Radioimmuno targeting (^{99m})technetium labeled anti-epidermal growth factor receptor monoclonal antibodies in experimental tumor models. *The quarterly journal of nuclear medicine: official publication of the Italian Association of Nuclear Medicine* 47:139–144
140. Meier, D., D. J. Wagenaar, G. Maehlum, B. Sundal, B.E. Patt, S. Chen, J. Xu, J. Yu, B. M. W. Tsui, M. J. Hamamura, W. W. Roeck, S.H. Ha, and O. Nalcioglu. 2009. 'A SPECT camera for simultaneous SPECT/MRI', *IEEE Nuclear Science Symposium Conference Record*, J01-1
141. Melis M, de Swart J, de Visser M, Berndsen SC, Koelwijn S, Valkema R, Boerman OC, Krenning EP, de Jong M (2010) Dynamic and static small-animal SPECT in rats for monitoring renal function after ¹⁷⁷Lu-labeled Tyr3-octreotate radionuclide therapy. *Journal of nuclear medicine: official publication, Society of Nuclear Medicine* 51:1962–1968
142. Melis M, Vegt E, Konijnenberg MW, de Visser M, Bijster M, Vermeij M, Krenning EP, Boerman OC, de Jong M (2010) Nephrotoxicity in mice after repeated imaging using ¹¹¹In-labeled peptides. *Journal of nuclear medicine: official publication, Society of Nuclear Medicine* 51:973–977
143. Merron A, Baril P, Martin-Duque P, de la Vieja A, Tran L, Briat A, Harrington KJ, McNeish IA, Vassaux G (2010) Assessment of the Na/I symporter as a reporter gene to

- visualize oncolytic adenovirus propagation in peritoneal tumours. *Eur J Nucl Med Mol Imaging* 37:1377–1385
144. Merron A, Peerlinck I, Martin-Duque P, Burnet J, Quintanilla M, Mather S, Hingorani M, Harrington K, Iggo R, Vassaux G (2007) SPECT/CT imaging of oncolytic adenovirus propagation in tumours in vivo using the Na/I symporter as a reporter gene. *Gene Ther* 14:1731–1738
 145. Milagre C, Dhomen N, Geyer FC, Hayward R, Lambros M, Reis-Filho JS, Marais R (2010) A mouse model of melanoma driven by oncogenic KRAS. *Can Res* 70:5549–5557
 146. Miller BW, Van Holen R, Barrett HH, Furenlid LR (2011) A System Calibration and Fast Iterative Reconstruction Method for Next-Generation SPECT Imagers. *IEEE Nucl Sci Symp Conf Rec* 1997(2011):3548–3553
 147. Miller BW, Van Holen R, Barrett HH, Furenlid LR (2012) A System Calibration and Fast Iterative Reconstruction Method for Next-Generation SPECT Imagers. *IEEE Trans Nucl Sci* 59:1990–1996
 148. Ming H, Fang L, Gao J, Li C, Ji Y, Shen Y, Hu Y, Li N, Chang J, Li W, Tan J (2017) Antitumor Effect of Nanoparticle (131)I-Labeled Arginine-Glycine-Aspartate-Bovine Serum Albumin-Polycaprolactone in Lung Cancer. *AJR Am J Roentgenol* 208:1116–1126
 149. Misri R, Meier D, Yung AC, Kozlowski P, Hafeli UO (2012) Development and evaluation of a dual-modality (MRI/SPECT) molecular imaging bioprobe. *Nanomedicine* 8:1007–1016
 150. Mitra D, Pan H, Alhassen F, Seo Y (2014) Parallelization of Iterative Reconstruction Algorithms in Multiple Modalities. *IEEE Nucl Sci Symp Conf Rec* 1997:2014
 151. Miwa K, Inubushi M, Takeuchi Y, Katafuchi T, Koizumi M, Saga T, Sasaki M (2015) Performance characteristics of a novel clustered multi-pinhole technology for simultaneous high-resolution SPECT/PET. *Ann Nucl Med* 29:460–466
 152. Moji V, Zeratkar N, Farahani MH, Aghamiri MR, Sajedi S, Teimourian B, Ghafarian P, Sarkar S, Ay MR (2014) Performance evaluation of a newly developed high-resolution, dual-head animal SPECT system based on the NEMA NU1-2007 standard. *J Appl Clin Med Phys* 15:4936
 153. Moore SC, Park MA, Liu Z, Lyon MC, Johnson LC, Lushear VH, Westberg JG, Metzler SD (2016) Design of a dual-resolution collimator for preclinical cardiac SPECT with a stationary triple-detector system. *Med Phys* 43:6336
 154. Mu Z, Dobrucki LW, Liu YH (2016) SPECT Imaging of 2-D and 3-D Distributed Sources with Near-Field Coded Aperture Collimation: Computer Simulation and Real Data Validation. *J Med Biol Eng* 36:32–43
 155. Muller C, Fischer E, Behe M, Koster U, Dorrer H, Reber J, Haller S, Cohrs S, Blanc A, Grunberg J, Bunka M, Zhernosekov K, van der Meulen N, Johnston K, Turler A, Schibli R (2014) Future prospects for SPECT imaging using the radiolanthanide terbium-155 - production and preclinical evaluation in tumor-bearing mice. *Nucl Med Biol* 41(Suppl):e58–e65
 156. Naqvi SA, Matzow T, Finucane C, Nagra SA, Ishfaq MM, Mather SJ, Sosabowski J (2010) Insertion of a lysosomal enzyme cleavage site into the sequence of a radiolabeled neuropeptide influences cell trafficking in vitro and in vivo. *Cancer biotherapy & radiopharmaceuticals* 25:89–95
 157. Nayak TR, Krasteva LK, Cai W (2013) Multimodality imaging of RNA interference. *Curr Med Chem* 20:3664–3675
 158. Nelson, S. J., J. Kurhanewicz, D. B. Vigneron, P. E. Larson, A. L. Harzstark, M. Ferrone, M. van Criekinge, J. W. Chang, R. Bok, I. Park, G. Reed, L. Carvajal, E. J. Small, P. Munster, V. K. Weinberg, J. H. Ardenkjaer-Larsen, A. P. Chen, R. E. Hurd, L. I. Odegaardstuen, F. J. Robb, J. Tropp, and J. A. Murray. 2013. ‘Metabolic imaging of patients with prostate cancer using hyperpolarized [1-(1)(3)C]pyruvate’, *Sci Transl Med*, 5: 198ra08
 159. Neyt S, Vliegen M, Verreut B, De Lombaerde S, Braeckman K, Vanhove C, Huisman MT, Dumolyn C, Kersemans K, Hulpia F, Van Calenbergh S, Mannens G, De Vos F (2016) Synthesis, in vitro and in vivo small-animal SPECT evaluation of novel technetium labeled

- bile acid analogues to study (altered) hepatic transporter function. *Nucl Med Biol* 43:642–649
160. Ni Y, Wang H, Chen F, Li J, DeKeyser F, Feng Y, Yu J, Bosmans H, Marchal G (2009) Tumor models and specific contrast agents for small animal imaging in oncology. *Methods* 48:125–138
 161. Nilsson C, Barrios-Lopez B, Kallinen A, Laurinmaki P, Butcher SJ, Raki M, Weisell J, Bergstrom K, Larsen SW, Ostergaard J, Larsen C, Urtti A, Airaksinen AJ, Yaghmur A (2013) SPECT/CT imaging of radiolabeled cubosomes and hexosomes for potential theranostic applications. *Biomaterials* 34:8491–8503
 162. Oliver PG, LoBuglio AF, Zinn KR, Kim H, Nan L, Zhou T, Wang W, Buchsbaum DJ (2008) Treatment of human colon cancer xenografts with TRA-8 anti-death receptor 5 antibody alone or in combination with CPT-11. *Clinical cancer research: an official journal of the American Association for Cancer Research* 14:2180–2189
 163. Padmanabhan P, Grosse J, Asad AB, Radda GK, Gelay X (2013) Gastrointestinal transit measurements in mice with ^{99m}Tc-DTPA-labeled activated charcoal using NanoSPECT-CT. *EJNMMI Res* 3:60
 164. Palmieri D, Smith QR, Lockman PR, Bronder J, Gril B, Chambers AF, Weil RJ, Steeg PS (2006) Brain metastases of breast cancer. *Breast disease* 26:139–147
 165. Pan H, Chang H, Mitra D, Gullberg GT, Seo Y (2017) Sparse domain approaches in dynamic SPECT imaging with high-performance computing. *Am J Nucl Med Mol Imaging* 7:283–294
 166. Pato LR, Vandenbergh S, Zedda T, Van Holen R (2015) Parallel-hole collimator concept for stationary SPECT imaging. *Phys Med Biol* 60:8791–8807
 167. Peerlinck I, Merron A, Baril P, Conchon S, Martin-Duque P, Hindorf C, Burnet J, Quintanilla M, Hingorani M, Iggo R, Lemoine NR, Harrington K, Vassaux G (2009) Targeted radionuclide therapy using a Wnt-targeted replicating adenovirus encoding the Na/I symporter. *Clinical cancer research: an official journal of the American Association for Cancer Research* 15:6595–6601
 168. Peterson TE, Furenlid LR (2011) SPECT detectors: the Anger Camera and beyond. *Phys Med Biol* 56:R145–R182
 169. Pino F, Roe N, Aguiar P, Falcon C, Ros D, Pavia J (2015) Improved image quality in pinhole SPECT by accurate modeling of the point spread function in low magnification systems. *Med Phys* 42:703–714
 170. Pomper MG, Hammond H, Yu X, Ye Z, Foss CA, Lin DD, Fox JJ, Cheng L (2009) Serial imaging of human embryonic stem-cell engraftment and teratoma formation in live mouse models. *Cell Res* 19:370–379
 171. Prior P, Timmins R, Petryk J, Strychorst J, Duan Y, Wei L, Glenn Wells R (2016) A modified TEW approach to scatter correction for In-111 and Tc-99m dual-isotope small-animal SPECT. *Med Phys* 43:5503
 172. Ray GL, Baidoo KE, Wong KJ, Williams M, Garmestani K, Brechbiel MW, Milenic DE (2009) Preclinical evaluation of a monoclonal antibody targeting the epidermal growth factor receptor as a radioimmunodiagnostic and radioimmunotherapeutic agent. *Br J Pharmacol* 157:1541–1548
 173. Rokugawa T, Uehara T, Higaki Y, Matsushima S, Obata A, Arano Y, Abe K (2014) Potential of (^{99m}Tc)-MIBI SPECT imaging for evaluating non-alcoholic steatohepatitis induced by methionine-choline-deficient diet in mice. *EJNMMI Res* 4:57
 174. Rosol TJ, Tannehill-Gregg SH, LeRoy BE, Mandl S, Contag CH (2003) Animal models of bone metastasis. *Cancer* 97:748–757
 175. Sanches PG, Peters S, Rossin R, Kaijzel EL, Que I, Lowik CW, Grull H (2015) Bone metastasis imaging with SPECT/CT/MRI: a preclinical toolbox for therapy studies. *Bone* 75:62–71

176. Sanchez F, Orero A, Soriano A, Correcher C, Conde P, Gonzalez A, Hernandez L, Moliner L, Rodriguez-Alvarez MJ, Vidal LF, Benlloch JM, Chapman SE, Leevy WM (2013) ALBIRA: a small animal PETSPECTCT imaging system. *Med Phys* 40:051906
177. Santini C, Kuil J, Bunschoten A, Pool S, de Blois E, Ridwan Y, Essers J, Bernsen MR, van Leeuwen FW, de Jong M (2016) Evaluation of a Fluorescent and Radiolabeled Hybrid Somatostatin Analog In Vitro and in Mice Bearing H69 Neuroendocrine Xenografts. *J Nucl Med* 57:1289–1295
178. Sausville, E. A., and A. M. Burger. 2006. 'Contributions of human tumor xenografts to anticancer drug development', *Cancer research*, 66: 3351–4, discussion 54
179. Schillaci O, Spanu A, Madeddu G (2005) [^{99m}Tc]sestamibi and [^{99m}Tc]tetrofosmin in oncology: SPET and fusion imaging in lung cancer, malignant lymphomas and brain tumors. *The quarterly journal of nuclear medicine and molecular imaging: official publication of the Italian Association of Nuclear Medicine* 49:133–144
180. Shih BB, Chang YF, Cheng CC, Yang HJ, Chang KW, Ho AS, Lin HC, Yeh C, Chang CC (2017) SPECT imaging evaluation of (¹¹¹)indium-chelated cetuximab for diagnosing EGFR-positive tumor in an HCT-15-induced colorectal xenograft. *J Chin Med Assoc* 80:766–773
181. Si C, Mok GS, Chen L, Tsui BM (2016) Design and evaluation of an adaptive multipinhole collimator for high-performance clinical and preclinical imaging. *Nucl Med Commun* 37:313–321
182. Sosabowski JK, Matzow T, Foster JM, Finucane C, Ellison D, Watson SA, Mather SJ (2009) Targeting of CCK-2 receptor-expressing tumors using a radiolabeled divalent gastrin peptide. *Journal of nuclear medicine: official publication, Society of Nuclear Medicine* 50:2082–2089
183. Stephenson KA, Zubieta J, Banerjee SR, Levadala MK, Taggart L, Ryan L, McFarlane N, Boreham DR, Maresca KP, Babich JW, Valliant JF (2004) A new strategy for the preparation of peptide-targeted radiopharmaceuticals based on an fmoc-lysine-derived single amino acid chelate (SAAC). automated solid-phase synthesis, NMR characterization, and in vitro screening of fMLF(SAAC)G and fMLF[(SAAC-Re(CO)₃)+]G. *Bioconj Chem* 15:128–136
184. Stolin A, Pole D, Majewski S, Kross B, Weisenberger A, Wojcik R, Williams MB (2005) Design and characteristics of a small animal multi-modality scanner. In: Bo Yu (ed) *IEEE Nuclear Science Symposium Conference Record*. Puerto Rico, Fajardo, pp 2183–2186
185. Strydhorst JH, Ruddy TD, Wells RG (2015) Effects of CT-based attenuation correction of rat microSPECT images on relative myocardial perfusion and quantitative tracer uptake. *Med Phys* 42:1818–1824
186. Takahashi, T., and S. Watanabe. 2001. 'Recent Progress in CdTe and CdZnTe detectors', *IEEE transactions on nuclear science*, 48
187. Tan JW, Cai L, Meng LJ (2009) A prototype of the MRI-compatible ultra-high resolution SPECT for in vivo mice brain imaging. *IEEE Nuclear Science Symposium Conference Record M05:2800–2805*
188. Tang L, Peng C, Tang B, Li Z, Wang X, Li J, Gao F, Huang L, Xu D, Zhang P, Zhuang R, Su X, Chen X, Zhang X (2018) Radioiodinated Small-Molecule Tyrosine Kinase Inhibitor for HER2-Selective SPECT Imaging. *J Nucl Med* 59:1386–1391
189. Tibbelin S, Nillius P, Danielsson M (2012) Simulation of HyperSPECT: a high-resolution small-animal system with in-line x-ray optics. *Phys Med Biol* 57:1617–1629
190. Timmermand OV, Tran TA, Strand SE, Axelsson J (2015) Intratherapeutic biokinetic measurements, dosimetry parameter estimates, and monitoring of treatment efficacy using cerenkov luminescence imaging in preclinical radionuclide therapy. *J Nucl Med* 56:444–449
191. Tseng YC, Xu Z, Guley K, Yuan H, Huang L (2014) Lipid-calcium phosphate nanoparticles for delivery to the lymphatic system and SPECT/CT imaging of lymph node metastases. *Biomaterials* 35:4688–4698

192. Uchida E, Matsushita A, Yanagi K, Hiroi M, Aimoto T, Nakamura Y, Yokoyama T, Tajiri T (2008) 'Experimental pancreatic cancer model using PGHAM-1 cells: characteristics and experimental therapeutic trials', *J Nippon Medical School = Nihon Ika Daigaku zasshi*, 75:325–31
193. Umeda IO, Tani K, Tsuda K, Kobayashi M, Ogata M, Kimura S, Yoshimoto M, Kojima S, Moribe K, Yamamoto K, Moriyama N, Fujii H (2012) High resolution SPECT imaging for visualization of intratumoral heterogeneity using a SPECT/CT scanner dedicated for small animal imaging. *Ann Nucl Med* 26:67–76
194. Vaissier PE, Goorden MC, Vastenhouw B, van der Have F, Ramakers RM, Beekman FJ (2012) Fast spiral SPECT with stationary gamma-cameras and focusing pinholes. *J Nucl Med* 53:1292–1299
195. Van Audenhaege K, Van Holen R, Vandenberghe S, Vanhove C, Metzler SD, Moore SC (2015) Review of SPECT collimator selection, optimization, and fabrication for clinical and preclinical imaging. *Med Phys* 42:4796–4813
196. Van Holen R, Vandeghinste B, Deprez K, Vandenberghe S (2013) Design and performance of a compact and stationary microSPECT system. *Med Phys* 40:112501
197. van Oosterom MN, Kreuger R, Buckle T, Mahn WA, Bunschoten A, Josephson L, van Leeuwen FW, Beekman FJ (2014) U-SPECT-BioFluo: an integrated radionuclide, bioluminescence, and fluorescence imaging platform. *EJNMMI Res* 4:56
198. van Weerden WM, Bangma C, de Wit R (2009) Human xenograft models as useful tools to assess the potential of novel therapeutics in prostate cancer. *Br J Cancer* 100:13–18
199. Vandeghinste B, Van Holen R, Vanhove C, De Vos F, Vandenberghe S, Staelens S (2014) Use of a ray-based reconstruction algorithm to accurately quantify preclinical microSPECT images. *Mol Imaging* 13:1–13
200. Vangestel C, Peeters M, Mees G, Oltenfreiter R, Boersma HH, Elsinga PH, Reuteling-sperger C, Van Damme N, De Spiegeleer B, Van de Wiele C (2011) In vivo imaging of apoptosis in oncology: an update. *Mol Imaging* 10(5):340–358
201. Vanhove C, Defrise M, Bossuyt A, Lahoutte T (2011) Improved quantification in multiple-pinhole SPECT by anatomy-based reconstruction using microCT information. *Eur J Nucl Med Mol Imaging* 38:153–165
202. Veres DS, Mathe D, Futo I, Horvath I, Balazs A, Karlinger K, Szigeti K (2014) Quantitative liver lesion volume determination by nanoparticle-based SPECT. *Mol Imaging Biol* 16:167–172
203. Verhaar MJ, Keep PA, Hawkins RE, Robson L, Casey JL, Pedley B, Boden JA, Begent RH, Chester KA (1996) Technetium-99m radiolabeling using a phage-derived single-chain Fv with a C-terminal cysteine. *Journal of nuclear medicine: official publication, Society of Nuclear Medicine* 37:868–872
204. Verhaegen F, Dubois L, Gianolini S, Hill MA, Karger CP, Lauber K, Prise KM, Sarrut D, Thorwarth D, Vanhove C, Vojnovic B, Weersink R, Wilkens JJ, Georg D (2018) ESTRO ACROP: Technology for precision small animal radiotherapy research: Optimal use and challenges. *Radiother Oncol* 126:471–478
205. Virzi F, Fritz B, Rusckowski M, Gionet M, Misra H, Hnatowich DJ (1991) 'New indium-111 labeled biotin derivatives for improved immunotargeting', *International journal of radiation applications and instrumentation*. Part B, Nuclear medicine and biology 18:719–726
206. Voskoglou-Nomikos T, Pater JL, Seymour L (2003) Clinical predictive value of the in vitro cell line, human xenograft, and mouse allograft preclinical cancer models. *Clinical cancer research: an official journal of the American Association for Cancer Research* 9:4227–4239
207. Vrigneaud JM, Courteau A, Ranouil J, Morgand L, Raguin O, Walker P, Oudot A, Collin B, Brunotte F (2013) Application of the optically stimulated luminescence (OSL) technique for mouse dosimetry in micro-CT imaging. *Med Phys* 40:122102

208. Walker KL, Judenhofer MS, Cherry SR, Mitchell GS (2015) Un-collimated single-photon imaging system for high-sensitivity small animal and plant imaging. *Phys Med Biol* 60:403–420
209. Wang Y, Tseng JC, Sun Y, Beck AH, Kung AL (2015) Noninvasive imaging of tumor burden and molecular pathways in mouse models of cancer. *Cold Spring Harb Protoc* 2015:135–144
210. Wang, Y., H. Xue, J. C. Cutz, J. Bayani, N. R. Mawji, W. G. Chen, L. J. Goetz, S. W. Hayward, M. D. Sadar, C. B. Gilks, P. W. Gout, J. A. Squire, G. R. Cunha, and Y. Z. Wang. 2005. 'An orthotopic metastatic prostate cancer model in SCID mice via grafting of a transplantable human prostate tumor line', *Laboratory investigation*, 85:1392–404
211. Weisenberger AG, Kross B, Majewski S, Popov V, Smith MF, Welch B, Wojcik R, Goddard J, Gleason SS, Paulus MJ, Meikle SR, Pomper M (2005) A small animal SPECT imaging system utilizing position tracking of unanesthetized mice. In: Kupinski MA, Barrett HH (eds) *Small-Animal SPECT Imaging*. New York, Springer
212. Weisenberger AG, Wojcik R, Bradley EL, Brewer P, Majewski S, Qian J, Ranck A, Saha MS, Smith K, Smith MF, Welsh RE (2003) SPECT-CT system for small animal imaging. *IEEE Trans Nucl Sci* 50:74–79
213. Weisenberger, A.G., B. Kross, S. Majewski, V. Popov, M.F. Smith, V.H. Tran, B. Welch, J. Baba, J. Goddard, M. Pomper, and B. Tsui. 2006. "Instrumentation Development of a SPECT-CT System to Image Awake Mice. In: *IEEE Nuclear Science Symposium Conference Record*, 3000–3003
214. Woods A, Patel A, Spina D, Riffo-Vasquez Y, Babin-Morgan A, de Rosales RT, Sunassee K, Clark S, Collins H, Bruce K, Dailey LA, Forbes B (2015) In vivo biocompatibility, clearance, and biodistribution of albumin vehicles for pulmonary drug delivery. *J Control Release* 210:1–9
215. Workman P, Aboagye EO, Balkwill F, Balmain A, Bruder G, Chaplin DJ, Double JA, Everitt J, Farningham DAH, Glennie MJ, Kelland LR, Robinson V, Stratford IJ, Tozer GM, Watson S, Wedge SR, Eccles SA (2010) Guidelines for the welfare and use of animals in cancer research. *Br J Cancer* 102:1555–1577
216. Wu C, van der Have F, Vastenhout B, Dierckx RA, Paans AM, Beekman FJ (2010) Absolute quantitative total-body small-animal SPECT with focusing pinholes. *Eur J Nucl Med Mol Imaging* 37:2127–2135
217. Wu Y, Sun Y, Zhu X, Liu Q, Cao T, Peng J, Yang Y, Feng W, Li F (2014) Lanthanide-based nanocrystals as dual-modal probes for SPECT and X-ray CT imaging. *Biomaterials* 35:4699–4705
218. Xie T, Zaidi H (2016) Development of computational small animal models and their applications in preclinical imaging and therapy research. *Med Phys* 43:111
219. Xie, Z., S. Li, K. Yang, B. Xu, and Q. Ren. 2016. 'Evaluation of a Wobbling Method Applied to Correcting Defective Pixels of CZT Detectors in SPECT Imaging', *Sensors (Basel)*, 16
220. Xue S, Zhang C, Yang Y, Zhang L, Cheng D, Zhang J, Shi H, Zhang Y (2015) ^{99m}Tc-Labeled Iron Oxide Nanoparticles for Dual-Contrast (T1/T2) Magnetic Resonance and Dual-Modality Imaging of Tumor Angiogenesis. *J Biomed Nanotechnol* 11:1027–1037
221. Yamamoto S, Watabe H, Kanai Y, Shimosegawa E, Hatazawa J (2012) Development of a pixelated GSO gamma camera system with tungsten parallel hole collimator for single photon imaging. *Med Phys* 39:581–588
222. Yang S, Dong Q, Yao M, Shi M, Ye J, Zhao L, Su J, Gu W, Xie W, Wang K, Du Y, Li Y, Huang Y (2009) Establishment of an experimental human lung adenocarcinoma cell line SPC-A-1BM with high bone metastases potency by (99m)Tc-MDP bone scintigraphy. *Nucl Med Biol* 36:313–321

223. Yang Y, Sun Y, Cao T, Peng J, Liu Y, Wu Y, Feng W, Zhang Y, Li F (2013) Hydrothermal synthesis of NaLuF₄:153Sm, Yb, Tm nanoparticles and their application in dual-modality upconversion luminescence and SPECT bioimaging. *Biomaterials* 34:774–783
224. Youn H, Chung JK (2013) Reporter gene imaging. *AJR Am J Roentgenol* 201:W206–W214
225. Yu M, Zhou H, Liu X, Huo Y, Zhu Y, Chen Y (2010) Study on biodistribution and imaging of radiiodinated arginine-arginine-leucine peptide in nude mice bearing human prostate carcinoma. *Ann Nucl Med* 24:13–19
226. Zan Y, Boutchko R, Huang Q, Li B, Chen K, Gullberg GT (2013) Fast direct estimation of the blood input function and myocardial time activity curve from dynamic SPECT projections via reduction in spatial and temporal dimensions. *Med Phys* 40:092503
227. Zeraatkar N, Farahani MH, Rahmim A, Sarkar S, Ay MR (2016) Design and assessment of a novel SPECT system for desktop open-gantry imaging of small animals: A simulation study. *Med Phys* 43:2581
228. Zeraatkar N, Sajedi S, Farahani MH, Arabi H, Sarkar S, Ghafarian P, Rahmim A, Ay MR (2014) Resolution-recovery-embedded image reconstruction for a high-resolution animal SPECT system. *Phys Med* 30:774–781
229. Zhang M, Jasim DA, Menard-Moyon C, Nunes A, Iijima S, Bianco A, Yudasaka M, Kostarelos K (2016) Radiolabeling, whole-body single photon emission computed tomography/computed tomography imaging, and pharmacokinetics of carbon nanohorns in mice. *Int J Nanomedicine* 11:3317–3330
230. Zhang X, You L, Chen S, Gao M, Guo Z, Du J, Lu J, Zhang X (2018) Development of a novel (99m) Tc-labeled small molecular antagonist for CXCR4 positive tumor imaging. *J Labelled Comp Radiopharm* 61:438–446
231. Zhang C, Yu X, Gao L, Zhao Y, Lai J, Lu D, Bao R, Jia B, Zhong L, Wang F, Liu Z (2017) Noninvasive Imaging of CD206-Positive M2 Macrophages as an Early Biomarker for Post-Chemotherapy Tumor Relapse and Lymph Node Metastasis. *Theranostics* 7:4276–4288
232. Zhao Q, Yan P, Yin L, Li L, Chen XQ, Ma C, Wang RF (2013) ‘Validation study of (1)(3) (1)I-RRL: assessment of biodistribution. SPECT imaging and radiation dosimetry in mice’, *Mol Med Rep* 7:1355–1360
233. Zhou HE, Li CL, Chung LW (2000) Establishment of human prostate carcinoma skeletal metastasis models. *Cancer* 88:2995–3001
234. Zhou Y, Shao G, Liu S (2012) Monitoring Breast Tumor Lung Metastasis by U-SPECT-II/CT with an Integrin alpha(v)beta(3)-Targeted Radiotracer(99m)Tc-3P-RGD (2). *Theranostics* 2:577–588
235. Zhu X, Li J, Hong Y, Kimura RH, Ma X, Liu H, Qin C, Hu X, Hayes TR, Benny P, Gambhir SS, Cheng Z (2014) 99mTc-labeled cystine knot peptide targeting integrin alphavbeta6 for tumor SPECT imaging. *Mol Pharm* 11:1208–1217



Preclinical Applications of Magnetic Resonance Imaging in Oncology

12

Wilfried Reichardt and Dominik von Elverfeldt

Contents

12.1	Introduction.....	406
12.2	Experimental Models of Cancer	407
12.3	Small Animal Molecular Imaging.....	408
12.4	Magnetic Resonance Imaging and Spectroscopy	409
12.4.1	Contrast Agents	411
12.4.2	Dynamic Contrast-Enhanced MRI	413
12.4.3	Steady-State Susceptibility-Contrast MRI.....	413
12.4.4	Diffusion-Weighted MRI.....	415
12.4.5	Arterial Spin Labeling	418
12.4.6	¹³ C Hyperpolarization	419
12.5	Applications	420
12.5.1	Metabolism	420
12.5.2	Hypoxia.....	421
12.5.3	Angiogenesis.....	423
12.5.4	Cellular Imaging.....	424
12.6	Summary and Outlook	427
	References	428

W. Reichardt (✉) · D. von Elverfeldt
Medical Physics, Department of Radiology, Faculty of Medicine,
University of Freiburg, Freiburg, Germany
e-mail: wilfried.reichardt@uniklinik-freiburg.de

D. von Elverfeldt
e-mail: dominik.elverfeldt@uniklinik-freiburg.de

W. Reichardt
German Consortium for Translational Cancer Research (DKTK), Heidelberg, Germany
German Cancer Research Center (DKFZ), Heidelberg, Germany

© Springer Nature Switzerland AG 2020
O. Schober et al. (eds.), *Molecular Imaging in Oncology*,
Recent Results in Cancer Research 216,
https://doi.org/10.1007/978-3-030-42618-7_12

405

12.1 Introduction

Non-invasive *in vivo* imaging techniques have been used as biomarker of disease in oncology, mainly involved in (i) pretreatment tissue characterization and monitoring tumor progression, (ii) therapy planning, and (iii) therapy response evaluation, and follow-up. In this context, imaging has been generally based on basic morphological criteria of tumor size and location, which are probably not influenced in the early and potentially main relevant phases of modern cancer therapies. However, current advances in molecular cancer biology, genetics, and imaging technology shift imaging paradigms away from solely morphological imaging toward molecular imaging MI, which is defined as the direct or indirect assessment of spatial and/or temporal distribution of physiologic, metabolic, and cellular or molecular processes within tissues *in vivo* especially with the development of high-field MR imaging [39].

Besides detection, (differential) diagnosis, and staging of neoplastic tissue during disease progression, tissue characterization with MI techniques also enables the assessment of therapeutically relevant biological properties such as metabolism, proliferation, hypoxia, angiogenesis, apoptosis, and gene and receptor expression of tumors. Such features are related to important hallmarks of cancer [42] and themselves targets for modern treatment strategies. Thus, thorough evaluation of biological tumor characteristics may impact the currently morphology-based treatment planning and help to improve future therapeutical strategies. Therefore, it is of great importance to assess changes in cancer biology in response to a specific therapy early on during the course of treatment, even before apparent changes in morphological imaging become visible. This will allow timely adjusting potentially ineffective treatment concepts that may be expensive and largely impacting on patients' quality of life. Consequently, MI will likely contribute to the realization of concepts of modern individualized medicine.

Animal models of cancer have ever played an important role in oncological research. Current and future MI developments have been and will be almost exclusively tested and optimized in preclinical studies. With the development of novel experimental tumor models based on recent developments in molecular biology and genetics [113, 152], their value for the evaluation of new therapeutic concepts, ongoing methodological developments, and underlying imaging principles is constantly growing.

Investigation of physiologic, metabolic, and cellular or molecular processes *in vivo* in experimental tumor models can be performed non-invasively with a variety of small animal imaging modalities, which all have their inherent strengths and weaknesses. Here, we will focus on magnetic resonance imaging (MRI) and spectroscopy (MRS) that are widely accessible and clinically well established, thus allowing fast translation of experimental imaging findings into clinics.

In the first chapter, we will comment on the use of experimental animal models of cancer and associated challenges for imaging. We introduce basic principles, values, and limitation of MRI/MRS as MI modalities. Finally, we present

applications in preclinical cancer research, indicating the high potential of MI to non-invasively assess information on hypoxia, angiogenesis, apoptosis, gene expression, metabolism, and cell migration in tumors.

12.2 Experimental Models of Cancer

Oncological studies in human patients confront strict ethical regulations and are time- and resource-intensive often with shortages of sound scientific evidence. However, *in vitro* cell culture and biochemical assays usually may not adequately reflect *in vivo* conditions. The use of clinically relevant animal tumor models as workable surrogates for human patients represents an important step in translational research bridging the gap between cell laboratory and clinical application. In the European Union, approximately 99% of laboratory animals used in 2011 in the field of cancer research were mice (94%) and rats (5%) (European Commission 2013). Consequently, a variety of animal tumor models in mice and rats exist in experimental oncology [91, 113, 125, 152]. They possess rather widely differing features such as growth pattern (diffuse over body vs. single solid lesion), dignity (less differentiated malignant tumor with infiltrating growth and raised metastatic potential vs. well-differentiated benign tumor with expanding growth and encapsulation), vascularity (highly vascularized vs. avascular), and incidence of spontaneous necrosis. Primary tumors (malignant or benign) can be spontaneously formed or artificially induced by chemicals, ionizing radiation, and genetic engineering, whereas secondary tumors (only malignant) can be created as allografts (from the same species) or xenografts (across different species; most often from human to animal) by cell suspension inoculation or tissue piece implantation. Xenograft tumor models may successfully be established only in immune-suppressed animals. Tumors may grow ectopically (in an unusual place), such as most subcutaneous tumor models, or orthotopically (in the usual position), like lymphoma in spleen. However, available animal models are still discussed rather controversially for their capabilities in efficient cancer therapy development [34, 56, 113, 152]. Although ectopic human tumor xenograft models of non-small cell lung and ovarian cancers may predict phase II clinical trial performance of cancer drugs, they have not yet proven to be general predictors of clinical outcome. This might be due to various variables impacting on outcome of therapeutic experimental models: site of implantation, growth properties of xenograft and size at treatment initiation, agent formulation, scheduling, route of administration and dose, and the selected endpoint for assessing activity. In studies of antiangiogenic or anti-vascular and immunotherapeutical strategies, the targeted structures of interest in xenografts are predominantly of host origin. They are also less useful for assessment of anti-metastatic strategies since subcutaneously implanted tumors generally do not metastasize. Animal models using orthotopically implanted tumors may be more appropriate [113, 125, 126]. Due to these shortcomings, there has been much interest in genetically engineered models, in which genes of interest can

be selectively overexpressed, additionally inserted or deleted in all cells or only in a specific tissue compartment and/or developmental stage [104, 113, 125]. Such sophisticated models are able to produce orthotopic primary tumors that closely mimic human cancer. However, the use of artificial promoters which drive transgene expression can influence the affected cell type, vary the expression based on genetic background, and decrease cellular heterogeneity, which, in turn, can affect tumor progression and metastasis [125].

Although the ideal experimental cancer model that can reliably predict the extent of clinical efficacy has not yet been identified, selection of models suiting the desired research purpose may finally be achieved by thoroughly taking into account the specialties and features of present tumor models [113]. If particular abnormalities of human cancer are sufficiently represented, experimental tumor models can still be valuable for in vivo proof-of-principle of new therapeutic concepts such as target identification, optimization of pharmaceutically tractable molecules, selection of lead candidates for clinical evaluation, optimization of scheduling, and combination with other drugs to guide clinical development and to study acquired drug resistance (and its circumvention). Furthermore, it can be used to develop new imaging concepts such as tracer and contrast agent development, visualization and quantification of biological tumor properties, and validation of non-invasive cancer biomarkers. For many applications, it will be critical to incorporate pharmacological and toxicological considerations as well as mechanistic concepts of tumor induction, progression, and metastasis. Some models may be even more suited for diagnostic rather than therapeutic assessments. Molecular imaging can promote development of improved animal models and anticancer agents by providing a time- and labor-efficient way of non-invasively evaluating effectiveness of novel treatment strategies to identify most promising candidates for clinical application. In contrast to biomarkers circulating in blood or tissue sampling, non-invasive imaging biomarkers may more efficiently sample tumor heterogeneity and thus impact on the proposed treatment scheme. Conversely, new insights in cancer biology may also stimulate the development of innovative imaging approaches.

12.3 Small Animal Molecular Imaging

Imaging experimental models of cancer in small animals requires special consideration of their altered morphology and physiology with respect to humans. Selected morphological and physiological characteristics of mice, rats, and humans are summarized in Table 12.1 [147]. In order to obtain comparable resolution—related to body size—as in human imaging, voxel dimensions need to be scaled down in small animal imaging by a factor of approximately 10 (in every spatial direction), which will result in 1,000-fold less signal. This has led to the development of dedicated scanners, which are particularly designed to meet small animal imaging needs. With current advances in clinical scanner and detector technology, small animal imaging can successfully be performed using clinical scanners too

Table 12.1 Selected characteristic morphological and physiological values for mouse, rat, and human (reprinted with permission of Informa Healthcare from [147])

	Mouse	Rat	Human
Body mass (g)	20–40	250–400	70,000
Blood volume (ml)	1.5–3.2	15–28	6,000–7,000
Brain size (mm)	6	10	105
Heart mass (g)	0.1	1	300
Heart rate (min^{-1})	630	330–480	60–80
Breathing rate (min^{-1})	163	66–114	12–18

[8, 147]. Dedicated small animal scanners typically present better imaging performance, but their clinical counterparts can compete in many applications and warrant a better availability and potential translatability of experimental imaging methods into clinics. Nevertheless, applications with ultrahigh-resolution requirements, as well as advanced functional imaging are usually restricted to dedicated scanners exclusively.

Most widely used modalities in molecular imaging include PET, SPECT, MRI, and MRS, which are clinically well established. Optical imaging [40] is also very powerful in experimental molecular imaging but clinically less relevant except for surgical guidance. Other modalities like ultrasound [59, 160] and computed tomography [25] are progressively developing MI capabilities.

12.4 Magnetic Resonance Imaging and Spectroscopy

Magnetic resonance (MR) techniques rely on the behavior of nuclei in strong magnetic fields under the influence of radiofrequency (RF) waves. To be actively exploited with MR, isotopes must possess a nuclear spin (e.g., hydrogen (^1H), carbon (^{13}C), fluorine (^{19}F), sodium (^{23}Na), and phosphorus (^{31}P)). In living subjects, the protons (^1H) of water and lipids are the primary signal source, whereas other isotopes are less abundant, and thus more difficult to assess. In a magnetic field, protons act as little bar magnets. According to Boltzmann distribution, they tend to orient themselves parallel (spin up) and anti-parallel (spin down) with respect to the direction of the externally applied magnetic field, respectively, thereby building up a net equilibrium magnetization. Typically, the number of excess spins in energetically more favorable parallel alignment is in the order of 10 in one million at clinically relevant field strengths. Additionally, spins precess at a frequency proportional to magnetic field strength, which is known as Larmor frequency. Excitation of spins with a sequence of RF pulses at the Larmor frequency disturbs the thermal equilibrium spin distribution and temporarily promotes spins to the high-energy anti-parallel alignment. This tilts overall magnetization away from the static magnetic field direction, thus decreasing longitudinal and increasing transverse magnetization components. Relaxation of excited spins to their thermal

equilibrium state is governed by realignment with the main magnetic field (B_0) and recovery of longitudinal magnetization (T_1 relaxation) as well as dephasing due to local and global field inhomogeneities and decay of transverse magnetization (T_2^* relaxation). RF waves sent out during relaxation are detected with specialized coils and amplified to form the MR signal.

In MRI, spatial information of each voxel within the imaging volume is encoded in the signal by application of magnetic field gradients during and in between RF pulses and signal reception. From raw data, an image is reconstructed using Fourier transformation. Since relaxation times differ among tissues, MRI can be predominantly weighted by proton density, T_1 or T_2^* relaxation time, depending on timing of RF pulse excitation, and signal detection. Additionally, sophisticated MR techniques enable the generation of contrast based on diffusion or perfusion of nuclei.

MRS utilizes the fact that spins resonate at slightly different frequencies (chemical shift) depending on different nuclear shielding by electrons due to the molecular chemical environment. This is expressed in a spectrum of resonance lines stemming from endogenous as well as exogenous substances, thus enabling the investigation of molecular composition of tissues and metabolism of pharmaceuticals. The most commonly used nucleus in MRS is ^1H . It offers the best sensitivity and spatial resolution but also necessitates the suppression of highly abundant water and lipid signals in order to detect metabolites. MRS enables the detection of metabolites, amino acids, and lipids, among other biomolecules, in tumors of live mouse models of cancer [20]. Other nuclei used in MRS comprise ^{19}F , ^{23}Na , ^{31}P , and ^{13}C . Especially, ^{19}F is nearly as sensitive as ^1H and has no endogenous physiological background, thus offering straightforward molecular identification. The features of spatial resolution of MRI and spectral resolution of MRS can be combined in magnetic resonance spectroscopic imaging (MRSI), which is able to generate spatially resolved maps of tumor metabolic markers for cancer diagnosis, metabolic phenotyping, and characterization of tumor microenvironment [20].

MR techniques offer the advantages of not exposing subjects to ionizing radiation, thus enabling repeated measurements, high spatial and temporal resolution, and high imaging flexibility with various contrast mechanisms (e.g., T_1 , T_2^* , proton density, diffusion, perfusion) for excellent tissue characterization. MR techniques, including imaging, functional MRI, and spectroscopy, are able to assess morphological, physiological, functional, and metabolic information in one session. However, MR is expensive and demands a rather high level of expertise. Due to safety considerations, MR is not amenable for some subjects. Most inauspicious for molecular imaging with MRI is the inherently low sensitivity in the micro- to millimolar range as compared to PET. Therefore, it is essential to employ efficient signal amplification strategies.

12.4.1 Contrast Agents

Contrast agents (CAs) are being continuously developed and employed as signal amplifiers to overcome the inherently low sensitivity of MRI [122]. CAs may be either (i) targeted to directly image molecular and cellular processes (MI in its strictest sense) [15], (ii) activated to generate contrast only in response to changes in their physical environment to indirectly image underlying biological processes [26, 77], or (iii) non-targeted to image surrogate biomarkers of function and physiology (MI in its broadest sense) [54]. Strategies to modify contrast in proton MRI are based on alteration of T_1 and T_2 relaxation times, proton density, and nuclear polarization, respectively. Alternatively, CAs based on non-proton nuclei like ^{19}F can be used to produce MR signal without physiological background.

T_1 contrast agents most commonly incorporate paramagnetic ions, e.g., gadolinium (Gd), manganese (Mn), and lead to positive signal enhancement in T_1 -weighted imaging by locally increasing the longitudinal relaxation rate ($R_1 = 1/T_1$) of water protons. Sensitivity of commercially available Gd-based small molecules, e.g., Gd-DTPA (Magnevist[®]), Gd-DTPA-BMA (Omniscan[®]), and Gd-DOTA (Dotarem[®]), is typically in the millimolar range [122], which precludes direct imaging of molecular receptors with typically nanomolar abundance. Nevertheless, they are extensively used to assess functional and physiological biomarkers of cancer using dynamic contrast-enhanced MRI [54, 66, 84]). Unfortunately, commonly applied small-molecule CAs are known to diffuse quickly from blood into extracellular space for both normal and pathologic tissues. This can be overcome with the use of macromolecular CAs [100], which cannot easily leak out of normal vasculature. The apparent threshold in effective molecular weight with no measurable leakage into normal tissue is between 194 and 323 kDa [24]. High sensitivity can be attained by exploiting macromolecules or nanocarriers (e.g., micelles, microemulsions, liposomes) containing hundreds to thousands of Gd entities [6] (Mulder et al. 2006; Gore et al. 2009). For the detection of vascular endothelial growth factor (VEGF) receptor with a small lysine-based dendron consisting of eight Gd-DOTA units conjugated to a specific dimeric peptoid, the in vitro detection limit was in the submicromolar range (790 nM) (De-Rodriguez et al. 2009).

T_2^* contrast agents are usually iron oxide particles which typically result in signal loss in T_2^* -weighted images by dramatically increasing transverse relaxation rate ($R_2^* = 1/T_2^*$) due to induction of strong local susceptibility differences. Iron oxide nanoparticles are available with different magnetic properties and in various sizes, e.g., superparamagnetic iron oxide (SPIO) nanoparticles (50–150 nm), ultrasmall superparamagnetic iron oxide (USPIO) nanoparticles (20–30 nm), very small superparamagnetic iron oxide particles (VSOP; 7–10 nm), microparticles of iron oxide (MPIO; 0.35–1.6 μm), cross-linked iron oxide (CLIO) nanoparticles (30–50 nm), monocrystalline iron oxide nanoparticles (MION), and magnetism-engineered iron oxide (MEIO) nanoparticles, and are usually coated with polymers or monomers that prevent aggregation and allow functionalization [72, 86]. They have been used as organ-specific contrast agent, for vascular characterization,

tumor targeting, and cell labeling (Yan et al. 2007) [48, 86]. The detection threshold of iron oxide agents is suggested in the submicromolar range [76] (Gore et al. 2009), but for SPIO-labeled cells even PET-comparable sensitivity in the pico- to femtomolar range was reported [45, 46].

Reduction of total water signal (proton density) can be achieved with chemical exchange saturation transfer (CEST) agents. This interesting and comparatively new CA class relies on diamagnetic [139] or paramagnetic [149] compounds with slowly exchanging protons, which possess a largely different resonance frequency than protons of the bulk water pool. Irradiation at the resonance frequency of exchangeable protons leads to a reduction of bulk water signal via saturation transfer due to chemical exchange of protons from CEST agent and water pool. Interestingly, CEST contrast can be turned on or off at will, since saturation transfer can only occur, if exchangeable protons are irradiated at the proper resonance frequency. The sensitivity of CEST agents is in the millimolar range for low-molecular-weight small molecules and can be enhanced to micromolar concentrations with macromolecular compounds [6] (Gore et al. 2009). Liposome-trapped CEST (LIPOCEST) agents increase sensitivity even up to sub-nanomolar (90 pM) concentrations (Aime et al. 2005a). They can be designed to be sensitive to glucose concentration [105, 155], lactate concentration [5], enzymatic activity [17, 153], pH [4], or temperature [73, 156]. Additionally, the concept of CEST contrast can be extended to simultaneously detect two CEST agents (Ali et al. 2009b) or diamagnetic multi-label polypeptide CEST (DIACEST) agents [78] at different resonance frequencies in the same region. This has been demonstrated to work in phantoms (Aime et al. 2005b) [78], in vitro in labeled rat tumor hepatoma cells (Aime et al. 2005b), and in vivo in a mouse model of mammary carcinoma (Ali et al. 2009a). Thus, CEST agents bear a high potential for MI applications.

Thermal equilibrium of spin distribution (nuclear polarization) can be artificially changed in favor of energetically lower state by hyperpolarization techniques which results in huge signal enhancement (>100,000), thus enabling imaging with non-proton nuclei like ^{13}C (Golman et al. 2003) and ^{19}F [67]. The half-life of hyperpolarization is limited by T_1 relaxation time. Hyperpolarized ^{13}C -labeled pyruvate and its metabolites lactate and alanine could be successfully imaged in vivo in rat tumors using MRSI [20].

An alternative to generate contrast in MRI is the utilization of nuclei other than ^1H . ^{19}F appears to be especially suited since it is nearly as sensitive as ^1H and lacks endogenous physiological background signal while featuring 100% natural abundance. Several fluorine-containing agents ranging from small molecules to nanoparticulate assemblies are used in ^{19}F MRI and MRS to derive information on various subjects including pH, tissue oxygenation and hypoxia, metabolism, inflammation, and cellular imaging [2, 30, 93, 97]. To obtain detectable signals, sufficient amounts of the fluorinated probe must be administered, but care must be given to avoid physiological perturbations or toxic side effects.

12.4.2 Dynamic Contrast-Enhanced MRI

Dynamic contrast-enhanced (DCE)-MRI serially monitors signal intensity after intravenous administration of CA using either T_2^* - or T_1 -weighted sequences [54]. On the one hand, T_2^* - or dynamic susceptibility-contrast (DSC)-MRI can be used within first few seconds after contrast bolus injection to observe the transient first-pass effects of contrast agent, i.e., initial rapid drop and fast subsequent recovery of signal intensity. On the other hand, T_1 -weighted DCE-MRI is used to observe the extravasation of CA from vascular to interstitial space over several minutes. Pharmacokinetic modeling of the dynamic signal change can provide useful hemodynamic parameters of tumor vasculature including tumor perfusion, vascular permeability, and blood volume [66].

Measurements of tumor microvasculature with DCE-MRI have been correlated with prognostic factors (e.g., tumor grade, metastatic potential) and with recurrence and survival outcomes. DCE-MRI parameters were found to be associated with common angiogenesis markers (e.g., microvascular density (MVD), VEGF expression), thus indicating the enormous potential of DCE-MRI as non-invasive biomarker for tumor detection and characterization, monitoring tumor response to anticancer therapies that affect angiogenesis or perfusion, and outcome prediction [54]. In human lung tumor xenografts, the effects of antiangiogenic treatment on tumor vasculature were evaluated *in vivo* using DCE-MRI. Treated tumors showed decreased contrast uptake and transfer constant on day 7 of treatment, which was associated with significant growth retardation and lower MVD compared with controls [89]. DCE-MRI with intravascular macromolecular CA in breast and prostate cancer xenograft models of different metastatic potentials revealed higher blood volume and permeability in metastatic tumors, which also matched VEGF expression [146]. The assessment of vascular endothelial leakiness using new PEG-core, (Gd-DOTA)-conjugated macromolecular contrast agents proved applicable for the differentiation of human breast cancer from normal soft tissue [24].

12.4.3 Steady-State Susceptibility-Contrast MRI

Steady-state susceptibility-contrast (ssSC) MRI after application of CA allows the assessment of vessel morphology and blood volume [131]. Intravascular CAs induce long-range field perturbations that extend into tissues and increase transverse relaxation rates R_2 and R_2^* . These effects are differently expressed in spin-echo- and gradient-echo-type MRI in dependence on vessel size. Thus, from measured changes in relaxation times (ΔR_2 and ΔR_2^*) induced by CA injection, maps of vessel size index and additionally fractional blood volume can be estimated. CAs with high T_2^* relaxivity (e.g., SPIO) increase induced changes in transverse relaxation rates, which allows assessing smaller vessel size differences. In comparison to DSC-MRI, steady-state methods offer the potential of a higher signal-to-noise ratio, and thus a higher spatial resolution.

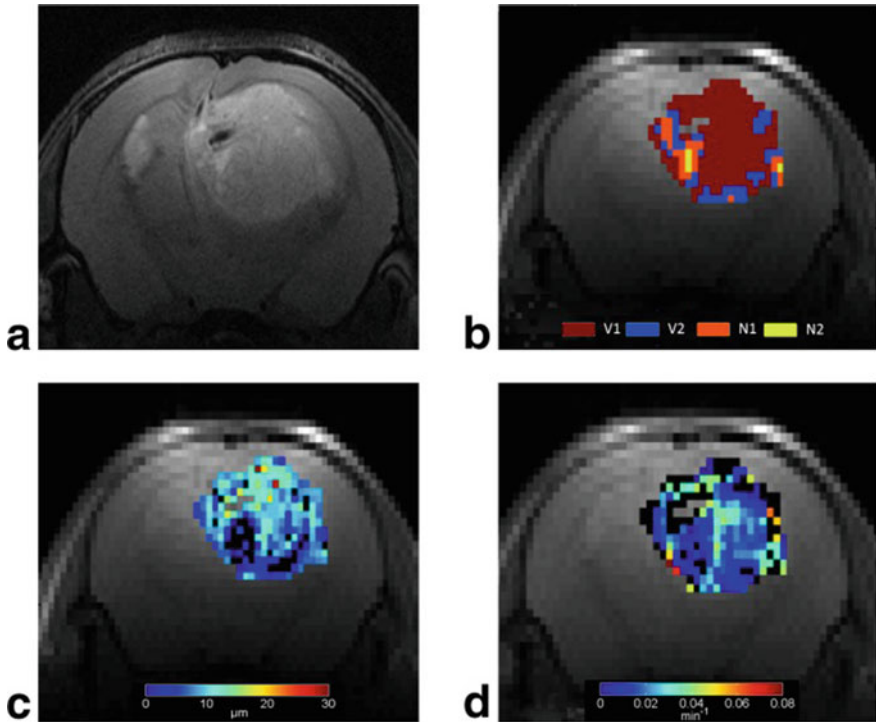


Fig. 12.1 Exemplary T2-weighted RARE image (a) and corresponding segmentation (b), VSI (c), and Ktrans map (d) of one animal of the control. Regions of necrosis (N2+N1) are white in T2-weighted RARE images and yellow in the segmented map. Viable tumor is shown in red (V1) in the segmented images and in blue (V2). N1 is shown in orange and is mostly found around N2, illustrated in yellow [66]

This imaging approach can be used to assess differences in morphology of neoplastic and normal vessels and response to therapies directed to tumor vasculature. In a rat glioma model, vessel size imaging revealed larger mean vessel size in tumors than in surrounding normal brain, which was correlated significantly with histological data [132]. Another study [66] showed that it is possible to extract VSI data and DCI data simultaneously from a multiparametric imaging approach using Gd-based CA (Fig. 12.1).

In GH3 prolactinoma and RIF-1 fibrosarcoma grown in mice, ssSC MRI with a blood pool CA could correctly identify the larger blood volume (fourfold) and capillary size (twofold) in GH3 tumors in agreement with histological analysis of MVD, perfused MVD, and perfused vessel fraction. In two rat glioma (C6 and RG2) models, repeated SPIO-enhanced MRI of blood volume fraction and vessel size index indicated significantly different microvascular evolutions during tumor progression between the two models. These results were in good agreement with

histology-derived vascular parameters (MVD, vascular fraction), expression of angiogenic factors (VEGF, angiopoietin-2), and activities of matrix metalloproteinases (Valable et al. 2008). Repeated injection of SPIO particles as CA did not affect the physiological status of animals and the accuracy of MR estimates of microvascular parameters. In melanoma tumors overexpressing platelet-derived growth factor, thus leading to enhanced blood vessel pericyte coverage, ssSC MRI with USPIO particles revealed a significant reduction in vessel size index compared to control melanoma, which was validated histologically by the presence of significantly smaller, and more punctate blood vessels [109]. In colon carcinoma mouse models, steady-state MRI with intravascular paramagnetic or superparamagnetic CA demonstrated highly sensitive and early reduction of tumor blood volume in response to antiangiogenic treatment with a VEGF receptor tyrosine kinase inhibitor, concomitant to increased apoptosis of tumor and endothelial cells, and decreased vascular density [63] (Reichardt et al. 2005). In a squamous cell carcinoma tumor model, a strong decrease of blood volume 4 days after antiangiogenic treatment initiation was observed, which was in line with MVD assessment [55].

12.4.4 Diffusion-Weighted MRI

Diffusion-weighted imaging (DWI) assesses the random translational (Brownian) motion (diffusion) of water molecules in tissues. Generally, MRI sequences are made sensitive to diffusion through application of a pair of strong magnetic field gradients, which induce a controlled position-dependent spread of resonance frequency. The first gradient is used to encode initial spin position, while the second gradient encodes final position. Diffusion leads to an imbalance of dephasing effects due to the first and second gradient. This, finally, results in signal attenuation due to incomplete spin rephasing. The amount of diffusion weighting in final MRI signal depends on gradient parameters (strength, duration, separation) which are collectively summarized in the b value. From a series of differently diffusion-weighted images, diffusion can be quantified by means of apparent diffusion coefficient (ADC). Reduced diffusion leads to less dephasing and appears bright on DWI and dark on ADC maps.

DWI is sensitive to tissue microstructure on a cellular level including cellularity, presence and integrity of membranes, extracellular matrix composition, interaction with intracellular elements, and water distribution between intra- and extracellular space [19, 95, 98]. Additionally, perfusion in capillaries, ducts, and interstitial space may also impact DWI leading to deviations from monoexponential signal decay, DCI and VSI. As an example, Fig. 12.1 shows the parameter maps of a tumor in a murine glioma xenograft model.

Pathological processes or therapeutic interventions that alter tissue microstructure and microcirculation affect water mobility, and thus are accessible by DWI. The basic principle of cancer detection and therapy response monitoring with DWI is schematically illustrated in Fig. 12.2. Normal appearing non-diseased tissue

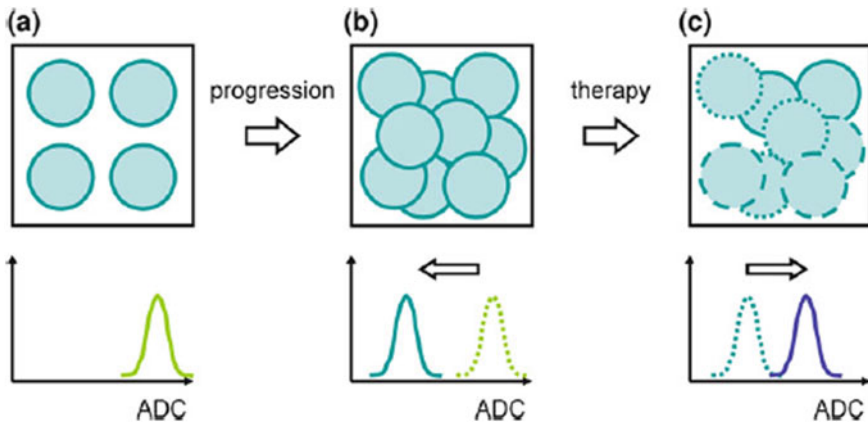


Fig. 12.2 Illustration of principles of cancer detection and therapy monitoring with DWI: Progression from loosely packed (normal) tissue associated with high ADC due to comparatively unrestricted diffusion (a) toward pathologically changed (cancer) tissue of high cellular density leads to decreased ADC due to diffusion restriction (b). Successful cancer therapy leads to early disintegration of cells, and thus less restricted diffusion (c). This is reflected by an increasing ADC, already before changes in morphological size criteria become obvious

shows up with low cell density and exhibit comparatively free water diffusion (high ADC) (a). During tumor progression enhanced cell and matrix proliferation lead to increased tissue cellularity (b) which becomes obvious in reduced diffusion (lower ADC) of water molecules through these pathologically changed areas. Correspondingly, changes in tissue microstructure in response to successful therapy (c) usually result in increased diffusion (higher ADC). This can be detected with DWI and quantified by ADC before any detectable change in size occurs (Pickles et al. 2006). DWI has indicated its potential as imaging biomarker in oncology in tissue characterization and differentiation, therapy response monitoring, and outcome prediction.

DWI has been used in tissue characterization for improved detection of small (<1 mm) prostate tumors in a transgenic mouse model [120] and nodal staging with less false-positive results than PET/CT [92]. It may potentially differentiate among benign and malignant primary and metastatic lesions with fewer false-positives for active inflammatory lesions than PET (Mori et al. 2008) [150], identify viable and necrotic tumor regions [28, 124, 154] and discriminate tumor recurrence, and post-therapeutic tissue change (Asao et al. 2005) [134]. A very important potential application of DWI is to monitor early tumor response to treatment [81, 95]. Successful applications have shown early effects on ADC in various tumor entities in response to chemotherapy, as shown in Fig. 12.3 (Reichardt et al. 2009), chemoradiotherapy [63], antiangiogenic treatment, anti-vascular therapy [129, 137], and apoptosis-inducing antibody treatment [61]. An example for identification of early response to therapy using DWI is presented in Fig. 12.3. In a human tumor

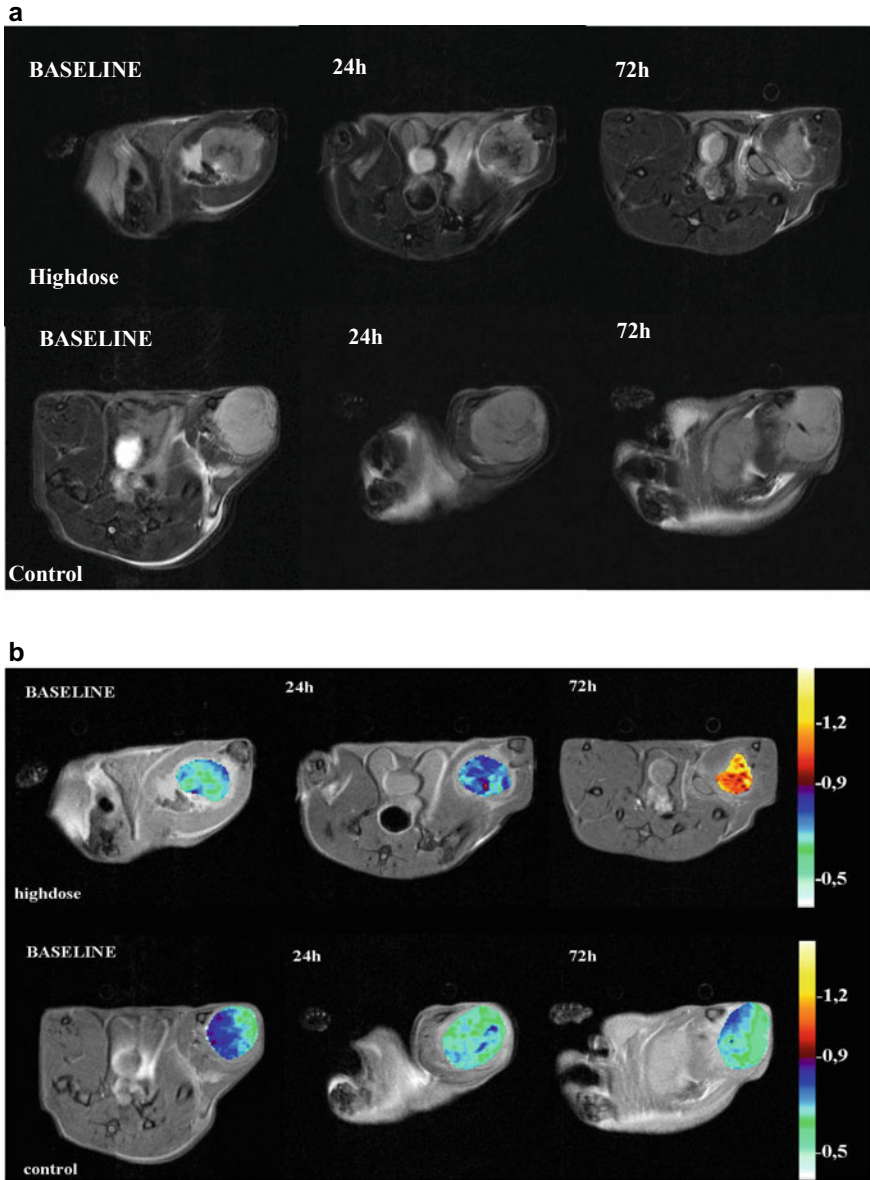


Fig. 12.3 **a** T2-RARE images of tumors at three different time points of the therapy (0, 24, and 72 h). **b** Corresponding T1 images with color-coded ADC maps of the complete tumor. Shown are the ADC measurements at different time points of the therapy given as overlay image. The color bar is indicating ADC values ($\times 10^{-3}$) (Reichardt et al. 2009)

xenograft model, we observed a significantly higher ADC in tumors receiving chemotherapy in a high dosage versus tumors receiving a low dosage.

Furthermore, DWI has been evaluated as prognostic biomarker of outcome. Pretreatment ADC was indicative of survival in postoperative radiation therapy of malignant supratentorial astrocytoma in patients [87] and in a colon carcinoma mouse model treated with chemotherapy [112]. Early ADC changes were reported to be predictive of survival in gene-dependent enzyme prodrug therapies in an orthotopic animal model of high-grade glioma [41], combined anti-death receptor 5 antibody, and gemcitabine treatment in orthotopic pancreatic tumor xenografts [62], and radiotherapy in rabbit VX2 tumor model [74].

The widespread implementation of DWI to assess cancer is currently challenged by a lack of methodological standardization across instruments, data acquisition protocols, and analysis methods between and among manufacturers, accepted quality assurance standards and realistic phantoms as well as proper evaluation of reproducibility, thus rendering multicenter studies practically unfeasible. In order to assess reproducibility of DWI, Wolf et al. have designed a tissue-equivalent phantom, which resembles T_1 , T_2 , and ADC of various tissues (Wolf et al. 2012a). Using this phantom in different scanners at different centers revealed a high inter-scanner ADC variability of 15% (range: 10–37%), while intra-scanner variability (assessed in the same scanner over several weeks) ranged between 3 and 6% depending on the instrument. Additionally, the underlying biological principles of DWI at the microscopic level are still only poorly understood. However, recommendations on how to perform DWI in clinical cancer imaging [95] as well as special advice on practical aspects of technical adaptation and optimization of protocols for DWI of small rodents with tumors in clinical scanners have been published [18].

12.4.5 Arterial Spin Labeling

An alternative to contrast-enhanced MRI for assessment of perfusion is arterial spin labeling (ASL). Instead of exogenous CA, ASL utilizes endogenous contrast which can be generated by magnetically inverting inflowing arterial blood prior to entering the imaging plane. The small ASL signal change, obtained as difference of tag and control experiment with labeled and unlabeled blood, respectively, is directly related to absolute blood perfusion. ASL has been shown to correlate with blood flow measures from ^{15}O -water PET [151] and DSC-MRI [141] in normal brain tissue. However, ASL is one of the more demanding MRI techniques associated with potential issues including low sensitivity, inaccurate bolus preparation, and complex flow quantification [38], which has been partly addressed in recent methodological developments [79].

However, ASL perfusion imaging shows promising results for potential application in tumor detection and monitoring of interventions. In experimental brain tumor models, blood flow exhibited pronounced heterogeneity, corresponding to MVD, with much higher blood flow in normal brain than in tumor periphery, and

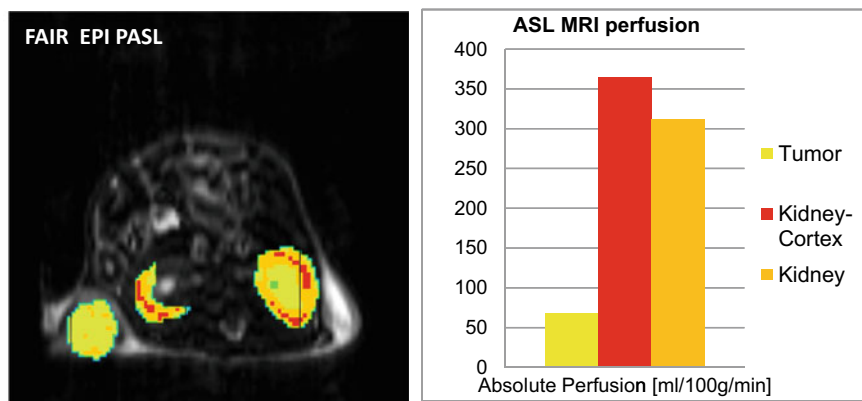


Fig. 12.4 **Left:** color-coded map of average blood perfusion values determined with PASL. **Right:** the detected values for absolute blood perfusion in the subcutaneous tumor models were in good correlation to literature values

tumor core [123]. Changes in blood flow could be detected in animal models of renal carcinoma [103], experimental glioma models in response to vasodilatation by carbogen breathing [82], and inhibition of vascular endothelial growth factor [83], as well as different animal strains [69]. Figure 12.4 shows an example for the detection of absolute blood flow in a mouse tumor model, and the kidneys as internal reference.

12.4.6 ^{13}C Hyperpolarization

Recent advances in the ability to detect cancer metabolism have generated considerable interest among clinicians. However, until now the only imaging agent regularly used in the clinic to assess metabolism is the glucose analog [^{18}F] fluorodeoxyglucose (FDG), a positron emission tomography (PET) tracer that reports on local glucose uptake in many cancers, inflammations, and other processes (Kurhanewicz et al. 2019). While FDG PET has been an extremely successful approach, it cannot assess downstream metabolism that is often important to more fully understand cancer. Hyperpolarized magnetic resonance imaging (HP MRI) provides a unique window into metabolic alterations based on its ability to measure molecular transformations of the imaging agent. Until now primarily ^{13}C -based Hyperpolarization is used for the characterization of tumor metabolism and is on its path to its clinical translation (Kurhanewicz et al. 2019). Especially, techniques using hyperpolarized ^{13}C -labeled pyruvate infusion to monitor increased glycolysis in cancer have the potential to improve the way MRI is used for detection and characterization of cancer [43, 53, 96, 114]. The level of hyperpolarized [$1-^{13}\text{C}$] lactate that is detectable after intravenous injection of ^{13}C pyruvate is correlated with cancer progression and is lower after therapy [68]. The exchange

of hyperpolarized ^{13}C between pyruvate and lactate has been used by Haris and coworkers [43] to visualize prostate cancer. A study measuring the levels of hyperpolarized ^{13}C lactate in a transgenic prostate cancer mouse model showed that the hyperpolarized lactate level was positively correlated with cancer aggressiveness and histological grading (Albers et al. 2008). Other studies detected the absence of lactate production in mutant gliomas [16]. In a study with a mouse lymphoma tumor model, hyperpolarized ^{13}C glucose has been used to monitor the glycolytic flux [111] to monitor therapeutic effects. A signal from 6-phosphogluconate could be detected which is generated through the *PPP*. However, there was an obvious difference in the level of detected hyperpolarized ^{13}C lactate when hyperpolarized ^{13}C glucose was infused compared to the infusion of hyperpolarized ^{13}C pyruvate. Nonetheless, this method could provide a new way to monitor the glycolytic flux and *PPP* activity in tumor.

Recently, a new technique to realize ^{13}C hyperpolarization in aqueous solution with Synthesis Amid the Magnet Bore and Dramatically Enhanced Nuclear Alignment (SAMBADENA) was developed that could permit a higher polarization at the time of detection at a fraction of the cost and complexity of external polarizers, as the hyperpolarization takes place inside the animal scanner in direct conjunction with the animal bed. This development is particularly promising in light of the recently extended portfolio of biomedically relevant para-hydrogen tracers and may lead to new diagnostic applications [53, 114].

Finally, it has been shown that the tissue pH can be mapped through hyperpolarized MRI [33]. Since there are a lot of pathological changes associated with pH changes, monitoring the pH *in vivo* can provide useful information about the tissue pathological stage. A pH map that can be generated non-invasively by targeting conversion of the injected hyperpolarized ^{13}C -labeled bicarbonate to hyperpolarized carbon dioxide in tumor tissues [33]. As pH changes in a tumor can be related to treatment efficacy, the monitoring of the tumor pH is well suited for the design of effective cancer treatment protocols. Furthermore, by using hyperpolarizing techniques the treatment response can be monitored very time efficient and a more effective treatment could be initiated based on this observation.

12.5 Applications

12.5.1 Metabolism

Tumors, generally, present severely altered metabolic properties compared to normal tissue. Increased metabolism of glucose, amino acids, nucleosides, and lipids and their changes may be exploited to image neoplastic disease, and monitor cancer treatment. MRS can be used to repeatedly and non-invasively study metabolism of tumors *in vivo* [11]. It can detect several metabolites in one measurement without prior specification, particularly phospholipid metabolites (e.g., phospho-monoesters, phosphodiester, choline/phosphocholine, glycerophosphocholine),

bioenergetic metabolites (e.g., creatine/phosphocreatine, nucleotide triphosphates, inorganic phosphate), and glycolytic metabolites (e.g., glucose, glutamine/glutamate, lactate). Tumors, typically, show characteristic metabolic features in ^1H and ^{31}P MRS (e.g., high levels of phosphomonoesters, phosphodiester, total choline), which are often reversed on successful treatment with chemo- or radiotherapy and currently considered as biomarkers for tumor diagnosis, staging, and clinical response monitoring [11]. High glucose consumption and lactate production in tumors can be monitored in preclinical models of cancer with ^1H and ^{13}C MRS [145]. Preclinical studies have demonstrated the potential of spectroscopic measurements to non-invasively detect the action of new therapeutic agents [11]. A limitation associated mostly with ^{31}P and ^{13}C MRS is their low sensitivity, which leads to long data acquisition times and poor spectral resolution. In this respect, MRS benefits from high magnetic field strength offered by dedicated small animal scanners. Alternatively, hyperpolarization of exogenous probe molecules could greatly enhance sensitivity and enables *in vivo* metabolic imaging of tumors (Golman et al. 2006). Additionally, MRI with a PARACEST agent may provide metabolic maps of glucose over a range of physiologic interest (Zhang et al. [155] b). MRSI finally has the potential to detect and evaluate tumor metabolic markers for cancer diagnosis, metabolic phenotyping, and characterization of tumor microenvironment [20].

12.5.2 Hypoxia

Hypoxia is a characteristic pathophysiological property of many cancers, commonly arising as regions of low oxygen concentration as a result of increased oxygen consumption in neoplastic tissue and/or inadequate oxygen supply [135]. It is associated with an aggressive tumor phenotype, risk of invasion and metastasis, treatment resistance, and poor prognosis [127, 143]. Knowledge of oxygenation status of tumors may help to improve tumor therapy and select patients that may benefit from novel therapy options or eventually exclude patients with limited chance of cure from more invasive therapeutic strategies [13, 144].

MRI and MRS may contribute to hypoxia imaging by several approaches including BOLD MRI, ^{19}F MRI/MRS of fluorinated substances, and indirectly lactate imaging, respectively [127] (Padhani et al. 2007).

Since BOLD MRI is sensitive to the oxygenation status of hemoglobin in perfused blood vessels, which might not generally be the case in tumor vasculature, it reflects more the effects of acute hypoxia [10]. Therefore, only qualitative but no direct correlation between R_2^* and tissue $p\text{O}_2$ was found [31], and knowledge of blood volume distribution is necessary to correctly infer tissue oxygenation status from R_2^* . However, changes in R_2^* can be used to measure changes in tissue $p\text{O}_2$ upon vasomodulation. This technique has been demonstrated to predict radiotherapeutic response in rodent tumors [110]. BOLD contrast may be confounded by blood flow effects, which may be uncoupled from static R_2^* effects (Howe et al. 2001).

^{19}F MRI can be used to assess tissue oxygenation using perfluorocarbons and fluorinated nitroimidazoles [107]. Perfluorocarbon reporter molecules may determine absolute oxygen levels with estimated precision of 1–3 mm Hg in the crucial low oxygen tension range (<5 mm Hg) (Zhao et al. 2003). Perfluorocarbons display temperature-dependent transverse relaxation rates (R_1) that linearly relate to $p\text{O}_2$ (Yu et al. 2005). Importantly, R_1 of perfluorocarbons is essentially independent on pH, carbon dioxide, paramagnetic ions, common proteins, mixing with blood or emulsification, and dilution. They may be introduced by direct intratumoral injection or systemic application of biocompatible emulsions, thus providing oxygen levels consistent with electrode and fiber optic measurements, while being less invasive, covering multiple locations simultaneously and allowing sequential assessments (Yu et al. 2005). Measurements after systemic application of perfluorocarbon emulsions may be subject to flow effects, represent only the most well-perfused areas in tumor periphery, and require large injection volumes since most material is sequestered in the reticuloendothelial system, which may lead to adverse side effects [94]. Instead, most successful approaches used intratumoral injections of perfluorocarbons that exhibit only a single resonance line (e.g., hexafluorobenzene), thus maximizing signal-to-noise ratio, and $p\text{O}_2$ -sensitive R_1 across the entire range of oxygenation, including anoxia, hypoxia, normoxia, hyperoxia, and even hyperbaric [127]. In analogy to PET, ^{19}F -labeled nitroimidazoles have been evaluated to assess hypoxia by ^{19}F MRS. ^{19}F -TFMISO was suggested as a potential MR hypoxia marker [101]. On the other hand, ^{19}F -EF5 could not be evaluated as a valid MR indicator of hypoxia [50]. Additionally, these approaches generally require large amounts of reporter molecule to be present in the region of interest, which may be associated with adverse side effects. Upon chemical trapping in hypoxic cells, multiple ^{19}F -labeled species (including macromolecular) with individual chemical shifts may be generated contributing to poor signal-to-noise ratio, which necessitates long acquisition times. Moreover, retention of ^{19}F -labeled nitroimidazoles did not demonstrate clear correlation with tissue $p\text{O}_2$ in analogy to their analogs for PET and histology.

Due to limited clinical availability of ^{19}F imaging capabilities, proton imaging of silanes for tissue oxygen levels (PISTOL) has been proposed as an alternative [65]. The reporter molecule hexamethyldisiloxane (HMDSO) exhibits strong hydrophobicity, high oxygen solubility, low toxicity, ready availability, inertness, and most importantly oxygen-sensitive T_1 relaxation. Its single resonance line is far away from water and fat signal, and thus can be readily detected after water and fat suppression to interrogate tissue oxygen level after direct intratumoral injection.

Lactate accumulates in tumors as a consequence of hypoxia. Lactate levels have been indicative of metastasis and survival and may provide metabolic classification of tumors that might lead to improved prognosis in clinical oncology [136]. Lactate can be quantified non-invasively in an animal model of glioma for therapy monitoring by ^1H MRS [22] and Lactate Chemical Exchange Saturation Transfer (LATEST) [27], which may, therefore, represent (although not directly) tissue $p\text{O}_2$.

12.5.3 Angiogenesis

Angiogenesis is a critical requirement of cancer progression. Tumors reaching a few millimeters in size need an increased supply of oxygen and nutrients, which activates the development of new vasculature characterized by aberrant vascular structure, altered endothelial cell–pericyte interactions, abnormal blood flow, increased permeability, enlargement of vessel diameter, basement membrane degradation, thin endothelial cell lining, increased number of endothelial cells, decreased number of pericytes, and delayed maturation. The process of angiogenesis generally encompasses several mechanisms like sprouting angiogenesis, intussusceptive angiogenesis, recruitment of endothelial progenitor cells, vessel cooption, vasculogenic mimicry, and lymphangiogenesis [47]. It is regulated by a variety of pro- and antiangiogenic factors, of which $\alpha_v\beta_3$ integrins and VEGF, and its receptors are considered key regulators (Ferrara and Kerbel 2005) [80]. Angiogenesis has become an important therapeutic target, mainly directed against either existing tumor blood vessels (vascular disrupting agents), or tumor blood vessel development (antiangiogenic agents) (Ferrara and Kerbel 2005) [7, 57]. MI may explore new molecular measures of biological response based on targeting molecules selectively expressed by angiogenic vessels. In addition, morphological and functional imaging biomarkers of tumor vasculature (e.g., blood flow, blood volume, vessel permeability, vessel size, vessel density) may also be promising for therapy evaluation [9, 58, 90].

Current MR approaches in angiogenesis imaging rely mainly on indirect imaging of biomarkers of vascular morphology and function and targeted imaging of $\alpha_v\beta_3$ integrin, respectively.

Non-targeted imaging with advanced MRI techniques like ASL, BOLD MRI, DCE-MRI, and ssSC MRI can be used to indirectly characterize angiogenic tumor vasculature and treatment-related changes of vascular function [9, 58, 90]. High-resolution MR angiography allowed non-invasive characterization of intratumoral vasculature. Vessels diameters down to 100–200 μm can be visualized accordingly in clinical scanners using optimized instrumentation and long scan times. ssSC MRI can quantify vessel size and blood volume and changes due to angiogenesis or therapy. A multiparametric approach has combined microscopic MR angiography and ssSC MRI blood volume mapping to simultaneously provide high-resolution 3-D information on morphology, in vivo microvascular architecture, and hemodynamic response, which can be used to monitor changes in microvasculature [75]. DCE-MRI, preferably with macromolecular CAs, can be used to assess vascular permeability, which develops as an immediate consequence of VEGF stimulation. In DCE-MRI in an experimental tumor treatment model, fractional plasma volume and transendothelial permeability decreased significantly in response to treatment with anti-VEGF monoclonal antibody using macromolecular CA but did not change significantly using low-molecular-weight CAs [133]. Additionally, DCE-MRI and ASL can monitor blood perfusion and blood flow during angiogenesis or in response to antiangiogenic treatment. In human lung tumor xenografts, DCE-MRI could evaluate the effects of antiangiogenic treatment

on tumor vasculature, which was associated with growth retardation and lower MVD compared with controls [89]. In rat glioma models, ASL and ssSC MRI showed significant change in tumor blood flow and blood volume in dependence on VEGF expression levels [83]. Perfusion changes in response to vasomodulation can be used to probe vascular maturation with BOLD MRI, which revealed pericyte-dependent changes in function of perfused tumor vasculature under normal, hypercapnic, and hyperoxic conditions in a mouse melanoma model [109].

Targeted MRI of angiogenesis for the most part explored binding of RGD-linked nanoparticles to $\alpha_v\beta_3$ integrins [14]. In human melanoma tumor xenografts, angiogenic vasculature could be successfully detected and characterized in vivo with positive MRI contrast using $\alpha_v\beta_3$ integrin-targeted paramagnetic nanoparticles [116] and paramagnetically labeled micelle-coated quantum dots (Mulder et al. 2009a), which additionally allowed fluorescence imaging. Alternatively, RGD-conjugated USPIO nanoparticles showed efficient targeting of $\alpha_v\beta_3$ -integrin and were able to non-invasively distinguish between tumors with different integrin expressions [157]. A bimodal ^{64}Cu -DOTA-labeled RGD-conjugated iron oxide probe showed efficient integrin binding in vitro and delivery to glioblastoma in vivo with both MRI and PET [71]. This probe combines high sensitivity of PET and high spatial resolution of MRI, which will become increasingly important with the ongoing development of combined PET/MRI technology. In squamous cell carcinomas with up-regulated microvasculature, ^{19}F diffusion-weighted MRS has been used to detect specific binding of integrin-targeted perfluorocarbon nanoparticles, while selectively suppressing background ^{19}F signal from unbound, freely circulating nanoparticles [140]. We believe that ^{19}F MRI/MRS will develop into a viable alternative to current standard MR measures, if ^{19}F imaging capabilities will become more broadly available (which is currently only rarely the case, especially with clinical equipment). Targeted MRI of VEGF receptors is currently hardly performed. However, in 2010, there was a study reporting on the detection of increased VEGF receptor 2 expression in vivo in a rat glioma model using CLIO-conjugated anti-VEGF receptor 2 antibodies, which were specifically retained in tumor tissue as evident from signal loss in T_2 -weighted MRI and histological evaluations [130].

Additionally, magnetically labeled stem/progenitor cells, which are known to migrate to areas of active angiogenesis [80], have been used to assess neovascularization in tumors with MRI. For example, MRI has demonstrated the incorporation of SPIO-labeled endothelial progenitor cells in tumors at sites of active angiogenesis a few days after systemic administration (Arbab et al. 2006; Schindler et al. 2010).

12.5.4 Cellular Imaging

With advances in cell-based therapies, such as the use of stem cells to replace defective cell populations or to deliver therapeutic agents [21] (Kosztowski et al. 2009), non-invasive detection and tracking of transplanted or transfused cells

in vivo become increasingly important [1]. Cellular imaging may contribute to the understanding of the current role of certain cell populations in disease and repair processes and help to guide further developments. For example, endothelial progenitor cells are known to migrate to areas of active angiogenesis and contribute to neovascularization [80]. Cancer stem cells have attracted much of recent scientific interest in cancer therapy [64]. Given the current progress in molecular and cellular imaging, non-invasive in vivo detection of cancer stem cells as potential therapeutic targets may ultimately come into reach (Hart and El-Deiry 2008).

Although MRI is limited by inherently low sensitivity compared to PET, it is the most widely applied modality for in vivo cellular imaging [48, 60] (Reichardt et al. 2008), since it offers high-resolution anatomical imaging with excellent contrast. In order to visualize cells against the background of host cells and to increase sensitivity, MRI-based cellular imaging generally requires labeling of cells with CAs. Incorporation of CA into cells can be achieved with several strategies (e.g., transfection, electroporation) without adverse effects on cell proliferation, differentiation, and migration or cell toxicity (Bulte 2006) [48]. CAs used for cell labeling comprise mainly SPIO nanoparticles, but also paramagnetic Gd chelates, CEST agents, or fluorine-containing compounds have been used. However, cellular labeling with exogenous substances may lead to label dilution upon cell division and disables differentiation between dead and live cells, thus limiting their potential for long-term non-invasive monitoring of cell therapy. A viable alternative may be reporter genes that encode for proteins specifically influencing MR contrast [37, 48].

Cell labeling with SPIO leads to signal loss in T_2^* -weighted MRI. Sensitivity comparable to PET was reported [44]. Detection limits of SPIO-labeled cells are currently in the range of 100–500 cells down to single cells in non-clinical dedicated animal scanners at high field [86]. For example, the trafficking of dendritic cells (DC) through ipsilateral lymph nodes (Fig. 12.5) can be monitored in a mouse model after the dendritic cells had been labeled externally and implanted (Reichardt et al. 2008).

Equivalently, SPIO-labeled AC133+ progenitor cells could be detected at 3 days after intravenous injection to traffic to sites of tumor angiogenesis in glioma xenografts (Arbab et al. 2006). SPIO-labeled and genetically transformed AC133+ progenitor cells were found to accumulate in subcutaneous breast cancer xenografts after intravenous administration and selectively express human sodium iodide symporter gene at tumor site, indicating that such multifunctional cells can be used as both cellular probes and gene carrier systems for cancer treatment [102].

SPIOs could be used not only to track cells in vivo but also to investigate the migration of bacteria in a mouse model for GvHD, indicating that they play a role in GvHD-related tissue damage [118].

Although paramagnetic Gd chelates lead to positive contrast, due to the relatively lower sensitivity, large amounts of intracellular Gd-CA are needed. It was suggested that with clinically approved CAs of low relaxivity about 10^9 Gd complexes per cell [3] or cellular Gd concentrations exceeding 50 μM are required to provide sufficient contrast for MRI visualization. In a phantom, the detection limit

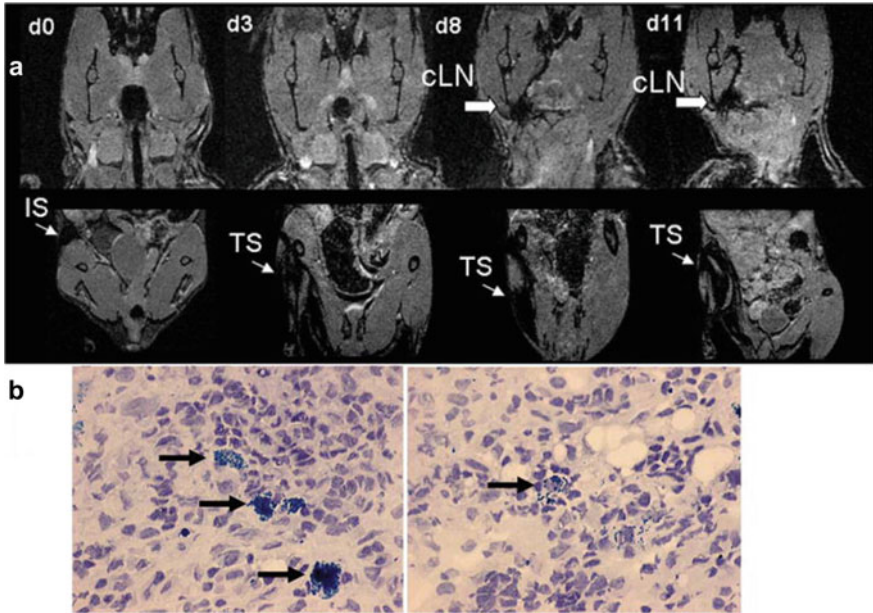


Fig. 12.5 MRI and IFM demonstrate migration of SPIO+DC from the injection site toward cervical lymph nodes day 8 after BMT. **a** i.m. injection of luc+SPIO+CD11c+ cells in the right proximal leg 1 h after BMT (C57B/6→BALB/c). Trafficking is monitored by MRI using the three-dimensional FLASH sequence on the indicated days in the cervical region (upper row) and lower extremities (lower row). The thin arrow indicates signal disruption within the right leg injection site (IS) within the muscle tissue (TS) and the bold arrow indicates signal disruption within the cervical lymph node (cLN) region. Experiments were repeated two times. **b** Detection of Fe within the cervical lymph node (black arrow) of an animal receiving local SPIO+CD11c+ cells in the right proximal leg as indicated by Prussian blue stain. Counterstained with Hematoxylin, original magnification $\times 400$ (Reichardt et al., Copyright 2008. The American Association of Immunologists, Inc.)

of cells labeled with a Gd chelate was estimated to approximately 2,000–3,000 cells [23].

With the recent rise of immune therapy, the tracking of immune cells *in vivo* is getting increasingly important [117]. In this context, understanding how the immune system affects cancer development and progression has been one of the most challenging questions in immunology. Research over the past two decades has helped explaining why the answer to this question has evaded us for so long. It has been found that the immune system plays a dual role in cancer: It can not only suppress tumor growth by destroying cancer cells or inhibiting their outgrowth but also promote tumor progression, either by selecting out tumor cells that are more fit to survive in an immunocompetent host or by establishing conditions within the tumor microenvironment that facilitate tumor outgrowth. Immunotherapy in cancer is using antibodies, cytokines, or immune cells to activate the immune system to

strengthen the defense for destruction of tumor cells. Immune cells can be affected by cytokines such as interferon or by antibodies (ABs) to exert an antitumoral effect. For example, immunization against cancer is attempted with injections of specific tumor antigens or activated immune cells (dendritic cells or T cells). Antibodies can activate a variety of immune cells including monocytes and T cells. This leads to a massive infiltration of activated immune cells into the tumor and lymph nodes (Postow et al. 2011). CD40 is expressed in dendritic cells, B cells, and macrophages and is required for their activation. So when treated with stimulating anti-CD40 ABs, cytotoxic T cells and B cells are activated. Anti-CD40 ABs are being tested in clinical trials. On the other hand, the PD-L1 surface molecule shuts down T cells and serves as a self-protection of the body's own cells from the immune system. Some tumors also express PD-L1 and thus prevent destruction by the immune system. Blockade of PD-L1 with an AB increases the number of T cells and cytokine production (which in turn can cause infiltration of macrophages) in the tumor (Iwai et al. 2005). Anti-PD-L1 ABs are in clinical trials, e.g., in bladder cancer [99] and kidney cancer (Tykodi et al. 2014). Common to all immunotherapeutic approaches is the lack of information about the migratory pattern and activity of those cells once they are activated. Perfluorocarbons (PFC) are taken up by monocytes *in vivo* after intravenous (i.v.) injection. Thus, PFC injection can serve as a tracer for immune cell tracking as these PFCs can be detected with ^{19}F MRI [1, 121, 128]. The ^{19}F nucleus is very sensitive for MR imaging. Therefore, the signal from the exogenous tracer can be detected and localized with high sensitivity if ^{19}F cell loading and the number of cells in the region of interest are sufficient. Additionally, MRI-detectable ^{19}F is virtually absent in the body. Externally supplied ^{19}F -containing substances can, therefore, be detected with high sensitivity as there is no background signal from the body. PFCs are commercially available. Ideally, they are coupled to fluorescence dye, which allows detection of the tracer in the excised tissue with optical imaging. ^{19}F MRI in combination with i. v. injected PFCs may serve as a tool for detection of inflammation and for monitoring of immunotherapies.

Externally PFC-labeled dendritic cells were used in a mouse tumor model to track their migratory patterns [12]. Immune cells were also detected *ex vivo* in a mouse tumor xenograft model using a combined PFC i.v. fluorescent contrast agent approach (Balducci et al. 2013) [142].

12.6 Summary and Outlook

MI aims at understanding biological processes of cancer *in vivo* at the levels of compartments, organs, tissues, cells, or molecules. It has been proven in preclinical experiments as a powerful tool in cancer characterization and treatment monitoring, mainly facilitated by tremendous developments in imaging technology, and contrast agents. MRI has in many aspects highlighted its potential as MI modalities. MRI is still challenged by its inherently low sensitivity, but efficient signal amplification

strategies are pushing limits forward toward higher sensitivity. Especially, the use of integrated MRI scanner technology in combination with multifunctional imaging probes seems to be very promising for the future. In addition, probe development may concentrate on multi-purpose agents that combine diagnostic and therapeutic functionality, thus enabling theranostic imaging.

MI has changed the way we are looking at tumors and shifts imaging paradigms away from classical morphological measures toward functional assessments, thus finally leading to personalized treatment of patients. Preclinical experiments in animal models have provided numerous diagnostic agents and imaging approaches. These possibilities need to be selected and translated to clinical practice to diagnose disease and to monitor treatment. The selection of suitable experimental imaging methodology needs to be based on sound scientific rationale, substantial and immediate impacts on patient care, and easy accessibility to patients and referring clinicians. Considering these factors, MRI will continue to be one of the dominant molecular imaging modalities for clinical imaging in near future. Furthermore, the successful translation into clinical applications will require thorough clinical validation of methods and careful correlation with established prognostic markers, standardization and active interdisciplinary collaboration among basic researchers, imaging experts, and referring clinicians. Thus, higher investments in the quality of clinical studies are necessary. To better realize the potential of new developments for clinical translation already in an early preclinical stage, improved *in vitro* models and animal models of disease that closely represent patient requirements are highly needed. Currently available genomic information of species can be used to develop animal models that better recapitulate human disease at both the phenotypic and the genomic levels. Despite all challenges, MI is already approaching clinical reality.

Acknowledgments The authors are supported by the Federal Ministry of Education and Research, Germany (German Consortium for Translational Cancer Research).

References

1. Ahrens ET, Bulte JWM (2013) Tracking immune cells *in vivo* using magnetic resonance imaging. *Nat Rev Immunol* 13:755–763
2. Ahrens ET, Helfer BM, O'Hanlon CF, Schirda C (2014) Clinical cell therapy imaging using a perfluorocarbon tracer and fluorine-19 MRI. *Magn Reson Med* 72:1696–1701
3. Aime S, Barge A, Batsanov AS, Botta M, Castelli DD, Fedeli F, Mortillaro A, Parker D, Puschmann H (2002) Controlling the variation of axial water exchange rates in macrocyclic lanthanide(III) complexes. *Chem Commun (Camb)* 10:1120–1121
4. Aime S, Barge A, Delli Castelli D, Fedeli F, Mortillaro A, Nielsen FU, Terreno E (2002) Paramagnetic lanthanide(III) complexes as pH-sensitive chemical exchange saturation transfer (CEST) contrast agents for MRI applications. *Magn Reson Med* 47:639–648
5. Aime S, Cabella C, Colombatto S, Geninatti Crich S, Gianolio E, Maggioni F (2002) Insights into the use of paramagnetic Gd(III) complexes in MR-molecular imaging investigations. *J Magn Reson Imaging* 16:394–406

6. Aime S, Castelli DD, Crich SG, Gianolio E, Terreno E (2009) Pushing the sensitivity envelope of lanthanide-based magnetic resonance imaging (MRI) contrast agents for molecular imaging applications. *Acc Chem Res* 42:822–831
7. Alessi P, Ebbinghaus C, Neri D (2004) Molecular targeting of angiogenesis. *Biochim Biophys Acta* 1654:39–49
8. Almeida GS, Panek R, Hallsworth A, Webber H, Papaevangelou E, Boulton JK, Jamin Y, Chesler L, Robinson SP (2017) Pre-clinical imaging of transgenic mouse models of neuroblastoma using a dedicated 3-element solenoid coil on a clinical 3T platform. *Br. J. Cancer* 117:791–800; Bajada S, Mazakova I, Richardson JB, Ashammakhi N (2008) Updates on stem cells and their applications in regenerative medicine. *J Tissue Eng Regen Med* 2:169–183
9. Barrett T, Brechbiel M, Bernardo M, Choyke PL (2007) MRI of tumor angiogenesis. *J Magn Reson Imaging* 26:235–249
10. Baudelet C, Ansiaux R, Jordan BF, Havaux X, Macq B, Gallez B (2004) Physiological noise in murine solid tumours using T2*-weighted gradient-echo imaging: a marker of tumour acute hypoxia? *Phys Med Biol* 49:3389–3411
11. Belouche-Babari M, Chung Y-L, Al-Saffar NMS, Falck-Miniotis M, Leach MO (2010) Metabolic assessment of the action of targeted cancer therapeutics using magnetic resonance spectroscopy. *Br J Cancer* 102:1–7
12. Bonetto F, Srinivas M, Heerschap A, Mailliard R, Ahrens ET, Figdor CG, de Vries IJM (2011) A novel (19)F agent for detection and quantification of human dendritic cells using magnetic resonance imaging. *Int J Cancer* 129:365–373
13. Brown JM, Wilson WR (2004) Exploiting tumour hypoxia in cancer treatment. *Nat Rev Cancer* 4:437–447
14. Cai W, Chen X (2008) Multimodality molecular imaging of tumor angiogenesis. *J Nucl Med* 49(Suppl 2):113S–128S
15. Caruthers SD, Winter PM, Wickline SA, Lanza GM (2006) Targeted magnetic resonance imaging contrast agents. *Methods Mol Med* 124:387–400
16. Chaumeil MM, Radoul M, Najac C, Eriksson P, Viswanath P, Blough MD, Chesnelong C, Luchman HA, Cairncross JG, Ronen SM (2016) Hyperpolarized (13)C MR imaging detects no lactate production in mutant IDH1 gliomas: Implications for diagnosis and response monitoring. *Neuroimage Clin* 12:180–189
17. Chauvin T, Durand P, Bernier M, Meudal H, Doan B-T, Noury F, Badet B, Beloeil J-C, Tóth E (2008) Detection of enzymatic activity by PARACEST MRI: a general approach to target a large variety of enzymes. *Angew Chem Int Ed Engl* 47:4370–4372
18. Chen F, De Keyser F, Wang H, Vandecaveye V, Landuyt W, Bosmans H, Hermans R, Marchal G, Ni Y (2007) Diffusion weighted imaging in small rodents using clinical MRI scanners. *Methods* 43:12–20
19. Chenevert TL, Sundgren PC, Ross BD (2006) Diffusion imaging: insight to cell status and cytoarchitecture. *Neuroimaging Clin N Am* 16:619–632, viii–ix
20. Cheng M, Glunde K (2018) Magnetic resonance spectroscopy studies of mouse models of cancer. *Methods Mol Biol* 1718:331–345
21. Corsten MF, Shah K (2008) Therapeutic stem-cells for cancer treatment: hopes and hurdles in tactical warfare. *Lancet Oncol* 9:376–384
22. Crémillieux Y, Salvati R, Dumont U, Pinaud N, Bouchaud V, Sanchez S, Glöggler S, Wong A (2018) Online 1 H-MRS measurements of time-varying lactate production in an animal model of glioma during administration of an anti-tumoral drug. *NMR Biomed* 31
23. Crich SG, Biancone L, Cantaluppi V, Duò D, Esposito G, Russo S, Camussi G, Aime S (2004) Improved route for the visualization of stem cells labeled with a Gd-/Eu-chelate as dual (MRI and fluorescence) agent. *Magn Reson Med* 51:938–944

24. Cyran CC, Fu Y, Raatschen H-J, Rogut V, Chaopathomkul B, Shames DM, Wendland MF, Yeh BM, Brasch RC (2008) New macromolecular polymeric MRI contrast agents for application in the differentiation of cancer from benign soft tissues. *J Magn Reson Imaging* 27:581–589
25. Danad I, Fayad ZA, Willemink MJ, Min JK (2015) New applications of cardiac computed tomography: dual-energy, spectral, and molecular CT imaging. *JACC Cardiovasc Imaging* 8:710–723
26. De Leon-Rodriguez LM, Lubag AJM, Malloy CR, Martinez GV, Gillies RJ, Sherry AD (2009) Responsive MRI agents for sensing metabolism in vivo. *Acc Chem Res* 42:948–957
27. DeBrosse C, Nanga RPR, Bagga P, Nath K, Haris M, Marincola F, Schnall MD, Hariharan H, Reddy R (2016) Lactate chemical exchange saturation transfer (LATEST) imaging in vivo a biomarker for LDH activity. *Sci Rep* 6:19517
28. Deng J, Rhee TK, Sato KT, Salem R, Haines K, Paunesku T, Mulcahy MF, Miller FH, Omary RA, Larson AC (2006) In vivo diffusion-weighted imaging of liver tumor necrosis in the VX2 rabbit model at 1.5 Tesla. *Invest Radiol* 41:410–414
29. Deng L, Liang H, Burnette B, Beckett M, Darga T, Weichselbaum RR, Fu Y-X (2014) Irradiation and anti-PD-L1 treatment synergistically promote antitumor immunity in mice. *J Clin Invest* 124:687–695
30. Ebner B, Behm P, Jacoby C, Burghoff S, French BA, Schrader J, Flögel U (2010) Early assessment of pulmonary inflammation by 19F MRI in vivo. *Circ Cardiovasc Imaging* 3:202–210
31. Fan X, River JN, Zamora M, Al-Hallaq HA, Karczmar GS (2002) Effect of carbogen on tumor oxygenation: combined fluorine-19 and proton MRI measurements. *Int J Radiat Oncol Biol Phys* 54:1202–1209
32. Ferrara N, Gerber H-P, LeCouter J (2003) The biology of VEGF and its receptors. *Nat Med* 9:669–676
33. Gallagher FA, Kettunen MI, Brindle KM (2011) Imaging pH with hyperpolarized ¹³C. *NMR Biomed* 24:1006–1015
34. García-Figueiras R, Padhani AR, Baleato-González S (2016) Therapy monitoring with functional and molecular MR imaging. *Magn Reson Imaging Clin N Am* 24:261–288
35. Gaustad J-V, Simonsen TG, Smistad R, Wegner CS, Andersen LMK, Rofstad EK (2015) Early effects of low dose bevacizumab treatment assessed by magnetic resonance imaging. *BMC Cancer* 15:900
36. Gilad AA, McMahon MT, Walczak P, Winnard PT, Raman V, van Laarhoven HWM, Skoglund CM, Bulte JWM, van Zijl PCM (2007) Artificial reporter gene providing MRI contrast based on proton exchange. *Nat Biotechnol* 25:217–219
37. Gilad AA, Ziv K, McMahon MT, van Zijl PCM, Neeman M, Bulte JWM (2008) MRI reporter genes. *J Nucl Med* 49:1905–1908
38. Golay X, Hendrikse J, Lim TCC (2004) Perfusion imaging using arterial spin labeling. *Top Magn Reson Imaging* 15:10–27
39. Gore JC, Zu Z, Wang P, Li H, Xu J, Dortch R, Gochberg DF (2017) “Molecular” MR imaging at high fields. *Magn Reson Imaging* 38:95–100
40. Gujrati V, Mishra A, Ntziachristos V (2017) Molecular imaging probes for multi-spectral optoacoustic tomography. *Chem Commun (Camb)* 53:4653–4672
41. Hamstra DA, Lee KC, Tychevicz JM, Schepkin VD, Moffat BA, Chen M, Dornfeld KJ, Lawrence TS, Chenevert TL, Ross BD et al (2004) The use of 19F spectroscopy and diffusion-weighted MRI to evaluate differences in gene-dependent enzyme prodrug therapies. *Mol Ther* 10:916–928
42. Hanahan D, Weinberg RA (2011) Hallmarks of cancer: the next generation. *Cell* 144:646–674
43. Haris M, Yadav SK, Rizwan A, Singh A, Wang E, Hariharan H, Reddy R, Marincola FM (2015) Molecular magnetic resonance imaging in cancer. *J Transl Med* 13:313
44. Heyn C, Bowen CV, Rutt BK, Foster PJ (2005) Detection threshold of single SPIO-labeled cells with FIESTA. *Magn Reson Med* 53:312–320

45. Heyn C, Ronald JA, Mackenzie LT, MacDonald IC, Chambers AF, Rutt BK, Foster PJ (2006) In vivo magnetic resonance imaging of single cells in mouse brain with optical validation. *Magn Reson Med* 55:23–29
46. Heyn C, Ronald JA, Ramadan SS, Snir JA, Barry AM, MacKenzie LT, Mikulis DJ, Palmieri D, Bronder JL, Steeg PS et al (2006) In vivo MRI of cancer cell fate at the single-cell level in a mouse model of breast cancer metastasis to the brain. *Magn Reson Med* 56:1001–1010
47. Hillen F, Griffioen AW (2007) Tumour vascularization: sprouting angiogenesis and beyond. *Cancer Metastasis Rev* 26:489–502
48. Himmelreich U, Dresselaers T (2009) Cell labeling and tracking for experimental models using magnetic resonance imaging. *Methods* 48:112–124
49. Hitchens TK, Ye Q, Eytan DF, Janjic JM, Ahrens ET, Ho C (2011) 19F MRI detection of acute allograft rejection with in vivo perfluorocarbon labeling of immune cells. *Magn Reson Med* 65:1144–1153
50. Hoff MN, Yapp DT, Yung AC, Oliver TS, Kozlowski P (2008) In vivo measurement of the hypoxia marker EF5 in Shionogi tumours using (19)F magnetic resonance spectroscopy. *Int J Radiat Biol* 84:237–242
51. Hövener J-B, Bär S, Leupold J, Jenne K, Leibfritz D, Hennig J, Duckett SB, von Elverfeldt D (2013) A continuous-flow, high-throughput, high-pressure parahydrogen converter for hyperpolarization in a clinical setting. *NMR Biomed* 26:124–131
52. Hövener J-B, Schwaderlapp N, Lickert T, Duckett SB, Mewis RE, Highton LAR, Kenny SM, Green GGR, Leibfritz D, Korvink JG et al (2013) A hyperpolarized equilibrium for magnetic resonance. *Nat Commun* 4:2946
53. Hövener J-B, Pravdivtsev AN, Kidd B, Bowers CR, Glöggler S, Kovtunov KV, Plaumann M, Katz-Brull R, Buckenmaier K, Jerschow A et al (2018) Parahydrogen-based hyperpolarization for biomedicine. *Angew Chem Int Ed Engl* 57:11140–11162
54. Hylton N (2006) Dynamic contrast-enhanced magnetic resonance imaging as an imaging biomarker. *J Clin Oncol* 24:3293–3298
55. Hyodo F, Chandramouli GVR, Matsumoto S, Matsumoto K-I, Mitchell JB, Krishna MC, Munasinghe JP (2009) Estimation of tumor microvessel density by MRI using a blood pool contrast agent. *Int J Oncol* 35:797–804
56. Jackson SJ, Thomas GJ (2017) Human tissue models in cancer research: looking beyond the mouse. *Dis Model Mech* 10:939–942
57. Jain RK (2005) Normalization of tumor vasculature: an emerging concept in antiangiogenic therapy. *Science* 307:58–62
58. Kiessling F, Jugold M, Woenne EC, Brix G (2007) Non-invasive assessment of vessel morphology and function in tumors by magnetic resonance imaging. *Eur Radiol* 17:2136–2148
59. Kiessling F, Huppert J, Palmowski M (2009) Functional and molecular ultrasound imaging: concepts and contrast agents. *Curr Med Chem* 16:627–642
60. Kim D, Hong KS, Song J (2007) The present status of cell tracking methods in animal models using magnetic resonance imaging technology. *Mol Cells* 23:132–137
61. Kim H, Morgan DE, Buchsbaum DJ, Zeng H, Grizzle WE, Warram JM, Stockard CR, McNally LR, Long JW, Sellers JC et al (2008) Early therapy evaluation of combined anti-death receptor 5 antibody and gemcitabine in orthotopic pancreatic tumor xenografts by diffusion-weighted magnetic resonance imaging. *Cancer Res* 68:8369–8376
62. Kim H, Morgan DE, Zeng H, Grizzle WE, Warram JM, Stockard CR, Wang D, Zinn KR (2008) Breast tumor xenografts: diffusion-weighted MR imaging to assess early therapy with novel apoptosis-inducing anti-DR5 antibody. *Radiology* 248:844–851
63. Kim S, Loevner L, Quon H, Sherman E, Weinstein G, Kilger A, Poptani H (2009) Diffusion-weighted magnetic resonance imaging for predicting and detecting early response to chemoradiation therapy of squamous cell carcinomas of the head and neck. *Clin Cancer Res* 15:986–994; Kim YR, Yudina A, Figueiredo J, Reichardt W, Hu-Lowe D, Petrovsky A,

- Kang HW, Torres D, Mahmood U, Weissleder R et al (2005) Detection of early antiangiogenic effects in human colon adenocarcinoma xenografts: in vivo changes of tumor blood volume in response to experimental VEGFR tyrosine kinase inhibitor. *Cancer Res* 65:9253–9260
64. Koch U, Krause M, Baumann M (2010) Cancer stem cells at the crossroads of current cancer therapy failures—radiation oncology perspective. *Semin Cancer Biol* 20:116–124
65. Kodibagkar VD, Wang X, Pacheco-Torres J, Gulaka P, Mason RP (2008) Proton imaging of siloxanes to map tissue oxygenation levels (PISTOL): a tool for quantitative tissue oximetry. *NMR Biomed* 21:899–907
66. Kording F, Weidensteiner C, Zwick S, Osterberg N, Weyerbrock A, Staszewski O, von Elverfeldt D, Reichardt W (2014) Simultaneous assessment of vessel size index, relative blood volume, and vessel permeability in a mouse brain tumor model using a combined spin echo gradient echo echo-planar imaging sequence and viable tumor analysis. *J Magn Reson Imaging* 40:1310–1318
67. Kuhn LT, Bommerich U, Bargon J (2006) Transfer of parahydrogen-induced hyperpolarization to 19F. *J Phys Chem A* 110:3521–3526
68. Kurhanewicz J, Vigneron DB, Brindle K, Chekmenev EY, Comment A, Cunningham CH, Deberardinis RJ, Green GG, Leach MO, Rajan SS et al (2011) Analysis of cancer metabolism by imaging hyperpolarized nuclei: prospects for translation to clinical research. *Neoplasia* 13:81–97
69. Larkin JR, Simard MA, Khrapitchev AA, Meakin JA, Okell TW, Craig M, Ray KJ, Jezzard P, Chappell MA, Sibson NR (2018) Quantitative blood flow measurement in rat brain with multiphase arterial spin labelling magnetic resonance imaging. *J Cereb Blood Flow Metab*. 271678X18756218
70. Lee KC, Hamstra DA, Bhojani MS, Khan AP, Ross BD, Rehemtulla A (2007) Noninvasive molecular imaging sheds light on the synergy between 5-fluorouracil and TRAIL/Apo2L for cancer therapy. *Clin Cancer Res* 13:1839–1846
71. Lee H-Y, Li Z, Chen K, Hsu AR, Xu C, Xie J, Sun S, Chen X (2008) PET/MRI dual-modality tumor imaging using arginine-glycine-aspartic (RGD)-conjugated radiolabeled iron oxide nanoparticles. *J Nucl Med* 49:1371–1379
72. Lee J-H, Lee K, Moon SH, Lee Y, Park TG, Cheon J (2009) All-in-one target-cell-specific magnetic nanoparticles for simultaneous molecular imaging and siRNA delivery. *Angew Chem Int Ed Engl* 48:4174–4179
73. Li AX, Wojciechowski F, Suchy M, Jones CK, Hudson RHE, Menon RS, Bartha R (2008) A sensitive PARACEST contrast agent for temperature MRI: Eu³⁺-DOTAM-glycine (Gly)-phenylalanine (Phe). *Magn Reson Med* 59:374–381
74. Li S, Xue H-D, Wang X-H, Sun F, Jiang B, Liu D, Lei J, Jin Z-Y (2008) MR diffusion weighted imaging for evaluation of radiotherapeutic effects on rabbit VX2 tumor model. *Chin Med Sci J* 23:172–177
75. Lin C-Y, Lin M-H, Cheung W-M, Lin T-N, Chen J-H, Chang C (2009) In vivo cerebrovasculature visualization using 3D DeltaR2-based microscopy of magnetic resonance angiography (3DDeltaR2-mMRA). *Neuroimage* 45:824–831
76. Mahmood U, Josephson L (2005) Molecular MR imaging probes. *Proc IEEE Inst Electr Electron Eng* 93:800–808
77. Major JL, Meade TJ (2009) Bioresponsive, cell-penetrating, and multimeric MR contrast agents. *Acc Chem Res* 42:893–903
78. McMahon MT, Gilad AA, DeLiso MA, Berman SMC, Bulte JWM, van Zijl PCM (2008) New “multicolor” polypeptide diamagnetic chemical exchange saturation transfer (DIA-CEST) contrast agents for MRI. *Magn Reson Med* 60:803–812
79. Meng Y, Lei H (2009) A novel continuous arterial spin labeling approach for CBF measurement in rats with reduced labeling time and optimized signal-to-noise ratio efficiency. *MAGMA* 22:135–142

80. Milkiewicz M, Ispanovic E, Doyle JL, Haas TL (2006) Regulators of angiogenesis and strategies for their therapeutic manipulation. *Int J Biochem Cell Biol* 38:333–357
81. Moffat BA, Hall DE, Stojanovska J, McConville PJ, Moody JB, Chenevert TL, Rehemtulla A, Ross BD (2004) Diffusion imaging for evaluation of tumor therapies in preclinical animal models. *MAGMA* 17:249–259
82. Moffat BA, Chenevert TL, Hall DE, Rehemtulla A, Ross BD (2005) Continuous arterial spin labeling using a train of adiabatic inversion pulses. *J Magn Reson Imaging* 21:290–296
83. Moffat BA, Chen M, Kariaapper MST, Hamstra DA, Hall DE, Stojanovska J, Johnson TD, Blaivas M, Kumar M, Chenevert TL et al (2006) Inhibition of vascular endothelial growth factor (VEGF)-A causes a paradoxical increase in tumor blood flow and up-regulation of VEGF-D. *Clin Cancer Res* 12:1525–1532
84. Moroz J, Reinsberg SA (2018) Dynamic contrast-enhanced MRI. *Methods Mol Biol* 1718:71–87
85. von Morze C, Larson PEZ, Hu S, Keshari K, Wilson DM, Ardenkjaer-Larsen JH, Goga A, Bok R, Kurhanewicz J, Vigneron DB (2011) Imaging of blood flow using hyperpolarized [(13)C]urea in preclinical cancer models. *J Magn Reson Imaging* 33:692–697
86. Muja N, Bulte JWM (2009) Magnetic resonance imaging of cells in experimental disease models. *Prog Nucl Magn Reson Spectrosc* 55:61–77
87. Murakami R, Sugahara T, Nakamura H, Hirai T, Kitajima M, Hayashida Y, Baba Y, Oya N, Kuratsu J-I, Yamashita Y (2007) Malignant supratentorial astrocytoma treated with postoperative radiation therapy: prognostic value of pretreatment quantitative diffusion-weighted MR imaging. *Radiology* 243:493–499
88. Muruganandham M, Alfieri AA, Matei C, Chen Y, Sukenick G, Schemainda I, Hasmann M, Saltz LB, Koutcher JA (2005) Metabolic signatures associated with a NAD synthesis inhibitor-induced tumor apoptosis identified by 1H-decoupled-31P magnetic resonance spectroscopy. *Clin Cancer Res* 11:3503–3513
89. Muruganandham M, Lupu M, Dyke JP, Matei C, Linn M, Packman K, Kolinsky K, Higgins B, Koutcher JA (2006) Preclinical evaluation of tumor microvascular response to a novel antiangiogenic/antitumor agent RO0281501 by dynamic contrast-enhanced MRI at 1.5 T. *Mol Cancer Ther* 5:1950–1957
90. Neeman M (2018) Perspectives: MRI of angiogenesis. *J Magn Reson* 292:99–105
91. Ni Y, Wang H, Chen F, Li J, DeKeyser F, Feng Y, Yu J, Bosmans H, Marchal G (2009) Tumor models and specific contrast agents for small animal imaging in oncology. *Methods* 48:125–138
92. Nomori H, Mori T, Ikeda K, Kawanaka K, Shiraishi S, Katahira K, Yamashita Y (2008) Diffusion-weighted magnetic resonance imaging can be used in place of positron emission tomography for N staging of non-small cell lung cancer with fewer false-positive results. *J Thorac Cardiovasc Surg* 135:816–822
93. O'Hanlon CF, Fedczyna T, Eaker S, Shingleton WD, Helfer BM (2017) Integrating a 19F MRI tracer agent into the clinical scale manufacturing of a T-cell immunotherapy. *Contrast Media Mol Imaging* 2017:9548478
94. Oyen WJG, Kaanders JH, Bussink J (2013) Molecular imaging of hypoxia. *Q J Nucl Med Mol Imaging* 57:217–218
95. Padhani AR, Liu G, Koh DM, Chenevert TL, Thoeny HC, Takahara T, Dzik-Jurasz A, Ross BD, Van Cauteren M, Collins D et al (2009) Diffusion-weighted magnetic resonance imaging as a cancer biomarker: consensus and recommendations. *Neoplasia* 11:102–125
96. Park I, Larson PEZ, Zierhut ML, Hu S, Bok R, Ozawa T, Kurhanewicz J, Vigneron DB, Vandenberg SR, James CD et al (2010) Hyperpolarized 13C magnetic resonance metabolic imaging: application to brain tumors. *Neuro-Oncology* 12:133–144
97. Partlow KC, Chen J, Brant JA, Neubauer AM, Meyerrose TE, Creer MH, Nolte JA, Caruthers SD, Lanza GM, Wickline SA (2007) 19F magnetic resonance imaging for stem/progenitor cell tracking with multiple unique perfluorocarbon nanobeacons. *FASEB J* 21:1647–1654

98. Patterson DM, Padhani AR, Collins DJ (2008) Technology insight: water diffusion MRI—a potential new biomarker of response to cancer therapy. *Nat Clin Pract Oncol* 5:220–233
99. Powles T, Eder JP, Fine GD, Braiteh FS, Loria Y, Cruz C, Bellmunt J, Burris HA, Petrylak DP, Teng S et al (2014) MPDL3280A (anti-PD-L1) treatment leads to clinical activity in metastatic bladder cancer. *Nature* 515:558–562
100. Preda A, van Vliet M, Krestin GP, Brasch RC, van Dijke CF (2006) Magnetic resonance macromolecular agents for monitoring tumor microvessels and angiogenesis inhibition. *Invest Radiol* 41:325–331
101. Procissi D, Claus F, Burgman P, Kozirowski J, Chapman JD, Thakur SB, Matei C, Ling CC, Koutcher JA (2007) In vivo ¹⁹F magnetic resonance spectroscopy and chemical shift imaging of tri-fluoro-nitroimidazole as a potential hypoxia reporter in solid tumors. *Clin Cancer Res* 13:3738–3747
102. Rad AM, Iskander ASM, Janic B, Knight RA, Arbab AS, Soltanian-Zadeh H (2009) AC133 + progenitor cells as gene delivery vehicle and cellular probe in subcutaneous tumor models: a preliminary study. *BMC Biotechnol* 9:28
103. Rajendran R, Liang J, Tang MYA, Henry B, Chuang K-H (2015) Optimization of arterial spin labeling MRI for quantitative tumor perfusion in a mouse xenograft model. *NMR Biomed* 28:988–997
104. Raman V, Pathak AP, Glunde K, Artemov D, Bhujwala ZM (2007) Magnetic resonance imaging and spectroscopy of transgenic models of cancer. *NMR Biomed* 20:186–199
105. Ren J, Trokowsky R, Zhang S, Malloy CR, Sherry AD (2008) Imaging the tissue distribution of glucose in livers using a PARACEST sensor. *Magn Reson Med* 60:1047–1055
106. Reynolds S, Metcalf S, Cochrane EJ, Collins RC, Jones S, Paley MNJ, Tozer GM (2017) Direct arterial injection of hyperpolarized ¹³C-labeled substrates into rat tumors for rapid MR detection of metabolism with minimal substrate dilution. *Magn Reson Med* 78:2116–2126
107. Robinson SP, Griffiths JR (2004) Current issues in the utility of ¹⁹F nuclear magnetic resonance methodologies for the assessment of tumour hypoxia. *Philos Trans R Soc Lond B Biol Sci* 359:987–996
108. Robinson SP, Rijken PFJW, Howe FA, McSheehy PMJ, van der Sanden BPJ, Heerschap A, Stubbs M, van der Kogel AJ, Griffiths JR (2003) Tumor vascular architecture and function evaluated by non-invasive susceptibility MRI methods and immunohistochemistry. *J Magn Reson Imaging* 17:445–454
109. Robinson SP, Ludwig C, Paulsson J, Ostman A (2008) The effects of tumor-derived platelet-derived growth factor on vascular morphology and function in vivo revealed by susceptibility MRI. *Int J Cancer* 122:1548–1556
110. Rodrigues LM, Howe FA, Griffiths JR, Robinson SP (2004) Tumor R2* is a prognostic indicator of acute radiotherapeutic response in rodent tumors. *J Magn Reson Imaging* 19:482–488
111. Rodrigues TB, Serrao EM, Kennedy BWC, Hu D-E, Kettunen MI, Brindle KM (2014) Magnetic resonance imaging of tumor glycolysis using hyperpolarized ¹³C-labeled glucose. *Nat Med* 20:93–97
112. Roth Y, Tichler T, Kostenich G, Ruiz-Cabello J, Maier SE, Cohen JS, Orenstein A, Mardor Y (2004) High-b-value diffusion-weighted MR imaging for pretreatment prediction and early monitoring of tumor response to therapy in mice. *Radiology* 232:685–692
113. Ruggeri BA, Camp F, Miknyoczki S (2014) Animal models of disease: pre-clinical animal models of cancer and their applications and utility in drug discovery. *Biochem Pharmacol* 87:150–161
114. Schmidt AB, Berner S, Schimpf W, Müller C, Lickert T, Schwaderlapp N, Knecht S, Skinner JG, Dost A, Rovedo P et al (2017) Liquid-state carbon-13 hyperpolarization generated in an MRI system for fast imaging. *Nat Commun* 8:14535
115. Schmidt AB, Berner S, Braig M, Zimmermann M, Hennig J, von Elverfeldt D, Hövener J-B (2018) In vivo ¹³C-MRI using SAMBADENA. *PLoS ONE* 13:e0200141

116. Schmieder AH, Winter PM, Caruthers SD, Harris TD, Williams TA, Allen JS, Lacy EK, Zhang H, Scott MJ, Hu G et al (2005) Molecular MR imaging of melanoma angiogenesis with alphanubeta3-targeted paramagnetic nanoparticles. *Magn Reson Med* 53:621–627
117. Schreiber RD, Old LJ, Smyth MJ (2011) Cancer immunoediting: integrating immunity's roles in cancer suppression and promotion. *Science* 331:1565–1570
118. Schwab L, Goroncy L, Palaniyandi S, Gautam S, Triantafyllou A, Mocsai A, Reichardt W, Karlsson FJ, Radhakrishnan SV, Hanke K et al (2014) Neutrophil granulocytes recruited upon translocation of intestinal bacteria enhance graft-versus-host disease via tissue damage. *Nat Med* 20:648–654
119. Shah K, Weissleder R (2005) Molecular optical imaging: applications leading to the development of present day therapeutics. *NeuroRx* 2:215–225
120. Song S-K, Qu Z, Garabedian EM, Gordon JI, Milbrandt J, Ackerman JJH (2002) Improved magnetic resonance imaging detection of prostate cancer in a transgenic mouse model. *Cancer Res* 62:1555–1558
121. Srinivas M, Turner MS, Janjic JM, Morel PA, Laidlaw DH, Ahrens ET (2009) In vivo cytometry of antigen-specific T cells using 19F MRI. *Magn Reson Med* 62:747–753
122. Strijkers GJ, Mulder WJM, van Tilborg GAF, Nicolay K (2007) MRI contrast agents: current status and future perspectives. *Anticancer Agents Med Chem* 7:291–305
123. Sun Y, Schmidt NO, Schmidt K, Doshi S, Rubin JB, Mulkern RV, Carroll R, Ziu M, Erkmann K, Poussaint TY et al (2004) Perfusion MRI of U87 brain tumors in a mouse model. *Magn Reson Med* 51:893–899
124. Sun X, Wang H, Chen F, De Keyzer F, Yu J, Jiang Y, Feng Y, Li J, Marchal G, Ni Y (2009) Diffusion-weighted MRI of hepatic tumor in rats: comparison between in vivo and postmortem imaging acquisitions. *J Magn Reson Imaging* 29:621–628
125. Talmadge JE, Singh RK, Fidler IJ, Raz A (2007) Murine models to evaluate novel and conventional therapeutic strategies for cancer. *Am J Pathol* 170:793–804
126. Taromi S, Kayser G, von Elverfeldt D, Reichardt W, Braun F, Weber WA, Zeiser R, Burger M (2016) An orthotopic mouse model of small cell lung cancer reflects the clinical course in patients. *Clin Exp Metastasis* 33:651–660
127. Tatum JL, Kelloff GJ, Gillies RJ, Arbeit JM, Brown JM, Chao KSC, Chapman JD, Eckelman WC, Fyles AW, Giaccia AJ et al (2006) Hypoxia: importance in tumor biology, noninvasive measurement by imaging, and value of its measurement in the management of cancer therapy. *Int J Radiat Biol* 82:699–757
128. Sebastian T, Florian B, Jürgen S, Ulrich F (2012) 19F magnetic resonance imaging of endogenous macrophages in inflammation. *Wiley Interdiscipl Rev: Nanomed Nanobiotechnol* 4:329–343
129. Thoeny HC, De Keyzer F, Vandecaveye V, Chen F, Sun X, Bosmans H, Hermans R, Verbeke EK, Boesch C, Marchal G et al (2005) Effect of vascular targeting agent in rat tumor model: dynamic contrast-enhanced versus diffusion-weighted MR imaging. *Radiology* 237:492–499
130. Towner RA, Smith N, Asano Y, Doblaz S, Saunders D, Silasi-Mansat R, Lupu F (2010) Molecular magnetic resonance imaging approaches used to aid in the understanding of the tissue regeneration marker Met in vivo: implications for tissue engineering. *Tissue Eng Part A* 16:365–371
131. Tropès I, Grimault S, Vaeth A, Grillon E, Julien C, Payen JF, Lamalle L, Décorps M (2001) Vessel size imaging. *Magn Reson Med* 45:397–408
132. Tropès I, Lamalle L, Péoc'h M, Farion R, Usson Y, Décorps M, Rémy C (2004) In vivo assessment of tumoral angiogenesis. *Magn Reson Med* 51:533–541
133. Turetschek K, Preda A, Novikov V, Brasch RC, Weinmann HJ, Wunderbaldinger P, Roberts TPL (2004) Tumor microvascular changes in antiangiogenic treatment: assessment by magnetic resonance contrast media of different molecular weights. *J Magn Reson Imaging* 20:138–144

134. Vandecaveye V, de Keyzer F, Vander Poorten V, Deraedt K, Alaerts H, Landuyt W, Nuyts S, Hermans R (2006) Evaluation of the larynx for tumour recurrence by diffusion-weighted MRI after radiotherapy: initial experience in four cases. *Br J Radiol* 79:681–687
135. Vaupel P, Mayer A (2007) Hypoxia in cancer: significance and impact on clinical outcome. *Cancer Metastasis Rev* 26:225–239
136. Walenta S, Mueller-Klieser WF (2004) Lactate: mirror and motor of tumor malignancy. *Semin Radiat Oncol* 14:267–274
137. Wang H, Sun X, Chen F, De Keyzer F, Yu J, Landuyt W, Vandecaveye V, Peeters R, Bosmans H, Hermans R et al (2009) Treatment of rodent liver tumor with combretastatin a4 phosphate: noninvasive therapeutic evaluation using multiparametric magnetic resonance imaging in correlation with microangiography and histology. *Invest Radiol* 44:44–53
138. Wang K, Wang K, Shen B, Huang T, Sun X, Li W, Jin G, Li L, Bu L, Li R et al (2010) MR reporter gene imaging of endostatin expression and therapy. *Mol Imaging Biol* 12:520–529
139. Ward KM, Aletras AH, Balaban RS (2000) A new class of contrast agents for MRI based on proton chemical exchange dependent saturation transfer (CEST). *J Magn Reson* 143:79–87
140. Waters EA, Chen J, Yang X, Zhang H, Neumann R, Santeford A, Arbeit J, Lanza GM, Wickline SA (2008) Detection of targeted perfluorocarbon nanoparticle binding using 19F diffusion weighted MR spectroscopy. *Magn Reson Med* 60:1232–1236
141. Weber M-A, Günther M, Lichy MP, Delorme S, Bongers A, Thilmann C, Essig M, Zuna I, Schad LR, Debus J et al (2003) Comparison of arterial spin-labeling techniques and dynamic susceptibility-weighted contrast-enhanced MRI in perfusion imaging of normal brain tissue. *Invest Radiol* 38:712–718
142. Weibel S, Basse-Luesebrock TC, Hess M, Hofmann E, Seubert C, Langbein-Laugwitz J, Gentschev I, Sturm VJF, Ye Y, Kampf T et al (2013) Imaging of intratumoral inflammation during oncolytic virotherapy of tumors by 19F-magnetic resonance imaging (MRI). *PLoS ONE* 8:e56317
143. Weinmann M, Belka C, Plasswilm L (2004) Tumour hypoxia: impact on biology, prognosis and treatment of solid malignant tumours. *Onkologie* 27:83–90
144. Williams KJ, Cowen RL, Brown LM, Chinje EC, Jaffar M, Stratford IJ (2004) Hypoxia in tumors: molecular targets for anti-cancer therapeutics. *Adv Enzym Regul* 44:93–108
145. Wilson DM, Kurhanewicz J (2014) Hyperpolarized 13C MR for molecular imaging of prostate cancer. *J Nucl Med* 55:1567–1572
146. Winnard PT, Pathak AP, Dhara S, Cho SY, Raman V, Pomper MG (2008) Molecular imaging of metastatic potential. *J Nucl Med* 49(Suppl 2):96S–112S
147. Wolf G, Abolmaali N (2009) Imaging tumour-bearing animals using clinical scanners. *Int J Radiat Biol* 85:752–762
148. Wong FC, Kim EE (2009) A review of molecular imaging studies reaching the clinical stage. *Eur J Radiol* 70:205–211
149. Woods M, Woessner DE, Sherry AD (2006) Paramagnetic lanthanide complexes as PARACEST agents for medical imaging. *Chem Soc Rev* 35:500–511
150. Xue H-D, Li S, Sun H-Y, Jin Z-Y, Sun F (2008) Experimental study of inflammatory and metastatic lymph nodes with diffusion weighted imaging on animal model: comparison with conventional methods. *Chin Med Sci J* 23:166–171
151. Ye FQ, Berman KF, Ellmore T, Esposito G, van Horn JD, Yang Y, Duyn J, Smith AM, Frank JA, Weinberger DR et al (2000) H(2)(15)O PET validation of steady-state arterial spin tagging cerebral blood flow measurements in humans. *Magn Reson Med* 44:450–456
152. Yee NS, Ignatenko N, Finnberg N, Lee N, Stairs D (2015) Animal models of cancer biology. *Cancer Growth Metastasis* 8:115–118
153. Yoo B, Raam MS, Rosenblum RM, Pagel MD (2007) Enzyme-responsive PARACEST MRI contrast agents: a new biomedical imaging approach for studies of the proteasome. *Contrast Media Mol Imaging* 2:189–198

154. Youn BJ, Chung JW, Son KR, Kim H-C, Jae HJ, Lee JM, Song IC, Kim I-O, Park JH (2008) Diffusion-weighted MR: therapeutic evaluation after chemoembolization of VX-2 carcinoma implanted in rabbit liver. *Acad Radiol* 15:593–600
155. Zhang S, Trokowski R, Sherry AD (2003) A paramagnetic CEST agent for imaging glucose by MRI. *J Am Chem Soc* 125:15288–15289
156. Zhang S, Malloy CR, Sherry AD (2005) MRI thermometry based on PARACEST agents. *J Am Chem Soc* 127:17572–17573
157. Zhang C, Jugold M, Woenne EC, Lammers T, Morgenstern B, Mueller MM, Zentgraf H, Bock M, Eisenhut M, Semmler W et al (2007) Specific targeting of tumor angiogenesis by RGD-conjugated ultrasmall superparamagnetic iron oxide particles using a clinical 1.5-T magnetic resonance scanner. *Cancer Res* 67:1555–1562
158. Zhang M, Huang M, Le C, Zanzonico PB, Claus F, Kolbert KS, Martin K, Ling CC, Koutcher JA, Humm JL (2008) Accuracy and reproducibility of tumor positioning during prolonged and multi-modality animal imaging studies. *Phys Med Biol* 53:5867–5882
159. Zhang M, Yao Z, Dubois S, Ju W, Müller JR, Waldmann TA (2009) Interleukin-15 combined with an anti-CD40 antibody provides enhanced therapeutic efficacy for murine models of colon cancer. *Proc Natl Acad Sci USA* 106:7513–7518
160. Zlitni A, Gambhir SS (2018) Molecular imaging agents for ultrasound. *Curr Opin Chem Biol* 45:113–120



Optical and Optoacoustic Imaging

13

Joanna Napp, Andrea Markus, and Frauke Alves

Contents

13.1	Introduction.....	441
13.2	Fluorescence Imaging.....	442
13.2.1	Principles of Fluorescence.....	442
13.2.2	Fluorescence Imaging Technologies.....	445
13.2.3	Optical Domains.....	448
13.2.4	In Vivo Applications of Fluorescence Imaging.....	451
13.3	Bioluminescence Imaging.....	459
13.3.1	Basics of Bioluminescence Imaging.....	460
13.3.2	Factors Affecting BLI.....	462
13.3.3	Genetically Engineered Luciferases, Modified Substrates, and Multicolor Reporter Systems.....	464

J. Napp (✉)

Image-Guided Nanotherapy and Diagnostic (IND), Institute of Diagnostic and Interventional Radiology, University Medical Center Goettingen (UMG), Robert-Koch-Str. 40, 37075 Goettingen, Germany
e-mail: joanna.napp@med.uni-goettingen.de

A. Markus

Translational Molecular Imaging, Max-Planck-Institute for Experimental Medicine, Hermann-Rein-Str. 3, 37075 Goettingen, Germany
e-mail: markus@em.mpg.de

F. Alves (✉)

Translational Molecular Imaging, Institute of Diagnostic and Interventional Radiology, Clinic of Hematology and Medical Oncology, University Medical Center Goettingen (UMG), Robert-Koch Str. 40, 37075 Goettingen, Germany
e-mail: falves@gwdg.de

F. Alves

Max-Planck-Institute for Experimental Medicine, Hermann-Rein-Str. 3, 37075 Goettingen, Germany

13.3.4 Applications of BLI.....	466
13.3.5 Bioluminescence Imaging Versus Fluorescence Imaging	470
13.4 Optoacoustic Imaging.....	471
13.4.1 Modes of Action.....	473
13.4.2 Sources of Contrast	473
13.5 Summary.....	482
References	482

Nomenclature

2D	Two-dimensional
3D	Three-dimensional
ACT	Adoptive T cell therapy
BLI	Bioluminescence imaging
BRET	Bioluminescence resonance energy transfer
CCD	Charged-coupled device
cRGD	Cyclic arginine–glycine–aspartic acid
CXCR4	CXC-Motiv-Chemokine receptor 4
DOX	Doxorubicin
DR5	Proapoptotic receptor death receptor 5
ECM	Extracellular matrix
EGFR	Epidermal growth factor receptor
EPR	Enhanced permeability and retention
ER	Endoplasmic reticulum
FGS	Fluorescence-guided surgery
FITC	Fluorescein isothiocyanate
FLIM	Fluorescence lifetime imaging
FLuc	Firefly luciferase
FRI	Fluorescence reflectance imaging
FTI	Fluorescence transillumination imaging
GFP	Green fluorescent protein
GLuc	<i>Gaussia</i> luciferase
GPCR	G protein-coupled receptor
hASCs	Human subcutaneous adipose tissue stem cells
HIF	Hypoxia-inducible factor
hMSCs	Human mesenchymal stem cells
ICG	Indo-cyanine green
LLC	Lewis lung cancer
MICAD	Molecular Imaging and Contrast Agent Database
MMPs	Matrix metalloproteinases
MRI	Magnetic resonance imaging
MSOT	Multispectral optoacoustic tomography
NFAT	Nuclear factor of activated T cells
NIR(F)	Near-infrared (fluorescence)
OAI	Optoacoustic imaging

OVA	Ovalbumin
PBLs	Peripheral blood lymphocytes
PCA	Protein fragment complementation assay
PDGFR	Platelet-derived growth factor receptor
PEG	Polyethylene glycol
PKA	Protein kinase A
PSA	Prostate-specific antigen
QY	Quantum yield
RFP	Red fluorescent protein
RLuc	<i>Renilla</i> luciferase
SLNs	Sentinel lymph node(s)
SNR	Signal-to-noise ratio
SPCD	Single-photon counting detector
SPR	Surface plasmon resonance
TILs	Tumor-infiltrating lymphocytes
TME	Tumor microenvironment
TNF	Tumor necrosis factor
TRAIL	Tumor necrosis factor (TNF)-related apoptosis-inducing ligand
UV	Ultraviolet
VEGF	Vascular endothelial growth factor
Vluc	Vargula luciferase

13.1 Introduction

The spatiotemporal determination of molecular events and cells is important for understanding disease processes, especially in oncology, and thus for the development of novel treatments. Equally important is the knowledge of the biodistribution, localization, and targeted accumulation of novel therapies as well as monitoring of tumor growth and therapeutic response. Optical imaging provides an ideal versatile platform for imaging of all these problems and questions. While each of the three modalities presented here—bioluminescence, fluorescence, and optoacoustic imaging—has its advantages and disadvantages, they serve numerous applications, of which only a few are named here:

- Detection and monitoring of targeted proteins for providing information on biodistribution, accumulation, and specificity of imaging probes and therapies.
- Monitoring of cell trafficking or cell migration such as stem cells or T-lymphocytes.
- Tracking of tumor growth, cancer cell metastasis, migration, and invasion.
- Monitoring of therapeutic response.
- Visualization of enzymatic activity such as proteases.

- Visualization of physiologic changes in tissues, such as hypoxia.
- Localization and trafficking of proteins through different cellular compartments using fluorescent reporters fused to proteins of interest.
- Monitoring of gene expression using DNA-binding responsive elements.

At the same time, fluorescent and bioluminescent optical imaging modalities are simple, less expensive, more convenient, and more user-friendly than other imaging modalities and thus often the first choice for preclinical imaging in oncology. Due to the general safety of optical imaging, in particular, fluorescence and optoacoustic imaging, a major advantage of these modalities is the possibility of longitudinal studies which are most valuable in efficacy and pharmacokinetic studies.

The field of optical imaging has recently received a further boost with the development of novel optical probes. The list of fluorescent probes is steadily growing and competing with novel more sophisticated applications such as activatable probes, fluorescent nanoparticles as well as sensing probes, which have significantly increased both the sensitivity and specificity of detection and assessment of biological processes *in vivo*.

This chapter will introduce the principles of fluorescence, bioluminescence, and optoacoustic imaging and will provide appropriate examples of how these modalities have shaped the *in vivo* preclinical research of cancer.

13.2 Fluorescence Imaging

13.2.1 Principles of Fluorescence

Fluorescence is the property of certain molecules (**fluorophores, fluorochromes, or fluorescent dyes**) to absorb light or other electromagnetic radiation at one wavelength and to emit light at another (Fig. 13.1). Thereby, the absorption of the photon of energy ($h\nu$) transfers the molecule to the excited electronic singlet state. The excited state of a fluorophore is characterized by a very short half-life, usually

Fig. 13.1 Jablonski diagram of absorbance, non-radiative decay, and fluorescence

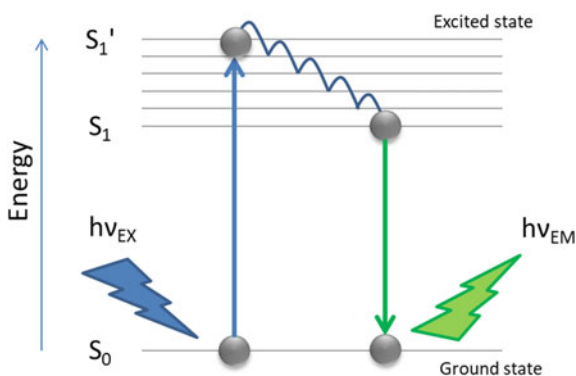
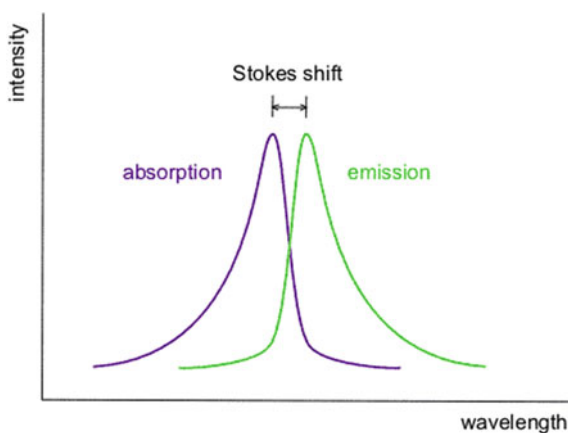


Fig. 13.2 The difference between the maximum emission and excitation wavelengths is termed Stokes shift



in the order of a few nanoseconds, after which the molecule returns to the ground state emitting a photon of usually lower energy and consequently longer wavelength. The average time, which a molecule spends in the excited state, is called **lifetime** and is specific for each fluorophore.

Usually, a molecule does not absorb and emit only one particular wavelength, but a whole range of wavelengths that can be represented in the form of absorption and emission spectra with bandwidths and maxima specific for each particular fluorophore. The difference between the maximum excitation and emission is termed **Stokes shift**, after Sir George Stokes, who first described this phenomenon in 1852 (Fig. 13.2). The Stokes shift is a distinct characteristic of each fluorophore. In fluorophores with very small Stokes shifts, excitation and emission wavelengths greatly overlap and the emitted fluorescence is difficult to distinguish from the excitation light. A large Stokes shift is therefore usually preferred for in vivo imaging.

The process of fluorescence is not very efficient and not every absorption event ends up in an emission of the photon. The efficiency of the fluorescence is described by the **quantum yield (QY; Φ)**, a parameter, which is defined as the number of times a specific event occurs per photon absorbed by the molecule. The QY ranges from 0 (non-fluorescent molecule) to 1 (100% efficiency). Another parameter that describes the efficiency of the fluorescence process is the **molar extinction coefficient (ϵ)**, which defines how strongly a molecule absorbs light at a given wavelength (per molar concentration). The intensity of fluorescence output per fluorophore is proportional to the product of the extinction coefficient (at the relevant excitation wavelength) and the fluorescence QY.

Fluorescence is a “cyclic” process, meaning that a molecule can be repeatedly excited after the light emission unless it is destroyed, e.g., because of prolonged exposure to the excitation source or due to exposure to high-intensity excitation light. This irreversible destruction of the fluorophore is called **bleaching or photobleaching**.

All cells contain endogenous fluorophores, which become fluorescent when excited with the suitable wavelength. This characteristic is generally called **autofluorescence** and is one of the major drawbacks of in vivo fluorescence imaging. Among autofluorescent tissue components, NADPH and flavins are the most common, but also other structures such as some lipopigments or aromatic amino acids (tryptophan, tyrosine, and phenylalanine) and extracellular tissue components with a high content of collagen and elastin demonstrate measurable levels of autofluorescence [87]. Most of these molecules absorb and emit ultraviolet (UV) or visible light, hampering fluorescence imaging in this light spectrum.

Furthermore, light passing through tissues undergoes **absorption** and **scattering**. As already mentioned, the majority of tissue components absorb short-wavelength UV and visible light, meaning that longer wavelengths are more favorable for in vivo applications.

Photon penetration into living tissue is highly dependent on the absorption and scattering properties of tissue components [31]. The major tissue absorbers are hemoglobin and water, but the lowest absorption occurs in the near-infrared (NIR) region at 650–950 nm, a wavelength region called “optical window” [144]. At wavelengths longer than 950 nm, absorption by water and lipids increases again, but at the same time, the tissue autofluorescence decreases, making the wavelength range between 1000 and 1350 nm, the so-called “second optical window”, particularly favorable for in vivo imaging (Fig. 13.3). Optical imaging at this wavelength has been slowed down by the lack of sensitive and low-cost detectors, but with the recent progress in technology and the development of appropriate fluorescent probes the second optical window offers a tremendous new opportunity for sensitive in vivo fluorescence imaging of small animals [119].

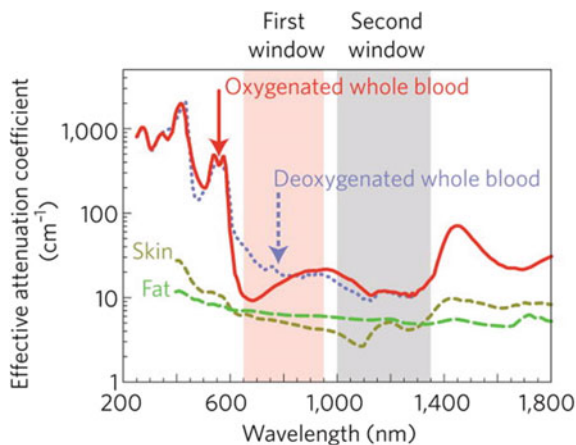


Fig. 13.3 First and second NIR windows for optical imaging. Effective attenuation coefficient (on a log scale) corresponding to absorption and scattering from oxygenated blood, deoxygenated blood, skin, and fatty tissue are plotted versus wavelength [119]

13.2.2 Fluorescence Imaging Technologies

In general, fluorescence imaging requires a light source and a detector, both of which have to match the absorption and emission spectra of the fluorescent molecule or the fluorophore. A simple lamp or a laser can serve as a source of light, while the emitted fluorescence can be detected with an appropriate camera, such as a low-noise charged-coupled device (CCD) camera, or with a photomultiplier tube. In the majority of *in vivo* imaging systems, the light source and the detector are placed in a dark box that usually also contains an animal holder and anesthesia equipment.

The question of which kind of imager to buy or build is dependent on many factors, and users should carefully consider these before making a choice. Variables include the type of application (planar or tomographic), the animal species and numbers, the disease model and questions to be answered, the dyes and type of probe to be used, sensitivity of the system, flexibility (multiple and upgradable filters and lasers for instance), ease of use and, last but not least, the price.

Fluorophores can either be expressed endogenously, by genetically modified cells or organisms, or can be applied extrinsically, e.g., in the form of dyes attached to the molecule of interest (antibody, peptide, enzyme, etc.), dye-loaded nanoparticles, quantum dots, etc. [145]. This enables a wide range of applications including, for example, the assessment of the location and dynamics of gene and protein expression, or of molecular interactions, but also the analysis of the biodistribution of applied probes, monitoring of drug release, or analyte sensing (e.g., O_2 or pH) in cells and tissues. Especially the use of probes/labels that absorb an emitting NIR light allows for relatively high penetration depths of up to ~ 2 cm.

In vivo fluorescence imaging can be performed as planar (two-dimensional, 2D) or tomographic (three-dimensional, 3D) approaches. While planar imaging is relatively simple and measures the fluorescence intensity over the body surface, tomographic imaging requires more complex reconstruction of raw data by a model algorithm, delivering additional information about the depth of the fluorescence signal within the object. Planar fluorescence imaging can be performed either in epi-illumination, also called fluorescence reflectance imaging (FRI), or in transillumination mode, known as fluorescence transillumination imaging (FTI).

13.2.2.1 Fluorescence Reflectance Imaging (FRI)

In FRI, the source of excitation light and the detector are located on the same side of the object or subject (Fig. 13.4 upper panel). The buildup is thus simple and does not require any special animal table or holder. As the excitation light is strongly absorbed and scattered by tissues, the intensity of the excitation light rapidly decays with increasing depth, meaning that deeper located fluorophores will be less excited than the ones near the surface. At the same time, fluorescent signals derived from deeper locations will also be more absorbed and scattered than those on the surface. As a consequence, the acquired signals are dominated by surface-near fluorescence events and deeper signals appear more diffuse than those near the surface. The largest disadvantage of the FRI approach is the fact that the autofluorescence from

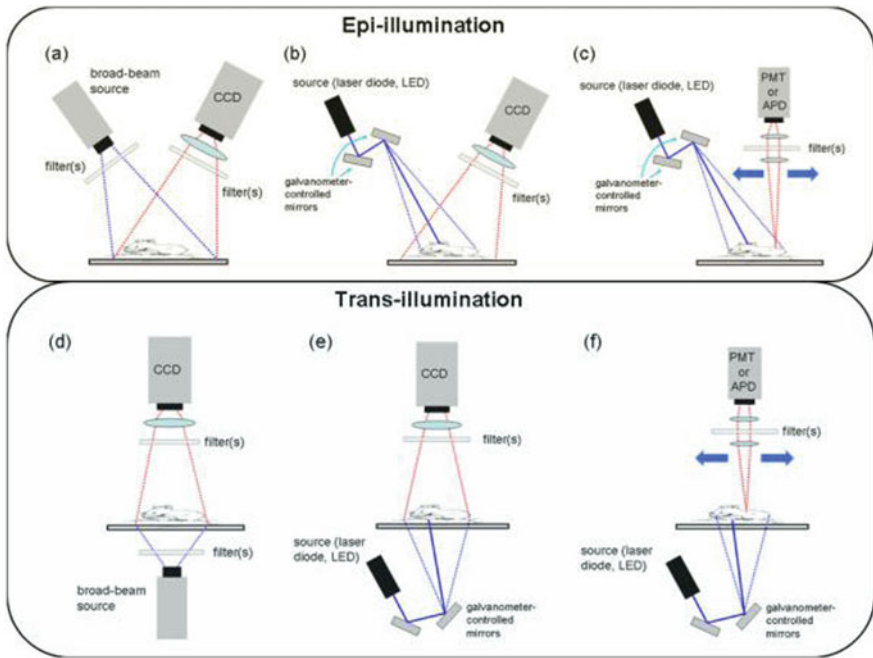


Fig. 13.4 Principle of optical fluorescence imaging techniques that can be used for whole-body fluorescence imaging. The upper panel shows epi-illumination geometries: **a** broad beam illumination with wide-field camera detection; **b** raster-scan illumination with wide-field camera detection, **c** raster-scan illumination and detection. The lower panel shows the corresponding transillumination configurations **d–f**: different possible set-ups of transillumination techniques. Not shown in the figure are configurations optimized for tomography imaging and fiber-based planar configurations. Figure taken from Leblond et al. [61], with permission from the Journal of Photochemistry and Photobiology/Elsevier

subsurface tissues will be more excited and thus better detected than possible deeper located fluorescent signals, consequently strongly contributing to surface-weighted images.

13.2.2.2 Fluorescence Transillumination Imaging (FTI)

In FTI, the excitation light source and the detector are located on opposite sides of the object or subject (Fig. 13.4 lower panel). The advantage is that, in contrast to FRI, the fluorescence generated within the body dominates the overall measurement, since the autofluorescence generated from the skin and blood vessels on the excitation side needs to penetrate the whole animal before detection, reducing overall autofluorescence [101]. However, FTI has some restrictions: (i) the animal holder must be transparent at least to the particular light used and (ii) the emitted

light needs to travel through the remaining dimension of the animal. Therefore, transillumination cannot be applied for larger animals.

13.2.2.3 Fluorescence Tomography

In planar fluorescence intensity maps, which are typically overlaid with photographic images of the subject, detected signals are often surface-weighted and deeper signals appear weaker and distorted due to the absorbance and scattering of light. Furthermore, fluorescence sources within the body of the animal can be shielded by other organs/structures lying in the path of the light between source and detector. This means, with a 2D approach, it is impossible to determine if a detected weak fluorescence signal is related to a low near-surface concentration of the fluorescent dye or from a high concentration of the fluorescent probe located deeper in the body, restricting a reliable quantification of the data (Fig. 13.5).

Tomographic fluorescence approaches are obviously advantageous since they allow the assessment of the location/depth of the signal source within the tissue and therefore provide more quantifiable data. However, especially due to the strong light absorption by biological samples, generation of reliable 3D NIR fluorescence (NIRF) images is far less straightforward as with other tomographic imaging modalities and requires information about the tissue composition. Based on this,

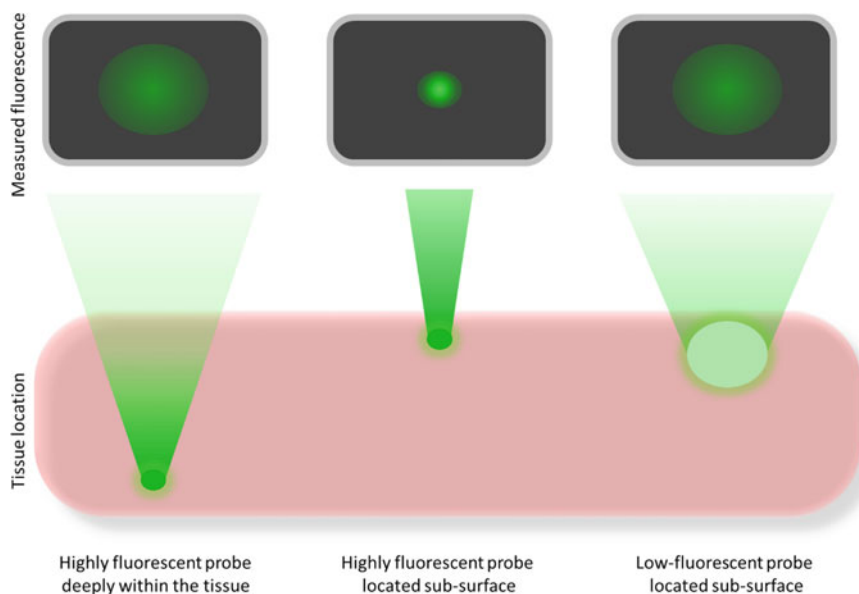


Fig. 13.5 Limitations of planar fluorescence imaging for data quantification: a deeply located small target with a bright fluorescent probe (left) will appear larger and less bright due to light scattering and absorption than the same target/probe located near the surface and will possibly deliver similar results as a large target detected with a low-fluorescent probe at a subsurface location (right)

light propagation models for specific samples are developed and complex algorithms are then applied to calculate the distribution of fluorescent sources within the tissues.

3D fluorescent images can be produced by either rotating a single detector around the subject, or by combining multiple images from different detectors placed around the subject, or by using a tomographic approach based on transillumination [96, 100, 126].

13.2.3 Optical Domains

13.2.3.1 Intensity Domain

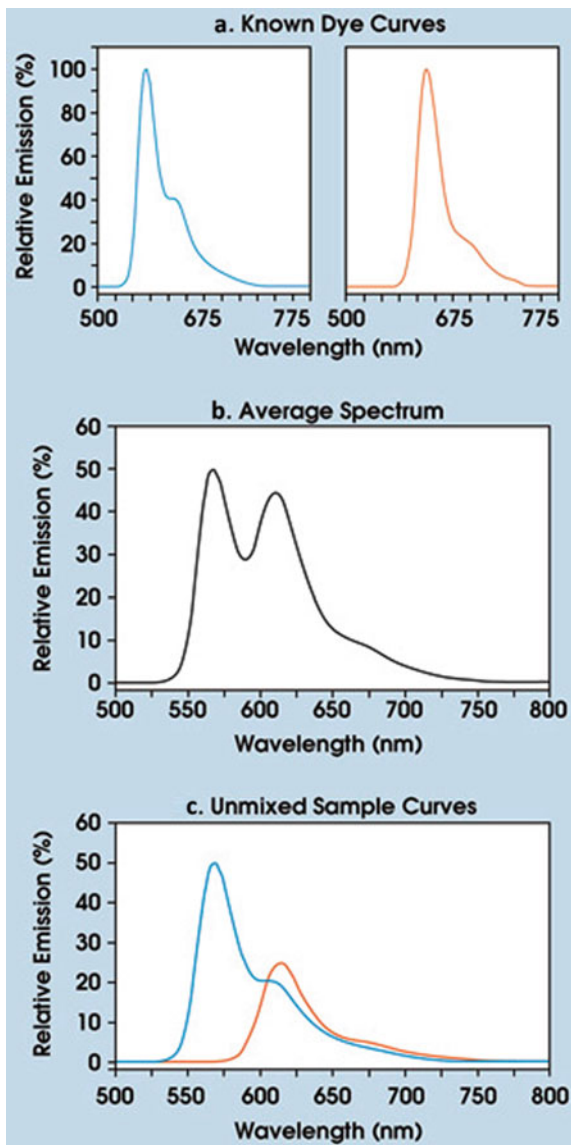
Imaging in the intensity domain is the simplest form of fluorescence imaging. Here, the whole animal is illuminated with a broad beam constant intensity light source and the emitted light is detected with a low-noise CCD, both equipped with appropriate filters to meet the excitation and emission wavelengths of the fluorophore. In the classical approach, NIRF imaging devices operate in the intensity domain by simply integrating the measured fluorescence signal over a certain time interval, and the output is fluorescence intensity.

The fluorescence intensity depends non-linearly on the excitation wavelength and the spectral properties of the fluorophores are usually known before the experiment. Since the intensity measured on the surface is the sum of all intensities from all the sources in the animal body, decoupling methods that allow a separation of different signals (e.g., endogenous and injected fluorophores) are necessary. One possibility to do this is “spectral unmixing”, where the spectral characteristics of different sources are analyzed and used to decouple signals from different sources (Fig. 13.6).

13.2.3.2 Time Domain

Time-domain imaging is a particular mode, which allows the assessment of fluorescence lifetime. In contrast to intensity domain imaging, in time-domain imaging, the subject is illuminated with short laser pulses. After each single excitation pulse, the first photon response is measured using time-resolved detectors (for instance, with “single-photon counting detector” SPCD or “fluorescence lifetime imaging” FLIM detectors) and is used to calculate the fluorescence lifetime [100]. In contrast to conventional imaging, in which the whole animal is usually illuminated at once, in lifetime imaging, the measurement is performed by raster scanning of the desired area. The arrival of photons can be depicted for each individual measurement point as a function of time, in form of the so-called photon-time-of-flight histogram (an average time, which a photon needs to reach the detector, after an excitation pulse). This information enables the calculation of the fluorescence decay time, also termed fluorescence lifetime. Since the emission of fluorescence is a statistic process, the evaluation of the fluorescence lifetime requires time-resolved and repeated measurements as well as the use of pulsed laser diodes, resulting in higher costs and increased acquisition times.

Fig. 13.6 Spectral unmixing of two dyes with defined emission spectra. **a** Dye spectra. **b** The average spectrum of the experimental sample containing a mixture of the two dyes. The unmixed spectra show quantitative fluorophore contributions. The data was acquired using an MAG Biosystems SpecEM spectral imaging system. Adapted with permission from Photonics Media



Fluorescence lifetime imaging offers two major advantages. Firstly, the lifetime of fluorescent probes, although sometimes influenced by the environment (e.g., pH) usually clearly differs from the lifetime of autofluorescent sources. Secondly, the lifetime parameter is independent of the intensity, making the interpretation of weak signals more reliable. It should be noted though that lifetime data usually contain a mixture of probe-derived and (various) endogenous lifetimes, making two-component models for lifetime calculation more reliable.

An example of using time-domain imaging to decouple probe-derived signals and autofluorescence has been shown by Napp et al. [94]. The group analyzed fluorescence lifetimes in different regions of the body before and after the injection of Cy5.5-labeled tumor-targeting antibody into mice bearing orthotopic pancreatic tumors and detected two different lifetimes. The first one corresponded to the *in vitro* measured lifetime of the Cy5.5 probe and was detected over the tumor area only in the probe-injected mice, while the second lifetime was much longer and was detected over the gastrointestinal tract in both naive and probe-injected animals and thus assumed to be an autofluorescence component. Setting lifetime gates which removed the second, longer lifetime, allowed for visualization of NIRF-antibody specific signals (Fig. 13.7).

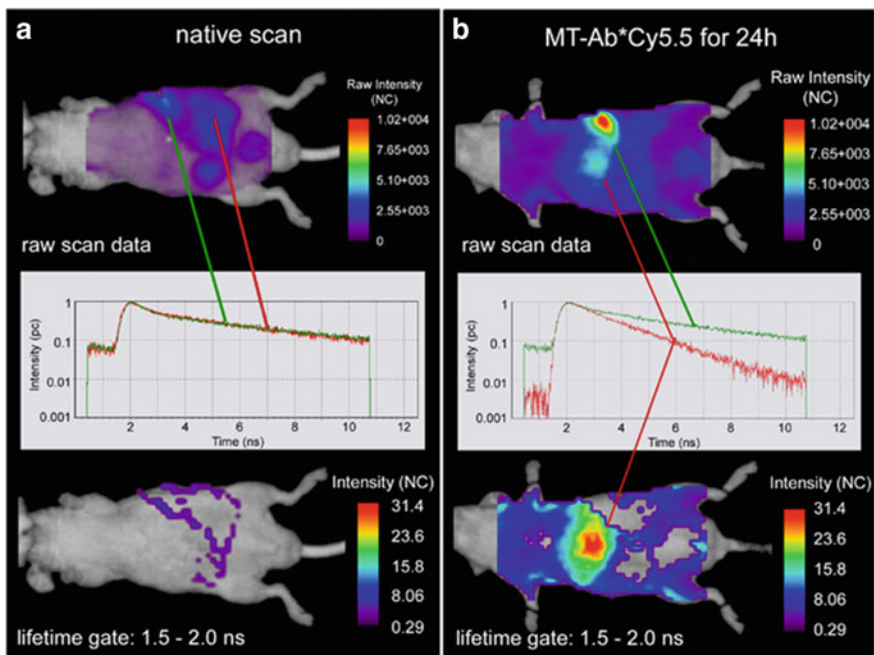


Fig. 13.7 An example of lifetime imaging for improved detection of probe-derived fluorescence. A mouse bearing an orthotopic pancreatic tumor was scanned either before (A; native scan) or 24 h after (B) injection of fluorescence-labeled tumor-targeting antibody (MT-Ab*Cy5.5). Upper panels show unprocessed intensity maps, middle panels show photon-time-of-flight histograms used for lifetime calculation, and lower panels show intensity maps after lifetime gating. For the areas over the gastrointestinal tract, lifetimes exceeding 2.5 ns were measured in both the native scan and the scan after injection of the specific probe. Therefore, these signals were considered as autofluorescence. After application of the probe, additional signals with a lifetime of 1.7 ns (red line) were detected over the primary tumor which were defined as probe-derived. After narrowing the lifetime gate to 1.5–2.0 ns (lower panel), only the specific fluorescence over the tumor area remained on the intensity maps. Adapted with permission from [94]

The following section supplies a selection of *in vivo* applications of 2D fluorescence imaging in the field of oncology. These examples are by no means complete, but merely intend to provide the reader with an idea of how and to what extent this 2D optical imaging method can be useful for preclinical studies.

13.2.4 In Vivo Applications of Fluorescence Imaging

In vivo fluorescence imaging is unequivocally the most versatile visualization modality, due to its ease of use, low costs as well as high sensitivity and relatively high spatial resolution. It has become especially attractive for the noninvasive preclinical assessment of disease development, progression, and therapeutic efficacy for a wide range of pathologies [4]. The development of appropriate low-cost clinical instrumentation is ongoing, and the design and clinical approval of novel targeted probes have already promoted the translation into the clinic.

13.2.4.1 Imaging of Tumors

Cancer research is one of the largest application fields for fluorescence imaging. Here, it is routinely applied to unravel molecular mechanisms underlying the disease, to obtain information about tumor progression, or about specific processes of interest such as the localization of certain proteins/tumor markers or the assessment of enzymatic activity of tumor-relevant enzymes *in vivo*. Furthermore, it is used to assess noninvasively the biodistribution, binding kinetics, toxicity, and effects of various compounds such as therapeutic drugs, or to track various cell types over time.

Activatable Probes

A major disadvantage of fluorescence imaging is the limited penetration depth and the relatively low and depth-dependent spatial resolution. As tumors are often located deep within the body (unless it is a tumor of the skin), they are usually difficult to image. The choice of highly specific probes and good controls is therefore crucial to overcome a weak signal, i.e., sensitive probes with little background and high specificity to cells or molecules are needed. Accordingly, smart probes have been the tools of choice for many researchers, in particular, protease-activatable probes because they are only activated at the site of interest. Proteolytic enzymes are frequently overexpressed in tumors, where they play a role in metastasis formation, invasion, and angiogenesis. Additionally, they are expressed at an early stage of tumor formation and therefore represent an attractive target for both diagnostic and therapeutic approaches in oncology. The visualization of the enzyme activity of matrix metalloproteinases (MMPs) in tumors in combination with planar fluorescence imagers has, for example, been applied by Lee et al. [62]. A convincing example of multimodal imaging using bioluminescence, macroscopic *in vivo* fluorescence, and *in vivo* confocal laser microscopy was presented by von Burstin et al. by imaging early-stage pancreatic tumors in combination with commercially available cathepsin and MMP-sensitive probes [140].

A similar multimodal approach targeting MMPs was applied to target and resect orthotopic glioma [64]. A recent example of a prodrug-type, MMP-2-targeting nanoprobe was reported for the specific detection of several different tumor entities [142]. Noninvasive detection of epidermal growth factor receptor (EGFR) inhibition on colon tumorigenesis using the commercial activatable NIRF Probe ProSense was limited to large tumors [24].

Furthermore, Weissleder and other groups have published several reviews on the use of monitoring protease activities in optical imaging of cancer [26, 76].

Sensing Probes

With the gradual realization, that tumors interact with the extracellular matrix (ECM), blood vessels, and immune cells in their environment and that this tumor microenvironment (TME) is crucial for tumor development, invasion and metastasis, the detection of physiological changes that take place in the TME and also in the tumors, became a target of novel smart probes. A good example of the use of such smart probes in oncology is the detection of hypoxia. Hypoxia is a typical feature of advanced solid cancers, and hypoxic tumor cells are more resistant to radio- and chemotherapy [139]. A recent example of hypoxia detection was presented by Zheng et al., who used a highly sensitive and specific two-component probe, of which the first component, a NIR phosphorescent iridium (III) complex, was quenched by oxygen in normal tissues but turned on at the reduced oxygen level in tumor tissues, allowing hypoxia deep tissue imaging with minimal background interference. The second component was a hydrophilic poly (N-vinylpyrrolidone) (PVP) polymer that improved tumor retention time via the enhanced permeation and retention effect [153].

In an impressive approach by Conway et al., dual intravital imaging facilitated live tracking of moving hypoxic regions in different pancreatic ductal adenocarcinoma mouse models. The combination with a hypoxia-activated prodrug simultaneously alleviated hypoxia-induced resistance [19]. In earlier work, an oxygen-dependent degradation protein probe was used for the in vivo detection of hypoxia-inducible factor (HIF) activity, a master transcriptional regulator for adaptation to hypoxia, employing bimodal imaging of fluorescence and bioluminescence [58] and our own group used nanoparticles doped with an oxygen-sensing dye to monitor hypoxic areas of a subcutaneous pancreatic AsPC-1 adenocarcinoma [93].

Using FRI, pH-sensing probes have also been utilized to differentiate cancer from healthy tissue. An example of measuring extracellular pH was provided by Loja et al. [71]. In the same year, we showed that a fluorescent probe which is activated by the acidic pH of HER2-positive breast tumors is able to achieve a more specific signal than an “always-on” Alexa Fluor 647-conjugated HER2 probe (Fig. 13.8) [82].

Theranostic Probes

Fluorescence imaging is, furthermore, an ideal method to optimize targeted strategies to different tumor entities before entering the clinic. In fact, the field of

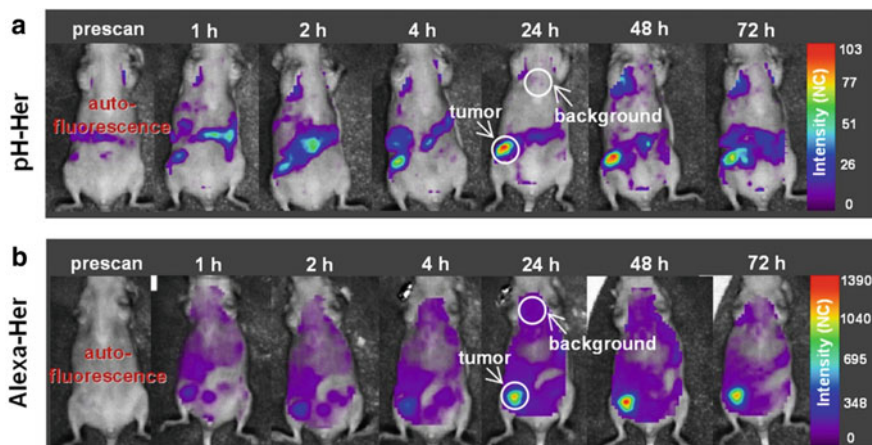


Fig. 13.8 An example of improved tumor-imaging specificity using a pH-sensing probe. KPL-4 breast tumor-bearing mice were imaged using an epi-fluorescence imaging system in a ventral position before (prescan) and 1 to 72 h after i.v. injection of the tumor-targeting pH-sensing probe (**a**; pH-Her) and a control always-on probe (**b**; Alexa-Her). In the mouse that received pH-Her, probe-derived signals are mainly detected in the tumor (characterized by low pH), while the probe present in the circulation is not activated and therefore does not affect the detection of target-derived fluorescence. In the mouse that received Alexa-Her, probe-derived signals are obtained in the tumor as well as the background. Adapted with permission of [82]

so-called theranostics, i.e., the combination of diagnostic and therapeutic approaches, has rocketed with the advent of nanosized drug delivery systems.

As an example, methods to improve the solubilization of poorly water-soluble drugs, such as glycol chitosan nanoparticles for paclitaxel, have been explored by 2D fluorescence imaging and found to be promising carriers for paclitaxel delivery in cancer therapy [113].

As early as 2004, Shah et al. coupled the regulation of a therapeutic protein, Tumor Necrosis Factor (TNF)-Related Apoptosis-Inducing Ligand (TRAIL) with the activation of an herpes simplex virus (HSV)-1-specific NIRF probe by engineering an endoplasmic reticulum (ER)-targeted-TRAIL that is retained in the ER, where it is inactive until selectively released by the HSV-1 viral protease. *In vivo* FRI was thus used to monitor gene delivery by systemic administration of an NIRF probe activated by the protease [116].

A recent study by Li et al. showed the development of an activatable theranostic nanoplatform that was able to delineate the tumor in real time with NIRF signals during surgery, and at the same time mediated intraoperative targeted phototherapeutic treatment to eliminate unresected ovarian cancer sites [68].

In vivo fluorescence imaging has therefore reached a new level of sophistication by using probes which not only target biomarkers but can be simultaneously used as therapeutic drugs. Diagnosis, monitoring, and treatment of the disease can hereby

be achieved by employing a single probe. Several recent reviews are available that discuss the current advances in tumor theranostics [6, 39, 105, 125].

13.2.4.2 Imaging of Apoptosis

Apoptosis is a highly regulated form of cell suicide that plays a significant role in the maintenance of tissue homeostasis. One of the characteristics of growing tumors is their capability to escape the apoptotic death, and various therapeutic concepts are being developed, that target receptors or ligands to promote cancer cell death while sparing normal cells. In this context, noninvasive and longitudinal detection of apoptotic events is especially valuable for assessment of treatment efficacy in preclinical settings, but it would also be of enormous benefit in the clinic for the improvement of patient management.

One of the key players in the apoptosis process is Annexin V, which is a small 35–36 kD calcium-dependent protein that specifically binds to phosphatidylserine. In healthy cells, phosphatidylserine is located in the inner membrane and inaccessible to Annexin V binding, but it translocates to the outer leaflet of the membrane upon induction of apoptosis. Application of fluorescent Annexin V conjugates provides a quick and straightforward method for identification of early stages of apoptosis in living animals, but also in cells or tissues, albeit with the drawback of some false-positive signals from necrotic cells. An early example of imaging of apoptosis as a sign of tumor response to chemotherapy was published by Petrovsky et al., who used Annexin V with a NIRF label to detect gliosarcoma and lung carcinoma in female *nu/nu* mice with an FRI system [107]. Alternatively, small fluorescent molecules binding to phosphatidylserine or phosphatidylethanolamine like PSVue® or duramycin may be applied, which in comparison to Annexin have better tissue penetration and thus their accumulation is less dependent on the vascular integrity.

Another approach is to monitor specific apoptosis signaling molecules such as caspases. In this context, Lee et al. proposed a new apoptosis nanoprobe (Apo-NP) that efficiently delivers chemically labeled, dual-quenched caspase-3-sensitive fluorogenic peptides into cells, allowing caspase-3-dependent strong fluorescence amplification. This probe was used to image both apoptotic cells in real time and at high resolution and monitoring therapeutic efficacy of apoptotic drugs in cancer treatment [63]. A similar approach was used by Bullock et al., who used a small membrane-permeable and caspase-activatable fluorescent peptide for in vivo visualization of apoptosis in colorectal cancer [15].

There are a number of publications that introduce other novel NIRF-labeled probes which were assessed for their ability to detect cell death in animal models [83, 120]. Most of these are published in the Molecular Imaging and Contrast Agent Database (MICAD), an online source of scientific information regarding molecular imaging and contrast agents (under development, in clinical trials or commercially available for medical applications) that have in vivo data (animal or human) published in peer-reviewed scientific journals (“Molecular Imaging and Contrast Agent Database (MICAD) [2004]—PubMed—NCBI”, 2004).

Two potential targets for tumor therapy via induction of apoptosis are the TNF-related apoptosis-inducing ligand (TRAIL) and its proapoptotic receptor death receptor 5 (DR5). In subcutaneous xenografts in mice, Zhou et al. showed that *in vivo* NIRF imaging of death-inducing ligand–receptor interaction was consistent with the apoptosis readout, which they evaluated by imaging NIRF-labeled Annexin V and *ex vivo* tumor tissue-activated caspase-3 staining [154]. *In vivo* molecular imaging of TRAIL receptor expression correlated with the response to TRAIL therapy and an apoptotic response *in vivo* [47]. Jiang used fluorescently labeled TRAIL conjugates for *in vivo* monitoring of TRAIL delivery to subcutaneous A549 tumors, as a pre-evaluation study before testing the efficacy of a TRAIL/DOX (Doxorubicin, an intracellular-acting small-molecule drug) co-delivery system.

Single-cell imaging of retinal ganglion cell apoptosis was demonstrated with a cell-penetrating, caspase-activatable peptide probe in an *in vivo* glaucoma model [10]. However, fluorescence imaging was then performed on *ex vivo* retina using a fluorescence stereomicroscope.

An update of *in vivo* imaging of apoptosis in oncology has been given by Vangestel et al., highlighting that NIRF imaging shows great potential in small animal imaging, but its usefulness for *in vivo* imaging in humans is limited to superficially located structures in the human body [138].

13.2.4.3 Imaging of Angiogenesis

Angiogenesis is a key biological process not only in cancer but also in many other clinically relevant diseases, such as atherosclerosis or autoimmune diseases.

The simplest setup for noninvasive imaging of tumor vascularization in animal models is the general visualization of blood vessels, which can easily be achieved by using non-targeting blood pool imaging agents. The requirements for such a contrast agent are relatively simple: it has to have a sufficient blood half-life and low extravasation. There are multiple such contrast agents commercially available. A simple example of *in vivo* imaging with blood pool contrast agents for visualization of vessels and a highly vascularized tumor is shown in Fig. 13.9 [82].

A pioneering role in the combinatorial use of fluorescent optical tomography and intravascular probes for the determination of vascular volume fraction in subcutaneous as well as in deeply located tumors was provided by the Weissleder research group. They imaged the natural course of angiogenesis as well as reliably monitored its inhibition as dose response to antivascular endothelial growth factor antibody [90].

Furthermore, Backer et al. employed a single-chain vascular endothelial growth factor (VEGF)-based NIRF probe to detect angiogenic vasculature by planar fluorescence imaging in Balb/c and SCID/NCr mice. The fluorescent signal received was matched with the bioluminescent signal from a luciferase-expressing orthotopically grown mammary adenocarcinoma [7].

Some of the most important molecules in the process of angiogenesis in general and in neoangiogenesis of neoplastic tissues are the cell adhesion molecules, integrins, with $\alpha V\beta 3$ being a key player. Imaging approaches using NIRF-labeled probes that take advantage of the high integrin-targeting efficacy of the cyclic

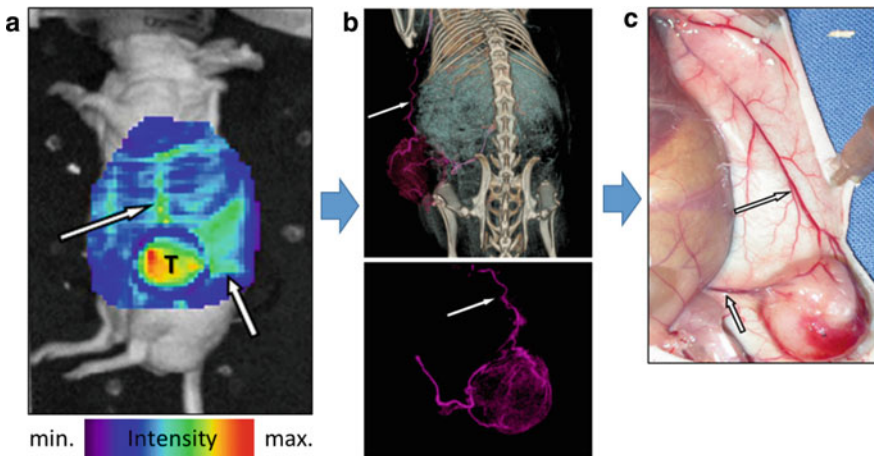


Fig. 13.9 Visualization of tumor vascularization using a blood pool contrast agent. **a** NIRF image acquired 1 h after intravenous injection of the contrast agent into a nude mouse bearing a subcutaneous glioblastoma xenograft. Strong fluorescence is measured over the tumor (T) indicating high vascularization. Two large tumor-supplying vessels show strong fluorescence (arrows). **b** High-resolution anatomical scan, performed by flat-panel volume computer tomography, 90 s after intravenous application of 150 μ l iodine-containing blood pool agent confirmed the localization of the same two large blood vessels (arrows) detected in (a), and also shows smaller tumor vessels (pink). **c** Macroscopic image of the same mouse confirms the presence of the two large vessels (arrows) Adapted with permission of Napp [82]

arginine–glycine–aspartic acid (cRGD) peptides have been reviewed by Cai et al. [16]. Several groups have later used this approach, for instance, by multimodal imaging of mouse mammary tumors or glioblastoma xenografts [28, 70, 81].

Another method for quantifying tumor angiogenesis is the assessment of microvessel density based on CD105 staining, which is an independent prognostic factor for survival in patients with most solid tumor types. Yang et al. recently showed that an NIRF-labeled human/murine chimeric anti-CD105 antibody (TRC105) was able to specifically recognize CD105 on 4T1 murine breast tumors and showed significantly stronger signal intensities than the controls [149]. The authors suggest that this probe may be used in the clinic for imaging tumor angiogenesis within the lesions close to the skin surface, tissues accessible by endoscopy, or during image-guided surgery.

13.2.4.4 Cell Tracking

Three major applications of optical imaging have to be mentioned in the field of cell tracking: in vivo visualization of cancer cell migration within the lymphatic system, T cell tracking, and stem cell migration.

These areas have benefited enormously from new optical devices and more specific probes. However, most of these applications use microscopy, in particular, intravital microscopy. Important work in this regard has been achieved by

Kobayashi and colleagues, who simultaneously visualized the migration of quantum dot-labeled melanoma cells and the lymphatics using optically labeled dendrimers *in vivo* [54]. For further information on intravital microscopy, we would like to refer to several reviews [41, 97, 109].

Whole-body reflectance or transillumination fluorescence imaging is rather difficult for cell tracking, as the resolution achieved by these techniques is too low to distinguish individual cells. However, a study by Eisenblätter et al. was able to visualize and quantify early inflammatory processes by tracing the migration of fluorescence-labeled murine macrophages in a cutaneous granuloma model by FRI [29]. The same modality was used to demonstrate that immunotherapeutic natural killer cells labeled with fluorescent nanocrystals can be employed for the effective tracking of injected therapeutic cells and their therapeutic effect using optical imaging technology [69].

T cells are increasingly studied in the context of cancer immunotherapy. Genetic modification of T cells usually aims at the improvement of their homing properties to the tumor site for increased efficacy. *In vivo* fluorescence imaging was applied to track such modified T cells in various preclinical settings. Foster and colleagues labeled, for example, Epstein–Barr virus-specific T cells with the NIRF dye IRDye800CW by simple co-incubation of cells with the dye, which bound to T cell surface proteins without affecting T cell function. These cells were then applied *in vivo*, to visualize their migration to the tumor site. Homing of the labeled T cells to the tumor was demonstrated by the increased fluorescence intensity over the tumor area following intravenous injection [30]. A similar experiment was described by the group of Weissleder, who labeled T cells with the NIR dye VT680 and followed their accumulation in tumor and lymph nodes by *in vivo* FMT [129].

13.2.4.5 Imaging of Autofluorescence

For a long time, autofluorescence was considered as a major drawback of *in vivo* fluorescence imaging, because it often impairs the detection of specific, probe-derived signals, especially in the visible wavelength range. However, since some of the autofluorescent sources can be assigned to specific tissue structures or molecular events, autofluorescence can indeed be actively chosen for *in vivo* imaging with the great advantage that it does not require any fluorophore injection or expression by cells/organisms. This makes autofluorescence imaging especially attractive for clinical translation. Studies have thus already shown that autofluorescence has a high potential to minimize unnecessary biopsies or even to define margins of a lesion during surgical procedures.

Yet, the method suffers from the well-known drawback that fluorescence in general is only measurable at the surface, after it travels through the tissues. Since autofluorescence is relatively weak and usually has low contrast and less specificity than fluorescent dyes, only exposed structures, such as oral tissues, skin, or gut, are suitable for this kind of imaging approach.

Pathophysiological processes such as cancer can influence the amount and distribution of endogenous fluorophores in autofluorescent proteins, thus allowing a certain degree of distinction between healthy and diseased tissue by means of

autofluorescence measurement [33]. Huang et al. found that, by using autofluorescence microscopy, differences in the clinically measured autofluorescence spectra between normal and cancerous colonic tissue were mainly due to thickening of the tumor mucosa, resulting in a reduced submucosa fluorescence contribution, as well as due to increased hemoglobin absorption in tumor tissue [42].

The distinct autofluorescence properties of healthy and cancerous tissue have already been exploited in several human tumor entities, such as colon cancer [117], oral neoplasms [45], skin cancer [13], and cervical lesions [147]. These studies suggested that autofluorescence signals can indeed be used for noninvasive tumor diagnostics and for the detection of tumor margins.

In vivo NIR autofluorescence imaging has also been employed for the detection of cutaneous melanins in human skin [38]. The study suggested that NIR autofluorescence detection could be useful for the diagnosis and clinical evaluation of melanomas. Combined with other techniques, such as Raman spectroscopy, NIR autofluorescence spectroscopy was even more useful [42].

As early as 2000, Delank et al. attempted autofluorescence-based endoscopy of laryngeal cancer. The group found that this approach exceeded the sensitivity of white-light endoscopy and microscopic laryngoscopy. However, the method was not specific for laryngeal cancer but resulted in false-positive signals due to inflammation, hypervascularization, and edema [22]. Other endoscopic procedures, such as those for diagnosis of colorectal cancers [91] and bladder cancers [72], have benefited from the use of autofluorescence.

13.2.4.6 Intraoperative Fluorescence Imaging

For a long time, fluorescence imaging was restricted to preclinical research but has recently found its way into the clinics. One of the most promising clinical applications of NIRF and at the same time one of the most notable advances in surgical oncology is image- or fluorescence-guided surgery (FGS). For the excision of tumor lesions, surgeons used to rely mostly on their experience, visual examination, or palpation. FGS now offers the advantage of fluorescence labeling of tumor tissues and other structures such as lymph nodes to help navigate during the surgical intervention.

The principles of intraoperative fluorescence imaging are the same as for the above-described FRI.

The multispectral strategy has to allow for color imaging and simultaneous sensitive fluorescence detection. The camera system should consist of a CCD for sensitive fluorescence detection and two separate cameras for the detection of intrinsic fluorescence and color. Thus, data are acquired in parallel by all cameras so that color, light attenuation images, and fluorescence images are simultaneously collected [136].

While dozens of different fluorescent labels are used in preclinical routine, only a very few of them are approved for application in humans [37]. Among them is indo-cyanine green (ICG) which is the most common clinical label used for intraoperative discrimination of malignant from benign breast lesions or identification and

staging of sentinel lymph nodes, but also for other applications such as intraoperative angiography or lymphography [110, 115]. ICG is a non-specific probe which accumulates in tumors only due to the leaky vasculature and due to the enhanced permeability and retention (EPR) effect. Furthermore, it suffers from a rapid liver clearance and fairly poor quantum yield. Imaging in the visible light spectrum, using a fluorescein isothiocyanate (FITC)-coupled imaging probe, has also been described [132, 136], but these have the well-known disadvantage of autofluorescence. Thus, there is a great need for the development of novel specific tumor labels in the NIR for FGS [5]. New handheld devices have also been developed and clinically used [86, 88, 134].

13.2.4.7 Conclusion

Two-dimensional optical fluorescence imaging is a valuable asset for the preclinical assessment of disease development, progression, and therapies for a wide range of oncologic pathologies. Its most important advantages are the possibility for in vivo evaluation at a relatively low cost, the versatility of probes available, and a fairly high sensitivity. Its main limitation, the low tissue penetration, can be improved by the use of NIRF probes. By using activatable probes, lifetime imaging, and multimodality instruments, 2D fluorescence imaging is not only a very valuable technique for preclinical use in small animals but may have a significant contribution to endoscopy or surgery. With the increasing development of 3D techniques, 2D optical imaging may eventually become the lesser used option of the two.

13.3 Bioluminescence Imaging

Bioluminescence is the general ability of living organisms to produce light. The light is generated via a biochemical reaction in which chemical energy is converted into light, meaning that bioluminescence is a form of chemiluminescence.

The reaction depends on two major components: (1) a substrate, which is an oxidizable organic molecule, generally called “luciferin” and (2) an enzyme catalyzing the reaction, which is specific for different organisms, generally “luciferase”. Some luciferases may also require cofactors such as Ca^{2+} , Mg^{2+} , or ATP. During the reaction, luciferin is oxidized by molecular oxygen yielding an excited state intermediate that releases light photons upon relaxation to the ground state to become a nonreactive product and CO_2 . This means that, in contrast to fluorescence, the release of photons during the bioluminescence process does not necessitate any external light source for excitation and the light emission continues until all the available luciferin is oxidized (Fig. 13.10).

In nature, bioluminescence has been found in almost all major taxonomic groups, e.g., bacteria, hydrozoa, siphonophores, fungi, insects such as click beetle or firefly, various types of fish such as lanternfish, anglerfish, or dragonfish, and many others. Production of light provides various adaptational advantages to the host and serves important ecological roles and functions. The most common ones

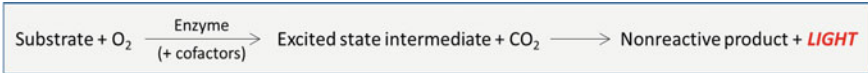


Fig. 13.10 Generalized bioluminescence reaction

are offence (e.g., hunting or prey attraction), defense (e.g., camouflage or distraction), and communication (e.g., sexual attraction). Interestingly, approximately 80% of luminescent organisms are marine species [36].

Different species or groups of organisms developed different luciferin–luciferase systems with different light emission characteristics adapted to their ecological needs. For example, as the water absorbs red-yellow-green light more than blue light, the majority of marine bioluminescent organisms emit blue light, while the terrestrial ones emit rather longer wavelengths from green to red.

13.3.1 Basics of Bioluminescence Imaging

Bioluminescence imaging (BLI) utilizes the naturally occurring process of bioluminescence to study various molecular processes *in vivo*. As luciferases are not expressed by ordinary model organisms such as mice, they need to be artificially introduced into the cells/tissues in form of reporter gene constructs, while the substrate necessary for the reaction is usually delivered by systemic injection shortly before the imaging experiment. Typically, the luciferase gene is cloned under the control of a specific promoter and is delivered into the cells using plasmid or viral transfection or transduction of cells. Luciferase-expressing cells can be then followed *in vivo* using an ultra-sensitive CCD camera (Fig. 13.11).

BLI is relatively simple to perform and enables longitudinal monitoring of the localization and serial quantification of a variety of biological processes throughout

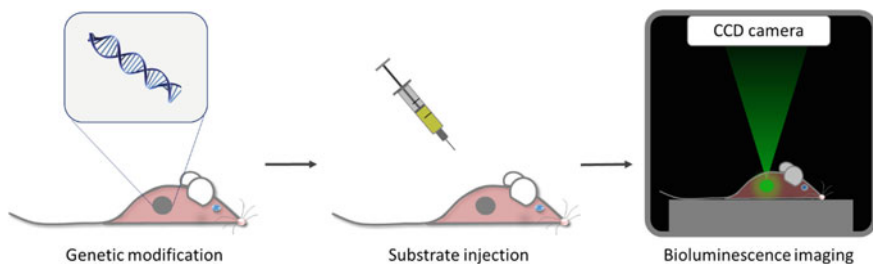


Fig. 13.11 In vivo bioluminescence imaging (BLI) experiment. Left: A reporter gene, encoding for the enzyme luciferase is incorporated into the genome of a model organism. Middle: The substrate luciferin is injected directly before the imaging experiment. Right: The light is measured using a highly sensitive CCD camera

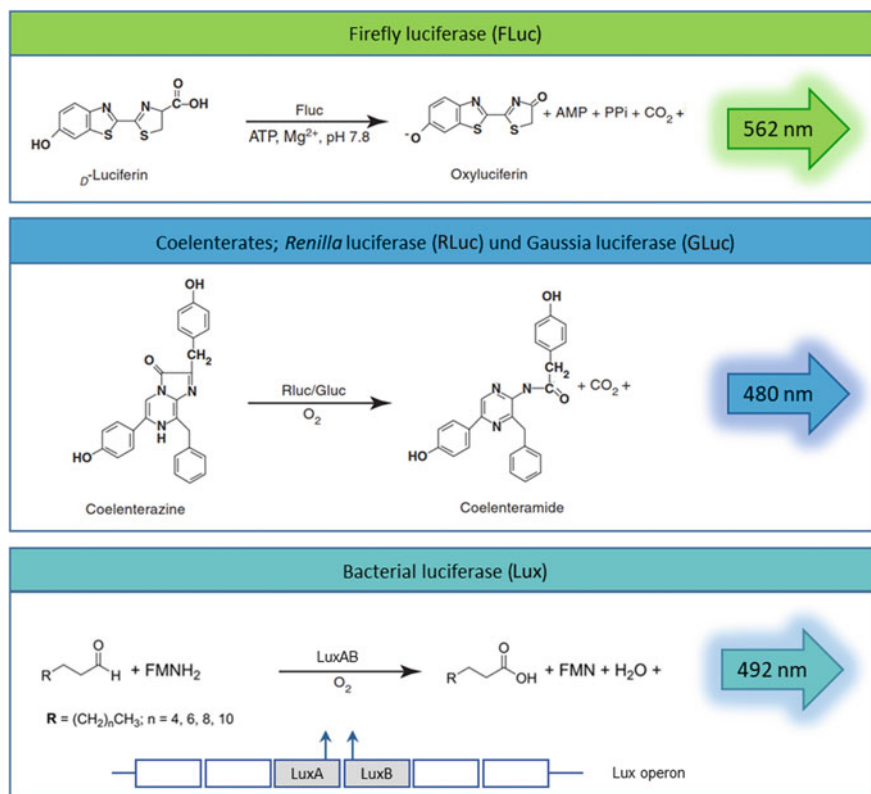


Fig. 13.12 The chemistry of the most common bioluminescent reporters. Modified from [8, 14]

the course of disease. Furthermore, since mammalian tissues lack intrinsic bioluminescence, a remarkably high signal-to-noise ratio can be achieved by BLI.

Many of the bioluminescent systems occurring in nature have been isolated, cloned, and characterized, and some of them have been further modified to adapt the biochemical properties of their light emission to biomedical needs. The most common reporter gene systems utilize luciferases from firefly (*Photinus pyralis*) or from coelenterates, sea pansy (*Renilla reniformis*), and marine copepod (*Gaussia princeps*), while the bioluminescent bacteria utilize a very unique system, not found in any other species (Fig. 13.12).

Firefly luciferase (FLuc) is a monomeric protein of 61 kDa, found in the light-emitting organ of the firefly *Photinus pyralis*, and emits greenish-yellow light with a peak at 562 nm. In addition to the substrate beetle D-luciferin, which is a benzothiazole, FLuc requires ATP and magnesium as cofactors to produce light. FLuc is characterized by an extremely high QY of $\sim 48\%$, which is defined as the ability to produce a photon from a single reactant molecule [99]. The reaction catalyzed by FLuc is the so-called “glow-type” luminescence reaction, which

means that the enzyme and the substrate react slowly to emit a stable glow lasting over several minutes or hours. These characteristics make FLuc especially attractive for in vivo imaging.

Renilla luciferase (RLuc) is a monomeric protein of 36 kDa. In contrast to FLuc, the reaction catalyzed by RLuc does not require any cofactors and the catalyzed oxidative decarboxylation of the substrate coelenterazine results in emission of blue light of 480 nm. It also has a much lower QY of only about 6%, which, together with the blue emission, makes it less suitable for in vivo imaging [12]. Furthermore, the reaction catalyzed by RLuc is a flash-type reaction that occurs very quickly within seconds or minutes to emit a single, brief flash of luminescence.

Similar to RLuc, **Gaussia luciferase (GLuc)** also catalyzes a flash-type bioluminescent reaction that does not require any cofactors, but the substrate coelenterazine. With 19.9 kDa, GLuc is the smallest luciferase known and emits blue light of 480 nm with a broad emission spectrum extending to 600 nm and with an intensity at least 200-fold higher than that of FLuc. GLuc is naturally secreted and thus an optimal luciferase system for in vitro assays based on analysis of cell media.

Bacterial luciferase (Lux) is a unique luciferase that has been found in bioluminescent bacteria (*Photobacterium luminescens*; *Vibrio harveyi*). In contrast to eukaryotic luciferases, Lux is a heterodimer consisting of two homologous subunits, designated as the α - and β -subunits. It catalyzes the production of light through oxidation of a long-chain fatty aldehyde in the presence of oxygen and reduced riboflavin phosphate. The Lux operon is a unique bioreporter system organized in a cassette of five genes (luxCDABE) that not only express the two Lux subunits, but also genes coding for the fatty acid reductase complex responsible for synthesizing fatty aldehydes for the luminescence reaction. This means that bacteria do not require the addition of exogenous substrate as they generate their own substrate. The bioluminescence QY of bacterial luciferase is approximately 10–16% but they are rarely expressed in mammalian cells [14, 84]. The codon-optimized version of this luciferase expressed in mammalian cells has been recently proposed for in vivo imaging but it is less robust than firefly luciferase [18].

13.3.2 Factors Affecting BLI

In the past decades, BLI has increasingly become a method of choice for noninvasive monitoring of biologic phenomena in living cells or in animals. However, several aspects have to be considered before planning, analyzing, and quantifying a BLI experiment.

As bioluminescence depends on the presence of the enzyme expressed by living cells, but also on other components such as oxygen and the exogenously administered luciferin, the measured light emission will not be a true representation of luciferase activity if any of these components is limited. Furthermore, the **reaction kinetics** in animals will also depend on the substrate delivery and therefore also on the route of substrate administration (intravenous, intraperitoneal). This means that

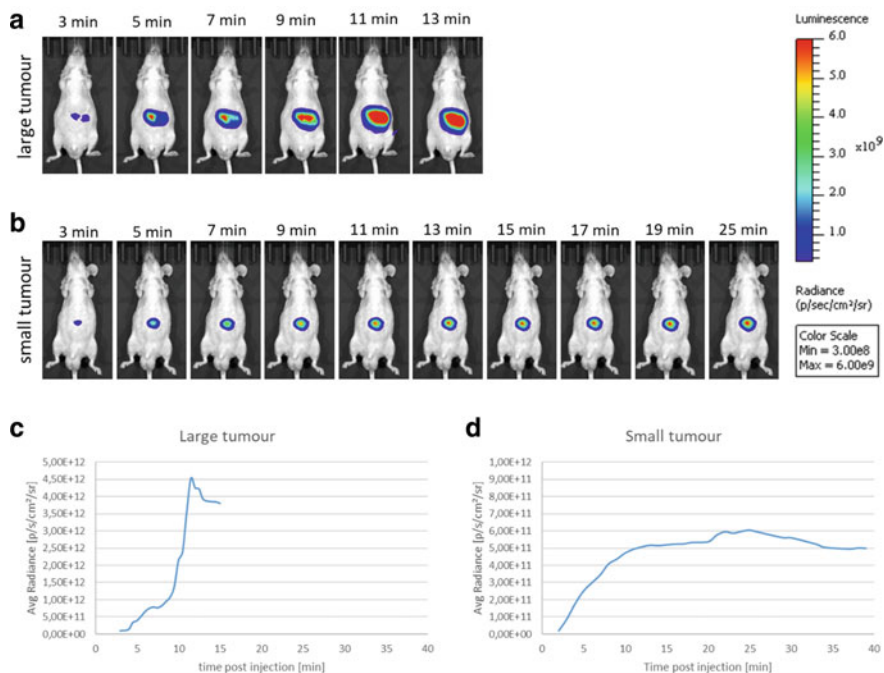


Fig. 13.13 The kinetics of the bioluminescence reaction differs depending on the size of the tumor. **a–b** Mice with **(a)** large and **(b)** small orthotopic pancreatic tumors were injected with the same amounts of luciferase, and imaged with BLI over time, showing bioluminescence intensities correlating with tumor sizes. While the mouse with large tumor shows a relatively fast increase in the measured bioluminescence intensity which peaks at 12–13 min after substrate injection, most probably due to a limitation in luciferin, **(c)** the bioluminescence of the mouse with small tumor also increases but reaches a long-lasting plateau **(d)** (Napp, unpublished data)

the measured bioluminescence intensity varies depending on the time after substrate injection, with a signal increase during substrate distribution in the animal body, a specific maximum (e.g., for firefly luciferase the reaction peaks ~ 10 – 12 min after injection of luciferin; Fig. 13.13a,c) and a slow decrease as the substrate is consumed. In addition, large bioluminescent tissues (e.g., tumors) will obviously need more substrate and will utilize it faster than smaller tissues (Fig. 13.13b,d). Therefore, to achieve comparable results, the optimal time for BLI (the time between injection of the substrate and the start of measurement) as well as the optimal dose of administered substrate should be standardized for each study.

As only viable cells express the enzyme and as oxygen is required for the bioluminescent reaction, the **presence of necrotic or hypoxic areas** within the tissues will also have an effect on the measured bioluminescence intensity. This can be an issue, e.g., when tumor progression is assessed in response to treatment in preclinical animal studies. Decreasing bioluminescence intensity could be an indicator of a decreasing tumor size but it could also be caused by the presence of

hypoxic areas in still-growing or not-shrinking tumors, which potentially contain “quiescent” cells and low oxygen levels leading to reduced bioluminescence intensities.

Penetration depth also has an impact on bioluminescence intensity, since light in general, and especially visible light emitted by the majority of bioluminescent reporter systems, is strongly absorbed by tissues. Furthermore, light is scattered by tissues and the tissue geometry (e.g., presence of bones, scars, vessels) will have an additional impact on the scattering. This means that BLI always results in surface-weighted images, where subsurface structures appear smaller and brighter while deeper structures appear larger but less intense.

Taken together, one has to consider that the simple quantification of the light emission usually does not provide accurate information but only delivers semi-quantitative information of the biological process.

Also, the choice of an **appropriate promoter** can be a crucial parameter for obtaining reliable data, as the promoter will regulate transcriptional activity of the luciferase gene construct and therefore the efficacy of the bioluminescence reaction. Typically, for experiments involving cell tracking or monitoring of tumor growth, constitutive promoters, such as CMV, CAG, or SV40, are used, aiming at a strong constant expression of the reporter gene construct. However, it has been shown that the transcriptional activity of such promoters is not always constant and can be modulated, e.g., by the cell cycle.

When using BLI for monitoring the expression of a particular gene, the luciferase reporter is typically cloned under the control of the gene of interest; its expression should reflect the expression of the gene of interest. The insertion per se though can affect regulatory processes and transcriptional activity in the cells, which also needs to be taken into account when designing BLI experiments.

13.3.3 Genetically Engineered Luciferases, Modified Substrates, and Multicolor Reporter Systems

Although *Gausia*, *Renilla*, and firefly luciferases are still the most commonly applied luciferases for BLI, novel discoveries, and research on new luciferase genes and genetic variants as well as novel modified substrates have emerged over the past decades. Research especially aims at improved bioluminescence in terms of higher sensitivity, as well as optimized, preferentially NIR emission that allows for improved tissue penetration and increased light emission. Furthermore, the development of multicolor reporter systems is of growing interest, since multiplex imaging allows simultaneous visualization of different processes in the same animal, such as multiple molecular events, molecular interactions, or different cell types, reducing the number of animals used per experiment.

Simultaneous in vivo monitoring of two or more genes expressing different luciferases requires readily distinguishable signals with intense emission and preferentially narrow emission spectra. Here, the most common combination of luciferase systems for dual-color imaging is based on firefly and *Renilla* luciferases,

which require two different substrates (luciferin and coelenterazine, respectively) exclusively for the corresponding luciferase. Furthermore, it has to be considered that the kinetics of light production are distinct, with the Rluc reaction peaking quickly and the Fluc reaction being slower and resulting in a longer lasting luminescence. BLI of different molecular events using Fluc and Rluc can either be acquired sequentially in separate imaging sessions, after separate injections of luciferin and coelenterazine, or after simultaneous injections of the two substrates, using multiple image acquisitions of the different reaction kinetics as an additional parameter to separate the reporter protein signal [12].

New optimized luciferases with red-shifted emission offer an improvement in two- or multicolor BLI. The group of Löwik et al. described, for example, a red-emitting codon-optimized mutant of Fluc, called Ppy RE8 that has been used in combination with the green click beetle luciferase, CBG99 for dual-color imaging. Here, both luciferases share a single substrate, luciferin, but show distinct emission peaks with a peak emission at 618 nm for Ppy RE8 luciferase and a peak around 540 nm for the click beetle luciferase. Multi-wavelength image acquisition and application of spectral unmixing algorithms achieved good separation and reliable quantification of the dual bioluminescence signals in a mixed population of cells in vitro and in vivo [85].

Multi-reporter/multicolor imaging is more challenging, since it requires a combination of three or more different luciferase systems with efficient expression of comparable expression levels, well-separable emission spectra, and preferentially each enzyme having also an individual substrate. A triple-color BLI has been achieved by multiplexing a codon-optimized *Vargula* luciferase (Vluc) together with Gluc and Fluc. Vluc is a luciferase from cypridina ostracods habituating Japanese waters, *Vargula hilgendorfi*. It is a 62 kDa protein naturally secreted from cells. It oxidizes the substrate vargulin, resulting in the emission of blue light at 462 nm. Combination of the Vluc, Gluc, and Fluc with the corresponding substrates vargulin, coelenterazine, and luciferin, respectively, for sequential imaging allowed monitoring of three distinct cellular phenomena in the same biological system [75].

In addition to the optimization of the existing luciferases via various mutation strategies in order to obtain red-shifted light emission and brighter luminescent probes with improved expression in mammalian systems, luciferases can also be fused to fluorescent proteins, resulting in the expression of chimeric constructs capable of intramolecular bioluminescence resonance energy transfer (BRET). Briefly, in BRET the luciferase serves as a donor, while the fluorescent protein acts as an acceptor and allows to tune the bioluminescence spectrum toward NIR [55]. Interestingly, BRET is a naturally occurring phenomenon found, for example, in the jellyfish, *Aequorea*. Here, the bioluminescent protein aequorin is associated with the green fluorescent protein (GFP), which accepts the energy from green-emitting aequorin, thus shifting the emission to produce green light.

Various BRET systems have been introduced aiming especially at NIR shift of the emission for deeper tissue penetration and improved QY for high detection efficiency, but also at tuning of the bioluminescence spectra for simultaneous

multicolor imaging of multiple events [128, 131]. Attempts in obtaining NIR emission in longer wavelengths are still rare though, and the most BRET systems emit in the range of ~ 600 nm [150]. Recently, a NIR BRET imaging platform reaching ~ 300 nm blue-to-NIR shift (400–717 nm) has been described. The platform is based on a fusion protein between a modified Rluc and the red fluorescent protein iRFP, and an array of 18 novel coelenterazine derivatives serving as substrates for the reaction [98].

13.3.4 Applications of BLI

13.3.4.1 Imaging of Cancer

Imaging of cancer and cancer-related events are the most common applications of BLI. In the simplest form, bioluminescent tumor cells are transplanted subcutaneously or orthotopically into the host animal, and their location and tumor growth and progression are tracked over time. Different orthotopic tumors such as brain [48], prostate [73], breast [46], colon [108], pancreatic [34], bladder [137] and hepatic tumors [114], lymphoma [27] or melanoma [21] have already been visualized with BLI. Thus, in addition to functioning as a quantitative measure for cell number, BLI also provides information on cell viability within the tumor mass. Furthermore, BLI is routinely applied in the development of novel therapies and assessment of their efficacy, tracking of tumor stem cells or transformed adult cells, as well as assessment of events leading to malignant transformation. These applications are important preclinical approaches in the process of drug discovery and optimization. Since BLI is a very sensitive method, a few hundred or even dozen of cells are usually sufficient to produce well-detectable signals *in vivo*. The use of engineered, highly efficient luciferase systems allows for even more sensitive detection, showing that even a single tumorigenic cell can be visualized *in vivo* under optimal conditions [43, 51].

In more sophisticated experimental setups, transgenic animals are produced, where luciferase is set under the control of a cell- or tissue-specific promoter, or a promoter whose activity is strictly related to specific cancer cellular processes.

The group of Jenkins et al. cloned, for example, the FLuc gene under the control of the human prostate-specific antigen (PSA) promoter and achieved specific and robust expression in the prostate glands of transgenic mice. This PSA-Luc mouse was used not only to noninvasively image SV40 T antigen-induced prostate tumorigenesis *in vivo* over time but also to assess tumor response to androgen ablation, allowing also for rapid identification of individual animals that were capable of sustaining tumor growth in the absence of androgen [73].

A similar approach was applied to noninvasively assess the onset, growth, and progression of brain tumors, using a transgenic mouse model (Ef-luc). In this model, the luciferase gene was encoded under the promoter of human E2F1, a gene that is only active in proliferating cells. Treatment of the mice with chemotherapeutics such as inhibitors of either the platelet-derived growth factor receptor (PDGFR) or the mammalian target of rapamycin (mTOR) led to a reduction of E2F1

promoter activity and could be measured in vivo by the decrease of bioluminescence intensity [133].

Furthermore, Cre-dependent bioluminescent reporter mice ubiquitously expressing conditional (Cre/Lox) luciferase transgene were developed and applied to image spontaneously arising tumor burden. Crossing of those mice with Cre/LoxP-dependent models of cancer drives the expression of luciferase in cells that have undergone Cre-mediated recombination. This allows for specific imaging of tumor-related events such as the number and size of spontaneously arising tumors. Such a model was, for example, applied for longitudinal noninvasive visualization of lung tumorigenesis after crossing the reporter mice with transgenic mice, specifically expressing conditional oncogenic Kras in lung epithelial cells [74]. In a Cre-dependent mouse model of glioblastoma, crossing the mice with the reporter strain allowed for specific monitoring of tumor initiation and progression with BLI over time [146].

Lung cancer progression and lung metastasis have been studied using Lewis lung cancer (LLC) cells labeled with GFP and luciferase reporter [122]. It was shown that bioluminescence is detectable from day 24 after intravenous LLC cell injection with an intensity correlating to the number of metastases. The same model was used to study malignant pleural effusion, showing that also in this model, bioluminescence intensity correlates with the number of tumors and BLI can be applied as an indicator of tumor burden.

Although studies involving bioluminescent bacteria are mainly performed in the context of infectious diseases, recently, it has been shown that if administered systemically, bacteria are naturally capable of homing to the tumors and can potentially be applied for efficient DNA or drug delivery into cells or neoplastic tissues. Following this hypothesis, several bioluminescent bacterial strains were imaged in tumor models in order to systematically analyze their homing and therapeutic potential. Min and colleagues showed that genetically modified bioluminescent *E.coli* strains can be applied to visualize the process of bacterial tumor targeting, to quantify bacterial growth noninvasively in target tissues, and to monitor bacterial migration in real time in different mouse models of cancer. They showed that in mice with colon carcinoma or breast cancer, intravenously applied bacteria distributed to the liver early after injection but subsequently migrated to tumor sites, where they remained throughout the course of imaging up to 12 days [87].

A similar approach was used by Cronin and colleagues, who additionally performed dual-reporter imaging to co-localize bacteria and neoplastic tissues. This study implemented FLuc-expressing subcutaneous tumor xenografts and non-pathogenic bioluminescent bacterial strains: *E.coli* *Bifidobacterium breve* and *Salmonella typhimurium*, each expressing the Lux operon. In vivo BLI showed specific co-localization of bacterial Lux and tumor-derived FLuc bioluminescence, pointing to the potential of non-pathogenic bacteria as vectors for the delivery of anticancer therapies [20].

13.3.4.2 Imaging of Cancer-Related Inflammation and the Immune System

It is well known that cancer is closely linked to the process of inflammation, and the related molecular events and functional link are being intensively investigated.

Epidemiologic studies have shown that chronic inflammation can predispose individuals to various types of cancer, and the inflammatory microenvironment promotes the development of tumors by triggering the proliferation and survival of malignant cells, angiogenesis, and metastasis. Furthermore, inflammatory processes can affect adaptive immune responses and alter the response to chemotherapeutic treatments, all extensively reviewed elsewhere [80].

One of the factors that play a relevant role in tumor-related inflammation is NF- κ B (nuclear factor “kappa-light-chain-enhancer” of activated B cells). Carlsen and colleagues developed a transgenic mouse model that expresses luciferase under the control of NF- κ B. They showed that these mice can be used for real-time *in vivo* imaging of NF- κ B activity in live animals, in the context of tumor-related inflammation, but also other inflammatory disorders such as rheumatoid arthritis [17].

Rauch and colleagues developed an even more sophisticated mouse model, in which the bioluminescence emission was coupled to the malignant transformation and development of spontaneous lymphoma. The group applied these mice for imaging of spontaneous tumor development, showing that microscopic intra-epithelial lesions precede the onset of peripheral subcutaneous tumors, proving that the model can be used to study the association of inflammation and tumor initiation processes [111].

13.3.4.3 Tracking of Immune Cells/T Cell Imaging

Anticancer immunotherapies that emerged in the recent decade aim at priming the immune system to recognize and destroy tumor cells. Adoptive T cell therapy (ACT) is a powerful approach that relies on the infusion of tumor-specific T cells. For this purpose, tumor-infiltrating lymphocytes (TILs) are isolated directly from the tumor, expanded, and then re-injected in the patient, taking advantage of the natural tumor-homing properties of TILs. In a more sophisticated form, the so-called CAR-T cell therapy, patient-derived T cells are isolated from the blood (peripheral blood lymphocytes, PBLs). Since PBLs show less or no tumor-homing properties, they are genetically modulated to express tumor-recognizing receptors and thus gain the capacity to distinguish tumor from healthy tissue, before being expanded and re-injected into the patient. T cell therapies have emerged as a powerful and potentially curative therapy for several cancers and have been extensively reviewed by [106].

However, while very promising and already clinically available for treatment of leukemia, adoptive T cell therapies for solid tumors are still under development. To study the course and the efficacy of such therapies in solid tumors, Na and colleagues generated a transgenic mouse model which allows for simultaneous *in vivo* BLI of migration and activation of T cells with a nuclear factor of activated T cells

(NFAT)-dependent click beetle luciferase (imaging of activation) and a constitutive *Renilla* luciferase (imaging of migration) [92, 130].

The same model was used recently by Kleinovink and colleagues to follow T cell localization and activation in vaccine-draining lymph nodes of ovalbumin (OVA)-vaccinated mice. They showed that the system can be applied in non-cancerous experimental models to study the location and functional state of T cells [53].

13.3.4.4 Stem Cell Tracking

Stem cell therapy is an emerging strategy aiming at repair response and regeneration of damaged, dysfunctional, or diseased tissues by applying stem cells. The therapeutic efficacy depends on the *in vivo* behavior of the transplanted stem cells, including their migration, tissue-specific accumulation, long-term survival, morphological differentiation, or generation of the repaired tissues. For all of these, BLI is a valuable tool both *in vitro* and *in vivo*. For example, Allen and colleagues used BLI for long-term *in vivo* monitoring of subcutaneous hydrogel scaffold transplants loaded with luciferase-expressing human mesenchymal stem cells (hMSCs) and showed that the bioluminescence signal remained predictive of live cell number for at least a week [3]. Luciferase-expressing hMSCs were applied to study stem cell tropism in tumors and inflammatory sites and to determine conditions under which those cells selectively engraft in sites of inflammation. Using BLI, the group could demonstrate not only specific homing of hMSC to injured sites in wounded mice, but also accumulation at the sites of tumor development in mouse breast carcinoma xenografts [50].

Studies have also been conducted aiming at the improvement of stem cell homing to the desired sites, such as infarcted areas or tumors, which can be achieved for example by overexpression of certain molecules on the stem cell surface. One such factor is CXC-Motiv-Chemokine receptor 4 (CXCR4), which has been shown to improve the migratory capacity of stem cells *in vitro*. *In vivo*, BLI studies confirmed that intravenous infusion of MSCs overexpressing CXCR4 increased their ability to home to the tumor [49].

In a non-cancerous context, BLI was used to determine the survival and migration of an intramyocardially injected regenerative cell population derived from human subcutaneous adipose tissue stem cells (hASCs) in an experimental model of myocardial infarction. Long-term BLI demonstrated that injected hASCs engrafted and persisted in the myocardium for at least 10 weeks [9].

Numerous reviews have been published, describing applications of BLI to track transplanted cells, such as stem cells or cancer cells, and to follow their fate [25, 104].

13.3.4.5 Imaging of Protein–Protein Interactions

Imaging of protein–protein interactions typically utilizes the so-called split luciferases, in which the enzyme is expressed as two independent N-terminal and C-terminal fragments (NLuc and CLuc, respectively), which on their own are enzymatically inactive. Only when both are close enough to form an active protein,

the bioluminescence reaction will be catalyzed and light emission takes place. By fusing such split luciferases with interacting proteins, the visualization of the restored luciferase activity and thus the bioluminescence intensity will be a measure of the protein–protein interaction.

Stefan and colleagues designed such a *Renilla* luciferase (*Rluc*)-based method for investigation of dynamic protein complexes which they called protein fragment complementation assay (PCA). This assay was successfully applied for G protein-coupled receptor (GPCR)-induced disassembly of protein kinase A (PKA) regulatory and catalytic subunits, a key effector of GPCR signaling, allowing for accurate measurements of live changes in protein complex assembly and disassembly as well as cellular imaging and dynamic localization of protein complexes [123].

A similar approach was used to measure the activity of the serine/threonine kinase Akt, which is a mediator of mitogenic and antiapoptotic responses. The group applied split-luciferase-based BLI imaging to monitor quantitatively and dynamically Akt activity in response to activation or inhibition pathways in mouse tumor xenografts [152].

The application of split luciferases for preclinical imaging of cancer-related processes has also been reviewed elsewhere [59].

13.3.5 Bioluminescence Imaging Versus Fluorescence Imaging

Fluorescence and bioluminescence imaging are two optical imaging modalities which are routinely applied to study cancer and a number of non-cancerous diseases in preclinical settings. Due to the different origins of the light emission process, each method has a number of advantages and disadvantages which have to be considered before choosing the appropriate system.

First of all, in bioluminescence, the energy to excite the electrons derives from a chemical reaction while exogenous illumination is necessary for fluorescence to excite the electrons to a higher energy level, leading to photon emission during the electrons' return to their ground state. The exciting photons contribute greatly to tissue autofluorescence by exciting endogenous fluorophores. Therefore, background levels in BLI are extremely low, and the signal-to-noise ratio (SNR) can be very high. By comparison, fluorescence imaging often suffers from strong autofluorescence signals, which can even exceed the detection of the specific event.

Another advantage of BLI over fluorescence imaging is its high sensitivity, because of its independence of excitation photons. In fluorescence imaging, excitation photons need to travel through the tissue, where they undergo absorption and scattering before they reach the target. As a consequence, only a small amount of the applied photons will indeed reach the target, negatively affecting the detection efficacy. In bioluminescence, the light is produced directly at the target, making the light emission much more efficient. Furthermore, BLI offers much better quantification accuracy due to the light production by an enzymatic reaction occurring only in live cells.

However, the major drawback of BLI is the necessity of genetic modification of the host to express luciferases, which are normally not present in the genome of model organisms. As a consequence, this imaging modality will never find application in humans.

Another important drawback of both *in vivo* optical imaging modalities, resulting from light attenuation (absorbance and scattering) in biological tissues, is the poor spatial resolution with increasing depth and the generally limited penetration depth. Therefore, other optical imaging technologies have to be chosen when aiming at deep tissue imaging.

13.4 Optoacoustic Imaging

Optoacoustic imaging (OAI; also called photoacoustic imaging) is a technology based on detection of acoustic waves, which occur in response to the absorption of light photons by molecules. This phenomenon of sound generation by light, the so-called photoacoustic effect, was first described in 1880 by Alexander Graham Bell in his pioneering work on a device called “photophone”, a prototype of what we now know as wireless communication [11].

During OAI, tissues are illuminated with short laser light pulses of a specific wavelength causing photons to propagate diffusely inside. When the wavelength of the applied light meets the spectroscopic characteristics of an absorber molecule within the tissue, the light photons are specifically absorbed, causing a brief thermoelastic expansion of the absorber molecule. This in turn leads to the formation of a transient pressure, which distributes through the tissues in form of spherical acoustic waves with an ultrasound frequency that can be detected on the body

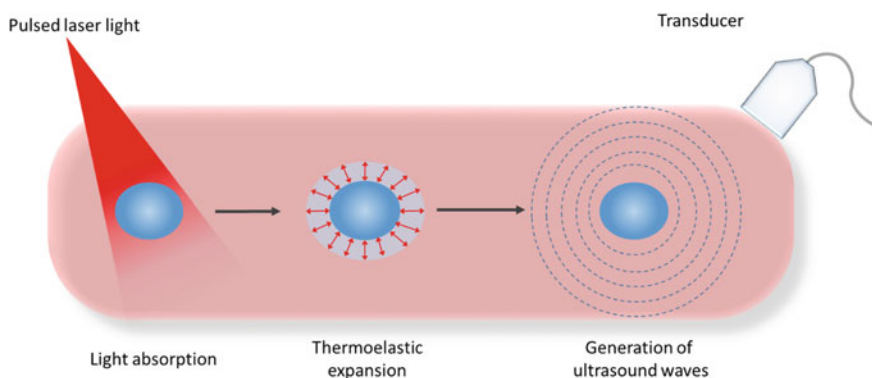


Fig. 13.14 The general principle of OAI. Absorption of the energy of a pulsed laser light by chromophores within the tissue (blue) leads to a short thermoelastic expansion of the absorber. This process generates acoustic waves which distribute through the tissue and can be measured with an ultrasonic transducer and reconstructed as a 3D image

surface with ultrasound transducers and then analyzed to produce 3D images. These basic principles of OAI are illustrated in Fig. 13.14.

OAI relies on the absorption of light for signal generation and the detection of ultrasound waves for signal acquisition and thus combines advantages of both fluorescence and ultrasound imaging.

OAI offers an increased penetration depth in comparison to fluorescence imaging, because it uses light only for the signal generation, but acoustic waves for signal detection. Light photons of different wavelengths, especially those in the visible range, are intensely absorbed by the tissue components. Furthermore, light is strongly scattered within the tissues, which dramatically reduces the resolution of optical imaging with increasing depth. In contrast, the scattering of ultrasound waves in tissue is approximately two to three orders of magnitude weaker than optical scattering. This means that sound waves can propagate much greater distances than photons without losing their original direction. Therefore, OAI allows much higher spatial resolution in deep tissues and improved penetration depths of several centimeters when compared to traditional fluorescence imaging [148]. At the same time, OAI clearly exceeds the soft tissue contrast of ultrasonic imaging allowing for improved specificity and higher contrast/excellence of structure differentiation and surpasses the spectral tuning of optical imaging. This is because the differences between the absorbance of light by various tissue components/chromophores are typically much higher than those of the acoustic waves. In addition, when compared to ultrasound imaging which does not provide certain physiological parameters, OAI enables label-free imaging of endogenous chromophores supplies, for instance, highly specific information on blood oxygen saturation. Finally, OAI sustains the advantages of both imaging modalities (ultrasound and fluorescence) of being harmless (non-ionizing, noninvasive) and easy to use.

In general, two types of molecules can serve as source of contrast for OAI: (a) exogenous absorbers such as hemoglobin, melanin, water, and lipids or (b) endogenous contrast agents.

Each of the absorber molecules has its own absorbance spectrum with an ideal wavelength for optimal targeting. Single-wavelength OAI can be applied to detect a particular chromophore molecule, such as the distribution of a contrast agent in live mice based on the signal intensity. However, in most cases, the detected signal is only semiquantitative, as it is influenced by background signals unrelated to those derived from the contrast agent and the measurement is therefore prone to error.

As molecules such as hemoglobin or melanin differ in their absorption characteristics, they can usually be easily resolved using the different excitation wavelengths. The simplest spectroscopic method involves measurements at two optical wavelengths. The ratio between the two measured optoacoustic signals can be used to estimate the ratio between two defined tissue components, e.g., oxygenated and deoxygenated hemoglobin to define tissue oxygenation status or to measure the activation state of an activatable contrast agent. Here, the major limitation is that only two absorbers can be resolved. An alternative technique requires a reasonable estimation of the anticipated absorbers within the tissue and a multi-wavelength excitation. Each pixel of the measurement is excited at different wavelengths and then

correlated to the spectrum of one selected absorber. The method does not necessarily reflect true values as the assumption that one pixel contains only one single absorber is incorrect in the majority of cases. Finally, a spectroscopic approach can be applied, by which tissues are illuminated with a number of wavelengths using, for example, a tunable laser. Each pixel is treated as a combination of different absorbers, and linear models are used to estimate the relative contribution of each absorber to the overall spectrum. This method is the most accurate as tissues always contain a combination of different absorbers, but it requires well-designed and reliable algorithms and good knowledge of the spectra of the major tissue components [135].

In each aforementioned method, the choice of optical wavelengths is critically important. The unique spectral features of each absorber must be captured by a discrete set of wavelengths. Information on tissue composition, i.e., relative concentrations of (de)oxyhemoglobin, water, lipid, or an injected imaging agent, can be calculated by combining photoacoustic data acquired at multiple wavelengths.

13.4.1 Modes of Action

OAI has two general modes of action. The first one is based on the focusing of an ultrasonic transducer, which can be either simply focused on one plane and results in two-dimensional images or combined with time-resolved recordings of the pressure. With the knowledge of the speed of sound, the time-varying detected ultrasound signals can then be reconstructed to three-dimensional images, supplying information about the spatial origin of the optical absorption. This particularly requires perfect time synchronization between the laser pulses used for signal generation and the acquisition times of the transducer in order to ensure accurate localization of the event. As the transducer is positioned on a single plane, it only records part of the spherical wavefront, leading to a loss in image contrast. The second mode of action is called optoacoustic tomography. Here, typically a large diameter laser beam is applied to achieve a larger field illumination of the tissue. The use of NIR light adds to the deeper penetration and light scattering within the tissue, facilitating a relatively homogenous tissue illumination where the photons can reach most absorber molecules. Scanning is achieved either by mechanical moving of a focused ultrasound transducer over the tissue or by using multiple transducers arranged around the tissue (Fig. 13.15). The latter usually requires a more complex image reconstruction, similar to that for X-ray tomography, and therefore also longer image-generation times, but at the same time it offers more control over the data acquisition [135].

13.4.2 Sources of Contrast

As mentioned above, OAI can be performed either using the endogenous tissue contrast obtained from physiologically specific absorption of endogenous chromophores or by applying exogenous chromophores which target specific structures or processes in the body.

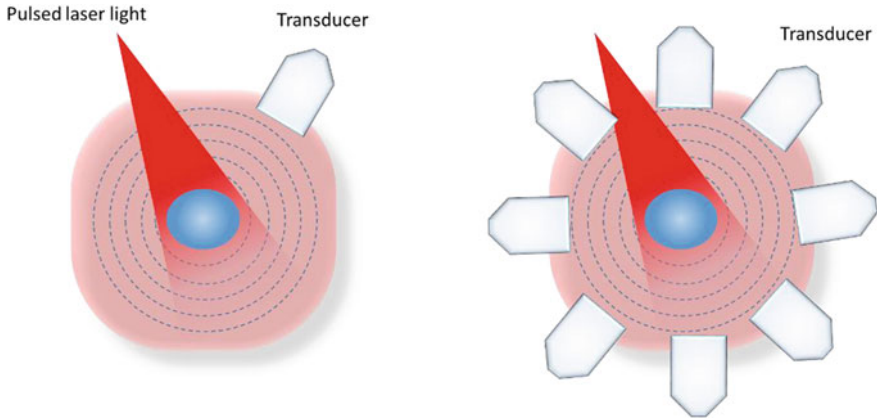
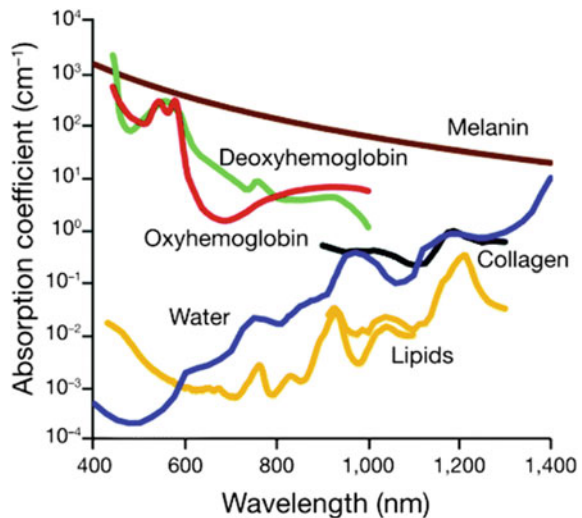


Fig. 13.15 Operation modes in OAI. Left: The classical approach, where a single transducer is located at a fixed position which therefore records only a part of the emerging ultrasonic waves (dashed circles). Right: Tomographic approach, where either a single transducer is rotated around the tissue or multiple transducers arranged in a circular array surrounding the tissue are used for data acquisition in a manner comparable to X-ray tomography

The major tissue absorbers are melanin, hemoglobin, water, and lipids (Fig. 13.16). Hemoglobin is of particular interest as the oxygenated and deoxygenated hemoglobin differ in their absorbance spectra. This not only allows for the detection of the general tissue vascularization or (micro-)circulation within the area of interest, but also provides information about the tissue oxygenation, allowing to distinguish between hypoxic, normoxic, or hyperoxic areas or to quantify hemoglobin oxygenation within single vessels in real time.

Fig. 13.16 Absorption coefficient spectra of endogenous tissue chromophores at their typical concentrations in the human body: oxyhemoglobin, red line; deoxyhemoglobin, green line; water, blue line; lipids, yellow lines; melanin, brown line; and collagen, black line. Data from <http://omlc.ogi.edu/spectra/> [143]



Next to the intrinsic chromophores, genetically encoded fluorophores can be used as a source of contrast for OAI, since fluorescent proteins are typically strong light absorbers and therefore capable of generating optoacoustic signals. However, the majority of genetically encoded fluorescent proteins, such as GFP or red fluorescent protein (RFP), absorb and emit in the visible spectrum, where the light penetration is hindered by an extremely high absorption by water and hemoglobin, limiting the use of genetically encoded fluorescence reporters. In recent years, several red-shifted fluorescent proteins have been developed with OAI-optimized absorbance spectra. Alas, the *in vivo* detection of the majority of GFP-like fluorescent proteins often suffers from limited photostability and low efficiency in the generation of photoacoustic signals, restricting their application. Still, the use of OAI based on reporter gene detection may be of benefit where the application of extrinsic chromophores is unwanted and the intrinsic ones do not deliver the desired information [143].

In general, all fluorescent molecules can be used as optoacoustic reporters as all of them are capable of absorbing photons. However, an optimal contrast agent for OAI should fulfill the following criteria. First, the molecule should have a high molar extinction coefficient (ϵ), which is a measure of how strongly a chemical species or substance absorbs light at a particular wavelength. At the same time, it should have a low QY, which is a measure of photon emission efficiency as defined by the ratio of the number of photons emitted to the number of photons absorbed, in order to maximize the non-radiative conversion of light energy to acoustic waves. This means that all the fluorescent molecules, which are relatively poor contrast agents for optical imaging, due to the low QY, are the most optimal sources of contrast for OAI. A sharply peaked absorbance spectrum, although not mandatory, is also advantageous for OAI, as it allows for spectral distinction between different signal sources.

A peak absorption in the NIT range offers another advantage for the OAI. Although, in general, both visible (~ 400 – 650 nm) and NIR (650 – 950 nm) light are suitable as a source of contrast in OAI, the visible light is predominantly absorbed by the intrinsic chromophores and the use of NIR light will maximize the penetration depth.

The optimal contrast agent should also have a high photostability, in order to ensure stable signals upon light irradiation. Furthermore, similar to fluorescence imaging agents, the OAI probe needs to fulfill certain biological properties in order to ensure the specific detection of the anticipated event. It means that it either has to selectively recognize a specific biological target, or it has to accumulate in a desired tissue, e.g., at the tumor site, due to the EPR effect or it has to be specifically activated via a physiological or pathophysiological process. Furthermore, the OAI probe needs to have high biocompatibility, no, or negligible toxicity and circulation times which are sufficient for binding/accumulation/activation [143].

13.4.2.1 Hemoglobin

Hemoglobin is one of the major absorbers in mammalian tissues and therefore one of the most valuable intrinsic contrast agents for OAI. OAI of hemoglobin can, for

example, be applied for the detection and characterization of vasculature, e.g., in longitudinal imaging of (tumor-) angiogenesis.

At shorter wavelengths, ranging in the visible spectrum, hemoglobin is the major tissue absorber, with the absorbance of at least two orders of magnitude higher than the other tissue absorbers such as water or lipids (see Fig. 13.16). At the same time, melanin, which has even a higher absorption coefficient than hemoglobin, especially in the NIR range, remains localized to some specific regions such as skin and retina and, therefore, usually does not affect the measurement of hemoglobin much. In this way, precise information about the total hemoglobin concentration within tissues can be obtained at shorter wavelengths.

As the two forms of hemoglobin have very similar molar extinction coefficients at ~ 580 nm, measurements at this wavelength allow the detailed depiction of the (micro-) vasculature but no information about the oxygenation [151]. Similar depiction of the vasculature can be achieved by measuring the optoacoustic signals at 800 nm, where the oxygen binding does also not affect the absorbance coefficient of hemoglobin (see Fig. 13.16).

Malignant tumors are characterized by disorganized and dense vasculature. Therefore, simple hemoglobin-based OAI can often be used for the detection of tumors by distinguishing them from healthy less vascularized tissue with homogenous vessel structure. Such approaches have already been applied for the detection of breast tumors in human patients. An initial study revealed higher intensity regions which were attributed to the vascular distribution associated with cancer [79].

Kruger and colleagues developed a breast photoacoustic mammography (PAM) system. The device is a tomographic setup, based on multiple detectors surrounding the tissue and allows for imaging of even large breasts of more than 1.5 L with a penetration depth of >5 cm and submillimeter spatial resolution [56].

Since photoacoustic imaging is noninvasive and harmless, longitudinal studies can be performed to assess tumor neovascularization or even to determine the time point when the tumor switches to malignancy. This has been shown by Siphanto et al., who monitored the formation of tumor vessels in subcutaneously transplanted tumors in rats. Using OAI, the onset of neovascularization could be observed as early as 3 days after transplantation [118].

As the hemoglobin changes its molecular and electronic structure upon oxygen binding, the two hemoglobin isoforms, oxyhemoglobin and deoxyhemoglobin, differ in their absorbance spectra (see Fig. 13.16). Thus, OAI can also be applied for the assessment of the oxygenation status/hypoxia levels of tissues or even of particular vessels. For this purpose, oxyhemoglobin and deoxyhemoglobin are treated as the dominant absorbing compounds, and their relative concentrations are calculated on the basis of their molar extinction spectra from spectral measurements of the total absorption coefficient. This requires the acquisition of an optoacoustic signal using at least two wavelengths at which each compound emission dominates, although multi-wavelength measurements are obviously better to obtain more reliable results.

Oxygenation levels in healthy tissues range between 95% and 100% in the arteries and 60% and 80% in the veins [40]. Tumors have usually higher oxygen consumption rates than the surrounding tissues. Especially, fast-growing tumors develop low-oxygenated hypoxic areas in the tumor center, due to the insufficient neovascularization and the increased oxygen consumption. Hypoxic tumors are often more resistant to therapies and associated with poor prognosis. Therefore, assessment of the oxygenation levels within the neoplastic tissue can be an important prognostic parameter. In this context, Mallidi and colleagues showed that tumor oxygenation levels measured with OAI can be a surrogate marker for predicting treatment efficacy and tumor recurrence. In this study, they applied photodynamic therapy to mice with subcutaneous tumors and measured oxygenation levels with OAI before and after therapy. They showed that only the responder group showed strong changes in tumor oxygenation by 24 h post-therapy, while the non-responsive mice had continuously constant tumor oxygen levels [78].

The recent advances in the measurement of oxygenation levels in tumors have also been reviewed elsewhere [66].

13.4.2.2 Melanin

As already mentioned, melanin is one of the endogenous chromophores, which can be utilized for OAI. It is a natural pigment produced by melanocytes located for example in the deeper layer of the epidermis but also in the eyes or some areas of the brain. Due to its function, melanin is an extremely effective absorber of light, as its main purpose is to protect the organisms against UV-induced damage.

Melanoma is a form of skin cancer that develops from the pigment-containing cells, the melanocytes. Although it is not the most common one, melanoma is undoubtedly the most dangerous of all skin cancers as it is prone to metastasize early into the lymph nodes, brain, or other organs. Due to the high melanin content, melanoma and its metastatic nodules can efficiently be detected and characterized using OAI.

The group of Oh et al. applied, for example, microscopic OAI to detect subcutaneously transplanted B16 skin melanoma cells in nude mice as early as 4 days after the transplantation, when the transversal size of the tumor was in submillimeter range. By applying double-wavelength optoacoustic microscopy and the combination of visible and NIR light for signal generation, they were able to distinguish melanoma tissue from the blood vessels due to the large difference in the absorption coefficients of light in melanin and in blood [102]. With NIR light (excitation 764 nm), the absorption of melanin is much higher than the one of blood, so that the photoacoustic signals from the blood vessels were far below the noise level of the system and only melanin, but not blood could be measured exactly from the images. In contrast, epidermal and the tumor-nourishing vasculature could be almost exclusively depicted with visible light (584 nm), as photoacoustic signals at this wavelength from the blood vessels were around 1.5–2.5 times higher than those from the melanoma. Here, the total blood content was assessed as at this wavelength since measurements with visible light are insensitive to hemoglobin oxygenation. Combining the two images from these two spectral

regions reveals the 3D morphology of both the melanoma and the surrounding vasculature [102, 151].

Another question for which melanin-based OAI can be applied is the identification of melanoma-positive sentinel lymph nodes, either before/during the resection, or during the biopsy examination to determine the presence of metastatic tissue. Stoffels et al. applied multispectral optoacoustic tomography (MSOT) to image sentinel lymph nodes (SLNs) *ex vivo* and to determine their metastatic status in melanoma patients. The subsequent spectral analysis allowed the quantification of melanin signal throughout the SLN and excellent correlation between intact photoacoustic melanin detection and localization of metastatic cells by histology [124]. Finally, it was also shown that melanin-based OAI can be used to detect circulating melanoma tumor cells with a sensitivity of one cell per mL of blood [32].

A major problem that melanoma patients face is the development of brain metastases, resulting in a very poor prognosis and a poor median survival of 4–5 months. Therefore, an early detection and characterization of brain metastases is crucial for the selection of an appropriate therapeutic approach and the patient's overall survival. As the melanoma brain metastases, similar to the primary tumors, contain high levels of melanin, they can be easily visualized using OAI based on the endogenous melanin contrast. Lavaud et al., for example, applied multispectral (680–924 nm) transcranial OAI for the noninvasive examination of B16F10 melanoma brain metastases in nude mice. Subsequent spectral unmixing analyses of the spectroscopic data revealed the presence of melanin in tumor-bearing brains and allowed the visualization of tumor nodules. Furthermore, the unmixing of oxy- and deoxyhemoglobin spectra enabled the characterization of the oxygen distribution in the tumor and to visualize hypoxic areas near the tumor center [60].

Staley and colleagues applied a similar approach, in which they used photoacoustic microscopy to monitor growth of melanoma-derived brain metastasis over the course of the disease (two weeks). They were able to detect tumors of sub-millimeter size and monitor their growth through the skull [121].

13.4.2.3 Lipids

Absorption of light by lipids is in general lower than the one by melanin or hemoglobin. However, the lipids' absorption spectrum is very different from that of other tissue components and shows several characteristics which can be exploited for OAI. Lipids exhibit several absorption peaks, the most prominent one is the strong and sharp absorption peak at 1210 nm, together with the weaker absorption peaks at 920 and 1040 nm. At the same time, the absorbance of melanin and hemoglobin are reduced at longer wavelengths, which makes the 1210 nm peak especially optimal for the *in vivo* detection of lipid-rich structures.

Lipid imaging can be applied, for example, for the detection and characterization of arteriosclerotic plaques adding valuable information to the already existing diagnostic techniques. Vulnerable plaques, which are particularly susceptible to disruption causing acute coronary events, are described as those having a thin inflamed fibrous cap over a very large lipid core. Lipids, therefore, can be utilized as an endogenous contrast agent to reveal the plaque's vulnerability. This can be

assessed, for example, by applying low-invasive intravascular OAI, which requires the insertion of the imaging probe into the vessel of interest such as a coronary artery. Here, spectroscopic imaging has already been shown to provide highly detailed information about the tissue composition, e.g., to outline fat deposits and to discriminate between the normal arterial areas, lipid-rich arteriosclerotic plaques, atheromas, and those which contain other components such as fibrous or calcified compounds [44].

13.4.2.4 Exogenous Probes

Aside from endogenous contrast agents, a diversity of exogenous contrast agents or targeted probes can be applied for OAI, providing additional contrast and valuable information about the disease-specific events. Such probes include fluorescent dyes, liposomes, polymeric nanoparticles, gold or carbon nanoparticles, nanodroplets, or quantum dots, which can be conjugated to antibodies or ligands to image disease-specific receptors that do not provide OAI contrast per se [135].

Fluorescent Dyes

NIR-absorbing dyes such as ICG or IRDye 800/IRDye 800 CW are the most common dyes used for OAI, both with a relatively narrow absorbance peak around 800 and 780 nm, respectively, and thus easily distinguishable from endogenous chromophores, especially oxy and deoxyhemoglobin. Both dyes are particularly interesting for OAI as they are already applied for various applications in clinical practice and would thus have great potential for clinical translation.

ICG is a non-specific probe, which distributes through the vasculature and accumulates in tumors or inflammatory sites due to the EPR effect. It has short clearance times and is extracted fast by the liver into bile juice. Clinically, ICG is applied as an intraoperative fluorescence contrast agent, e.g., for the visualization of lymph or blood vessels during angio- or lymphography, for example, in liver surgery to measure hepatic blood flow or during reconstructive microsurgery, yet all of them with strongly limited penetration depth [2]. In contrast, it has been shown that using OAI, ICG can be reliably detected in biological tissues at tissue depths exceeding 5 cm, which increases the potential field of clinical application [57]. In a mouse model, ICG-based OAI has already been applied to measure the extravasation in tumors noninvasively and in real time and has been shown to have a high potential to facilitate the early detection of changes in vascular permeability during cancer therapy [103]. In combination with (polyethylene glycol) PEG, added to increase the circulation times, ICG has been used to perform angiography of rat brains, significantly improving the contrast between vessels and the surrounding tissues [141].

IRDye 800 is increasingly gaining clinical attention, especially during fluorescence-guided surgical interventions. Similar to ICG, IRDye 800CW is a suitable contrast agent for OAI because of its spectroscopic characteristics, but at the same time, it has the advantage of an improved conjugation capability. This means that the dye cannot only be used for perfusion studies or the assessment of passive accumulation in tissues but also for molecular analyses, e.g., of target

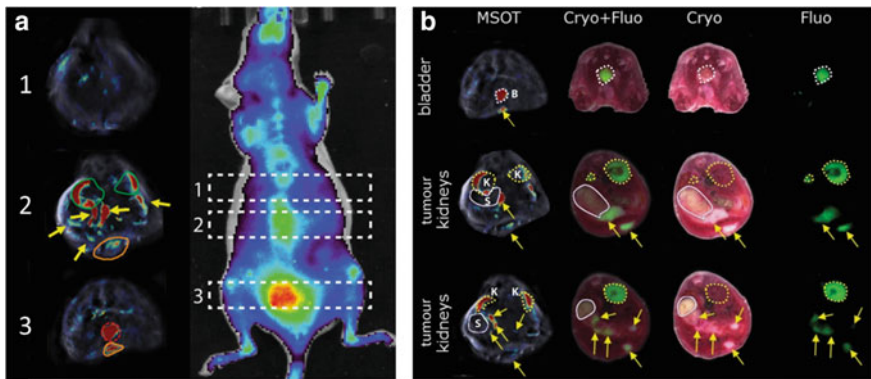


Fig. 13.17 OAI for visualization of orthotopic pancreatic tumors in mice. **a** Left: Three selected transversal slices performed 6 h after intravenous injection of cRGD-IRDye800CW, showing the detection of pancreatic tumor nodules. Right: Corresponding planar fluorescence image of the same mouse showing the location of the three transversal slices. **b** Verification of the in vivo recorded optoacoustic data (left) to the anatomical structures (Cryo) and fluorescence images (Fluo) of the cryosliced mouse. Yellow arrows: tumor nodules, K-kidneys, B-bladder, S-stomach, orange line subcutaneous tumor mass at the scar [95]

expression or drug biodistribution. In combination with an integrin-targeting probe, it has been applied for OAI of orthotopically transplanted glioblastoma [65].

Our group has recently published a study in which we used cRGD peptide labeled with a fluorescent dye, IRDye800CW, for the perioperative detection of pancreatic tumor nodules. cRGD peptide specifically targets integrins, which are overexpressed in various cancer types and are playing a key role in the early phase of tumor angiogenesis and in tumor cell migration. We showed that the applied probe can be visualized with both planar fluorescence imaging, allowing for the general assessment of tumor location, and OAI, allowing for precise visualization of particular tumor nodules located deeply within the mouse body (Fig. 13.17) [95].

Nanoparticles

Nanoparticles are currently the largest class of OAI contrast agents. These include gold-, carbon-, and polymer-based nanoparticles, quantum dots, or even contrast agents used in other imaging modalities, such as microbubbles or iron oxide particles.

Nanoparticles can have different forms and sizes. One of the biggest advantages of nanoparticles is their tunable surface properties that can be adapted, e.g., to increase circulation times, modify stability and reduce toxicity, or achieve molecular targeting. Furthermore, nanoparticles have large surface areas; hence, numerous targeting moieties can be attached per particle, increasing the probability of target binding. Depending on their composition, nanoparticles can also be loaded with drugs, dyes or other substances and used for their delivery and for simultaneous monitoring of distribution and/or release.

However, due to their size nanoparticles have the disadvantage that they often accumulate in the reticuloendothelial system for long periods, resulting in possible long-term toxicity and thus restricting their clinical application.

Plasmonic nanoparticles of different forms, including nanoshells, nanorods, and nanocages, usually made of gold, represent a particular group of nanoparticles and are promising contrast agents for OAI. Here, the signal generation is based on the surface plasmon resonance (SPR) effect that takes place when light (electromagnetic waves) interacts with the conduction electrons on the nanoparticle surface. This interaction causes the resonant oscillation of conduction electrons and leads to an optical absorption that is several orders of magnitude higher than the absorption of organic dyes. The great advantage of using SPR nanoparticles is the tunable optical absorption, which is dependent on the size and shape of the gold nanoparticles and can easily be adapted to the biomedical need. A disadvantage of plasmonic nanoparticles is their possible deformation upon long-term irradiation which can affect their absorption properties. Furthermore, similar to other nanoparticles they can also show long-term toxicity. Nevertheless, plasmonic nanoparticles have already been applied in different settings, e.g., for OAI of imaging of cancer, atherosclerotic plaques, brain function, or image-guided therapy [67].

Mallidi et al. applied gold nanoparticles targeting the epidermal growth factor receptor (EGFR) for highly selective and sensitive detection of EGFR-expressing cancer cells in mice [77]. Similarly, antibody-conjugated gold nanorods were developed for specific detection of tumor nodules [1]. Gold-plated carbon nanotubes conjugated to antibody targeting lymphatic vascular endothelial hyaluronan receptor-1 LYVE-1 have been shown to detect heterogeneities in lymphatic vasculature such as those in tumors and to measure changes in response to treatment with therapeutic agents [52].

Quantum dots are also interesting contrast agents for OAI. Sun et al. introduced titanium sulfonate-black phosphorus quantum dots that efficiently accumulate in the MCF-7 tumor xenografts in mice and showed a high potential for application as efficient optoacoustic agents in bio-imaging of cancer [127]. Ding and colleagues presented recently another interesting theranostic system, in which quantum dots were used simultaneously as an optoacoustic contrast agent for monitoring the delivery and as a therapeutic agent for photothermal/photodynamic combined cancer treatment [23].

Iron oxide nanoparticles are particularly interesting for OAI of cancer, because they were originally developed as contrast agent for MRI and are thus already approved for use in patients. In a rat model of prostate cancer, superparamagnetic iron oxide nanoparticles were used for ex vivo staging of lymph nodes. However, although the group observed a good correlation of the optoacoustic data with metastatic involvement measured by MRI and histology, proposing OAI as potential valuable tool for nodal staging, the application of iron oxide nanoparticles suffers from low optoacoustic contrast, reducing their optoacoustic detection in vivo [35].

13.5 Summary

The main field of application of OAI is undoubtedly in preclinical cancer research. Here, both endogenous and applied chromophores are commonly used as a source of contrast for the identification of tumor nodules and metastatic spread, for the assessment of the efficacy of therapeutic interventions, detection of metastatic lymph nodes, or characterization of tumor status and vascularization.

As the penetration of light into the tissue is limited by the absorbance of light photons by endogenous absorber molecules—reaching a maximum penetration depth of a few centimeters—the clinical application of OAI will remain restricted to the detection and characterization of surface-near structures or endoscopic procedures, such as the detection of lesions in the gastrointestinal tract, bladder, or possibly also prostate (transrectal) and ovaries (transvaginal). Nevertheless, as the technique uses non-ionizing radiation and is capable of utilizing endogenous tissue contrast to provide various information about disease-relevant events, its clinical use is versatile and clinical translation is relatively simple and therefore wanted.

References

1. Agarwal A, Huang SW, O'Donnell M, Day KC, Day M, Kotov N, Ashkenazi S (2007) Targeted gold nanorod contrast agent for prostate cancer detection by photoacoustic imaging. *J Appl Phys* 102:064701. <https://doi.org/10.1063/1.2777127>
2. Alander JT, Kaartinen I, Laakso A, Pätälä T, Spillmann T, Tuchin VV, Venermo M, Välisuo P (2012) A review of indocyanine green fluorescent imaging in surgery. *Int J Biomed Imaging* 2012:1–26. <https://doi.org/10.1155/2012/940585>
3. Allen AB, Gazit Z, Su S, Stevens HY, Guldberg RE (2014) In vivo bioluminescent tracking of mesenchymal stem cells within large hydrogel constructs. *Tissue Eng Part C Methods* 20:806–816. <https://doi.org/10.1089/ten.tec.2013.0587>
4. Alves F, Dullin C, Napp J, Missbach-Guentner J, Jannasch K, Mathejczyk J, Pardo LA, Stühmer W, Tietze L-F (2009) Concept of a selective tumour therapy and its evaluation by near-infrared fluorescence imaging and flat-panel volume computed tomography in mice. *Eur J Radiol* 70:286–293. <https://doi.org/10.1016/j.ejrad.2009.01.048>
5. Ankersmit M, van Dam DA, van Rijswijk A-S, van den Heuvel B, Tuynman JB, Meijerink WJHJ (2017) Fluorescent imaging with indocyanine green during laparoscopic cholecystectomy in patients at increased risk of bile duct injury. *Surg Innov* 24:245–252. <https://doi.org/10.1177/1553350617690309>
6. Ardeshipour Y, Chernomordik V, Capala J, Hassan M, Zielinsky R, Griffiths G, Achilefu S, Smith P, Gandjbakhchke A (2011) Using in-vivo fluorescence imaging in personalized cancer diagnostics and therapy, an image and treat paradigm. *Technol Cancer Res Treat* 10:549–560
7. Backer MV, Levashova Z, Patel V, Jehning BT, Claffey K, Blankenberg FG, Backer JM (2007) Molecular imaging of VEGF receptors in angiogenic vasculature with single-chain VEGF-based probes. *Nat Med* 13:504–509. <https://doi.org/10.1038/nm1522>
8. Badr CE, Tannous BA (2011) Bioluminescence imaging: progress and applications. *Trends Biotechnol* 29:624–633. <https://doi.org/10.1016/j.tibtech.2011.06.010>
9. Bai X, Yan Y, Coleman M, Wu G, Rabinovich B, Seidensticker M, Alt E (2011) Tracking long-term survival of intramyocardially delivered human adipose tissue-derived stem cells using bioluminescence imaging. *Mol Imaging Biol* 13:633–645. <https://doi.org/10.1007/s11307-010-0392-z>

10. Barnett EM, Zhang X, Maxwell D, Chang Q, Piwnica-Worms D (2009) Single-cell imaging of retinal ganglion cell apoptosis with a cell-penetrating, activatable peptide probe in an in vivo glaucoma model. *Proc Natl Acad Sci U S A* 106:9391–9396. <https://doi.org/10.1073/pnas.0812884106>
11. Bell AG (1880) On the production and reproduction of sound by light. *Am J Sci Series 3* 20:305–324. <https://doi.org/10.2475/ajs.s3-20.118.305>
12. Bhaumik S, Gambhir SS (2002) Optical imaging of Renilla luciferase reporter gene expression in living mice. *Proc Natl Acad Sci U S A* 99:377–382. <https://doi.org/10.1073/pnas.012611099>
13. Brancalion L, Durkin AJ, Tu JH, Menaker G, Fallon JD, Kollias N (2001) In vivo fluorescence spectroscopy of nonmelanoma skin cancer. *Photochem Photobiol* 73:178–183
14. Brodl E, Winkler A, Macheroux P (2018) Molecular mechanisms of bacterial bioluminescence. *Comput Struct Biotechnol J* 16:551–564. <https://doi.org/10.1016/j.csbj.2018.11.003>
15. Bullok KE, Maxwell D, Kesarwala AH, Gammon S, Prior JL, Snow M, Stanley S, Piwnica-Worms D (2007) Biochemical and in vivo characterization of a small, membrane-permeant, caspase-activatable far-red fluorescent peptide for imaging apoptosis. *Biochemistry* 46:4055–4065. <https://doi.org/10.1021/bi061959n>
16. Cai W, Sam Gambhir S, Chen X (2005) Multimodality tumor imaging targeting integrin $\alpha v \beta 3$. *Biotechniques* 39:S14–S25. <https://doi.org/10.2144/000112091>
17. Carlsen H, Moskaug JØ, Fromm SH, Blomhoff R (2002) In vivo imaging of nf- κ b activity. *J Immunol* 168:1441–1446. <https://doi.org/10.4049/jimmunol.168.3.1441>
18. Close DM, Patterson SS, Ripp S, Baek SJ, Sanseverino J, Sayler GS (2010) Autonomous bioluminescent expression of the bacterial luciferase gene cassette (lux) in a mammalian cell line. *PLoS ONE* 5:e12441. <https://doi.org/10.1371/journal.pone.0012441>
19. Conway JRW, Warren SC, Herrmann D, Murphy KJ, Cazet AS, Vennin C, Shearer RF, Killen MJ, Magenau A, Méléneć P, Pinese M, Nobis M, Zaratzian A, Boulghourjian A, Da Silva AM, Del Monte-Nieto G, Adam ASA, Harvey RP, Haigh JJ, Wang Y, Croucher DR, Sansom OJ, Pajic M, Caldon CE, Morton JP, Timpson P (2018) Intravital imaging to monitor therapeutic response in moving hypoxic regions resistant to PI3K pathway targeting in pancreatic cancer. *Cell Rep* 23:3312–3326. <https://doi.org/10.1016/j.celrep.2018.05.038>
20. Cronin M, Akin AR, Collins SA, Meganck J, Kim J-B, Baban CK, Joyce SA, van Dam GM, Zhang N, van Sinderen D, O’Sullivan GC, Kasahara N, Gahan CG, Francis KP, Tangney M (2012) High resolution in vivo bioluminescent imaging for the study of bacterial tumour targeting. *PLoS ONE* 7:e30940. <https://doi.org/10.1371/journal.pone.0030940>
21. David S, Carmoy N, Resnier P, Denis C, Misery L, Pitard B, Benoit J-P, Passirani C, Montier T (2012) In vivo imaging of DNA lipid nanocapsules after systemic administration in a melanoma mouse model. *Int J Pharm, Spec Issue: Drug Deliv Imaging Cancer* 423:108–115. <https://doi.org/10.1016/j.ijpharm.2011.06.031>
22. Delank W, Khanavkar B, Nakhosteen JA, Stoll W (2000) A pilot study of autofluorescent endoscopy for the in vivo detection of laryngeal cancer. *Laryngoscope* 110:368–373. <https://doi.org/10.1097/00005537-200003000-00007>
23. Ding D, Guo W, Guo C, Sun J, Zheng N, Wang F, Yan M, Liu S (2017) MoO₃ - x quantum dots for photoacoustic imaging guided photothermal/photodynamic cancer treatment. *Nanoscale* 9:2020–2029. <https://doi.org/10.1039/C6NR09046J>
24. Ding S, Blue RE, Moorefield E, Yuan H, Lund PK (2017) Ex vivo and in vivo noninvasive imaging of epidermal growth factor receptor inhibition on colon tumorigenesis using activatable near-infrared fluorescent probes. *Mol Imaging* 16:1536012117729044. <https://doi.org/10.1177/1536012117729044>
25. Dothager RS, Flentie K, Moss B, Pan M-H, Kesarwala A, Piwnica-Worms D (2009) Advances in bioluminescence imaging of live animal models. *Curr Opin Biotechnol, Anal Biotechnol* 20:45–53. <https://doi.org/10.1016/j.copbio.2009.01.007>

26. Edgington LE, Verdoes M, Bogyo M (2011) Functional imaging of proteases: recent advances in the design and application of substrate-based and activity-based probes. *Curr Opin Chem Biol* 15:798–805. <https://doi.org/10.1016/j.cbpa.2011.10.012>
27. Edinger M, Cao Y-A, Verneris MR, Bachmann MH, Contag CH, Negrin RS (2003) Revealing lymphoma growth and the efficacy of immune cell therapies using in vivo bioluminescence imaging. *Blood* 101:640–648. <https://doi.org/10.1182/blood-2002-06-1751>
28. Edwards WB, Akers WJ, Ye Y, Cheney PP, Bloch S, Xu B, Laforest R, Achilefu S (2009) Multimodal imaging of integrin receptor-positive tumors by bioluminescence, fluorescence, gamma scintigraphy, and single-photon emission computed tomography using a cyclic RGD peptide labeled with a near-infrared fluorescent dye and a radionuclide. *Mol Imaging* 8:101–110
29. Eisenblätter M, Ehrchen J, Varga G, Sunderkötter C, Heindel W, Roth J, Bremer C, Wall A (2009) In vivo optical imaging of cellular inflammatory response in granuloma formation using fluorescence-labeled macrophages. *J Nucl Med* 50:1676–1682. <https://doi.org/10.2967/jnumed.108.060707>
30. Foster AE, Kwon S, Ke S, Lu A, Eldin K, Sevick-Muraca E, Rooney CM (2008) In vivo fluorescent optical imaging of cytotoxic T lymphocyte migration using IRDye800CW near-infrared dye. *Appl Opt* 47:5944–5952
31. Frangioni JV (2003) In vivo near-infrared fluorescence imaging. *Curr Opin Chem Biol* 7:626–634. <https://doi.org/10.1016/j.cbpa.2003.08.007>
32. Galanzha EI, Shashkov EV, Spring PM, Suen JY, Zharov VP (2009) In vivo, noninvasive, label-free detection and eradication of circulating metastatic melanoma cells using two-color photoacoustic flow cytometry with a diode laser. *Cancer Res* 69:7926–7934. <https://doi.org/10.1158/0008-5472.CAN-08-4900>
33. Georgakoudi I, Jacobson BC, Müller MG, Sheets EE, Badizadegan K, Carr-Locke DL, Crum CP, Boone CW, Dasari RR, Van Dam J, Feld MS (2002) NAD(P)H and collagen as in vivo quantitative fluorescent biomarkers of epithelial precancerous changes. *Cancer Res* 62:682–687
34. Giannuzzo A, Saccomano M, Napp J, Ellegaard M, Alves F, Novak I (2016) Targeting of the P2X7 receptor in pancreatic cancer and stellate cells: Targeting of the P2X7 receptor in pancreatic cancer and stellate cells. *Int J Cancer* 139:2540–2552. <https://doi.org/10.1002/ijc.30380>
35. Grootendorst DJ, Fratila RM, Visscher M, Haken BT, van Wezel RJA, Rottenberg S, Steenbergen W, Manohar S, Ruers TJM (2013) Intra-operative ex vivo photoacoustic nodal staging in a rat model using a clinical superparamagnetic iron oxide nanoparticle dispersion. *J Biophotonics* 6:493–504. <https://doi.org/10.1002/jbio.201200204>
36. Haddock SHD, Moline MA, Case JF (2010) Bioluminescence in the Sea. *Annu Rev Mar Sci* 2:443–493. <https://doi.org/10.1146/annurev-marine-120308-081028>
37. Hadjipanayis CG, Widhalm G, Stummer W (2015) What is the surgical benefit of utilizing 5-aminolevulinic acid for fluorescence-guided surgery of malignant gliomas?: *Neurosurgery* 77:663–673. <https://doi.org/10.1227/NEU.0000000000000929>
38. Han X, Lui H, McLean DI, Zeng H (2009) Near-infrared autofluorescence imaging of cutaneous melanins and human skin in vivo. *J Biomed Opt* 14:024017. <https://doi.org/10.1117/1.3103310>
39. Han X, Xu K, Taratula O, Farsad K (2019) Applications of nanoparticles in biomedical imaging. *Nanoscale* 11:799–819. <https://doi.org/10.1039/C8NR07769J>
40. Harrop GA (1919) The oxygen and carbon dioxide content of arterial and of venous blood in normal individuals and in patients with anemia and heart disease. *J Exp Med* 30:241–257
41. Hart LS, El-Deiry WS (2008) Invincible, but not invisible: imaging approaches toward in vivo detection of cancer stem cells. *J Clin Oncol* 26:2901–2910. <https://doi.org/10.1200/JCO.2008.16.9573>
42. Huang Z, Zheng W, Xie S, Chen R, Zeng H, McLean DI, Lui H (2004) Laser-induced autofluorescence microscopy of normal and tumor human colonic tissue. *Int J Oncol* 24:59–63

43. Iwano S, Sugiyama M, Hama H, Watakabe A, Hasegawa N, Kuchimaru T, Tanaka KZ, Takahashi M, Ishida Y, Hata J, Shimozone S, Namiki K, Fukano T, Kiyama M, Okano H, Kizaka-Kondoh S, McHugh TJ, Yamamori T, Hioki H, Maki S, Miyawaki A (2018) Single-cell bioluminescence imaging of deep tissue in freely moving animals. *Science* 359:935–939. <https://doi.org/10.1126/science.aag1067>
44. Jansen K, van der Steen AFW, Wu M, van Beusekom HMM, Springeling G, Li X, Zhou Q, Shung KK, de Kleijn DP, van Soest G (2014) Spectroscopic intravascular photoacoustic imaging of lipids in atherosclerosis. *JBO* 19:026006. <https://doi.org/10.1117/1.JBO.19.2.026006>
45. Jayanthi JL, Subhash N, Stephen M, Philip EK, Beena VT (2011) Comparative evaluation of the diagnostic performance of autofluorescence and diffuse reflectance in oral cancer detection: a clinical study. *J Biophotonics* 4:696–706. <https://doi.org/10.1002/jbio.201100037>
46. Jenkins DE, Hornig YS, Oei Y, Dusich J, Purchio T (2005) Bioluminescent human breast cancer cell lines that permit rapid and sensitive in vivo detection of mammary tumors and multiple metastases in immune deficient mice. *Breast Cancer Res* 7:R444. <https://doi.org/10.1186/bcr1026>
47. Jiang T, Sun W, Zhu Q, Burns NA, Khan SA, Mo R, Gu Z (2015) Furin-mediated sequential delivery of anticancer cytokine and small-molecule drug shuttled by Graphene. *Adv Mater* 27:1021–1028. <https://doi.org/10.1002/adma.201404498>
48. Jost SC, Collins L, Travers S, Piwnica-Worms D, Garbow JR (2009) Measuring Brain Tumor Growth: A Combined BLI/MRI Strategy. *Mol Imaging* 8:245–253
49. Kalimuthu S, Oh JM, Gangadaran P, Zhu L, Lee HW, Rajendran RL, Baek S-H, Jeon YH, Jeong SY, Lee S-W, Lee J, Ahn B-C (2017) In vivo tracking of chemokine receptor CXCR4-engineered mesenchymal stem cell migration by optical molecular imaging [WWW Document]. *Stem Cells Int*. <https://doi.org/10.1155/2017/8085637>
50. Kidd S, Spaeth E, Dembinski JL, Dietrich M, Watson K, Klopp A, Battula L, Weil M, Andreeff M, Marini FC (2009) Direct evidence of mesenchymal stem cell tropism for tumor and wounding microenvironments using in vivo bioluminescence imaging. *Stem Cells* 27:2614–2623. <https://doi.org/10.1002/stem.187>
51. Kim J-B, Urban K, Cochran E, Lee S, Ang A, Rice B, Bata A, Campbell K, Coffee R, Gorodinsky A, Lu Z, Zhou H, Kishimoto TK, Lassota P (2010) Non-invasive detection of a small number of bioluminescent cancer cells in vivo. *PLoS ONE* 5:e9364. <https://doi.org/10.1371/journal.pone.0009364>
52. Kim J-W, Galanzha EI, Shashkov EV, Moon H-M, Zharov VP (2009) Golden carbon nanotubes as multimodal photoacoustic and photothermal high-contrast molecular agents. *Nat Nanotechnol* 4:688–694. <https://doi.org/10.1038/nnano.2009.231>
53. Kleinovink JW, Mezzanotte L, Zambito G, Fransen MF, Cruz LJ, Verbeek JS, Chan A, Ossendorp F, Löwik C (2019) A dual-color bioluminescence reporter mouse for simultaneous in vivo imaging of T cell localization and function. *Front. Immunol.* 9. <https://doi.org/10.3389/fimmu.2018.03097>
54. Kobayashi H, Ogawa M, Kosaka N, Choyke PL, Urano Y (2009) Multicolor imaging of lymphatic function with two nanomaterials: quantum dot-labeled cancer cells and dendrimer-based optical agents. *Nanomedicine (Lond)* 4:411–419. <https://doi.org/10.2217/nmm.09.15>
55. Kojima R, Takakura H, Ozawa T, Tada Y, Nagano T, Urano Y (2013) Rational design and development of near-infrared-emitting firefly luciferins available in vivo. *Angew Chem Int Ed* 52:1175–1179. <https://doi.org/10.1002/anie.201205151>
56. Kruger RA, Kuzmiak CM, Lam RB, Reinecke DR, Del Rio SP, Steed D (2013) Dedicated 3D photoacoustic breast imaging. *Med Phys* 40:113301. <https://doi.org/10.1118/1.4824317>
57. Ku G, Wang LV (2005) Deeply penetrating photoacoustic tomography in biological tissues enhanced with an optical contrast agent. *Opt Lett* 30:507. <https://doi.org/10.1364/OL.30.000507>

58. Kuchimaru T, Kadonosono T, Tanaka S, Ushiki T, Hiraoka M, Kizaka-Kondoh S (2010) In vivo imaging of HIF-active tumors by an oxygen-dependent degradation protein probe with an interchangeable labeling system. *PLoS One* 5. <https://doi.org/10.1371/journal.pone.0015736>
59. Lake MC, Aboagye EO (2014) Luciferase fragment complementation imaging in preclinical cancer studies. *Oncoscience* 1:310–325. <https://doi.org/10.18632/oncoscience.45>
60. Lavaud J, Henry M, Coll JL, Jossierand V (2017) Exploration of melanoma metastases in mice brains using endogenous contrast photoacoustic imaging. *Int J Pharm, SFNano 2016 meeting* 532:704–709. <https://doi.org/10.1016/j.ijpharm.2017.08.104>
61. Leblond F, Davis SC, Valdés PA, Pogue BW (2010) Pre-clinical whole-body fluorescence imaging: Review of instruments, methods and applications. *J Photochem Photobiol B* 98:77–94. <https://doi.org/10.1016/j.jphotobiol.2009.11.007>
62. Lee C-M, Jang D, Cheong S-J, Jeong M-H, Kim E-M, Kim DW, Lim ST, Sohn M-H, Jeong H-J (2012) Optical imaging of MMP expression and cancer progression in an inflammation-induced colon cancer model. *Int J Cancer* 131:1846–1853. <https://doi.org/10.1002/ijc.27451>
63. Lee S, Choi KY, Chung H, Ryu JH, Lee A, Koo H, Youn I-C, Park JH, Kim I-S, Kim SY, Chen X, Jeong SY, Kwon IC, Kim K, Choi K (2011) Real time, high resolution video imaging of apoptosis in single cells with a polymeric nanoprobe. *Bioconjug Chem* 22:125–131. <https://doi.org/10.1021/bc1004119>
64. Li L, Du Y, Chen X, Tian J (2018) Fluorescence molecular imaging and tomography of matrix metalloproteinase-activatable near-infrared fluorescence probe and image-guided orthotopic glioma resection. *Mol Imaging Biol* 20:930–939. <https://doi.org/10.1007/s11307-017-1158-7>
65. Li M, Oh J, Xie X, Ku G, Wang W, Li C, Lungu G, Stoica G, Wang LV (2008) Simultaneous molecular and hypoxia imaging of brain tumors in vivo using spectroscopic photoacoustic tomography. *Proc IEEE* 96:481–489. <https://doi.org/10.1109/JPROC.2007.913515>
66. Li M, Tang Y, Yao J (2018) Photoacoustic tomography of blood oxygenation: a mini review. *Photoacoustics* 10:65–73. <https://doi.org/10.1016/j.pacs.2018.05.001>
67. Li W, Chen X (2015) Gold nanoparticles for photoacoustic imaging. *Nanomedicine* 10:299–320. <https://doi.org/10.2217/nmm.14.169>
68. Li X, Schumann C, Albarqi HA, Lee CJ, Alani AWG, Bracha S, Milovancev M, Taratula Olena, Taratula Oleh (2018) A tumor-activatable theranostic nanomedicine platform for NIR fluorescence-guided surgery and combinatorial phototherapy. *Theranostics* 8:767–784. <https://doi.org/10.7150/thno.21209>
69. Lim YT, Cho MY, Noh Y-W, Chung JW, Chung BH (2009) Near-infrared emitting fluorescent nanocrystals-labeled natural killer cells as a platform technology for the optical imaging of immunotherapeutic cells-based cancer therapy. *Nanotechnology* 20:475102. <https://doi.org/10.1088/0957-4484/20/47/475102>
70. Liu Z, Liu Shuanglong, Niu G, Wang F, Liu Shuang, Chen X (2010) Optical imaging of integrin α v β 3 expression with near-infrared fluorescent RGD dimer with tetra (ethylene glycol) linkers. *Mol Imaging* 9:21–29
71. Loja MN, Luo Z, Farwell DG, Luu QC, Donald PJ, FRCS, Amott D, Truong AQ, Gandour-Edwards RF, Nitin N (2013) Optical molecular imaging detects changes in extracellular pH with the development of head and neck cancer. *Int J Cancer* 132:1613–1623. <https://doi.org/10.1002/ijc.27837>
72. Lopez A, Liao JC (2014) Emerging endoscopic imaging technologies for bladder cancer detection. *Curr Urol Rep* 15:406. <https://doi.org/10.1007/s11934-014-0406-5>
73. Lyons SK, Lim E, Clermont AO, Dusich J, Zhu L, Campbell KD, Coffee RJ, Grass DS, Hunter J, Purchio T, Jenkins D (2006) noninvasive bioluminescence imaging of normal and spontaneously transformed prostate tissue in mice. *Cancer Res* 66:4701–4707. <https://doi.org/10.1158/0008-5472.CAN-05-3598>

74. Lyons SK, Meuwissen R, Krimpenfort P, Berns A (2003) The generation of a conditional reporter that enables bioluminescence imaging of Cre/loxP-dependent tumorigenesis in mice. *Cancer Res* 63:7042–7046
75. Maguire CA, Bovenberg MS, Crommentuijn MH, Niers JM, Kerami M, Teng J, Sena-Esteves M, Badr CE, Tannous BA (2013) Triple bioluminescence imaging for in vivo monitoring of cellular processes. *Mol Therapy—Nucleic Acids* 2. <https://doi.org/10.1038/mtna.2013.25>
76. Mahmood U, Weissleder R (2003) Near-infrared optical imaging of proteases in cancer. *Mol Cancer Ther* 2:489–496
77. Mallidi S, Larson T, Tam J, Joshi PP, Karpiouk A, Sokolov K, Emelianov S (2009) Multiwavelength photoacoustic imaging and plasmon resonance coupling of gold nanoparticles for selective detection of cancer. *Nano Lett* 9:2825–2831. <https://doi.org/10.1021/nl802929u>
78. Mallidi S, Watanabe K, Timerman D, Schoenfeld D, Hasan T (2015) Prediction of tumor recurrence and therapy monitoring using ultrasound-guided photoacoustic imaging. *Theranostics* 5:289–301. <https://doi.org/10.7150/thno.10155>
79. Manohar S, Vaartjes SE, van Hespden JCG, Klaase JM, van den Engh FM, Steenbergen W, van Leeuwen TG (2007) Initial results of in vivo non-invasive cancer imaging in the human breast using near-infrared photoacoustics. *Opt Express* 15:12277–12285. <https://doi.org/10.1364/oe.15.012277>
80. Mantovani A, Allavena P, Sica A, Balkwill F (2008) Cancer-related inflammation. *Nature* 454:436–444. <https://doi.org/10.1038/nature07205>
81. Mathejczyk JE, Pauli J, Dullin C, Napp J, Tietze L-F, Kessler H, Resch-Genger U, Alves F (2011) Spectroscopically well-characterized RGD optical probe as a prerequisite for lifetime-gated tumor imaging. *Mol Imaging* 10:469–480
82. Mathejczyk JE, Pauli J, Dullin C, Resch-Genger U, Alves F, Napp J (2012) High-sensitivity detection of breast tumors in vivo by use of a pH-sensitive near-infrared fluorescence probe. *J Biomed Opt* 17:076028. <https://doi.org/10.1117/1.JBO.17.7.076028>
83. Maxwell D, Chang Q, Zhang X, Barnett EM, Piwnica-Worms D (2009) An improved cell-penetrating, caspase-activatable, near-infrared fluorescent peptide for apoptosis imaging. *Bioconjug Chem* 20:702–709. <https://doi.org/10.1021/bc800516n>
84. Meighen EA (1991) Molecular biology of bacterial bioluminescence. *Microbiol Rev* 55:123–142
85. Mezzanotte L, Que I, Kaijzel E, Branchini B, Roda A, Löwik C (2011) Sensitive dual color in vivo bioluminescence imaging using a new red codon optimized firefly luciferase and a green click beetle luciferase. *PLoS ONE* 6:e19277. <https://doi.org/10.1371/journal.pone.0019277>
86. Mieog JSD, Vahrmeijer AL, Hutteman M, van der Vorst JR, Drijfhout van Hooff M, Dijkstra J, Kuppen PJK, Keijzer R, Kaijzel EL, Que I, van de Velde CJH, Löwik CWGM (2010) Novel intraoperative near-infrared fluorescence camera system for optical image-guided cancer surgery. *Mol Imaging* 9:223–231
87. Min J-J, Nguyen VH, Kim H-J, Hong Y, Choy HE (2008) Quantitative bioluminescence imaging of tumor-targeting bacteria in living animals. *Nat Protoc* 3:629–636. <https://doi.org/10.1038/nprot.2008.32>
88. Mohs AM, Mancini MC, Singhal S, Provenzale JM, Leyland-Jones B, Wang MD, Nie S (2010) Hand-held spectroscopic device for in vivo and intraoperative tumor detection: contrast enhancement, detection sensitivity, and tissue penetration. *Anal Chem* 82:9058–9065. <https://doi.org/10.1021/ac102058k>
89. Monici M (2005) Cell and tissue autofluorescence research and diagnostic applications. In: *Biotechnology annual review*. Elsevier, pp. 227–256. [https://doi.org/10.1016/S1387-2656\(05\)11007-2](https://doi.org/10.1016/S1387-2656(05)11007-2)

90. Montet X, Figueiredo J-L, Alencar H, Ntziachristos V, Mahmood U, Weissleder R (2007) Tomographic fluorescence imaging of tumor vascular volume in mice. *Radiology* 242:751–758. <https://doi.org/10.1148/radiol.2423052065>
91. Moriichi K, Fujiya M, Okumura T (2016) The efficacy of autofluorescence imaging in the diagnosis of colorectal diseases. *Clin J Gastroenterol* 9:175–183. <https://doi.org/10.1007/s12328-016-0658-3>
92. Na I-K, Markley JC, Tsai JJ, Yim NL, Beattie BJ, Klose AD, Holland AM, Ghosh A, Rao UK, Stephan MT, Serganova I, Santos EB, Brentjens RJ, Blasberg RG, Sadelain M, van den Brink MRM (2010) Concurrent visualization of trafficking, expansion, and activation of T lymphocytes and T-cell precursors in vivo. *Blood* 116:e18–e25. <https://doi.org/10.1182/blood-2009-12-259432>
93. Napp J, Behnke T, Fischer L, Würth C, Wottawa M, Katschinski DM, Alves F, Resch-Genger U, Schäferling M (2011) Targeted luminescent near-infrared polymer-nanoprobes for in vivo imaging of tumor hypoxia. *Anal Chem* 83:9039–9046. <https://doi.org/10.1021/ac201870b>
94. Napp J, Dullin C, Müller F, Uhland K, Petri JB, van de Loch A, Steinmetzer T, Alves F (2010) Time-domain in vivo near infrared fluorescence imaging for evaluation of matriptase as a potential target for the development of novel, inhibitor-based tumor therapies. *Int J Cancer* 127:1958–1974. <https://doi.org/10.1002/ijc.25405>
95. Napp J, Stammes MA, Claussen J, Prevoo HAJM, Sier CFM, Hoeben FJM, Robillard MS, Vahrmeijer AL, Devling T, Chan AB, de Geus-Oei L-F, Alves F (2018) Fluorescence- and multispectral optoacoustic imaging for an optimized detection of deeply located tumors in an orthotopic mouse model of pancreatic carcinoma. *Int J Cancer* 142:2118–2129. <https://doi.org/10.1002/ijc.31236>
96. Niedre MJ, de Kleine RH, Aikawa E, Kirsch DG, Weissleder R, Ntziachristos V (2008) Early photon tomography allows fluorescence detection of lung carcinomas and disease progression in mice in vivo. *Proc Natl Acad Sci USA* 105:19126–19131. <https://doi.org/10.1073/pnas.0804798105>
97. Niesner RA, Hauser AE (2011) Recent advances in dynamic intravital multi-photon microscopy. *Cytometry Part A* 79A:789–798. <https://doi.org/10.1002/cyto.a.21140>
98. Nishihara R, Paulmurugan R, Nakajima T, Yamamoto E, Natarajan A, Afjei R, Hiruta Y, Iwasawa N, Nishiyama S, Citterio D, Sato M, Kim SB, Suzuki K (2019) Highly bright and stable NIR-BRET with blue-shifted coelenterazine derivatives for deep-tissue imaging of molecular events in vivo. *Theranostics* 9:2646–2661. <https://doi.org/10.7150/thno.32219>
99. Niwa K, Ichino Y, Kumata S, Nakajima Y, Hiraishi Y, Kato D, Viviani VR, Ohmiya Y (2010) Quantum yields and kinetics of the firefly bioluminescence reaction of beetle luciferases. *Photochem Photobiol* 86:1046–1049. <https://doi.org/10.1111/j.1751-1097.2010.00777.x>
100. Ntziachristos V, Ripoll J, Wang LV, Weissleder R (2005a) Looking and listening to light: the evolution of whole-body photonic imaging. *Nat Biotechnol* 23:313. <https://doi.org/10.1038/nbt1074>
101. Ntziachristos V, Turner G, Dunham J, Windsor S, Soubret A, Ripoll J, Shih HA (2005b) Planar fluorescence imaging using normalized data. *J Biomed Opt* 10:064007. <https://doi.org/10.1117/1.2136148>
102. Oh J-T, Li M-L, Zhang HF, Maslov K, Stoica G, Wang LV (2006) Three-dimensional imaging of skin melanoma in vivo by dual-wavelength photoacoustic microscopy. *J Biomed Opt* 11:034032. <https://doi.org/10.1117/1.2210907>
103. Okumura K, Yoshida K, Yoshioka K, Aki S, Yoneda N, Inoue D, Kitao A, Ogi T, Kozaka K, Minami T, Koda W, Kobayashi S, Takuwa Y, Gabata T (2018) Photoacoustic imaging of tumour vascular permeability with indocyanine green in a mouse model. *Eur Radiol Exp* 2:5. <https://doi.org/10.1186/s41747-018-0036-7>

104. Ozawa T, Yoshimura H, Kim SB (2013) Advances in fluorescence and bioluminescence imaging. *Anal Chem* 85:590–609. <https://doi.org/10.1021/ac3031724>
105. Pandey RK, James NS, Chen Y, Missert J, Sajjad M (2010) Bifunctional agents for imaging and therapy. *Methods Mol Biol* 635:223–259. https://doi.org/10.1007/978-1-60761-697-9_16
106. Perica K, Varela JC, Oelke M, Schneck J (2015) Adoptive T cell immunotherapy for cancer. *Rambam Maimonides Med J* 6. <https://doi.org/10.5041/RMMJ.10179>
107. Petrovsky A, Schellenberger E, Josephson L, Weissleder R, Bogdanov A (2003) Near-infrared fluorescent imaging of tumor apoptosis. *Cancer Res* 63:1936–1942
108. Pichorner A, Sack U, Kobelt D, Kelch I, Arlt F, Smith J, Walther W, Schlag PM, Stein U (2012) In vivo imaging of colorectal cancer growth and metastasis by targeting MACC1 with shRNA in xenografted mice. *Clin Exp Metastasis* 29:573–583. <https://doi.org/10.1007/s10585-012-9472-6>
109. Pittet MJ, Weissleder R (2011) Intravital imaging. *Cell* 147:983–991. <https://doi.org/10.1016/j.cell.2011.11.004>
110. Porcu EP, Salis A, Gavini E, Rassu G, Maestri M, Giunchedi P (2016) Indocyanine green delivery systems for tumour detection and treatments. *Biotechnol Adv* 34:768–789. <https://doi.org/10.1016/j.biotechadv.2016.04.001>
111. Rauch D, Gross S, Harding J, Niewiesk S, Lairmore M, Piwnica-Worms D, Ratner L (2009) Imaging spontaneous tumorigenesis: inflammation precedes development of peripheral NK tumors. *Blood* 113:1493–1500. <https://doi.org/10.1182/blood-2008-07-166462>
112. Revealing lymphoma growth and the efficacy of immune cell therapies using in vivo bioluminescence imaging. *Blood J* [WWW Document], n.d. <http://www.bloodjournal.org/content/101/2/640.long>. Accessed 23 May 2019)
113. Saravanakumar G, Min KH, Min DS, Kim AY, Lee C-M, Cho YW, Lee SC, Kim K, Jeong SY, Park K, Park JH, Kwon IC (2009) Hydrotropic oligomer-conjugated glycol chitosan as a carrier of paclitaxel: synthesis, characterization, and in vivo biodistribution. *J Control Release* 140:210–217. <https://doi.org/10.1016/j.jconrel.2009.06.015>
114. Sarraf-Yazdi S, Mi J, Dewhirst MW, Clary BM (2004) Use of in vivo bioluminescence imaging to predict hepatic tumor burden in mice. *J Surg Res* 120:249–255. <https://doi.org/10.1016/j.jss.2004.03.013>
115. Sevcik-Muraca EM (2012) Translation of near-infrared fluorescence imaging technologies: emerging clinical applications. *Annu Rev Med* 63:217–231. <https://doi.org/10.1146/annurev-med-070910-083323>
116. Shah K, Tung C-H, Yang K, Weissleder R, Breakefield XO (2004) Inducible release of TRAIL fusion proteins from a proapoptotic form for tumor therapy. *Cancer Res* 64:3236–3242
117. Shao X, Zheng W, Huang Z (2011) In vivo diagnosis of colonic precancer and cancer using near-infrared autofluorescence spectroscopy and biochemical modeling. *J Biomed Opt* 16:067005. <https://doi.org/10.1117/1.3589099>
118. Siphanto RI, Thumma KK, Kolkman RGM, van Leeuwen TG, de Mul FFM, van Neck JW, van Adrichem LNA, Steenbergen W (2005) Serial noninvasive photoacoustic imaging of neovascularization in tumor angiogenesis. *Opt Express* 13:89–95. <https://doi.org/10.1364/opex.13.000089>
119. Smith AM, Mancini MC, Nie S (2009) Second window for in vivo imaging. *Nat Nanotechnol* 4:710–711. <https://doi.org/10.1038/nnano.2009.326>
120. Smith BA, Xiao S, Wolter W, Wheeler J, Suckow MA, Smith BD (2011) In vivo targeting of cell death using a synthetic fluorescent molecular probe. *Apoptosis* 16:722–731. <https://doi.org/10.1007/s10495-011-0601-5>
121. Staley J, Grogan P, Samadi AK, Cui H, Cohen MS, Yang X (2010) Growth of melanoma brain tumors monitored by photoacoustic microscopy. *J Biomed Opt* 15:040510. <https://doi.org/10.1117/1.3478309>

122. Stathopoulos GT, Zhu Z, Everhart MB, Kalomenidis I, Lawson WE, Bilaceroglu S, Peterson TE, Mitchell D, Yull FE, Light RW, Blackwell TS (2006) Nuclear factor-kappaB affects tumor progression in a mouse model of malignant pleural effusion. *Am J Respir Cell Mol Biol* 34:142–150. <https://doi.org/10.1165/rcmb.2005-0130OC>
123. Stefan E, Aquin S, Berger N, Landry CR, Nyfeler B, Bouvier M, Michnick SW (2007) Quantification of dynamic protein complexes using Renilla luciferase fragment complementation applied to protein kinase a activities in vivo. *PNAS* 104:16916–16921. <https://doi.org/10.1073/pnas.0704257104>
124. Stoffels I, Morscher S, Helfrich I, Hillen U, Leyh J, Burton NC, Sardella TCP, Claussen J, Poepfel TD, Bachmann HS, Roesch A, Griewank K, Schadendorf D, Gunzer M, Klode J (2015) Metastatic status of sentinel lymph nodes in melanoma determined noninvasively with multispectral optoacoustic imaging. *Sci Trans Med* 7:317ra199–317ra199. <https://doi.org/10.1126/scitranslmed.aad1278>
125. Strijkers GJ, Kluzza E, Van Tilborg GAF, van der Schaft DWJ, Griffioen AW, Mulder WJM, Nicolay K (2010) Paramagnetic and fluorescent liposomes for target-specific imaging and therapy of tumor angiogenesis. *Angiogenesis* 13:161–173. <https://doi.org/10.1007/s10456-010-9165-1>
126. Stuker F, Ripoll J, Rudin M (2011) Fluorescence molecular tomography: principles and potential for pharmaceutical research. *Pharmaceutics* 3:229–274. <https://doi.org/10.3390/pharmaceutics3020229>
127. Sun Z, Zhao Y, Li Z, Cui H, Zhou Y, Li W, Tao W, Zhang H, Wang H, Chu PK, Yu X-F (2017) TiL4-coordinated black phosphorus quantum dots as an efficient contrast agent for in vivo photoacoustic imaging of cancer. *Small* 13:1602896. <https://doi.org/10.1002/smll.201602896>
128. Suzuki K, Kimura T, Shinoda H, Bai G, Daniels MJ, Arai Y, Nakano M, Nagai T (2016) Five colour variants of bright luminescent protein for real-time multicolour bioimaging. *Nat Commun* 7:13718. <https://doi.org/10.1038/ncomms13718>
129. Swirski FK, Berger CR, Figueiredo J-L, Mempel TR, von Andrian UH, Pittet MJ, Weissleder R (2007) A near-infrared cell tracker reagent for multiscope in vivo imaging and quantification of leukocyte immune responses. *PLoS ONE* 2:e1075. <https://doi.org/10.1371/journal.pone.0001075>
130. Szyska M, Herda S, Althoff S, Heimann A, Russ J, D'Abundo D, Dang TM, Durieux I, Dörken B, Blankenstein T, Na I-K (2018) A transgenic dual-luciferase reporter mouse for longitudinal and functional monitoring of T Cells in vivo. *Cancer Immunol Res* 6:110–120. <https://doi.org/10.1158/2326-6066.CIR-17-0256>
131. Takai A, Nakano M, Saito K, Haruno R, Watanabe TM, Ohyanagi T, Jin T, Okada Y, Nagai T (2015) Expanded palette of Nano-lanterns for real-time multicolor luminescence imaging. *PNAS* 112:4352–4356. <https://doi.org/10.1073/pnas.1418468112>
132. Themelis G, Yoo JS, Soh K-S, Schulz R, Ntziachristos V (2009) Real-time intraoperative fluorescence imaging system using light-absorption correction. *J Biomed Opt* 14:064012. <https://doi.org/10.1117/1.3259362>
133. Uhrbom L, Nerio E, Holland EC (2004) Dissecting tumor maintenance requirements using bioluminescence imaging of cell proliferation in a mouse glioma model. *Nat Med* 10:1257. <https://doi.org/10.1038/nm1120>
134. Valdés PA, Leblond F, Kim A, Harris BT, Wilson BC, Fan X, Tosteson TD, Hartov A, Ji S, Erkmann K, Simmons NE, Paulsen KD, Roberts DW (2011) Quantitative fluorescence in intracranial tumor: implications for ALA-induced PpIX as an intraoperative biomarker. *J Neurosurg* 115:11–17. <https://doi.org/10.3171/2011.2.JNS101451>
135. Valluru KS, Willmann JK (2016) Clinical photoacoustic imaging of cancer. *Ultrasonography* 35:267–280. <https://doi.org/10.14366/usg.16035>

136. van Dam GM, Themelis G, Crane LMA, Harlaar NJ, Pleijhuis RG, Kelder W, Sarantopoulos A, de Jong JS, Arts HJG, van der Zee AGJ, Bart J, Low PS, Ntziachristos V (2011) Intraoperative tumor-specific fluorescence imaging in ovarian cancer by folate receptor- α targeting: first in-human results. *Nat Med* 17:1315–1319. <https://doi.org/10.1038/nm.2472>
137. van der Horst G, van Asten JJ, Figdor A, van den Hoogen C, Cheung H, Bevers RFM, Pelger RCM, van der Pluijm G (2011) Real-time cancer cell tracking by bioluminescence in a preclinical model of human bladder cancer growth and metastasis. *Eur Urol* 60:337–343. <https://doi.org/10.1016/j.eururo.2011.05.005>
138. Vangestel C, Peeters M, Mees G, Oltenfreiter R, Boersma HH, Elsinga PH, Reutlingsperger C, Van Damme N, De Spiegeleer B, Van de Wiele C (2011) In vivo imaging of apoptosis in oncology: an update. *Mol Imaging* 10:340–358. <https://doi.org/10.2310/7290.2010.00058>
139. Vaupel P, Mayer A (2007) Hypoxia in cancer: significance and impact on clinical outcome. *Cancer Metastasis Rev* 26:225–239. <https://doi.org/10.1007/s10555-007-9055-1>
140. von Burstin J, Eser S, Seidler B, Meining A, Bajbouj M, Mages J, Lang R, Kind AJ, Schnieke AE, Schmid RM, Schneider G, Saur D (2008) Highly sensitive detection of early-stage pancreatic cancer by multimodal near-infrared molecular imaging in living mice. *Int J Cancer* 123:2138–2147. <https://doi.org/10.1002/ijc.23780>
141. Wang X, Xie X, Ku G, Wang LV, Stoica G (2006) Noninvasive imaging of hemoglobin concentration and oxygenation in the rat brain using high-resolution photoacoustic tomography. *JBO* 11:024015. <https://doi.org/10.1117/1.2192804>
142. Wang Y, Lin T, Zhang W, Jiang Y, Jin H, He H, Yang VC, Chen Y, Huang Y (2015) A Prodrug-type, MMP-2-targeting nanoprobe for tumor detection and imaging. *Theranostics* 5:787–795. <https://doi.org/10.7150/thno.11139>
143. Weber J, Beard PC, Bohndiek SE (2016) Contrast agents for molecular photoacoustic imaging. *Nat Methods* 13:639–650. <https://doi.org/10.1038/nmeth.3929>
144. Weissleder R (2001) A clearer vision for in vivo imaging. *Nat Biotechnol* 19:316. <https://doi.org/10.1038/86684>
145. Weissleder R, Pittet MJ (2008) Imaging in the era of molecular oncology. *Nature* 452:580–589. <https://doi.org/10.1038/nature06917>
146. Woolfenden S, Zhu H, Charest A (2009) A Cre/LoxP conditional luciferase reporter transgenic mouse for bioluminescence monitoring of tumorigenesis. *Genesis* 47:659–666. <https://doi.org/10.1002/dvg.20545>
147. Wu T, Qu J, Cheung T-H, Lo K, Yu M-Y (2003) Preliminary study of detecting neoplastic growths in vivo with real time calibrated autofluorescence imaging. *Opt Express* 11:291–298. <https://doi.org/10.1364/oe.11.000291>
148. Xu M, Wang LV n.d. Photoacoustic imaging in biomedicine. *Rev Sci Instrum* 23
149. Yang Y, Zhang Y, Hong H, Liu G, Leigh BR, Cai W (2011) In vivo near-infrared fluorescence imaging of CD105 expression during tumor angiogenesis. *Eur J Nucl Med Mol Imaging* 38:2066–2076. <https://doi.org/10.1007/s00259-011-1886-x>
150. Yeh H-W, Karmach O, Ji A, Carter D, Martins-Green MM, Ai H (2017) Red-shifted luciferase-luciferin pairs for enhanced bioluminescence imaging. *Nat Methods* 14:971–974. <https://doi.org/10.1038/nmeth.4400>
151. Zhang HF, Maslov K, Stoica G, Wang LV (2006) Functional photoacoustic microscopy for high-resolution and noninvasive in vivo imaging. *Nat Biotechnol* 24:848–851. <https://doi.org/10.1038/nbt1220>
152. Zhang L, Lee KC, Bhojani MS, Khan AP, Shilman A, Holland EC, Ross BD, Rehemtulla A (2007) Molecular imaging of Akt kinase activity. *Nat Med* 13:1114–1119. <https://doi.org/10.1038/nm1608>

153. Zheng X, Wang X, Mao H, Wu W, Liu B, Jiang X (2015) Hypoxia-specific ultrasensitive detection of tumours and cancer cells in vivo. *Nat Commun* 6:5834. <https://doi.org/10.1038/ncomms6834>
154. Zhou L, Wang W, Dicker DT, Humphreys RC, El-Deiry WS (2011) Prediction of proapoptotic anticancer therapeutic response in vivo based on cell death visualization and TRAIL death ligand-receptor interaction. *Cancer Biol Ther* 12:335–348. <https://doi.org/10.4161/cbt.12.4.17174>

Joanna Napp studied biology at the Nicolaus Copernicus University in Torun, Poland. She did her Ph.D. at the Max-Planck-Institute (MPI) of Experimental Medicine and the European Neuroscience Institute in Goettingen. In 2006, she joined the Translational Molecular Imaging Group of Frauke Alves, established at the MPI and at the University Medical Center Goettingen (UMG). In 2015, she started her research group Image-based Nanotherapy and Diagnostics at the UMG, supported with a guest-scientist position at the MPI. She has specialized in the *in vivo* imaging of animal disease models, particularly focusing on development and evaluation of novel tumor therapies.

Andrea Markus received her degree in biology from the Johannes Gutenberg University, Mainz. Following her Ph.D. in 1998 at the Helmholtz Center in Munich, she moved to Australia, where she worked for many years in molecular biology of cancer at the University of Sydney. In 2010, she returned to Germany and took up a position at the Department of Hematology/Oncology at the University Medicine Göttingen and then at the Max-Planck Institute for Experimental Medicine in the group of Translational Molecular Imaging.

Frauke Alves received 2009 her professorship in Internal Medicine. As a clinician she developed a thorough bench to bedside approach in the cancer field by heading a tandem research group at the University Medical Center and the Max-Planck-Institute for Experimental Medicine, Goettingen. The focus of her interdisciplinary group is the development and preclinical evaluation of novel therapeutic concepts and diagnostic procedures in oncology and inflammatory lung diseases by applying molecular imaging strategies. She established a small animal imaging platform that includes *in vivo* technologies such as x-ray based—and optical imaging, as well as *ex-vivo* imaging methods such as high resolution phase contrast CT and two-photon microscopy.



Sonja Schelhaas

Contents

14.1 Introduction.....	493
14.2 Challenges of Small Animal PET.....	494
14.3 Tumor Characterization.....	498
14.4 Evaluation of Therapy Response.....	500
14.5 Therapy Development.....	501
14.6 Multimodal PET Imaging.....	503
14.7 Conclusion.....	504
References.....	504

14.1 Introduction

Specific accumulation of radioactive tracers can provide insights into physiological processes within a body. Even more meaningful information can be gathered when radioactivity is assessed in a tomographic manner, which also provides information on tumor heterogeneity. These imaged processes comprise functional, metabolic, cellular, and molecular activities. These data can be obtained in a longitudinal manner, enabling evaluation of changes over time. Nuclear medicine approaches to do so comprise single-photon emission computed tomography (SPECT) and positron emission tomography (PET). Both of these methods are already widely used in the field of oncology in the clinical scenario. However, preclinical studies are indispensable for developing new imaging paradigms and understanding the biology underlining specific processes, as preclinical setups harbor potentials of

S. Schelhaas (✉)

European Institute for Molecular Imaging, University of Münster, Waldeyerstr. 15,
48149 Münster, Germany
e-mail: sonja.schelhaas@uni-muenster.de

image validation by *ex vivo* analyses. Those are only exceptional in the clinical situation. Here, we will focus on small animal PET. Aspects covering preclinical SPECT are described in the chapter “Preclinical SPECT and SPECT-CT”.

PET relies on exogenous application of a positron-emitting substance. During the radioactive decay, a proton is converted to a neutron, while also a positron (e^+) is released. The positron undergoes an annihilation reaction with a nearby electron (e^-), resulting in the emission of two high-energy photons (γ -rays, 511 keV each) which are emitted in exactly opposing directions. The simultaneous detection (within a few nanoseconds) of this pair of photons by the detector allows the determination of the line of incidence (also called line of response) facilitating the reconstruction of the source of radioactivity. The degree of the two emitted photons is not always exactly 180° , based on the residual momentum of the positron and the electron at the time of annihilation. This non-collinearity ($\pm 0.25^\circ$) and also the fact that the positron particles travel a certain distance in tissue before the annihilation reaction (positron range, depending on the radionuclide and its energy spectrum) lead to limitations in the maximal achievable spatial resolution [10, 30].

There is no depth limitation in the detection of γ -rays. The half-life of the isotopes used for PET can differ from minutes (e.g., ^{15}O : 2 min, ^{11}C : 20 min) to hours (^{68}Ga : 68 min, ^{18}F : 110 min) or days (^{124}I : 4.2 d). Importantly, PET provides a very high detection sensitivity down to picomolar concentrations—which is about two to three orders of magnitude higher than for SPECT [39]. Hence, the amount of the radioactive substances applied is very low (tracer principle), and there is almost no interference with normal regular processes underlying the tracer accumulation or the body physiology.

In this chapter, we will give an overview of small animal PET imaging with regard to (i) challenges, and its applications in oncology in the fields of (ii) tumor characterization, (iii) therapy response evaluation, and (iv) therapy development.

14.2 Challenges of Small Animal PET

There are several aspects that have to be considered when applying small animal PET imaging, especially with respect to potential transfer of results to humans. First of all, the size of animal models is smaller than the size of humans. This bears technical challenges, as a spatial resolution of ~ 1 cm, which is usually achieved with clinical scanners, is not suitable to image processes within mice or rats. For this need, dedicated small animal PET cameras have been developed, which have a spatial resolution of ~ 1 mm [58]. One example of a small animal PET scanner is depicted in Fig. 14.1.

The reduced blood volume of rodent models in comparison to humans also has implication on the volume that can be injected into the animal. These volumes are generally regulated by national institutions, such as the USDA in the US or the GV-SOLAS in Germany. Especially in the context of small animal PET imaging, this is of importance. The half-life of the radiotracers employed for PET is in general

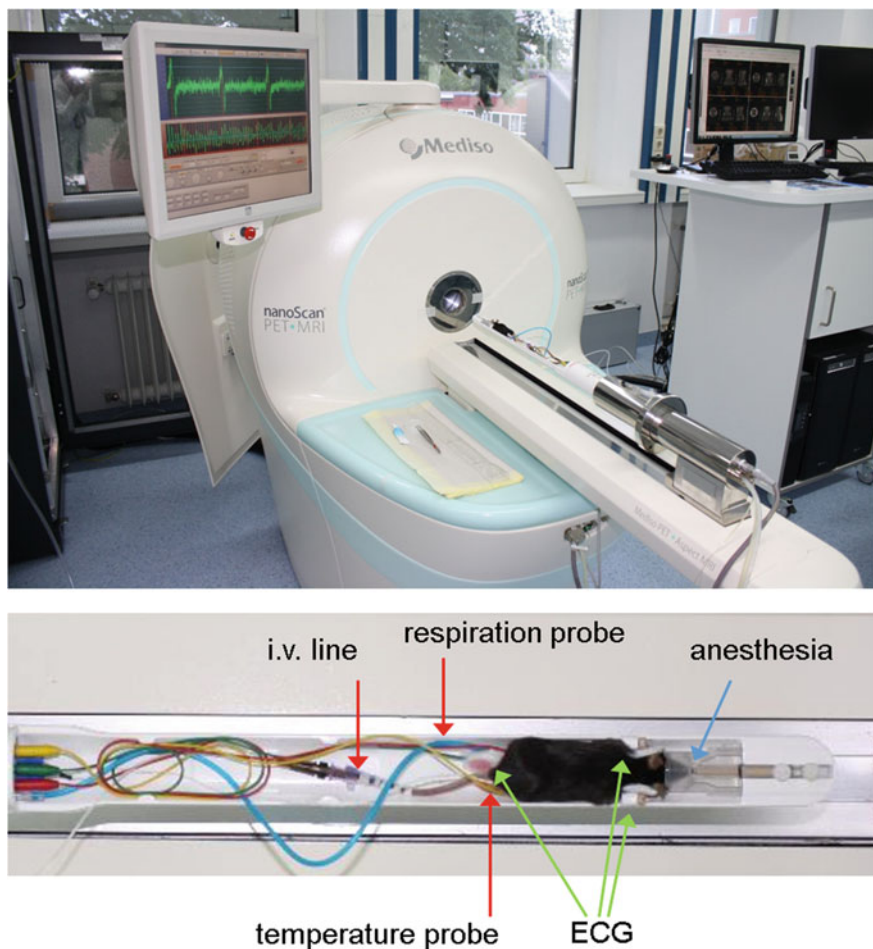


Fig. 14.1 Example of a small animal PET camera and a respective animal cradle. Depicted is a combined PET/MR system. Most modern preclinical PET cameras allow arrangement of the narcotized mouse on an animal bed equipped with respiration, heartbeat (ECG), and temperature control

relatively short. Due to the radioactive decay, the amount of the tracer might have to be increased for animals injected at a later time point. This does not only affect the total volume, which can impact pharmacology or physiology, but also the amounts of solvents like ethanol increase, potentially resulting in undesirable side effects.

Upon that, breathing and heart rate, as well as metabolism differ between humans and rodents. Consequently, the distribution of radioactive tracers might differ between species. The biodistribution of 3'-Deoxy-3'- ^{18}F -Fluorothymidine (^{18}F -FLT) may serve as an example. This thymidine analog visualizes cellular

proliferation. Due to differences in thymidine levels in blood as well as in thymidine metabolism, the biodistribution of ^{18}F -FLT also differs. For example, accumulation of ^{18}F -FLT in the liver is low in dogs compared to humans [47] and the biodistribution in mice was reported to vary in different strains [32]. This does not imply that results obtained in animals cannot be transferred to patients. However, species-specific differences might have to be considered.

To obtain sufficient PET image quality, image acquisition has to occur in the range of minutes. While this is no issue in adult patients, which can lie still in a scanner for this period of time, this is a challenge in small animal imaging. There are approaches to perform PET imaging in awake rodents [62]. However, in general, the animals are immobilized by means of narcosis. The narcotic agent can potentially interfere with blood flow, tissue oxygenation, body temperature, and metabolism of an organism and hence with the distribution of a tracer. This has been well studied with ^{18}F -FDG. For instance, warming of anesthetized animals diminishes accumulation of this tracer in brown fat tissue [16], and the choice of narcosis affects insulin levels. This in turn regulates blood glucose concentrations and consequently ^{18}F -FDG uptake [27]. Figure 14.2 shows a mouse undergoing an

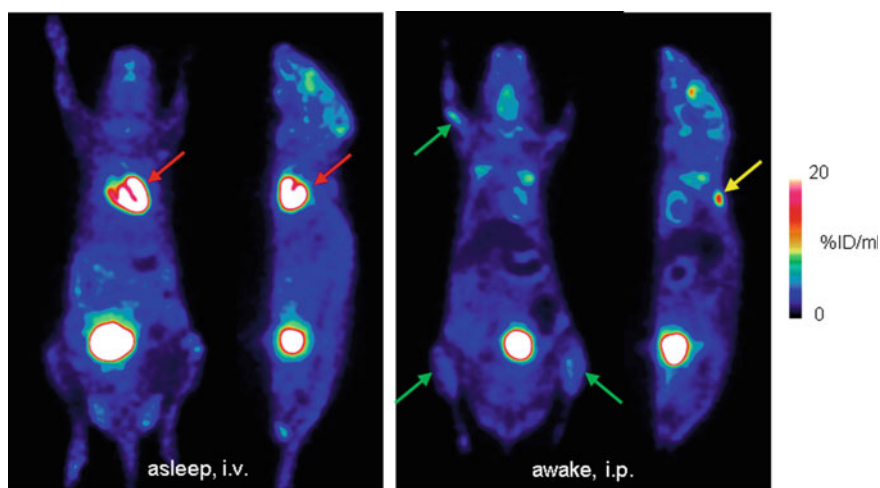


Fig. 14.2 Choice of narcosis affects distribution of ^{18}F -FDG in a C57/BL6 mouse. Images show two ^{18}F -FDG PET studies of the same mouse where each PET acquisition was performed under isoflurane narcosis 50–60 min after injection of 10 MBq ^{18}F -FDG. In the first example (left panel), ^{18}F -FDG injection and biodistribution took place under isoflurane anesthesia, while the mouse was positioned on a heating mat. In the second example (right panel), ^{18}F -FDG was injected intraperitoneally (i.p.) in an awake mouse. Coronal and sagittal planes focusing on the heart are shown here. Note the increased ^{18}F -FDG uptake of the myocardium under isoflurane narcosis (red arrows), resulting from altered glucose metabolism and effects of the narcotic agents on perfusion [11]. Brown fat (yellow arrow) is not visible in the PET images if the mouse was warmed during the tracer uptake period [16]. The increased activity of skeletal muscles of awake mice is reflected by increased ^{18}F -FDG uptake (green arrows)

^{18}F -FDG PET scan under different narcotic conditions. These data show that it is important to carefully consider animal handling conditions and keep them constant during the course of an experiment. Also, hypothermia of the animals must be avoided and fasting can be an important issue when dealing with ^{18}F -FDG.

A further issue that has to be considered when performing preclinical PET is radiation exposure, especially when serial imaging in combination with CT is performed. The whole-body dose of a single PET scan is in the range of 0.06–0.9 Gy for mice and 0.01–0.27 Gy for rats [17]. Radiation doses resulting from CT scans highly depend on the instrument settings and range from 0.017 Gy–0.78 Gy [8]. These values are not negligible, taking into account that the lethal dose for 50% of a population 30 d after whole-body irradiation ($\text{LD}_{50/30}$) is in the range of 5 Gy for mice [19]. Exact values vary with mouse strain and age. Gene expression can already be altered with doses as low as 0.2 Gy [2]. Hence, effects of PET/CT imaging on experimental outcome cannot be excluded.

The setup of the infrastructure for small animal PET imaging might be challenging. This method requires positron-emitting isotopes. Hence, especially when using short-lived radiotracers, a nearby cyclotron and the respective radiochemistry have to be localized in close proximity. Furthermore, the equipment is very expensive, and there is a need for the setup of a radioactive control area. Last but not least, the logistics of the animals might be a hurdle, especially when performing longitudinal studies. Many research institutes are depending on a central animal facility. Due to hygiene and in general legislative restrictions, and also due to radiation limits, transport of animals back to this central facility is not always possible. Consequently, adequate animal housing might have to be implemented within the institution.

One additional hurdle in small animal PET imaging is the choice of the animal model. As it is a model, it is in itself artificial and can resemble the situation in a human being only to a limited extent. One also has to keep in mind that therapies that address issues of the host organism, such as vascularization or the immune system, might act differently in rodents and other animals. For oncology research, there exist various mouse tumor models [13, 41]. Most commonly, xenograft models are used. For these, tumor cells, mostly originating from human cancers, are cultivated *in vitro* and transferred to an immunocompromised mouse, either ectopically (mostly subcutaneously), orthotopically (in the usual position, like gliomas in the brain), or systemically. These tumors are less heterogeneous than patient cancer tissues. However, this also makes animal experiments more reproducible than results obtained from more heterogeneous samples. Moreover, the cell lines can be genetically modified, enabling the evaluation of the importance of specific genes for tumor development or tracer accumulation. The microenvironment of tumor xenografts does not quite resemble the clinical situation, especially in the case of subcutaneous tumor implantation. Patient-derived xenograft (PDX) models, which are directly originating from clinical tumor samples, are supposed to more closely resemble the heterogeneity observed in patients. For most of these models, the use of immunocompromised mice is necessary, as the host immune system would successfully fight the cancer. Allografts (cells derived from

the same species) can be implanted in a similar manner, and the host can be immunocompetent.

In the clinical scenario, the potential of malignant tumors to spread and form metastases is in general associated with a poor prognosis. The differentiation level of metastasized tumor cells often differs from the primary tumor, thereby complicating the choice of an adequate therapy. To mimic and investigate the metastatic behavior of tumors in a preclinical setting is challenging. Injection of tumor cells into the bloodstream does not resemble metastasis-initiating steps. When working with primary tumors, these are in general growing so fast that the animal has to be sacrificed before metastases are detectable. One possible approach is to surgically remove the primary tumor and follow the metastases in the upcoming weeks [6]. There also exists a range of genetic engineered mouse models (GEMMs) of cancer in immunocompetent mice. In many instances, these more closely resemble the nature of human cancers, ranging from tumor initiating steps to metastasis formation [25].

14.3 Tumor Characterization

Assessment of tumor biology is a crucial step in understanding the disease and developing novel therapies. What is the vascularization state? Is there an overexpression of a specific antigen? These questions might arise and be of fundamental importance for the success of a diagnostic or therapeutic approach. Consequently, characterization of a tumor in a non-invasive manner by means of PET can provide information on metabolic modifications of a cancer over time and can aid in deciding for a treatment paradigm. Especially when employing multiple modalities, profiling of a tumor is possible. In general, features of cancers, which could potentially be imaged, are mostly related to the hallmarks of cancers, as summarized by Hanahan and Weinberg [20].

In the clinical setting, PET imaging does have a prominent role in detection, diagnosis, and staging of tumors. For preclinical models, tumor detection and follow up in itself might be of less value than in the clinic, as in most instances the localization is known, and the size itself can be assessed by more easily accessible methods, such as CT. However, tracers used for clinical cancer diagnostics do in one way or another also provide information on characteristics of tumors.

The rate of aerobic glycolysis in tumors is generally high due to the Warburg effect [51, 53]. Hence, tumors make use of glucose from the extracellular space and consequently take up glucose analogs, such as fluorodeoxyglucose (^{18}F -FDG). ^{18}F -FDG is the most commonly used PET tracer for clinical molecular imaging and has applications in detection, staging, and therapy response assessment. Also in the preclinical setting, it has been used for the analysis of tumor engraftment or metastasis detection. Figure 14.3 shows ^{18}F -FDG PET images of a mouse with subcutaneous tumors. PET visualizes the growth of the tumor over time in terms of metabolic tumor volume (MTV), which parallels tumor volumes as assessed by

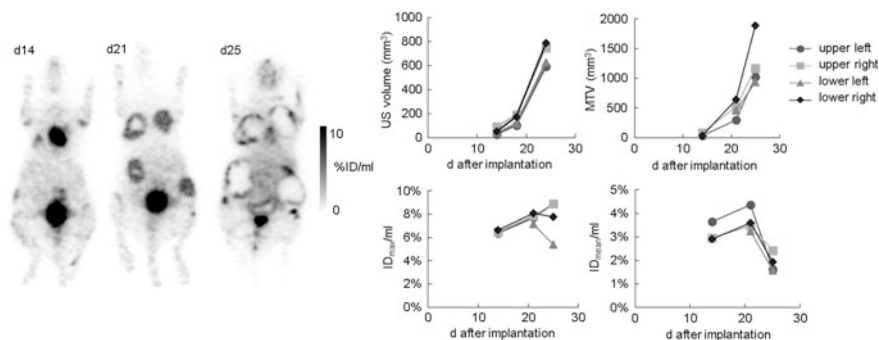


Fig. 14.3 ^{18}F -FDG PET imaging to monitor tumor growth. Coronal planes of ^{18}F -FDG PET images of a nude mouse harboring four subcutaneous U87 glioblastomas are shown here at different days (d) after tumor implantation. Tumor volumes as measured by ultrasound (US) are increasing during the course of time, which is also reflected in the metabolic tumor volume (MTV) assessed on the PET images. The amount of central necrosis visible on the PET images is increasing during tumor growth, resulting in decreasing mean radiotracer uptake

ultrasound (US). In this experimental setup, maximal tracer uptake (expressed as percent injected dose: $\%ID_{\text{max}}/\text{ml}$) is mostly unaffected by tumor growth, while average tracer uptake in the tumor (here expressed as $\%ID_{\text{mean}}/\text{ml}$) is decreasing with increasing tumor size. The latter is related to an increase in necrosis within the tumors, which is visible on the PET images. Hence, these data show that the mode of data analysis should be wisely chosen.

Not only (anaerobic) glycolysis, but many metabolism pathways are deregulated in cancers. Consequently, a range of tracers have been developed to visualize processes such as amino acid transport (L-[methyl- ^{11}C]methionine (^{11}C -MET) or *O*-(2-[^{18}F]fluoroethyl)-L-tyrosine (^{18}F -FET)), fatty acid synthesis (^{11}C -acetate), membrane phospholipid synthesis (^{11}C -choline), or proliferation (^{18}F -FLT) [31, 54].

The vasculature is of crucial importance for delivery of nutrients and oxygen to tissues. In the case of tumor development, as soon as the tumor reaches a size of a few millimeters, there is a need for the development of new vasculature, which is characterized by increased permeability, increased vessel diameter, and delayed maturation [4]. As angiogenesis might be an attractive target for tumor therapy, there is a need to non-invasively monitor the angiogenic state of a tumor. Key regulators are $\alpha_v\beta_3$ integrins and the vascular endothelial growth factor (VEGF). $\alpha_v\beta_3$ integrins are upregulated during angiogenesis. Small peptides containing an arginine-glycine-aspartic acid (RDG) sequence are ligands of $\alpha_v\beta_3$ and might serve as lead structures for $\alpha_v\beta_3$ targeting tracers, such as ^{18}F -FRGD2 [61]. Also, radiolabeled VEGF has been successfully employed to monitor the vascularization in a preclinical setup [7]. The perfusion itself can be assessed by tracers like H_2^{15}O [3].

Vascularization has an impact on the oxygen level within tumors. Oxygen consumption of tumors is generally high, whereas the oxygen supply might be low, potentially resulting in hypoxic conditions within a tumor. Hypoxia is associated

with tumor aggressiveness, risk of metastasis formation, or treatment resistance [49]. Hence, imaging of hypoxia might be helpful for tumor characterization and therapy decisions. ^{18}F -labeled nitroimidazoles are reduced to reactive intermediary species binding to intracellular proteins in hypoxic cells. ^{18}F -FMISO (^{18}F -fluoromisonidazole) is the most widely used hypoxia imaging agent, which accumulates in tissue when $p\text{O}_2 < 10$ mm Hg [36].

Characterization of a tumor by means of PET can be helpful in patient stratification. In a recently published study, Sun et al. designed a radiotracer (*N*-(3-chloro-4-fluorophenyl)-7-(2-(2-(^{18}F -fluoroethoxy) ethoxy) ethoxy) ethoxy)-6-methoxyquinazolin-4-amine, ^{18}F -MPG) that targets a specific mutation in the epidermal growth factor receptor (EGFR). Non-small cell lung cancer models with varying mutations in this receptor showed comparable accumulation of ^{18}F -FDG, whereas uptake of ^{18}F -MPG was in line with the specific EGFR mutation and with response to treatment with the tyrosine kinase inhibitor gefitinib in lung cancer. After this successful preclinical validation, the authors demonstrated that this tracer facilitates clinical treatment decisions [48].

14.4 Evaluation of Therapy Response

PET has the potential to monitor therapeutic effects, ideally before morphological changes in tumor volume are visible. This is because PET can directly visualize processes within a cancer that ultimately can result in a rest in tumor growth or even a morphological shrinkage of the tumor. These processes include tumor proliferation, cell death, and energy metabolism. Therapies might target cells outside a cancer such as the vascularization or immune cells that can also be visualized by PET. Hence, looking beyond the tumor might also provide information on therapeutic effects.

The most widely used PET tracer ^{18}F -FDG has successfully been applied in a range of preclinical studies monitoring therapy response [23]. Reduction in glucose metabolism appears to be a good predictor for treatment response, also in the clinical setting. However, uptake of this tracer is not tumor-specific, as it also accumulates in inflammatory lesions. Tumor therapies can cause massive cell death, which in turn initiates an inflammatory response similar to a wound-healing process [40]. These recruited immune cells might result in a transient increase in ^{18}F -FDG uptake, masking a potential reduction of the glycolytic activity of the tumor [5, 18]. Hence, there is a need for more tumor-specific tracers to evaluate treatment response.

Many tumor therapies have an anti-proliferative effect. Hence, visualization of tumor proliferation is an approach that can be applied to a range of treatment strategies. One of the key steps in tumor cell proliferation is the synthesis of novel DNA strands. Consequently, radiolabeled DNA building blocks might be employed for imaging proliferation. As thymidine is exclusive for DNA (and not RNA), it can be employed for imaging of tumor proliferation. While ^{11}C -thymidine has only a

short half-life and is rapidly degraded in vivo, 3'-deoxy-3-¹⁸F-fluorothymidine (¹⁸F-FLT) shows superior imaging qualities. It has been used in a range of pre-clinical and clinical studies, demonstrating a reduction in tracer uptake after therapy in line with treatment response and/or changes in immunohistochemical markers of proliferation [44]. However, when therapeutic agents interfere with the thymidine de novo pathway [28, 42] or compete with thymidine for cellular uptake [46], changes in tracer uptake are uncoupled from changes in proliferation. This demonstrates that a detailed understanding of the mechanism of tracer and drug accumulation is indispensable for an understanding of treatment-induced changes in PET images. Especially this detailed understanding can be gained with preclinical analyses, as imaging findings can easily be corroborated by ex vivo analyses. This is not only true for changes within the solid tumor. Proliferation might also be affected in hematopoietic organs (bone marrow and spleen). Many therapies exert a transient myelosuppressive effect. This effect, and subsequent recovery, is visible on ¹⁸F-FLT PET scans, not only in the preclinical setting [45], but also in the clinical scenario [29]. Hence, one should also pay attention to regions outside of the tumor, as the whole-body imaging method PET can show a whole lot more than a single lesion.

Tumor therapy often induces apoptosis, a form of cell death, which is accompanied by a range of morphological and biochemical alterations, such as phosphatidylserine (PS) externalization, caspase-3 activation, DNA degradation, and cellular shrinkage. These targets harbor potential for molecular imaging. When imaging caspase activation, the tracer has to be able to cross the cell membrane, due to the intracellular localization of the target. Isatin-5-sulfonamide (¹⁸F-ICMT11) is one example of a PET radiotracer targeting activated caspase-3 [34]. Alterations occurring on the cell surface of cells undergoing apoptosis can be detected, e.g., with 2-(5-fluoro-pentyl)-2-methyl-malonic acid (¹⁸F-ML-10) [14] or with radiolabeled annexin V [38, 57]. However, reports on treatment monitoring with cell death tracers are limited, implying that this is a field that needs further improvement.

14.5 Therapy Development

What is the anatomical distribution of a specific therapeutic agent? Does it accumulate within a primary tumor or metastases? Next to the therapy-induced impact on the tumor biology, these are questions that can potentially be answered by PET and they are of special interest in preclinical evaluations of novel treatment approaches.

Drug delivery systems, like liposomes or nanoparticles, can be designed in a way to contain a PET radioisotope [9]. Drugs might also be directly labeled with a radionuclide. ¹¹C-labeling of DNA-intercalating agents was helpful in preclinical evaluation of the most promising candidates for future clinical applications [35]. Mathematical modeling of tissue distribution from dynamic PET scans can provide further information on free concentrations or clearance from plasma to tissue [33].

However, blood concentration (plasma input function) of the radiotracer has to be known for accurate quantitative analysis, usually derived from arterial blood sampling, which is challenging in rodents due to their limited blood volume. Image-derived input functions can serve as an alternative.

When analyzing the distribution of a radiolabeled drug, one has to keep in mind that the radiolabel might affect the drug in terms of activity, affinity, or pharmacokinetics. Moreover, the distribution within a body also depends on the concentration of a specific agent. Hence, larger concentrations than tracer amounts are necessary for reliable predictions.

Also, cells might be used for the therapy of cancers. For instance, stem cells can be employed to deliver therapeutic agents [12, 60]. Non-invasive detection and tracking of these applied cells can provide information on the accumulation of the cells and therewith the therapeutic agent. For all cell tracking approaches, it is crucial to verify that the labeling does not interfere with the mode of action of the cells. For instance, proliferation or activation patterns can potentially be altered. These issues have to be evaluated beforehand, which is usually done by *in vitro* assays. Cell tracking also holds great promise for immunotherapies, which employ the host immune system to detect and fight the cancer. This approach might make use of cells that are infused into the subject (adoptive cell transfer). These cells can be visualized by PET by different means [15, 59]. They can be labeled directly with a radioactive agent, such as ^{64}Cu -pyruvaldehyde-bis(N4-methylthiosemicarbazone) (^{64}Cu -PTSM) [1] or ^{89}Zr -Oxine [43]. These approaches are relatively easy and straightforward. However, they have the drawback that the cells can only be tracked for a limited period of time, due to the limited radioactive half-life of the tracers. But even when employing long-lived radioactive isotopes, the radioactivity can leak out of the cells and will be diluted when cells are dividing.

Specific tracers can also aid in visualizing cells. These tracers might target cell surface-specific molecules, e.g., ^{64}Cu -radiolabeled anti-CD4 and anti-CD8 cys-diabodies targeting T cells [50] or radiolabeled interleukin-2 (IL-2) targeting the corresponding IL-2 receptor (CD25) highly expressed on activated T cells [21].

The use of reporter genes is an alternative approach to visualize externally transfused cells. For this purpose, the cells have to be genetically manipulated to express the respective gene, which triggers the accumulation of radiotracers. This gene might code either for an enzyme (such as herpes simplex virus thymidine kinase (HSV-TK) accumulating 9-(4- ^{18}F -fluoro-3-hydroxymethylbutyl)guanine (^{18}F -FHBG)), a transporter (e.g., sodium iodide transporter, NIS, accumulating ^{18}F -tetrafluoroborate (^{18}F -BF₄)), or a receptor (e.g., dopamine D2 receptor, accumulating 3-(2'- ^{18}F -fluoroethyl)spiperone (^{18}F -FESP)) [56].

Reporter gene approaches can also be applied in the context of gene therapies. For this purpose, DNA encoding for a therapeutic gene is combined with a DNA encoding for an imaging gene. Hence, cells expressing the gene of interest can be visualized by imaging. By this means, it can be evaluated if the gene therapy vector reaches its target specifically and the gene delivery protocol can be optimized in

terms of route of application, timing, or dosing [52]. In a theranostic approach, Jacobs et al. showed that HSV-TK expression as determined by ^{18}F -FHBG PET correlates with glioma response to ganciclovir therapy, a prodrug activated by HSV-TK [22]. The imaging gene, as well as the therapeutic gene, can also be controlled by regulatory elements, allowing visualization of specific inducible processes [55].

14.6 Multimodal PET Imaging

One of the major drawbacks of PET is the fact that no morphological information is provided by this method, making the localization of signals challenging. For this reason, PET is often performed in combination with computer tomography (CT). Upon that, (pre)clinical PET-MR scanners are on the rise. The morphological information can aid in the definition of regions of interest (ROIs) used for quantification and facilitate the exact measurement of organ sizes. CT and MR can not only provide information on anatomy, but they can also aid in attenuation or motion correction and also report on other molecular processes, such as cell death, as described in detail in the respective chapters. This complementary information not only stands for its own, but a direct overlay of these images provides useful information on tumor biology. By performing simultaneous PET-MRI, the group of Pichler demonstrated that areas of high ^{18}F -FLT overlap with areas of fast contrast agent enrichment in T1-weighted MR images, representing viable tumor regions as identified by immunohistochemistry [24]. Moreover, coregistration of PET and MR images acquired in the same imaging session allows for voxel-wise comparison of the data obtained by these two modalities as demonstrated in Fig. 14.4. PET has recently also been used in combination with ultrafast ultrasound, allowing the simultaneous coregistration of tumor vasculature with metabolism during tumor growth [37].

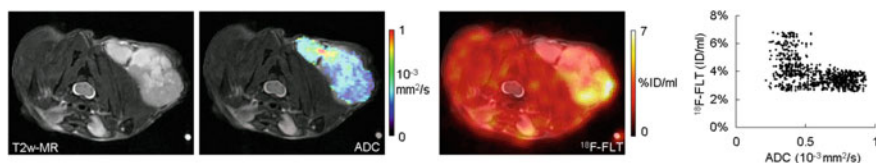


Fig. 14.4 Coregistration of PET and MR images allows identification of relationships between the different modalities on a voxel-wise basis. T2-weighted MR image (left panel) allows detection of a subcutaneous Colo-205 tumor implanted subcutaneously on the right shoulder in a CD1 nude mouse on an anatomical level. The apparent diffusion coefficient (ADC) determined by diffusion-weighted MRI shows variability of water diffusion, as an indicator of cell death. In this tumor, ADC negatively correlates with proliferation determined by ^{18}F -FLT PET (Pearson correlation coefficient = -0.50 , $P < 0.0001$)

14.7 Conclusion

As the incidence of oncological diseases is on the rise, due to the increasing age of our population, there is a need for a mechanistic understanding of the processes underlying tumor development and therapies. PET imaging is a valuable tool to non-invasively and longitudinally monitor tumors and treatment-induced changes on a functional level, facilitating personalized cancer therapies. Preclinical experiments are helpful in defining novel imaging or therapy approaches, especially as in vivo results can be corroborated by ex vivo analyses. There is still a need for improved animal models, better reflecting the situation in patients. The future in preclinical PET imaging will most likely be largely influenced by advances in (automated) image analysis, comprising also the analysis of advanced features by means of radiomics [26] and the mathematical modeling in a holistic approach (systems biology).

References

1. Adonai N, Nguyen KN, Walsh J et al (2002) Ex vivo cell labeling with ^{64}Cu -pyruvaldehyde-bis(N4-methylthiosemicarbazone) for imaging cell trafficking in mice with positron-emission tomography. *Proc Natl Acad Sci* 99:3030–3035
2. Amundson SA, Bittner M, Meltzer P et al (2001) Induction of gene expression as a monitor of exposure to ionizing radiation. *Radiat Res* 156:657–661
3. Beaney RP, Lammertsma AA, Jones T et al (1984) Positron emission tomography for in-vivo measurement of regional blood flow, oxygen utilisation, and blood volume in patients with breast carcinoma. *Lancet (London, England)* 1:131–134
4. Bergers G, Benjamin LE (2003) Tumorigenesis and the angiogenic switch. *Nat Rev Cancer* 3:401–410
5. Brepoels L, Stroobants S, Verhoef G et al (2009) $(^{18}\text{F})\text{-FDG}$ and $(^{18}\text{F})\text{-FLT}$ uptake early after cyclophosphamide and mTOR inhibition in an experimental lymphoma model. *J Nucl Med* 50:1102–1109
6. Bulk E, Hascher A, Liersch R et al (2008) Adjuvant therapy with small hairpin RNA interference prevents non-small cell lung cancer metastasis development in mice. *Cancer Res* 68:1896–1904
7. Cai W, Chen K, Mohamedali KA et al (2006) PET of vascular endothelial growth factor receptor expression. *J Nucl Med* 47:2048–2056
8. Carlson SK, Classic KL, Bender CE, Russell SJ (2007) Small animal absorbed radiation dose from serial micro-computed tomography imaging. *Mol Imaging Biol* 9:78–82
9. Chakravarty R, Hong H, Cai W (2014) Positron emission tomography image-guided drug delivery: current status and future perspectives. *Mol Pharm* 11:3777–3797
10. Cherry SR (2004) In vivo molecular and genomic imaging: new challenges for imaging physics. *Phys Med Biol* 49:R13–R48
11. Cicone F, Viertl D, Quintela Pousa AM et al (2017) Cardiac radionuclide imaging in rodents: a review of methods, results, and factors at play. *Front Med* 4:35
12. Corsten MF, Shah K (2008) Therapeutic stem-cells for cancer treatment: hopes and hurdles in tactical warfare. *Lancet Oncol* 9:376–384
13. de Jong M, Essers J, van Weerden WM (2014) Imaging preclinical tumour models: improving translational power. *Nat Rev Cancer* 14:481–493

14. Demirci E, Ahmed R, Ocak M et al (2017) Preclinical evaluation of 18F-ML-10 to determine timing of apoptotic response to chemotherapy in solid tumors. *Mol Imaging* 16:1536012116685941
15. Fruhwirth GO, Kneilling M, de Vries IJM et al (2018) The potential of in vivo imaging for optimization of molecular and cellular anti-cancer immunotherapies. *Mol Imaging Biol* 20:696–704
16. Fueger BJ, Czernin J, Hildebrandt I et al (2006) Impact of animal handling on the results of 18F-FDG PET studies in mice. *J Nucl Med* 47:999–1006
17. Funk T, Sun M, Hasegawa BH (2004) Radiation dose estimate in small animal SPECT and PET. *Med Phys* 31:2680–2686
18. Graf N, Herrmann K, Nummerger B et al (2013) [18F]FLT is superior to [18F]FDG for predicting early response to antiproliferative treatment in high-grade lymphoma in a dose-dependent manner. *Eur J Nucl Med Mol Imaging* 40:34–43
19. Grahn D, Hamilton KF (1957) Genetic variation in the acute lethal response of four inbred mouse strains to whole body X-irradiation. *Genetics* 42:189–198
20. Hanahan D, Weinberg RA (2011) Hallmarks of cancer: the next generation. *Cell* 144:646–674
21. Hartimath SV, Draghiciu O, van de Wall S et al (2017) Noninvasive monitoring of cancer therapy induced activated T cells using [18 F]FB-IL-2 PET imaging. *Oncoimmunology* 6: e1248014
22. Jacobs AH, Rueger MA, Winkeler A et al (2007) Imaging-guided gene therapy of experimental gliomas. *Cancer Res* 67:1706–1715
23. Jensen MM, Kjaer A (2015) Monitoring of anti-cancer treatment with (18)F-FDG and (18) F-FLT PET: a comprehensive review of pre-clinical studies. *Am J Nucl Med Mol Imaging* 5:431–456
24. Judenhofer MS, Wehrl HF, Newport DF et al (2008) Simultaneous PET-MRI: a new approach for functional and morphological imaging. *Nat Med* 14:459–465
25. Kersten K, de Visser KE, van Miltenburg MH, Jonkers J (2017) Genetically engineered mouse models in oncology research and cancer medicine. *EMBO Mol Med* 9:137–153
26. Lambin P, Rios-Velazquez E, Leijenaar R et al (2012) Radiomics: extracting more information from medical images using advanced feature analysis. *Eur J Cancer* 48:441–446
27. Lee K-H, Ko B-H, Paik J-Y et al (2005) Effects of anesthetic agents and fasting duration on 18F-FDG biodistribution and insulin levels in tumor-bearing mice. *J Nucl Med* 46:1531–1536
28. Lee SJ, Kim SY, Chung JH et al (2010) Induction of thymidine kinase 1 after 5-fluorouracil as a mechanism for 3'-deoxy-3'-[18F]fluorothymidine flare. *Biochem Pharmacol* 80:1528–1536
29. Leimgruber A, Moller A, Everitt SJ et al (2014) Effect of platinum-based chemoradiotherapy on cellular proliferation in bone marrow and spleen, estimated by 18F-FLT PET/CT in patients with locally advanced non-small cell lung cancer. *J Nucl Med* 55:1075–1080
30. Levin CS, Hoffman EJ (1999) Calculation of positron range and its effect on the fundamental limit of positron emission tomography system spatial resolution. *Phys Med Biol* 44:781–799
31. Lewis DY, Soloviev D, Brindle KM (2015) Imaging tumor metabolism using positron emission tomography. *Cancer J* 21:129–136
32. Mankoff DA, Shields AF, Krohn KA (2005) PET imaging of cellular proliferation. *Radiol Clin North Am* 43:153–167
33. Matthews PM, Rabiner EA, Passchier J, Gunn RN (2012) Positron emission tomography molecular imaging for drug development. *Br J Clin Pharmacol* 73:175–186
34. Nguyen Q-D, Challapalli A, Smith G et al (2012) Imaging apoptosis with positron emission tomography: 'Bench to bedside' development of the caspase-3/7 specific radiotracer [18F] ICMT-11. *Eur J Cancer* 48:432–440
35. Osman S, Rowlinson-Busza G, Luthra SK et al (2001) Comparative biodistribution and metabolism of carbon-11-labeled N-[2-(dimethylamino)ethyl]acridine-4-carboxamide and DNA-intercalating analogues. *Cancer Res* 61:2935–2944
36. Padhani AR, Krohn KA, Lewis JS, Alber M (2007) Imaging oxygenation of human tumours. *Eur Radiol* 17:861–872

37. Provost J, Garofalakis A, Sourdon J et al (2018) Simultaneous positron emission tomography and ultrafast ultrasound for hybrid molecular, anatomical and functional imaging. *Nat Biomed Eng* 2:85–94
38. Qin H, Zhang M-R, Xie L et al (2015) PET imaging of apoptosis in tumor-bearing mice and rabbits after paclitaxel treatment with (18)F(-)-Labeled recombinant human His10-annexin V. *Am J Nucl Med Mol Imaging* 5:27–37
39. Rahmim A, Zaidi H (2008) PET versus SPECT: strengths, limitations and challenges. *Nucl Med Commun* 29:193–207
40. Rock KL, Kono H (2008) The inflammatory response to cell death. *Annu Rev Pathol* 3:99–126
41. Ruggeri BA, Camp F, Miknyoczki S (2014) Animal models of disease: Pre-clinical animal models of cancer and their applications and utility in drug discovery. *Biochem Pharmacol* 87:150–161
42. Saito Y, Furukawa T, Arano Y et al (2008) Comparison of semiquantitative fluorescence imaging and PET tracer uptake in mesothelioma models as a monitoring system for growth and therapeutic effects. *Nucl Med Biol* 35:851–860
43. Sato N, Wu H, Asiedu KO et al (2015) ⁸⁹Zr-Oxine Complex PET cell imaging in monitoring cell-based therapies. *Radiology* 275:490–500
44. Schelhaas S, Heinzmann K, Bollineni VR, et al (2017) Preclinical applications of 3'-deoxy-3'-[¹⁸F]fluorothymidine in oncology - A systematic review. *Theranostics* 7(1):40–50
45. Schelhaas S, Held A, Bäumer N et al (2016a) Preclinical evidence that 3'-deoxy-3'-[¹⁸F]fluorothymidine PET can visualize recovery of hematopoiesis after gemcitabine chemotherapy. *Cancer Res* 76(24):7089–7095
46. Schelhaas S, Held A, Wachsmuth L et al (2016b) Gemcitabine mechanism of action confounds early assessment of treatment response by 3'-Deoxy-3'-[¹⁸F]fluorothymidine in preclinical models of lung cancer. *Cancer Res* 76(24):7096–7105
47. Shields AF, Grierson JR, Dohmen BM et al (1998) Imaging proliferation in vivo with [F-18]FLT and positron emission tomography. *Nat Med* 4:1334–1336
48. Sun X, Xiao Z, Chen G et al (2018) A PET imaging approach for determining EGFR mutation status for improved lung cancer patient management. *Sci Transl Med* 10:eaan8840
49. Tatum JL, Kelloff GJ, Gillies RJ et al (2006) Hypoxia: importance in tumor biology, noninvasive measurement by imaging, and value of its measurement in the management of cancer therapy. *Int J Radiat Biol* 82:699–757
50. Tavaré R, McCracken MN, Zettlitz KA et al (2015) Immuno-PET of murine T cell reconstitution postadoptive stem cell transplantation using anti-CD4 and Anti-CD8 Cys-diabodies. *J Nucl Med* 56:1258–1264
51. Vander Heiden MG, Cantley LC, Thompson CB (2009) Understanding the Warburg effect: the metabolic requirements of cell proliferation. *Science* 324:1029–1033
52. Waerzeggers Y, Monfared P, Viel T et al (2009) Methods to monitor gene therapy with molecular imaging. *Methods* 48:146–160
53. Warburg O, Wind F, Negelein E (1927) The metabolism of tumors in the body. *J Gen Physiol* 8:519–530
54. Wester H-J (2007) Nuclear imaging probes: from bench to bedside. *Clin Cancer Res* 13:3470–3481
55. Winkler A, Sena-Esteves M, Paulis LEM et al (2007) Switching on the lights for gene therapy. *PLoS ONE* 2:e528
56. Yaghoubi SS, Campbell DO, Radu CG, Czernin J (2012) Positron emission tomography reporter genes and reporter probes: gene and cell therapy applications. *Theranostics* 2:374–391
57. Yagle KJ, Eary JF, Tait JF et al (2005) Evaluation of 18F-annexin V as a PET imaging agent in an animal model of apoptosis. *J Nucl Med* 46:658–666
58. Yao R, Lecomte R, Crawford ES (2012) Small-animal PET: what is it, and why do we need it? *J Nucl Med Technol* 40:157–165

59. Zeelen C, Paus C, Draper D et al (2018) In-vivo imaging of tumor-infiltrating immune cells: implications for cancer immunotherapy. *Q J Nucl Med Mol Imaging* 62:56–77
60. Zhang C-L, Huang T, Wu B-L et al (2017) Stem cells in cancer therapy: opportunities and challenges. *Oncotarget* 8:75756–75766
61. Zhang X, Xiong Z, Wu Y et al (2006) Quantitative PET imaging of tumor integrin alphavbeta3 expression with 18F-FRGD2. *J Nucl Med* 47:113–121
62. Zhou VW, Kyme AZ, Meikle SR, Fulton R (2008) An event-driven motion correction method for neurological PET studies of awake laboratory animals. *Mol Imaging Biol* 10:315–324



Jasmin Baier, Anne Rix, and Fabian Kiessling

Contents

15.1	Introduction.....	510
15.2	Ultrasound Contrast Agents	511
15.2.1	Microbubbles	511
15.2.2	Liposomes.....	512
15.2.3	Nanobubbles	513
15.2.4	Phase-Change Nanodroplets.....	513
15.3	Active and Passive Targeting.....	513
15.4	Ligands for Molecular CEUS	514
15.5	Detection of Targeted Contrast Agents	515
15.5.1	Dwell-Time Imaging	516
15.5.2	Destruction-Replenishment Imaging	517
15.5.3	Sensitive Particle Acoustic Quantification (SPAQ).....	517
15.6	Preclinical Applications.....	518
15.6.1	Imaging Angiogenesis	518
15.6.2	Further Molecular Targets.....	521
15.6.3	Nanobubbles and Nanoparticles for Preclinical Molecular Ultrasound Imaging	523
15.7	Clinical Application.....	524
15.8	Targeted Ultrasound-Mediated Drug Delivery	524
	References	526

J. Baier · A. Rix · F. Kiessling (✉)

Institute for Experimental Molecular Imaging Organization University Clinics, RWTH Aachen University, Forckenbeckstrasse 55 52074 Aachen, Germany

e-mail: fkiessling@ukaachen.de

J. Baier

e-mail: jbaier@ukaachen.de

A. Rix

e-mail: arix@ukaachen.de

15.1 Introduction

Ultrasound is a cost-effective imaging technology that offers high spatial resolution, portability, and lack of irradiation [19]. The most commonly used ultrasound contrast agents for functional and molecular contrast-enhanced ultrasound (CEUS) are microbubbles. They consist of an echogenic gas core encapsulated by a stabilizing shell of proteins, lipids, or biopolymers [35]. Next to microbubbles, nano-sized contrast agents like liposomes, nanobubbles, and phase-changing nano-droplets are described. For molecular CEUS, contrast agents are decorated with site-specific ligands, such as antibodies or peptides [39] to examine receptor expression of a specific marker [77]. The ligands can be attached directly to the microbubble shell either covalently or by use of a spacer. Another alternative is the biotin–avidin binding system, which is often preferred in preclinical applications as any biotinylated ligand can be attached just by mixing with streptavidin-coated microbubbles. However, they cannot be used in humans due to their high immunogenic potential [48].

After intravenous injection, molecular microbubbles bind to their specific target and can be detected in the late-phase enhancement. For quantification of the molecular signal, several techniques were developed like the destruction-replenishment, sensitive particle acoustic quantification (SPAQ), and dwell-time imaging.

Since microbubbles are not able to extravasate from the vascular system due to their size of 1–8 μm , target receptors for molecular CEUS have to be present in the tumor vasculature [35]. In tumor imaging, the most common markers for molecular CEUS are related to neoangiogenesis and include the vascular endothelial growth factor receptor-2 (VEGFR2) and $\alpha_v\beta_3$ integrin. Besides angiogenesis, intravascular targets related to inflammation can be assessed, like E-selectin, Thy-1, and B7-H3. Numerous preclinical studies confirm the ability of molecular ultrasound to detect angiogenesis and inflammation, to longitudinally monitor receptor expression during tumor growth, and to assess therapy responses. Recently, the first VEGFR2-targeted phospholipid microbubble agent was applied in clinical trials. Promising results were obtained regarding patient safety and the detection of malignant lesions in the prostate, ovary, and breast.

Finally, ultrasound contrast agents can be used as drug delivery systems to increase the drug accumulation in tumors. The application of ultrasound pulses facilitates triggered drug release from the contrast agent. Furthermore, sonopermeabilization and sonopermeation of the tissue enable a better accumulation of drugs in the tumor.

The present chapter introduces the composition of different ultrasound contrast agents and explains how they can be modified to enable molecular imaging. Furthermore, multiple preclinical and clinical applications with regard to tumor imaging are described. In the final part, the use of ultrasound contrast agents as theranostics is discussed.

15.2 Ultrasound Contrast Agents

In the late 1980s, first attempts were made to image blood vessels in tumors with color Doppler ultrasound [4]. However, for detailed investigations of microvessels, Doppler ultrasound is limited since slow blood velocities cannot be assessed at clinically applied frequencies and frame rates. To overcome this limitation, the blood contrast can be enhanced by contrast agents [16]. Ultrasound contrast agents create a distinct acoustic impedance mismatch with surrounding tissues, resulting in an increased ultrasound reflection [39]. For molecular ultrasound investigations, the contrast agent is decorated with a site-specific ligand. Although microbubbles are the most commonly used ultrasound contrast agent class with a size of 1–8 μm , they are not able to leave the vasculature. As a consequence, only targets inside the blood vessels can be reached. Therefore, nano-sized contrast agents like liposomes, nanoparticles, nanodroplets, and nanobubbles have been designed and evaluated for functional and molecular ultrasound imaging (Fig. 15.1). However, their detection with conventional ultrasound methods is often much more difficult due to their lower acoustic reflectivity [19].

15.2.1 Microbubbles

The first contrast agents for ultrasound imaging were free air bubbles produced by agitation of saline solution to generate contrast in ultrasound examinations only of the right heart, as these bubbles were not able to cross the pulmonary capillary bed [37]. The encapsulation with a stabilizing shell protects the microbubbles from immediate destruction in the lungs and, therefore, facilitates CEUS in the whole

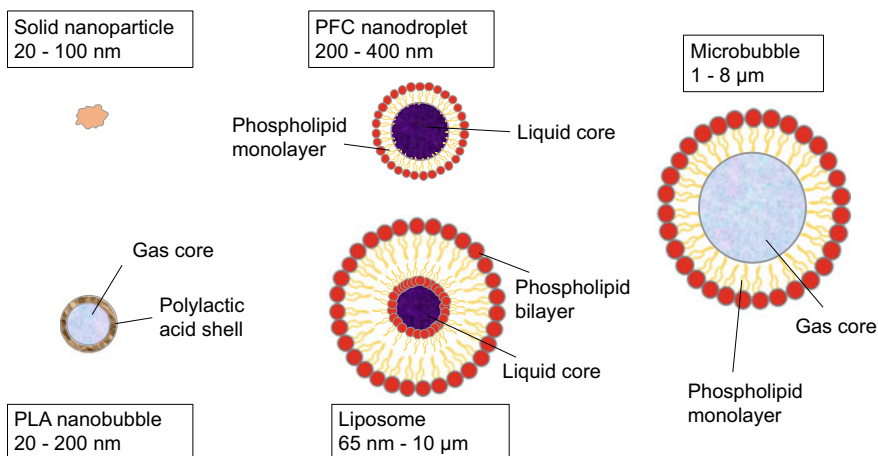


Fig. 15.1 Different types of ultrasound contrast agents

body. Furthermore, the shell can be engineered to prevent gas leakage and aggregation [19], optimize pharmacokinetic properties [35], and enable ligand attachment [27, 54]. Depending on the chemical composition of the shell, microbubbles can be divided into soft-shell and hard-shell microbubbles.

Soft-shell microbubbles usually consist of a thin palmitic acid or lipid monolayer. In this regard, Levovist® are air-filled microbubbles stabilized by a matrix of galactose and palmitic acid. The contact with blood plasma dissolves the galactose matrix and releases palmitic acid-coated microbubbles [37]. Phospholipid microbubbles represent the most used type of contrast agent for ultrasound imaging. They can be easily produced and enable the incorporation of different lipid headgroups or post-production bioconjugation [36]. In this regard, additional polyethylene glycol (PEG) coatings were reported to further prevent microbubble aggregation (Deshpande et al. 2010). Furthermore, they have a good stability and echogenicity, and several phospholipid-based contrast agents are approved for clinical use [37].

In comparison to soft-shell microbubbles, hard-shell microbubbles consist of a stiffer shell made out of proteins or polymers. Protein-based microbubbles are produced by sonication of heat-denatured proteins, mostly albumin [36]. Next to proteins, hard-shell microbubbles can be produced by cross-linking of polylactide-derived or cyanoacrylate polymers. They have a very high in vivo stability and provide a higher echogenicity in high-intensity ultrasound applications [49].

The echogenic gas core of microbubbles is composed of air or perfluorochemicals (PFCs) like perfluorobutane, perfluoropropane [17], or octafluoropropane [37]. Since the PFC gas core is hardly water-soluble and not metabolized in the body, it enhances the stability of the microbubbles and prolongs their circulation time from seconds to minutes compared to air-filled microbubbles [35].

Independently of their composition, microbubbles typically have a size of 1–8 μm and are, therefore, not able to leave the vascular system. This can be advantageous on the one hand, as they do not accumulate unspecifically in the interstitial space. On the other hand, the application of targeted microbubbles is restricted to molecules present in the vasculature [35].

15.2.2 Liposomes

Echogenic liposomes (ELIPs) for contrast-enhanced ultrasound examinations have a size range of 65–10 μm [24]. They consist of a lipid bilayer made of phosphatidylcholine (PC), cholesterol, phosphatidylethanolamine (PE), or phosphatidylglycerol (PG) [30], and an aqueous core [59]. Their echogenicity is enabled by various air inclusions in the bilayer [59]. In general, liposomes with higher saturated lipids emit a longer ultrasound signal than those with unsaturated lipids. ELIPs can be used as drug delivery systems by enclosing hydrophilic or lipophilic drugs inside the ELIPs that can be released at the desired target site after ultrasound stimulation [33].

15.2.3 Nanobubbles

Nanobubbles have a diameter of less than 1 μm . They typically consist of a polymer or phospholipid shell, stabilized by tensides, and a core that can be gaseous (e.g., perfluorocarbons) [79], liquid or solid [72]. Although nanobubbles can be used to detect targets outside the vasculature, they still have a poor in vivo stability [79], and they are too big to easily overcome biological barriers. One method to increase their stability without affecting their flexibility is the incorporation of a cross-linked polymer to phospholipid-based nanobubbles in order to reduce the gas core diffusion [52].

15.2.4 Phase-Change Nanodroplets

Phase-change nanodroplets have a size of 200 nm–1 μm [46], can leave the vasculature, and are suitable tracers for the lymphatic duct [73]. They are usually made out of a perfluorocarbon or perfluoropentane core [46] with an organic or inorganic shell (e.g., PLGA) [73, 79]. Nanodroplets can be synthesized from commercially available micron-sized particles through condensation with increased surrounding pressure or decreased temperature [79]. Phase-change nanodroplets keep their shape and size (diameter) until they are exposed to a high-energy pulse induced by ultrasound waves. In their liquid state, they are almost invisible to ultrasound imaging [25]. After the pulse, the droplets change their state from liquid to a gaseous phase, vaporize into microbubbles, and can then be detected by ultrasound [79].

15.3 Active and Passive Targeting

The retention of an ultrasound contrast agent at a target site can be induced by passive and active targeting strategies [18]. In this regard, passive targeting describes the retention of contrast agents at a target site due to their physico-chemical properties. One modification to enable passive targeting can be the incorporation of negatively charged phosphatidylserine in the shell of phospholipid microbubbles to promote attachment to activated leukocytes [44]. Here, instead of directly targeting inflammation-related markers, the leukocyte adhesion to activated endothelium is detected (Fig. 15.2a) [18]. Passive targeting can be used for the detection of vascular inflammation regarding plaques or thrombi as well as for the detection of sentinel lymph nodes or liver lesions [18].

For active targeting (Fig. 15.2b), the shell of the contrast agent needs to be decorated with a ligand. The ligand, e.g., a peptide or antibody, is attached to the surface of the contrast agent via covalent or non-covalent bonds [39]. Afterwards, the microbubble can bind to specific receptors [19, 34].

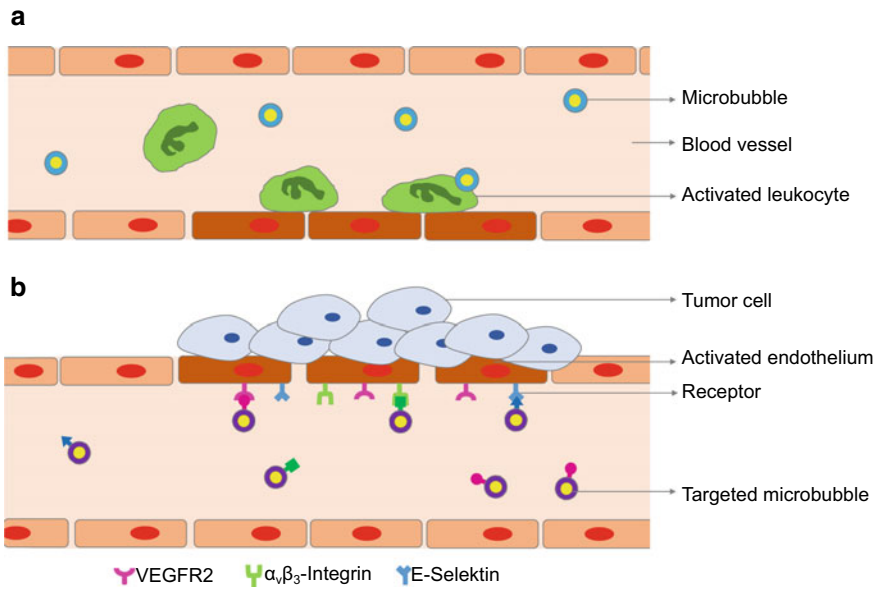


Fig. 15.2 Passive and active targeting strategies, **a** Passive targeting of inflammation with microbubbles binding to activated leukocytes **b** Active microbubble targeting of receptors that are overexpressed on activated tumor endothelium

15.4 Ligands for Molecular CEUS

Ligands for molecular CEUS should have a high target specificity and affinity as well as high mechanical and chemical stability. Furthermore, no immune or physiological reactions should be induced by the modified contrast agent [18].

Ligands can be attached either non-covalently or covalently. One of the most popular and strongest non-covalent coupling strategies is the avidin–biotin interaction. Avidin, a 66 kD glycoprotein, is bound to the microbubble shell facilitating the attachment of any biotinylated ligand [36] (Fig. 15.3a). Advantages of this

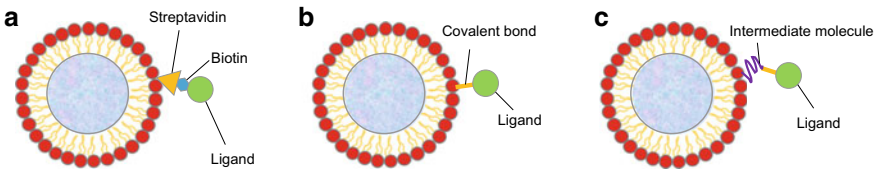


Fig. 15.3 Strategies for the attachment of binding moieties to the microbubble surface. **a** Binding of a biotinylated targeting ligand to streptavidin on the microbubble surface, **b** Covalent binding of the targeting ligand to the microbubble, **c** Covalent binding of the targeting ligand to an intermediate molecule at the microbubble surface

technique are the high stability and selectivity of the biotin–avidin bond and the high application flexibility as many molecules are available in a biotinylated form [37]. However, due to the high immunogenicity of (strep)avidin in patients, its use is restricted to preclinical applications [23].

The preparation of targeted contrast agents for clinical use can be achieved by covalently binding the ligand to the microbubble surface (Fig. 15.3b). In this regard, proteins are most commonly coupled to a free carboxyl or maleimide group on the microbubble surface. Through chemical activation, the carboxyl group forms an active ester, which in turn reacts with a ligand amino group, resulting in an amide bond. Since the amide bond can lead to random binding of the targeting moiety to the microbubbles and thus, to reduced targeting efficacy, maleimide groups are preferred for covalent bonds. Therefore, a thiol group of the ligand is coupled to a free maleimide group on the microbubble shell via thioether bonds resulting in directed coupling, which enables a high microbubble affinity to the targeted receptor [65].

To further increase the binding efficiency of targeted microbubbles, a polyethylene glycol (PEG) spacer arm can be used to create a distance between the ligand and the microbubble shell of up to 30 nm (Fig. 15.3c). Furthermore, the use of an intermediate spacer improves microbubble adhesion and retention at the receptor as shown for BR55 microbubbles [65].

The most commonly used ligands for molecular ultrasound imaging are antibodies and peptides [12, 30]. Antibodies are available for many intravascular targets [6]. Especially monoclonal antibodies from the immunoglobulin- γ (IgG) family have been used for cell surface receptor targeting [23]. However, their production is cost-intensive, and they carry the risk of being immunogenic [23]. Alternatively, affibodies can be used as targeting moieties. These small, synthetically produced proteins derive from the immunoglobulin G-binding domain of protein A and belong to the class of antibody mimetics. They have proven promising as targeting moieties of nanobubbles and nanoparticles, to which they were conjugated via biotin–avidin or covalent bonds [72]. Peptides are an even smaller and cheaper alternative, and in particular the RGD sequence, generating probe specificity to $\alpha_v\beta_3$ integrin, has been popular in the molecular imaging field. Table 15.1 provides an overview of the most commonly used molecular CEUS contrast agents and their shell and core composition.

15.5 Detection of Targeted Contrast Agents

A prerequisite for sensitive ultrasound contrast agent detection is a high contrast to the tissue background. Compared with other ultrasound contrast agents, microbubbles have the highest acoustic impedance difference to their surrounding tissue and therefore can be detected with highest sensitivity [12]. Ultrasound pulses with a low mechanical index and alternating positive and negative pressure cause the microbubbles to contract and expand. This oscillation is non-linear, and the

Table 15.1 Most commonly used molecular CEUS contrast agent compositions

Category	Shell	Filling	Ligand	Target
Microbubbles	Streptavidin-coated lipid shell	Perfluorocarbon	Antibody	$\alpha_v\beta_3$ integrin VEGFR2 [61]
	Streptavidin-coated lipid shell	Perfluorocarbon	Peptide	$\alpha_v\beta_3$ integrin [70]
	Streptavidin-coated PBCA	Air	Antibody	$\alpha_v\beta_3$ integrin [50]
	PBCA	Air	Peptide	E-selectin [62]
	Albumin, avidin	Perfluoropropane	Antibody	Endoglin [38]
	Lipids (DSPC, DSPE, PEG2K)	Perfluorobutane	Peptide	Nucleolin [76]
	Lipids (PEG)	Perfluorobutane	Antibody	SFRP2 [64]
Nanobubbles	Lipids (PEG)	Octafluoropropane	Antibody	CA-125 [29]
Liposome	Lipids and Rhodamine	Deionized water and air inclusions	Antibody	ICAM-1 [31]
PCD (Phase-change droplets)	Lipids	Perfluoropentane	Folate (Vitamin)	Folate receptor [46]
GGNPs (Gas-generating nanoparticles)	PLGA	CaCO ₃	Peptide	Neuroblastoma [40]

resulting microbubble-specific signal can be determined by harmonic imaging, respectively, contrast-specific scan modes [1]. The general modes of microbubble detection are described in Chap. 4. The present chapter focuses on the detection and quantification of bound microbubbles for molecular imaging.

Except for dwell-time imaging, molecular imaging is usually performed 5–10 min after microbubble injection, when most of the microbubbles are bound to the target and freely circulating microbubbles are almost cleared from the bloodstream [35].

15.5.1 Dwell-Time Imaging

A nearly real-time method for the detection of bound microbubbles was introduced by Pysz et al. in 2012 and relies on the measurement of the microbubbles dwell time in the acoustic field [55]. First, a baseline value is acquired for each pixel in the area of interest before microbubble injection. Then, the change of acoustic intensities after microbubble injection is measured over a defined time period. Microbubbles are considered as bound if their detected signal is present for more than 80% of the acquisition time at the same location. Then, the percent coverage area is determined, that is, the percentage of voxels in the field of view, where a bound microbubble was present [55].

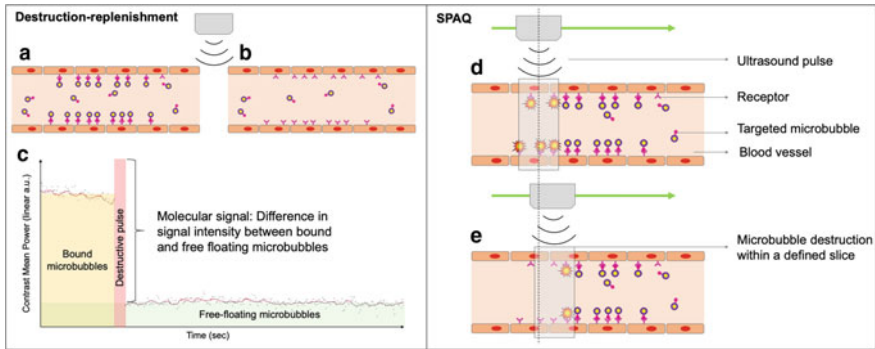


Fig. 15.4 Destruction-replenishment microbubble detection. Signal intensity difference before (a) and after (b) a destructive pulse represents signal from bound microbubbles (c); SPAQ: Initially microbubbles are destroyed in a broad slice (d), while destruction of microbubbles in subsequent measurements only occurs in the non-overlapping volume defined by the step size (e)

15.5.2 Destruction-Replenishment Imaging

The destruction-replenishment technique was introduced in 1998 by Wei and colleagues [68] for the quantification of tissue perfusion [7]. For signal quantification of bound microbubbles, two sets of real-time images are needed. The first set is taken in the late-phase enhancement, approximately 5–10 min after the microbubble injection [35]. Here, the detected signal results from the tissue, bound and remaining freely circulating microbubbles. Subsequently, an ultrasound pulse with a high mechanical index (MI) is applied [7], which leads to fragmentation of all microbubbles in the acoustic window (Fig. 15.4). The acquisition of a second set of images, recorded directly after the destructive pulse, detects the signal from the tissue and freely circulating microbubbles reperfusing the tumor. The signal intensity (SI) of bound microbubbles is then indicated by the difference between the mean SI of the first set of images and the mean SI of the second set of images [35].

15.5.3 Sensitive Particle Acoustic Quantification (SPAQ)

Sensitive particle acoustic quantification (SPAQ) is a 3D technique that was introduced in 2005 by Reinhardt et al. and is able to quantify microbubbles within a whole tumor [57]. For SPAQ, the transducer has to be moved in a defined step size over the tumor during a destructive Doppler scan [35]. The destruction of microbubbles generates a strong non-linear signal, known as loss of correlation, which is interpreted as a strong movement and detected by Doppler imaging. The first destructive pulse destroys microbubbles in a broad slice, while in the following measurements only destruction of microbubbles in the non-overlapping volume defined by the step size is detected (Fig. 15.4). With SPAQ, a quantification of

bound microbubbles in a whole tumor volume is possible, which makes the approach particularly suitable to characterize tumors with a heterogeneous receptor expression [36].

15.6 Preclinical Applications

Molecular targets for ultrasound imaging using microbubbles must be located on the endothelium, as microbubbles are not able to leave the vasculature due to their size of 1–8 μm . Furthermore, the target expression on the endothelium should be low under physiological conditions, whereas pathological alterations, like tumor growth, should lead to an upregulation of the target molecule. Several targets of angiogenesis and inflammation have been identified and tested for molecular ultrasound imaging.

15.6.1 Imaging Angiogenesis

Angiogenesis, one of the hallmarks of cancer [28], describes the formation of new vessels from previously existing vessels. Physiologically, angiogenesis plays a crucial role in embryogenesis and is essential for wound healing. The fact that in most tissues angiogenesis is almost absent makes it a promising target for tumor detection and characterization.

15.6.1.1 Vascular Endothelial Growth Factor Receptor 2

The most prominent marker in molecular ultrasound imaging of tumor angiogenesis is the vascular endothelial growth factor receptor-2 (VEGFR2). The binding of vascular endothelial growth factor to VEGFR2 leads to activation of a signaling cascade, which results in the enhancement of endothelial proliferation and migration [14]. In various preclinical molecular ultrasound studies, VEGFR2 targeting has been successfully used to specifically and sensitively detect angiogenesis in tumor models, e.g., of pancreas [56], colon [6, 66], ovary [11, 71], prostate [63], and breast [3, 8] in various animal species including mouse [8, 56, 71], rat [63], or hens [11].

Next to the detection of tumor angiogenesis, molecular ultrasound imaging targeting VEGFR2 enables a discrimination of differently aggressive breast cancer subtypes [13]. In this regard, Bzyl and coworkers compared highly aggressive, estrogen-independent (MDA-MB-231) and low-aggressive, estrogen-dependent (MCF-7) breast cancer xenografts by functional and molecular ultrasound imaging. The degree of vascularization and angiogenesis measured by ultrasound imaging was in accordance with results obtained by immunofluorescence analyses. Importantly, it was found that the molecular information regarding angiogenesis discriminated both tumors better than the information about the vascularization.

Furthermore, Deshpande and coworkers longitudinally evaluated different tumor models of breast, ovarian, and pancreatic cancer regarding the expression patterns of three angiogenic markers (VEGFR2, endoglin, and $\alpha_v\beta_3$ integrin) during tumor growth. Molecular ultrasound imaging enabled the longitudinal, non-invasive evaluation of molecular expression profiles in different tumor models, and, therefore, in the regulation of tumor angiogenesis [20].

The ability of molecular ultrasound to longitudinally track receptor expression during tumor growth opens the possibility to monitor antiangiogenic treatment responses. Zafarnia and coworkers applied VEGFR2 targeted microbubbles to assess the response of desmoplastic breast tumors in mice to either nilotinib, anti-VEGFR2 antibody DC101 (inhibition of angiogenesis), or a combination of both. Surprisingly, nilotinib inhibited vessel maturation and lead to enhanced angiogenesis and tumor growth. In line with this, molecular ultrasound imaging revealed an increase in VEGFR2 expression in nilotinib-treated tumors. In contrast, DC101 treatment decreased VEGFR2 expression and tumors treated with a combination of both substances showed a VEGFR2 expression similar to untreated control tumors. These findings matched well with immunohistochemical analyses and confirmed the ability of VEGFR2-targeting microbubbles to detect the tumors' response to therapy sensitively and accurately [75].

The same type of microbubbles was used to simultaneously assess a functional (tumor perfusion) and molecular (VEGFR2 expression) information from squamous cell carcinoma bearing mice treated with an anti-VEGF antibody. This study showed that the first-pass kinetic of VEGFR2-targeted microbubbles is not affected by early binding of microbubbles to the receptor. Therefore, first-pass analysis can be used to determine tumor perfusion, while the late accumulation phase provides the molecular information. Furthermore, antiangiogenic therapy effects could be detected earlier and more distinctly by the molecular compared to the functional ultrasound parameters [10] (Fig. 15.5).

The combination of functional and molecular imaging was also applied in a rat model of colorectal adenocarcinoma treated with the multi-tyrosine kinase inhibitor regorafenib. The reduced perfusion and VEGFR2 expression in regorafenib-treated animals correlated well with DCE MRI data, postprocessed using a two-compartment-model, and the immunohistochemical analyses, respectively [22].

15.6.1.2 $\alpha_v\beta_3$ Integrin

Another promising marker for the detection of angiogenesis with molecular ultrasound imaging is $\alpha_v\beta_3$ integrin, a member of the integrin family of heterodimeric surface glycoproteins. $\alpha_v\beta_3$ integrin plays an important role in tumor growth [5] and metastasis by mediating cell adhesion to components of the extracellular matrix and influencing the proliferation and survival of cells. $\alpha_v\beta_3$ integrins are highly expressed on the activated endothelium during angiogenesis, whereas quiescent endothelial cells only show a weak expression [35]. In this regard, several studies used $\alpha_v\beta_3$ integrin-targeted microbubbles successfully for the detection of tumor angiogenesis in different preclinical tumor models like glioma [21], ovarian [20, 71], breast [5, 67], liver [74], or skin [50] cancer.

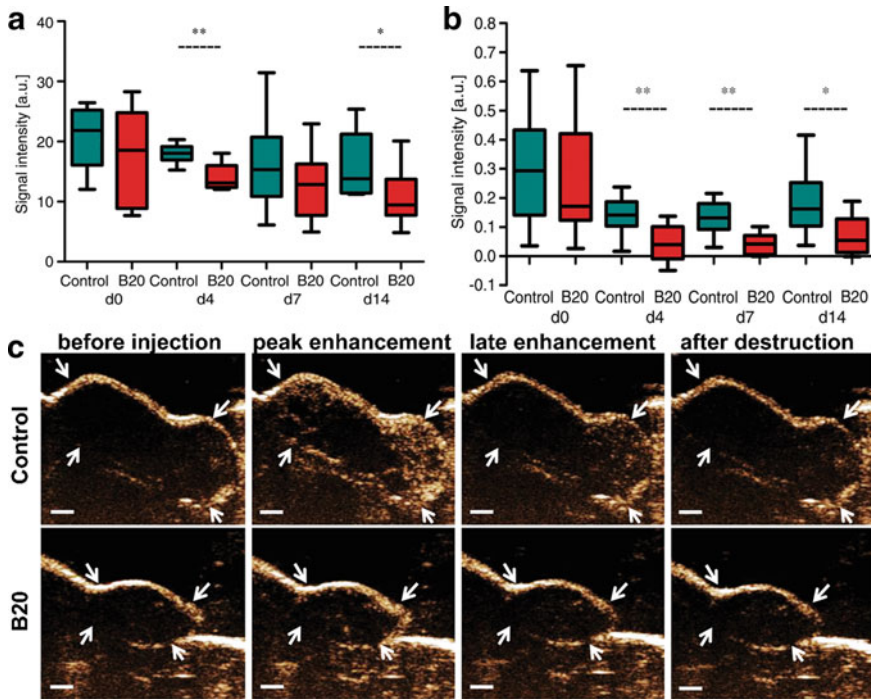


Fig. 15.5 Simultaneous assessment of functional and molecular information from squamous cell carcinomas in nude mice. **a** First-pass analysis of BR55 and postprocessing with maximum intensity over time (MIOT) in B20-treated (anti-VEGFR2 antibody) and control tumors. Data are presented as median and IQRs. * = $p < 0.05$. **b** From day 4 of therapy on, B20-treated tumors show a significantly decreased amount of bound BR55 microbubbles compared with untreated tumors. Results are presented as difference in US imaging signal before and after application of a destructive pulse. Data are presented as median and IQRs. * = $p < 0.05$, ** = $p < 0.01$. **c** Representative US images of control and B20-treated squamous cell carcinomas at day 14 of therapy before and after injection of BR55 microbubbles show a higher peak enhancement in the control tumor compared with the B20-treated tumor. The late enhancement (8 min after microbubble injection) shows a higher signal of bound BR55 microbubbles in control tumors that disappears after application of a destructive pulse. Arrows indicate tumor margins. Bar = 1 mm (reproduced with permission from [10] ©RSNA Radiology, 2014)

The detection of $\alpha_v\beta_3$ integrin expression can be facilitated with different kinds of ligands. In this regard, Ellegala and colleagues used contrast-enhanced ultrasound with $\alpha_v\beta_3$ integrin-targeted microbubbles to image angiogenesis in athymic, malignant glioma (humane U87MG)-bearing rats. For this purpose, a highly $\alpha_v\beta_3$ integrin affine polypeptide (echistatin) was bound to the microbubbles. Longitudinal ultrasound investigations showed an increasing $\alpha_v\beta_3$ integrin-targeted microbubble signal within the tumors over two weeks. The signal was most pronounced at the tumor periphery, the place with the highest $\alpha_v\beta_3$ integrin expression, which correlated with immunohistochemistry [21].

Other studies used different peptides to explore the potential of $\alpha_v\beta_3$ integrin targeting for tumor angiogenesis detection. Willmann and coworkers tested disulfide-constraining cystine knot peptides coupled to perfluorocarbon-filled microbubbles for targeted molecular ultrasound imaging of human ovarian adenocarcinoma xenograft tumors in mice. There, the imaging signal of microbubble–knotting peptide combinations in the tumor was even higher than the signal emitted by larger microbubble–antibody combinations [70]. Another study performed by Anderson et al. in a murine mammary carcinoma model showed similar results, when microbubbles were conjugated with $\alpha_v\beta_3$ integrin affine arginine–glycine–aspartic acid (RGD) [5].

In addition, $\alpha_v\beta_3$ integrin-targeted microbubbles can be used to longitudinally assess vascular responses to therapy. In this regard, Palmowski and coworkers successfully evaluated $\alpha_v\beta_3$ integrin-targeted microbubbles to detect acute radiotherapy effects. In rat prostate tumors, a single 16 Gy irradiation with carbon ions resulted in enhanced $\alpha_v\beta_3$ integrin expression, while tumor perfusion hardly changed [51]. Therapeutic effects of bevacizumab on 2LMP breast cancer in mice was examined by Sorace and colleagues using triple-targeted molecular ultrasound microbubbles (antibodies against $\alpha_v\beta_3$ integrin, P-selectin, and VEGFR2). Although no changes in tumor size could be detected three days after bevacizumab injection, molecular ultrasound imaging indicated a decrease in microvessel density. Hence, molecular ultrasound imaging can be used to obtain information about the early therapy response even before a change in tumor size occurs [61]. However, the need of investigating molecular information and vascularization in concert to distinguish between vascular regression and changes in the molecular expression of angiogenesis markers at the endothelium has to be noted [50].

15.6.1.3 Endoglin

Endoglin is a marker of tumor-related angiogenesis and neovascularization. It is expressed and up-regulated on proliferating endothelial cells and serves as an accessory receptor for the transforming growth factor-beta (TGF- β). Several studies showed the suitability of this angiogenesis marker for the detection of tumor neovascularization in mouse glioma xenografts [45] and the longitudinal monitoring of receptor expression in breast, ovarian, and pancreatic cancer in mice [20]. Furthermore, it could be applied successfully to monitor therapy response of mouse melanoma to sorafenib treatment [41] and mouse pancreatic tumor response to monoclonal antibody (VEGF) alone or in combination with gemcitabine therapy [38].

15.6.2 Further Molecular Targets

Next to these well-known markers of tumor angiogenesis, several less-known markers related to angiogenesis were successfully evaluated by molecular ultrasound imaging. The expression of secreted frizzled-related protein-2 (SFRP-2) was captured in tumor vessels of murine angiosarcoma [64]. In addition, neuropilin-1 [77] and nucleolin [76] could be visualized on murine breast cancer vasculature.

Furthermore, inflammation-related markers, like E-selectin, B7-H3, or the thymocyte differentiation antigen 1 (Thy-1), have been targeted in tumors using molecular ultrasound imaging (Table 15.2). Of those, E-selectin was most commonly addressed. In this regard, Fokong and coworkers developed microbubbles decorated with a peptide that specifically targets E-selectin, an important mediator for the adhesion of leukocytes that is involved in tumor metastasis and progression. In line with this, significant binding of E-selectin targeted microbubbles was found in human ovarian carcinoma xenografts [26]. Using the same microbubbles, Spivak and colleagues performed a dosing experiment aiming to reach the microdose range

Table 15.2 Overview of currently used markers for molecular ultrasound imaging with micro- or nanobubbles

Contrast agent	Marker	Pathway	Cancer model
Microbubbles	VEGFR2	Endothelial proliferation and migration, angiogenesis	Pancreatic [38, 56]
			Ovarian [11, 71]
			Prostate [63]
			Breast [3, 8, 13, 75]
			Squamous cell carcinoma [10]
			Colon [6, 22, 66]
			Skin [50]
	Integrin	Cell movement, leukocyte adhesion, angiogenesis	Glioma [21]
			Ovarian [20, 70]
			Breast [5, 20, 61, 67]
			Liver [74]
			Prostate [51]
			Skin [50]
Endoglin (CD105)	Tumor growth, metastasis, angiogenesis	Pancreatic [20, 38]	
		Ovarian [20]	
		Melanoma [41]	
SFRP2	Angiogenesis	Angiosarcoma [64]	
Neuropilin-1	Angiogenesis	Breast [77]	
Nucleolin	Synthesis and maturation of ribosomes	Breast [78]	
E-selectin	Inflammation	Ovarian [26, 62]	
Thy1 (CD90)	Nerve regeneration, metastasis, inflammation, apoptosis	Pancreatic [2]	
B7-H3 (CD276)	Tumor immunology, inflammation	Breast [9]	
Nanobubbles	CA-125	Tumorigenesis, proliferation	Ovarian [29]
Phase-shift nanoparticles	Folate receptor	Tumor cells	Ovarian [43]
Nanoparticles	SHP2	Tumor cells	Thyroid [32]

in human carcinoma xenografts of the ovary and epidermis in mice. Although the microdose range could not be achieved, changes in E-selectin expression after antiangiogenic treatment in human ovarian carcinoma xenografts in mice could be captured with microbubble doses of 7×10^7 microbubbles/kg body weight [62].

15.6.3 Nanobubbles and Nanoparticles for Preclinical Molecular Ultrasound Imaging

In contrast to microbubbles, whose application is restricted to the vascular compartment, nano-sized contrast agents can leave the vasculature and, therefore, reach molecular targets outside the blood vessels.

15.6.3.1 Nanobubbles

In 2017, Gao and colleagues demonstrated targeting of the cancer antigen 125 (CA-125) with antibody functionalized nanobubbles in positive OVCAR-3 tumor-bearing mice. Ca-125, a protein located in mesothelial cells, is involved in tumor proliferation and tumorigenesis. The study showed a high tumor accumulation of the targeted nanobubbles, increased retention, and an enhanced ultrasound signal [29].

15.6.3.2 Phase-Shift Nanoparticles

Phase-shift nanoparticles represent a compromise between microbubbles that have a high echogenicity and nanoemulsions that can leave the vascular bed [43]. An ultrasound-triggered phase transition of the nanoparticles leads to a microbubble in the tumor tissue and enables the detection via ultrasound. In a recent study by Li and coworkers, liquid perfluorohexane nanoparticles with a size of 280 nm and encapsulated by poly lactic-co-glycolic acid were investigated. Perfluorohexane has a low boiling point and can, therefore, undergo the phase transition with low-intensity focused ultrasound. These particles were decorated with a folate-targeting group as many epithelial-derived tumors show an overexpression of the folate receptor. They show the ability of their nanoparticles to undergo the phase shift and performed *in vivo* competition with free folic acid to verify specific accumulation in ovarian cancer xenografts that were also confirmed by fluorescence histology [43].

Another approach to overcome the penetration limitations of microbubbles by using phase-changeable perfluorocarbon nanoparticles focused on the targeting of Src homology 2 domain-containing phosphotyrosine phosphatase 2 (SHP-2) in thyroid tumors. PLGA nanoparticles encapsulating perfluoropentane were decorated with an SHP-2 binding antibody. Their ability to undergo low-intensity-focused ultrasound induced phase transition and their binding specificity to human thyroid cancer xenografts could be verified [32].

15.7 Clinical Application

Currently, BR55 is the only molecularly targeted ultrasound contrast agent that received the Investigational New Drug Approval from the US Food and Drug Administration. The phospholipid-based microbubble is filled with a mixture of perfluorobutane and nitrogen and functionalized by incorporation of a kinase insert domain receptor (KDR)-targeting phospholipid heteropeptide into the microbubble shell [53]. The peptide has a high specificity to KDR, also known as human VEGFR2, which was introduced previously in this chapter.

Prior to the application in patients, BR55 was extensively tested in preclinical settings to demonstrate its potential for tumor characterization [13, 53, 56, 63] and therapy response evaluation [75, 78] in animal models of prostate [63], breast [13, 53, 75] and colon [56, 78] cancer in mice [13, 75, 78] and rats [53, 63].

In 2017, Smeenge and coworkers reported on the first application of BR55 in humans. In this phase 0 study, the feasibility and safety of BR55 to detect prostate cancer in patients was investigated [60]. BR55 showed a good safety profile as no serious adverse events occurred, and malignant lesions were detected with a high accuracy and in good correlation with histopathology.

Another study carried out by Willmann and coworkers used BR55 to assess KDR expression in focal ovarian and breast lesions of patients [69]. Here, only few mild to moderate self-resolving adverse events were found that were related to the microbubble injection. They claim that these adverse events were comparable to those occurring in controlled clinical trials using non-targeted microbubbles approved by the US Food and Drug Administration. Furthermore, the results from KDR-targeted molecular ultrasound imaging matched well with KDR expression of focal ovarian and breast lesions evaluated with immunohistochemistry (Fig. 15.6).

A recently completed clinical trial tested the efficacy of BR55 to detect prostate cancer prior to radical prostatectomy using volumetric ultrasound imaging (ClinicalTrials.gov identifier: NCT02142608). However, the outcome is not yet open to the public.

These promising results of first-in-human proof of concept trials show the diagnostic potential of molecularly targeted ultrasound imaging and should stimulate further research on the exploration of this non-harming imaging modality as an alternative or complementary tool to other molecular imaging modalities discussed in this book.

15.8 Targeted Ultrasound-Mediated Drug Delivery

Besides their diagnostic application, microbubbles can be used to enhance therapeutic effects by mediating a transient permeabilization of cell membranes. This is caused by the oscillation of microbubbles as a response to ultrasound pressure waves. In this context, stable cavitation occurs when ultrasound is applied at low

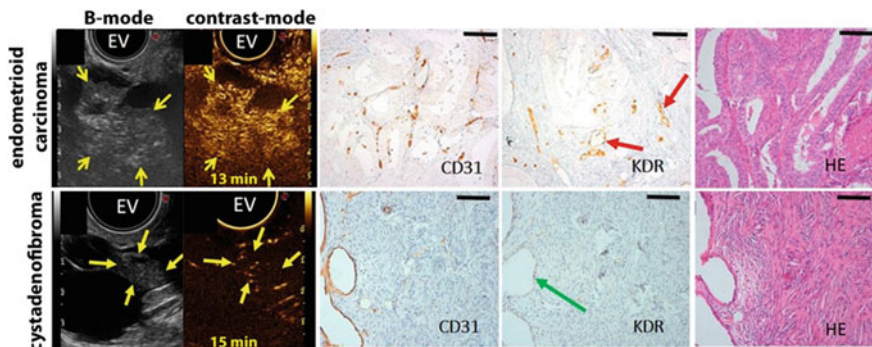


Fig. 15.6 Assessment of KDR expression in focal ovarian lesions of patients. Upper panel: Endometrioid carcinoma in a 50-year-old woman: the transverse endovaginal B-mode ultrasound image of the right ovary shows a 5.2-cm-large mixed cystic and solid lesion (yellow arrows = solid lesion) that also shows a strong imaging signal 13 min after intravenous injection of BR55. KDR expression on the tumor-associated neovasculature (CD31-positive, red arrows) was confirmed by immunohistochemistry. Lower panel: Benign serous cystadenofibroma in a 65-year-old woman: the transverse endovaginal B-mode ultrasound image of the right ovary presents a 4.8-cm-large, mixed cystic and solid ovarian mass (yellow arrows = solid lesion) with only minimal background signal after injection of BR55. Immunohistochemistry shows only minimal KDR expression (green arrow) on CD31-positive vasculature. Scale bar immunohistochemistry images: 100 μ m (reproduced with permission from [69] ©American Society of Clinical Oncology)

intensities, whereas high ultrasound intensities lead to inertial cavitation that can result in the destruction of microbubbles [42].

Sonopermeabilization can be used to temporarily open biological barriers to improve drug delivery to tissues. The term sonopermeation describes the use of contrast-enhanced ultrasound to locally increase perfusion and tissue permeability. This can be of special interest for opening of the blood–brain barrier, which prevents the entrance of substances from the blood into brain tissue. There are many interesting studies on sonoporation ongoing using clinical scale ultrasound contrast agents [58]. However, it needs to be mentioned that this paragraph only considers applications with targeted microbubbles.

In this context, Chang and coworkers investigated cationic microbubbles carrying a suicide (pHSV-TK) and a reporter gene (red firefly luciferase gene). Additionally, the microbubbles were decorated with an anti-VEGFR2 antibody to target the vasculature of rat glioma. The application of focused ultrasound leads to a strong oscillation of bound microbubbles resulting in permeabilization of the blood–brain barrier to enable trans-vascular gene delivery. At the same time, a disintegration of the microbubbles into nanometer-sized fragments enables the introduction of DNA into perivascular cells. They showed an increased gene concentration in the target cells and a reduction of tumor growth. However, a limitation of this method is the difficulty to transfect tissue beyond the vasculature since the gene delivery primarily occurs in cells with direct contact to microbubbles [15].

A possibility to overcome the limited penetration of microbubbles into the tumor tissue could be the use of phase-changeable nanoparticles as drug delivery systems. In this regard, Liu and coworkers established nanodroplets with a liquid phase-changeable perfluoropentane core and a shell composed of cholesterol and phospholipids with conjugated folic acid. Furthermore, the nanodroplets were loaded with superparamagnetic iron oxide nanoparticles (to be visible in MRI and photoacoustics), and the anticancer drug 10-hydroxycamptothecin was incorporated. The passive (enabled by the small particle size and extravasation through leaky tumor vessels) and active (enabled by targeting to folic acid receptor) accumulation of nanodroplets in murine ovarian cancers could successfully be visualized by MRI and photoacoustic imaging. Furthermore, low-intensity-focused ultrasound induced the phase transition of accumulated nanoparticles in the tumor into microbubbles that resulted in an enhanced echo intensity in ultrasound measurements. The release of drugs from the phase-changeable nanoparticles during the phase transition resulted in enhanced tumor growth inhibition compared to treatment with the drug alone [47].

Although both approaches are showing promising results, there are still many open questions regarding the ability of the contrast agents to overcome biological barriers inside the tumors, the biological processes induced at the cell membrane, and the most effective therapy protocol.

References

1. Abou-Elkacem L, Bachawal SV, Willmann JK (2015) Ultrasound molecular imaging: Moving toward clinical translation. *Eur J Radiol* 84(9):1685–1693. <https://doi.org/10.1016/j.ejrad.2015.03.016>
2. Abou-Elkacem L, Wang H, Chowdhury SM, Kimura RH, Bachawal SV, Gambhir SS, Tian L, Willmann JK (2018) Thy1-targeted microbubbles for ultrasound molecular imaging of pancreatic ductal adenocarcinoma. *Clin Cancer Res* 24(7):1574–1585. <https://doi.org/10.1158/1078-0432.CCR-17-2057>
3. Abou-Elkacem L, Wilson KE, Johnson SM, Chowdhury SM, Bachawal S, Hackel BJ, Tian L, Willmann JK (2016) Ultrasound molecular imaging of the breast cancer neovasculature using engineered fibronectin scaffold ligands: a novel class of targeted contrast ultrasound agent. *Theranostics* 6(11):1740–1752. <https://doi.org/10.7150/thno.15169>
4. Adler DD, Carson PL, Rubin JM, Quinn-Reid D (1990) Doppler ultrasound color flow imaging in the study of breast cancer: preliminary findings. *Ultrasound Med Biol* 16(6):553–559
5. Anderson CR, Hu X, Zhang H, Tlaxca J, Decleves AE, Houghtaling R, Sharma K, Lawrence M, Ferrara KW, Rychak JJ (2011) Ultrasound molecular imaging of tumor angiogenesis with an integrin targeted microbubble contrast agent. *Invest Radiol* 46(4):215–224. <https://doi.org/10.1097/RLI.0b013e3182034fed>
6. Anderson CR, Rychak JJ, Backer M, Backer J, Ley K, Klibanov AL (2010) scVEGF microbubble ultrasound contrast agents: a novel probe for ultrasound molecular imaging of tumor angiogenesis. *Invest Radiol* 45(10):579–585. <https://doi.org/10.1097/RLI.0b013e3181efd581>
7. Arditi M, Frinking PJ, Zhou X, Rognin NG (2006) A new formalism for the quantification of tissue perfusion by the destruction-replenishment method in contrast ultrasound imaging. *IEEE Trans Ultrason Ferroelectr Freq Control* 53(6):1118–1129

8. Bachawal SV, Jensen KC, Lutz AM, Gambhir SS, Tranquart F, Tian L, Willmann JK (2013) Earlier detection of breast cancer with ultrasound molecular imaging in a transgenic mouse model. *Cancer Res* 73(6):1689–1698. <https://doi.org/10.1158/0008-5472.CAN-12-3391>
9. Bachawal SV, Jensen KC, Wilson KE, Tian L, Lutz AM, Willmann JK (2015) Breast cancer detection by B7-H3-Targeted ultrasound molecular imaging. *Cancer Res* 75(12):2501–2509. <https://doi.org/10.1158/0008-5472.CAN-14-3361>
10. Baetke SC, Rix A, Tranquart F, Schneider R, Lammers T, Kiessling F, Lederle W (2016) Squamous cell carcinoma xenografts: use of VEGFR2-targeted microbubbles for combined functional and molecular US to monitor antiangiogenic therapy effects. *Radiology* 278(2):430–440. <https://doi.org/10.1148/radiol.2015142899>
11. Barua A, Yellapa A, Bahr JM, Machado SA, Bitterman P, Basu S, Sharma S, Abramowicz JS (2014) Enhancement of ovarian tumor detection with alphavbeta3 integrin-targeted ultrasound molecular imaging agent in laying hens: a preclinical model of spontaneous ovarian cancer. *Int J Gynecol Cancer* 24(1):19–28. <https://doi.org/10.1097/IGC.0000000000000040>
12. Buchanan KD, Huang S, Kim H, Macdonald RC, McPherson DD (2008) Echogenic liposome compositions for increased retention of ultrasound reflectivity at physiologic temperature. *J Pharm Sci* 97(6):2242–2249. <https://doi.org/10.1002/jps.21173>
13. Bzyl J, Lederle W, Rix A, Grouls C, Tardy I, Pochon S, Siepmann M, Penzkofer T, Schneider M, Kiessling F, Palmowski M (2011) Molecular and functional ultrasound imaging in differently aggressive breast cancer xenografts using two novel ultrasound contrast agents (BR55 and BR38). *Eur Radiol* 21(9):1988–1995. <https://doi.org/10.1007/s00330-011-2138-y>
14. Cebe-Suarez S, Zehnder-Fjallman A, Ballmer-Hofer K (2006) The role of VEGF receptors in angiogenesis; complex partnerships. *Cell Mol Life Sci* 63(5):601–615. <https://doi.org/10.1007/s00018-005-5426-3>
15. Chang EL, Ting CY, Hsu PH, Lin YC, Liao EC, Huang CY, Chang YC, Chan HL, Chiang CS, Liu HL, Wei KC, Fan CH, Yeh CK (2017) Angiogenesis-targeting microbubbles combined with ultrasound-mediated gene therapy in brain tumors. *J Control Release* 255:164–175. <https://doi.org/10.1016/j.jconrel.2017.04.010>
16. Cosgrove D, Harvey C (2009) Clinical uses of microbubbles in diagnosis and treatment. *Med Biol Eng Comput* 47(8):813–826. <https://doi.org/10.1007/s11517-009-0434-3>
17. Cui W, Bei J, Wang S, Zhi G, Zhao Y, Zhou X, Zhang H, Xu Y (2005) Preparation and evaluation of poly(L-lactide-co-glycolide) (PLGA) microbubbles as a contrast agent for myocardial contrast echocardiography. *J Biomed Mater Res B Appl Biomater* 73(1):171–178. <https://doi.org/10.1002/jbm.b.30189>
18. Dayton PA, Rychak JJ (2007) Molecular ultrasound imaging using microbubble contrast agents. *Front Biosci* 12:5124–5142
19. Deshpande N, Needles A, Willmann JK (2010) Molecular ultrasound imaging: current status and future directions. *Clin Radiol* 65(7):567–581. <https://doi.org/10.1016/j.crad.2010.02.013>
20. Deshpande N, Ren Y, Foygel K, Rosenberg J, Willmann JK (2011) Tumor angiogenic marker expression levels during tumor growth: longitudinal assessment with molecularly targeted microbubbles and US imaging. *Radiology* 258(3):804–811. <https://doi.org/10.1148/radiol.10101079>
21. Ellegala DB, Leong-Poi H, Carpenter JE, Klibanov AL, Kaul S, Shaffrey ME, Sklenar J, Lindner JR (2003) Imaging tumor angiogenesis with contrast ultrasound and microbubbles targeted to alpha(v)beta3. *Circulation* 108(3):336–341. <https://doi.org/10.1161/01.CIR.0000080326.15367.0C>
22. Eschbach RS, Clevert DA, Hirner-Eppeneder H, Ingrisch M, Moser M, Schuster J, Tadros D, Schneider M, Kazmierczak PM, Reiser M, Cyran CC (2017) Contrast-enhanced ultrasound with VEGFR2-targeted microbubbles for monitoring regorafenib therapy effects in experimental colorectal adenocarcinomas in rats with DCE-MRI and immunohistochemical validation. *PLoS ONE* 12(1):e0169323. <https://doi.org/10.1371/journal.pone.0169323>

23. Ferrara K, Pollard R, Borden M (2007) Ultrasound microbubble contrast agents: fundamentals and application to gene and drug delivery. *Annu Rev Biomed Eng* 9:415–447. <https://doi.org/10.1146/annurev.bioeng.8.061505.095852>
24. Ferrara KW, Borden MA, Zhang H (2009) Lipid-shelled vehicles: engineering for ultrasound molecular imaging and drug delivery. *Acc Chem Res* 42(7):881–892. <https://doi.org/10.1021/ar8002442>
25. Fix SM, Novell A, Yun Y, Dayton PA, Arena CB (2017) An evaluation of the sonoporation potential of low-boiling point phase-change ultrasound contrast agents in vitro. *J Ther Ultrasound* 5:7. <https://doi.org/10.1186/s40349-017-0085-z>
26. Fokong S, Fragoso A, Rix A, Curaj A, Wu Z, Lederle W, Iranzo O, Gatjens J, Kiessling F, Palmowski M (2013) Ultrasound molecular imaging of E-selectin in tumor vessels using poly n-butyl cyanoacrylate microbubbles covalently coupled to a short targeting peptide. *Invest Radiol* 48(12):843–850. <https://doi.org/10.1097/RLI.0b013e31829d03ec>
27. Fokong S, Siepmann M, Liu Z, Schmitz G, Kiessling F, Gatjens J (2011) Advanced characterization and refinement of poly N-butyl cyanoacrylate microbubbles for ultrasound imaging. *Ultrasound Med Biol* 37(10):1622–1634. <https://doi.org/10.1016/j.ultrasmedbio.2011.07.001>
28. Fouad YA, Aanei C (2017) Revisiting the hallmarks of cancer. *Am J Cancer Res* 7(5):1016–1036
29. Gao Y, Hernandez C, Yuan HX, Lilly J, Kota P, Zhou H, Wu H, Exner AA (2017) Ultrasound molecular imaging of ovarian cancer with CA-125 targeted nanobubble contrast agents. *Nanomedicine* 13(7):2159–2168. <https://doi.org/10.1016/j.nano.2017.06.001>
30. Hamilton AJ, Huang SL, Warnick D, Rabbat M, Kane B, Nagaraj A, Klegerman M, McPherson DD (2004) Intravascular ultrasound molecular imaging of atheroma components in vivo. *J Am Coll Cardiol* 43(3):453–460. <https://doi.org/10.1016/j.jacc.2003.07.048>
31. Hitchcock KE, Caudell DN, Sutton JT, Klegerman ME, Vela D, Pyne-Geithman GJ, Abruzzo T, Cyr PE, Geng YJ, McPherson DD, Holland CK (2010) Ultrasound-enhanced delivery of targeted echogenic liposomes in a novel ex vivo mouse aorta model. *J Control Release* 144(3):288–295. <https://doi.org/10.1016/j.jconrel.2010.02.030>
32. Hu Z, Yang B, Li T, Li J (2018) Thyroid cancer detection by ultrasound molecular imaging with SHP2-targeted perfluorocarbon nanoparticles. *Contrast Media Mol Imaging* 2018:8710862. <https://doi.org/10.1155/2018/8710862>
33. Huang SL, MacDonald RC (2004) Acoustically active liposomes for drug encapsulation and ultrasound-triggered release. *Biochim Biophys Acta* 1665(1–2):134–141. <https://doi.org/10.1016/j.bbamem.2004.07.003>
34. Ignee A, Atkinson NS, Schuessler G, Dietrich CF (2016) Ultrasound contrast agents. *Endosc Ultrasound* 5(6):355–362. <https://doi.org/10.4103/2303-9027.193594>
35. Kiessling F, Fokong S, Bzyl J, Lederle W, Palmowski M, Lammers T (2014) Recent advances in molecular, multimodal and theranostic ultrasound imaging. *Adv Drug Deliv Rev* 72:15–27. <https://doi.org/10.1016/j.addr.2013.11.013>
36. Kiessling F, Fokong S, Koczera P, Lederle W, Lammers T (2012) Ultrasound microbubbles for molecular diagnosis, therapy, and theranostics. *J Nucl Med* 53(3):345–348. <https://doi.org/10.2967/jnumed.111.099754>
37. Kiessling F, Huppert J, Palmowski M (2009) Functional and molecular ultrasound imaging: concepts and contrast agents. *Curr Med Chem* 16(5):627–642
38. Korpanty G, Carbon JG, Grayburn PA, Fleming JB, Brekken RA (2007) Monitoring response to anticancer therapy by targeting microbubbles to tumor vasculature. *Clin Cancer Res* 13(1):323–330. <https://doi.org/10.1158/1078-0432.CCR-06-1313>
39. Lanza GM, Wickline SA (2003) Targeted ultrasonic contrast agents for molecular imaging and therapy. *Curr Probl Cardiol* 28(12):625–653. <https://doi.org/10.1016/j.cpcardiol.2003.11.001>

40. Lee J, Min HS, You DG, Kim K, Kwon IC, Rhim T, Lee KY (2016) Theranostic gas-generating nanoparticles for targeted ultrasound imaging and treatment of neuroblastoma. *J Control Release* 223:197–206. <https://doi.org/10.1016/j.jconrel.2015.12.051>
41. Leguermey I, Scoazec JY, Gadot N, Robin N, Penault-Llorca F, Victorin S, Lassau N (2015) Molecular ultrasound imaging using contrast agents targeting endoglin, vascular endothelial growth factor receptor 2 and integrin. *Ultrasound Med Biol* 41(1):197–207. <https://doi.org/10.1016/j.ultrasmedbio.2014.06.014>
42. Lentacker I, De Cock I, Deckers R, De Smedt SC, Moonen CT (2014) Understanding ultrasound induced sonoporation: definitions and underlying mechanisms. *Adv Drug Deliv Rev* 72:49–64. <https://doi.org/10.1016/j.addr.2013.11.008>
43. Li M, Luo H, Zhang W, He K, Chen Y, Liu J, Chen J, Wang D, Hao L, Ran H, Zheng Y, Wang Z, Li P (2018) Phase-shift, targeted nanoparticles for ultrasound molecular imaging by low intensity focused ultrasound irradiation. *Int J Nanomedicine* 13:3907–3920. <https://doi.org/10.2147/IJN.S166200>
44. Lindner JR, Dayton PA, Coggins MP, Ley K, Song J, Ferrara K, Kaul S (2000) Noninvasive imaging of inflammation by ultrasound detection of phagocytosed microbubbles. *Circulation* 102(5):531–538
45. Liu C, Yan F, Xu Y, Zheng H, Sun L (2018) InVivo molecular ultrasound assessment of glioblastoma neovasculature with endoglin-targeted microbubbles. *Contrast Media Mol Imaging* 2018:8425495. <https://doi.org/10.1155/2018/8425495>
46. Liu J, Shang T, Wang F, Cao Y, Hao L, Ren J, Ran H, Wang Z, Li P, Du Z (2017) Low-intensity focused ultrasound (LIFU)-induced acoustic droplet vaporization in phase-transition perfluoropentane nanodroplets modified by folate for ultrasound molecular imaging. *Int J Nanomedicine* 12:911–923. <https://doi.org/10.2147/IJN.S122667>
47. Liu J, Xu F, Huang J, Xu J, Liu Y, Yao Y, Ao M, Li A, Hao L, Cao Y, Hu Z, Ran H, Wang Z, Li P (2018) Low-intensity focused ultrasound (LIFU)-activated nanodroplets as a theranostic agent for noninvasive cancer molecular imaging and drug delivery. *Biomater Sci* 6(11):2838–2849. <https://doi.org/10.1039/c8bm00726h>
48. Marshall D, Pedley RB, Boden JA, Boden R, Melton RG, Begent RH (1996) Polyethylene glycol modification of a galactosylated streptavidin clearing agent: effects on immunogenicity and clearance of a biotinylated anti-tumour antibody. *Br J Cancer* 73(5):565–572
49. Paefgen V, Doleschel D, Kiessling F (2015) Evolution of contrast agents for ultrasound imaging and ultrasound-mediated drug delivery. *Front Pharmacol* 6:197. <https://doi.org/10.3389/fphar.2015.00197>
50. Palmowski M, Huppert J, Ladewig G, Hauff P, Reinhardt M, Mueller MM, Woenne EC, Jenne JW, Maurer M, Kauffmann GW, Semmler W, Kiessling F (2008) Molecular profiling of angiogenesis with targeted ultrasound imaging: early assessment of antiangiogenic therapy effects. *Mol Cancer Ther* 7(1):101–109. <https://doi.org/10.1158/1535-7163.MCT-07-0409>
51. Palmowski M, Peschke P, Huppert J, Hauff P, Reinhardt M, Maurer M, Karger CP, Scholz M, Semmler W, Huber PE, Kiessling FM (2009) Molecular ultrasound imaging of early vascular response in prostate tumors irradiated with carbon ions. *Neoplasia* 11(9):856–863
52. Perera RH, Wu H, Peiris P, Hernandez C, Burke A, Zhang H, Exner AA (2017) Improving performance of nanoscale ultrasound contrast agents using N, N-Diethylacrylamide Stabilization. *Nanomedicine* 13(1):59–67. <https://doi.org/10.1016/j.nano.2016.08.020>
53. Pochon S, Tardy I, Bussat P, Bettinger T, Brochot J, von Wronski M, Passantino L, Schneider M (2010) BR55: a lipopeptide-based VEGFR2-targeted ultrasound contrast agent for molecular imaging of angiogenesis. *Invest Radiol* 45(2):89–95. <https://doi.org/10.1097/RLI.0b013e3181c5927c>
54. Postema M, Schmitz G (2007) Ultrasonic bubbles in medicine: influence of the shell. *Ultrason Sonochem* 14(4):438–444. <https://doi.org/10.1016/j.ultsonch.2006.09.013>
55. Pysz MA, Guracar I, Tian L, Willmann JK (2012) Fast microbubble dwell-time based ultrasonic molecular imaging approach for quantification and monitoring of angiogenesis in

- cancer. *Quant Imaging Med Surg* 2(2):68–80. <https://doi.org/10.3978/j.issn.2223-4292.2012.06.05>
56. Pysz MA, Machtaler SB, Seeley ES, Lee JJ, Brentnall TA, Rosenberg J, Tranquart F, Willmann JK (2015) Vascular endothelial growth factor receptor type 2-targeted contrast-enhanced US of pancreatic cancer neovasculature in a genetically engineered mouse model: potential for earlier detection. *Radiology* 274(3):790–799. <https://doi.org/10.1148/radiol.14140568>
 57. Reinhardt M, Hauff P, Briel A, Uhlendorf V, Linker RA, Maurer M, Schirner M (2005) Sensitive particle acoustic quantification (SPAQ): a new ultrasound-based approach for the quantification of ultrasound contrast media in high concentrations. *Invest Radiol* 40(1):2–7
 58. Rix A, Lederle W, Theek B, Lammers T, Moonen C, Schmitz G, Kiessling F (2018) Advanced ultrasound technologies for diagnosis and therapy. *J Nucl Med* 59(5):740–746. <https://doi.org/10.2967/jnumed.117.200030>
 59. Schroeder A, Kost J, Barenholz Y (2009) Ultrasound, liposomes, and drug delivery: principles for using ultrasound to control the release of drugs from liposomes. *Chem Phys Lipids* 162(1–2):1–16. <https://doi.org/10.1016/j.chemphyslip.2009.08.003>
 60. Smeenge M, Tranquart F, Mannaerts CK, de Reijke TM, van de Vijver MJ, Laguna MP, Pochon S, de la Rosette J, Wijkstra H (2017) First-in-human ultrasound molecular imaging with a VEGFR2-specific ultrasound molecular contrast agent (BR55) in prostate cancer: a safety and feasibility pilot study. *Invest Radiol* 52(7):419–427. <https://doi.org/10.1097/RLI.0000000000000362>
 61. Sorace AG, Saini R, Mahoney M, Hoyt K (2012) Molecular ultrasound imaging using a targeted contrast agent for assessing early tumor response to antiangiogenic therapy. *J Ultrasound Med* 31(10):1543–1550
 62. Spivak I, Rix A, Schmitz G, Fokong S, Iranzo O, Lederle W, Kiessling F (2016) Low-dose molecular ultrasound imaging with E-selectin-targeted PBCA microbubbles. *Mol Imaging Biol* 18(2):180–190. <https://doi.org/10.1007/s11307-015-0894-9>
 63. Tardy I, Pochon S, Theraulaz M, Emmel P, Passantino L, Tranquart F, Schneider M (2010) Ultrasound molecular imaging of VEGFR2 in a rat prostate tumor model using BR55. *Invest Radiol* 45(10):573–578. <https://doi.org/10.1097/RLI.0b013e3181ee8b83>
 64. Tsuruta JK, Klauber-DeMore N, Streeter J, Samples J, Patterson C, Mumper RJ, Ketelsen D, Dayton P (2014) Ultrasound molecular imaging of secreted frizzled related protein-2 expression in murine angiosarcoma. *PLoS ONE* 9(1):e86642. <https://doi.org/10.1371/journal.pone.0086642>
 65. Unnikrishnan S, Klibanov AL (2012) Microbubbles as ultrasound contrast agents for molecular imaging: preparation and application. *AJR Am J Roentgenol* 199(2):292–299. <https://doi.org/10.2214/AJR.12.8826>
 66. Wang S, Herbst EB, Mauldin FW Jr, Diakova GB, Klibanov AL, Hossack JA (2016) Ultra-low-dose ultrasound molecular imaging for the detection of angiogenesis in a mouse murine tumor model: how little can we see? *Invest Radiol* 51(12):758–766. <https://doi.org/10.1097/RLI.0000000000000310>
 67. Warram JM, Sorace AG, Saini R, Humphrey HR, Zinn KR, Hoyt K (2011) A triple-targeted ultrasound contrast agent provides improved localization to tumor vasculature. *J Ultrasound Med* 30(7):921–931
 68. Wei K, Jayaweera AR, Firoozan S, Linka A, Skyba DM, Kaul S (1998) Quantification of myocardial blood flow with ultrasound-induced destruction of microbubbles administered as a constant venous infusion. *Circulation* 97(5):473–483
 69. Willmann JK, Bonomo L, Carla Testa A, Rinaldi P, Rindi G, Valluru KS, Petrone G, Martini M, Lutz AM, Gambhir SS (2017) Ultrasound molecular imaging With BR55 in patients with breast and ovarian lesions: first-in-human results. *J Clin Oncol* 35(19):2133–2140. <https://doi.org/10.1200/JCO.2016.70.8594>
 70. Willmann JK, Kimura RH, Deshpande N, Lutz AM, Cochran JR, Gambhir SS (2010) Targeted contrast-enhanced ultrasound imaging of tumor angiogenesis with contrast

- microbubbles conjugated to integrin-binding knottin peptides. *J Nucl Med* 51(3):433–440. <https://doi.org/10.2967/jnumed.109.068007>
71. Willmann JK, Lutz AM, Paulmurugan R, Patel MR, Chu P, Rosenberg J, Gambhir SS (2008) Dual-targeted contrast agent for US assessment of tumor angiogenesis in vivo. *Radiology* 248(3):936–944. <https://doi.org/10.1148/radiol.2483072231>
 72. Yang H, Cai W, Xu L, Lv X, Qiao Y, Li P, Wu H, Yang Y, Zhang L, Duan Y (2015) Nanobubble-Affibody: novel ultrasound contrast agents for targeted molecular ultrasound imaging of tumor. *Biomaterials* 37:279–288. <https://doi.org/10.1016/j.biomaterials.2014.10.013>
 73. Yang L, Cheng J, Chen Y, Yu S, Liu F, Sun Y, Chen Y, Ran H (2017) Phase-transition nanodroplets for real-time photoacoustic/ultrasound dual-modality imaging and photothermal therapy of sentinel lymph node in breast cancer. *Sci Rep* 7:45213. <https://doi.org/10.1038/srep45213>. <https://www.nature.com/articles/srep45213#supplementary-information>
 74. Yuan HX, Wang WP, Wen JX, Lin LW, Exner AA, Guan PS, Chen XJ (2018) Dual-targeted microbubbles specific to integrin α V β 3 and vascular endothelial growth factor receptor 2 for ultrasonography evaluation of tumor angiogenesis. *Ultrasound Med Biol* 44(7):1460–1467. <https://doi.org/10.1016/j.ultrasmedbio.2018.03.022>
 75. Zafarnia S, Bzyl-Ibach J, Spivak I, Li Y, Koletnik S, Doleschel D, Rix A, Pochon S, Tardy I, Koyadan S, van Zandvoort M, Palmowski M, Kiessling F, Lederle W (2017) Nilotinib enhances tumor angiogenesis and counteracts VEGFR2 blockade in an orthotopic breast cancer xenograft model with desmoplastic response. *Neoplasia* 19(11):896–907. <https://doi.org/10.1016/j.neo.2017.08.009>
 76. Zhang H, Ingham ES, Gagnon MK, Mahakian LM, Liu J, Foiret JL, Willmann JK, Ferrara KW (2017) In vitro characterization and in vivo ultrasound molecular imaging of nucleolin-targeted microbubbles. *Biomaterials* 118:63–73. <https://doi.org/10.1016/j.biomaterials.2016.11.026>
 77. Zhang H, Tam S, Ingham ES, Mahakian LM, Lai CY, Tumbale SK, Teesalu T, Hubbard NE, Borowsky AD, Ferrara KW (2015) Ultrasound molecular imaging of tumor angiogenesis with a neuropilin-1-targeted microbubble. *Biomaterials* 56:104–113. <https://doi.org/10.1016/j.biomaterials.2015.03.043>
 78. Zhou J, Wang H, Zhang H, Lutz AM, Tian L, Hristov D, Willmann JK (2016) VEGFR2-targeted three-dimensional ultrasound imaging can predict responses to antiangiogenic therapy in preclinical models of colon cancer. *Cancer Res* 76(14):4081–4089. <https://doi.org/10.1158/0008-5472.CAN-15-3271>
 79. Zlitni A, Gambhir SS (2018) Molecular imaging agents for ultrasound. *Curr Opin Chem Biol* 45:113–120. <https://doi.org/10.1016/j.cbpa.2018.03.017>



Molecular Imaging in Oncology: Advanced Microscopy Techniques

16

Dimitrios Kapsokalyvas and Marc A. M. J. van Zandvoort

Contents

16.1	Introduction.....	534
16.2	Fluorescence and Labelling.....	535
16.2.1	Chemical Labelling.....	536
16.2.2	Immunofluorescence.....	536
16.2.3	Fluorescent Proteins.....	536
16.2.4	Photo-Switching Dyes.....	537
16.3	Fluorescence Microscopy Techniques.....	537
16.3.1	Confocal Microscopy.....	537
16.3.2	Light-Sheet Microscopy.....	539
16.3.3	Two-Photon Microscopy.....	540
16.3.4	Super-Resolution Microscopy Techniques.....	541
16.3.5	Single-Molecule Localization Microscopy—SMLM.....	542
16.3.6	Structured Illumination Microscopy—SIM.....	543
16.4	Applications.....	544
16.4.1	Confocal Microscopy.....	544
16.4.2	Light-Sheet Microscopy—LSM.....	544
16.4.3	Two-Photon Microscopy.....	545
16.4.3.1	Ex Vivo.....	545
16.4.3.2	Metabolic Imaging.....	546
16.4.3.3	Multiphoton Imaging of Skin.....	547
16.4.3.4	Intravital Imaging with Two-Photon Microscopy.....	549
16.4.3.5	Second Harmonic Generation Imaging of Collagen.....	550
16.4.3.6	Higher Order Fluorescence and Harmonics.....	551
16.4.3.7	Endomicroscopy.....	552

D. Kapsokalyvas · M. A. M. J. van Zandvoort (✉)

School for Oncology and Developmental Biology GROW and School for Cardiovascular Diseases CARIM, Maastricht University, Maastricht, The Netherlands
e-mail: mamj.vanzandvoort@maastrichtuniversity.nl

D. Kapsokalyvas · M. A. M. J. van Zandvoort

Institut für Molekulare Kreislaufforschung, Universitätsklinikum Aachen, Aachen, Germany

© Springer Nature Switzerland AG 2020

533

O. Schober et al. (eds.), *Molecular Imaging in Oncology*,

Recent Results in Cancer Research 216,

https://doi.org/10.1007/978-3-030-42618-7_16

16.4.4 Super-Resolution Microscopy	553
16.4.5 Multimodal Techniques	554
16.5 Conclusion	556
References	556

16.1 Introduction

As the field of oncology is expanding, new processes are revealed, and many more questions arise. Investigation at subcellular resolution is not possible in the clinical setting, and therefore a preclinical platform is needed. This is offered by the use of immortalized cell lines where cellular and molecular dynamics can be investigated. However, it is often criticized that such cell lines resemble the clinical malignant tissue only to a limited extent. To address this issue, the use of small animals has been increasingly employed in oncology studies. This includes the use of wild but also transgenic species, modified to investigate the effect of different factors in oncological development or processes. Sample analysis can be done using molecular techniques, such as western blots, HPLC, mass spectroscopy, or through visualization using microscopy.

Imaging of tissue or cells with subcellular resolution is important for delineating molecular processes. Techniques that offer this kind of information include optical microscopy techniques (wide-field fluorescence, confocal laser scanning microscopy—CLSM, super-resolution microscopy—SRM, and two-photon laser scanning microscopy—TPM), and electron microscopy techniques (TEM, AFM, SEM, etc.). In this chapter, we will review only advanced optical fluorescence techniques since they are minimally invasive or non-invasive and require minimal sample preparation. Moreover, as it will be shown below, some of these techniques can be also applied *in vivo* offering a unique tool for investigating tumour dynamics and processes.

A plethora of techniques that offer resolution around 1 μm or better and are fluorescence-based is available. Each of them offers unique advantages. We will review the potential of each technique and highlight their strengths. These techniques include confocal laser scanning microscopy (CLSM), light-sheet microscopy (LSM), two-photon microscopy (TPM), and super-resolution microscopy (SRM) techniques.

16.2 Fluorescence and Labelling

Fluorescence-based microscopy techniques use the phenomenon of fluorescence as contrast mechanism. Fluorescence occurs when an excited molecule transitions from the first excited electronic state to the ground electronic state by emitting a photon. There are also other de-excitation mechanisms which are radiationless; therefore, they do not contribute to fluorescence. In fluorescence-based microscopy techniques, molecules with high fluorescence rates are used. In such techniques usually, excitation is accomplished with a laser line. A typical Jablonski diagram of de-excitation transitions of the microscopy techniques described in this chapter is depicted in Fig. 16.1. Traditional bright-field microscopy, as the one used for histopathologic examination of tissue slides, relies on the phenomenon of absorption or scattering for contrast. This limits the number of contrast agents, as absorption spectra are generally broad and overlap, and additionally out of focus signal significantly blurs the image. In fluorescence, emission spectra are generally narrower, since only two electronic states are involved in the process. As a result, it is easier to control excitation and detection, by using a specific excitation wavelength for each fluorophore and selecting only a small wavelength bandwidth for detection. In this way, three or more fluorophores can be combined in a single sample and the excitation of each fluorophore can be controlled independently. Conventional wide-field fluorescence microscopy is not reviewed in this chapter as it offers lower axial resolution compared to the other techniques.

In microscopy, fluorescence is used to increase contrast. In order to achieve this contrast, the structure under investigation, e.g. a protein, DNA, has to be labelled with a fluorescent marker. To achieve this, several methods for labelling have been developed.

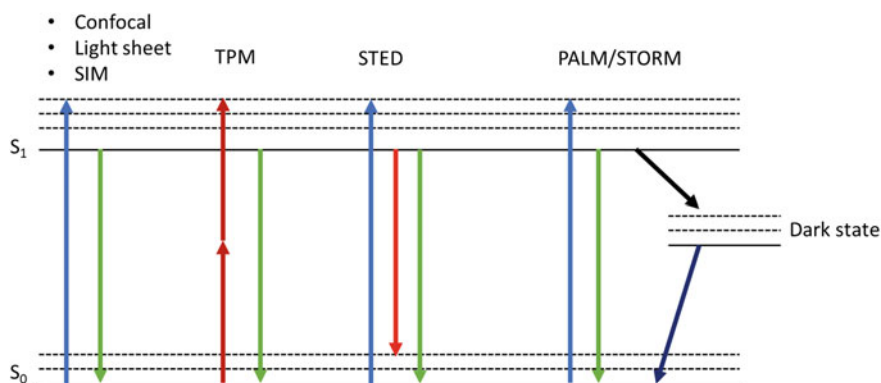


Fig. 16.1 Jablonski diagram of the molecular transitions of fluorophores in different microscopy techniques

16.2.1 Chemical Labelling

In this case, a molecule, a peptide, or a chemical agent in general that is shown to preferentially bind to a specific structure is used for direct labelling. When the chemical agent is not fluorescent itself, it is conjugated to a fluorescent dye. Examples of such agents include DAPI and Hoechst, commonly used for nuclear staining. Other examples are specific mitochondrial dyes (such as Mitotracker, TMR, or JC-1, the latter with fluorescence colour depending on mitochondrial membrane potential), actin dyes (such as phalloidin or SiR-actin), or membrane dyes (such as DiI, WGA, and MemBrite). This kind of labelling is relatively easy and usually requires a single step of incubation, after which the labelled structure becomes visible on a dark background.

16.2.2 Immunofluorescence

Immunofluorescence staining involves the use of antibodies that target specific proteins in the cell. The primary antibody can be linked to a fluorescent probe directly. More commonly, a secondary antibody carrying the probe (usually organic dyes) is used to target the unlabelled primary antibody. In the case of using secondary antibodies, more than one secondary antibody can bind to the primary antibody, therefore increasing the fluorophore density, and thereafter signal. The advantage of antibody labelling is that any structure in the cell can be specifically labelled. The disadvantage, however, is that it can only be performed on fixed samples. Antibody labelling, in general, is a multistep process that requires fixation, permeabilization, and staining of the sample, and several washing cycles in between. In intact tissues and living animals, the antibodies cannot penetrate deep enough. They can certainly not enter intact cells, allowing only labelling of external targets.

To address issues concerning the size of conventional antibodies especially in applications of super-resolution microscopy, new generation of markers has been developed. These include affibody proteins [1], which are small synthesized peptides designed to target a specific protein, and antibody fragments [2], which are engineered to retain the targeting properties of the full antibody but be smaller in size. One could also consider chromobodies as an example of this type of staining, since the cell is transfected with the heavy chain fragment of a lama antibody to a specific protein. Such staining agents can either be conjugated to a fluorophore or be followed by an additional step of secondary labelling, similar to classical immunostaining.

16.2.3 Fluorescent Proteins

In this case, the DNA of the host is modified to express a fluorescent protein (FP) such as green fluorescent protein (GFP), and yellow fluorescent protein (YFP) in the target structure. This can be achieved temporarily by transfecting the

cell with a plasmid that contains the FP's DNA. Transfection efficiency can vary due to competing mechanisms in the cell and as a result transfection efficiency can vary significantly from cell to cell. To address this issue, the DNA of the host can be modified permanently to express the FPs. The later method is more challenging to achieve but offers more reliable results. It can be performed on cell lines or even small animals such as mice, rats, and zebrafish. FPs are not as bright as organic dyes; however, they are expressed specifically on the desired target (e.g. a protein like LaminA, Actin). Furthermore, since they are expressed naturally by cells, FPs are optimal for live-cell imaging.

In more advanced applications where signal intensity is important for applications, such as live-cell imaging or single-molecule microscopy, the so-called SNAP [3], Halo-, and CLIP-tag methods can be used [4]. These are self-labelling enzymes which can be fused to a target protein and can covalently bond to a labelled ligand. The advantage of this method is that organic dyes can be used for ligand labelling, which are brighter than FPs.

16.2.4 Photo-Switching Dyes

Photo-switching dyes are used in super-resolution techniques. SRM techniques rely on their ability to drive the dye in states that are fluorescent—the ON state—and states that are non-fluorescent—the OFF state—in a controlled manner [5] (Fig. 16.1). This includes dyes that can reversibly photoswitch between an OFF and ON state (such as *cis-trans* isomerization of FPs, or dyes in the presence of strong reducing solutions [6]), dyes that irreversibly photoswitch from an OFF state to an ON state, and dyes that are irreversibly photoconverted from one fluorescence state to another red-shifted fluorescence state. Their emission state can be controlled, and the emission from a single molecule can be recorded independently of neighbouring molecules. This method provides a detailed and high-resolution “map” of each fluorophore. Such dyes are commonly used in PALM/STORM-related techniques.

16.3 Fluorescence Microscopy Techniques

In this chapter, we will discuss the most frequently used microscopy techniques in oncological research. We refer to Fig. 16.2 for a detailed schedule of the individual setups.

16.3.1 Confocal Microscopy

Confocal laser scanning microscopy (CLSM) was conceptualized in the late 60s; however, it became widely applicable in the late 80s and early 90s. Developments in laser technology and electronics allowed the construction of electronic microscopes.

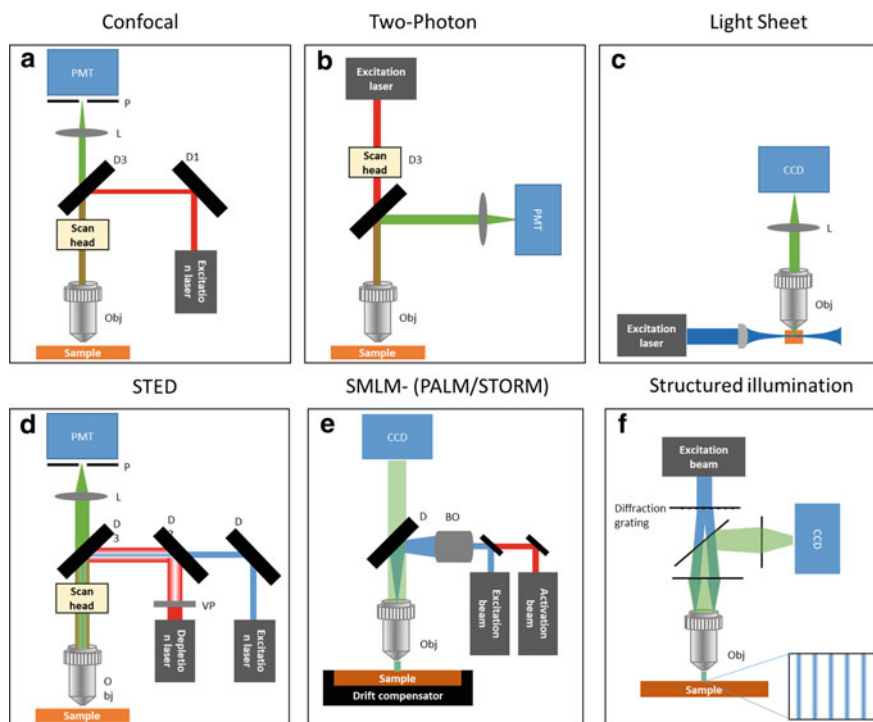


Fig. 16.2 Schematic overview of different fluorescence microscopy techniques. **a** Confocal microscopy, the sample is scanned with a laser source and fluorescence is detected by a photon detector PMT. Out of focus light is rejected by the pinhole (P). **b** Two-photon microscopy, a pulsed near-infrared laser source is scanning the sample and a PMT is detecting the signal. **c** Light-sheet microscopy, a sheet of light excites the sample from the side and a perpendicularly positioned objective lens is collecting fluorescence to form the image on the CCD or sCMOS camera. **d** STED, it is a confocal-based method where additionally a depletion beam is scanning the sample along with the excitation beam. **e** SMLM, activation and excitation beams are used at different frequencies and intensities to drive molecules stochastically in and out of the fluorescence state. **f** SIM, a diffracting element is used to create a striped illumination pattern at the focal point. This pattern is rotated, and subsequent images are post-processed

Combined with the use of a high intensity collimated light source—the laser—and multiple electronic systems that could be synchronized and controlled by a computer, this allowed the production of high-resolution tomographic images. Nowadays, confocal microscopy is a standard technique for light microscopy facilities [7]. Contrast is based on fluorescence and any conventional dye (using the labelling techniques described above) can be used for imaging. A pinhole is used to reject the out of focus light and restrict the axial dimensions of the section being imaged. Such detection requires high levels of signal, since signal mainly form the focal spot that is mainly collected; therefore, in practice modern bright dyes that are less sensitive to photobleaching are favoured. Typically, resolution in confocal microscopy is around

250 nm in XY and 700 nm in axial dimension. Confocal microscopy can be used for imaging of any type of cell process in culture, in both fixed and living cells. It can also be used as an alternative to histopathology, where biopsies can be imaged immediately after removal in order to define tumour margins and type [8]. The advantage is the 3D sectioning and higher resolution compared to conventional wide-field microscopy. Contrast and resolution of confocal images can be further improved by post-processing based on deconvolution algorithms. This technique is very efficient in reducing noise and enhancing contrast of subtle structures, therefore increasing resolution, especially in “noisy” images [7].

16.3.1.1 Limitations

Confocal microscopy uses visible light for excitation. Visible light has low penetration depth; therefore, thicker tissues cannot be visualized. Penetration depends on the sample absorption and scattering properties, and typically is in the 50–100 μm range. At deeper layers, out of focus fluorescence cannot be rejected anymore, due to scattering, and images become blurry. Another limitation is the number of fluorescent probes that can be used. Commonly, three different probes can be used without complications, using sequential imaging. Use of more probes is possible, though the risk of fluorescence cross-talk from one channel to the other increases. Because it is a scanning technique, it is slower compared to conventional wide-field fluorescence. To increase scanning speed resonant scanners can be used, which can acquire images at video rate (30 frames per second-fps) with good signal-to-noise ratio (SNR). Another application which can increase acquisition speed is the *spinning disc confocal*. In this case, instead of scanning the laser beam over the sample, two discs, one containing microlenses and the other individual pinholes, are rotated in tandem to scan the sample, and the image is projected on a camera such as a CCD or sCMOS. Spinning disc offers high-speed scanning, but resolution is inferior to classical CLSM due to pinhole cross-talk.

16.3.2 Light-Sheet Microscopy—LSM

Light-sheet microscopy (LSM) or selective plane illumination, a technique recently introduced [9, 10], has received a lot of attention. Light sheet, instead of using the same path for excitation and detection as in CLSM and TPM, uses a thin sheet of light to excite a layer of the sample. Another objective placed perpendicular to the excitation light sheet is used to collect the generated signal. By doing so, the entire illuminated (and excited) section of the sample can be used to collect signal from. Since there are full field excitation and image formation, LSM is very fast. Its resolution is mainly dependent on the thickness of the light sheet, typically being in the 1–2 μm range. The extension of the light sheet over which it can maintain a relative homogeneous thickness defines the maximum field of view, typically around 0.5–1 mm. LSM typically offers less resolution compared to CLSM and TPM, but it is much faster (several frames per second) and allows imaging of large

fields of view. However, samples need to be transparent, for example, embryos (such as drosophila, zebrafish), and small organoids, and cleared organs [11].

Recently, super-resolution variations of LSM, such as lattice light sheet, have been reported, which offer reduced field of view and penetration depth but are significantly fast [12]. Also, a non-invasive *in vivo* application was presented, which gives promise for further development of the intravital application of the technique [13]. This opens up the potential for intravital imaging also in oncology with very high-resolution and video-rate acquisition.

16.3.2.1 Limitations

Because of its orthogonal excitation detection geometry, LSM poses limitations on the objectives that can be used and on the sample positioning in the microscope. In routine applications, resolution is inferior to that of CLSM or TPM; therefore, if the structure of interest is below the 1 μm range, super-resolution techniques will have to be preferred instead. Additionally, penetration depth can be a concern; therefore, if the tissue is not transparent, either naturally (embryos) or by clearing, penetration is limited in the 50–100 μm range depending on the sample.

16.3.3 Two-Photon Microscopy

Two-photon microscopy (TPM) (also referred to as two-photon excitation, two-photon laser scanning, multiphoton, or non-linear microscopy) was invented in the early 90s [14]. Its development was facilitated by the presence of very fast laser-pulsed systems (80 MHz) able to deliver very short pulses in the range of hundreds of femtoseconds with high enough intensity. Because light scattering and absorption in biological samples for the near-infrared laser sources (usually 740–860 nm) used in two-photon microscopy is much lower than that for the visible spectrum, near-infrared light can penetrate deeper. This property allows high-resolution imaging deep in tissue sections, organs, and organisms *in vitro* and *in vivo*. The actual penetration depth depends on the optical properties of the tissue and can range from 200 μm [15] in skin up to 1 mm in brain [16]. Additionally, due to the fact that excitation takes place only in the focal plane, a pinhole is not needed. Therefore, detectors can be placed closer to the sample and as a result detection can be more efficient. Like confocal microscopy, it is a scanning technique and again similar to confocal can produce 3D images. Resolution in TPM on very thin samples, such as cells or surface of tissues, is worse than confocal due to the longer excitation wavelength used. However, at deeper layers, confocal resolution worsens significantly due to scattering, while in TPM resolution is less affected (since fluorescence originates from the focal spot), so as a result resolution of TPM becomes better compared to confocal at deeper layers. Since in TPM excitation only takes place in the focus of the objective, photobleaching and photodamage are overall less compared to that in confocal microscopy. However, photobleaching rate can be significantly higher in the focus, compared to confocal, due to non-linear processes [17].

Typically, in TPM, objectives with lower numerical aperture (0.8–1 NA) and low magnification (20X) are used. Such objectives offer bigger field of view (500–700 μm), have longer working distances (2–8 mm), and are water immersion. This facilitates the application of tissue imaging where deeper penetration is needed, water immersion is more compatible with tissues, especially when doing intravital imaging, and capturing as more as possible of bigger morphological structures is required. Resolution for such objectives is around 500 nm in the lateral plane, and 1.5 μm in the axial direction.

Another advantage of TPM is that it can effectively excite and detect endogenous fluorophores as well as image collagen in the extracellular matrix based on the second harmonic signal (SHG). There are several natural fluorophores in tissue such as keratin, melanin, NDH, FAD, collagen, and elastin. These can be used to visualize tissue, which is usually termed as autofluorescence. In TPM, many probes and/or autofluorescent structures can be excited with a single wavelength (for example, 800 nm). This in contrast to the sequential imaging needed in CLSM. This is especially relevant in intravital imaging or in imaging in living cells. When considering intravital applications the advantage is that instead of UV light that would be required for one-photon excitation, such as in confocal microscopy, a near-infrared source is used which is not damaging DNA. Additionally, the SHG of collagen is commonly used as a label-free method to image the extracellular matrix (collagen). Another tissue element that can emit SHG is striated muscle; however, it is not usually relevant in oncology.

Several reviews already exist on this topic [18–23]. In this section, we will review the most important applications.

16.3.3.1 Limitations

TPM can efficiently excite autofluorescent molecules of the samples but when exogenous labelling is used, autofluorescence can be a problem as it adds an unwanted fluorescence background. Protocols to decrease autofluorescence background have been proposed [24], but they do not apply for every tissue and are not applicable in vivo. Due to the NIR wavelength used for excitation, resolution is lower compared to CLSM.

16.3.4 Super-Resolution Microscopy Techniques

Key contributors to the development of super-resolution techniques have been awarded the Nobel prize in chemistry in 2014. The most common techniques are simulated emission depletion (STED), photo-activatable localization microscopy (PALM), stochastic optical reconstruction microscopy (STORM), and structured illumination microscopy (SIM).

STED

STED is a confocal-based technique that additionally employs a depletion beam (usually in the red-infrared spectrum) to eliminate fluorescence emitted around the central point of excitation. This reduces the excitation region leading to improved resolution [25]. Resolution can be tuned by adjusting the depletion beam intensity according to the fluorophore, and the sample's properties. In biological specimens, resolution can be down to 70 nm in XY- and Z-directions. Since it is confocal-based method, it can offer sectioning capabilities and 3D imaging up to 50 μm in the sample, especially with refractive index correction objectives. Also, compared to other super-resolution techniques, it is fast (20 images per second in resonant scanner mode) and no post-processing is needed. Consequently, it can be used to study dynamic processes in living cells. Resolution in STED depends on the intensity of the depletion beam. Therefore, resolution can be tuned according to the desired resolution or the (bleaching) properties of the fluorophore.

16.3.4.1 Limitations

In STED, two laser beams are applied, one in the visible spectrum for excitation and another in the red-infrared spectrum for depletion. Usually, high levels of light are used for the depletion. This can lead to fast photobleaching of the sample. Therefore, dyes that are very photostable and bright are needed. Furthermore, an absolute prerequisite is that the probe does not absorb at the depletion wavelength. Imaging deeper sections of the sample are possible; however, penetration depth is similar to that of confocal and limited to 50–100 μm depending on the sample properties.

16.3.5 Single-Molecule Localization Microscopy—SMLM

Single-molecule localization microscopy (SMLM) techniques, such as PALM [26] and STORM [27], rely on determining the exact localization of a fluorophore in the sample. This is achieved by means of stochastic excitation of a subset of fluorophores. Comparing with conventional fluorescence microscopy, fluorescence still takes place, but a “dark state” (a state from which the fluorophore cannot fluoresce) is also involved in the fluorophore transitions. In a typical SMLM experiment, all fluorophores are in a “dark state” and then with low-intensity light a subgroup is activated and transitions to the “bright state” in which the molecule can transition between the singlet electronic states and emit fluorescence as depicted in Fig. 16.1. After the fluorophore has emitted sufficient photons for accurate localization transition to the “dark state” or can be permanently turned off by photobleaching. It is a repetitive process, until all fluorophores have been sufficiently interrogated. The resulting image is a map of the localization of the fluorophores. Resolution depends on the density of the fluorophores and on the number of photons collected.

The density should be chosen in agreement with the size of the structure to be imaged. A pitfall in this case is that when the density is too high, the simultaneous activation of fluorophores within the same diffraction-limited volume can take place, resulting in artefacts. Also, dyes have limitations on the number of photons that they can emit before entering a non-fluorescent state. The typical resolution that can be achieved is in the range of 20–50 nm. Several variations of these techniques have been developed to improve speed, specificity, photon collection efficiency, and resolution

16.3.5.1 Limitations

SMLM techniques are rather slow; acquisition of a single final image is in the order of seconds in modern setups. This severely hampers the imaging of fast processes in living cells. Furthermore, only images up to a depth of 1 μm can be made (using special cylindrical lenses), excluding visualization of processes and morphology deeper in cells. Finally, only certain types of dyes in combination with dedicated mounting methods can be used.

16.3.6 Structured Illumination Microscopy—SIM

In structured illumination microscopy (SIM) [28, 29], the sample is illuminated with a pattern of alternating bright and dark stripes. This pattern is usually created by using a diffractive mask, or by using a spatial light modulator (SLM). This pattern is then rotated, and the acquired images are post-processed. This method of illumination creates the so-called Moiré fringes, highlighting sub-diffraction features. With post-processing of the images, the high spatial frequency components of the image (higher order details) are extracted, and consequently resolution is improved up to twofold (~ 120 nm). Further improvement in resolution can be achieved by modifications to this technique, i.e. Saturated SIM (SSIM) [30, 31]. Resolution improvement is limited compared to other super-resolution techniques, but advantages of SIM are that there are no specific requirements for the dye selection, so any conventional dye is adequate. Additionally, since excitation light is usually low in intensity, photodamage and photobleaching are reduced. SIM is most commonly applied to wide-field microscopes, but application to scanning microscopes is also possible. It can also be used for *in vivo* studies; however, images will require post-processing to extract super-resolution.

16.3.6.1 Limitations

Image acquisition involves the acquisition of several sequential images of the same region. When imaging dynamic processes, this can be an issue if the acquisition time is larger than the period of the process investigated. Moreover, images need to be processed in order to construct the final image, which increases the total imaging time and the processing needs of this technique. Resolution improvement is limited to up to twofold which is not as high as the other SRM techniques offer (STED: 70 nm, SMLM: 20 nm).

16.4 Applications

16.4.1 Confocal Microscopy

CLSM is one of the most common microscopy techniques used in life science, found in most research institutes. It has been used in numerous studies studying the molecular basics of cancer. The major advantages are that it can provide high-resolution tomographic images of cells and subcellular compartments. For example, it has been used for investigating tumour initialization and analysing stem cell dynamics where it was shown that evolution of malignant mutations is not deterministic and that also the environment can affect their evolution [32]. Confocal microscopy was also used to investigate the kinetics of tumour cells and the effect on DNA damage. It was shown that tumour cells can reshape in order to migrate through very small openings, and even though nuclear envelope can rupture during this process and sustain DNA damage, they have repair mechanisms [33]. Another example includes the use of confocal microscopy to investigate the cell renewal of cancer stem cells on organoids developed from patient cells and implanted on mice [34]. The parameters leading to tumour regression were also visualized with CLSM.

Similar to the CLSM method based on fluorescence, a sister technique based on reflection (Reflectance CLSM) from tissue has been developed. This method has found applications that are closer to the clinical setting as no staining is required, since signal originates from the reflectance signal of the tissue itself. It has been particularly useful in clinical applications of imaging skin lesions [35, 36]. Another example is the use of these techniques for imaging breast needle core biopsies [37] which could provide an alternative to the classical histopathologic investigation of biopsies (Fig. 16.3).

16.4.2 Light-Sheet Microscopy—LSM

LSM microscopy with tissue clearing techniques was used to image whole solid tumours with high resolution [38]. The phenotype and heterogeneity of solid tumours were visualized in terms of vascularization and vessel thickness. Moreover, cancer pattern heterogeneities regarding E-cadherin, N-cadherin, vimentin, and CD34 were also visualized. What was also important was that the tissue used was paraffin embedded and deparaffinized for imaging and afterwards re-embedded for storage and future re-evaluation. This approach has the potential of more accurate identification of phenotypic patterns which can be discerned better in the 3D image compared to the 2D images of histopathology [39] (Fig. 16.4). Targeting at the diagnostic advantages that LSM can have over conventional histopathology, it was used to image thick histological sections (0.4 cm) of tissue. The advantages were that thick tissue slices could be imaged very fast, and structures of interest were not distorted due to μm slicing, as it could happen with conventional histopathology [40].

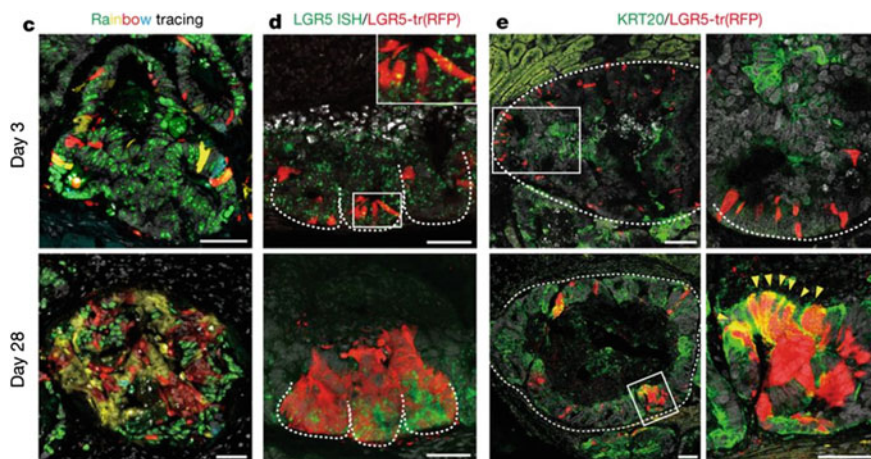


Fig. 16.3 Confocal images of cancer stem cell (LGR5-CreER) tracing in organoids. Cells have been modified to express different fluorescent proteins—nGFP (green), EYFP (yellow), CFP (cyan), and RFP (red). The results of treatment with tamoxifen after 3 days (upper row) and after 28 days (bottom row) are visualized. A number of clones have decreased after 28 days. Scale bars first, second, and fourth column: 50 μm , third column: 100 μm . Adapted from [34]

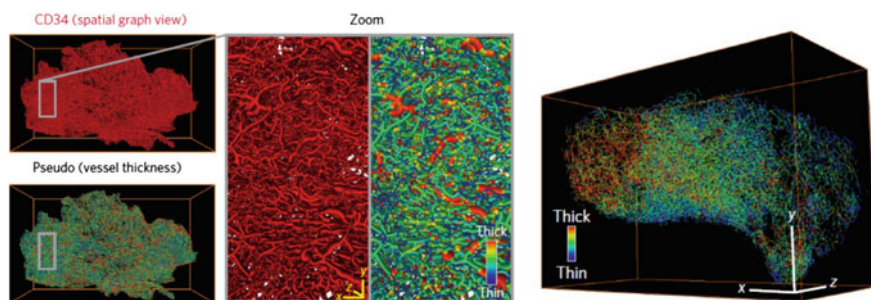


Fig. 16.4 LSM images of cleared human tumour sample. CD34 immunolabelling reveals the vasculature. In the zoom inset vessels are colour coded for different thicknesses (x, y, z indicators 80 μm). On the right, the entire reconstructed tumour sample with vessel thickness colour coding (x, y, z indicators, 100 μm). Adapted from [39]

16.4.3 Two-Photon Microscopy

16.4.3.1 Ex Vivo

Two-photon has been used to elucidate tumour molecular processes in various organs. It has often been used to compare histopathological results of standard H&E staining with those of TPM. Usually, TPM imaging is based on endogenous signal

of the tissue. Spectral properties that differentiate in malignant tissue are used for tumour identification and delineation. Examples include imaging of colorectal cancer tissue [41] where identification was based on nuclear size and collagen intensity, healthy bladder mucosa, and carcinoma in situ [42], where morphological and spectral emission differences between healthy and malignant lesions were identified, and in breast cancer [43]. Common findings in these cases were that nuclear morphology is irregular in malignant tissue, extracellular matrix organization is disrupted by tumour cells, and often spectral shifting is observed.

16.4.3.2 Metabolic Imaging

One of the advantages of endogenous fluorophore imaging is the ability to monitor the metabolic state of cells. This has been successfully used to monitor differences in metabolic activity of various grade cancer cells. The technique is based on measuring the autofluorescence levels of coenzymes that play key roles in the respiratory chain of cells, such as nicotinamide adenine dinucleotide (NADH) and flavin adenine dinucleotide (FAD) [44–46]. Cells produce energy in the form of ATP mainly through oxidation–reduction (redox) reactions, where NADH and FAD are involved. NADH and of FAD are autofluorescent, also under two-photon excitation at 740 nm and 820 nm, respectively [47]. Since they have distinct spectral emissions profiles, they can be separated, and their contribution measured. The ratio of their fluorescence intensities can be used to calculate the redox state of a cell. Increased ratio of FAD over NADH is associated with oxidative activity, whereas decrease of this ratio is correlated with glycolytic activity. These properties have been used to evaluate redox level in epithelial precancer cells [44] and breast cancer [48].

Other studies have focused on the fluorescence decay characteristics of NADH and FAD. More specifically, the reduced form of NADH fluoresces with a characteristic fluorescence lifetime depending on whether it is bound to a protein or free. The free form of NADH has a short fluorescence lifetime (0.4–0.8 ns) and is often associated with glycolytic activity. The bound form has a longer fluorescence lifetime (2–4 ns) and is associated with oxidative phosphorylation. The oxidized NAD^+ is not fluorescent. FAD is autofluorescent in a different emission range and when bound to a protein has a short fluorescence lifetime (0.8 ns), whereas when free has a long fluorescence lifetime (2.0 ns).

Changes in the mean lifetime of NADH have been observed in cancerous and precancerous cells [44] (Fig. 16.5), the proliferative state of the cell [49], the differentiation pathway of stem cells [50], or the cell response to toxic agents [51]. These reports suggest that the mean NADH lifetime is associated with the metabolic state of tissue. Since in cancer metabolism shifts towards anaerobic glycolysis (the Warburg effect), it is expected that this shift would be reflected in NADH lifetime. This technique has been used to identify precancerous epithelia [44], changes in bladder carcinoma in situ [42], and malignant skin lesions [52].

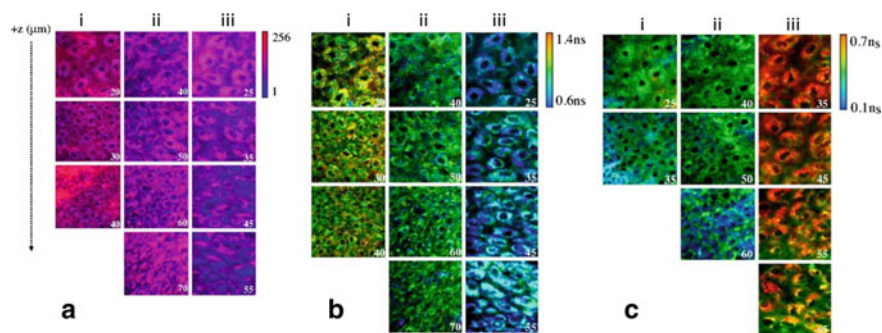


Fig. 16.5 **a** Redox ratio (FAD/NADH), **b** mean NAD lifetime, and **c** mean FAD lifetime of normal low-grade and high-grade precancer endothelial cells. Z-axis indicates depth inside the tissue. Adapted from [44]

16.4.3.3 Multiphoton Imaging of Skin

Skin, as it is the outermost human organ, is easily accessible for non-invasive imaging with TPM. For this reason, TPM has been particularly applied in imaging skin lesions in model organisms, such as mice [53] and ex vivo human biopsies [54], and later in human skin in vivo [15, 55].

In vivo application poses several limitations, most significantly the restricted use of light intensity in the order of 20–40 mW and absence of compatible in vivo labels. Skin imaging is therefore based completely on endogenous fluorophores. Luckily enough, there are several endogenous fluorophores present in skin [56, 57]. Most abundant are keratin, melanin, NADH, FAD, and lipofuscin in the epidermis, collagen, and elastin in the dermis. Detection of the endogenous signal is adequate to visualize cells and subcellular components, such as mitochondria. Usually, cell nuclei are identified as dark regions, since they don't exhibit autofluorescence, inside a bright autofluorescent cytoplasm. In the dermis, SHG from collagen and fluorescence from elastin offer a detailed view of the extracellular matrix morphology. Melanin is brightly fluorescent and can also be visualized in melanocytic skin lesions. Stratum corneum contains significant amounts of keratin and also lipofuscin. Changes in the morphology of skin lesions compared to normal skin, but also spectral and fluorescence decay properties of individual fluorophores, are used to identify and diagnose skin lesions. Advances in speed have allowed mesoscopic imaging of skin lesions [58] (Fig. 16.6).

TPM has been applied in imaging skin tumours, such as squamous cell carcinoma [59], basal cell carcinoma [60–62], and melanoma [63]. It was also shown that imaging of mitochondrial dynamics could be used for diagnosis of early-stage malignancies in vivo, based on the differences in mitochondria organization patterns [52] (Fig. 16.7).

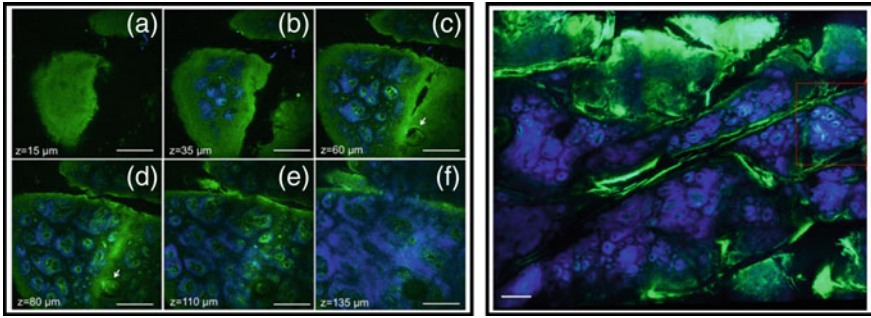


Fig. 16.6 TPM images of human skin. Colour coding green: autofluorescence from cells, blue: collagen. Left: Images of skin at different depths. Close to the surface keratin is well visible (green), and some cellular components are less visible (green punctuate) while deeper dermal papillae (blue) become visible. Scale bar is 200 μm. Right: A wide-area field of view ($3.1 \times 2.5 \text{ mm}^2$) of dermo-epidermal junction, the region where skin folds are deep enough to the level of papillary dermis. Scale bar is 0.25 mm. Adapted from [58]

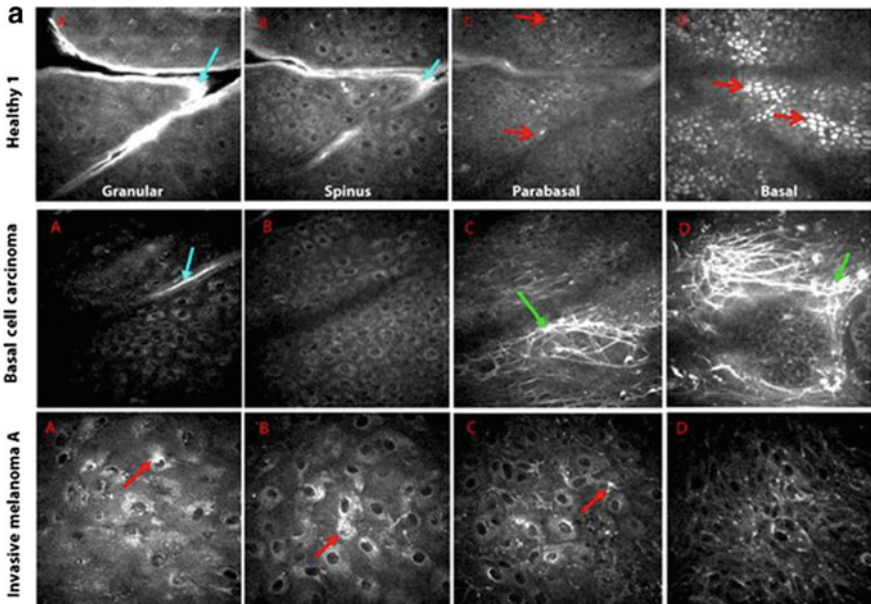


Fig. 16.7 Morphological and functional differences are detected in in vivo endogenous TPEF images of normal and cancerous human epithelia. Adapted from [52]

16.4.3.4 Intravital Imaging with Two-Photon Microscopy

The ability for deep penetration and relatively reduced photodamage/photobleaching has made TPM the technique of choice for intravital imaging of small rodents such as mice and rats. Its potential applications in intravital imaging have been recognized since early times [64]. It can be used in a non-invasive way when imaging external organs such as skin, but for imaging non-superficial organs a certain degree of invasiveness is required. A general protocol requires that the animal must be anaesthetized, where subsequently a minimal surgical intervention to expose the organ of interest follows. Such organs can be the bladder [65], the carotid [66], the gastrointestinal tract [67], and others [68]. A more elaborate method to monitor a region of interest for longer periods is to attach a glass window on the region of interest. Especially in the field of brain imaging, a cranial window is permanently attached to the scalp of mice and multiple imaging session can be performed over the course of several months [69], and even in freely moving animals [70] (Fig. 16.8).

One consideration when imaging intravitaly is motion artefacts and speed. Traditional scanning methods with frame rates above 1 frame per second (fps) are too slow for acquiring static images. One has to consider the normal breathing patterns of the animal, as well as the cardiovascular pulsing. To overcome this problem without significant improvement in speed, the solution of triggered imaging has been suggested, where a monitor observes both heart rate and breathing rate and at appropriate time the trigger to image is sent [71]. Although this technique is practical, it is not real time and is not fast enough. Another method to overcome this problem is to increase the scanning speed. In this regime, there are two solutions: (a) use of a resonant scanner and (b) use of multi-spot beam [72, 73]. Resonant scanners are very fast galvo-scanners operating at a fixed speed which can acquire images with video rate [74] and higher. This has allowed intravital imaging

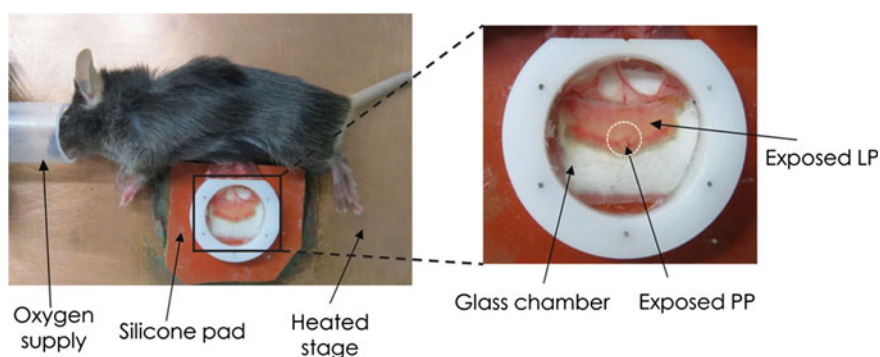


Fig. 16.8 TPM intravital imaging of gastrointestinal tract. The organ is exposed and mounted on an optical window, while the animal is anaesthetized. This can also be done with windows for tumour imaging. Adapted from [67]

with very good results. One consideration is that noise levels are high; therefore, this has to be compensated by using high concentration of dyes, and/or increasing excitation intensity. The use of hybrid detectors certainly reduces noise levels and is favoured when available. The other possibility of going faster is to use the multi-spot beam. In this case, the single laser beam is divided into many beams, typically 8–64 beams, which scan the sample simultaneously, therefore reducing scanning time 8–64-fold. In multi-spot TPM, instead of a point detector such as a PMT, a camera is used to collect the spatially separated signal. Cameras have a higher detection efficiency (or quantum efficiency—QE) compared to PMTs (Camera QE: ~90%, PMTs QE: ~40%). However, going deeper usually is accompanied by higher degrees of scattering and as a result signal from adjacent beams are detected. This introduces artefacts and limits the achievable resolution deeper in tissues.

Tumour growth is dynamic and takes place at variable rates and with different mechanisms [75, 76]. To elucidate the dynamics of these processes, an *in vivo* model is crucial. Several applications using *in vivo* environments by either using engineered tissue or small animal have been reported. To image the dynamic growth of cancer and invasion, Koehl et al. developed a modified skin-fold chamber model for orthotopic implantation in mice and subsequent injection of a solid cancer cell pellet [77]. They were able to monitor a slow and linear pre-angiogenic tumour growth phase at the beginning which was followed by rapid growth afterwards. They used an additional laser line at 1100 nm for imaging a near-infrared dextran variant which was helpful in separating its signal from EGFP to DsRed2. They were able to image vessels, cellular morphology, and nuclear states. Dondossola et al. using TPM and an imaging window investigated the osteolytic progression of cancer tumours on mice models and reported on the reduction of osteoclast kinetics and osteolysis, with no effect on tumour growth after bisphosphonate treatment [78]. Studies on cancer tissue such as on breast cancer [79, 80], cancer cells *in vivo* [81, 82], murine cutaneous squamous cell carcinoma [83], glioblastoma [84], tumour microcirculation [85], and melanoma cells [86] have been reported on intravital imaging. Several pathways for cell migration and therapy have been investigated with intravital TPM [87, 88].

16.4.3.5 Second Harmonic Generation Imaging of Collagen

SHG is an efficient label-free method for imaging collagen [89]. Apart as a contrast for visualizing the extension of extracellular matrix in connective tissue, the evolution and morphological alterations of collagen matrix have been shown to correlate with tumour growth and metastasis [18, 90]. Such changes involve collagen synthesis, increases in organization, and compaction of collagen fibres and change in their diameter. Such changes have been observed in different malignancies, and several quantification tools [91] have been proposed which could be useful for future diagnostic purposes and possibly automatic classification.

16.4.3.6 Higher Order Fluorescence and Harmonics

In the field of non-linear microscopy, the applications of three-photon excitation and third harmonic generation have been explored [92]. The advantage of three-photon excitation is that a more red-shifted laser line is required (~ 1200 nm), which allows deeper penetration inside tissues, while the emission profile of fluorophores does not change. However, higher intensities are required, and photobleaching rate can become significant. Third harmonic generation offers contrast on refractive index changes. Therefore, it provides contrast on interfaces in tissue with change in refractive index, such as the presence of membranes, blood cells, fat, and tissue layers. Together, this technique combined with TPM and SHG provides a full arsenal of tools for imaging tissue with as many details as possible [93, 94]. In practice, this allows for label-free imaging of tumour cells, red blood cells, macrophages, adipocytes, connective tissue, and the surrounding microvasculature of tissue and tumour microenvironment. Three-photon imaging has allowed imaging even through intact skull [95], and short femtosecond pulsed lasers optimized for exciting GFPs and RFPs have been demonstrated for deep tissue imaging [96] (Fig. 16.9).

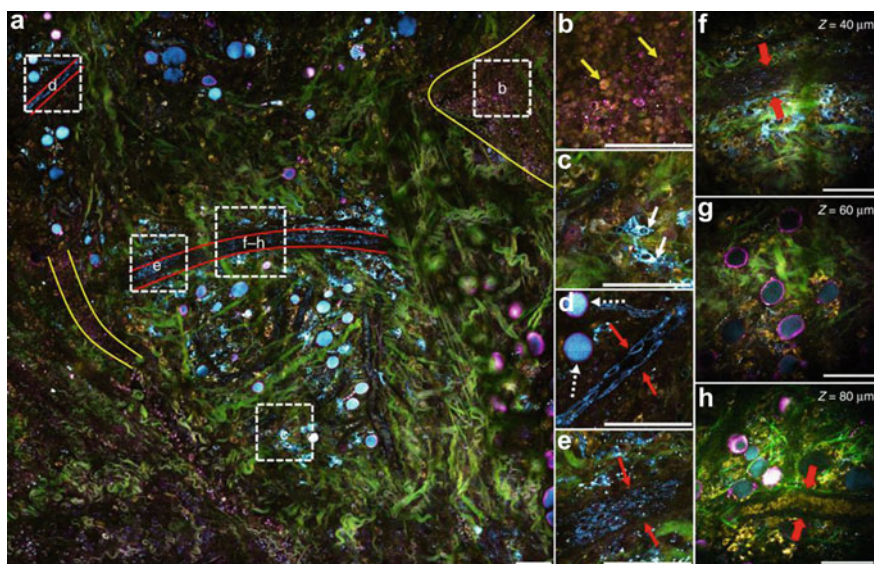


Fig. 16.9 Large field of view image (1.5×1.5 mm²) of label-free multi-harmonic image of *in vivo* rat mammary tumour microenvironment. Colour coding, Green: SHG (collagen fibres), Magenta: THG (from interfaces- membranes); Yellow: two-photon excited fluorescence (mainly FAD in cells); Cyan: three-photon excited fluorescence (mainly NADH in cells). Connective tissue appears green, macrophages appear cyan with a magenta boundary and can also be identified by their morphology, tumour cells appear yellow with magenta boundary and within tumour regions magenta punctuate originating from tumour-associated vesicles are visible. Scale bar: 100 μ m. Adapted from [94]

Another application to increase penetration depth and speed is wide-field two- [97, 98] and three-photon excitation [99]. Wide-field illumination ensures increased speed (frame rates of 100 Hz), since the sample is not scanned but illuminated in a similar manner as in wide-field microscopy. The apparent advantage in speed, however, is offset but reduced axial resolution, but in application such as optogenetics where speed is more important, compromise in resolution is welcome. The combination with three-photon excitation can increase penetration depth to 700 μm [99] without photodamage.

16.4.3.7 Endomicroscopy

So far, the potential and requirements of TPM have been described in detail. The potential of *in vivo* use has been demonstrated in small animals and in human skin imaging. If the technique were to be translated to the clinical setting, a miniaturization process is necessary. For this reason, efforts to convert this method to endomicroscopy have been made. The main difficulty has been the miniaturization of the lens and scanning head. In modern applications, this was achieved by the use of the gradient-index (GRIN) lens [57], where gradients in refractive index are used to focus light. Although this offers a compact solution for TPM, it poses a problem because chromatic aberration is significant between excitation and emission light. More recently, custom-made miniature lenses that can integrate diffractive elements [100, 101] (Fig. 16.10) have been proposed to compensate for aberrations. Scanning is performed in the miniaturized probe tip by using a piezoelectric ceramic tube [102, 103].

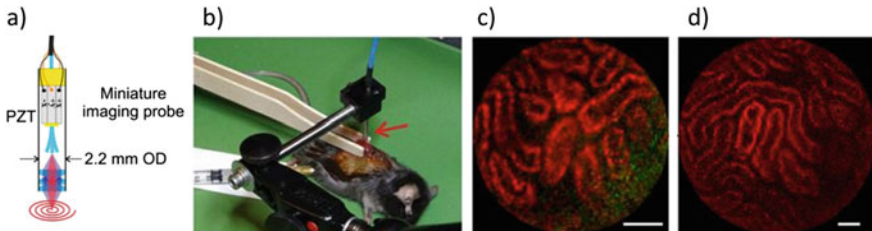


Fig. 16.10 Tip of a fibre-optic scanning two-photon endo-microscope. **a** The tip includes a piezoelectric element (PZT) for circular scanning, a miniature objective and is around 2 mm wide. **b** Anaesthetized mouse during endomicroscopic imaging. **c** TPM image of kidney, red autofluorescence, green collagen—SHG. **d** Same as in **c** but larger field of view, 450 μm . Scale bars, 50 μm . Adapted from [100]

16.4.4 Super-Resolution Microscopy

Several applications investigating oncological molecular process in this new range of resolution have been reported [104]. Resolution is very much improved in STED, but this is accompanied with reduced field of view and penetration depth. Therefore, STED is optimal when imaging molecular processes in subcellular level on cell cultures of primary or immortalized cell lines. In cancer research, some examples include imaging of ovarian cancer cells [105], rectal cancer [106] (Fig. 16.11), metastasizing cells [107], or the visualization of vimentin collapse [108] which is correlated with reduced cancer cell stiffness.

SMLM techniques have also been used in oncology studies. They constitute an obvious super-resolution alternative to confocal microscopy as they share similar limitations of sample thickness but offer one order of magnitude improved resolution. CLSM resolution is ~ 200 nm while with SMLM it can be 20 nm. SMLM was effectively used to re-image archived formalin-fixed paraffin-embedded samples of breast cancer tissue. This technique was used to investigate ultrastructural features of mitochondria and nuclei, not visible with conventional techniques [109] (Fig. 16.12). This method holds potential for investigating already archived tissue samples that could be used for investigating new parameters in diagnostic procedures.

SIM has also been used in oncology research. As with previous techniques, it has also been used in imaging biopsy tissue section of benign and malignant tissue. In a study on prostate cancer tissue slides, it was shown that application of fast

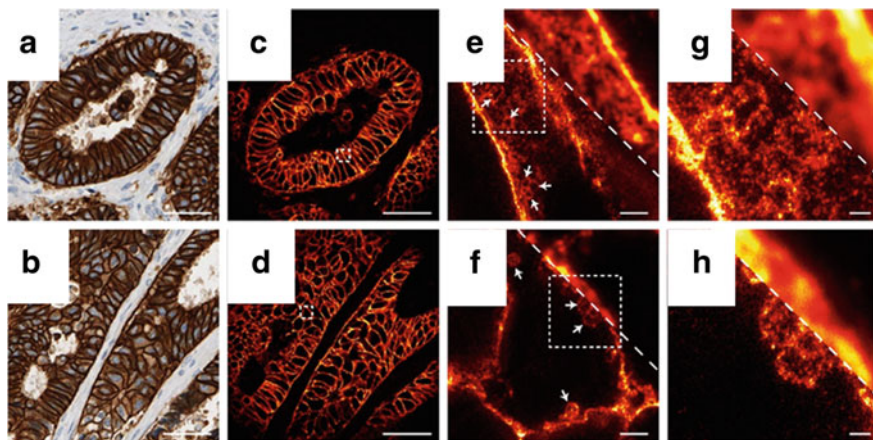


Fig. 16.11 Imaging of deparaffinized tissue slices of breast cancer tissue with conventional wide-field microscopy **a** and **b**, confocal **c–d**, **e**, **f** Magnified insets from **c** and **f**. **g** and **h** further magnification of (**e**), (**f**) Adapted from [106]

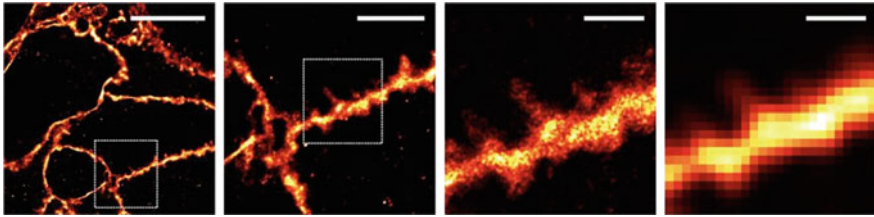


Fig. 16.12 SMLM images of HER2-positive cancer cells. The protrusions of the extracellular membrane are better visible in the SMLM images. From left to right increasing magnification insets (scale bars from left to right 10, 4, 1 to 1 μm). Last image in right is the conventional confocal microscopy image. Adapted from [109]

staining with acridine orange can produce images with similar contrast to that of Haematoxylin and Eosin (H&E). Such images feature super-resolution and additionally mosaics of the entire tissue section is possible with video-rate acquisition [110] (Fig. 16.13).

16.4.5 Multimodal Techniques

All these fluorescence-based techniques can offer new insight to different processes in the oncology field, but they can also be combined with another fluorescence-based technique to improve resolution or penetration or be combined with methods based on different contrast mechanisms.

In the field of skin imaging, confocal microscopy was combined with optical coherence tomography [111] (OCT), in a hand-held implementation [112], to detect margins of basal cell carcinoma in vivo, with the possibility of translating this technique in the clinic for diagnostic purposes. Two-photon microscopy was combined with coherent anti-Stokes Raman spectroscopy (CARS) a scattering-based method that can offer good visualization of lipids, for imaging tumour microenvironment and tracking of tumour cells and margins [113].

TPM was further combined with SIM. This combination offers the advantage of deeper penetration of the TPM beam and improved resolution offered by SIM. This multimodal technique was further combined with multifocal excitation in order to increase the speed of acquisition. This resulted in fast imaging with super-resolution of thick scattering samples such as *C. Elegans* embryos, *Drosophila Melanogaster* larval salivary glands, mouse liver tissue, and fast process in live zebrafish embryos [114–116].

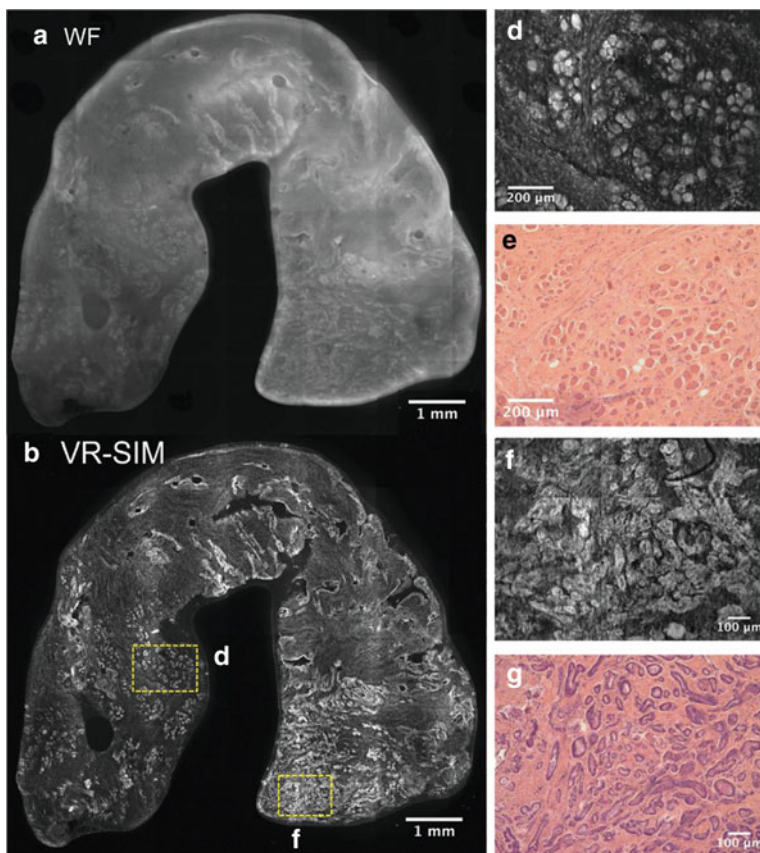


Fig. 16.13 SIM images of prostate cancer tissue section. **a** Wide-field and **b** the same section with SIM. Increase contrast is achieved with acridine orange staining. Magnified insets of **b** in **d–g** **c** and **d** areas of normal skeletal muscle and fibrous stroma. **f** and **g** depict areas of malignant glands. **d** and **f** SIM images. **e** and **g** H&E staining. Adapted from [110]

TPM microscopy has been also combined with optoacoustic imaging [117]. Two-photon images can be overlaid with optoacoustic images, resulting from the ultrasound signal due to the absorption of light at the focus of the objective, and offer contrast on vasculature and melanoma cells in vivo [118]. Such hybrid applications combine the advantages of TPM in deep penetration and high resolution with increased detection efficiency at deeper layers of tissue (Table 16.1).

Table 16.1 Characteristics of imaging techniques

	In vivo	Penetration depth	Resolution radial (XY)/axial (Z)	Label-free	Acquisition speed
TPM	Yes	200 μm	500/1500 nm	Yes	Video rate
CLSM/reflectance CLSM	Yes	50 μm /100 μm	250/750 nm–500/1500 nm	No/Yes	Video rate
LSM	Yes	50 μm /1–4 mm (in cleared samples)	1/1 μm	No	Video rate
STED	Yes	50 μm	70/120 nm	No	Video rate
SMLM	No	1–2 μm	20/100 nm	No	Seconds to minutes per frame
SIM	Yes	100 μm	120/400 nm	No	Video rate

16.5 Conclusion

Developments in advanced optical microscopy are fast. A whole plethora of techniques, all with their specific advantages, disadvantages, strongholds, and applications, is already available. Undoubtedly, new developments will come up, such as the combination of expansion and super-resolution microscopy. What we hope to have clarified is the enormous potential of advanced optical microscopy, both in fundamental research and in a more (pre)clinical setting. In that respect, especially interesting is the translation of these techniques to the clinic, e.g. by using micro-endoscopy or microscopy-at-the bedside. It definitely is worthwhile to look beyond gold standards and broadly applied techniques towards new developments.

References

1. Orlova A et al (2006) Tumor imaging using a picomolar affinity HER2 binding affibody molecule. *Cancer Res* 66:4339–4348
2. Holliger P, Hudson PJ (2005) Engineered antibody fragments and the rise of single domains. *Nat Biotechnol* 23:1126–1136
3. Keppler A et al (2003) A general method for the covalent labeling of fusion proteins with small molecules in vivo. *Nat Biotechnol* 21:86–89
4. Liss V, Barlag B, Nietschke M, Hensel M (2015) Self-labelling enzymes as universal tags for fluorescence microscopy, super-resolution microscopy and electron microscopy. *Sci Rep* 5
5. Chozinski TJ, Gagnon LA, Vaughan JC (2014) Twinkle, twinkle little star: photoswitchable fluorophores for super-resolution imaging. *FEBS Lett* 588:3603–3612
6. Van De Linde S et al (2011) Direct stochastic optical reconstruction microscopy with standard fluorescent probes. *Nat Protoc* 6:991–1009
7. Pawley JB (2006) *Handbook of biological confocal microscopy*, 3rd edn. <https://doi.org/10.1007/978-0-387-45524-2>

8. Dobbs J et al (2015) Confocal fluorescence microscopy for rapid evaluation of invasive tumor cellularity of inflammatory breast carcinoma core needle biopsies. *Breast Cancer Res Treat* 149:303–310
9. Huiskens J, Swoger J, Del Bene F, Wittbrodt J, Stelzer E. HK (2004) Optical sectioning deep inside live embryos by selective plane illumination microscopy. *Science* 305:1007–1009
10. Method of the Year 2014 (2014) *Nat Methods* 12:1
11. Keller PJ, Dodt HU (2012) Light sheet microscopy of living or cleared specimens. *Curr Opin Neurobiol* 22:138–143
12. Chen BC et al (2014) Lattice light-sheet microscopy: imaging molecules to embryos at high spatiotemporal resolution. *Science* 346
13. Liu TL et al (2018) Observing the cell in its native state: imaging subcellular dynamics in multicellular organisms. *Science*. <https://doi.org/10.1126/science.aag1392>
14. Denk W, Strickler JH, Webb WW (1990) Two-photon laser scanning fluorescence microscopy. *Science* 248:73–76
15. Masters BR, So PTC, Gratton E (1997) Multiphoton excitation fluorescence microscopy and spectroscopy of in vivo human skin. *Biophys J* 72:2405–2412
16. Helmchen F, Denk W (2005) Deep tissue two-photon microscopy. *Nat Methods* 2:932–940
17. Patterson GH, Piston DW (2000) Photobleaching in two-photon excitation microscopy. *Biophys J* 78:2159–2162
18. Perry SW, Burke RM, Brown EB (2012) Two-photon and second harmonic microscopy in clinical and translational cancer research. *Ann Biomed Eng* 40:277–291
19. Liu J (2015) Two-photon microscopy in pre-clinical and clinical cancer research. *Front Optoelectron* 8:141–151
20. Condeelis J, Weissleder R (2010) In vivo imaging in cancer. *Cold Spring Harbor Perspect Biol* 2
21. Provenzano PP, Eliceiri KW, Keely PJ (2009) Multiphoton microscopy and fluorescence lifetime imaging microscopy (FLIM) to monitor metastasis and the tumor microenvironment. *Clin Exp Metas* 26:357–370
22. König K (2000) Multiphoton microscopy in life sciences. *J Microsc* 200:83–104
23. Wang BG, König K, Halbhauer KJ (2010) Two-photon microscopy of deep intravital tissues and its merits in clinical research. *J Microsc* 238:1–20
24. Staughton TJ, McGillicuddy CJ, Weinberg PD (2001) Techniques for reducing the interfering effects of autofluorescence in fluorescence microscopy: improved detection of sulphorhodamine B-labelled albumin in arterial tissue. *J Microsc* 201:70–76
25. Hell SW (2009) Microscopy and its focal switch. *Nat Methods* 6:24–32
26. Betzig E et al (2006) Imaging intracellular fluorescent proteins at nanometer resolution. *Science* 313:1642–1645
27. Rust MJ, Bates M, Zhuang X (2006) Sub-diffraction-limit imaging by stochastic optical reconstruction microscopy (STORM). *Nat Methods* 3:793–795
28. Gustafsson MGL (2000) Surpassing the lateral resolution limit by a factor of two using structured illumination microscopy. *J Microsc* 198:82–87
29. Heintzmann R, Huser T (2017) Super-resolution structured illumination microscopy. *Chem Rev* 117:13890–13908
30. Heintzmann R, Jovin TM, Cremer C (2002) Saturated patterned excitation microscopy—a concept for optical resolution improvement. *J Opt Soc Am A* 19:1599
31. Gustafsson MGL (2005) Nonlinear structured-illumination microscopy: wide-field fluorescence imaging with theoretically unlimited resolution. *Proc Natl Acad Sci* 102:13081–13086
32. Vermeulen L et al (2013) Defining stem cell dynamics in models of intestinal tumor initiation. *Science* 342:995–998
33. Denais CM et al (2016) Nuclear envelope rupture and repair during cancer cell migration. *Science* 352:353–358
34. Shimokawa M et al (2017) Visualization and targeting of LGR5 + human colon cancer stem cells. *Nature* 545:187–192

35. Que S (2015) Non-invasive imaging technologies for the delineation of basal cell carcinomas. *J Invest Dermatol* 135:S32
36. Que SKT (2015) Research techniques made simple: noninvasive imaging technologies for the delineation of basal cell carcinomas. *J Invest Dermatol* 136:e33–e38
37. Schiffhauer LM et al (2009) Confocal microscopy of unfixed breast needle core biopsies: a comparison to fixed and stained sections. *BMC Cancer* 9
38. Tanaka N et al (2017) Whole-tissue biopsy phenotyping of three-dimensional tumours reveals patterns of cancer heterogeneity. *Nat Biomed Eng* 1:796–806
39. Uhlén P, Tanaka N (2018) Improved pathological examination of tumors with 3D light-sheet microscopy. *Trends Cancer* 4:337–341
40. Glaser AK et al (2017) Light-sheet microscopy for slide-free non-destructive pathology of large clinical specimens. *Nat Biomed Eng* 1
41. Matsui T et al (2017) Non-labeling multiphoton excitation microscopy as a novel diagnostic tool for discriminating normal tissue and colorectal cancer lesions. *Sci Rep* 7
42. Cicchi R et al (2010) Time- and Spectral-resolved two-photon imaging of healthy bladder mucosa and carcinoma in situ. *Opt Express* 18:3840–3849
43. Wu X et al (2013) Label-free detection of breast masses using multiphoton microscopy. *PLoS One* 8
44. Skala MC et al (2007) In vivo multiphoton microscopy of NADH and FAD redox states, fluorescence lifetimes, and cellular morphology in precancerous epithelia. *Proc Natl Acad Sci USA* 104:19494–19499
45. Ostrander JH et al (2010) Optical redox ratio differentiates breast cancer cell lines based on estrogen receptor status. *Cancer Res* 70:4759–4766
46. Liu Z et al (2018) Mapping metabolic changes by noninvasive, multiparametric, high-resolution imaging using endogenous contrast. *Sci Adv* 4
47. Huang S, Heikal AA, Webb WW (2002) Two-photon fluorescence spectroscopy and microscopy of NAD(P)H and flavoprotein. *Biophys J* 82:2811–2825
48. Alhallak K et al (2016) Optical redox ratio identifies metastatic potential-dependent changes in breast cancer cell metabolism. *Clin Oncol* 34:2303–2311
49. Patalay R et al (2011) Quantification of cellular autofluorescence of human skin using multiphoton tomography and fluorescence lifetime imaging in two spectral detection channels. *Biomed Opt Express* 2:3295–3308
50. Stringari C, Nourse JL, Flanagan LA, Gratton E (2012) Phasor fluorescence lifetime microscopy of free and protein-bound NADH reveals neural stem cell differentiation potential. *PLoS ONE*. <https://doi.org/10.1371/journal.pone.0048014>
51. Stuntz E et al (2017) Endogenous two-photon excited fluorescence imaging characterizes neuron and astrocyte metabolic responses to manganese toxicity/631/378/1689/364/639/624/1111/55/14/69/14/63/123 article. *Sci Rep*. <https://doi.org/10.1038/s41598-017-01015-9>
52. Pouli D et al (2016) Imaging mitochondrial dynamics in human skin reveals depth-dependent hypoxia and malignant potential for diagnosis. *Sci Transl Med* 8
53. So P, Kim H, Kochevar I (1998) Two-photon deep tissue ex vivo imaging of mouse dermal and subcutaneous structures. *Opt Express* 3:339–350
54. König K, Riemann I (2003) High-resolution multiphoton tomography of human skin with subcellular spatial resolution and picosecond time resolution. *J Biomed Opt* 8:432–439
55. König K, König K (2008) Clinical multiphoton tomography. *J Biophotonics* 1:13–23
56. Breunig HG, Studier H, König K (2010) Multiphoton excitation characteristics of cellular fluorophores of human skin in vivo. *Opt Express* 18:7857–7871
57. König K et al (2007) Clinical two-photon microendoscopy. *Microsc Res Tech* 70:398–402
58. Balu M, Mikami H, Hou J, Potma EO, Tromberg BJ (2016) Rapid mesoscale multiphoton microscopy of human skin. *Biomed Opt Express* 7:4375
59. Heuke S et al (2013) Detection and discrimination of non-melanoma skin cancer by multimodal imaging. *Healthcare* 1:64–83

60. Balu M et al (2015) In vivo multiphoton microscopy of basal cell carcinoma. *JAMA Dermatol* 151:1068–1074
61. Cicchi R et al (2007) Multidimensional non-linear laser imaging of basal cell carcinoma. *Opt Express* 15:10135
62. Patalay R et al (2012) Multiphoton multispectral fluorescence lifetime tomography for the evaluation of basal cell carcinomas. *PLoS One* 7
63. Seidenari S et al (2013) Multiphoton laser tomography and fluorescence lifetime imaging of melanoma: morphologic features and quantitative data for sensitive and specific non-invasive diagnostics. *PLoS One* 8:e70682
64. Flesken-Nikitin A, Williams RM, Zipfel WR, Webb WW, Nikitin AY (2004) Use of multiphoton imaging for studying cell migration in the mouse. *Methods Mol Biol* 294(335–46):335–346
65. Sano T et al (2016) Intravital imaging of mouse urothelium reveals activation of extracellular signal-regulated kinase by stretch-induced intravesical release of ATP. *Physiol Rep* 4
66. Wu Z et al (2017) Multi-photon microscopy in cardiovascular research. *Methods* 130:79–89
67. Kolesnikov M, Farache J, Shakhar G (2015) Intravital two-photon imaging of the gastrointestinal tract. *J Immunol Methods* 421:73–80
68. Wyckoff J, Gligorijevic B, Entenberg D, Segall J, Condeelis J (2011) High-resolution multiphoton imaging of tumors in vivo. *Cold Spring Harb Protoc* 6:1167–1184
69. Drew PJ et al (2010) Chronic optical access through a polished and reinforced thinned skull. *Nat Methods* 7:981–984
70. Sawinski J et al (2009) Visually evoked activity in cortical cells imaged in freely moving animals. *Proc Natl Acad Sci* 106:19557–19562
71. Megens RTA et al (2010) In vivo high-resolution structural imaging of large arteries in small rodents using two-photon laser scanning microscopy. *J Biomed Opt* 15:11108
72. Bewersdorf J, Pick R, Hell SW (1998) Multifocal multiphoton microscopy. *Opt Lett* 23:655
73. Niesner R, Andresen V, Neumann J, Spiecker H, Gunzer M (2007) The power of single and multibeam two-photon microscopy for high-resolution and high-speed deep tissue and intravital imaging. *Biophys J* 93:2519–2529
74. Kirkpatrick N et al (2012) Video-rate resonant scanning multiphoton microscopy: an emerging technique for intravital imaging of the tumor microenvironment. *IntraVital* 1:60–68
75. Condeelis J, Segall JE (2003) Intravital imaging of cell movement in tumours. *Nat Rev Cancer* 3:921–930
76. Friedl P, Gilmour D (2009) Collective cell migration in morphogenesis, regeneration and cancer. *Nat Rev Mol Cell Biol* 10:445–457
77. Alexander S, Koehl GE, Hirschberg M, Geissler EK, Friedl P (2008) Dynamic imaging of cancer growth and invasion: a modified skin-fold chamber model. *Histochem Cell Biol* 130:1147–1154
78. Dondossola E et al (2018) Intravital microscopy of osteolytic progression and therapy response of cancer lesions in the bone. *Sci Transl Med* 10
79. Iina O et al (2018) Intravital microscopy of collective invasion plasticity in breast cancer. *Dis Model Mech* 11
80. Patsialou A et al (2013) Intravital multiphoton imaging reveals multicellular streaming as a crucial component of in vivo cell migration in human breast tumors. *IntraVital* 2:e25294
81. Le Dévédec SE et al (2011) Two-photon intravital multicolour imaging to study metastatic behaviour of cancer cells in vivo. *Methods Mol Biol*. https://doi.org/10.1007/978-1-61779-207-6_22
82. Koga S et al (2014) In vivo subcellular imaging of tumors in mouse models using a fluorophore-conjugated anti-carcinoembryonic antigen antibody in two-photon excitation microscopy. *Cancer Sci* 105:1299–1306

83. Thomas G et al (2014) In vivo nonlinear spectral imaging as a tool to monitor early spectroscopic and metabolic changes in a murine cutaneous squamous cell carcinoma model. *Biomed Opt Express* 5:4281
84. Kantelhardt SR et al (2016) In vivo multiphoton tomography and fluorescence lifetime imaging of human brain tumor tissue. *J Neurooncol* 127:473–482
85. Lunt SJ, Gray C, Reyes-Aldasoro CC, Matcher SJ, Tozer GM (2010) Application of intravital microscopy in studies of tumor microcirculation. *J Biomed Opt* 15:011113
86. Bentolila NY, Barnhill RL, Lugassy C, Bentolila LA (2018) Intravital imaging of human melanoma cells in the mouse ear skin by two-photon excitation microscopy. In: Damoiseaux R, Hasson S (eds) *BT—reporter gene assays: methods and protocols*. Springer, New York, pp 223–232. https://doi.org/10.1007/978-1-4939-7724-6_15
87. Alexander S, Weigel B, Winkler F, Friedl P (2013) Preclinical intravital microscopy of the tumour-stroma interface: invasion, metastasis, and therapy response. *Curr Opin Cell Biol* 25:659–671
88. Beerling E, Ritsma L, Vrisekoop N, Derksen PWB, van Rheenen J (2011) Intravital microscopy: new insights into metastasis of tumors. *J Cell Sci* 124:299–310
89. Chen X, Nadiarynkh O, Plotnikov S, Campagnola PJ (2012) Second harmonic generation microscopy for quantitative analysis of collagen fibrillar structure. *Nat Protoc* 7:654–669
90. Provenzano PP et al (2006) Collagen reorganization at the tumor-stromal interface facilitates local invasion. *BMC Med* 4
91. Tilbury K, Campagnola PJ (2015) Applications of second-harmonic generation imaging microscopy in ovarian and breast cancer. *Perspect Med Chem* 7:21–32
92. Horton NG et al (2013) In vivo three-photon microscopy of subcortical structures within an intact mouse brain. *Nat Photonics* 7:205–209
93. Weigel B, Bakker G-J, Friedl P (2012) Intravital third harmonic generation microscopy of collective melanoma cell invasion. *IntraVital* 1:32–43
94. You S et al (2018) Intravital imaging by simultaneous label-free autofluorescence-multiharmonic microscopy. *Nat Commun* 9
95. Wang T et al (2018) Three-photon imaging of mouse brain structure and function through the intact skull. *Nat Methods* 15:789–792
96. Guesmi K et al (2018) Dual-color deep-tissue three-photon microscopy with a multiband infrared laser. *Light Sci Appl* 7
97. Hwang JY et al (2011) Multimodal wide-field two-photon excitation imaging: characterization of the technique for in vivo applications. *Biomed Opt Express* 2:356
98. Cheng L-C et al (2012) Spatiotemporal focusing-based widefield multiphoton microscopy for fast optical sectioning. *Opt Express* 20:8939
99. Rowlands CJ et al (2017) Wide-field three-photon excitation in biological samples. *Light Sci Appl* 6
100. Ducourthial G et al (2015) Development of a real-time flexible multiphoton microendoscope for label-free imaging in a live animal. *Sci Rep* 5
101. Liang W, Hall G, Messerschmidt B, Li MJ, Li X (2017) Nonlinear optical endomicroscopy for label-free functional histology in vivo. *Light Sci Appl* 6
102. Kundrat MJ, Reinhall PG, Lee CM, Seibel EJ (2011) High performance open loop control of scanning with a small cylindrical cantilever beam. *J Sound Vib* 330:1762–1771
103. Zhao Y, Nakamura H, Gordon RJ (2010) Development of a versatile two-photon endoscope for biological imaging. *Biomed Opt Express* 1:1159
104. Blom H, Widengren J (2017) Stimulated emission depletion microscopy. *Chem Rev* 117:7377–7427
105. Sharma S et al (2012) Correlative nanomechanical profiling with super-resolution F-actin imaging reveals novel insights into mechanisms of cisplatin resistance in ovarian cancer cells. *Nanomedicine Nanotechnol Biol Med*. <https://doi.org/10.1016/j.nano.2011.09.015>
106. Igen P et al (2014) STED super-resolution microscopy of clinical paraffin-embedded human rectal cancer tissue. *PLoS One* 9

107. Rönnlund D, Gad AKB, Blom H, Aspenström P, Widengren J (2013) Spatial organization of proteins in metastasizing cells. *Cytom Part A* 83:855–865
108. Rathje L-SZ et al (2014) Oncogenes induce a vimentin filament collapse mediated by HDAC6 that is linked to cell stiffness. *Proc Natl Acad Sci* 111:1515–1520
109. Creech MK, Wang J, Nan X, Gibbs SL (2017) Superresolution imaging of clinical formalin fixed paraffin embedded breast cancer with single molecule localization microscopy. *Sci Rep* 7
110. Wang M et al (2015) High-resolution rapid diagnostic imaging of whole prostate biopsies using video-rate fluorescence structured illumination microscopy. *Cancer Res* 75:4032–4041
111. Wang J, Xu Y, Boppart SA (2017) Review of optical coherence tomography in oncology. *J Biomed Opt* 22:1
112. Iftimia N et al (2017) Handheld optical coherence tomography–reflectance confocal microscopy probe for detection of basal cell carcinoma and delineation of margins. *J Biomed Opt* 22:076006
113. Lee M et al (2015) In vivo imaging of the tumor and its associated microenvironment using combined CARS/2-photon microscopy. *IntraVital* 4:e1055430
114. Andresen, V. *et al.* High-Resolution Intravital Microscopy. *PLoS One* 7, (2012)
115. York AG et al (2012) Resolution doubling in live, multicellular organisms via multifocal structured illumination microscopy. *Nat Methods* 9:749–754
116. Ingaramo M et al (2014) Two-photon excitation improves multifocal structured illumination microscopy in thick scattering tissue. *Proc Natl Acad Sci* 111:5254–5259
117. Tservelakis GJ, Soliman D, Omar M, Ntziachristos V (2014) Hybrid multiphoton and optoacoustic microscope. *Opt Lett* 39:1819
118. Kellnberger S et al (2018) Optoacoustic microscopy at multiple discrete frequencies. *Light Sci Appl* 7:109

Part III
Clinical Applications



Quantitative SPECT/CT—Technique and Clinical Applications

17

Philipp Ritt and Torsten Kuwert

Contents

17.1	Introduction.....	565
17.2	Quantitative SPECT/CT	567
17.2.1	SPECT/CT Instrumentation	568
17.2.2	Registration of Multimodal Images	570
17.2.3	Attenuation Correction of SPECT	570
17.2.4	Image Reconstruction	572
17.2.5	Scatter Correction	574
17.2.6	Partial Volume Correction.....	576
17.2.7	Calibration	578
17.3	Quantitative Accuracy	579
17.4	Clinical Aspects of Quantitative SPECT	580
17.5	Summary and Outlook	583
	References	584

17.1 Introduction

Single Photon Emission Computed Tomography (SPECT) is widely used in the field of Nuclear Medicine for various purposes. The most important diagnostic applications nowadays are skeletal imaging using Tc-99m-labeled polyphosphonates,

P. Ritt (✉) · T. Kuwert
Clinic of Nuclear Medicine, University Hospital Erlangen,
Ulmenweg 18, 91054 Erlangen, Germany
e-mail: philipp.ritt@uk-erlangen.de

© Springer Nature Switzerland AG 2020
O. Schober et al. (eds.), *Molecular Imaging in Oncology*,
Recent Results in Cancer Research 216,
https://doi.org/10.1007/978-3-030-42618-7_17

565

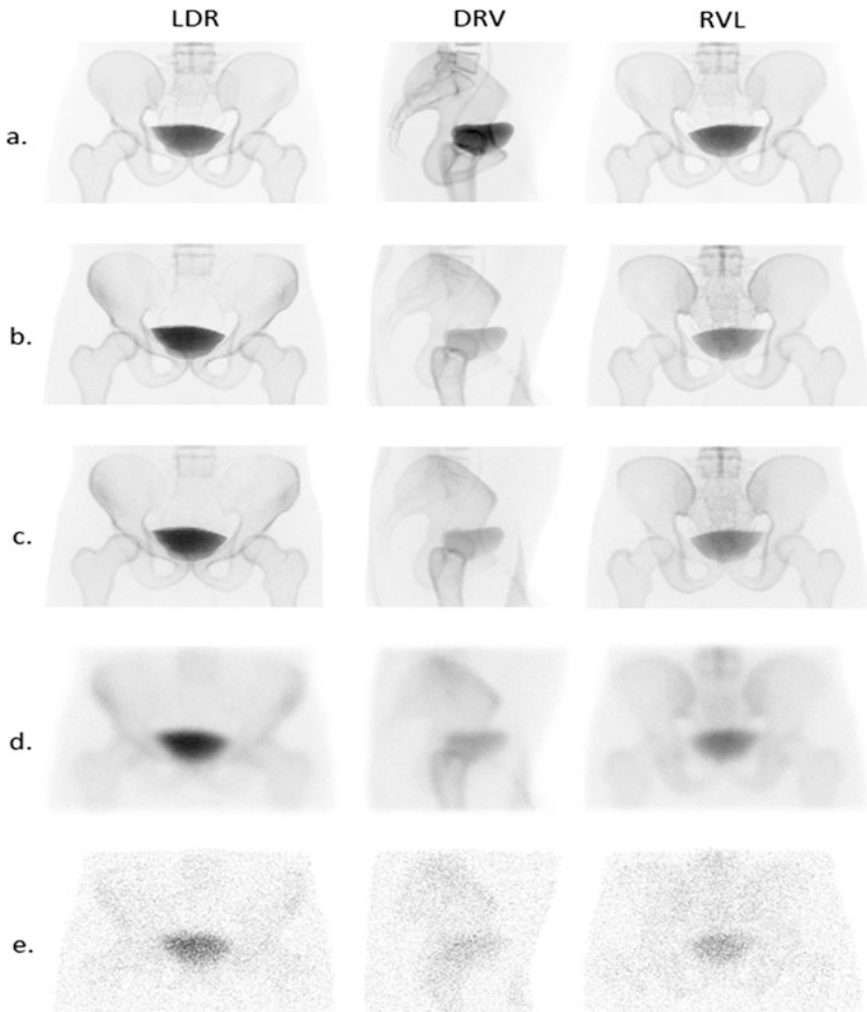


Fig. 17.1 Illustration of several image degrading effects based on simulated SPECT projection data. **a** perfect image, no degrading factors. **b** added photon attenuation, especially deep organs such as bladder appear at lower intensities. **c** added photon scatter, effect is noticeable as slight blurring, e.g., at the edge of bony structures. **d** realistic spatial resolution, depending on the activity distribution, counts are distributed outside (spill-out) or integrated into (spill-in) a region-of-interest. **e** realistic photon count level and noise

assessment of cardiac perfusion using Tc-99m-MIBI, and thyroid imaging using Tc-99m-pertechnetate. Additionally, SPECT is frequently applied for the confirmation of desired tracer distribution under I-131 therapy or the diagnosis of diseases of the neuronal system like Tc-99m-HMPAO for epilepsy or I-123-FP-CIT for dopamine transporter function.

Another established field of application is the individualized dosimetry for, e.g., I-131, Y-90, or Lu-177 labeled antibody therapies. For this purpose, an exact representation of the radioactive substance is especially desirable, which leads to the need of absolute quantification with SPECT. This process is compromised by photon scatter [1–3], photon attenuation [4–7], and partial volume artifacts [8, 9] (see Fig. 17.1 for an overview of image degrading effects). Thus, the following chapters are focused on SPECT/CT instrumentation, correction techniques of the aforementioned effects, and additional steps that are necessary for quantitative accurate absolute quantification in clinical application.

17.2 Quantitative SPECT/CT

SPECT allows the visualization of the distribution of radioactivity within the human body. The modality is widely used for clinical purposes (for more details, see the articles by, e.g., Bockisch et al. [10] or Schulthess et al. [11]). SPECT also holds the promise to exactly quantify the concentration of radioactivity within a given volume in absolute units, e.g., as kBq/cm³. This process is heavily compromised by photon scatter [1–3], photon attenuation [4–7], and partial volume artifacts [8, 9]. In SPECT, technical progress in that regard has been considerably slower than in PET. Various reports point to its lack of quantitative abilities [12–14].

In the present chapter, we outline the recent progress in that field for SPECT/CT. A simplified diagram of the image formation chain for quantitative SPECT is given in Fig. 17.2 for the purpose of orientation. We will begin with the reconstruction

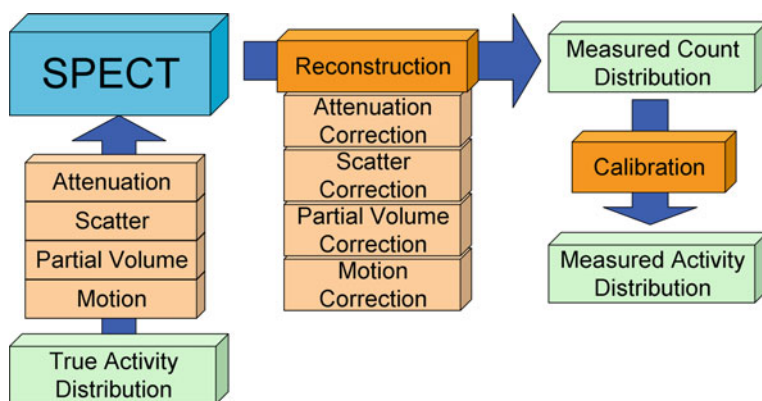


Fig. 17.2 Illustration of a simplified image formation chain. The image of the true activity distribution is influenced by several effects, namely, attenuation, scatter, partial volume, and motion. The SPECT reconstruction, along with possible corrections for those effects, results in a measured, 3-dimensional count distribution. By calibration, the count distribution can be translated into a measured activity distribution. Image adapted from [122]

methods that nowadays incorporate many corrections mentioned in the latter paragraphs. We will then focus on scatter and partial volume artifacts: In each of these paragraphs, a short explanation of the underlying physical effect and an overview of the appropriate correction techniques are given. In addition, we will briefly introduce an easy calibration technique.

Please note: In the following, it has to be assumed that the kinetics of the radioactive tracer of interest are slow with respect to the imaging time. If this is not true, significant quantification errors are very likely to occur and other approaches (e.g., dynamic SPECT) should be considered [15].

17.2.1 SPECT/CT Instrumentation

Modern SPECT devices are based on the gamma camera principle by Hal Anger [16, 17]. Its main components are a collimator, a scintillation crystal (mainly NaI), which is read out by photomultipliers, and subsequent electronics. The unit of these components is commonly referred to as detector. The detector itself is mounted onto a gantry, which allows movements of the detector head. For SPECT, nowadays the application of dual detector head cameras can be considered as the standard, single or triple detector head cameras are more uncommon (Fig. 17.3).

The SPECT camera setup is completed by the patient bed and computers for the data processing.



Fig. 17.3 Examples of SPECT/CT Systems. Image adapted from [123]. Upper left—GE Discovery NM/CT 670, two gamma camera heads here configured at 90° combined with a CT System. Upper right—Philips BrightView XCT, two gamma camera heads with a flat-panel detector. Lower image—Siemens Intevo, two gamma camera heads combined with a CT system

Image spatial resolution is in the following defined as the full width half maximum (FWHM) of a point source. In SPECT, it is mainly limited by collimator performance. SPECT utilizes absorptive collimation to identify the direction of the photon line-of-response (LOR). Positron emission tomography (PET), for example, uses electronic (coincidence) collimation to identify the LORs. Only a little fraction of the gamma quanta that reach the collimator surface pass through it. As a consequence the detection efficiency of SPECT when compared to PET (see, e.g., Cherry et al. [18] p. 340) is diminished to a large extent. It is important to notice that there is always a trade-off between spatial resolution and detection efficiency in SPECT. The collimators are typically designed with the maximum allowable resolution in order to partially compensate for the limited detection efficiency.

The achievable spatial resolution is also influenced by the detectors' intrinsic resolution defined as the spatial resolution of the detector without a collimator. The detectors of most clinical SPECT systems are made of a single crystal plate of NaI, which acts as scintillator and illuminates an array of photomultipliers. The intrinsic resolution of the detector depends on the photopeak energy of the radionuclide used and the crystal thickness of the NaI. Higher gamma quantum energy allows a better intrinsic resolution due to the higher light output of the scintillation. Larger crystal thickness increases intrinsic resolution. This is a consequence of the broader spread of the scintillation light before it exits the crystal and is detected with the photomultipliers.

In recent years, alternatives to the Anger camera have been introduced into clinical practice. Solid-state detectors, relying on materials like, e.g., cadmium telluride (CdTe) and cadmium zinc telluride (CZT) convert the gamma photons directly into electrical signals and offer better performance when converting gamma photons to electrons; this leads to an increased energy resolution ($\sim 5\%$ vs. $\sim 10\%$ at 140 keV) as compared to the Anger technique [19]. Additionally, the linear attenuation coefficient of CZT is slightly higher than that of NaI ($\sim 3 \text{ cm}^{-1}$ vs. $\sim 2 \text{ cm}^{-1}$ at 140 keV), which could potentially lead to an increased sensitivity [18], although this benefit is often foregone when it is decided, for economic reasons, to limit the thickness of the semiconductors. In fact, the considerable advantages in terms of the photon sensitivity (regularly reported to be 4–8 times higher) and resolution [20] of these cameras are achieved through changes to features other than just the detector material, e.g., through special geometries, adapted collimation, and pixelated detectors [21].

Typical SPECT detectors have an intrinsic spatial resolution in the range of 3–5 mm for Tc-99m. However, the image resolution for the whole SPECT system depends mainly on the collimator design and the source-to-collimator distance. For parallel-hole collimation of Tc-99m and typical source-to-collimator distances, it ranges from 7 to 15 mm FWHM. This is considerably higher than that seen in PET (2–5 mm FWHM). By using other collimator geometries, e.g., (multi-) pinhole, even lower spatial resolution than in PET can be achieved [22]. Branderhorst et al. [23], for example, obtained sub-millimeter (FWHM) resolution for their small animal SPECT camera for Tc-99m. However, these collimator geometries nowadays seem to be used more frequently for small animal studies than in clinical

practice. An in-detail description on collimator geometries can be found in [18]. An improved spatial resolution of the imaging system helps to avoid partial volume effects.

The SPECT/CT is a combination of a SPECT camera and an X-ray computed tomography (CT). SPECT and CT are in these systems installed in sequential order, attached to a common gantry with just one patient bed.

This setup helps to solve two major problems, registration and attenuation correction, of multi-modality imaging at the same time, as will be discussed in the following chapters.

17.2.2 Registration of Multimodal Images

In typical systems, SPECT and CT data acquisition is performed sequentially: Usually, SPECT is carried out first, followed by CT. The patients are transferred by a table movement from one modality to the other. A huge advantage of this procedure is that the patient is scanned by both modalities in roughly the same position. SPECT and CT thus are acquired in good approximation at the same patient position. Together with the information of the parameters of the table movement between both acquisitions, this can be used to facilitate a precise assignment between functional (SPECT) and anatomical (CT) images. This so-called “hardware fusion” is, in general, superior to retrospective fusion with regard to image alignment. The registration accuracy of the hardware fusion reaches 1–2 mm for organs which are not affected by respiratory movement [24]. However, the registration accuracy for organs that are affected by respiratory movements is reported to be significantly higher (5–7 mm) [25]. Partially, this is caused by differences in acquisition time between the modalities. While a SPECT scan usually takes 10–30 min and spans over a lot of respiratory cycles, a CT scan often is acquired in one phase of the respiratory cycle only. Nevertheless, in order to minimize misalignment, the CT should be acquired in a resting expiratory position [26].

17.2.3 Attenuation Correction of SPECT

SPECT images are heavily affected by the effect of photon attenuation (see Fig. 17.4).

The probability P_{Det} for gamma quanta emitted at \vec{a} for reaching a detector at position \vec{D} (under the assumption that it is emitted in the proper direction) is calculated according to Eq. 17.1:

$$P_{Det} = \exp\left\{\int_{\vec{a}}^{\vec{D}} -\mu(\vec{r})d\vec{r}\right\} \quad (17.1)$$

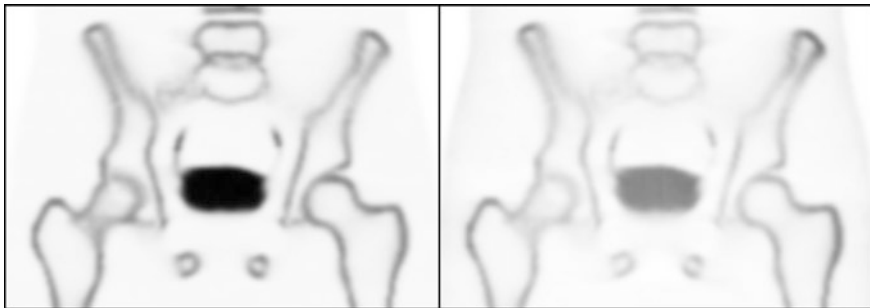


Fig. 17.4 A reconstructed SPECT image of simulated bone scintigraphy (Tc-99m). In the simulation, photon attenuation could be either simulated or omitted. The image with realistic photon attenuation (right side) shows a relative overestimation of the activity at the rim of the patient and an underestimation at the center when compared to the image without photon attenuation (left side)

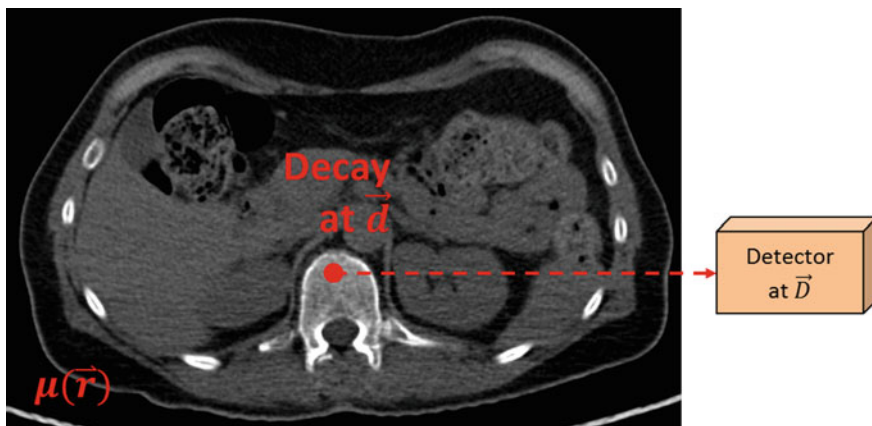


Fig. 17.5 A simplified illustration of the detection of a decay event: The signal from the decay at position \vec{d} is lowered by photon attenuation. The amount of attenuation depends on the spatially non-constant linear attenuation coefficients $\mu(\vec{r})$ and on the distance between the detector and the decay, $|\vec{D} - \vec{d}|$. Image adapted from [122]

The line integral covers the path of the radiation from its origin through the object, to the location of its detection (see Fig. 17.5 for a simplified illustration).

For SPECT imaging, the probability depends on the (unknown) location of the decay \vec{d} and on the linear attenuation coefficients $\mu(\vec{r})$ of the object.

For the correction of the attenuation effect, the spatial distribution of the attenuation coefficients of the examined object for the photon energy of the used

radionuclide needs to be known. The distribution of attenuation coefficients (called attenuation map) can be generated through a simple transformation of a transmission scan. First, the transmission images need to be converted to the attenuation factors valid at the effective energy of the emission scan (140 keV for Tc-99m); then, they need to be corrected for the spatial registration between the emission and transmission images. The resulting attenuation map can, for example, be integrated into the reconstruction step in order to correct for photon attenuation.

Before the introduction of hybrid SPECT/CT devices, radionuclide (source-based) transmission measurements (e.g., using Gd-153, Tc-99m, or Ba-133) were used for obtaining the attenuation map.

With the availability of SPECT/CT hybrid devices, and with their ability to perform highly correlated high quality X-ray CT transmission scans, it is nowadays the clinical standard to use these scans not only for fused viewing, but also for attenuation correction. The CT scans are obtained in Hounsfield units. These units have to be converted to the linear attenuation coefficients valid at the respective photon energy of the radionuclide, which is for, e.g., Tc-99m 140 keV.

In some cases, patient motion could occur between the emission and transmission acquisitions in a hybrid system. This can lead to artifacts in reconstructed attenuation-corrected images, which in turn could lead to false readings of the corrected SPECT images. A manual post-registration could help to prevent such artifacts [27].

Still, the methods that rely on the segmentation of contours in SPECT can be sufficient for SPECT quantification in “easy” anatomies like the brain. Nevertheless, the attenuation correction by SPECT/CT has become the clinical standard and is, in general, highly recommended. Attenuation and other corrections are obligatory for accurate quantification with SPECT/CT, which will be discussed in the following chapter.

17.2.4 Image Reconstruction

Image reconstruction is the technique used to transform the measured 2-D projection data into a 3-D activity distribution. In contrast to CT, which often employs analytic techniques like back projection, iterative reconstruction techniques prevail in SPECT. For a review of the different algorithms, see [28].

Most iterative techniques rely on mathematical models which assume a linear dependency of the image f (vector with elements f_j representing the voxels of the activity distribution) and the projection data p (vector with elements p_i representing detector pixels) via the system matrix A . Each element A_{ij} describes the probability that a photon originating from voxel j is detected at pixel i . The projection data thus can be expressed as a multiplication of the system matrix A by f (Eq. 17.2):

$$A\mathbf{f} = \mathbf{p} \quad (17.2)$$

The most common iterative techniques are the ML-EM algorithm and its accelerated version, OS-EM. ML-EM was first applied to SPECT in 1984 [29, 30]. Its relatively high computational requirements (compared with filtered back projection) delayed its widespread use until the late 1990s. It is based on the fact that the image f consists of Poisson-distributed random variables and it seeks to maximize the likelihood of the observed data given the source f . The well-known update rule of the iterative ML-EM algorithm is given in Eq. 17.3.

$$f_j^{new} = \frac{f_j^{old}}{\sum_l a_{lj}} \sum_i a_{ij} \frac{P_i}{\sum_k a_{ik} f_k^{old}} \quad (17.3)$$

Besides explicit Poisson-noise modeling, an important additional advantage of ML-EM is its capacity to implement the crucial attenuation and scatter corrections and to model the collimator-detector response (CDR) directly into the reconstruction. While the attenuation and scatter corrections model the interaction of the photons with the imaged object, the latter represents their interaction with the detection system (collimator, crystal, and electronics). The most important components of the CDR are: (a) the intrinsic response that is caused by scatter occurring in the crystal itself and the uncertainty of the position estimation of the detected photon, (b) the geometric response which represents a distance-dependent spatial resolution caused by the finite bore length and width of the collimator, (c) scatter in the collimator itself, and (d) septal penetration when photons are detected after passing through the walls of the collimator holes.

The CDR is commonly assumed to be Gaussian and modeled as such in the reconstruction. In general, it is reported that this leads to significantly improved image quality [31–33]. The importance of CDR compensation was shown in a large multi-center study [34] that compared a variety of advanced SPECT/CT reconstruction algorithms for cardiac phantoms and found considerable improvements in image quality. The study used the full width at half maximum (FWHM) of the wall thickness of the left ventricle as a measure of the spatial resolution and reported a significant reduction relative to FBP (on average 22.0 mm FWHM) for OS-EM without CDR modeling (20.6 mm FWHM) and with CDR modeling and corrections for scatter (16.2 mm FWHM). Similar trends in favor of the advanced reconstruction techniques are reported for other image quality metrics like contrast and background homogeneity. Additionally, several studies found that with iterative reconstruction techniques, the acquisition time or patient dose could be reduced by a factor of up to two, for example in cardiac [35, 36] and skeletal examinations [37].

Still, it is clear that the Gaussian modeling approach has only limited precision since significant differences between the model and the real CDR can be found, especially in regions on the edge of the geometric response. There, the Gaussian model systematically underestimates the number of detected counts. Additionally, a rotationally invariant function like the Gaussian cannot express the contours found in real CDRs which mimic the shape of the collimator bore. Multiple solutions have

been proposed for further improving the modeling: MC simulations can be used to calculate the CDR during reconstruction [38] or prior to reconstruction [39]. In later approaches, a set of distance-dependent CDRs is calculated, stored and then used in the iterative reconstruction. Other approaches rely on more sophisticated mathematical models and fit their free parameters to a set of point source measurements [40]. Nevertheless, Gaussian modeling is the method that is applied in most clinically available tools.

17.2.5 Scatter Correction

Scatter is another factor which degrades the quality of SPECT images, although its correction is somewhat less important [41] than the corrections for the collimator-detector response or for photon attenuation. However, since very accurate technical solutions for these latter problems are already available in clinical practice, scatter remains a major limiting factor of the image quality and quantitative accuracy of current SPECT systems, particularly when using isotopes with complex emission spectra. There exist numerous techniques for scatter correction; describing them all is beyond the scope of this article, but an extensive review can be found in [42].

The Compton Effect is the dominant process for scattering of photons in the patient and in the collimators at clinically relevant energies in Nuclear Medicine. Coherent scattering, an interaction between the photons and atoms or molecules, which is another phenomenon capable of deflecting photons from their original direction, is important only for energies below 50 keV. With Compton scattering, the photon transfers part of its energy to an electron and should be detected at lower energies in an ideal detector with perfect energy resolution. In a real detector, the uncertainty of energy determination limits the detectable energy loss. In general, the amount of energy loss depends on the scatter angle. The result of this relationship is that scattered photons are often detected at locations unrelated to their initial trajectories, leading to a loss of information about the activity distribution being imaged. The proportion of scattered photons in a particular acquisition is object dependent but can be rather high. One study reports that the ratio of scattered to unscattered photons in myocardial Tc-99m imaging is typically 0.34 [43]. The amount of Compton scatter originating in the collimators is most likely negligible for 140 keV Tc-99m imaging but increases with increasing energy and thus is considerably higher for I-131 at 364 keV [44]. In order to minimize the amount of scatter and to exclude photons that do not originate from the decay of the respective radionuclide, energy windows around the photopeak of interest are applied. Nevertheless, due to the limited energy resolution of SPECT detectors and the typical width of the photopeak windows, a considerable amount of scattered photons is still recorded.

A very common approach in clinical routine is based on utilizing dual-[1], triple-[45], or even multi-energy [2] windows. The additional scatter energy windows are placed below and/or above the photopeak energy window. Additional projections

are acquired at those windows simultaneously to the image at the photopeak window. Subsequently, for each pixel of the projections at the photopeak window, the amount of scattered radiation can be estimated from the scatter window images. This amount is subtracted from the projections or incorporated in the iterative reconstruction.

This underlines the fact that additional techniques are necessary to account and correct for scatter. First, the amount of scattered photons in the photopeak window needs to be estimated. Here, two paradigms are possible: estimates based on directly measured data or estimates based on modeling. The most common approach, i.e., that of measuring the counts in multiple additional energy windows [1, 45] adjacent to the photopeak window, belongs to the former paradigm. For the triple energy window (TEW) technique, the scattered photons in the photopeak can be calculated according to Eq. 17.4 for every pixel. Here, n_s are the counts of the pixel that were scattered and n_l , n_u are the measured counts in the lower and upper scatter windows. The widths of the photopeak, the lower scatter, and upper scatter window are denoted by w_p , w_l , and w_u .

$$n_s = \left(\frac{n_l}{w_l} + \frac{n_u}{w_u} \right) \times \frac{1}{2} w_p \quad (17.4)$$

The calculated amount of scattered photons is then incorporated into the image reconstruction. This can be achieved in multiple ways. The simplest approach is to subtract the counts from the photopeak window. However, it was found [46] that incorporating the amount of scatter directly into the forward projector in the maximum likelihood expectation maximization (ML-EM) algorithm is a superior approach in terms of image quality and quantitative accuracy. This is to a large extent explained by the high amount of noise in the scatter window data which is due to the generally low count number in these windows.

As an extension of the TEW method, so-called spectral models can be applied. Such methods try to improve the accuracy and the noise properties of the scatter estimates via a finer sampling of the energy distribution of the photons that reach each detector pixel. Ideally, one would record the energy of each photon individually (list-mode acquisition). With this information, models that predict the amount of scatter in the photopeak window could be estimated with good confidence and low noise [47]. Despite the high accuracy of these methods, to the best of our knowledge, no scientific studies in this field have been published in recent years. However, we assume that such approaches might attract renewed interest if list-mode acquisitions become routinely available on commercial SPECT systems.

Scatter estimation and correction with the help of full Monte Carlo (MC) simulations has been a trend in research in recent years. These simulations are supported by the availability of faster computational hardware and the development of accelerated versions of the MC algorithms [48]. Two important prerequisites for these simulations are the estimates of the spatial distributions of the radioactive source and of the probability that scatter occurs. For this reason, MC simulations are usually carried out in each step of the iterative SPECT reconstruction, since the

source distribution is not known a priori and is therefore updated at each iteration [49]. The probability that scatter occurs can be estimated using transmission scans of the object, which are readily available with SPECT/CT systems. Drawbacks of these methods are the still comparatively long calculation times and the inability to account for photons that originate from outside the camera's field of view. A faster method that relies on partial MC simulations and approximated scatter patterns is called effective source scatter estimation [50].

However, despite the availability of very sophisticated scatter correction methods, the estimation of scatter by either TEW or DEW (the dual energy window approach that neglects upper scatter) and its correction in the ML-EM or in the ordered subset expectation maximization (OS-EM) algorithm is still the standard approach in clinical SPECT.

17.2.6 Partial Volume Correction

Partial volume effects are caused by the limited spatial resolution of the SPECT device. Radioactivity concentration in regions of interest (ROI) in structures smaller than approximately 2–3 times of the FWHM is mis-quantified: The activity in ROIs of that size is either under- or over-estimated, depending on the combination of “spill-in” and “spill-out” effects. Spill-in means that activity from outside the ROI or structure due to the limited spatial resolution is integrated (added) to the activity inside the ROI: The activity inside the ROI is erroneously increased. Spill-out implies that the activity of the ROI or structure is distributed over its borders (again due to limited spatial resolution) and therefore “lost”: The activity measured inside the ROI is then underestimated.

Most importantly, the degree of the partial volume effect depends on the system resolution of the imaging system relative to the size of structures in which activity is to be quantified. Patient motion can be another cause for increased partial volume effects, especially in clinical settings.

The approaches for a correction of the partial volume effect are divided into two groups: Approaches that are based on additional information from images (e.g., CT and MR) of the structures in question and methods that work solely on the emission images.

If only the average activity concentration in a sufficiently large object is of interest, like, e.g., in organ-based dosimetry, one simple way of compensating the partial volume effect is by careful definition of the region/volume of interest (ROI/VOI) for the evaluation of the activity. As mentioned above, the counts registered by the detector are distributed over an area which is larger than the physical extent of the object of interest. Thus, for “hot” objects in a comparably “cold” background, one could dilate the VOI over the actual physical extent as given by CT and partially recover the counts otherwise lost due to spill-out. The extent of dilation should be carefully chosen based on the target-to-background ratio and the spatial resolution of the SPECT acquisition. The accuracy of this method is varying strongly, depending on the activity distribution that surrounds the

VOI. Alternatively, for large objects that can be assumed having homogenous tracer uptake, one could draw a smaller spherical VOI, in a sub-region unaffected by partial volume effect and extrapolate to the whole VOI [51, 52].

Another common and still simple post-reconstruction approach in the latter group is founded on measurements with physical phantoms, simulation studies, or theoretical derivations: As outlined by Hoffman et al. [53] and Kessler et al. [8] recovery coefficients (the ratio of apparent activity concentration to true activity concentration) for simple geometries (e.g., spheres, discs, and cylinders) can be measured or estimated and consequently be used to calculate corrected values for the amount of radioactivity in those structures. Several groups report that this successfully improves quantification accuracy [5, 9, 54]. However, a limitation of this approach is its applicability to only simple geometries; in general, the radioactive distribution in a patient will not follow this assumption. Another method is the deconvolution-based partial volume correction: Seo et al. [55] report with their implementation an accuracy of 10% for In-111 in lesions with a volume of down to 8 ml.

Every technique that results in an improved spatial resolution of the imaging system helps to avoid or lower the influence of the partial volume effect. For example, some methods that are described in the *Image Reconstruction* paragraph which incorporate information about the collimator-detector response function will improve the systems spatial resolution to some extent and therefore can be interpreted as partial volume correction technique. For example Hutton et al. [56] report improved accuracy for the simulated Mathematical Cardiac Torso (MCAT) phantom for their implementation of the detector-response modeling into the ML-EM and OS-EM reconstruction.

The other group of methods utilizes structural and anatomical information in the form of segmented images from another imaging modality (CT, MR, and US) for partial volume correction. The segmentation itself can be done in a fully automatic fashion or by manually outlining ROIs. The simple methods rely on multiple two-class segmentation (regions with activity and regions without activity). Pretorius et al. [57], Da Silva et al. [58], and Tang et al. [59] apply this approach to co-registered myocardial CT images on the MCAT phantom and are able to obtain improved visual characteristics as well as a higher quantitative accuracy of the corrected SPECT data.

$$\begin{bmatrix} t_1 \\ t_2 \\ \vdots \\ t_n \end{bmatrix} = \begin{bmatrix} \omega_{11} & \omega_{21} & \cdots & \omega_{n1} \\ \omega_{12} & \ddots & & \omega_{n2} \\ \vdots & & \ddots & \vdots \\ \omega_{1n} & \omega_{2n} & \cdots & \omega_{nn} \end{bmatrix} \times \begin{bmatrix} T_1 \\ T_2 \\ \vdots \\ T_n \end{bmatrix}. \quad (17.5)$$

A more complex method is based on the geometric transfer matrix (GTM), which was first applied by Rousset et al. [60, 61] on brain PET studies: It basically can handle any desired number n of regions, in which the activity distribution is

assumed to be homogenous. The observed activity t_i of a tissue class i is modeled as a linear combination of the true activities T_j of all other tissues classes $j = 1 \dots n$. The spatial definition of those regions is done by segmenting (automatically or manually) CT or MRI images. The matrix components ω_{ij} describe the regional transfer coefficients: The diagonal terms represent the spill-out of the regions; the off-diagonal terms define the spill-in from other regions. The ω_{ij} can be modeled on basis of the definition of the regions and the point spread function of the SPECT system. As soon as all the components ω_{ij} are known (full-rank transfer matrix) the true activities T_j can be computed by solving the linear equation defined in Eq. 17.5.

Du et al. [62] compare variants of the GTM approach to uncorrected images in a physical brain phantom for Tc-99m; they find a substantial reduction of the bias caused by the partial volume effect. Soret et al. [63] studied the effect of the GTM correction on I-123 using a physical brain phantom and segmentation of CT images. They found an underestimation of up to 50% when compared to the true activity concentration for uncorrected images and small structures (e.g., putamen). The application of the partial volume correction leads to an overestimation of about 10%, which is a significant improvement.

17.2.7 Calibration

$$S_{Vol} = \frac{R}{V_{VOI} \cdot c_{Vol}} \times \exp\left(\frac{T_0 - T_{cal}}{T_{1/2}} \cdot \ln 2\right) \times \left(\frac{T_{acq}}{T_{1/2}} \cdot \ln 2\right) \times \left(1 - \exp\left(-\frac{T_{acq}}{T_{1/2}} \cdot \ln 2\right)\right)^{-1} \quad (17.6)$$

An important requirement for quantitative accurate SPECT is the determination of the system volume sensitivity S_{Vol} (Eq. 17.6). This is needed for the calibration of the scanner to absolute values and typically obtained by a correlation of measured results to a calibrated well counter. This process is standardized and its description can be found in detail, for example, in the NEMA protocols [64]. Its principle is briefly outlined in the following: In order to avoid partial volume effects, a large cylindrical phantom with known activity concentration c_{Vol} is scanned with the SPECT system. Subsequently corrections for attenuated and scattered photons are applied and a large VOI with volume V_{VOI} is defined in the reconstructed image. T_0 is the start time, T_{acq} the duration of the acquisition. $T_{1/2}$ is the half time of the used radionuclide, T_{cal} the time of the activity calibration, and R represents the counting rate measured in the VOI. Finally, based on Eq. 17.4, a calibration factor, which allows conversion from detected counts per second to Becquerel is calculated.

This calibration factor is specific for every radionuclide as well as for different intrinsic detector sensitivities and collimators. It is possible and in some cases

beneficial to have count rate dependent calibration factors. Reasons for this are thought to be non-linearities of the detector at the different count rates and dead time effects at high activities. Those effects will be stronger for higher energy radionuclides (e.g., I-131). Dewaraja et al. [65] report about dead time and pulse pile-up effects for the SPECT quantification of therapeutic activities of 2–6 GBq I-131.

Another important development for SPECT was the commercial introduction and availability of SPECT/CT systems and reconstruction workstations which provide images in quantitative units (often Bq/mL) as output. For most of these systems, one first needs to determine a proper calibration factor which is then applied in the image reconstruction. One exception is the xSPECT Quant technique introduced by Siemens Healthineers [66]. It relies on NIST-traceable quantitative sources and currently offers quantitative capabilities for the radionuclides (Tc-99m, I-123, In-111, and Lu-177). This promises to minimize the variability of quantitative data obtained at different centers/hospitals and helps to standardize quantitative SPECT, which could be advantageous for multi-centric studies.

17.3 Quantitative Accuracy

Based on 21 evaluated studies from the literature [67–87], average quantitative errors of $3.8 \pm 0.8\%$, $6.6 \pm 1.4\%$, $5.5 \pm 1.7\%$, and $9.4 \pm 2.0\%$ (all mean \pm standard error) were reported for Tc-99m, Lu-177, I-131, and PET (Fig. 17.6). The accuracy for Lu-177 and I-131 appears to be lower than for Tc-99m, which could be

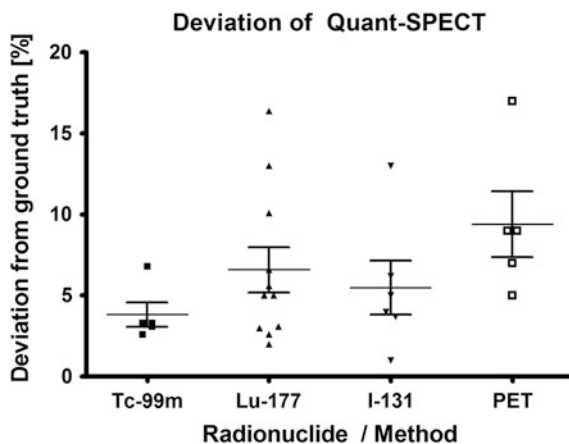


Fig. 17.6 Overview of the results of 21 studies reporting on the quantitative accuracy of SPECT and PET, separated by method and, in the case of SPECT, by radionuclide. Markers indicate the average deviation between ground-truth and imaging-derived quantitative values, as reported by the respective study. Additionally, mean values and standard error of the mean are provided for each group

due to higher scatter fraction, lower spatial resolution, and pulse pile-up. Generally, quantitative accuracy in PET is in the same range, at least for sufficiently large structures. Nevertheless, for smaller structures, PET will most likely achieve better quantitative accuracy due to its higher spatial resolution. Generally, a quantitative accuracy of within 10% error could be achieved.

17.4 Clinical Aspects of Quantitative SPECT

The literature on the clinical use of quantitative SPECT/CT is still scarce. A Pubmed research using the key words “Quantitative SPECT/CT patients” conducted end of March 2019 yielded altogether 168 hits. By screening this list and disregarding, in particular, papers dealing primarily with methodological issues, we identified 33 original publications that reported the use of quantitative SPECT/CT for predominantly clinical purposes. This database was complemented by some other evidence found in less formalized literature searches as basis for the subsequent review. In 2010, it was first shown that a commercially available SPECT/CT system has the potential to quantify regional radioactivity concentrations in absolute units [82]. At this point in time, quantitative SPECT/CT had to recur to research protocols, accessible only in specialized institutions. In 2015, SPECT/CT hybrid systems allowing for true quantitative SPECT/CT have become commercially available. Since then, a moderate number of papers dealing with this topic have been published (Fig. 17.7a). As a variety of clinically relevant SPECT/CT examinations exists, it is also not surprising that the topics addressed by these publications are heterogeneous as well (Fig. 17.7b): Quantifying radioactivity concentration in the skeleton has been the most frequent indication, followed by the use of quantitative SPECT/CT for dosimetry and its application to thyroid disease.

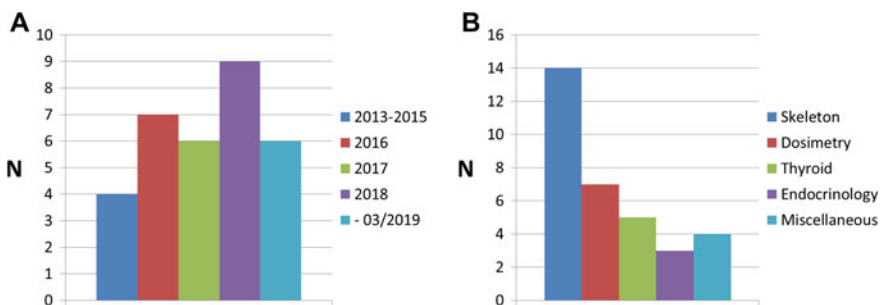


Fig. 17.7 Results of a PubMed search using “quantitative SPECT/CT patients” as keywords. **a** provides the number of papers found per year of publication, **b** the number of papers found per organ system examined

Calculating normal ranges for different skeletal sites would, in principle, improve the diagnosis of osseous disease. Directly after development of the methodology, Cachovan et al. measured the radioactivity concentration in spongy bone of the vertebral bodies of women injected by Tc-99m-methylenediphosphonate for routine bone scintigraphy, reporting a value of 48.15 kBq/ml [88]. This translated into standardized uptake values (SUV) of approximately 6, corresponding in magnitude to SUV values reported for F-18-fluoride-PET/CT of approximately 5 [89]. Arvola and coworkers could demonstrate a highly significant correlation between SUV values determined in osseous structures by F-18-fluoride-PET/CT and those of SPECT/CT with Tc-99m-HDP [90]. As yet, normal ranges determined in sufficiently large groups of subjects have, however, not been published. Nevertheless, several authors have reported the use of SUV values to differentiate between benign and malignant skeletal foci of prostate cancer with the goal to determine total tumor burden in automated approaches: Umeda and coworkers, e.g., performed receiver operation characteristic (ROC) analyses and reported an SUV threshold of 7 for this purpose [91]. Kuji et al. demonstrated that osseous metastases of prostate cancer could be reliably differentiated from hot spots due to degenerative alterations on the basis of their SUV values [92]. Quantitative skeletal SPECT/CT for diagnosing bone disease may also help in risk stratification for surgical treatment of accessory navicular bones [93], in the diagnosis of transthyretin cardiac amyloid [94], and in the evaluation of temporal mandibular joint disorder [95]. Evidence also exists with regard to the potential value of quantitative skeletal SPECT/CT to evaluate painful prostheses and the severity of osteoarthritis [96, 97].

The growth of bone metastases is difficult to assess by medical imaging. This is due to the following methodological reasons: Osteolytic metastases usually lack clearly defined borders, their size is, therefore, difficult to determine precisely on CT or MRI images. Using these modalities, it is also not reliably possible to diagnose whether sclerotic foci are still vital or represent healed and inactive disease. Bone scintigraphy is, in principle, suited to provide information on at least the regression of malignant skeletal foci, but changes in activity are difficult to assess by visual interpretation only: Beck and coworkers demonstrated in a small group of subjects that visual evaluation of changes in activity of bone metastases was erroneous in every third patient when compared to quantitative SPECT/CT as the gold standard [98]. No paper has as yet studied the value of quantitative SPECT/CT for monitoring the activity of bone metastases. It is clear that in this context also the flare phenomenon will have to be considered. A prospective study using F-18-fluoride-PET/CT to monitor response to treatment in metastatic prostate cancer to the bone could, however, demonstrate a strong correlation of PET response with progression-free survival [99]; this suggests that skeletal SPECT/CT could be used analogously in the future.

Quantitative SPECT/CT holds some promise to improve dosimetry of molecular radiotherapy. The increasing need for the latter arises from narrow risk-benefit ratios encountered in the new therapies available in clinical nuclear medicine such as those directed against metastatic neuroendocrine tumors or metastatic prostate cancer. Until the development of quantitative SPECT/CT, dosimetry employed

planar imaging only, often relying on the calculation of geometric means of organ uptake to account for variations in the localization of organs and neoplastic lesions. However, the accuracy of this approach is confounded by activity from overlying organs. This restriction does not apply to quantitative SPECT/CT. Using this technology, Delprete and coworkers (2019) conceived a personalized protocol for Lu-177-octreotate peptide receptor radionuclide therapy (PRRT), in which the activity given to the patients was adjusted to deliver to the kidney the maximally tolerable dose [100]. They could demonstrate that there was a median 1.26-fold increase in the cumulated maximal tumor absorbed dose when compared to a protocol in which fixed empirical doses would have been used. Dittmann and coworkers compared the performance of planar scans and quantitative SPECT/CT to calculate the lung shunt fraction before radioembolization of liver tumors [101]. In their paper, the lung shunt fraction determined using SPECT/CT was considerably lower than that measured on planar images, potentially allowing the use of higher doses in radioembolization of patients with significant shunting to the lung. SPECT/CT approaches to dose calculation for radioembolization have been reported also by other authors [102–104]. Therapy of prostate cancer using Lu-177-labeled radioligands against the prostate membrane specific antigen (PSMA) has entered the field quite recently [105] and might also benefit from the increase in accuracy afforded by the use of SPECT/CT in dose calculation [106]. Clearly, the accuracy of internal dosimetry does not only depend on the accuracy in the measurement of regional survival radioactivity concentrations, but also on other factors such as the determination of the kinetics of the therapeutic radiopharmaceutical in normal organs and tumor deposits as well as on tumor-related factors such as heterogeneity of uptake (for a review, see [107]). Furthermore, evidence of higher quality would be needed before establishing personalized protocols of molecular radiotherapy as routine clinical tools.

The determination of myocardial blood flow (MBF) in absolute units has been the domain of PET/CT for many years. MBF measurement may improve the diagnosis of coronary artery disease (CAD), in particular, when MBF is diffusely decreased such as in three-vessel disease. Using dynamic quantitative SPECT/CT, Klein and coworkers demonstrated that MBF could also be measured with this technology [108]. Furthermore, subsequently, this group of researchers showed in a small group of subjects that diagnostic accuracy was higher when MBF was determined than when not [109].

The uptake of Tc-99m-pertechnetate (TcTU) by the thyroid gland provides information on synthesis rates of thyroid hormones. Traditionally, this variable is determined using planar scintigraphy. Lee and coworkers compared TcTU determined on planar scans with that obtained by quantitative SPECT/CT in a group of 50 subjects with various thyroid diseases [110]. They demonstrated a significant overestimation of this variable by planar imaging due to its inability to differentiate thyroid uptake from that in salivary glands and saliva. Researchers from the same institution used quantitative SPECT/CT to differentiate destructive thyroiditis from euthyroid patients and to diagnose Graves disease [111, 112]. In these papers, quantitative SPECT/CT was not compared to planar imaging. It, therefore, remains

unclear whether SPECT/CT offers clinical advantages over planar imaging with regard to quantitation of TcTU.

Some evidence has been published on miscellaneous other potential indications for quantitative SPECT/CT as well: So has this technology been employed to calculate glomerular filtration rate from images of renal uptake of Tc-99m-DTPA [113], obviating the need of blood radioactivity measurements. Furthermore, decreases in lung perfusion caused by irradiation are now also amenable to diagnosis by quantitative SPECT/CT [114]. Other possible applications of this new tool include the diagnosis of parathyroid adenomas [115], of salivary dysfunction [116], of pheochromocytoma [117], and of Alzheimer's disease [118].

Quantitative SPECT/CT is feasible, yielding acceptable accuracy. It constitutes a new clinical tool in nuclear medicine. Evidence is accumulating suggesting its clinical usefulness, but is still scarce for many potential applications. Particularly interesting is the use of this new tool for dosimetry of molecular radiotherapy as well as for monitoring response to therapy. It may also provide a basis for novel automated approaches to image analysis and help in diagnosis as well as in standardization of the interpretation of clinical SPECT/CT images.

17.5 Summary and Outlook

The continuous development of SPECT and SPECT/CT over the past 50 years has led to remarkable improvements in image quality and diagnostic confidence. The most influential developments include, to name but a few, the realization of hybrid SPECT/CT devices, the implementation of attenuation correction, and iterative reconstruction techniques.

In recent years, some interesting approaches in detector technology have found their way into commercial products. For example, some SPECT cameras dedicated to specific organs use semi-conductive materials like CZT as detector material. It has been shown that this could help to further increase the obtainable image quality.

New trends in the ongoing development of SPECT/CT are quite diverse. For example, whole-body SPECT/CT images consisting of acquisitions from multiple consecutive bed positions, similar to PET/CT, have begun to increase. Yet the relatively long SPECT acquisition times (typically 15 min per bed position and 30–45 min for the trunk), together with the increased radiation dose from the extended CT field of view, are likely to hamper the routine application of these acquisitions in clinical practice. Even though new reconstruction techniques already allow for acquisition time reduction, in the future, new collimator and detector designs with higher photon sensitivity could further support this development. Additionally, this trend could be facilitated by the incorporation of low-dose concepts applicable to CT like, for example, the use of iterative CT reconstruction in SPECT/CT.

As with PET, the availability of SPECT list-mode data could allow an enormous gain of information. This information could be used to improve estimation and correction of confounding factors like patient motion [119] and scattered radiation

[120]. Unfortunately, to the best of our knowledge, such techniques are so far available only for research and not for clinical use.

Another recent development has been the incorporation of additional information obtained from the CT images into the SPECT reconstruction, in other words the use of CT data for more than just attenuation correction and image fusion. This development could lead to improved spatial resolution and reduced partial volume effects. This technique has been commercially introduced for Tc-99m bone scans only. However, it could be extremely useful with other tracers as well.

Another important aspect of SPECT/CT is the fact that the technique, like PET, allows quantification of the amount of tracer in terms of Bq/mL or as a SUV. Numerous publications have shown that absolute quantification is feasible [82, 88, 121]. This can be expected to further boost diagnostic confidence, e.g., for judging the efficacy of a treatment through follow-up acquisitions from the same patient or for improving dosimetry for radionuclide therapy [69].

The ever-increasing number of publications on SPECT/CT show that this modality is of great clinical interest. New technical developments will strengthen this trend and ensure that SPECT/CT remains the workhorse of nuclear medicine, even when compared to other strong contenders like PET/CT or PET/MRI.

References

1. Jaszczak RJ, Greer KL, Floyd CEJ, Harris CC, Coleman RE (1984) Improved SPECT quantification using compensation for scattered photons. *J Nucl Med* 25(8):893–900
2. Koral KF, Wang X, Rogers WL, Clinthorne NH, Wang X (1988) SPECT compton-scattering correction by analysis of energy spectra. *J Nucl Med* 29(2):195–202
3. Frey EC, Tsui BMW (1994) Modeling the scatter response function in inhomogenous scattering media for SPECT. *IEEE Trans Nucl Sci* 41(4):1585–1593
4. LaCroix KJ, Tsui BMW, Hasegawa BH, Brown JK (1994) Investigation of the use of X-ray CT images for attenuation compensation in SPECT. *IEEE Trans Nucl Sci* 41(6):2793–2799
5. Blankespoor SC, Xu X, Kaiki K, Brown JK, Tang HR, Cann CE et al (1996) Attenuation correction of SPECT using X-ray CT on an emission-transmission CT system: myocardial perfusion assessment. *IEEE Trans Nucl Sci* 43(4):2263–2274
6. Römer W, Reichel N, Vija HA, Nickel I, Hornegger J, Bautz W et al (2006) Isotropic reconstruction of SPECT data using OSEM3D: correlation with CT. *Acad Radiol.* 13 (4):496–502
7. El Fakhri GN, Buvat I, Péligrini M, Benali H, Almeida P, Bendriem B et al (1999) Respective roles of scatter, attenuation, depth-dependent collimator response and finite spatial resolution in cardiac single-photon emission tomography quantitation: a Monte Carlo study. *Eur J Nucl Med Mol Imaging* 26(5):437–446
8. Kessler RM, Ellis JRJ, Eden M (1984) Analysis of emission tomographic scan data: limitations imposed by resolution and background. *J Comput Assist Tomogr* 8(3):514–522
9. Geworski L, Knoop BO, de Cabrejas ML, Knapp WH, Munz DL (2000) Recovery correction for quantitation in emission tomography: a feasibility study. *Eur J Nucl Med* 27 (2):161–169
10. Bockisch A, Freudenberg LS, Schmidt D, Kuwert T (2009) Hybrid imaging by SPECT/CT and PET/CT: proven outcomes in cancer imaging. *Semin Nucl Med* 39(4):276–289
11. von Schulthess GK, Steinert HC, Hany TF (2006) Integrated PET/CT: current applications and future directions. *Radiology* 238(2):405–422

12. Germain P, Baruthio J, Roul G, Dumitresco B (eds) (2000) First-pass MRI compartmental analysis at the chronic stage of infarction: myocardial flow reserve parametric map. *Comput Cardiol*
13. Lewis DH, Bluestone JP, Savina M, Zoller WH, Meshberg EB, Minoshima S (2006) Imaging cerebral activity in recovery from chronic traumatic brain injury: a preliminary report. *J Neuroimaging* 16(3):272–277
14. Sidoti C, Agrillo U (2006) Chronic cortical stimulation for amyotrophic lateral sclerosis: a report of four consecutive operated cases after a 2-year follow-up: technical case report. *Neurosurgery* 58(2):E384. <https://doi.org/10.1227/01.NEU.0000195115.30783.3A>
15. Gullberg GT et al (2010) Dynamic single photon emission computed tomography: basic principles and cardiac applications. *Phys Med Biol* 55(20):R111
16. Anger HO (1958) Scintillation camera. *Rev Sci Instrum* 29(1):27–33
17. Anger HO (1964) Scintillation camera with multichannel collimators. *J Nucl Med* 5(7):515–531
18. Cherry SR, Sorenson JA, Phelps ME (2003) *Physics in nuclear medicine*, 3rd edn. Elsevier, Philadelphia
19. Bocher M, Blevis IM, Tsukerman L, Shrem Y, Kovalski G, Volokh L (2010) A fast cardiac gamma camera with dynamic SPECT capabilities: design, system validation and future potential. *Eur J Nucl Med Mol Imaging* 37(10):1887–1902
20. Imbert L, Poussier S, Franken PR, Songy B, Verger A, Morel O et al (2012) Compared performance of high-sensitivity cameras dedicated to myocardial perfusion SPECT: a comprehensive analysis of phantom and human images. *J Nucl Med* 53(12):1897–1903
21. Slomka PJ, Berman DS, Germano G (2014) New cardiac cameras: single-photon emission CT and PET. *Semin Nucl Med* 44(4):232–251
22. Schramm NU, Ebel G, Engeland U, Schurrat T, Behe M, Behr TM (2003) High-resolution SPECT using multipinhole collimation. *IEEE Trans Nucl Sci* 50(3):315–320
23. Branderhorst W, Vastenhouw B, van der Have F, Blezer E, Bleeker W, Beekman F (2010) Targeted multi-pinhole SPECT. *Eur J Nucl Med Mol Imaging* 1–10
24. Nömayr A, Römer W, Strobel D, Bautz W, Kuwert T (2006) Anatomical accuracy of hybrid SPECT/spiral CT in the lower spine. *Nucl Med Commun* 27(6):521–528
25. Han J, Köstler H, Bennewitz C, Kuwert T, Hornegger J (2008) Computer-aided evaluation of anatomical accuracy of image fusion between X-ray CT and SPECT. *Comput Med Imaging Graph* 32(5):388–395
26. Gilman MD, Fischman AJ, Krishnasetty V, Halpern EF, Aquino SL (2006) Optimal ct breathing protocol for combined thoracic PET/CT. *Am J Roentgenol* 187(5):1357–1360
27. Chen J, Caputlu-Wilson S, Shi H, Galt J, Faber T, Garcia E (2006) Automated quality control of emission-transmission misalignment for attenuation correction in myocardial perfusion imaging with SPECT-CT systems. *J Nucl Cardiol*. 13(1):43–49
28. Bruyant PP (2002) Analytic and iterative reconstruction algorithms in SPECT. *J Nucl Med* 43(10):1343–1358
29. Shepp LA, Vardi Y (1982) Maximum likelihood reconstruction for emission tomography. *IEEE Trans Med Imaging* 1(2):113–122
30. Lange K, Carson R (1984) EM reconstruction algorithms for emission and transmission tomography. *J Comput Assist Tomogr* 8(2):306–316
31. Arosio M, Pasquali C, Crivellaro C, De Ponti E, Morzenti S, Guerra L et al (2011) Performance of a SPECT collimator-detector response reconstruction algorithm: phantom studies and validation in inflammation clinical studies. *Q J Nucl Med Mol Imaging*. 55(6):671–679
32. Aldridge MD, Waddington WW, Dickson JC, Prakash V, Ell PJ, Bomanji JB (2013) Clinical evaluation of reducing acquisition time on single-photon emission computed tomography image quality using proprietary resolution recovery software. *Nucl Med Commun* 34(11):1116–1123

33. Kalantari F, Rajabi H, Saghari M (2012) Quantification and reduction of the collimator-detector response effect in SPECT by applying a system model during iterative image reconstruction: a simulation study. *Nucl Med Commun* 33(3):228–238
34. Zoccarato O, Scabbio C, De Ponti E, Matheoud R, Leva L, Morzenti S, et al (2014) Comparative analysis of iterative reconstruction algorithms with resolution recovery for cardiac SPECT studies. A multi-center phantom study. *J Nucl Cardiol* 21(1):135–148
35. Druz RS, Phillips LM, Chugkowski M, Boutis L, Rutkin B, Katz S (2011) Wide-beam reconstruction half-time SPECT improves diagnostic certainty and preserves normalcy and accuracy: a quantitative perfusion analysis. *J Nucl Cardiol*. 18(1):52–61
36. Venero CV, Heller GV, Bateman TM, McGhie AI, Ahlberg AW, Katten D et al (2009) A multicenter evaluation of a new post-processing method with depth-dependent collimator resolution applied to full-time and half-time acquisitions without and with simultaneously acquired attenuation correction. *J Nucl Cardiol*. 16(5):714–725
37. Stansfield EC, Sheehy N, Zurakowski D, Vija AH, Fahey FH, Treves ST (2010) Pediatric ^{99m}Tc-MDP bone SPECT with ordered subset expectation maximization iterative reconstruction with isotropic 3D resolution recovery. *Radiology* 257(3):793–801
38. Liu S, Farncombe TH, (eds) (2007) Collimator-detector response compensation in quantitative SPECT reconstruction. In: Nuclear science symposium conference record, NSS'07 Oct 26–Nov 3 2007 IEEE
39. Du Y, Tsui BM, Frey EC (2006) Model-based compensation for quantitative ¹²³I brain SPECT imaging. *Phys Med Biol* 51(5):1269–1282
40. Se Young C, Fessler JA, Dewaraja YK (2013) Correction for collimator-detector response in SPECT using point spread function template. *IEEE Trans Med Imaging* 32(2):295–305
41. El Fakhri G, Buvat I, Benali H, Todd-Pokropek A, Di Paola R (2000) Relative impact of scatter, collimator response, attenuation, and finite spatial resolution corrections in cardiac SPECT. *J Nucl Med* 41(8):1400–1408
42. Hutton BF, Buvat I, Beekman FJ (2011) Review and current status of SPECT scatter correction. *Phys Med Biol* 56(14):R85–112
43. King MA, Tsui BMW, Pan T-S (1995) Attenuation compensation for cardiac single-photon emission computed tomographic imaging: part 1. Impact of attenuation and methods of estimating attenuation maps. *J Nucl Cardiol* 2(6):513–24
44. Zaidi H, Koral KF (2004) Scatter modelling and compensation in emission tomography. *Eur J Nucl Med Mol Imaging* 31(5):761–782
45. Ogawa K, Harata Y, Ichihara T, Kubo A, Hashimoto S (1991) A practical method for position-dependent Compton-scatter correction in single photon emission CT. *IEEE Trans Med Imaging* 10(3):408–412
46. King MA, DeVries DJ, Pan TS, Pretorius PH, Case JA (1997) An investigation of the filtering of TEW scatter estimates used to compensate for scatter with ordered subset reconstructions. *IEEE Trans Nucl Sci* 44(3):1140–1145
47. Buvat I, Rodriguez-Villafuerte M, Todd-Pokropek A, Benali H, Di Paola R (1995) Comparative assessment of nine scatter correction methods based on spectral analysis using Monte Carlo simulations. *J Nucl Med* 36(8):1476–1488
48. Sohlberg A, Watabe H, Iida H (2008) Acceleration of Monte Carlo-based scatter compensation for cardiac SPECT. *Phys Med Biol* 53(14):N277–N285
49. Beekman FJ, De Jong HWAM, van Geloven S (2002) Efficient fully 3-D iterative SPECT reconstruction with Monte Carlo-based scatter compensation. *IEEE Trans Medical Imaging*, 21(8):867–877
50. Frey EC, Tsui BMW (eds) (1996) A new method for modeling the spatially-variant, object-dependent scatter response function in SPECT. In: Nuclear science symposium, 1996 conference record, 2–9 Nov 1996. IEEE
51. Vicente EM, Lodge MA, Rowe SP, Wahl RL, Frey EC (2017) Simplifying volumes-of-interest (VOIs) definition in quantitative SPECT: beyond manual definition of 3D whole-organ VOIs. *Med Phys* 44(5):1707–1717

52. Sandström M, Garske U, Granberg D, Sundin A, Lundqvist H (2010) Individualized dosimetry in patients undergoing therapy with ^{177}Lu -DOTA-D-Phe (1)-Tyr (3)-octreotate. *Eur J Nucl Med Mol Imaging* 37
53. Hoffman EJ, Huang S-C, Phelps ME (1979) Quantitation in positron emission computed tomography: 1. effect of object size. *J Comput Assist Tomogr* 3(3):299–308
54. Chen CH, Muzic RF Jr, Nelson AD, Adler LP (1998) A nonlinear spatially variant object-dependent system model for prediction of partial volume effects and scatter in PET. *IEEE Trans Med Imaging* 17(2):214–227
55. Seo Y, Aparici CM, Cooperberg MR, Konety BR, Hawkins RA (2009) In Vivo Tumor Grading of Prostate Cancer Using Quantitative ^{111}In -Capromab Pendetide SPECT/CT. *J Nucl Med* 51(1):31–36
56. Hutton BF, Lau YH (1998) Application of distance-dependent resolution compensation and post-reconstruction filtering for myocardial SPECT. *Phys Med Biol* 43(6):1679
57. Pretorius PH, King MA (2009) Diminishing the impact of the partial volume effect in cardiac SPECT perfusion imaging. *Med Phys* 36(1):105–115
58. Da Silva AJ, Tang HR, Wong KH, Wu MC, Dae MW, Hasegawa BH (2001) Absolute quantification of regional myocardial uptake of $^{99\text{m}}\text{Tc}$ -Sestamibi with SPECT: experimental validation in a porcine model. *J Nucl Med* 42(5):772–779
59. Tang HR, Brown JK, Hasegawa BH (eds) (1996) Use of X-ray CT-defined regions of interest for the determination of SPECT recovery coefficients. In: Nuclear science symposium, conference record, IEEE
60. Rousset O, Ma Y, Kamber M, Evans AC (1993) 3D simulations of radiotracer uptake in deep nuclei of human brain. *Comput Med Imaging Graph* 17(4–5):373–379
61. Rousset OG, Ma Y, Evans AC (1998) Correction for partial volume effects in PET: principle and validation. *J Nucl Med* 39(5):904–911
62. Du Y, Tsui BMW, Frey EC (2005) Partial volume effect compensation for quantitative brain SPECT imaging. *IEEE Trans Med Imaging* 24(8):969–976
63. Soret M, Koulibaly PM, Darcourt J, Hapdey S, Buvat I (2003) Quantitative accuracy of dopaminergic neurotransmission imaging with ^{123}I SPECT. *J Nucl Med* 44(7):1184–1193
64. Performance measurements of gamma cameras (2007) NEMA NU 1-2007. National Electrical Manufacturers Association, Rosslyn, VA
65. Dewaraja Y, Ljungberg M, Koral K. Effects of dead time and pile up on quantitative SPECT for I-131 dosimetric studies. *J Nucl Med Meet Abstr* 49(MeetingAbstracts_1):47P-c-
66. Vija AH (2013) White paper: introduction to xSPECT technology: evolving multi-modal SPECT to become context-based and quantitative. Siemens Medical Solutions USA, Inc
67. Sanders JC, Kuwert T, Hornegger J, Ritt P (2015) Quantitative SPECT/CT imaging of ^{177}Lu with in vivo validation in patients undergoing peptide receptor radionuclide therapy. *Mol Imaging Biol.* 17(4):585–593
68. Zimmerman BE, Grosev D, Buvat I, Coca Perez MA, Frey EC, Green A et al (2017) Multi-centre evaluation of accuracy and reproducibility of planar and SPECT image quantification: an IAEA phantom study. *Z Med Phys* 27(2):98–112
69. Beaugerard JM, Hofman MS, Pereira JM, Eu P, Hicks RJ (2011) Quantitative (^{177}Lu) SPECT (QSPECT) imaging using a commercially available SPECT/CT system. *Cancer Imaging* 11:56–66
70. D’Arienzo M, Cazzato M, Cozzella ML, Cox M, D’Andrea M, Fazio A et al (2016) Gamma camera calibration and validation for quantitative SPECT imaging with (^{177}Lu). *Appl Radiat Isot* 112:156–164
71. de Nijs R, Lagerburg V, Klausen TL, Holm S (2014) Improving quantitative dosimetry in (^{177}Lu)-DOTATATE SPECT by energy window-based scatter corrections. *Nucl Med Commun* 35(5):522–533
72. Gils CAJv, Beijst C, Rooij Rv, Jong HWAMd (2016) Impact of reconstruction parameters on quantitative I-131 SPECT. *Phys Med Biol* 61(14):5166

73. Israel O, Iosilevsky G, Front D, Bettman L, Frenkel A, Ish-Shalom S et al (1990) SPECT quantitation of iodine-131 concentration in phantoms and human tumors. *J Nucl Med* 31 (12):1945–1949
74. Koral KF, Yendiki A, Dewaraja YK (2007) Recovery of total I-131 activity within focal volumes using SPECT and 3D OSEM. *Phys Med Biol* 52(3):777
75. Marin G, Vanderlinden B, Karfis I, Guiot T, Wimana Z, Flamen P et al (2017) Accuracy and precision assessment for activity quantification in individualized dosimetry of ¹⁷⁷Lu-DOTATATE therapy. *EJNMMI Phys* 4(1):7
76. Mezzenga E, D’Errico V, D’Arienzo M, Strigari L, Panagiota K, Matteucci F et al (2017) Quantitative accuracy of ¹⁷⁷Lu SPECT imaging for molecular radiotherapy. *PLoS ONE* 12 (8):e0182888
77. Shcherbinin S, Celler A, Belhocine T, Vanderwerf R, Driedger A (2008) Accuracy of quantitative reconstructions in SPECT/CT imaging. *Phys Med Biol* 53(17):4595
78. Shcherbinin S, Piwowska-Bilska H, Celler A, Birkenfeld B (2012) Quantitative SPECT/CT reconstruction for ¹⁷⁷Lu and ¹⁷⁷Lu/ ⁹⁰Y targeted radionuclide therapies. *Phys Med Biol* 57(18):5733
79. Uribe CF, Esquinas PL, Tanguay J, Gonzalez M, Gaudin E, Beauregard JM et al (2017) Accuracy of ¹⁷⁷Lu activity quantification in SPECT imaging: a phantom study. *EJNMMI Phys.* 4(1):2
80. Willowson K, Bailey DL, Bailey EA, Baldock C, Roach PJ (2010) In vivo validation of quantitative SPECT in the heart. *Clin Physiol Funct Imaging* 30(3):214–219
81. Willowson K, Bailey DL, Baldock C (2008) Quantitative SPECT reconstruction using CT-derived corrections. *Phys Med Biol* 53(12):3099
82. Zeintl J, Vija AH, Yahil A, Hornegger J, Kuwert T (2010) Quantitative accuracy of clinical ^{99m}Tc SPECT/CT using ordered-subset expectation maximization with 3-dimensional resolution recovery, attenuation, and scatter correction. *J Nucl Med* 51(6):921–928
83. Chipiga L, Sydoff M, Zvonova I, Bernhardsson C (2016) Investigation of partial volume effect in different PET/CT systems: a comparison of results using the madeira phantom and the NEMA NU-2 2001 phantom. *Radiat Prot Dosimetry* 169(1–4):365–370
84. Jonsson L, Stenvall A, Mattsson E, Larsson E, Sundlov A, Ohlsson T et al (2018) Quantitative analysis of phantom studies of (¹¹¹In and (⁶⁸Ga) imaging of neuroendocrine tumours. *EJNMMI Phys.* 5(1):5
85. Maus J, Hofheinz F, Schramm G, Oehme L, Beuthien-Baumann B, Lukas M et al (2014) Evaluation of PET quantification accuracy in vivo. Comparison of measured FDG concentration in the bladder with urine samples. *Nuklearmedizin* 53(3):67–77
86. Maus J, Schramm G, Hofheinz F, Oehme L, Lougovski A, Petr J et al (2015) Evaluation of in vivo quantification accuracy of the Ingenuity-TF PET/MR. *Med Phys* 42(10):5773–5781
87. Zhu Y, Geng C, Huang J, Liu J, Wu N, Xin J et al (2018) Measurement and evaluation of quantitative performance of PET/CT images before a multicenter clinical trial. *Sci Rep* 8 (1):9035
88. Cachovan M, Vija A, Hornegger J, Kuwert T (2013) Quantification of ^{99m}Tc-DPD concentration in the lumbar spine with SPECT/CT. *EJNMMI Research* 3(1):45
89. Ayubcha C, Zirakchian Zadeh M, Stochkendahl MJ, Al-Zaghal A, Hartvigsen J, Rajapakse CS et al (2018) Quantitative evaluation of normal spinal osseous metabolism with ^{18F}-NaF PET/CT. *Nucl Med Commun* 39(10):945–950
90. Arvola S, Jambor I, Kuisma A, Kemppainen J, Kajander S, Seppanen M et al (2019) Comparison of standardized uptake values between (^{99m}Tc)-HDP SPECT/CT and (¹⁸F)-NaF PET/CT in bone metastases of breast and prostate cancer. *EJNMMI research.* 9(1):6
91. Umeda T, Koizumi M, Fukai S, Miyaji N, Motegi K, Nakazawa S et al (2018) Evaluation of bone metastatic burden by bone SPECT/CT in metastatic prostate cancer patients: defining threshold value for total bone uptake and assessment in radium-223 treated patients. *Ann Nucl Med* 32(2):105–113

92. Kuji I, Yamane T, Seto A, Yasumizu Y, Shirotake S, Oyama M (2017) Skeletal standardized uptake values obtained by quantitative SPECT/CT as an osteoblastic biomarker for the discrimination of active bone metastasis in prostate cancer. *Eur J Hybrid Imaging* 1(1):2
93. Bae S, Kang Y, Song YS, Lee WW (2019) Maximum standardized uptake value of foot SPECT/CT using Tc-99 m HDP in patients with accessory navicular bone as a predictor of surgical treatment. *Medicine* 98(2):e14022
94. Ramsay SC, Lindsay K, Fong W, Patford S, Younger J, Atherton J (2018) Tc-HDP quantitative SPECT/CT in transthyretin cardiac amyloid and the development of a reference interval for myocardial uptake in the non-affected population. *Eur J Hybrid Imaging* 2(1):17
95. Suh MS, Lee WW, Kim YK, Yun PY, Kim SE (2016) Maximum Standardized Uptake Value of (99 m)Tc Hydroxymethylene Diphosphonate SPECT/CT for the Evaluation of Temporomandibular Joint Disorder. *Radiology* 280(3):890–896
96. Kim J, Lee HH, Kang Y, Kim TK, Lee SW, So Y et al (2017) Maximum standardised uptake value of quantitative bone SPECT/CT in patients with medial compartment osteoarthritis of the knee. *Clin Radiol* 72(7):580–589
97. Barthassat E, Afifi F, Konala P, Rasch H, Hirschmann MT (2017) Evaluation of patients with painful total hip arthroplasty using combined single photon emission tomography and conventional computerized tomography (SPECT/CT)—a comparison of semi-quantitative versus 3D volumetric quantitative measurements. *BMC Med Imaging* 17(1):31
98. Beck M, Sanders JC, Ritt P, Reinfelder J, Kuwert T (2016) Longitudinal analysis of bone metabolism using SPECT/CT and (99m)Tc-diphosphono-propanedicarboxylic acid: comparison of visual and quantitative analysis. *EJNMMI research* 6(1):60
99. Harmon SA, Perk T, Lin C, Eickhoff J, Choyke PL, Dahut WL et al (2017) Quantitative assessment of early [(18)F]sodium fluoride positron emission tomography/computed tomography response to treatment in men with metastatic prostate cancer to bone. *J Clin Oncol: Off J Am Soc Clin Oncology* 35(24):2829–2837
100. Del Prete M, Buteau FA, Arsenault F, Saighi N, Bouchard LO, Beaulieu A et al (2019) Personalized (177)Lu-octreotate peptide receptor radionuclide therapy of neuroendocrine tumours: initial results from the P-PRRT trial. *Eur J Nucl Med Mol Imaging* 46(3):728–742
101. Dittmann H, Kopp D, Kupferschlaeger J, Feil D, Groezinger G, Syha R et al (2018) A prospective study of quantitative SPECT/CT for evaluation of lung shunt fraction before SIRT of liver tumors. *J Nucl Med: Off Publ, Soc Nucl Medicine* 59(9):1366–1372
102. Garin E, Rolland Y, Pracht M, Le Sourd S, Laffont S, Mesbah H et al (2017) High impact of macroaggregated albumin-based tumour dose on response and overall survival in hepatocellular carcinoma patients treated with (90) Y-loaded glass microsphere radioembolization. *Liver Int: Off J Int Assoc Study Liver* 37(1):101–110
103. Kappadath SC, Mikell J, Balagopal A, Baladandayuthapani V, Kaseb A, Mahvash A (2018) Hepatocellular Carcinoma Tumor Dose Response After (90)Y-radioembolization With Glass Microspheres Using (90)Y-SPECT/CT-Based Voxel Dosimetry. *Int J Radiat Oncol Biol Phys* 102(2):451–461
104. Gnesin S, Canetti L, Adib S, Cherbuin N, Silva Monteiro M, Bize P et al (2016) Partition model-based 99mTc-MAA SPECT/CT predictive dosimetry compared with 90Y TOF PET/CT posttreatment dosimetry in radioembolization of hepatocellular carcinoma: a quantitative agreement comparison. *J Nucl Med: Off Publ, Soc Nucl Medicine* 57(11):1672–1678
105. Delker A, Fendler WP, Kratochwil C, Brunegraf A, Gosewisch A, Gildehaus FJ et al (2016) Dosimetry for (177)Lu-DKFZ-PSMA-617: a new radiopharmaceutical for the treatment of metastatic prostate cancer. *Eur J Nucl Med Mol Imaging* 43(1):42–51
106. Violet J, Jackson P, Ferdinandus J, Sandhu S, Akhurst T, Iravani A et al (2019) Dosimetry of (177)Lu-PSMA-617 in metastatic castration-resistant prostate cancer: correlations between pretherapeutic imaging and whole-body tumor dosimetry with treatment outcomes. *J Nucl Med* 60(4):517–523

107. Lassmann M, Eberlein U (2018) The Relevance of Dosimetry in Precision Medicine. *Journal of nuclear medicine: official publication, Society of Nuclear Medicine*. 59(10):1494–1499
108. Klein R, Hung GU, Wu TC, Huang WS, Li D, deKemp RA et al (2014) Feasibility and operator variability of myocardial blood flow and reserve measurements with (9)(9) mTc-sestamibi quantitative dynamic SPECT/CT imaging. *J Nucl Cardiol: Off Publ Am Soc Nucl Cardiology* 21(6):1075–1088
109. Hsu B, Chen FC, Wu TC, Huang WS, Hou PN, Chen CC et al (2014) Quantitation of myocardial blood flow and myocardial flow reserve with 99mTc-sestamibi dynamic SPECT/CT to enhance detection of coronary artery disease. *Eur J Nucl Med Mol Imaging* 41(12):2294–2306
110. Lee H, Kim JH, Kang YK, Moon JH, So Y, Lee WW (2016) Quantitative single-photon emission computed tomography/computed tomography for technetium pertechnetate thyroid uptake measurement. *Medicine* 95(27):e4170
111. Kim JY, Kim JH, Moon JH, Kim KM, Oh TJ, Lee DH et al (2018) Utility of Quantitative Parameters from Single-Photon Emission Computed Tomography/Computed Tomography in Patients with Destructive Thyroiditis. *Korean J Radiol* 19(3):470–480
112. Dong F, Li L, Bian Y, Li G, Han X, Li M et al (2019) Standardized uptake value using thyroid quantitative SPECT/CT for the diagnosis and evaluation of graves' disease: a prospective multicenter study. *Biomed Res Int* 2019:7589853
113. Park J, Bae S, Seo S, Park S, Bang JI, Han JH et al (2019) Measurement of glomerular filtration rate using quantitative SPECT/CT and deep-learning-based kidney segmentation. *Sci Rep* 9(1):4223
114. Liss AL, Marsh RB, Kapadia NS, McShan DL, Rogers VE, Balter JM et al (2017) Decreased lung perfusion after breast/chest wall irradiation: quantitative results from a prospective clinical trial. *Int J Radiat Oncol Biol Phys* 97(2):296–302
115. Robin P, Klein R, Gardner J, Ziebarth B, Bazarjani S, Razavi S et al (2019) Quantitative analysis of technetium-99m-sestamibi uptake and washout in parathyroid scintigraphy supports dual mechanisms of lesion conspicuity. *Nucl Med Commun*
116. Kim J, Lee H, Lee H, Bang JI, Kang YK, Bae S et al (2018) Quantitative single-photon emission computed tomography/computed tomography for evaluation of salivary gland dysfunction in sjogren's syndrome patients. *Nucl Med Mol Imaging* 52(5):368–376
117. Nakamoto R, Nakamoto Y, Ishimori T, Togashi K (2016) Clinical significance of quantitative 123I-MIBG SPECT/CT analysis of pheochromocytoma and paraganglioma. *Clin Nucl Med* 41(11):e465–e472
118. Welz F, Sanders JC, Kuwert T, Maler J, Kornhuber J, Ritt P (2016) Absolute SPECT/CT quantification of cerebral uptake of 99mTc-HMPAO for patients with neurocognitive disorders. *Nucl Nucl Med* 55(4):158–165
119. Schleyer PJ, O'Doherty MJ, Barrington SF, Marsden PK (2009) Retrospective data-driven respiratory gating for PET/CT. *Phys Med Biol* 54(7):1935–1950
120. Hapdey S, Soret M, Buvat I (2006) Quantification in simultaneous (99m)Tc/(123)I brain SPECT using generalized spectral factor analysis: a Monte Carlo study. *Phys Med Biol* 51(23):6157–6171
121. Bailey DL, Willowson KP (2014) Quantitative SPECT/CT: SPECT joins PET as a quantitative imaging modality. *Eur J Nucl Med Mol Imaging* 41(1):17–25
122. Ritt P, Vija H, Hornegger J, Kuwert T (2011) Absolute quantification in SPECT. *Eur J Nucl Med Mol Imaging* 38(1):69–77
123. Ritt P, Sanders J, Kuwert T (2014) SPECT/CT technology. *Clin Transl Imaging* 1–13



Fluorescence Imaging of Breast Tumors and Gastrointestinal Cancer

18

Dirk Grosenick and Christoph Bremer

Contents

18.1	Introduction.....	592
18.2	Fluorescence Imaging of Breast Cancer	593
18.2.1	Basics of Breast Optical Imaging and Endogenous Tumor Contrast	593
18.2.2	Contrast Agents for Breast Optical Imaging	594
18.2.3	Breast Tumor Detection by ICG Using Vascular Contrast.....	596
18.2.4	Breast Tumor Imaging and Differentiation by ICG Using Vessel Permeability	599
18.2.5	Imaging of Breast Cancer with Omocianine	604
18.2.6	Fluorescence-Guided Breast Cancer Surgery.....	606
18.3	Cancer and Early Malignancies of the Gastrointestinal Tract.....	608
18.3.1	Protoporphyrin IX as Tumor Marker.....	609
18.3.2	Time-Gated Fluorescence Imaging of Protoporphyrin IX.....	610
18.3.3	Targeted Molecular Imaging in Gastrointestinal Endoscopy	613
18.4	Outlook	617
	References	618

D. Grosenick (✉)

Physikalisch-Technische Bundesanstalt (PTB), Abbestr. 2-12, 10587 Berlin, Germany

e-mail: dirk.grosenick@ptb.de

C. Bremer

Klinik für Radiologie, St. Franziskus Hospital GmbH, Hohenzollernring 70,

48145 Münster, Germany

e-mail: bremerc@uni-muenster.de

© Springer Nature Switzerland AG 2020

O. Schober et al. (eds.), *Molecular Imaging in Oncology*,

Recent Results in Cancer Research 216,

https://doi.org/10.1007/978-3-030-42618-7_18

591

18.1 Introduction

Optical imaging of head, breast, and skin, as well as of inner cavities of the human body, e.g., bladder or colon, is a powerful diagnostic tool with high potential for early detection of tumors. Besides the measurement of intrinsic tissue optical parameters like absorption, scattering, hemoglobin (Hb) concentration, and blood oxygen saturation, fluorescence imaging has attracted increasing interest in medical diagnostics and therapy over many years now [72, 75, 102]. In particular, it plays an important role for the increasing number of molecular probes developed to exploit tumor-specific molecular targets and processes for optical imaging [3, 7, 56, 106].

When performing fluorescence imaging on superficial tissue structures, scattering of light in the tissue is of low importance, and wavelengths across the whole spectrum of light can be applied to excite fluorescence of appropriate exogenous contrast agents or endogenous markers. Typically, the tissue region of interest is homogeneously illuminated with a laser or LED to excite the fluorophores, and a sufficiently sensitive camera equipped with a long pass or bandpass filter for blocking of the excitation light is employed to record the fluorescence images in reflection. Often, this flat-field fluorescence imaging approach is combined with white-light imaging, and the fluorescent tissue structures are overlaid on the conventional color image. Besides endoscopes with a fluorescence detection channel, several new research and commercial devices have been developed for flat-field fluorescence imaging with the main focus on application for fluorescence-guided open surgery of cancer and fluorescence-assisted sentinel lymph node detection [19, 49, 86, 89, 92].

When deeper tissue layers have to be investigated, the strong scattering of light in biological tissue plays an important role. Both, the excitation light and the emitted fluorescence light are scattered multiple times and the corresponding optical path lengths are significantly increased. To obtain a sufficient penetration depth of the excitation light and a measurable fluorescence signal, excitation and emission wavelengths have to fall into the so-called diagnostic window between approximately 650 and 1000 nm where light absorption of the tissue is moderate. Recent developments in experimental methods have allowed to extend the application of fluorescence imaging to diseases of highly scattering tissue such as breast cancer [14, 36, 97], stroke [53], or rheumatoid arthritis [24]. These techniques offer ways to translate corresponding probes for molecular imaging from preclinical research to clinical application.

In the following, we discuss two applications for fluorescence-assisted clinical diagnosis and therapy of tumors. As an example for imaging in highly scattering tissue we review results on the detection of carcinomas in the female breast. We focus on the nonspecific contrast agents indocyanine green (ICG) and omocyanine and report on a recently explored method to characterize differences in the extravasation of ICG between malignant and benign breast lesions utilizing vessel permeability. Then, we discuss first results with targeted and activatable probes aiming at the reliable detection of tumor margins in breast surgery. As an example

of superficial lesions, tumor detection in the gastrointestinal tract by fluorescence endoscopy will be explained. We report on results with protoporphyrin IX which acts as an endogenous specific target for malignancy. Finally, we briefly discuss exogenous targeted and activatable probes for esophageal and colorectal tumors.

18.2 Fluorescence Imaging of Breast Cancer

Due to the high prevalence of breast cancer, many efforts are undertaken to develop targeted contrast agents for early detection of this disease. Hereby, optical imaging plays an important role in understanding the properties of the agent and its action on the cellular level. By adding a fluorescent moiety to the carrier molecule of the probe fluorescence imaging can be applied as a sensitive method to detect the probe in the tissue. Basic investigations on new probes are often performed on small animal models [9, 20]. Due to the small dimensions of such animal models, tumors are easily accessible by optical methods, since they are situated directly on or close to the tissue surface. Accordingly, simple wide-field fluorescence imaging is sufficient for their detection. In contrast, optical imaging of a molecular contrast agent in the human breast is much more challenging due to the drastically enlarged tissue dimensions compared to a small animal breast tumor model.

Numerous investigations have shown that the human breast can be transilluminated by near-infrared light due to the low absorption of breast tissue in this spectral range [35]. The challenge in generating optical images of the breast is the separation of tissue absorption and fluorescence on one side and tissue scattering properties on the other side. Compared to x-ray mammography and magnetic resonance (MR) imaging of the breast, optical imaging is not able to visualize morphological characteristics in the breast with adequate spatial resolution. Instead, important physiological properties of the tissue can be derived.

18.2.1 Basics of Breast Optical Imaging and Endogenous Tumor Contrast

The original idea of optical mammography comprised the diagnosis of breast cancer by exploiting endogenous contrast arising from differences in the total Hb concentration and the blood oxygen saturation (StO_2) between carcinomas and the surrounding healthy tissue. Near-infrared light is an almost perfect tool to determine the tissue concentrations of oxygenated (HbO_2) and deoxygenated hemoglobin (HbR) since these two substances dominate the absorption of light in breast tissue for wavelengths between about 650 and 900 nm. The expected higher concentration of Hb is a direct implication of neoangiogenesis in the carcinoma. Accordingly, all relevant *in vivo* studies confirmed the increased Hb concentration in breast carcinomas. On average, the increase was estimated to be about two to threefold with respect to the surrounding healthy tissue [35].

For blood oxygen saturation a decrease was originally expected for carcinomas due to their high metabolic activity and the related demand on energy. This expectation was supported by measurements of the O_2 tension in breast carcinomas [99] showing hypoxic behavior. In some studies on optical mammography, it was concluded that the hypoxia could be seen from near-infrared measurements as well [13, 64]. However, other clinical studies revealed that blood oxygen saturation is not a characteristic biomarker for breast cancers. There are carcinomas with decreased blood oxygen saturation as well as carcinomas with no characteristic deviation of this parameter from the surrounding healthy tissue [35].

Besides oxygenated and deoxygenated Hb other tissue constituents with absorption in the near-infrared were considered as possible biomarkers for the detection of carcinomas. In particular, increased content of water [12] and collagen [74] were reported for breast carcinomas. Furthermore, several groups could show an increased scattering coefficient of breast carcinomas compared to healthy tissue [35]. To assess the diagnostic potential of the endogenous contrast in breast optical imaging it is necessary to evaluate the differentiation between carcinomas and benign alterations. Corresponding investigations on arbitrary patient populations revealed a limited specificity only [25, 31, 78], in particular, since many benign tissue alterations show increased Hb concentration, similar to carcinomas. Whereas the endogenous optical contrast seems to be insufficient for cancer diagnostic and differentiation, it has high potential for monitoring the progress of neoadjuvant chemotherapy. In this application, the shrinking of a known lesion prior to surgery is studied by frequent observation of the Hb concentration [81, 91]. Another possible application of intrinsic near-infrared breast imaging is the assessment of tumor risk by considering the tissue collagen content [87]. Also, several groups pursue optical breast imaging as an adjunct modality to x-ray mammography [22], MR breast imaging [64, 84] or ultrasound [100].

18.2.2 Contrast Agents for Breast Optical Imaging

To improve the diagnostic and differentiation of breast cancer, and, more recently, to improve the detection of tumor margins during breast cancer surgery several contrast agents have been investigated. Most of the diagnostic studies were performed with ICG. This dye is clinically approved and well accepted as a safe contrast agent in various clinical applications for many years. It is routinely used for ocular fundus fluorescence angiography, for examination of the hepatic function and cardiac output measurements [17, 61]. A newer application is the study of the microcirculation in the human hand to diagnose rheumatic diseases [24, 82]. Besides these approved applications with intravenous injection, ICG has been used in many studies on sentinel lymph node detection for various types of tumors where it is directly injected into the tumor or the adjacent tissue [73, 109].

The spectral properties of ICG are almost perfect for the application in near-infrared diffuse optical imaging, since it shows absorption around 760 nm and fluorescence around 830 nm (in tissue). After intravenous injection, ICG binds

immediately to plasma proteins and is distributed in the vascular compartment. Since carcinomas are characterized by a locally increased vessel density, a higher tissue concentration of ICG in the carcinoma compared to healthy breast tissue should be detectable. After about 10 min of circulation ICG has been cleared from the blood by the liver. Clinical studies that looked on the increased ICG concentration during the circulation (vascular phase) are discussed in Sect. 18.2.3. A more promising method is the detection of extravasated ICG that settled in the carcinoma during the vascular phase. Corresponding investigations are discussed in Sect. 18.2.4.

The research on new contrast agents for the diagnosis of breast cancer by optical imaging has already been started at a time at which basic experimental concepts and theoretical models for diffuse optical imaging of the human breast were still under development [76]. In particular, fluorescence imaging systems for the breast were not yet available. The agents were derived from ICG with the aims to overcome the short plasma lifetime of ICG, its low fluorescence quantum yield, and its instability in aqueous solution which all were considered as disadvantages for fluorescence-assisted breast cancer detection [76]. Finally, the new dye omocianine found the way to clinical trials [71, 97]. Compared to ICG, omocianine (also known as TSC) has a weaker binding to plasma proteins and a higher fluorescence quantum yield [68]. Furthermore, the absorption and emission bands are slightly shifted to shorter wavelengths. Whereas ICG is washed out from the blood by the liver within typically 10 min, omocianine remains in the blood vessels for more than 24 h. Clinical results on this dye are presented in Sect. 18.2.5.

In the past, many efforts were undertaken to develop specific molecular probes to improve early diagnosis and therapy of breast cancer [8, 9, 96]. Up to date, such probes did not yet find application for breast cancer diagnostics by optical imaging. A few molecular probes are currently under investigation in clinical trials on tumor margin detection during breast cancer surgery [44, 61]. The probe bevacizumab-IRDye800CW targets the vascular endothelial growth factor A (VEGF-A) [88]. It is a conjugation of the therapeutic agent bevacizumab (Roche AG) and the near-infrared dye IRDye800CW (LI-COR Biosciences Inc.). The target protein VEGF-A is involved in tumor angiogenesis [1] and frequently overexpressed in breast cancer [54]. The molecular probe EC17 (On Target Laboratories LLC, West Lafayette, USA) targets the tumor-specific overexpression of the folate receptor alpha [94]. It consists of a folate analogue conjugated to 5-fluorescein isothiocyanate (FITC) which fluoresces at 520–530 nm. Because of this short wavelength EC17 seems to be preferably suited for imaging of superficial structures. It was already investigated on several types of cancer [90].

LUM015 is a protease activatable probe that consists of a polyethylene glycol, the near-infrared dye Cy5 (emission wavelength about 665 nm), and a fluorescence quencher [107]. Cathepsins being overexpressed by tumors [105] cleave the probe thus enabling tumor-specific fluorescence of Cy5. AVB-620 is another protease activatable fluorescent probe [58]. It utilizes the increased proteolytic activity from matrix metalloproteinases (MMPs) in tumors and the surrounding stromal microenvironment. AVB-620 contains Cy5 and Cy7 fluorescent molecules. The

intact agent shows fluorescence by Cy7. Its hydrolysis by MMPs results in a shift of fluorescence emission to Cy5 [58].

Besides molecular probes, also the classical perfusion type contrast agents ICG [90] and methylene blue [93] have been investigated in clinical trials for tumor margin detection in breast surgery.

18.2.3 Breast Tumor Detection by ICG Using Vascular Contrast

The first application of ICG in optical mammography was demonstrated by Ntziachristos et al. [63] who compared ICG absorption contrast with Gadolinium (Gd) enhancement in concurrently recorded MR images. Hereby, a time-domain NIR imager with a fixed grid of source and detector optical fibers was implemented into a 1.5 T MR breast imager with slight compression of the breast between two parallel plates. The investigations comprised Gadolinium enhanced MR imaging of the breast followed by optical imaging prior to, during, and after a bolus injection of ICG. The optical measurements were restricted to the tumor region known from the MR images. The increase in absorption at 830 nm observable about 3 min after ICG bolus injection was reconstructed for a slice selected at the known tumor position using a perturbation model of diffusion theory.

These absorption images showed good correlation to the structures with Gd enhancement in the MR images for all three cases investigated. A 1 cm invasive ductal carcinoma was optically visible by a local absorption increase of about 0.05 cm^{-1} , and a 1.5 cm fibroadenoma by an absorption increase of about 0.03 cm^{-1} . ICG induced absorption enhancement in other regions as well as for the third case without a lesion did not exceed 0.025 cm^{-1} . The authors discussed that the ICG molecules (due to their binding to the large plasma proteins) behave like macromolecules, and that extravasation of these macromolecules through leaky tumor capillaries should be a slow process not yet being visible at the early time of measurement. Accordingly, the absorption images are vascularization maps. As discussed in Sect. 18.2.2, such maps have been recorded by several groups exploiting the intrinsic Hb contrast. Ntziachristos et al. [63] suggested measurements of ICG absorption over a longer time period to study ICG kinetics and to possibly quantify vessel permeability as an additional feature for cancer differentiation.

Intes et al. [42] used a single-wavelength continuous-wave optical imager to measure the kinetics of an ICG bolus on three patients. The 2D circular tomographic arrangement of light sources and detectors was positioned around the freely pending breast such that it covered the lesion position known from palpation. A perturbation model was used to reconstruct 2D-maps of the absorption change due to the ICG bolus. Figure 18.1 displays the ICG kinetics for the three cases investigated.

The adenocarcinoma and the invasive ductal carcinoma are characterized by a significantly slower inflow, and the invasive ductal carcinoma, in addition, by a

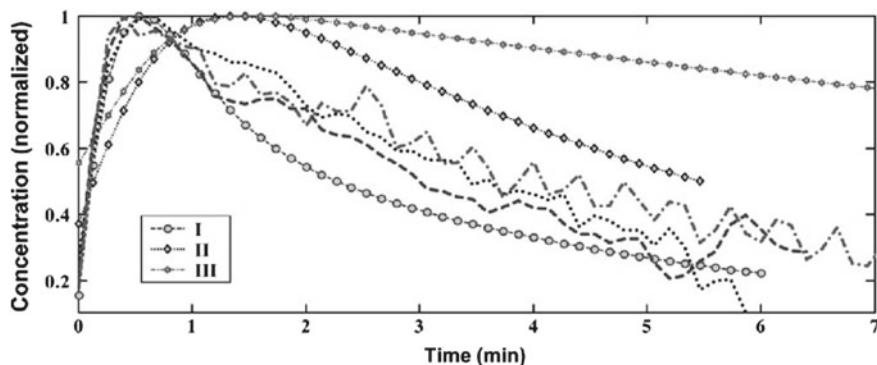


Fig. 18.1 ICG concentration kinetics for three patients with breast tumors; case I: fibroadenoma (diameter 1–2 cm), case II: adenocarcinoma (diameter 2–3 cm), case III: invasive ductal carcinoma (size 4 cm × 3 cm); curves with markers: tumors, curves without markers: healthy tissue of the suspicious breast (reprinted with permission from [42])

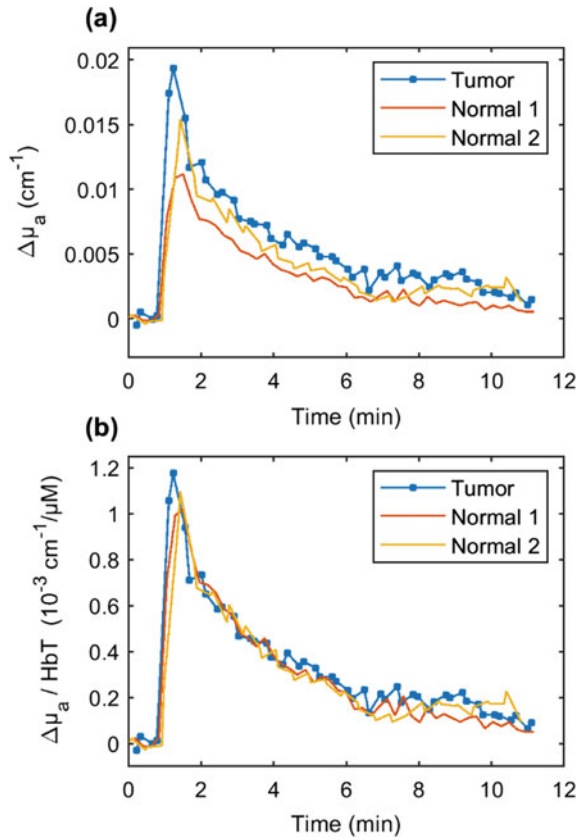
strongly delayed washout compared to the healthy tissue reference data. The benign fibroadenoma behaves similar to the healthy tissue. Obviously, the vessels in the two carcinomas have an increased resistance to blood flow possibly arising from a chaotic vessel structure in the carcinomas. The delay in the washout could be an indicator for extravasation of the ICG-plasma protein macromolecules [42].

Rinneberg et al. [78] performed a study on ICG bolus kinetics on 11 patients with breast cancer using a time-domain optical mammograph. Before bolus injection, the positions of the carcinomas were determined by recording transmission optical mammograms at 675 and 785 nm. Then, transmission at 785 nm was sampled continuously at the tumor position and at two reference positions to observe ICG inflow and washout. These measurements showed a strong patient-to-patient variation of the washout time. However, the temporal characteristics of the carcinoma and the reference positions of the same breast were almost identical in each case.

Figure 18.2a shows an example of the absorption change induced by the ICG bolus illustrating the higher ICG concentration in the carcinoma compared to the two healthy tissue reference positions. To compare the temporal characteristic, the three curves were normalized to the total Hb concentration at each position derived from the intrinsic absorption maps at 675 and 785 nm. Figure 18.2b shows that the normalized ICG absorption is essentially the same for the carcinoma and the healthy references during the about 10 min long measurement time. This result corresponds to the expectation that almost all ICG is contained in the vessels due to the strong plasma binding. Similar ICG kinetics was obtained for the other 10 cases. Hence, the carcinomas in this study did not show increased resistance to blood flow, in contrast to the two carcinomas discussed in Fig. 18.1.

The signal-to-noise ratio in the measurement of ICG absorption is limited due to the high intrinsic tissue absorption. Fluorescence imaging of ICG offers the advantage of an almost background free measurement. On the other hand, the

Fig. 18.2 Washout kinetics of ICG for an invasive carcinoma (size 2 cm) and two (healthy) reference positions with different vascularizations in the same breast; **a** absorption change $\Delta\mu_a$ by ICG bolus, **b** absorption change $\Delta\mu_a$ normalized to local total Hb concentration HbT



fluorescence signal is expected to be small due to the low fluorescence quantum yield of ICG in tissue making its detection challenging. The first successful detection of ICG fluorescence on patients with breast cancer was reported by Corlu et al. [14]. Using a frequency-domain parallel plate optical mammograph and 3D reconstruction, the ICG concentrations were determined 10.2 min after bolus injection. For the three patients with invasive ductal carcinomas investigated in this study a 4:1–6:1 contrast of the ICG concentration between carcinoma and healthy tissue was obtained whereas the contrast in the total Hb concentration was about 1.3:1 only. This result has been interpreted as an indicator for remarkable extravasation of ICG around 10 min after bolus injection due to high permeability of the tumor vessels for macromolecules [14].

The different studies with ICG discussed so far give a nonuniform picture about the advantages of the contrast agent. Corlu et al. reported ICG extravasation about 10 min after bolus injection, whereas Rinneberg et al. got ICG contrast comparable to Hb contrast at this time. And Intes et al. observed a remarkably delayed inflow of ICG into malignant lesion. One case with a delayed ICG inflow was reported also in a later study conducted by Poellinger et al. [70]. This delay was explained by

histologically confirmed necrotic tissue in the tumor whereas the other lesions in this study did not show such an abnormality. Since the study by Poellinger et al. differs in several aspects from the investigations discussed above, it is presented in detail in the next section.

18.2.4 Breast Tumor Imaging and Differentiation by ICG Using Vessel Permeability

The clinical results discussed in the preceding section could not yet fully elucidate the role of ICG extravasation. In general, due to its high binding to plasma proteins ICG should act as a macromolecule. According to the enhanced permeability and retention (EPR) effect [55] this macromolecule is expected to extravasate in a malignant tumor, and to stay in the extracellular space for a longer time. In contrast, vessels in the healthy tissue, and most likely in benign lesions, too, should not allow extravasation of the macromolecules.

The above investigations hamper from the high absorption or fluorescence signal of ICG circulating in the vessels. The promising way to get a signal from extravasated ICG exclusively is a measurement with high fluorescence detection sensitivity at a sufficiently late time when ICG has been totally washed out from the vascular system. This way was pursued in the study by Poellinger et al. [70], already briefly mentioned above. The device used in this study was designed to detect the fluorescence of ICG as well as absorption and scattering properties of the tissue at selected near-infrared wavelengths [36]. Figure 18.3 illustrates the block diagram.

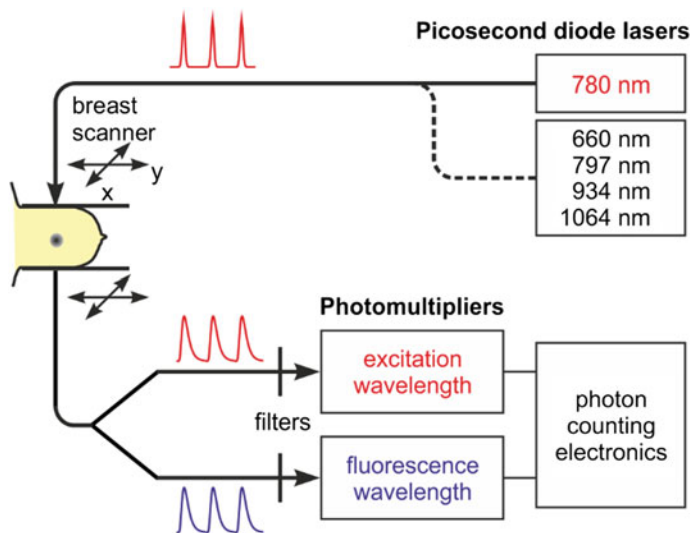


Fig. 18.3 Block diagram of the PTB fluorescence mammograph developed by Hagen et al. [36]

Images of the breast being gently compressed between two parallel glass plates were generated within about 3–10 min by continuously moving source and detector fibers in tandem across the tissue. Fluorescence of the contrast agent was excited by a module with four synchronized picosecond diode lasers (wavelength 780 nm, 15 mW average power at the breast surface). The central detection fiber bundle was bifurcated to guide the transmitted light to the fluorescence and the excitation wavelength detection channels. Time-correlated single-photon counting ensured a high light detection sensitivity. Fluorescence and excitation light information were combined in a fluorescence ratio mammogram. Without this normalization (or an appropriate reconstruction) fluorescent lesions appear with reduced contrast, or contrast could even be canceled out due to the absorption of fluorescence photons by the locally enhanced Hb in the lesion [36]. The optical mammograph was equipped with six more detection fiber bundles and photomultipliers (not shown in Fig. 18.3) to derive 3D information about the breast tissue and with four additional picosecond diode lasers (660, 797, 934, and 1066 nm) for spectroscopic measurements [34].

The device was used in a feasibility study on 20 patients with malignant and benign lesions [70]. This study differed from the previous trials with ICG discussed in Sect. 18.2.3 by two main points: (i) imaging of ICG extravasated from the blood vessels was done at a late time when ICG has been completely washed out from the vascular system, and (ii) ICG was injected by a combination of a bolus and a 20 min long infusion to elongate the interaction time with the vessels. Figure 18.4 summarizes the examination protocol of the study.

Mammograms of the suspicious breast were recorded at three different times: (i) prior to application of ICG (native phase), (ii) two times during the infusion period (when the dye was distributed in the blood vessels—vascular phase), and (iii) two times starting about 20 min after the end of the infusion (when the dye had been washed out from the blood by the liver—extravascular phase). During the

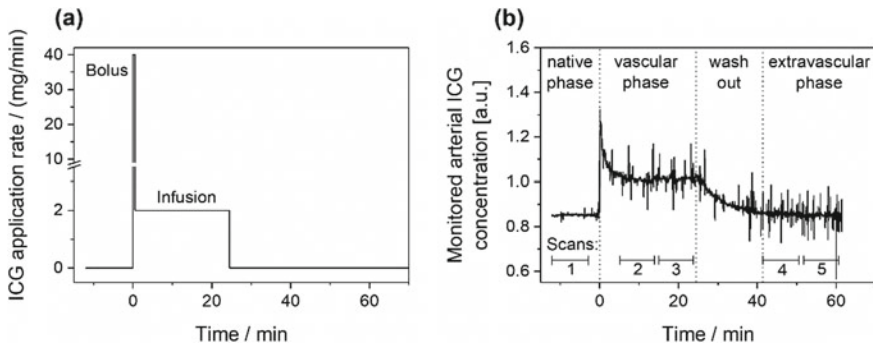


Fig. 18.4 Examination protocol; **a** temporal profile of ICG application, **b** monitored arterial ICG concentration (finger clip) with labeling of the various phases of the examination and of the time intervals of the five breast scans performed (data refer to the case in Fig. 18.5)

examination, the plasma level of ICG was monitored by conventional transcutaneous pulse densitometry using a finger clip [36].

To demonstrate typical results of the approach, we consider two cases with invasive ductal carcinomas, an older and a younger woman, and a third example with a fibroadenoma as a benign tumor. The first case is a 72-years-old patient with a histologically proven medium differentiated invasive ductal carcinoma with a maximum extension of 1.6 cm in the right breast. Since the breast of this older woman consisted mainly of adipose tissue, it was radiologically transparent, and the carcinoma was clearly visible in the x-ray mammogram. Similarly, the breast is highly transparent for optical radiation. Figure 18.5a, b shows the intrinsic absorption maps at 660 and 797 nm recorded prior to the application of ICG. Data refer to normalized photon counts in the so-called “late time window” of the time-domain technique [33].

At 660 nm, the carcinoma is clearly visible at high contrast, at 797 nm it has a contrast compared to the superficial blood vessels which appear as elongated structures. Since 797 nm is close to the isosbestic point of oxy- and deoxyhemoglobin absorption, Fig. 18.5b is a qualitative map of the total Hb concentration, i.e. the lesion has an increased Hb concentration as expected. The stronger tumor absorption at 660 nm reflects a high concentration of deoxyhemoglobin, i.e. the carcinoma is characterized by a decrease in blood oxygen saturation compared to the surrounding tissue which is a sign of high metabolic activity. Figure 18.5c shows the breast absorption at the excitation wavelength (780 nm) for the first scan during the vascular phase. Now, absorption is enhanced by ICG which is distributed in the vessels at this measurement time. According to the discussion in Sect. 18.2.3, the mammogram gives the same information as the intrinsic absorption image at the

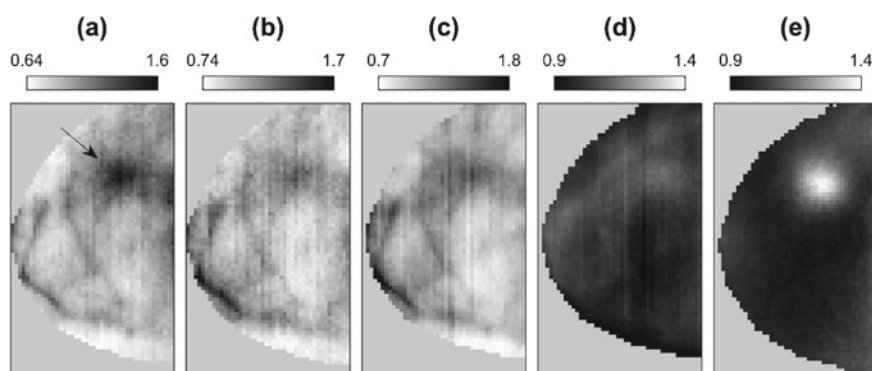


Fig. 18.5 Optical mammograms (case 1, craniocaudal view) of a 72-years-old patient with an invasive ductal carcinoma in the right breast, indicated by the arrow; **a** intrinsic absorption at 660 nm (native phase), **b** intrinsic absorption at 797 nm, **c** contrast-enhanced absorption during vascular phase, **d** fluorescence ratio mammogram of the vascular phase, and **e** fluorescence ratio mammogram of the extravascular phase. The absorption mammograms (**a–c**) display normalized reciprocal photon counts in a late time window

nearby wavelength of 797 nm (cf. Fig. 18.5b) due to the strong binding of ICG to plasma proteins.

Figure 18.5d shows the corresponding fluorescence ratio mammogram for the vascular phase, and Fig. 18.5e displays the fluorescence ratio mammogram for the second scan of the extravascular phase. For comparison, these two images are given with the same grayscale. Bright structures in the mammograms indicate a locally enhanced concentration of ICG. In Fig. 18.5d fluorescence can be seen at the site of the (vascularized) carcinoma, as well as for the superficial blood vessels. The visibility of the carcinoma is comparable to Fig. 18.5b, c. The fluorescence ratio mammogram for the extravascular phase (Fig. 18.5e) displays the carcinoma with the highest contrast due to extravasation of ICG and its retention in the carcinoma. All other structures, that appear in the native phase absorption mammograms and during the vascular phase, are suppressed now. It should be noted, however, that a fluorescence background signal was obtained at all scan positions, which indicates a low extravasation in all parts of the breast.

The second patient is a 51-years-old woman with a well-differentiated invasive ductal carcinoma. The size given by histology was $1.1 \times 1.0 \times 0.8 \text{ cm}^3$. The suspicious lesion was found by ultrasound. The x-ray mammogram revealed dense glandular tissue and showed only a poorly visible architectural distortion. The expected position of the lesion in the optical mammograms was derived from dynamic contrast-enhanced MRI measurements which showed the lesion at the lateral side of the breast close to the chest wall. MRI offered a second lesion nearby, which was histologically classified as low-grade ductal carcinoma in situ.

Figure 18.6a, b displays the absorption at 660 and 797 nm without contrast agent (native phase). Both images show a lesion of strongly increased absorption in the upper left part in accordance with the location expected from MR imaging. However, the location differs between both wavelengths making a decision about lesion visibility for the native phase difficult. As for the first case, the contrast-enhanced absorption mammogram for the vascular phase (Fig. 18.6c) is very similar to the intrinsic absorption mammogram at 797 nm. Figure 18.6d, e displays the fluorescence ratio mammograms for this patient. Similar to case 1, the image for the vascular phase is of flat contrast only when compared to the extravascular phase. The latter mammogram clearly displays the strong enrichment of the contrast agent at the expected tumor position. Besides the carcinoma, we observe a moderate fluorescence signal from the tissue close to the chest wall in the lower left part of the mammograms in Fig. 18.6d, e, and some contrast behind the nipple position. Compared to the carcinoma, these regions did not essentially change contrast from the vascular to the extravascular phase. The deviation of the shape of the breast in Fig. 18.6e from the other mammograms is caused by slightly different positioning of the breast during recompression for the extravascular phase measurements. Therefore, the location of the lesion in Fig. 18.6e cannot be directly transferred to the other mammograms.

The third case is an example of a benign lesion. The 52-years-old patient had a fibroadenoma in her left breast, which was finally validated by histology. From ultrasound examination, the size of the lesion was estimated as $1.8 \text{ cm} \times 1.0 \text{ cm}$.

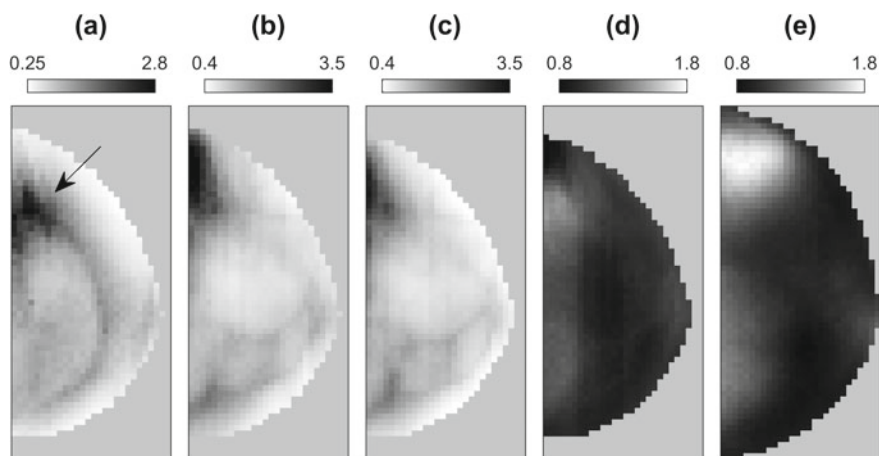


Fig. 18.6 Optical mammograms (case 2, craniocaudal view) of a 51-years-old patient with an invasive ductal carcinoma in the left breast, indicated by the arrow; **a** intrinsic absorption at 660 nm (native phase), **b** intrinsic absorption at 797 nm, **c** contrast-enhanced absorption at 780 nm during vascular phase, **d** fluorescence ratio mammogram for the vascular phase, and **e** fluorescence ratio mammogram for the extravascular phase. The absorption mammograms (**a–c**) display normalized reciprocal photon counts in a late time window

The x-ray image did not show any abnormality. For this patient, data were recorded in the native phase at the excitation wavelength (780 nm, see Fig. 18.7a). It was known from ultrasound that the fibroadenoma lies in the left part of the breast. Having in mind that fibroadenomas often exhibit increased absorption due to an increased hemoglobin concentration [21, 25, 77], its position most probably corresponds to the absorbing region in the left part of the breast, indicated by the arrow in Fig. 18.7a. However, there remains some uncertainty in this decision. Similar to the other two cases, the contrast-enhanced absorption mammogram for the vascular phase in Fig. 18.7b shows the same structures as the intrinsic absorption mammogram in Fig. 18.7a.

In Fig. 18.7c, d the fluorescence ratio mammograms for the vascular and the extravascular phase are displayed. Apart from the blood vessels, which are only visible in Fig. 18.7c, both images are very similar. Hence, the fibroadenoma does not show any particular enrichment of ICG due to extravasation. This result corroborates the expectation that the capillary walls in benign lesions are not sufficiently leaky to allow enhanced extravasation of macromolecules.

Confirmed by the results on the other cases of the trial, the study has shown that fluorescence images recorded in the extravascular phase enable the detection of extravasated ICG, which offers a way to improve the specificity in breast cancer detection by exploiting vessel permeability for macromolecules to differentiate malignant from benign lesions [70]. Furthermore, this study enabled a comparison of the permeability specific images with endogenous contrast optical mammograms

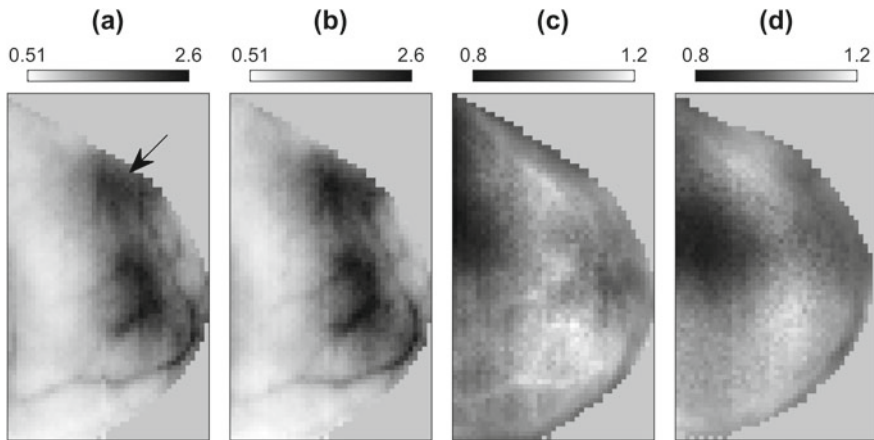


Fig. 18.7 Optical mammograms (case 3, craniocaudal view) of a 52-years-old patient with a fibroadenoma in the left breast. The presumed position of the lesion is indicated by the arrow; **a** intrinsic absorption at 780 nm (native phase), **b** contrast-enhanced absorption during vascular phase, **c** fluorescence ratio mammogram for the vascular phase, and **d** fluorescence ratio mammogram for the extravascular phase. Absorption mammograms display normalized reciprocal photon counts in a late time window

of the same patients representing total Hb or deoxyhemoglobin distributions, and with ICG enhanced vascular contrast mammograms. In this way, the advantages of the permeability specific measurements could be convincingly demonstrated. Larger clinical studies are required to confirm the potential of the method.

The EPR effect is also considered for improving the specificity in MR imaging of breast tumors. Gd-based contrast agents used in clinical routine act as small molecules that non-selectively extravasate in tumors as well as in healthy tissue. To obtain a more specific enhancement, several macromolecular contrast agents for MRI are under development [16, 108]. Up to now no such agent became available for clinical applications. A main problem is safety concerns related to the slow excretion and high tissue accumulation of toxic Gd ions [23, 108]. In contrast, the approved contrast agent ICG offers a safe way to exploit the EPR effect. However, visualization of ICG in the breast by fluorescence imaging is hampered by the low spatial resolution of diffuse optical imaging.

18.2.5 Imaging of Breast Cancer with Omocianine

The small molecular contrast agent omocianine was used in two pilot studies. One study comprised the examination of 11 patients with a continuous-wave (CW) fluorescence and absorption tomography system developed by Philips Healthcare (Best, The Netherlands) [97]. This device uses a high-density

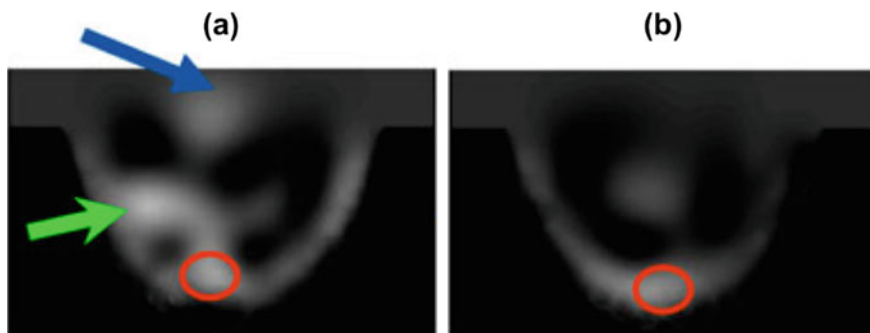


Fig. 18.8 Reconstructed fluorescence images of a patient with an invasive lobular carcinoma obtained 8 h after administration of omocianine; **a** left breast with carcinoma (green arrow) and a reconstruction artifact at the chest wall (blue arrow), **b** right breast. The red circles indicate the nipple positions (reprinted with permission from [97])

source-detector fiber system arranged around a cup unit for investigation of the freely pending breast. Optical contact is supported by a matching fluid. Omocianine was administered intravenously as a bolus. Four different doses were used with three cases in each group (two cases for the highest dose). At the two lowest doses, five out of six malignant lesions were detected in the reconstructed fluorescence images whereby the missed lesion was out of the field of view. No lesions could be seen in the two highest dose groups for which reconstruction was problematic due to the non-negligible absorption of the contrast agent. Best lesion-to-background contrast was obtained 8 h after injection ranging between 1.8 and 2.8. Figure 18.8 shows the reconstructed fluorescence image for a case with a 2.5 cm diameter invasive lobular carcinoma. The result for the contralateral breast is given as well.

Besides the lesion (green arrow) other fluorescent structures are visible such as the nipples of both breasts (red circles) and glandular tissue. The study showed that glandular tissue generally exhibited an enhancement pattern similar to the carcinomas making a reliable detection of carcinomas with omocianine probably problematic. The authors concluded that target-specific contrast agents will be crucial to translate fluorescence molecular breast imaging to clinical application [97].

The second study was a multicenter clinical trial with 52 patients who received omocianine and 9 patients who got placebos instead [71]. Fluorescence and absorption images of the freely pending suspicious breast were acquired with a tomographic device from Imaging Diagnostics Systems, Inc. (Ft. Lauderdale, FL, USA) using a vertically moveable ring arrangement of light sources and detectors. Omocianine was administered at five different doses. The best performance was obtained at a dose of 0.1 mg omocianine per kg body weight which was the highest dose in the first study discussed above. All 7 malignant lesions were detected, whereas the two benign lesions in this group did not show enhanced fluorescence. However, the neighboring dose groups of 0.2 and 0.05 mg/kg yielded carcinoma detection rates of about 50% only, and 1 false positive result each. Furthermore, the

time point of the best lesion contrast in this study showed a strong spread. On average, the optimal detection time lay between 3 and 4 h compared to the stable result of 8 h observed by van de Ven et al. There was a tendency for earlier imaging time points for malignant in contrast to the visible benign lesions. Eventually, the authors concluded the need for improvements in the technique and the development of cancer-specific, targeted contrast agents [71].

The studies with omocyanine revealed some preliminary technical problems that limited the value of the results. These problems may be overcome by improving data acquisition and reconstruction. However, both studies ended up with significant limitations due to the nonspecific nature of this contrast agent. In comparison, the contrast agent ICG has the advantage that the vessel permeability can be exploited as a characteristic feature of malignant tumors.

18.2.6 Fluorescence-Guided Breast Cancer Surgery

During breast conserving cancer surgery, it is required to reliably recognize the borders between tumor and healthy tissue. Commonly, surgeons have to rely on visual inspection. Along with this technique, incomplete resections were reported for 20–40% of the patients [69]. Near-infrared fluorescence imaging is a promising technique to improve intraoperative tumor margin detection. Hereby, the fluorescent contrast agent should either actively or passively accumulate in the tumor, but not in the surrounding healthy tissue.

The extravasation of ICG in carcinomas according to the EPR effect offers potential to delineate tumor margins during surgery. As reviewed by Tipirneni et al. [90], several clinical trials have been conducted to study the visualization of tumor margins with ICG. However, no published data are available so far.

Tummers et al. [93] investigated the application of methylene blue for tumor margin detection. Intraoperative fluorescence imaging was conducted with a combined white-light and fluorescence detection system. Fluorescence was searched in the wound bed and on the surface of the resected specimens. Two out of the 24 cases in this study showed fluorescence at these locations after conventional cancer resection. For both cases, histopathology finally confirmed positive resection margins. As an example, Fig. 18.9 displays intraoperatively taken images for one of these cases.

Overall, 20 out of the 24 resected carcinomas in this study contained methylene blue as confirmed by fluorescence measurements after pathological bisection of the specimens. In one of the remaining 4 cases without methylene blue enrichment histology revealed positive resection margins, too.

The four molecular probes listed in Sect. 18.2.2 were investigated in exploratory studies on tumor margin detection. The probe bevacizumab-IRDye800CW targeting the vascular epithelial growth factor VEGF-A was applied in a study on 20 patients [51]. Fluorescence and white-light images were recorded with a custom-made device with an excitation laser at 750 nm and a high-end cooled EMCCD camera for sensitive fluorescence detection. The contrast agent was

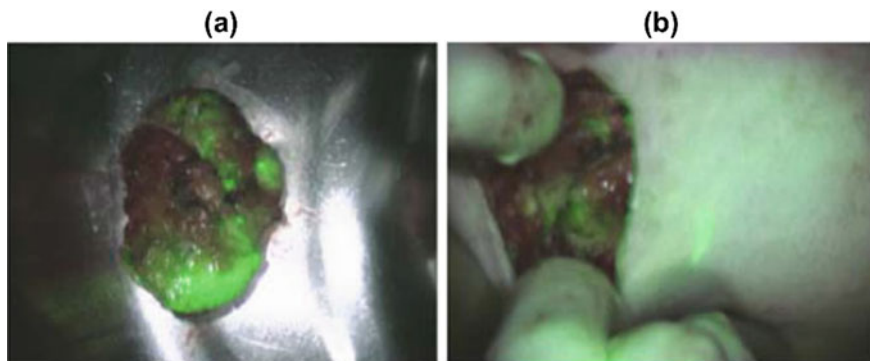


Fig. 18.9 **a** Resected breast cancer specimen, **b** wound bed after resection. Both images show fluorescence from methylene blue (overlaid as green color) indicating incomplete cancer removal (reprinted with permission from [93])

administered intravenously at a microdose level. During surgery, fluorescence images were recorded at several predefined time points. After tumor removal, the surgical field was inspected again for fluorescence, and the excised specimens were imaged, too. Histopathology identified two patients with incomplete tumor removal. For both these cases, positive resection margins were visible in the fluorescence images recorded from the tissue lumps directly after removal. However, no residual fluorescence was seen in the wound bed. Final investigations on excised and sliced specimens showed IRDye800CW fluorescence in 19 of the 20 carcinomas. Microscopy revealed complete overlap of the molecular probe and VEGF-A regions in 6 and adjacent location in 12 cases. In the remaining two cases IRDye800CW and VEGF-A positions did not overlap.

The folate receptor alpha targeting agent EC17 was applied for intraoperative imaging on 3 patients with breast cancer [94]. Images of the surgical field, the excised specimens and of the wound bed were recorded with the Artemis fluorescence imaging system (Quest Medical Imaging, The Netherlands) specially configured to generate excitation light for EC17 at 490 nm. Tumor-specific fluorescence could be observed during surgery for all three cases. However, autofluorescence of normal breast tissue strongly hampered tumor identification. Autofluorescence was also visible in fluorescence microscopy of the sliced tissue specimens. Nevertheless, clear accumulation of EC17 in tumor cells could be seen here.

The activatable probe LUM 15 was investigated on 15 patients having either breast cancer or soft-tissue sarcoma [107]. Fluorescence measurements were done ex vivo on resected tissue samples whereby a significantly higher fluorescence was observed for the tumors compared to normal tissue. The activatable probe AVB-620 was applied in a study on 27 patients who underwent surgical excision of breast cancer [95]. The probe was administered by an infusion 2–20 hours before surgery. Fluorescence images were taken from the surgical field as well as from the

excised specimens. The study demonstrated measurable changes between tumor-positive and tumor-negative tissue classified by pathology.

In summary, the first results with specific molecular probes for breast cancer applied on humans show tumor-specific fluorescence signals. Contrast seems not yet sufficiently stable for a reliable detection of tumor margins during surgery, and further research is required. Furthermore, it remains an open question, whether molecular probes could help to develop fluorescence imaging toward a diagnostic tool with high sensitivity and specificity for breast cancer. In fact, a highly specific molecular probe will be suitable for only a small fraction of cancer entities, since the pathology of tumor tissue differs widely among breast cancer patients.

18.3 Cancer and Early Malignancies of the Gastrointestinal Tract

The characterization of breast tumors discussed in the preceding section requires the use of near-infrared light in combination with advanced light detection techniques. In contrast, tumors of the gastrointestinal (GI) tract are superficial lesions which can easily be accessed in reflection geometry by light from the whole visible spectral range. The conventional technique for the detection of premalignant changes and early-stage carcinomas in the esophagus and the colon and rectum is white-light endoscopy [28, 104]. Since patients with inflammations of the GI tract have a high risk in the development of malignancies, they are advised to regularly undergo surveillance examinations. However, the detection of lesions developing from inflamed tissue is difficult since the mucosa appears flat in the endoscopic images. Thus, for patients with ulcerative colitis about 30% of flat intraepithelial neoplasias are not visible by conventional white-light endoscopy [80]. Similarly, the detection rate of neoplasia for patients with Barrett's esophagus is insufficient so far [101].

Over the years, enhanced optical imaging techniques have been developed for GI endoscopy [39]. Narrowband imaging and autofluorescence imaging use endogenous tissue contrast. Recent studies suggested that narrowband imaging does not really improve neither the detection of esophageal neoplasia [29] nor the detection of colorectal dysplasia [41, 52]. Likewise, autofluorescence imaging of the esophagus was found to be of limited value only for early detection of lesions [5, 29]. Chromoendoscopy uses a dye spray to improve lesion detection. First studies with this technique demonstrated a 3–5-fold increase in the probability of detecting colorectal dysplasia [40, 48, 83]. In 2015, chromoendoscopy became part of a consensus statement on surveillance and management of dysplasia in inflammatory bowel disease [50]. In a recent study, Mooiweer et al. [60] assessed more critically that chromoendoscopy of the colon does not yield enhanced performance compared to white-light endoscopy.

Another advanced technique is confocal laser endomicroscopy which provides microscopic details of the gastrointestinal mucosa *in vivo* [28, 30]. Studies on patients with Barrett's esophagus and with ulcerative colitis, performed in

combination with chromoendoscopy using intravenous injection of fluorescein, demonstrated high diagnostic accuracy [30], whereas a later study on patients with Crohn's disease showed a lower diagnostic yield [103]. Moreover, confocal laser endomicroscopy yielded good or, at least reasonable, diagnostic accuracy for investigations on patients with long-standing ulcerative colitis and with primary sclerosing cholangitis associated inflammatory bowel disease [18, 79, 98]. A main limitation of confocal laser endoscopy is that this technique is not suited for investigation of the full hollow organ. It requires preselection of suspicious regions by, e.g., white-light or chromoendoscopy, where it is then applied as a point technique to improve diagnosis [39].

Similar to other organs, further improvements of performance and diagnostic accuracy in endoscopy of the GI tract are expected by application of tumor-specific molecular probes. In the following, we start with a discussion of 5-aminolevulinic acid, which is transformed into protoporphyrin IX preferentially in tumor tissue. Then we review recent results obtained with targeting peptides and antibodies, as well as activatable probes.

18.3.1 Protoporphyrin IX as Tumor Marker

Protoporphyrin IX (PpIX) is a natural precursor in the synthesis of heme. Its conversion to heme by insertion of a ferrous ion is catalyzed by the enzyme ferrochelatase. Tumor cells show an accumulation of PpIX which is assumed to be caused by a reduced activity of ferrochelatase [26, 47] and a relative enhancement of porphobilinogen deaminase activity [32]. The endogenous small molecule 5-aminolevulinic acid (5-ALA) acts as a precursor in the biosynthesis of PpIX. When 5-ALA is additionally administered as an exogenous agent the synthesis of PpIX is enforced and its accumulation in tumor cells is increased [43]. PpIX can be made visible by fluorescence imaging using blue or green light for excitation. 5-ALA supported PpIX accumulation has been applied for investigations on oral cancer [4], bladder cancer [11, 43], lung cancer [37], and skin cancer [15]. Also, several studies were conducted on tumors of the GI tract.

Mayinger et al. [57] investigated 22 patients with known or treated malignant and precancerous lesions of the esophagus. 5-ALA was orally administered with a dose of 15 mg/kg body weight. Fluorescence and white-light endoscopy were conducted about 6 h later. The fiberoptic endoscope was connected to a light source capable of emitting violet-blue light, and a CCD camera for detection of the red fluorescence light. In this study, 85% of the biopsy sites with histologically confirmed premalignant or malignant tissue exhibited PpIX fluorescence. In contrast, only 25% of them were detected with white light.

The study by Brand et al. [6] aimed at differentiation between Barrett's mucosa with and without dysplasia. 20 patients obtained 10 mg/kg of 5-ALA orally 3 h before endoscopy of the esophagus. Fluorescence was excited with a wavelength of 400 nm from a dye laser, and fluorescence intensities were measured quantitatively at 635 and 480 nm to account for PpIX and autofluorescence, respectively.

By using the PpIX fluorescence intensity alone, high-grade dysplasia could be distinguished from nondysplastic tissue with a sensitivity of 77% and a specificity of 71%. Since the study showed a decreased autofluorescence intensity for nodular high-grade dysplasia, too, Brand et al. calculated the fluorescence intensity ratio of 635 and 480 nm signals. In this way, high-grade dysplasia could be differentiated from nondysplastic tissue with 100% sensitivity and 100% specificity. This result demonstrates the necessity to consider the fluorescence of PpIX with respect to the autofluorescence background. A similar approach was already successfully demonstrated in a study on naturally accumulated PpIX in esophageal dysplasia without additional administration of 5-ALA [67].

18.3.2 Time-Gated Fluorescence Imaging of Protoporphyrin IX

Another approach to obtain a high sensitivity and specificity in dysplasia detection of the esophagus and the colon is time-gated fluorescence imaging and spectroscopy. As demonstrated earlier for skin cancer, this method utilizes the fluorescence lifetime as an additional parameter to improve the detection of PpIX fluorescence versus the tissue autofluorescence background [15]. Figure 18.10 illustrates the main components of the research setup for time-gated fluorescence endoscopy developed at the PTB [65].

The endoscope in this setup has two working channels. The first one contains an optical fiber to guide the excitation light to the tissue. This fiber was also used to collect fluorescence light from the tissue for spectral analysis. The second working channel was equipped with an auxiliary image guide for the acquisition of fluorescence images by an intensified CCD camera. A bandpass filter in front of the camera suppressed the excitation light. The image guide was fixed in such a way that nearly the same field of view was covered by fluorescence and white-light images. The excitation light pulses were generated by an optical parametric oscillator (OPO), pumped by the third harmonic of a Q-switched Nd:YAG laser. Generally, the OPO could be tuned between 410 nm and 2.2 μm . For the investigations on PpIX fluorescence, a wavelength of 505 nm was chosen. The pulse duration was about 3 ns. After attenuation to the appropriate power, the light pulses were guided through a dichroic beam splitter into the illumination fiber of the endoscope.

To record fluorescence spectra, the fluorescence light collected by the illumination fiber was guided through the dichroic beam splitter to a polychromator. Similar to the intensified CCD camera for imaging, the cooled detector array of the polychromator was equipped with an intensifier. This intensifier was opened for 20 ns after each laser pulse. Furthermore, an electrical delay enabled to start the recording of fluorescence spectra either immediately or with a delay time of 20 ns with respect to the excitation pulse. Figure 18.11 illustrates the differences in the fluorescence spectra of normal mucosa and of a carcinoma of the colon obtained in this way. Data were acquired about 2 h after topical administration of 5-ALA.

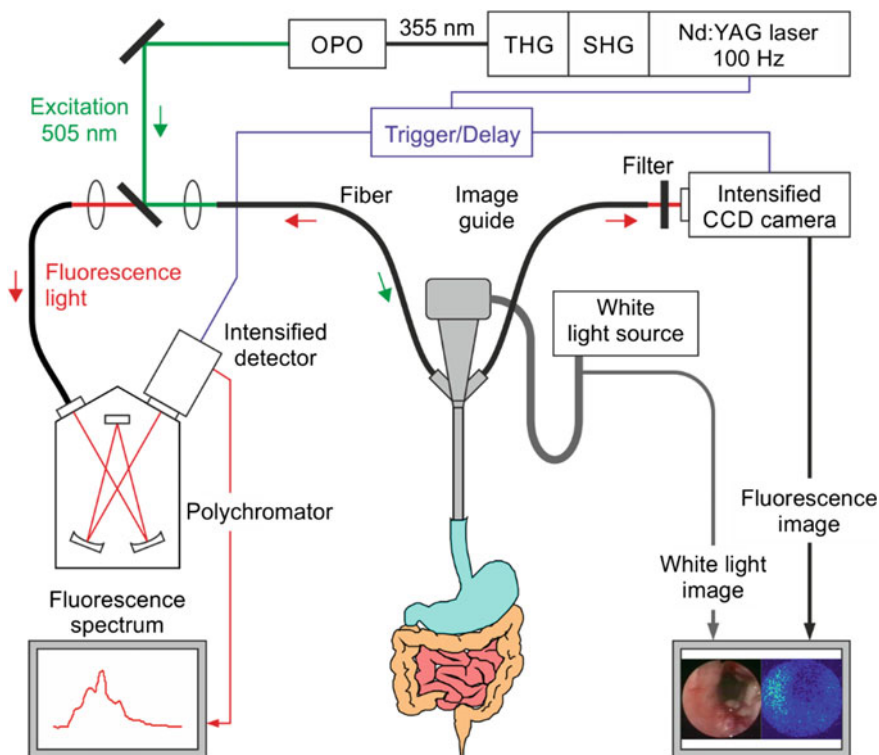
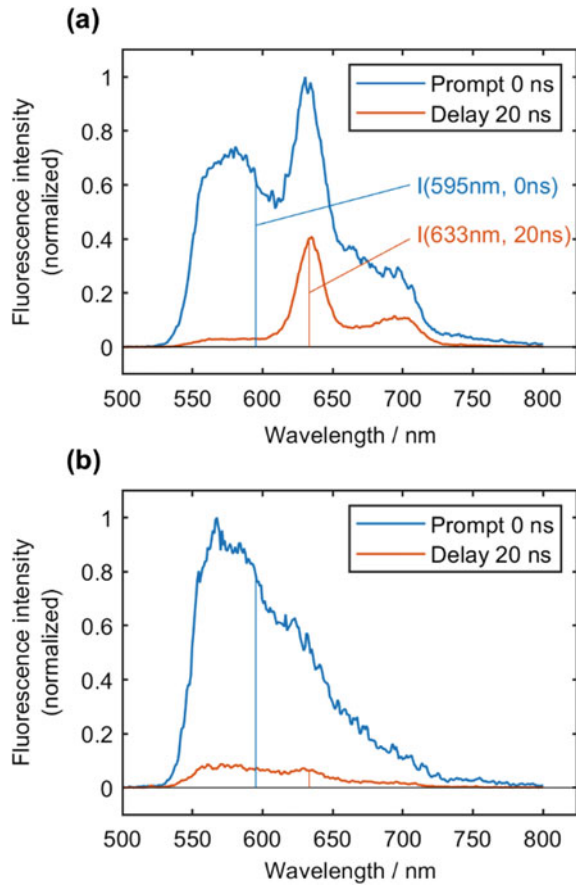


Fig. 18.10 Typical scheme of a setup for endoscopic investigation of time-delayed fluorescence of the gastrointestinal tract after topical application of 5-aminolevulinic acid

Normal mucosa shows a broad and flat emission spectrum. When the delay of 20 ns is applied then the fluorescence emission is almost down due to the short autofluorescence lifetime of about 3 ns [59]. The immediate spectrum of the carcinoma has the well-defined fluorescence peak of PpIX around 633 nm and a second minor band at about 700 nm. Both are overlaid on the flat autofluorescence background being similar to that of normal mucosa. The delayed spectrum is almost free of the autofluorescence background, and the tumor-specific fluorescence bands at 633 and 700 nm are clearly visible due to the longer fluorescence lifetime of PpIX (about 16 ns [59]). In order to quantify the tumor-specific fluorescence, the ratio R of the delayed fluorescence intensity at 633 nm and of the immediate fluorescence intensity at 595 nm according to $R = I(633 \text{ nm}, 20 \text{ ns})/I(595 \text{ nm}, 0 \text{ ns})$ can be utilized [59].

The time-gated laser-induced fluorescence endoscopy technique was applied in clinical trials on the esophagus [65] and the colon [27, 66]. In both studies, 5-ALA was topically administered to the patient about 2 h before the measurement. The investigations on a total of 141 esophageal lesions showed that the above-defined ratio R enables reliable differentiation of low-grade dysplasia from nondysplastic

Fig. 18.11 Normalized fluorescence intensity of PpIX and autofluorescence background in dependence on wavelength. **a** Immediate and time-delayed fluorescence spectrum of a carcinoma in vivo and **b** immediate and time-delayed fluorescence spectrum of normal mucosa in vivo



mucosa in Barret's esophagus. Furthermore, the higher performance of the time-gated technique could clearly be demonstrated. Compared to screening white-light endoscopy, dysplasia was detected at a 2.8-fold higher rate. In addition, three early carcinomas were visible from the time-gated technique only [65]. Besides spectroscopic investigations, the time-gated technique can also be used to take prompt and delayed fluorescence images of lesions together with white-light images. Due to the short gate time, there is no significant background to the fluorescence signal from the white-light source. As an example, Fig. 18.12 shows the delayed fluorescence image of a carcinoma in the esophagus together with the white-light image. The fluorescence image displays the carcinoma with its strong PpIX signal almost free of autofluorescence background. The slight discrepancy between both images in Fig. 18.12 is caused by the slow refreshment rate of the fluorescence image (2 images/s). The images were processed in real time in order to identify malignant spots in the white-light image for biopsy. Using this technique, the number of biopsies could be decreased.

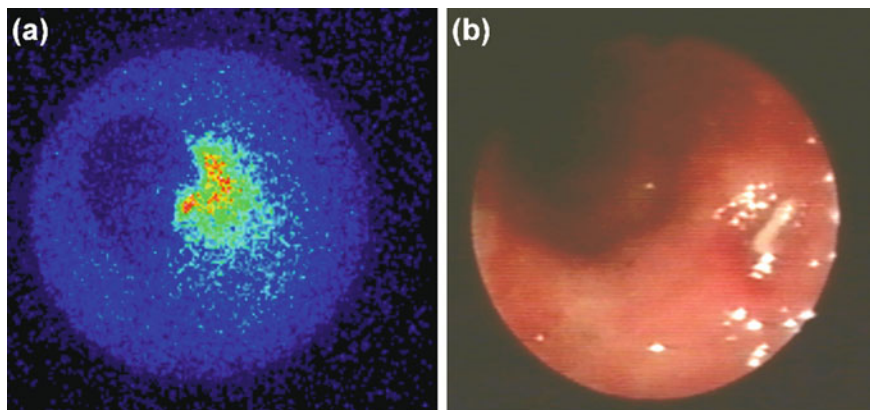


Fig. 18.12 **a** Fluorescence image taken with 20 ns delay and **b** corresponding white-light image of an esophageal carcinoma

The study on time-gated fluorescence colonoscopy was conducted on 42 patients with long-standing ulcerative colitis. Conventional white-light endoscopy with 4-quadrant biopsies detected invisible flat intraepithelial neoplasia in 3 patients, and time-gated fluorescence endoscopy in 10 patients. With the time-gated fluorescence ratio technique, dysplastic and nondysplastic mucosa could be discriminated with a sensitivity and specificity of 73% and 81%, respectively [66].

Overall, the results on time-gated fluorescence endoscopy with PpIX as tumor marker underline that this technique is superior to conventional white-light endoscopy. In particular, the detection limit is clearly improved after suppression of the short lifetime tissue autofluorescence. As demonstrated on colorectal cancers and their metastases, PpIX fluorescence can even be detected without amplification by 5-ALA administration [59]. However, time-gated fluorescence endoscopy requires advanced detection systems together with pulsed lasers which are expensive and, thus, hamper its translation to clinical routine.

5-ALA and PpIX have also been considered for the detection of other tumors, including bladder cancer, glioma, and squamous cell carcinoma [43, 44]. Some studies on the brain have shown that PpIX can accumulate in nonmalignant tissue, too [44], making its specificity for malignant tissue questionable. Besides their application in diagnostics, 5-ALA and PpIX play an important role in photodynamic therapy [2].

18.3.3 Targeted Molecular Imaging in Gastrointestinal Endoscopy

As for cancer in general, targeted molecular probes are also considered as a promising approach for the early detection of tumors in the GI tract by fluorescence

measurements. The targeted antibody bevacizumab-IR800CW and the activatable peptide LUM015 which have both been applied for fluorescence-guided surgery of breast cancer (cf. Sects. 18.2.2 and 18.2.6), are also investigated for the detection of cancer in the GI tract. Bevacizumab-IR800CW, which targets the vascular epithelial growth factor A, was applied in a study on 14 patients with Barrett's esophagus having known lesions [62]. For this study, the working channel of a high definition white-light endoscope was equipped with a fiber bundle connected to a custom-build fluorescence imaging setup with a 750 nm laser for fluorescence excitation and a short-pass filtered white-light LED for the generation of overlay images. Two cameras positioned behind a dichroic beam splitter were used to acquire fluorescence and (short-pass restricted) white-light images simultaneously in real time. Five patients received the agent through an intravenous bolus 2 days before endoscopy, the other nine patients topically by spraying immediately before fluorescence endoscopy.

Fluorescence imaging visualized 16 out of the 17 dysplastic and neoplastic lesions detected by conventional white-light endoscopy. Hereby, the missed lesion was not accessible, since its position at the gastric cardia could not be reached by the separate fiber bundle due to bending restrictions. In addition, fluorescence imaging found four more dysplastic and neoplastic lesions. As an example, Fig. 18.13 displays images of an early adenocarcinoma that was seen exclusively by fluorescence imaging. The smaller field of view in the overlay and the fluorescence image compared to the conventional endoscopic image is caused by the smaller aperture of the inserted fiber bundle. Compared to systemic administration, the topical administration was found to give a slightly higher tumor-to-background ratio of 4.30 ± 0.41 . The high number of lesions found only after administration of bevacizumab emphasizes the high potential of targeted imaging for early detection of esophageal cancer.

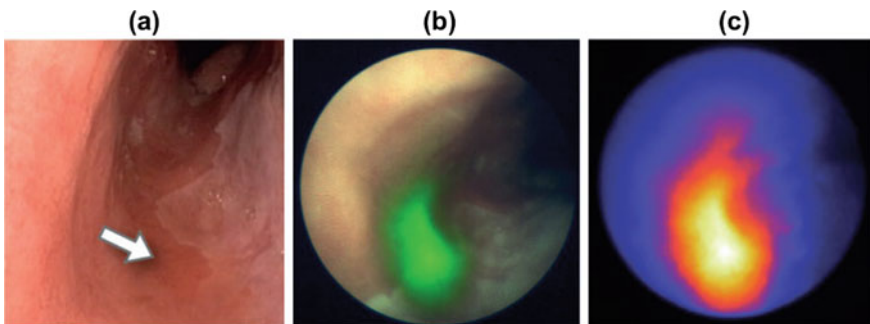


Fig. 18.13 In vivo detection of an early esophageal adenocarcinoma by targeted imaging with bevacizumab-IR800CW; **a** conventional white-light image without abnormality at the carcinoma position (arrow), **b** overlay image with fluorescence indicated in green, and **c** fluorescence image (reprinted with permission from [62])

The probe LUM015 which is activated by cathepsins currently undergoes a phase 1 clinical trial for assessing its safety and efficacy on patients with colorectal, pancreatic, and esophageal cancers [44]. As part of this study, fluorescence signals from specimens of resected tumors will be compared to histological findings (clinical trial number NCT02584244, clinicaltrials.gov). Likewise, the lectin *wisteria floribunda* which has been labeled with fluorescein is currently being evaluated in a phase 1 clinical trial for early detection of colorectal cancer. Lectins are expected to specifically detect cell-surface glycans that are altered in cancer [44].

There are also several peptides under consideration for tumor detection in the GI tract. Compared to antibodies, peptides have the advantages of lower costs and limited immunogenicity. The peptide GE-137 shows specific binding to c-Met, a protooncogene that encodes a transmembrane receptor tyrosine kinase to stimulate tumor progression and metastases [10]. Fluorescence is emitted by the conjugated dye Cy5. Intravenously injected GE-137 is well-tolerated in humans. A pilot study using white-light and fluorescence colonoscopy has shown that GE-137 enabled visualization of all 38 neoplastic colon polyps that were visible with white light. Moreover, the detection of nine additional polyps demonstrated that GE-137 may enable the detection of polyps missed by other techniques [10].

The specific peptides QRHKPRE and KSPNPRF are in the phase of first clinical trials for safety and efficacy evaluation [44]. QRHKPRE is considered for colorectal cancers. It binds to the epidermal growth factor receptor (EGFR) overexpressed in epithelial cancers. The peptide KSPNPRF has undergone a clinical trial on esophageal cancer. It targets the epidermal growth factor receptor 2 (Her2) which is known to be overexpressed in colon and esophageal as well as several other cancers.

Several peptides have been identified empirically using phage display by screening against cancer [44]. The peptide VRPMLQ was found to bind to pre-malignant rather than normal colonic crypts [38]. Using confocal endomicroscopy on 20 patients, a high tumor-to-background ratio of 17.9 ± 4.2 between adenomas and normal colonocytes was found after topical administration. However, this peptide has not yet been successfully applied in wide-field fluorescence endoscopy. The suspicious sites for performing endomicroscopy were selected by white-light endoscopy.

Sturm et al. [85] selected the peptide ASYNDA and labeled it with FITC for fluorescence imaging. The peptide was investigated in a study on 25 patients with Barrett's esophagus having a history with biopsy-proven high-grade dysplasia of esophageal adenocarcinoma. Suspicious regions were selected by white-light endoscopy. The peptide was sprayed to the corresponding site by a catheter. After a waiting time of 5 min an endomicroscope was placed in contact to take confocal fluorescence images of the lesion and normal-appearing squamous mucosa. By using a tumor-to-background fluorescence intensity ratio of 4.2 as threshold, high-grade dysplasia and adenocarcinoma could be differentiated from normal tissue with a sensitivity and specificity of 75% and 97%, respectively.

ASYNDA was used later by the same research group in a study with a multi-modal wide-field endoscope [45]. Besides white-light images, this endoscope

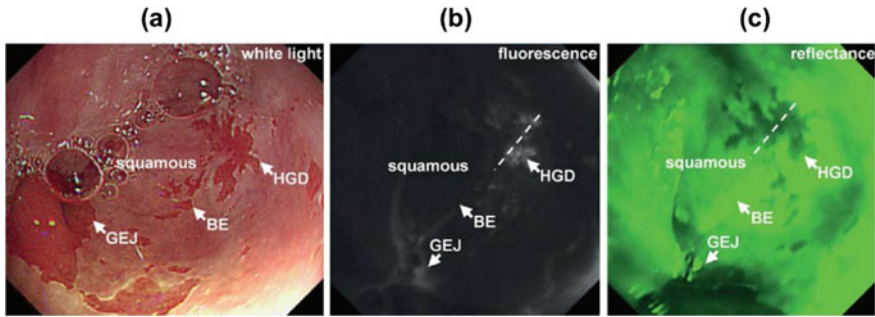


Fig. 18.14 In vivo detection of a high-grade dysplasia in the esophagus by targeted imaging with ASYNDA; **a** white-light image with several areas of Barrett's esophagus (BE), a high-grade dysplasia (HGD), squamous epithelium, and the gastroesophageal junction (GEJ); **b** fluorescence image; and **c** reflectance image co-registered with the fluorescence image. The dashed line indicates a cut through the lesion used for further analysis (reprinted with permission from [45])

collected fluorescence images and reflectance images in an alternating manner at 20 frames per second. The reflectance measured with illumination at 540–560 nm was used to normalize the fluorescence images in order to correct the shadowing of the raw data due to the large acceptance angle in image acquisition. Figure 18.14 shows a representative example of the three images for a region with a histologically confirmed high-grade dysplasia. The dysplasia can already be seen in the raw fluorescence image whereas Barrett's esophagus and squamous epithelium are almost free of fluorescence. In the lower part, some fluorescence from the gastroesophageal junction is visible. Using the normalized fluorescence images, sensitivity and specificity for the detection of high-grade dysplasia and early adenocarcinoma amounted to 76% and 94%, respectively.

The peptide KCCFPAQ was found to bind specifically to sessile serrated adenomas of the colon [46]. It did not show any toxic effects in animals and patients. KCCFPAQ was topically administered in a pilot study on 38 patients, having high risk for colorectal cancer, or having a suspected unresected proximal colonic polyp. Using wide-field fluorescence endoscopy, regions of sessile serrated adenomas were found to have a 2.4-fold higher mean fluorescence intensity than normal colonic mucosa. They could be distinguished with 89% sensitivity and 92% specificity. As described above for wide-field endoscopy with ASYNDA, this study used the same concept of fluorescence-to-reflectance ratio images to improve lesion detection [46].

In summary, there is a growing number of molecular probes that has entered clinical trials for the detection of carcinomas in the GI tract. In particular, the antibody bevacizumab-IR800CW and the specifically binding peptide GE-137 could already reveal their high potential by visualizing lesions that would have been missed by conventional white-light microscopy. Furthermore, the application of molecular probes in confocal endomicroscopy could become a way for the evaluation of suspicious regions without the necessity of taking biopsy samples.

18.4 Outlook

The discussed results on molecular imaging of carcinomas in the breast and GI tract underline the huge efforts undertaken to improve the early detection of cancer. Promising results on optical detection and differentiation of breast cancer have been obtained by exploiting the enhanced permeability and retention effect of solid carcinomas using the nontargeted contrast agent ICG. Specific binding markers as well as activatable probes have not yet been applied for breast cancer diagnosis, although proposed more than 20 years ago. In part, this slow development could be caused by the general limitations in optical imaging of the breast arising from the diffusive nature of light propagation in tissue. The detection of small concentrations of a tumor marker through several centimeters of tissue is a challenging task requiring advanced and expensive fluorescence imaging techniques. Furthermore, the spatial resolution of diffuse optical imaging will never be competitive with other imaging modalities. However, structural features (requiring high spatial resolution) are highly important for early clinical diagnosis of breast cancer.

The situation is different when the cancerous tissue in the breast has to be visualized during surgery. In this scenario, the cancer tissue is directly exposed to the surgical situs and optical imaging is the best-suited method for the surgeon. Accordingly, there is significant progress in the development of molecular probes for fluorescence-guided breast cancer surgery. Here we should expect the translation of molecular probes to clinical routine in the next future. This expectation is supported by the increasing number of fluorescence imaging systems approved for intraoperative use. However, the clinical development of highly specific molecular probes is limited by the selectivity of these contrast agents making them (commercially) relevant only for a defined subgroup of patients.

High-grade dysplasia and early carcinomas of the GI tract are superficial lesions as well. Whereas the intrinsic tumor marker PpIX was of high interest over years, molecular probes are more and more entering the field of GI tract imaging now. Having the number of probes in mind, that is just in the phase of safety investigations, we can expect that several probes will find their way into clinical routine over the next years. These probes may considerably improve the early detection of carcinomas in the GI tract. However, the same basic considerations concerning clinical probe development as pointed out for breast cancer apply for GI tumors as well.

Present results indicate that a tumor-to-background ratio in the order of 4:1 will be realistic. Since this number is not big, we can expect that quantitative imaging methods will become of high importance here. Similarly, the decision on tumor margins will depend on threshold values. Overall, quantification in fluorescence imaging might be an important step for the characterization of tumor grades as well as for the reliable resection of tumors.

References

1. Amini A, Masoumi Moghaddam S, Morris DL, Pourgholami MH (2012) The critical role of vascular endothelial growth factor in tumor angiogenesis. *Curr Cancer Drug Targets* 12:23–43. <https://doi.org/10.2174/156800912798888956>
2. Baumgartner R, Krammer B, Pottier R, Stepp H (eds) (2007) *Photodynamic therapy with ALA*. Royal Society of Chemistry, Cambridge
3. Becker A, Hessenius C, Licha K et al (2001) Receptor-targeted optical imaging of tumors with near-infrared fluorescent ligands. *Nat Biotechnol* 19:327–331. <https://doi.org/10.1038/86707>
4. Betz CS, Stepp H, Janda P et al (2002) A comparative study of normal inspection, autofluorescence and 5-ALA-induced PPIX fluorescence for oral cancer diagnosis. *Int J Cancer* 97:245–252. <https://doi.org/10.1002/ijc.1596>
5. Boerwinkel DF, Holz JA, Kara MA et al (2014) Effects of autofluorescence imaging on detection and treatment of early neoplasia in patients with Barrett's esophagus. *Clin Gastroenterol Hepatol* 12:774–781. <https://doi.org/10.1016/j.cgh.2013.10.013>
6. Brand S, Wang TD, Schomacker KT et al (2002) Detection of high-grade dysplasia in Barrett's esophagus by spectroscopy measurement of 5-aminolevulinic acid-induced protoporphyrin IX fluorescence. *Gastrointest Endosc* 56:479–487. <https://doi.org/10.1067/mge.2002.128172>
7. Bremer C, Tung C-H, Weissleder R (2001) In vivo molecular target assessment of matrix metalloproteinase inhibition. *Nat Med* 7:743–748. <https://doi.org/10.1038/89126>
8. Bremer C, Tung C-H, Bogdanov A, Weissleder R (2002) Imaging of differential protease expression in breast cancers for detection of aggressive tumor phenotypes. *Radiology* 222:814–818. <https://doi.org/10.1148/radiol.2223010812>
9. Bremer C, Ntziachristos V, Weitekamp B et al (2005) Optical imaging of spontaneous breast tumors using protease sensing “smart” optical probes. *Invest Radiol* 40:321–327. <https://doi.org/10.1097/01.rli.0000163797.23172.90>
10. Burggraaf J, Kamerling IMC, Gordon PB et al (2015) Detection of colorectal polyps in humans using an intravenously administered fluorescent peptide targeted against c-Met. *Nat Med* 21:955–961. <https://doi.org/10.1038/nm.3641>
11. Cauberg ECC, de Bruin DM, Faber DJ et al (2009) A new generation of optical diagnostics for bladder cancer: technology, diagnostic accuracy, and future applications. *Eur Urol* 56:287–297. <https://doi.org/10.1016/j.eururo.2009.02.033>
12. Cerussi AE, Shah N, Hsiang D et al (2006) In vivo absorption, scattering, and physiologic properties of 58 malignant breast tumors determined by broadband diffuse optical spectroscopy. *J Biomed Opt* 11:044005. <https://doi.org/10.1117/1.2337546>
13. Chance B, Nioka S, Zhang J et al (2005) Breast cancer detection based on incremental biochemical and physiological properties of breast cancers: a six-year, two-site study. *Acad Radiol* 12:925–933. <https://doi.org/10.1016/j.acra.2005.04.016>
14. Corlu A, Choe R, Durduran T et al (2007) Three-dimensional in vivo fluorescence diffuse optical tomography of breast cancer in humans. *Opt Express* 15:6696–6716. <https://doi.org/10.1364/oe.15.006696>
15. Cubeddu R, Pifferi A, Taroni P et al (1999) Fluorescence lifetime imaging: an application to the detection of skin tumors. *IEEE J Sel Top Quantum Electron* 5:923–929. <https://doi.org/10.1109/2944.796312>
16. Daldrup-Link HE, Brasch RC (2003) Macromolecular contrast agents for MR mammography: current status. *Eur Radiol* 13:354–365. <https://doi.org/10.1007/s00330-002-1719-1>
17. Desmettre T, Devoisselle JM, Mordon S (2000) Fluorescence properties and metabolic features of indocyanine green (ICG) as related to angiography. *Surv Ophthalmol* 45:15–27. [https://doi.org/10.1016/S0039-6257\(00\)00123-5](https://doi.org/10.1016/S0039-6257(00)00123-5)

18. Dlugosz A, Barakat AM, Björkström NK et al (2016) Diagnostic yield of endomicroscopy for dysplasia in primary sclerosing cholangitis associated inflammatory bowel disease: a feasibility study. *Endosc Int Open* 4:E901–E911. <https://doi.org/10.1055/s-0042-111203>
19. DSouza AV, Lin H, Henderson ER et al (2016) Review of fluorescence guided surgery systems: identification of key performance capabilities beyond indocyanine green imaging. *J Biomed Opt* 21:80901. <https://doi.org/10.1117/1.JBO.21.8.080901>
20. Ebert B, Sukowski U, Grosenick D et al (2001) Near-infrared fluorescent dyes for enhanced contrast in optical mammography: phantom experiments. *J Biomed Opt* 6:134–140. <https://doi.org/10.1117/1.1350561>
21. Enfield LC, Gibson AP, Everdell NL et al (2007) Three-dimensional time-resolved optical mammography of the uncompressed breast. *Appl Opt* 46:3628–3638. <https://doi.org/10.1364/ao.46.003628>
22. Fang Q, Selb J, Carp SA et al (2011) Combined optical and X-ray tomosynthesis breast imaging. *Radiology* 258:89–97. <https://doi.org/10.1148/radiol.10082176>
23. Feng Y, Jeong E-K, Mohs AM et al (2008) Characterization of tumor angiogenesis with dynamic contrast-enhanced MRI and biodegradable macromolecular contrast agents in mice. *Magn Reson Med* 60:1347–1352. <https://doi.org/10.1002/mrm.21791>
24. Fischer T, Ebert B, Voigt J et al (2010) Detection of rheumatoid arthritis using non-specific contrast enhanced fluorescence imaging. *Acad Radiol* 17:375–381. <https://doi.org/10.1016/j.acra.2009.09.016>
25. Floery D, Helbich TH, Riedl CC et al (2005) Characterization of benign and malignant breast lesions with computed tomography laser mammography (CTLM). *Invest Radiol* 40:328–335. <https://doi.org/10.1097/01.rli.0000164487.60548.28>
26. Fukuda H, Casas A, Batlle A (2005) Aminolevulinic acid: from its unique biological function to its star role in photodynamic therapy. *Int J Biochem Cell Biol* 37:272–276. <https://doi.org/10.1016/j.biocel.2004.04.018>
27. Fusco V, Ebert B, Weber-Eibel J et al (2012) Cancer prevention in ulcerative colitis: long-term outcome following fluorescence-guided colonoscopy. *Inflamm Bowel Dis* 18:489–495. <https://doi.org/10.1002/ibd.21703>
28. Galanopoulos M, Tsoukali E, Gkeros F et al (2018) Screening and surveillance methods for dysplasia in inflammatory bowel disease patients: Where do we stand? *World J Gastrointest Endosc* 10:250–258. <https://doi.org/10.4253/wjge.v10.i10.250>
29. Giacchino M, Bansal A, Kim RE et al (2013) Clinical utility and interobserver agreement of autofluorescence imaging and magnification narrow-band imaging for the evaluation of Barrett’s esophagus: a prospective tandem study. *Gastrointest Endosc* 77:711–718. <https://doi.org/10.1016/j.gie.2013.01.029>
30. Goetz M, Kiesslich R (2008) Confocal endomicroscopy: in vivo diagnosis of neoplastic lesions of the gastrointestinal tract. *Anticancer Res* 28:353–360
31. Götz L, Heywang-Kobrunner S, Schütz O, Siebold H (1998) Optische Mammographie an präoperativen Patientinnen. *Aktuelle Radiol* 8:31–33
32. Greenbaum L, Katcoff DJ, Dou H et al (2003) A porphobilinogen deaminase (PBGD) Ran-binding protein interaction is implicated in nuclear trafficking of PBGD in differentiating glioma cells. *Oncogene* 22:5221–5228. <https://doi.org/10.1038/sj.onc.1206723>
33. Grosenick D, Wabnitz H, Rinneberg H et al (1999) Development of a time-domain optical mammograph and first in vivo applications. *Appl Opt* 38:2927. <https://doi.org/10.1364/AO.38.002927>
34. Grosenick D, Hagen A, Steinkellner O et al (2011) A multichannel time-domain scanning fluorescence mammograph: performance assessment and first in vivo results. *Rev Sci Instrum* 82:024302. <https://doi.org/10.1063/1.3543820>
35. Grosenick D, Rinneberg H, Cubeddu R, Taroni P (2016) Review of optical breast imaging and spectroscopy. *J Biomed Opt* 21:091311. <https://doi.org/10.1117/1.JBO.21.9.091311>

36. Hagen A, Grosenick D, Macdonald R et al (2009) Late-fluorescence mammography assesses tumor capillary permeability and differentiates malignant from benign lesions. *Opt Express* 17:17016. <https://doi.org/10.1364/OE.17.017016>
37. Hautmann H, Pichler JP, Stepp H et al (2007) In-vivo kinetics of inhaled 5-aminolevulinic acid-induced protoporphyrin IX fluorescence in bronchial tissue. *Respir Res* 8:33. <https://doi.org/10.1186/1465-9921-8-33>
38. Hsiung P-L, Hardy J, Friedland S et al (2008) Detection of colonic dysplasia in vivo using a targeted heptapeptide and confocal microendoscopy. *Nat Med* 14:454–458. <https://doi.org/10.1038/nm1692>
39. Hundorfean G, Pereira SP, Karstensen JG et al (2018) Modern endoscopic imaging in diagnosis and surveillance of inflammatory bowel disease patients. *Gastroenterol Res Pract* 2018:5738068. <https://doi.org/10.1155/2018/5738068>
40. Hurlstone D, Sanders D, McAlindon M et al (2006) High-magnification chromoscopic colonoscopy in ulcerative colitis: a valid tool for in vivo optical biopsy and assessment of disease extent. *Endoscopy* 38:1213–1217. <https://doi.org/10.1055/s-2006-944732>
41. Ignjatovic A, East JE, Subramanian V et al (2012) Narrow band imaging for detection of dysplasia in colitis: a randomized controlled trial. *Am J Gastroenterol* 107:885–890. <https://doi.org/10.1038/ajg.2012.67>
42. Intes X, Ripoll J, Chen Y et al (2003) In vivo continuous-wave optical breast imaging enhanced with Indocyanine Green. *Med Phys* 30:1039. <https://doi.org/10.1118/1.1573791>
43. Jochem D, Stepp H, Waidelich R (2008) Photodynamic diagnosis in urology: state-of-the-art. *Eur Urol* 53:1138–1150. <https://doi.org/10.1016/j.eururo.2007.11.048>
44. Joshi BP, Wang TD (2018) Targeted optical imaging agents in cancer: focus on clinical applications. *Contrast Media Mol Imaging* 2018:2015237. <https://doi.org/10.1155/2018/2015237>
45. Joshi BP, Duan X, Kwon RS et al (2016) Multimodal endoscope can quantify wide-field fluorescence detection of Barrett’s neoplasia. *Endoscopy* 48:A1–A13. <https://doi.org/10.1055/s-0034-1392803>
46. Joshi BP, Dai Z, Gao Z et al (2017) Detection of sessile serrated adenomas in the proximal colon using wide-field fluorescence endoscopy. *Gastroenterology* 152:1002–1013.e9. <https://doi.org/10.1053/j.gastro.2016.12.009>
47. Kemmner W, Wan K, Rüttinger S et al (2008) Silencing of human ferrochelatase causes abundant protoporphyrin-IX accumulation in colon cancer. *FASEB J* 22:500–509. <https://doi.org/10.1096/fj.07-8888com>
48. Kiesslich R, Fritsch J, Holtmann M et al (2003) Methylene blue-aided chromoendoscopy for the detection of intraepithelial neoplasia and colon cancer in ulcerative colitis. *Gastroenterology* 124:880–888. <https://doi.org/10.1053/gast.2003.50146>
49. Kitai T, Inomoto T, Miwa M, Shikayama T (2005) Fluorescence navigation with indocyanine green for detecting sentinel lymph nodes in breast cancer. *Breast Cancer* 12:211–215. <https://doi.org/10.2325/jbcs.12.211>
50. Laine L, Kaltenbach T, Barkun A et al (2015) SCENIC international consensus statement on surveillance and management of dysplasia in inflammatory bowel disease. *Gastrointest Endosc* 81:489–501.e26. <https://doi.org/10.1016/j.gie.2014.12.009>
51. Lamberts LE, Koch M, de Jong JS et al (2017) Tumor-specific uptake of fluorescent bevacizumab-IRDye800CW microdosing in patients with primary breast cancer: a phase I feasibility study. *Clin Cancer Res* 23:2730–2741. <https://doi.org/10.1158/1078-0432.CCR-16-0437>
52. Leifeld L, Rogler G, Stallmach A et al (2015) White-light or narrow-band imaging colonoscopy in surveillance of ulcerative colitis: a prospective multicenter study. *Clin Gastroenterol Hepatol* 13:1776–1781.e1. <https://doi.org/10.1016/j.cgh.2015.04.172>
53. Liebert A, Wabnitz H, Obrig H et al (2006) Non-invasive detection of fluorescence from exogenous chromophores in the adult human brain. *Neuroimage* 31:600–608. <https://doi.org/10.1016/j.neuroimage.2005.12.046>

54. Liu Y, Tamimi RM, Collins LC et al (2011) The association between vascular endothelial growth factor expression in invasive breast cancer and survival varies with intrinsic subtypes and use of adjuvant systemic therapy: results from the Nurses' Health Study. *Breast Cancer Res Treat* 129:175–184. <https://doi.org/10.1007/s10549-011-1432-3>
55. Maeda H, Wu J, Sawa T et al (2000) Tumor vascular permeability and the EPR effect in macromolecular therapeutics: a review. *J Control Release* 65:271–284. [https://doi.org/10.1016/s0168-3659\(99\)00248-5](https://doi.org/10.1016/s0168-3659(99)00248-5)
56. Mahmood U (2004) Near infrared optical applications in molecular imaging. Earlier, more accurate assessment of disease presence, disease course, and efficacy of disease treatment. *IEEE Eng Med Biol Mag* 23:58–66. <https://doi.org/10.1109/MEMB.2004.1337950>
57. Mayinger B, Neidhardt S, Reh H et al (2001) Fluorescence induced with 5-aminolevulinic acid for the endoscopic detection and follow-up of esophageal lesions. *Gastrointest Endosc* 54:572–578. <https://doi.org/10.1067/mge.2001.118642>
58. Miampamba M, Liu J, Harootunian A et al (2017) Sensitive in vivo visualization of breast cancer using ratiometric protease-activatable fluorescent imaging agent, AVB-620. *Theranostics* 7:3369–3386. <https://doi.org/10.7150/thno.20678>
59. Moesta KT, Ebert B, Handke T et al (2001) Protoporphyrin IX occurs naturally in colorectal cancers and their metastases. *Cancer Res* 61:991–999
60. Mooiweer E, van der Meulen-de Jong AE, Ponsioen CY et al (2015) Chromoendoscopy for surveillance in inflammatory bowel disease does not increase neoplasia detection compared with conventional colonoscopy with random biopsies: results from a large retrospective study. *Am J Gastroenterol* 110:1014–1021. <https://doi.org/10.1038/ajg.2015.63>
61. Nagaya T, Nakamura YA, Choyke PL, Kobayashi H (2017) Fluorescence-guided surgery. *Front Oncol* 7:314. <https://doi.org/10.3389/fonc.2017.00314>
62. Nagengast WB, Hartmans E, Garcia-Allende PB et al (2019) Near-infrared fluorescence molecular endoscopy detects dysplastic oesophageal lesions using topical and systemic tracer of vascular endothelial growth factor A. *Gut* 68:7–10. <https://doi.org/10.1136/gutjnl-2017-314953>
63. Ntzichristos V, Yodh AG, Schnall MD, Chance B (2000) Concurrent MRI and diffuse optical tomography of breast after indocyanine green enhancement. *Proc Natl Acad Sci USA* 97:2767–2772. <https://doi.org/10.1073/pnas.040570597>
64. Ntzichristos V, Yodh AG, Schnall MD, Chance B (2002) MRI-guided diffuse optical spectroscopy of malignant and benign breast lesions. *Neoplasia* 4:347–354. <https://doi.org/10.1038/sj.neo.7900244>
65. Ortner M-A, Ebert B, Hein E et al (2003) Time gated fluorescence spectroscopy in Barrett's oesophagus. *Gut* 52:28–33. <https://doi.org/10.1136/gut.52.1.28>
66. Ortner M-A, Fusco V, Ebert B et al (2010) Time-gated fluorescence spectroscopy improves endoscopic detection of low-grade dysplasia in ulcerative colitis. *Gastrointest Endosc* 71:312–318. <https://doi.org/10.1016/j.gie.2009.09.029>
67. Panjehpour M, Overholt BF, Vo-Dinh T et al (1996) Endoscopic fluorescence detection of high-grade dysplasia in Barrett's esophagus. *Gastroenterology* 111:93–101. <https://doi.org/10.1053/gast.1996.v111.pm8698231>
68. Perlitz C, Licha K, Scholle F-D et al (2005) Comparison of two tricarbocyanine-based dyes for fluorescence optical imaging. *J Fluoresc* 15:443–454. <https://doi.org/10.1007/s10895-005-2636-x>
69. Pleijhuis RG, Graafland M, de Vries J et al (2009) Obtaining adequate surgical margins in breast-conserving therapy for patients with early-stage breast cancer: current modalities and future directions. *Ann Surg Oncol* 16:2717–2730. <https://doi.org/10.1245/s10434-009-0609-z>
70. Poellinger A, Burock S, Grosenick D et al (2011) Breast cancer: early-and late-fluorescence near-infrared imaging with indocyanine green—a preliminary study. *Radiology* 258:409–416. <https://doi.org/10.1148/radiol.10100258>

71. Poellinger A, Persigehl T, Mahler M et al (2011) Near-infrared imaging of the breast using omocyanine as a fluorescent dye: results of a placebo-controlled, clinical, multicenter trial. *Invest Radiol* 46:697–704. <https://doi.org/10.1097/RLI.0b013e318229ff25>
72. Pogue BW, Zhu TC, Ntzachristos V et al (2018) Fluorescence-guided surgery and intervention—an AAPM emerging technology blue paper. *Med Phys* 45:2681–2688. <https://doi.org/10.1002/mp.12909>
73. Polom K, Murawa D, Rho Y-S et al (2011) Current trends and emerging future of indocyanine green usage in surgery and oncology: a literature review. *Cancer* 117:4812–4822. <https://doi.org/10.1002/cncr.26087>
74. Quarto G, Spinelli L, Pifferi A et al (2014) Estimate of tissue composition in malignant and benign breast lesions by time-domain optical mammography. *Biomed Opt Express* 5:3684–3698. <https://doi.org/10.1364/BOE.5.003684>
75. Richards-Kortum R, Sevick-Muraca E (1996) Quantitative optical spectroscopy for tissue diagnosis. *Annu Rev Phys Chem* 47:555–606. <https://doi.org/10.1146/annurev.physchem.47.1.555>
76. Riefke B, Licha K, Semmler W et al (1996) In vivo characterization of cyanine dyes as contrast agents for near-infrared imaging. *Proc SPIE* 2927:199–208. <https://doi.org/10.1117/12.260652>
77. Rinneberg H, Grosenick D, Moesta KT et al (2005) Scanning time-domain optical mammography: detection and characterization of breast tumors in vivo. *Technol Cancer Res Treat* 4:483–496. <https://doi.org/10.1177/153303460500400503>
78. Rinneberg H, Grosenick D, Moesta KT et al (2008) Detection and characterization of breast tumours by time-domain scanning optical mammography. *Opto-Electron Rev* 16:147–162. <https://doi.org/10.2478/s11772-008-0004-5>
79. Rispo A, Castiglione F, Staibano S et al (2012) Diagnostic accuracy of confocal laser endomicroscopy in diagnosing dysplasia in patients affected by long-standing ulcerative colitis. *World J Gastrointest Endosc* 4:414. <https://doi.org/10.4253/wjge.v4.i9.414>
80. Rubin DT, Rothe JA, Hetzel JT et al (2007) Are dysplasia and colorectal cancer endoscopically visible in patients with ulcerative colitis? *Gastrointest Endosc* 65:998–1004. <https://doi.org/10.1016/j.gie.2006.09.025>
81. Schaafsma BE, van de Giessen M, Charehbili A et al (2015) Optical mammography using diffuse optical spectroscopy for monitoring tumor response to neoadjuvant chemotherapy in women with locally advanced breast cancer. *Clin Cancer Res* 21:577–584. <https://doi.org/10.1158/1078-0432.CCR-14-0736>
82. Schäfer VS, Hartung W, Hoffstetter P et al (2013) Quantitative assessment of synovitis in patients with rheumatoid arthritis using fluorescence optical imaging. *Arthritis Res Ther* 15:R124. <https://doi.org/10.1186/ar4304>
83. Soetikno R, Subramanian V, Kaltenbach T et al (2013) The detection of nonpolypoid (flat and depressed) colorectal neoplasms in patients with inflammatory bowel disease. *Gastroenterology* 144:1349–1352.e6. <https://doi.org/10.1053/j.gastro.2013.04.008>
84. Srinivasan S, Carpenter CM, Ghadyani HR et al (2010) Image guided near-infrared spectroscopy of breast tissue in vivo using boundary element method. *J Biomed Opt* 15:061703. <https://doi.org/10.1117/1.3499419>
85. Sturm MB, Joshi BP, Lu S et al (2013) Targeted imaging of esophageal neoplasia with a fluorescently labeled peptide: first-in-human results. *Sci Transl Med* 5:184ra61–184ra61. <https://doi.org/10.1126/scitranslmed.3004733>
86. Szcyc Ł, Bonifer S, Walter A et al (2015) Development of a handheld fluorescence imaging camera for intraoperative sentinel lymph node mapping. *J Biomed Opt* 20:051025. <https://doi.org/10.1117/1.JBO.20.5.051025>
87. Taroni P, Quarto G, Pifferi A et al (2015) Breast tissue composition and its dependence on demographic risk factors for breast cancer: non-invasive assessment by time domain diffuse optical spectroscopy. *PLoS ONE* 10:e0128941. <https://doi.org/10.1371/journal.pone.0128941>

88. Ter Weele EJ, Terwisscha van Scheltinga AGT, Linsen MD et al (2016) Development, preclinical safety, formulation, and stability of clinical grade bevacizumab-800CW, a new near infrared fluorescent imaging agent for first in human use. *Eur J Pharm Biopharm* 104:226–234. <https://doi.org/10.1016/j.ejpb.2016.05.008>
89. Themelis G, Yoo JS, Soh K-S et al (2009) Real-time intraoperative fluorescence imaging system using light-absorption correction. *J Biomed Opt* 14:064012. <https://doi.org/10.1117/1.3259362>
90. Tipirneni KE, Warram JM, Moore LS et al (2017) Oncologic procedures amenable to fluorescence-guided surgery. *Ann Surg* 266:36–47. <https://doi.org/10.1097/SLA.0000000000002127>
91. Tromberg BJ, L'Heureux D, Mankoff D et al (2011) OT2-05-02: ACRIN 6691 monitoring and predicting breast cancer neoadjuvant chemotherapy response using diffuse optical spectroscopic imaging (DOSI). *Cancer Res* 71:OT2-05–02. <https://doi.org/10.1158/0008-5472.sabcs11-ot2-05-02>
92. Troyan SL, Kianzad V, Gibbs-Strauss SL et al (2009) The FLARE intraoperative near-infrared fluorescence imaging system: a first-in-human clinical trial in breast cancer sentinel lymph node mapping. *Ann Surg Oncol* 16:2943–2952. <https://doi.org/10.1245/s10434-009-0594-2>
93. Tummers QRJG, Verbeek FPR, Schaafsma BE et al (2014) Real-time intraoperative detection of breast cancer using near-infrared fluorescence imaging and Methylene Blue. *Eur J Surg Oncol* 40:850–858. <https://doi.org/10.1016/j.ejso.2014.02.225>
94. Tummers QRJG, Hoogstins CES, Gaarenstroom KN et al (2016) Intraoperative imaging of folate receptor alpha positive ovarian and breast cancer using the tumor specific agent EC17. *Oncotarget* 7:32144–32155. <https://doi.org/10.18632/oncotarget.8282>
95. Unkart JT, Chen SL, Wapnir IL et al (2017) Intraoperative tumor detection using a ratiometric activatable fluorescent peptide: a first-in-human phase 1 study. *Ann Surg Oncol* 24:3167–3173. <https://doi.org/10.1245/s10434-017-5991-3>
96. van Brussel ASA, Adams A, Oliveira S et al (2016) Hypoxia-targeting fluorescent nanobodies for optical molecular imaging of pre-invasive breast cancer. *Mol Imaging Biol* 18:535–544. <https://doi.org/10.1007/s11307-015-0909-6>
97. van de Ven SMWY, Wiethoff A, Nielsen T et al (2010) A novel fluorescent imaging agent for diffuse optical tomography of the breast: first clinical experience in patients. *Mol Imaging Biol* 12:343–348. <https://doi.org/10.1007/s11307-009-0269-1>
98. van den Broek FJC, van Es JA, van Eeden S et al (2011) Pilot study of probe-based confocal laser endomicroscopy during colonoscopic surveillance of patients with longstanding ulcerative colitis. *Endoscopy* 43:116–122. <https://doi.org/10.1055/s-0030-1255954>
99. Vaupel P, Schlenger K, Knoop C, Höckel M (1991) Oxygenation of human tumors: evaluation of tissue oxygen distribution in breast cancers by computerized O₂ tension measurements. *Cancer Res* 51:3316–3322
100. Vavadi H, Mostafa A, Zhou F et al (2018) Compact ultrasound-guided diffuse optical tomography system for breast cancer imaging. *J Biomed Opt* 24:1. <https://doi.org/10.1117/1.JBO.24.2.021203>
101. Vieth M, Ell C, Gossner L et al (2004) Histological analysis of endoscopic resection specimens from 326 patients with Barrett's esophagus and early neoplasia. *Endoscopy* 36:776–781. <https://doi.org/10.1055/s-2004-825802>
102. Wagnieres G, Hadjir C, Grosjean P et al (1998) Clinical evaluation of the cutaneous phototoxicity of 5,10,15,20-tetra(m-hydroxyphenyl)chlorin. *Photochem Photobiol* 68:382–387
103. Wanders LK, Kuiper T, Kiesslich R et al (2016) Limited applicability of chromoendoscopy-guided confocal laser endomicroscopy as daily-practice surveillance strategy in Crohn's disease. *Gastrointest Endosc* 83:966–971. <https://doi.org/10.1016/j.gie.2015.09.001>

104. Wang KK, Sampliner RE (2008) Updated guidelines 2008 for the diagnosis, surveillance and therapy of Barrett's esophagus. *Am J Gastroenterol* 103:788–797. <https://doi.org/10.1111/j.1572-0241.2008.01835.x>
105. Weissleder R, Mahmood U (2001) Molecular imaging. *Radiology* 219:316–333. <https://doi.org/10.1148/radiology.219.2.r01ma19316>
106. Weissleder R, Tung CH, Mahmood U, Bogdanov A (1999) In vivo imaging of tumors with protease-activated near-infrared fluorescent probes. *Nat Biotechnol* 17:375–378. <https://doi.org/10.1038/7933>
107. Whitley MJ, Cardona DM, Lazarides AL et al (2016) A mouse-human phase 1 co-clinical trial of a protease-activated fluorescent probe for imaging cancer. *Sci Transl Med* 8:320ra4. <https://doi.org/10.1126/scitranslmed.aad0293>
108. Yan Y, Sun X, Shen B (2017) Contrast agents in dynamic contrast-enhanced magnetic resonance imaging. *Oncotarget* 8:43491–43505. <https://doi.org/10.18632/oncotarget.16482>
109. Zeng H-C, Hu J-L, Bai J-W, Zhang G-J (2018) Detection of sentinel lymph nodes with near-infrared imaging in malignancies. *Mol Imaging Biol*. <https://doi.org/10.1007/s11307-018-1237-4>



Juliane Becker, Sarah M. Schwarzenböck, and Bernd J. Krause

Contents

19.1	Introduction.....	626
19.2	Clinical Applications of FDG PET/CT in Oncology	626
19.2.1	Non-small Cell Lung Cancer (NSCLC) and Small Cell Lung Cancer (SCLC).....	627
19.2.2	Thyroid Cancer.....	631
19.2.3	Head and Neck Cancer.....	633
19.2.4	Oesophageal Cancer	635
19.2.5	Gastric Cancer and Gastrointestinal Stromal Tumour (GIST)	637
19.2.6	Colorectal Cancer	638
19.2.7	Pancreatic Cancer	640
19.2.8	Melanoma	641
19.2.9	Lymphoma.....	644
19.2.10	Sarcoma	648
19.2.11	Breast Cancer.....	650
19.2.12	Ovarian Cancer.....	652
19.2.13	Testicular Cancer.....	653
19.2.14	Penile Cancer.....	655
19.2.15	Prostate Cancer.....	656
19.2.16	Cancer of Unknown Primary	656
	References	657

J. Becker · S. M. Schwarzenböck · B. J. Krause (✉)
Department of Nuclear Medicine, University Medicine Rostock, Gertrudenplatz 1,
18057 Rostock, Germany
e-mail: bernd.krause@med.uni-rostock.de

© Springer Nature Switzerland AG 2020
O. Schober et al. (eds.), *Molecular Imaging in Oncology*,
Recent Results in Cancer Research 216,
https://doi.org/10.1007/978-3-030-42618-7_19

19.1 Introduction

Molecular imaging with positron emission tomography (PET) using tumour-seeking radiopharmaceuticals has gained wide acceptance in oncology with many clinical applications. Since its first *in vivo* application in the 1970s [4, 55] the glucose analogue 18-F-fluorodeoxyglucose (FDG) is the most common PET radiopharmaceutical in clinical routine, especially in oncology. *In vivo* FDG acts similar to glucose, but being trapped within the cells ('metabolic trapping') and not being metabolised any further. Increased consumption of glucose is a characteristic of most tumour cells and is mainly related to overexpression of the GLUT-1 glucose transporters and increased hexokinase activity [102, 159]. FDG enables to visualise regional glucose metabolism with high sensitivity but somewhat lower specificity. Despite the high sensitivity of FDG PET/computed tomography (CT) false-positive findings may occur due to physiologic processes such as brown fat, colonic and gynaecologic activity, infectious and inflammatory processes and rebound thymus hyperplasia. False-negative findings can occur, e.g. in the assessment of brain lesions as a consequence of physiologically high glucose uptake by surrounding normal brain. FDG accumulation can be assessed visually, semi-quantitatively and quantitatively. The most commonly used technique is the standardised uptake value (SUV): a semi-quantitative index of tumour uptake normalised to injected dose and a measure of the total volume distribution, such as the patient's body weight.

The hybrid imaging modality PET/CT has been clinically introduced in the late 1990s. PET/CT imaging allows assessing molecular as well as morphologic information at the same time. Nowadays, PET/CT represents a state of the art tool for whole-body staging and re-staging in oncology within one imaging modality. PET/CT outperforms PET or CT alone by improving lesion localisation and lesion characterisation in oncology imaging.

19.2 Clinical Applications of FDG PET/CT in Oncology

This chapter provides an overview of the main clinical applications of FDG PET/CT in oncology.

FDG PET/CT plays an integral role in diagnosis, staging and re-staging of disease in oncology. In addition, there is increasing evidence that FDG PET/CT can also significantly contribute to evaluation of therapy response, tumour control, and prediction of prognosis in oncologic patients (for a review see Herrmann et al. [65]). Conventional imaging modalities are of limited use to assess response to therapy. FDG has been proposed as an imaging surrogate parameter of therapy response. It provides highly reproducible quantitative parameters of tumour glucose metabolism. Changes of tumour consumption can therefore be used to define metabolic response to therapy. For this reason, FDG PET/CT was introduced for the early sequential monitoring of tumour response of breast cancer in 1993 [158].

FDG PET/CT can be used to assess response to therapy early and late in the course of treatment. From the perspective of a clinician, it is very important to differentiate non-responders to therapy early in the course of treatment (especially, if several cycles of a therapy have to be applied, e.g. chemotherapy or immunotherapy) in order to possibly change the therapeutic management. The schedule for PET timing is always dependent on the type of tumour and the treatment plan, often there is no standardised recommendation due to a lack of (randomised, multicentre, prospective) studies. However, a baseline scan is indispensable in any case, followed usually by a second scan after the first or second cycle of therapy. Changes in FDG uptake between the pre-therapeutic and early follow-up scan are used to predict histopathological response and patient outcome. The standardised uptake value is the most widely used FDG PET parameter, and in most studies relative changes (%) are calculated to quantify metabolic response.

Early therapy response as assessed by FDG PET/CT has shown promising results in single-centre studies and should be evaluated in randomised, prospective, multicentre trials in order to implement FDG PET/CT in clinical practice for this concern in the future. In this context, standardisation of patient preparation, data acquisition and processing, and data interpretation are important issues. In order to establish criteria to assess therapy response with the help of PET/CT, e.g. PERCIST criteria have been developed and implemented (PERCIST 1.0, PET Response Criteria In Solid Tumours) [157].

In this chapter, special emphasis will be on the use of FDG PET/CT for therapy response assessment being discussed in separate paragraphs for almost all of the listed tumour entities.

19.2.1 Non-small Cell Lung Cancer (NSCLC) and Small Cell Lung Cancer (SCLC)

19.2.1.1 Diagnosis, Staging and Radiation Treatment Planning in NSCLC Patients

Lung cancer is the most common cancer and the leading cause of cancer-related deaths worldwide [38].

Accurate diagnostic work-up and staging of NSCLC is mandatory with respect to mediastinal lymph node involvement and distant metastases affecting therapy management and prognosis. In particular, it is necessary to differentiate patients with potentially curable and resectable disease at early stages from those, who are not suitable for radical surgery, following the currently used staging system based on the tumour–node–metastasis (TNM) classification (description of primary tumour (T), lymph node involvement (N), and presence of distant metastases (M)).

FDG PET/CT allows staging of NSCLC with high diagnostic accuracy [6] and improves staging as compared to CT alone [40, 137] (Fig. 19.1). Several guidelines and professional societies strongly recommend the use of FDG PET/CT for diagnosis/staging (e.g. Interdisciplinary guideline of the German Respiratory Society/German Guidelines Programme Oncology, Cancer Care Ontario (CCO),

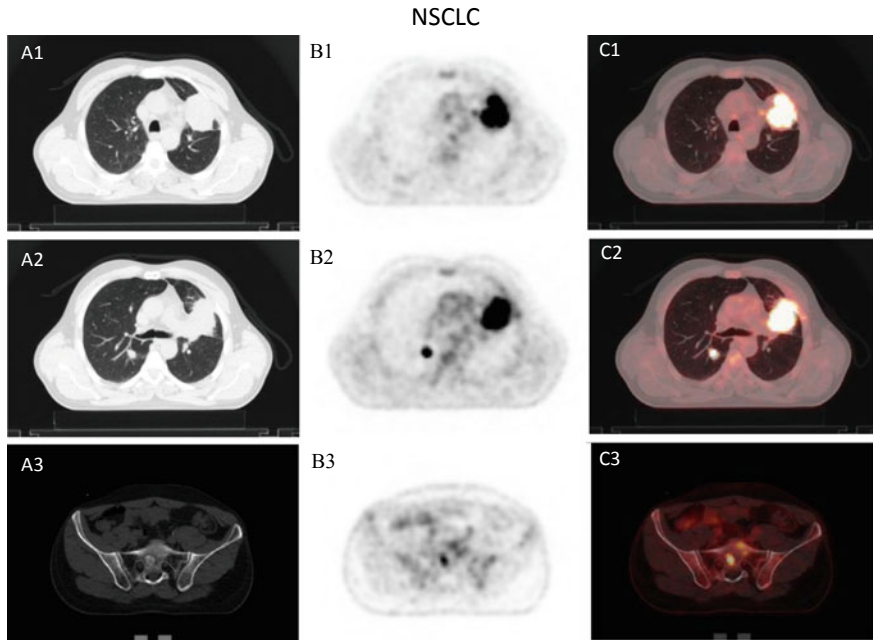


Fig. 19.1 47-year old male patient with histopathologically proven non-small cell lung cancer of the left upper lung lobe, referred to FDG PET/CT for primary staging. FDG PET/CT confirmed FDG -positive primary tumour and an already suspected contralateral lung metastasis (cM1a); furthermore, PET/CT revealed an FDG-positive bone metastasis in the Os sacrum (cM1b); (A1-3) CT-Scan, (B1-3) PET scan, (C1-3) PET/CT fused images

American Colleges of Chest Physicians and Radiologists (ACP/ACR)) [8, 9, 21, 134] as well as for detection of recurrence/re-staging (e.g. Society of Nuclear Medicine and Molecular Imaging (SNMMI)) [74], partly under special conditions such as planned curatively intended treatment.

The use of PET in the Dutch randomised controlled PLUS trial allowed for avoidance of futile thoracotomies in about 20% of patients with NSCLC (21% as compared to 41% of patients in the group with conventional work-up that did not undergo PET; relative risk reduction of 51% in favour of PET, $p = 0.003$) [152]. In another trial, Maziak et al. showed that in 337 patients with confirmed clinical stage I, II, or IIIA NSCLC and being considered for surgery (170 assigned to PET/CT and 167 to conventional staging including CT of liver and adrenal glands as well as whole-body bone scan) disease was correctly up-staged in 23 of 167 PET/CT patients and in 11 of 162 conventional staging patients (13.8% vs. 6.8%), thereby sparing these patients from surgery. On the other hand, disease was incorrectly up-staged in 8 PET/CT patients and 1 conventional staging patient (4.8% vs. 0.6%), and it was incorrectly under-staged in 25 PET/CT patients and 48 conventional staging patients, respectively (14.9% vs. 29.6%) [104]. In a recent retrospective

study, Kung et al. included 186 potentially operable NSCLC patients, who underwent whole-body FDG PET/CT examination in 2012. Due to disease up-staging 34.9% (65 patients) became inoperable by the results of PET/CT; 102 of the remaining 121 patients received surgery—97 of those proceeded to surgery without further (neoadjuvant) treatment or investigation, 4 received neoadjuvant treatment and 1 had further investigations after PET/CT. As a consequence, changes in management plans occurred in 37.6% due to PET/CT—the authors concluded that PET/CT had great clinical impact with a significant reduction of futile surgery [86].

Schreyögg et al. evaluated the diagnostic accuracy and cost-effectiveness of integrated PET/CT for the staging of NSCLC patients. The authors reported a diagnostic effectiveness in terms of correct TNM staging of 40% for CT alone and 60% for PET/CT. For the assessment of resectability, 84% of patients were staged correctly by PET/CT vs. 70% by CT alone. The cost-effectiveness analysis showed that costs for PET/CT were within the commonly accepted range for diagnostic tests or therapies [129].

With respect to the detection of mediastinal lymph node metastases several studies exist—although FDG PET/CT is more accurate than CT for the staging of mediastinal lymph nodes [137], it is still limited in its ability to differentiate between benign and metastatic lymph nodes. There can be false-negative findings, e.g. due to micrometastases, but false-positive findings seem to be the more decisive problem, e.g. due to inflammation [89]. To solve this problem Rogasch et al. chose an approach similar to the Cheson/Deauville criteria for judging residual lymphoma tumour masses either as vital or not based on a visual scale [28]—after standardised windowing (threshold: $2 \times$ liver SUV_{mean}) they used a 4-point scale as follows: (1) lymph node (LN) uptake \leq mediastinal blood pool structures (MBPS); (2) MBPS < LN < liver; (3) liver \leq LN < ‘black’; (4) LN appears ‘black’. As an optimal cut-off to differentiate benign vs. metastatic LNs they found a score >3 , reaching high sensitivities (88.9–90.7%), high specificities (92.0–94.6%), high negative predictive values (NPV) (97.2–97.6%), and high accuracies (91.4–93.5%) for different readers with different levels of experience (positive predictive values (PPV) 72.7–80.0%) [125]. There are several other approaches, partly based on SUV_{max} [89] and on a ratio of lymph node SUV_{max} to primary tumour SUV_{max} [30], respectively, or even based on a decision tree model for predicting mediastinal lymph node metastases (including morphologic and functional criteria) [116]. Taken together, more studies applying this or similar decision tree models should be conducted to develop tools for FDG PET/CT readers and to make FDG PET/CT-based nodal staging more reliable.

Distant metastatic spread typically involves the adrenal glands, bones, brain, or liver. Regarding a curative treatment intent, it is of particular interest, whether there are distant metastases present or not, especially if they are unexpected, such as in a low tumour stage. However, the rate of unexpected distant metastases rises with the tumour stage as a prospective Australian trial by MacManus et al. [98] showed including tumour stage I–III patients: at tumour stage I the rate was 7.5%, at stage II 18% and at stage III 24%, which underlines the value of FDG PET/CT also in the staging of (locally) advanced patients, especially with respect to overall survival

[144]. FDG PET/CT is suitable for the detection of metastases of the adrenal glands, bones, and liver [6]. For bone metastases, it is superior to conventional bone scintigraphy (with sensitivity, specificity, NPV, PPV and accuracy >90% each) [135], confirmed by similar results of Chang et al. [25]. In contrary, FDG PET/CT is not suitable for the detection of brain metastases due to the high glucose consumption of the normal surrounding brain tissue resulting in an overall poor sensitivity [6]. Thus, additional Magnetic Resonance Imaging (MRI) of the brain should be performed in all symptomatic patients and high-risk patients with curative intention (German S3 guideline, see AWMF [9]).

There are further reasons for false-negative findings on FDG PET/CT, mainly due to small lesion size (<5 mm, partial volume effect). Moreover, FDG PET sensitivity may be reduced in specific tumour types showing variable FDG uptake such as bronchiolo-alveolar carcinoma, mucinous forms and neuroendocrine tumours [6].

Finally, in NSCLC patients FDG PET/CT should be used for radiation treatment planning, since it is more accurate in defining the tumour extent than CT alone [16], resulting in a reduction of the dose delivered to normal surrounding tissue (if the PET tumour area is smaller than the one defined on CT) and in the inclusion of areas with viable tumour cells outside the CT-based radiation fields (if PET detects a tumour area more extensive than CT), thus, affecting the target volume definition and the patient's radiation exposure. In a systematic review and meta-analysis by Hallqvist et al. including 35 cross-sectional studies and one observational study there was a significant change in target delineation in approximately 40% of the patients [61].

19.2.1.2 Therapy Response Assessment in NSCLC Patients

So far, neoadjuvant chemotherapy is not a standard procedure in NSCLC patients. However, there are many advantages to this treatment modality. First of all, by a neoadjuvant treatment regimen potentially micrometastatic disease should be affected, which accounts for a 5% absolute increase in survival as compared to solely adjuvant chemotherapy [111]. Second, the tissue resected at surgery can serve as a gold standard to evaluate response to a neoadjuvant treatment, as it is already a standard in the assessment of treatment response in early stage breast cancer. And finally, neoadjuvant chemotherapy seems to be better tolerated than adjuvant therapy and the compliance seems to be higher [24].

In a meta-analysis conducted by Zhang et al. evaluating 13 studies with a total of 414 patients a pooled sensitivity, specificity, PPV and NPV for PET-predicted response of 83%, 84%, 74% and 91%, respectively, were reported. All included studies had used pathological outcome as the gold standard. The predictive value of PET in NSCLC patients for evaluating pathological response was significantly higher than that of CT in this meta-analysis [168].

The NEOSCAN trial intended to assess the value of FDG PET/CT for an interim staging in the setting of neoadjuvant chemotherapy in order to guide further neoadjuvant treatment, dependent on response or non-response. 40 stage IB-IIIa lung cancer patients were included, receiving for 2 cycles either cisplatin/carboplatin plus pemetrexed (adenocarcinoma) or cisplatin/carboplatin plus gemcitabine (squamous cell carcinoma). A decrease by at least 35% in SUV_{peak} in the primary

tumour was considered as response, going along with continuation of the same therapy regime for 2 more cycles, whereas therapy of non-responders was switched to vinorelbine plus docetaxel for 2 cycles. In all, 15 patients (38%) were non-responders, of which 10 patients (67%) reacted to vinorelbine plus docetaxel with partial or complete metabolic response as assessed by modified PERCIST criteria, one of those achieving major pathologic response. For all patients, response assessed by PET after 2 and 4 cycles of treatment correlated with major pathologic response ($p = 0.016$ and 0.034 , respectively), whereas CT-based response assessment did not [24].

19.2.1.3 Staging in SCLC Patients

SCLC is more aggressive than NSCLC and tends to spread with distant metastases much faster. There is a two-staged classification differentiating limited disease (LD) and extensive disease (ED) according to the Veterans Administration Lung Group (VALSG) that was first introduced in the 1950s. Limited disease is defined as disease confined to one hemithorax, the mediastinum and the supraclavicular lymph nodes. All other patients are classified as having ED, including those with malignant pleural effusion [124].

Most of the spare literature concerning FDG PET/CT and SCLC is analysing pre-therapeutic staging. In a systematic review and meta-analysis, Lu et al. showed that among 12 studies with a total of 369 patients the pooled estimated sensitivity and specificity were 97.5% and 98.2%, respectively, for the detection of ED by FDG PET and FDG PET/CT. They regarded FDG PET/CT as a valuable imaging tool for the pre-therapeutic assessment of ED in patients with SCLC [97]. The results of patients with an up-staging after undergoing FDG PET/CT as compared to conventional imaging are similar among several studies, e.g. Zer et al. found a change in the tumour stage up to extensive disease in 6/55 patients (10.9%) [168].

19.2.2 Thyroid Cancer

19.2.2.1 Diagnosis, Staging and Re-staging

Differentiated thyroid cancer (papillary or follicular) represents about 1% of all malignant tumours and is the most frequent endocrine cancer [14]. It is generally considered to be highly treatable and curable. However, approximately 30% of all patients with recurrence will develop local recurrence or metastases, which cannot be detected by Iodine-131 whole-body scintigraphy due to a loss of the ability of the tumour cells to concentrate iodine in the process of dedifferentiation [52]. According to the in 2015 revised guidelines of the American Thyroid Association (ATA) ^{18}F FDG PET/CT scanning should be considered in high-risk DTC [differentiated thyroid cancer] patients with elevated serum Tg [thyroglobulin] (generally >10 ng/mL) with negative RAI [radioiodine] imaging (strong recommendation, moderate-quality evidence). Furthermore, it 'may also be considered as [...] a part of initial staging in poorly differentiated thyroid cancers and invasive Hürthle cell carcinomas [...] (weak recommendation, low-quality evidence)' [63].

In the situation of suspected recurrence, elevated Tg levels, and negative RAI scintigraphy FDG PET/CT is also recommended by The Royal College of Radiologists (RCR) [142]. The European Society for Medical Oncology (ESMO) (working group ‘thyroid cancer’) emphasises the main indication of FDG PET/CT in metastatic patients who have lost radioiodine uptake [115].

With respect to Tg level ‘cut-off’ for the use of FDG PET/CT, studies have shown controversial results. However, a ‘cut-off’ of 10 ng/ml seems to be a reasonable value maintaining high accuracy in terms of a good compromise between sensitivity and specificity [14]. The sensitivity depends on the histological subtype and FDG PET is more sensitive in more aggressive subtypes such as poorly differentiated, tall cell, and Hürthle cell thyroid cancer. Thus, the Tg ‘cut-off’ needs to be adapted and lowered in case of aggressive pathological variants of thyroid cancer that may produce low amounts of serum Tg [63]. The diagnostic accuracy of FDG PET/CT is generally high in patients with negative RAI scans and high Tg levels [14] (Fig. 19.2).

In a recent meta-analysis enrolling 20 studies with 958 thyroid cancer patients with a previous negative RAI scan the combined sensitivity and specificity for conventional FDG PET were both found to be 84%; for FDG PET/CT they were

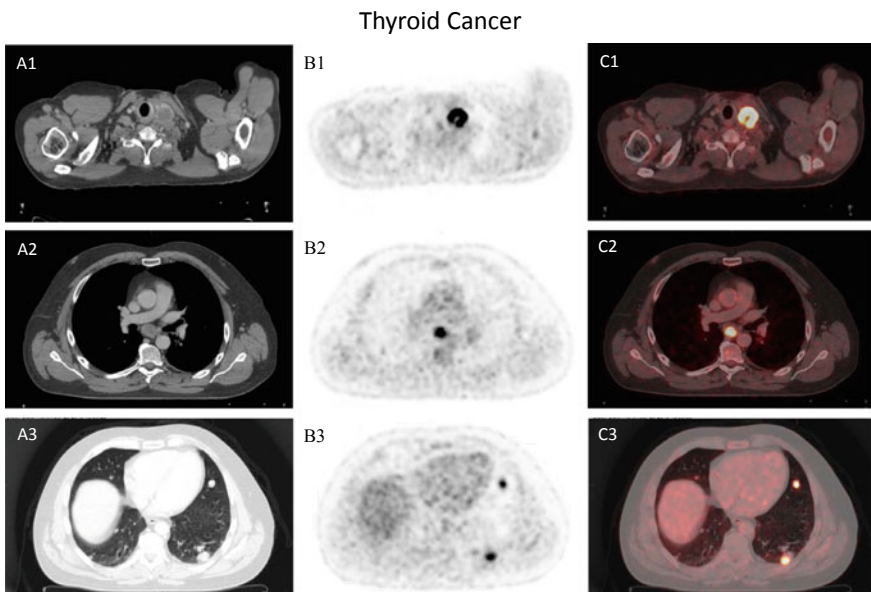


Fig. 19.2 53-year old male patient with minimally invasive follicular thyroid cancer, referred to FDG PET/CT for re-staging with known Iodine-131 positive local recurrence and a thyroglobulin level of 319 $\mu\text{g/l}$ under TSH suppression. Besides the local recurrence FDG PET/CT showed an infracarineral FDG-positive lymph node metastasis and multiple FDG-positive pulmonary metastases; (A1-3) CT-Scan, (B1-3) PET scan, (C1-3) PET/CT fused images

93% and 81%, respectively, and the overall accuracies were 91% and 93%, respectively [19].

For detecting recurrence with FDG PET/CT Choi et al. reported a sensitivity, specificity, accuracy, PPV and NPV of 64%, 94%, 83%, 86% and 81%, respectively, including 84 papillary thyroid cancer patients with negative RAI scans and high Tg levels. They also investigated the effect of thyroid-stimulating hormone (TSH) stimulation in comparison with TSH suppression and could not find an added value for TSH stimulation [32].

However, the impact of TSH on FDG PET/CT imaging is still an open issue, no consensus has been reached about the usefulness of high TSH levels. Levothyroxine withdrawal or alternatively the use of recombinant TSH might be preferable, especially in cases of relatively low Tg levels (<10 ng/ml) trying to improve sensitivity of FDG PET [14]. According to ATA guidelines ‘To date, there is no evidence that TSH stimulation improves the prognostic value of ¹⁸F-DG-PET imaging’ [63].

19.2.3 Head and Neck Cancer

19.2.3.1 Diagnosis, Staging and Re-staging

Cancers of the oral cavity and lips were the tenth most common cause of death in males living in developing countries in 2012 worldwide, representing the eighth most common cancers in the same population. Smoking, alcohol use, smokeless tobacco use, and human papillomavirus (HPV) infection are the major risk factors for oral cavity cancer, with smoking and alcohol having synergistic effects [146]. The incidence of HPV-associated head and neck cancer is increasing, most commonly arising from the oropharynx [103].

Histopathologically squamous cell carcinomas account for the vast majority of head and neck cancers with >90% [1, 29]. Most common site is the larynx, followed by oral cavity including tongue, lips and salivary glands [1].

A decisive prognostic factor is the metastatic involvement of cervical lymph nodes, crucial for an adequate therapeutic management [139]. For this reason, the role of FDG PET/CT in initial staging of head and neck cancer patients was investigated in many studies.

The use of FDG PET/CT in primary diagnostics/staging is usually not recommended, with the exception of cancers of unknown primary (CUP) with manifestation in cervical lymph node metastases (to learn more about the use of FDG PET/CT in CUPs please note the additional section following below). Cacicedo et al. conducted a prospective study enrolling 84 patients with newly diagnosed, locally advanced head and neck squamous cell carcinoma (stage III–IV disease according to the American Joint Committee on Cancer (AJCC) classification (seventh edition), histologically confirmed). After conventional work-up (physical examination, CT imaging of the head, neck and chest) each patient underwent FDG PET/CT and the results were separately discussed in multidisciplinary tumour boards—TNM stage was determined and afterwards validated by histopathological

analysis. The authors found a discordance for 32/84 (38%) patients between the results of conventional work-up and FDG PET/CT with the highest impact on N stage (in 21/32, 65.7%), followed by a change in patient management in 22/84 patients (26%)—PET/CT TNM-classification was significantly more accurate (92.5% vs. 73.7%) than conventional staging with a p-value < 0.001 [18].

There is an ongoing debate, if FDG PET/CT should be implemented in the routine diagnostic work-up of locally advanced head and neck cancers—the National Comprehensive Cancer Network (NCCN) guidelines recommend consideration of FDG PET/CT in the assessment of the initial treatment strategy for loco-regionally advanced disease to evaluate for distant metastases [36]; also RCR recommends the use in this patient population or if initial imaging is inconclusive/with equivocal findings that would preclude radical treatment [142].

However, the main field of FDG PET/CT in head and neck cancer patients is the follow-up and treatment response assessment after chemoradiotherapy.

In routine follow-up, FDG PET/CT is usually recommended after inconclusive conventional imaging to differentiate treatment effects from tumour residuals/recurrence [142] or if there is a high risk for distant metastases due to initial TNM stage, especially in patients considered for major salvage treatment [8]. Recurrence or relapse mostly occurs within the first 2–3 years after first diagnosis [29, 64, 131].

In the management of local recurrence, direct laryngoscopic techniques and physical examination remain key aspects, followed by PET/CT or other imaging modalities as important adjuncts in detecting recurrence in lymph nodes and more distant sites [74] (Fig. 19.3).

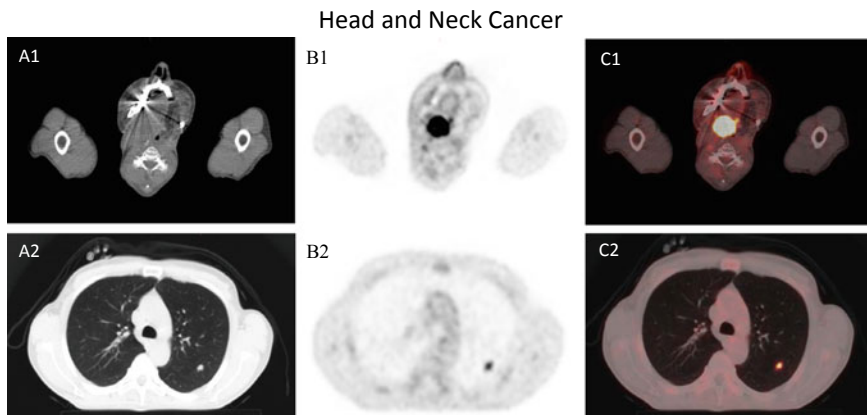


Fig. 19.3 55-year old male patient with histopathologically proven second local recurrence of oropharyngeal carcinoma (initially TNM-classification pT2 pN0 L0 V0 R0 cM0, first recurrence r_pT3 pN0 L0 V0 Pn1 cM0), referred to FDG PET/CT for re-staging. FDG PET/CT confirmed FDG-positive recurrence in the right oropharynx; furthermore, PET/CT revealed an FDG-positive lung metastasis in the left upper lung lobe (cM1); (A1-2) CT-Scan, (B1-2) PET scan, (C1-2) PET/CT fused images

A recent meta-analysis evaluating 23 studies (constituting 2,247 PET/CT examinations) found a pooled sensitivity and specificity of 92% and 87%, respectively, for detection of recurrence in general (local, regional and distant) in head and neck cancer patients by FDG PET/CT. The pooled sensitivity and specificity of scans performed 4–12 months after treatment were 95% and 78%, respectively, with similar sensitivity but higher specificity for scans performed ≥ 12 months after treatment with 92% and 91%, respectively [131]. In order to differentiate between the primary site, the loco-regional site and the distant site another meta-analysis including 27 studies (1,195 patients) was conducted recently: the authors found a pooled sensitivity and specificity of 86.2% and 82.3%, respectively, for detecting recurrence at the primary site, of 72.3% and 88.3%, respectively, at the loco-regional (neck) site and of 84.6% and 94.9%, respectively, for distant metastases [29].

19.2.3.2 Therapy Response Assessment

The prospective randomised PET-Neck trial investigated the role of FDG PET/CT performed 12 weeks after the end of chemoradiotherapy in 564 N2- or N3-patients to decide about the conduction of neck dissection, which was only employed if PET/CT showed an equivocal or incomplete response. PET/CT surveillance resulted in fewer neck dissections than did planned surgery (54 vs. 221), the 2-year overall survival rate was 84.9% in the surveillance group and 81.5% in the planned-surgery group—additionally PET/CT surveillance was more cost-effective over the duration of the trial [105].

The use of FDG PET/CT in follow-up after chemoradiotherapy was also recommended by other authors. There is a broad consensus that a period of at least 12 weeks after the completion of treatment and the scan should be kept to avoid non-specific chemoradiotherapy-related inflammatory FDG uptake [131]. It is still unclear, if HPV-positive patients should undergo FDG PET/CT at a later time after completion of primary treatment, since nodal disease might take longer to respond and regress in these patients [64, 69].

In an effort to standardise image interpretation, Marcus and colleagues proposed the so-called ‘Hopkins criteria’ in order to assess therapy response for head and neck cancers from the results of a post-therapy PET/CT-scan by using a 5-point scale comparing the intensity (as compared to SUV values of the liver and the internal jugular vein) and pattern (focal or diffuse) of FDG PET uptake in primary tumour and neck nodes. This assessment was shown to be highly specific with 92.2% and to carry a high NPV of 91.1% in an evaluated patient collective (57.5% HPV positive) [103].

19.2.4 Oesophageal Cancer

19.2.4.1 Diagnosis, Staging and Re-Staging

Oesophageal cancer is one of the most common cancers worldwide being the ninth most common cancer and the sixth most common cause of cancer-related deaths

[88]. There are two major histological subtypes of oesophageal cancer: squamous cell carcinoma and adenocarcinoma, the first being previously much more common than the second one. However, a marked increase in the incidence of oesophageal adenocarcinoma in Europe, North America and Australia has been observed during the past four decades, so the incidence of oesophageal adenocarcinoma has surpassed that of oesophageal squamous cell carcinoma in many western countries [88]. Oesophageal adenocarcinoma is mostly originating in the lower third of the oesophagus, often involving the oesophago-gastric junction. The main pathophysiological pathway of oesophageal adenocarcinoma is likely to be chronic gastro-oesophageal reflux, causing a metaplasia known as 'Barrett's oesophagus'.

Relevant pre-therapeutic prognostic factors are local tumour invasion, loco-regional lymph node and distant metastases. Endoscopic ultrasound and CT represent the most widely used imaging modalities for the assessment of local tumour invasion (T stage), loco-regional lymph node involvement (N stage) and also distant metastases stage (M stage) [161].

Sensitivity and specificity of FDG PET/CT for staging oesophageal cancer have been investigated in many studies. For instance, Purandare et al. conducted a study enrolling 156 patients with potentially curable oesophageal adenocarcinoma and they found a change in the intent of treatment in 16% of the patients by detecting M1b disease with high sensitivity, specificity, PPV, NPV and accuracy (83.3%, 98.4%, 92.5%, 96.1% and 95.3%, respectively). The authors concluded that FDG PET/CT should be implemented in the initial staging work-up [121].

In their systematic review and meta-analysis Goense et al. assessed the performance of FDG PET/CT for the detection of recurrent oesophageal cancer after curatively intended treatment. Evaluating 8 studies, they found a high sensitivity (96%) and moderate specificity (78%), concluding that histopathologic confirmation of PET/CT-suspected lesions remains necessary due to a considerable false-positive rate [56].

In international guidelines, the recommendation for the use of FDG PET/CT in staging and re-staging of oesophageal cancer differs—in some guidelines the use is recommended for a certain patient cohort, e.g. ESMO where FDG PET/CT should be carried out in candidates for oesophagectomy to exclude distant metastases [94], whereas other guidelines (NCCN) advise FDG PET/CT in initial staging as routine clinical work-up if there is no evidence of M1-disease. Similar to ESMO, NCCN also advises FDG PET/CT in re-staging before surgery for the detection of distant metastases for all patients who receive chemoradiotherapy either as neoadjuvant or definitive treatment [3]. According to the German S3 guideline FDG PET/CT may be used for locally advanced cancers (cT2-4, cN+) to exclude distant metastases prior to curatively intended treatment in anticipation of clinical consequences [120]. The use of FDG PET/CT is also recommended by some societies, e.g. RCR for staging/re-staging of patients suitable for radical treatment, including patients who have received neoadjuvant treatment, and for evaluation of suspected recurrence when other imaging is negative or equivocal [142].

19.2.4.2 Therapy Response Assessment

The MUNICON I trial was one of the first clinical trials to provide evidence that FDG PET can be used to individualise neoadjuvant therapy—in this trial chemotherapy in patients with locally advanced oesophageal adenocarcinoma. Treatment was adapted based upon PET results conducted 2 weeks after chemotherapy induction in the way that metabolic responders (predefined as decreases of SUV values by 35% or more) received more cycles of chemotherapy for a maximum of 12 weeks, whereas metabolic non-responders underwent surgery immediately [95].

The prospective MUNICON II trial was designed to potentially improve the clinical outcome of metabolic non-responders by applying a salvage neoadjuvant chemoradiotherapy; the authors found an increased histopathologic response rate as compared to the results of the MUNICON I trial, but the primary endpoint of the study—to increase the R0-resection rate—was not met [171].

In contrast, if FDG PET/CT is used to assess therapy response in squamous cell carcinoma patients, it should be conducted after completion of the neoadjuvant therapy [113].

19.2.5 Gastric Cancer and Gastrointestinal Stromal Tumour (GIST)

19.2.5.1 Diagnosis, Staging and Re-staging in Gastric Cancer Patients

Gastric cancer is the fourth most common cancer and the second leading cause of cancer-related deaths worldwide [92]. Gastric adenocarcinoma accounts for about 95% of all types of gastric cancer. There are two major subtypes according to Lauren's classification: intestinal type, which often evolves from the distal stomach in association with chronic *Helicobacter pylori* infection, and diffuse or signet ring type (non-intestinal type), which commonly evolves from the proximal stomach and is more often found in Western patients combined with chronic reflux and obesity [82].

In the staging of gastric cancer the use FDG PET/CT is limited by a reduced sensitivity. Only about 60% of locally advanced gastric cancers are FDG avid [138]. Especially tumours with non-intestinal type histology are often not FDG avid and can therefore not be imaged by FDG PET/CT. Furthermore, FDG non-avidity is associated with small tumour size, mucinous content and localisation in the distal third of the stomach [65]. For the detection of gastric cancer by FDG PET sensitivities range from 47 to 96% (mean sensitivity 77%, mean specificity 99%) [66]. For detection of loco-regional lymph nodes FDG PET/CT seems to be more specific, but less sensitive as compared to CT alone—FDG PET/CT sensitivity, specificity and accuracy range from 41 to 74%, 75 to 100% and 51 to 76%, respectively, whereas these parameters for contrast-enhanced CT range from 70 to 83%, 62 to 92% and 67 to 80%, respectively [82].

Wu et al. carried out a systematic review and meta-analysis to evaluate the use of FDG PET for the detection of recurrent gastric cancer. Across 9 studies (526 patients) the overall sensitivity of FDG PET was found to be 78% and the overall specificity 82% [162]. A more recent meta-analysis enrolling 14 studies with 828 patients reported a high sensitivity of 85% and a moderate specificity of 78% for FDG PET or FDG PET/CT for diagnosing recurrent gastric cancer—the authors concluded that FDG PET has a great value in the detection of recurrent gastric cancer after surgical resection, which might become more important in the future given the high recurrence rates of gastric cancer [92].

19.2.5.2 Diagnosis, Staging and Re-staging in GIST Patients

Most of gastrointestinal stromal tumours (GISTs) are found in the stomach (60%), another third is found in the small intestine [126]. Since GISTs often show a high FDG avidity, FDG PET/CT can be used to evaluate these tumours and their response to therapy [150]. A correlation between the FDG uptake and the malignant potential of GISTs presented by the Ki67 labelling index as a mitotic index has been reported by Kamiyama et al. [80].

FDG PET/CT is suitable for the initial staging of GIST patients, since at least half of the patients present with distant metastases at the time of diagnosis [101]. Most common sites for distant metastases are the liver and the peritoneum; loco-regional lymph node metastases are very uncommon [126]. Nevertheless, there is a significant number of patients with GISTs of about 10% that do not show the typically strong FDG uptake on baseline PET scan—this might be related to a high degree of tumour necrosis and myxoid/zystoid degeneration [101, 126].

19.2.5.3 Therapy Response Assessment in GIST Patients

Metabolic response as assessed by FDG PET/CT is closely related to clinical outcome for GIST patients. Changes of FDG uptake occur early, whereas morphological changes occur late in the course of imatinib therapy [147]. In a systematic review and meta-analysis, Hassanzadeh-Rad et al. found out that the accuracy of FDG PET/CT is higher in detection of treatment failure (e.g. non-responders) than in prediction of good response to therapy [62].

19.2.6 Colorectal Cancer

19.2.6.1 Diagnosis, Staging and Re-staging

In the United States in 2017 colorectal cancer was supposed to be the second leading cause of estimated cancer-related deaths in men and the third leading cause in women, even though, its incidence has decreased continually since 2004 by approximately 3% per year until 2013 [132].

At an early stage surgery is a curative treatment approach; however, for locally advanced cancers (pT3-4 or any T N1) usually a multimodality treatment approach is chosen, which includes pre-operative concomitant chemotherapy and radiotherapy [82].

In general, FDG PET/CT is considered not ‘useful’ in the initial staging of colorectal cancer patients, since the added value as compared to conventional imaging seems to be too little [82]. However, in a retrospective study, Petersen et al. analysed the data from 67 patients, who underwent FDG PET/CT additionally to conventional imaging (CT, MRI and/or ultrasound) for initial staging—they found a change in treatment plans in 30% of the cases due to FDG PET/CT, another third of this 30% was either a change from intended curative to palliative therapy or vice versa [118]. Lee and Lee also conducted a retrospective study enrolling 266 colon cancer patients also undergoing both FDG PET/CT and conventional imaging. Multidetector CT and FDG PET/CT showed similar accuracy in detecting lymph node metastases in patients with clinical stage III (36.2% vs. 42%, $p = 0.822$) and stage IV (60.3% vs. 63.5%, $p = 0.509$) disease. However, FDG PET/CT results led to a change in management for 1 of 40 (2.5%) with clinical stage I, 0 of 25 (0%) with stage II, 9 of 138 (6.5%) with stage III, and 8 of 63 patients (12.7%) with stage IV disease. The authors concluded that FDG PET/CT might be considered as a routine staging tool for clinical stage III and IV colon cancers [90].

Considering the M stage, liver metastases are most common in colorectal cancer patients with an incidence of approximately 50–60%, of which about one-third are diagnosed at the same time as the primary tumour is detected [82]. A recent meta-analysis by Maffione et al. including a total of 1,059 patients reported a high accuracy for FDG PET and FDG PET/CT for the detection and staging of liver lesions in colorectal cancer (pooled sensitivity and specificity of 93% in patient-based analysis, and 60% and 79%, respectively, in lesion-based analysis). PET showed a lower sensitivity as compared to MRI and CT in patient-based analysis (93%, 100% and 98%, respectively) and lesion-based analysis (66%, 89% and 79%, respectively); however, PET was more specific as compared to MRI and CT in both patient-based and lesion-based analysis (81%, 70% and 70%, respectively, and 86%, 81% and 67%, respectively). FDG PET and PET/CT results led to a change in management in an average of 24% of patients, entailing both exclusion from curative surgery and modification of the surgical approach. The mean incidence of extra-hepatic disease shown by FDG PET or PET/CT, but not detected by conventional imaging was 32% [99].

In the follow-up and detection of recurrent colorectal cancer, FDG PET/CT is regarded as a valuable tool. In a Danish study conducted by Engelmann et al. with a total of 66 prospectively included patients FDG PET/CT detected all relapses occurring within the first 2 years. Cumulative relapse incidences for clinical stages I–III ($n = 42$ patients) at 6, 12, 18 and 24 months were 7.1%, 14.3%, 19% and 21.4% [45]. A recent meta-analysis including 26 studies (1,794 patients) revealed a pooled sensitivity and specificity of 94% each for FDG PET and PET/CT in the detection of locally recurrent colorectal cancer [166]. Based on rising CEA levels (biochemical recurrence) many studies were conducted examining the usefulness of FDG PET/CT in this situation. In a systematic review and meta-analysis enrolling 11 studies with 510 patients Lu et al. found a pooled sensitivity and specificity of 90.3% and 80.0%, respectively, for FDG PET and a pooled sensitivity and

specificity of 94.1% and 77.2%, respectively, for FDG PET/CT in the detection of recurrence in colorectal cancer patients with elevated CEA levels [96].

The use of FDG PET/CT in colorectal cancer patients is recommended by some professional societies such as RCR, seeing the usefulness in many indications, e.g. initial staging of patients with synchronous metastases suitable for resection, re-staging of patients with recurrence (suspected by rising tumour markers and/or clinical suspicion of recurrence with normal or equivocal findings on other imaging), especially if being considered for radical treatment and/or invasive targeted techniques, or assessment of treatment response in patients with rectal carcinoma post (chemo)radiotherapy with indeterminate findings on other imaging [142]. Also SNMMI recommends the use of FDG PET/CT in re-staging for local recurrence and (distant) metastases, especially in the case of rising tumour markers with negative or equivocal findings on conventional imaging [74]. Furthermore, in the initial staging FDG PET/CT ‘may be appropriate’, if distant metastases are suspected in the pre-treatment staging of colorectal cancer according to the ACR Appropriateness Criteria® [51].

According to NCCN guidelines, FDG PET/CT is not indicated for pre-operative staging of rectal cancer in general, and should only be used to evaluate an equivocal finding on a contrast-enhanced CT-scan or in patients with a strong contraindication to intravenous contrast [13]. Following ESMO guidelines, PET/CT ‘may be helpful’ to characterise extra-hepatic disease [149].

19.2.6.2 Therapy Response Assessment

For therapy response assessment in rectal cancer patients a meta-analysis conducted by Maffione et al. (34 studies, 1,526 patients) found a high pooled accuracy for FDG PET and PET/CT to predict therapy response for the global cohort at the end of treatment (pooled sensitivity 73%, pooled specificity 77%), and especially for early interim PET performed between 1 and 2 weeks after the initiation of neoadjuvant chemoradiotherapy (pooled sensitivity 84%, pooled specificity 81%) [100].

19.2.7 Pancreatic Cancer

19.2.7.1 Diagnosis, Staging and Re-Staging

Pancreatic cancer is one of the most lethal cancers with a very poor prognosis and poor overall survival (5-year survival rate of about 4% [154]) as curative therapy is restricted to patients suffering from limited disease referred to surgery.

Commonly used imaging tools for the diagnosis of exocrine pancreatic cancer are ultrasound, endosonography, CT, MRI, and magnetic resonance and endoscopic retrograde cholangiopancreatography (MRCP and ERCP). Since 70–90% of exocrine pancreatic cancers show a high FDG uptake, FDG PET/CT was introduced to potentially improve detection of pancreatic adenocarcinomas.

Tang et al. assessed the diagnostic impact of FDG PET versus FDG PET/CT versus endoscopic ultrasonography in diagnosis of patients with pancreatic carcinoma. The authors reported that FDG PET/CT had a high pooled sensitivity of 90.1%, whereas the specificity was moderate with 80.1% in comparison with endoscopic ultrasonography with a pooled sensitivity and specificity of 81.2% and 93.2%, respectively. They concluded that FDG PET/CT and endoscopic ultrasonography might have different (complementary) roles under different conditions in diagnosing pancreatic carcinoma [141].

Fletcher et al. reported that PET improved differentiation between benign and malignant pancreatic tissue in the diagnostic work-up of patients with suspected pancreatic lesions and might reduce the need for biopsy and surgery influencing morbidity. They recommended FDG PET(/CT) as an additional tool in selected patients demonstrating inconclusive conventional imaging findings [49].

In the situation of potentially operable pancreatic adenocarcinoma an FDG PET/CT-scan is also recommended after inconclusive imaging by RCR [142]. CCO even recommends PET/CT staging in surgery candidates to confirm conventional staging: 'PET is recommended for staging if a patient is a candidate for potentially curative surgical resection as determined by conventional staging' [21].

Recently, several studies were conducted to investigate the usefulness of FDG PET/CT in the follow-up after curative surgery and in suspected recurrence, especially if tumour marker levels (CA 19-9) are high and conventional imaging is equivocal. Jung et al. investigated the usefulness of FDG PET/CT in the follow-up of curatively resected pancreatic cancer patients in comparison with CT alone: PET/CT showed a higher sensitivity (84.5% vs. 75.0%) and accuracy (84.5% vs. 74.5%) than CT alone, also in the detection of distant metastases (sensitivities 83.1% vs. 67.7%). In 19 out of 110 patients, recurrences were only seen on PET/CT [79].

In another study, the additional value of FDG PET/CT in unresectable pancreatic carcinoma patients prior to chemoradiotherapy was examined as compared to conventional imaging—in 19 out of 71 (26.8%) PET/CT staging showed distant metastases not detected by conventional staging, entailing a change in the conduction of chemoradiotherapy (or chemotherapy alone, respectively). The authors concluded that PET/CT-based staging might help to select the patients who are suitable for chemoradiotherapy, sparing those patients with metastases from futile radical protocols [145].

19.2.8 Melanoma

19.2.8.1 Diagnosis, Staging and Re-staging

Malignant melanoma is one of the most common tumour entities in both sexes worldwide—in the United States there were to be expected an estimated 6% of new cases in males (5th most common) and an estimated 4% in women (6th most common) in 2017, but due to new efficient treatment options like immunotherapies melanoma was not to be expected among the 10 cancer entities with the highest

mortality rates [132]. Incidence rates have been rising for many years worldwide by approximately 3% per year since 2004 [123].

Since tumour stage is the most important predictive factor for survival rates, initial staging of the disease is crucial. Surgery remains the gold standard in the treatment of loco-regional disease, but even in stage IV-patients (according to AJCC) survival rates have been improved by metastasectomy [123]. In general, FDG PET/CT has a higher sensitivity and specificity for detecting (distant) metastases as compared to conventional imaging. However, additional MRI of the head should be performed to exclude brain metastases, which might not be detected by PET/CT due to the high physiologic cerebral uptake and a resulting diminished sensitivity. Furthermore, by virtue of limited spatial resolution FDG PET/CT is inferior to sentinel lymph node biopsy in the detection of clinically occult lymph node metastases.

According to NCCN guidelines, PET/CT is recommended in patients equal or higher than stage III with clinically suspicious lymph nodes or with in-transit metastases (IIIB or higher) [35]. ESMO guidelines state that ‘before undertaking additional aggressive local surgical treatments, a detailed staging investigation, that includes high-resolution imaging techniques, such as PET, CT or magnetic resonance imaging is necessary to exclude distant metastases’, and specify that ‘in pT stages > pT3a [i.e. in patients equal or higher than stage IIA], computed tomography (CT) or positron emission tomography (PET) scans are recommended before surgical treatment and sentinel node biopsy’ [43] (Fig. 19.4). The German S3 guideline is not in agreement with ESMO guidelines by stating PET/CT shall not be performed routinely as initial staging procedure up to stage IIA/IIIB (suggesting to treat stage IIC patients like high-risk patients); however, in the primary staging of stage III patients and higher it has been shown that PET/CT is superior to the other methods in diagnostic accuracy [10].

A meta-analysis conducted by Xing et al. enrolling 10,528 patients (regardless of stage) investigated the utility of ultrasonography, CT, PET and PET/CT for staging and surveillance of melanoma patients—in the staging of distant metastases the

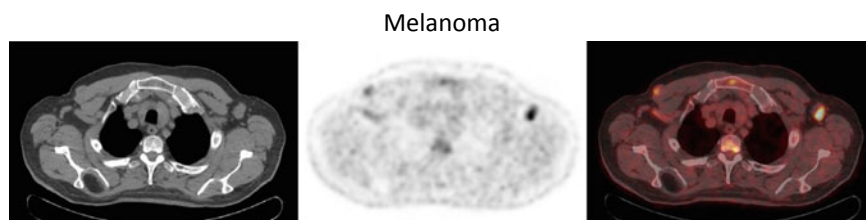


Fig. 19.4 78-year old male patient with melanoma of the left shoulder, pT4b, corresponding to AJCC stage IIC, referred to FDG PET/CT for initial staging after primary resection without sentinel lymph node biopsy. FDG PET/CT showed an FDG-positive lymph node metastasis in the left axilla and revealed another suspicious FDG-positive nodule adjacent to the right musculus pectoralis major; (A1) CT-Scan, (B1) PET scan, (C1) PET/CT fused images

highest sensitivity of 80% was found for PET/CT, going along with a moderate specificity of 87%. Similar results were found in the surveillance of patients with the help of PET/CT to exclude distant metastases [164]. A more recent meta-analysis aimed to review the utility of FDG PET in the detection of systemic metastases in patients with stage III melanoma, including 623 patients. The authors found a sensitivity and specificity of 89.42% and 88.78%, respectively; the area under the operating curve was 0.94. A change in stage and/or management was noted in 22% of patients [123].

In suspected recurrent disease, employment of FDG PET/CT is highly recommended by SNMMI [74], by CCO if just a solitary metastasis is identified at the time of recurrence prior to metastasectomy [21] and by NCCN in the case of nodal recurrence 'to evaluate specific signs or symptoms' [35].

A prospective multicentre PET registry study was conducted in Ontario (Canada) to assess the use of PET in advanced or high-risk melanoma as adjunct to clinical and standard radiologic investigation. Approximately 319 patients with potentially resectable high-risk melanoma or recurrent disease under evaluation for isolated metastasis underwent PET/CT, 10 of those already presenting with M1 stage (stage IV). A significant increase in stage to M1 was found after PET/CT in 17.6% of the patients, resulting in significantly more distant surgical interventions in this group as compared to the group without up-staging. None of the already assigned M1 patients was down-staged after PET/CT. The authors concluded that PET/CT has a significant impact on surgical management [136].

Usually, FDG PET/CT is not recommended for routine follow-up; however, according to ESMO guidelines and the German S3 guideline high-risk patients (starting from stage IIC onwards) should routinely undergo cross-sectional imaging, which may include cranial MRI and PET/CT, whole-body MRI or whole-body CT (German S3 guideline, AWMF [10] or 'ultrasound of lymph nodes, CT or whole-body PET or PET/CT scans' (ESMO, see Dummer et al. [43], respectively).

In order to assess the value of FDG PET/CT for patient management of melanoma patients Mena et al. carried out a retrospective study including 71 patients (regardless of stage) with 4 or more post-operative follow-up PET/CT-scans (246 scans). Recurrence was found in 39.0% of the scans, the examinations resulted in a change of patient's management in approximately 16.7% of the scans. Change in management was significantly higher in patients with prior clinical suspicion of malignancy recurrence than without prior clinical suspicion. There was a statistically significant difference in the overall survival between patients with at least 1 positive scan and patients with 4 or more negative subsequent follow-up scans at patient level [106]. More recently, a retrospective study analysed the data of 238 patients with 526 scans in Denmark—since 2015 PET/CT has been implemented in the Danish national follow-up programme as a routine examination at 6, 12 and 24 months after treatment for malignant melanoma of stage IIB or higher. However, in the analysis melanoma patients were included regardless of stage (starting from stage IA onwards). The authors found a sensitivity, specificity, PPV and NPV of 89%, 92%, 78% and 97%, respectively. Here there was no significant difference in the diagnostic accuracy of PET/CT between patients referred with or without

clinical suspicion of relapse [153]. A prospective study including 170 post-operative stage III patients with a total of 502 scans and a median follow-up of 47 months found relapses in 38% of the patients, the majority of them being asymptomatic. Overall sensitivity and specificity of the approach of sub-stage specific (IIIA/B/C) PET surveillance were 70% and 87%, respectively. PPV and NPV were calculated sub-stage- and time point-dependent—a negative PET at 18 months implied NPVs of 80–84% for true non-recurrence in the follow-up period. The authors considered PET/CT to be suitable to detect (asymptomatic) resectable and potentially curable disease at relapse [91].

19.2.8.2 Therapy Response Assessment

The therapy of unresectable metastatic melanoma has changed significantly by the introduction of immune check-point inhibitor therapy—the first FDA approved one was ipilimumab in 2011 for the treatment of malignant melanoma.

Sachpekidis et al. studied 41 patients with advanced melanoma prior to and after 2 cycles of ipilimumab treatment with FDG PET/CT (interim PET/CT). Earlier the authors had found that the absolute number of new lesions is a better parameter for prediction of immunotherapy response than changes in SUV and established the so-called PET Response Evaluation Criteria for Immunotherapy (PERCIMP). In this study therapy response assessment was based both on European Organization for Research and Treatment of Cancer (EORTC) criteria from 1999 and the proposed PERCIMP criteria. The patients were dichotomized into those with clinical benefit (CB including stable disease (SD), partial response (PR) and complete response (CR)), accounting for 31 patients, and those without CB (no-CB) showing progressive disease (PD), affecting the remaining 10 patients. According to EORTC criteria interim PET/CT demonstrated PD (meaning no-CB) in 20 patients, according to PERCIMP criteria PD was seen in 9 patients; SD and PR were seen in 19 patients according to EORTC criteria and in 30 patients according to PERCIMP criteria, and CR was seen in 2 patients according to both criteria, resulting in sensitivities (correctly predicting CB), specificities (correctly predicting no-CB), PPV, NPV and accuracies of 64.5%, 90.0%, 95.2%, 45.0% and 70.7%, respectively, for EORTC criteria, and 93.6%, 70.0%, 90.6%, 77.8% and 87.8%, respectively, for PERCIMP criteria [128].

19.2.9 Lymphoma

19.2.9.1 Diagnosis, Staging and Re-staging

Lymphomas are a heterogeneous group of malignancies characterised by diverse morphologies, immunophenotypes and cytogenetics. The major subdivision into Hodgkin's lymphoma (HL) and non-Hodgkin lymphoma (NHL) is following histopathological criteria, with HL presenting 'Sternberg-Reed cells' microscopically. Although the World Health Organisation (WHO) does not recommend a 'grouping' of lymphomas, there is a further classification dividing NHLs into indolent (low-risk) and aggressive/highly aggressive (intermediate- and high-risk)

NHLs, based on terms of biologic behaviour and the subsequently required aggressiveness of the treatment [75].

With an estimated 4% (women) and 5% (men) of new cases in 2017 in the United States, NHLs were supposed to be the 7th most common malignancy in both men and women [132].

In international guidelines and recommendations by professional societies, FDG PET/CT is often recommended in the initial staging work-up of lymphoma patients, especially in HL patients, e.g. RCR [142], NCCN [68] and ESMO [44]. While HL patients usually display a high FDG avidity on PET/CT-scans, the FDG avidity of NHL patients differs. However, almost all histological (nodal) NHL subtypes were reported to be highly FDG avid with the exception of extra-nodal marginal zone lymphoma and small lymphocytic lymphoma [160], and lymphoplasmacytic lymphoma/Waldenström's macroglobulinemia and mycosis fungoides (unless there is a suspicion of aggressive transformation) [28].

Based on published data, a consensus statement of the Malignant Lymphomas Imaging Working Group (MLIWG) on International Conferences in 2011 and in 2013 (Lugano, Switzerland) recommended the use of PET/CT in the staging of all FDG avid lymphomas, including indolent subtypes [28].

A prospective multicentre PET registry study published in 2017 was conducted to evaluate the clinical impact of pre-treatment FDG PET/CT on the staging and management of apparent limited-stage indolent lymphoma being considered for curative radiation therapy. Significantly, 47 patients (23.9%) of the included 197 patients were up-staged by the PET/CT result from the presumed limited-stage (stage I–II according to Cotswold-modified Ann Arbor classification) to advanced-stage disease (stage III–IV). Vice versa, 10 patients (5.1%) were down-staged, 4 of those patients from advanced-stage to limited-stage disease. After PET/CT (available data of 155 patients), 95 patients (61.3%) were planned to receive active treatment, of whom 59 patients were assigned to undergo the initially planned radiation therapy alone—finally, 34 patients of those received this treatment. The authors concluded that PET/CT should be implemented in the standard work-up of indolent lymphoma patients, as there was a significant impact on further clinical treatment in their study [107].

Instead of TNM staging, the staging of lymphoma patients follows the so-called 'Ann Arbor classification', lastly modified in Cotswold in 1988, which takes the site and the dissemination of involved lymphoid and extra-nodal tissue into account. The highest stage IV includes extra-nodal involvement other than contiguous/proximal lesions to the known nodal site, e.g. bone marrow involvement. Since bone marrow biopsy is an invasive method and gives information only about a small part of the bone marrow, many studies were conducted to investigate the sensitivity and specificity of FDG PET/CT in the assessment of bone marrow involvement in lymphoma patients. Recently, in a retrospective analysis evaluating 832 HL patients from the German Hodgkin Study Group trials HD16, HD17 and HD18, the results of bone marrow biopsy and PET scans (either in combination with CT or MRT and in 31 patients (4%) PET alone) were compared. With bone marrow biopsy as reference standard PET showed a sensitivity, specificity, PPV,

and NPV of 95.0%, 86.5%, 14.7% and 99.9%, respectively. Considering both bone marrow biopsy and PET as gold standard, sensitivity, specificity, PPV, and NPV of PET were 99.2%, 100%, 100% and 99.9%, respectively. PET found 110 additional patients with suspect focal bone marrow lesions who would have been considered negative by biopsy. Regarding these results, bone marrow biopsy seems to be futile in PET negative HL patients and the authors recommended biopsies only in PET positive patients that would undergo a changed treatment protocol as a result of the suspected bone marrow involvement [155].

Also in diffuse large B-cell lymphoma, the most common subtype with 30–35% of all NHL lymphomas, FDG PET/CT was reported to be more sensitive than bone marrow biopsy for the detection of bone marrow involvement [28]. In their systematic review and meta-analysis, Adams et al. included 7 studies with a total of 654 patients. The pooled estimates for sensitivity and specificity of FDG PET/CT for detecting bone marrow involvement were 88.7% and 99.8%, respectively. The weighted summary proportion of FDG PET/CT negative patients with positive bone marrow biopsy was 3.1%. In conclusion, FDG PET/CT was considered as a complementary tool to bone marrow biopsy for detecting bone marrow involvement, since it cannot be ruled out by a negative FDG PET/CT-scan [2]. However, even if positive PET findings were reported to be highly predictive and are considered usually sufficient to define advanced-stage disease [28], there is no consensus whether diffuse FDG bone marrow uptake should be regarded as positive or negative for involvement [2]. Furthermore, the histological type of lymphomatous cells in the bone marrow (small or large cells meaning discordant or concordant involvement) might have an influence on FDG avidity with FDG PET/CT being more sensitive in concordant bone marrow involvement [2].

Another retrospective study enrolling 185 patients with newly diagnosed lymphoma including indolent subtypes (47 patients, 30 follicular lymphomas and 17 marginal zone lymphomas) found a high concordance rate between bone marrow biopsy and PET/CT in the detection of bone marrow involvement for aggressive B-cell lymphoma (88.1%) and HL (93.8%), as well as high NPVs for PET/CT in the same histological subtypes (93.2% for aggressive B-cell lymphoma and 100% for HL). However, the concordance rate and NPV were much lower in indolent B-NHL with 66.0% and 66.7%, respectively—the authors considered bone marrow biopsy as an indispensable staging procedure in indolent lymphoma patients [31].

In follow-up, routine surveillance scans with FDG PET/CT are not recommended, since there is a high number of false-positive scans (>20%), leading to further unnecessary investigations, such as biopsies, and to increased patient anxiety. Therefore, follow-up scans should be based on clinical indications [28].

19.2.9.2 Therapy Response Assessment

According to the ‘Lugano Classification’ based on the results of the already mentioned 2 international conferences in Lugano, therapy response assessment is recommended to be performed by FDG PET/CT using the 5-point scale (Cheson/Deauville criteria) both for interim and end-of treatment response for all

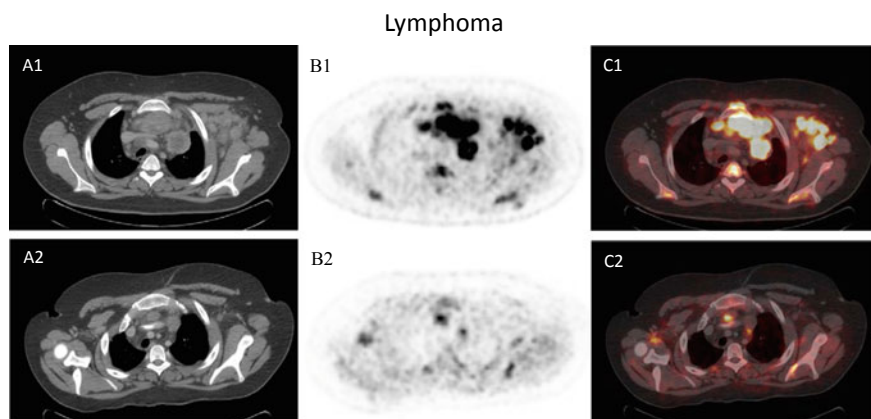


Fig. 19.5 19-year old male patient with Hodgkin lymphoma, referred to FDG PET/CT for initial staging (August 2015; images A1/B1/C1) and for re-staging (January 2016; images A2/B2/C2) after chemotherapy (6 cycles of BEACOPP August-December 2015). Initial FDG PET/CT showed manifestations of lymphoma on both sites of the diaphragm (Ann Arbor stage III), FDG PET/CT after chemotherapy showed vital lymphoma residuals in the mediastinum (visually Cheson/Deauville score 3–4, which means $>$ mediastinal blood pool uptake, but \leq liver uptake and moderately above liver uptake, respectively). As a consequence the patient was referred to adjuvant radiotherapy; (A1-2) CT-Scan, (B1-2) PET scan, (C1-2) PET/CT fused images

FDG avid lymphomas within clinical trials [28]. So far, therapy response should be assessed only visually, since there are not enough data for an SUV-based cut-off assessment. However, in NHL patients there are controversies about the interreader agreement after PET/CT applying the 5-point scale [11]. For end-of-treatment assessment, PET/CT is the standard of care for remission assessment in FDG-avid lymphoma (Fig. 19.5). However, for interim assessment, there are ongoing clinical trials evaluating and also questioning the usefulness of interim FDG PET/CT in therapy response assessment, especially during *immunochemotherapy* in diffuse large B-cell lymphomas [11].

There are a lot of studies investigating the usefulness of FDG PET/CT in interim therapy response assessment in HL patients, also at advanced-stage disease. In an international prospective multicentre trial, 1,119 patients with advanced-stage HL underwent interim PET/CT-scans, of whom 937 patients showed negative scans. Those patients with negative PET findings after 2 cycles of ABVD (doxorubicin, bleomycin, vinblastine and dacarbazine) chemotherapy were randomly assigned to continue ABVD or omit bleomycin in the following 4 cycles. The 3-year progression-free survival rate and overall survival rate in the ABVD group were 85.7% and 97.2%, respectively; the corresponding rates in the AVD group were 84.4% and 97.6%, respectively. In summary, the omission of bleomycin from the ABVD regimen after negative interim PET/CT resulted in a lower incidence of

pulmonary toxic effects than with continued ABVD but not significantly lower efficacy [77].

Recently, in an open-label international phase 3 trial 1,013 advanced-stage HL patients were randomised after negative interim FDG PET/CT (after 2 cycles of chemotherapy) to receive either standard eBEACOPP (in all 8 (before June 2011) or 6 cycles (after June 2011)) of bleomycin, etoposide, doxorubicin, cyclophosphamide, vincristine, procarbazine and prednisone in escalated doses) or de-escalated protocol with 4 cycles eBEACOPP in all (experimental arm). In PET negative patients the 5-year progression-free survival rates in the standard and experimental arm were 90.8% and 92.2%, respectively. Furthermore, the application of only 4 cycles of eBEACOPP was associated with fewer severe infections (8% vs. 15% after 6/8 cycles) and organ toxicities (8% vs. 18% after 6/8 cycles). The authors concluded that interim PET negativity allows for a reduction to only 4 cycles of eBEACOPP without loss of tumour control [15].

19.2.10 Sarcoma

19.2.10.1 Diagnosis, Staging and Re-staging

Sarcomas are a rare heterogeneous group of tumours composing about 1% of all malignancies [156], but carrying a high mortality rate, and presenting with varied radiologic appearances.

Primarily, sarcomas are divided into sarcomas originating from bone and cartilage, respectively, (such as osteosarcoma, Ewing's sarcoma or chondrosarcoma) or originating from soft tissue (such as liposarcoma, leiomyosarcoma and GIST).

With respect to the biologic potential, WHO has classified soft tissue tumours in four categories: benign, intermediate (locally aggressive), intermediate (rarely metastasising) and malignant [48]. The histological grade of soft tissue sarcomas and chondrosarcomas is supposed to be the most important prognostic factor in those cancer groups [33, 34].

A meta-analysis of FDG PET studies in patients with sarcoma concluded that FDG PET could discriminate between benign tumours and low-grade tumours and intermediate and high-grade tumours [12]. Also other authors found an accurate discrimination at least between low- and high-grade sarcomas employing FDG PET [26]. However, by use of FDG PET it remains difficult to distinguish low-grade tumours from benign tumours, as also confirmed by other studies, e.g. Ioannidis and Lau found FDG PET to be positive in all intermediate and high-grade soft tissue tumours, in 74.4% of low-grade soft tissue tumours and still in 39.3% of benign lesions [71]. Czernin et al. investigated the baseline glucose metabolic phenotype of sarcoma in more than 100 patients with soft tissue sarcoma. The SUV differed considerably and significantly among the many histological subtypes. Liposarcomas, especially the myxoid variants, exhibited low FDG uptake. Sarcomas not otherwise specified (NOS), the most dedifferentiated variants, showed the highest FDG uptake. Overall, SUV_{max} was significantly higher in high-grade than in low-grade sarcomas (11.7 ± 9.1 g/ml vs. 3.7 ± 1.8 g/ml; $p < 0.001$) [37].

FDG PET/CT can be useful in the evaluation of soft tissue tumours for guiding biopsy, helping to sample in the area with the highest glucose utilisation [122]. ESMO guidelines also see a role for FDG PET/CT in defining the area a biopsy should be taken from [23]. Furthermore, according to the NCCN guidelines there is a role for FDG PET/CT in the staging, prognostication and therapy response assessment in patients with soft tissue sarcomas of the extremities, the superficial trunk or head and neck, but not in surveillance [156].

A meta-analysis from 2012 enrolling 89 patients focused on the primary staging of high-grade bone and soft tissue sarcomas—the authors found a high sensitivity, specificity, PPV and NPV for the presence of distant metastases detected by FDG PET/CT with 95%, 96%, 87% and 98%, respectively. However, in the detection of lymph node metastases, the PPV was very low with 27%, but there were similarly high rates for sensitivity, specificity and NPV with 100%, 90% and 100%, respectively. The authors considered the use of FDG PET/CT to be ‘feasible’ in the initial assessment of patients with high-grade bone and soft tissue sarcoma. Furthermore, they found the SUV_{max} of the primary tumour to be a strong prognostic predictor of survival [53].

A more recent review and meta-analysis investigated the role of FDG PET and PET/CT in diagnosis, staging and recurrence assessment of bone sarcoma enrolling 42 trials with a total of 1,530 patients; for discriminating primary bone sarcomas from benign lesions the authors found a pooled sensitivity of 96% and a pooled specificity of 79%, for detecting distant metastases the pooled results on a lesion-based level were 90% and 85% for sensitivity and specificity, respectively, and for detecting recurrence the pooled results on an examination-based level were 92% (sensitivity) and 93% (specificity), respectively (all values referring to PET/CT, even though, results for PET only were comparable) [93].

There are sarcomas that preferably occur in children and adolescents such as Ewing’s sarcoma and rhabdomyosarcoma. In a study conducting 46 PET scans in 25 paediatric patients with Ewing’s sarcoma or neuroectodermal sarcoma or rhabdomyosarcoma a favourable accuracy was found for FDG PET (sensitivity, specificity, PPV and NPV were 86%, 80%, 89% and 67%, respectively) [108].

19.2.10.2 Therapy Response Assessment

Czernin et al. investigated the evaluation of therapy response in soft tissue sarcomas by determining the degree of FDG uptake decrease before and after treatment: In these studies, decreases of tumour FDG uptake by 35% after a single cycle and by >60% at the end of treatment identified all pathological treatment responders, predicting the amount of necrotic tissue in excised tumour tissue (>95% necrosis) [37].

In osteosarcomas Hongtao et al. carried out a meta-analysis examining the therapy response as assessed by FDG PET/CT—they showed that SUVs measured before and after treatment are valuable for predicting the histological response to chemotherapy [67].

19.2.11 Breast Cancer

19.2.11.1 Diagnosis, Staging and Re-staging

Breast cancer is the most common type of cancer in women worldwide [119]. In 2014, breast cancer was the second leading cause of cancer-related deaths in women in the United States, in the group of 20–39 years of age it was even the first reason for cancer-related deaths in women [132].

Invasive ductal carcinoma is the most common histopathological subtype of invasive breast cancer accounting for 50–70% of all cases, followed by invasive lobular carcinoma with 5–15%, and finally mucinous and tubular carcinoma representing 1–6% and 1–2% of the cases, respectively. Invasive lobular, mucinous and tubular carcinomas are considered to be low FDG avid [117]; depending on the size and cell density this often also applies to carcinoma in situ [54].

Mammography remains the principal imaging tool to screen for breast cancer. Small lesions cannot be characterised by FDG PET/CT due to the partial volume effect and limited spatial resolution—sensitivities of 59% in T1a–b (<10 mm) and 98% in T1c (11–20 mm) tumours have been reported [83]. According to NCCN guidelines, FDG PET/CT can be used for the staging from stage IIIA onwards (T3 N1 M0), optionally [57]. In a clinical trial Koolen et al. enrolled 154 patients with primary stage II and III breast cancer to evaluate the role of FDG PET/CT in the staging work-up in comparison with conventional imaging techniques (bone scintigraphy, liver ultrasound and chest radiography) to exclude distant metastases prior to neoadjuvant chemotherapy. They found a sensitivity, specificity, PPV, NPV and accuracy of 100%, 96%, 80%, 100% and 97%, respectively; in 16 of 20 patients additional (distant) lesions, metastatic disease or new primary malignancy, were exclusively seen by PET/CT, leading to a change in treatment in 13 of 154 patients (8%). The authors concluded that FDG PET/CT is superior to conventional imaging techniques in the detection of distant metastases in untreated stage II and III breast cancer patients and may be of additional value prior to neoadjuvant chemotherapy [84]. For a recent retrospective study in a total of 234 stage I, II and III breast cancer patients FDG PET/CT was performed before (114 patients) or after surgery (120 patients)—hypermetabolic extra-axillary lymph nodes were detected in 42/234 patients (17.9%) and hypermetabolic distant metastases in 65/234 patients (27.7%), leading to a modification in the staging in 82/234 patients (35%) and in patient management in 69/234 patients (29.4%) [165]. Thus, FDG PET/CT seems to be of additional value in the staging starting already from stage II onwards (for more information also see Groheux [58]).

A meta-analysis conducted by Sun et al. including 6 studies with 609 patients at any disease stage and regardless of treatment status concluded that FDG PET/CT outperforms conventional imaging by far and has an excellent diagnostic performance in staging of distant metastasis in breast cancer patients indicated by a sensitivity of 99% and a specificity of 95% as compared to conventional imaging with a sensitivity of 57% and a specificity of 88% [140].

Since about 30–35% of all patients ultimately relapse after initial (radical) treatment [119, 163], surveillance of breast cancer patients with initially advanced

tumour stage is of special importance. Two-thirds of breast tumour recurrences are local and detection of local recurrence is a domain of mammography and/or ultrasound and, if inconclusive, MRI [119]. However, the 5-year survival rate in patients with distant metastases (mediastinal lymph nodes, bones, lungs, liver and brain) is markedly lower (25% vs. 80% in patients with loco-regional recurrence) [163]. Especially if there are equivocal findings on conventional imaging (CT, MRI, bone scintigraphy) the use of FDG PET/CT is recommended by some professional societies to identify or exclude a relapse, e.g. by ESMO [22], and also for detection of local recurrence by SNMMI [74], and in particular in patients with dense breasts by RCR/RCP [142].

In a recent meta-analysis and systematic review including 26 studies with 1,752 patients with suspected recurrent breast cancer FDG PET or PET/CT was shown to be a highly sensitive and moderately specific imaging modality for the detection of relapse with a sensitivity of 90% and a specificity of 81% [163]. A retrospective clinical study conducted by Jung et al. enrolling 1,162 patients with 1,819 examinations assessed the role of FDG PET/CT in the detection of loco-regional recurrence or distant metastases as compared to conventional imaging (mammography, breast ultrasound, bone scintigraphy and chest radiography)—the authors found a sensitivity, specificity, PPV and NPV of 97.5%, 98.8%, 95.4% and 99.4%, respectively, for FDG PET/CT, the corresponding values for conventional imaging were 75.4%, 98.7%, 93.4% and 94.3%, respectively; thus, the sensitivity of FDG PET/CT was shown to be significantly higher as compared to conventional imaging. The authors considered FDG PET/CT as an acceptable diagnostic imaging modality for post-operative surveillance [78] (Fig. 19.6).

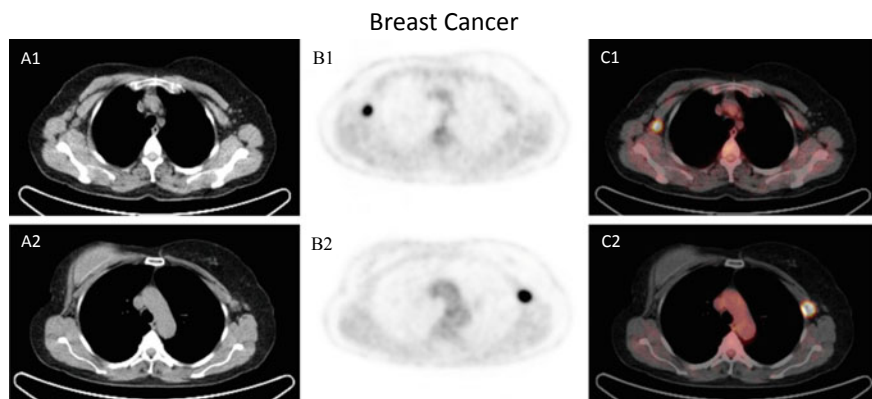


Fig. 19.6 56-year old female patient with history of breast cancer of the right breast (initially TNM-classification pT1b pN0 L0 V0 R0 G3) after surgery and adjuvant radiation therapy, referred to FDG PET/CT for re-staging; clinically already suspicious focal tumour in the right axilla. FDG PET/CT confirmed FDG-positive lymph node metastasis in the right axilla; furthermore, PET/CT revealed an FDG-positive node contralateral in the left axilla, either contralateral primary tumour or further lymph node metastasis; (A1-2) CT-Scan, (B1-2) PET scan, (C1-2) PET/CT fused images

19.2.11.2 Therapy Response Assessment

For breast cancer, FDG PET/CT was examined in many studies in the setting of neoadjuvant chemotherapy to assess therapy response. A meta-analysis from 2012 enrolling 17 studies with 781 patients summarised a good pooled sensitivity of 84.0%, but only a moderate pooled specificity of 71.3%; however, the studies included were quite heterogeneous. For instance, only 11 studies had reported the receptor status (estrogen, progesterone and human epidermal growth factor receptor (HER) 2). The authors recommended a combination of FDG PET/CT with other imaging modalities such as MRI, ultrasound and mammography to assess therapy response [27].

More recently, Tian et al. conducted a meta-analysis enrolling 22 studies with 1,119 patients; the pathological response in both breast tissues and in the axillary lymph nodes and the accordance with FDG PET/CT results were evaluated. They found a pooled sensitivity of 81.9% and a better-pooled specificity of 79.3% as compared to the results of Cheng et al. the area under the curve being 0.87. Among the included studies there was also a high heterogeneity, the sensitivities in the different studies ranged from 63 to 100% and the specificities ranged from 38 to 97%—the authors suggested that only tumour subtypes with relevant FDG uptake at baseline can be assessed in the course of chemotherapy. In tumours with low initial FDG avidity change in glucose utilisation cannot reasonably be used for therapy response assessment in the course of chemotherapy, but obviously those tumour subtypes were also evaluated in the included studies [143].

In general, therapy response assessment determined by FDG PET/CT seems to be of special interest in more aggressive subtypes like triple negative and HER2-positive breast cancers. The optimal timing of interim PET/CT is still an ongoing issue of research, but seems to depend on the histological cancer subtype and (chemo-/immuno-) therapy regimen [59].

19.2.12 Ovarian Cancer

19.2.12.1 Diagnosis, Staging and Re-staging

Nearly 90% of ovarian cancers arise from the epithelium, the remaining 10% are germ cell and stromal tumours [130]. Ovarian cancer is the leading cause of death from gynaecologic cancer in the Western World [85]. The poor prognosis results from an advanced cancer stage, which affects about 70% of patients at the time of diagnosis [46]. Ovarian cancer spreads mainly by local extension, by early implantation on both the parietal and the visceral peritoneum, by lymphatic dissemination (involving the inguinal, pelvic, paraaortic and mediastinal lymph nodes) and rarely through the blood vessels [46]. The serum tumour marker CA-125 is widely used to assess the effectiveness of therapy and to detect tumour recurrence.

Unclear ovarian masses are evaluated with ultrasound, CT and/or MRI, usually followed by ‘staging laparotomy’. Surgical exploration remains the standard reference for the initial staging of ovarian cancer [46, 130]. In the primary staging FDG PET/CT has no definite role, but ‘may be appropriate’ according to the ACR Appropriateness Criteria[®] in the staging and follow-up of ovarian cancer [81]. FDG

PET/CT was shown to be limited in the diagnosis of cancer of the ovaries due to physiologic FDG uptake observed in the ovaries of women at reproductive age; for this reason the examination should be conducted during the postmenstrual phase in premenopausal women. However, focal uptake in the region of the ovaries in postmenopausal women is suspicious of malignancy and should be further evaluated. False-positive results may also occur, e.g. when physiologic bowel activity is mixed up with peritoneal spread [46]. On the other hand, FDG PET/CT may lead to false-negative results in borderline tumours, in lesions smaller than 5 mm (such as carcinomatosis), in women with cystic or necrotic lesions and in mucinous tumours. Still, FDG PET/CT is more sensitive than CT alone in detecting small peritoneal deposits [50, 85]. Furthermore, women with ovarian cancer confined to the pelvis may benefit from a pre-operative FDG PET/CT in order to identify nodal metastases—in a prospective study enrolling 68 patients FDG PET/CT showed a high sensitivity, specificity, accuracy, PPV and NPV of 83.3%, 98.2%, 95.6%, 90.9% and 96.5%, respectively, in a patient-based analysis. The authors concluded that due to the high NPV systematic pelvic and aortic lymphadenectomy could be avoided in many patients [133]. In addition, FDG PET/CT has the advantage of a whole-body examination ('one-stop shop'), hence it might also detect supradiaphragmatic involvement at the time of primary staging. Therefore, it is recommended in the guidelines of the European Society of Urogenital Radiology (ESUR) in suspected stage IV disease (advanced ovarian cancer) and in the presence of indeterminate lymph node appearance [50].

The most important role of FDG PET/CT in ovarian cancer patients is the evaluation of tumour recurrence, especially when CA-125 levels are rising and conventional imaging is inconclusive or negative [46, 50, 85, 130]. Referring to the ACR Appropriateness Criteria[®], in this situation FDG PET/CT is considered 'usually appropriate' [81] and is also recommended by RCR [142].

19.2.12.2 Therapy Response Assessment

In the future, there might be a further role in monitoring response to treatment in advanced ovarian cancer, as FDG PET/CT is supposed to be more accurate in characterising residual disease after chemotherapy as compared to CT alone and as a molecular imaging technique it might also identify responders and non-responders [127]. However, so far it has not replaced second-look laparotomy, maybe also due to issues of cost-effectiveness [85, 130].

19.2.13 Testicular Cancer

19.2.13.1 Diagnosis, Staging and Re-staging

Most testicular neoplasms (90–95%) are germ cell tumours [7]. The other 5–10% include stromal tumours, lymphoma and metastases. Testicular germ cell tumours, representing a rare malignancy and occurring most frequently in Caucasian young males aged 15–40 years [112], are divided into seminoma and non-seminoma (tous germ cell tumours ((NSGCT)) with 50% each [112].

The NSGCT group consists of embryonic cell carcinomas including undifferentiated teratomas, differentiated teratomas (with varying degrees of differentiation, and immature and mature teratomas, respectively), yolk sac tumours such as choriocarcinomas and mixed tumours in every possible combination, also in combination with seminoma components. Mature teratomas do not show increased FDG uptake due to a low proliferation rate [5]. As mature teratoma is present in 30–45% of resected residual masses in NSGCT patients, this is a major source of false-negative results in PET scans prior to resection. In seminomas the fraction of mature teratoma in residual lesions is much lower (<5%). Therefore, FDG PET/CT has a greater role in evaluating patients with residual seminoma as compared to NSGCT patients with residuals [39].

However, FDG PET/CT does not contribute to initial staging and has no role in the routine follow-up (ESMO, see Oldenburg et al. [112]), for both of which usually CT is applied.

In contrary, FDG PET/CT is most helpful in the setting of tumour recurrence (when relapse is suspected, e.g. by elevated tumour marker levels, especially in combination with normal conventional imaging findings) and in the evaluation of chemotherapy response.

19.2.13.2 Therapy Response Assessment

Therapy response was evaluated in detail for residual tumour masses after chemotherapy in seminoma patients with suspicion of viable tumour residuals. Treglia et al. published a systematic review and meta-analysis referring to this question—pooled sensitivity and specificity of FDG PET or PET/CT were 78% and 86%, respectively; FDG showed a high NPV of 94% with a moderate PPV of 58% and a high accuracy of 84%. In addition, they found a significantly higher sensitivity for patients with residual masses >3 cm as compared to those <3 cm (89% vs. 47%) [148].

Thus, the main indication of FDG PET/CT in testicular cancer is the differentiation of residual tumour from fibrosis in seminoma patients, in particular in lesions >3 cm, as also recommended by CCO Cancer Care Ontario [21] and RCR [142]. In the assessment of residual tumour tissue after chemotherapy FDG PET/CT should be performed with a minimum of 6 weeks after the end of the treatment, as earlier imaging may lead to false-positive results due to inflammation following therapy. In the case of a positive PET scan, the probability of residual seminoma is high and a biopsy might be carried out before re-treatment by irradiation or resection [112].

There might be a future role for FDG PET/CT in the assessment of response to Cisplatin, Etoposide and Bleomycin (PEB) chemotherapy in metastatic seminoma patients, as Nechhi et al. pointed out: after 2 cycles of PEB 72.9% of the included 37 patients achieved a complete response (CR) and none of them relapsed (median follow-up of 18 months)—the authors concluded that patients showing CR on PET/CT-scan do not need additional treatment after (according to risk stratification 3 or 4 cycles of) PEB [110]. Further research in larger cohorts is necessary to confirm these results.

19.2.14 Penile Cancer

19.2.14.1 Diagnosis, Staging and Re-staging

In Europe and North America or in general in developed countries, penile cancer has a low incidence (≤ 1 per 100,000) that increases with age, with a peak during the sixth decade [60, 114]. As there is a strong correlation with human papillomavirus (HPV) (one-third of cases can be attributed to HPV-related carcinogenesis), this might explain regional differences in epidemiology with higher incidence rates in South America, Southeast Asia and parts of Africa [60]. The following section focuses on penile squamous cell carcinoma, which represents the vast majority of penile cancer subtypes [114].

As metastatic involvement of regional lymph nodes is a strong prognostic factor (excellent prognosis in N0-patients with cure in up to 90% [41, 114], invasive lymph node staging is required in patients at intermediate or high risk (intermediate risk: not well-differentiated pT1; high risk: pT2 or higher plus all G3 tumours) of lymphatic spread, i.e. either modified radical inguinal lymphadenectomy (ILND) or dynamic sentinel node biopsy (DSNB) [60]. In enlarged palpable inguinal lymph nodes the presence of metastases is more likely, but even in clinical unsuspecting lymph nodes micrometastases occur with a frequency of about 20–25% [41, 60]. Despite its poorer prognosis, cure is still possible in lymph node-positive disease—for this reason, improved imaging tools are needed to identify those patients. Due to low sensitivities for smaller metastases, FDG PET/CT is not recommended for cN0-patients [114]. Though there was an attempt by a Danish group to combine FDG PET/CT with sentinel node biopsy in cN0-patients and this combined approach showed a sensitivity of 94.4% [76]. In another prospective study, 41 cN0-patients underwent FDG PET/CT prior to bilateral modified or radical ILND—FDG PET/CT showed a high sensitivity but moderate specificity with 80% and 68%, respectively, as well as a high NPV of 91% (although low PPV of 44%). The authors concluded that FDG PET/CT cannot replace invasive nodal staging [42].

In clinically suspicious palpable lymph nodes FDG PET/CT can identify metastases and confirm lymph node involvement [60]. In nodal-positive patients, radical ILND with curative intention is indicated. FDG PET/CT might also help to identify pelvic lymph node metastases, if these are initially suspicious due to enlargement [151].

In follow-up, FDG PET/CT can improve the detection of early regional lymph node involvement and reveals more distant metastases, especially in patients with inguinal node-positive penile cancer (ESMO, see Van Poppel et al. [151]). In a recent study, Zhang et al. showed an overall sensitivity of 82% and specificity of 93% for the detection of distant metastases by FDG PET/CT in a patient-based analysis in 42 stage III- and IV-patients with advanced penile cancer, mostly in the clinical setting of re-staging/evaluation of suspected recurrence (65% of the patients) [169].

19.2.15 Prostate Cancer

19.2.15.1 Diagnosis, Staging and Re-staging

FDG PET/CT has shown only a limited sensitivity for the detection of differentiated prostate cancer and imaging of recurrent prostate cancer in various studies. Increased FDG uptake and accumulation is regularly only found in dedifferentiated and aggressive prostate cancer, given a Gleason score >7 , and the sensitivity for the detection of metastases increases with increasing serum PSA levels (for more information also see Jadvar [72, 73] and the chapter concerning molecular imaging of prostate cancer in this book).

19.2.16 Cancer of Unknown Primary

19.2.16.1 Diagnosis/Detection and Staging

About 3–5% of all malignancies are cancers of unknown primary (CUP) [47], mostly associated with a poor prognosis. By definition, CUPs present with histologically proven metastatic disease for which the site of origin cannot be identified at the time of diagnosis despite extensive diagnostic work-up. The biology of those tumours is still not fully understood [47], although one might hypothesise that the detection of the primary tumour might lead to a more distinctive treatment. The primary tumour can often not be identified on conventional imaging, thus, PET may improve the detection rate of CUPs and potentially improve patient outcome by optimising treatment planning.

A special patient sub-group in the group with those heterogeneous malignancies are patients with neck lymph node metastases from an occult primary who account for up to 10% of all patients with carcinoma of unknown primary site [20]. Since the most frequent histological finding in neck lymph node metastases is squamous cell carcinoma, particularly when the upper neck is involved [20], and squamous cell carcinomas are usually FDG avid, there is a high probability to find the primary tumour by virtue of FDG PET/CT, at least if the tumour size is not below resolution limit. Zhu et al. conducted a meta-analysis including 246 patients and with 44, 97 and 68% for detection rate, sensitivity and specificity, respectively, they found a moderate detection rate, a high sensitivity and a low specificity [170].

Despite the lack of recommendations in official guidelines, a multidisciplinary expert panel of oncologists, radiologists and nuclear physicians with expertise in PET/CT concluded that the use of FDG PET(/CT) is beneficial in the diagnostic work-up of patients with cervical CUPs [49].

At the moment also in extra-cervical CUPs evidence seems to be too rare to recommend the use of FDG PET/CT in guidelines in first line diagnostic work-up with exception of the German Society of Haematology and Oncology, which prefers FDG PET/CT for the detection of the primary tumour instead of CT thorax/abdomen alone [70]. RCR recommends FDG PET/CT for the ‘detection of the primary site when imaging and histopathology has failed to show a primary site, where the site of tumour will influence choice of chemotherapy’ [142].

A meta-analysis by Kwee et al. reported a primary tumour detection rate of 37%. Lung, oropharyngeal and pancreatic cancer were reported to represent the most frequently detected primary tumours [87]. Another meta-analysis was conducted by Moller et al., who found a detection rate of 39.5% for the primary site in patients with extra-cervical CUP, the pooled estimates for sensitivity, specificity and accuracy were 87%, 88% and 87.5%, respectively. The lungs were again the most commonly detected primary tumour site with 50% [109]. A more recent meta-analysis enrolling 1,942 patients came to a similar result with an overall detection rate of 40.93%—the authors concluded that up-front application of FDG PET/CT might have a role in CUP patients by obviating many futile diagnostic procedures [17].

References

1. Abouzi MM, Fathala A, Alsugair A, Muhaideb AIA, Qahtani MHA (2017) Role of fluorodeoxyglucose-positron emission tomography/computed tomography in the evaluation of head and neck carcinoma. *World J Nucl Med.* 16(4):257–265
2. Adams HJ, Kwee TC, de Keizer B, Fijnheer R, de Klerk JM, Nievelstein RA (2014) FDG PET/CT for the detection of bone marrow involvement in diffuse large B-cell lymphoma: systematic review and meta-analysis. *Eur J Nucl Med Mol Imaging* 41(3):565–574
3. Ajani JA, D’Amico TA, Almhanna K, Bentrem DJ, Besh S, Chao J et al (2015) Esophageal and esophagogastric junction cancers, version 1.2015. *J Natl Compr Canc Netw* 13(2):194–227
4. Alavi A, Reivich M (2002) Guest editorial: the conception of FDG-PET imaging. *Semin Nucl Med* 32(1):2–5
5. Albers P, Bender H, Yilmaz H, Schoeneich G, Biersack HJ, Mueller SC (1999) Positron emission tomography in the clinical staging of patients with stage I and II testicular germ cell tumors. *Urology* 53(4):808–811
6. Ambrosini V, Nicolini S, Caroli P, Nanni C, Massaro A, Marzola MC et al (2012) PET/CT imaging in different types of lung cancer: an overview. *Eur J Radiol* 81(5):988–1001
7. Ambrosini V, Zucchini G, Nicolini S, Berselli A, Nanni C, Allegri V et al (2014) ¹⁸F-FDG PET/CT impact on testicular tumours clinical management. *Eur J Nucl Med Mol Imaging* 41(4):668–673
8. American College of Radiology (ACR) Appropriateness Criteria® (2013). <https://acsearch.acr.org/list>. Accessed 12 Sept 2018
9. AWMF (2018) Leitlinienprogramm Onkologie (Deutsche Krebsgesellschaft, Deutsche Krebshilfe, AWMF): Prävention, Diagnostik, Therapie und Nachsorge des Lungenkarzinoms, Langversion 1.0, 2018, AWMF-Registernummer: 020/007OL, <http://leitlinienprogramm-onkologie.de/Lungenkarzinom.98.0.html>. Accessed 3 Jan 2019
10. AWMF (2018) Leitlinienprogramm Onkologie (Deutsche Krebsgesellschaft, Deutsche Krebshilfe, AWMF): Diagnostik, Therapie und Nachsorge des Melanoms, Langversion 3.1, 2018, AWMF Registernummer: 032/024OL, <http://www.leitlinienprogramm-onkologie.de/leitlinien/melanom/>. Accessed 3 Jan 2019
11. Barrington SF, Mikhael NG, Kostakoglu L, Meignan M, Hutchings M, Müeller SP et al (2014) Role of imaging in the staging and response assessment of lymphoma: consensus of the International Conference on Malignant Lymphomas Imaging Working Group. *J Clin Oncol* 32(27):3048–3058

12. Bastiaannet E, Groen H, Jager PL, Cobben DC, van der Graaf WT, Vaalburg W et al (2004) The value of FDG-PET in the detection, grading and response to therapy of soft tissue and bone sarcomas; a systematic review and meta-analysis. *Cancer Treat Rev* 30(1):83–101
13. Benson AB, Venook AP, Al-Hawary MM, Cederquist L, Chen YJ, Ciombor KK et al (2018) Rectal cancer, version 2.2018, NCCN clinical practice guidelines in oncology. *J Natl Compr Canc Netw* 16(7):874–901
14. Bertagna F, Biasiotto G, Orlando E, Bosio G, Giubbini R (2010) Role of ^{18}F -fluorodeoxyglucose positron emission tomography/computed tomography in patients affected by differentiated thyroid carcinoma, high thyroglobulin level, and negative ^{131}I scan: review of the literature. *Jpn J Radiol* 28(9):629–636
15. Borchmann P, Goergen H, Kobe C, Lohri A, Greil R, Eichenauer DA et al (2018) PET-guided treatment in patients with advanced-stage Hodgkin's lymphoma (HD18): final results of an open-label, international, randomised phase 3 trial by the German Hodgkin Study Group. *Lancet* 390(10114):2790–2802
16. Bradley J, Thorstad WL, Mutic S, Miller TR, Dehdashti F, Siegel BA et al (2004) Impact of FDG-PET on radiation therapy volume delineation in non-small-cell lung cancer. *Int J Radiat Oncol Biol Phys* 59(1):78–86
17. Burglin SA, Hess S, Høilund-Carsen PF, Gerke O (2017) ^{18}F -FDG PET/CT for detection of the primary tumor in adults with extracervical metastases from cancer of unknown primary: A systematic review and meta-analysis. *Medicine (Baltimore)* 96(16):e6713
18. Cacicedo J, Fernandez I, Del Hoyo O, Dolado A, Gómez-Suarez J, Hortelano E et al (2015) Should PET/CT be implemented in the routine imaging work-up of locally advanced head and neck squamous cell carcinoma? A prospective analysis. *Eur J Nucl Med Mol Imaging* 42(9):1378–1389
19. Caetano R, Bastos CR, de Oliveira IA, da Silva RM, Fortes CP, Pepe VL et al (2016) Accuracy of positron emission tomography and positron emission tomography-CT in the detection of differentiated thyroid cancer recurrence with negative (131) I whole-body scan results: a meta-analysis. *Head Neck* 38(2):316–327
20. Calabrese L, Jereczek-Fossa BA, Jassem J, Rocca A, Bruschini R, Orecchia R et al (2005) Diagnosis and management of neck metastases from an unknown primary. *Acta Otorhinolaryngol Ital* 25(1):2–12
21. Cancer Care Ontario (2009). <https://www.cancercareontario.ca/en/guidelines-advice/types-of-cancer>. Accessed 12 Sept 2018
22. Cardoso F, Harbeck N, Fallowfield L, Kyriakides S, Senkus E, Group EGW (2012) Locally recurrent or metastatic breast cancer: ESMO Clinical Practice Guidelines for diagnosis, treatment and follow-up. *Ann Oncol* 23 Suppl 7:vii11-9
23. Casali PG, Abecassis N, Bauer S, Biagini R, Bielack S, Bonvalot S et al (2018) Soft tissue and visceral sarcomas: ESMO-EURACAN Clinical Practice Guidelines for diagnosis, treatment and follow-up. *Ann Oncol*
24. Chaft JE, Dunphy M, Naidoo J, Travis WD, Hellmann M, Woo K et al (2016) Adaptive neoadjuvant chemotherapy guided by (18)F-FDG PET in resectable non-small cell lung cancers: the NEOSCAN trial. *J Thorac Oncol* 11(4):537–544
25. Chang MC, Chen JH, Liang JA, Lin CC, Yang KT, Cheng KY et al (2012) Meta-analysis: comparison of F-18 fluorodeoxyglucose-positron emission tomography and bone scintigraphy in the detection of bone metastasis in patients with lung cancer. *Acad Radiol* 19(3):349–357
26. Charest M, Hickeyson M, Lisbona R, Novales-Diaz JA, Derbekyan V, Turcotte RE (2009) FDG PET/CT imaging in primary osseous and soft tissue sarcomas: a retrospective review of 212 cases. *Eur J Nucl Med Mol Imaging* 36(12):1944–1951
27. Cheng X, Li Y, Liu B, Xu Z, Bao L, Wang J (2012) ^{18}F -FDG PET/CT and PET for evaluation of pathological response to neoadjuvant chemotherapy in breast cancer: a meta-analysis. *Acta Radiol* 53(6):615–627

28. Cheson BD, Fisher RI, Barrington SF, Cavalli F, Schwartz LH, Zucca E et al (2014) Recommendations for initial evaluation, staging, and response assessment of Hodgkin and non-Hodgkin lymphoma: the Lugano classification. *J Clin Oncol* 32(27):3059–3068
29. Cheung PK, Chin RY, Eslick GD (2016) Detecting residual/recurrent head neck squamous cell carcinomas using PET or PET/CT: systematic review and meta-analysis. *Otolaryngol Head Neck Surg* 154(3):421–432
30. Cho J, Choe JG, Pakh K, Choi S, Kwon HR, Eo JS et al (2017) Ratio of mediastinal lymph node SUV to primary tumor SUV in ^{18}F -FDG PET/CT for nodal staging in non-small-cell lung cancer. *Nucl Med Mol Imaging*. 51(2):140–146
31. Cho SF, Chang CC, Liu YC, Chang CS, Hsiao HH, Liu TC et al (2015) Utilization of ^{18}F -FDG PET/CT as a staging tool in patients with newly diagnosed lymphoma. *Kaohsiung J Med Sci* 31(3):130–137
32. Choi SJ, Jung KP, Lee SS, Park YS, Lee SM, Bae SK (2016) Clinical usefulness of F-18 FDG PET/CT in papillary thyroid cancer with negative radioiodine scan and elevated thyroglobulin level or positive anti-thyroglobulin antibody. *Nucl Med Mol Imaging*. 50(2):130–136
33. Chow WA (2007) Update on chondrosarcomas. *Curr Opin Oncol* 19(4):371–376
34. Coindre JM, Terrier P, Guillou L, Le Doussal V, Collin F, Ranchère D et al (2001) Predictive value of grade for metastasis development in the main histologic types of adult soft tissue sarcomas: a study of 1240 patients from the French Federation of Cancer Centers Sarcoma Group. *Cancer* 91(10):1914–1926
35. Coit DG, Thompson JA, Algazi A, Andtbacka R, Bichakjian CK, Carson WE et al (2016) Melanoma, version 2.2016, NCCN clinical practice guidelines in oncology. *J Natl Compr Canc Netw* 14(4):450–473
36. Colevas AD, Yom SS, Pfister DG, Spencer S, Adelstein D, Adkins D et al (2018) NCCN guidelines insights: head and neck cancers, version 1.2018. *J Natl Compr Canc Netw* 16(5):479–490
37. Czernin J, Benz MR, Allen-Auerbach MS (2010) PET/CT imaging: The incremental value of assessing the glucose metabolic phenotype and the structure of cancers in a single examination. *Eur J Radiol* 73(3):470–480
38. de Groot PM, Wu CC, Carter BW, Munden RF (2018) The epidemiology of lung cancer. *Transl Lung Cancer Res* 7(3):220–233
39. De Santis M, Pont J (2004) The role of positron emission tomography in germ cell cancer. *World J Urol* 22(1):41–46
40. De Wever W, Ceyskens S, Mortelmans L, Stroobants S, Marchal G, Bogaert J et al (2007) Additional value of PET-CT in the staging of lung cancer: comparison with CT alone, PET alone and visual correlation of PET and CT. *Eur Radiol* 17(1):23–32
41. Djajadiningrat RS, Graafland NM, van Werkhoven E, Meinhardt W, Bex A, van der Poel HG et al (2014) Contemporary management of regional nodes in penile cancer—improvement of survival? *J Urol* 191(1):68–73
42. Dräger DL, Heuschkel M, Protzel C, Erbersdobler A, Krause BJ, Hakenberg OW et al (2018) [^{18}F]FDG PET/CT for assessing inguinal lymph nodes in patients with penile cancer—correlation with histopathology after inguinal lymphadenectomy. *Nuklearmedizin* 57(1):26–30
43. Dummer R, Hauschild A, Lindenblatt N, Pentheroudakis G, Keilholz U, Committee EG (2015) Cutaneous melanoma: ESMO Clinical Practice Guidelines for diagnosis, treatment and follow-up. *Ann Oncol* 26(Suppl 5):v126–v132
44. Eichenauer DA, Aleman BMP, André M, Federico M, Hutchings M, Illidge T et al (2018) Hodgkin lymphoma: ESMO Clinical Practice Guidelines for diagnosis, treatment and follow-up. *Ann Oncol* 29(Supplement_4):iv19–iv29
45. Engelmann BE, Loft A, Kjær A, Nielsen HJ, Berthelsen AK, Binderup T et al (2014) Positron emission tomography/computed tomography for optimized colon cancer staging and follow up. *Scand J Gastroenterol* 49(2):191–201

46. Fischerova D, Burgetova A (2014) Imaging techniques for the evaluation of ovarian cancer. *Best Pract Res Clin Obstet Gynaecol* 28(5):697–720
47. Fizazi K, Greco FA, Pavlidis N, Daugaard G, Oien K, Pentheroudakis G et al (2015) Cancers of unknown primary site: ESMO Clinical Practice Guidelines for diagnosis, treatment and follow-up. *Ann Oncol* 26(Suppl 5):v133–v138
48. Fletcher C, Unni K, Mertens F (2002) WHO classification of tumours: pathology and genetics of tumours of soft tissue and bone. IARC Press, Lyon
49. Fletcher JW, Djulbegovic B, Soares HP, Siegel BA, Lowe VJ, Lyman GH et al (2008) Recommendations on the use of ^{18}F -FDG PET in oncology. *J Nucl Med* 49(3):480–508
50. Forstner R, Sala E, Kinkel K, Spencer JA, Radiology ESOU (2010) ESUR guidelines: ovarian cancer staging and follow-up. *Eur Radiol* 20(12):2773–2780
51. Fowler KJ, Kaur H, Cash BD, Feig BW, Gage KL, Garcia EM et al (2017) ACR appropriateness criteria[®] pretreatment staging of colorectal cancer. *J Am Coll Radiol* 14(5S):S234–S244
52. Frilling A, G6rges R, Tecklenborg K, Gassmann P, Bockhorn M, Clausen M et al (2000) Value of preoperative diagnostic modalities in patients with recurrent thyroid carcinoma. *Surgery* 128(6):1067–1074
53. Fugl6 HM, J6rgensen SM, Loft A, Hovgaard D, Petersen MM (2012) The diagnostic and prognostic value of ^{18}F -FDG PET/CT in the initial assessment of high-grade bone and soft tissue sarcoma. A retrospective study of 89 patients. *Eur J Nucl Med Mol Imaging* 39(9):1416–1424
54. Fujioka T, Kubota K, Toriihara A, Machida Y, Okazawa K, Nakagawa T et al (2016) Tumor characteristics of ductal carcinoma in situ of breast visualized on [^{18}F] fluorodeoxyglucose-positron emission tomography/computed tomography: results from a retrospective study. *World J Radiol* 8(8):743–749
55. Gallagher BM, Ansari A, Atkins H, Casella V, Christman DR, Fowler JS et al (1977) Radiopharmaceuticals XXVII. ^{18}F -labeled 2-deoxy-2-fluoro-d-glucose as a radiopharmaceutical for measuring regional myocardial glucose metabolism in vivo: tissue distribution and imaging studies in animals. *J Nucl Med* 18(10):990–996
56. Goense L, van Rossum PS, Reitsma JB, Lam MG, Meijer GJ, van Vulpen M et al (2015) Diagnostic performance of ^{18}F -FDG PET and PET/CT for the detection of recurrent esophageal cancer after treatment with curative intent: a systematic review and meta-analysis. *J Nucl Med* 56(7):995–1002
57. Gradishar WJ, Anderson BO, Balassanian R, Blair SL, Burstein HJ, Cyr A et al (2015) Breast cancer version 2.2015, NCCN Clinical Practice Guidelines in oncology. *J Natl Compr Canc Netw* 13(4):448–475
58. Groheux D (2017) FDG-PET/CT for systemic staging of patients with newly diagnosed breast cancer. *Eur J Nucl Med Mol Imaging* 44(9):1417–1419
59. Groheux D, Mankoff D, Espi6 M, Hindi6 E (2016) ^{18}F -FDG PET/CT in the early prediction of pathological response in aggressive subtypes of breast cancer: review of the literature and recommendations for use in clinical trials. *Eur J Nucl Med Mol Imaging* 43(5):983–993
60. Hakenberg OW, Comp6rat EM, Minhas S, Necchi A, Protzel C, Watkin N (2015) EAU guidelines on penile cancer: 2014 update. *Eur Urol* 67(1):142–150
61. Hallqvist A, Alverbratt C, Strandell A, Samuelsson O, Bj6rkander E, Liljegren A et al (2017) Positron emission tomography and computed tomographic imaging (PET/CT) for dose planning purposes of thoracic radiation with curative intent in lung cancer patients: a systematic review and meta-analysis. *Radiother Oncol* 123(1):71–77
62. Hassanzadeh-Rad A, Yousefifard M, Katal S, Asady H, Fard-Esfahani A, Moghadas Jafari A et al (2016) The value of (^{18}F) F-fluorodeoxyglucose positron emission tomography for prediction of treatment response in gastrointestinal stromal tumors: a systematic review and meta-analysis. *J Gastroenterol Hepatol* 31(5):929–935
63. Haugen BR, Alexander EK, Bible KC, Doherty GM, Mandel SJ, Nikiforov YE et al (2016) 2015 American Thyroid Association Management Guidelines for adult patients with thyroid

- nodules and differentiated thyroid cancer: the american thyroid association guidelines task force on thyroid nodules and differentiated thyroid cancer. *Thyroid* 26(1):1–133
64. Helsen N, Van den Wyngaert T, Carp L, Stroobants S (2018) FDG-PET/CT for treatment response assessment in head and neck squamous cell carcinoma: a systematic review and meta-analysis of diagnostic performance. *Eur J Nucl Med Mol Imaging* 45(6):1063–1071
 65. Herrmann K, Benz MR, Krause BJ, Pomykala KL, Buck AK, Czernin J (2011) (18) F-FDG-PET/CT in evaluating response to therapy in solid tumors: where we are and where we can go. *Q J Nucl Med Mol Imaging* 55(6):620–632
 66. Herrmann K, Ott K, Buck AK, Lordick F, Wilhelm D, Souvatzoglou M et al (2007) Imaging gastric cancer with PET and the radiotracers ^{18}F -FLT and ^{18}F -FDG: a comparative analysis. *J Nucl Med* 48(12):1945–1950
 67. Hongtao L, Hui Z, Bingshun W, Xiaojin W, Zhiyu W, Shuier Z et al (2012) ^{18}F -FDG positron emission tomography for the assessment of histological response to neoadjuvant chemotherapy in osteosarcomas: a meta-analysis. *Surg Oncol* 21(4):e165–e170
 68. Hoppe RT, Advani RH, Ai WZ, Ambinder RF, Aoun P, Bello CM et al (2017) Hodgkin lymphoma version 1.2017, NCCN clinical practice guidelines in oncology. *J Natl Compr Canc Netw* 15(5):608–638
 69. Huang SH, O'Sullivan B, Xu W, Zhao H, Chen DD, Ringash J et al (2013) Temporal nodal regression and regional control after primary radiation therapy for N2-N3 head-and-neck cancer stratified by HPV status. *Int J Radiat Oncol Biol Phys* 87(5):1078–1085
 70. Hübner G, Borner M, Neben K, Stöger H (2018) CUP-Syndrom—Krebserkrankungen mit unbekanntem Primärtumor. DGHO (Deutsche Gesellschaft für Hämatologie und Onkologie). Onkopedia. <https://www.onkopedia.com/de/onkopedia/guidelines/cup-syndrom-krebserkrankungen-mit-unbekanntem-primartumor/@@view/html/index.html>. Accessed 1 Sept 2018
 71. Ioannidis JP, Lau J (2003) ^{18}F -FDG PET for the diagnosis and grading of soft-tissue sarcoma: a meta-analysis. *J Nucl Med* 44(5):717–724
 72. Jadvar H (2013) Imaging evaluation of prostate cancer with ^{18}F -fluorodeoxyglucose PET/CT: utility and limitations. *Eur J Nucl Med Mol Imaging* 40(Suppl 1):S5–10
 73. Jadvar H (2016) Is there use for FDG-PET in prostate cancer? *Semin Nucl Med* 46(6):502–506
 74. Jadvar H, Colletti PM, Delgado-Bolton R, Esposito G, Krause BJ, Iagaru AH et al (2017) Appropriate Use Criteria for ^{18}F -FDG-PET/CT in Restaging and Treatment Response Assessment of Malignant Disease. *J Nucl Med* 58(12):2026–2037
 75. Jakić-Razumović J, Aurer I (2002) The World Health Organization classification of lymphomas. *Croat Med J* 43(5):527–534
 76. Jakobsen JK, Alslev L, Ipsen P, Costa JC, Krarup KP, Sommer P et al (2016) DaPeCa-3: promising results of sentinel node biopsy combined with (18) F-fluorodeoxyglucose positron emission tomography/computed tomography in clinically lymph node-negative patients with penile cancer—a national study from Denmark. *BJU Int* 118(1):102–111
 77. Johnson P, Federico M, Kirkwood A, Fosså A, Berkahn L, Carella A et al (2016) Adapted Treatment guided by interim PET-CT scan in advanced Hodgkin's lymphoma. *N Engl J Med* 374(25):2419–2429
 78. Jung NY, Yoo IR, Kang BJ, Kim SH, Chae BJ, Seo YY (2016) Clinical significance of FDG-PET/CT at the postoperative surveillance in the breast cancer patients. *Breast Cancer* 23(1):141–148
 79. Jung W, Jang JY, Kang MJ, Chang YR, Shin YC, Chang J et al (2016) The clinical usefulness of ^{18}F -fluorodeoxyglucose positron emission tomography-computed tomography (PET-CT) in follow-up of curatively resected pancreatic cancer patients. *HPB (Oxford)* 18(1):57–64
 80. Kamiyama Y, Aihara R, Nakabayashi T, Mochiki E, Asao T, Kuwano H et al (2005) ^{18}F -fluorodeoxyglucose positron emission tomography: useful technique for predicting malignant potential of gastrointestinal stromal tumors. *World J Surg* 29(11):1429–1435

81. Kang SK, Reinhold C, Atri M, Benson CB, Bhosale PR, Jhingran A et al (2018) ACR Appropriateness Criteria[®] staging and follow-up of ovarian cancer. *J Am Coll Radiol* 15 (5S):S198–S207
82. Kitajima K, Nakajo M, Kaida H, Minamimoto R, Hirata K, Tsurusaki M et al (2017) Present and future roles of FDG-PET/CT imaging in the management of gastrointestinal cancer: an update. *Nagoya J Med Sci* 79(4):527–543
83. Koolen BB, van der Leij F, Vogel WV, Rutgers EJ, Vrancken Peeters MJ, Elkhuzen PH et al (2014) Accuracy of ¹⁸F-FDG PET/CT for primary tumor visualization and staging in T1 breast cancer. *Acta Oncol* 53(1):50–57
84. Koolen BB, Vrancken Peeters MJ, Aukema TS, Vogel WV, Oldenburg HS, van der Hage JA et al (2012) ¹⁸F-FDG PET/CT as a staging procedure in primary stage II and III breast cancer: comparison with conventional imaging techniques. *Breast Cancer Res Treat* 131 (1):117–126
85. Kumar Dhingra V, Kand P, Basu S (2012) Impact of FDG-PET and -PET/CT imaging in the clinical decision-making of ovarian carcinoma: an evidence-based approach. *Womens Health (Lond)* 8(2):191–203
86. Kung BT, Yong TK, Tong CM (2017) The pearl of FDG PET/CT in preoperative assessment of patients with potentially operable non-small-cell lung cancer and its clinical impact. *World J Nucl Med* 16(1):21–25
87. Kwee TC, Kwee RM (2009) Combined FDG-PET/CT for the detection of unknown primary tumors: systematic review and meta-analysis. *Eur Radiol* 19(3):731–744
88. Lagergren J, Smyth E, Cunningham D, Lagergren P (2017) Oesophageal cancer. *Lancet* 390 (10110):2383–2396
89. Lee AY, Choi SJ, Jung KP, Park JS, Lee SM, Bae SK (2014) Characteristics of metastatic mediastinal lymph nodes of non-small cell lung cancer on preoperative F-18 FDG PET/CT. *Nucl Med Mol Imaging* 48(1):41–46
90. Lee JH, Lee MR (2014) Positron emission tomography/computed tomography in the staging of colon cancer. *Ann Coloproctol* 30(1):23–27
91. Lewin J, Sayers L, Kee D, Walpole I, Sanelli A, Te Marvelde L et al (2018) Surveillance imaging with FDG-PET/CT in the post-operative follow-up of stage 3 melanoma. *Ann Oncol* 29(7):1569–1574
92. Li P, Liu Q, Wang C, Wang T, Liu J, Huang G et al (2016) Fluorine-18-fluorodeoxyglucose positron emission tomography to evaluate recurrent gastric cancer after surgical resection: a systematic review and meta-analysis. *Ann Nucl Med* 30(3):179–187
93. Liu F, Zhang Q, Zhu D, Li Z, Li J, Wang B et al (2015) Performance of positron emission tomography and positron emission tomography/computed tomography using fluorine-18-fluorodeoxyglucose for the diagnosis, staging, and recurrence assessment of bone sarcoma: a systematic review and meta-analysis. *Medicine (Baltimore)* 94(36):e1462
94. Lordick F, Mariette C, Haustermans K, Obermannová R, Arnold D, Committee EG (2016) Oesophageal cancer: ESMO Clinical Practice Guidelines for diagnosis, treatment and follow-up. *Ann Oncol* 27(suppl 5):v50–v57
95. Lordick F, Ott K, Krause BJ, Weber WA, Becker K, Stein HJ et al (2007) PET to assess early metabolic response and to guide treatment of adenocarcinoma of the oesophagogastric junction: the MUNICON phase II trial. *Lancet Oncol* 8(9):797–805
96. Lu YY, Chen JH, Chien CR, Chen WT, Tsai SC, Lin WY et al (2013) Use of FDG-PET or PET/CT to detect recurrent colorectal cancer in patients with elevated CEA: a systematic review and meta-analysis. *Int J Colorectal Dis* 28(8):1039–1047
97. Lu YY, Chen JH, Liang JA, Chu S, Lin WY, Kao CH (2014) ¹⁸F-FDG PET or PET/CT for detecting extensive disease in small-cell lung cancer: a systematic review and meta-analysis. *Nucl Med Commun* 35(7):697–703
98. MacManus MP, Hicks RJ, Matthews JP, Hogg A, McKenzie AF, Wirth A et al (2001) High rate of detection of unsuspected distant metastases by pet in apparent stage III non-small-cell

- lung cancer: implications for radical radiation therapy. *Int J Radiat Oncol Biol Phys* 50 (2):287–293
99. Maffione AM, Lopci E, Bluemel C, Giammarile F, Herrmann K, Rubello D (2015) Diagnostic accuracy and impact on management of (18)F-FDG PET and PET/CT in colorectal liver metastasis: a meta-analysis and systematic review. *Eur J Nucl Med Mol Imaging* 42(1):152–163
 100. Maffione AM, Marzola MC, Capirci C, Colletti PM, Rubello D (2015) Value of (18)F-FDG PET for predicting response to neoadjuvant therapy in rectal cancer: systematic review and meta-analysis. *AJR Am J Roentgenol* 204(6):1261–1268
 101. Malle P, Sorschag M, Gallowitsch HJ (2012) FDG PET and FDG PET/CT in patients with gastrointestinal stromal tumours. *Wien Med Wochenschr* 162(19–20):423–429
 102. Mamede M, Higashi T, Kitaichi M, Ishizu K, Ishimori T, Nakamoto Y et al (2005) [18F] FDG uptake and PCNA, Glut-1, and Hexokinase-II expressions in cancers and inflammatory lesions of the lung. *Neoplasia* 7(4):369–379
 103. Marcus C, Ciarallo A, Tahari AK, Mena E, Koch W, Wahl RL et al (2014) Head and neck PET/CT: therapy response interpretation criteria (Hopkins Criteria)—interreader reliability, accuracy, and survival outcomes. *J Nucl Med* 55(9):1411–1416
 104. Maziak DE, Darling GE, Incelet RI, Gulenchyn KY, Driedger AA, Ung YC et al (2009) Positron emission tomography in staging early lung cancer: a randomized trial. *Ann Intern Med* 151(4):221–228, W-48
 105. Mehanna H, Wong WL, McConkey CC, Rahman JK, Robinson M, Hartley AG et al (2016) PET-CT surveillance versus neck dissection in advanced head and neck cancer. *N Engl J Med* 374(15):1444–1454
 106. Mena E, Taghipour M, Sheikhabahaei S, Mirpour S, Xiao J, Subramaniam RM (2016) ¹⁸F-FDG PET/CT and melanoma: value of fourth and subsequent posttherapy follow-up scans for patient management. *Clin Nucl Med* 41(9):e403–e409
 107. Metser U, Dubebout J, Baetz T, Hodgson DC, Langer DL, MacCrostie P et al (2017) [18 F]-FDG PET/CT in the staging and management of indolent lymphoma: a prospective multicenter PET registry study. *Cancer* 123(15):2860–2866
 108. Mody RJ, Bui C, Hutchinson RJ, Yanik GA, Castle VP, Frey KA et al (2010) FDG PET imaging of childhood sarcomas. *Pediatr Blood Cancer* 54(2):222–227
 109. Moller AK, Loft A, Berthelsen AK, Damgaard Pedersen K, Graff J, Christensen CB et al (2011) ¹⁸F-FDG PET/CT as a diagnostic tool in patients with extracervical carcinoma of unknown primary site: a literature review. *Oncologist* 16(4):445–451
 110. Necchi A, Nicolai N, Alessi A, Miceli R, Giannatempo P, Raggi D et al (2016) Interim (18) F-Fluorodeoxyglucose positron emission tomography for early metabolic assessment of response to cisplatin, etoposide, and bleomycin chemotherapy for metastatic seminoma: clinical value and future directions. *Clin Genitourin Cancer* 14(3):249–254
 111. NSCLC Meta-analysis Collaborative Group (2014) Preoperative chemotherapy for non-small-cell lung cancer: a systematic review and meta-analysis of individual participant data. *Lancet* 383(9928):1561–1571
 112. Oldenburg J, Fosså SD, Nuver J, Heidenreich A, Schmoll HJ, Bokemeyer C et al (2013) Testicular seminoma and non-seminoma: ESMO Clinical Practice Guidelines for diagnosis, treatment and follow-up. *Ann Oncol* 24 Suppl 6:vi125–vi132
 113. Ott K, Schmidt T, Lordick F, Herrmann K (2014) Importance of PET in surgery of esophageal cancer. *Chirurg* 85(6):505–512
 114. Ottenhof SR, Leone AR, Horenblas S, Spiess PE, Vegt E (2017) Advancements in staging and imaging for penile cancer. *Curr Opin Urol* 27(6):612–620
 115. Pacini F, Castagna MG, Brilli L, Pentheroudakis G, Group EGW (2012) Thyroid cancer: ESMO Clinical Practice Guidelines for diagnosis, treatment and follow-up. *Ann Oncol* 23 Suppl 7:viii10–viii19

116. Pak K, Kim K, Kim MH, Eom JS, Lee MK, Cho JS et al (2018) A decision tree model for predicting mediastinal lymph node metastasis in non-small cell lung cancer with F-18 FDG PET/CT. *PLoS ONE* 13(2):e0193403
117. Park HL, Yoo IR, O JH, Kim H, Kim SH, Kang BJ (2018) Clinical utility of ¹⁸F-FDG PET/CT in low ¹⁸F-FDG-avidity breast cancer subtypes: comparison with breast US and MRI. *Nucl Med Commun* 39(1):35–43
118. Petersen RK, Hess S, Alavi A, Høilund-Carlsen PF (2014) Clinical impact of FDG-PET/CT on colorectal cancer staging and treatment strategy. *Am J Nucl Med Mol Imaging*. 4(5):471–482
119. Piva R, Ticconi F, Ceriani V, Scalorbi F, Fiz F, Capitanio S et al (2017) Comparative diagnostic accuracy of ¹⁸F-FDG PET/CT for breast cancer recurrence. *Breast Cancer (Dove Med Press)* 9:461–471
120. Porschen R, Buck A, Fischbach W, Gockel I, Görling U, Grenacher L et al (2015) S3-Leitlinie Diagnostik und Therapie der Plattenepithelkarzinome und Adenokarzinome des Ösophagus (Langversion 1.0—September 2015, AWMF-Registernummer: 021/023OL). *Z Gastroenterol* 53(11):1288–1347
121. Purandare NC, Pramesh CS, Karimundackal G, Jiwnani S, Agrawal A, Shah S et al (2014) Incremental value of ¹⁸F-FDG PET/CT in therapeutic decision-making of potentially curable esophageal adenocarcinoma. *Nucl Med Commun* 35(8):864–869
122. Rakheja R, Makis W, Skamene S, Nahal A, Brimo F, Azoulay L et al (2012) Correlating metabolic activity on ¹⁸F-FDG PET/CT with histopathologic characteristics of osseous and soft-tissue sarcomas: a retrospective review of 136 patients. *AJR Am J Roentgenol* 198(6):1409–1416
123. Rodriguez Rivera AM, Alabbas H, Ramjaun A, Meguerditchian AN (2014) Value of positron emission tomography scan in stage III cutaneous melanoma: a systematic review and meta-analysis. *Surg Oncol* 23(1):11–16
124. Rodriguez E, Lilenbaum RC (2010) Small cell lung cancer: past, present, and future. *Curr Oncol Rep* 12(5):327–334
125. Rogasch JM, Apostolova I, Steffen IG, Steinkrüger FL, Genseke P, Riedel S et al (2016) Standardized visual reading of F18-FDG-PET in patients with non-small cell lung cancer scheduled for preoperative thoracic lymph node staging. *Eur J Radiol* 85(8):1345–1350
126. Ronellenfitch U, Wängler B, Niedermoser S, Dimitrakopoulou-Strauss A, Hohenberger P (2014) Importance of PET for surgery of gastrointestinal stromal tumors. *Chirurg* 85(6):493–499
127. Rubello D, Marzola MC, Colletti PM (2018) The prognostic value of ¹⁸F-FDG PET/CT in monitoring chemotherapy in ovarian cancer both at initial diagnosis and at recurrent disease. *Clin Nucl Med* 43(10):735–738
128. Sachpekidis C, Anwar H, Winkler J, Kopp-Schneider A, Larribere L, Haberkorn U et al (2018) The role of interim ¹⁸F-FDG PET/CT in prediction of response to ipilimumab treatment in metastatic melanoma. *Eur J Nucl Med Mol Imaging* 45(8):1289–1296
129. Schreyögg J, Weller J, Stargardt T, Herrmann K, Bluemel C, Dechow T et al (2010) Cost-effectiveness of hybrid PET/CT for staging of non-small cell lung cancer. *J Nucl Med* 51(11):1668–1675
130. Schwarz JK, Grigsby PW, Dehdashti F, Delbeke D (2009) The role of ¹⁸F-FDG PET in assessing therapy response in cancer of the cervix and ovaries. *J Nucl Med* 50(Suppl 1):64S–73S
131. Sheikhabaehi S, Taghipour M, Ahmad R, Fakhry C, Kiess AP, Chung CH et al (2015) Diagnostic accuracy of follow-up FDG PET or PET/CT in patients with head and neck cancer after definitive treatment: a systematic review and meta-analysis. *AJR Am J Roentgenol* 205(3):629–639
132. Siegel RL, Miller KD, Jemal A (2017) Cancer statistics, 2017. *CA Cancer J Clin* 67(1):7–30

133. Signorelli M, Guerra L, Pirovano C, Crivellaro C, Fruscio R, Buda A et al (2013) Detection of nodal metastases by ^{18}F -FDG PET/CT in apparent early stage ovarian cancer: a prospective study. *Gynecol Oncol* 131(2):395–399
134. Silvestri GA, Gonzalez AV, Jantz MA, Margolis ML, Gould MK, Tanoue LT et al (2013) Methods for staging non-small cell lung cancer: diagnosis and management of lung cancer, 3rd ed: American College of Chest Physicians evidence-based clinical practice guidelines. *Chest* 143(5 Suppl):e211S–e50S
135. Silvestri GA, Gould MK, Margolis ML, Tanoue LT, McCrory D, Toloza E et al (2007) Noninvasive staging of non-small cell lung cancer: ACCP evidenced-based clinical practice guidelines (2nd edn). *Chest* 132(3 Suppl):178S–201S
136. Singnurkar A, Wang J, Joshua AM, Langer DL, Metser U (2016) ^{18}F -FDG-PET/CT in the staging and management of melanoma: a prospective multicenter ontario PET registry study. *Clin Nucl Med* 41(3):189–193
137. Sobic-Saranovic D, Petrusic I, Artiko V, Pavlovic S, Subotic D, Saranovic D et al (2015) Comparison of ^{18}F -FDG PET/CT and MDCT for staging/restaging of non-small cell lung cancer. *Neoplasma* 62(2):295–301
138. Stahl A, Ott K, Weber WA, Becker K, Link T, Siewert JR et al (2003) FDG PET imaging of locally advanced gastric carcinomas: correlation with endoscopic and histopathological findings. *Eur J Nucl Med Mol Imaging* 30(2):288–295
139. Sun R, Tang X, Yang Y, Zhang C (2015) ^{18}F -FDG-PET/CT for the detection of regional nodal metastasis in patients with head and neck cancer: a meta-analysis. *Oral Oncol* 51(4):314–320
140. Sun Z, Yi YL, Liu Y, Xiong JP, He CZ (2015) Comparison of whole-body PET/PET-CT and conventional imaging procedures for distant metastasis staging in patients with breast cancer: a meta-analysis. *Eur J Gynaecol Oncol* 36(6):672–676
141. Tang S, Huang G, Liu J, Liu T, Treven L, Song S et al (2011) Usefulness of ^{18}F -FDG PET, combined FDG-PET/CT and EUS in diagnosing primary pancreatic carcinoma: a meta-analysis. *Eur J Radiol* 78(1):142–150
142. The Royal College Of Radiologists; Royal College Of Physicians Of London; Royal College Of Physicians And Surgeons Of Glasgow; Royal College Of Physicians Of Edinburgh; British Nuclear Medicine Society; Administration Of Radioactive Substances Advisory Committee (2016) Evidence-based indications for the use of PET-CT in the United Kingdom 2016. *Clin Radiol* 71(7):e171–188
143. Tian F, Shen G, Deng Y, Diao W, Jia Z (2017) The accuracy of ^{18}F -FDG PET/CT in predicting the pathological response to neoadjuvant chemotherapy in patients with breast cancer: a meta-analysis and systematic review. *Eur Radiol* 27(11):4786–4796
144. Tönnies S, Bauer TT, Misch D, Boch C, Blum T, Bittner RC et al (2012) Staging with ^{18}F -FDG-PET/CT influences stage-specific survival in advanced non-small cell lung cancer (NSCLC). *Pneumologie* 66(4):212–217
145. Topkan E, Parlak C, Yapar AF (2013) FDG-PET/CT-based restaging may alter initial management decisions and clinical outcomes in patients with locally advanced pancreatic carcinoma planned to undergo chemoradiotherapy. *Cancer Imaging* 13(3):423–428
146. Torre LA, Bray F, Siegel RL, Ferlay J, Lortet-Tieulent J, Jemal A (2015) Global cancer statistics, 2012. *CA Cancer J Clin* 65(2):87–108
147. Treglia G, Mirk P, Stefanelli A, Rufini V, Giordano A, Bonomo L (2012) ^{18}F -Fluorodeoxyglucose positron emission tomography in evaluating treatment response to imatinib or other drugs in gastrointestinal stromal tumors: a systematic review. *Clin Imaging* 36(3):167–175
148. Treglia G, Sadeghi R, Annunziata S, Caldarella C, Bertagna F, Giovannella L (2014) Diagnostic performance of fluorine-18-fluorodeoxyglucose positron emission tomography in the postchemotherapy management of patients with seminoma: systematic review and meta-analysis. *Biomed Res Int* 2014:852681

149. Van Cutsem E, Cervantes A, Adam R, Sobrero A, Van Krieken JH, Aderka D et al (2016) ESMO consensus guidelines for the management of patients with metastatic colorectal cancer. *Ann Oncol* 27(8):1386–1422
150. Van den Abbeele AD (2008) The lessons of GIST—PET and PET/CT: a new paradigm for imaging. *Oncologist* 13(Suppl 2):8–13
151. Van Poppel H, Watkin NA, Osanto S, Moonen L, Horwich A, Kataja V et al (2013) Penile cancer: ESMO Clinical Practice Guidelines for diagnosis, treatment and follow-up. *Ann Oncol* 24 Suppl 6:vi115–24
152. van Tinteren H, Hoekstra OS, Smit EF, van den Bergh JH, Schreurs AJ, Stallaert RA et al (2002) Effectiveness of positron emission tomography in the preoperative assessment of patients with suspected non-small-cell lung cancer: the PLUS multicentre randomised trial. *Lancet* 359(9315):1388–1393
153. Vensby PH, Schmidt G, Kjaer A, Fischer BM (2017) The value of FDG PET/CT for follow-up of patients with melanoma: a retrospective analysis. *Am J Nucl Med Mol Imaging* 7(6):255–262
154. Vincent A, Herman J, Schulick R, Hruban RH, Goggins M (2011) Pancreatic cancer. *Lancet* 378(9791):607–620
155. Voltin CA, Goergen H, Baues C, Fuchs M, Mettler J, Kreissl S et al (2018) Value of bone marrow biopsy in Hodgkin lymphoma patients staged by FDG PET: results from the German Hodgkin Study Group trials HD16, HD17, and HD18. *Ann Oncol* 29(9):1926–1931
156. von Mehren M, Randall RL, Benjamin RS, Boles S, Bui MM, Ganjoo KN et al (2018) Soft tissue sarcoma, Version 2.2018, NCCN clinical practice guidelines in oncology. *J Natl Compr Canc Netw* 16(5):536–563
157. Wahl RL, Jacene H, Kasamon Y, Lodge MA (2009) From RECIST to PERCIST: evolving considerations for PET response criteria in solid tumors. *J Nucl Med* 50(Suppl 1):122S–150S
158. Wahl RL, Zasadny K, Helvie M, Hutchins GD, Weber B, Cody R (1993) Metabolic monitoring of breast cancer chemohormonotherapy using positron emission tomography: initial evaluation. *J Clin Oncol* 11(11):2101–2111
159. Warburg O (1928) The chemical constitution of respiration ferment. *Science* 68(1767):437–443
160. Weiler-Sagie M, Bushelev O, Epelbaum R, Dann EJ, Haim N, Avivi I et al (2010) (18)F-FDG avidity in lymphoma readdressed: a study of 766 patients. *J Nucl Med* 51(1):25–30
161. Wong WL, Chambers RJ (2008) Role of PET/PET CT in the staging and restaging of thoracic oesophageal cancer and gastro-oesophageal cancer: a literature review. *Abdom Imaging* 33(2):183–190
162. Wu LM, Hu JN, Hua J, Gu HY, Zhu J, Xu JR (2012) ¹⁸F-fluorodeoxyglucose positron emission tomography to evaluate recurrent gastric cancer: a systematic review and meta-analysis. *J Gastroenterol Hepatol* 27(3):472–480
163. Xiao Y, Wang L, Jiang X, She W, He L, Hu G (2016) Diagnostic efficacy of ¹⁸F-FDG-PET or PET/CT in breast cancer with suspected recurrence: a systematic review and meta-analysis. *Nucl Med Commun* 37(11):1180–1188
164. Xing Y, Bronstein Y, Ross MI, Askew RL, Lee JE, Gershenwald JE et al (2011) Contemporary diagnostic imaging modalities for the staging and surveillance of melanoma patients: a meta-analysis. *J Natl Cancer Inst* 103(2):129–142
165. Yazarbas U, Avci NC, Yeniay L, Argon AM (2018) The value of ¹⁸F-FDG PET/CT imaging in breast cancer staging. *Bosn J Basic Med Sci.* 18(1):72–79
166. Yu T, Meng N, Chi D, Zhao Y, Wang K, Luo Y (2015) Diagnostic Value of (18)F-FDG PET/CT in detecting local recurrent colorectal cancer: a pooled analysis of 26 individual studies. *Cell Biochem Biophys* 72(2):443–451
167. Zer A, Domachevsky L, Rapson Y, Nidam M, Flex D, Allen AM et al (2016) The role of ¹⁸F-FDG PET/CT on staging and prognosis in patients with small cell lung cancer. *Eur Radiol* 26(9):3155–3161

168. Zhang C, Liu J, Tong J, Sun X, Song S, Huang G (2013) ^{18}F -FDG-PET evaluation of pathological tumour response to neoadjuvant therapy in patients with NSCLC. *Nucl Med Commun* 34(1):71–77
169. Zhang S, Li W, Liang F (2016) Clinical value of fluorine-18 2-fluoro-2-deoxy-D-glucose positron emission tomography/computed tomography in penile cancer. *Oncotarget* 7 (30):48600–48606
170. Zhu L, Wang N (2013) ^{18}F -fluorodeoxyglucose positron emission tomography-computed tomography as a diagnostic tool in patients with cervical nodal metastases of unknown primary site: a meta-analysis. *Surg Oncol* 22(3):190–194
171. zum Büschenfelde CM, Herrmann K, Schuster T, Geinitz H, Langer R, Becker K et al (2011) ^{18}F -FDG PET-guided salvage neoadjuvant radiochemotherapy of adenocarcinoma of the esophagogastric junction: the MUNICON II trial. *J Nucl Med* 52(8):1189–1196



Egesta Lopci and Stefano Fanti

Contents

20.1	Introduction to Non-FDG PET Tracers	670
20.2	Clinical Applications of ¹¹ C/ ¹⁸ F-Choline	671
20.3	Clinical Applications of ¹¹ C-Acetate	674
20.4	Clinical Applications of ⁶⁸ Ga-PSMA	676
20.5	Clinical Applications of ¹⁸ F-FACBC.....	678
20.6	Clinical Applications of ¹¹ C-Methionine.....	679
20.7	Clinical Applications of ¹⁸ F-FET.....	682
20.8	Clinical Applications of ¹⁸ F-DOPA.....	684
20.9	Clinical Applications of ⁶⁸ Ga-DOTA-Peptides	688
20.10	Clinical Applications of ¹⁸ F-FLT.....	691
20.11	Clinical Applications of ¹⁸ F-Fluoride	693
20.12	Clinical Applications of ¹²⁴ I-Na.....	695
20.13	Clinical Potential of PET Tracers for Hypoxia	697
20.14	Clinical Potential of PET Tracers for Angiogenesis	698
20.15	Clinical Potential of Immune-PET Tracers.....	699
	References.....	700

E. Lopci (✉)

Nuclear Medicine Department, Humanitas Clinical and Research Hospital—IRCCS,
Via Manzoni 56, 20089 Rozzano, MI, Italy

e-mail: egesta.lopci@gmail.com; egesta.lopci@cancercenter.humanitas.it

S. Fanti

Metropolitan Nuclear Medicine, University Hospital S. Orsola-Malpighi, Alma Mater
Studiorum, University of Bologna, Via Massarenti 9, 40138 Bologna, Italy

e-mail: stefano.fanti@aosp.bo.it

© Springer Nature Switzerland AG 2020

O. Schober et al. (eds.), *Molecular Imaging in Oncology*,

Recent Results in Cancer Research 216,

https://doi.org/10.1007/978-3-030-42618-7_20

20.1 Introduction to Non-FDG PET Tracers

In 2011, the medical oncologist Siddhartha Mukherjee was assigned the Pulitzer Prize for publishing “The Emperor of All Maladies: A Biography of Cancer” [246]. Along with a brilliant summary of cancer history, the book clearly stated already in the cover the undisputable relevance that cancer has in human life. Undoubtedly, with longer life expectancy in modern era, humankind has found a new “Black Death” in oncologic pathologies. Consequently, timely diagnosis has become as crucial as treatment itself. Hence, a big leap in medical diagnosis was determined with the introduction of molecular imaging, positron emission tomography (PET/CT) and all the associated compounds allowing cancer detection and clinical assessment in different oncologic settings.

Since its approval by the Food and Drug Administration in 2000, a major breakthrough for PET imaging was represented by the introduction in clinical practice of 18F-Fluorodeoxyglucose (18F-FDG). Up to now, more than 90% of worldwide studies with PET are performed using 18F-FDG. Although 18F-FDG PET performs with a high sensitivity and specificity in the majority of cancer types, it remains independently a “nonspecific” tracer. As a glucose analogue, it provides functional information on cellular metabolism, and as an oncologic tracer, its use is essentially based on the so-called Warburg effect [364]. The phenomenon, however, is not a transversal characteristic for all tumours, and some of them on contrary can show a reduced 18F-FDG uptake. Many malignancies, in fact, are poorly imaged by 18F-FDG, comprising prostate cancer [182, 183, 306], hepatocellular carcinoma (HCC) [150], renal cell carcinoma (RCC), low-grade sarcomas, low-grade lymphomas, brain tumours, well-differentiated neuroendocrine tumours, etc. [79, 179, 263]. Moreover, this PET tracer cannot differentiate between cells that have a high metabolic rate associated with neoplasia and those with increased metabolism due to other conditions, such as infection, inflammation or even normal physiological uptake.

The acquired knowledge on cancer features, however, have allowed the recognition in the last decades of multiple metabolic or pathogenic pathways within the cancer cells. Consequently, the development of new radiotracers has become of utmost importance in clinical practice. Many alternative PET tracers have been proposed and evaluated in preclinical and clinical studies and, in the last decades, an endless list of PET tracers, substantially covering all hallmarks of cancer, has entered the clinical routine.

However, just a limited portrayal of them guards a relevant impact on clinical practice and this chapter aims describing the most significant representatives. Some necessary space will be still dedicated to three large families of special compounds bearing on counterpart a huge clinical potential.

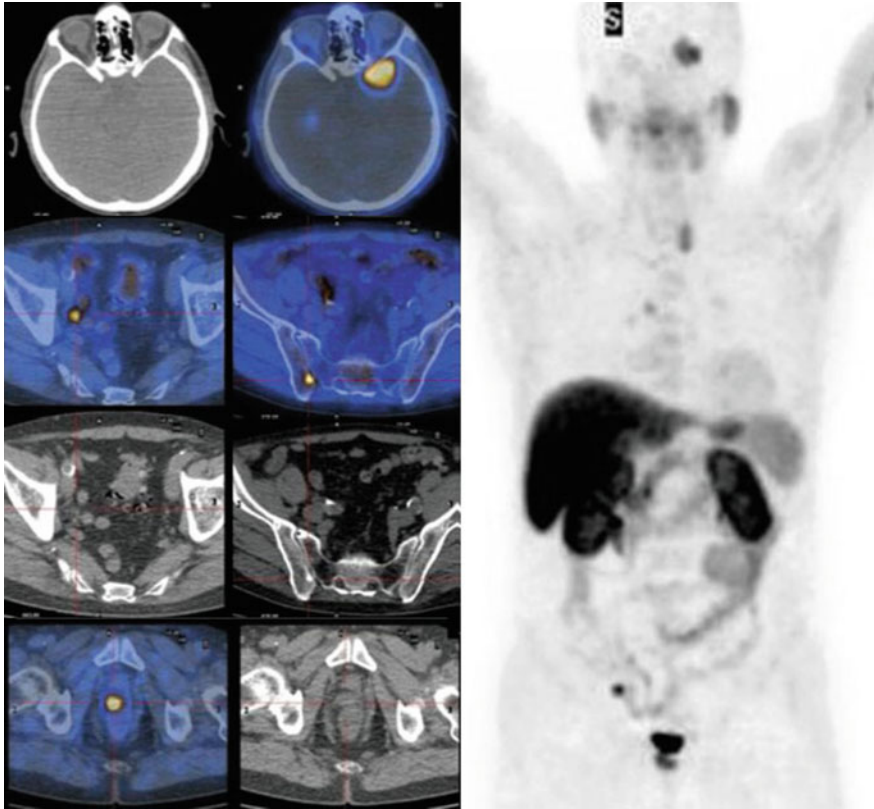


Fig. 20.1 MIP image of ^{11}C -Choline PET/CT (right-sided panel of the figure), with transversal images of single pathologic findings in a high-risk PCa patient at initial staging; local recurrence (inferior view); imaging bone lesion and nodal involvement (mid views); a large malignant lesion is also visible in the brain (superior view)

20.2 Clinical Applications of $^{11}\text{C}/^{18}\text{F}$ -Choline

Carbon-11 choline (^{11}C -Choline) is a small molecule that was at first introduced in PET imaging in 1997 [132] for the detection of brain and prostatic cancer. It is rapidly taken up, phosphorylated by choline kinase to phosphocholine and trapped within the cell to be integrated into cellular membranes, as a precursor for the biosynthesis of phospholipids (phosphatidilcholine) [266, 382]. The uptake of ^{11}C -choline is a marker for membrane turnover and metabolism [356], which are reported to be substantially increased in malignant cells [1, 282, 335].

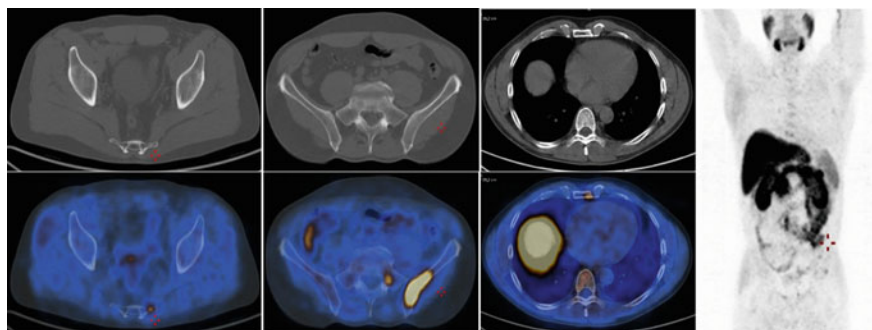


Fig. 20.2 MIP image of ^{11}C -Choline PET/CT (right-sided panel of the figure), with transversal images of the multiple pathological bony lesions in a PCa patient with biochemical relapse after radical prostatectomy (PSA 8.8 ng/ml)

The physiological distribution of ^{11}C -Choline includes the salivary glands, liver, renal parenchyma and pancreas, which can be detected already a few minutes after the injection (3–5 min). Some faint uptake can be visualized also in the spleen, bone marrow, muscles and bowel. ^{11}C -Choline is successfully taken up in various tumours with a high signal-to-background ratio, including slowly growing ones, and presents a late urinary excretion phase, which makes it a good tracer for the detection of prostate and bladder cancers [130, 133, 196, 279].

The main drawbacks of this tracer are related to the short half-life of the radionuclide ^{11}C ($T_{1/2}$ 20 min) and the rapid *in vivo* oxidation [356], which led to the development of ^{18}F -labelled choline analogues, such as ^{18}F -fluorocholine (FCH) [64, 71, 131]. The synthesis of FCH was first described by Degrado et al. [71]. Normal biodistribution of FCH shows relatively high uptake in the salivary and lachrymal glands, pancreas, liver, spleen and kidneys; mild uptake in the bone marrow and variable uptake in the bowel. No substantial differences have been detected in between the two radiolabelled-choline tracers, except for the earlier urinary appearance of ^{18}F -fluorocholine, probably due to an incomplete tubular reabsorption [162].

As an oncologic tracer, $^{11}\text{C}/^{18}\text{F}$ -choline has a potential role in any neoplasia, although in clinical practice it has found a principal application in prostate cancer [24, 174, 130, 199, 278].

PET imaging with ^{11}C -choline has been proposed to early detect primary prostate cancer, to stage/restage the tumour (Fig. 20.1), but the prevailing utility appears to be the detection of tumour recurrence in case of biochemical relapse (Fig. 20.2) [96, 355].

At staging ^{11}C -choline has been utilized prevalently to assess nodal and bone metastasis in prostate cancer patients [174, 130, 196, 284, 315], while less for primary tumour (T staging) [119]. The main reason is the difficulty to discriminate between malignant lesions and benign disease (i.e. prostatitis, benign prostatic

hyperplasia) by pure choline uptake [97], and second, due to the limited spatial resolution of the method (~ 5 mm), the method has a low accuracy in the detection of extra-capsular and seminal vesicle extension [315]. In particular, 11C-choline PET appears significantly less sensitive than the standard of reference (MRI) for extraprostatic extension, with a sensitivity of 22% versus 63% for MRI [239]. The same study group performed also a direct comparison of PET with sextant results of step-section histopathology and found a sensitivity, specificity and accuracy of 66%, 81% and 71%, respectively [97].

A more relevant role for 11C-choline PET in staging prostate cancer is reported in selected high-risk patients (high levels of PSA or Gleason score, etc.), with the intent to assess extraprostatic metastases. Even with respect to clinical nomograms [38], 11C-choline PET seems to perform better in the detection of nodal metastasis [315]. As reported in literature [174, 70, 278, 348, 376], 11C-choline PET accuracy (sensitivity 80%; specificity 96%; accuracy 93%) is generally better than that of conventional imaging techniques (CI) for primary PCa staging.

The main application of 11C-choline PET, however, remains the evaluation of prostate cancer relapse in previously treated patients, presenting with rising PSA serum level and negative conventional imaging procedures [50, 49]. The higher sensitivity is seen for the detection of early nodal involvement and secondary bone lesions [130, 199, 314]. Since 11C-choline uptake in malignant metastatic cells occurs before bone osteoblastic changes, the method permits the detection of bone lesions even before bone scintigraphy [174, 109, 277]. On a lesion-based analysis, 11C-choline PET shows a sensitivity, specificity and accuracy of 64%, 90% and 77%, respectively [314]. Although with a lower accuracy than for other sites of disease, 11C-choline PET is useful also in detecting local recurrence [37, 174, 277].

11C-choline PET still has an imperfect overall detection rate (39–56%) [50, 199]. This can be significantly ameliorated by adopting other parameters, such as PSA kinetics. Therefore, trigger PSA, PSA velocity and PSA doubling time [50, 49, 119, 199] can contribute to increasing the probability of having positive finding at PET, since they express somehow the malignancy of the disease relapse.

Other oncologic conditions have been successfully studied with 11C-choline PET, starting with the bladder cancer [132, 279]. Thanks to the late urinary excretion and low background activity, 11C-choline allows for a good identification of the primary bladder cancer (sensitivity 96% for PET versus 84% CT) and its proper nodal staging (sensitivity and specificity, respectively, 62% and 100% for PET versus 50% and 75% for CT) [279].

Brain tumours too are an interesting indication for 11C-choline PET [134], which, in very limited studies, have shown a potentially equal or slightly better tumour delineating capability [250]. However, it is not able to substitute amino acid radiopharmaceuticals in this context, such as 11C-methionine or 18F-FET.

11C-choline and its fluorinated analogue has been utilized with success also for imaging hepatocellular carcinoma (HCC) (Fig. 20.3) [51, 233, 377, 340, 341]. In comparison to morphological imaging (i.e. CT or MRI), 11C-choline PET has demonstrated a sensitivity and specificity of 88% and 90%, respectively, which resulted significantly higher especially in case of extra-hepatic tumour detection

[233]. This determined a modification in HCC management in 24% of the patients. The highest accuracy, however, was obtained when combining PET and CT/MRI; the diagnostic accuracy could reach 92% on a scan-based and 96% on a lesion-based analysis. Similarly, in the study from Castilla-Lièvre et al., when comparing 11C-choline with 18F-FDG PET, the sensitivity of the modalities resulted 75% for 11C-choline, 36% for 18F-FDG and 93% by combining the two scans [51].

Some preliminary results have shown for 11C-choline PET also a potential role in multiple myeloma. It seems that the tracer is capable to detect more myelomatous lesions than 18F-FDG PET, although the difference between the two tracers is not reported to be statistically significant in mean number of lesions [247, 349]. Despite the potentialities of this tracer in detecting many malignancies, 11C-choline and its fluorinated analogues, at present find a proper use in clinical practice mainly in prostate cancer patients.

20.3 Clinical Applications of 11C-Acetate

Radiolabelled acetate (11C-Acetate) was proposed as a PET compound almost 3 decades ago for tracing regional blood flow, cardiac physiology or tissue lipogenesis [10, 11]. Once injected, 11C-acetate is rapidly cleared from the bloodstream and activated within the cells into 11C-acetyl-CoA [160]. This activation may happen in the cytosol, like in cells with high lipogenic activity, such as liver, salivary glands, spleen and also many cancers [235, 336], Vallabhajosula [356], or may occur within the mitochondria, where 11C-acetyl-CoA enters the tricarboxylic acid (TCA) cycle, used for either catabolic or anabolic purpose [56, 243, 338].

The first pathway leads to the synthesis of cholesterol and fatty acids, which are incorporated into cell membranes [160], while the second, in normal cells and myocardium, leads to complete oxidation of 11C-acetyl-CoA to 11C-CO₂ and H₂O [200]. This background is the rationale for the use of 11C-acetate as a PET tracer for studying myocardial blood flow and oxidative metabolism [305, 338], as well as for visualizing certain tumours in which 18F-FDG PET is of limited use, such as prostate cancer, hepatocarcinoma and bladder cancer. [77, 79, 151, 150, 262, 264]. Also, other tumour types can show an increased uptake of 11C-acetate thanks to the above-mentioned mechanisms [283, 332, 334, 336]; i.e. meningioma, glioma, nasopharyngeal carcinoma, lymphoma, non-small cell lung cancer, colon cancer, renal cell carcinoma, ovarian cancer, etc. [79, 227, 228, 329, 378].

Yet, in tumour imaging, 11C-acetate has been mainly used for prostate cancer [79, 381] at diagnosis [61], staging/restaging [332] and detection of recurrence in biochemical relapse [9, 264]. According to the literature, the tracer is sensitive in the detection of primary tumour [262] with good accuracy in N- and M-staging, and in the detection of disease relapse [197, 264]. Haseebuddin et al. for instance, analyzed 107 men with intermediate-risk or high-risk localized PCa at diagnosis

[137]. Despite the presence of negative conventional imaging, 11C-acetate PET/CT showed positive findings for pelvic nodes or distant metastasis in 36 out of 107 patients (34%). The sensitivity, specificity, positive predictive value (PPV) and negative predictive value (NPV) resulted 68%, 78%, 49% and 89%, respectively.

One of the other indications for PCa concerns biochemical recurrence after radical prostatectomy or radiotherapy. As per tumour detection in this context, 11C-acetate PET shows a sensitivity which is variable and dependent from PSA levels. In the paper from Oyama et al. [264], the overall detection rate for 46 patients (30 after radical prostatectomy and 16 after radiation therapy) resulted 59%. When categorizing the performance based on PSA levels, 13 out of 22 (59%) had positive scan with serum PSA > 3 ng/mL, while only 1 out of 24 patients (4%) with lower serum PSA levels [264]. Higher detection rate has been demonstrated by other authors, such as Sandblom et al. [310]. With a mean PSA level of 2 ng/mL, their findings report 15 out of the 20 patients analyzed as having a positive 11C-acetate PET. On the other hand, due to the favourable tracer distribution, with no interference in the urinary tract, 11C-acetate can better detect local relapse. This is the case of the 50 patients investigated by Watcher et al. with combined 11C-acetate PET/MRI modality at biochemical relapse [60]. Based on the information provided by 11C-acetate PET, treatment management was changed in 28% of the cases, and after fusion with MRI, the number of equivocal findings was completely reduced. In general, however, the clinical applications of 11C-acetate match with those of 11C-choline PET, and, although the latter is more widely used as PET compound, the two tracers seem to yield almost identical results in patients with prostate cancer [245, 345].

Interesting data are available also for bladder cancer imaging with 11C-acetate PET. The prospective analysis from Vargas et al. [358], for instance, reports a sensitivity of 11C-acetate PET/CT for N staging of 100%, and a specificity of 71%. In the same cohort, the sensitivity and specificity for lymph node metastases were 50% and 71% for MRI, and 50% and 79% for CT, respectively. More recently, in the multicenter ACEBIB trial analyzing 11C-acetate PET/MRI for the detection of muscle invasive bladder cancer [309], the diagnostic performance was confirmed superimposable with reported sensitivity, specificity and accuracy of 100%, 69% and 73%, respectively.

Another clinical indication for 11C-acetate PET/CT concerns the investigation of HCC (Fig. 20.4). In this context, the tracer has demonstrated a higher sensitivity in patients (83–87%) as compared to 18F-FDG PET (40–47%) [164]. These data are not surprising, as it is already known that HCC is one of those tumours that may exhibit a glycolysis similar to or even lower than normal liver parenchyma [150, 170]. When combined, however, the two PET-studies may show a complementary role: when primary HCC has a low 18F-FDG uptake, there is an avid 11C-acetate uptake, and vice versa [164]. These information can be an outmost value in case of advanced treatment planning alone or in combination to loco-regional therapy, such as transarterial chemoembolization [224].

20.4 Clinical Applications of 68Ga-PSMA

Prostate specific membrane antigen (PSMA) is a type II transmembrane glycoprotein, also known as glutamate carboxypeptidase II, which results significantly overexpressed in prostate cancer (PCa) [34, 330]. PSMA is typically located in the cytosol of normal prostate [118] and acts as glutamate carboxypeptidase for folate substrate and neuropeptide N-acetyl-L-aspartyl-L-glutamate [47]. In PCa cells, it turns into a membrane-bound protein composed of three parts, internal portion, transmembrane portion and external portion [3]. The internal portion has represented the target for Indium-111 (111In) capromab pentetide (ProstaScint®; Cytogen Corporation, Princeton, NJ), used for prostate imaging with gamma camera [342]. Recently, radiopharmaceuticals targeting the extracellular component have been developed for PET imaging [20, 83].

PSMA is overexpressed 100–1000 times in PCa compared to normal tissue [159], and its expression increases with tumour dedifferentiation, in metastatic and hormone-refractory cancers [118, 167]. Despite its commonly used name, PSMA is not a prostate exclusive molecule, because it is reported overexpressed in numerous other tissues, including kidney, liver, spleen, small and large bowel, bladder, thyroid and salivary glands [189, 190, 330], as well as in several tumour types, such as transitional cell carcinoma, renal cell carcinoma, colon carcinoma and in the peritumoural neovasculature and endotumoural endothelial cells [6, 54, 330]. These characteristics have promoted the targeting of the extracellular portion of PSMA for imaging and therapy. Although potentially applicable in different cancer types, the principal reports concern prostate cancer indications.

The first 68Ga-labelled PSMA ligands were synthesized at the Johns Hopkins University, while later on developed in Heidelberg [20, 83]. Currently, many of tracers are available in the market and comprise either 68Ga-labelled compounds (68Ga-PSMA), such as 68Ga-PSMA-11 [20], 68Ga-PSMA-617 or 68Ga-PSMA-I&T [2, 142], or 18F-d ligands, including 18F-DCFBC [62], 18F-DCFPyL [337] or 18F-PSMA-1007 [116]. If we exclude some differences in biodistribution, the above-mentioned tracers result substantially interchangeable.

The principal indication for PSMA concerns PCa restaging after biochemical recurrence (BCR) (Fig. 20.5). The majority of papers published so far, although in a vast proportion retrospective, analyze the 68Ga-PSMA PET/CT in this setting [159, 274]. Overall, the rate of positive 68Ga-PSMA PET in BCR results 76%. Compared to other PET tracers, PSMA PET demonstrates a higher detection rate in BCR that goes up to 90% based on the cohort [4, 86], and reaches 58% for PSA values <0.5 ng/ml (Fig. 20.6) or 42% for PSA between 0 and 0.2 ng/ml [274]. As expected, detection rates for PSMA PET too result in a positive correlation with PSA levels, PSA kinetics (PSA Doubling Time, PSA velocity), initial Gleason Score and ongoing androgen deprivation therapy (ADT). On pooled analysis, on a per-patient basis, the sensitivity and specificity for PSMA PET are reported both 86%. While, on a per-lesion basis, the pooled sensitivity and specificity result 80% and 97%, respectively [159, 274].

The use of PSMA PET determines in addition a significant change in management. In the meta-analysis published recently, in 1163 patients (15 studies) with biochemical failure, the pooled proportion of change in management was 54% [129]. According to the type of treatment, the percentage of radiotherapy, surgery, focal therapy and multimodal treatment varied from 56% to 61%, from 1% to 7%, from 1% to 2% and from 2% to 6%, respectively. Conversely, the proportion of systemic treatment versus no therapy at all passed from 26% to 12% and 14% to 11%, respectively [129].

The other possible indication for PSMA PET/CT concerns primary staging in high-risk PCa (i.e. Gleason Score > 7, PSA > 20 ng/ml, clinical stage of T2c–3a) before surgery or radiotherapy. Some significant data derive with this regard from prospective studies. Firstly, Eiber et al. [85] used 68Ga-PSMA PET for preoperative imaging in 37 intermediate-risk and high-risk patients undergoing radical prostatectomy and extended pelvic lymph node dissection. Overall, on a patient-based analysis, the sensitivity and specificity of the modality resulted 75% and 96%, respectively, while on a field-based analysis, the sensitivity and specificity were 65% and 98%, respectively [85, 159]. More recently, van Leeuwen et al. [216] reported results of primary nodal staging in 30 patients with high risk. The performance of PSMA PET/CT in this case was 64% sensitivity and 95% specificity in the patient-based analysis; while, on a region-based analysis, sensitivity and specificity resulted 56% and 98%, respectively.

PSMA PET/CT outperforms also other imaging modalities for primary PCa staging, including CT and bone scintigraphy [21, 288]. In the report from Pyka et al. [288], in 126 patients (1115 examined bone regions), the overall sensitivity and specificity regarding bone involvement resulted 98.7–100% and 88.2–100% for PET, compared to 86.7–89.3% and 60.8–96.1% for bone scan, respectively. On a region-based analysis, the sensitivity and specificity obtained were 98.8–99.0% and 98.9–100% for PET and 82.4–86.6% and 91.6–97.9% for bone scan. In both types of analysis, the difference in diagnostic performance was statistically significant ($p < 0.001$).

One of the biggest advantages of PSMA in PCa is related to the theranostic potential of the tracer, which can be labelled with beta-emitters, such as ^{177}Lu , to treat metastatic cancer. The ligand investigated so far for this purpose, ^{177}Lu -PSMA-617, has been used for radionuclide therapy of metastatic patients in different countries and is currently being evaluated in some multicenter studies in Germany and Australia [118]. PSMA PET/CT would necessarily be of help in this context for the diagnostic/therapeutic pathway of PCa by allowing patient selection and response assessment in the case of radionuclide treatment with ^{177}Lu -PSMA-617.

Since PSMA is overexpressed also in other tumours, some preliminary reports concern its use in RCC [331], HCC [186], Thyroid cancer [237], demonstrating very promising results.

20.5 Clinical Applications of 18F-FACBC

18F-anti-1-amino-3-18F-fluorocyclobutane-1-carboxylic acid (FACBC or fluciclovine) is a synthetic amino acid investigated in the last years for oncology imaging, mainly focusing on prostate cancer [92, 93, 323, 322]. The rationale behind the use of this radiopharmaceutical relies on the known overexpression of several amino acid transporter systems in cancer cells, including prostate [172, 242]. This characteristic relates also to higher tumour aggressiveness and poorer prognosis [322].

18F-FACBC, as other amino acids, is excreted via urinary tract, although it presents with a lower bladder accumulation at early imaging [321]. Being a not natural synthetic amino acid, fluciclovine is not metabolized or incorporated into proteins; hence, its uptake depends on the sodium-independent L large-neutral amino acid transport system [321]. Normal distribution includes high intensity of uptake in the pancreas, less in liver, bone marrow, salivary glands, lymphoid tissues and pituitary.

The primary reports on fluciclovine in prostate cancer investigated biochemical recurrence after radical prostatectomy (Fig. 20.7) and radiotherapy [325, 324]. At first, Schuster et al. demonstrated a higher diagnostic performance for 18F-FACBC compared to ^{111}In -capromab in 93 patients, leading to a disease upstage in 26% of the cases [325]. Pathologically proved analyses on a per-patient basis reported a true positivity rate of 96%. The ability of fluciclovine to detect disease was classified also according to the site, either prostate or prostate bed (90% sensitivity, 40% specificity and 74% accuracy) or extraprostatic localizations (55% sensitivity, 97% specificity and 73% accuracy) [325, 322]. These findings are in line with the pooled data obtained from the meta-analysis published in 2016, summarizing 251 patients (six studies) with suspicion of prostate carcinoma recurrence. Overall, 18F-FACBC PET reached a pooled sensitivity of 87%, a pooled specificity of 66%, with an area under the ROC curve of 0.93 on a per-patient-based analysis [300].

There seems to be some advantage in terms of image quality and acquisition protocol for 18F-FACBC over radiolabelled choline [92, 93]. This advantage is translated into a better performance, as reported by Nanni et al. [248], where a statistically significantly better detection rate was defined for fluciclovine compared to choline in all PSA levels, either low (<1 ng/ml), intermediate (1–2 ng/ml) or high (>2 ng/ml).

More recently, Turkbey et al. reported and investigated the role of fluciclovine for primary PCa detection [354]. In this context, however, 18F-FACBC was reported to have a worse diagnostic performance. Sector-based comparison with pathology revealed a sensitivity and specificity of 67% and 66%, respectively, for 18F-FACBC PET and 73% and 79%, respectively, for MRI. The main limitation, similar to that with choline PET, was due to the high tracer uptake in benign lesions, such as BPH [212].

Other cancer types along with prostate are being investigated with 18F-fluciclovine, nevertheless, so far the only FDA approval for the radiopharmaceutical is to identify prostate cancer recurrence in men with elevated levels of PSA following prior treatment.

20.6 Clinical Applications of 11C-Methionine

11C-Methionine is the radiolabelled variant of the essential amino acid methionine, used as a surrogate marker for the protein metabolism of tumour cells. Hence, its uptake reflects the increased amino acid transport and is related to cellular proliferative activity [138]. The precise mechanism of accumulation is not fully clear, but methionine is known to be necessary for protein synthesis and results involved in crucial pathways, all accelerated in malignant cells [158].

Since the first report [67], L-methyl-11C-methionine is documented as a potential agent in imaging different malignancies, like brain and lung tumours, melanoma lymphoma, breast, pelvic, prostate and head and neck tumours [68, 127, 256, 206, 223–219]. At present, the principal clinical application of 11C-methionine PET concerns central nervous system (CNS) tumours.

Brain has a physiologically intense uptake of 18F-FDG, because glucose is the main metabolic substrate for CNS, and consequently it is very difficult to distinguish malignant lesions in the contest of a hypermetabolic background [188, 201]. Both high-grade (HGG) and low-grade glioma (LGG) may be obscured by adjacent activity or confused with other benign lesions such as infection, infarction or haemorrhage [260, 304, 365, 375]. Conventional imaging methods too, including CT and especially MRI, apart from providing excellent anatomical information with a 65–100% sensitivity, are deficient in differentiating tumours from other non-pathological findings, as well as tumour grades and volumes [128, 375].

11C-Methionine, in contrast, is not physiologically taken up by brain and benign conditions such as fibrosis, necrosis or edema (Fig. 20.8), which are imaged as cold areas in PET [78, 138, 163]. On the contrary, malignant lesions present with an increased 11C-methionine uptake due to an increased protein metabolism and increased vascular permeability [32, 180, 259, 281, 311, 312, 351, 201]. Because of its high contrast, the method seems to allow the identification of low- and high-grade lesions and provides an initial prognostic value [161, 181]. In fact, 11C-methionine uptake and tumour-to-normal brain tissue ratios are reported to correlate with patient prognosis, Ki-67 expression and proliferating cell nuclear antigen (PCNA) expression [188, 251, 347].

The use, however, of 11C-methionine in grading tumours is yet controversial; while some authors report a correlation between tracer uptake and glioma grade [178], others have not demonstrated any significant differences in uptake between gliomas grade I and II, or III and IV, respectively, although 11C-methionine uptake directly correlates with microvessel density [198]. More recent reports [230], however, define the uptake on 11C-methionine PET as significantly correlated to histological grade and other molecular markers, such as IDH1 (isocitrate dehydrogenase 1) mutation status. Commonly, a max tumour-to-brain ratio of 1.3 is used to differentiate neoplasia from other non-neoplastic lesions, as well as to define tumour extent [113, 209].

The overall sensitivity of 11C-methionine PET for gliomas is estimated around 89%, with a specificity of almost 100%, but with lower figures in low-grade tumours (65–85%) [36, 63, 141]. Other intracranial tumours too can show a high 11C-methionine uptake, including pituitary adenomas, ependimomas, lymphomas or brain metastases. A recent study performed on 80 patients with brain tumours documented a sensitivity, specificity and accuracy for 11C-methionine of 88, 80 and 86%. In addition, in 50% of the cases, PET findings had a direct impact on the therapeutic management of the patient [379].

The better tumour delineation of 11C-methionine PET is applied in clinical radiotherapy planning [126, 257]. Both in high-grade and low-grade gliomas, the gross tumour volume (GTV) defined by 11C-methionine is reported to be more precise than that defined by MRI. The difference in accuracy becomes highly relevant in post-therapeutic lesions, when conventional imaging fails to distinguish between residual disease and post-treatment alterations [257].

11C-Methionine PET has a potential use also in stereotactic brain biopsy, especially for distinguishing neoplastic sites from necrotic areas, which are neither easily detectable by MRI nor 18F-FDG PET [120].

The post-treatment evaluation represents another main application for 11C-methionine PET (Fig. 20.9), thanks to its capability to differentiate recurrent brain tumours from radiation necrosis [225, 258, 352]. The sensitivity, specificity and accuracy in detecting tumour recurrence range from 78–100%, 60–100% and

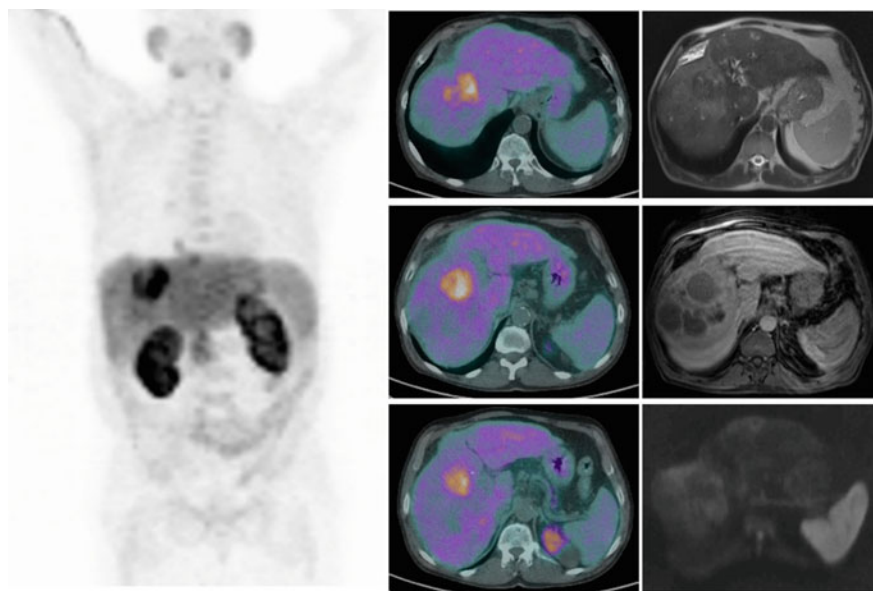


Fig. 20.3 MIP image of 11C-Choline PET/CT of a patient with HCC (left-sided panel of the figure), plus transversal fused images at the level of the liver and corresponding MRI, respectively, in top-down order: T2-weighted haste, T1-weighted vide and Diffusion-weighted views

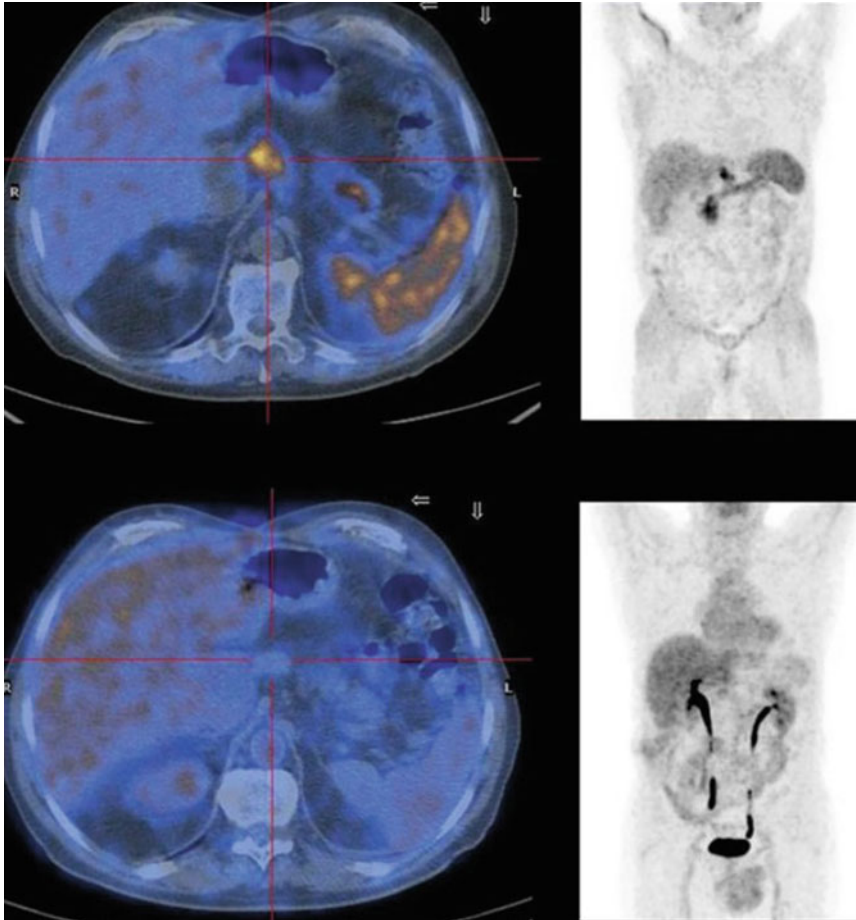


Fig. 20.4 MIP images of a nodal recurrence of HCC studied with ^{11}C -Acetate PET/CT (upper view) and ^{18}F -FDG PET/CT (lower view); FDG-PET shows no pathology uptake, while Acetate-PET clearly detects nodal involvement

about 82%, respectively [352, 353]. False positive cases, however, can be related to acute inflammation, ischemic stroke with reperfusion, etc., but not in chronic inflammatory or radiogenic lesions [169, 198, 353].

^{11}C -methionine PET has been successfully applied also in certain non-oncological fields, such as the diagnostic work-up of patients with hyperparathyroidism, compared to conventional nuclear medicine examination based on $^{99\text{m}}\text{Tc}$ -SESTAMIBI [145, 308, 343]. Other authors, however, demonstrate an inferior sensitivity of ^{11}C -methionine PET in primary hyperparathyroidism with respect to ultrasonography and scintigraphy [145], but a superior accuracy in detecting secondary hyperparathyroidism in patients with renal failure and hypercalcemia [308].

20.7 Clinical Applications of 18F-FET

Tyrosine was radiolabelled and introduced for PET imaging for the first time in 1989 [66]. As an amino acid, it follows the protein synthesis pathways and therefore its uptake reflects the metabolism of malignant cells too [371].

Among the possible radiolabelled forms, 18F-fluoroethyltyrosine (18F-FET) yields the most promising results [98]. Although it is not incorporated into proteins, 18F-FET PET shows a high accuracy in the diagnostics of tumours, such as gliomas, probably due to intracellular tracer entrapment secondary to increased amino acid transport within the cells [139, 204, 369].

18F-FET exhibits a high in vivo stability, low uptake in inflammatory tissue and suitable uptake kinetics for clinical imaging [177, 285]. In addition, it can be produced with high efficiency and therefore offers the opportunity for commercial distribution [204, 333].

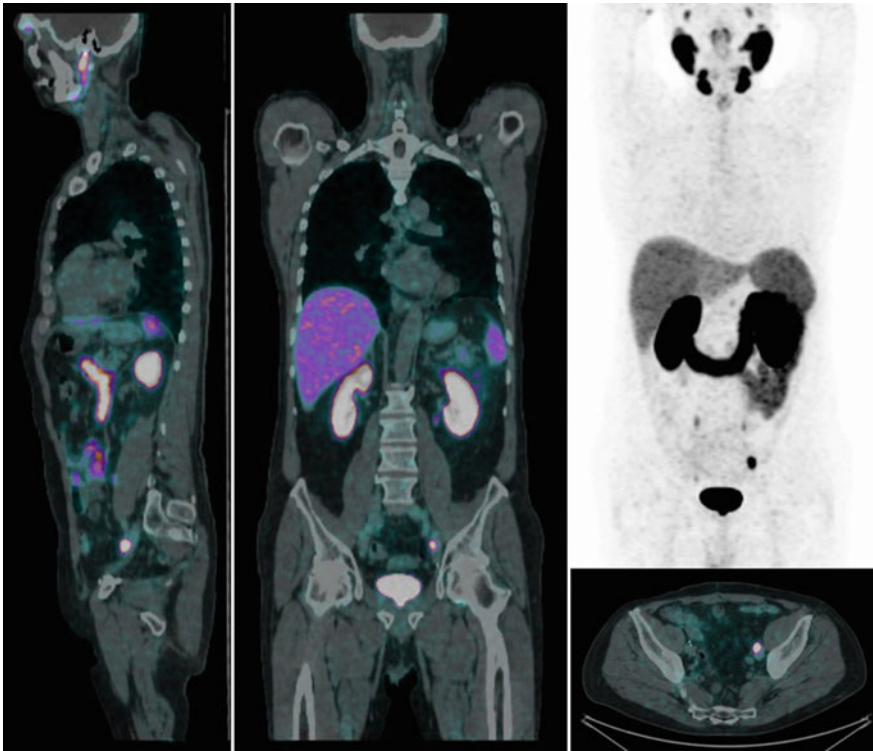


Fig. 20.5 MIP and multi-axial views of ^{68}Ga -PSMA PET/CT in a PCa patient with biochemical relapse (PSA 1.86 ng/ml) after radical prostatectomy; the nodal involvement in the left iliac region is clearly visible in all views, respectively, from left to right: sagittal, coronal, MIP plus axial

Several studies have demonstrated the benefit of ^{18}F -FET PET for the management of patients with gliomas in terms of differential diagnosis and grading [104, 268, 367], prediction of prognosis [104], monitoring of therapy response [289], radiotherapy planning [366] and detection and diagnosis of tumour recurrence [290, 291, 293]. In this context, ^{18}F -FET PET shows a sensitivity and specificity of 96% and 53%, respectively, in the detection of tumour tissue [268]. In non-neoplastic brain lesions, however, an increase in ^{18}F -FET uptake may indicate reactive astrocytosis. In more recent data from 13 studies (462 patients), ^{18}F -FET PET yielded a pooled sensitivity and specificity of 82% and 76%, respectively, for the diagnosis of primary brain tumours [82]. Reference thresholds to differentiate primary neoplasia from non-neoplastic lesions can be used: i.e. mean and max tumour-to-brain ratio (TBR) of 1.6 and 2.1, respectively [209, 296]. The main limitation to be considered for ^{18}F -FET PET is acquisition protocol. According to the EANM/EANO/RANO practice guidelines/SNMMI procedure standards [209], acquisition can be performed with 20 min static images, obtained 20 min after injection, or by means of dynamic images starting 10–50 min after. Other authors propose earlier acquisition, from 5 to 15 min for better differentiating HGG from LGG [7]. The rationale for this suggestion relies on the common behaviour of HGG showing an early peak 10–15 min after injection followed by a progressive and rapid decrease of uptake; on counterpart, LGG is usually present with a delayed and steady increase of tracer uptake [292].

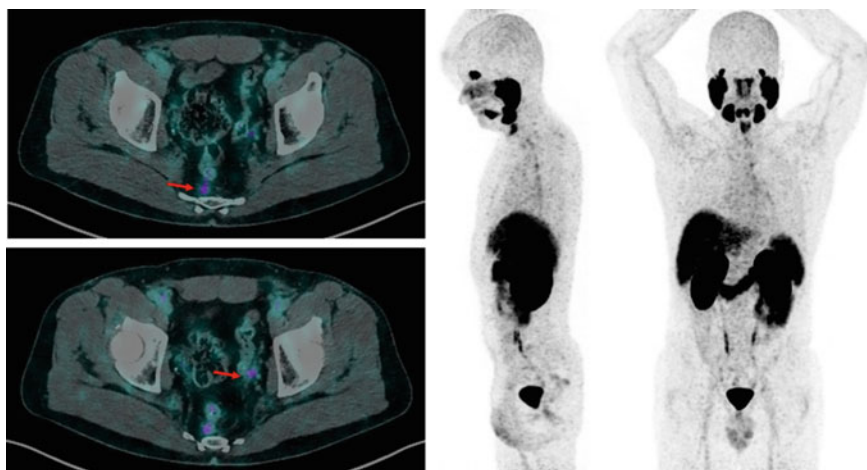


Fig. 20.6 Anterior and lateral MIP views of ^{68}Ga -PSMA PET/CT in a PCa patient with biochemical relapse having a very low trigger PSA (0.41 ng/ml) after radical prostatectomy; red arrows indicate the locations of nodal involvements, respectively, at the presacral and left obturator region

18F-FET PET has also demonstrated a good sensitivity and specificity in head and neck cancers of 75% and 95%, respectively, with an overall accuracy of 90% [269]. When comparing, however, the diagnostic value with that of 18F-FDG PET, the latter results more accurate, but 18F-FET uptake yields a better differentiation of tumour tissue from inflammatory disease [269].

20.8 Clinical Applications of 18F-DOPA

18F-DOPA (18F-dihydroxy-phenylalanine) is a positron emitter compound applied in clinical practice since the 80s [103, 114] as a marker for the basal ganglia dopamine production [370]. It is the fluorinated form of L-DOPA, which represents the immediate precursor of dopamine [234], a central nervous system neurotransmitter predominantly found in the nigro-striatal region and related to neuro-degenerative and movement disorders, such as Parkinson's disease (PD) (AGID 1991). Unlike dopamine, L-DOPA is actively transported through the blood-brain barrier, and then converted into dopamine by the action of L-aromatic amino acid decarboxylase [234] and at last stored in intraneuronal vesicles, ready for release in the various dopaminergic pathways, such as the pre-synaptic space.

The objective of the *in vivo* detection of dopaminergic degeneration in PD by the means of 18F-DOPA is related to the early diagnosis and monitoring of disease progression [87, 215, 313]. The method has in fact demonstrated a high sensitivity and specificity in the diagnosis of PD, ranging from 91–100% and 90–100%, respectively [90], although some papers report a paradoxical up-regulation of decarboxylase activity and consequently a possibly increased trapping of 18F-DOPA in the pre-synaptic vesicles during the earlier stage of the disease [168, 213].

Main drawbacks, however, of the method are related to the need of a cyclotron-based radiopharmacy and the relatively complicated synthesis of 18F-DOPA [362]. The commercial presence of other valid alternatives, such as 123I-FP-CIT SPECT, a marker of the pre-synaptic dopamine transporter (DAT) expression [121], directly correlated to PD alterations and disease stage, with similar features to the 18F-DOPA diagnostic value [90, 91], makes this latter one not of routine use in clinical practice, despite the unquestionable advantages over 123I-FP-CIT in terms of length of the procedure and image quality.

A mechanism similar to the above-mentioned one, characterized by active uptake and decarboxylation of amines precursors, is noticed also in other brain regions and in extracranial tissues, giving way to the possibility of 18F-DOPA to be used in the detection of pathological situation such as brain tumours [140], neural crest derived neoplasms [154] and pancreatic islets hyper-function (i.e. primary hyperinsulinism) [135].

In oncology, 18F-DOPA has been initially proposed as a marker for melanomas [80], thanks to the ability of neural crest derived tumours, which are now defined as neuroendocrine tumours (NET), to accumulate and decarboxylate L-DOPA as a

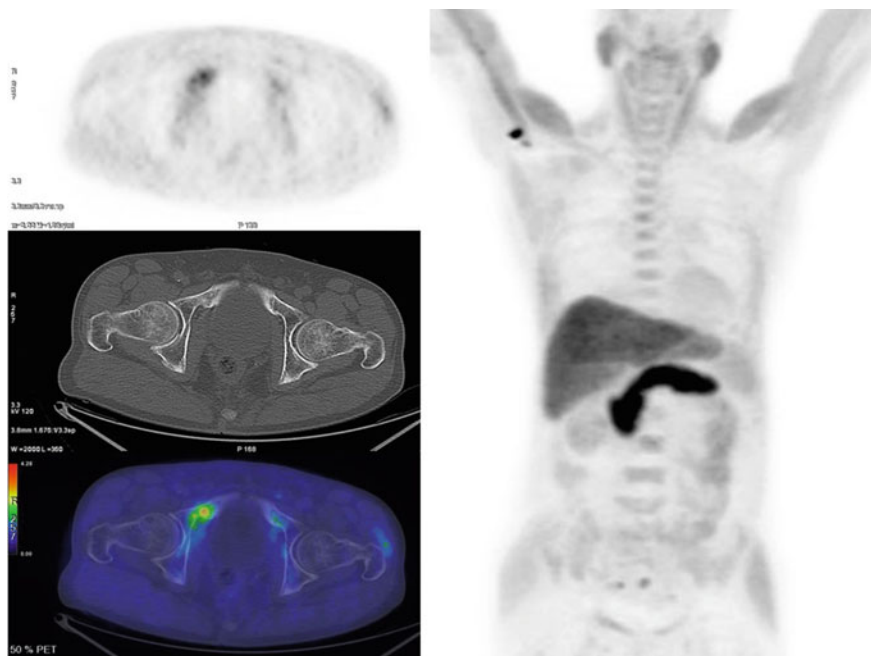


Fig. 20.7 MIP image of ^{18}F -FACBC PET/CT (right-sided panel of the figure), with transversal images of the pathological bony lesion documented in a PCa patient with biochemical relapse after radical prostatectomy (PSA 4 ng/ml); note how the corresponding localization CT of the right pubic bone shows no significant alterations (*Courtesy of Dr. Cristina Nanni and Dr. Lucia Zanoni, University Hospital S. Orsola-Malpighi, Bologna, Italy*)

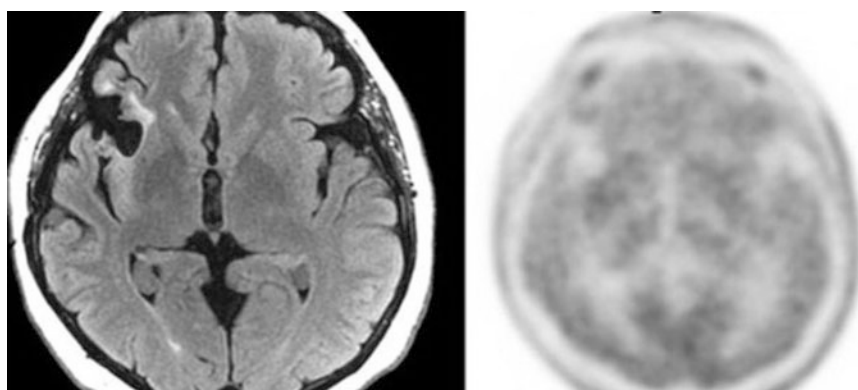


Fig. 20.8 Example of no pathologic uptake of ^{11}C -Methionine (right-sided view) in the suspected right fronto-temporal lesion described at T1 weighted MRI (left-sided view)

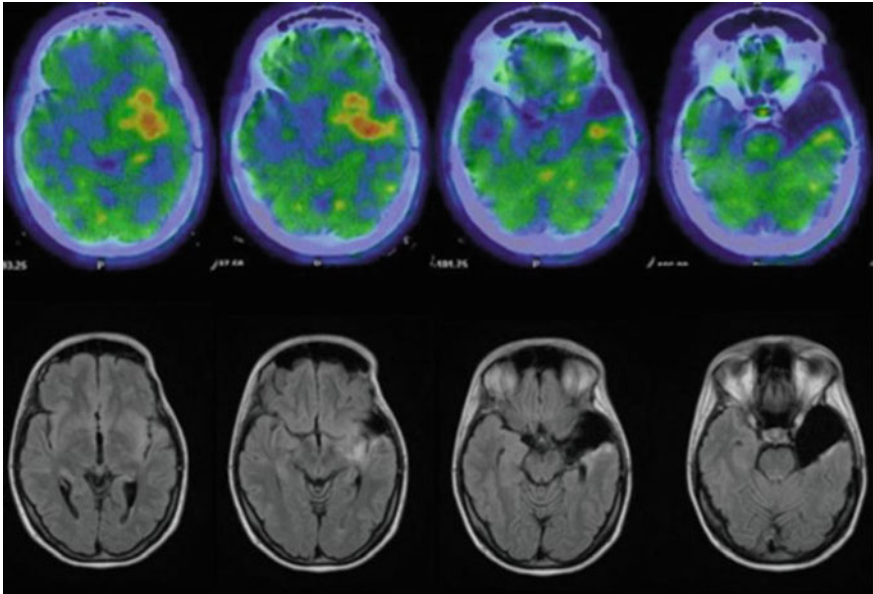


Fig. 20.9 Transversal images of ^{11}C -Methionine PET/CT referred to the corresponding T1 weighted MRI; (upper study) perilesional recurrence at the level of surgical crater, both at the MRI (inferior views) and Methionine-PET (superior views)

precursor of dopamine. The amine precursor uptake and decarboxylation (APUD) concept was introduced in 1969 [271] and consequently, the known increased activity of L-DOPA decarboxylase in NET [25, 115] permitted their visualization through positron emitters. The first PET compound, however, was ^{11}C -labelled DOPA used by Ahlström for NET imaging [5].

At present, ^{18}F -DOPA PET is a well-assessed procedure in the detection of primary and metastatic NET (carcinoids, gastroenteropancreatic tumours (GEP), glomus tumour, medullary thyroid cancer, small cell lung cancer, neuroblastoma, paraganglioma, pheochromocytoma, etc. (Fig. 20.10)) [122, 161–157, 171, 249]. Its diagnostic accuracy is reported higher than the other conventional imaging techniques, including CT/MRI, ^{123}I -MIBG and ^{111}In -Octreoscan [25, 102, 166]. However, the group of neoplasms which mostly benefit from ^{18}F -DOPA imaging are of NET associated with excessive catecholamine release (sensitivity of 73–90%) [102] and particularly pheochromocytomas (sensitivity, 85%; specificity, 100%; accuracy, 92%) [166] (Fig. 15.1).

PET imaging with ^{18}F -DOPA, compared to the other radionuclide methods, has in addition a better spatial resolution (~ 5 mm versus 10–15 mm) and a higher signal-to-background ratio, with physiological uptake of the tracer situated only in the basal ganglia, bile ducts, gallbladder, adrenals and excretory tract [154]. To further improve the method and, in particular, to reduce the high renal excretion of

the tracer, oral premedication with carbidopa (decarboxylase inhibitor) is suggested to block the aromatic amino acid decarboxylase enzyme [205]. This leads to a six-fold decreased renal excretion while the tumour uptake increased three-fold, hence improving the visualization of neuroendocrine tumours [88].

When comparing 18F-DOPA to other PET tracers, such as the 68Ga-labelled somatostatin analogues, whose rationale is based on the well-known overexpression of somatostatin receptors in NET [302], the latter ones show a slightly better accuracy [17, 18].

However, the substantially different pathways of the two kinds of tracers suggest a more likely complementary function in the detection of NET sites, in accordance with the natural heterogeneity and development history of these neoplasms.

Being an amino acid, 18F-DOPA PET has found a clinical application also in brain tumour imaging [140]. The new joint EANM/EANO/RANO guidelines [209] and previous recommendations in 2016 [8, 7] report on the use of this amino acid and other tracers in glioma imaging. The sensitivity of 18F-DOPA PET for primary detection of histologically proven glioma is 95% compared to 91% for MRI [53]. The use of thresholds for uptake can in addition help differentiate high-grade and low-grade primary glioma with a sensitivity and specificity of 70% and 90%, respectively, (i.e. $SUV_{mean} = 2.5$) [374]. Another reference for glioma detection relies on relative uptake with respect to basal ganglia accumulation [326]. In the case of recurrence, 18F-DOPA PET reaches a sensitivity, a specificity and an accuracy of 100%, 86% and 96%, respectively [363]. In this case, when a threshold of 1.8 is used, the sensitivity and specificity of 18F-DOPA PET reaches 100% and 80%, respectively [374]. Also, metabolic changes with 18F-DOPA during treatment can be applied to determine the patient outcome, by predicting longer PFS and OS [319]. Its impact in altering treatment plan can be seen in 41% of cases [28, 244].

Another important application of 18F-DOPA is the identification of hyperinsulinism in infants. Otonkoski et al. were the first to suggest a possible use of 18F-DOPA in congenital hyperinsulinism [261] based on the fact that several studies showed that normal pancreatic β -cells take up L-DOPA [33, 226]. The preliminary results were very encouraging, and the accuracy of this technique seems to range from 96 to 100% for the diagnosis of diffused disease and for the localization of focal lesions [135]. In subsequent studies, the diagnosis of focal or diffuse hyperinsulinism was possible in 88%, with 18F-DOPA scans diagnosing 75% of focal cases and correctly identifying all sites of disease [136].

Very recently, a new application of 18F-DOPA in children has been investigated, and this concerns Neuroblastoma [231, 276]. The results are quite encouraging and are worthy assessed in a larger study population.

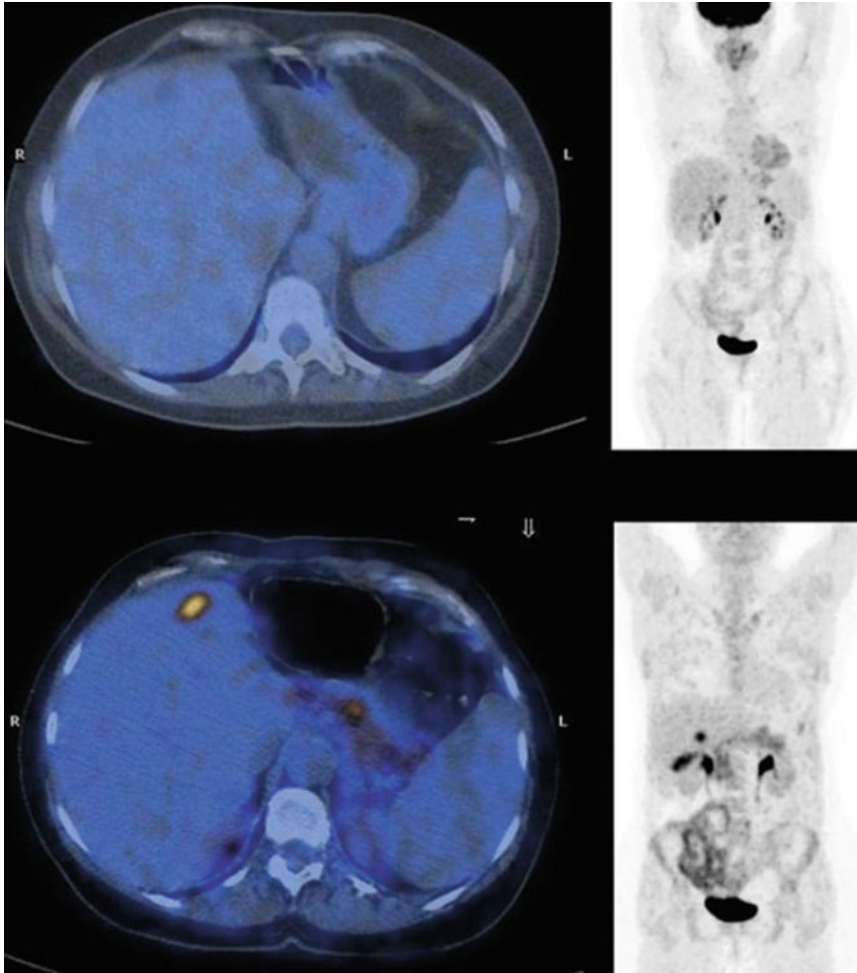


Fig. 20.10 MIP images of ^{18}F -FDG PET/CT (upper image) and ^{18}F -DOPA PET/CT (lower image), with transversal views demonstrating a single small liver metastasis derived from a previously operated intestinal carcinoid; the lesion is visible only on the ^{18}F -DOPA images and appears undetectable on ^{18}F -FDG PET/CT

20.9 Clinical Applications of ^{68}Ga -DOTA-Peptides

^{68}Ga -labelled DOTA-peptides represent a group of PET radiopharmaceuticals specifically targeting somatostatin receptors (SSTRs) at variable affinity [14, 270]. SSTRs are G-protein coupled membrane receptors, first described in rat pituitary tumour cells by Schonbrunn and Tashjian [270, 320]. SSTRs are present also in a

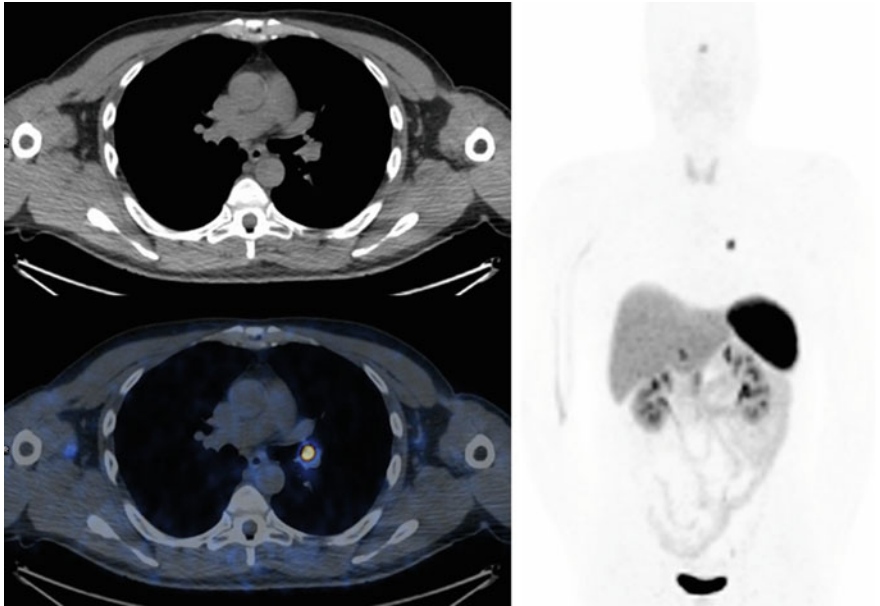


Fig. 20.11 MIP image of ^{68}Ga -DOTATOC PET/CT (right-sided panel of the figure), with transversal images of the pathological lesion in the left bronchus corresponding to a pulmonary neuroendocrine tumour; note the appearance of the small tumour detectable on localization CT as endobronchial nodule

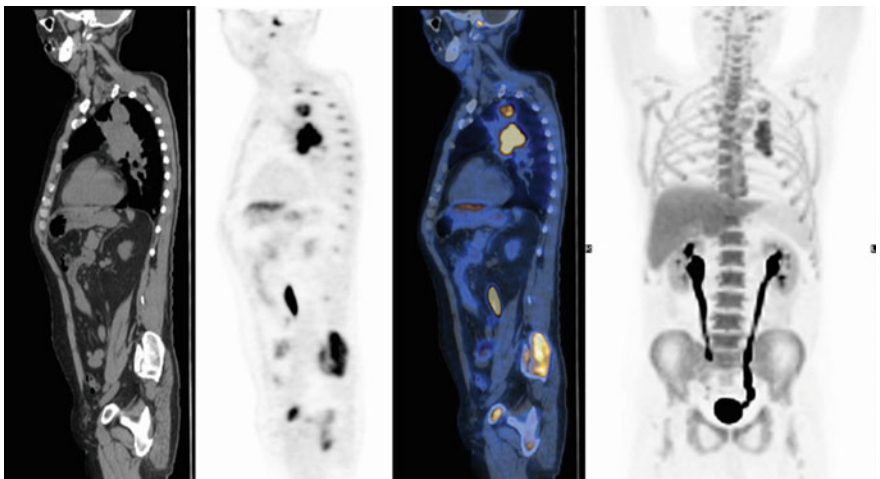


Fig. 20.12 MIP image of ^{18}F -FLT PET/CT (right-sided panel of the figure), with sagittal images of a patient with NSCLC of the left upper lobe associated to large hilar adenopathies. Note the diffusely increased uptake of the tracer in the bone marrow, as physiological distribution

wide range of normal tissues, such as the spleen, adrenals, pituitary gland, pancreas, liver, gastro-intestinal tract, kidneys and lungs, which are characterized by various levels of expression of the SSTR subtypes (SSTR1, 3, 4 and 5) [303, 304]. Their introduction in clinical practice has significantly improved the diagnostic, and subsequently the therapeutic, pathway of neuroendocrine tumours (NETs) that are known to overexpress in 80–100% of the cases of SSTRs, of which SSTR2 represents the principal subtype [267].

The most common ^{68}Ga -DOTA-peptides (DOTA-TOC, DOTA-NOC, DOTA-TATE) are all composed by a chelant (DOTA) for the nuclide (^{68}Ga) and a ligand of SSTR (i.e. NOC, TOC or TATE): all above-mentioned peptides are agonists of SSTRs and bind to SSTR2 and to SSTR5, while ^{68}Ga -DOTA-NOC binds with a good affinity also to SSTR3 [14, 19]. More recently, radiolabelled antagonists (i.e. ^{68}Ga -NODAGA-JR11) have been investigated and reported to have considerably more binding sites than agonists [117, 255, 373].

So far, the main indications of ^{68}Ga -DOTA-peptides PET in NETs relate to disease staging/restaging (Fig. 20.11), detection of unknown primary tumour, selection of patients for target radionuclide therapy (PPRT) and detection of relapse during follow-up. In this context, the overall sensitivity and specificity in NET range between 90–98% and 92–98%, respectively [13, 14, 111]. Findings demonstrate that DOTA-peptides are superior to either Octreoscan (In-111 somatostatin receptor scintigraphy; SRS) or computed tomography (CT), proving an accuracy of 96% versus 75% for CT and 58% for SRS [111]. PET/CT was in particular more accurate for the detection of nodal, bony and liver lesions. ^{68}Ga -DOTA-peptides can consequently change the clinical management of patients with NET [14]. This is the case of 90 patients with biopsy-proved NET, for which ^{68}Ga -DOTA-NOC PET affected stage classification or therapy in half the patients [12]. The advantage in treatment change is confirmed in 14% of the cases compared with SRS and in 21% compared with CT [111]. In a more recent meta-analysis, for a total of 1,561 patients, change in management after ^{68}Ga -DOTA-peptides PET/CT occurred in 44% of the cases [21].

^{68}Ga -DOTA-peptides PET/CT can be successfully used also for the detection of the unknown primary NET. For example, in the paper from Prasad et al. [286], in 59% of the patients, ^{68}Ga -DOTA-NOC PET/CT localized the site of the primary tumour, while CT alone could confirm the findings in only 12 of 59 patients (20%). Also in the case of suspicious NET, ^{68}Ga -DOTA-peptides can help identify the presence of the tumour [15]. Overall, 131 suspected NET with either increased blood markers, inconclusive conventional imaging (CI), clinical signs or symptoms, equivocal ^{18}F -FDG PET or SRS or a combination of them were analyzed [15]. ^{68}Ga -DOTA-NOC PET in this case detected NET in 19/131 patients (15%), with an overall sensitivity and specificity of 90% and 100%, respectively. The occurrence of NET was higher in the case of inconclusive findings at conventional imaging (13/41).

The information provided by ^{68}Ga -DOTA-peptides can help define the outcome of the tumour based on the intensity of uptake in patients with G1 and G2 NET of the pancreas (pNET) [16]. In the cohort studied by the group from Bologna, the best cutoff for SUV_{max} ranged between 37.8 and 38.0. pNET having a higher risk of progression

presented with an SUV_{max} < 37.8 (HR, 3.09; *p* = 0.003), a Ki-67 > 5% (HR, 2.89; *p* = 0.009) and medical therapy alone (HR, 2.36; *p* = 0.018) [16].

Semi-quantitative and visual analysis for ⁶⁸Ga-DOTA-peptides uptake is used also to guide targeted peptide radionuclide therapy with ¹⁷⁷Lu-DOTA-TATE or ⁹⁰Y-DOTA-TOC or a combination of the two [112].

20.10 Clinical Applications of 18F-FLT

18F-3'-deoxy-3'-18F-fluorothymidine (18F-FLT) is the fluorinated analogue of thymidine, one of the four DNA bases, introduced as a PET tracer for measuring tissue and tumour proliferation in 1998 [127, 328]. The rationale for using thymidine analogues is based on the knowledge that this pyrimidine base is rapidly incorporated into newly synthesized DNA, and this led to the first attempts in the 80s to utilize the native form labelled with ¹¹C (¹¹C-thymidine) for the evaluation of DNA synthesis in vivo [238, 368]. The carbon labelled tracer, however, turned out not suitable for routine clinical use due to the short half-life of ¹¹C and the rapid in vivo degradation of ¹¹C-thymidine. Therefore, 18F-FLT, which derives from the cytostatic drug azidovudine (AZT), was preferred for this purpose [328].

Despite following the natural pathway of thymidine, 18F-FLT is trapped in cells after phosphorylation by thymidine kinase 1, but it is not or only marginally incorporated into the growing DNA chain (<2%) [26, 41, 301]. This means that 18F-FLT uptake is not a direct representative of DNA synthesis, but rather of cellular S-phase [23, 41]. Noteworthy, a significant correlation has been reported between this tracer uptake and cellular proliferation in various malignant tumours, such as lung cancer (Fig. 20.12), breast cancer, colorectal cancer, gliomas, sarcomas and lymphomas [41–42, 55, 106, 184, 223], also with respect to the proliferation fraction in biopsied tissues as indicated by Ki-67 immunohistochemistry [41, 42, 360].

18F-FLT PET yields images of high contrast, with good tumour-to-background ratio. Physiological uptake of 18F-FLT is noticed in the bone marrow, due to elevated cell proliferation, in the liver, secondary to hepatic glucuronidation and in the urinary tract, as part of the renal clearance of the tracer [327]. According to this pattern of distribution, these areas represent the main limits of the method with respect to accuracy.

Malignant lymphomas, both aggressive and indolent subtypes, are reported to show high 18F-FLT uptake, with an excellent overall sensitivity up to 100%. Similar results were reported in non-small cell lung cancer, with a sensitivity of up to 90% [41]. However, the detection rate decreases markedly when considering lymphogenic spread (53%) and distant metastases (67%), resulting in a lower accuracy of 18F-FLT PET in tumour staging [41, 65, 81].

Additionally, the baseline uptake of 18F-FLT in aggressive lymphoma [143] has been reported to correlate with treatment response, while its change already 1 week after the start of chemotherapy can be predictive of clinical response and survival

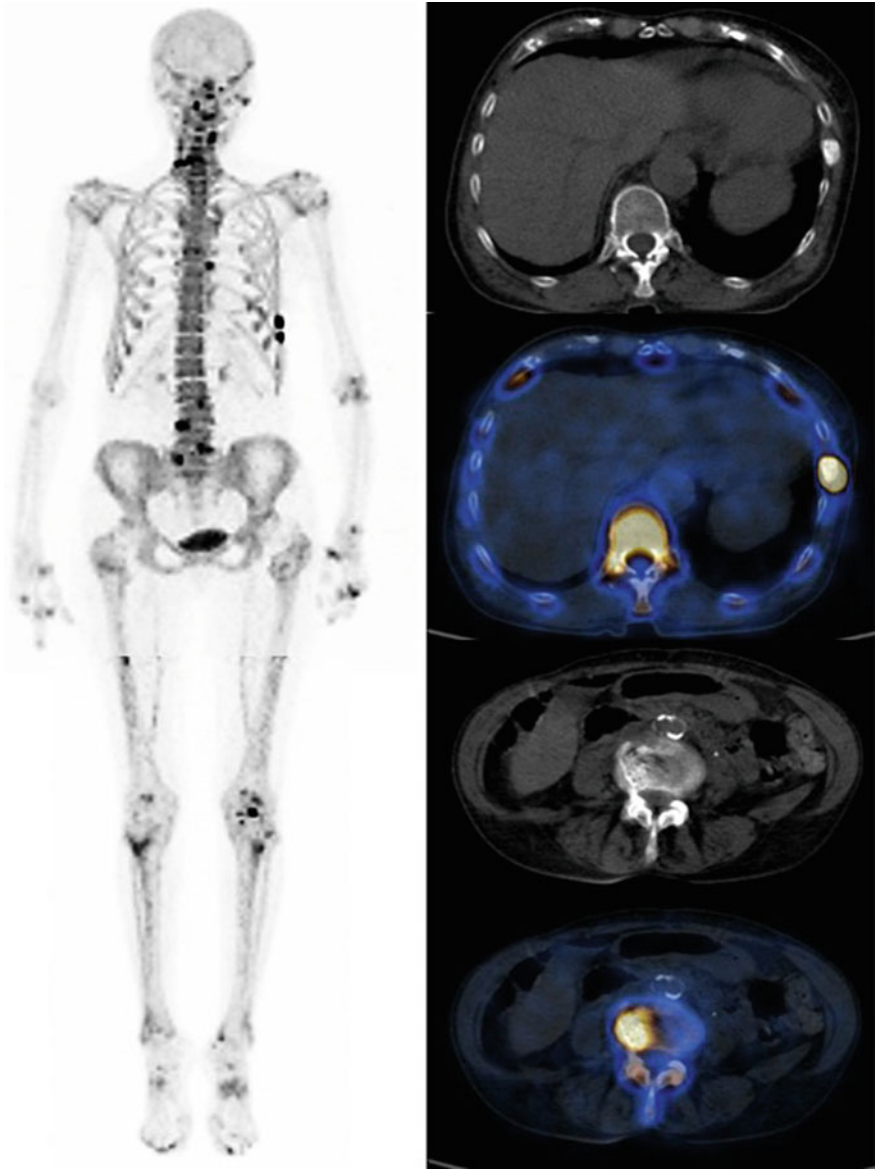


Fig. 20.13 MIP image of ^{18}F -Fluoride PET/CT (left-sided panel of the figure), with axial images of a patient referred for suspicious bone metastases from breast cancer; no clear malignant lesions were documented, however the patient presented with diffuse degenerative alterations and left-sided rib fractures (axial views on the right panels)

[144, 214]. Also in acute myeloid leukaemia (AML), 18F-FLT PET can serve as an early biomarker of response [357].

In colorectal cancer, both 18F-FLT and 18F-FDG PET has shown a good visualization of the primary tumours, however, only 34% of liver metastases can be detected with 18F-FLT versus 97% with 18F-FDG PET [106]. As per response to treatment in colorectal cancer, the weight of 18F-FLT flare during 5-FU infusion resulted correlated with treatment response; patients with low flare on day 2 had a longer survival than those with a high 18F-FLT PET flare (2-year overall survival rate 78% versus 44%, $p = 0.051$) [31, 176].

18F-FLT PET role has been investigated also in brain tumours, where its uptake seems to correlate better with Ki-67 proliferation index. In this context, a higher accuracy for the detection of recurrent brain tumours has been reported when compared with 18F-FDG PET [55]. No clear advantage, however, is known over standard brain imaging with amino acid tracers, i.e. 11C-methionine, 18F-FET, etc., except for the ability of early 18F-FLT uptake reduction after few cycles of therapy to correlate with clinical outcome [58]. In fact, the most promising application appears to be monitoring of therapeutic response with 18F-FLT PET. In animal models of fibrosarcoma and lymphoma [22, 43], and in preliminary studies in primary breast tumours and metastases, when compared to 18F-FDG, 18F-FLT has shown a more significant decrease in uptake [22, 223]. A more favourable outcome is reported also for head and neck cancer in case of greater reduction of 18F-FLT uptake in the second week of treatment with radiotherapy or chemoradiotherapy [31, 153].

Generally, the mean 18F-FLT uptake in tumours is reported to be significantly lower when compared to the respective 18F-FDG uptake [41]. Overall 18F-FLT PET appears to be less accurate in tumour detection than 18F-FDG PET, however, as a proliferation tracer, 18F-FLT is more specific than 18F-FDG and therefore, the principal role of this tracer can be assessed in monitoring treatment response in the clinical setting.

20.11 Clinical Applications of 18F-Fluoride

Sodium (18F)fluoride or 18F-NaF is a bone-seeking radiopharmaceutical utilized for bone imaging with PET and initially introduced by Blau et al. [30]. 18F-Fluoride represents the simplest fluorinated radiopharmaceutical adopted in PET imaging. The rationale for its utilization in bone imaging is the same for diphosphonates and is based on the physiological absorption of fluoroderivates in the bone matrix as fluoroapatite [361], Vallabhajosula [356]. 18F-Fluoride accumulation reflects the regional bone blood flow and osteoblastic activity. As such, the tracer is a marker of osteoblastic metabolism. When compared to the γ -emitter ^{99m}Tc -phosphonates, 18F-fluoride benefits from several advantages related to faster extraction from blood pool [205], higher capillary permeability, and significantly higher pathologic-to-normal bone fluoride uptake [29]. It has in fact a high

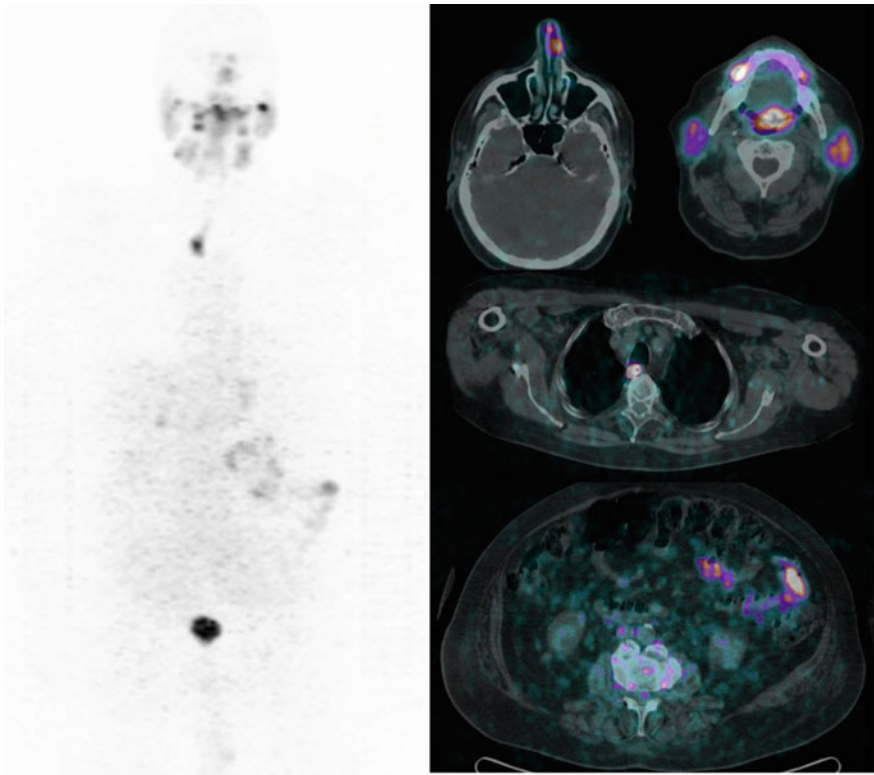


Fig. 20.14 MIP image of ^{124}I -Iodine PET/CT (left-sided panel of the figure), with axial images of a patient referred for suspicious thyroid cancer relapse; the scan is negative for metastases, but shows multiple findings related to unspecific iodine accumulations; from top to bottom: nasal, salivary, buccal, esophageal and in intestinal uptake

blood to bone clearance, similar to $^{99\text{m}}\text{Tc}$ -methylenediphosphonate ($^{99\text{m}}\text{Tc}$ -MDP), and imaging is instantaneously available after ^{18}F -fluoride administration [127, 205]. In addition, ^{18}F -fluoride PET has shown an increased diagnostic sensitivity for bone lesions as compared with $^{99\text{m}}\text{Tc}$ -diphosphonates, thanks to the better spatial resolution provided by PET/CT technology [356].

^{18}F -Fluoride bone uptake has been reported in both sclerotic and lytic metastases [94, 316] and there is a documented evidence that the diagnostic accuracy of ^{18}F -fluoride PET is better than that of $^{99\text{m}}\text{Tc}$ -MDP scintigraphy for detecting bone metastases in several cancers, such as lung, prostate and breast cancer [95, 127, 147, 317]. In an investigation of patients with prostate cancer [94, 95] ^{18}F -fluoride PET/CT, detected bone metastases with a sensitivity and specificity of 100%, whereas $^{99\text{m}}\text{Tc}$ -MDP scintigraphy had a sensitivity and a specificity of 92% and 82%, respectively [127]. Also in a recent review from Evangelista et al. [92, 93] summarizing the diagnostic performance of ^{18}F -fluoride PET, the mean weighted

sensitivity, specificity, PPV, NPV of the method resulted very high: 96% (range 81–100%), 77% (range 54–100%), 85% (74–100%), 95% (78–100%) and 79% (65–100%), respectively.

The main limit, however, for this tracer is the fact that as a bone agent ^{18}F -fluoride cannot be considered as tumour specific (Fig. 20.13). Similar to $^{99\text{m}}\text{Tc}$ -diphosphonates, it may be taken up in benign pathologies and nonmalignant orthopaedic problems (Vallabhajosula [356]. Also, osteomedullary malignant lesions can be missed, if neither bone formation (*Osteosclerotic mets*) nor sufficient bone destruction (osteolytic mets) are seen with ^{18}F -Fluoride PET and corresponding CT images. The favourable imaging performance however and the clinical utility of ^{18}F -fluoride PET [123], compared with $^{99\text{m}}\text{Tc}$ -diphosphonate scintigraphy, support the potential use of ^{18}F -fluoride as a routine bone imaging agent.

20.12 Clinical Applications of ^{124}I -Na

Conventional imaging with radioactive iodine (^{131}I or ^{123}I) represents the fundamentals of diagnostic and therapeutic approach to differentiated thyroid cancer (DTC). The equivalent PET nuclide, i.e. iodine-124 (^{124}I), allows for an additional amelioration of the detectability of residual or recurrent thyroid cancer [48] with a higher sensitivity than conventional ^{131}I scintigraphy [275].

Iodine-124 has several advantages in terms of image quantification, derived from radionuclide characteristics and whole-body PET acquisition. However, Iodine-124 is an impure positron emitter with a long half-life of 4.2 days and a complex decay scheme that produces a low positron abundance (23%) of maximal energy of 0.603 MeV [232]. Simultaneously to positrons, ^{124}I decay scheme contains gamma rays that lead to spurious coincidences. The result can be more noisy images, although the spatial resolution and image quality are significantly improved in modern PET/CT scanners.

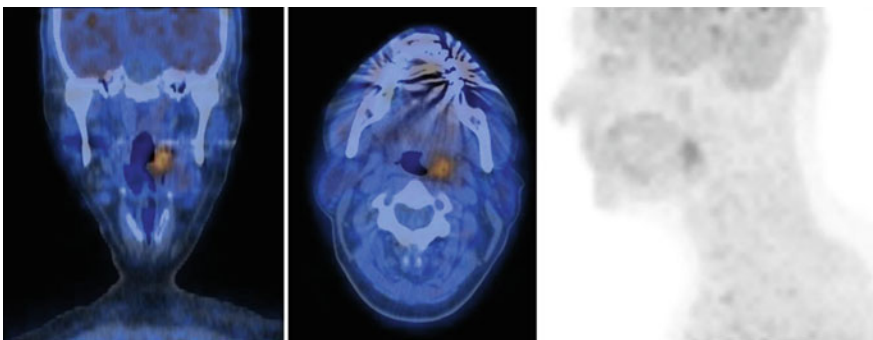


Fig. 20.15 MIP image of ^{64}Cu -ATSM PET/CT (right-sided panel of the figure), with axial and coronal images of a patient with HNSCC referred hypoxia detection

Iodine-124 is a very versatile nuclide that can be used for labelling also other molecules or compounds, such as MIBG (metaiodobenzylguanidine), IAZA (iodoazomycin arabinoside), FIAU (2'-fluoro-2'-deoxy-1-D-arabinofuranosyl-5-iodouracil), and β -Cit (2 beta-carbomethoxy-3 beta-(4-iodophenyl)tropane). [48].

Its pure use as 124I-iodine in thyroid cancer (Fig. 20.14), either alone or in combination with FDG PET, can improve restaging and detection of recurrent DTC [48, 108]. The higher diagnostic accuracy can help modulate in addition the therapeutic radioiodine activity [89, 203]. Still the experience in clinical practice is limited. Freudenberg et al. [108, 107] in their report in 12 thyroid cancer patients demonstrated a lesion delectability of 87% and 100% for 124I-PET and combined 124I-PET/CT, respectively. Lesion delectability in the same cohort for 131I scintigraphy was 83%. A clear diagnostic advantage compared to 131I scan was reported also by Phan et al. [275], who were able to detect more abnormalities with 124I PET and in more patients. Out of the 20 patients enrolled, only 3 cases presented with pathological uptake on the diagnostic 131I scan out of the 11 patients with positive 124I-PET. When compared to therapeutic 131I scintigraphy, all PET positive cases were confirmed. Two more additional patients are presented with abnormal uptake on therapeutic 131I scan; in one, the uptake was confirmed by MRI, whereas in the other, no clear anatomical localisation was documented [275].

124I-PET can help in parallel for the diagnosis and for the therapeutic outcome prediction with 131I radionuclide treatment. The report from Wierts et al. in 47 patients scheduled for radioiodine therapy revealed that pre-therapeutic 124I PET/CT dosimetry can be used to predict lesion-based 131I therapy response, having an area under the curve of 0.76 for thyroid remnants and 0.97 for metastases [372]. On the other hand, 124I-PET cannot be considered a screening tool for the selection of patients with detectable Thyroglobulin (Tg) in case of negative scan. In fact, Khorjekar et al. retrospectively determined patients who had an elevated Tg, a negative diagnostic 131I/123I scan, a negative diagnostic 124I-PET and a prior 131I therapy with a subsequent positive post-131I scan [187]. Out of the 12 patients filling the inclusion criteria, 10 cases (83%) had positive foci on post-therapy 131I scan, despite a negative 124I-PET.

The THYROPET study [191] reports in addition the role of iodine-124 imaging in DTC patients with detectable Tg and a negative neck US undergoing blind 131I therapy. Although the multicentric study was designed for 100 patients, the trial was stopped after the first 17 cases because the stopping rule had been met. Still, on a patient-based analysis, the sensitivity, specificity, negative predictive value and positive predictive value of 124I-PET were 44%, 100%, 62% and 100%, respectively. Overall, 8 cases out of 17 post-therapy 131I scans were negative (47%); all correctly predicted by a negative 124I-PET. However, of the 13 negative 124I-PET scans, 5 cases resulted as false negative (29%). As a conclusion, in patients with biochemical recurrence of DTC, 124I PET/CT before blind 131I therapy can correctly predict tumour positive uptake and thus be used for dosimetric evaluation. However, it should not preclude treatment in case of negative result, due to its false negative rate.

20.13 Clinical Potential of PET Tracers for Hypoxia

A major challenge in treating tumours is related to the low levels of tissue oxygenation [39, 344]. As a consequence of the reduced oxygen supply, inadequate to cover the cellular metabolic demand, tumour tissue experiences hypoxia. Onset of hypoxia is often the result of abnormal perfusion, insufficient oxygen diffusion or altered oxygen transport [229]. Response to chemo- and radiotherapy is strongly determined by this fact and it is already reported that acquired resistance and increased probability for precocious relapse are largely influenced by the fraction of hypoxic tissue in the tumour [69, 125, 221, 222, 280].

The classical methods to directly assess tumour hypoxia are rather invasive and difficult to perform [52, 199] consequently, indirect methods of hypoxia measurement have been development. Imaging modalities appear with this regard the most appealing, because they can identify the phenomenon non-invasively and provide a whole-tumour assessment of hypoxia. Multiple PET radiopharmaceuticals are studied and can be potentially used in clinics. In general, they can be categorized into two large groups: nitroimidazole family and non-nitroimidazole compounds.

18F-Fluoromisonidazole (18F-FMISO) was the first PET tracer for mapping the *in vivo* tissue oxygenation [194, 299, 297]. When 18F-FMISO encounters hypoxic environment, it is reduced and bound to intracellular macromolecules, preventing the usual back-diffusion occurring in normal oxygenation conditions [46, 60, 127]. 18F-FMISO PET has been used to monitor hypoxia in the hearts of patients with myocardial ischemia [356], in lung cancer [193], in sarcomas [295], in breast cancer [59], in renal carcinoma [211], in brain and head and neck cancer [148, 254, 294], demonstrating a good correlation between of 18F-FMISO uptake and poor outcome to radiation treatment and chemotherapy.

However, the tracer has some limitations related to the presence of high normal liver uptake and urinary excretion. Although, the most important drawbacks are the absence of tracer accumulation in necrotic tissue and the modest signal-to-noise ratio, leading to unfavourable imaging characteristics.

Similar in principle to 18F-FMISO, but with better imaging qualities, are the most recently introduced hypoxic tracers, such as 18F-fluoroazomycin arabinoside (18F-FAZA) [280], 18F-fluoroery-thronitroimidazole (18F-FETNIM) [380], 18F-fluoroetanidazole (18F-FETA) [298], 18F-2-nitroimidazol-pentafluoropropyl acetamide (18F-EF5) [195, 208] and 18F-2 nitroimidazol-trifluoropropyl acetamide (18F-EF3) [175].

The group of non-nitroimidazole compounds has different mechanisms of accumulation and is represented by radiotracers such as ⁶⁴Cu-methylthiosemicarbazone (⁶⁴Cu-ATSM) [110] or iodine-labelled antibody Grawitz250 (124I-cG250) [210]. ⁶⁴Cu-ATSM appears to be rather promising for imaging tumour hypoxia with PET [265]. The mechanism of retention is largely attributed to the low oxygen tensions and the altered redox environment of hypoxic tumours [265]. This results in an optimal signal-to-background ratio, with absent ⁴⁶Cu-ATSM in normal tissue and

almost exclusive uptake in the hypoxic areas (Fig. 20.15). Physiologic distribution of the tracer is characterized by an elevated uptake in the liver, to a minor degree in the kidneys and, on delayed acquisitions, within the intestine secondary to biliary excretion [202]. At present, several preclinical and clinical studies have evaluated and validated the use of ^{64}Cu -ATSM for imaging hypoxia in tumours and other tissues [75–74, 110, 220, 221, 230, 240]. This is the case for lung and cervical cancers [75, 76, 230], head and neck tumour [124], glioma [345], where the ^{64}Cu -ATSM uptake was a good predictor of patient outcome, by discriminating those likely to respond to therapy from non-responders [339].

More limited evidence exists for ^{124}I -cG250 PET and much more need to be investigated on the clinical impact of hypoxic tracers in cancer treatment.

20.14 Clinical Potential of PET Tracers for Angiogenesis

Angiogenesis represents one of the key processes in tumour progression; therefore, many efforts have been made to identify antiangiogenic molecules and design antiangiogenic strategies for cancer treatment [44, 45, 105, 185]. Molecular imaging has consequently followed this step way by implementing radiolabelled compounds for non-invasive imaging. Principally, two different angiogenesis-related molecular targets have been studied the most; one is integrin ($\alpha v\beta 3$), while the second is vascular endothelial growth factor receptor (VEGFR) [45].

Integrins are a family of adhesion molecules actively involved in tumour angiogenesis and metastasis [165]. Among them, we find integrin $\alpha v\beta 3$, which binds to arginine-glycine-aspartic acid (RGD), and is known to be significantly upregulated on tumour vasculature but not on quiescent endothelium. Molecular imaging tracers containing RGD peptide have been promptly radiolabelled with numerous PET nuclides (^{18}F , ^{64}Cu , ^{68}Ga) for non-invasive monitoring of tumour angiogenesis via integrin $\alpha v\beta 3$ expression [27, 45, 57].

The other mechanism involved in the modulation of angiogenesis is VEGF/VEGFR signalling pathway, which is significant in both normal and pathologic vasculature development [99, 101]. At present, seven subtypes of VEGF and two different endothelium-specific receptors, VEGFR-1 and VEGFR-2, are known Hicks et al. [148]. There seems to be the worst prognosis when a VEGF/VEGFR overexpression is documented [100]. Therefore, VEGFR-targeted molecular imaging can serve as a new paradigm for assessing the efficacy of antiangiogenic therapeutics and patients outcome. For this purpose, PET imaging of VEGFR has been reported over the past several years [45].

Many antiangiogenic drugs have up to now been introduced for tumour treatment, like bevacizumab, sunitinib, sorafenib, etc., demonstrating therapeutic efficacy in several solid cancers [35, 236, 287]. However, this sort of molecular targeted therapy is not adequate in all patients. The main reason for imaging application in this field relies primarily on the possibility to precociously detect cancer patients who might benefit from a targeted antiangiogenic therapy.

Encouraging results have been reported on several radiopharmaceuticals, such as RGD radiolabelled peptides (18F-Galacto-RGD, 68Ga-NOTA-RGD, etc.) [173, 318] and VEGF radiolabelled tracers (64Cu-DOTA-VEGF) [44]. Further studies are, however, required to confirm the potentials of targeted antiangiogenic therapy imaging.

20.15 Clinical Potential of Immune-PET Tracers

The growing relevance of tumour immunology and immunotherapy with checkpoint inhibitors has promoted the development of molecular imaging agents targeting antibodies and antibody fragments for Immuno-PET [307]. Its application has for a long period been mostly limited to preclinical studies, although the radiopharmaceuticals have a huge potential for the prediction of response to immunotherapy [192]. The principal targets for immuno-PET comprise the major checkpoints, such as CTLA-4 or Cytotoxic T-Lymphocyte Antigen 4, the programmed death-1 (PD-1) and PD-ligand 1 (PD-L1), but also some of the principal representatives of tumour microenvironment and immune infiltrate, including CD3, CD8 TILs (tumour-infiltrating lymphocytes). For this purpose, either intact antibodies or smaller fragments can be radiolabelled, preferably with long half-live nuclides, such as iodine-124 (124I, 4.2 days), zirconium-89 (89Zr, 3.2 days), copper-64 (64Cu, 12.7 h) and yttrium-86 (86Y, 14.7 h) [272, 273, 350, 359].

One of the first compounds developed for this purpose was the 64Cu-labelled anti-mouse-CTLA-4 monoclonal antibody (64Cu-DOTA-anti-CTLA-4 mAb) [149]. The authors use the tracer to evaluate CTLA-4 expression in normal colon tissues, cultured CT26 cells (an undifferentiated colon carcinoma cell line) and CT26 colon cancer-bearing mice. In their study, higher CTLA-4 expression and significantly higher 64Cu-DOTA-anti-CTLA-4 mAb accumulation was noted in CT26 tumour tissue compared to control [149]. CTLA-4 expression was the target also for Ehlerding et al. [84], who utilized 64Cu-DOTA-ipilimumab in three NSCLC cell lines (A549, H460 and H358). Ipilimumab, a fully human Ig1 anti-CTLA-4 monoclonal antibody, has been the first checkpoint inhibitor approved in 2011 by FDA (Food and Drug Administration) for the treatment of advanced melanoma [152]. Similar to previous report, the authors suggest that 64Cu-DOTA-ipilimumab PET can help identify CTLA-4 expression in living tissues [84, 149].

An interesting target is representing also by the PD-1/PD-L1 blockade. One example is provided by Natarajan et al. [253], who labelled the anti-mouse PD-1 antibody (IgG) with copper-64 to image PD-1 expression on TILs in melanoma xenograft. Later on, the same researchers [252] labelled the anti-PD-1 human antibody (IgG; Keytruda) with either Zr-89 or Cu-64 for Immuno-PET of NOD-scid IL-2R γ null (NSG) mice (hNSG) bearing A375 human skin melanoma tumours. In the study, human TILs in melanoma of hNSG-non blocking mice exhibited at 24 h higher tracer uptake (either 89Zr-Keytruda or 64Cu-Keytruda) compared to NSG-control mice.

Other reports have targeted PD-L1 or PD-1 with either NOTA or DOTA conjugates [146, 241]. Hettich et al. [146] found that the tracer uptake was higher in the tumour, where the majority of induced TILs were CD8+ and expressed PD-1 on their cell surface. Maute et al. [241] radiolabelled the high affinity protein (HAC)-PD1 showing a nearly two-fold increase uptake for PD-L1 positive tumours over negative ones. Other authors evaluated CD3 (89Zr-p-isothiocyanatobenzyl-deferoxamine-CD3) and CD8 (89Zr-desferrioxamine-labelled anti-CD8 cys-diabody) expression in tumours during immunotherapy [207, 346].

Larimer et al. [207] showed that a high CD3 PET uptake in the anti-CTLA-4-treated mice correlated with tumour volume reduction and was predictive of response. Tavare et al. [346] demonstrated specific targeting of CD8 in vivo for wild-type mice versus a decreased uptake in lymphoid organs of CD8-blocked mice.

The above-mentioned preclinical studies, as well as other available in literature, show the potentials of immune-PET in providing the necessary tools to select patients, investigate response to checkpoint blockade and better understand immunotherapy efficacy.

References

1. Ackerstaff E, Pflug BR, Nelson JB et al (2001) Detection of increased choline compounds with proton nuclear magnetic resonance spectroscopy subsequent to malignant transformation of human prostatic epithelial cells. *Cancer Res* 61:3599–3603
2. Afshar-Oromieh A, Avtzi E, Giesel FL et al (2015) The diagnostic value of PET/CT imaging with the (68)Ga-labelled PSMA ligand HBED-CC in the diagnosis of recurrent prostate cancer. *Eur J Nucl Med Mol Imaging* 42(2):197–209
3. Afshar-Oromieh A, Babich JW, Kratochwil C et al (2016) The rise of PSMA ligands for diagnosis and therapy of prostate cancer. *J Nucl Med* 57:79S–89S
4. Afshar-Oromieh A, Hetzheim H, Kratochwil C et al (2015) The theranostic PSMA ligand PSMA-617 in the diagnosis of prostate cancer by PET/CT: biodistribution in humans, radiation dosimetry, and first evaluation of tumor lesions. *J Nucl Med* 56:1697–1705
5. Ahlström H, Eriksson B, Bergstrom M et al (1995) Pancreatic neuroendocrine tumors: diagnosis with PET. *Radiology* 195:333–337
6. Ahn T, Roberts MJ, Abduljabar A et al (2019) A review of prostate-specific membrane antigen (PSMA) positron emission tomography (PET) in renal cell carcinoma. *Mol Imaging Biol.* <https://doi.org/10.1007/s11307-018-01307-0>. (Epub ahead of print)
7. Albert NL, Winkelmann I, Suchorska B et al (2016) Early static (18)F-FET-PET scans have a higher accuracy for glioma grading than the standard 20–40 min scans. *Eur J Nucl Med Mol Imaging* 43:1105–1114
8. Albert NL, Weller M, Suchorska B, et al (2016) Response assessment in neuro-oncology working group and European association for neuro-oncology recommendations for the clinical use of PET imaging in gliomas. *Neuro Oncol* 18(9):1199–1208
9. Albrecht S, Buchegger F, Soloviev D et al (2007) (11)C-Acetate PET in the early evaluation of prostate cancer recurrence. *Eur J Nucl Med Mol Imaging* 34:185–196
10. Allan RM, Pike VW, Maseri A et al (1981) Myocardial metabolism of ¹¹C-acetate: experimental and patient studies. *Circulation* 64(Suppl IV):IV–75, (Abst)
11. Allan RM, Selwyn AP, Pike VW et al (1980) In vivo experimental and clinical studies of normal and ischemic myocardium using ¹¹C-acetate. *Circulation* 62 (Suppl III):111–174, (Abst)

12. Ambrosini V, Campana D, Bodei L et al (2010) 68Ga-DOTANOC PET/CT clinical impact in patients with neuroendocrine tumors. *J Nucl Med* 51(5):669–673
13. Ambrosini V, Campana D, Tomassetti P et al (2012) 68Ga-labelled peptides for diagnosis of gastroenteropancreatic NET. *Eur J Nucl Med Mol Imaging* 39(Suppl 1):S52–S60
14. Ambrosini V, Fanti S (2014) 68Ga-DOTA-peptides in the diagnosis of NET. *PET Clin.* 9 (1):37–42
15. Ambrosini V, Campana D, Nanni C et al (2012) Is 68Ga-DOTA-NOC PET/CT indicated in patients with clinical, biochemical or radiological suspicion of neuroendocrine tumour? *Eur J Nucl Med Mol Imaging* 39(8):1278–1283
16. Ambrosini V, Campana D, Polverani G et al (2015) Prognostic value of 68Ga-DOTANOC PET/CT SUVmax in patients with neuroendocrine tumors of the pancreas. *J Nucl Med* 56 (12):1843–1848
17. Ambrosini V, Marzola MC, Rubello D et al (2009) (68)Ga-somatostatin analogues PET and (18)F-DOPA PET in medullary thyroid carcinoma. *Eur J Nucl Med Mol Imaging*
18. Ambrosini V, Tomassetti P, Castellucci P et al (2008) Comparison between 68Ga-DOTA-NOC and 18F-DOPA PET for the detection of gastro-entero-pancreatic and lung neuro-endocrine tumours. *Eur J Nucl Med Mol Imaging* 35(8):1431–1438
19. Antunes P, Ginj M, Zhang H et al (2007) Are radiogallium-labelled DOTA-conjugated somatostatin analogues superior to those labelled with other radiometals? *Eur J Nucl Med Mol Imaging* 34(7):982–993
20. Banerjee SR, Pullambhatla M, Byun Y et al (2010) 68Ga-labeled inhibitors of prostate-specific membrane antigen (PSMA) for imaging prostate cancer. *J Med Chem* 53:5333–5341
21. Barrio M, Czernin J, Fanti S et al (2017) The impact of somatostatin receptor-directed PET/CT on the management of patients with neuroendocrine tumor: a systematic review and meta-analysis. *J Nucl Med* 58(5):756–761
22. Barthel H, Cleij MC, Collingridge DR et al (2003) 3'-Deoxy-3'-(¹⁸F)fluorothymidine as a new marker for monitoring tumor response to antiproliferative therapy in vivo with positron emission tomography. *Cancer Res* 63:3791–3798
23. Barthel H, Perumal M, Latigo J et al (2005) The uptake of 3'-deoxy-3'-(¹⁸F) fluorothymidine into L178Y tumours in vivo is dependent on thymidine kinase 1 protein levels. *Eur J Nucl Med Mol Imaging* 32(3):257–263
24. Bauman G, Belhocine T, Kovacs M et al (2012) 18F-fluorocholine for prostate cancer imaging: a systematic review of the literature. *Prostate Cancer Prostatic Dis* 15:45–55
25. Becherer A, Szabó M, Karanikas G et al (2004) Imaging of advanced neuroendocrine tumors with (18)F-FDOPA PET. *J Nucl Med* 45(7):1161–1167
26. Been LB, Suurmeijer AJH, Cobben DCP et al (2004) (18F) FLT-PET in oncology: current status and opportunities. *Eur J Nucl Med Mol Imaging* 31:1659–1672
27. Beer AJ, Haubner R, Sarbia M et al (2006) Positron emission tomography using (18F) galacto-RGD identifies the level of integrin $\alpha v \beta 3$ expression in man. *Clin Cancer Res* 12:3942–3949
28. Bell C, Dowson N, Puttick S et al (2015) Increasing feasibility and utility of (18)F-FDOPA PET for the management of glioma. *Nucl Med Biol* 42(10):788–795
29. Blake GM, Park-Holohan SJ, Cook GJ et al (2001) Quantitative studies of bone with the use of 18F-fluoride and 99mTc-methylene diphosphonate. *Semin Nucl Med* 31:28–49
30. Blau M, Nagler W, Bender MA (1962) A new isotope for bone scanning. *J Nucl Med* 3:332–334
31. Bollineni VR, Kramer GM, Jansma EP et al (2016) A systematic review on ((18)F)FLT-PET uptake as a measure of treatment response in cancer patients. *Eur J Cancer* 55:81–97
32. Borbély K, Nyáry I, Tóth M et al (2006) Optimization of semi-quantification in metabolic PET studies with 18F-fluorodeoxyglucose and 11C-methionine in the determination of malignancy of gliomas. *J Neurol Sci* 15:85–94

33. Borelli MI, Villar MJ, Orezza A et al (1997) Presence of DOPA decarboxylase and its localisation in adult rat pancreatic islet cells. *Diabetes Metab* 23:161–163
34. Bostwick DG, Pacelli A, Blute M et al (1998) Prostate specific membrane antigen expression in prostatic intraepithelial neoplasia and adenocarcinoma: a study of 184 cases. *Cancer* 82:2256–2261
35. Brandi G, Nannini M, Pantaleo MA et al (2008) Molecular imaging suggests efficacy of bevacizumab beyond the second line in advanced colorectal cancer patients. *Chemotherapy* 54(6):421–424
36. Braun V, Dempf S, Weller R et al (2002) Cranial neuronavigation with direct integration of (11)C methionine positron emission tomography (PET) data—results of a pilot study in 32 surgical cases. *Acta Neurochir* 144:777–782
37. Breeuwsma AJ, Pruijm J, Van den Bergh AC et al (2009) Detection of local, regional, and distant recurrence in patients with PSA relapse after external-beam radiotherapy using (11) C-Choline positron emission tomography. *Int J Radiat Oncol Biol Phys*
38. Briganti A, Chun FK-H, Salonia A et al (2006) Validation of a nomogram predicting the probability of lymph node invasion among patients undergoing radical prostatectomy and an extended pelvic lymphadenectomy. *Eur Urol* 49:1019–1027
39. Brown JM (1999) The hypoxic cell: A target for selective cancer therapy—Eighteenth Bruce F. Cain Memorial Award Lecture. *Cancer Res* 59:5863–5870
40. Buck AK, Herrmann K, Buschenfelde CM et al (2008) Imaging bone and soft tissue tumors with the proliferation marker (18F)fluorothymidine. *Clin Cancer Res* 14(10):2970–2977
41. Buck AK, Hetzel M, Schirrmeister H et al (2005) Clinical relevance of imaging proliferative activity in lung nodules. *Eur J Nucl Med Mol Imaging* 32:525–533
42. Buck AK, Schirrmeister H, Hetzel M et al (2002) 3-Deoxy-3-(¹⁸F)fluorothymidine-positron emission tomography for noninvasive assessment of proliferation in pulmonary nodules. *Cancer Res* 62:3331–3334
43. Buck AK, Vogg ATJ, Glatting G et al (2004) (¹⁸F)FLT for monitoring response to antiproliferative therapy in a mouse lymphoma xenotransplant model. *J Nucl Med* 45:434
44. Cai W, Chen K, Mohamedali KA et al (2006) PET of vascular endothelial growth factor receptor expression. *J Nucl Med* 47:2048–2056
45. Cai W, Gambhir SS, Chen X (2008) Chapter 7. Molecular imaging of tumor vasculature. *Methods Enzymol* 445:141–176
46. Caldwell JH, Revenaugh JR, Martin GV et al (1995) Comparison of fluorine-18-fluorodeoxyglucose and tritiated fluoromisonidazole uptake during low-flow ischemia. *J Nucl Med* 36:1633–1638
47. Carter RE, Feldman AR, Coyle JT (1996) Prostate-specific membrane antigen is a hydrolase with substrate and pharmacologic characteristics of a neuropeptidase. *Proc Natl Acad Sci USA* 93:749–753
48. Cascini GL, Niccoli Asabella A, Notaristefano A et al (2014) 124 Iodine: a longer-life positron emitter isotope—new opportunities in molecular imaging. *Biomed Res Int* 2014:672094
49. Castellucci P, Fuccio C, Rubello D et al (2011) Is there a role for 11C-choline PET/CT in the early detection of metastatic disease in surgically treated prostate cancer patients with a mild PSA increase < 1,5 ng/ml? *Eur J Nucl Med Mol Imaging* 38(1):55–63
50. Castellucci P, Fuccio C, Nanni C et al (2009) Influence of trigger PSA and PSA kinetics on 11C-Choline PET/CT detection rate in patients with biochemical relapse after radical prostatectomy. *J Nucl Med* 50(9):1394–1400
51. Castilla-Lièvre MA, Franco D, Gervais P et al (2016) Diagnostic value of combining 11C-choline and 18F-FDG PET/CT in hepatocellular carcinoma. *Eur J Nucl Med Mol Imaging* 43(5):852–859
52. Cater DB, Silver IA (1960) Quantitative measurements of oxygen tension in normal tissues and in tumors of patients before and after radiotherapy. *Acta Radiol* 53:233–256

53. Chan JL, Lee SW, Fraass BA et al (2002) Survival and failure patterns of high-grade gliomas after three-dimensional conformal radiotherapy. *J Clin Oncol* 20(6):1635–1642
54. Chang SS, Reuter VE, Heston WD, Gaudin PB (2001) Metastatic renal cell carcinoma neovasculature expresses prostate-specific membrane antigen. *Urology* 57:801–805
55. Chen W, Cloughesy T, Kamdar N et al (2005) Imaging proliferation in brain tumors with 18F-FLT PET: comparison with 18F-FDG. *J Nucl Med* 46(6):945–952
56. Chen S, Ho C, Feng D et al (2004) Tracer kinetic modeling of 11Cacetate applied in the liver with positron emission tomography. *IEEE Trans Med Imaging* 23(4):426–432
57. Chen X, Sievers E, Hou Y et al (2005) Integrin α v β 3-targeted imaging of lung cancer. *Neoplasia* 7:271–279
58. Chen W, Delaloye S, Silverman DHS et al (2007) Predicting treatment response of malignant gliomas to bevacizumab and irinotecan by imaging proliferation with (18F) fluorothymidine positron emission tomography: a pilot study. *J Clin Oncol* 25(30):4714e21
59. Cheng J, Lei L, Xu J et al (2013) 18F-Fluoromi-sonidazole PET/CT: a potential tool for predicting primary endocrine therapy resistance in breast cancer. *J Nucl Med* 54:333–340
60. Cher LM, Murone C, Lawrentschuck N et al (2006) Correlation of hypoxic cell fraction and angiogenesis with glucose metabolic rate in gliomas using 18F-fl uoromisonidazole, 18F-FDG PET, and immunohistochemical studies. *J Nucl Med* 47:410–418
61. Chierichetti F, Lessi G, Bissoli S et al (2005) Preliminary experience with 11C-Acetate and PET/CT in prostate cancer. *J Nucl Med* (Supplement 2):46
62. Cho SY, Gage KL, Mease RC et al (2012) Biodistribution, tumor detection, and radiation dosimetry of 18F-DCFBC, a low-molecular-weight inhibitor of prostate-specific membrane antigen, in patients with metastatic prostate cancer. *J Nucl Med* 53:1883–1891
63. Chung JK, Kim YK, Kim SK et al (2002) Usefulness of 11C-methionine PET in the evaluation of brain lesions that are hypo- or isometabolic on 18F-FDG PET. *Eur J Nucl Med Mol Imaging* 29:176–182
64. Cimitan M, Bortolus R, Morassut S et al (2006) (18F)fluorocholine PET/CT imaging for the detection of recurrent prostate cancer at PSA relapse: experience in 100 consecutive patients. *Eur J Nucl Med Mol Imaging* 33(12):1387–1398
65. Cobben DC, Elsinga PH, Hoekstra HJ et al (2004) Is 18F-3'-fl uoro-3'-deoxy-L-thymidine useful for the staging and restaging of non-small cell lung cancer? *J Nucl Med* 45:1677–1682
66. Coenen HH, Kling P, Stocklin G (1989) Cerebral metabolism of L-(2-18F)fluorotyrosine, a new PET tracer of protein synthesis. *J Nucl Med* 30:1367–1372
67. Comar D, Cartron JC, Maziere M et al (1976) Labeling and metabolism of methionine-methyl-11C. *Eur J Nucl Med* 1:11–14
68. Cook GJ, Maisey MN, Fogelman I (1999) Normal variants, artefacts and interpretative pitfalls in PET imaging with 18-fl uoro-2-deoxyglucose and carbon-11 methionine. *Eur J Nucl Med* 26:1363–1378
69. Crabtree HG, Cramer W (1933) The action of radium on cancer cells I and II. Some factors determining the susceptibility of cancer cells to radium. *Proc R Soc Ser B* 113:238–250
70. De Jong IJ, Pruim J, Elsinga PH et al (2002) Visualization of bladder cancer using ¹¹C-choline PET: first clinical experience. *Eur J Nucl Med* 29:1283–1288
71. DeGrado TR, Coleman RE, Wang S et al (2001) Synthesis and evaluation of 18F labeled choline as an oncologic tracer for positron emission tomography: Initial findings in prostate cancer. *Cancer Res* 61:110–117
72. Dearling JLD, Lewis JS, Mullen GE et al (1998) Design of hypoxia-targeting radiopharmaceuticals: Selective uptake of copper-64 complexes in hypoxic cells in vitro. *Eur J Nucl Med* 25:788–792
73. Dearling JL, Lewis JS, Mullen GE et al (2002) Copper bis(thiosemicarbazone) complexes as hypoxia imaging agents: structure-activity relationships. *J Biol Inorg Chem* 7:249–259
74. Dearling JLD, Lewis JS, Welch MJ et al (1998) Redox-active complexes for imaging hypoxic tissues: Structure-activity relationships in copper(II)bis(thiosemicarbazone) complexes. *Chem Commun* 22:2531–2533

75. Dehdashti F, Grigsby PW, Mintun MA et al (2003) Assessing tumor hypoxia in cervical cancer by positron emission tomography with ^{60}Cu -ATSM: relationship to therapeutic response—a preliminary report. *Int J Radiat Oncol Biol Phys* 55:1233–1238
76. Dehdashti F, Mintun MA, Lewis JS et al (2003) In vivo assessment of tumor hypoxia in lung cancer with ^{60}Cu -ATSM. *Eur J Nucl Med Mol Imaging* 30:844–850
77. Delbeke D, Pinson CW (2003) ^{11}C -acetate: a new tracer for the evaluation of hepatocellular carcinoma. *J Nucl Med* 44:222–223
78. Derlon JM, Bourdet C, Bustany P et al (1989) ^{11}C L-methionine uptake in gliomas. *Neurosurgery* 25:720–728
79. Dimitrakopoulou-Strauss A, Strauss LG (2003) PET imaging of prostate cancer with ^{11}C -acetate. *J Nucl Med* 44:556–558
80. Dimitrakopoulou-Strauss A, Strauss LG, Burger C (2001) Quantitative PET studies in pretreated melanoma patients: a comparison of 6-(^{18}F)fluoro-L-dopa with ^{18}F -FDG and (^{15}O)-water using compartment and noncompartment analysis. *J Nucl Med* 42(2):248–256
81. Dittman H, Dohmen BM, Paulsen F et al (2003) ^{18}F FLT PET for diagnosis and staging of thoracic tumours. *Eur J Nucl Med Mol Imaging* 30:1407–1412
82. Dunet V, Rossier C, Buck A et al (2012) Performance of ^{18}F -fluoro-ethyl-tyrosine (^{18}F -FET) PET for the differential diagnosis of primary brain tumor: a systematic review and metaanalysis. *J Nucl Med* 53:207–214
83. Eder M, Schafer M, Bauder-Wust U et al (2012) ^{68}Ga -complex lipophilicity and the targeting property of a urea-based PSMA inhibitor for PET imaging. *Bioconjug Chem* 23:688–697
84. Ehlerding EB, England CG, Majewski RL et al (2017) ImmunoPET imaging of CTLA-4 expression in mouse models of non-small cell lung cancer. *Mol Pharm* 14(5):1782–1789
85. Eiber M, Maurer T, Beer AJ et al (2014) Prospective evaluation of PSMA-PET imaging for preoperative lymph node staging in prostate cancer. *J Nucl Med* 55(Suppl 1):20
86. Eiber M, Maurer T, Souvatzoglou M et al (2015) Evaluation of hybrid ^{68}Ga -PSMA Ligand PET/CT in 248 patients with biochemical recurrence after radical prostatectomy. *J Nucl Med* 56:668–674
87. Eidelberg D (1992) Positron emission tomography studies in parkinsonism. *Neurol Clin* 10:421–433
88. Eriksson B, Bergstrom M, Sundin A et al (2002) The role of PET in localization of neuroendocrine and adrenocortical tumors. *Ann NY Acad Sci* 970:159–169
89. Eschmann SM, Reischl G, Bilger K et al (2002) Evaluation of dosimetry of radioiodine therapy in benign and malignant thyroid disorders by means of iodine-124 and PET. *Eur J Nucl Med Mol Imaging* 29:760–767
90. Eshuis SA, Jager PL, Maguire RP et al (2009) Direct comparison of FP-CIT SPECT and F-DOPA PET in patients with Parkinson's disease and healthy controls. *Eur J Nucl Med Mol Imaging* 36:454–462
91. Eshuis SA, Maguire RP, Leenders KL et al (2006) Comparison of FP-CIT SPECT with F-DOPA PET in patients with de novo and advanced Parkinson's disease. *Eur J Nucl Med Mol Imaging* 33(2):200–209
92. Evangelista L, Bertoldo F, Boccardo F et al (2016) Diagnostic imaging to detect and evaluate response to therapy in bone metastases from prostate cancer: current modalities and new horizons. *Eur J Nucl Med Mol Imaging* 43(8):1546–1562
93. Evangelista L, Briganti A, Fanti S, et al (2016) New clinical indications for ^{18}F /(^{11}C)-choline, new tracers for positron emission tomography and a promising hybrid device for prostate cancer staging: a systematic review of the literature. *Eur Urol* 70(1):161–175
94. Even-Sapir E, Metser U, Flusser G et al (2004) Assessment of malignant skeletal disease with ^{18}F -fluoride PET/CT. *J Nucl Med* 45:272–278
95. Even-Sapir E, Metser U, Mishani E et al (2006) The Detection of bone metastases in patients with high-risk prostate cancer: $^{99\text{m}}\text{Tc}$ -MDP planar bone scintigraphy, single- and multi-field-of-view SPECT, ^{18}F -Fluoride PET, and ^{18}F -Fluoride PET/CT. *J Nucl Med* 47:287–297

96. Fanti S, Nanni C, Ambrosini V et al (2007) PET in genitourinary tract cancers. *Q J Nucl Med Mol Imaging* 51(3):260–271
97. Farsad M, Schiavina R, Castellucci P et al (2005) Detection and localization of prostate cancer: correlation of ¹¹C-choline PET/CT with histopathologic step-section analysis. *J Nucl Med* 46(10): 1642–1649
98. Fedorova OS, Kuznetsova OF, Shatik SV et al (2009) (¹⁸F)-labeled tyrosine derivatives: synthesis and experimental studies on accumulation in tumors and abscesses. *Bioorg Khim* 35(3):334–343
99. Ferrara N (2002) VEGF and the quest for tumour angiogenesis factors. *Nat Rev Cancer* 2:795–803
100. Ferrara N (2004) Vascular endothelial growth factor: Basic science and clinical progress. *Endocr Rev* 25:581–611
101. Ferrara N (2005) The role of VEGF in the regulation of physiological and pathological angiogenesis. *EXS* 94:209–231
102. Fiebrich HB, Brouwers AH, Kerstens MN et al (2009) 6-(F-18)Fluoro-L-dihydroxyphenylalanine positron emission tomography is superior to conventional imaging with (¹²³I)-metaiodobenzylguanidine scintigraphy, computer tomography, and magnetic resonance imaging in localizing tumors causing catecholamine excess. *J Clin Endocrinol Metab* 94(10):3922–3930
103. Firnau G, Chiakal R, Garnett ES (1984) Aromatic radiofluorination with ¹⁸F fluorine gas: 6-(¹⁸F)fluoro-L-dopa. *J Nucl Med* 25:1228–1233
104. Floeth FW, Pauleit D, Sabel M et al (2007) Prognostic value of O-(2-¹⁸F-fluoroethyl)-L-tyrosine PET and MRI in low-grade glioma. *J Nucl Med* 48:519–527
105. Folkman J (2007) Angiogenesis: an organizing principle for drug discovery? *Nat. Rev Drug Discov* 6:273–286
106. Francis DL, Visvikis D, Costa DC et al (2003) Potential impact of (¹⁸F)3'-deoxy-3'-fluorothymidine versus (¹⁸F)fluoro-2-deoxy-D-glucose in positron emission tomography for colorectal cancer. *Eur J Nucl Me Mol Imaging* 30(7):988–994
107. Freudenberg LS, Antoch G, Jentzen W et al (2004) Value of ¹²⁴I-PET/CT in staging of patients with differentiated thyroid cancer. *Eur Radiol* 14:2092–2098
108. Freudenberg LS, Antoch G, Jentzen W et al (2004) Value of (¹²⁴I)-I-PET/CT in staging of patients with differentiated thyroid cancer. *Eur Radiol* 14(11):2092–2098
109. Fuccio C, Castellucci P, Schiavina R et al (2010) Role of ¹¹C-choline PET/CT in the restaging of prostate cancer patients showing a single lesion on bone scintigraphy. *Ann Nucl Med* 24(6):485–492
110. Fujibayashi Y, Taniuchi H, Yonekura Y et al (1997) Copper-62-ATSM: a new hypoxia imaging agent with high membrane permeability and low redox potential. *J Nucl Med* 38:1155–1160
111. Gabriel M, Decristoforo C, Kendler D et al (2007) ⁶⁸Ga-DOTA-Tyr3-octreotide PET in neuroendocrine tumors: comparison with somatostatin receptor scintigraphy and CT. *J Nucl Med* 48(4):508–518
112. Gabriel M, Andergassen U, Putzer D et al (2010) Individualized peptide-related-radiionuclide-therapy concept using different radiolabelled somatostatin analogs in advanced cancer patients. *Q J Nucl Med Mol Imaging* 54(1):92–99
113. Galldiks N, Ullrich R, Schroeter M et al (2010) Volumetry of ((¹¹C)-methionine PET uptake and MRI contrast enhancement in patients with recurrent glioblastoma multiforme. *Eur J Nucl Med Mol Imaging* 37:84–92
114. Garnett ES, Firnau G, Nahmias C (1983) Dopamine visualized in the basal ganglia of living man. *Nature* 305:137–138
115. Gazdar AF, Helman LJ, Israel MA et al (1988) Expression of neuroendocrine cell markers L-dopa decarboxylase, chromogranin A, and dense core granules in human tumors of endocrine and nonendocrine origin. *Cancer Res* 48:4078–4082

116. Giesel FL, Hadaschik B, Cardinale J et al (2016) F-18 labelled PSMA-1007: biodistribution, radiation dosimetry and histopathological validation of tumor lesions in prostate cancer patients. *Eur J Nucl Med Mol Imaging* 44:678–688
117. Ginj M, Zhang H, Waser B et al (2006) Radiolabeled somatostatin receptor antagonists are preferable to agonists for in vivo peptide receptor targeting of tumors. *Proc Natl Acad Sci U S A* 103:16436–16441
118. Giovacchini G, Giovannini E, Riondato M, Ciarmiello A (2018) PET/CT With 68Ga-PSMA in prostate cancer: radiopharmaceutical background and clinical implications. *Curr Radiopharm* 11(1):4–13
119. Giovacchini G, Picchio M, Coradeschi E et al (2008) ((11)C)choline uptake with PET/CT for the initial diagnosis of prostate cancer: relation to PSA levels, tumour stage and anti-androgenic therapy. *Eur J Nucl Med Mol Imaging* 35(6):1065–1073
120. Goldman S, Levivier M, Pirotte B et al (1997) Regional methionine and glucose uptake in high-grade gliomas: a comparative study on PET-guided stereotactic biopsy. *J Nucl Med* 38:1459–1462
121. Goodman MM, Keil R, Shoup TM et al (1997) Fluorine-18-FPCT: a PET radiotracer for imaging dopamine transporters. *J Nucl Med* 38:119–126
122. Gourgiotis L, Sarlis NJ, Reynolds JC et al (2003) Localization of medullary thyroid carcinoma metastasis in a multiple endocrine neoplasia type 2A Patient by 6-(18F)-Fluorodopamine positron emission tomography. *J Clin Endocrinol Metab* 88(2):637–641
123. Grant FD, Fahey FH, Packard AB et al (2008) Skeletal PET with 18F-fluoride: applying new technology to an old tracer. *J Nucl Med* 49(1):68–78
124. Grassi I, Nanni C, Cicoria G et al (2014) Usefulness of 64Cu-ATSM in head and neck cancer: a preliminary prospective study. *Clin Nucl Med* 39:e59–e63
125. Gray LH, Conger AD, Ebert M et al (1953) Concentration of oxygen dissolved in tissues at the time of irradiation as a factor in radiotherapy. *Br J Radiol* 26:638–648
126. Grosu AL, Weber WA, Riedel E et al (2005) L-(methyl-11C) methionine positron emission tomography for target delineation in resected high-grade gliomas before radiotherapy. *Int J Radiat Oncol Biol Phys* 63(1):64–74
127. Groves AM, Win Th, Ben Haim S et al (2007) Non-(18F)FDG PET in clinical oncology. *Lancet Oncol* 8:822–830
128. Gumprecht H, Grosu AL, Souvatsoqlou M et al (2007) 11C-Methionine positron emission tomography for preoperative evaluation of suggestive low-grade gliomas. *Zentralbl Neurochir* 68:19–23
129. Han S, Woo S, Kim YJ, Suh CH (2018) Impact of 68Ga-PSMA PET on the management of patients with prostate cancer: a systematic review and meta-analysis. *Eur Urol* 74(2):179–190
130. Hara T, Kosaka N, Kishi H (1998) PET imaging of prostate cancer using carbon-11-choline. *J Nucl Med* 39:990–995
131. Hara T, Kosaka N, Kishi H (2002) Development of (18F)-Fluoroethylcholine for cancer imaging with PET: synthesis, biochemistry, and prostate cancer imaging. *J Nucl Med* 43:187–199
132. Hara T, Yuasa M, Yoshida H (1997) Automated synthesis of fluorine-18 labeled choline analogue: 2-fluoroethyl- dimethyl-2-oxethylammonium (abstract). *J Nucl Med* 38:44P
133. Hara, T, Kosada N, Kondo T et al (1997) Imaging of brain tumor, lung cancer, esophageal cancer, colon cancer, prostate cancer and bladder cancer with (C-11)choline. *J Nucl Med* 38:250P (Abstract)
134. Hara T, Kondo T, Hara T et al (2003) Use of 18F-choline and 11C-choline as contrast agents in positron emission tomography imaging-guided stereotactic biopsy sampling of gliomas. *J Neurosurg* 99(3):474–479
135. Hardy O, Hernandez-Pampaloni M, Saffer JR et al (2007) Diagnosis and localization of focal congenital hyperinsulinism by 18F-fluorodopa PET scan. *J Pediatr* 150(2):140–145

136. Hardy OT, Hernandez-Pampaloni M, Saffer JR et al (2007) Accuracy of (18F)fluorodopa positron emission tomography for diagnosing and localizing focal congenital hyperinsulinism. *J Clin Endocrinol Metab* 92(12):4706–4711
137. Haseebuddin M, Dehdashti F, Siegel BA et al (2013) 11C-acetate PET-CT before radical prostatectomy: Nodal staging and treatment failure prediction. *J Nucl Med* 54(5):699–706
138. Hatazawa J, Ishiwata K, Itoh M et al (1989) Quantitative evaluation of L-(methyl-C-11) methionine uptake in tumor using positron emission tomography. *J Nucl Med* 30:1809–1813
139. Heiss P, Mayer S, Herz M et al (1999) Investigation of transport mechanism and uptake kinetics of O-(2-¹⁸F-fluoroethyl)-L-tyrosine in vitro and in vivo. *J Nucl Med* 40:1367–1373
140. Heiss WD, Wienhard K, Wagner R et al (1996) F-Dopa as an amino acid tracer to detect brain tumours. *J Nucl Med* 37(7):1180–1182
141. Herholz K, Hölzer T, Bauer B et al (1998) 11-C-methionine PET for differential diagnosis of low-grade gliomas. *Neurology* 50:1316–1322
142. Herrmann K, Bluemel C, Weineisen M et al (2015) Biodistribution and radiation dosimetry for a probe targeting prostate-specific membrane antigen for imaging and therapy. *J Nucl Med* 56:855–861
143. Herrmann K, Buck AK, Schuster T et al (2011) Predictive value of initial 18F-FLT uptake in patients with aggressive non-hodgkin lymphoma receiving R-CHOP treatment. *J Nucl Med* 52(5):690–696
144. Herrmann K, Buck AK, Schuster T et al (2014) Week one FLT-PET response predicts complete remission to R-CHOP and survival in DLBCL. *Oncotarget* 5(12):4050–4059
145. Herrmann K, Takei T, Kanegae K et al (2009) Clinical value and limitations of 11(C)-Methionine PET for detection and localization of suspected parathyroid adenomas. *Mol Imaging Biol* 11(5):356–363
146. Hettich M, Braun F, Bartholoma MD et al (2016) High-resolution PET imaging with therapeutic antibody-based PD-1/PD-L1 checkpoint tracers. *Theranostics* 6(10):1629–1640
147. Hetzel M, Arslanemir C, König HH et al (2003) F-18 NaF PET for detection of bone metastases in lung cancer: accuracy, cost-effectiveness, and impact on patient management. *J Bone Miner Res* 18:2206–2214
148. Hicks RJ, Rischin D, Fisher R et al (2005) Utility of FMISO PET in advanced head and neck cancer treated with chemoradiation incorporating a hypoxia-targeting chemotherapy agent. *Eur J Nucl Med Mol Imaging* 32:1384–1391
149. Higashikawa K, Yagi K, Watanabe K et al (2014) 64Cu-DOTA-Anti-CTLA-4 mAb enabled PET visualization of CTLA-4 on the T-Cell infiltrating tumor tissues. *PLoS ONE* 9(11): e109866
150. Ho CL, Yu SC, Yeung DW (2003) 11C-acetate PET imaging in hepatocellular carcinoma and other liver masses. *J Nucl Med* 44:213–221
151. Ho CL, Chen S, Yeung DW et al (2007) Dual-tracer PET/CT imaging in evaluation of metastatic hepatocellular carcinoma. *J Nucl Med* 48(6):902–909
152. Hodi FS, O'Day SJ, McDermott DF et al (2010) Improved survival with ipilimumab in patients with metastatic melanoma. *N Engl J Med* 363:711–723
153. Hoeben BAW, Troost EGC, Span PN et al (2013) 18F-FLT PET during radiotherapy or chemoradiotherapy in head and neck squamous cell carcinoma is an early predictor of outcome. *J Nucl Med* 54(4):532e40
154. Hoegerle S, Althoefer C, Ghanem N et al (2001) Whole Body 18F-DOPA PET for detection of gastrointestinal carcinoid tumors. *Radiology* 220:373–380
155. Hoegerle S, Althoefer C, Ghanem N et al (2001) 18F-DOPA positron emission tomography for tumour detection in patients with medullary thyroid carcinoma and elevated calcitonin levels. *Eur J Nucl Med* 28(1):64–71
156. Hoegerle S, Ghanem N, Althoefer C et al (2003) 18F-DOPA positron emission tomography for the detection of glomus tumours. *Eur J Nucl Med Mol Imaging* 30(5):689–694
157. Hoegerle S, Nitzsche E, Althoefer C et al (2002) Pheochromocytomas: detection with 18F DOPA whole body PET—initial results. *Radiology* 222(2):507–512

158. Hoffman RM (1984) Altered methionine metabolism, DNA methylation and oncogenic expression in carcinogenesis. *Biochem Biophys Acta* 738:49–87
159. Hofman MS, Irvani A (2017) Gallium-68Prostate-specific membrane antigen PET imaging. *PET Clin* 12(2):219–234
160. Howard BV, Howard WJ (1975) Lipids in normal and tumor cells in culture. *Prog Biochem Pharmacol* 10:135–166
161. Huang MC, Shih MH, Chung WY et al (2005) Malignancy of intracerebral lesions evaluated with 11C-methionine-PET. *J Clin Neurosci* 12:775–780
162. Husarik DB, Miralbell R, Dubs M et al (2008) Evaluation of ((18)F)-choline PET/CT for staging and restaging of prostate cancer. *Eur J Nucl Med Mol Imaging* 35(2):253–263
163. Hustinx R, Pourdehnad M, Kaschten B et al (2005) PET imaging for differentiating recurrent brain tumours from radiation necrosis. *Radiol Clin North Am* 43:35–47
164. Hwang KH, Choi DJ, Lee SY et al (2009) Evaluation of patients with hepatocellular carcinomas using ((11)C)acetate and ((18)F)FDG PET/CT: A preliminary study. *Appl Radiat Isot* 67(7–8):1195–1198
165. Hynes RO (2002) Integrins: bidirectional, allosteric signaling machines. *Cell* 110:673–687
166. Imani F, Agopian VG, Auerbach MS et al (2009) 18F-FDOPA PET and PET/CT accurately localize pheochromocytomas. *J Nucl Med* 50(4):513–519
167. Israeli RS, Powell CT, Corr JG et al (1994) Expression of the prostate-specific membrane antigen. *Cancer Res* 54:1807–1811
168. Ito Y, Fujita M, Shimada S et al (1999) Comparison between the decrease of dopamine transporter and that of L-DOPA uptake for detection of early to advanced stage of Parkinson's disease in animal models. *Synapse* 31:178–185
169. Iwai Y, Yamanaka K, Oda J et al (2001) Tracer accumulation in radiation necrosis of the brain after thallium-201 SPECT and ((11)C)methionine PET: case report. *Neurol Med Chir (Tokyo)* 41:415–418
170. Iwata Y, Shiomi S, Sasaki N et al (2000) Clinical usefulness of positron emission tomography with fluorine-18-fluorodeoxyglucose in the diagnosis of liver tumors. *Ann Nucl Med* 14:121–126
171. Jacob T, Grahek D, Younsi N et al (2003) Positron emission tomography with (18F)FDOPA and (18F)FDG in the imaging of small cell lung carcinoma: preliminary results. *Eur J Nucl Med Mol Imaging* 30:1266–1269
172. Jager PL, Vaalburg W, Pruijm J et al (2001) Radiolabeled amino acids: Basic aspects and clinical applications in oncology. *J Nucl Med* 42(3):432–445
173. Jeong JM, Hong MK, Chang YS et al (2008) Preparation of a promising angiogenesis PET imaging agent: 68Ga-labeled c(RGDyK)-isothiocyanatobenzyl-1,4,7-triazacyclononane-1,4,7-triacetic acid and feasibility studies in mice. *J Nucl Med* 49(5):830–836
174. De Jong I, Pruijm J, Elsinga PH et al (2003) 11C-choline positron emission tomography for the evaluation after treatment of localized prostate cancer. *Eur Urol* 44:32–38
175. Josse O, Labar D, Georges B, Gregoire V, Marchand-Brynaert J (2001) Synthesis of (18F)-labeled EF3 (2-(2-Nitroimidazol-1yl)-N-(3,3,3-trifluoropropyl)-acetamide), a Marker for PET Detection of Hypoxia. *Bioorg Med Chem* 9:665–675
176. Kahraman D, Holstein A, Scheffler M et al (2012) Tumor lesion glycolysis and tumor lesion proliferation for response prediction and prognostic differentiation in patients with advanced non-small cell lung cancer treated with erlotinib. *Clin Nucl Med* 37(11):1058–1064
177. Kaim AH, Weber B, Kurrer MO et al (2002) ¹⁸F-FDG and ¹⁸F-FET uptake in experimental soft tissue infection. *Eur J Nucl Med Mol Imaging* 29:648–654
178. Kameyama M, Shirane R, Itoh J et al (1990) The accumulation of 11C-methionine in cerebral glioma patients studied with PET. *Acta Neurochir (Wien)* 104:8–12
179. Kang DE, White RL Jr, Zuger JH et al (2004) Clinical use of fluorodeoxyglucose F 18 positron emission tomography for detection of renal cell carcinoma. *J Urol* 171:1806–1809
180. Kaschten B, Stevenaert A, Sadzot B et al (1998) Preoperative evaluation of 54 gliomas by PET with fluorine-18- fluorodeoxyglucose and/or carbon-11-methionine. *J Nucl Med* 39:778–785

181. Kato TJ, Shinoda N, Oka K et al (2008) Analysis of 11C-methionine uptake in low-grade gliomas and correlation with proliferative activity. *Am J Neuroradiol* 29:1867–1871
182. Kayani I, Groves AM (2006) 18F-fl uorodeoxyglucose PET/CT in cancer imaging. *Clin Med* 6:240–244
183. Kelloff GJ, Hoff man JM, Johnson B et al (2005) Progress and promise of FDG-PET imaging for cancer patient management and drug development. *Clin Cancer Res* 11:2785–2808
184. Kenny LM, Vigushin DM, Al-Nahhas A et al (2005) Quantification of cellular proliferation in tumor and normal tissues of patients with breast cancer by (18F)fluorothymidine-positron emission tomography imaging: evaluation of analytical methods. *Cancer Res* 65(21):10104–10112
185. Kerbel R, Folkmal J (2002) Clinical translation of angiogenesis inhibitors. *Nat Rev Cancer* 2:727–739
186. Kesler M, Levine C, Hershkovitz D et al (2018) 68Ga-PSMA is a novel PET-CT tracer for imaging of hepatocellular carcinoma: a prospective pilot study. *J Nucl Med pii: jnumed.118.214833*. <https://doi.org/10.2967/jnumed.118.214833>. (Epub ahead of print)
187. Khorjekar GR, Van Nostrand D, Garcia C et al (2014) Do negative ¹²⁴I pretherapy positron emission tomography scans in patients with elevated serum thyroglobulin levels predict negative ¹³¹I posttherapy scans? *Thyroid* 24:1394–1399
188. Kim S, Chung JK, Im SH et al (2005) 11C-methionine PET as a prognostic marker in patients with glioma: comparison with 18F-FDG PET. *Eur J Nucl Med Mol Imaging* 32:52–59
189. Kinoshita Y, Kuratsukuri K, Landas S et al (2006) Expression of prostate-specific membrane antigen in normal and malignant human tissues. *World J Surg* 30:628–636
190. Kirchner J, Schaarschmidt BM, Sawicki LM et al (2017) Evaluation of practical interpretation hurdles in 68Ga-PSMA PET/CT in 55 patients: physiological tracer distribution and incidental tracer uptake. *Clin Nucl Med* 42:e322–e327
191. Kist JW, de Keizer B, van der Vlies M et al (2016) 124I PET/CT to predict the outcome of blind 131I treatment in patients with biochemical recurrence of differentiated thyroid cancer: results of a multicenter diagnostic cohort study (THYROPET). *J Nucl Med* 57(5):701–707
192. Knowles SM, Am Wu (2012) Advances in immuno-positron emission tomography: antibodies for molecular imaging in oncology. *J Clin Oncol* 30(31):3884–3892
193. Koh WJ, Bergman KS, Rasey JS et al (1995) Evaluation of oxygenation status during fractionated radiotherapy in human nonsmall cell lung cancers using (F- 18)fluoromisonidazole positron emission tomography. *Int J Radiat Oncol Biol Phys* 33:391–398
194. Koh W-J, Rasey JS, Evans ML (1992) Imaging of hypoxia in human tumors with (F-18) fluoromisonidazole. *Int J Radiat Oncol Biol Phys* 22:199–212
195. Komar G, Seppänen M, Eskola O et al (2008) 18F-EF5: a new PET tracer for imaging hypoxia in head and neck cancer. *J Nucl Med* 49:1944–1951
196. Kotzerke J, Prang J, Neumaier B et al (2000) Experience with carbon-11 choline positron emission tomography in prostate carcinoma. *Eur J Nucl Med* 27:1415–1419
197. Kotzerke J, Volkmer BJ, Neumaier B et al (2002) Carbon-11 acetate positron emission tomography can detect local recurrence of prostate cancer. *Eur J Nucl Med* 29:1380–1384
198. Kracht LW, Friese M, Herholz K et al (2003) Methyl-(11C)-lmethionine uptake as measured by positron emission tomography correlates to microvessel density in patients with glioma. *Eur J Nucl Med Mol Imaging* 30:868–873
199. Krause BJ, Souvatzoglou M, Tinsel M et al (2008) The detection rate of 11-C choline PET/TC depends on the serum PSA-value in patients with biochemical recurrence of prostate cancer. *Eur J Nucl Med Mol Imaging* 35:18–23
200. Krebs HA (1948) The tricarboxylic acid cycle. *Harvey Lect Series* 44:165–199
201. Van Laere K, Ceyssens S, Van Calenberg F et al (2005) Direct comparison of 18F-FDG and 11C-methionine PET in suspected recurrence of glioma: sensitivity, inter-observer variability and prognostic value. *Eur J Nucl Med Mol Imaging* 32:39–51
202. Laforest R, Dehdashti F, Lewis J et al (2005) Dosimetry of 60/61/62/64 Cu-ATSM: a hypoxia imaging agent for PET. *Eur J Nucl Med Mol Imaging* 32:764–770

203. Lambrecht RM, Woodhouse N, Phillips R et al (1988) Investigational study of iodine-124 with a positron camera. *Am J Physiol Imaging* 3(4):197–200
204. Langen KJ, Hamacher K, Weckesser M et al (2006) O-(2-(18F)fluoroethyl)-L-tyrosine: uptake mechanisms and clinical applications. *Nucl Med Biol* 33(3):287–294
205. Langsteger W, Heinisch M, Fogelman I (2006) The role of fluorodeoxyglucose, 18F-dihydroxyphenylalanine, 18F-choline, and 18F-fluoride in bone imaging with emphasis on prostate and breast. *Semin Nucl Med* 36:73–92
206. Lapela M, Leskinen-Kallio S, Varpula M et al (1994) Imaging of uterine carcinoma by carbon-11-methionine and PET. *J Nucl Med* 35(10):1618–1623
207. Larimer BM, Wehrenberg-Klee E, Caraballo A, Mahmood U (2016) Quantitative CD3 PET imaging predicts tumor growth response to Anti-CTLA-4 therapy. *J Nucl Med* 57(10):1607–1611
208. Laughlin KM, Evans SM, Jenkins WT et al (1996) Biodistribution of the nitroimidazole EF5 (2-(2-nitro-1H-imidazol-1-yl)-N-(2,2,3,3,3-pentafluoropropyl) acetamide) in mice bearing subcutaneous EMT6 tumors. *J Pharmacol Exp Ther* 277:1049–1057
209. Law I, Albert NL, Arbizu J et al (2018) Joint EANM/EANO/RANO practice guidelines/SNMMI procedure standards for imaging of gliomas using PET with radiolabelled amino acids and (18F)FDG: version 1.0. *Eur J Nucl Med Mol Imaging*. <https://doi.org/10.1007/s00259-018-4207-9>. (Epub ahead of print)
210. Lawrentschuk N, Lee FT, Jones G, Rigopoulos A, Mountain A, O’Keefe G, Papenfuss AT, Bolton DM, Davis ID, Scott AM (2011) Investigation of hypoxia and carbonic anhydrase IX expression in a renal cell carcinoma xenograft model with oxygen tension measurements and 124I-cG250 PET/CT. *Urol Oncol* 29:411–420
211. Lawrentschuk N, Poon AMT, Foo SS, Johns LG, Putra J, Murone C, Davis ID, Bolton DM, Scott AM (2005) Assessing regional hypoxia in human renal tumours using 18F-fluoromisonidazole positron emission tomography. *BJU Int* 96:540–546
212. Lazzeri M, Lopci E, Lughezzani G et al (2017) Targeted 11C-choline PET-CT/TRUS software fusion-guided prostate biopsy in men with persistently elevated PSA and negative mpMRI after previous negative biopsy. *Eur J Hybrid Imaging* 1(1):9
213. Lee CS, Samii A, Sossi V et al (2000) In vivo positron emission tomographic evidence for compensatory changes in presynaptic dopaminergic nerve terminals in Parkinson’s disease. *Ann Neurol* 47:493–503
214. Lee H, Kim S-K, Kim Y-I et al (2014) Early determination of prognosis by interim 30-deoxy-30-18F-fluorothymidine PET in patients with non-Hodgkin lymphoma. *J Nucl Med* 55(2):216e22
215. Leenders KL, Salmon EP, Tyrrell P et al (1990) The nigro-striatal dopaminergic system assessed in vivo by positron emission tomography in healthy volunteer subjects and patients with Parkinson’s disease. *Arch Neurol* 47:1290–1298
216. van Leeuwen PJ, Emmett L, Ho B et al (2017) Prospective evaluation of 68Gallium-PSMA positron emission tomography/computerized tomography for preoperative lymph node staging in prostate cancer. *BJU Int* 119:209–215
217. Leskinen-Kallio S, Minn H, Joensuu H (1990) PET and (11C)methionine in assessment of response in non-Hodgkin lymphoma. *Lancet* 336(8724):1188
218. Leskinen-Kallio S, Nägren K, Lehtikoinen P et al (1991) Uptake of 11C-methionine in breast cancer studied by PET. An association with the size of S-phase fraction. *Br J Cancer* 64(6):1121–1124
219. Leskinen-Kallio S, Nägren K, Lehtikoinen P et al (1992) Carbon-11-methionine and PET is an effective method to image head and neck cancer. *J Nucl Med* 33(5):691–695
220. Lewis JS, McCarthy DW, McCarthy TJ et al (1999) Evaluation of 64Cu-ATSM in vivo and in vitro in a hypoxic tumor model. *J Nucl Med* 40:177–183
221. Lewis JS, Sharp TL, Laforest R et al (2001) Tumor uptake of copper-diacetyl-bis(N4-methylthiosemicarbazone): effect of changes in tissue oxygenation. *J Nucl Med* 42:655–661
222. Lewis JS, Welch MJ (2001) PET imaging of hypoxia. *Q J Nucl Med* 45(2):183–188

223. Leyton J, Latigo J, Perumal M et al (2005) Early detection of tumor response to chemotherapy by 3'-deoxy-3'-(18F)fluorothymidine positron emission tomography: the effect of cisplatin on the fibrosarcoma tumor model in vivo. *Cancer Res* 65(10):4202–4210
224. Li S, Peck-Radosavljevic M, Ubl P et al (2017) The value of (11C)-acetate PET and (18F)-FDG PET in hepatocellular carcinoma before and after treatment with transarterial chemoembolization and bevacizumab. *Eur J Nucl Med Mol Imaging* 44(10):1732–1741
225. Lilja A, Lundqvist H, Olsson Y et al (1989) Positron emission tomography and computed tomography in differential diagnosis between recurrent or residual glioma and treatment-induced brain lesions. *Acta Radiol* 30:121–128
226. Lindstrom P, Sehlin J (1986) Aromatic amino acids and pancreatic islet function: a comparison of L-tryptophan and L-5-hydroxytryptophan. *Mol Cell Endocrinol* 48:121–126
227. Liu RS (2000) Clinical application of (C-11)acetate in oncology (abstract). *Clin Positron Imaging* 3:185
228. Liu RS, Chang CP, Chu LS et al (2006) PET imaging of brain astrocytoma with 1-11C-acetate. *Eur J Nucl Med Mol Imaging* 33:420–427
229. Lopci E, Grassi I, Chiti A et al (2014) PET radiopharmaceuticals for imaging of tumor hypoxia: a review of the evidence. *Ann J Nucl Med Mol Imaging* 4:365–384
230. Lopci E, Grassi I, Rubello D et al (2016) Prognostic evaluation of disease outcome in solid tumors investigated with 64Cu-ATSM PET/CT. *Clin Nucl Med* 41:e87–e92
231. Lopci E, Piccardo A, Nanni C et al (2012) 18F-DOPA PET/CT in neuroblastoma: comparison of conventional imaging with CT/MR. *Clin Nucl Med* 37(4):e73–e78
232. Lopci E, Chiti A, Castellani MR et al (2011) Matched pairs dosimetry: 124I/131I metaiodobenzylguanidine and 124I/131I and 86Y/90Y antibodies. *Eur J Nucl Med Mol Imaging* 38(Suppl 1):S28–S40
233. Lopci E, Torzilli G, Poretti D et al (2015) Diagnostic accuracy of ¹¹C-choline PET/CT in comparison with CT and/or MRI in patients with hepatocellular carcinoma. *Eur J Nucl Med Mol Imaging* 42(9):1399–1407
234. Lovenberg W, Weissbach H, Udenfriend S (1962) Aromatic L-amino acid decarboxylase. *J Biol Chem* 237:89–93
235. Luong A, Hannah VC, Brown MS et al (2000) Molecular characterization of human acetyl-CoA synthetase, an enzyme regulated by sterol regulatory element-binding proteins. *J Biol Chem* 275(34):26458–26466
236. Lyrdal D, Boijesen M, Suurkula M et al (2009) Evaluation of sorafenib treatment in metastatic renal cell carcinoma with 2-fluoro-2-deoxyglucose positron emission tomography and computed tomography. *Nucl Med Commun.* 30(7):519–524
237. Lütje S, Gomez B, Cohnen J et al (2017) Imaging of prostate-specific membrane antigen expression in metastatic differentiated thyroid cancer using 68Ga-HBED-CC-PSMA PET/CT. *Clin Nucl Med* 42(1):20–25
238. Martiat P, Ferrant A, Labar D et al (1988) In vivo measurement of carbon-11 thymidine uptake in non-Hodgkin's lymphoma using positron emission tomography. *J Nucl Med* 29:1633–1637
239. Martorana G, Schiavina R, Corti B et al (2006) 11C-choline positron emission tomography/computerized tomography for tumor localization of primary prostate cancer in comparison with 12-core biopsy. *J Urol* 176:954–960, Discussion 960
240. Maurer RI, Blower PJ, Dilworth JR et al (2002) Studies on the mechanism of hypoxic selectivity in copper bis(thiosemicarbazone) radiopharmaceuticals. *J Med Chem* 45:1420–1431
241. Maute RL, Gordon SR, Mayer AT et al (2015) Engineering high-affinity PD-1 variants for optimized immunotherapy and immuno-PET imaging. *Proc Natl Acad Sci U S A* 112(47):E6506–E6514
242. McConathy J, Yu W, Jarkas N et al (2012) Radiohalogenated nonnatural amino acids as PET and SPECT tumor imaging agents. *Med Res Rev* 32(4):868–905
243. Mittendorf B, Sidossis LS, Walser E et al (1998) Regional acetate kinetics and oxidation in human volunteers. *Am J Physiol* 274(6 Pt 1):E978–E983

244. Mongiardi MP (2012) Angiogenesis and hypoxia in glioblastoma: a focus on cancer stem cells. *CNS Neurol Disord Drug Targets* 11(7):878–883
245. Morris MJ, Scher HI (2007) 11C-acetate PET imaging in prostate cancer. *Eur J Nucl Med Mol Imaging* 34(2):181–184
246. Mukherjee S (2010) *The emperor of all maladies: a biography of cancer*. Scribner, New York
247. Nanni C, Castellucci P, Farsad M et al (2007) 11C/18F-choline PET or 11C/8F-acetate PET in prostate cancer: may a choice be recommended? *Eur J Nucl Med Mol Imaging* 34:1704–1705
248. Nanni C, Schiavina R, Brunocilla E et al (2015) 18F-Fluciclovine PET/CT for the detection of prostate cancer relapse. a comparison to 11C-Choline PET/CT. *Clin Nucl Med* 40:e386–e391
249. Nanni C, Zamagni E, Cavo M et al (2007) 11C-choline vs. 18F-FDG PET/CT in assessing bone involvement in patients with multiple myeloma. *World J Surg Oncol* 5:68
250. Narayanan TK, Said S, Mukherjee J et al (2002) A comparative study on the uptake and incorporation of radiolabeled methionine, choline and fluorodeoxyglucose in human astrocytoma. *Mol Imaging Biol* 4(2):147–156
251. Nariai T, Tanaka Y, Wakimoto H et al (2005) Usefulness of L-(methyl-11C) methionine-positron emission tomography as a biological monitoring tool in the treatment of glioma. *J Neurosurg* 103:498–507
252. Natarajan A, Mayer AT, Reeves RE et al (2017) Development of novel immunoPET tracers to image human PD-1 checkpoint expression on tumor-infiltrating lymphocytes in a humanized mouse model. *Mol Imaging Biol* 19(6):903–914
253. Natarajan A, Mayer AT, Xu L et al (2015) Novel radiotracer for immunoPET imaging of PD-1 checkpoint expression on tumor infiltrating lymphocytes. *Bioconjug Chem* 26 (10):2062–2069
254. Ng P, Rajendran JG, Schwartz DL et al (2003) Can (F-18) fluoromisonidazole PET imaging predict treatment response in head and neck cancer? *J Nucl Med* 44:128P
255. Nicolas GP, Schreiter N, Kaul F et al (2018) Sensitivity comparison of (68)Ga-OPS202 and (68)Ga-DOTATOC PET/CT in patients with gastroenteropancreatic neuroendocrine tumors: a prospective phase II imaging study. *J Nucl Med* 59:915–921
256. Nunez R, Macapinlac H, Yeung HWD et al (2002) Combined 18F-FDG and 11C-methionine PET scans in patients with newly progressive metastatic prostate cancer. *J Nucl Med* 43:46–55
257. Nuutinen J, Sonninen P, Lehtikoinen P et al (2000) Radiotherapy treatment planning and long-term follow-up with (11C)methionine PET in patients with low-grade astrocytoma. *Int J Radiat Oncol Biol Phys* 48(1):43–52
258. Ogawa T, Kanno I, Shishido F et al (1991) Clinical value of PET with ¹⁸F-fluorodeoxyglucose and L-methyl-¹¹C-methionine for diagnosis of recurrent brain tumor and radiation injury. *Acta Radiol* 32:197–202
259. Ogawa T, Shishido F, Kanno I et al (1993) Cerebral gliomas: evaluation with methionine-PET. *Radiology* 186:45–53
260. Oriuchi N, Tomiyoshi K, Inoue T et al (1996) Independent thallium-201 accumulation and fluorine-18-fluorodeoxyglucose metabolism in glioma. *J Nucl Med* 37:457–462
261. Otonkoski T, Veijola R, Huopio H et al (2003) Diagnosis of focal persistent hyperinsulinism of infancy with 18F-fluoro-L-DOPA PET. In: Program of the 42nd annual meeting of the European society for paediatric endocrinology (ESPE), Ljubljana, Slovenia, p 2 (Abstract 5.09)
262. Oyama N, Akino H, Kanamaru H et al (2002) 11C-acetate PET imaging of prostate cancer. *J Nucl Med* 43(2):181–186
263. Oyama N, Akino H, Suzuki Y et al (1999) The increased accumulation of (18F) fluorodeoxyglucose in untreated prostate cancer. *Jpn J Clin Oncol* 29:623–629
264. Oyama N, Miller TR, Dehdashti F et al (2003) 11C-acetate PET imaging of prostate cancer: detection of recurrent disease at PSA relapse. *J Nucl Med* 44(4):556–558
265. Padhani A (2006) PET imaging of tumour hypoxia. *Cancer Imaging* 6:S117–S121

266. Pascali C, Bogni A, Iwata R et al (2000) (¹¹C)methylation on a C18 Sep-Pak cartridge: a convenient way to produce (N-methyl-¹¹C)choline. *J Label Comput Radiopharm* 43:195–203
267. Patel YC (1999) Somatostatin and its receptor family. *Front Neuroendocrinol* 20:157–198
268. Pauleit D, Floeth F, Hamacher K et al (2005) O-(2-(¹⁸F)fluoroethyl)-L-tyrosine PET combined with MRI improves the diagnostic assessment of cerebral gliomas. *Brain* 128:678–687
269. Pauleit D, Zimmermann A, Stoffels G et al (2006) 18F-FET PET compared with 18F-FDG PET and CT in patients with head and neck cancer. *J Nucl Med* 47(2):256–261
270. Pauwels E, Cleeren F, Bormans F et al (2018) Somatostatin receptor PET ligands—the next generation for clinical practice. *Am J Nucl Med Mol Imaging*. 8(5):311–331
271. Pearse AG (1969) The cytochemistry and ultrastructure of polypeptide hormone-producing cells of the APUD series and the embryologic, physiologic and pathologic implications of the concept. *J Histochem Cytochem* 17:303–313
272. Pentlow KS, Graham MC, Lambrecht RM et al (1996) Quantitative imaging of iodine-124 with PET. *J Nucl Med* 37(9):1557–1562
273. Pentlow KS, Finn RD, Larson SM et al (2000) Quantitative imaging of Yttrium-86 with PET. The occurrence and correction of anomalous apparent activity in high density regions. *Clin Positron Imaging* 3(3):85–90
274. Perera M, Papa N, Christidis D et al (2016) Sensitivity, specificity, and predictors of positive 68Ga-Prostate-specific membrane antigen positron emission tomography in advanced prostate cancer: a systematic review and meta-analysis. *Eur Urol* 70(6):926–937
275. Phan HT, Jager PL, Paans AM et al (2008) The diagnostic value of 124I-PET in patients with differentiated thyroid cancer. *Eur J Nucl Med Mol Imaging* 35(5):958–965
276. Piccardo A, Lopci E, Conte M et al (2012) Comparison of 18F-dopa PET/CT and 123I-MIBG scintigraphy in stage 3 and 4 neuroblastoma: a pilot study. *Eur J Nucl Med Mol Imaging* 39:57–71
277. Picchio M, Landoni C, Messa C et al (2002) Positive 11C-choline and negative (18F)FDG with positron emission tomography in recurrence of prostate cancer. *AJR Am J Roentgenol* 179:482–484
278. Picchio M, Messa C, Landoni C et al (2003) Value of (11C)choline positron emission tomography for re-staging prostate cancer: a comparison with (18F)fluorodeoxyglucose positron emission tomography. *J Urol* 169:1337–1340
279. Picchio M, Treiber U, Beer AJ et al (2006) Value of 11C-choline PET and contrast-enhanced CT for staging of bladder cancer: correlation with histopathologic findings. *J Nucl Med* 47(6):938–944
280. Piert M, Machulla HJ, Picchio M et al (2005) Hypoxia-specific tumor imaging with 18F-fluoroazomycin arabinoside. *J Nucl Med* 46:106–113
281. Pirotte B, Goldman S, Massager N et al (2004) Comparison of 18F-FDG and 11C-methionine for PET-guided stereotactic brain biopsy of gliomas. *J Nucl Med* 45:1293–1298
282. Podo F (1999) Tumor phospholipid metabolism. *NMR Biomed* 12:413–414
283. Ponde DE, Oyama N, Dence CS et al (2003) (18F)-Fluoroacetate, an analogue of C-11 acetate for tumor imaging. *J Nucl Med* 44:296p
284. Powles T, Murray I, Brock C et al (2007) Molecular positron emission tomography and PET/CT imaging in urological malignancies. *Eur Urol* 51:1511–1521
285. Prante O, Blaser D, Maschauer S et al (2007) In vitro characterization of the thyroidal uptake of O-(2-(¹⁸F)fluoroethyl)-L-tyrosine. *Nucl Med Biol* 34:305–314
286. Prasad V, Ambrosini V, Hommann M et al (2010) Detection of unknown primary neuroendocrine tumours (CUP-NET) using (68)Ga-DOTA-NOC receptor PET/CT. *Eur J Nucl Med Mol Imaging* 37(1):67–77
287. Prior JO, Montemurro M, Orcurto MV et al (2009) Early prediction of response to sunitinib after imatinib failure by 18F-fluorodeoxyglucose positron emission tomography in patients with gastrointestinal stromal tumor. *J Clin Oncol* 27(3):439–445

288. Pyka T, Okamoto S, Dahlbender M et al (2016) Comparison of bone scintigraphy and ⁶⁸Ga-PSMA PET for skeletal staging in prostate cancer. *Eur J Nucl Med Mol Imaging* 43:2114–2121
289. Pöpperl G, Goldbrunner R, Gildehaus FJ et al (2005) O-(2-(¹⁸F)Fluoroethyl)-L-tyrosine PET for monitoring the effects of convection-enhanced delivery of paclitaxel in patients with recurrent glioblastoma. *Eur J Nucl Med Mol Imaging* 32:1018–1025
290. Pöpperl G, Gotz C, Rachinger W et al (2004) Value of O-(2-(¹⁸F)fluoroethyl)-L-tyrosine PET for the diagnosis of recurrent glioma. *Eur J Nucl Med Mol Imaging* 31:1464–1470
291. Pöpperl G, Kreth FW, Herms J et al (2006) Analysis of ¹⁸F-FET PET for grading of recurrent gliomas: is evaluation of uptake kinetics superior to standard methods? *J Nucl Med* 47:393–403
292. Pöpperl G, Kreth FW, Mehrkens JH et al (2007) FET PET for the evaluation of untreated gliomas: correlation of FET uptake and uptake kinetics with tumour grading. *Eur J Nucl Med Mol Imaging* 34:1933–1942
293. Rachinger W, Goetz C, Pöpperl G et al (2005) Positron emission tomography with O-(2-(¹⁸F)fluoroethyl)-l-tyrosine versus magnetic resonance imaging in the diagnosis of recurrent gliomas. *Neurosurgery* 57:505–511
294. Rajendran JG, Mankoff DA, O'Sullivan F et al (2004) Hypoxia and glucose metabolism in malignant tumors: evaluation by (18F)fluoromisonidazole and (18F)fluorodeoxyglucose positron emission tomography imaging. *Clin Cancer Res* 10:2245–2252
295. Rajendran JG, Wilson DC, Conrad EU et al (2003) (18F)FMISO and ((18F)FDG PET imaging in soft tissue sarcomas: correlation of hypoxia, metabolism and VEGF expression. *Eur J Nucl Med Mol Imaging* 30:695–704
296. Rapp M, Heinzel A, Galldiks N et al (2013) Diagnostic performance of 18F-FET PET in newly diagnosed cerebral lesions suggestive of glioma. *J Nucl Med* 54:229–235
297. Rasey JS, Grunbaum Z, Magee S et al (1987) Characterization of radiolabeled fluoromisonidazole as a probe for hypoxic cells. *Radiat Res* 111:292–304
298. Rasey JS, Hofstrand PD, Chin LK, Tewson TJ (1999) Characterization of (F-18) fluoroetanidazole, a new radiopharmaceutical for detecting tumor hypoxia. *J Nucl Med* 40:1072–1079
299. Rasey J, Koh W, Evans M et al (1996) Quantifying regional hypoxia in human tumors with positron emission tomography of (18F)fluoromisonidazole: a pretherapy study of 37 patients. *Int J Radiat Oncol Biol Phys* 24:417–428
300. Ren J, Yuan L, wen G, Yang J (2016) The value of anti-1-amino-3-18F-fluorocyclobutane-1-carboxylic acid PET/CT in the diagnosis of recurrent prostate carcinoma: a meta-analysis. *Acta Radiol* 57(4):487–493
301. Reske SN, Deisenhofer S (2006) Is 3'-deoxy-3'-18F-fluorothymidine a better marker for tumour response than 18F-fluorodeoxyglucose? *Eur J Nucl Med Mol Imaging* 33:S38–S43
302. Reubi JC (2004) Somatostatin and other Peptide receptors as tools for tumor diagnosis and treatment. *Neuroendocrinology* 80(Suppl 1):51–56
303. Reubi JC, Kvolts L, Krenning E, Lamberts SW (1990) Distribution of somatostatin receptors in normal and tumor tissue. *Metabolism* 39:78–81
304. Ricci PE, Karis JP, Heiserman JE et al (1998) Differentiating recurrent tumor from radiation necrosis: time for re-evaluation of positron emission tomography? *AJNR* 19:407–413
305. Rigo P, De Landsheere C, Melon P et al (1990) Imaging of myocardial metabolism by positron emission tomography. *Cardiovasc Drugs Ther* 4(Suppl 4):847–851
306. Rohren EM, Turkington TG, Coleman RE (2004) Clinical applications of PET in oncology. *Radiology* 231:305–332
307. Rossi S, Toschi L, Castello A et al (2017) Clinical characteristics of patient selection and imaging predictors of outcome in solid tumors treated with checkpoint-inhibitors. *Eur J Nucl Med Mol Imaging* 44(13):2310–2325

308. Rubello D, Fanti S, Nanni C et al (2006) 11-C methionine PET/TC in 99m tc-sestamibi negative hyperparathyroidism in patients with renal failure on chronic haemodialysis. *Eur J Nucl Med Mol Imaging* 33(4):453–459
309. Salminen A, Jambor I, Merisaari H et al (2018) 11C-acetate PET/MRI in bladder cancer staging and treatment response evaluation to neoadjuvant chemotherapy: a prospective multicenter study (ACEBIB trial). *Cancer Imaging*. 18(1):25
310. Sandblom G, Sorensen J, Lundin N et al (2006) Positron emission tomography with 11C-acetate for tumor detection and localization in patients with prostate-specific antigen relapse after radical prostatectomy. *Urology* 67(5):996–1000
311. Sasaki M, Kuwabara Y, Yoshida T et al (1998) A comparative study of thallium-201 SPET, carbon-11 methionine PET and fluorine-18 fluorodeoxyglucose PET for the differentiation of astrocytic tumours. *Eur J Nucl Med* 25:1261–1269
312. Sato N, Suzuki M, Kuwata N et al (1999) Evaluation of the malignancy of glioma using 11C-methionine positron emission tomography and proliferating cell nuclear antigen staining. *Neurosurg Rev* 22:210–214
313. Sawle GV (1993) The detection of pre-clinical Parkinson's disease: what is the role of positron emission tomography? *Mov Disord* 8:271–277
314. Scattoni V, Picchio M, Suardi N et al (2007) Detection of lymph-node metastases with integrated (11C)choline PET/CT in patients with PSA failure after radical retropubic prostatectomy: results confirmed by open pelvic- retroperitoneal lymphadenectomy. *Eur Urol* 52(2):423–429
315. Schiavina R, Scattoni V, Castellucci P et al (2008) 11C-choline positron emission tomography/computerized tomography for preoperative lymph-node staging in intermediate-risk and high-risk prostate cancer: comparison with clinical staging nomograms. *Eur Urol* 54(2):392–401
316. Schiepers C, Nuytes J, Bormans G et al (1997) Fluoride kinetics of the axial skeleton measured in vivo with fluorine-18-fluoride PET. *J Nucl Med* 38:1970–1976
317. Schirmmeister H, Glatting G, Hetzel J et al (2001) Prospective evaluation of the clinical value of planar bone scans, SPECT, and (18)F-labeled NaFPET in newly diagnosed lung cancer. *J Nucl Med* 42:1800–1804
318. Schnell O, Krebs B, Carlsen J et al (2009) Imaging of integrin alpha(v)beta(3) expression in patients with malignant glioma by (18F) Galacto-RGD positron emission tomography. *Neuro Oncol* 11(6):861–870
319. Schomas DA, Laack NNI, Rao RD et al (2009) Intracranial low-grade gliomas in adults: 30-year experience with long-term follow-up at Mayo clinic. *Neuro-Oncology* 11(4):437–445
320. Schonbrunn A, Tashjian H Jr (1978) Characterization of functional receptors for somatostatin in rat pituitary cells in culture. *J Biol Chem* 253:6473–6483
321. Schuster DM, Nanni C, Fanti S et al (2014) Anti-1-amino-3-18F-fluorocyclobutane-1-carboxylic acid: physiologic uptake patterns, incidental findings, and variants that may simulate disease. *J Nucl Med* 55:1986–1992
322. Schuster DM, Nanni C, Fanti S (2016) PET tracers beyond FDG in prostate cancer. *Semin Nucl Med* 45:507–521
323. Schuster D, Nye J, Nieh P et al (2009) Initial experience with the radiotracer anti-1-amino-3-(F-18)fluorocyclobutane-1-carboxylic acid (Anti-(F-18)FACBC) with PET in renal carcinoma. *Mol Imaging Biol* 11(6):434–438
324. Schuster DM, Savir-Baruch B, Nieh PT et al (2011) Detection of recurrent prostate carcinoma with anti-1-amino-3-18F-fluorocyclobutane-1-carboxylic acid PET-CT and 111In-capromab pendetide SPECT/CT. *Radiology* 259(3):852–861
325. Schuster D, Votaw J, Nieh P et al (2007) Initial experience with the radiotracer anti-1-amino-3-F-18-fluorocyclobutane-1-carboxylic acid with PET-CT in prostate carcinoma. *J Nucl Med* 48(1):56–63

326. Schwarzenberg J, Czernin J, Cloughesy TF et al (2014) Treatment response evaluation using 18F-FDOPA PET in patients with recurrent malignant glioma on bevacizumab therapy. *Clin Cancer Res* 20:3550–3559
327. Shields AF (2006) Positron emission tomography measurement of tumor metabolism and growth: its expanding role in oncology. *Mol Imaging Biol* 8:141–150
328. Shields AF, Grierson JR, Dohmen BM et al (1998) Imaging proliferation in vivo with (¹⁸F)FLT and positron emission tomography. *Nat Med* 4:1334–1336
329. Shreve P, Chiao PC, Humes HD et al (1995) Carbon-11-acetate PET imaging in renal disease. *J Nucl Med* 36:1595–1601
330. Silver DA, Pellicer I, Fair WR et al (1997) Prostate-specific membrane antigen expression in normal and malignant human tissues. *Clin Cancer Res* 3(1):81–85
331. Siva S, Callahan J, Pryor D et al (2017) Utility of 68Ga prostate specific membrane antigen—positron emission tomography in diagnosis and response assessment of recurrent renal cell carcinoma. *J Med Imaging Radiat Oncol* 61(3):372–378
332. Soloviev D, Fini A, Chierichetti F et al (2008) PET imaging with 11C-acetate in prostate cancer: a biochemical, radiochemical and clinical perspective. *Eur J Nucl Med Mol Imaging* 35(5):942–949
333. Stadlbauer A, Prante O, Nimsy C et al (2008) Metabolic imaging of cerebral gliomas: spatial correlation of changes in O-(2-18F-fluoroethyl)-L-tyrosine PET and proton magnetic resonance spectroscopic imaging. *J Nucl Med* 49(5):721–729
334. Sun A, Sörensen J, Karlsson M et al (2007) 1-(11C)-acetate PET imaging in head and neck cancer—a comparison with 18F-FDG-PET: implications for staging and radiotherapy planning. *Eur J Nucl Med Mol Imaging* 34(5):651–657
335. Sutinen E, Nurmi M, Roivainen A et al (2003) Kinetics of (11C)choline uptake in prostate cancer: a PET study. *Eur J Nucl Med Mol Imaging* 31:317–324
336. Swinnen JV, Van Veldhoven PP, Timmermans L et al (2003) Fatty acid synthase drives the synthesis of phospholipids partitioning into detergent-resistant membrane microdomains. *Biochem Biophys Res Commun* 302:898–903
337. Szabo Z, Mena E, Rowe SP et al (2015) Initial evaluation of ((18F)DCFPyL for prostate-specific membrane antigen (PSMA)-targeted PET imaging of prostate cancer. *Mol Imaging Biol* 17:565–574
338. Sörensen J, Andrén B, Blomquist G et al (2006) The central circulation in congestive heart failure non-invasively evaluated with dynamic positron emission tomography. *Clin Physiol Funct Imaging* 26(3):171–177
339. Takahashi N, Fujibayashi Y, Yonekura Y et al (2000) Evaluation of ⁶²Cu labeled diacetyl-bis(N4-methylthiosemicarbazone) as a hypoxic tissue tracer in patients with lung cancer. *Ann Nucl Med* 14:323–328
340. Talbot JN, Fartoux L, Balogova S et al (2010) Detection of hepatocellular carcinoma with PET/CT: a prospective comparison of 18F-fluorocholine and 18F-FDG in patients with cirrhosis or chronic liver disease. *J Nucl Med* 51(11):1699–1706
341. Talbot JN, Gutman F, Fartoux L et al (2006) PET/CT in patients with hepatocellular carcinoma using ((18F)fluorocholine: preliminary comparison with ((18F)FDG PET/CT. *Eur J Nucl Med Mol Imaging* 33(11):1285–1289
342. Taneja SS (2004) ProstaScint® Scan: contemporary use in clinical practice. *Rev Urol* 6 (Suppl 10):S19–S28
343. Tang BN, Moreno-reyes R, Blocket D et al (2008) Accurate preoperative localization of pathological parathyroid glands using 11C- methionine PET/TC. *Contrast Media Mol Imaging* 3(4):157–163
344. Tannock I, Guttman P (1981) Responses of Chinese hamster ovary cells to anticancer drugs under aerobic and hypoxic conditions. *Br J Cancer* 42:245–248
345. Tateichi K, Tateishi U, Sato M et al (2013) Application of ⁶²Cu-diacetyl-bis (N4-methylthiosemicarbazone) PET imaging to predict highly malignant tumor grades and

- hypoxia-inducible factor-1 α expression in patients with glioma. *AJNR Am J Neuroradiol* 34:92–99
346. Tavare R, Escuin-Ordinas H, Mok S et al (2016) An effective immuno-PET imaging method to monitor CD8-dependent responses to immunotherapy. *Cancer Res* 76(1):73–82
347. Terakawa Y, Tsuyuguchi N, Iwai Y et al (2008) Diagnostic accuracy of ¹¹C-Methionine PET for differentiation of recurrent brain tumors from radiation necrosis after radiotherapy. *J Nucl Med* 49(5):694–699
348. Testa C, Schiavina R, Lodi R et al (2007) Prostate cancer: sextant localization with MR imaging, MR spectroscopy, and ¹¹Ccholine PET/CT. *Radiology* 244:797–806
349. Tian M, Zhang H, Higuchi T et al (2004) Oncological diagnosis using (11) C-choline-positron emission tomography in comparison with 2-deoxy-2-((¹⁸F) fluoro-D-glucose-positron emission tomography. *Mol Imaging Biol* 6(3):172–179
350. Tolmachev V, Stone-Elander V (2010) Radiolabelled proteins for positron emission tomography: pros and cons of labelling methods. *Biochim Biophys Acta* 1800(5):487–510
351. Torii K, Tsuyuguchi N, Kawabe J et al (2005) Correlation of amino-acid uptake using methionine PET and histological classifications in various gliomas. *Ann Nucl Med* 19:677–683
352. Tsuyuguchi N, Sunada I, Iwai Y et al (2003) Methionine positron emission tomography of recurrent metastatic brain tumor and radiation necrosis after stereotactic radiosurgery: is a differential diagnosis possible? *J Neurosurg* 98(5):1056–1064
353. Tsuyuguchi N, Takami T, Sunada I et al (2004): Methionine positron emission tomography for differentiation of recurrent brain tumor and radiation necrosis after stereotactic radiosurgery—in malignant glioma. *Ann Nucl Med* 18(4):291–296
354. Turkbey B, Mana E, Shih J et al (2014) Localised prostate cancer detection with ¹⁸F FACBC PET/CT: comparison with MR imaging and histopathologic analysis. *Radiology* 270:849–856
355. Umbehr MH, Muntener M, Hany T et al (2013) The role of ¹¹C-choline and ¹⁸F-fluorocholine positron emission tomography (PET) and PET/CT in prostate cancer: a systematic review and meta-analysis. *Eur Urol* 64:106–117
356. Vallabhajosula S (2007) ¹⁸F-labeled positron emission tomographic radiopharmaceuticals in oncology: an overview of radiochemistry and mechanisms of tumor localization. *Semin Nucl Med* (37):400–419
357. Vanderhoek M, Juckett MB, Perlman SB et al (2011) Early assessment of treatment response in patients with AML using (¹⁸F)FLT PET imaging. *Leuk Res* 35(3):310e6
358. Vargas HA, Akin O, Schöder H et al (2012). Prospective evaluation of MRI, ¹¹C-acetate PET/CT and contrast-enhanced CT for staging of bladder cancer. *Eur J Radio* 81(12):4131–4137
359. Verel I, Visser GW, Boellaard R et al (2003) ⁸⁹Zr immuno-PET: comprehensive procedures for the production of ⁸⁹Zr-labeled monoclonal antibodies. *J Nucl Med* 44(8):1271–1281
360. Vesselle H, Grierson J, Muzi M et al (2002) In vivo validation of 3'-deoxy-3'-((¹⁸F) fluorothymidine ((¹⁸F)FLT) as a proliferation imaging tracer in humans: correlation of (¹⁸F) FLT uptake by positron emission tomography with Ki-67 immunohistochemistry and flow cytometry in human lung tumors. *Clin Cancer Res* 8:3315–3323
361. Volker JF et al (1940) The absorption of fluorides by enamel, dentin, bone, and hydroxyapatite as shown by the radioactive isotope. *J Biol Chem* 134:543–548
362. De Vries EFJ, Luurtsema G, Brussermann M et al (1999) Fully automated synthesis module for the high yield one-pot preparation of 6-((¹⁸F)fluoro-L-DOPA. *Appl Radiat Isot* 51:389–394
363. van Waarde A, Cobben DC, Suurmeijer AJ et al (2004) Selectivity of ¹⁸F-FLT and ¹⁸F-FDG for differentiating tumor from inflammation in a rodent model. *J Nucl Med* 45 (4):695–700
364. Warburg O (1956) On the origin of cancer cells. *Science* 123(3191):309–314
365. Weber W, Bartenstein P, Gross MW et al (1997) Fluorine-18-FDG PET and iodine-123-IMT SPECT in the evaluation of brain tumors. *J Nucl Med* 38:802–808

366. Weber DC, Zilli T, Buchegger F et al (2008) ((18)F)Fluoroethyltyrosine-positron emission tomography-guided radiotherapy for high-grade glioma. *Radiat Oncol* 3:44
367. Weckesser M, Langen KJ, Rickert CH et al (2005) O-(2-(¹⁸F)Fluoroethyl)-L-tyrosine PET in the clinical evaluation of primary brain tumours. *Eur J Nucl Med Mol Imaging* 32:422–429
368. Wells P, Gunn RN, Alison M et al (2002) Assessment of proliferation in vivo using 2-(¹¹C) thymidine positron emission tomography in advanced intra-abdominal malignancies. *Cancer Res* 62:5698–5702
369. Wester HJ, Herz M, Weber W et al (1999) Synthesis and radiopharmacology of O-(2-¹⁸F-fluoroethyl)-L-tyrosine for tumor imaging. *J Nucl Med* 40:205–212
370. Whal L, Nahmias C (1997) Modeling of fluorine-18-6-fluoro-L-Dopa in humans. *J Nucl Med* 37(3):432–437
371. Wienhard K, Herholz K, Coenen HH et al (1991) Increased amino acid transport into brain tumors measured by PET of L-(2-18F)fluorotyrosine (see comments). *J Nucl Med* 32:1338–1346
372. Wierts R, Brans B, Havekes B et al (2016) Dose-response relationship in differentiated thyroid cancer patients undergoing radioiodine treatment assessed by means of 124I PET/CT. *J Nucl Med* 57(7):1027–1032
373. Wild D, Fani M, Behe M et al (2011) First clinical evidence that imaging with somatostatin receptor antagonists is feasible. *J Nucl Med* 52:1412–1417
374. De Witte O, Levivier M, Violon P et al (1996) Prognostic value positron emission tomography with (18F)fluoro-2-deoxy-d-glucose in the low-grade glioma. *Neurosurgery* 39(3):470–477
375. Wong TZ, Van der Westhuizen GJ, Coleman RE (2002) Positron emission tomography imaging of brain tumours. *Neuroimaging Clin N Am* 12:615–626
376. Yamaguchi T, Lee J, Uemura H et al (2005) Prostate cancer: a comparative study of (11) C-choline PET and MR imaging combined with proton MR spectroscopy. *Eur J Nucl Med Mol Imaging* 32:742–748
377. Yamamoto Y, Nishiyama Y, Kameyama R et al (2008) Detection of hepatocellular carcinoma using 11C-choline PET: comparison with 18-F-FDG PET. *J Nucl Med* 49(8):1245–1248
378. Yamamoto Y, Nishiyama Y, Kimura N et al (2008) 11C-Acetate PET in the Evaluation of Brain Glioma: comparison with 11C-Methionine and 18F-FDG-PET. *Mol Imaging Biol* 10:281–287
379. Yamane T, Sakamoto S, Senda M (2009) Clinical impact of (11)C-methionine PET on expected management of patients with brain neoplasm. *Eur J Nucl Med Mol Imaging*
380. Yang DJ, Wallace S, Cherif A, Li C, Gretzer MB, Kim EE, Podoloff DA (1995) Development of F-18-labeled fluoroerythronitroimidazole as a PET agent for imaging tumor hypoxia. *Radiology* 194:795–800
381. Yoshimoto M, Waki A, Yonekura Y et al (2001) Characterization of acetate metabolism in tumor cells in relation to cell proliferation: acetate metabolism in tumor cells. *Nucl Med Biol* 28:117–122
382. Zeisel SH (1981) Dietary choline: biochemistry, physiology and pharmacology. *Annu Rev Nutr* 1:95–121



Daniel Paech and Heinz-Peter Schlemmer

Contents

21.1	Diffusion-Weighted Imaging (DWI)	720
21.1.1	Diffusion-Weighted Imaging in Brain Cancer Patients	720
21.1.2	Prostate MRI with Diffusion-Weighted Imaging	721
21.1.3	MR Mammography Using Diffusion-Weighted Imaging	722
21.2	Perfusion MRI	723
21.2.1	Perfusion MRI in the Brain	724
21.2.2	Arterial Spin Labeling (ASL) in Brain Tumors	725
21.2.3	Breast Perfusion Imaging	726
21.2.4	Prostate Perfusion Imaging	726
21.2.5	Abdominal Perfusion MRI	727
21.3	Susceptibility-Weighted Imaging (SWI)	727
21.4	Magnetic Resonance Spectroscopy (MRS)	728
21.5	Protein-Weighted MRI Using Chemical Exchange Saturation Transfer (CEST)	730
21.5.1	Brain Tumors	730
21.5.2	Applications of CEST MRI in Other Organs	732
21.6	Dynamic Glucose-Enhanced (DGE) MRI	732
21.7	MR Fingerprinting for Quantitative Relaxometry (T1 and T2 Mapping)	733
21.7.1	Prostate Relaxometry	733
21.7.2	Brain Relaxometry	735
21.8	Challenges to Implement Clinical MR Biomarkers in Multicenter Trials	735
	References	736

D. Paech · H.-P. Schlemmer (✉)

Division of Radiology, German Cancer Research Center (DKFZ), Im Neuenheimer Feld 280, 69120 Heidelberg, Germany
e-mail: h.schlemmer@dkfz.de

D. Paech

e-mail: d.paech@dkfz.de

21.1 Diffusion-Weighted Imaging (DWI)

Diffusion-weighted imaging sequences (DWI) provide complementary information to conventional MR techniques by adding information on microstructural tissue correlates, indicating such as cellularity and tissue integrity. DWI provides a measure of diffusion motion of water molecules, which is assumed to be more restricted in malignant tumors than in benign lesions due to higher cellularity in neoplasia. DWI has emerged as a powerful method with a variety of clinical applications in oncologic imaging. For example, applications in brain, prostate, and breast cancer are pointed out.

21.1.1 Diffusion-Weighted Imaging in Brain Cancer Patients

DWI has become an essential part of most MRI protocols in neuroradiology with a crucial role in the management of both stroke and brain tumor patients. The apparent diffusion coefficient (ADC) is the most common DWI-derived imaging biomarker with broad clinical applications. The majority of studies published in the literature showed an inverse correlation between the ADC and tumor cellularity in tumors [1–4]. Among brain tumors, gliomas are the most common type of primary intra-axial neoplasms in adults [5]. The World Health Organization (WHO) classification of brain tumors is commonly used as the primary basis to guide therapy and to assess overall prognosis [6]. Patient prognosis and survival depend to a great extent on the tumor grade and histopathological characteristics, particularly the Isocitrate dehydrogenase (IDH) mutation status and the O6-methylguanine-DNA-methyltransferase (MGMT) promoter methylation status [7–10]. Several studies reported an association overall survival (OS) and progression-free survival (PFS) with MRI parameters, particularly employing advanced imaging techniques at 3T, such as the ADC. The majority of these studies found decreased ADC values in brain tumors to be correlated with worse outcome (OS and/or PFS) [11–16]. These results are in line with multiple investigators reporting an inverse relationship with malignancy (WHO grade) and ADC [17–20] including non-enhancing high-grade gliomas [21].

Regarding therapy response assessment, changes in ADC have been shown to be associated with treatment response in glioma patients early after radiation therapy [22–24]. These changes have been hypothesized to be linked to cellular structure reflecting apoptosis and/or necrosis [22–24]. This information may be valuable for early individualized treatment strategies of glioma patients.

Furthermore, DWI sequences can be used to measure the apparent diffusion tensor of water D in each voxel of an image [25]. It has been reported that diffusion tensor imaging (DTI) can be used to differentiate normal white matter, edematous brain, and enhancing tumor margins [26]. Moreover, DTI has been applied in perioperative assessment of glioma patients in order to identify possible pyramidal tract involvement [27]. The authors concluded that DTI-based functional

neuronavigation contributes to maximal safe resection of cerebral gliomas with PT involvement, thereby decreasing postoperative motor deficits [27].

Diffusion kurtosis imaging (DKI), an extension of DTI, allows the simultaneous estimation of the ADC and the apparent excess kurtosis coefficient (AKC) on a direction-dependent basis [28, 29]. Investigations in glioma patients yielded significant differences in kurtosis parameters between high-grade and low-grade gliomas; hence, better separation was achieved with these parameters than with conventional diffusion imaging parameters [28].

21.1.2 Prostate MRI with Diffusion-Weighted Imaging

DWI has established as one of the most important imaging sequences in the standardized PI-RADS (Prostate Imaging Reporting and Data System) reading scheme (Fig. 20.1). Multiple studies have shown that DWI, combined with various mathematical models, improves differentiation between malignant and benign tissue

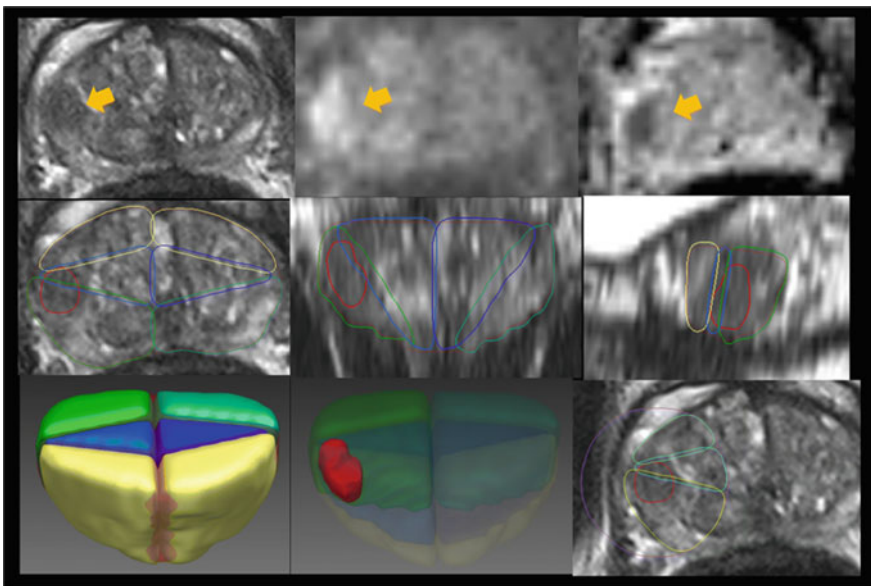


Fig. 20.1 Multiparametric MRI of the prostate. Top panel: axial T2-weighted image (left), DWI $b = 1500 \text{ s/mm}^2$ image (middle) and ADC map (right) demonstrate a suspicious lesion (arrows) with marked signal increase on $b = 1500$, a markedly decreased ADC value and suspicious homogeneous hypointensity on the T2w image, PI-RADS 5. Middle panel: sextants are spatially defined for right and left anterior (yellow), middle (blue), and posterior (green) locations and shown together with the radiologically defined lesion (red) in axial (left), coronal (middle), and sagittal (right) planes. Bottom panel: volume renderings of the prostate segmentation seen from anteriorly superiorly with sextants shown (left) and lesion shown by decreasing the opacity of the sextant volumes (middle) © *European Radiology*, Bonekamp et al. (Epub ahead of print) [186]

changes in prostate cancer [30–37]. Thereby, documented studies have shown statistically significant correlations between the ADC and the Gleason score (GS) of prostate cancer (PCa) [30–33]. Few studies showed that ADC may additionally be useful to predict prognosis for patients undergoing active surveillance and biochemical recurrence after radical prostatectomy [38, 39].

Also histogram analysis of intravoxel incoherent motion (IVIM) has been reported to be feasible and to enable stratification of prostate cancer grades, according to the Gleason score [40]. Recent investigations showed that D performed better in distinguishing low-grade from high-grade carcinomas than the conventional ADC [40]. However, none of these approaches can currently replace lesion biopsy followed by histologic analysis. Therefore, the development of a reliable non-invasive tool to distinguish benign lesions, low-grade PCa, and high-grade PCa would be a major advance and would have a significant benefit for individualized treatment options [40].

21.1.3 MR Mammography Using Diffusion-Weighted Imaging

Diffusion-weighted imaging has extended the repertoire of non-invasive biomarkers also in MR mammography. Particularly in abbreviated, non-contrast-enhanced breast imaging protocols, DWI has become an integral part [41] (Fig. 20.2). Decreased ADC has been shown to be associated with malignant breast tumors, which contributes to differential diagnosis of unclarified lesions [42]. Furthermore, the ADC has been reported to correlate with pathologic biomarkers such as tumor cellularity, Ki67, and peritumoral lymphocytic infiltrate (PLI) in patients with estrogen receptor (ER)-positive breast cancer [43]. Consequently, DWI MRI is helpful for non-invasive further characterization of suspicious breast masses and can increase the accuracy of conventional breast MRI assessment [44–46].

Besides the Apparent Diffusion Coefficient (ADC), diffusion kurtosis imaging (DKI) parameters and Fractional Order Calculus Models (FROC) might provide insights into tissue heterogeneity [47–49]. Particularly, DKI, which quantifies the diffusion restriction, showed higher specificity than did conventional diffusion-weighted imaging for assessment of benign and malignant breast lesions [48].

Intravoxel incoherent motion (IVIM) models use low b -values to calculate the perfusion fraction through bi-exponential fitting [50, 51]. Diffusion tensor imaging (DTI) measures the direction of diffusion restriction and has been shown to correlate with the fibroglandular microarchitecture [52]. DWI can, however, be challenging in breast tissue due to, e.g., insufficient fat suppression and the heterogeneous tissue structure of the female breast [41, 53]. Additionally, there are differences in image acquisition protocols and post processing methods that prevent a standardized clinical application [54]. Sufficient evidence for equality of non-contrast-enhanced imaging protocols as compared to contrast-enhanced full

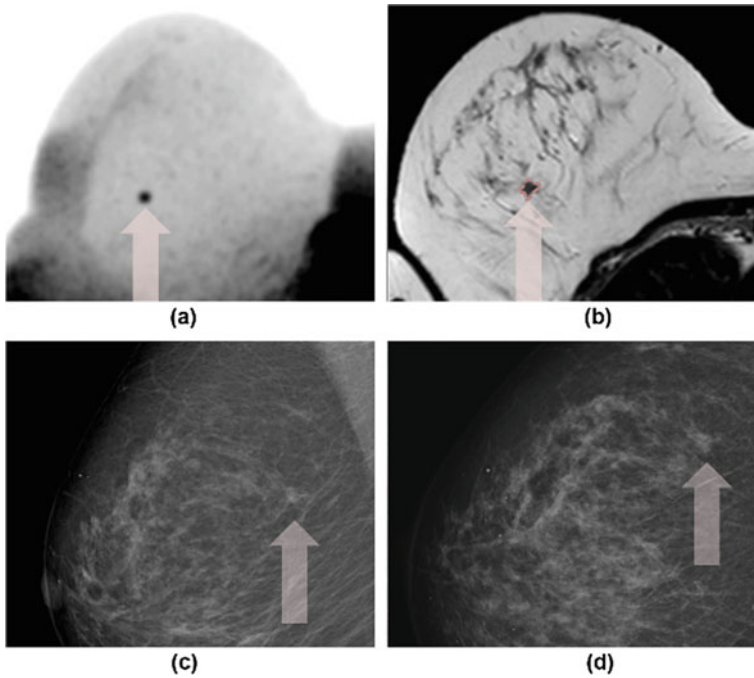


Fig. 20.2 Example of a female breast cancer screening participant with a suspicious lesion detected on X-ray mammography. **a** The MIBDI-MRI image (maximum intensity projection of diffusion-weighted imaging with background suppression, $b = 1500 \text{ s/mm}^2$, displayed with black-white-inversion) demonstrates a focal lesion within the breast parenchyma (as shown in the left image marked by the rose arrow). **b** Corresponding T2w-morphology (T2-TSE) that was evaluated in every patient with a lesion detected on the MIBDI-MRI confirming the suspicious character of the lesion. Histopathology revealed an Invasive Ductal Carcinoma (IDC, 4 mm). X-ray mammography depicting the suspicious lesion (arrows) in mediolateral oblique. **(c)** and craniocaudal views. **(d)**. © *Clinical Radiology*, Bickelhaupt and Paech et al. 72 (2017) 900.e1–900.e8 [187]

diagnostic MR mammography is, therefore, still lacking. Consequently, gadolinium contrast-enhanced MR mammography is currently considered the gold standard in MR mammography.

21.2 Perfusion MRI

Perfusion is an important biomarker indicating the viability and aggressive potential of tumors. For this, medical imaging techniques greatly benefit from the application of contrast agents. Gadolinium-based contrast agents (GBCA) are most commonly used in MRI. Due to its paramagnetic properties, GBCA enhance the local nuclear

relaxation rates of adjacent protons and thus modify signal intensities in the images. Furthermore, the acquisition of time-resolved data, following the administration of contrast agent, enables derivation of quantitative parameters related to tissue perfusion and microvasculature. Clinical applications of dynamic contrast-enhanced (DCE) MRI include a variety of tumors from all body parts. A promising alternative to image perfusion without the need of GBCA is arterial spin labeling (ASL).

21.2.1 Perfusion MRI in the Brain

In the healthy brain, GBCA is confined to the vascular spaces by the blood–brain barrier (BBB). Malignant gliomas often exhibit a disrupted BBB causing further leakage of contrast agent into the extracellular-extravascular space (EES). Hence, T1w-GdCE MRI is used as the gold standard in clinical routine for diagnostics of brain tumors.

Dynamic susceptibility contrast (DSC) and dynamic contrast-enhanced (DCE) MRI have been widely applied to assess perfusion-related properties of brain tumors. DSC MRI is most commonly used in clinical routine to obtain semi-quantitative biomarkers such as the relative cerebral blood volume (rCBV) or the relative cerebral blood flow (rCBF) [55] (Fig. 20.3). Quantitative MR biomarkers can be determined through pharmacokinetic modeling analyses based on DCE-MRI data. Both approaches have been successfully applied for the assessment of parameters linked to blood volume, perfusion, and disruption of BBB in malignant gliomas [56–61].

rCBV is widely used to assess tumor vascularity and has been shown to be increased in high-grade tumors compared to low-grade tumors [62, 63]. Peak height and the percentage of signal intensity recovery derived from DSC perfusion MRI have additionally been reported to enable differentiation of glioblastoma from brain metastases [64]. Moreover, different investigators reported significantly increased rCBV in IDH-wt versus IDH-mut tumors of glioma patients [58, 65] and 1p/19q co-deleted tumors (1p19q⁻) versus non-1p/19q co-deleted tumors (1p19q⁺) [66]. Therefore DSC by means of rCBV may enable early characterization of histologic and genetic subtypes in glioma patients prior to invasive procedures. Accordingly, increased rCBV values in the tumor region of glioma patients were reported to be associated with worse outcome (OS and/or PFS) [12, 66–68]. However, rCBV did not enable prediction of chemosensitivity prior to treatment [66].

The degree of endothelial permeability is typically represented by the endothelial permeability surface area product or the transfer coefficient transfer constant (K^{trans}) [61]. K^{trans} is commonly determined on DCE-MRI data using the Tofts and Ker-mode model [56]. Besides permeability, K^{trans} also depends on several other factors, including vascular surface area and flow [61]. It has been reported to be significantly correlated with the tumor grade of gliomas [59–61]. This correlation reflects a more pronounced BBB disruption in high-grade gliomas compared to low-grade tumors.

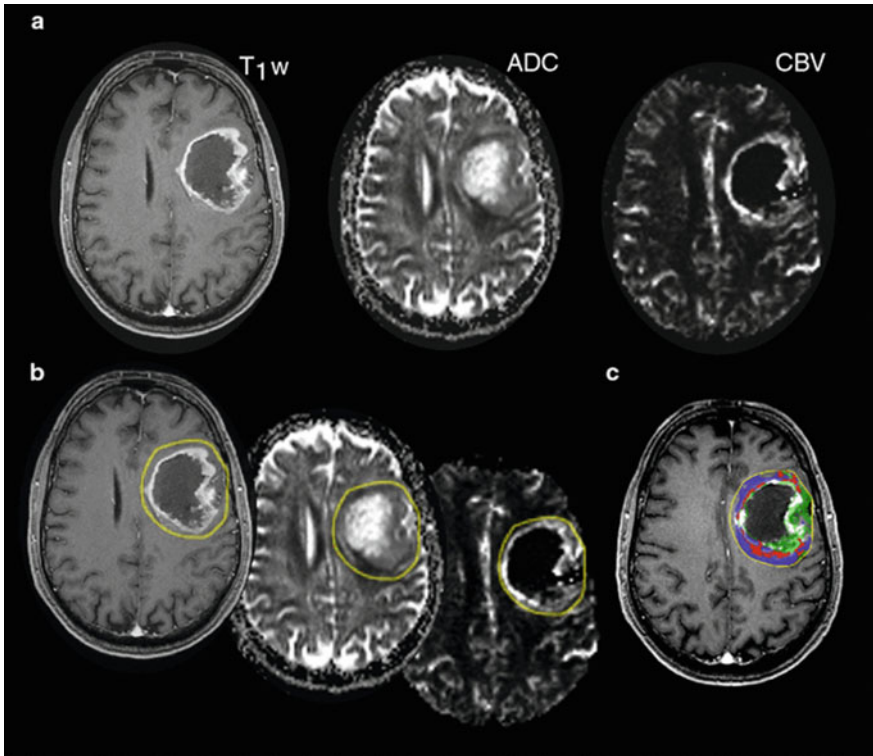


Fig. 20.3 Patient with a left frontal glioblastoma. **a** Gdce T1-w (left) image, ADC map (middle), and CBV map (right) shown. Decreased ADC values and increased CBV values can be observed especially in the tumor rim, partially overlapping with the Gd contrast enhancement. **b** Delineation of a region of interest (ROI) including the tumor and tumor periphery (yellow line). **c** Subsequently, an automatic identification algorithm has been applied to identify ADC hypointensities ($ADC_{\min} = 30^{\text{th}}$ signal percentile blue) and CBV hyperintensities ($CBV_{\max} = 70^{\text{th}}$ signal percentile = green) within the ROI. Red pixels represent regions where ADC_{\min} and CBV_{\max} match. © *J Neurooncol*, Deik et al. (2016) 126: 463 [187]

The volume fraction of extravascular extracellular space (v_e) is given by the leakage volume due to contrast extravasation outside the vascular space. It is considered as an index of tumor necrosis and an inverse index of tumor cellularity [22]. Few studies demonstrated that v_e may be useful to distinguish intra- from extra-axial masses and to be also positively correlated with tumor grade [69–71].

21.2.2 Arterial Spin Labeling (ASL) in Brain Tumors

A promising alternative for gadolinium-dependent perfusion MRI is given by non-contrast arterial spin labeling (ASL). Here, magnetically labeled blood water is

used as an endogenous flow tracer to provide CBF quantification without the need for contrast media administration.

The label is usually performed by saturating or inverting the magnetization of the blood water molecules. After inversion delay (TI) a so-called tagged image is acquired and compared with a reference image without inverted or saturated blood water magnetization. The signal difference between these two images is proportional to the amount of magnetization delivered to the tissue and reflects local perfusion [72]. Thus, ASL which was first described by Detre et al. [73] and Kwong et al. [74] in 1992 represents a promising technique for non-contrast perfusion MRI today. Especially, the clinical application of ASL in malignant brain tumors may be useful as an adjunctive modality due to characteristically increased perfusion and angiogenesis. In this respect, several studies have already shown the possibility to discriminate low and high-grade gliomas using ASL [75].

21.2.3 Breast Perfusion Imaging

Gadolinium contrast-enhanced sequences are commonly used in breast MRI for the detection of abnormalities. Increased contrast enhancement of lesions agent is a central imaging finding of malignant breast tumors which is caused by physiologically increased perfusion and leakage of the blood-tissue-barrier.

Contrast-enhanced breast MRI enables fast and robust image acquisition with high spatial and temporal resolution. Using abbreviated contrast-enhanced MR protocols for breast cancer detection high diagnostic sensitivities of up to 100% and a high negative predictive value (NPV) of up to 99.8% have been reported [76]. Using maximum intensity projections (MIPs), generated from only one pre- and one post-contrast acquisition and their derived images (first postcontrast subtracted [FAST]) and maximum intensity projection [MIP] images has been shown to yield diagnostic accuracy equivalent to that of the regular full diagnostic protocol and resulted in an additional cancer detection of 18.2 per 1,000 [76]. Besides identification of suspicious lesions, a positive correlation of initial contrast enhancement ratios with tumor grade has been reported [77]. However, this method has its limits in breast tissue with a high degree of background parenchymal enhancement (BPE), since high BPE might mask focal suspicious contrast enhancement [78]. Additional hemodynamic properties of malignant lesions can also be acquired and quantified using advanced imaging techniques such as time-resolved angiography with interleaved stochastic trajectories (TWIST) which may help to further increase diagnostic accuracy of Breast DCE-MRI [79].

21.2.4 Prostate Perfusion Imaging

However, non-malignant diseases such as prostatitis or benign prostatic hyperplasia are also known to enhance avidly with an enhancement pattern similar to prostate cancer [80]. Therefore, prostate DCE-MRI alone has limited specificity and should

only be interpreted together with other sequences such as T2-w imaging and ADC (derived from DWI) as recommended by the Prostate Imaging Reporting and Data System (PI-RADS).

DCE-MRI assessment of patients with prostate cancer during and after primary proton and carbon ion irradiation revealed increased transfer constant (K^{trans}) and leakage space volume (v_e) in antihormonal therapy (AHT) naïve patients with persistent PSA elevation compared to those with PSA suppression. Consequently, these quantitative biomarkers may also aid in the assessment of treatment response in prostate cancer [81].

21.2.5 Abdominal Perfusion MRI

Main applications in abdominal DCE-MRI, both non-quantitative and quantitative parameters, include renal, hepatic, and pancreatic lesion characterization. MRI can classify different liver lesions more accurately than multi-detector CT [82, 83]. The majority of incidental liver findings can easily be depicted and correctly identified by combination of the information from the comprehensive liver magnetic resonance examination: These include malignant tumors, cysts, haemangiomas, focal nodular hyperplasia, adenomas, and other benign hepatic diseases [83]. Typically three phases of contrast enhancement are clinically assessed to characterize liver tumors: (1) arterial phase images, (2) portal venous phase images, and (3) delayed equilibrium phase images. These three sequences take advantage of the dual blood supply to the liver via the hepatic artery and the portal vein to visualize different phases of liver and tumor enhancement [83]. Thereby, perfusion data provides information on the tumor microvasculature and alterations in tumor perfusion that can be used to evaluate response to chemotherapy, antiangiogenic treatment, or percutaneous ablation of liver tumors [84–87]. Besides liver imaging, DCE-MRI has proven its utility in predicting and monitoring the effects of a variety of oncologic treatments in bone sarcomas and renal, bladder, and pancreatic cancers [88–91]. For instance, quantitative measures of K^{trans} in pancreatic tumors have been shown to enable prediction of response to combined chemotherapy and antiangiogenic therapy [91]. The ability to detect and visualize tumor perfusion yields a more accurate diagnosis and improves the assessment of tumor treatment response [83]. Consequently, DCE-MRI provides crucial complementary information to morphological sequences in the assessment of tumors.

21.3 Susceptibility-Weighted Imaging (SWI)

Susceptibility-weighted imaging (SWI) is a magnetic resonance imaging (MRI) technique that detects susceptibility differences between tissues by combining magnitude and phase information in gradient echo data [92]. SWI is sensitive to both paramagnetic and diamagnetic substances, particularly to

deoxygenated blood and intracranial calcifications. SWI has therefore been applied to various pathologies including intracranial hemorrhage, traumatic brain injury, stroke, neoplasm, and multiple sclerosis [92–97]. SWI does however not provide quantitative measures of magnetic susceptibility, since phase information is non-local and orientation-dependent. This major limitation can be overcome using quantitative susceptibility mapping (QSM) approaches which yield susceptibility values of each voxel as a scalar quantity [92]. Furthermore, QSM can remove so-called blooming artifacts (as observed in conventional T2*w images), thus providing an accurate definition of the distribution of magnetic biomaterials in MRI [98, 99].

Clinical applications of QSM are currently being probed mainly in neurodegenerative and inflammatory diseases, to assess hemorrhage, to measure metabolic consumption of oxygen [98]. QSM can detect calcifications in neurocysticercosis and tumors with high sensitivity [100, 101] and has been demonstrated to be superior to phase imaging for the detection of intracranial hemorrhage and calcification [102]. QSM can also be used to measure the loss of myelin [103]. Furthermore, multiple sclerosis (MS) lesion susceptibility values have been reported to increase significantly as the lesion evolves from enhanced-with-Gd to not-enhanced-with-Gd, therefore, serving as a disease biomarker [104, 105]. In first investigations outside the brain, QSM has additionally been proven to be feasible for applications in other body parts including the breast, extremity, and abdominal imaging [106].

21.4 Magnetic Resonance Spectroscopy (MRS)

MR spectroscopy (MRS) allows to non-invasively detect metabolic features of tumor tissue *in vivo*. Proton MRS is essentially applied in clinical practice either as single voxel or multivoxel method because protons have the highest MR sensitivity, therefore enabling higher spatial resolution than MR spectroscopy of x-nuclei (nuclei other than protons).

Proliferative tumor tissue of various tumor types appears in proton MR spectra generally by intense resonances of choline-containing compounds (Cho) and the technique can easily be performed on clinical 1.5 T MR scanners using routine receiver coils, sequence protocols and evaluation software [107–109] (Fig. 20.4). MRS has to be considered as part of a combined diagnostic approach including morphologic and functional MR imaging (MRI), e.g., for detecting areas of increased tumor vascularization by dynamic contrast-enhanced MRI. The metabolic information can then be used for (1) differentiating malignant from benign mass lesions, (2) grading the aggressiveness of malignant tumors, (3) guiding biopsy in heterogeneous mass lesions, (4) treatment planning in radiotherapy, chemotherapy, and surgery, and (5) monitoring treatment effects of different chemo- and/or radiotherapy regimes [109–114]. However, MRS is not as robust as MRI and the spectral quality strongly depends on the magnetic field homogeneity which is

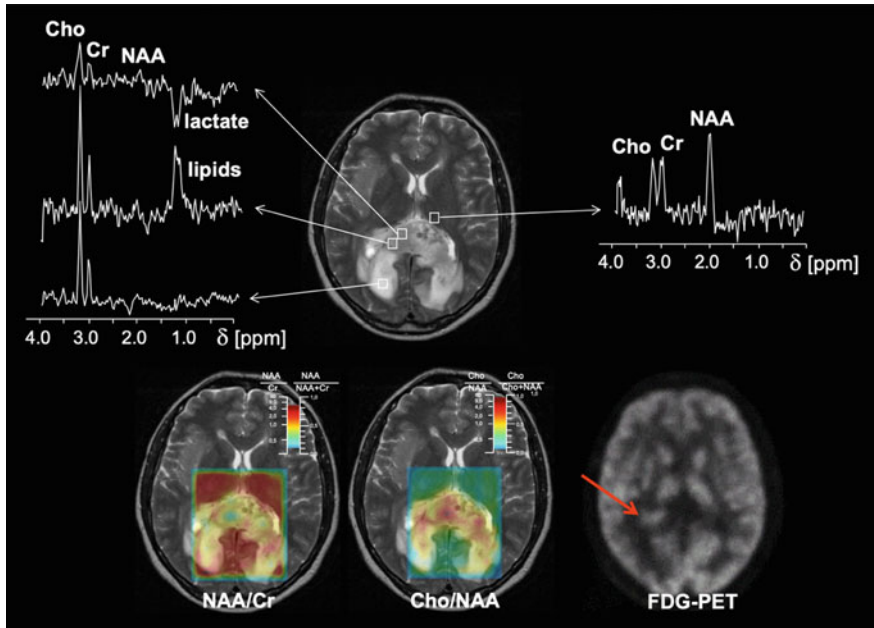


Fig. 20.4 39-year-old patient with a recurrent grade II astrocytoma after stereotactic irradiation with 54 Gy. Axial T2-weighted MRI 8 months after irradiation reveals a posterior mass with surrounding edema. The white grid on the T2w MRI marks the area of ^1H -CSI examined (PRESS, TE = 135 ms). The ^1H MR spectra measured in the mass (voxels 1, 2) show markedly increased signal intensity ratios from Cho to Cr and Cho to NAA. At the tumor margin (voxel 3) a lower relative signal intensity of the Cho resonance, but an additional lactate peak. Voxel 4 shows the spectrum of a normal appearing brain region. The recurrent tumor has high Cho or Cho/NAA and Cho/(Cho + NAA) values as well as low NAA and NAA/Cr and NAA/(NAA + Cr) values. However, the absolute signal intensity of the Cho resonance varies considerably in the tumor region (e.g., different SNR spectrum 1 and 2 and the inhomogeneous color distribution of the Cho image in the tumor)

influenced by the examined anatomic region and tissue characteristics. Additionally, the specificity of MRS is limited because increased Cho levels are also observed in benign disorders, e.g., in inflammation. In brain tumors and prostate cancer, however, MRS has been proven in large clinical trials as a valuable diagnostic tool for staging and therapy monitoring. It is well-known from the literature that various cancer cells tend to have increased lactate and lipid production associated with altered pH values in the tumor microenvironment [115, 116]. These metabolic changes cause an acidification of the extracellular compartment (pHe) and an alkalization of the intracellular space (pHi) [117–119]. Decreased pHe values were shown to enhance tumor invasiveness [120–122] and angiogenesis [123, 124]. Increased pHi values have been reported to increase cancer resistance to radiation and chemotherapy [125, 126], as well as to contribute to enhanced

proliferation [121] and reduced apoptosis [121, 127]. In this context, *in vitro* 1H MRS studies of astrocytoma biopsies have shown that lipid levels correlate with tumor necrosis [128]. Mobile lipids have also been shown to arise in some tumor cells under hypoxic stress prior to necrosis [129, 130]. Therefore, such insights into metabolic features could furthering our understanding of the pathophysiologically altered metabolism in tumors with impact on therapy planning and prognostication [121, 131].

21.5 Protein-Weighted MRI Using Chemical Exchange Saturation Transfer (CEST)

Chemical exchange saturation transfer (CEST) magnetic resonance imaging (MRI) represents a novel technique that enables large signal amplification of low-concentration molecules *in vivo*. CEST contrasts make use of the spontaneous chemical exchange between solute-bound protons and protons of free bulk water that to a large extent depends on the concentration of cellular proteins. Therefore, CEST MRI may add valuable information in diagnostic oncology prior to invasive procedures as well as in the follow-up setting for therapy monitoring.

Proteins and peptides have amide groups, which resonate around +3.5 parts per million (ppm) relative to the water proton signal. The majority of CEST studies published in the literature aimed at quantifying the amide proton transfer (APT) effect, most commonly assessed using the magnetization transfer ratio asymmetry (MTR_{asym}) approach proposed by Zhou et al. [132]. The resulting contrast is usually referred to as APT-weighted APT-w MRI in the literature.

Besides APT, relayed nuclear Overhauser effects (rNOE) and amine resonances can be observed in the so-called Z-Spectrum (Fig. 20.5) which is commonly acquired in CEST MRI through selective radiofrequency (RF) saturation [133]. Recently, more sophisticated approaches have been proposed enabling simultaneous quantification of multiple CEST pools by using Lorentzian fit analysis on data with high spectral resolution obtained at 7.0 T (Fig. 20.1) [134–138]. CEST MRI significantly extends the currently available repertoire of MR biomarkers in diagnostic oncology and has recently been investigated in numerous clinical studies with a large majority applied to neuro-oncologic diseases.

21.5.1 Brain Tumors

Pre-operative assessment of glioma with APT(-w) CEST MRI has been shown to correlate with WHO tumor grade [139–143] and has the potential to distinguish high and low-grade glioma also for non-enhancing lesions [144] (Fig. 20.6). For rNOE mediated CEST effects, correlation with tumor grade [145] and cellularity have also been reported [146]. While increased APT effects are observed in high-grade glioma, decreased rNOE signals were reported in both high-grade and

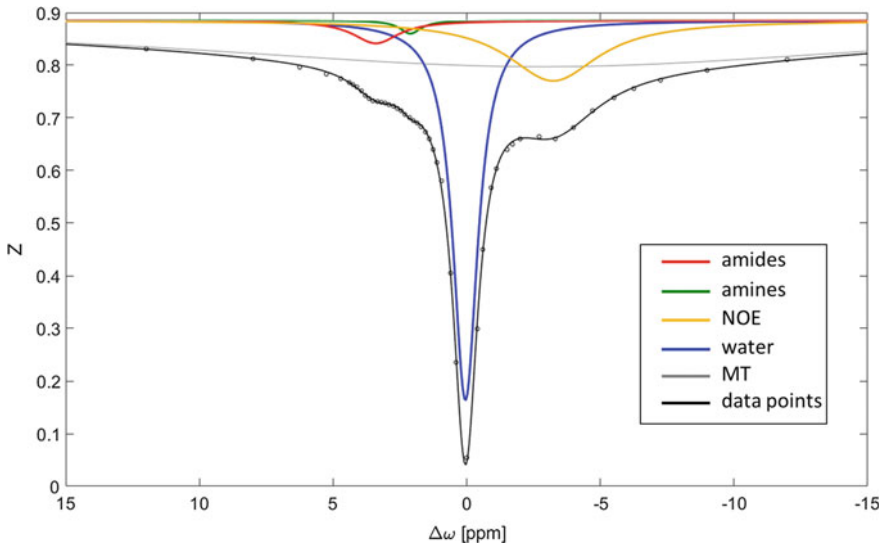


Fig. 20.5 CEST effects in the Z-spectrum at 7.0 T. The most prominent resonances downfield from the water resonance can be assigned to the amide protons ($\Delta\omega = +3.5$ ppm) and fast-exchanging amines ($\Delta\omega = +2.7$ ppm). Upfield ($\Delta\omega = -2.0$ ppm to -5.0 ppm), a broader resonance can be observed, which is due to relayed nuclear Overhauser effects (rNOE). Z-spectrum acquired in the brain of a healthy volunteer at a 7 T whole body MRI scanner. (Parameters: 120 Gaussian-shaped pulses à 15 ms; $B_1 = 0.9 \mu\text{T}$; 60 offsets, read out: FoV 195×170 , matrix 128×112 , slice 5 mm, TE = 3.61 ms, TR = 7.4 ms, flip angle 10°)

low-grade glioma (Fig. 20.6) [134, 135, 143, 145, 147]. Recently, different approaches of APT mediated CEST MRI were shown to be associated with the IDH-mutation status in newly diagnosed gliomas [143, 148]. This finding is plausible since mutations in IDH gene-encoded enzymes cause widespread alterations of amino acid concentrations with a global downregulation of protein expression [148]. Therefore, APT CEST MRI may represent an alternative MR biomarker that may help to determine IDH-mutation status non-invasively.

Prognostication and early response assessment are major challenges in daily clinical decision-making in glioma patients [149]. Recent studies reported increased APT-w signals in progressive tumors compared with treatment-related changes [150, 151] and to be associated with survival and progression-free survival (PFS) in glioma patients [152]. Furthermore, investigations of early treatment response in glioblastoma patients during ongoing radiotherapy enabled to distinguish treatment responders from non-responders, at a time point as early as two weeks after start of radiochemotherapy based on APT and rNOE imaging [153]. APT and rNOE mediated CEST contrasts were additionally shown to enable prognostication of response to first-line chemo-radiation therapy prior to treatment [152–154]. However, these promising results need to be confirmed in larger prospective study cohorts.

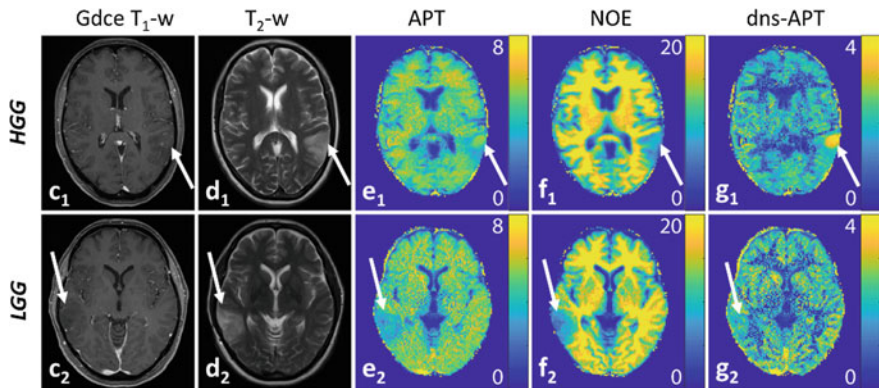


Fig. 20.6 Association CEST MRI and WHO tumor grade (HGG vs. LGG) in newly diagnosed untreated glioma patients. Two exemplary patients with high-grade glioma (HGG: glioblastoma, c_1 – g_1) and low-grade glioma (LGG: Oligodendroglioma II, c_2 – g_2) shown: c_i : Gdce T1-w, d_i : T2-w (TSE), relaxation-compensated multi-pool CEST MRI at 7T with separated APT (e_i), NOE (f_i), and downfield NOE-suppressed (dns)-APT (g_i) effects [unit: %]. Increased APT signals can be observed in the HGG tumor, especially at dns-APT imaging whereas the LGG tumor displays hypo-/isointense to surrounding normal appearing tissue. The glioblastoma patient shows only a small spot-like contrast enhancement in the tumor region (c_1) while a clear hyperintensity displays within the tumor at dns-APT imaging (g_1 , white arrow). © *Neuro-Oncology*, Oxford Academic, Paech et al. Volume 20, Issue 12, 12 November 2018, pp. 1661–1671

21.5.2 Applications of CEST MRI in Other Organs

CEST MRI has also been demonstrated to be feasible in other oncologic diseases. In 2011, CEST MRI was applied for the first time in twelve patients with biopsy-proven prostate cancer [155]. The study showed that APT mediated CEST effects were significantly increased in the tumor region compared with benign tissue of the peripheral zone [155]. Moreover, another study found a correlation between the APT signal intensity in prostate tumors and the Gleason score [156]. Investigations in breast cancer patients showed a positive correlation between APT CEST signal intensity and tumor grades [157, 158]. Apart from that, the APT CEST contrast was recently also used to distinguish benign and malignant pulmonary lesions [159] as well as benign and malignant head and neck tumors [160]. All these recent studies indicate the high potential of CEST MRI as an additional, non-invasive tool in diagnostic oncology.

21.6 Dynamic Glucose-Enhanced (DGE) MRI

Most common MRI contrast agents are based on the paramagnetic metal gadolinium (Gd), which enhances the nuclear relaxation rates of adjacent protons, thereby modifying signal intensities in the acquired images. Recently, Gd-based contrast

agents (GBCA) have been subject to criticism, since several studies reported accumulation of gadolinium in deep gray matter nuclei after serial application [161–166]. Besides, there is a known risk of developing nephrogenic systemic fibrosis for patients with renal failure [167]. Consequently, the development of novel MRI techniques using biodegradable contrast agents is highly desirable. A promising substance for such a new type of contrast agent is natural D-glucose, since it can be detected through chemical exchange saturation transfer (CEST) [168–170] or chemical exchange sensitive spin-lock (CESL) [171, 172]. The basic idea of these approaches is to measure signal changes after intravenous glucose administration with sufficiently high temporal and spatial resolution. The feasibility of dynamic glucose-enhanced DGE-MRI in humans has recently been proven in independent studies employing both CEST and CESL-based techniques [172–175]. Figure 20.7 shows glucose-enhanced images of a patient with newly diagnosed right-frontal glioblastoma [173]. The tumor regions of patients with glioblastoma showed increased glucose concentrations partially overlapping with the corresponding gadolinium-enhancement and relative cerebral blood volume (rCBV) maps, which are routinely acquired in diagnostic neuro-oncology [173]. However, also beyond disrupted blood–brain barrier regions, increased signal intensities can be observed at glucose-enhanced images (Fig. 20.7). Origins of signal changes in DGE-MRI are still under debate. Generally, glucose signal can result from concentration changes in three different compartments: (1) the intravascular space, (2) the extravascular and extracellular space (EES), and (3) the intracellular space. The latest results indicate major contributions of tissue perfusion and blood–brain barrier (BBB) leakage [173, 175, 176]. Besides, DGE-MRI contrasts may be additionally altered by local pH, since an acidic tumor microenvironment enhances DGE signals through the modulation of the proton exchange rate.

21.7 MR Fingerprinting for Quantitative Relaxometry (T1 and T2 Mapping)

Magnetic Resonance Fingerprinting (MRF) is an imaging approach to quantitatively measure multiple tissue properties simultaneously. This technique has been shown to enable rapid acquisition T1 and T2 maps with good correlation with conventional T1 and T2 mapping methods [177, 178]. Initial clinical studies employing MRF-based techniques have reported promising results in brain and prostate cancer [179].

21.7.1 Prostate Relaxometry

A study performed by Yu and colleagues employed a MRF-based T1, T2, and standard apparent diffusion coefficient (ADC) mapping approach to differentiate cancer lesions in the peripheral zone from normal prostate tissue [180]. They

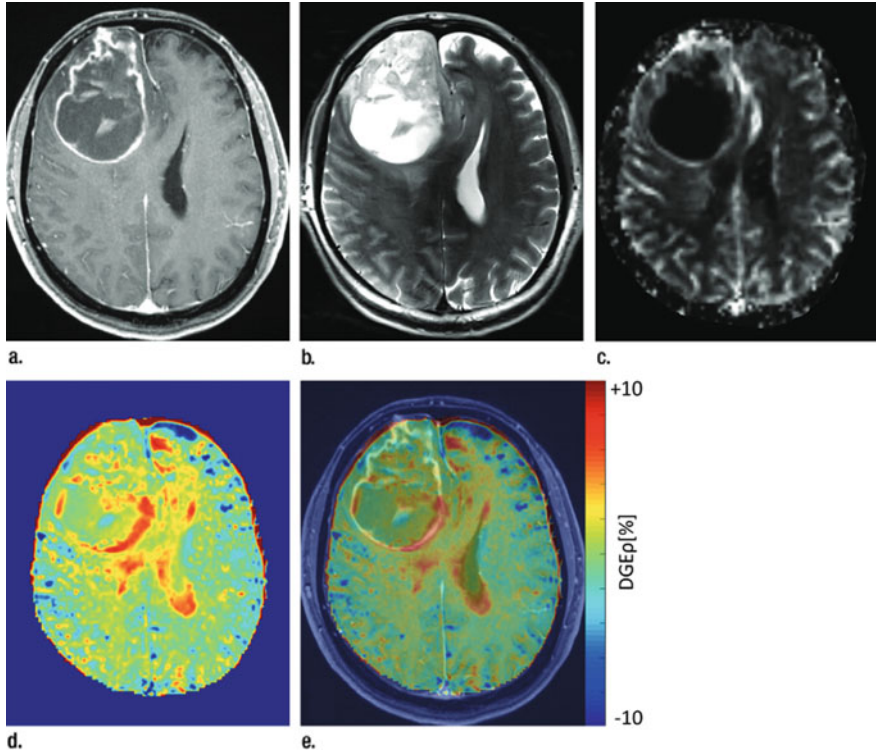


Fig. 20.7 $T1\rho$ -weighted dynamic glucose-enhances ($DGE\rho$) MRI at 7T in a patient with newly diagnosed glioblastoma, compared with GdCE T1-w, T2-w and perfusion imaging. **a** GdCE T1-w images, **b** T2-w images and **c** rCBV maps displayed. T2-w and **d** $DGE\rho$ images obtained at 7T. **e** Fusion images of GdCE T1-w and $DGE\rho$ images. The $DGE\rho$ contrast displays regions of increased signal intensity, particularly in the dorsomedial tumor region (overlapping with the ring-enhancement on GdCE-T1), and beyond the borders of BBB disruption (**e**). Some regions of increased glucose uptake cannot be delineated on the GdCE T1-w, T2-w, and perfusion images. Partial overlap can be observed between $DGE\rho$ and rCBV images. Original figure from Paech et al. [173] with reprint permission from RSNA

reported that T1, T2, and ADC were all significant univariate predictors in the differentiation between histologically proved prostate cancer normal-appearing peripheral zone (NPZ). Moreover, MRF-derived T2 and ADC helped to separate high- or intermediate-grade prostate cancer from low-grade cancer [180]. Ultimately, T1, T2, and ADC were all significant predictors in the differentiation between histologically proved prostatitis and NPZ while the combination of T1 and ADC yielded the best discrimination [180].

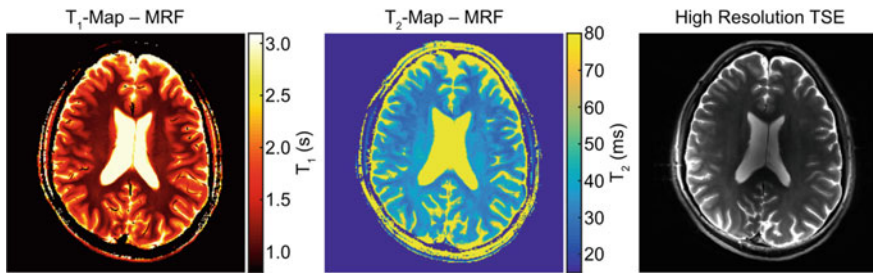


Fig. 20.8 Brain relaxometry: Quantitative T1 and T2 maps derived from MR Fingerprinting in a healthy volunteer at 7 T using a fast imaging with steady-state precession (FISP)-based sequence. Figure courtesy of Sebastian Flassbeck, MSc, German Cancer Research Center, Division of Medical Physics in Radiology

21.7.2 Brain Relaxometry

MR fingerprinting allows rapid simultaneous T1 and T2 measurement in brain tumors and surrounding tissues [181] (Fig. 20.8). The first clinical application in a study cohort of 31 patients with untreated intra-axial brain tumors showed that MRF-derived T1 and T2 maps have the potential to distinguish between gliomas and brain metastases [181]. Broader applications and investigations in larger study cohorts are needed to assess the full diagnostic potential of MRF-derived biomarkers.

21.8 Challenges to Implement Clinical MR Biomarkers in Multicenter Trials

Application of MR biomarkers on a larger scale for tumor staging and therapy response assessment is still challenging. In multicenter clinical studies as well as in clinical routine standardization of examination protocols, data evaluation algorithms, documentation procedures, and quality assurance measures are essentially required. To develop imaging biomarkers for different human body regions and for particular clinical questions, information platforms are needed that include centers of excellence, ongoing imaging biomarker research projects, clinical studies, and educational activities. International collaborative organizations tackle key issues by coordinating research activities on quantitative imaging biomarkers and by providing recommendations. Goal of the Quantitative Imaging Biomarkers Alliance (QIBA) of the Radiologic Society of North America (RSNA) is to provide technical performance standards and tools for producing reliable quantitative imaging biomarkers for use in the clinical imaging community, e.g., for improved precision of DWI and DCE-MRI derived biomarkers in multicenter oncology trials [182]. The QIBA accredits centers suitable for multicenter trials based on certain

quality criteria. The European Imaging Biomarker Alliance (EIBALL) is a subcommittee of the European Society for Radiology (ESR) supported for its operational activities by the European Institute for Biomedical Imaging Research (EIBIR). In order to exploit synergies with other societies active on imaging biomarker research EIBALL works in collaboration with QIBA and other European imaging societies, e.g., European Society of Molecular and Functional Imaging (ESMOFIR) and the European Society of Magnetic Resonance in Medicine and Biology (ESMRMB). EIBALL lists for example core institutions and networks of collaborating institutions in Europe involved in imaging biomarker development and publish white papers and recommendations [183–185]. Potential imaging sites can be identified which qualify for multicenter clinical trials concerning biological validation as well as application, e.g., by the European Organization of Research and Treatment of Cancer (EORTC). These activities should enable, that clinical trials can use advanced imaging biomarkers, in particular when imaging is used as early response marker and primary endpoint.

References

1. Ellingson BM, Malkin MG, Rand SD et al (2010) Validation of functional diffusion maps (fDMs) as a biomarker for human glioma cellularity. *J Magn Reson Imaging* 31:538–548
2. Sugahara T, Korogi Y, Kochi M et al (1999) Usefulness of diffusion-weighted MRI with echo-planar technique in the evaluation of cellularity in gliomas. *J Magn Reson Imaging* 9:53–60
3. Kono K, Inoue Y, Nakayama K et al (2001) The role of diffusion-weighted imaging in patients with brain tumors. *AJNR Am J Neuroradiol* 22:1081–1088
4. Gupta RK, Cloughesy TF, Sinha U et al (2000) Relationships between choline magnetic resonance spectroscopy, apparent diffusion coefficient and quantitative histopathology in human glioma. *J Neuro-oncol* 50:215–226
5. Porter KR, McCarthy BJ, Freels S, Kim Y, Davis FG (2010) Prevalence estimates for primary brain tumors in the United States by age, gender, behavior, and histology. *Neuro Oncol* 12:520–527
6. Louis DN, Perry A, Reifenberger G et al (2016) The 2016 World Health Organization classification of tumors of the central nervous system: a summary. *Acta Neuropathol* 131:803–820
7. Wen PY, Kesari S (2008) Malignant gliomas in adults. *N Engl J Med* 359:492–507
8. Hegi ME, Diserens AC, Gorlia T et al (2005) MGMT gene silencing and benefit from temozolomide in glioblastoma. *N Engl J Med* 352:997–1003
9. Platten M, Bunse L, Wick W, Bunse T (2016) Concepts in glioma immunotherapy. *Cancer Immunol Immunother* 65:1269–1275
10. Yan H, Parsons DW, Jin G et al (2009) IDH1 and IDH2 mutations in gliomas. *N Engl J Med* 360:765–773
11. Pope WB, Qiao XJ, Kim HJ et al (2012) Apparent diffusion coefficient histogram analysis stratifies progression-free and overall survival in patients with recurrent GBM treated with bevacizumab: a multi-center study. *J Neurooncol* 108:491–498
12. Oh J, Henry RG, Pirzkall A et al (2004) Survival analysis in patients with glioblastoma multiforme: predictive value of choline-to-n-acetylaspartate index, apparent diffusion coefficient, and relative cerebral blood volume. *J Magn Reson Imaging* 19:546–554

13. Ellingson BM, Cloughesy TF, Lai A et al (2011) Graded functional diffusion map–defined characteristics of apparent diffusion coefficients predict overall survival in recurrent glioblastoma treated with bevacizumab. *Neuro-Oncology* 13:1151–1161
14. Higano S, Yun X, Kumabe T et al (2006) Malignant astrocytic tumors: clinical importance of apparent diffusion coefficient in prediction of grade and prognosis. *Radiology* 241:839–846
15. Hamstra DA, Chenevert TL, Moffat BA et al (2005) Evaluation of the functional diffusion map as an early biomarker of time-to-progression and overall survival in high-grade glioma. *Proc Natl Acad Sci USA* 102:16759–16764
16. Murakami R, Sugahara T, Nakamura H et al (2007) Malignant supratentorial astrocytoma treated with postoperative radiation therapy: prognostic value of pretreatment quantitative diffusion-weighted MR imaging. *Radiology* 243:493–499
17. Kono K, Inoue Y, Nakayama K et al (2001) The role of diffusion-weighted imaging in patients with brain tumors. *Am J Neuroradiol* 22:1081–1088
18. Sugahara T, Korogi Y, Kochi M et al (1999) Usefulness of diffusion-weighted MRI with echo-planar technique in the evaluation of cellularity in gliomas. *J Magn Reson Imaging Official J Int Soc Magn Reson Med* 9:53–60
19. Yang D, Korogi Y, Sugahara T et al (2002) Cerebral gliomas: prospective comparison of multivoxel 2D chemical-shift imaging proton MR spectroscopy, echoplanar perfusion and diffusion-weighted MRI. *Neuroradiology* 44:656–666
20. Yamasaki F, Kurisu K, Satoh K et al (2005) Apparent diffusion coefficient of human brain tumors at MR imaging. *Radiology* 235:985–991
21. Lee E, Lee S, Agid R, Bae J, Keller A (2008) Preoperative grading of presumptive low-grade astrocytomas on MR imaging: diagnostic value of minimum apparent diffusion coefficient. *Am J Neuroradiol* 29:1872–1877
22. Mills SJ, Soh C, Rose CJ et al (2010) Candidate biomarkers of extravascular extracellular space: a direct comparison of apparent diffusion coefficient and dynamic contrast-enhanced MR imaging—derived measurement of the volume of the extravascular extracellular space in glioblastoma multiforme. *Am J Neuroradiol* 31:549–553
23. Moffat BA, Chenevert TL, Lawrence TS et al (2005) Functional diffusion map: a noninvasive MRI biomarker for early stratification of clinical brain tumor response. *Proc Natl Acad Sci* 102:5524–5529
24. Chenevert TL, Stegman LD, Taylor JM et al (2000) Diffusion magnetic resonance imaging: an early surrogate marker of therapeutic efficacy in brain tumors. *JNCI J Natl Cancer Inst* 92:2029–2036
25. Basser PJ, Mattiello J, LeBihan D (1994) Estimation of the effective self-diffusion tensor from the NMR spin echo. *J Magn Reson Ser B* 103:247–254
26. Sinha S, Bastin ME, Whittle IR, Wardlaw JM (2002) Diffusion tensor MR imaging of high-grade cerebral gliomas. *Am J Neuroradiol* 23:520–527
27. Zhou L-F, Du G-H, Wu J-S et al (2007) Clinical evaluation and follow-up outcome of diffusion tensor imaging-based functional neuronavigation: a prospective, controlled study in patients with gliomas involving pyramidal tracts. *Neurosurgery* 61:935–949
28. Cauter SV, Veraart J, Sijbers J et al (2012) Gliomas: diffusion kurtosis MR imaging in grading. *Radiology* 263:492–501
29. Poot DH, Arnold J, Achten E, Verhoye M, Sijbers J (2010) Optimal experimental design for diffusion kurtosis imaging. *IEEE Trans Med Imaging* 29:819–829
30. Vargas HA, Akin O, Franiel T et al (2011) Diffusion-weighted endorectal MR imaging at 3 T for prostate cancer: tumor detection and assessment of aggressiveness. *Radiology* 259:775–784
31. Langer DL, van der Kwast TH, Evans AJ et al (2010) Prostate tissue composition and MR measurements: investigating the relationships between ADC, T2, K trans, Ve, and corresponding histologic features. *Radiology* 255:485–494

32. Turkbey B, Shah VP, Pang Y et al (2011) Is apparent diffusion coefficient associated with clinical risk scores for prostate cancers that are visible on 3-T MR images? *Radiology* 258:488–495
33. Hambrock T, Somford DM, Huisman HJ et al (2011) Relationship between apparent diffusion coefficients at 3.0-T MR imaging and Gleason grade in peripheral zone prostate cancer. *Radiology* 259:453–461
34. Barentsz JO, Richenberg J, Clements R et al (2012) ESUR prostate MR guidelines 2012. *Eur Radiol* 22:746–757
35. Jung SI, Donati OF, Vargas HA, Goldman D, Hricak H, Akin O (2013) Transition zone prostate cancer: incremental value of diffusion-weighted endorectal MR imaging in tumor detection and assessment of aggressiveness. *Radiology* 269:493–503
36. Jambor I, Merisaari H, Taimen P et al (2015) Evaluation of different mathematical models for diffusion-weighted imaging of normal prostate and prostate cancer using high b-values: a repeatability study. *Magn Reson Med* 73:1988–1998
37. Bonekamp D, Kohl S, Wiesenfarth M et al (2018) Radiomic machine learning for characterization of prostate lesions with MRI: comparison to ADC values. *Radiology* 289:128–137
38. Morgan V, Riches S, Thomas K et al (2011) Diffusion-weighted magnetic resonance imaging for monitoring prostate cancer progression in patients managed by active surveillance. *Br J Radiol* 84:31–37
39. Park SY, Kim CK, Park BK, Lee HM, Lee KS (2011) Prediction of biochemical recurrence following radical prostatectomy in men with prostate cancer by diffusion-weighted magnetic resonance imaging: initial results. *Eur Radiol* 21:1111–1118
40. Zhang Y-D, Wang Q, Wu C-J et al (2015) The histogram analysis of diffusion-weighted intravoxel incoherent motion (IVIM) imaging for differentiating the gleason grade of prostate cancer. *Eur Radiol* 25:994–1004
41. Deike-Hofmann K, Koenig F, Paech D et al (2019) Abbreviated MRI protocols in breast cancer diagnostics. *J Magn Reson Imaging* 49(3):647–658
42. Marini C, Iacconi C, Giannelli M, Cilotti A, Moretti M, Bartolozzi C (2007) Quantitative diffusion-weighted MR imaging in the differential diagnosis of breast lesion. *Eur Radiol* 17:2646–2655
43. Shin HJ, Kim SH, Lee HJ et al (2016) Tumor apparent diffusion coefficient as an imaging biomarker to predict tumor aggressiveness in patients with estrogen-receptor-positive breast cancer. *NMR Biomed* 29:1070–1078
44. Bickelhaupt S, Tesdorff J, Laun FB et al (2017) Independent value of image fusion in unenhanced breast MRI using diffusion-weighted and morphological T2-weighted images for lesion characterization in patients with recently detected BI-RADS 4/5 x-ray mammography findings. *Eur Radiol* 27:562–569
45. Yabuuchi H, Matsuo Y, Sunami S et al (2011) Detection of non-palpable breast cancer in asymptomatic women by using unenhanced diffusion-weighted and T2-weighted MR imaging: comparison with mammography and dynamic contrast-enhanced MR imaging. *Eur Radiol* 21:11–17
46. Ei Khouli RH, Jacobs MA, Mezban SD et al (2010) Diffusion-weighted imaging improves the diagnostic accuracy of conventional 3.0-T breast MR imaging. *Radiology* 256:64–73
47. Jensen JH, Helpert JA, Ramani A, Lu H, Kaczynski K (2005) Diffusional kurtosis imaging: The quantification of non-gaussian water diffusion by means of magnetic resonance imaging. *Magn Reson Med* 53:1432–1440
48. Sun K, Chen X, Chai W et al (2015) Breast cancer: diffusion kurtosis MR imaging—diagnostic accuracy and correlation with clinical-pathologic factors. *Radiology* 277:46–55
49. Bickelhaupt S, Steudle F, Paech D et al (2017) On a fractional order calculus model in diffusion weighted breast imaging to differentiate between malignant and benign breast lesions detected on X-ray screening mammography. *PLoS ONE* 12:e0176077

50. Le Bihan D, Breton E, Lallemand D, Aubin M, Vignaud J, Laval-Jeantet M (1988) Separation of diffusion and perfusion in intravoxel incoherent motion MR imaging. *Radiology* 168:497–505
51. Liu C, Liang C, Liu Z, Zhang S, Huang B (2013) Intravoxel incoherent motion (IVIM) in evaluation of breast lesions: comparison with conventional DWI. *Eur J Radiol* 82:e782–e789
52. Eyal E, Shapiro-Feinberg M, Furman-Haran E et al (2012) Parametric diffusion tensor imaging of the breast. *Invest Radiol* 47:284–291
53. Partridge SC, McDonald ES (2013) Diffusion weighted magnetic resonance imaging of the breast: protocol optimization, interpretation, and clinical applications. *Magn Reson Imaging Clin* 21:601–624
54. Rahbar H, Partridge SC (2016) Multiparametric MR imaging of breast cancer. *Magn Reson Imaging Clin N Am* 24:223–238
55. Nguyen TB, Cron GO, Perdrizet K et al (2015) Comparison of the diagnostic accuracy of DSC- and dynamic contrast-enhanced MRI in the preoperative grading of astrocytomas. *Am J Neuroradiol* 36:2017–2022
56. Tofts PS, Kermode AG (1991) Measurement of the blood-brain barrier permeability and leakage space using dynamic MR imaging. 1 Fundamental concepts. *Magn Reson Med* 17:357–367
57. Sourbron S, Ingrisch M, Siefert A, Reiser M, Hermann K (2009) Quantification of cerebral blood flow, cerebral blood volume, and blood-brain-barrier leakage with DCE-MRI. *Magn Reson Med* 62:205–217
58. Leu K, Ott GA, Lai A et al (2017) Perfusion and diffusion MRI signatures in histologic and genetic subtypes of WHO grade II–III diffuse gliomas. *J Neurooncol* 134:177–188
59. Lacerda S, Law M (2009) Magnetic resonance perfusion and permeability imaging in brain tumors. *Neuroimaging Clin N Am* 19:527–557
60. Thompson G, Mills SJ, Stivaros SM, Jackson A (2010) Imaging of brain tumors: perfusion/permeability. *Neuroimaging Clin N Am* 20:337–353
61. Cha S, Yang L, Johnson G et al (2006) Comparison of microvascular permeability measurements, K^{trans} , determined with conventional steady-state T1-weighted and first-pass T2*-weighted MR imaging methods in gliomas and meningiomas. *Am J Neuroradiol* 27:409–417
62. Boxerman J, Schmainda K, Weisskoff R (2006) Relative cerebral blood volume maps corrected for contrast agent extravasation significantly correlate with glioma tumor grade, whereas uncorrected maps do not. *Am J Neuroradiol* 27:859–867
63. Aronen HJ, Gazit IE, Louis DN et al (1994) Cerebral blood volume maps of gliomas: comparison with tumor grade and histologic findings. *Radiology* 191:41–51
64. Cha S, Lupo JM, Chen M-H et al (2007) Differentiation of glioblastoma multiforme and single brain metastasis by peak height and percentage of signal intensity recovery derived from dynamic susceptibility-weighted contrast-enhanced perfusion MR imaging. *Am J Neuroradiol* 28:1078–1084
65. Tan W, Xiong J, Huang W, Wu J, Zhan S, Geng D (2017) Noninvasively detecting Isocitrate dehydrogenase 1 gene status in astrocytoma by dynamic susceptibility contrast MRI. *J Magn Reson Imaging* 45:492–499
66. Jenkinson MD, Smith TS, Joyce KA et al (2006) Cerebral blood volume, genotype and chemosensitivity in oligodendroglial tumours. *Neuroradiology* 48:703–713
67. Law M, Young RJ, Babb JS et al (2008) Gliomas: predicting time to progression or survival with cerebral blood volume measurements at dynamic susceptibility-weighted contrast-enhanced perfusion MR imaging. *Radiology* 247:490–498
68. Bonekamp D, Deike K, Wiestler B et al (2015) Association of overall survival in patients with newly diagnosed glioblastoma with contrast-enhanced perfusion MRI: Comparison of intraindividually matched T1- and T2*-based bolus techniques. *J Magn Reson Imaging* 42:87–96

69. Lüdemann L, Grieger W, Wurm R, Wust P, Zimmer C (2005) Quantitative measurement of leakage volume and permeability in gliomas, meningiomas and brain metastases with dynamic contrast-enhanced MRI. *Magn Reson Imaging* 23:833–841
70. Lüdemann L, Grieger W, Wurm R, Budzisch M, Hamm B, Zimmer C (2001) Comparison of dynamic contrast-enhanced MRI with WHO tumor grading for gliomas. *Eur Radiol* 11:1231–1241
71. Zhu X, Li K, Kamaly-Asl I et al (2000) Quantification of endothelial permeability, leakage space, and blood volume in brain tumors using combined T1 and T2* contrast-enhanced dynamic MR imaging. *J Magn Reson Imaging* 11:575–585
72. Telischak NA, Detre JA, Zaharchuk G (2015) Arterial spin labeling MRI: clinical applications in the brain. *J Magn Reson Imaging* 41:1165–1180
73. Detre JA, Leigh JS, Williams DS, Koretsky AP (1992) Perfusion imaging. *Magn Reson Med* 23:37–45
74. Kwong KK, Belliveau JW, Chesler DA et al (1992) Dynamic magnetic resonance imaging of human brain activity during primary sensory stimulation. *Proc Natl Acad Sci U S A* 89:5675–5679
75. Kong L, Chen H, Yang Y, Chen L (2017) A meta-analysis of arterial spin labelling perfusion values for the prediction of glioma grade. *Clin Radiol* 72:255–261
76. Kuhl CK, Schradang S, Strobel K, Schild HH, Hilgers R-D, Bieling HB (2014) Abbreviated breast Magnetic Resonance Imaging (MRI): first postcontrast subtracted images and maximum-intensity projection—a novel approach to breast cancer screening with MRI. *J Clin Oncol*. <https://doi.org/10.1200/jco.2013.52.5386>
77. Heacock L, Melsaether AN, Heller SL et al (2016) Evaluation of a known breast cancer using an abbreviated breast MRI protocol: correlation of imaging characteristics and pathology with lesion detection and conspicuity. *Eur J Radiol* 85:815–823
78. Klifa C, Suzuki S, Aliu S et al (2011) Quantification of background enhancement in breast magnetic resonance imaging. *J Magn Reson Imaging* 33:1229–1234
79. Mann RM, Mus RD, van Zelst J, Geppert C, Karssemeijer N, Platel B (2014) A novel approach to contrast-enhanced breast magnetic resonance imaging for screening: high-resolution ultrafast dynamic imaging. *Invest Radiol* 49:579–585
80. Padhani AR, Gapinski CJ, Macvicar DA et al (2000) Dynamic contrast enhanced MRI of prostate cancer: correlation with morphology and tumour stage, histological grade and PSA. *Clin Radiol* 55:99–109
81. Bonekamp D, Wolf MB, Edler C et al (2016) Dynamic contrast enhanced MRI monitoring of primary proton and carbon ion irradiation of prostate cancer using a novel hypofractionated raster scan technique. *Radiother Oncol* 120:313–319
82. Semelka RC, Martin DR, Balci C, Lance T (2001) Focal liver lesions: comparison of dual-phase CT and multisequence multiplanar MR imaging including dynamic gadolinium enhancement. *J Magn Reson Imaging Official J Int Soc Magn Reson Med* 13:397–401
83. Low RN (2007) Abdominal MRI advances in the detection of liver tumours and characterisation. *Lancet Oncol* 8:525–535
84. Pandharipande PV, Krinsky GA, Rusinek H, Lee VS (2005) Perfusion imaging of the liver: current challenges and future goals. *Radiology* 234:661–673
85. Ichikawa T, Haradome H, Hachiya J, Nitatori T, Araki T (1998) Characterization of hepatic lesions by perfusion-weighted MR imaging with an echoplanar sequence. *AJR Am J Roentgenol* 170:1029–1034
86. Cuenod CA, Leconte I, Siauve N et al (2001) Early changes in liver perfusion caused by occult metastases in rats: detection with quantitative CT. *Radiology* 218:556–561
87. Padhani AR (2002) Dynamic contrast-enhanced MRI in clinical oncology: current status and future directions. *J Magn Reson Imaging Official J Int Soc Magn Reson Med* 16:407–422

88. Barentsz JO, Berger-Hartog O, Witjes JA et al (1998) Evaluation of chemotherapy in advanced urinary bladder cancer with fast dynamic contrast-enhanced MR imaging. *Radiology* 207:791–797
89. Reddick WE, Taylor JS, Fletcher BD (1999) Dynamic MR imaging (DEMRI) of microcirculation in bone sarcoma. *J Magn Reson Imaging Official J Int Soc Magn Reson Med* 10:277–285
90. Rosen MA, Schnall MD (2007) Dynamic contrast-enhanced magnetic resonance imaging for assessing tumor vascularity and vascular effects of targeted therapies in renal cell carcinoma. *Clin Cancer Res* 13:770s–776s
91. Akisik MF, Sandrasegaran K, Bu G, Lin C, Hutchins GD, Chiorean EG (2010) Pancreatic cancer: utility of dynamic contrast-enhanced MR imaging in assessment of antiangiogenic therapy. *Radiology* 256:441–449
92. Liu C, Li W, Tong KA, Yeom KW, Kuzminski S (2015) Susceptibility-weighted imaging and quantitative susceptibility mapping in the brain. *J Magn Reson Imaging JMRI* 42:23–41
93. Haacke EM, Xu Y, Cheng Y-CN, Reichenbach JR (2004) Susceptibility weighted imaging (SWI). *Magn Reson Med* 52:612–618
94. Reichenbach JR, Venkatesan R, Schillinger DJ, Kido DK, Haacke EM (1997) Small vessels in the human brain: MR venography with deoxyhemoglobin as an intrinsic contrast agent. *Radiology* 204:272–277
95. Essig M, Reichenbach JR, Schad LR, Schoenberg SO, Debus J, Kaiser WA (1999) High-resolution MR venography of cerebral arteriovenous malformations. *Magn Reson Imaging* 17:1417–1425
96. Tong KA, Ashwal S, Holshouser BA et al (2003) Hemorrhagic shearing lesions in children and adolescents with posttraumatic diffuse axonal injury: improved detection and initial results. *Radiology* 227:332–339
97. Idbaih A, Boukobza M, Crassard I, Porcher R, Bousser M-G, Chabriat H (2006) MRI of clot in cerebral venous thrombosis. *Stroke* 37:991–995
98. Wang Y, Liu T (2015) Quantitative susceptibility mapping (QSM): Decoding MRI data for a tissue magnetic biomarker. *Magn Reson Med* 73:82–101
99. Li J, Chang S, Liu T et al (2012) Reducing the object orientation dependence of susceptibility effects in gradient echo MRI through quantitative susceptibility mapping. *Magn Reson Med* 68:1563–1569
100. Huisman TA (2005) Intracranial hemorrhage: ultrasound, CT and MRI findings. *Eur Radiol* 15:434–440
101. Makariou E, Patsalides AD (2009) Intracranial calcifications. *Appl Radiol* 38:48
102. Chen W, Zhu W, Kovanlikaya I et al (2014) Intracranial calcifications and hemorrhages: characterization with quantitative susceptibility mapping. *Radiology* 270:496–505
103. Liu C, Li W, Johnson GA, Wu B (2011) High-field (9.4 T) MRI of brain dysmyelination by quantitative mapping of magnetic susceptibility. *NeuroImage* 56:930–938
104. Wisnieff C, Ramanan S, Olesik J, Gauthier S, Wang Y, Pitt D (2015) Quantitative susceptibility mapping (QSM) of white matter multiple sclerosis lesions: interpreting positive susceptibility and the presence of iron. *Magn Reson Med* 74:564–570
105. Zhang Y, Gauthier SA, Gupta A et al (2016) Longitudinal change in magnetic susceptibility of new enhanced multiple sclerosis (MS) lesions measured on serial quantitative susceptibility mapping (QSM). *J Magn Reson Imaging* 44:426–432
106. Xie L, Sparks MA, Li W et al (2013) Quantitative susceptibility mapping of kidney inflammation and fibrosis in type 1 angiotensin receptor-deficient mice. *NMR Biomed* 26:1853–1863
107. Horská A, Barker PB (2010) Imaging of brain tumors: MR spectroscopy and metabolic imaging. *Neuroimaging Clin N Am* 20:293–310
108. Ma FH, Qiang JW, Cai SQ, Zhao SH, Zhang GF, Rao YM (2015) MR spectroscopy for differentiating benign from malignant solid adnexal tumors. *Am J Roentgenol* 204:W724–W730

109. Leclerc X, Huisman TA, Sorensen AG (2002) The potential of proton magnetic resonance spectroscopy (1H-MRS) in the diagnosis and management of patients with brain tumors. *Curr Opin Oncol* 14:292–298
110. Negendank W (1992) Studies of human tumors by MRS: a review. *NMR Biomed* 5:303–324
111. Preul MC, Caramanos Z, Collins DL et al (1996) Accurate, noninvasive diagnosis of human brain tumors by using proton magnetic resonance spectroscopy. *Nat Med* 2:323–325
112. Castillo M, Smith JK, Kwok L (2000) Correlation of myo-inositol levels and grading of cerebral astrocytomas. *Am J Neuroradiol* 21:1645–1649
113. Schlemmer HP, Bachert P, Herfarth KK, Zuna I, Debus J, van Kaick G (2001) Proton MR spectroscopic evaluation of suspicious brain lesions after stereotactic radiotherapy. *Am J Neuroradiol* 22:1316–1324
114. Schlemmer H-P, Bachert P, Henze M et al (2002) Differentiation of radiation necrosis from tumor progression using proton magnetic resonance spectroscopy. *Neuroradiology* 44:216–222
115. Gatenby RA, Gillies RJ (2004) Why do cancers have high aerobic glycolysis? *Nat Rev Cancer* 4:891–899
116. Kugel H, Heindel W, Ernestus R, Bunke J, Du Mesnil R, Friedmann G (1992) Human brain tumors: spectral patterns detected with localized H-1 MR spectroscopy. *Radiology* 183:701–709
117. Fais S, Venturi G, Gatenby B (2014) Microenvironmental acidosis in carcinogenesis and metastases: new strategies in prevention and therapy. *Cancer Metastasis Rev* 33:1095–1108
118. Huber V, De Milito A, Harguindey S et al (2010) Proton dynamics in cancer. *J Transl Med* 8:57
119. Webb BA, Chimenti M, Jacobson MP, Barber DL (2011) Dysregulated pH: a perfect storm for cancer progression. *Nat Rev Cancer* 11:671
120. Harris RJ, Cloughesy TF, Liau LM et al (2015) pH-weighted molecular imaging of gliomas using amine chemical exchange saturation transfer MRI. *Neuro-oncology* 17:1514–1524
121. Wenger KJ, Hattingen E, Franz K, Steinbach JP, Bähr O, Pilatus U (2017) Intracellular pH measured by 31P-MR-spectroscopy might predict site of progression in recurrent glioblastoma under antiangiogenic therapy. *J Magn Reson Imaging* 46:1200–1208
122. Martínez-Zaguilán R, Seftor EA, Seftor RE, Chu Y-W, Gillies RJ, Hendrix MJ (1996) Acidic pH enhances the invasive behavior of human melanoma cells. *Clin Exp Metas* 14:176–186
123. Fukumura D, Xu L, Chen Y, Gohongi T, Seed B, Jain RK (2001) Hypoxia and acidosis independently up-regulate vascular endothelial growth factor transcription in brain tumors in vivo. *Can Res* 61:6020–6024
124. Griffiths L, Dachs GU, Bicknell R, Harris AL, Stratford IJ (1997) The influence of oxygen tension and pH on the expression of platelet-derived endothelial cell growth factor/thymidine phosphorylase in human breast tumor cells grown in vitro and in vivo. *Can Res* 57:570–572
125. Freeman M, Sierra E (1984) An acidic extracellular environment reduces the fixation of radiation damage. *Radiat Res* 97:154–161
126. Reichert M, Steinbach JP, Supra P, Weller M (2002) Modulation of growth and radiochemosensitivity of human malignant glioma cells by acidosis: a new look at the efficacy of nitrosoureas. *Cancer* 95:1113–1119
127. Lagadic-Gossmann D, Huc L, Lecreur V (2004) Alterations of intracellular pH homeostasis in apoptosis: origins and roles. *Cell Death Differ* 11:953
128. Kuessel AC, Sutherland GR, Halliday W, Smith IC (1994) 1H MRS of high grade astrocytomas: mobile lipid accumulation in necrotic tissue. *NMR Biomed* 7:149–155
129. Howe FA, Barton SJ, Cudlip SA et al (2003) Metabolic profiles of human brain tumors using quantitative in vivo 1H magnetic resonance spectroscopy. *Magn Reson Med* 49:223–232

130. Barba I, Cabañas ME, Arús C (1999) The relationship between nuclear magnetic resonance-visible lipids, lipid droplets, and cell proliferation in cultured C6 cells. *Can Res* 59:1861–1868
131. Maintz D, Heindel W, Kugel H, Jaeger R, Lackner KJ (2002) Phosphorus-31 MR spectroscopy of normal adult human brain and brain tumours. *NMR Biomed* 15:18–27
132. Zhou J, Payen J-F, Wilson DA, Traystman RJ, van Zijl PCM (2003) Using the amide proton signals of intracellular proteins and peptides to detect pH effects in MRI. *Nat Med* 9:1085–1090
133. Ward KM, Aletras AH, Balaban RS (2000) A new class of contrast agents for MRI based on proton Chemical Exchange Dependent Saturation Transfer (CEST). *J Magn Reson* 143:79–87
134. Jones CK, Huang A, Xu J et al (2013) Nuclear overhauser enhancement (NOE) imaging in the human brain at 7 T. *Neuroimage* 77:114–124
135. Zaiss M, Windschuh J, Paech D et al (2015) Relaxation-compensated CEST-MRI of the human brain at 7 T: Unbiased insight into NOE and amide signal changes in human glioblastoma. *NeuroImage* 112:180–188
136. Zaiß M, Schmitt B, Bachert P (2011) Quantitative separation of CEST effect from magnetization transfer and spillover effects by Lorentzian-line-fit analysis of z-spectra. *J Magn Reson* 211:149–155
137. Zaiss M, Xu J, Goerke S et al (2014) Inverse Z-spectrum analysis for spillover-, MT-, and T1-corrected steady-state pulsed CEST-MRI—application to pH-weighted MRI of acute stroke. *NMR Biomed* 27:240–252
138. Zaiss M, Windschuh J, Goerke S et al (2017) Downfield-NOE-suppressed amide-CEST-MRI at 7 Tesla provides a unique contrast in human glioblastoma. *Magn Reson Med* 77(1):196–208
139. Togao O, Yoshiura T, Keupp J et al (2014) Amide proton transfer imaging of adult diffuse gliomas: correlation with histopathological grades. *Neuro Oncol* 16:441–448
140. Bai Y, Lin Y, Zhang W et al (2017) Noninvasive amide proton transfer magnetic resonance imaging in evaluating the grading and cellularity of gliomas. *Oncotarget* 8:5834–5842
141. Sakata A, Okada T, Yamamoto A et al (2015) Grading glial tumors with amide proton transfer MR imaging: different analytical approaches. *J Neurooncol* 122:339–348
142. Choi YS, Ahn SS, Lee S-K et al (2017) Amide proton transfer imaging to discriminate between low- and high-grade gliomas: added value to apparent diffusion coefficient and relative cerebral blood volume. *Eur Radiol* 27:3181–3189
143. Paech D, Windschuh J, Oberhollenzer J et al (2018) Assessing the predictability of IDH mutation and MGMT methylation status in glioma patients using relaxation-compensated multi-pool CEST MRI at 7.0 Tesla. *Neuro-Oncology* 20(12):1661–1671
144. Togao O, Hiwatashi A, Yamashita K et al (2017) Grading diffuse gliomas without intense contrast enhancement by amide proton transfer MR imaging: comparisons with diffusion- and perfusion-weighted imaging. *Eur Radiol* 27:578–588
145. Heo H-Y, Jones CK, Hua J et al (2016) Whole-brain amide proton transfer (APT) and nuclear overhauser enhancement (NOE) imaging in glioma patients using low-power steady-state pulsed chemical exchange saturation transfer (CEST) imaging at 7T. *J Magn Reson Imaging* 44:41–50
146. Paech D, Burth S, Windschuh J et al (2015) Nuclear overhauser enhancement imaging of glioblastoma at 7 Tesla: region specific correlation with apparent diffusion coefficient and histology. *PLoS ONE* 10:e0121220
147. Paech D, Zaiss M, Meissner J-E et al (2014) Nuclear overhauser enhancement mediated chemical exchange saturation transfer imaging at 7 Tesla in glioblastoma patients. *PLoS ONE* 9:e104181
148. Jiang S, Zou T, Eberhart CG et al (2017) Predicting IDH mutation status in grade II gliomas using amide proton transfer-weighted (APT_w) MRI. *Magn Reson Med* 78:1100–1109

149. Wen PY, Macdonald DR, Reardon DA et al (2010) Updated response assessment criteria for high-grade gliomas: response assessment in neuro-oncology working group. *J Clin Oncol* 28:1963–1972
150. Park KJ, Kim HS, Park JE, Shim WH, Kim SJ, Smith SA (2016) Added value of amide proton transfer imaging to conventional and perfusion MR imaging for evaluating the treatment response of newly diagnosed glioblastoma. *Eur Radiol* 26:4390–4403
151. Park JE, Kim HS, Park KJ, Kim SJ, Kim JH, Smith SA (2016) Pre- and posttreatment glioma: comparison of amide proton transfer imaging with MR spectroscopy for biomarkers of tumor proliferation. *Radiology* 278:514–523
152. Paech D, Dreher C, Regnery S et al (2019) Relaxation-compensated amide proton transfer (APT) MRI signal intensity is associated with survival and progression in high-grade glioma patients. *Eur Radiol* 29(9):4957–4967
153. Mehrabian H, Myrehaug S, Soliman H, Sahgal A, Stanisiz GJ (2018) Evaluation of glioblastoma response to therapy with chemical exchange saturation transfer. *Int J Radiat Oncol Biol Phys* 101:713–723
154. Regnery S, Adeberg S, Dreher C et al (2018) Chemical exchange saturation transfer MRI serves as predictor of early progression in glioblastoma patients. *Oncotarget* 9:28772–28783
155. Jia G, Abaza R, Williams JD et al (2011) Amide proton transfer MR imaging of prostate cancer: a preliminary study. *J Magn Reson Imaging* 33:647–654
156. Takayama Y, Nishie A, Sugimoto M et al (2016) Amide proton transfer (APT) magnetic resonance imaging of prostate cancer: comparison with Gleason scores. *MAGMA* 29:671–679
157. Zhang S, Seiler S, Wang X et al (2018) CEST-Dixon for human breast lesion characterization at 3 T: a preliminary study. *Magn Reson Med* 80:895–903
158. Dula AN, Arlinghaus LR, Dortch RD et al (2013) Amide proton transfer imaging of the breast at 3 T: establishing reproducibility and possible feasibility assessing chemotherapy response. *Magn Reson Med* 70:216–224
159. Ohno Y, Kishida Y, Seki S et al (2018) Amide proton transfer-weighted imaging to differentiate malignant from benign pulmonary lesions: comparison with diffusion-weighted imaging and FDG-PET/CT. *J Magn Reson Imaging* 47:1013–1021
160. Choi SH (2018) Can amide proton transfer MRI distinguish benign and malignant head and neck tumors? *Radiology* 288:791–792
161. Radbruch A, Weberling LD, Kieslich PJ et al (2015) Gadolinium retention in the dentate nucleus and globus pallidus is dependent on the class of contrast agent. *Radiology* 275:783–791
162. Kanda T, Ishii K, Kawaguchi H, Kitajima K, Takenaka D (2014) High signal intensity in the dentate nucleus and globus pallidus on unenhanced T1-weighted MR Images: relationship with increasing cumulative dose of a gadolinium-based contrast material. *Radiology* 270:834–841
163. Kanda T, Osawa M, Oba H et al (2015) High signal intensity in dentate nucleus on unenhanced T1-weighted MR Images: association with linear versus macrocyclic gadolinium chelate administration. *Radiology* 275:803–809
164. McDonald RJ, McDonald JS, Kallmes DF et al (2015) Intracranial gadolinium deposition after contrast-enhanced MR imaging. *Radiology* 275:772–782
165. Radbruch A, Haase R, Kickingereder P et al (2017) Pediatric brain: no increased signal intensity in the dentate nucleus on unenhanced T1-weighted MR images after consecutive exposure to a macrocyclic gadolinium-based contrast agent. *Radiology* 283:828–836
166. Radbruch A (2016) Are some agents less likely to deposit gadolinium in the brain? *Magn Reson Imaging* 34:1351–1354
167. Thomsen HS, Morcos SK, Almén T et al (2012) Nephrogenic systemic fibrosis and gadolinium-based contrast media: updated ESUR Contrast Medium Safety Committee guidelines. *Eur Radiol* 23:307–318

168. Chan K W Y, McMahon M T, Kato Y et al (2012) Natural D-glucose as a biodegradable MRI contrast agent for detecting cancer. *Magn Reson Med* 68:1764–1773
169. Rivlin M, Horev J, Tsarfaty I, Navon G (2013) Molecular imaging of tumors and metastases using chemical exchange saturation transfer (CEST) MRI. *Sci Rep* 3
170. Walker-Samuel S, Ramasawmy R, Torrealdea F et al (2013) In vivo imaging of glucose uptake and metabolism in tumors. *Nat Med* 19:1067–1072
171. Jin T, Mehrens H, Hendrich K S, Kim S-G (2014) Mapping brain glucose uptake with chemical exchange-sensitive spin-lock magnetic resonance imaging. *J Cereb Blood Flow Metab* 34:1402–1410
172. Schuenke P, Koehler C, Korzowski A et al (2017) Adiabatically prepared spin-lock approach for T1 ρ -based dynamic glucose enhanced MRI at ultrahigh fields. *Magn Reson Med* 78:215–225
173. Paech D, Schuenke P, Koehler C et al (2017) T1 ρ -weighted dynamic glucose-enhanced MR imaging in the human brain. *Radiology* 285:914–922
174. Schuenke P, Paech D, Koehler C et al (2017) Fast and quantitative T1 ρ -weighted dynamic glucose enhanced MRI. *Sci Rep* 7:42093
175. Xu X, Yadav N N, Knutsson L et al (2015) Dynamic Glucose-Enhanced (DGE) MRI: translation to human scanning and first results in glioma patients. *Tomogr J Imaging Res* 1:105
176. Tao J, Bistra I, Kevin H T et al (2018) Chemical exchange-sensitive spin-lock (CESL) MRI of glucose and analogs in brain tumors. *Magn Reson Med* 80:488–495
177. Jiang Y, Ma D, Seiberlich N, Gulani V, Griswold M A (2015) MR fingerprinting using fast imaging with steady state precession (FISP) with spiral readout. *Magn Reson Med* 74:1621–1631
178. Chen Y, Jiang Y, Pahwa S et al (2016) MR fingerprinting for rapid quantitative abdominal imaging. *Radiology* 279:278–286
179. Panda A, Mehta B B, Coppo S et al (2017) Magnetic resonance fingerprinting—an overview. *Curr Opin Biomed Eng* 3:56–66
180. Yu A C, Badve C, Ponsky L E et al (2017) Development of a combined MR fingerprinting and diffusion examination for prostate cancer. *Radiology* 283:729–738
181. Badve C, Yu A, Dastmalchian S et al (2017) MR fingerprinting of adult brain tumors: initial experience. *Am J Neuroradiol* 38:492–499
182. Shukla-Dave A, Obuchowski N A, Chenevert T L et al (2018) Quantitative imaging biomarkers alliance (QIBA) recommendations for improved precision of DWI and DCE-MRI derived biomarkers in multicenter oncology trials. *J Magn Reson Imaging*. <https://doi.org/10.1002/jmri.26518>
183. European Society of R (2013) ESR statement on the stepwise development of imaging biomarkers. *Insights Imaging* 4:147–152
184. European Society of R (2015) Magnetic resonance fingerprinting—a promising new approach to obtain standardized imaging biomarkers from MRI. *Insights Imaging* 6:163–165
185. European Society of R (2010) White paper on imaging biomarkers. *Insights Imaging* 1:42–45
186. Bonekamp D, Schelb P, Wiesenfarth M et al (2018) Histopathological to multiparametric MRI spatial mapping of extended systematic sextant and MR/TRUS-fusion-targeted biopsy of the prostate. *Eur Radiol*. <https://doi.org/10.1007/s00330-018-5751-1>
187. Bickelhaupt S, Paech D, Laun F B et al (2017) Maximum intensity breast diffusion MRI for BI-RADS 4 lesions detected on X-ray mammography. *Clin Radiol* 72:900.e901–900.e908



Wolfgang Weber

Contents

22.1	Fundamental Differences Between PET/MR and PET/CT Imaging in Oncology	748
22.2	Clinical Studies Evaluating PET/MR in Different Oncological Diseases.....	751
22.2.1	Head and Neck Cancers.....	751
22.2.2	Non-small Cell Lung Cancer	752
22.2.3	Gastrointestinal Cancers and Neuroendocrine Tumors.....	754
22.2.4	Gynecologic Malignancies	755
22.2.5	Breast Cancer.....	755
22.2.6	Lymphoma.....	758
22.2.7	Prostate Cancer.....	758
22.2.8	PET/MR in Children	759
22.3	Conclusions.....	761
	References.....	761

The introduction of clinical PET/CT in 2000 has led to a dramatic increase in FDG PET in clinical research and patient management (Fig. 22.1). When integrated PET/MR systems entered the clinic about 10 years later, it was expected that PET/MR may have a similar impact. However, research activity as well as clinical acceptance of PET/MR have been much slower (Fig. 22.1). MR imaging provides several advantages when compared to CT, including lack of ionizing radiation high soft tissue contrast, and ability to measure physiologic parameters as well as multi-parametric imaging. Therefore, there were good reasons to believe that PET/MR would improve staging accuracy, treatment monitoring, as well as bio-

W. Weber (✉)

Department of Nuclear Medicine, School of Medicine, Technical University Munich, Ismaningerstr 22, 81675 Munich, Germany
e-mail: w.weber@tum.de

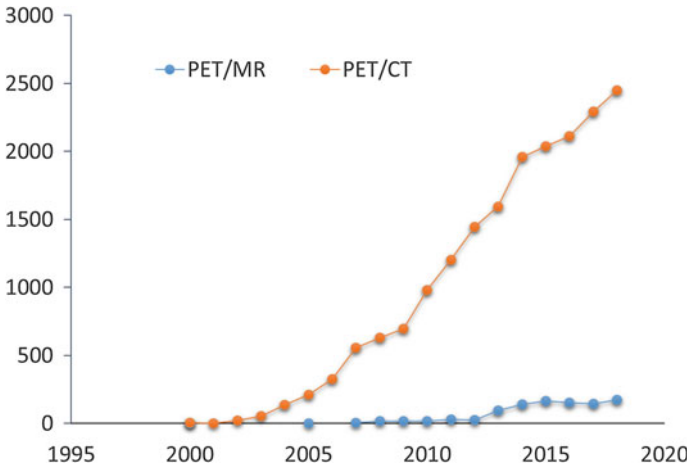


Fig. 22.1 Number of publications in the database Medline including the term PET/CT or PET/MR

logical characterization of the tumor tissue. Combining the molecular information of PET with MR in one examination was thus anticipated to spark clinical research and result in new clinical indications for imaging in oncologic patients.

22.1 Fundamental Differences Between PET/MR and PET/CT Imaging in Oncology

In retrospect, there are several reasons why oncologic research and clinical applications of PET/MR developed more slowly compared to PET/CT. First, accurate attenuation correction proved more difficult to establish than expected. Therefore, PET/MR research focused for several years on methodological aspects instead of studies of tumor biology or development of new clinical applications [1, 2]. Accurate attenuation correction is a prerequisite for research applications of PET/MR which require quantitative data. It is also a prerequisite for some clinical applications of PET/MR such as treatment monitoring. Attenuation correction is particularly challenging for oncologic PET which typically involves whole-body imaging, and thus requires attenuation correction to be accurate for different body regions. Furthermore, the normal anatomy is frequently distorted by previous treatments, treatment-related complications, or tumor progression. For example, air-filled lung tissue may be replaced by pleural effusions or bone structures may be replaced by a metal implant. Therefore, atlas-based approaches that “convert” an MR image into a “synthetic” CT for attenuation correction are more difficult to implement than for brain imaging studies. While some inaccuracies compared to PET/CT remain, the problem of attenuation correction has probably now been

solved with reasonable accuracy for many research and clinical applications, i.e., errors due to attenuation correction are reasonably small when compared to the expected biological signals.

Second, many whole PET/MR protocols were typically lengthy because they acquired a combination of a dedicated MR of one body region with a whole-body MRI. For whole-body MRI, several MR sequences were acquired as it is standard for standalone whole-body MR (e.g., T1 VIBE Dixon, Diffusion weighted EPI, T2 weighted TIRM, T2 weighted HASTE, T1 weighted vibs post-contrast) [3]. Each of these imaging sequences may show specific artifacts, e.g., due to patient motion. This made whole-body PET/MR not only time consuming to acquire (45–60 min per scan), but also challenging to interpret because of the enormous number of images to be reviewed. Typical scan times for PET/MR are 2–3 times longer than for a PET/CT with contrast-enhanced CT. In contrast to PET/CT—which had drastically reduced acquisition times of PET due to the fast CT-based attenuation correction—integrated PET/MR has considerably increased the duration of a PET scan. Combined with the high costs of PET/MR installation and maintenance, this has limited clinical interest in replacing PET/CT with PET/MR for whole-body staging (Fig. 22.1).

However, for specific applications, imaging times have been reduced to less than 30 min for PET/MR which will likely improve clinical acceptance [3–6]. Long acquisition times may therefore become less of an issue in the future.

Third, and probably most importantly, the introduction of PET/CT provides for the first time spatially well-matched anatomical information for findings on PET. With PET/CT, the anatomical location of abnormal findings on PET could be

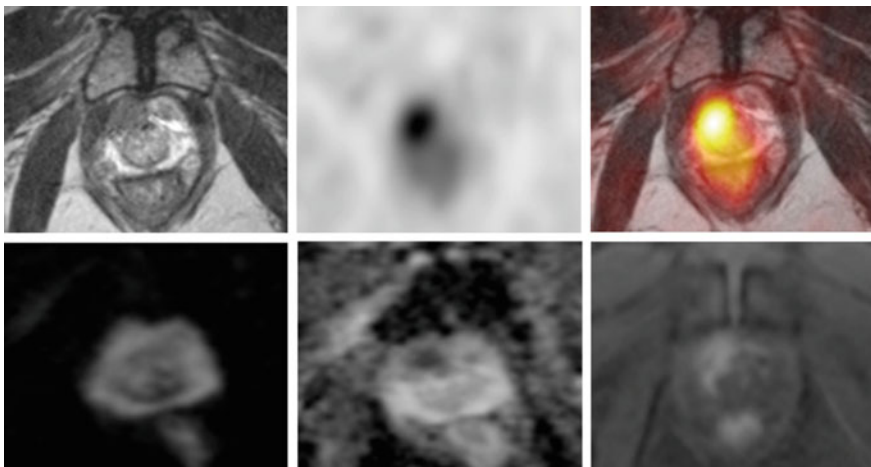


Fig. 22.2 Concordant detection of prostate cancer by MP-MRI and Ga-68-PSMA-11 PET/MR in a patient with elevated PSA (10.1 ng/mL) and a negative prostate biopsy. The MP-MRI study shows a T2 hypo-intense, contrast-enhancing lesion with restricted diffusion on the ADC map (PIRADS 5). There intense tracer uptake on the corresponding PET images. Prostate cancer was confirmed on targeted biopsy (Gleason 4 + 3)

precisely described, and focal hypermetabolic lesions on PET could be matched with subtle abnormalities on the corresponding CT scan. Conversely, a malignant lesion can frequently be ruled out based on the lack of a corresponding finding on CT. This allowed for a much more specific interpretation of PET and has greatly increased the confidence of clinicians in PET findings. The ability to precisely correlate PET and CT findings has also led to some new scientific discoveries. For example, the existence of substantial amounts of metabolically active brown adipose tissue in adults was not known until PET/CT scans showed that linear FDG uptake in the neck was not located in cervical muscles, but in fatty tissue.

With respect to anatomic correlation and precise localization of PET findings, the introduction of PET/MR was a less significant step than the advent of PET/CT. Standalone PET provided (almost) no anatomical information and the anatomical data provided by combining PET with CT were entirely new. Especially when performed as a combination of PET and contrast-enhanced CT, PET/CT already provided quite detailed information which was only incrementally improved by PET/MR. Thus, PET/CT very quickly stimulated research and clinical applications whereas the impact of PET/MR is more subtle.

Lastly, CT is the standard imaging modality for staging of many of the cancers for which FDG PET has been found to be most clinically useful. These include, for example, lung cancer, melanoma, and lymphomas. Instead of performing separate CT and PET scans, it was obvious to image these tumors with an integrated PET/CT system. Subsequently, clinical studies quickly showed that integrated PET/CT is not only logistically easier to perform and read than two separate studies, but also provides increased staging accuracy due to the exact co-localization of CT and PET findings. Of course, MR is also used clinically for imaging of many malignancies, but often not as the primary staging modality, rather as a “problem-solving modality” if uncertainties remain on CT. CT remains the preferred imaging modality because of its robustness, speed, and higher sensitivity for detection of lung metastases. Since whole-body imaging for staging and restaging is by far the most common application of FDG PET in oncology, there were obvious indications for PET/CT imaging. This was less the case for PET/MR, because MR is much less commonly used for whole-body imaging than CT. For the same reason, it is not too surprising that for many cancers, PET/MR has not shown superior staging accuracy when compared to PET with contrast-enhanced CT (see following section).

This may now change due to the success of PSMA PET for imaging of prostate cancer. In prostate cancer, MR is increasingly being used for detection and primary staging while the role of CT is quite limited. Specifically, CT has a low sensitivity to detect the primary tumor and bone marrow/osseous metastases because of its low soft tissue contrast. Combining PSMA PET and MRI is thus a promising PET/MR application. With prostate cancer now being the most common malignancy in men in many countries, detection, staging, restaging, and therapy, monitoring of patients with prostate cancer may well become a key application of PET/MR.

Against this backdrop, this chapter provides an overview on the use of FDG PET/MR for whole-body staging while focusing on applications where PET/MR with FDG or PSMA ligands is used for locoregional staging.

22.2 Clinical Studies Evaluating PET/MR in Different Oncological Diseases

Spick et al. have summarized the results of studies comparing PET/CT and PET/MR imaging published until 2016 [7]. Their review includes 46 comparative studies in a total of 2340 patients. MR was mostly used for anatomical localization of abnormal findings on PET. There were 7 studies in head and neck cancer, 6 studies in lung cancer, 7 in gastrointestinal cancers and neuroendocrine, 5 in gastrointestinal and neuroendocrine tumors, 5 in gynecological cancers and breast cancer, 3 in prostate cancer, 5 in lymphoma, and 13 in mixed populations. Except for three studies in prostate cancer and two studies in neuroendocrine tumors, all studies used FDG as the imaging agent. In the following sections, the results from the analysis by Spicks et al. [7] combined with results from more recent papers and reviews will be presented.

Spicks et al. [7] focused on the question if PET/MR is superior to PET/CT. A different way to look at the available clinical studies is to ask if PET/MR is superior to standalone MR. This perspective will also be included in the following summary of the clinical literature.

22.2.1 Head and Neck Cancers

A total of 369 patients with squamous cell carcinomas of the head and neck were included in the analysis by Spicke et al., and the impact of FDG PET/MR on T, N and M staging was evaluated. With respect to T staging PET/MR was equivalent to PET/CT in 3 studies and superior in one study [8]. However, this holds true only for

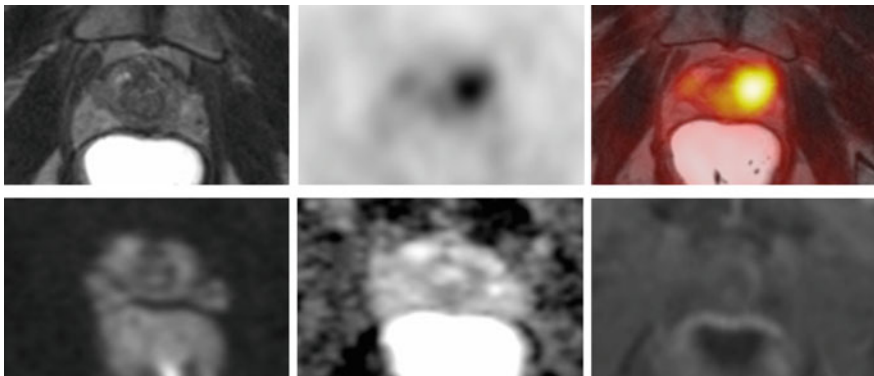


Fig. 22.3 Detection of MP-MRI occult prostate cancer by Ga-68-PSMA-11 PET/MR in a patient with elevated PSA (9.2) and a negative prostate biopsy. MP-MR images of the prostate (T2 weighted, diffusion-weighted, ADC map and T1 contrast enhanced) shows no evidence of prostate cancer (PIRADS score 1). In contrast, there is intense tracer uptake in the left prostate, consistent with malignancy. Prostate cancer (Gleason 4 + 3) was confirmed by targeted biopsy

a relatively “soft” criterion, “lesions conspicuity.” There were no statistically significant differences between PET/MR and PET/CT with respect to detection of lymph node and distant metastases [7]. Considering that PET/MR imaging is substantially more complex and expensive than PET/CT, this can be seen as a negative result. However, this analysis as well as some newer studies also indicate that PET/MR improves certain aspects of tumor staging compared to standalone MR. PET/MR facilitates the interpretation of the images by head and neck surgeons due to the typical high contrast between tumor and surrounding normal tissues [9]. Several studies also report that PET/MR improves the detection of tumor infiltration in neighboring structures which is essential for planning of surgical procedures and radiotherapy [8, 10–14]. With the existing data, this potential improvement of T staging is difficult to analyze statistically because patient populations are quite heterogeneous (Table 22.1), and different anatomical structures are involved depending on the exact tumor location. This aspect of tumor staging should therefore be studied systematically for different tumor locations.

However, there is already some evidence that PET/MR improves the detection of lymph node metastases when compared to standalone MR (Table 22.1). Here, FDG PET/MR has been shown to be consistently superior to standalone MR. Therefore, in patients scheduled to undergo an MRI of the head and neck for locoregional staging and surgical or radiotherapy planning, PET/MR may be a superior alternative, especially for more advanced tumor stages and a relevant risk for development of lymph node and distant metastases. Since most of the available literature are retrospective case series, further prospective evaluation of FDG PET/MR as an alternative to standalone MR is therefore warranted.

22.2.2 Non-small Cell Lung Cancer

For the use of PET/MR in non-small cell lung cancer (NSCLC) Spicks et al. analyzed 6 studies including a total of 194 patients. No statistically significant differences between PET/CT and PET/MR with respect to T and N staging were observed [7]. However, PET/MR was less sensitive than PET/CT for detection of small pulmonary metastases or second primary tumors (e.g., multifocal adenocarcinomas). This is not an unexpected finding, considering artifacts from respiratory motion on whole-body MRI that limit the detection of small pulmonary nodules as well as the limited sensitivity of current PET systems for detection of hypermetabolic pulmonary lesions with a diameter of less than 1 cm. On a patient level, however, these differences between PET/CT and PET/MRI did not affect management in a statistically significant way [7]. As CT is the primary imaging modality for NSCLC and MR is only used in selected cases with unclear findings on CT, it is unlikely that FDG PET/MR will become an alternative to FDG PET/CT in NSCLC.

Table 22.1 Detection of lymph node metastases in newly diagnosed patients with squamous cell carcinomas of the head and neck

Authors	Year	Cancer types	N	Reference Positive LN regions/total	FDG PET/MR		Comparator	Sensitivity (%)	Specificity (%)
					Sensitivity (%)	Specificity (%)			
Schaarschmit et al. [12]	2016	Tonsil (3), base of tongue (3), tongue (2), CUP (2), hypopharynx (1), larynx (1)	12	NR	81	99	MR neck	78	99
Platzcek et al. [46]	2014 ¹	Floor of the mouth (10), tongue (9), mandible (7), maxilla (3), larynx (2), piriform sinus (2), other (5)	38	38/391	90	95	MR neck	66	97
Chan [47]	2018	Nasopharynx	113	NR	100	99	MR neck	94	100
Kanda et al. [48]	2013 ^a	Tongue (12), floor of mouth (3), buccal (1), hypopharynx (8)	30	39/244	77*	96	MR neck	49*	99

Results are presented for neck lymph node regions. N—Number of patients. NR—not reported. *Statistically significant difference compared to comparator.
^aRetrospective fusion of PET and MR, not an integrated PET/MR. PET/CT was performed with IV contrast in all studies

22.2.3 Gastrointestinal Cancers and Neuroendocrine Tumors

Most studies on the use of PET/MR in gastrointestinal cancers are small pilot studies that lack the statistical power to reliably detect differences in sensitivity and specificity between PET/MR and PET/CT. Among the 7 studies including 201 patients reviewed by Spicks et al. [7], only one study reported a superior diagnostic accuracy of PET/MR as compared to PET/CT. However, one potential advantage of PET/MR is the high sensitivity of MRI for detection of liver metastases. Thus, several studies have reported that PET/MR can detect small liver metastases that are not found on PET or CT [15, 16].

Conversely, however, it is not clear if PET can detect a substantial number of liver metastases that are negative on MRI. In a group of 18 patients with neuroendocrine tumors, DOTANOC PET combined with a diffusion-weighted MRI of the liver had the same diagnostic accuracy for detection of liver metastases as liver MRI with the MR contrast agent gadoxetate [17]. Lee et al. [18] compared contrast-enhanced multidetector CT, FDG PET/MR and MR with liver-specific contrast agents in 55 patients with colorectal cancer and suspected liver metastases. The diagnostic performance of FDG PET/MR was significantly higher than that of CT, but there was no significant difference between MR with liver-specific contrast agents and PET/MR. Eighteen patients had undergone neoadjuvant chemotherapy prior to imaging. Residual FDG uptake after therapy was associated with a markedly worse prognosis following surgical resection. The one year recurrence free survival of patients with no hypermetabolic metastases after neoadjuvant therapy ($n = 6$) was 80% as compared to only 14% for patients with hypermetabolic liver lesions after therapy [18]. This suggests that PET/MR may be helpful to assess response to neoadjuvant therapy. However, this needs to be further studied in larger series of patients.

The advantages of PET/MR over PET/CT for the detection of liver metastases are of course highly dependent on the MR and CT protocol used. For example, FDG PET/MR with only T1 and T2 weighted images had a similar diagnostic accuracy as FDG PET combined with a contrast-enhanced CT in a study of 55 patients with suspected liver metastases from gastrointestinal cancers [19]. In this study, 120 liver lesions were analyzed of which 79 were considered to be metastases. In contrast, 25% of the liver metastases seen on PET/MR were false negative on FDG PET combined with low-dose CT [19]. In a similar study, Beiderwellen et al. [20] compared FDG PET/CT (with IV contrast) and liver MRI including T1wFLASH before and after contrast, T1w dynamic VIBE, T2wHASTE, T2wTSEIn, and DWI. A total of 32 patients was included and 113 lesions were analyzed. In this patient population, the sensitivity of PET/MR (92%) was significantly higher than that of PET/CT (68%) at similar specificities (100% vs. 97%).

In addition, criteria for interpretation will also affect the reported sensitivity and specificity. For example, are lesions without FDG uptake above liver background considered as suspicious for metastases when they meet the criteria for malignancy on CT or MR? Finally, it is often not feasible to use histology as the reference standard in studies of the diagnostic accuracy of imaging tests to detect liver metastases. Lesions are often too small for biopsies, and in patients with multifocal

disease not all lesions can be validated by histology. Therefore, a combination of histology and follow-up imaging is commonly used as a reference standard. However, follow-up may be incomplete, particularly in retrospective studies; growth of metastases may be inhibited by effective therapies; the criteria for “significant growth” of metastases may differ between studies, etc. Therefore, comparisons of the diagnostic accuracy of imaging technologies for the detection of liver metastases need to be interpreted with caution. Overall, detection of liver metastases by PET/MR needs further evaluation in prospective clinical studies with rigorous endpoints that define the diagnostic accuracy and prognostic value of PET/MR in this setting.

22.2.4 Gynecologic Malignancies

MR is commonly used for the staging of pelvic malignancies due to its high soft tissue contrast that allows better definition of tumor extension and therefore more accurate staging. In the review by Spicks et al., the results of 5 studies including a total of 154 patients were analyzed. In these studies, FDG PET/CT and FDG PET/MR had been compared for the detection and staging of primary and recurrent gynecologic cancers. As seen for several other tumor types, FDG PET/MR increased interpreter confidence when compared to FDG PET/CT, but there was no statistically significant difference in staging accuracy or patient management (Tables 22.2 and 22.3). However, in recurrent gynecological cancers, a recently published study in 71 patients has indicated [21] that FDG PET/MR significantly improves the detection of recurrent tumors on the patient level, as well as staging accuracy on a lesion level (Tables 22.2 and 22.3). A clear limitation of this and other studies (Tables 22.2 and 22.3) are the heterogeneous patient populations that are frequently a mix of several gynecologic tumor types. These tumors differ markedly in the frequency of metastases, the typical sites of metastases, and the metabolic activity of tumor tissue. Therefore, future prospective studies in well-defined patient populations are necessary to determine if PET/MR should be used instead of standalone MR in certain patient populations.

22.2.5 Breast Cancer

MR plays a central part in the initial diagnosis and staging of breast cancer as well as in restaging of recurrent breast cancer. Therefore, there are multiple possible applications of FDG PET/MR in breast cancer, ranging from more accurate cancer detection in patients with suspected breast cancer to monitoring response to systemic therapy in patients with advanced disease. In their review, Spicks et al. [7] identified only two studies on the use of FDG PET/MR in breast cancer which only described the feasibility of FDG PET/MR for staging and restaging of breast cancer patients [22, 23]. Since then, a few additional studies have investigated the potential clinical utility of FDG PET/MR in breast cancer. Botsikas et al. evaluated in a

Table 22.2 Detection of recurrent malignancies of the female pelvis by PET/MR on a patient basis

Authors	Year	Cancer types	N	Recurrence by reference standard	FDG PET/MR				
Specificity	Yes	No		Sensitivity (%)	Comparator				
				Specificity	Sensitivity (%)				
Sawicki [21]	2018	Cervical (32), ovarian (26), endometrial (7), vulvar (4), vaginal (2)	71	55	16	100*	MRI	86	94%
Beiderwellen [49]	2015	Ovarian (11), cervical (8)	19	16	3	100	PET/CT	100	NR
Grueneisen [50]	2014	Ovarian (16), cervical (18)	34	25	9	100	MRI	92	NR
Kirchner [6]	2017	Ovarian (23), cervical (12), endometrial (3), vulvar (3), vaginal (1)	43	38	5	95	PET/CT	97	80%
Kitajima [6]	2014 ^a	Cervical (15), ovarian (9), endometrial (6)	30	16	14	88	PET/CT	100	73%
Grueneisen [3]	2015	Ovarian (13), cervical (7), endometrial (4)	24	21	3	95	PET/CT	95	NR

NR—not reported. *Statistically significant difference compared to comparator. ^aRetrospective fusion of PET and MR, not an integrated PET/MR. N—number of patients. PET/CT was performed with IV contrast in all studies

Table 22.3 Detection of recurrent malignancies of the female pelvis by PET/MR on a lesion basis

Authors	Year	N	Reference standard		FDG PET/MR		Comparator	Sensitivity	Specificity
			Malignant	Benign	Sensitivity	Specificity			
Sawicki [21]	2018	241	181	60	100%	96%	MRI	81%*	93%
Beiderwellen [49]	2015	78	58	20	100%	95%	PET/CT	100%	90%
Grueneisen [50]	2014	118	89	29	99%	89%	MRI	89%	83%
Kirchner [6]	2017	154	113	41	98%	83%	PET/CT	97%	83%
Kitajima [6]	2014 ^a	NR	NR	NR	NR	NR	PET/CT	NR	NR
Grueneisen [3]	2015	104	81	23	82%	91%	PET/CT	85%	87%

N—Number of analyzed lesions. NR—not reported. *Statistically significant difference compared to comparator. ^aRetrospective fusion of PET and MR, not an integrated PET/MR. PET/CT was performed with IV contrast in all studies

retrospective study the sensitivity of breast MR and FDG PET/MR for detection of primary breast cancers, lymph node, and distant metastases in 58 patients who were imaged prior to surgery. FDG PET/MR did not improve the sensitivity for detection of primary tumors or lymph node metastases [24]. The same group also compared FDG PET/MR and FDG PET/CT in patients with newly diagnosed or recurrent breast cancer. FDG PET/MR was more sensitive than FDG PET/CT for the detection of osseous metastases on a lesion basis. However, this had no effect on M staging on a per patient basis. There was also no significant difference in the accuracy of N staging [25]. Wang et al. [26] used FDG PET/MR to monitor tumor response to neoadjuvant chemotherapy in a small group of 14 patients with newly diagnosed invasive breast cancer. FDG PET was performed before neoadjuvant therapy and after first or second chemotherapy cycle. Standardized uptake values of the tumor tissue and total lesion glycolysis were measured on PET; choline signal-to-noise ratios, peak enhancement ratios from dynamic contrast-enhanced MRI, and ADC coefficients were measured on MRI. A combination of PET and MR parameters, the ratio of change in SUV divided by change in ADC showed the closest correlation with histologic response to therapy. While these findings need to be confirmed in larger patient populations, they are promising and one of the few examples where a true multimodal and multi-parametric combination of PET and MR parameters is used to address a clinical question [26].

22.2.6 Lymphoma

FDG PET/CT is the imaging modality of choice in FDG avid lymphomas. Most of the diagnostic information is derived from the PET part of the PET/CT study, and CT imaging mostly serves to provide anatomical correlation and exclude non-malignant causes of increased FDG uptake, such as FDG uptake by activated brown adipose tissue. It is therefore not surprising that FDG PET/MR has not been found to be superior to FDG PET/CT for imaging of lymphoma patients [7].

22.2.7 Prostate Cancer

Over the last 5 years, multi-parametric MR of the prostate (MP-MRI) has become a central part of the initial staging and restaging of patients with prostate cancer. MP-MRI involves T2-weighted, diffusion-weighted, and dynamic contrast-enhanced MR of the prostate. MP-MRI has been shown to improve the diagnosis of prostate cancer in randomized controlled trials [27, 28] and is now widely adopted to evaluate patients with elevated PSA in order to decide if a prostate biopsy should be performed [29].

However, MP-MRI of the prostate is far from perfect, and the cancer detection rate of MP-MRI guided targeted biopsy is in the range of 11–54% [29] clearly indicating that MR findings are not specific for prostate cancer. There is therefore a significant potential to improve the diagnostic accuracy of MP-MRI by PET/MR.

MP-MRI has also limitations in sensitivity, especially in the transition zone. Reporting of MP-MRI has been standardized by the Prostate Imaging Reporting and Data System (PIRADS), but the reproducibility of the image interpretation is only modest even among experienced radiologists [30, 31].

Conversely, MP-MRI can improve the diagnostic accuracy of PET imaging in two ways. First, it can identify tumors that are negative for molecular markers detected by PET imaging. For example, about 10% of primary prostate cancers do not express PSMA and cannot be detected by PSMA PET/CT [32]. These are typically rather poorly differentiated tumors that can be well detected by MP-MRI. In addition, there are typical MP-MRI characteristics of benign prostatic nodules caused by prostate hyperplasia (BPH). Thus, MP-MRI can decrease the number of false positive PET studies for ligands that accumulate in BPH, such as choline analogs and to a lesser degree PSMA ligands.

A recent meta-analysis by Li et al. [31] has identified 9 studies that have compared prostate MR with PET/MR [32–40]. In all these studies a MP-MRI and a PET/MR were performed in the same patient. Two studies used F-18-fluorocholine as the radiotracer and one the amino acid analog F-18-FACBC as the radiotracer. The other 6 PET/MR studies were performed with PSMA ligand Ga-68-PSMA-11. Overall, the studies included a total of 353 patients (Table 22.4). The studies used different reference standards and different statistical approaches to determine sensitivity and specificity (on a lesion basis or various number of prostate regions ranging from 2 to 30, Table 22.4). Despite this heterogeneity, PET/MR consistently improved sensitivity in 5 of the 6 studies. Specificity was higher for PET/MR in 3 studies, identical in one, and lower in one study (Table 22.4). Choline PET/MR also demonstrated higher sensitivity than MP-MRI, albeit at lower specificity. In the one study with F-18-FACBC, sensitivity of PET/MR was slightly higher than of MP-MRI and specificity slightly lower (Table 22.4).

In the meta-analysis of all nine studies, the pooled sensitivity and specificity of PET/MR was 78 and 90% as compared to 60% and 88% for MP-MRI. In a ROC (receiver operator characteristic curve) analysis the area under the curve of PET/MR (0.93) was significantly larger than of MP-MRI (0.84) indicating a higher diagnostic accuracy of PET/MR as compared to MP-MRI [31].

22.2.8 PET/MR in Children

The radiation exposure of the CT part of a PET/CT contributes to up to two-thirds of the total effective dose of a PET/CT scan with FDG if the CT is performed as a “diagnostic” CT [4, 41]. Using a so-called low-dose CT approach the radiation exposure from CT can be markedly reduced, but at the cost of a significant loss of anatomical information and spatial resolution. Many institutions therefore acquire low-dose CTs that still result about the same effective dose as an FDG PET scan.

There is a long-standing controversy if reducing radiation exposure from CT is meaningful in adult patients [42, 43]. However, for pediatric patients there is more

Table 22.4 Detection of prostate cancer on PET/MRI as compared to MP-MRI

Authors	Year	N patients	Tracer	Analysis approach	Positive/Total	PET/MR		MP-MRI		Reference standard
						Sensitivity (%)	Specificity (%)	Sensitivity (%)	Specificity (%)	
Eiber et al. [32]	2016	53	Ga-68-PSMA-11	6 segments	202/318	76	97	58	82	Step sections
Al-Bayati et al. [33]	2018	22	Ga-68-PSMA-11	Lesions	32/41	88	100	59	67	Biopsy
Taneja et al. [34]	2018	35	Ga-68-PSMA-11	Lesions	6/35	93	83	97	67	Biopsy
Hicks et al. [35]	2018	32	Ga-68-PSMA-11	30 Regions	412/960	74	88	50	90	Step sections
Jena et al. [36]	2018	82	Ga-68-PSMA-11	Lesions	63/84	90	86	76	86	Biopsy
Park et al. [39]	2018	33	Ga-68-PSMA-11	Lobes	57/66	86	88	53	100	Step sections
Jambor et al. [36]	2018	26	F-18-FACBC	12 Regions	164/313	88	93	77	99	Step sections
Perrot et al. [40]	2014	23	F-18-fluorocholine	8 Segments	NA	75	73	58	79	Step sections
Lee et al. [38]	2017	31	F-18-fluorocholine	6 segments	NA	73	81	58	87	Step sections

N—Number of patients. Analysis Approach: Number of analyzed regions per prostate or analysis on a lesion basis. NA—Not available

or less consensus that radiation exposure from imaging studies should be as low as reasonably achievable. Acquiring high-quality anatomic images with MR instead of CT is therefore of significant interest. Furthermore, bone and soft tissue sarcomas are common tumor types in children and MR is the imaging method choice for staging because of its high soft tissue contrast [44]. However, a limitation of PET/MR in younger children is the long acquisition times which require anesthesia. Monitoring anesthetized children inside the PET/MR can be logistically challenging, because the PET/MR scans need to be coordinated with the anesthesiology department and all equipment needs to be compatible with the magnetic field of the MR. Repeated anesthesia in early childhood, e.g., for follow-up imaging studies, may have long-term adverse effects on cognitive development [45]. Therefore, development of optimized imaging protocols that limit scan duration will be important for the broader use of PET/MR in pediatric patients [41].

22.3 Conclusions

Whole-body FDG PET/MR is feasible in oncologic patients, but overall does not provide a substantially higher accuracy for staging than FDG PET/CT. With the substantially higher costs of PET/MR systems and the longer acquisition times, it is unlikely that FDG PET/MR will replace FDG PET/CT, except perhaps in pediatric patients. However, as PET/CT has replaced standalone CT for certain indications (e.g., treatment monitoring in lymphoma), PET/MR may replace standalone MR for some specific applications where the anatomic information from MR is fundamental for tumor detection and staging, but diagnostic accuracy can be improved by the additional functional or molecular information from a PET scan. Currently developing applications in this area include imaging of head and neck cancers, gynecologic malignancies, and prostate cancer (with PSMA ligands). In these areas, truly multimodal and multi-parametric imaging, i.e., imaging that fully utilizes the diagnostic capabilities of PET and MR may become feasible in the near future.

References

1. Bailey DL, Barthel H, Beyer T, Boellaard R, Guckel B, Hellwig D et al (2013) Summary report of the first international workshop on PET/MR imaging, March 19–23, 2012, Tubingen, Germany. *Mol Imaging Biol* 15:361–371
2. Bailey DL, Antoch G, Bartenstein P, Barthel H, Beer AJ, Bisdas S et al (2015) Combined PET/MR: the real work has just started. In: Summary report of the third international workshop on PET/MR imaging, 17–21 February 2014, Tubingen, Germany. *Mol Imaging Biol* 17:297–312
3. Grueneisen J, Schaarschmidt BM, Heubner M, Suntharalingam S, Milk I, Kinner S et al (2015) Implementation of FAST-PET/MRI for whole-body staging of female patients with recurrent pelvic malignancies: a comparison to PET/CT. *Eur J Radiol* 84:2097–2102

4. Grueneisen J, Sawicki LM, Schaarschmidt BM, Suntharalingam S, von der Ropp S, Wetter A et al (2016) Evaluation of a fast protocol for staging lymphoma patients with integrated PET/MRI. *PLoS ONE* 11:e0157880
5. Grueneisen J, Sawicki LM, Wetter A, Kirchner J, Kinner S, Aktas B et al (2017) Evaluation of PET and MR datasets in integrated 18F-FDG PET/MRI: a comparison of different MR sequences for whole-body restaging of breast cancer patients. *Eur J Radiol* 89:14–19
6. Kirchner J, Sawicki LM, Suntharalingam S, Grueneisen J, Ruhlmann V, Aktas B et al (2017) Whole-body staging of female patients with recurrent pelvic malignancies: ultra-fast 18F-FDG PET/MRI compared to 18F-FDG PET/CT and CT. *PLoS ONE* 12:e0172553
7. Spick C, Herrmann K, Czernin J (2016) 18F-FDG PET/CT and PET/MRI perform equally well in cancer: evidence from studies on more than 2,300 patients. *J Nucl Med* 57:420–430
8. Kuhn FP, Hullner M, Mader CE, Kastrinidis N, Huber GF, von Schulthess GK et al (2014) Contrast-enhanced PET/MR imaging versus contrast-enhanced PET/CT in head and neck cancer: how much MR information is needed? *J Nucl Med* 55:551–558
9. Hayashi K, Kikuchi M, Imai Y, Yamashita D, Hino M, Ito K et al (2019) Clinical value of fused PET/MRI for surgical planning in patients with oral/oropharyngeal carcinoma. *Laryngoscope*
10. Kubiessa K, Purz S, Gawlitza M, Kuhn A, Fuchs J, Steinhoff KG et al (2014) Initial clinical results of simultaneous 18F-FDG PET/MRI in comparison to 18F-FDG PET/CT in patients with head and neck cancer. *Eur J Nucl Med Mol Imaging* 41:639–648
11. Platzek I (2016) (18)F-Fluorodeoxyglucose PET/MR imaging in head and neck cancer. *PET Clin* 11:375–386
12. Schaarschmidt BM, Heusch P, Buchbender C, Ruhlmann M, Bergmann C, Ruhlmann V et al (2016) Locoregional tumour evaluation of squamous cell carcinoma in the head and neck area: a comparison between MRI, PET/CT and integrated PET/MRI. *Eur J Nucl Med Mol Imaging* 43:92–102
13. Sekine T, de Galiza Barbosa F, Kuhn FP, Burger IA, Stolzmann P, Huber GF et al (2017) PET + MR versus PET/CT in the initial staging of head and neck cancer, using a trimodality PET/CT + MR system. *Clin Imaging* 42:232–239
14. Szyszko TA, Cook GJR (2018) PET/CT and PET/MRI in head and neck malignancy. *Clin Radiol* 73:60–69
15. Hope TA, Pampaloni MH, Nakakura E, VanBrocklin H, Slater J, Jivan S et al (2015) Simultaneous (68)Ga-DOTA-TOC PET/MRI with gadoxetate disodium in patients with neuroendocrine tumor. *Abdom Imaging* 40:1432–1440
16. Kirchner J, Sawicki LM, Deuschl C, Gruneisen J, Beiderwellen K, Lauenstein TC et al (2017) 18 F-FDG PET/MR imaging in patients with suspected liver lesions: value of liver-specific contrast agent Gadobenate dimeglumine. *PLoS ONE* 12:e0180349
17. Mayerhoefer ME, Ba-Ssalamah A, Weber M, Mitterhauser M, Eidherr H, Wadsak W et al (2013) Gadoxetate-enhanced versus diffusion-weighted MRI for fused Ga-68-DOTANOC PET/MRI in patients with neuroendocrine tumours of the upper abdomen. *Eur Radiol* 23:1978–1985
18. Lee DH, Lee JM, Hur BY, Joo I, Yi NJ, Suh KS et al (2016) Colorectal cancer liver metastases: diagnostic performance and prognostic value of PET/MR imaging. *Radiology* 280:782–792
19. Reiner CS, Stolzmann P, Husmann L, Burger IA, Hullner MW, Schaefer NG et al (2014) Protocol requirements and diagnostic value of PET/MR imaging for liver metastasis detection. *Eur J Nucl Med Mol Imaging* 41:649–658
20. Beiderwellen K, Geraldo L, Ruhlmann V, Heusch P, Gomez B, Nensa F et al (2015) Accuracy of [18F]FDG PET/MRI for the detection of liver metastases. *PLoS ONE* 10:e0137285
21. Sawicki LM, Kirchner J, Grueneisen J, Ruhlmann V, Aktas B, Schaarschmidt BM et al (2018) Comparison of (18)F-FDG PET/MRI and MRI alone for whole-body staging and potential impact on therapeutic management of women with suspected recurrent pelvic cancer: a follow-up study. *Eur J Nucl Med Mol Imaging* 45:622–629

22. Grueneisen J, Nagarajah J, Buchbender C, Hoffmann O, Schaarschmidt BM, Poeppel T et al (2015) Positron emission tomography/magnetic resonance imaging for local tumor staging in patients with primary breast cancer: a comparison with positron emission tomography/computed tomography and magnetic resonance imaging. *Invest Radiol* 50:505–513
23. Pace L, Nicolai E, Luongo A, Aiello M, Catalano OA, Soricelli A et al (2014) Comparison of whole-body PET/CT and PET/MRI in breast cancer patients: lesion detection and quantitation of 18F-deoxyglucose uptake in lesions and in normal organ tissues. *Eur J Radiol* 83:289–296
24. Botsikas D, Kalovidouri A, Becker M, Copercini M, Djema DA, Bodmer A et al (2016) Clinical utility of 18F-FDG-PET/MR for preoperative breast cancer staging. *Eur Radiol* 26:2297–2307
25. Botsikas D, Bagetakos I, Picarra M, Da Cunha Afonso Barisits AC, Boudabbous S, Montet X et al (2019) What is the diagnostic performance of 18-FDG-PET/MR compared to PET/CT for the N- and M- staging of breast cancer? *Eur Radiol* 29:1787–1798
26. Wang J, Shih TT, Yen RF (2017) Multiparametric evaluation of treatment response to neoadjuvant chemotherapy in breast cancer using integrated PET/MR. *Clin Nucl Med* 42:506–513
27. Kasivisvanathan V, Rannikko AS, Borghi M, Panebianco V, Mynderse LA, Vaarala MH et al (2018) MRI-targeted or standard biopsy for prostate-cancer diagnosis. *N Engl J Med* 378:1767–1777
28. Ahmed HU, El-Shater Bosaily A, Brown LC, Gabe R, Kaplan R, Parmar MK et al (2017) Diagnostic accuracy of multi-parametric MRI and TRUS biopsy in prostate cancer (PROMIS): a paired validating confirmatory study. *Lancet* 389:815–822
29. Lindenberg ML, Turkbey B, Mena E, Choyke PL (2017) Imaging locally advanced, recurrent, and metastatic prostate cancer: a review. *JAMA Oncol* 3:1415–1422
30. Rosenkrantz AB, Ginocchio LA, Cornfeld D, Froemming AT, Gupta RT, Turkbey B et al (2016) Interobserver reproducibility of the PI-RADS version 2 Lexicon: a multicenter study of six experienced prostate radiologists. *Radiology* 280:793–804
31. Li M, Huang Z, Yu H, Wang Y, Zhang Y, Song B (2019) Comparison of PET/MRI with multiparametric MRI in diagnosis of primary prostate cancer: a meta-analysis. *Eur J Radiol* 113:225–231
32. Eiber M, Weirich G, Holzapfel K, Souvatzoglou M, Haller B, Rauscher I et al (2016) Simultaneous (68)Ga-PSMA HBED-CC PET/MRI improves the localization of primary prostate cancer. *Eur Urol* 70:829–836
33. Al-Bayati M, Grueneisen J, Lutje S, Sawicki LM, Suntharalingam S, Tschirdewahn S et al (2018) Integrated 68Gallium labelled prostate-specific membrane antigen-11 positron emission tomography/magnetic resonance imaging enhances discriminatory power of multi-parametric prostate magnetic resonance imaging. *Urol Int* 100:164–171
34. Taneja S, Jena A, Taneja R, Singh A, Ahuja A (2018) Effect of combined (68) Ga-PSMAHBED-CC uptake pattern and multiparametric MRI derived with simultaneous PET/MRI in the diagnosis of primary prostate cancer: initial experience. *AJR Am J Roentgenol* 210:1338–1345
35. Hicks RM, Simko JP, Westphalen AC, Nguyen HG, Greene KL, Zhang L et al (2018) Diagnostic accuracy of (68)Ga-PSMA-11 PET/MRI compared with multiparametric MRI in the detection of prostate cancer. *Radiology* 289:730–737
36. Jambor I, Kuisma A, Kahkonen E, Kempainen J, Merisaari H, Eskola O et al (2018) Prospective evaluation of (18)F-FACBC PET/CT and PET/MRI versus multiparametric MRI in intermediate- to high-risk prostate cancer patients (FLUCIPRO trial). *Eur J Nucl Med Mol Imaging* 45:355–364
37. Jena A, Taneja R, Taneja S, Singh A, Kumar V, Agarwal A et al (2018) Improving diagnosis of primary prostate cancer with combined (68)Ga-Prostate-Specific Membrane Antigen-HBED-CC simultaneous PET and multiparametric MRI and clinical parameters. *AJR Am J Roentgenol* 211:1246–1253

38. Lee MS, Cho JY, Kim SY, Cheon GJ, Moon MH, Oh S et al (2017) Diagnostic value of integrated PET/MRI for detection and localization of prostate cancer: comparative study of multiparametric MRI and PET/CT. *J Magn Reson Imaging* 45:597–609
39. Park SY, Zacharias C, Harrison C, Fan RE, Kunder C, Hatami N et al (2018) Gallium 68 PSMA-11 PET/MR imaging in patients with intermediate- or high-risk prostate cancer. *Radiology* 288:495–505
40. de Perrot T, Rager O, Scheffler M, Lord M, Puzstaszeri M, Iselin C et al (2014) Potential of hybrid (1)(8)F-fluorocholine PET/MRI for prostate cancer imaging. *Eur J Nucl Med Mol Imaging* 41:1744–1755
41. Muehe AM, Theruvath AJ, Lai L, Aghighi M, Quon A, Holdsworth SJ et al (2018) How to provide gadolinium-free PET/MR cancer staging of children and young adults in less than 1 h: the Stanford approach. *Mol Imaging Biol* 20:324–335
42. Siegel JA, Pennington CW, Sacks B (2017) Subjecting radiologic imaging to the linear no-threshold hypothesis: a non sequitur of non-trivial proportion. *J Nucl Med* 58:1–6
43. Weber W, Zanzonico P (2017) The controversial linear no-threshold model. *J Nucl Med* 58:7–8
44. Kwatra NS, Lim R, Gee MS, States LJ, Vossough A, Lee EY (2019) PET/MR imaging: current updates on pediatric applications. *Magn Reson Imaging Clin N Am* 27:387–407
45. Schneuer FJ, Bentley JP, Davidson AJ, Holland AJ, Badawi N, Martin AJ et al (2018) The impact of general anesthesia on child development and school performance: a population-based study. *Paediatr Anaesth* 28:528–536
46. Platzek I, Beuthien-Baumann B, Schneider M, Gudziol V, Kitzler HH, Maus J et al (2014) FDG PET/MR for lymph node staging in head and neck cancer. *Eur J Radiol* 83:1163–1168
47. Chan SC, Yeh CH, Yen TC, Ng SH, Chang JT, Lin CY et al (2018) Clinical utility of simultaneous whole-body (18)F-FDG PET/MRI as a single-step imaging modality in the staging of primary nasopharyngeal carcinoma. *Eur J Nucl Med Mol Imaging* 45:1297–1308
48. Kanda T, Kitajima K, Suenaga Y, Konishi J, Sasaki R, Morimoto K et al (2013) Value of retrospective image fusion of (18)F-FDG PET and MRI for preoperative staging of head and neck cancer: comparison with PET/CT and contrast-enhanced neck MRI. *Eur J Radiol* 82:2005–2010
49. Beiderwellen K, Grueneisen J, Ruhlmann V, Buderath P, Aktas B, Heusch P et al (2015) [(18)F]FDG PET/MRI vs. PET/CT for whole-body staging in patients with recurrent malignancies of the female pelvis: initial results. *Eur J Nucl Med Mol Imaging* 42:56–65
50. Grueneisen J, Beiderwellen K, Heusch P, Gratz M, Schulze-Hagen A, Heubner M et al (2014) Simultaneous positron emission tomography/magnetic resonance imaging for whole-body staging in patients with recurrent gynecological malignancies of the pelvis: a comparison to whole-body magnetic resonance imaging alone. *Invest Radiol* 49:808–815



Advanced Ultrasound Imaging for Patients in Oncology: DCE-US

23

Nathalie Lassau

Neovascularization is a key stage in the growth of malignancies beyond 2–3 mm³. This neoangiogenesis is an important target for novel anticancer treatments [1], and many new antiangiogenesis or antivascular treatments aim at destroying or limiting the growth of tumor vessels [2].

Antiangiogenic treatments are disrupting signaling pathways that lead to the formation of new cancer blood vessels and by inhibiting factors that promote the structural integrity of neovascular endothelium.

Standard tumor response evaluation criteria, such as WHO [3] and RECIST [4], have limited applicability in antiangiogenic treatment monitoring, since reduction in tumor vascularization in responders occurs much earlier than decrease in tumor size. Successful antiangiogenic treatment often induces lesion edema with an increase in tumor volume, resulting in pseudoprogression when evaluated by RECIST, in particular in gastrointestinal stromal tumors (GIST) treated with imatinib targeted c-Kit. Therefore, alternative methods of treatment response assessment based on vascularization biomarkers are urgently needed. Ultrasound with Doppler imaging has a limited role in tumor vascularity assessment due to the inability to visualize flow on the capillary level, where the majority of early antiangiogenic effects occur.

A new area of clinical utility for dynamic contrast enhanced ultrasound (DCE-US) has emerged for monitoring the response to these drugs (Fig. 23.1).

N. Lassau (✉)
Institut Gustave Roussy, Villejuif, France
e-mail: nathalie.lassau@gustaveroussy.fr; lassau@igr.fr
Université de Paris-Saclay, Villejuif, France

© Springer Nature Switzerland AG 2020
O. Schober et al. (eds.), *Molecular Imaging in Oncology*,
Recent Results in Cancer Research 216,
https://doi.org/10.1007/978-3-030-42618-7_23

765

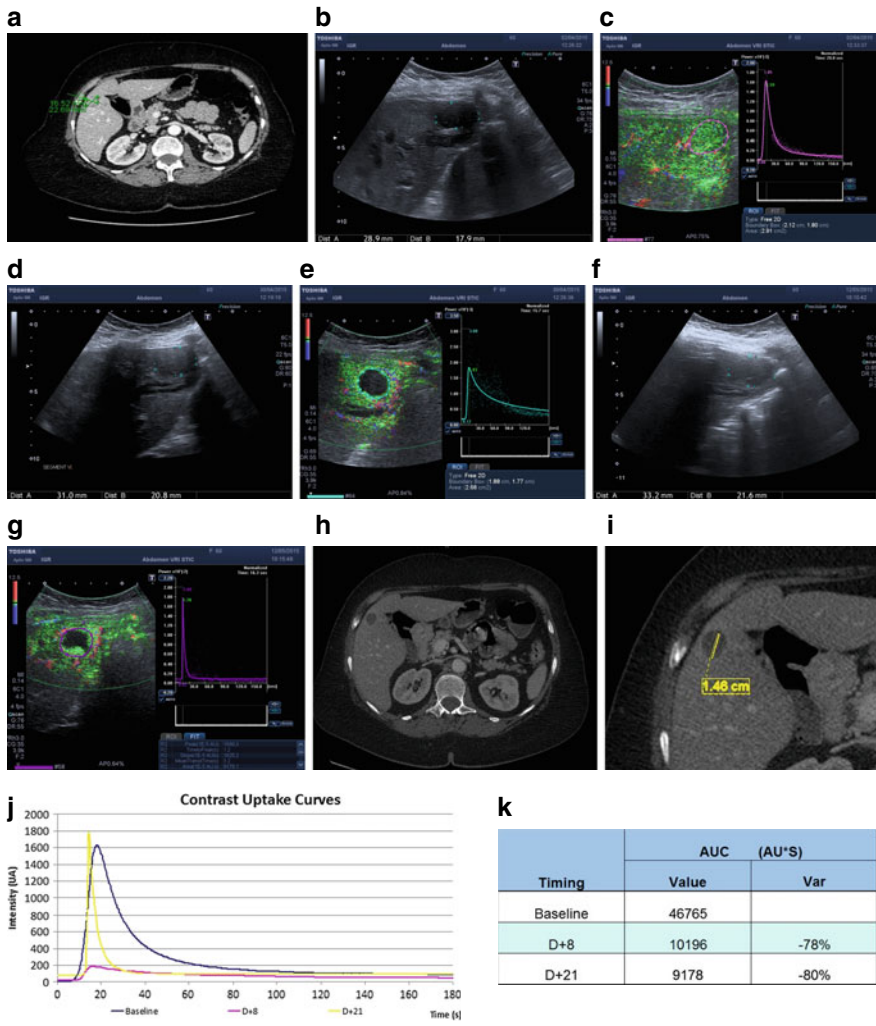


Fig. 23.1 A woman 61 years old with metastasis from Uterine leiomyosarcoma was treated by antiangiogenic treatment. The targeted lesion was located in segment V of the liver. At baseline, a CT-scan **a** and DCE-US were performed. The lesion was hypoechoic on B mode (**b**) and hypervascularized on VRI (vascular recognition imaging) mode (**c**) after injection on 4.8 ml of contrast agent. DCE-US was performed at D8 after the start of therapy showing the same size on B mode (**d**) but a strong decrease in vascularization at the arterial peak (**e**). The results were confirmed at D 21 with DCE-US on B mode (**f**) et VRI mode (**g**). The CT-scan was performed after 2 months demonstrating a decreasing size of the hypodense nodule (1.46 mm) **h, i**. The graph (**j**) and the table (**k**) confirm that the biomarker AUC on DCE-US decreases more than 40% at day 8 and day 21

DCE-US is better suited for tumor perfusion monitoring than non contrast enhanced Doppler, since it can detect and quantify flow in much smaller vessels with a diameter as small as 40 μm [5, 6].

Imaging biomarkers for the evaluation of tumor perfusion have been developed using DCE-MRI, DCE-CT, and DCE-US. DCE-CT is based on the analysis of temporal changes in attenuation numbers within blood vessels and tissues. DCE-MRI is used to measure tissue perfusion, vessel wall endothelium permeability, and extravascular volume ratio. DCE-US is used to measure intratumoral blood flow velocity and blood volume [7]. Why does DCE-US challenge these other techniques? DCE-US has many advantages over DCE-CT and DCE-MRI, such as ease of use, high throughput, low-cost examinations, and well-tolerated contrast agents approved since 2003 in Europe [8]. DCE-US has been proven to provide valuable biomarkers of treatment efficacy for a number of antiangiogenic therapies in patients with metastatic renal cell carcinoma [9–11], sarcoma [12], hepatocellular carcinoma [13–15], gastrointestinal stromal tumor [16, 17], and metastatic colon cancer [18, 19]. In these mono-centric studies, DCE-US has been shown to be predictive of progression free survival and overall survival, which are the best end points for oncologists.

DCE-US can be conducted as follows: First, an anatomical study using B-mode US is performed, aiming to detect the target tumor. The DCE-US is performed with high-dose injection of ultrasound contrast agent (4.8 mL of Lumason/SonoVue) immediately flushed with 5–10 mL of normal saline. The increased dosing of contrast is necessary since a large number of primary and metastatic malignancies demonstrate hypoenhancement, when imaged with standard doses of contrast. For each examination, DCE-US ultrasound images of the lesion are recorded for 3 min after the injection of the contrast agent. Contrast cine loops from raw linear data [20] are analyzed, and tumor contrast enhancement time-intensity curves are composed.

DCE-US criteria for treatment response evaluation [21] are as follows:

Blood Volume Criteria

- peak contrast enhancement intensity
- AUC
- AUC during contrast wash-in
- AUC during contrast wash-out

Blood Flow Criteria

- time to peak contrast intensity
- slope of the contrast wash-in

Mean Transit Time

Among these criteria, the change from baseline of the AUC is consistently found to be related to the treatment outcomes. The validation of AUC as a biomarker was performed in a clinical multicenter study [22, 23]. Seventy-five expert panels, assembled by Cancer Research UK and the European Organisation for Research

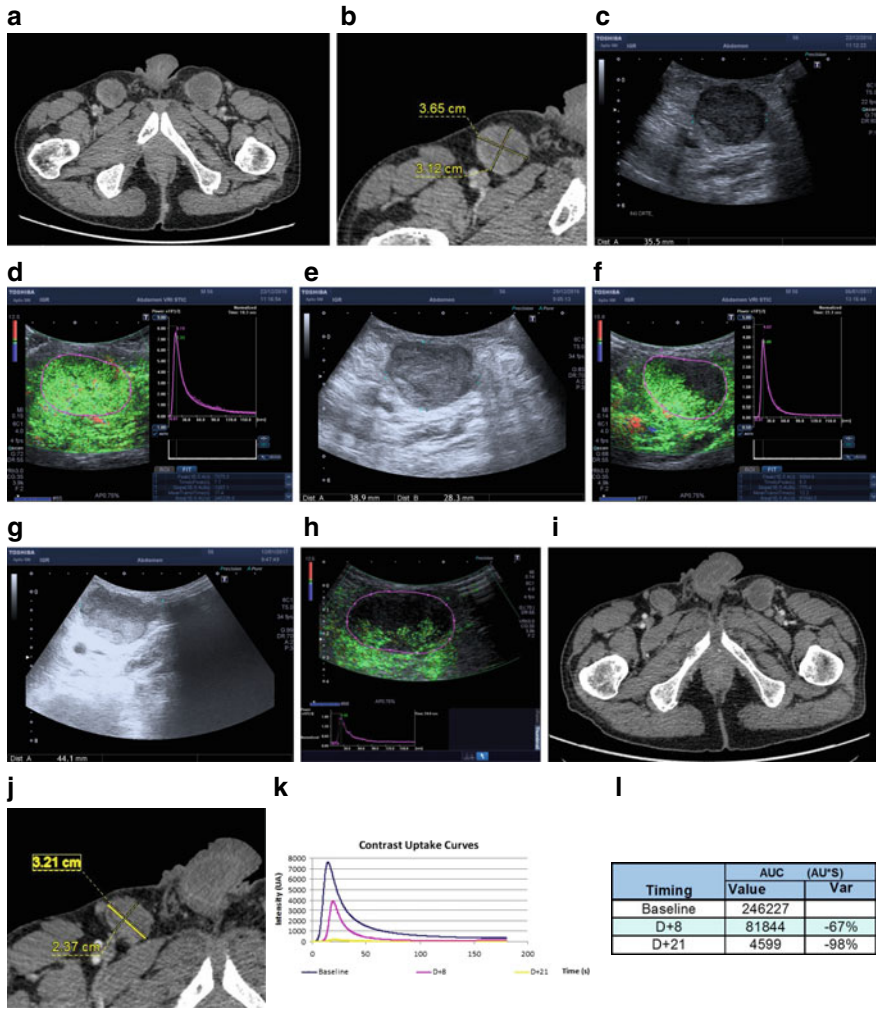


Fig. 23.2 A 57 years old man with metastasis from melanoma was treated by a combination of two immunotherapies. The targeted lesion was an inguinal lymph node. At baseline, a CT-scan (a, b) and DCE-US were performed. The lesion was hypoechoic on B mode (c) and hypervascularized on VRI (vascular recognition imaging) mode (d) after injection on 4.8 ml of contrast agent. The DCE-US was performed at D8 after the start of therapy showing the same size on B mode (e) but a decrease of vascularization at the peak arterial (f). The results were confirmed on day 21 with DCE-US in B mode (g) and VRI mode (h). The CT-scan shown in (i, j) was performed after 2 months of therapy, indicating stable disease of the lymph node. The graph (k) and the table (l) confirm AUC as a suitable DCE-US biomarker that compared to baseline decreased more than 40% at day 8 and day 21

and Treatment of Cancer [24] had this biomarker in their evaluation because of its correlation with overall survival. Based on AUC analysis, it is also relatively straightforward to distinguish the responders from non-responders. Responders will demonstrate a substantial decrease in target tumor perfusion with a significant drop of contrast enhancement AUC (more than 40% at one month in patients treated with tyrosine kinase inhibitors). Non-responders will demonstrate either no change, minimal change, or increase in tumor perfusion on CEUS, as detected by contrast enhanced AUC (Fig. 23.2).

Furthermore, with DCE-US, it might be possible to distinguish responding and non-responding metastatic colon cancer patients to anti VEGF therapies (bevacizumab) after only 1 week since the initiation of treatment, which is particularly possible with the parameter mean transit time (MTT) [21]. Compared to this, CT and MRI typically take 3–6 months to demonstrate the effects of systemic cancer treatments. The specificity of ultrasound could even be increased using targeted microbubbles. However, this is still at an early stage and until now most studies were performed in mice and only a few in phase 1 proof of concept studies in humans were reported on breast and ovarian tumors [25] (see also Chap. 15).

References

1. Ferrara N, Kerbel RS (2005) Angiogenesis as a therapeutic target. *Nature* 438:967–974
2. Kessler T, Bayer M, Schwoppe C, Liersch R, Mesters RM, Berdel WE (2010) Compounds in clinical Phase III and beyond. *Recent Results Cancer Res* 180:137–163
3. World Health Organisation (1979) WHO Handbook for Reporting Results of Cancer Treatment. World Health Organisation Offset Publication, Geneva, Switzerland
4. Therasse P, Arbuck SG, Eisenhauer EA, Wanders J, Kaplan RS, Rubinstein L, Verweij J et al (2000) New guidelines to evaluate the response to treatment in solid tumors. European Organization for Research and Treatment of cancer, National Cancer Institute of the United States, National Cancer Institute of Canada. *J Natl Cancer Inst* 92:205–216
5. Dietrich CF, Averkioui MA, Correas JM, Lassau N, Leen E, Piscaglia F (2012) An EFSUMB introduction into dynamic contrast-enhanced ultrasound (DCE-US) for quantification of tumour perfusion. *Ultraschall Med*
6. Forsberg F, Kuruvilla B, Pascua MB, Chaudhari MH, Merton DA, Palazzo JP, Goldberg BB (2008) Comparing contrast-enhanced color flow imaging and pathological measures of breast lesion vascularity. *Ultrasound Med Biol* 34:1365–1372
7. Cosgrove D, Lassau N (2010) Imaging of perfusion using ultrasound. *Eur J Nucl Med Mol Imaging* 37(Suppl 1):S65–S85
8. Sidhu PS et al (2018) The EFSUMB guidelines and recommendations for the clinical practice of contrast-enhanced ultrasound (CEUS) in non-hepatic applications: update 2017 (Long Version). *Ultraschall Med* 39(2):e2–e44
9. Lamuraglia M, Escudier B, Chami L, Schwartz B, Leclere J, Roche A, Lassau N (2006) To predict progression-free survival and overall survival in metastatic renal cancer treated with sorafenib: pilot study using dynamic contrast-enhanced Doppler ultrasound. *Eur J Cancer* 42:2472–2479
10. Lassau N, Koscielny S, Albiges L, Chami L, Benatsou B, Chebil M, Roche A et al (2010) Metastatic renal cell carcinoma treated with sunitinib: early evaluation of treatment response using dynamic contrast-enhanced ultrasonography. *Clin Cancer Res* 16:1216–1225

11. Hudson JM, Bailey C, Atri M, Stanisz G, Milot L, Williams R, Kiss A, Burns PN, Bjamason GA (2018) The prognostic and predictive value of vascular response parameters measured by dynamic contrast-enhanced-CT, -MRI and -US in patients with metastatic renal cell carcinoma receiving sunitinib. *Eur Radiol* 28(6):2281–2290
12. Lazar V, Lassau N, Meurice G, Loriot Y, Peña C, Massard C, Robert C, Robert T, Le Berre MA, de Baere T, Dessen P, Soria JC, Armand JP (2014) Sorafenib plus dacarbazine in solid tumors: a phase I study with dynamic contrast-enhanced ultrasonography and genomic analysis of sequential tumor biopsy samples. *Invest New Drugs* 32(2):312–322
13. Lassau N, Koscielny S, Chami L, Chebil M, Benatsou B, Roche A, Ducreux M et al (2010) Advanced hepatocellular carcinoma: early evaluation of response to bevacizumab therapy at dynamic contrast-enhanced US with quantification—preliminary results. *Radiology* 258:291–300
14. Frampas E, Lassau N, Zappa M, Vullierme MP, Koscielny S, Vilgrain V (2013) Advanced Hepatocellular Carcinoma: early evaluation of response to targeted therapy and prognostic value of Perfusion CT and dynamic contrast enhanced-ultrasound. Preliminary results. *Eur J Radiol* 82(5):e205–e211
15. Lo GM, Al Zahrani H, Jang HJ, Menezes R, Hudson J, Burns P, McNamara MG, Kandel S, Khalili K, Knox J, Rogalla P, Kim TK (2016) Detection of early tumor response to axitinib in advanced hepatocellular carcinoma by dynamic contrast enhanced ultrasound. *Ultrasound Med Biol* 42(6):1303–1311
16. De Giorgi U, Aliberti C, Benea G, Conti M, Marangolo M (2005) Effect of angiosonography to monitor response during imatinib treatment in patients with metastatic gastrointestinal stromal tumors. *Clin Cancer Res* 11:6171–6176
17. Lassau N, Chami L, Koscielny S, Chebil M, Massard C, Benatsou B, Bidault S et al (2012) Quantitative functional imaging by dynamic contrast enhanced ultrasonography (DCE-US) in GIST patients treated with masatinib. *Invest New Drugs* 30:765–771
18. Wu Z, Yang X, Chen L, Wang Z, Shi Y, Mao H, Dai G, Yu X (2017) Anti-angiogenic therapy with contrast-enhanced ultrasound in colorectal cancer patients with liver metastasis. *Medicine* 96(20):e6731
19. Lassau N, Coiffier B, Kind M, Vilgrain V, Lacroix J, Cuinet M, Taieb S, Aziza R, Sarran A, Labbe-Devilliers C, Gallix B, Lucidarme O, Ptak Y, Rocher L, Caquot LM, Chagnon S, Marion D, Luciani A, Feutray S, Uzan-Augui J, Benatsou B, Bonastre J, Koscielny S (2016) Selection of an early biomarker for vascular normalization using dynamic contrast-enhanced ultrasonography to predict outcomes of metastatic patients treated with bevacizumab. *Ann Oncol* 27(10):1922–1928
20. Peronneau P, Lassau N, Leguierney I, Roche A, Cosgrove D (2010) Contrast ultrasonography: necessity of linear data processing for the quantification of tumor vascularization. *Ultraschall Med* 31:370–378
21. Lassau N, Coiffier B, Faivre L, Benatsou B, Bidault S, Girard E, Asselain B, Pitre-Champagnat S, Koscielny S (2017) Study of inpatient variability and reproducibility of quantitative tumor perfusion parameters evaluated with dynamic contrast-enhanced ultrasonography. *Invest Radiol* 52(3):148–154
22. Lassau N, Chapotot L, Benatsou B, Vilgrain V, Kind M, Lacroix J, Cuinet M, Taieb S, Aziza R, Sarran A, Labbe C, Gallix B, Lucidarme O, Ptak Y, Rocher L, Caquot LM, Chagnon S, Marion D, Luciani A, Uzan-Augui J, Koscielny S (2012) Standardization of dynamic contrast-enhanced ultrasound for the evaluation of antiangiogenic therapies: the French multicenter support for innovative and expensive techniques study. *Invest Radiol* 47(12):711–716
23. Lassau N, Bonastre J, Kind M, Vilgrain V, Lacroix J, Cuinet M, Taieb S, Aziza R, Sarran A, Labbe-Devilliers C, Gallix B, Benastou B, Koscielny Lucidarme O, Ptak Y, Rocher L, Caquot LM, Chagnon S, Marion D, Luciani A, Feutray S, Uzan-Augui J, Coiffier BS (2014) Validation of dynamic contrast-enhanced ultrasound in predicting outcomes of antiangiogenic

- therapy for solid tumors: the French multicenter support for innovative and expensive techniques study. *Invest Radiol* 49(12):794–800
24. O'Connor JP, Aboagye EO, Adams JE, Aerts HJ, Barrington SF, Beer AJ, Boellaard R, Bohndiek SE, Brady M, Brown G, Buckley DL, Chenevert TL, Clarke LP, Collette S, Cook GJ, deSouza NM, Dickson JC, Dive C, Evelhoch JL, Faivre-Finn C, Gallagher FA, Gilbert FJ, Gillies RJ, Goh V, Griffiths JR, Groves AM, Halligan S, Harris AL, Hawkes DJ, Hoekstra OS, Huang EP, Hutton BF, Jackson EF, Jayson GC, Jones A, Koh DM, Lacombe D, Lambin P, Lassau N, Leach MO, Lee TY, Leen EL, Lewis JS, Liu Y, Lythgoe MF, Manoharan P, Maxwell RJ, Miles KA, Morgan B, Morris S, Ng T, Padhani AR, Parker GJ, Partridge M, Pathak AP, Peet AC, Punwani S, Reynolds AR, Robinson SP, Shankar LK, Sharma RA, Soloviev D, Stroobants S, Sullivan DC, Taylor SA, Tofts PS, Tozer GM, van Herk M, Walker-Samuel S, Wason J, Williams KJ, Workman P, Yankeelov TE, Brindle KM, McShane LM, Jackson A, Waterton JC (2017) Imaging biomarker roadmap for cancer studies. *Nat Rev Clin Oncol*. 14(3):169–186
 25. Willmann JK, Bonomo L, Carla Testa A, Rinaldi P, Rindi G, Valluru KS, Petrone G, Martini M, Lutz AM, Gambhir SS (2017) Ultrasound molecular imaging with BR55 in patients with breast and ovarian lesions: first-in-human results. *J Clin Oncol* 35(19):2133–2140



Image-Guided Radiooncology: The Potential of Radiomics in Clinical Application

24

Jan C. Peeken, Benedikt Wiestler, and Stephanie E. Combs

Contents

24.1	Introduction.....	775
24.1.1	Definition of “Radiomics”.....	775
24.1.2	Machine Learning—The Toolbox for the Generation of Radiomics Models... ..	778
24.1.3	Moving the Field Forward—The Role of “Deep Learning”.....	779
24.1.4	Radiomics and Molecular Imaging.....	780
24.1.5	Technical Challenges of Radiomics.....	780
24.2	The Clinical Potential of Radiomics.....	782
24.2.1	Radio-Oncomics.....	782
24.2.2	Radiogenomics.....	784
24.2.3	The Radiomics Target Volume Concept.....	784
24.3	Clinical Applications of Radiomics.....	784
24.3.1	NSCLC.....	785
24.3.2	HNSCC.....	786
24.3.3	Soft-Tissue Sarcoma (STS).....	787
24.3.4	Glioma.....	787
24.3.5	Challenges Before Clinical Applications.....	789
24.4	Conclusion.....	790
	References.....	790

J. C. Peeken (✉) · B. Wiestler · S. E. Combs
Department of Radiation Oncology, Klinikum Rechts der Isar, Technical University of Munich (TUM), Ismaninger Straße 22, 81675 Munich, Germany
e-mail: jan.peeken@tum.de

J. C. Peeken · S. E. Combs
Department of Radiation Sciences (DRS), Institute of Radiation Medicine (IRM), Helmholtz Zentrum München, Ingolstaedter Landstrasse 1, 85764 Neuherberg, Germany
Deutsches Konsortium Für Translationale Krebsforschung (DKTK), Partner Site Munich, Munich, Germany

List of Abbreviations

BraTS	Brain Tumor Segmentation Challenge
CERR	Computational environment for radiological research
CNN	Convolutional neural network
CT	Computer tomography
CTV	Clinical target volume
DTI	Diffusion tensor imaging
EGFR	Epidermal growth factor receptor
EORTC	European Organisation for Research and Treatment of Cancer
FET	¹⁸ F-fluoroethyl-1-tyrosine
FDG	¹⁸ F-fluorodeoxyglucose
GLCM	Gray-level co-occurrence matrix
GLDM	Gray-level dependence matrix
GLRLM	Gray-level run length matrix
GUI	Graphical user interface
IBSI	Imaging biomarker standardization initiative
IHC	Immunohistochemistry
GTV	Gross tumor volumes
HPV	Human papillomavirus
LBP	Local binary pattern
ML	Machine learning
MITK	Medical imaging tool kit
MRI	Magnetic resonance imaging
mpMRI	Multiparametric magnetic resonance imaging
NGTDM	Neighboring gray tone difference matrix
NSCLC	Non-small cell lung cancer
PET	Positron emission tomography
PD1	Programmed cell death protein 1
PDGFRA	Platelet-derived growth factor receptor A
PD-L1	Anti-programmed cell death ligand 1
RT	Radiotherapy
ROC	Receiver operator characteristic
SUV	Standardized uptake value
TKI	Tyrosine kinase inhibitor
TRIPOD	Transparent reporting of a multivariable prediction model for individual prognosis or diagnosis
VOI	Volume of interest

24.1 Introduction

24.1.1 Definition of “Radiomics”

The term “Radiomics” has first been introduced by Lambin et al. in [1]. It generally describes the extraction of quantitative features from medical imaging studies and inclusion into predictive models to predict clinical endpoints or tissue characteristics. Quantification of imaging properties has long been performed before, especially in the field of nuclear medicine or functional imaging. Radiomics in its current form, however, encompasses a two-step process: *First*, extraction of large-scale imaging features representing a multitude of image properties. *Secondly*, sophisticated modeling strategies involving dimensionality reduction methods and statistical or machine learning (ML) methods for the generation of optimal and valid prediction models [2].

Some studies have evaluated the value of semantic imaging features as a human equivalent to radiomics [3]. However, such features can only be of qualitative or semi-quantitative nature and suffer from a lack of reproducibility. In contrast, computational features quantitatively describe a volume of interest (VOI) more objectively. The commonly extracted radiomics features range from simple intensity metrics to complex textural analyses. Many of these features originally stem from the field of computer vision and pattern recognition in picture processing. Features are always extracted from a predefined volume of interest (VOI) (e.g., a gross tumor volume (GTV)).

Depending on the exact implementation of a predefined feature, results from the same image may differ significantly impairing reproducibility and hence clinical usefulness. The imaging biomarker standardization initiative (IBSI) has defined guidelines on the extraction of radiomics parameters, image preprocessing, recommendations on the reporting of radiomics studies, and tools to verify radiomics software implementations [4]. The main focus of IBSI was the exact mathematical description to allow for better comparability of radiomics features used in scientific studies. This aims to improve reproducibility and facilitate clinical applications. The authors provide a detailed mathematical description of all radiomics features and preprocessing steps [4].

In principle, radiomics features can be calculated in two dimensions (i.e., one slice), 2.5 dimensions (multiple averaged slices), or three-dimensionally. Most recent studies use three-dimensional features representing the total VOI.

The most commonly used feature types are described in the following (see Fig. 24.1).

24.1.1.1 First-Order Intensity Features

First-order intensity features describe the distribution of voxel intensity values within the VOI. They summarize the original image by simple statistical measures such as “mean”, “range”, or “kurtosis”.

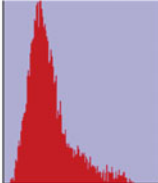
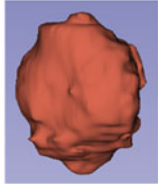

Radiomics Feature Type	Examples	Graphical Depiction																									
<i>Intensity based statistics</i>	Maximum, Mean, Range, Kurtosis, Entropy...																										
<i>Texture features</i>	<i>Gray Level Co-occurrence Matrix (GLCM) features:</i> Cluster tendency, Joint Average, Correlation...	<table border="1"> <tr> <td>1</td> <td>2</td> <td>2</td> <td>1</td> <td>0</td> </tr> <tr> <td>2</td> <td>0</td> <td>0</td> <td>1</td> <td>0</td> </tr> <tr> <td>2</td> <td>1</td> <td>0</td> <td>1</td> <td>2</td> </tr> <tr> <td>2</td> <td>0</td> <td>1</td> <td>3</td> <td>3</td> </tr> <tr> <td>0</td> <td>0</td> <td>1</td> <td>1</td> <td>3</td> </tr> </table>	1	2	2	1	0	2	0	0	1	0	2	1	0	1	2	2	0	1	3	3	0	0	1	1	3
1	2	2	1	0																							
2	0	0	1	0																							
2	1	0	1	2																							
2	0	1	3	3																							
0	0	1	1	3																							
<i>Morphology</i>	Volume, Elongation, Sphericity, Surface Area...																										
<i>Filters</i>	Laplacian of Gaussian, Wavelet Decomposition, Local Binary Pattern ...																										

Fig. 24.1 Exemplary illustration of the radiomics feature types. Subfigures were adapted from Peeken et al. [5]

24.1.1.2 Morphology Features

Morphology or “shape” features quantify the geometrical shape of a VOI. Thus, the features are independent on image gray values and only depend on the specific VOI mask. Important variables include the number of voxels, the surface area, or axis length. Features range from the VOI “volume”, over the quantification of the “elongation” (the relationship between the two principal axis lengths) to “sphericity” (a measure to quantify the roundness of a shape).

24.1.1.3 Second-Order Texture Features

Texture features include multiple distinct feature types that derive information from the spatial distribution of intensity values. Intensity values must be discretized before textural analysis.

The *gray-level co-occurrence matrix (GLCM)* quantifies the frequency of gray-level pairs that are neighbored in a predefined direction and distance. Features are generated by quantifying the *GLCM* matrix (such as “Cluster Tendency” as a measure for the grouping of similar intensity voxels) (see Fig. 24.1 for an exemplary *GLCM*).

The *gray-level run length matrix (GLRLM)* assesses the length of a sequence of equal gray values in neighboring voxels in a predefined direction. An exemplary feature, the “Long Run Emphasis,” is a measure of the distribution of long-run length indicating the coarseness of a texture.

If the *GLCM* or *GLRLM* features are averaged for every possible directional angle, the mean of these values represents a rotationally invariant measure which is frequently used in radiomics studies.

The *gray-level size zone matrix (GLSZM)* quantifies the occurrence of voxel zones with an equal gray value connected in all directions yielding a rotational invariant matrix. An exemplary feature, the “Zone Entropy” quantifies the randomness in the distribution of gray-level zone sizes indicating a measure of heterogeneity.

In the *gray-level dependence matrix (GLDM)*, the number of dependent voxels, which are defined as neighboring voxels in a predefined distance with a predefined maximal gray value difference, is quantified yielding a rotationally invariant matrix. The exemplary feature “Dependence Non-Uniformity” assesses the similarity between all dependencies within the *VOI* as an indicator of the homogeneity of a texture.

The *neighboring gray tone difference matrix (NGTDM)* determines the mean difference in gray values between the voxel of interest and its connected voxels yielding a rotational invariant matrix. An exemplary feature represents the “Busyness” which assesses the number of rapid intensity changes between voxels and their surroundings.

Finally, the less common *gray-level distance zone matrix (GLDZ)* combines the gray value zone matrix obtained as for the *GLSZM* features and a distance map assessing the distance of each voxel to the *VOI* edge. The combined matrix assesses the number of voxel groups with equal gray value and equal distance to the *VOI* edge. The feature derivation is similar to the *GLRLM*. In this case, the “Large distance emphasis” assesses gray zones with a large distance to the *VOI* edge.

24.1.1.4 Image Filtering

First-order and second-order features can be calculated from the original image or from a transformed image which has been modified by the application of a *filter*. As for the abovementioned features, filters find frequent application in image processing. Depending on the filter type, certain properties of the image are altered leading to different feature values. Thus, a radiomics feature is always defined by the applied filter and the actual feature algorithm. By the multiplication of the available feature algorithm and a series of different filters, large numbers of radiomics features can be extracted from single images.

The “*Laplacian of Gaussian*” filter computes the second spatial derivative of the input image which highlights areas of rapid intensity change such as edges. To reduce the effect of noise, a Gaussian smoothing filter is applied beforehand. The “*wavelet decomposition*” filter yields eight distinct decompositions. Each decomposition constitutes a unique combination of applying a low-pass or high-pass filter in all three dimensions.

The “*Local Binary Pattern*” (LBP) filter assigns a new value to each voxel defined by the relative intensity of the neighboring voxels. LBP-based features introduce directionality in addition to rotational invariance. Each surrounding voxel is labeled with 1 or 0 depending on whether the intensity value is larger or smaller than the voxel of interest. Each combination of all surrounding voxels is assigned as a novel intensity value. As a consequence, semantic structures such as edges or corners can be quantified.

24.1.2 Machine Learning—The Toolbox for the Generation of Radiomics Models

In order to make a prediction on clinically relevant questions, radiomics features need to be used as input features for predictive models. Since a large proportion of radiomics features are inter-correlated, feature reduction methods are often reduced to the most important features. Common techniques include “least absolute shrinkage and selection operator,” “minimum redundancy maximum relevance,” or “principal component analysis.” The remaining features can be used for model building [6].

If a sufficient feature reduction is possible, *statistical methods* such as logistic regression or Cox proportional hazard models can be trained. These methods bear the advantage of simple interpretability with the disadvantage of small input feature numbers and the incapability of modeling non-linear relationships. Other statistical methods such as ridge regression can fit prediction models based on a large number of input features by reducing the regression coefficients of unimportant features without setting them to zero.

Alternatively, a diverse set of *ML methods* can be applied for predictive modeling, allowing larger input feature numbers, potential handling of missing data points, and modeling of interaction or non-linear relationships at the expense of interpretability [7]. Commonly used models include decision tree methods such as random forest, bagging or boosting techniques, support vector machines, or neural networks [6].

Today, most applications rely on *supervised learning*, where a computer learns “by example”. The process of training such an ML model involves an (expert-) annotated training set. *Supervised learning* is highly efficient and has achieved unprecedented performance in many machine learning tasks. More recently, *semi-supervised* and *unsupervised* architectures, where computers learn the complex relations of data by themselves, have been more extensively studied. Such approaches are very attractive, as they at least partly abolish the need for

time-consuming and error-prone manual annotation of data. However, defining a learning objective in such scenarios is more difficult.

Scientific studies have compared the performance of different ML methods [6]. Depending on the specific dataset predictive performances differed significantly between arbitrarily chosen models [8]. Ensemble learning strategies in which several distinct ML models are combined to one model may compensate for this disadvantage.

24.1.3 Moving the Field Forward—The Role of “Deep Learning”

Deep Learning has emerged as a powerful technique in medical image analysis. Algorithmic advances in parallel with the broad availability of computing power (in particular, GPU) have enabled computers to take over tasks previously unthinkable [9]. This ranges from playing *Go* at a super-human level to correctly classifying skin lesions on par with expert dermatologists [10].

Deep Learning is a member of a broader family of machine learning methods. Setting *Deep Learning* apart from traditional machine learning algorithms like *Support Vector Machines* or *Random Forests* is their typical architecture, comprised of a large number of layers interconnected to form an *artificial neural network*. This architecture, coupled with non-linear activation functions, enables these networks to learn complex, non-linear decision functions. In medical image analysis, the use of *convolutional neural networks* (CNN) has integrated the process of feature definition and extraction into the learnable network and has therefore further improved the versatility of *Deep Learning*, as computers learn the relevant features themselves instead of relying on expert-defined features. CNNs are characterized by a series of convolutional layers, which apply a linear filtering operation on the image and thus extract features from the filter’s receptive field. These layers are combined with pooling layers, which subsample the image and a final fully connected layer for classification.

Neural networks as well can be trained in a *supervised* or *non-supervised* manner. During supervised training, the network aims to minimize a loss function (e.g., the number of wrongly classified cases) by optimizing network parameters yielding excellent predictive performances compared to other techniques.

Deep Learning is the current state of the art in most image analysis tasks and achieves unprecedented performance. However, there are several aspects that impede a more successful translation of these models in clinical practice. Most prominent among these are *generalizability* and *explainability*. *Generalizability* refers to the ability of a network to correctly process new, unseen cases. Especially in medical image analysis, a plethora of factors, including patient selection, scanner hardware, sequence and post-processing parameters influence the robustness of a network. This can partly be compensated by employing a large number of diverse training cases (Chilamkurthy et al. trained their model on >250,000 cranial computer tomography (CT) images [11]), but still remains a challenge. This is further

complicated by the “black box” nature of networks, where it is typically difficult to understand what the network has learned exactly. Having networks better “explain” what they have learned is; therefore, a major research focuses on AI research. These explanations could take many forms, such as visual (e.g., reconstruction of the final feature layer in CNN) or textual explanations.

Despite these obstacles, *Deep Learning* has already begun to influence image analysis workflow and will do so even more in the future.

24.1.4 Radiomics and Molecular Imaging

Quantitative imaging has been an integral part of nuclear medicine for decades. Tracer uptake in positron emission tomography (PET) studies quantified as standardized uptake value (SUV) was predominantly limited to simple “intensity features” such as the maximum or mean values [12]. Besides these features, morphology information such as the metabolic tumor volume has also been linked to prognostic prediction or tumor grading [12]. Analysis of heterogeneity of tracer uptake in PET has been introduced at the end of the 2000s [13]. Since then, a multitude of publications has shown a prognostic benefit by applying radiomics analyses to PET imaging for multiple tumor types such as cervical cancer, head and neck squamous cell carcinoma (HNSCC), or non-small cell lung cancer (NSCLC) (see below) [14–16]. In contrast to other imaging modalities such as CT, PET imaging bears the disadvantage of providing inferior spatial resolutions. As a consequence, the number of voxels per VOI is small impairing the informative power of texture features due to a direct correlation to the VOI volume as shown by Hatt et al. [17]. The same authors proposed a minimum VOI volume of 10 cm^3 . Hence, radiomics analysis of PET imaging with various tracers may play an important role in the future in sufficiently large tumors.

24.1.5 Technical Challenges of Radiomics

Generalizing a radiomics model to patients and scanners the model has not seen during training is key for a successful clinical application. To achieve this, there are several important challenges that need to be completed.

For multimodal image analysis, registration and resampling is a crucial first step. Registration performs an alignment of two imaging studies into one coordinate system [18]. After successful registration, VOIs can be transferred or direct voxel-wise comparisons can be performed. Dependent on the matching base, it can be performed landmark-based, surface-based, intensity-based, feature-based, or manually. Further on, the type of transformation differentiates rigid, affine, and deformable transformations. In rigid registration, the images are fused by linear three-dimensional translation and rotational movements. This conserves the distance between all points in the image but may come to its limits in multimodality registration, in studies from different time points and in the case of movement of

anatomical structures. The affine transformation adds scaling and shearing allowing better alignment with the cost of differing distances between image points. Deformable registration allows for voxel-directed spatially variant transformations which can lead to significant distortion of the image.

Especially for MR images, visible differences can exist between seemingly similar sequences, e.g., T1 images from different scanners. This is further complicated by a plethora of other confounding factors such as bias-field inhomogeneities. Especially when this variability has not been captured during training, this can pose a real problem for applying radiomics models on unseen data. To improve domain adaptation, software packages for important preprocessing steps such as bias-field correction or intensity normalization have been developed [19, 20]. Lately, deep-learning-based approaches have been evaluated for this task, too [21].

After first radiomics studies used self-built radiomics tool kits, multiple open-source software packages have been published and are now in use by the research community. The Matlab® (The Mathworks, Natick, MA)-based radiomics package for the “computational environment for radiological research” (CERR) combines radiomics feature extraction following the IBSI feature definition with the diverse functions of the CERR toolbox [22]. Further on, it allows for segmentation, visualization of radiomics feature maps, and direct DICOM import. An application programming interface has been developed for integration with the clinical software MIM (MIMvista, MIM Software Inc., Cleveland, OH). Based on Matlab® and C++, the software IBEX was one of the first softwares providing a graphical user interface (GUI), built-in segmentation, and DICOM support. Following its early release, however, features were not defined following the IBSI definitions [23].

Based on C++, the medical imaging tool kit (MITK) “phenotyping” provides a large toolchain ranging from DICOM import, registration, resampling, and segmentation to radiomics feature extraction of all IBSI-defined features [24]. It can be accessed using a GUI, by scripting languages or directly via a command-line tool.

LifeX is a Java-based GUI providing import of DICOM and non-DICOM files, segmentation tools, preprocessing, and IBSI-defined feature extraction [25]. It can also be run via a scripting interface. In contrast, Rayweb constitutes the only web-based tool providing decentralized segmentation, feature extraction, and data sharing [26]. Following the growing influence of Python on medical image analyses, the Python package pyradiomics has seen frequent use in recent radiomics studies providing a large library of feature extraction, preprocessing and visualization tools [27]. However, so far, no support for the DICOM format is available. Slicer radiomics constitutes a 3D slicer extension for pyradiomics providing a GUI for the usage of pyradiomics [28].

MaZda constitutes a non-open-source software that offers in-built segmentation and radiomics map visualization. Radiomics feature extraction is, however, limited to only a subset of the IBSI-defined features [29].

The company Oncoradiomics has recently introduced a commercial “Discovery Toolbox” for automated radiomics feature extraction and automatic machine learning building. Further on, a second software may soon become the first clinically usable radiomics software.

24.2 The Clinical Potential of Radiomics

24.2.1 Radio-Oncomics

The current limitations of radiation oncology may lie in the limited use of the full imaging information in the current radiation oncology workflow. We are using imaging to semantically characterize the underlying disease, discriminate affected tissues from healthy organs, and to provide a diagnosis for the physicians treating the disease. Always strongly depending on the disease, limitations lie in the sensitivity and specificity regarding tumor characterization and classification. In radiation oncology, essential information extracted from CT, magnetic resonance imaging (MRI), and/or PET images are used for treatment planning. Treatment planning delineation includes the GTV, potential areas of immediate risk of infiltration defined as the clinical target volume (CTV), and organs at risk (normal tissue) to determine the lowest possible dose in the treatment planning process.

The concept of “Radio-oncomics” defines the use of imaging information beyond pure tumor volumes and simple morphological changes [30]. It describes the use of radiomics information for tumor targeting, risk prediction, early tumor recurrence identification, as well as normal tissue characterization. Within the radio-oncomics concept, the information extracted from images is included in the radiation oncology treatment and follow-up loop. It is used for patient stratification, treatment planning, and early response assessment. See Fig. 24.2 for an overview of the structure of scientific radiomics studies.

Since its introduction, radiomics has been directed to predict a multitude of clinical or biological endpoints extracting information beyond the current applications. The most frequently predicted endpoint has been overall survival (OS) or relevant prognostic endpoints such as local (LPFS) or distant progression-free survival (DPFS). In these models, the performance of a radiomics model always needs to be compared to known clinically relevant prognostic factors such as tumor size, location, TNM staging, and patient-specific factors such as age or Karnofsky performance score [5, 31].

Further on, a large proportion of studies aimed to characterize biological tumor properties which may replace or act complementary to current pathology exams. Predicted tumor properties include tumor grading, Gleason score, or histological subtypes as surrogates for tumor aggressiveness [30]. Moreover, early responses may be detected before tumor volume changes generally defined by RECIST criteria (one-dimensional) or WHO criteria (two-dimensional), and lastly treatment response prediction may become possible enabling early personalization of patients’ follow-up [30]. For example, the differentiation of semantically similar imaging phenomena can be improved such as the differentiation of radiation necrosis and tumor progression based on 18F-fluoroethyl-l-tyrosine (FET) PET/MRI imaging [32]. Further on, radiomics has been used for radiotherapy (RT)-dependent toxicity predictions [33]. Figure 24.3 allocates the different areas of application to the radiation oncology workflow.

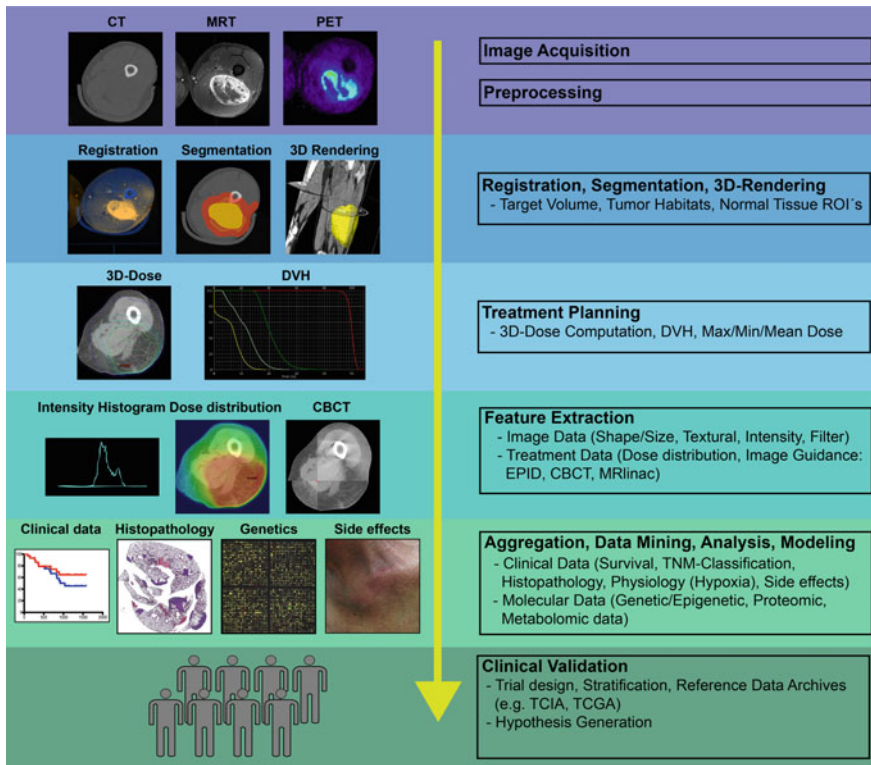


Fig. 24.2 Overview of the structure of scientific radiomics studies. Adapted by permission from Springer Nature Customer Service Centre GmbH [30]

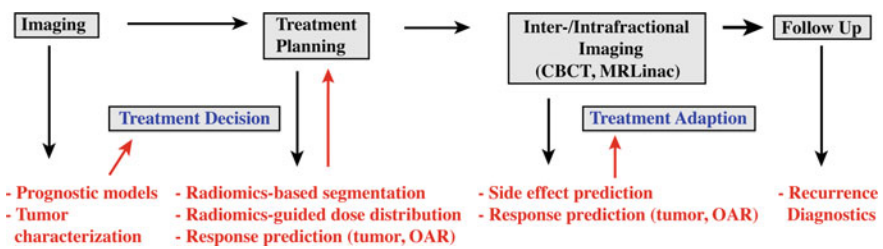


Fig. 24.3 Potential applications of radiomics in the radiation oncology workflow. OAR: organs at risk. Adapted by permission from Springer Nature Customer Service Centre GmbH [16]

24.2.2 Radiogenomics

The concept of “Radiogenomics” describes the direct correlation of a radiomics phenotype to underlying molecular aberrations. The hypothesis is that tissue imaging correlates with tissue pathology. A whole set of publications demonstrated successful prediction of genetic mutations, chromosomal aberrations, and transcriptional programs (RNA, miRNA) [34]. Radiogenomic prediction of molecular aberrations related to radiation sensitivity may pose a powerful tool for therapy adjustment or dose painting approaches (see below).

These principles were recently used to develop a cancer-independent immunogenic phenotype. The prediction model was able to predict tumor-infiltrating CD8+ T-cells and the response to anti-programmed cell death protein 1 (PD1) or anti-programmed cell death ligand 1 (PD-L1) immunotherapies [35].

24.2.3 The Radiomics Target Volume Concept

A clear potential lies in the use of radiomics and radiogenomic information for advanced target volume definition. With the information derived from small sub-volumes of tumors (“habitats”) and normal tissue, areas of high risk for tumor recurrence might be identified and targeted. Such high-risk habitats could be targeted using higher radiation doses. Additionally, normal tissue may be characterized more in detail and areas at high risk for side effects can be detected requiring advanced protection even from low-dose irradiation. Exemplarily, our group analyzed imaging for treatment planning in glioblastomas focusing on MRI. We could characterize an infiltrative GTV inside of the FLAIR hyperintense regions which correlated with tumor recurrences. A novel target volume was developed to specifically target such regions reducing the total treatment volume [36]. Others have shown that multiparametric MRI (mpMRI) signal intensities can be enhanced by radiomics information to target prostate cancer lesions; they applied radiomics along with deformable co-registration tools to generate targeted focal RT treatment plans including external beam RT and brachytherapy [37]. Clinical studies validating these new target volume concepts are necessary and have to be performed for each tumor entity before target volume guidelines can be adapted.

24.3 Clinical Applications of Radiomics

In the following section, the current literature on radiomics models for selected malignant entities will be discussed.

24.3.1 NSCLC

NSCLC has been among the first malignant tumor entities to be studied by radiomics. Aerts et al. first established a radiomics workflow based on NSCLC patients that has since been used as a role model for many subsequent studies in the following years [38]. The authors first demonstrated that a radiomics classifier based on four features showed significant prognostic value with a C-index of 0.65 and the propensity of significant patient risk stratification. Significant correlations between the radiomics signature and gene expression patterns were found as a biological basis.

Although prediction of local recurrence remained challenging, analyzing the influence of RT on NSCLC radiomics feature changes obtained before and after RT (“delta radiomics”) increased the predictive performance allowing significant patient stratification into patients with high or low risk of local tumor recurrence [39].

Besides, delta radiomics features assessed after RT changed significantly in a dose-dependent manner and were able to predict radiation pneumonitis grade II or higher with an AUC of up to 0.75, however, without external validation [33]. In a different study, the propensity to predict radiation pneumonitis based on CT-based radiomics features could further be increased by the inclusion of the SUV standard deviation of 18F-fluorodeoxyglucose (FDG) PET scans up to a mean AUC difference of 0.08 [40].

Multiple further studies have evaluated the potential of radiomics analysis of FDG PET imaging. In contrast to standard measures such as maximum or mean SUV, certain radiomics features were associated with OS independent from known clinical factors [15].

In general, a prognostic assessment was possible independent of the therapy delivered (stereotactic body RT versus surgery) in stage I NSCLC patients [41].

Radiogenomic analyses provided radiomics phenotypes predictive for frequently occurring genetic mutations such as epidermal growth factor receptor (*EGFR*) and *KRAS* mutations [42]. These phenotypes were also able to improve prognostic evaluations. Taking the idea one step further, a further study was able to demonstrate that a delta radiomics response phenotype for *EGFR* mutations comprising of features obtained from pre-therapeutic and post-therapeutic scans 3 weeks after initiation of therapy showed better prediction of *EGFR* mutational status than pre-treatment features [43]. The simple measure of volume change, however, was the most predictive factor with an AUC of 0.91.

An additional novel concept could demonstrate the capability of deep learning to integrate a temporal dimension for prognostic prediction. On the basis of one pre-therapeutic CT scans, subsequent serial CT scans from sequential time points of the patients’ follow-up were added as training basis for prognostic assessment. The underlying network was able to capture an RT response phenotype increasing the predictive performance for OS from follow-up to follow-up up to a maximum AUC of 0.74 [44].

24.3.2 HNSCC

The previously mentioned radiomics classifier developed for NSCLC patients was originally also tested in HNSCC patients. Interestingly, predictive performance was even better for HNSCC as for NSCLC patients with an AUC of 0.69 on two independent validation sets [38]. Shortly later, novel CT-based radiomics models for the prediction of LPFS and DPFS based on FDG PET and CT imaging were published [16]. Especially, the prediction of DPFS showed a good predictive performance with a C-index of 0.88 in the validation set significantly outperforming a clinical model and tumor volume.

RT dose escalation or de-escalation has long been a matter of research. The observed favorable prognosis of human papillomavirus (HPV) positive HNSCC has led to a series of dose de-escalation trials. In clinical practice, the p16 tumor suppressor protein expression determined by immunohistochemistry (IHC) is often used as a surrogate for HPV infections. Bogowicz et al. developed radiomics models to predict IHC-based p16 positivity with good performance achieving an AUC of 0.78 in the testing set [45]. IHC-based measurement of p16 has been described to have a good sensitivity of 96.8% with a specificity of 83.8% for the determination of HPV infections determined by RNA amplification [46]. In a further study, radiomics models were trained to predict HPV status determined by detection of HPV-specific RNA in whole-transcriptome sequencing (RNA-seq). In the testing set which provided IHC-based p16 status, a similar predictive performance compared to the previous study could be found with an AUC of 0.76 [47]. A clinical model that was largely dominated by the anatomic side achieved the best predictive performance with an AUC of 0.86. In a side-restricted analysis, however, the radiomics model retained better performance than a clinical model (radiomics AUC: 0.79, clinical AUC: 0.61). To conclude, such HPV models may one day be used for patient stratification or even spatial dose de-escalations in radiomics target volumes in clinically relevant patient subcohorts.

Most radiomics studies have focused on pre-therapeutic imaging. However, radiomics analysis after the first 2 weeks of RT treatment appears to bear information regarding therapy response triggering superior prognostic capabilities increasing the predictive performance from 0.65 (pre-therapy) to 0.79 (2 weeks) [48]. Such information may be used as well for treatment adaptations in the future.

The definitive treatment of HNSCC enables long-time survival in a large proportion of patients. As a consequence, many patients suffer from chronic RT side effects such as xerostomia. Current risk models are predominantly based on RT dose metrics. The inclusion of the individual tissue susceptibility may help to predict salivary gland toxicity more accurately. First radiomics studies were able to identify MRI-based texture features associated with xerostomia development [49].

Radiomics feature can also be used for tumor segmentation. Yu et al. identified relevant radiomics texture features of registered FDG PET/CT scans for automated GTV definitions [50]. The proposed segmentation strategies outperformed former segmentation approaches, e.g., based on SUV thresholding, in terms of sensitivity and specificity compared to expert delineations.

24.3.3 Soft-Tissue Sarcoma (STS)

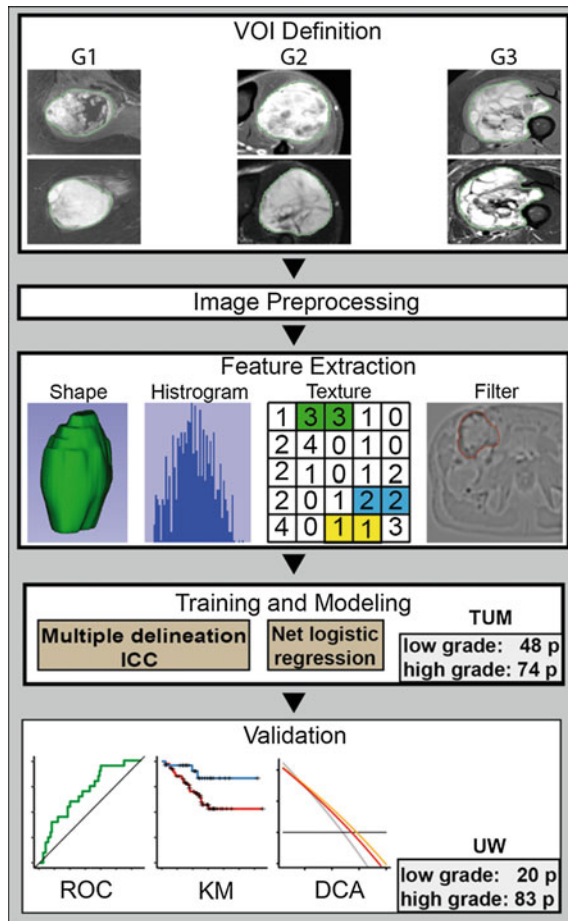
One of the first studies that analyzed tracer uptake heterogeneity of FDG PET imaging was performed within patients suffering from STS showing independent prognostic relevance in cox proportional hazard models [51]. One of the first multimodal radiomics studies combining PET imaging with MRI was applied to STS, too [52]. This work demonstrated the potential of predicting the occurrence of lung metastases albeit lacking an external validation cohort. Later, Spraker et al. could demonstrate and externally validate a radiomics model for OS based on contrast-enhanced T1-weighted MRI sequences [53]. The developed model predicted OS with a C-index of 0.68. The performance of a clinical model could be improved after combination with the radiomics model from 0.71 to 0.78 on an independent validation cohort. Further on, radiomics models based on planning CT data of neoadjuvantly treated STS achieved predictive performances for OS, DPFS, and LPFS [5]. Interestingly, the prognostic performance was even better compared to the MRI-based model with a C-index of 0.73 despite the unfavorable soft tissue resolution of CT imaging underlining the potential of radiomics. A combined radiomics-clinical model outperformed a clinical model and the AJCC staging system with a C-index of 0.76 (clinical: 0.69, AJCC: 0.68). Significant patient stratification was possible for all three endpoints. Moreover, a recent study has demonstrated the possibility of quantifying intra-tumoral changes following neoadjuvant chemotherapy (delta radiomics) as a predictive marker for therapy response [54]. The proposed model achieved an accuracy of 74.6% classifying patient with good response.

In terms of tumor characterization, first studies showed the potential of differentiating G1 (“low grade”) from G2/G3 (“high grade”) or G2 from G3 sarcomas on CT or MRI imaging data (see Fig. 24.4 for a related workflow) [55]. G2 versus G3 differentiation on CT achieved only moderate performances with a testing AUC of 0.64 [5]. Differentiation of “low-grade” from “high-grade” STS, however, was achieved with an AUC of 0.78 in the independent validation set. Adding the radiomics model to the AJCC staging system further increased the total prognostic performance by 0.05 C-index showing an incremental clinical net benefit. Further on, the differentiation between benign and malign soft tissue lesions appeared to be possible as well in a further study [56].

24.3.4 Glioma

Reliable tumor segmentation is an essential first step in virtually all radiomics pipelines and RT treatment planning. The development of segmentation strategies based on U-Nets [57] has led to algorithms that today perform glioma segmentation well within the performance level of expert human raters, as highlighted in the brain tumor segmentation (BraTS) challenge [58]. U-Nets are fully convolutional neural networks, which consist of a contracting encoder and an expansive decoder (giving the architecture a U-like shape). In order to forward spatial information through the

Fig. 24.4 Exemplary radiomics workflow for the development of tumor grading models in soft tissue sarcomas. Adapted from Peeken et al. [55]



network skip connections are introduced. Those connections concatenate feature maps of the downsampling path with the corresponding layers of the upsampling [57]. Importantly, the clinical value of these algorithms has been successfully demonstrated in a translational study: In a retrospective analysis of multicentre prospective “European Organisation for Research and Treatment of Cancer” (EORTC) trial data, automated glioma response assessment based on computational tumor segmentation outperformed human readers in terms of predicting survival [59].

In gliomas, machine learning methods have demonstrated their ability to predict key genomic alterations from MR images in *radiogenomics* studies. Capitalizing on the ability of medical imaging to capture spatial heterogeneity in these tumors well beyond histological analysis, more recent studies have investigated the ability of machine learning to predict spatial heterogeneity of key genomic alterations in newly diagnosed glioblastomas [60]. In their analysis, Hu et al. demonstrated that typical genomic alterations in glioblastomas, such as *EGFR* or platelet-derived

growth factor receptor A (*PDGFRA*) copy-number alterations, show regional heterogeneity, and that the molecular status of these genes could be predicted by ML-based image analysis. In the light of better understanding resistance of tumors to molecularly targeted therapies, these results point to an important role of image analysis, albeit further studies and validation are necessary.

Diffusion tensor imaging (DTI) has seen an increased use for prediction of tumor infiltration in gliomas. However, the analysis of DTI data is impeded by the corruption of the true diffusion signal by water signal especially in areas of peritumoral edema, which, on the other hand, also is the most likely area of tumor recurrence. To disentangle the true DTI signal from water contamination, a *Deep-Learning*-based model was trained [61]. Using these water contamination corrected maps, tumor infiltration maps can be calculated from the DTI data and used for radiotherapy planning. In a pilot study, these maps demonstrated their potential to serve as a basis for individualized therapy planning [36].

Considering the rich information on tumor biology contained in medical images, strategies for exploiting this data for better personalizing treatment are attractive. Based on pre-operative multimodal PET/MR imaging in newly diagnosed glioblastomas, a personalized growth model based on a reaction–diffusion equation was recently proposed. Through Bayesian inference, this model infers patient-specific growth parameters like the proliferation rate and cell density from FET PET and anatomic MR images and uses this information to model tumor growth. In a small study with eight patients, this system yielded smaller, more personalized clinical target volumes (CTV), while still covering recurrence. Also, this model might also guide local dose escalations more reliably than FET PET-based planning. While promising, future prospective evaluations of these algorithms for personalizing radiotherapy are necessary [62].

24.3.5 Challenges Before Clinical Applications

The literature in the field of radiomics has grown exponentially in the last years. So far, none of the proposed models has yet found its way into daily clinical practice though. There are several hurdles to take before clinical translation: *First*, many models have been externally validated using predominantly retrospective patient cohorts. Optimal validation, however, would include validation in *prospective trials* without access to the development data (i.e., type IV validation following the “transparent reporting of a multivariable prediction model for individual prognosis or diagnosis” (TRIPOD) statement) [63]. *Secondly*, the reproducibility of radiomics models is largely prone to variations in scanner models, acquisition parameters and radiomics software implementations hindering safe widespread use. CT data with its absolute real-world measures appears to show the best reproducibility. Limited preprocessing procedures may be sufficient to allow widespread usage. On the contrary, *harmonization* of MRI- and PET-based features constitutes a significantly

more complex task requiring further research. *Thirdly*, prognostic models should ideally be used in *therapeutic trials* for patient risk stratification and selection to demonstrate a benefit to the patients. *Fourthly*, *software solutions* providing standardized and easy-to-use radiomics analysis have not yet arrived in clinical practice.

24.4 Conclusion

Radiomics constitutes a powerful and cost-effective tool to extract additional information from daily acquired medical imaging studies. Areas of application include diagnostics, prognostic patient risk stratifications, therapy response monitoring, radiogenomic analysis of molecular aberrations, or tissue characterization. The principle finds application in all imaging modalities. However, for each specific task, the optimal modality and the true incremental benefit of a novel prediction model must be evaluated. PET-based radiomics models may play an important role in large growing tumors such as cervical cancer, NSCLC, or HNSCC. Before widespread clinical usage, several limiting factors need to be solved signaling the need for further research.

References

1. Lambin P, Rios-Velazquez E, Leijenaar R, Carvalho S, van Stiphout RGPM, Granton P et al (2012) Radiomics: extracting more information from medical images using advanced feature analysis. *Eur J Cancer* Mar 48(4):441–446
2. Peeken JC, Bernhofer M, Wiestler B, Goldberg T, Cremers D, Rost B et al (2018) Radiomics in radiooncology – challenging the medical physicist. *Phys Medica* 48:27–36
3. Peeken JC, Kessel KA, Nüsslin F, Braun AE, Combs SE (2018) Semantic imaging features predict disease progression and survival in glioblastoma multiforme patients. *Strahlentherapie und Onkol* 194(9):824–834
4. Zwanenburg A, Vallières M, Abdalah MA, Aerts HJWL, Andrearczyk V, Apte A et al (2020) The image biomarker standardization initiative: standardized quantitative radiomics for high-throughput image-based phenotyping. *Radiology* (5):191145
5. Peeken JC, Bernhofer M, Spraker MB, Pfeiffer D, Devecka M, Thamer A et al (2019) CT-based radiomic features predict tumor grading and have prognostic value in patients with soft tissue sarcomas treated with neoadjuvant radiation therapy. *Radiother Oncol* 135:187–196
6. Parmar C, Grossmann P, Bussink J, Lambin P, Aerts HJWL (2015) Machine learning methods for quantitative radiomic biomarkers. *Sci Rep* 5(1):13087. <http://www.ncbi.nlm.nih.gov/pubmed/26278466>. Accessed 17 Oct 2016
7. Peeken JC, Goldberg T, Knie C, Komboz B, Bernhofer M, Pasa F et al (2018) Treatment-related features improve machine learning prediction of prognosis in soft tissue sarcoma patients. *Strahlentherapie und Onkol* 194(9):824–834. <http://link.springer.com/10.1007/s00066-018-1294-2>
8. Deist TM, Dankers FJWM, Valdes G, Wijsman R, Hsu IC, Oberije C et al (2018) Machine learning algorithms for outcome prediction in (chemo)radiotherapy: an empirical comparison of classifiers. *Med Phys* 45(7):3449–3459

9. LeCun Y, Bengio Y, Hinton G (2015) Deep learning. *Nature* 521(7553):436–444. <http://www.nature.com/articles/nature14539>
10. Esteva A, Kuprel B, Novoa RA, Ko J, Swetter SM, Blau HM et al (2017) Dermatologist-level classification of skin cancer with deep neural networks. *Nature* 542(7639):115–118. <http://www.nature.com/doi/10.1038/nature21056>. Accessed 20 Mar 2017
11. Chilamkurthy S, Ghosh R, Tanamala S, Biviji M, Campeau NG, Venugopal VK et al (2018) Deep learning algorithms for detection of critical findings in head CT scans : a retrospective study. *Lancet* 392(10162):2388–2396. [http://dx.doi.org/10.1016/S0140-6736\(18\)31645-3](http://dx.doi.org/10.1016/S0140-6736(18)31645-3)
12. Pyka T, Gempt J, Hiob D, Ringel F, Schlegel J, Bette S et al (2016) Textural analysis of pre-therapeutic [18F]-FET-PET and its correlation with tumor grade and patient survival in high-grade gliomas. *Eur J Nucl Med Mol Imaging* 43(1):133–141
13. Yu H, Caldwell C, Mah K, Mozeg D (2009) Coregistered FDG PET/CT-based textural characterization of head and neck cancer for radiation treatment planning. *IEEE Trans Med Imaging* 28(3):374–383. <http://ieeexplore.ieee.org/document/4601461/>. Accessed 4 Dec 2016
14. Lucia F, Visvikis D, Vallières M, Desseroit M, Miranda O, Robin P et al (2019) External validation of a combined PET and MRI radiomics model for prediction of recurrence in cervical cancer patients treated with chemoradiotherapy. *Eur J Nucl Med Mol Imaging* 46(4):864–877. <http://link.springer.com/10.1007/s00259-018-4231-9>
15. Arshad MA, Thornton A, Lu H, Tam H, Wallitt K, Rodgers N et al (2019) Discovery of pre-therapy 2-deoxy-2-18F-fluoro-D-glucose positron emission tomography-based radiomics classifiers of survival outcome in non-small-cell lung cancer patients. *Eur J Nucl Med Mol Imaging* [Internet] 46(2):455–466. Available from: <http://link.springer.com/10.1007/s00259-018-4139-4>, <http://www.ncbi.nlm.nih.gov/pubmed/30173391>
16. Vallières M, Kay-Rivest E, Perrin LJ, Liem X, Furstoss C, Aerts HJWL et al (2017) Radiomics strategies for risk assessment of tumour failure in head-and-neck cancer. *Sci Rep* 7(1):10117. <http://www.ncbi.nlm.nih.gov/pubmed/28860628>. Accessed 9 Oct 2017
17. Hatt M, Majdoub M, Vallieres M, Tixier F, Le Rest CC, Groheux D et al (2015) 18F-FDG PET uptake characterization through texture analysis: investigating the complementary nature of heterogeneity and functional tumor volume in a multi-cancer site patient cohort. *J Nucl Med* 56(1):38–44. <http://jnm.snmjournals.org/cgi/doi/10.2967/jnumed.114.144055>
18. Brock KK, Mutic S, McNutt TR, Li H, Kessler ML (2017) Use of image registration and fusion algorithms and techniques in radiotherapy: report of the AAPM radiation therapy committee task group no. 132: report. *Med Phys* 44(7):e43–76
19. Tustison NJ, Gee JC (2009) N4ITK: Nick’s N3 ITK implementation for MRI bias field correction. *Insight J* 1–8. <http://www.insight-journal.org/browse/publication/640%5Cnpapers2://publication/uuid/BB26233C-D637-405C-A49E-4E487427AE18%5Cnpapers2://publication/uuid/D6B8F005-7D75-45B7-8014-172867966A98>
20. Shinohara RT, Sweeney EM, Goldsmith J, Shiee N, Mateen FJ, Calabresi PA et al (2014) Statistical normalization techniques for magnetic resonance imaging. *NeuroImage Clin* 6:9–19. <http://dx.doi.org/10.1016/j.nicl.2014.08.008>
21. Baur C, De Benedikt Wiestler CB, Albarqouni S, Navab N (2019) Fusing unsupervised and supervised deep learning for white matter lesion segmentation. *Proc Mach Learn Res* 102:63–72. <https://openreview.net/pdf?id=ryxNhZGlxV>
22. Apte AP, Iyer A, Crispin-Ortuzar M, Pandya R, van Dijk LV, Spezi E et al (2018) Technical note: extension of CERR for computational radiomics: a comprehensive MATLAB platform for reproducible radiomics research. *Med Phys* 45(8):3713–3720. <http://doi.wiley.com/10.1002/mp.13046>
23. Zhang L, Fried D V, Fave XJ, Hunter LA (2015) ibex : an open infrastructure software platform to facilitate collaborative work in radiomics 42(3):1341–1353
24. Götz M, Nolden M, Maier-Hein K (2019) MITK phenotyping: an open-source toolchain for image-based personalized medicine with radiomics. *Radiother Oncol* 131:108–111. <https://doi.org/10.1016/j.radonc.2018.11.021>

25. Nioche C, Orlhac F, Boughdad S, Reuzé S, Goya-Outi J, Robert C et al (2018) LIFEx: a freeware for radiomic feature calculation in multimodality imaging to accelerate advances in the characterization of tumor heterogeneity. *Cancer Res* canres.0125.2018. <http://www.ncbi.nlm.nih.gov/pubmed/29959149>
26. Yuan R, Shi S, Chen J, Cheng G (2019) Radiomics in RayPlus: a web-based tool for texture analysis in medical images. *J Digit Imaging* 32(2):269–275. <http://link.springer.com/10.1007/s10278-018-0128-1>
27. van Griethuysen JJM, Fedorov A, Parmar C, Hosny A, Aucoin N, Narayan V et al (2017) Computational radiomics system to decode the radiographic phenotype. *Cancer Res* 77(21):e104–e107
28. Fedorov A, Beichel R, Kalpathy-Cramer J, Finet J, Fillion-Robbin J-C, Pujol S et al (2012) 3D slicers as an image computing platform for the quantitative imaging network. *Magn Reson Imaging* 30(9):1323–1341
29. Szczypiński PM, Strzelecki M, Materka A, Klepaczko A (2009) MaZda-A software package for image texture analysis. *Comput Methods Programs Biomed* 94(1):66–76
30. Peeken JC, Nüsslin F, Combs SE (2017) “Radio-oncomics” - the potential of radiomics in radiation oncology. *Strahlentherapie und Onkol* 193(10):767–779
31. Peeken JC, Goldberg T, Pyka T, Bernhofer M, Wiestler B, Kessel KA et al (2019) Combining multimodal imaging and treatment features improves machine learning-based prognostic assessment in patients with glioblastoma multiforme. *Cancer Med* 8(1):128–136. <http://doi.wiley.com/10.1002/cam4.1908>
32. Lohmann P, Kocher M, Cecon G, Bauer EK, Stoffels G, Viswanathan S et al (2018) Combined FET PET/MRI radiomics differentiates radiation injury from recurrent brain metastasis. *NeuroImage Clin* 20:537–542
33. Cunliffe A, Armato SG, Castillo R, Pham N, Guerrero T, Al-Hallaq HA et al (2015) Lung texture in serial thoracic computed tomography scans: correlation of radiomics-based features with radiation therapy dose and radiation pneumonitis development. *Int J Radiat Oncol Biol Phys* 91(5):1048–1056. <http://www.ncbi.nlm.nih.gov/pubmed/25670540>. Accessed 18 Oct 2016
34. Gillies RJ, Kinahan PE, Hricak H (2015) Radiomics: images are more than pictures, they are data. *Radiology* [Internet] 278(2):151169. Available from: <http://pubs.rsna.org/doi/10.1148/radiol.2015151169>
35. Sun R, Limkin EJ, Vakalopoulou M, Dercle L, Champiat S, Han SR et al (2018) A radiomics approach to assess tumour-infiltrating CD8 cells and response to anti-PD-1 or anti-PD-L1 immunotherapy: an imaging biomarker, retrospective multicohort study. *Lancet Oncol* 2045(18):1–12
36. Peeken JC, Molina-Romero M, Diehl C, Menze BH, Straube C, Meyer B et al (2019) Deep learning derived tumor infiltration maps for personalized target definition in Glioblastoma radiotherapy. *Radiother Oncol* 138:166–172. <https://doi.org/10.1016/j.radonc.2019.06.031>
37. Shiradkar R, Podder TK, Algohary A, Viswanath S, Ellis RJ, Madabhushi A (2016) Radiomics based targeted radiotherapy planning (Rad-TRaP): a computational framework for prostate cancer treatment planning with MRI. *Radiat Oncol* 11(1):148. <http://www.ncbi.nlm.nih.gov/pubmed/27829431>. Accessed 17 Nov 2016
38. Aerts HJWL, Velazquez ER, Leijenaar RTH, Parmar C, Grossmann P, Carvalho S et al (2014) Decoding tumour phenotype by noninvasive imaging using a quantitative radiomics approach. *Nat Commun* 5:4006. <http://www.ncbi.nlm.nih.gov/pubmed/24892406>. Accessed 24 July 2016
39. Fave X, Zhang L, Yang J, MacKin D, Balter P, Gomez D, et al (2017) Delta-radiomics features for the prediction of patient outcomes in non-small cell lung cancer. *Sci Rep* 7(1):1–11. <http://dx.doi.org/10.1038/s41598-017-00665-z>
40. Anthony GJ, Cunliffe A, Castillo R, Pham N, Guerrero T, Armato SG et al (2017) Incorporation of pre-therapy 18 F-FDG uptake data with CT texture features into a radiomics

- model for radiation pneumonitis diagnosis. *Med Phys* 44(7):3686–3694. <http://doi.wiley.com/10.1002/mp.12282>
41. Yu W, Tang C, Hobbs BP, Li X, Koay EJ, Wistuba II et al (2017) Development and validation of a predictive radiomics model for clinical outcomes in stage I non-small cell lung cancer. *Int J Radiat Oncol*. <https://www.sciencedirect.com/science/article/pii/S0360301617340610>. Accessed 2 Jan 2018
 42. Rios Velazquez E, Parmar C, Liu Y, Coroller TP, Cruz G, Stringfield O et al (2017) Somatic mutations drive distinct imaging phenotypes in lung cancer. *Cancer Res* 77(14):3922–3930
 43. Aerts HJWL, Grossmann P, Tan Y, Oxnard GG, Rizvi N, Schwartz LH et al (2016) Defining a radiomic response phenotype: a pilot study using targeted therapy in NSCLC. *Sci Rep* 6:33860. <http://www.ncbi.nlm.nih.gov/pubmed/27645803>. Accessed 17 Oct 2016
 44. Xu Y, Hosny A, Zeleznik R, Parmar C, Coroller T, Franco I et al (2019) Deep learning predicts lung cancer treatment response from serial medical imaging. *Clin Cancer Res* 1–11. <http://clincancerres.aacrjournals.org/lookup/doi/10.1158/1078-0432.CCR-18-2495>
 45. Bogowicz M, Riesterer O, Ikenberg K, Stieb S, Moch H, Studer G et al (2017) Computed tomography radiomics predicts HPV status and local tumor control after definitive radiochemotherapy in head and neck squamous cell carcinoma. *Int J Radiat Oncol Biol Phys* 99(4):921–928. <https://doi.org/10.1016/j.ijrobp.2017.06.002>
 46. Jordan RC, Lingen MW, Perez-Ordóñez B, He X, Pickard R, Koluder M et al (2012) Validation of methods for oropharyngeal cancer HPV status determination in US cooperative group trials. *Am J Surg Pathol* 36(7):945–954. <http://insights.ovid.com/crossref?an=00000478-201207000-00002>
 47. Huang C, Cintra M, Brennan K, Zhou M, Colevas AD, Fischbein N et al (2019) Development and validation of radiomic signatures of head and neck squamous cell carcinoma molecular features and subtypes. *EBioMedicine* 1–11. <https://doi.org/10.1016/j.ebiom.2019.06.034>
 48. Leger S, Zwanenburg A, Pilz K, Zschaek S, Zöphel K, Kotzerke J et al (2018) CT imaging during treatment improves radiomic models for patients with locally advanced head and neck cancer. *Radiother Oncol* 1–8. <https://doi.org/10.1016/j.radonc.2018.07.020>
 49. van Dijk LV, Thor M, Steenbakkens RJHM, Apte A, Zhai TT, Borra R et al (2018) Parotid gland fat related Magnetic Resonance image biomarkers improve prediction of late radiation-induced xerostomia. *Radiother Oncol* 128(3):459–466. <https://doi.org/10.1016/j.radonc.2018.06.012>
 50. Yu H, Caldwell C, Mah K, Poon I, Balogh J, MacKenzie R et al (2009) Automated radiation targeting in head-and-neck cancer using region-based texture analysis of PET and CT images. *Int J Radiat Oncol* 75(2):618–625. <https://linkinghub.elsevier.com/retrieve/pii/S036030160900618X>. Accessed 4 Dec 2016
 51. Eary JF, O’Sullivan F, O’Sullivan J, Conrad EU (2008) Spatial heterogeneity in sarcoma 18F-FDG uptake as a predictor of patient outcome. *J Nucl Med* 49(12):1973–1979
 52. Vallières M, Freeman CR, Skamene SR, El Naqa I (2015) A radiomics model from joint FDG-PET and MRI texture features for the prediction of lung metastases in soft-tissue sarcomas of the extremities. *Phys Med Biol* 60(14):5471–5496. <http://iopscience.iop.org/article/10.1088/0031-9155/60/14/5471>
 53. Spraker MB, Wootton LS, Hippe DS, Ball KC, Peeken JC, Macomber MW et al (2019) MRI radiomic features are independently associated with overall survival in soft tissue sarcoma. *Adv Radiat Oncol* 4(2):413–421. <https://doi.org/10.1016/j.adro.2019.02.003>
 54. Crombè A, Périer C, Kind M, De Senneville BD, Le Loarer F, Italiano A et al (2018) T2-based MRI Delta-radiomics improve response prediction in soft-tissue sarcomas treated by neoadjuvant chemotherapy. *J Magn Reson Imaging* 1–14
 55. Peeken JC, Spraker MB, Knebel C, Dapper H, Pfeiffer D, Devecka M et al (2019) Tumor grading of soft tissue sarcomas using MRI-based radiomics. *EBioMedicine*. <https://linkinghub.elsevier.com/retrieve/pii/S2352396419305821>

56. Wang H, Nie P, Wang Y, Xu W, Duan S, Chen H et al (2019) Radiomics nomogram for differentiating between benign and malignant soft-tissue masses of the extremities. *J Magn Reson Imaging*. <https://onlinelibrary.wiley.com/doi/abs/10.1002/jmri.26818>
57. Ronneberger O, Philipp F, Brox T (2015) U-Net: convolutional networks for biomedical image segmentation. In: *MICCAI. Lecture notes in computer science*, vol 9351, pp 234–241
58. Kwon D, Acharya G, Agarwal M, Alam M, Amorim HA, Amrutkar A et al, Identifying the best machine learning algorithms for brain tumor segmentation, progression assessment, and overall survival prediction in the BRATS challenge. <http://arxiv.org/abs/181102629>
59. Kickingereder P, Isensee F, Tursunova I, Petersen J, Neuberger U, Bonekamp D et al (2019) Automated quantitative tumour response assessment of MRI in neuro-oncology with artificial neural networks: a multicentre, retrospective study. *Lancet* 20:728–740
60. Hu LS, Ning S, Eschbacher JM, Baxter LC, Gaw N, Ranjbar S et al (2017) Radiogenomics to characterize regional genetic heterogeneity in glioblastoma. *Neuro-Oncol.* 19:128–137
61. Molina-Romero M, Wiestler B, Gomez P, Menzel M, Menze B (2018) Deep learning with synthetic diffusion MRI data for free-water elimination in glioblastoma cases. *Miccai (Md)*
62. Lipkova J, Angelikopoulos P, Wu S, Alberts E, Wiestler B, Diehl C et al (2019) Personalized radiotherapy design for glioblastoma: integrating mathematical tumor models, multimodal scans and bayesian inference. *IEEE Trans Med Imaging (c):1*. <http://arxiv.org/abs/1807.00499>, <https://doi.org/10.1109/TMI.2019.2902044>
63. Collins GS, Reitsma JB, Altman DG, Moons KGM (2015) Transparent reporting of a multivariable prediction model for individual prognosis or diagnosis (TRIPOD): the TRIPOD statement. *Eur Urol* 67(6):1142–1151



Non-invasive Imaging Techniques: From Histology to In Vivo Imaging

25

Chapter of Imaging in Oncology

Thomas Bocklitz, Anja Silge, Hyeonsoo Bae, Marko Rodewald,
Fisseha Bekele Legesse, Tobias Meyer, and Jürgen Popp

Contents

25.1 Introduction.....	795
25.2 Raman Spectral Imaging/Spectroscopy.....	797
25.3 Coherent Raman Spectroscopy and Spectromicroscopy: CARS and SRS.....	800
25.4 Non-linear Processes (SHG, THG, TPEF).....	802
25.5 Fluorescence Lifetime Imaging (FLIM).....	804
25.6 Machine Learning for Spectral and Image Data.....	806
25.7 Summary.....	808
References.....	809

25.1 Introduction

All imaging techniques are based on interactions of particles or waves with the molecules or atoms of the sample.¹ Particles, which are employed for imaging applications, are photons of various energy or electrons, while ultrasound waves are examples of waves utilized for imaging applications. After the interaction took

¹Due to the wave–particle duality, the separation between particles and waves is not strict and an object can be described as wave or particle.

T. Bocklitz (✉) · A. Silge · H. Bae · M. Rodewald · F. B. Legesse · T. Meyer · J. Popp (✉)
University of Jena, IPC, Helmholtzweg 4, 07743 Jena, Germany
e-mail: thomas.bocklitz@uni-jena.de

J. Popp
e-mail: juergen.popp@uni-jena.de

place, either new generated particles/waves or missing/generated particles/waves are measured [1]. The particles and waves utilized for imaging can be diverse and have to be selected according to the samples, which should be imaged. For example, in ultrasound imaging, ultrasound waves are used and the not absorbed fraction of these waves is detected. To review all interactions and the corresponding imaging techniques is beyond the scope of this chapter. Therefore, we will focus on photon–matter interactions and we will emphasize interactions, which do not destroy the molecules of the sample [2]. The imaging methods, which are derived from these interactions, can be utilized for destruction-free tissue imaging and an application *in vivo* is possible. Because the photon–matter interaction is composition dependent, all of these imaging methods can be used to highlight the chemical composition of the sample in general or the spatial distribution of some molecules or molecular groups within the sample.

The photon–matter interactions can be classified into three broad categories: absorption-based, emission-based, and scattering-based interactions. In the former interaction type, a photon is absorbed and its energy is transferred to the molecule. Here, we restrict ourselves to interactions where the energy transfers an electron to an excited state.² After a given time, the excited state is destroyed and a part of the energy is emitted again often as photon. In contrast, scattering interactions are working instantaneously, e.g., without time delay. The scattering processes are generating a time-dependent dipole in the molecule, which subsequently radiates. All photon–matter interaction types and the respective imaging techniques can be further categorized by their dependency on the excitation intensity, which is called order of the process.

Besides the discussed intensity dependency of the used processes, two additional aspects are important for imaging techniques of bio-medical specimen. The first aspect is, if the measurement techniques result in (hyper)-spectral scans or in low-dimensional images. While the former is called spectral imaging, the latter is called band integration or imaging mode. This property has an implication on the information depth and on the measurement time, which are higher for spectral imaging. The second aspect is the need of specific labels for imaging. We decided to review methods, which do not necessarily need a label for measurement. Therefore, all the presented techniques can be applied under *in vivo* conditions, because all reviewed methods are also non-destructive [2].

In this chapter, we will give a short introduction and review the applications of the following scattering-based techniques: We will review spontaneous Raman spectral imaging, coherent anti-Stokes Raman scattering (CARS), stimulated Raman scattering (SRS), second-harmonic generation (SHG), and third-harmonic generation (THG). Additionally, we will present absorption-based techniques, two-photon excited fluorescence (TPEF), and fluorescence lifetime imaging (FLIM). In both fluorescence-based imaging techniques, we focus on the label-free version of the technique, where intrinsic fluorophores of the samples are visualized. We do not review IR-absorption-based imaging in this chapter because an *in vivo*

²It should be noted here that an absorption can occur also into vibrational states. The corresponding imaging technology IR-absorption-based imaging is not described in this section.

application seems challenging. At the end of the chapter, a short review of chemometric methods and machine learning techniques is given. These techniques are necessary if the presented imaging techniques should be used for diagnostics applications.

25.2 Raman Spectral Imaging/Spectroscopy

The first imaging technique to be reviewed is Raman spectral imaging, which is based on inelastic light scattering on the vibrational states of the molecules within the sample. Therefore, Raman spectral imaging belongs to the scattering techniques. This imaging technique is optimally suited to measure bio-medical specimen, because it is non-destructive and label-free. By combining Raman spectroscopy with a microscope an imaging modality is generated, which allows a non-invasive and label-free measurement of the composition of bio-medical specimen.

The initial step of the Raman spectral imaging is the irradiation of a sample with laser light. The backscattered radiation of the illuminated sample area is subsequently spectroscopically detected and the elastic (Rayleigh) scattered photons, which feature the same frequency as the incoming photons are filtered. Besides this elastic scattered light, only a small percentage of the scattered light is frequency shifted. The frequency shifts are specific for the molecular vibrations within the excited sample area and represent indirectly the molecular composition. The result of the spectroscopic measurement of the inelastic scattered light is called a Raman spectrum. The scattering process can cause frequency shifts to lower energies ω_{L-vib} compared to the incoming radiation ω_L , which is called Stokes–Raman scattering. Additionally, the scattering process causes frequency shifts to higher energies as well, which is called anti-Stokes Raman ω_{L+vib} scattering. The Raman imaging techniques described in the following are utilizing Stokes–Raman scattering, because this effect is the dominant effect at room temperature.

Raman scattering can be observed through a microscope applying an instrumental setup presented in Fig. 25.1a. The laser light ω_L enters the microscope through a small pinhole and is focused by a microscope objective to a spot size corresponding to the diffraction limit. Typically, the scattered light from the illuminated spot is collected by the same objective in backscattering geometry and the Raman scattered light ω_{L-vib} is selectively guided to the spectrometer coupled to the microscope. By applying a Raman microscopic setup, Raman spectra of spatially resolved image points are collected. The focused laser can be moved over the sample to achieve a Raman spectral scan or the sample can be moved via high-precision Piezo stages with respect to the laser focus to achieve a high-resolution scanning pattern. Due to the confocal pinhole, e.g., an aperture, only the light from the respective focal volume is detected, leading to a depth resolution (Fig. 25.1b). Raman imaging produces datasets of several thousand individual spectra. The subsequent computer-based Raman image generation technique can be best described by a hyperspectral data cube visualized in

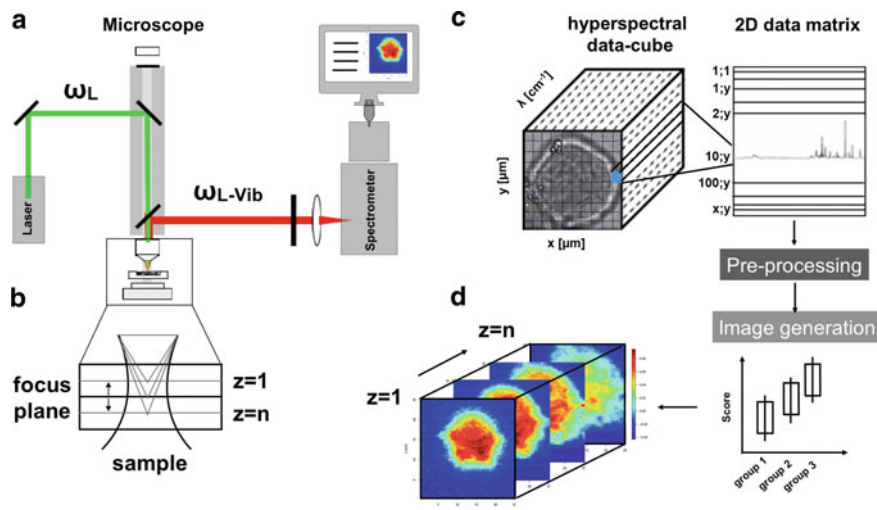


Fig. 25.1 Principles of the Raman spectral image generation. **a** Schematic of a confocal Raman microscope. The sample is probed by a laser ω_L focused through a microscope objective. The Stokes–Raman scattered light ω_{L-Vib} is guided to a spectrometer and detected. **b** Schematic of the confocal microscopic approach designed to probe spatially resolved image points. **c** Hyperspectral data cube, each pixel at position x, y represents a unique spectrum. **d** Data pipeline for feature extraction and generation of molecular images. See text for more details

Fig. 25.1c The x - and y -directions represent the spatial dimension of the image. The spectral dimension is plotted in z -direction. Within the data cube, each pixel at position x, y is containing a Raman spectrum. Therefore, each pixel contains the molecular fingerprint within the respective sampling volume on a given point x, y [3, 4].

The data analysis pipeline for such a Raman spectral data cube is described in Sect. 25.6 in detail, but it is roughly sketched here. To generate an image based on a Raman spectral scan, a reorientation of the hyperspectral data cube into a 2D data matrix is performed. In this matrix, every spectrum is pre-processed for a robust data analysis of the entire Raman scan. The pre-processing procedure includes calibration routines and corrections for artifacts and noise contributions. From every wavenumber slice of the data cube, a Raman false color image can be generated (Fig. 25.1d). In this manner, the spatial distribution of defined marker signals, e.g., Raman bands, can be visualized. For a deeper understanding, clustering algorithms as well as classification and regression methods are applied. The output of these multivariate methods can be utilized to calculate scores or to generate an image [5]. Besides image generation, the measured Raman spectra can be translated into bio-medical information, which can be further used by biologists or physicians. An example for such information would be the appearance of biomarkers, bio-chemical alterations, or the detection of concentration of substances. This translation is explained in Sect. 25.6 in more detail.

As described above, Raman spectroscopy detects the bio-chemical composition of the sample in a non-invasive, label-free, and non-destructive manner. Due to these properties, Raman spectroscopy is an ideal tool for investigations of bio-medical samples. Additionally, water is the optimal solvent for Raman spectral imaging allowing for in vivo measurements. Due to the mentioned properties, Raman spectral imaging can be applied to a broad range of biological specimens including yeast, plant, and eukaryotic cells [6]. In the field of cancer research, in vitro cell models are frequently studied by Raman spectral imaging to analyze sub-cellular structures and spectral changes induced by a treatment with chemotherapeutic agents or due to changed metabolisms [7–11]. Other studies explore intracellular lipid accumulations using Raman spectral imaging, which provided new insights into cancer progression [12]. The differentiation between cell types like normal and tumor cells circulating in body fluids based on Raman spectral signatures is another application in the field of cytopathology [13–15].

Tissue imaging and diagnostics enlarge the application field of Raman spectral imaging to clinically relevant questions. The Raman spectral imaging technique can support pathologists with information, which would need costly and time-consuming bio-assays or staining procedures, if they were measured classically. For example, the chemical contrast provided by Raman spectral imaging revealed a higher spectral contribution from nucleic acids analyzing high-grade brain tumor section in comparison with low-grade tumors [16]. For the detection of alterations in tissue, a spectral histopathology is utilized, which provides morphological and chemical details by visualizing the margins between normal and pathological tissue [17]. By using this spectral histopathology, chemical and molecular changes can be directly obtained from the examined samples and correlated with the histopathological gold standard hematoxylin and eosin staining (H&E) [18]. Briefly, the Raman spectral signatures of a specimen are linked to the pathologist's diagnosis and a classification model is constructed. The subsequent model can be applied for the differential diagnosis of new samples, e.g., the discrimination between normal and tumor regions. In [19], the adenoma–carcinoma sequence was studied using a Raman-based spectral histopathology. The introduced Raman-based workflow featured 100% mean sensitivity for the prediction of normal and tumor tissue compared to the gold standard diagnosis of an experienced pathologist [19, 20]. This spectral histopathology workflow was also tested for the Raman spectral imaging of brain metastases and a prediction of the primary tumor could be achieved with a high sensitivity [21]. A further development of the Raman spectral imaging concept is the use within a core needle biopsy system. The system allows an in situ tumor analysis by applying molecular Raman imaging and differentiates between healthy and tumor tissues before tissue harvesting [22]. Besides this core needle biopsy system, also direct Raman spectral measurements based on fibers can be performed. This procedure was successfully tested in a brain surgery to determine the tissue type shortly before resection of it [23].

25.3 Coherent Raman Spectroscopy and Spectromicroscopy: CARS and SRS

Linear Raman spectroscopy based imaging has a number of advantages as described above. Nevertheless, it has one major drawback, which is the low efficiency of the process leading to long measurement times. This drawback can be circumvented by non-linear Raman-spectroscopic techniques which can be applied for imaging a wide range of bio-medical samples. The most often applied imaging methods are coherent anti-Stokes Raman scattering (CARS) and stimulated Raman scattering (SRS) [24–29], which are third-order processes. Opposite to second-order processes, third-order processes can be induced in all materials, resulting in a wide range of potential applications. Both techniques, CARS and SRS, address one of the major limitations of linear Raman spectroscopy based methods, which is the low scattering cross section of spontaneous Raman scattering and the resulting low signal. This drawback leads to severe limitations in the field of imaging and results in the need for long acquisition times, constantly requiring compromises between image size and image resolution. “Spontaneous” in this context means that in linear Raman spectroscopy all individual molecular vibrations are excited independently of one another by a single laser frequency and don’t exhibit any phase relationship.

In coherent Raman spectroscopy, two frequencies, ω_p (p = pump) and ω_S (S = Stokes), instead of one Laser frequency are used and by matching the difference frequency (i.e., the beat-frequency) $\omega_p - \omega_S$ to a specific Raman active molecular vibration ω_R , those vibrations can be driven coherently. In CARS spectroscopy, a third photon can then be scattered in-elastically off this ensemble of coherently vibrating molecules. From simple energy conservation, it arises that $\omega_{as} = 2\omega_p - \omega_S$, as depicted in Fig. 25.2. Because of this blue-shift, the CARS signal does not interfere with fluorescence, which is a major drawback of Raman spectral imaging. Additionally, the CARS signal is significantly enhanced as compared to spontaneous Raman spectroscopy, opening the possibilities for fast imaging of large areas with high resolution and even video rate. These benefits come at the expense of a lower spectral information since a specific resonance has to be addressed by choosing ω_p and ω_S . To overcome this limitation, broadband laser sources for the Stokes beam are currently under development [30–32] enabling true spectral CARS and SRS imaging. Other drawbacks like the need to meet specific phase-matching criteria are no concerns under the tight focusing conditions of microscope lenses and therefore don’t cause inconvenience in the context of imaging [24]. The CARS signal is always accompanied by a non-resonant background according to Fig. 25.2 leading to a relatively poor contrast in CARS imaging. The non-resonant background is largely independent of the resonant signal and its effect is, therefore, more severe for modes with low Raman intensities.

In SRS spectroscopy, a photon of frequency ω_S stimulates the emission of a second photon of that frequency upon interaction with the virtual state reached by ω_p , if $\omega_p - \omega_S$ is equal to a vibrational resonance ω_R . This leads to an energy

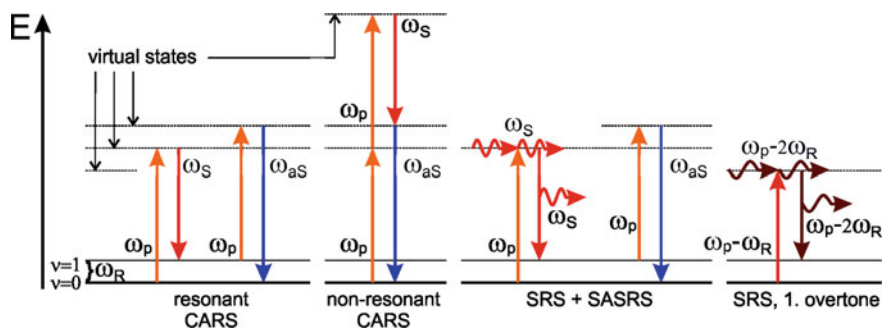


Fig. 25.2 Energy level diagram of different CARS and SRS processes. On the left side, the non-resonant and resonant CARS process is visualized. On the right side, the SRS processes are shown

transfer from the pump beam to the Stokes beam. Depending on whether the loss of intensity of the pump beam or the gain in intensity of the Stokes beam is detected, the technique is called stimulated Raman loss spectroscopy (SRLS) or stimulated Raman gain spectroscopy (SRGS). Since these losses or gains are usually small compared to the initial laser power, SRLS and SRGS rely on very sophisticated detection methods. In contrast to CARS, the generated signal is linearly dependent on the analyte concentration and has no intrinsic background, leading to easier quantification and better contrast in imaging applications.

Both CARS microscopy and SRS microscopy provide molecular information, which can be linked with pathological conditions [27, 33–37]. These molecular information are intrinsic to the respective sample, eliminating the need of introducing labels or staining techniques. Figure 25.3 shows an example of a CARS image of a human tissue sample. In this figure, three vibrational resonances ($2,845\text{ cm}^{-1}$, $2,930\text{ cm}^{-1}$, and $3,030\text{ cm}^{-1}$) were measured and the corresponding images are shown on the left. On the right, a combination of the individual images is shown enabling a non-invasive chemo-morphological characterization of the tissue. In this combination image nuclei are shown in green, the cytoplasm is represented by red, and water is shown in cyan. Thus, CARS and SRS might not only add to the repertoire of pathologists, but potentially even replace common staining techniques. The combination with computer-aided data analysis such as machine learning or deep learning [37–40] promises high diagnostic performance. The ultimate goal in this regard is fast and reliable on-site diagnostics, including *in vivo* imaging during surgery.

Typical samples for CARS and SRS microscopy are tissue sections and cell assays, but also bulk samples can be studied. The 3D imaging capabilities of the techniques vary depending on the sample type and the laser frequencies but usually

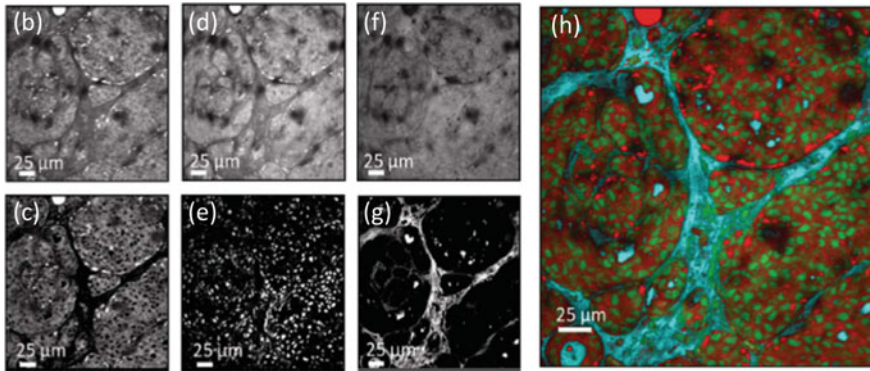


Fig. 25.3 Example CARS image of a human tissue sample. The small images on the top row left correspond to different mapped vibrations, namely, $2,845\text{ cm}^{-1}$, $2,930\text{ cm}^{-1}$ and $3,030\text{ cm}^{-1}$, while the images in the lower row show various difference images. The combined false color image on the right highlights nuclei in green, cytoplasm in red, and water in cyan Reprinted and adapted with permission from ref [33], Taylor and Francis Group, LLC

penetration depths of $100\text{--}200\text{ }\mu\text{m}$ are achievable [26] with some studies reporting even larger penetration depths by using adaptive optics [41]. The maximum resolution for a given set of wavelengths is slightly better than in diffraction-limited white light microscopy due to the non-linear nature of the processes. Nevertheless, a compromise between image size, acquisition speed, and resolution must be made. To meet clinical needs, considerable effort is put into miniaturizing of the devices as well as making them more reliable and easier to apply [42–45]. In view of the on-site diagnostic potential, many groups worldwide are currently working on integrating the technique into endoscopic devices.

Other imaging modalities like second-harmonic generation (SHG) and two-photon excited fluorescence (TPEF) are often seamlessly integrated into the same setup since the corresponding signals are generated by the strong laser fields as a side effect, thus providing additional valuable information. These techniques are described in the next section.

25.4 Non-linear Processes (SHG, THG, TPEF)

Like described in the previous chapter, non-linear phenomena, like CARS or SRS, occur, if high-intensity light is interacting with molecules in bio-medical samples. Besides these Raman-related processes, other non-linear processes are triggered by high intensities, like two-photon excited fluorescence (TPEF), second-harmonic generation (SHG), and third-harmonic generation (THG). If these processes are utilized in microscopic imaging techniques, a fast and non-invasive investigation of cells and tissue with high resolution and depth of penetration can be performed.

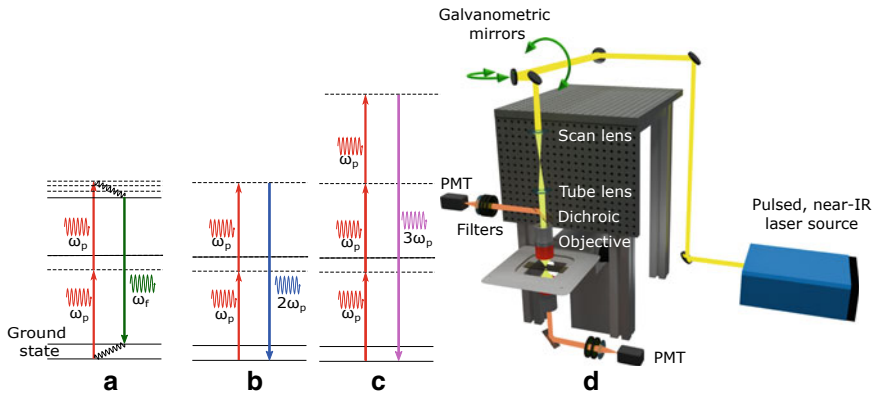


Fig. 25.4 Jablonski diagram of (a) two-photon excited autofluorescence (TPEF), (b) second-harmonic generation (SHG), and (c) third-harmonic generation (THG). (d) A laser scanning microscope (LSM) for non-linear imaging

These techniques also intrinsically offer optical sectioning and thus enable imaging inside thick tissue samples.

TPEF is a non-linear fluorescence technique in which two photons are simultaneously absorbed to excite a fluorophore which subsequently emits a fluorescence photon. Second-harmonic generation (SHG) is a second-order coherent scattering optical process wherein two photons of frequency ω are consumed to form a photon with twice the frequency 2ω of each incident photon. Analogous to SHG, in third-harmonic generation (THG) three photons of frequency ω are consumed to produce a photon with triple their frequency (3ω). The energy level diagrams for these particular non-linear processes are depicted in Fig. 25.4(a–c).

These non-linear techniques have been employed as a contrast mechanism for optical imaging purposes and have readily been incorporated into laser scanning microscopic (LSM) setups [46–48]. In LSMs, a laser beam is focused into a diffraction-limited spot and is raster scanned across the sample. The tight focusing and small temporal width of pulsed laser sources lead to high peak intensities strong enough to induce non-linear effects. A typical LSM used for non-linear imaging is shown in Fig. 25.4d. The output of a tunable pulsed near-IR laser source is coupled into the galvanometer mirrors of the LSM. The scanning module of the LSM consisting of a scan and tube lens directs the beam onto the rear aperture of the microscopic objective thereby translating the angular deflections of the galvanometer mirrors into lateral scanning of the focal spot in the focal plane. The signal generated is then collected either in the forward direction (using a condenser) or in epi-direction (with the focusing objective). Beam splitters are then needed to separate the generated signal from the excitation beam. The signal is eventually detected using a photomultiplier tube (PMT) after passing through a series of

detection filters, the selection of which is dependent on the specific non-linear imaging modality needed.

TPEF microscopy has been used to image a number of endogenous fluorophores in mammalian tissue. Among these imaged fluorophores are porphyrins, amino acids, macromolecular proteins like collagen and elastin as well as cofactors such as FAD and NAD(P)H [49]. Information about autofluorescence, particularly from NAD(P)H, has been found to be useful in differentiating between healthy and cancerous tissue [50]. In this regard, TPEF microscopy has been used for tumor tissue imaging and cancer diagnostics [49, 51].

SHG is a consequence of second-order non-linear susceptibility; therefore, the incoming photons need to simultaneously interact in a non-centrosymmetric media to generate the signal at the doubled frequency. Consequently, SHG maps the distribution of anisotropic biological structures with large hyper-polarizability [52, 53]. Most of the SHG signal in mammalian tissue arises from collagen, a highly ordered non-centrosymmetric structure [54]. The imaging of collagen with SHG has been demonstrated to provide information regarding the aging, healing, and tumor progression [51, 55].

Unlike the SHG process, THG is the result of third-order non-linear susceptibility, which is existing for all materials [48]. THG signal is dependent on optical heterogeneities of objects in the probed medium which allows the imaging of otherwise transparent samples [56]. For instance, THG has been used to image lipid droplets in the aqueous environment of cell cytoplasm using the significant differences in the optical properties of lipid and water [57]. THG also has found versatile applications in cell and tissue research within the context of cancer diagnostics [58].

In general, these non-linear techniques allow the characterization of morphological alterations associated with malignant transformation such as increase in nuclear size and nuclei-to-cytoplasm ratio and loss of epithelial architecture in a label-free manner [59, 60]. An example image of a larynx section combining CARS (red), SHG (blue), and TPEF (green) is shown in Fig. 25.5 together with a H&E stain of the same section [40]. It can be seen that different tissue structures can be differentiated either using the stained section or the multimodal image. In this image, fiber structures are highlighted by SHG in blue and the epithelium is characterized by an increased CARS signal in red.

25.5 Fluorescence Lifetime Imaging (FLIM)

Besides the above-described TPEF, also other fluorescence-based imaging techniques exist. The most prominent fluorescence-based imaging technique is one-photon fluorescence imaging, which is usually applied in combination with exogenous labeling. After labeling, the spatial distribution of the labels and hence the spatial distribution of the labeled structures can be visualized. Besides the fluorescence intensity of the fluorophores also the fluorescence lifetime features important information about the fluorophore of interest. Often fluorophores can be

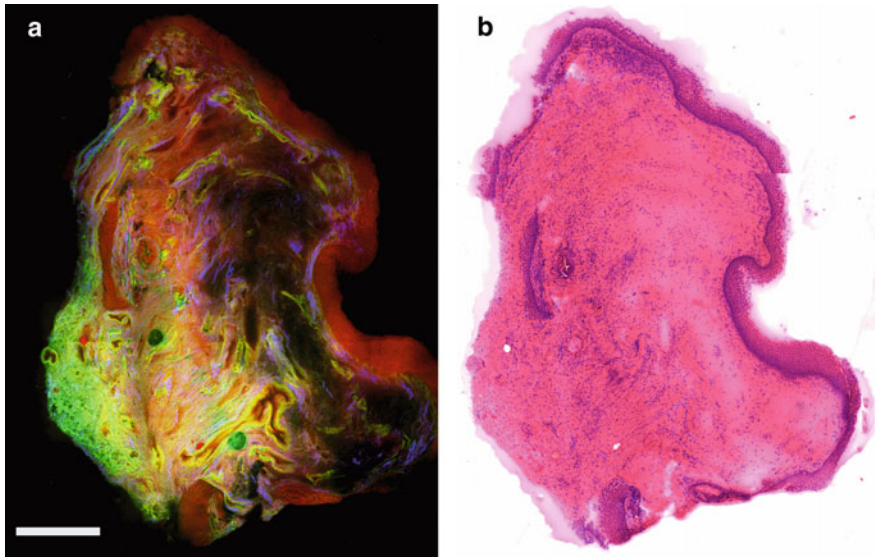


Fig. 25.5 Multimodal image of larynx tissue section (a) and the same section after a H&E stain (b) was applied. In the multimodal image, red, blue, and green represent CARS, SHG, and TPEF. The bar represents 500 μm and the images were taken from Heuke et al. [40]. See text for more details

differentiated by their lifetime even though a differentiation based on their spectrum is not possible leading to an increased multiplexing capability of fluorescence lifetime imaging (FLIM). The fluorescence lifetime of endogenous fluorophores in bio-medical samples typically varies in the range from hundreds to thousands of picoseconds [61, 62]. Because the fluorescence lifetime is sensitive to the local micro-environment of the fluorophore [63], FLIM can be used to monitor subtle changes in the chemical composition of tissues as it is induced by disease progression, e.g., by cancer growth [64, 65].

In general, two dominant methods are used for FLIM, the time-domain technique and the frequency-domain technique. In the time-domain technique, the fluorescence signal is acquired as function of time delay, while for the frequency-domain method the phase difference between excitation and fluorescence signal is measured [24]. There are many variations for each approach according to sampling techniques, detection techniques, and the type of microscope, which need to be selected according to the target application [24]. The most often applied (time-domain) FLIM detection techniques are time-correlated single photon counting (TCSPC) or the utilization of time-gated CCDs. Besides these FLIM concepts, also fiber-based FLIM measurement concepts exist [67]. Currently, two-photon FLIM (2p-FLIM) combining two-photon excited fluorescence (TPEF) and FLIM is a very active field of research [68]. 2p-FLIM setups are based on laser scanning microscopes equipped with ultrafast pulsed lasers in the near-infrared

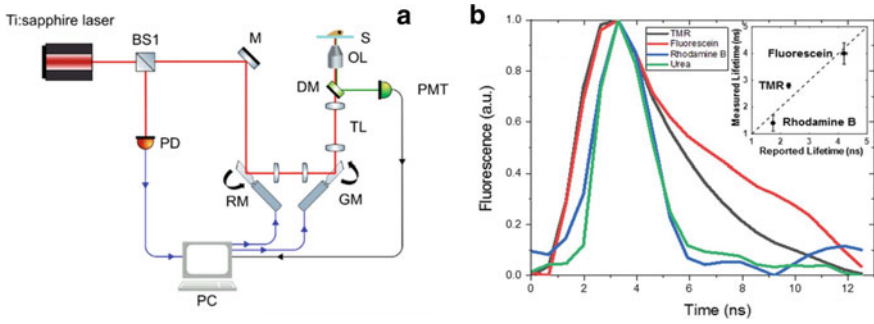


Fig. 25.6 2p-FLIM system design (a) and representative fluorescence decay curves of standard fluorescence dyes (b) Reprinted and adapted with permission from ref [66], OSA

range as excitation light source. This technique enables single-point fluorescence lifetime measurements with significantly reduced photo-bleaching and provides substantially deeper penetration into tissue samples.

An example of 2p-FLIM system and fluorescence decay curves from different dyes is described in Fig. 25.6 [66]. The beam is scanned by scanning mirrors (one is a resonant scanning mirror (RM) for the fast axis and another is a galvo-mirror (GM) for the slow axis) and focused on the sample through microscope optics. The synchronization of data sampling clock of the detected signal from PMT and laser pulse clock is precisely tuned to secure time-locked sampling of each dataset.

FLIM allows for imaging the metabolic activity within cells and tissues by differentiating quantitative shifts of NAD(P)H fluorescence lifetime. Thus, FLIM has the potential to study possible metabolic rearrangement in various pathologies, particularly in cancer [70]. Figure 25.7a [66] presents 2p-FLIM images of breast cancer cell lines of two different metabolic profiles, MDA-MB-231 and MCF-7, showing a dramatic increase in cytoplasmic NADH fluorescence lifetime in MCF-7 compared to MDA-MB-231. In addition to this, NADH fluorescence is clearly identified with shorter lifetime from elastin fluorescence of the seminiferous tubules.

Another example of FLIM is shown in Fig. 25.7b, which is a 3D image stack of fluorescence lifetime components and their fractional distribution for normal and pre-cancerous samples [69]. In the results, the distribution of each fluorophore at different layers can be estimated by visually color-coded images.

25.6 Machine Learning for Spectral and Image Data

The imaging modalities presented in the former sections result either in images or spectral scans. In order to use this data for diagnostic tasks, the data needs to be translated into medical relevant information. For images, this translation can be

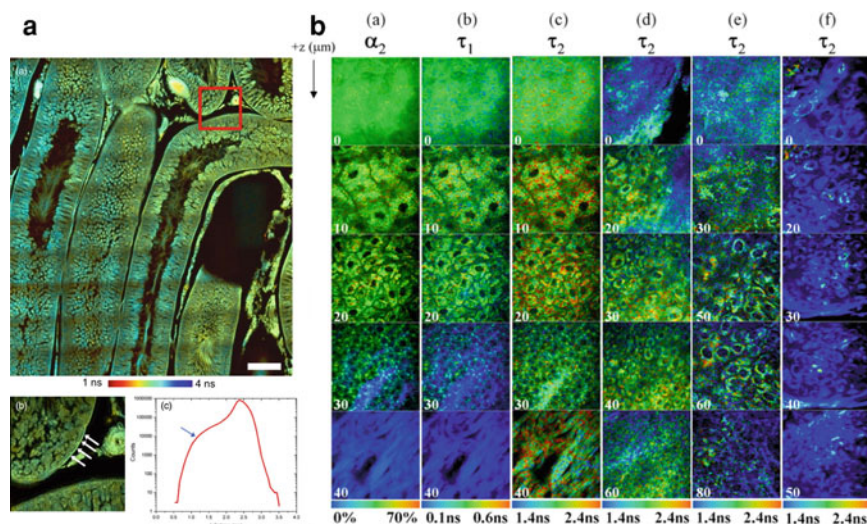


Fig. 25.7 FLIM images. **a** 2p-FLIM images. (a) tile image of size $2.5 \text{ mm} \times 2.5 \text{ mm}$ of a rat testis sample. (b) Zoom area of indicated area in (a). The white arrow corresponds to elastin fluorescence. (c) represents the lifetime histogram of (a). Blue arrow indicates the lifetime of elastin, while large peak corresponds to the lifetime of NADH. Reprinted and adapted with permission from ref [66], OSA. **b** FLIM images of normal and pre-cancerous hamster cheek pouch. While panel (a–c) represents normal tissue, (d–f) shows altered tissue. The column (a) represents α_2 , e.g., the contribution of the long lifetime component, while column (b) shows the short lifetime component τ_1 . The long lifetime τ_2 is visualized in panel (c–f). The image size is $100 \mu\text{m} \times 100 \mu\text{m}$ Reprinted and adapted with permission from ref [69], SPIE

done—in principle—by manual inspection. For higher dimensional spectral scans, this approach is not possible. Even though the manual inspection is possible for image data, an automatic approach is advisable for both data types, because such an approach can convert tiny spectral features and image structures into medical relevant information. To do so, either machine learning or chemometrics is applied [71]. Both techniques are not differing much, but the term “machine learning” [72] is often used for images, while “chemometrics” [73] is utilized for spectral data analysis models. We will stick to this terminology throughout the section.

If chemometrics is utilized to analyze spectral data, like the described Raman spectra (Sect. 25.2), CARS spectra, and SRS spectra (Sect. 25.3), automatic data pipelines to analyze the spectra are constructed. Such a data pipeline combines data pretreatment, data pre-processing, and analysis methods. For the Raman spectra, the pretreatment consists of a spike correction, wavenumber, and intensity calibration [74]. In the case of CARS spectra, additional phase retrieval methods have to be applied [75]. Thereafter, baseline correction, filtering, and normalization have to be combined [76] to pre-process and standardize the data. Analysis methods can be applied afterwards to the pretreated and pre-processed spectra. The analysis

methods can be either factor analysis methods, clustering, or classification methods. While factor methods can be utilized for a dimension reduction, clustering methods can be used to highlight different groups in the data without knowing them. Classification methods can be utilized to model group differences in a supervised manner. After training of such a classification model, it can be used as diagnostic model [72, 73].

Machine learning can be utilized to analyze image data and like described above a data analysis pipeline is constructed [71]. Image data can be derived in the case of TPEF, SHG, THG, FLIM, CARS, and SRS microscopies. For these image data, a pre-processing pipeline including flat-field correction [77], filtering and scaling needs to be applied. In the case of FLIM, the images, which should be analyzed, need to be generated first. This image generation is done by various fitting procedures, either in a global or individual manner [78]. The pre-processed or generated images are then analyzed using machine learning. In case of classical machine learning, first image features are extracted from the images, which are subsequently analyzed with the chemometric techniques described above [71]. The other option is the application of deep learning techniques, which perform an intrinsic feature extraction and modeling. Deep learning is constructing a highly parametrized model, which can be used as feature extraction method in combination with a classification model [72, 73].

25.7 Summary

In this chapter, we described imaging methods, which can be used to study bio-medical samples. We restricted ourselves to imaging modalities, which are non-destructive and can be used without adding a label, but leading to a quantification of the bio-chemical composition of the sample. In that way, the presented imaging techniques can be utilized to measure bio-medical samples and the information can be used for diagnostic applications or to gain deeper insight into the processes ongoing in the sample. We described a number of measurement techniques, namely, Raman spectral imaging, CARS, SRS, TPEF, FLIM, 2p-FLIM, SHG, and THG and shortly reviewed the application of these techniques for measurements of bio-medical samples with a focus on cancer diagnostics or oncological applications. At the end, we described how chemometrics and machine learning are utilized to extract bio-medical information from the generated data. The extracted information can be subsequently used for diagnostic applications or to gain a deeper insight into the bio-medical samples.

References

1. Popp J, Tuchin VV, Chiou A, Heinemann S (eds) (2011) Handbook of biophotonics. Basics and techniques, vol 1. Wiley-VCH
2. Vogler N, Heuke S, Bocklitz TW, Schmitt M, Popp J (2015) Multimodal imaging spectroscopy of tissue. *Annu Rev Anal Chem* 8:359–387
3. Abramczyk H, Brozek-Pluska B (2013) Raman imaging in biochemical and biomedical applications. diagnosis and treatment of breast cancer. *Chem Rev* 113(8):5766–5781
4. Stewart S, Priore RJ, Nelson MP, Treado PJ (2012) Raman imaging. *Annu Rev Anal Chem* 5:337–360
5. Bocklitz TW, Guo S, Ryabchykov O, Vogler N, Popp N (2016) Raman based molecular imaging and analytics: a magic bullet for biomedical applications!? *Anal Chem* 88:133–151
6. Petry R, Schmitt M, Popp J (2003) Raman spectroscopy—a prospective tool in the life sciences. *Chem Phys Chem* 4:14–30
7. Czamara K, Majzner K, Selmi A, Baranska M, Ozaki Y, Kaczor A (2017) Unsaturated lipid bodies as a hallmark of inflammation studied by Raman 2d and 3d microscopy. *Sci Rep* 7:40889
8. Heraud P, Marzec KM, Zhang Q-H, Yuen WS, Carroll J, Wood BR (2017) Label-free in vivo Raman microspectroscopic imaging of the macromolecular architecture of oocytes. *Sci Rep* 7(1):8945
9. Yildirim T, Matthäus C, Press AT, Schubert S, Bauer M, Popp J, Schubert US (2017) Uptake of retinoic acid-modified pmma nanoparticles in lx-2 and liver tissue by Raman imaging and intravital microscopy. *Macromol Biosci* 17(10):1700064
10. Bräutigam K, Bocklitz T, Schmitt M, Rösch P, Popp J (2013) Raman spectroscopic imaging for the real-time detection of chemical changes associated with docetaxel exposure. *Chem Phys Chem* 14:550–553
11. Mignolet A, Wood BR, Goormaghtigh E (2018) Intracellular investigation on the differential effects of 4 polyphenols on mcf-7 breast cancer cells by Raman imaging. *Analyst* 143(1):258–269
12. Tirinato L, Liberale C, Di Franco S, Candeloro P, Benfante A, La Rocca R, Potze L, Marotta R, Ruffilli R, Rajamanickam VP et al (2015) Lipid droplets: a new player in colorectal cancer stem cells unveiled by spectroscopic imaging. *Stem cells* 33(1):35–44
13. Dochow S, Krafft C, Neugebauer U, Bocklitz T, Henkel T, Albert J, Popp J (2011) Tumor cell identification by means of Raman spectroscopy in combination with optical traps. *Lab Chip* 11:1484–1490
14. Tolstik T, Marquardt C, Matthäus C, Bergner N, Bielecki C, Krafft C, Stallmach A, Popp J (2014) Discrimination and classification of liver cancer cells and proliferation states by Raman spectroscopic imaging. *Analyst* 139(22):6037–6044
15. Ramoji A, Neugebauer U, Bocklitz T, Förster M, Kiehnopf M, Bauer M, Popp J (2012) Toward a spectroscopic hemogram: Raman spectroscopic differentiation of the two most abundant leukocytes from peripheral blood. *Anal Chem* 84(12):5335–5342
16. Krafft C, Belay B, Bergner N, Romeike B, Reichart R, Kalf R, Popp J (2012) Advances in optical biopsy—correlation of malignancy and cell density of primary brain tumors using raman microspectroscopic imaging. *Analyst*
17. Diem M, Mazur A, Lenau K, Schubert J, Bird B, Miljković M, Krafft C, Popp J (2013) Molecular pathology via IR and Raman spectral imaging. *J Biophoton* 6(11–12):855–886
18. Krafft C, Schmitt M, Schie IW, Cialla-May D, Matthäus C, Bocklitz T, Popp J (2017) Label-free molecular imaging of biological cells and tissues by linear and nonlinear raman spectroscopic approaches. *Angewandte Chemie International Edition* 56(16):4392–4430
19. Vogler N, Bocklitz T, Salah FS, Schmidt C, Bräuer R, Cui T, Mireskandari M, Greten F, Schmitt M, Stallmach A, Petersen I, Popp J (2015) Systematic evaluation of colorectal tissue diagnostics based on the statistical analysis of Raman spectra. *J Biophoton* 9:533–541
20. Bocklitz T, Salah FS, Vogler N, Heuke S, Chernavskaia O, Schmidt C, Waldner M, Greten FR, Bräuer R, Schmitt M, Stallmach A, Petersen I, Popp J (2016) Pseudo-HE images

- derived from CARS/TPEF/SHG multimodal imaging in combination with Raman-spectroscopy as a pathological screening tool. *BMC Cancer* 16(1):1–11
21. Bergner N, Bocklitz T, Romeike BFM, Reichart F, Kalff R, Krafft C, Popp J (2012) Identification of primary tumors of brain metastases by Raman imaging and support vector machines. *Chemom Intell Laboratory Syst* 117:224–232
 22. Desroches J, Jermyn M, Pinto M, Picot F, Tremblay M-A, Obaid S, Marple E, Urmev K, Trudel D, Soulez G et al (2018) A new method using Raman spectroscopy for in vivo targeted brain cancer tissue biopsy. *Sci Rep* 8(1):1792
 23. Jermyn M, Mok K, Mercier J, Desroches J, Pichette J, Saint-Arnaud K, Bernstein L, Guiot M-C, Petrecca K, Leblond F (2015) Intraoperative brain cancer detection with Raman spectroscopy in humans. *Sci Transl Med* 7(274):274ra19–274ra19
 24. Popp J, Tuchin VV, Chiou A, Heinemann SH (2013) *Handbook of biophotonics*. Wiley-VCH Verlag GmbH and Co. KGaA, Weinheim, Germany
 25. Müller M, Zumbusch A (2007) Coherent anti-Stokes Raman scattering microscopy. *Chemphyschem: Eur J Chem Phys Phys Chem* 8(15):2156–2170
 26. Evans CL, Xie XS (2008) Coherent anti-Stokes Raman scattering microscopy: chemical imaging for biology and medicine. *Annu Rev Anal Chem (Palo Alto, Calif.)* 1:883–909
 27. Krafft Ch, Dietzek B, Popp J (2009) Raman and CARS microspectroscopy of cells and tissues. *Analyst* 134(6):1046–1057
 28. Rodriguez LG, Lockett SJ, Holtom GR (2006) Coherent anti-Stokes Raman scattering microscopy: a biological review. *Cytometry Part: J Int Soc Anal Cytol*, 69(8):779–791
 29. Zumbusch A, Holtom GR, Xie XS (1999) Three-dimensional vibrational imaging by coherent anti-Stokes Raman scattering. *Phys Rev Lett* 82(20):4142–4145
 30. Pohling C, Bocklitz T, Duarte AS, Emmanuello C, Ishikawa MS, Dietzeck B, Buckup T, Uckermann O, Schackert G, Kirsch M, Schmitt M, Popp J, Motzkus M (2017) Multiplex coherent anti-Stokes Raman scattering microspectroscopy of brain tissue with higher ranking data classification for biomedical imaging. *J Biomed Opt* 22:22–25
 31. Parekh SH, Lee YJ, Aamer KA, Cicerone MT (2010) Label-free cellular imaging by broadband coherent anti-Stokes Raman scattering microscopy. *Biophys J* 99(8):2695–2704
 32. Bocklitz T, Meyer T, Schmitt M, Rimke I, Hoffmann F, von Eggeling F, Ernst G, Guntinas-Lichius O, Popp J (2018) Comparison of hyperspectral coherent Raman scattering microscopies for biomedical applications. *APL Photonics* 3:092404
 33. Lee M, Downes A, Chau Y-Y, Serrels B, Hastie N, Elflick A, Brunton V, Frame M, Serrels A (2015) In vivo imaging of the tumor and its associated microenvironment using combined CARS/2-photon microscopy. *Intravital* 4(1):e1055430
 34. Cui S, Zhang S, Yue S (2018) Raman spectroscopy and imaging for cancer diagnosis. *J Healthc Eng* 2018:8619342
 35. Freudiger CW, Min W, Saar BG, Lu S, Holtom GR, He C, Tsai JC, Kang JX, Xie XS (2008) Label-free biomedical imaging with high sensitivity by stimulated Raman scattering microscopy. *Science (New York, N.Y.)* 322(5909):1857–1861
 36. Lu F-K, Calligaris D, Olubiyi OI, Norton I, Yang W, Santagata S, Xie XS, Golby AJ, Agar NYR (2016) Label-free neurosurgical pathology with stimulated Raman imaging. *Cancer Res* 76(12):3451–3462
 37. Weng S, Xu X, Li J, Wong STC (2017) Combining deep learning and coherent anti-stokes Raman scattering imaging for automated differential diagnosis of lung cancer. *J Biomed Opt* 22(10):1–10
 38. Chernavskaja O, Heuke S, Vieth M, Friedrich O, Schürmann S, Atreya R, Stallmach A, Neurath MF, Waldner M, Petersen I, Schmitt M, Bocklitz T, Popp J (2016) Beyond endoscopic assessment in inflammatory bowel disease: real-time histology of disease activity by non-linear multimodal imaging. *Sci Rep* 6:29239
 39. Rodner E, Bocklitz T, von Eggeling F, Ernst G, Chernavskaja O, Popp J, Denzler J, Guntinas-Lichius O (2019) Fully convolutional networks in multimodal nonlinear microscopy images for automated detection of head and neck carcinoma: a pilot study. *Head Neck* 41(1):116–121

40. Heuke S, Chernavskaja O, Bocklitz T, Legesse FB, Meyer T, Akimov D, Dirsch O, Ernst G, von Eggeling F, Petersen I, Guntinas-Lichius O, Schmitt M, Popp J (2016) Multimodal nonlinear microscopic investigations on Head and Neck squamous cell carcinoma—toward surgery assisting frozen section analysis. *Head Neck* 38(10):1545–1552
41. Wright AJ, Poland SP, Girkin JM, Freudiger CW, Evans CL, Xie XS (2007) Adaptive optics for enhanced signal in cars microscopy. *Opt Express* 15(26):18209–18219
42. Lombardini A, Mytskaniuk V, Sivankutty S, Andresen ER, Chen X, Wenger J, Fabert M, Joly N, Louradour F, Kudlinski A, Rigneault H (2018) High-resolution multimodal flexible coherent raman endoscope. *Light: Sci Appl* 7(1):aaa8870
43. Lukic A, Dochow S, Bae H, Matz G, Latka I, Messerschmidt B, Schmitt M, Popp J (2017) Endoscopic fiber probe for nonlinear spectroscopic imaging. *Optica* 4(5):496
44. Haohua T, Boppart SA (2014) Coherent anti-Stokes Raman scattering microscopy: overcoming technical barriers for clinical translation. *J Biophotonics* 7(1–2):9–22
45. Zirak P, Matz G, Messerschmidt B, Meyer T, Schmitt M, Popp J, Uckermann O, Galli R, Kirsch M, Winterhalder MJ, Zumbusch A (2018) Invited article: a rigid coherent anti-Stokes Raman scattering endoscope with high resolution and a large field of view. *APL Photonics* 3(9):092409
46. Denk W, Strickler JH, Webb WW (1990) Two-photon laser scanning fluorescence microscopy. *Science* 248(4951):73–76
47. Hellwarth R, Christensen P (1974) Nonlinear optical microscopic examination of structure in polycrystalline ZnSe. *Opt Commun* 12(3):318–322
48. Barad Y, Eisenberg H, Horowitz M, Silberberg Y (1997) Nonlinear scanning laser microscopy by third harmonic generation. *Appl Phys Lett* 70(8):922–924
49. Zipfel WR, Williams RM, Christie R, Nikitin AY, Hyman BT, Webb WW (2003) Live tissue intrinsic emission microscopy using multiphoton-excited native fluorescence and second harmonic generation. *Proc Natl Acad Sci* 100(12):7075–7080
50. Richards-Kortum R, Sevick-Muraca E (1996) Quantitative optical spectroscopy for tissue diagnosis. *Annu Rev Phys Chem* 47(1):555–606
51. Meyer T, Guntinas-Lichius O, von Eggeling F, Ernst G, Akimov D, Schmitt M, Dietzek B, Popp J (2013) Multimodal nonlinear microscopic investigations on head and neck squamous cell carcinoma: toward intraoperative imaging. *Head Neck* 35(9):E280–E287
52. Fine S, Hansen WP (1971) Optical second harmonic generation in biological systems. *Appl Opt* 10(10):2350–2353
53. Pavone FS, Campagnola PJ (2013) Second harmonic generation imaging. CRC Press
54. Mohler W, Millard AC, Campagnola PJ (2003) Second harmonic generation imaging of endogenous structural proteins. *Methods* 29(1):97–109
55. Cicchi R, Vogler N, Kapsokalyvas D, Dietzek B, Popp J, Pavone FS (2013) From molecular structure to tissue architecture: collagen organization probed by SHG microscopy. *J Biophotonics* 6:129–142
56. Müller M, Squier J, Wilson KR, Brakenhoff GJ (1998) 3d microscopy of transparent objects using third-harmonic generation. *J Microsc* 191(3):266–274
57. Débarre D, Supatto W, Pena A-M, Fabre A, Tordjmann T, Combettes L, Schanne-Klein M-C, Beaurépaire E (2006) Imaging lipid bodies in cells and tissues using third-harmonic generation microscopy. *Nat Methods* 3(1):47
58. Weigel B, Bakker G-J, Friedl P (2016) Third harmonic generation microscopy of cells and tissue organization. *J Cell Sci* jcs-152272
59. Heuke S, Vogler N, Meyer T, Akimov D, Kluschke F, Röwert-Huber H-J, Lademann J, Dietzek B, Popp J (2013) Multimodal mapping of human skin. *Br J Dermatol* 169(4):794–803
60. Adur J, Carvalho HF, Cesar CL, Casco VH (2014) Nonlinear optical microscopy signal processing strategies in cancer. *Cancer Inf* 13:CIN-S12419
61. Richards-Kortum R, Sevick-Muraca E (1996) Quantitative optical spectroscopy for tissue diagnosis. *Annu Rev Phys Chem* 47:555–606

62. Elson D, Requejo-Isidro J, Munro I, Reavell F, Siegel J, Suhling K, Tadrous P, Benninger R, Lanigan P, McGinty J, Talbot C, Treanor B, Webb S, Sandison A, Wallace A, Davis D, Lever J, Neil M, Phillips D, Stamp G, French P (2004) Time-domain fluorescence lifetime imaging applied to biological tissue. *Photochem Photobiol Sci: Off J Eur Photochem Assoc Eur Soc Photobiol* 3(8):795–801
63. Lakowicz JR (2010) *Principles of fluorescence spectroscopy*. 3 edn [4. corr. print.] edn. Springer, New York
64. Das BB, Liu F, Alfano RR (1997) Time-resolved fluorescence and photon migration studies in biomedical and model random media. *Rep Prog Phys* 60(2):227
65. Dowling K, Dayel MJ, Lever MJ, French PMW, Hares JD, Dymoke-Bradshaw AKL (1998) Fluorescence lifetime imaging with picosecond resolution for biomedical applications. *Opt Lett* 23(10):810–812
66. Bower AJ, Li J, Chaney EJ, Marjanovic M, Spillman DR, Boppart SA (2018) High-speed imaging of transient metabolic dynamics using two-photon fluorescence lifetime imaging microscopy. *Optica* 5(10):1290–1296
67. Liu J, Sun Y, Qi J, Marcu L (2012) A novel method for fast and robust estimation of fluorescence decay dynamics using constrained least-squares deconvolution with laguerre expansion. *Phys Med Biol* 57(4):843
68. Valeur B (2001) *Molecular fluorescence*. Wiley-VCH Verlag GmbH, Weinheim, FRG
69. Skala MC, Riching KM, Bird DK, Gendron-Fitzpatrick A, Eickhoff Jens, Eliceiri KW, Keely PJ, Ramanujam N (2007) In vivo multiphoton fluorescence lifetime imaging of protein-bound and free nicotinamide adenine dinucleotide in normal and precancerous epithelia. *J Biomed Opt* 12(2):024014
70. Blacker TS, Mann ZF, Gale JE, Ziegler M, Bain AJ, Szabadkai G, Duchon MR (2014) Separating nadh and nadph fluorescence in live cells and tissues using flim. *Nat Commun* 5:3936
71. Bocklitz T, Schmitt M, Popp J (2014) Ex-vivo and in-vivo optical molecular pathology. In: *Image processing—chemometric approaches to analyze optical molecular images*, Wiley-VCH Verlag GmbH and Co. KGaA, pp 215–248
72. Bishop CM (2011) *Pattern recognition and machine learning*. Information Science and Statistics, Springer
73. Tauler R, Walczak B, Brown SD (eds) (2009) *Comprehensive chemometrics: chemical and biochemical data analysis*. Elsevier
74. Dörfer T, Bocklitz T, Tarcea N, S M, Popp J (2011) Checking and improving calibration of Raman spectra using chemometric approaches. *ZPC (Zeitschrift für Physikalische Chemie)* 225:753–764
75. Vartiainen EM, Rinia HA, Muller M, Bonn M (2006) Direct extraction of Raman line-shapes from congested CARS spectra. *Opt Express* 14(8):3622–3630
76. Bocklitz T, Walter A, Hartmann K, R P, Popp J (2011) How to pre-process Raman spectra for reliable and stable models? *Anal Chim Acta* 704:47–56
77. Chernavskaja O, Bocklitz T, Meyer T, Vogler N, Akimov D, Heuke S, Guo S, Heintzmann R, Popp J (2017) Correction of mosaicking artefacts in multimodal images caused by uneven illumination. *J Chemom* 31(6):e2901
78. Suhling K, Hirvonen LM, Levitt JA, Chung PH, Tregidgo C, Le Marois A, Rusakov DA, Zheng K, Ameer-Beg S, Poland S et al (2015) Fluorescence lifetime imaging (flim): basic concepts and some recent developments. *Med Photonics* 27:3–40



Stephanie Schipmann-Miletić and Walter Stummer

Contents

26.1	Introduction.....	814
26.2	Conventional Intraoperative Imaging.....	814
26.2.1	Ultrasound.....	814
26.2.2	Neuronavigation.....	815
26.2.3	Intraoperative MRI (iMRI).....	817
26.3	Fluorescence-Guided Brain Surgery.....	817
26.3.1	5-Aminolevulinic Acid (5-ALA).....	818
26.3.1.1	5-Aminolevulinic Acid in High-Grade Gliomas.....	818
26.3.1.2	5-Aminolevulinic Acid in Recurrent High-Grade Gliomas.....	819
26.3.1.3	5-Aminolevulinic Acid in Low-Grade Gliomas.....	821
26.3.1.4	5-Aminolevulinic Acid in Other Brain Tumors.....	822
26.3.2	Fluorescein.....	823
26.3.2.1	Critical Points/Problems with the Usage of Fluorescein.....	824
26.3.2.2	Fluorescein-Guided Surgery for High-Grade Gliomas.....	824
26.3.2.3	Fluorescein-Guided Surgery for Cerebral Metastases.....	825
26.3.2.4	Fluorescein-Guided Surgery for Other CNS Tumors.....	825
26.3.3	Indocyanine Green (ICG).....	826
26.4	Novel Techniques.....	827
26.4.1	Tumor-Targeted Alkylphosphocholine Analogs for Intraoperative Visualization.....	827
26.4.2	Confocal Endomicroscopy.....	828
26.4.3	Raman Spectroscopy.....	828
26.4.4	BLZ-100 Fluorescence-Guided Brain Tumor Surgery.....	829
26.5	Combination of Different Techniques for Intraoperative Imaging.....	829
26.6	Future Directions.....	830
	References.....	833

S. Schipmann-Miletić (✉) · W. Stummer
Department of Neurosurgery, University Hospital Münster, Albert-Schweitzer-Campus 1,
Building A1, 48149 Münster, Germany
e-mail: Stephanie.schipmann@ukmuenster.de

26.1 Introduction

Over the past decades, brain tumor surgery has undergone large changes as medical technology and surgical experience have grown. A milestone was the introduction of the microscope and microsurgical techniques by Yasargil [129]. The paradigm of brain tumor surgery has shifted from removing tumor that is obvious to the human eye to resection of malignant cells beyond the scope of the microscope and visual inspection aided by technological innovations. In the treatment of gliomas, an independent factor for better outcome regarding overall survival (OS) and progression-free survival (PFS) that can be directly influenced by the neurosurgeon is the extent of resection (EOR) [7, 58, 65, 96, 115]. It is well known that gliomas infiltrate surrounding brain parenchyma in a manner that is not perceived by the human eye even with the aid of the surgical microscope and infiltrated brain often cannot be differentiated from normal brain tissue based on tactile features.

Therefore, several attempts have been undertaken during the last decades to develop techniques for better tumor visualization and identification, aiming at higher EOR. Among them are techniques such as neuronavigation, intraoperative ultrasound, intraoperative magnetic resonance imaging (iMRI), and, more recently, fluorescence-guided surgery (FGS). Especially the latter has taken the process of intraoperative tissue visualization to another level with the potential of true real-time imaging of tumor without any interruptions to surgery for identifying tumor. Recently, other highly precise techniques have been introduced and are being translated into clinical medicine, promising even more exact delineation of tumor tissue, such as confocal microscopy, Raman spectroscopy, or targeted fluorescence opening the frontiers to real-time intraoperative molecular and cellular imaging.

All these tools have improved the ability of the surgeon to identify tumor tissue and distinguish tumor from normal brain parenchyma. In this chapter, the different techniques with their applicability in brain tumor surgery and their benefits and limitations will be discussed.

26.2 Conventional Intraoperative Imaging

Conventional intraoperative imaging techniques like neuronavigation and ultrasound are the basis for most cases in brain tumor surgery and have been well integrated into the operative setting in neurosurgery.

26.2.1 Ultrasound

Intraoperative ultrasound provides an easy, cost-effective, and rapidly available method for localization of lesions prior to durotomy and residual tumor during tumor resection. It is a dynamic method that enables visualization of tumor borders and adjacent normal brain structures and anatomy [76]. It has been shown that use

of ultrasound has the potential to increase the grade of resection and thus improving outcome [93]. Ultrasound is more effective with cystic and heterogenous lesions with different echogenicities from the cortex. Some navigation systems use intraoperatively acquired data from the ultrasound to update navigational data to avoid the limitations of brain shift [67]. However, peritumoral edematous tissue also appears hyperechogenic and can be confused with brain tumor, potentially resulting in resections being carried into functional brain and thus potentially endangering the patient's neurological function [92] (Fig. 26.1a).

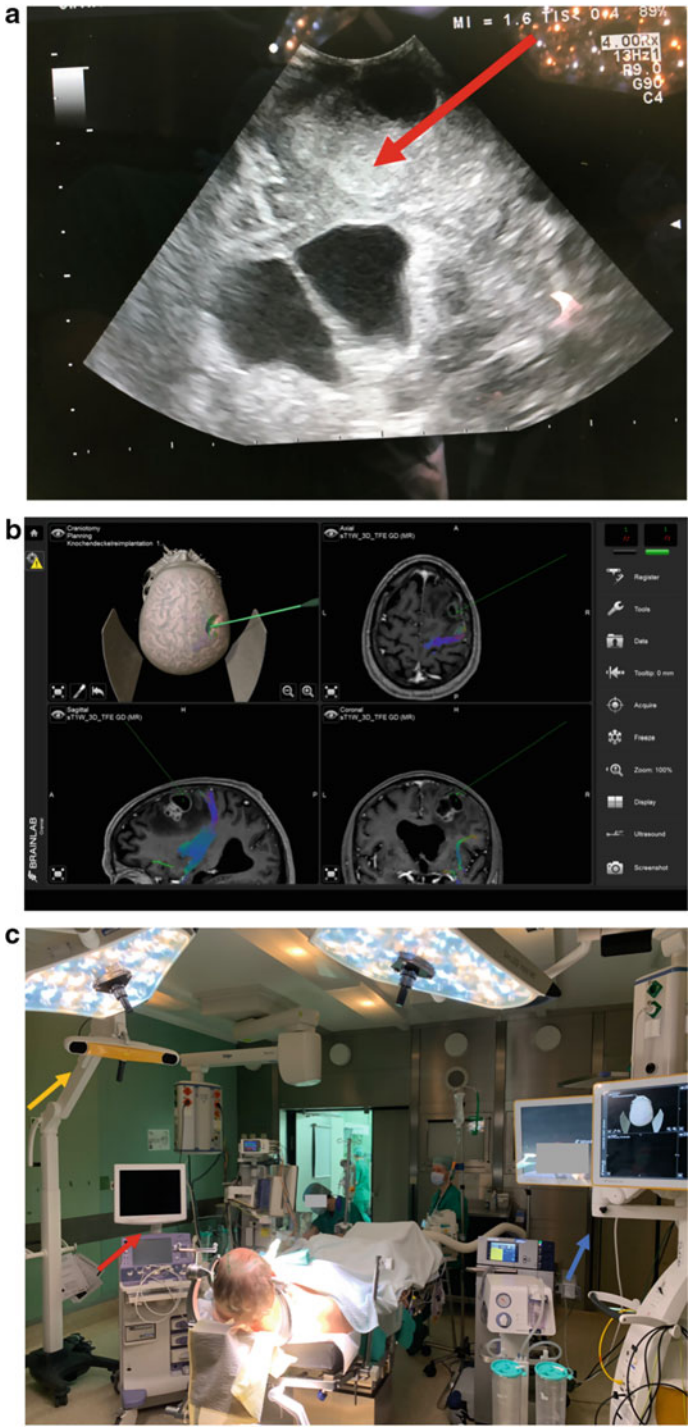
26.2.2 Neuronavigation

Neuronavigation has become a ubiquitously available and indispensable tool for the surgical treatment of brain tumors. Neuronavigation is based on three-dimensional preoperative radiological imaging data, which is merged with the patient's anatomy by registration [104]. The navigation system consists of a reference arm attached to the head clamp that is fixed to the surgical table. Infrared cameras track the position of the probe relative to the fixed reference arm and preoperative imaging is shown on the screen with the real-time intraoperative position of the probe [76]. Imaging acquired preoperatively, such as CT, MRI, and PET, can be entered into the neuronavigation software and provides the neurosurgeon with intraoperative almost real-time localization and orientation. Anatomical information and data on the extent of the tumor and its relation to adjacent structures can be gained from the system, leading to higher surgical accuracy and precision for the resection of brain tumors [104].

Furthermore, functional data can be incorporated into the neuronavigation system. Functional MRI (fMRI) can help identifying localization of functional brain regions, e.g., for language and motor functions [138].

Diffusion tensor imaging (DTI) is based on the preferential diffusion of water in the direction of white matter tracts within the central nervous system [3, 76]. These data can be added to the navigation system to give detailed information on subcortical fiber tracts, e.g., the corticospinal tract, that could be at risk during tumor resection [25]. In addition, neuronavigation is very useful for planning the surgical approach and craniotomy [42].

However, there are distinct limitations using neuronavigation. A major issue is loss of accuracy due to intraoperative brain shift caused by positioning, application of mannitol, drainage of cerebral spinal fluid (CSF), and bulk tumor resection, as navigational systems rely on preoperative imaging. A further limitation is that most navigational systems display the information used during surgery on a screen outside the surgical field, forcing the surgeon to draw his attention away from the surgical field to a screen. However, modern neuronavigational systems enable injecting navigational information into the display within the operating microscope (Fig. 26.1b, c).



- ◀ **Fig. 26.1** Techniques for intraoperative imaging. **a** Ultrasound. The lesion can be seen transdural and can be clearly distinguished from normal brain structures (red arrow). **b** MRI: Patient with fiber tracking (pyramid tract) for intraoperative orientation and planning of surgical approach. **c** Setting in the operating room with simultaneous use of ultrasound (red arrow), neuronavigation with display (blue arrow) and camera (yellow arrow)

26.2.3 Intraoperative MRI (iMRI)

Intraoperative MRI (iMRI) has been introduced in the 1990s [124] and has since undergone several improvements. iMRI has the propensity for providing images during surgery and for updating the information on the navigation system to correct for changes in anatomy due to brain shift [41]. In addition, iMRI can be used to identify residual tumor and to improve the extent of tumor resection. A randomized controlled trial evaluating the benefit of iMRI in glioma surgery performed by Senft et al. demonstrated a gross total resection (GTR) rate of 96% in the iMRI group versus 68% in the control group, operated with conventional microsurgery [106]. Especially, in the treatment of low-grade gliomas (LGG) several studies demonstrated the potential of iMRI, with a 30–60% of return to surgery after initial resection to address residual tumor identified on iMRI [55, 107, 108].

Despite the increasing use of iMRI, there are disadvantages as this technology comes with high costs, is time-consuming, and prolongs the duration of surgery and anesthesia. iMRI cannot be used for patients with ferromagnetic implants. Furthermore, the frequent application of gadolinium might lead to extravasation in the resection cavity, impeding interpretation of imaging.

26.3 Fluorescence-Guided Brain Surgery

For neurosurgeons, the ability to differentiate abnormal from normal tissues is of utmost importance in order to perform safe and effective surgery. In this regard, fluorescence-guided surgery (FGS) has shown to be extremely helpful for visualization and delineation of pathological tissues. In principle, FGS is based on the administration of optical imaging agents to patients prior or during surgery that are selectively accumulated in tumor tissues. FGS was first described for neurosurgery by George E. Moore in 1947, who showed that glioma and meningioma cells could be better visualized by fluorescence after intravenous application of fluorescein [70]. This ability of real-time intraoperative detection of tumor tissue has further developed throughout recent years with the great advantage of intraoperative visualization of tumor tissue independent from neuronavigation, which is often affected by brain shift [28]. Besides fluorescein, two further agents have been introduced into the field of neurosurgery, 5-aminolevulinic acid (5-ALA) [119] and indocyanine green (ICG) [83].

26.3.1 5-Aminolevulinic Acid (5-ALA)

5-aminolevulinic acid (5-ALA) is a natural metabolite in the hemoglobin pathway. 5-ALA is metabolized into protoporphyrin IX (PpIX), a strongly fluorescent precursor of heme. Glioma cells selectively take up 5-ALA, convert this to PpIX, resulting in tumor cell fluorescence [14, 117]. Fluorescence can be visualized by coupling the surgical microscope to a xenon light source that is capable of switching between white and violet-blue light (wavelength: 370–440 nm) and adding an emission filter in order to visualize the red tumor fluorescence at a peak of 635 and 704 nm [117]. Besides the visualization of fluorescence, the filters enable sufficient background discrimination in order to perform major parts of surgery under conditions suitable for visualizing fluorescence. At present, all modern surgical microscopes offer adjuncts with the ability to visualize PpIX fluorescence. 5-ALA (brand name Gliolan® in the EU or Gleolan® in the US) is administered as an oral solution at a dose of 20 mg/kg body weight 3 h before induction of anesthesia. Plasma clearance is achieved within 2 h after administration [118]. Peak fluorescence can be expected after about 6–8 h, with fluorescence beginning to become visible after about 3 h [48, 117, 120]. Typically, high-grade gliomas show solid red fluorescence with a slightly pink fluorescence at the tumor margins, representing the tumor-infiltrating zone [113]. Several studies demonstrate toxicological safety. At most, 5-ALA leads to transient skin phototoxicity or temporarily elevated liver enzymes [114, 128].

5-ALA is the most widely studied fluorescent agent worldwide and has been approved as the only optical imaging agent by both the U.S. Food and Drug Administration (FDA) and the European Medicines Agency (EMA) for real-time visualization of malignant tissue during glioma surgery. Next to its clinical application in malignant gliomas, several studies confirm benefit for resection in other primary and metastatic brain tumors, such as meningiomas, brain metastases, and pediatric brain tumors [19, 24, 38, 46, 71, 141].

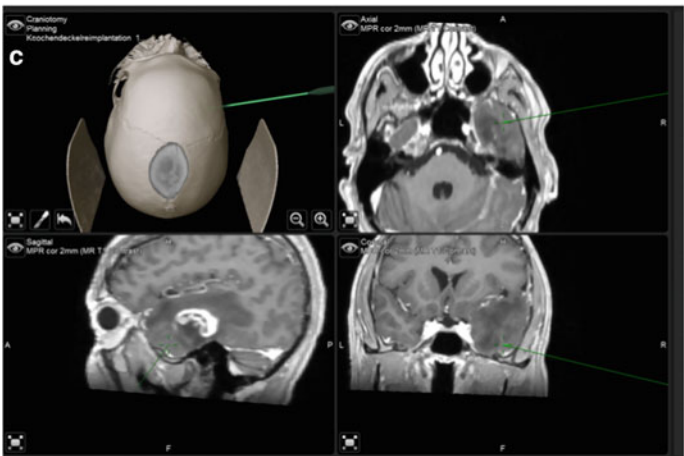
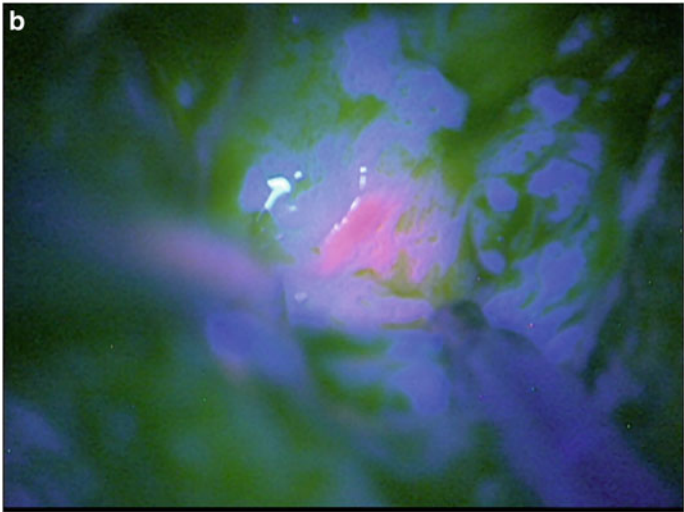
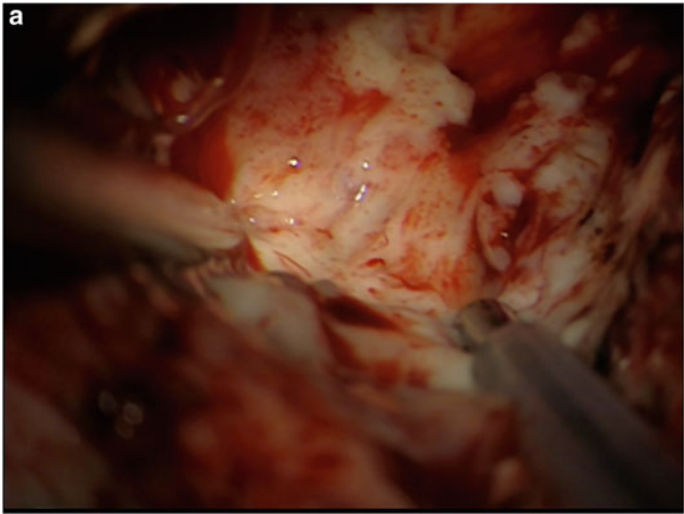
26.3.1.1 5-Aminolevulinic Acid in High-Grade Gliomas

High-grade gliomas (HGGs) are the most frequent primary malignant brain tumors in adults and are known to be highly infiltrative tumors [10]. Glioblastoma is characterized by a poor prognosis with median survival of 15 months and a 2-year survival rate of 17.4% [52, 78]. Typically, the solid tumor core is surrounded by normal brain with invading tumor cells and no histologically distinct border. Despite the fact that surgery is never curative, given the infiltrating nature of high-grade gliomas, the benefit of complete resection of contrast-enhancing tumor regarding overall survival has been shown in several studies, all supporting maximal safe resection [7, 58, 65, 96, 115]. Identification and complete resection of contrast-enhancing tumor only by the unenhanced visual impression or haptic information is almost impossible to achieve [75].

5-ALA can aid in the visualization of glioma tissue. The first clinical usage was reported in 1998 in a cohort of nine high-grade glioma patients, revealing a high sensitivity of 85% and specificity of 100% for detection of malignant tissue [119]. A phase III randomized controlled multicenter trial revealed that 5-ALA enables more complete resections of contrast-enhancing tumor (65% of patients assigned to the 5-ALA group compared with 36% of those assigned to the conventional surgery white light group, $p < 0.001$), leading to improved 6-month progression-free survival (41.0% in the 5-ALA group versus 21.1% in the white light group) [114]. Since this study, 5-ALA has been widely used in resection of high-grade glioma. The resection rates of 65% initially reported in that study have improved over the last years due to a gain in experience and the addition of modern intraoperative monitoring and brain mapping methodology, allowing safe resections even in eloquent regions. At present, resection rates between 80 and 100% are reported [13, 18]. Strong 5-ALA fluorescence shows a strong correlation with contrast enhancement on MRI, while marginal, weaker pink fluorescence often exceeds the contrast-enhancing margins, representing the infiltration zone [121] (Fig. 26.2). Strong correlations between histological grading, features of malignancy, a higher Ki-67/MIB-1 index, and the intensity of 5-ALA fluorescence were observed [37, 90].

26.3.1.2 5-Aminolevulinic Acid in Recurrent High-Grade Gliomas

In recurrent high-grade gliomas, several small non-randomized patient cohorts suggest that completeness of resection of contrast-enhancing tumor also results in better survival [82, 89, 122]. Therefore, 5-ALA-guided resection also seems to be an attractive approach for recurrent glioma, as corroborated by several studies. Mean rates of complete resection of 91% have been described using 5-ALA [32]. In addition, longer OS was associated with 5-ALA FGS in recurrent gliomas compared to patients undergoing repeat surgery without 5-ALA [32]. However, the utility of 5-ALA might be impacted by post-therapeutic tissue changes such as gliosis, necrosis, and vascular hyalinization [6, 17, 126], affecting specificity and sensitivity. Positive fluorescence was reported in the vast majority of recurrent high-grade gliomas and was regarded a good predictor for the presence of tumor [32, 45, 73, 133]. However, in contrast to the findings in primary glioma the absence of fluorescence is not essentially a reliable marker for absence of tumor [59]. In some cases, no active tumor tissue could be diagnosed despite visible fluorescence linked to reactive tissue changes or inflammation [45, 133]. In summary, the use of 5-ALA appears to be feasible in recurrent gliomas, keeping in mind possible false positive or negative fluorescence and the not yet understood impact of adjuvant tumor treatment on the degree of fluorescence.



- ◀ **Fig. 26.2** 5-ALA-guided resection of glioblastoma. **a** Tumor under white light, delineation between tumor and normal tissue is almost impossible. **b** Tumor under violet light, showing a clear and solid fluorescence in tumor tissue and a vague fluorescence at the border and infiltrating zone. **c** Screenshot from neuronavigation, demonstrating the area of the above-taken images. 5-ALA fluorescence goes beyond the borders of the contrast enhancement on MRI, enabling a higher extent of resection

26.3.1.3 5-Aminolevulinic Acid in Low-Grade Gliomas

There is clear evidence that more extensive resection of low-grade gliomas (LGG) results in improved outcomes [31, 94, 110]. Consequently, the aim of surgery is maximal safe tumor resection. A challenge in surgery of LGG is the fact that these tumors often show only slight differences in texture and consistency compared to normal brain. LGG often demonstrate histological heterogeneity with circumscribed areas of malignant transformation (anaplastic foci) [81]. Most LGG do not reveal visible 5-ALA fluorescence; however, several studies demonstrated correlations between 5-ALA fluorescence and patchy/faint contrast enhancement on preoperative MRI, areas with higher metabolic activity in PET and higher proliferation rate [26, 39, 140]. Consequently, the use of 5-ALA enables intraoperative identification of anaplastic foci, more precise histopathological diagnoses, reducing the risk of histopathological undergrading and enabling allocation of patients to proper adjuvant treatment. At present, the use of 5-ALA in suspected LGG is recommended in case of patchy or faint contrast enhancement on MRI and in case of ^{18}F -FET-PET hot spots with a standardized uptake value (SUV) greater than 1.9 [39] (Fig. 26.3).

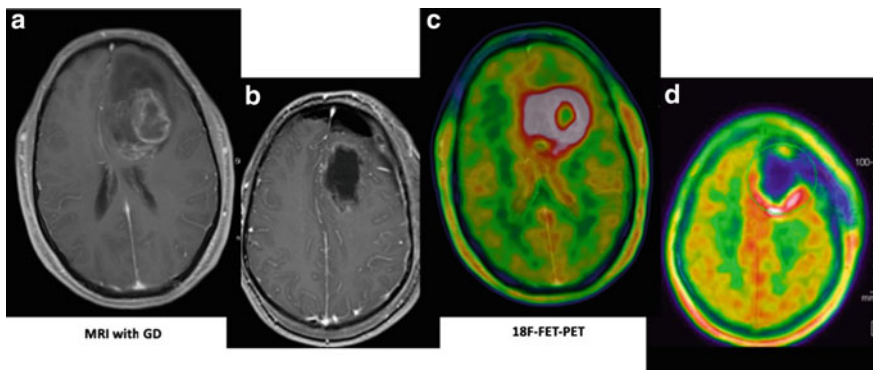


Fig. 26.3 a MRI T1+Gd before and after surgery (a and b) with corresponding F18-FET-PET imaging pre- and postoperatively (c and d). The enhanced metabolism of the tumor can be visualized using PET imaging. Images are reprinted with permission of the Department of Nuclear Medicine, University Hospital Münster, Germany

26.3.1.4 5-Aminolevulinic Acid in Other Brain Tumors

In addition to the wide use of 5-ALA for glioma surgery, several studies demonstrated the utility of 5-ALA as a surgical adjunct for resection of other brain tumors. In meningioma surgery, 5-ALA fluorescence can help to identify tumor infiltration of dura, brain, bone, and satellite lesions beyond the tumor bulk allowing to maximize resection [19, 69, 71, 134, 141] (Fig. 26.4).

Cerebral metastases have a high local recurrence rate even after assumed complete surgical resection, often due to residual tumor tissue [46]. In order to improve the degree of resection, some groups studied the use of 5-ALA for resection of cerebral metastases. Altogether, 5-ALA fluorescence has been observed in only half of all studied cerebral metastases [47, 131]. Studies suggested that 5-ALA does not allow reliable visualization of residual tumor after resection and so far, there are no known predictors for positive 5-ALA fluorescence in metastasis [46, 131].

Spinal cord ependymomas frequently show strong 5-ALA fluorescence and this technique was shown to be useful for differentiating tumor from normal tissue [38].

In the pediatric brain tumor population, promising results have been found regarding the use of 5-ALA for resection of astrocytomas, glioblastomas, ependymomas, and medulloblastomas [24, 91, 105, 116].

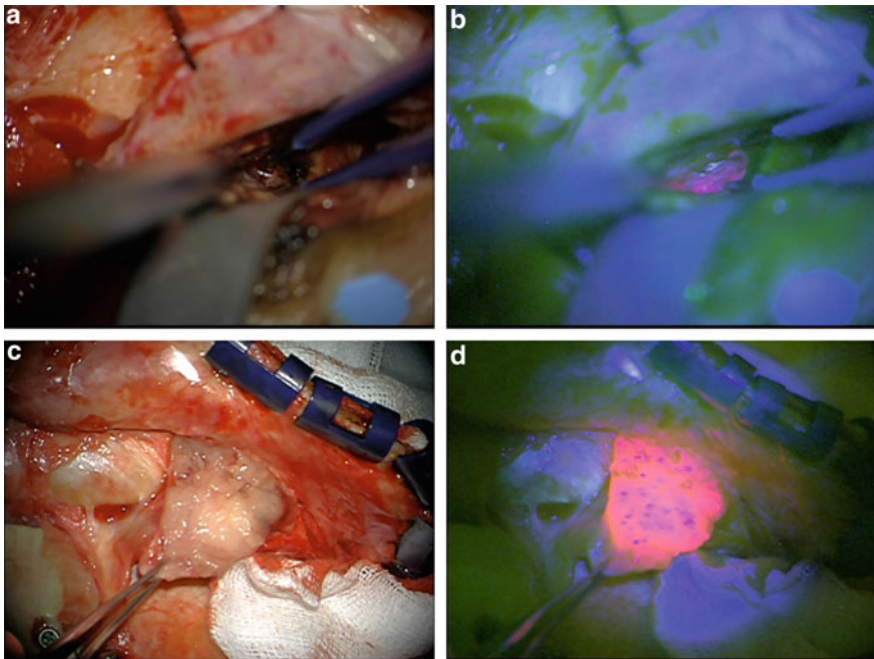


Fig. 26.4 Usage of 5-ALA in meningioma. After dural opening, 5-ALA-induced fluorescence of tumor tissue is visible (a, c: white light, b, d: violet light)

In cases of cerebral lymphoma, application of 5-ALA appears to help in obtaining representative biopsy samples as most lymphomas show positive 5-ALA fluorescence [142, 143].

In addition, 5-ALA fluorescence-guided surgery has been described in single cases for resection of hemangioblastoma [132], subependymomas [5], and germ cell tumors [127].

5-ALA appears to bear potential for the resection of different non-glioma brain tumors in individual cases; however, only case reports are available so far, with the difficulty of drawing conclusions at this time. Prospective studies are warranted to evaluate the benefit and full value of 5-ALA-guided surgery in these tumor entities.

26.3.2 Fluorescein

Fluorescein sodium has been discovered almost 150 years ago and is nowadays mostly used in ophthalmology for detection of corneal abrasions and for retinal angiography [85, 98]. A possible utility for neurosurgery was first suggested by George E. Moore in 1947, showing that glioma and meningioma cells could be differentially visualized by fluorescence after intravenous application of fluorescein [70]. Fluorescein is considered as a robust, inexpensive, and safe fluorescent biomarker with characteristic yellow-green fluorescence. Its peak absorption spectrum occurs at 465–490 nm with emission peaks at 500–530 nm. Fluorescein fluorescence can also be discriminated under white light [57, 109]. After intravenous administration, fluorescein is distributed systemically through the bloodstream and extravasates into regions with increased vascular permeability, abnormal vasculature, and neovascularization [70]. Under normal circumstances, circulating fluorescein is excluded from normal brain tissue by the blood–brain barrier (BBB) [100]. In case of disruption of the BBB, for example, in tumors, fluorescein accumulates in the extracellular space of tumor tissue and can be visualized under yellow-filtered (560 nm) light [57].

A surgical microscope enabling visualization of fluorescein was introduced for resection of high-grade glioma [57]. Nowadays, a variety of fluorescent filters are available, e.g., the YELLOW 560 system (Carl Zeiss) or the FL560 System (Leica Microscopes).

Fluorescein can also be visualized as a yellow dye under the white light of surgical microscopes at high concentrations. However, lower concentrations of fluorescein can be used when using specialized microscopes equipped with appropriate emission filters. A dose of 3–5 mg/kg body weight is administered intravenously after induction of anesthesia [22, 29]. Fluorescein is eliminated renally and mostly free of side effects apart from leading to transient discoloration of skin and urine after administration. Single cases of anaphylactic shock have been reported [23].

26.3.2.1 Critical Points/Problems with the Usage of Fluorescein

Recent studies have confirmed fluorescein staining not to be tumor-cell-specific [22]. Additionally, fluorescein mainly marks areas with BBB breakdown, which are somewhat, but not strictly related to tumor tissue. Thus, fluorescein serves as an excellent marker of edema propagation [111, 112]. There is no real consensus on timing of administration of fluorescein before surgery and dosage in the current literature, although this is critical due to the fact that extravasation and distribution of this agent follow a certain time course regarding plasma fluorescein contents, perfusion of brain, and finally extravasation. After a half-life of 4 and $\frac{1}{2}$ h, intravascular fluorescein will slowly subside, resulting in prolonged staining of normal perfused brain, while being extravasated and traveling with edema through peritumoral tissue, raising the danger of staining non-tumorous tissue [111]. Consequently, the timing of surgery is critical and duration of craniotomy and preparation before reaching the lesion have to be considered. A further aspect confounding applicability of fluorescein is the problem with surgical injury of normal brain tissue, which will lead to unselective extravasation of fluorescein from the bloodstream along the cut margins.

Consequently, further studies are required to evaluate fluorescein in the context of tumor histology, timing of administration, illumination, tissue perfusion, and edema. In summary, from the current point of view, the abovementioned confounders have to be considered using a fluorophore that does not have a specific tumor–fluorophore interaction and is rather a marker of BBB integrity.

26.3.2.2 Fluorescein-Guided Surgery for High-Grade Gliomas

With the success of 5-ALA-guided glioma resection regarding the improvement of the extent of resection, several studies have attempted to evaluate the use of the more inexpensive agent fluorescein regarding its usefulness in improving EOR in malignant gliomas [1, 11, 74, 88, 98]. The groups of Schebesch and Acerbi reported a gross total resection rate of 80% in their series of $n = 35$ and $n = 20$, respectively, high-grade glioma patients using YELLOW 560 filter [1, 100] (Fig. 26.5). Other studies reported GTR in up to 100% of cases using fluorescein, and additionally showing that intraoperative fluorescence correlated well with contrast enhancement on MRI scans [2, 22]. Sensitivity and specificity analyses after administration of low-dose fluorescein revealed a sensitivity of 94% and a specificity of 90% [1]. In 2011, a phase II trial (FLUOGLIO) started to evaluate the safety and efficacy of fluorescein-guided glioma surgery, showing that this approach is feasible, safe [2]. However, the current evidence for usage of fluorescein in high-grade gliomas is still limited to small cohort studies with inherent case selection issues. No further prospective randomized controlled trials are available that investigate the possible benefit of fluorescein in terms of survival and EOR.

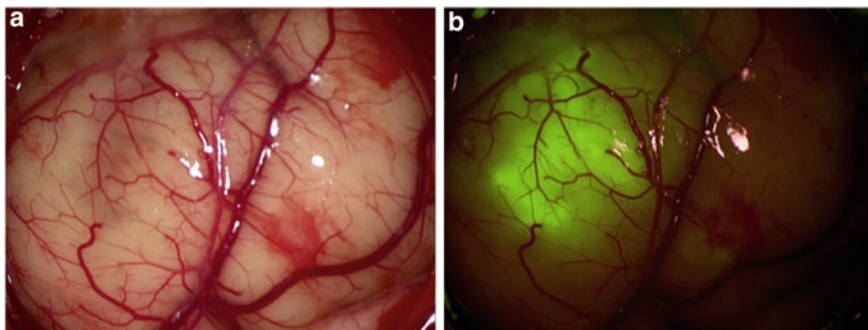


Fig. 26.5 Fluorescein-guided resection of malignant glioma. Intraoperative view of a malignant glioma under white light (a) and after application of fluorescein under YELLOW 560 filter (b) before corticotomy. Reprinted with permission [35]

Interestingly, the simultaneous usage of fluorescein with 5-ALA has been investigated for the resection of high-grade glioma. This concept results in better background discrimination from circulating fluorescein while retaining the selectivity of 5-ALA-induced porphyrins for discriminating tumor [123].

26.3.2.3 Fluorescein-Guided Surgery for Cerebral Metastases

GTR of cerebral metastases is known as an independent predictor of patient survival [44]. Consequently, intraoperative imaging that helps in increasing EOR is in focus to improve outcome. The benefit of fluorescein in improving extent of resection (EOR) has been shown for metastases, yielding 83–100% GTR. In comparison with traditional white light microscopy, GTR has been reported to be achieved in 54–74% [29, 35, 80].

26.3.2.4 Fluorescein-Guided Surgery for Other CNS Tumors

As in 5-ALA-guided surgery, more and more reports on fluorescein-guided resection of other CNS tumors are becoming available. However, so far, there are only studies with small patient numbers and without standardized protocols for the administration of fluorescein. Fluorescein has been described as helpful for resection of convexity meningioma, enabling visualization and differentiation of meningioma and its dural tail from normal brain and dura [16]. Furthermore, fluorescein might help to enhance contrast between normal brain structures and cranial nerves and meningiomas in skull base surgery [15]. Primary central nervous system (CNS) lymphomas are typically treated with radio- and chemotherapy. However, a surgical biopsy is usually required. Fluorescein has been shown to help visualizing lymphomas by delineating malignant tissue from normal brain [29, 99].

26.3.3 Indocyanine Green (ICG)

Indocyanine green (ICG) is a tricarboyanine with fluorescence in the near-infrared range with a peak emission at 780 nm and excitation at 810 nm. ICG was approved by the Food and Drug Administration (FDA) in 1959, providing information of liver and cardiocirculatory functions, and later widely used for ophthalmologic applications [12, 87]. The group of Raabe et al. was the first to describe the use of ICG for visualization of blood flow in cerebral vessels exposed in the surgical microscope field, a technique now known as ICG videoangiography [83]. ICG videoangiography was originally used to provide augmentive information on cerebrovascular pathologies and especially used for vascular cases (aneurysms and arteriovenous malformations) [30, 84]. In addition, the utility of ICG to help understand the angioarchitecture of hypervascular tumors, e.g., in case of hemangioblastomas and to identify surrounding vessels has been described. This helps in understanding the angioarchitecture related to the tumor and hereby increasing the safety of the procedure. Following the intravenous administration of 0.2–0.5 mg ICG/kg, NIR light (range 700–850 nm) is used to excite the dye, and a NIR camera—integrated into the latest generations of surgical microscopes—captures the emission at 780–950 nm of the molecules flowing through the vessels.

The use of ICG is safe with an incidence of adverse reactions ranging from 0.05% for severe side effects such as hypotension, arrhythmia, anaphylactic shock to 0.2% for mild or moderate side effects such as nausea, skin eruption, and pruritus [83].

A growing body of research has led to the utilization of ICG in neuro-oncological surgery as well. One technique has been referred to as second-window ICG (SWIG), a procedure in which higher doses up to 5.0 mg/kg are administered to the patient up to 24 h in advance of surgery with intraoperative imaging [61]. Within the 24 h, ICG accumulates in the tumor tissue due to enhanced permeability within the tumor and selective retention effects [125]. It is assumed that ICG binds to serum albumin and can pass through the disrupted blood–brain barrier. ICG is retained possibly due to a lack of drainage [61, 125]. However, the exact mechanisms of retention are not entirely clear.

Unlike 5-ALA-PpIX and fluorescein, which emit fluorescence within the visible spectrum, ICG's excitation and emission are in the near-infrared (NIR) region of the spectrum [137]. These properties enable visualization of ICG fluorophore situated deeper in the tissue since longer wavelength excitation and emission light undergo less absorption than shorter wavelength [137]. Therefore, ICG permits visualization of tumors up to a depth of 2 cm and through the dura, facilitating planning of dural opening and corticectomy. On the other hand, NIR cameras are necessary and for the moment ICG fluorescence can only be visualized on the video screen and not directly within the cavity during surgery.

Studies revealed ICG fluorescence to be detectable in contrast-enhancing gliomas and have discussed ICG's value for the detection of tumor margins. Strong tumor-to-background fluorescence ratios were found and fluorescence appeared to correlate with the degree of contrast enhancement on preoperative MRI [61]. So far,

there are no studies demonstrating a benefit for extent of resection in glioma surgery. Furthermore, ICG is not tumor-specific, incorporating the risk of resection of normal false positive tissue.

In addition, some authors suggest the usage of second-window ICG in order to visualize residual tumor and the margins in surgery for metastases and meningioma [62, 63]. However, the benefit of this intraoperative tool warrants further investigation.

26.4 Novel Techniques

Despite several advantages and the broad use of wide-field fluorescence imaging techniques, there are some limitations regarding sensitivity for the detection of malignant cells. Improvements in FGS are ongoing and further techniques are being developed to improve brain tumor surgery. Most of these advanced technologies are in their fledgling stage and are presently subject to intensive research.

26.4.1 Tumor-Targeted Alkylphosphocholine Analogs for Intraoperative Visualization

A major aim in surgery of malignant brain tumors is complete resection of tumor cells while sparing healthy brain parenchyma. To this end, cancer-targeted alkylphosphocholine analogs (APCs) attached to fluorophores are being explored for intraoperative visualization of tumor cells. APC analogs are small synthetic phospholipid ether molecules that are taken up by tumor cells through overexpressed lipid rafts and undergo prolonged retention due to decreased catabolism [33, 139]. APC analogs were originally developed for PET imaging and targeted radiotherapy and appear to have a broad tumor-targeting potential [139]. Two fluorescent APCs (CLR1501-green fluorescence and CLR1502-near-infrared fluorescence) have been found to label tumor cells in a glioblastoma xenograft model with a high cancer cell selectivity [125]. Future step of this technology, which is translating into clinical use, is the development of a dual-labeled APC enabling NIR fluorescence with deep tissue penetration and PET imaging with the same agent. This offers the possibility of synergistic diagnostic detection of tumor cells and usage at multiple phases of tumor management with regard to tumor resection, staging, and possible localized radiotherapy. However, up to date, these are preclinical data and the benefit in the management of brain tumor patients has yet to be determined [56, 144].

26.4.2 Confocal Endomicroscopy

A major problem with wide-field fluorescence-guided surgery is the lack of high resolution and the subjective interpretation of fluorescence intensities, challenging delineation of normal brain tissue and tumor tissue especially in glioma surgery and at the tumor margins. Predictions of grade to predict tumor grade from preoperative imaging in glioma surgery are often uncertain [72]. Therefore, time-consuming intraoperative frozen sections are regularly performed. However, there are some shortcomings about frozen-section pathology as it can be non-diagnostic or misleading in some cases [130].

To overcome these limitations, confocal endomicroscopy has been recently introduced into the field of neurosurgery, a technique that allows standard neuropathological diagnostics as a real-time intraoperative technique [27, 66]. The system consists of a handheld probe that uses a single optical fiber for illumination and detection and displays high-resolution images with up to 1000-fold magnification to a movable LCD workstation [34]. Tissue contrast is achieved by administration of fluorescent dyes, e.g., fluorescein [27].

This “optical biopsy” facilitates surgeons to detect tumor remnants at resection margins with higher accuracy and in especially critical and eloquent regions where an aggressive maximal extent of resection is not possible and can be probed with confocal endomicroscopy for measurement of tumor cell densities before resection.

In cases of LGG, which often do not show visible PPIX fluorescence, intraoperative confocal endomicroscopy is able to visualize the presence of even small amounts of fluorescence in tumor cells [97]. Furthermore, visualization of tumor cells with confocal endomicroscopy has been shown for a variety of brain tumors, including meningiomas, hemangioblastomas, gliomas, and neurocytomas [95].

Confocal endomicroscopy only enables a small field of view of about 0.5 mm in diameter and therefore cannot be used to scan the whole tumor area, but can be utilized at the end of surgery to detect malignant tissue remnants. To interpret the images, however, knowledge of histopathology or the presence of a neuropathologist is required [4].

26.4.3 Raman Spectroscopy

All previously mentioned visualization techniques rely on labeling agents that have limitations regarding sensitivity or specificity for tumor detection. Recently, label-free techniques have emerged in the field of intraoperative tumor visualization that depends on the intrinsic biochemical properties of normal versus pathological tissue to provide image contrast [36, 43, 77].

Raman spectroscopy is one such technique that is based on the findings of C.V. Raman in 1928 [86]. The Raman Effect refers to the scattering of monochromatic light. Most photons in the visible spectrum are scattered elastically when interacting with tissue or a media. However, a small portion of photons absorbs energy or transfers energy from or to the object being imaged. The transfer in energy results in

inelastic scattering and is called the Raman Effect. The Raman Effect can be captured using a sensitive spectrometer. Raman spectroscopy is used to provide information on the chemical composition of different tissues, e.g., their lipid and protein ratios, providing a structural fingerprint. Investigations have shown that Raman spectroscopy is helpful in delineating normal brain parenchyma from tumor tissue and necrosis [43, 50, 51, 54]. Accuracies of up to 98% for discrimination in frozen sections have been described [43].

Recently, a Raman spectroscopy handheld probe system for in vivo intraoperative use has been developed [20]. Jermyn et al. were able to distinguish normal brain from high- and low-grade gliomas invaded brain with high accuracy [40]. The aim of this method is to analyze the molecular nature of the tissue prior to resection, with the aim of improving cancer targeting and patient safety [21] (Fig. 26.6).

26.4.4 BLZ-100 Fluorescence-Guided Brain Tumor Surgery

Targeted fluorescence imaging using fluorescent-labeled probes with tumor-specific molecular targets is the next obvious step toward a higher accuracy for discriminating tumor-infiltrated tissue from normal brain. The combination of the fluorophore with a tumor-specific peptide enhances specificity for detection of malignant cells. BLZ-100 (tozuleristide) is such a molecule that consists of a tumor-targeting peptide, chlorotoxin, coupled to the near-infrared fluorophore ICG [79]. Chlorotoxin, extracted from the venom of scorpions, specifically binds to gliomas and tumors of neuroectodermal origin [64]. BLZ-100 is administered intravenously 24 h prior to surgery. As mentioned above, ICG fluorescence can be visualized using a NIR camera. A high affinity of BLZ-100 toward human gliomas has been demonstrated [8]. However, further trials are needed to determine the utility of BLZ-100 in glioma surgery.

26.5 Combination of Different Techniques for Intraoperative Imaging

The combination of different imaging modalities, e.g., neuronavigation with MRI and PET with specific biomarkers and FGS, allows the generation of comprehensive information on tumor location, extent, anatomy, metabolism, and function [60, 68].

Newer techniques might help to add additional information on the chemical or molecular composition of the tissue. Using different modalities helps to overcome limitations of single techniques, e.g., brain shift, using synergistic effects and utilizing the benefits of several techniques [53, 102, 103].

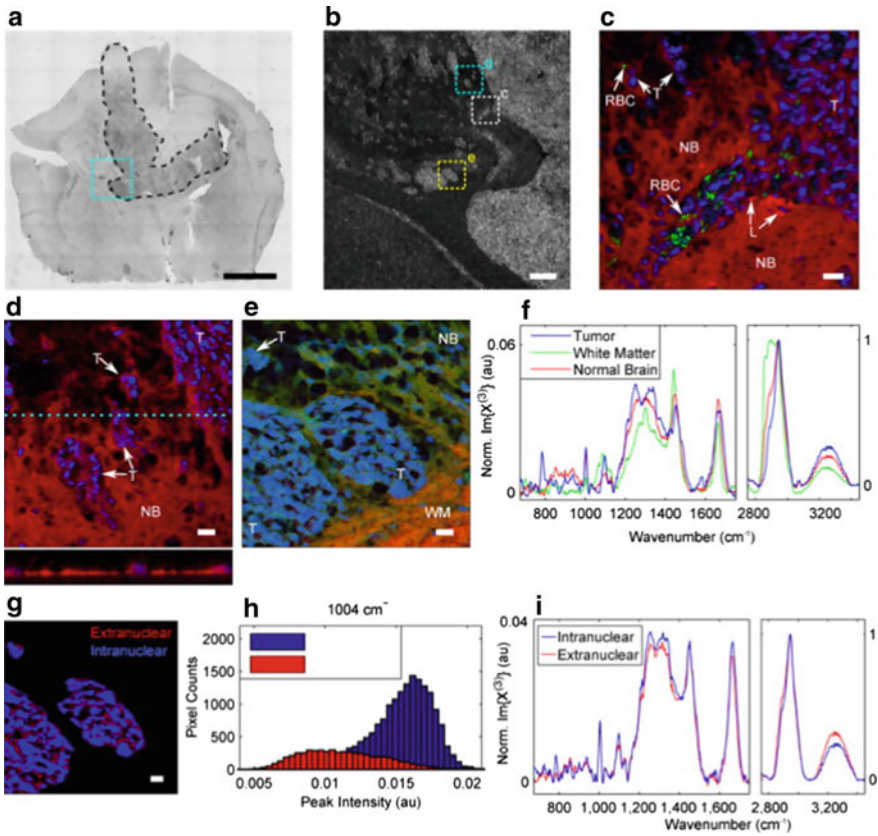


Fig. 26.6 Raman spectroscopy. **a** Brightfield image of xenograft glioblastoma in mouse brain outlining tumor hard boundary (black, dashed line), **b**, Cyan dashed box indicates region of interest (ROI). Scale bar, 2 mm. **b** Phase contrast micrograph of BCARS ROIs with boxes and associated subfigure labels. Scale bar, 200 μm . **c** Pseudocolor BCARS image of tumor and normal brain tissue highlighting nuclei (blue), lipid content (red), and red blood cells (green). **d** BCARS image and axial scan highlighting nuclei (blue) and lipid content (red). **e** BCARS image highlighting nuclei (blue), lipid content (red), and CH_3 -stretch- CH_2 -stretch (green). NB: normal brain; T: tumor cells; RBC: red blood cells; L: lipid bodies; WM: white matter. **f** Single-pixel spectra. **g** Spectrally segmented image of internuclear (blue) and extranuclear (red) tumoral spaces. **h** Histogram analysis of phenylalanine content. **i** Mean spectra from within tumor mass. **c–e** and **g**, Scale bars, 20 μm . Reproduced with permission [9]

26.6 Future Directions

All the developments discussed here aim at better intraoperative visualization in order to improve accuracy and extent of resection. However, current methods, which have been established in the clinical routine setting, face individual limitations. Consequently, further research is required to overcome these limitations. For

methods exploiting induced tissue fluorescence, quantitative as opposed to qualitative assessments require more scrutiny. At the moment, the decision of whether tissue is “fluorescent” relies on the subjective impression and assessment of the surgeon. Several attempts to measure and quantify fluorescence have been undertaken. One promising technology given quantitative information is fluorescence spectrography. Small handheld devices for intraoperative spectroscopy are available that enable determining the actual PpIX concentration in tumor tissue using 5-ALA FGS, even when no fluorescence is visible under the microscope [49, 121, 136]. Using this method, objective measurements of tissue fluorescence can be achieved. In addition, invisible PpIX accumulation, e.g., in patients with LGG, that would have gone unnoticed by the surgeon’s visual perception alone can be detected using spectroscopy. A 100-fold increase of sensitivity of fluorescence detection in LGG using handheld spectroscopy has been shown [135].

Furthermore, more specific labeling of tumor cells is under investigation, e.g., targeted fluorescence imaging. Innovations of neurosurgical microscopes will improve the view of the surgical field using all the mentioned visualization tools, detecting additional optical features in tumor tissue [137].

Multimodality in the applied imaging techniques and development of new techniques will provide comprehensive information derived from different sources regarding biological, metabolic, anatomical, and functional properties of tissue (Table 26.1). Neurosurgeons are beginning to integrate imaging concepts into their daily routine for brain tumor surgery, aiming at better extent of resection while lowering the risk of removal of functional non-tumor tissue.

Table 26.1 Overview on the current techniques for intraoperative tumor visualization with their advantages and disadvantages, modified from [101]

Technique	Advantages	Disadvantages
5-ALA	<ul style="list-style-type: none"> • Selectively absorbed by tumor cells and is converted into fluorescent PpIX • Low toxicity, high safety • Intraoperative real-time feedback • Brain shift does not interfere with this technique • Full integration into the surgical microscope • View of the full surgical field • Use without interruption to the surgical workflow • Reliable correlation with preoperative contrast enhancement on MRI • Correlation with histopathology • Metabolic labeling 	<ul style="list-style-type: none"> • Low background illumination, loss of normal optical information <ul style="list-style-type: none"> – Alternating between white light and fluorescence mode • Imaging surface tool, depth can limit visualization • Requires special microscope • Expensive • Bleaching effect • Time dependency • Subjective interpretation of fluorescence intensities

(continued)

Table 26.1 (continued)

Technique	Advantages	Disadvantages
Fluorescein	<ul style="list-style-type: none"> • Robust and inexpensive • Can be visualized by the naked eye (using higher concentrations) • Low toxicity, high safety • Intraoperative real-time feedback • Brain shift does not interfere with this technique • Full integration into the surgical microscope • View of the full surgical field • Use without interruption to the surgical workflow 	<ul style="list-style-type: none"> • Not tumor-cell-specific <ul style="list-style-type: none"> – Marker of BBB breakdown • Unselective extravasation during surgery • Time dependency • Subjective interpretation of fluorescence intensities • Passive labeling
Indocyanine green (ICG)	<ul style="list-style-type: none"> • Excitation and emission in the near-infrared region <ul style="list-style-type: none"> – Enables visualization of fluorescence situated deeper in the tissue • Less scatter of emitted light • Low tissue autofluorescence • Low toxicity, high safety • Intraoperative real-time feedback • Brain shift does not interfere with this technique • Full integration into the surgical microscope • View of the full surgical field • Use without interruption to the surgical workflow 	<ul style="list-style-type: none"> • Requires special cameras and instrumentation to visualize fluorescence • Not tumor-specific • Accumulates due to an enhanced permeability of the BBB • Time dependency • Subjective interpretation of fluorescence intensities • Passive labeling
Neuronavigation	<ul style="list-style-type: none"> • Ubiquitous • Several imaging modalities can be entered into the software, providing information on <ul style="list-style-type: none"> – Anatomy – Localization and orientation (almost real time) – Extent of tumor – Function (fMRI) – Fiber tracts (DTI) – Metabolic (PET) • Planning of surgical approach/craniotomy • Use without interruption to the surgical workflow 	<ul style="list-style-type: none"> • Loss of accuracy due to intraoperative brain shift caused by positioning, application of mannitol, and drainage of cerebral spinal fluid (CSF) • Information used during surgery is displayed on a screen outside the surgical field—interruptions to surgical workflow

References

1. Acerbi F et al (2014) Is fluorescein-guided technique able to help in resection of high-grade gliomas? *Neurosurg Focus* 36:E5. <https://doi.org/10.3171/2013.11.FOCUS13487>
2. Acerbi F et al (2018) Fluorescein-guided surgery for resection of high-grade gliomas: a multicentric prospective phase II study (FLUOGLIO). *Clin Cancer Res* 24:52–61. <https://doi.org/10.1158/1078-0432.ccr-17-1184>
3. Basser PJ, Mattiello J, LeBihan D (1994) Estimation of the effective self-diffusion tensor from the NMR spin echo. *J Magn Reson B* 103:247–254
4. Belykh E et al (2016) Intraoperative fluorescence imaging for personalized brain tumor resection: current state and future directions. *Front Surg* 3:55. <https://doi.org/10.3389/fsurg.2016.00055>
5. Bernal Garcia LM, Cabezudo Artero JM, Marcelo Zamorano MB, Gilete Tejero I (2015) Fluorescence-guided resection with 5-aminolevulinic Acid of subependymomas of the fourth ventricle: report of 2 cases: technical case report. *Neurosurgery* 11(Suppl 2):E364–E371; discussion E371. <https://doi.org/10.1227/NEU.0000000000000682>
6. Brandes AA, Tosoni A, Spagnoli F, Frezza G, Leonardi M, Calucci F, Franceschi E (2008) Disease progression or pseudoprogression after concomitant radiochemotherapy treatment: pitfalls in neurooncology. *Neuro Oncol* 10:361–367. <https://doi.org/10.1215/15228517-2008-008>
7. Brown TJ et al (2016) Association of the extent of resection with survival in glioblastoma: a systematic review and meta-analysis. *JAMA Oncol* 2:1460–1469. <https://doi.org/10.1001/jamaoncol.2016.1373>
8. Butte PV et al (2014) Near-infrared imaging of brain tumors using the tumor paint BLZ-100 to achieve near-complete resection of brain tumors. *Neurosurg Focus* 36:E1. <https://doi.org/10.3171/2013.11.fOCUS13497>
9. Camp CH Jr et al (2014) High-speed coherent Raman fingerprint imaging of biological tissues. *Nat Photonics* 8:627–634. <https://doi.org/10.1038/nphoton.2014.145>
10. Carlsson SK, Brothers SP, Wahlestedt C (2014) Emerging treatment strategies for glioblastoma multiforme. *EMBO Mol Med* 6:1359–1370. <https://doi.org/10.15252/emmm.201302627>
11. Chen B et al (2012) Gross total resection of glioma with the intraoperative fluorescence-guidance of fluorescein sodium. *Int J Med Sci* 9:708–714. <https://doi.org/10.7150/ijms.4843>
12. Cherrick GR, Stein SW, Leevy CM, Davidson CS (1960) Indocyanine green: observations on its physical properties, plasma decay, and hepatic extraction. *J Clin Invest* 39:592–600. <https://doi.org/10.1172/jci104072>
13. Coburger J, Hagel V, Wirtz CR, König R (2015) Surgery for glioblastoma: impact of the combined use of 5-aminolevulinic acid and intraoperative MRI on extent of resection and survival. *PLoS One* 10:e0131872. <https://doi.org/10.1371/journal.pone.0131872>
14. Colditz MJ, Leyen K, Jeffree RL (2012) Aminolevulinic acid (ALA)-protoporphyrin IX fluorescence guided tumour resection. Part 2: theoretical, biochemical and practical aspects. *J Clin Neurosci* 19:1611–1616. <https://doi.org/10.1016/j.jocn.2012.03.013>
15. da Silva CE, da Silva JL, da Silva VD (2010) Use of sodium fluorescein in skull base tumors. *Surg Neurol Int* 1:70. <https://doi.org/10.4103/2152-7806.72247>
16. da Silva CE, da Silva VD, da Silva JL (2014) Convexity meningiomas enhanced by sodium fluorescein. *Surg Neurol Int* 5:3. <https://doi.org/10.4103/2152-7806.124978>
17. de Wit MC, de Bruin HG, Eijkenboom W, Sillevs Smitt PA, van den Bent MJ (2004) Immediate post-radiotherapy changes in malignant glioma can mimic tumor progression. *Neurology* 63:535–537
18. Della Puppa A et al (2013) 5-aminolevulinic acid (5-ALA) fluorescence guided surgery of high-grade gliomas in eloquent areas assisted by functional mapping. Our experience and review of the literature. *Acta Neurochir (Wien)* 155:965–972; discussion 972. <https://doi.org/10.1007/s00701-013-1660-x>

19. Della Puppa A et al. (2014) Predictive value of intraoperative 5-aminolevulinic acid-induced fluorescence for detecting bone invasion in meningioma surgery *J Neurosurg* 120:840–845 <https://doi.org/10.3171/2013.12.jns131642>
20. Desroches J et al (2015) Characterization of a Raman spectroscopy probe system for intraoperative brain tissue classification. *Biomed Opt Express* 6:2380–2397. <https://doi.org/10.1364/BOE.6.002380>
21. Desroches J et al (2018) A new method using Raman spectroscopy for in vivo targeted brain cancer tissue biopsy. *Sci Rep* 8:1792. 10.1038/s41598-018-20233-3
22. Diaz RJ et al (2015) Study of the biodistribution of fluorescein in glioma-infiltrated mouse brain and histopathological correlation of intraoperative findings in high-grade gliomas resected under fluorescein fluorescence guidance. *J Neurosurg* 122:1360–1369. <https://doi.org/10.3171/2015.2.JNS132507>
23. Dilek O, Ihsan A, Tulay H (2011) Anaphylactic reaction after fluorescein sodium administration during intracranial surgery. *J Clin Neurosci* 18:430–431. <https://doi.org/10.1016/j.jocn.2010.06.012>
24. Eicker S et al (2011) ALA-induced porphyrin accumulation in medulloblastoma and its use for fluorescence-guided surgery. *Cent Eur Neurosurg* 72:101–103. <https://doi.org/10.1055/s-0030-1252010>
25. Elhawary H et al (2011) Intraoperative real-time querying of white matter tracts during frameless stereotactic neuronavigation. *Neurosurgery* 68:506–516; discussion 516. <https://doi.org/10.1227/neu.0b013e3182036282>
26. Ewelt C et al (2011) Finding the anaplastic focus in diffuse gliomas: the value of Gd-DTPA enhanced MRI, FET-PET, and intraoperative, ALA-derived tissue fluorescence. *Clin Neurol Neurosurg* 113:541–547. <https://doi.org/10.1016/j.clineuro.2011.03.008>
27. Foersch S et al (2012) Confocal laser endomicroscopy for diagnosis and histomorphologic imaging of brain tumors in vivo. *PLoS ONE* 7:e41760. <https://doi.org/10.1371/journal.pone.0041760>
28. Hadjipanayis CG, Widhalm G, Stummer W (2015) What is the surgical benefit of utilizing 5-aminolevulinic acid for fluorescence-guided surgery of malignant gliomas? *Neurosurgery* 77:663–673. <https://doi.org/10.1227/NEU.0000000000000929>
29. Hamamcioglu MK, Akcakaya MO, Goker B, Kasimcan MO, Kiris T (2016) The use of the YELLOW 560 nm surgical microscope filter for sodium fluorescein-guided resection of brain tumors: our preliminary results in a series of 28 patients. *Clin Neurol Neurosurg* 143:39–45. <https://doi.org/10.1016/j.clineuro.2016.02.006>
30. Hanggi D, Ertinan N, Steiger HJ (2010) The impact of microscope-integrated intraoperative near-infrared indocyanine green videoangiography on surgery of arteriovenous malformations and dural arteriovenous fistulae. *Neurosurgery* 67:1094–1103; discussion 1103–1094. <https://doi.org/10.1227/neu.0b013e3181eb5049>
31. Hervey-Jumper SL, Berger MS (2014) Role of surgical resection in low- and high-grade gliomas. *Curr Treat Options Neurol* 16:284. <https://doi.org/10.1007/s11940-014-0284-7>
32. Hickmann AK, Nadji-Ohl M, Hopf NJ (2015) Feasibility of fluorescence-guided resection of recurrent gliomas using five-aminolevulinic acid: retrospective analysis of surgical and neurological outcome in 58 patients. *J Neurooncol* 122:151–160. <https://doi.org/10.1007/s11060-014-1694-9>
33. Hilgard P, Klenner T, Stekar J, Unger C (1993) Alkylphosphocholines: a new class of membrane-active anticancer agents. *Cancer Chemother Pharmacol* 32:90–95
34. Hoffman A, Goetz M, Vieth M, Galle PR, Neurath MF, Kiesslich R (2006) Confocal laser endomicroscopy: technical status and current indications. *Endoscopy* 38:1275–1283. <https://doi.org/10.1055/s-2006-944813>
35. Hohne J, Hohenberger C, Proescholdt M, Riemenschneider MJ, Wendl C, Brawanski A, Schebesch KM (2017) Fluorescein sodium-guided resection of cerebral metastases-an update. *Acta Neurochir (Wien)* 159:363–367. <https://doi.org/10.1007/s00701-016-3054-3>

36. Hollon T, Lewis S, Freudiger CW, Sunney Xie X, Orringer DA (2016) Improving the accuracy of brain tumor surgery via Raman-based technology. *Neurosurg Focus* 40:E9. <https://doi.org/10.3171/2015.12.FOCUS15557>
37. Idoate MA, Diez Valle R, Echeveste J, Tejada S (2011) Pathological characterization of the glioblastoma border as shown during surgery using 5-aminolevulinic acid-induced fluorescence. *Neuropathology* 31:575–582. <https://doi.org/10.1111/j.1440-1789.2011.01202.x>
38. Inoue T, Endo T, Nagamatsu K, Watanabe M, Tominaga T (2013) 5-aminolevulinic acid fluorescence-guided resection of intramedullary ependymoma: report of 9 cases. *Neurosurgery* 72:ons159–168; discussion ons168. <https://doi.org/10.1227/neu.0b013e31827bc7a3>
39. Jaber M et al (2016) The value of 5-aminolevulinic acid in low-grade gliomas and high-grade gliomas lacking glioblastoma imaging features: an analysis based on fluorescence, magnetic resonance imaging, 18F-fluoroethyl tyrosine positron emission tomography, and tumor molecular factors. *Neurosurgery* 78:401–411; discussion 411. <https://doi.org/10.1227/neu.0000000000001020>
40. Jermyn M et al (2015) Intraoperative brain cancer detection with Raman spectroscopy in humans. *Sci Transl Med* 7:274ra219. <https://doi.org/10.1126/scitranslmed.aaa2384>
41. Jolesz FA (2011) Intraoperative imaging in neurosurgery: where will the future take us? *Acta Neurochir Suppl* 109:21–25. https://doi.org/10.1007/978-3-211-99651-5_4
42. Jung TY, Jung S, Kim IY, Park SJ, Kang SS, Kim SH, Lim SC (2006) Application of neuronavigation system to brain tumor surgery with clinical experience of 420 cases. *Minim Invasive Neurosurg* 49:210–215. <https://doi.org/10.1055/s-2006-948305>
43. Kalkanis SN et al (2014) Raman spectroscopy to distinguish grey matter, necrosis, and glioblastoma multiforme in frozen tissue sections. *J Neurooncol* 116:477–485. <https://doi.org/10.1007/s11060-013-1326-9>
44. Kalkanis SN, Linskey ME (2010) Evidence-based clinical practice parameter guidelines for the treatment of patients with metastatic brain tumors: introduction. *J Neurooncol* 96:7–10. <https://doi.org/10.1007/s11060-009-0065-4>
45. Kamp MA et al (2015) 5-ALA-induced fluorescence behavior of reactive tissue changes following glioblastoma treatment with radiation and chemotherapy. *Acta Neurochir (Wien)* 157:207–213; discussion 213–204. <https://doi.org/10.1007/s00701-014-2313-4>
46. Kamp MA et al (2016) 5-ALA fluorescence of cerebral metastases and its impact for the local-in-brain progression. *Oncotarget* 7:66776–66789. <https://doi.org/10.18632/oncotarget.11488>
47. Kamp MA, Grosser P, Felsberg J, Slotty PJ, Steiger HJ, Reifemberger G, Sabel M (2012) 5-aminolevulinic acid (5-ALA)-induced fluorescence in intracerebral metastases: a retrospective study. *Acta Neurochir (Wien)* 154:223–228; discussion 228. <https://doi.org/10.1007/s00701-011-1200-5>
48. Kaneko S, Suero Molina E, Ewelt C, Warneke N, Stummer W (2019) Fluorescence-based measurement of real-time kinetics of protoporphyrin IX after 5-aminolevulinic acid administration in human in situ malignant gliomas. *Neurosurgery*
49. Kim A, Khurana M, Moriyama Y, Wilson BC (2010) Quantification of in vivo fluorescence decoupled from the effects of tissue optical properties using fiber-optic spectroscopy measurements. *J Biomed Opt* 15:067006. <https://doi.org/10.1117/1.3523616>
50. Kirsch M, Schackert G, Salzer R, Krafft C (2010) Raman spectroscopic imaging for in vivo detection of cerebral brain metastases. *Anal Bioanal Chem* 398:1707–1713. <https://doi.org/10.1007/s00216-010-4116-7>
51. Kohler M, Machill S, Salzer R, Krafft C (2009) Characterization of lipid extracts from brain tissue and tumors using Raman spectroscopy and mass spectrometry. *Anal Bioanal Chem* 393:1513–1520. <https://doi.org/10.1007/s00216-008-2592-9>
52. Koshy M et al (2012) Improved survival time trends for glioblastoma using the SEER 17 population-based registries *J Neurooncol* 107:207–212 <https://doi.org/10.1007/s11060-011-0738-7>

53. Kracht LW et al (2004) Delineation of brain tumor extent with [¹¹C]L-methionine positron emission tomography: local comparison with stereotactic histopathology. *Clin Cancer Res* 10:7163–7170. <https://doi.org/10.1158/1078-0432.ccr-04-0262>
54. Krafft C, Neudert L, Simat T, Salzer R (2005) Near infrared Raman spectra of human brain lipids. *Spectrochim Acta A Mol Biomol Spectrosc* 61:1529–1535. <https://doi.org/10.1016/j.saa.2004.11.017>
55. Kremer P et al (2006) Intraoperative MRI for interventional neurosurgical procedures and tumor resection control in children. *Childs Nerv Syst* 22:674–678. <https://doi.org/10.1007/s00381-005-0030-2>
56. Kuo JS, Zhang RR, Pinchuk AN, Clark PA, Weichert JP (2016) Creation of a dual-labeled cancer-targeting alkylphosphocholine analog for dual modality quantitative positron emission tomography and intraoperative tumor visualization. *Neurosurgery* 63:208
57. Kuroiwa T, Kajimoto Y, Ohta T (1998) Development of a fluorescein operative microscope for use during malignant glioma surgery: a technical note and preliminary report. *Surg Neurol* 50:41–48; discussion 48–49
58. Lacroix M et al (2001) A multivariate analysis of 416 patients with glioblastoma multiforme: prognosis, extent of resection, and survival. *J Neurosurg* 95:190–198. <https://doi.org/10.3171/jns.2001.95.2.0190>
59. Lau D, Hervey-Jumper SL, Chang S, Molinaro AM, McDermott MW, Phillips JJ, Berger MS (2016) A prospective Phase II clinical trial of 5-aminolevulinic acid to assess the correlation of intraoperative fluorescence intensity and degree of histologic cellularity during resection of high-grade gliomas. *J Neurosurg* 124:1300–1309. <https://doi.org/10.3171/2015.5.jns1577>
60. Laukamp KR et al (2017) Multimodal imaging of patients with gliomas confirms (11)C-MET PET as a complementary marker to MRI for noninvasive tumor grading and intraindividual follow-up after therapy. *Mol Imaging* 16:1536012116687651. <https://doi.org/10.1177/1536012116687651>
61. Lee JY et al (2016) Intraoperative near-infrared optical imaging can localize gadolinium-enhancing gliomas during surgery. *Neurosurgery* 79:856–871. <https://doi.org/10.1227/NEU.0000000000001450>
62. Lee JYK, Pierce JT, Thawani JP, Zeh R, Nie S, Martinez-Lage M, Singhal S (2018) Near-infrared fluorescent image-guided surgery for intracranial meningioma. *J Neurosurg* 128:380–390. <https://doi.org/10.3171/2016.10.JNS161636>
63. Lee JYK, Pierce JT, Zeh R, Cho SS, Salinas R, Nie S, Singhal S (2017) Intraoperative near-infrared optical contrast can localize brain metastases. *World Neurosurg* 106:120–130. <https://doi.org/10.1016/j.wneu.2017.06.128>
64. Lyons SA, O'Neal J, Sontheimer H (2002) Chlorotoxin, a scorpion-derived peptide, specifically binds to gliomas and tumors of neuroectodermal origin. *Glia* 39:162–173. <https://doi.org/10.1002/glia.10083>
65. Marko NF, Weil RJ, Schroeder JL, Lang FF, Suki D, Sawaya RE (2014) Extent of resection of glioblastoma revisited: personalized survival modeling facilitates more accurate survival prediction and supports a maximum-safe-resection approach to surgery. *J Clin Oncol* 32:774–782. <https://doi.org/10.1200/JCO.2013.51.8886>
66. Martirosyan NL et al (2011) Use of in vivo near-infrared laser confocal endomicroscopy with indocyanine green to detect the boundary of infiltrative tumor. *J Neurosurg* 115:1131–1138. <https://doi.org/10.3171/2011.8.JNS11559>
67. Mercier L et al (2011) New prototype neuronavigation system based on preoperative imaging and intraoperative freehand ultrasound: system description and validation. *Int J Comput Assist Radiol Surg* 6:507–522. <https://doi.org/10.1007/s11548-010-0535-3>
68. Meyer GJ, Schober O, Hundeshagen H (1985) Uptake of ¹¹C-L- and D-methionine in brain tumors. *Eur J Nucl Med* 10:373–376

69. Millesi M et al (2016) Analysis of the surgical benefits of 5-ALA-induced fluorescence in intracranial meningiomas: experience in 204 meningiomas. *J Neurosurg* 125:1408–1419. <https://doi.org/10.3171/2015.12.jns151513>
70. Moore GE (1947) Fluorescein as an agent in the differentiation of normal and malignant tissues. *Science* 106:130–131. <https://doi.org/10.1126/science.106.2745.130-a>
71. Morofuji Y, Matsuo T, Hayashi Y, Suyama K, Nagata I (2008) Usefulness of intraoperative photodynamic diagnosis using 5-aminolevulinic acid for meningiomas with cranial invasion: technical case report. *Neurosurgery* 62:102–103; discussion 103–104. <https://doi.org/10.1227/01.neu.0000317378.22820.46>
72. Muragaki Y et al (2008) Low-grade glioma on stereotactic biopsy: how often is the diagnosis accurate? *Minim Invasive Neurosurg* 51:275–279. <https://doi.org/10.1055/s-0028-1082322>
73. Nabavi A et al (2009) Five-aminolevulinic acid for fluorescence-guided resection of recurrent malignant gliomas: a phase II study. *Neurosurgery* 65:1070–1076; discussion 1076–1077. <https://doi.org/10.1227/01.neu.0000360128.03597.c7>
74. Neira JA et al (2017) Aggressive resection at the infiltrative margins of glioblastoma facilitated by intraoperative fluorescein guidance. *J Neurosurg* 127:111–122. <https://doi.org/10.3171/2016.7.JNS16232>
75. Orringer D et al. (2012a) Extent of resection in patients with glioblastoma: limiting factors, perception of resectability, and effect on survival. *J Neurosurg* 117:851–859. <https://doi.org/10.3171/2012.8.jns12234>
76. Orringer DA, Golby A, Jolesz F (2012b) Neuronavigation in the surgical management of brain tumors: current and future trends. *Expert Rev Med Devices* 9:491–500. <https://doi.org/10.1586/erd.12.42>
77. Orringer DA et al. (2017) Rapid intraoperative histology of unprocessed surgical specimens via fibre-laser-based stimulated Raman scattering microscopy. *Nat Biomed Eng* 1. <https://doi.org/10.1038/s41551-016-0027>
78. Ostrom QT, Gittleman H, Truitt G, Boscia A, Kruchko C, Barnholtz-Sloan JS (2018) CBTRUS statistical report: primary brain and other central nervous system tumors diagnosed in the United States in 2011–2015. *Neuro Oncol* 20:iv1–iv86. <https://doi.org/10.1093/neuonc/ny131>
79. Parrish-Novak J et al (2017) Nonclinical profile of BLZ-100, a tumor-targeting fluorescent imaging agent. *Int J Toxicol* 36:104–112 <https://doi.org/10.1177/1091581817697685>
80. Patchell RA et al (1998) Postoperative radiotherapy in the treatment of single metastases to the brain: a randomized trial. *JAMA* 280:1485–1489
81. Paulus W, Peiffer J (1989) Intratumoral histologic heterogeneity of gliomas. A quantitative study. *Cancer* 64:442–447
82. Perrini P et al (2017) Survival outcomes following repeat surgery for recurrent glioblastoma: a single-center retrospective analysis. *J Neurooncol* 131:585–591. <https://doi.org/10.1007/s11060-016-2330-7>
83. Raabe A, Beck J, Gerlach R, Zimmermann M, Seifert V (2003) Near-infrared indocyanine green video angiography: a new method for intraoperative assessment of vascular flow. *Neurosurgery* 52:132–139; discussion 139
84. Raabe A et al (2005) Prospective evaluation of surgical microscope-integrated intraoperative near-infrared indocyanine green videoangiography during aneurysm surgery. *J Neurosurg* 103:982–989. <https://doi.org/10.3171/jns.2005.103.6.0982>
85. Rabb MF, Burton TC, Schatz H, Yannuzzi LA (1978) Fluorescein angiography of the fundus: a schematic approach to interpretation. *Surv Ophthalmol* 22:387–403
86. Raman C (1928) A new type of secondary radiation. *Nature* 121:501–502
87. Reinhart MB, Huntington CR, Blair LJ, Heniford BT, Augenstein VA (2016) Indocyanine green: historical context, current applications, and future considerations. *Surg Innov* 23:166–175. <https://doi.org/10.1177/1553350615604053>
88. Rey-Dios R, Hattab EM, Cohen-Gadol AA (2014) Use of intraoperative fluorescein sodium fluorescence to improve the accuracy of tissue diagnosis during stereotactic needle biopsy of

- high-grade gliomas. *Acta Neurochir (Wien)* 156:1071–1075; discussion 1075. <https://doi.org/10.1007/s00701-014-2097-6>
89. Ringel F et al (2016) Clinical benefit from resection of recurrent glioblastomas: results of a multicenter study including 503 patients with recurrent glioblastomas undergoing surgical resection. *Neuro Oncol* 18:96–104. <https://doi.org/10.1093/neuonc/nov145>
 90. Roberts DW et al (2011) Coregistered fluorescence-enhanced tumor resection of malignant glioma: relationships between delta-aminolevulinic acid-induced protoporphyrin IX fluorescence, magnetic resonance imaging enhancement, and neuropathological parameters. *Clinical Art J Neurosurg* 114:595–603. <https://doi.org/10.3171/2010.2.JNS091322>
 91. Ruge JR, Liu J (2009) Use of 5-aminolevulinic acid for visualization and resection of a benign pediatric brain tumor. *J Neurosurg Pediatr* 4:484–486. <https://doi.org/10.3171/2009.6.peds08428>
 92. Rygh OM, Selbekk T, Torp SH, Lydersen S, Hernes TA, Unsgaard G (2008) Comparison of navigated 3D ultrasound findings with histopathology in subsequent phases of glioblastoma resection. *Acta Neurochir (Wien)* 150:1033–1041; discussion 1042. <https://doi.org/10.1007/s00701-008-0017-3>
 93. Saether CA, Torsteinsen M, Torp SH, Sundstrom S, Unsgard G, Solheim O (2012) Did survival improve after the implementation of intraoperative neuronavigation and 3D ultrasound in glioblastoma surgery? a retrospective analysis of 192 primary operations. *J Neurol Surg A Cent Eur Neurosurg* 73:73–78. <https://doi.org/10.1055/s-0031-1297247>
 94. Sanai N, Berger MS (2008) Glioma extent of resection and its impact on patient outcome. *Neurosurgery* 62:753–764; discussion 264–756. <https://doi.org/10.1227/01.neu.0000318159.21731.cf>
 95. Sanai N et al. (2011a) Intraoperative confocal microscopy for brain tumors: a feasibility analysis in humans. *Neurosurgery* 68:282–290; discussion 290. <https://doi.org/10.1227/neu.0b013e318212464e>
 96. Sanai N, Polley MY, McDermott MW, Parsa AT, Berger MS (2011b) An extent of resection threshold for newly diagnosed glioblastomas. *J Neurosurg* 115:3–8. <https://doi.org/10.3171/2011.2.JNS10998>; <https://doi.org/10.3171/2011.7.JNS10238>
 97. Sanai N, Snyder LA, Honea NJ, Coons SW, Eschbacher JM, Smith KA, Spetzler RF (2011c) Intraoperative confocal microscopy in the visualization of 5-aminolevulinic acid fluorescence in low-grade gliomas. *J Neurosurg* 115:740–748. <https://doi.org/10.3171/2011.6.jns11252>
 98. Schebesch KM, Brawanski A, Hohenberger C, Hohne J (2016) Fluorescein sodium-guided surgery of malignant brain tumors: history, current concepts, and future project. *Turk Neurosurg* 26:185–194. <https://doi.org/10.5137/1019-5149.JTN.16952-16.0>
 99. Schebesch KM et al (2015) Fluorescein sodium-guided surgery in cerebral lymphoma. *Clin Neurol Neurosurg* 139:125–128. <https://doi.org/10.1016/j.clineuro.2015.09.015>
 100. Schebesch KM et al (2013) Sodium fluorescein-guided resection under the YELLOW 560 nm surgical microscope filter in malignant brain tumor surgery—a feasibility study. *Acta Neurochir (Wien)* 155:693–699. <https://doi.org/10.1007/s00701-013-1643-y>
 101. Schipmann S, Schwake M, Suero Molina E, Stummer W (2019) Markers for identifying and targeting glioblastoma cells during surgery. *Acta Neurochir (Wien)*
 102. Schober O, Creutzig H, Meyer GJ, Becker H, Schwarzrock R, Dietz H, Hundeshagen H (1985a) 11C-methionine PET, IMP-SPECT, CT and MRI in brain tumors. *Rofu* 143:133–136. <https://doi.org/10.1055/s-2008-1052777>
 103. Schober O, Meyer GJ, Stolke D, Hundeshagen H (1985b) Brain tumor imaging using C-11-labeled L-methionine and D-methionine. *J Nucl Med* 26:98–99
 104. Schulz C, Waldeck S, Mauer UM (2012) Intraoperative image guidance in neurosurgery: development, current indications, and future trends. *Radiol Res Pract* 2012:197364. <https://doi.org/10.1155/2012/197364>

105. Schwake M et al (2014) Kinetics of porphyrin fluorescence accumulation in pediatric brain tumor cells incubated in 5-aminolevulinic acid. *Acta Neurochir (Wien)* 156:1077–1084. <https://doi.org/10.1007/s00701-014-2096-7>
106. Senft C, Bink A, Franz K, Vatter H, Gasser T, Seifert V (2011) Intraoperative MRI guidance and extent of resection in glioma surgery: a randomised, controlled trial. *Lancet Oncol* 12:997–1003. [https://doi.org/10.1016/s1470-2045\(11\)70196-6](https://doi.org/10.1016/s1470-2045(11)70196-6)
107. Senft C, Franz K, Ulrich CT, Bink A, Szelenyi A, Gasser T, Seifert V (2010) Low field intraoperative MRI-guided surgery of gliomas: a single center experience. *Clin Neurol Neurosurg* 112:237–243. <https://doi.org/10.1016/j.clineuro.2009.12.003>
108. Senft C, Seifert V, Hermann E, Franz K, Gasser T (2008) Usefulness of intraoperative ultra low-field magnetic resonance imaging in glioma surgery. *Neurosurgery* 63:257–266; discussion 266–257. <https://doi.org/10.1227/01.neu.0000313624.77452.3c>
109. Shinoda J, Yano H, Yoshimura S, Okumura A, Kaku Y, Iwama T, Sakai N (2003) Fluorescence-guided resection of glioblastoma multiforme by using high-dose fluorescein sodium. Technical note. *J Neurosurg* 99:597–603. <https://doi.org/10.3171/jns.2003.99.3.0597>
110. Smith JS et al (2008) Role of extent of resection in the long-term outcome of low-grade hemispheric gliomas. *J Clin Oncol* 26:1338–1345. <https://doi.org/10.1200/JCO.2007.13.9337>
111. Stummer W (2015) Poor man's fluorescence? *Acta Neurochir (Wien)* 157:1379–1381. <https://doi.org/10.1007/s00701-015-2471-z>
112. Stummer W, Gotz C, Hassan A, Heimann A, Kempfski O (1993) Kinetics of Photofrin II in perifocal brain edema. *Neurosurgery* 33:1075–1081; discussion 1081–1072
113. Stummer W, Novotny A, Stepp H, Goetz C, Bise K, Reulen HJ (2000) Fluorescence-guided resection of glioblastoma multiforme by using 5-aminolevulinic acid-induced porphyrins: a prospective study in 52 consecutive patients. *J Neurosurg* 93:1003–1013. <https://doi.org/10.3171/jns.2000.93.6.1003>
114. Stummer W, Pichlmeier U, Meinel T, Wiestler OD, Zanella F, Reulen HJ, Group AL-GS (2006) Fluorescence-guided surgery with 5-aminolevulinic acid for resection of malignant glioma: a randomised controlled multicentre phase III trial. *Lancet Oncol* 7:392–401. [https://doi.org/10.1016/s1470-2045\(06\)70665-9](https://doi.org/10.1016/s1470-2045(06)70665-9)
115. Stummer W et al (2008) Extent of resection and survival in glioblastoma multiforme: identification of and adjustment for bias. *Neurosurgery* 62:564–576; discussion 564–576. <https://doi.org/10.1227/01.neu.0000317304.31579.17>
116. Stummer W et al (2014a) Predicting the “usefulness” of 5-ALA-derived tumor fluorescence for fluorescence-guided resections in pediatric brain tumors: a European survey. *Acta Neurochir (Wien)* 156:2315–2324. <https://doi.org/10.1007/s00701-014-2234-2>
117. Stummer W, Stepp H, Moller G, Ehrhardt A, Leonhard M, Reulen HJ (1998a) Technical principles for protoporphyrin-IX-fluorescence guided microsurgical resection of malignant glioma tissue. *Acta Neurochir (Wien)* 140:995–1000
118. Stummer W, Stepp H, Wiestler OD, Pichlmeier U (2017) Randomized, prospective double-blinded study comparing 3 different doses of 5-aminolevulinic acid for fluorescence-guided resections of malignant gliomas. *Neurosurgery* 81:230–239. <https://doi.org/10.1093/neuros/nyx074>
119. Stummer W et al (1998b) Intraoperative detection of malignant gliomas by 5-aminolevulinic acid-induced porphyrin fluorescence. *Neurosurgery* 42:518–525; discussion 525–516
120. Stummer W, Suero Molina E (2017) Fluorescence imaging/agents in tumor resection. *Neurosurg Clin N Am* 28:569–583. <https://doi.org/10.1016/j.nec.2017.05.009>
121. Stummer W et al (2014b) 5-Aminolevulinic acid-derived tumor fluorescence: the diagnostic accuracy of visible fluorescence qualities as corroborated by spectrometry and histology and postoperative imaging. *Neurosurgery* 74:310–319; discussion 319–320. <https://doi.org/10.1227/01.neu.0000000000000267>

122. Suchorska B et al (2016) Complete resection of contrast-enhancing tumor volume is associated with improved survival in recurrent glioblastoma-results from the DIRECTOR trial. *Neuro Oncol* 18:549–556. <https://doi.org/10.1093/neuonc/nov326>
123. Suero Molina E, Wolfer J, Ewelt C, Ehrhardt A, Brokinkel B, Stummer W (2018) Dual-labeling with 5-aminolevulinic acid and fluorescein for fluorescence-guided resection of high-grade gliomas: technical note. *J Neurosurg* 128:399–405. <https://doi.org/10.3171/2016.11.jns161072>
124. Sutherland GR, Kaibara T, Louw D, Hoult DI, Tomanek B, Saunders J (1999) A mobile high-field magnetic resonance system for neurosurgery. *J Neurosurg* 91:804–813. <https://doi.org/10.3171/jns.1999.91.5.0804>
125. Swanson KI, Clark PA, Zhang RR, Kandela IK, Farhoud M, Weichert JP, Kuo JS (2015) Fluorescent cancer-selective alkylphosphocholine analogs for intraoperative glioma detection *Neurosurgery* 76:115–123; discussion 123–114. <https://doi.org/10.1227/neu.0000000000000622>
126. Taal W et al (2008) Incidence of early pseudo-progression in a cohort of malignant glioma patients treated with chemoradiation with temozolomide. *Cancer* 113:405–410. <https://doi.org/10.1002/cncr.23562>
127. Takeda J et al. (2017) 5-ALA fluorescence-guided endoscopic surgery for mixed germ cell tumors. *J Neurooncol* 134:119–124. <https://doi.org/10.1007/s11060-017-2494-9>
128. Teixidor P et al (2016) Safety and efficacy of 5-aminolevulinic acid for high grade glioma in usual clinical practice: a prospective cohort study. *PLoS One* 11:e0149244. <https://doi.org/10.1371/journal.pone.0149244>
129. Tew JM (1999) M. Gazi Yasargil: neurosurgery's man of the century. *Neurosurgery* 45:1010–1014
130. Uematsu Y, Owai Y, Okita R, Tanaka Y, Itakura T (2007) The usefulness and problem of intraoperative rapid diagnosis in surgical neuropathology. *Brain Tumor Pathol* 24:47–52. <https://doi.org/10.1007/s10014-007-0219-z>
131. Utsuki S, Miyoshi N, Oka H, Miyajima Y, Shimizu S, Suzuki S, Fujii K (2007a) Fluorescence-guided resection of metastatic brain tumors using a 5-aminolevulinic acid-induced protoporphyrin IX: pathological study. *Brain Tumor Pathol* 24:53–55. <https://doi.org/10.1007/s10014-007-0223-3>
132. Utsuki S, Oka H, Kijima C, Miyajima Y, Hagiwara H, Fujii K (2011) Utility of intraoperative fluorescent diagnosis of residual hemangioblastoma using 5-aminolevulinic acid. *Neurol India* 59:612–615. <https://doi.org/10.4103/0028-3886.84349>
133. Utsuki S et al (2007b) Histological examination of false positive tissue resection using 5-aminolevulinic acid-induced fluorescence guidance. *Neurol Med Chir (Tokyo)* 47:210–213; discussion 213–214
134. Valdes PA et al (2014) 5-Aminolevulinic acid-induced protoporphyrin IX fluorescence in meningioma: qualitative and quantitative measurements in vivo. *Neurosurgery* 10(Suppl 1):74–82; discussion 82–73. <https://doi.org/10.1227/neu.0000000000000117>
135. Valdes PA, Jacobs V, Harris BT, Wilson BC, Leblond F, Paulsen KD, Roberts DW (2015) Quantitative fluorescence using 5-aminolevulinic acid-induced protoporphyrin IX biomarker as a surgical adjunct in low-grade glioma surgery. *J Neurosurg* 123:771–780. <https://doi.org/10.3171/2014.12.jns14391>
136. Valdes PA et al (2011) Quantitative fluorescence in intracranial tumor: implications for ALA-induced PpIX as an intraoperative biomarker. *J Neurosurg* 115:11–17. <https://doi.org/10.3171/2011.2.JNS101451>
137. Valdes PA, Roberts DW, Lu FK, Golby A (2016) Optical technologies for intraoperative neurosurgical guidance. *Neurosurg Focus* 40:E8. <https://doi.org/10.3171/2015.12.FOCUS15550>
138. Villanueva-Meyer JE, Mabray MC, Cha S (2017) Current clinical brain tumor imaging. *Neurosurgery* 81:397–415. <https://doi.org/10.1093/neuros/nyx103>

139. Weichert JP et al (2014) Alkylphosphocholine analogs for broad-spectrum cancer imaging and therapy. *Sci Transl Med* 6:240ra275. <https://doi.org/10.1126/scitranslmed.3007646>
140. Widhalm G et al (2013) 5-Aminolevulinic acid induced fluorescence is a powerful intraoperative marker for precise histopathological grading of gliomas with non-significant contrast-enhancement. *PLoS One* 8:e76988. <https://doi.org/10.1371/journal.pone.0076988>
141. Wilbers E, Hargus G, Wolfer J, Stummer W (2014) Usefulness of 5-ALA (Gliolan(R))-derived PPX fluorescence for demonstrating the extent of infiltration in atypical meningiomas. *Acta Neurochir (Wien)* 156:1853–1854. <https://doi.org/10.1007/s00701-014-2148-z>
142. Yamamoto T et al (2015) Photodynamic diagnosis using 5-aminolevulinic acid in 41 biopsies for primary central nervous system lymphoma. *Photochem Photobiol* 91:1452–1457. <https://doi.org/10.1111/php.12510>
143. Yun J, Iwamoto FM, Sonabend AM (2016) Primary central nervous system lymphoma: a critical review of the role of surgery for resection. *Arch Cancer Res* 4. <https://doi.org/10.21767/2254-6081.100071>
144. Zhang RR, Swanson KI, Hall LT, Weichert JP, Kuo JS (2016) Diaplectic cancer-targeting alkylphosphocholine analogs may advance management of brain malignancies. *CNS Oncol* 5:223–231. <https://doi.org/10.2217/cns-2016-0017>

Part IV
Image Guided Radiooncology



Molecular Imaging in Photon Radiotherapy

27

Jamina Tara Fennell, Eleni Gkika, and Anca L. Grosu

Contents

27.1 Brain Tumours.....	846
27.1.1 Gliomas.....	846
27.2 Meningiomas.....	848
27.3 Head and Neck Cancer.....	848
27.4 Lung Cancer.....	850
27.5 Esophageal Cancer.....	852
27.6 Prostate Cancer.....	853
27.6.1 Localized Prostate Cancer and Dose Escalation.....	853
27.6.2 Lymph Node Metastases.....	854
27.6.3 Recurrence.....	854
27.6.4 Bone Metastases.....	855
27.7 Uterine Cancer.....	855
27.7.1 Cervical Cancer.....	855
27.7.2 Endometrial Cancer.....	856
27.8 Conclusion and Outlook.....	856
References.....	856

Nowadays, more than ever before, the treatment of cancer patients requires an interdisciplinary approach. Radiation therapy (RT) has become an indispensable pillar of cancer treatment early on, offering a local, curative treatment option and symptom control in palliative cases. Due to technological advances of the last 30 years, the precision in RT planning has greatly improved, allowing the radiation oncologist to prescribe high radiation doses and by that assuring high local tumour control while sparing healthy tissue and thereby reducing side effects. One of the most important developments has been the widespread introduction of intensity-modulated RT (IMRT) allowing a steep dose gradient outside the target volume. But higher precision in RT delivery is only useful if the information about

J. T. Fennell · E. Gkika · A. L. Grosu (✉)
Department of Radiation Oncology, University of Freiburg, Freiburg, Germany
e-mail: anca.grosu@uniklinik-freiburg.de

© Springer Nature Switzerland AG 2020
O. Schober et al. (eds.), *Molecular Imaging in Oncology*,
Recent Results in Cancer Research 216,
https://doi.org/10.1007/978-3-030-42618-7_27

845

tumour spread is equally precise. Unlike the surgeon who can visually verify the preoperative staging and adapt the extent of the procedure accordingly, the radiation oncologist depends much more and sometimes even exclusively on imaging diagnostics to define the macroscopic (gross tumour volume (GTV)) and microscopic tumour spread (clinical tumour volume (CTV)).

Therefore, molecular imaging, especially positron emission tomography (PET) and multiparametric MRI offer exciting new possibilities to improve RT planning and monitoring. While radio-oncology has become a vast field, the following chapter is supposed to give an overview of the application of molecular imaging in photon RT, which is the most common type of RT, using the example of brain tumours, head and neck cancer, lung cancer, esophageal cancer, prostate cancer and uterine cancer.

27.1 Brain Tumours

27.1.1 Gliomas

The standard imaging modality for diagnosis of gliomas is MRI. T1 sequences with and without gadolinium contrast enhancement and T2/FLAIR sequences give a good indication about tumour spread and heterogeneity. While low-grade gliomas typically present themselves only as hypointense lesions in T1- and hyperintense lesions FLAIR/T2-sequences, high-grade gliomas often have additional contrast enhancement in T1-sequences with central necrosis.

Because of the high sensitivity of these MRI sequences, the European Organization for Research and Treatment of Cancer (EORTC) and Radiotherapy and Oncology Group (RTOG) recommend that target volume definition be based on them [1]. Unfortunately, this can result in large planning target volumes increasing the risk of side effects like radionecrosis when curative doses are administered. Therefore if critical structures like the optical nerves or brain stem are involved to any greater extent, the prescribed dose must be reduced even at the expense of local tumour control. But at the same time, peritumoural edema, post-therapeutic gliosis and radionecrosis, have similar imaging characteristics as malignant tissue in the aforementioned MRI sequences leading to a specificity of 50% and leaving considerable room for improvement [2].

Magnetic resonance spectroscopy (MRS) allows the comparison of chemical components between normal and abnormal brain tissue and thus offers information about the metabolism of the latter. Although MRS has only a low resolution, it has proven useful in distinguishing post-therapeutic tissue alterations from tumour recurrence [3]. Whether MRS should routinely be integrated into RT planning remains still to be seen. Preliminary results are encouraging: a small phase II trial has shown dose escalation to areas of high choline/N-acetylaspartate ratio in patients with glioblastoma to be feasible and indicated an improved overall survival compared to a historic control [4]. In the USA, a pilot study investigating the possibility of

MRS-guided dose escalation is recruiting since 2017 (NCT03137888). A large phase III trial is being prepared in France with the same objective [5].

Positron emission tomography (PET) is another way to increase the specificity of tumour detection. In case of gliomas, the most common PET tracers are the amino acids C11-methionine (MET) and 18F-(fluoroethyl)-L-tyrosin (FET). Comparative studies on patients with cerebral malignancies could not find a difference in uptake or tumour/brain ratio between the two tracers, and hence they are equivalent for the clinical practice and RT planning [6, 7]. Both FET- and MET-PET were attributed superior specificity (75–95%) compared to MRI alone [8, 9]. The troublesome nature of this discovery is further illustrated by a study conducted on 39 high-grade glioma patients, who underwent MET-PET, MRI and CT before receiving adjuvant RT, which showed that the GTV based on MET-PET corresponded only in 13% of cases to the GTV based on gadolinium contrast-enhanced MRI and exceeded in 50% even the hyperintense area in T2 [10]. In clinical practice, RT naïve patients receive FET- or MET-PET-based target volume definition only on a case by case basis, e.g. to decrease the high dose volume and spare healthy tissue (Fig. 27.1). Randomized trials, which prove that the use of PET in radiation planning translates into improved prognosis, are still lacking.

In patients with high-grade glioma recurrence after RT who are eligible for re-irradiation, biological imaging is more commonly used, but again not systematically. A study of 44 patients with recurrence of high-grade glioma who received RT based on biological imaging, CT and MRI showed improved overall survival compared to those patients whose RT relied only on CT and MRI [11]. While this small study offers promising results, the question whether increased specificity of PET/CT translates into improved prognosis remains uncertain. To finally answer

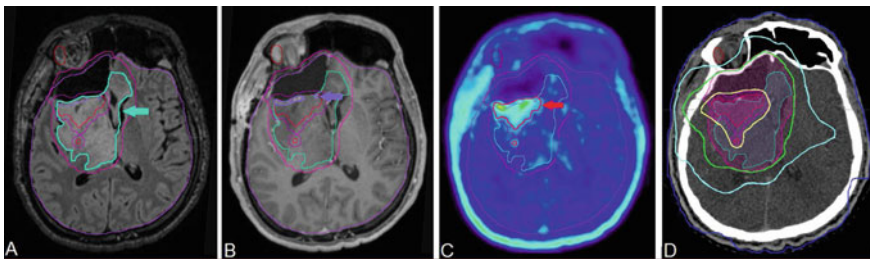


Fig. 27.1 Patient with oligodendroglioma WHO[°]III. After partial resection, imaging studies were performed for individual radiotherapy planning. **a** MRI-T2-weighted-fluid-attenuated inversion recovery (FLAIR) sequence: Gross tumour volume (GTV) according to FLAIR is highlighted in turquoise (->). **b** MRI-T1 sequence with gadolinium contrast enhancement (CE): GTV according to CE is highlighted in purple (->). **c** 18F-(fluoroethyl)-L-tyrosin positron emission tomography sequence (FET-PET): GTV according to FET-PET is highlighted in red (->). It is much larger than GTV-CE, but smaller than GTV-FLAIR, since it does not include edema. **d** Radiation plan using intensity-modulated radiotherapy (IMRT) with simultaneous integrated boost (SIB) to the GTV-FET; yellow: 95%-isodose (57 Gy), green: 76%-isodose (45.6 Gy), turquoise: 50%-isodose (30 Gy)

this question, the GLIAA trial, a prospective randomized multicenter phase II study, is currently recruiting patients with recurrent glioblastoma to treat them with re-irradiation either guided by PET/CT or by gadolinium enhancement on MRI (NCT01252459) [12]. Primary endpoint will be progression-free survival after 6 months and one of the secondary endpoints is overall survival.

27.2 Meningiomas

Similar to gliomas, MRI has been the imaging standard for diagnosis of meningiomas because of its morphological precision. According to the guidelines of the European Association of Neuro-Oncology (EANO), surgery remains the first-line treatment [13], but there are a considerable number of patients, who are either ineligible for surgery or whose meningioma can only be partially surgically removed and therefore require either primary, adjuvant or salvage RT. The most critical localization is the skull base, where any surgery has a considerable risk of neurological morbidity. Local tumour control after RT of skull base meningioma is excellent (86% after 10 years) [14]. However, the skull base is exactly the localization, where precise meningioma demarcation in MRI reaches its limitations especially around the cavernous sinus and the pituitary gland. Here PET/CT with either MET or 68-Ga-labelled DOTA (0)-D-Phe (1)-Tyr (3)-Octreotide (DOTATOC) decreases interobserver variability, identifies portions of meningioma undetected by MRI and CT and thereby significantly alters target volume definition [15–17].

27.3 Head and Neck Cancer

Irradiating patients with head and neck squamous cell carcinoma (HNSCC) poses a multitude of challenges. Lymph drainage in the mouth, throat and neck is rather complex, lymph nodes often are reactively enlarged due to inflammation or superinfection, RT is, in general, associated with considerable morbidity and prognosis depends heavily on individual tumour characteristics. The introduction of IMRT has already significantly reduced the risk of developing long-term side effects like xerostomia through conformal radiation dose delivery without jeopardizing tumour control [18]. However, in order to balance the need of tumour control on the one hand and the effort to improve treatment tolerance on the other hand, dose prescription needs to be optimized according to individual risk stratification.

Diffusion-weighted MRI (DW-MRI) which visualizes areas of high cellularity may present an easy and cost-effective way to increase the sensitivity of lymph node staging by MRI. Especially in cases of primary radiochemotherapy (RCT) the radiation oncologist has to rely on imaging to determine the extent of macroscopic tumour spread. T1 and T2 sequences offer morphological criteria whether or not a lymph node is involved, one of the most important criterion being a diameter larger

than 1 cm. In a study of 33 patients with head and neck cancer, the histopathology of 301 lymph nodes was correlated with information obtained by DW-MRI. DW-MRI proved to be superior to anatomical MRI in predicting metastasis in lymph nodes smaller than 1 cm (sensitivity 76% vs. 7%, respectively) [19]. According to several small studies, a low apparent diffusion coefficient values in DW-MRI during and near-term after RCT correlate with an unfavourable treatment response [20, 21] and are indicative of early recurrence with a reported accuracy of 90% [22]. Therefore, DW-MRI might be a useful monitoring tool to identify patients in need of early salvage therapy.

F18-fluorodeoxyglucose (FDG)-PET/CT may offer improved and new avenues to optimize target volume definition. A study, which compared target volume definition based on CT, MRI and FDG-PET with surgical specimens, found that GTV definition based on FDG-PET to be the most accurate, while GTVs based on CT and MRI were larger than the actual tumour [23]. Although the GTV receives in primary RCT a dose as high as 70 Gy, tumour recurrences occur most of the time in the high dose volume and even in 54% of cases inside the FDG-positive volume, indicating the tumour cells there to be highly radioresistant [24]. This may be overcome with dose escalation. In order to not increase treatment toxicity, investigators of a planning study used adaptive, voxel-by-voxel dose painting technology, so that only voxels with the highest FDG uptake would receive up to 86 Gy [25]. Obviously, this kind of methodology needs to be highly standardized in order to attempt any multicenter trials, which are necessary to evaluate the effect of these advanced treatment concepts on patient outcome [26].

PET/CT may also identify non-responders among patients with HNSCC treated with primary RCT through tumour hypoxia. The latter has proven to be a deciding factor for treatment resistance in a number of cancers but particularly in HNSCC [27, 28]. Using the PET-tracer fluoromisonidazole (FMISO) tumour hypoxia may be visualized non-invasively, which provides the possibility of monitoring hypoxia throughout RT [29]. Studies examining patients under RCT with serial FMISO-PET/CTs found that no hypoxia or hypoxia resolution early in therapy correlated with favourable outcomes [30, 31]. The hypoxic subvolume in patients with hypoxia persistence under RCT remains in the same topographical region [32]. The link between hypoxia and patient outcome prompted Lee et al. to de-escalate dose prescription to lymph nodes of patients with human papillomavirus-associated HNSCC if hypoxia measured by FMISO-PET/CT resolved after 1 week of RCT [33]. Thus, 30% of patients received 10 Gy less to lymph nodes without affecting clinical outcome after 2 years follow-up. While these endeavours pave the way to better treatment tolerance, simultaneously efforts are being made to improve tumour control in patients with unfavourable prognosis through dose escalation to areas of hypoxia persistence during RCT. Doses of up to 80.5 Gy can be attained in hypoxic subvolumes without violating the dose constraints of healthy surrounding tissue [34]. However, results whether this strategy has a clinical benefit remain to be seen: a randomized phase II study is currently recruiting patients to escalate the dose in FMISO-positive subvolume to 77 Gy (NCT02352792).

Follow-up and the early detection of recurrence after RCT for HNSCC are very challenging because post-treatment alterations, scar tissue and edema confound the sensitivity of CT and conventional MRI. Mehanna et al. could show that patients without residual activity in FDG-PET/CT 12 weeks after RCT could forego planned neck dissection without impacting clinical outcome [35]. FDG-PET has become an indispensable module of the diagnosis and treatment algorithm during follow-up of patients after RCT according to the NCCN guideline [36].

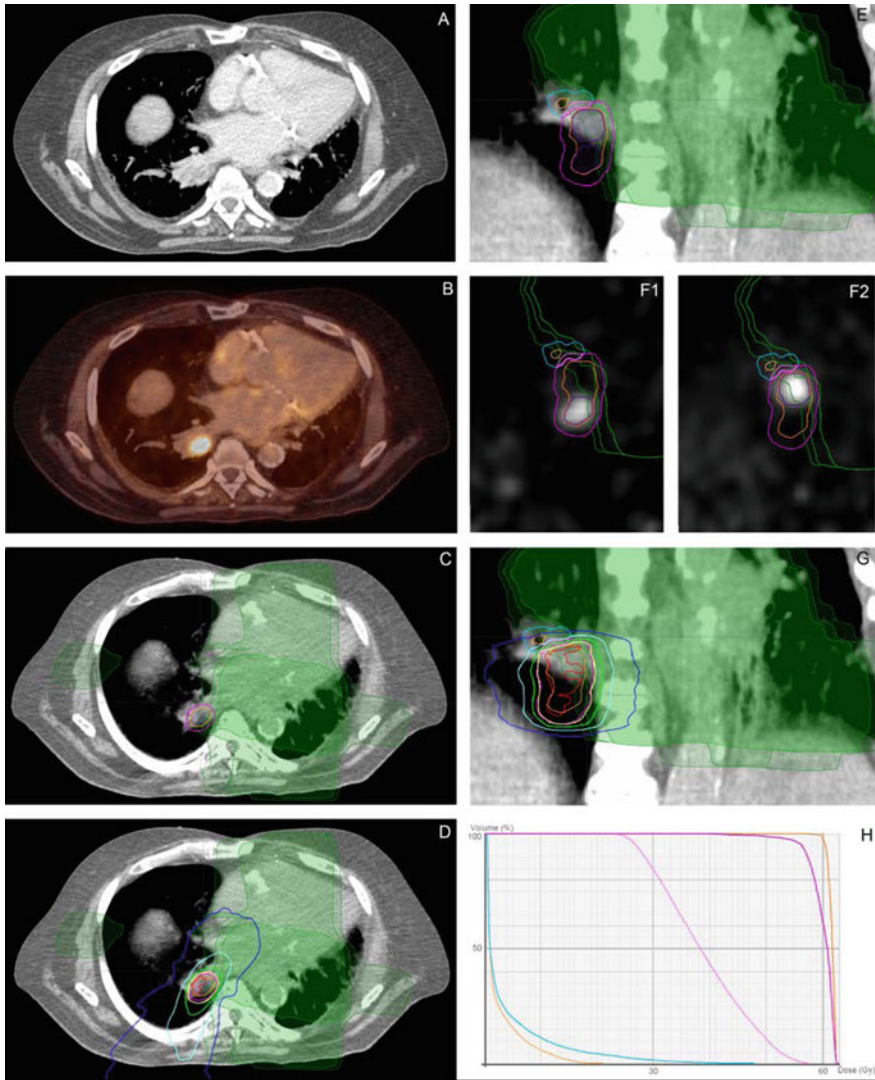
27.4 Lung Cancer

Non-small cell lung cancer (NSCLC) is one of the most common forms of cancer and the leading cause of death among all tumour entities. Nowadays, the usefulness of FDG-PET/CT for initial staging of patients with NSCLC is universally accepted in the medical community and mandatory prior treatment. Already 20 years ago radiation oncologists recognized the value of FDG-PET/CT for GTV definition of the primary tumour in case of atelectasis [37]. At the same time, FDG-PET/CT facilitates the identification of involved mediastinal lymph nodes [38].

PET/CT has significantly reduced interobserver variability and thusly has contributed to further standardization of treatment [39–41]. The diagnostic accuracy of FDG PET/CT compared with historical CT imaging makes it possible to adapt the target volumes. Several retrospective and single-centre analyses demonstrated an improvement of the inter-observer agreement for target volume delineation [42–44]. There have been efforts to even automatize GTV segmentation by defining a standard uptake value (SUV) threshold, which is viewed very critically by experts since healthy tissue like myocardium or brown fat has a high and necrosis a low SUV [45]. Therefore, qualitative interdisciplinary analysis of the PET/CT images and manual editing of the automatic-generated GTV remain indispensable [46, 47].

There are several pitfalls in the use of FDG-PET for RT planning. Most importantly the duration between the FDG-PET scan and the start of radiation treatment should not be more than three weeks. Then, it is paramount to standardize window/level settings to avoid discrepancies in tumour size and maintain a low intra- and interobserver variability. Furthermore, FDG-PET-based volumina often appear a little larger than their correlate in the CT scan due to respiratory motion during registration. Finally, FDG-PET/CT should be acquired in radiation position to allow optimal starting conditions for RT planning [48].

Depending on tumour stage there are two main ways to irradiate a patient with NSCLC: stereotactic body RT (SBRT) or conventionally fractionated radio(chemo)therapy. Patients with early stage tumours without nodal involvement are eligible for SBRT. In order to define the internal target volume (ITV), which respects the position of the GTV in all breathing cycles, a 4D-CT is mandatory. While this may be absolutely sufficient in case of peripheral tumours, centrally localized NSCLCs are far less easily marked out (Fig. 27.2). Interobserver variability profits from 4D-FDG-PET/CT [49]. It was also employed in the LungTech trial (EORTC



22,113-08,113) which investigates outcome after SBRT of centrally located NSCLCs. The results are still pending.

Patients with locally advanced NSCLC are treated with RCT. As mentioned above, PET/CT allows the distinction between atelectasis and tumour as well as reactive and involved lymph nodes. This harbours great potential for shrinking the radiation field and thereby allowing dose escalation. Until recently, it was unclear whether a smaller target volume would adversely affect prognosis. The results of the multicenter randomized phase II PET-Plan trial have been published in 2020 showing non-inferiority of FDG-PET/CT-based RT planning compared to

- ◀ **Fig. 27.2** Patient with non-small cell lung cancer (NSCLC) without lymph node or distant metastases. He was treated with neoadjuvant radiochemotherapy due to NSCLC of the contralateral lung 12 years ago with 50.4 Gy in 28 fractions. **a** Computer tomography (CT) with contrast enhancement (CE): right hilus is enlarged, but precise distinction between tumour and blood vessel is not possible. **b** 18F-fluorodeoxyglucose positron emission tomography/CT (FDG-PET/CT): the tumour is now plainly demarcated, due to high FDG uptake. **c** Planning CT: integral tumour volume (ITV) is highlighted in orange; planning target volume (PTV) is highlighted in dark pink; isodoses of the previous irradiation are shown in green (30, 40 and 50 Gy). **d** Treatment plan for 55 Gy in 10 fractions: red: 112%-isodose (61.6 Gy); yellow: 100%-isodose (55 Gy); bright green: 80%-isodose (44 Gy); turquoise: 50%-isodose (27.5 Gy); dark blue: 20%-isodose (11 Gy). **e** Planning CT in sagittal plane with extremes of breathing cycle delineated: dark purple: gross tumour volume during different breathing positions; orange: ITV; ocher: right bronchus; bright blue: planning organ at risk volume (PRV) of the right bronchus; bright pink: SIP (simultaneous integrated protection volume (overlap between PTV and PRV)) **F1/F2** FDG-PET-scan with respiratory gating. **G** Treatment plan in sagittal plane: SIP will only receive 28 Gy in 10 fractions in order to not exceed the constraint to the right bronchus (34 Gy). **G** Treatment plan for 55 Gy in 10 fractions in sagittal plane: red: 112%-isodose (61.6 Gy); yellow: 100%-isodose (55 Gy); bright green: 80%-isodose (44 Gy); turquoise: 50%-isodose (27.5 Gy); dark blue: 20%-isodose (11 Gy). **h** Dose volume histogram: The right bronchus receives less than 30 Gy, while 95% of the ITV will receive at least 60 Gy

conventional planning with a trend towards improved local control through isotoxic dose escalation [50].

27.5 Esophageal Cancer

Esophageal cancer can be treated by RT either neoadjuvantly or primarily. Lymph node involvement significantly impacts target volume definition, since either mediastinal, cervical or abdominal ones may be affected, depending on tumour location. Standard imaging consists of endoscopic ultrasound to evaluate locoregional lymph node metastases and mucosal tumour invasion and CT scan to again assess lymph nodes and distant metastases [51]. Furthermore, FDG-PET/CT is recommended for initial patient work-up according to international guidelines (NCCN, ESMO) [52]; While the sensitivity and specificity of FDG-PET/CT for detecting locoregional lymph node metastases vary from study to study (30–93% and 79–100%, respectively) and equal endoscopic ultrasound (45–100% and 44–100%, respectively), it supersedes conventional CT scans in the detection of distant metastases [53–55]. Thusly, patients, who are eligible for surgery based on the local medical findings but were identified as having distant metastases in the FDG-PET/CT scan, can be spared an invasive procedure. In case of oligometastatic disease, they may be eligible for an individualized treatment plan with RCT of the primary tumour and SBRT of the distant metastases. But even if there are no distant metastases detected, a study of 90 patients found that FDG-PET/CT leads to a change in the radiation treatment plan in around 50% of cases [56]. However, in the same study, PET/CT-based planning showed no benefit in terms of decreased locoregional recurrence.

There have been efforts to make FDG-PET/CT an even more integral part of esophageal cancer treatment. The MUNICON II trial subjected patients, who did not metabolically respond to neoadjuvant chemotherapy in FDG-PET/CT after 14 days to RCT of a total dose of 32 Gy. Unfortunately, that trial did not meet its primary end point of increased R0-resections which may be due to the rather low total dose [57]. Another clinical trial evaluated the impact of dose escalation in patients who did not respond or only responded partially to RCT up to 50.4 Gy according to serial FDG-PET/CT scans. They found improved 2-year overall survival and local tumour control between the control and investigative group. Further analysis revealed that only the patient with partial treatment response had a significant benefit from dose escalation [58].

27.6 Prostate Cancer

RT is highly effective in patients with prostate cancer as primary therapy in localized disease with curative intent or for symptom control in a palliative setting [59]. Prostate cancer is the most common tumour entity among men. The current guidelines recommend to forego any imaging for low-risk patients, whereas intermediate patients may and high-risk patients absolutely should receive multiparametric MRI (mpMRI) and a bone scan to exclude metastatic disease [59–61].

27.6.1 Localized Prostate Cancer and Dose Escalation

Target definition in localized prostate cancer is dependent upon tumour stage. Moreover, several trials dating from 10 years ago have shown an improved biochemical progression-free survival after primary RT with dose escalation to 74–80 Gy [62–66], which was accompanied with greater urogenital and/or gastrointestinal early and late toxicity [62–65], as the dose was homogeneously prescribed to the whole prostate. Since the malignant tissue seldom encompasses the whole prostate, the next logical step is to limit the dose escalation only to it, which would allow better protection for bladder and rectum. The prerequisite for this approach is the ability to precisely identify malignant tumour tissue in an organ of around 25 ml.

MpMRI, which entails T1, T2, DW and dynamic contrast-enhanced (DCE) sequences, has a good sensitivity (74–89%) and specificity (73–88%) for tumour detection [67, 68], and yet there is high interobserver variability in precise intraprostatic tumour delineation [69, 70] due partially to confounding factors like androgen deprivation therapy, previous biopsy or fiducial implantation [71], lesions smaller than 0.5 ml [72] and benign prostate hyperplasia [73]. The updated version of the Prostate Imaging Reporting and Data System (PI-RADSv2) endeavours to further standardize the evaluation of mpMRI and names the most significant sequences to detect malignant tissue in the different subregions of the prostate [74].

Different PET tracers have been investigated in terms of their usefulness to stage prostate cancer. FDG has been proven unreliable because of similar uptake in benign prostate hyperplasia, prostate cancer, prostatitis and normal prostate tissue [75]. Carbon-11-choline (11C-choline) has also failed to deliver reliable information about intraprostatic tumour spread [76, 77]. The rather new PET-tracer Prostate-specific membrane antigen (PSMA) has shown to be more promising especially in larger tumours [78]. However, current data suggest that the combination of PSMA-PET/CT and mpMRI will result in the highest sensitivity and specificity in tumour tissue detection compared to histopathological analysis [79, 80]. Several planning studies have demonstrated that integrated dose escalation to the intraprostatic PSMA-uptake volume is feasible with nearly no increased risk of increased bladder and rectum toxicity [81, 82]. Similar results could be found for integrated dose escalation to a GTV based on PSMA-PET and mpMRI [83]. Whether integrated dose escalation to intraprostatic tumour volume will actually prove beneficial for patients is being investigated in the prospective phase III trial (FLAME-study, NCT01168479) [84].

27.6.2 Lymph Node Metastases

Another important aspect in target volume definition of localized prostate cancer is the identification of lymph node metastases. Unfortunately, conventional MRI sequences possess only low sensitivity (39%) with a specificity of 82% [85]. Sensitivity seems to be improving after consideration of DW-MRI (sensitivity 84.6%, specificity 89%) [86].

PSMA-PET/CT is also superior to conventional MRI sequences in detecting lymph node metastases. Sensitivity and specificity in studies have been 64–67% and 81–98.9%, respectively [87–89]. The precise identification of lymph node metastases allows the radiation oncologist to formulate individual treatment plans with enlarged para-aortal radiation fields and dose escalation to only PSMA-positive lymph nodes.

27.6.3 Recurrence

RT is a common salvage therapy for patients with biochemical or macroscopic recurrence after primary treatment. An issue of contention is the PSA level which warrants imaging diagnostics. Here PSMA-PET/CT has proven to be valuable and significantly impacting the patient treatment plan in around 50% of cases [90, 91]. Currently, it may be performed at PSA levels as low as 0.2–0.5 ng/ml [92]. Of course, the likelihood of macroscopic tumour detection increases with absolute PSA value and PSA doubling time [92]. An analysis of 1007 with prostate cancer recurrence showed that in 79% of cases a macroscopic tumour could be detected [93].

27.6.4 Bone Metastases

Most of the distant metastases in prostate cancer are located in the bone. RT is indicated either in oligometastatic disease or in palliative setting to maintain bone stability, manage pain or prevent, respectively, treat neurological symptoms due to spinal cord or nerve compression. Standard staging modality is a bone scan.

While a meta-analysis has shown a very high pooled sensitivity and specificity for the detection of bone metastases with MRI (96 and 98%) and it can decidedly influence the treatment strategy in patients with high-risk prostate cancer [94, 95], depending on the country it may be difficult and costly to scan all the body regions necessary to have a complete staging.

PSMA-PET/CT performed superiorly compared to a standard bone scan in an analysis of 126 patients (sensitivity 98.7–100% versus 86.7–89.3% specificity 88.2–100% versus 60.8–96.1%) [96]. While still a costly imaging modality, PSMA-PET/CT has the added advantage of giving more information about bone stability due to the included CT scan and other metastases compared to bone scan and MRI.

27.7 Uterine Cancer

27.7.1 Cervical Cancer

Cervical cancer is the second most common tumour entity among women [97] and RT is often used primarily or adjuvantly in a curative intent. Nevertheless, especially in early stages, surgery presents the first-line approach. Therefore, traditionally, cervical cancer is classified by the International Federation of Gynecology and Obstetrics (FIGO) staging system, which is mainly based on clinical examination. But since risk factors like tumour size, stroma or lymph node involvement have been identified to significantly impact prognosis, imaging with MRI and CT is now routinely performed. Additionally, FDG-PET/CT has proven to be more and more relevant in recent years, so much so that it has been introduced into the major NCCN and ESMO guidelines [98, 99].

During initial patient work-up, FDG-PET/CT does not perform better than MRI with regard to assessing tumour volume and parametric invasion, since the latter is unparalleled in depicting soft tissue contrast and resolution. But FDG-PET/CT has shown a high sensitivity and specificity for the detection of pelvic (65–90% and 96–99%, respectively) and para-aortal lymph node metastases (68–94% and 89–98%, respectively) as well as distant metastases [100]. This information directly affects radiation treatment planning and may result in an extended radiation field or dose escalation to lymph nodes with increased FDG uptake. In order to avoid increased toxicity during and after RT of lymph node metastases, intensity-modulated RT should be used [101]. Thusly, a high local control rate may be achieved in field but unfortunately distant metastases are the most common failure site once there is lymph node involvement [102].

There are some studies exploring the feasibility of FDG-PET-guided HDR-brachytherapy, but the patient numbers are small and there is no comparison to MRI-guided brachytherapy.

27.7.2 Endometrial Cancer

Surgery as primary therapy or for the purpose of staging is often the first procedure that patients with endometrial cancer have to undergo. Depending on individual risk factors, RT is mostly indicated adjuvantly, but is an option for primary treatment if the patient is inoperable [103]. Nevertheless, assessment of pelvic and para-aortal lymph node is indispensable for target definition. FDG-PET/CT presents an appropriate alternative for surgical staging with high sensitivity and specificity (73–85% and 91–98%, respectively) [104–107].

27.8 Conclusion and Outlook

Biological imaging is a useful tool of the radiation oncologist for tumour detection and identification of high-risk subvolumes. This makes it possible to further individualize treatment either through dose escalation or deescalation.

A very promising prospect for future studies and clinical trials is radiomics, which may be the key to transcend the limitations of the human eye in the interpretation of imaging diagnostics and lead to improved treatment of cancer patients.

References

1. Zhao F, Li M, Kong L, Zhang G, Yu J (2016) Delineation of radiation therapy target volumes for patients with postoperative glioblastoma: a review. *OncoTargets Ther* 9:3197–3204
2. Weber WA, Grosu AL, Czernin J (2008) Technology Insight: advances in molecular imaging and an appraisal of PET/CT scanning. *Nat Clin Pract Oncol* 5:160–170
3. Nguyen ML, Willows B, Khan R, Chi A, Kim L, Nour SG, Sroka T, Kerr C, Godinez J, Mills M et al (2014) The potential role of magnetic resonance spectroscopy in image-guided radiotherapy. *Front Oncol* 4
4. Einstein DB, Wessels B, Bangert B, Fu P, Nelson AD, Cohen M, Sagar S, Lewin J, Sloan A, Zheng Y et al (2012) Phase II trial of radiosurgery to magnetic resonance spectroscopy-defined high-risk tumor volumes in patients with glioblastoma multiforme. *Int J Radiat Oncol Biol Phys* 84:668–674
5. Ken S, Vieilleveigne L, Franceries X, Simon L, Supper C, Lotterie J-A, Filleron T, Lubrano V, Berry I, Cassol E et al (2013) Integration method of 3D MR spectroscopy into treatment planning system for glioblastoma IMRT dose painting with integrated simultaneous boost. *Radiat Oncol Lond Engl* 8:1
6. Grosu A-L, Astner ST, Riedel E, Nieder C, Wiedenmann N, Heinemann F, Schwaiger M, Molls M, Wester H-J, Weber WA (2011) An interindividual comparison of O-(2-[18F]

- fluoroethyl)-L-tyrosine (FET)- and L-[methyl-11C]methionine (MET)-PET in patients with brain gliomas and metastases. *Int J Radiat Oncol Biol Phys* 81:1049–1058
7. Weber WA, Wester HJ, Grosu AL, Herz M, Dzewas B, Feldmann HJ, Molls M, Stöcklin G, Schwaiger M (2000) O-(2-[18F]fluoroethyl)-L-tyrosine and L-[methyl-11C]methionine uptake in brain tumours: initial results of a comparative study. *Eur J Nucl Med* 27:542–549
 8. Dunet V, Rossier C, Buck A, Stupp R, Prior JO (2012) Performance of 18F-fluoroethyl-tyrosine (18F-FET) PET for the differential diagnosis of primary brain tumor: a systematic review and metaanalysis. *J Nucl Med Off Publ Soc Nucl Med* 53:207–214
 9. Grosu A-L, Weber WA (2010) PET for radiation treatment planning of brain tumours. *Radiother Oncol J Eur Soc Ther Radiol Oncol* 96:325–327
 10. Grosu A-L, Weber WA, Riedel E, Jeremic B, Nieder C, Franz M, Gumprecht H, Jaeger R, Schwaiger M, Molls M (2005) L-(methyl-11C) methionine positron emission tomography for target delineation in resected high-grade gliomas before radiotherapy. *Int J Radiat Oncol Biol Phys* 63:64–74
 11. Grosu AL, Weber WA, Franz M, Stärk S, Piert M, Thamm R, Gumprecht H, Schwaiger M, Molls M, Nieder C (2005) Reirradiation of recurrent high-grade gliomas using amino acid PET (SPECT)/CT/MRI image fusion to determine gross tumor volume for stereotactic fractionated radiotherapy. *Int J Radiat Oncol Biol Phys* 63:511–519
 12. Oehlke O, Mix M, Graf E, Schimek-Jasch T, Nestle U, Götz I, Schneider-Fuchs S, Weyerbrock A, Mader I, Baumert BG et al (2016) Amino-acid PET versus MRI guided re-irradiation in patients with recurrent glioblastoma multiforme (GLIAA)—protocol of a randomized phase II trial (NOA 10/ARO 2013-1). *BMC Cancer* 16:769
 13. Goldbrunner R, Minniti G, Preusser M, Jenkinson MD, Sallabanda K, Houdart E, von Deimling A, Stavrinou P, Lefranc F, Lund-Johansen M et al (2016) EANO guidelines for the diagnosis and treatment of meningiomas. *Lancet Oncol* 17:e383–e391
 14. Combs SE, Farzin M, Boehmer J, Oehlke O, Molls M, Debus J, Grosu A-L (2018) Clinical outcome after high-precision radiotherapy for skull base meningiomas: pooled data from three large german centers for radiation oncology. *Radiother Oncol J Eur Soc Ther Radiol Oncol* 127:274–279
 15. Astner ST, Dobrei-Ciuchendea M, Essler M, Bundschuh RA, Sai H, Schwaiger M, Molls M, Weber WA, Grosu AL (2008) Effect of 11C-Methionine-Positron emission tomography on gross tumor volume delineation in stereotactic radiotherapy of skull base meningiomas. *Int J Radiat Oncol Biol Phys* 72:1161–1167
 16. Grosu A-L, Weber WA, Astner ST, Adam M, Krause BJ, Schwaiger M, Molls M, Nieder C (2006) 11C-methionine PET improves the target volume delineation of meningiomas treated with stereotactic fractionated radiotherapy. *Int J Radiat Oncol Biol Phys* 66:339–344
 17. Milker-Zabel S, Zabel-du Bois A, Henze M, Huber P, Schulz-Ertner D, Hoess A, Haberkorn U, Debus J (2006) Improved target volume definition for fractionated stereotactic radiotherapy in patients with intracranial meningiomas by correlation of CT, MRI, and [68 Ga]-DOTATOC-PET. *Int J Radiat Oncol Biol Phys* 65:222–227
 18. Marta GN, Silva V, de Carvalho AH, de Arruda FF, Hanna SA, Gadia R, da Silva JLF, Correa SFM, Abreu CECV, Riera R (2014) Intensity-modulated radiation therapy for head and neck cancer: systematic review and meta-analysis. *Radiother Oncol* 110:9–15
 19. Thoeny HC, De Keyzer F, King AD (2012) Diffusion-weighted MR imaging in the head and neck. *Radiology* 263:19–32
 20. Dirix P, Vandecaveye V, De Keyzer F, Stroobants S, Hermans R, Nuyts S (2009) Dose painting in radiotherapy for head and neck squamous cell carcinoma: value of repeated functional imaging with (18)F-FDG PET, (18)F-fluoromisonidazole PET, diffusion-weighted MRI, and dynamic contrast-enhanced MRI. *J Nucl Med Off Publ Soc Nucl Med* 50:1020–1027
 21. Vandecaveye V, Dirix P, De Keyzer F, de Beeck KO, Vander Poorten V, Roebben I, Nuyts S, Hermans R (2010) Predictive value of diffusion-weighted magnetic resonance imaging during chemoradiotherapy for head and neck squamous cell carcinoma. *Eur Radiol* 20:1703–1714

22. King AD, Mo FKF, Yu K-H, Yeung DKW, Zhou H, Bhatia KS, Tse GMK, Vlantis AC, Wong JKT, Ahuja AT (2010) Squamous cell carcinoma of the head and neck: diffusion-weighted MR imaging for prediction and monitoring of treatment response. *Eur Radiol* 20:2213–2220
23. Daisne J-F, Duprez T, Weynand B, Lonneux M, Hamoir M, Reyckler H, Grégoire V (2004) Tumor volume in pharyngolaryngeal squamous cell carcinoma: comparison at CT, MR imaging, and FDG PET and validation with surgical specimen. *Radiology* 233:93–100
24. Due AK, Vogelius IR, Aznar MC, Bentzen SM, Berthelsen AK, Korreman SS, Loft A, Kristensen CA, Specht L (2014) Recurrences after intensity modulated radiotherapy for head and neck squamous cell carcinoma more likely to originate from regions with high baseline [18F]-FDG uptake. *Radiother Oncol J Eur Soc Ther Radiol Oncol* 111:360–365
25. Differding S, Sterpin E, Janssens G, Hanin F-X, Lee JA, Grégoire V (2016) Methodology for adaptive and robust FDG-PET escalated dose painting by numbers in head and neck tumors. *Acta Oncol Stockh Swed* 55:217–225
26. Grégoire V, Bol A, Geets X, Lee J (2006) Is PET-based treatment planning the new standard in modern radiotherapy? The head and neck paradigm. *Semin Radiat Oncol* 16:232–238
27. Fleming IN, Manavaki R, Blower PJ, West C, Williams KJ, Harris AL, Domarkas J, Lord S, Baldry C, Gilbert FJ (2015) Imaging tumour hypoxia with positron emission tomography. *Br J Cancer* 112:238–250
28. Nordmark M, Bentzen SM, Rudat V, Brizel D, Lartigau E, Stadler P, Becker A, Adam M, Molls M, Dunst J et al (2005) Prognostic value of tumor oxygenation in 397 head and neck tumors after primary radiation therapy. An international multi-center study. *Radiother Oncol J Eur Soc Ther Radiol Oncol* 77:18–24
29. Gagel B, Reinartz P, DiMartino E, Zimny M, Pinkawa M, Maneschi P, Stanzel S, Hamacher K, Coenen HH, Westhofen M et al (2004) pO₂ Polarography Versus Positron Emission Tomography ([18F] Fluoromisonidazole, [18F]-2-Fluoro-2'-Deoxyglucose). *Strahlenther Onkol* 180:616–622
30. Wiedenmann NE, Bucher S, Hentschel M, Mix M, Vach W, Bittner M-I, Nestle U, Pfeiffer J, Weber WA, Grosu AL (2015) Serial [18F]-fluoromisonidazole PET during radiochemotherapy for locally advanced head and neck cancer and its correlation with outcome. *Radiother Oncol J Eur Soc Ther Radiol Oncol* 117:113–117
31. Zips D, Zöphel K, Abolmaali N, Perrin R, Abramyyuk A, Haase R, Appold S, Steinbach J, Kotzerke J, Baumann M (2012) Exploratory prospective trial of hypoxia-specific PET imaging during radiochemotherapy in patients with locally advanced head-and-neck cancer. *Radiother Oncol J Eur Soc Ther Radiol Oncol* 105:21–28
32. Bittner M-I, Wiedenmann N, Bucher S, Hentschel M, Mix M, Weber WA, Grosu A-L (2013) Exploratory geographical analysis of hypoxic subvolumes using 18F-MISO-PET imaging in patients with head and neck cancer in the course of primary chemoradiotherapy. *Radiother Oncol* 108:511–516
33. Lee N, Schoder H, Beattie B, Lanning R, Riaz N, McBride S, Katabi N, Li D, Yarusi B, Chan S et al (2016) Strategy of using intratreatment hypoxia imaging to selectively and safely guide radiation dose de-escalation concurrent with chemotherapy for locoregionally advanced human papillomavirus-related oropharyngeal carcinoma. *Int J Radiat Oncol Biol Phys* 96:9–17
34. Grosu AL, Souvatzoglou M, Röper B, Dobritz M, Wiedenmann N, Jacob V, Wester HJ, Reischl G, Machulla HJ, Schwaiger M et al (2007) Hypoxia imaging with FAZA-PET and theoretical considerations with regard to dose painting for individualization of radiotherapy in patients with head and neck cancer. *Int J Radiat Oncol Biol Phys* 69:541–551
35. Mehanna H, Wong W-L, McConkey CC, Rahman JK, Robinson M, Hartley AGJ, Nutting C, Powell N, Al-Booz H, Robinson M et al (2016) PET-CT Surveillance versus Neck Dissection in Advanced Head and Neck Cancer. *N Engl J Med* 374:1444–1454
36. Pfister DG, Foote RL, Gilbert J, Gillison ML, Ridge JA, Rocco J (2018) NCCN guidelines index table of contents discussion 227

37. Nestle U, Walter K, Schmidt S, Licht N, Nieder C, Motaref B, Hellwig D, Niewald M, Ukena D, Kirsch CM et al (1999) 18F-deoxyglucose positron emission tomography (FDG-PET) for the planning of radiotherapy in lung cancer: high impact in patients with atelectasis. *Int J Radiat Oncol Biol Phys* 44:593–597
38. De Ruyscher D, Wanders S, van Haren E, Hochstenbag M, Geeraedts W, Utama I, Simons J, Dohmen J, Rhami A, Buell U et al (2005) Selective mediastinal node irradiation based on FDG-PET scan data in patients with non-small-cell lung cancer: a prospective clinical study. *Int J Radiat Oncol Biol Phys* 62:988–994
39. Caldwell CB, Mah K, Ung YC, Danjoux CE, Balogh JM, Ganguli SN, Ehrlich LE (2001) Observer variation in contouring gross tumor volume in patients with poorly defined non-small-cell lung tumors on CT: the impact of 18FDG-hybrid PET fusion. *Int J Radiat Oncol Biol Phys* 51:923–931
40. Fox JL, Rengan R, O'Meara W, Yorke E, Erdi Y, Nehmeh S, Leibel SA, Rosenzweig KE (2005) Does registration of PET and planning CT images decrease interobserver and intraobserver variation in delineating tumor volumes for non-small-cell lung cancer? *Int J Radiat Oncol Biol Phys* 62:70–75
41. Hanna GG, McAleese J, Carson KJ, Stewart DP, Cosgrove VP, Eakin RL, Zafari A, Lynch T, Jarritt PH, Young VAL et al (2010) 18F-FDG PET-CT simulation for non-small-cell lung cancer: effect in patients already staged by PET-CT. *Int J Radiat Oncol Biol Phys* 77:24–30
42. Dwamena BA, Sonnad SS, Angobaldo JO, Wahl RL (1999) Metastases from non-small cell lung cancer: mediastinal staging in the 1990s—meta-analytic comparison of PET and CT. *Radiology* 213:530–536
43. De Ruyscher D, Wanders S, van Haren E et al (2005) Selective mediastinal node irradiation based on FDG-PET scan data in patients with non-small-cell lung cancer: a prospective clinical study. *Int J Radiat Oncol Biol Phys* 62:988–994
44. Nestle U, Walter K, Schmidt S et al (1999) 18F-deoxyglucose positron emission tomography (FDG-PET) for the planning of radiotherapy in lung cancer: high impact in patients with atelectasis. *Int J Radiat Oncol Biol Phys* 44:593–597
45. MacManus MP, Hicks RJ (2008) Where do we draw the line? Contouring tumors on positron emission tomography/computed tomography. *Int J Radiat Oncol Biol Phys* 71:2–4
46. Doll C, Duncker-Rohr V, Rücker G, Mix M, MacManus M, De Ruyscher D, Vogel W, Eriksen JG, Oyen W, Grosu A-L et al (2014) Influence of experience and qualification on PET-based target volume delineation. When there is no expert—ask your colleague. *Strahlenther Onkol Organ Dtsch Rontgengesellschaft A1* 190:555–562
47. MacManus M, Nestle U, Rosenzweig KE, Carrio I, Messa C, Belohlavek O, Danna M, Inoue T, Deniaud-Alexandre E, Schipani S et al (2009) Use of PET and PET/CT for radiation therapy planning: IAEA expert report 2006–2007. *Radiother Oncol J Eur Soc Ther Radiol Oncol* 91:85–94
48. Konert T, Vogel W, MacManus MP, Nestle U, Belderbos J, Grégoire V, Thorwarth D, Fidarova E, Paez D, Chiti A et al (2015) PET/CT imaging for target volume delineation in curative intent radiotherapy of non-small cell lung cancer: IAEA consensus report 2014. *Radiother Oncol* 116:27–34
49. Chirindel A, Adebahr S, Schuster D, Schimek-Jasch T, Schanne DH, Nemer U, Mix M, Meyer P, Grosu A-L, Brunner T et al (2015) Impact of 4D-(18)FDG-PET/CT imaging on target volume delineation in SBRT patients with central versus peripheral lung tumors. Multi-reader comparative study. *Radiother Oncol J Eur Soc Ther Radiol Oncol* 115:335–341
50. Nestle U, Schimek-Jasch T, Kremp S, Schaefer-Schuler A, Kuesters A, Tosch M, Hehr T, Eschmann S, Bultel Y, Hass P et al (2020) Imaging-based target volume reduction in chemoradiotherapy for locally advanced non-small-cell lung cancer (PET-Plan): a multicentre, open-label, randomised, controlled trial. *Lancet Oncol*. 21(4):581–592

51. Lordick F, Mariette C, Haustermans K, Obermannová R, Arnold D, Guidelines Committee ESMO (2016) Oesophageal cancer: ESMO clinical practice guidelines for diagnosis, treatment and follow-up. *Ann Oncol Off J Eur Soc Med Oncol* 27:v50–v57
52. Ajani JA, Barthel JS, Bentrem DJ, D'Amico TA, Das P, Denlinger CS, Fuchs CS, Gerdes H, Glasgow RE, Hayman JA et al (2011) Esophageal and esophagogastric junction cancers. *J Natl Compr Canc Netw* 9:830–887
53. Muijs CT, Beukema JC, Pruim J, Mul VE, Groen H, Plukker JT, Langendijk JA (2010) A systematic review on the role of FDG-PET/CT in tumour delineation and radiotherapy planning in patients with esophageal cancer. *Radiother Oncol J Eur Soc Ther Radiol Oncol* 97:165–171
54. van Vliet EPM, Heijenbrok-Kal MH, Hunink MGM, Kuipers EJ, Siersema PD (2008) Staging investigations for oesophageal cancer: a meta-analysis. *Br J Cancer* 98:547–557
55. van Westreenen HL, Westerterp M, Bossuyt PMM, Pruim J, Sloof GW, van Lanschot JJB, Groen H, Plukker JTM (2004) Systematic review of the staging performance of 18F-fluorodeoxyglucose positron emission tomography in esophageal cancer. *J Clin Oncol Off J Am Soc Clin Oncol* 22:3805–3812
56. Muijs CT, Beukema JC, Woutersen D, Mul VE, Berveling MJ, Pruim J, van der Jagt EJ, Hospers GAP, Groen H, Plukker JT et al (2014) Clinical validation of FDG-PET/CT in the radiation treatment planning for patients with oesophageal cancer. *Radiother Oncol J Eur Soc Ther Radiol Oncol* 113:188–192
57. zum Büschenfelde CM, Herrmann K, Schuster T, Geinitz H, Langer R, Becker K, Ott K, Ebert M, Zimmermann F, Friess H et al (2011) (18)F-FDG PET-guided salvage neoadjuvant radiochemotherapy of adenocarcinoma of the esophagogastric junction: the MUNICON II trial. *J Nucl Med Off Publ Soc Nucl Med* 52:1189–1196
58. Ma J, Wang Z, Wang C, Chen E, Dong Y, Song Y, Wang W, You D, Jiang W, Zang R (2017) Individualized radiation dose escalation based on the decrease in tumor FDG uptake and normal tissue constraints improve survival in patients with esophageal carcinoma. *Technol Cancer Res Treat* 16:75–80
59. Mohler, J.L., Lee, R.J., Antonarakis, E.S., Higano, C.S., and Richey, S. (2018). NCCN Guidelines Index Table of Contents. Prostate Cancer 151
60. Bekelman JE, Rumble RB, Freedland SJ (2018) Clinically localized prostate cancer: ASCO clinical practice guideline endorsement of an AUA/ASTRO/SUO guideline summary. *J Oncol Pract* 14:618–624
61. Mottet N, Bellmunt J, Bolla M, Briers E, Cumberbatch MG, De Santis M, Fossati N, Gross T, Henry AM, Joniau S et al (2017) EAU-ESTRO-SIOG guidelines on prostate cancer. Part 1: screening, diagnosis, and local treatment with curative intent. *Eur Urol* 71:618–629
62. Dearnaley DP, Sydes MR, Graham JD, Aird EG, Bottomley D, Cowan RA, Huddart RA, Jose CC, Matthews JH, Millar J et al (2007) Escalated-dose versus standard-dose conformal radiotherapy in prostate cancer: first results from the MRC RT01 randomised controlled trial. *Lancet Oncol* 8:475–487
63. Kuban DA, Tucker SL, Dong L, Starkschall G, Huang EH, Cheung MR, Lee AK, Pollack A (2008) Long-term results of the M. D. Anderson randomized dose-escalation trial for prostate cancer. *Int J Radiat Oncol Biol Phys* 70:67–74
64. Kuban DA, Levy LB, Cheung MR, Lee AK, Choi S, Frank S, Pollack A (2011) Long-term failure patterns and survival in a randomized dose-escalation trial for prostate cancer. Who dies of disease? *Int J Radiat Oncol Biol Phys* 79:1310–1317
65. Viani GA, Stefano EJ, Afonso SL (2009) Higher-than-conventional radiation doses in localized prostate cancer treatment: a meta-analysis of randomized, controlled trials. *Int J Radiat Oncol Biol Phys* 74:1405–1418
66. Zietman AL, DeSilvio ML, Slater JD, Rossi CJ, Miller DW, Adams JA, Shipley WU (2005) Comparison of conventional-dose vs high-dose conformal radiation therapy in clinically localized adenocarcinoma of the prostate: a randomized controlled trial. *JAMA* 294:1233–1239

67. de Rooij M, Hamoen EHJ, Fütterer JJ, Barentsz JO, Rovers MM (2014) Accuracy of multiparametric MRI for prostate cancer detection: a meta-analysis. *AJR Am J Roentgenol* 202:343–351
68. Woo S, Suh CH, Kim SY, Cho JY, Kim SH (2017) Diagnostic performance of prostate imaging reporting and data system version 2 for detection of prostate cancer: a systematic review and diagnostic meta-analysis. *Eur Urol* 72:177–188
69. van Schie MA, Dinh CV, van Houdt PJ, Pos FJ, Heijmink SWTJP, Kerkmeijer LGW, Kotte ANTJ, Oyen R, Haustermans K, van der Heide UA (2018) Contouring of prostate tumors on multiparametric MRI: Evaluation of clinical delineations in a multicenter radiotherapy trial. *Radiother Oncol J Eur Soc Ther Radiol Oncol* 128:321–326
70. Steenbergen, P., Haustermans, K., Lerut, E., Oyen, R., De Wever, L., Van den Bergh, L., Kerkmeijer, L.G.W., Pameijer, F.A., Veldhuis, W.B., van der Voort van Zyp, J.R.N., et al. (2015). Prostate tumor delineation using multiparametric magnetic resonance imaging: Inter-observer variability and pathology validation. *Radiother. Oncol. J. Eur. Soc. Ther. Radiol. Oncol.* 115, 186–190
71. Barrett T, Gill AB, Kataoka MY, Priest AN, Joubert I, McLean MA, Graves MJ, Stearn S, Lomas DJ, Griffiths JR et al (2012) DCE and DW MRI in monitoring response to androgen deprivation therapy in patients with prostate cancer: a feasibility study. *Magn Reson Med* 67:778–785
72. Schmuecking M, Boltze C, Geyer H, Salz H, Schilling B, Wendt TG, Kloetzer K-H, Marx C (2009) Dynamic MRI and CAD vs. choline MRS: where is the detection level for a lesion characterisation in prostate cancer? *Int J Radiat Biol* 85:814–824
73. Bonekamp D, Jacobs MA, El-Khouli R, Stoianovici D, Macura KJ (2011) Advancements in MR imaging of the prostate: from diagnosis to interventions. *Radiogr Rev Publ Radiol Soc N Am Inc* 31:677–703
74. Weinreb JC, Barentsz JO, Choyke PL, Cornud F, Haider MA, Macura KJ, Margolis D, Schnall MD, Shtern F, Tempany CM et al (2016) PI-RADS Prostate imaging—reporting and data system: 2015, Version 2. *Eur Urol* 69:16–40
75. Jadvar H (2011) Prostate cancer: PET with 18F-FDG, 18F- or 11C-acetate, and 18F- or 11C-choline. *J Nucl Med Off Publ Soc Nucl Med* 52:81–89
76. Bundschuh RA, Wendl CM, Weirich G, Eiber M, Souvatzoglou M, Treiber U, Kübler H, Maurer T, Gschwend JE, Geinitz H et al (2013) Tumour volume delineation in prostate cancer assessed by [11C]choline PET/CT: validation with surgical specimens. *Eur J Nucl Med Mol Imaging* 40:824–831
77. Grosu A-L, Weirich G, Wendl C, Prokic V, Kirste S, Geinitz H, Souvatzoglou M, Gschwend JE, Schwaiger M, Molls M et al (2014) 11C-Choline PET/pathology image coregistration in primary localized prostate cancer. *Eur J Nucl Med Mol Imaging* 41:2242–2248
78. Giesel FL, Sterzing F, Schlemmer HP, Holland-Letz T, Mier W, Rius M, Afshar-Oromieh A, Kopka K, Debus J, Haberkorn U et al (2016) Intra-individual comparison of (68) Ga-PSMA-11-PET/CT and multi-parametric MR for imaging of primary prostate cancer. *Eur J Nucl Med Mol Imaging* 43:1400–1406
79. Eiber M, Weirich G, Holzapfel K, Souvatzoglou M, Haller B, Rauscher I, Beer AJ, Wester H-J, Gschwend J, Schwaiger M et al (2016) Simultaneous 68 Ga-PSMA HBED-CC PET/MRI Improves the Localization of Primary Prostate Cancer. *Eur Urol* 70:829–836
80. Zamboglou C, Drendel V, Jilg CA, Rischke HC, Beck TI, Schultze-Seemann W, Krauss T, Mix M, Schiller F, Wetterauer U et al (2017) Comparison of 68 Ga-HBED-CC PSMA-PET/CT and multiparametric MRI for gross tumour volume detection in patients with primary prostate cancer based on slice by slice comparison with histopathology. *Theranostics* 7:228–237
81. Thomas L, Kantz S, Hung A, Monaco D, Gaertner FC, Essler M, Strunk H, Laub W, Bundschuh RA (2018) 68 Ga-PSMA-PET/CT imaging of localized primary prostate cancer patients for intensity modulated radiation therapy treatment planning with integrated boost. *Eur J Nucl Med Mol Imaging* 45:1170–1178

82. Zamboglou C, Sachpazidis I, Koubar K, Drendel V, Wiehle R, Kirste S, Mix M, Schiller F, Mavroidis P, Meyer PT et al (2017) Evaluation of intensity modulated radiation therapy dose painting for localized prostate cancer using 68Ga-HBED-CC PSMA-PET/CT: A planning study based on histopathology reference. *Radiother Oncol J Eur Soc Ther Radiol Oncol* 123:472–477
83. Zamboglou C, Thomann B, Koubar K, Bronsert P, Krauss T, Rischke HC, Sachpazidis I, Drendel V, Salman N, Reichel K et al (2018) Focal dose escalation for prostate cancer using 68Ga-HBED-CC PSMA PET/CT and MRI: a planning study based on histology reference. *Radiat Oncol Lond Engl* 13:81
84. Lips IM, van der Heide UA, Haustermans K, van Lin ENJT, Pos F, Franken SPG, Kotte ANTJ, van Gils CH, van Vulpen M (2011) Single blind randomized phase III trial to investigate the benefit of a focal lesion ablative microboost in prostate cancer (FLAME-trial): study protocol for a randomized controlled trial. *Trials* 12:255
85. Hövels AM, Heesakkers R a M, Adang, EM, Jager GJ, Strum S, Hoogeveen YL, Severens JL, Barentsz JO (2008) The diagnostic accuracy of CT and MRI in the staging of pelvic lymph nodes in patients with prostate cancer: a meta-analysis. *Clin Radiol* 63:387–395
86. Vallini V, Ortori S, Boraschi P, Manassero F, Gabelloni M, Faggioni L, Selli C, Bartolozzi C (2016) Staging of pelvic lymph nodes in patients with prostate cancer: Usefulness of multiple b value SE-EPI diffusion-weighted imaging on a 3.0 T MR system. *Eur J Radiol Open* 3:16–21
87. van Leeuwen PJ, Emmett L, Ho B, Delprado W, Ting F, Nguyen Q, Stricker PD (2017) Prospective evaluation of 68 Gallium-prostate-specific membrane antigen positron emission tomography/computed tomography for preoperative lymph node staging in prostate cancer. *BJU Int* 119:209–215
88. Maurer T, Gschwend JE, Rauscher I, Souvatzoglou M, Haller B, Weirich G, Wester H-J, Heck M, Kübler H, Beer AJ et al (2016) Diagnostic Efficacy of (68)Gallium-PSMA positron emission tomography compared to conventional imaging for lymph node staging of 130 consecutive patients with intermediate to high risk prostate cancer. *J Urol* 195:1436–1443
89. Öbek C, Doğanca T, Demirci E, Ocak M, Kural AR, Yıldırım A, Yücetaş U, Demirdağ Ç, Erdoğan SM, Kabasakal L et al (2017) The accuracy of 68 Ga-PSMA PET/CT in primary lymph node staging in high-risk prostate cancer. *Eur J Nucl Med Mol Imaging* 44:1806–1812
90. Habl G, Sauter K, Schiller K, Dewes S, Maurer T, Eiber M, Combs SE (2017) 68 Ga-PSMA-PET for radiation treatment planning in prostate cancer recurrences after surgery: Individualized medicine or new standard in salvage treatment. *Prostate* 77:920–927
91. Shakespeare TP (2015) Effect of prostate-specific membrane antigen positron emission tomography on the decision-making of radiation oncologists. *Radiat Oncol Lond Engl* 10:233
92. Verburg FA, Pfister D, Heidenreich A, Vogg A, Drude NI, Vöö S, Mottaghy FM, Behrendt FF (2016) Extent of disease in recurrent prostate cancer determined by [(68)Ga] PSMA-HBED-CC PET/CT in relation to PSA levels, PSA doubling time and Gleason score. *Eur J Nucl Med Mol Imaging* 43:397–403
93. Afshar-Oromieh A, Holland-Letz T, Giesel FL, Kratochwil C, Mier W, Haufe S, Debus N, Eder M, Eisenhut M, Schäfer M et al (2017) Diagnostic performance of 68 Ga-PSMA-11 (HBED-CC) PET/CT in patients with recurrent prostate cancer: evaluation in 1007 patients. *Eur J Nucl Med Mol Imaging* 44:1258–1268
94. Lecouvet FE, Geukens D, Stainier A, Jamar F, Jamart J, d’Othée BJ, Therasse P, Vande Berg B, Tombal B (2007) Magnetic resonance imaging of the axial skeleton for detecting bone metastases in patients with high-risk prostate cancer: diagnostic and cost-effectiveness and comparison with current detection strategies. *J Clin Oncol Off J Am Soc Clin Oncol* 25:3281–3287

95. Woo S, Suh CH, Kim SY, Cho JY, Kim SH (2018) Diagnostic Performance of Magnetic Resonance Imaging for the Detection of Bone Metastasis in Prostate Cancer: a Systematic Review and Meta-analysis. *Eur Urol* 73:81–91
96. Pyka T, Okamoto S, Dahlbender M, Tauber R, Retz M, Heck M, Tamaki N, Schwaiger M, Maurer T, Eiber M (2016) Comparison of bone scintigraphy and 68 Ga-PSMA PET for skeletal staging in prostate cancer. *Eur J Nucl Med Mol Imaging* 43:2114–2121
97. Parkin DM, Bray F, Ferlay J, Pisani P (2005) Global cancer statistics, 2002. *CA Cancer J Clin* 55:74–108
98. Koh W-J, Abu-Rustum NR, Bean S, Bradley K, Campos SM, Cho KR, Chon HS, Chu C, Clark R, Cohn D et al (2019) Cervical cancer, version 3.2019, NCCN clinical practice guidelines in oncology. *J Natl Compr Cancer Netw JNCCN* 17:64–84
99. Marth C, Landoni F, Mahner S, McCormack M, Gonzalez-Martin A, Colombo N (2017) Cervical cancer: ESMO clinical practice guidelines for diagnosis, treatment and follow-up. *Ann Oncol* 28:iv72–iv83
100. Havrilesky LJ, Kulasingam SL, Matchar DB, Myers ER (2005) FDG-PET for management of cervical and ovarian cancer. *Gynecol Oncol* 97:183–191
101. Kidd EA, Siegel BA, Dehdashti F, Rader JS, Mutic S, Mutch DG, Powell MA, Grigsby PW (2010) Clinical outcomes of definitive intensity-modulated radiation therapy with fluorodeoxyglucose-positron emission tomography simulation in patients with locally advanced cervical cancer. *Int J Radiat Oncol Biol Phys* 77:1085–1091
102. Grigsby PW, Singh AK, Siegel BA, Dehdashti F, Rader J, Zoberi I (2004) Lymph node control in cervical cancer. *Int J Radiat Oncol Biol Phys* 59:706–712
103. Koh W-J, Abu-Rustum NR, Bean S, Bradley K, Campos SM, Cho KR, Chon HS, Chu C, Cohn D, Crispens MA et al (2018) Uterine neoplasms, version 1.2018, NCCN clinical practice guidelines in oncology. *J Natl Compr Canc Netw* 16:170–199
104. Antonsen SL, Jensen LN, Loft A, Berthelsen AK, Costa J, Tabor A, Qvist I, Hansen MR, Fisker R, Andersen ES et al (2013) MRI, PET/CT and ultrasound in the preoperative staging of endometrial cancer—a multicenter prospective comparative study. *Gynecol Oncol* 128:300–308
105. Crivellaro C, Signorelli M, Guerra L, De Ponti E, Pirovano C, Fruscio R, Elisei F, Montanelli L, Buda A, Messa C (2013) Tailoring systematic lymphadenectomy in high-risk clinical early stage endometrial cancer: the role of 18F-FDG PET/CT. *Gynecol Oncol* 130:306–311
106. Husby JA, Reitan BC, Biermann M, Trovik J, Bjørge L, Magnussen IJ, Salvesen ØO, Salvesen HB, Haldorsen IS (2015) Metabolic tumor volume on 18F-FDG PET/CT improves preoperative identification of high-risk endometrial carcinoma patients. *J Nucl Med Off Publ Soc Nucl Med* 56:1191–1198
107. Signorelli M, Crivellaro C, Buda A, Guerra L, Fruscio R, Elisei F, Dolci C, Cuzzocrea M, Milani R, Messa C (2015) Staging of high-risk endometrial cancer with pet/ct and sentinel lymph node mapping. *Clin Nucl Med* 40:780–785
109. Oesophageal Cancer: ESMO Clinical Practice Guidelines|ESMO



Molecular Imaging for Particle Therapy: Current Approach and Future Directions

28

Katharina Seidensaal, Semi Ben Harrabi, and Jürgen Debus

Contents

28.1 Introduction.....	865
28.2 Sidenote: In situ beam monitoring by PET.....	867
28.3 Metabolic Activity: Imaging of Glucose Metabolism in Oncology.....	870
28.4 The New Tracer FAPI.....	871
28.5 Tumor-Specific Tracers: PSMA.....	872
28.6 Metabolic Activity: Amino Acid Metabolism in Brain Tumors.....	873
28.7 Tumor-Specific Markers: DOTATOC.....	874
28.8 Future Directions: Individualized Adaptive Treatment Planning Based on Functional and Biological Characteristics.....	875
References.....	876

28.1 Introduction

During the last decades, radiation oncology has been subject to a number of technological innovations. Over time, 2D treatment planning was replaced by CT-based 3D treatment planning. Computer algorithms that allowed to prescribe a maximum tolerated dose to an organ at risk led to the introduction of inverse treatment planning and made the development of intensity-modulated radiotherapy (IMRT) possible. Further techniques such as radiosurgery by gammaknife, cyberknife, or specialized linear accelerators were consequently introduced into the clinical practice. With those technical advances, a high level of precision was achieved.

K. Seidensaal · S. B. Harrabi · J. Debus (✉)

Department of Radiation Oncology, Heidelberg University Hospital, Heidelberg, Germany
e-mail: Juergen.debus@med.uni-heidelberg.de

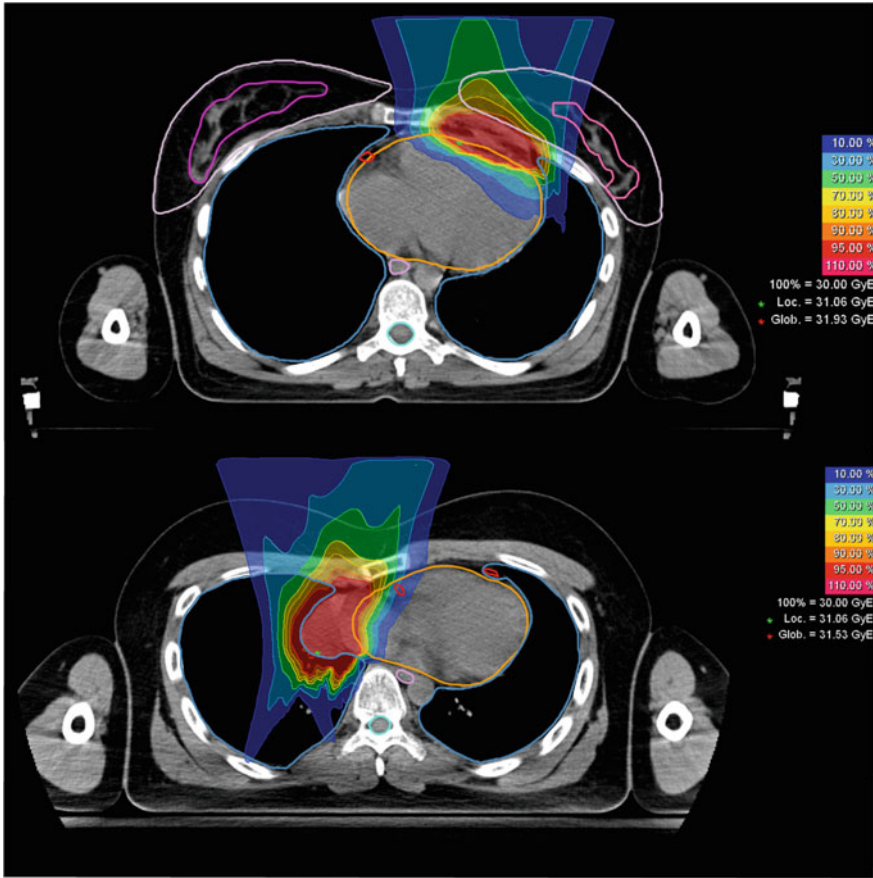


Fig. 28.1 Consolidation proton radiotherapy for mediastinal lymphoma: the characteristic features of protons allow to spare dose to the heart and to breast tissue reducing the risk of coronary heart disease and secondary malignancy; the upper picture shows a 25-year-old female patient and the lower a 22-year-old male, both suffering from nodular sclerosing Hodgkin Lymphoma with a pericardial bulky disease at diagnosis, and treatment was performed up to the total dose of 30 Gy (RBE), single dose 2 Gy (RBE), 15 fractions

Particle therapy evolved in parallel to the modern high-precision photon radiotherapy techniques and offers a superior dose distribution with decreased integral dose to healthy tissue compared to most modern photon techniques. Protons and carbon ions are currently the only two clinically used charged particles, but helium ions might be implemented in the near future. Due to the complexity of particle therapy, facility availability is limited, while around 70 proton facilities are in operation, there are only 12 carbon ion facilities worldwide (Particle Therapy

Co-Operative Group, PTCOG, January 2019). Particle beams offer unique physical and biological characteristics. The inverse depth-dose profile is characteristic; the energy deposition in the healthy tissue in the entrance channel is low, and the dose increases only slowly with penetration depth until the end of the range where the dose increase and fall-off are steep and result in the so-called Bragg peak. It is worth noting that the lateral dose width (penumbra) of carbon ions is significantly smaller than the penumbra of protons. The biological characteristics of particle therapy are based on the energy loss in tissue. The linear energy transfer (LET) of carbon ions is higher than that of protons. While the relative biological effectiveness (RBE) of protons is comparable to photons, the RBE of carbon ions is higher and it varies based on different parameters and has to be calculated by complex biological models. Different possibilities of beam application with varying doses to normal tissue due to neutron production exist, with active beam delivery being superior over passive scattering.

With advancing precision of treatment, the necessity for accurate and confident target volume delineation is rising. Due to the steep dose gradients, inaccuracy in delineation of the tumor can lead to an inadequate dose coverage. Morphological imaging has limitations in distinguishing vital tumor cells against benign tissues like scar tissue. Identifying the exact margins of the tumor can be a challenge for poorly marginated, heterogeneous, and infiltrative tumors particularly after several previous treatments.

Functional and biological information from positron emission tomography (PET) can provide additional information for target volume delineation. The implementation in the daily clinical routine is subject to discussion and certain challenges have yet to be solved. The edges of tumors avid to certain PET tracers can blur due to partial volume effect and limited spatial resolution. Altering the standardized uptake scale (SUV) can change the apparent tumor volume. Automated processes are generally considered more consistent than visual interpretation; however, no consensus is reached on the optimal segmentation approach. Besides target volume delineation PET plays an established role in the initial staging and an emerging role in the adaptation of the target volume during treatment as well as in the evaluation and prognostication of treatment response after its completion. The following chapter summarizes the current role and prospective developments of molecular imaging for particle therapy.

28.2 Sidenote: In situ beam monitoring by PET

In carbon ion radiotherapy, nuclear fragmentation contributes to the characteristic depth-dose distribution. Those nuclear reactions lead to creation of lighter ions, which continue the path of the primary ion with approximately the same velocity. However, those fragments have a larger penetration depth as they are lighter and thus they form the characteristic dose tail at the distal end of the Bragg peak. In this

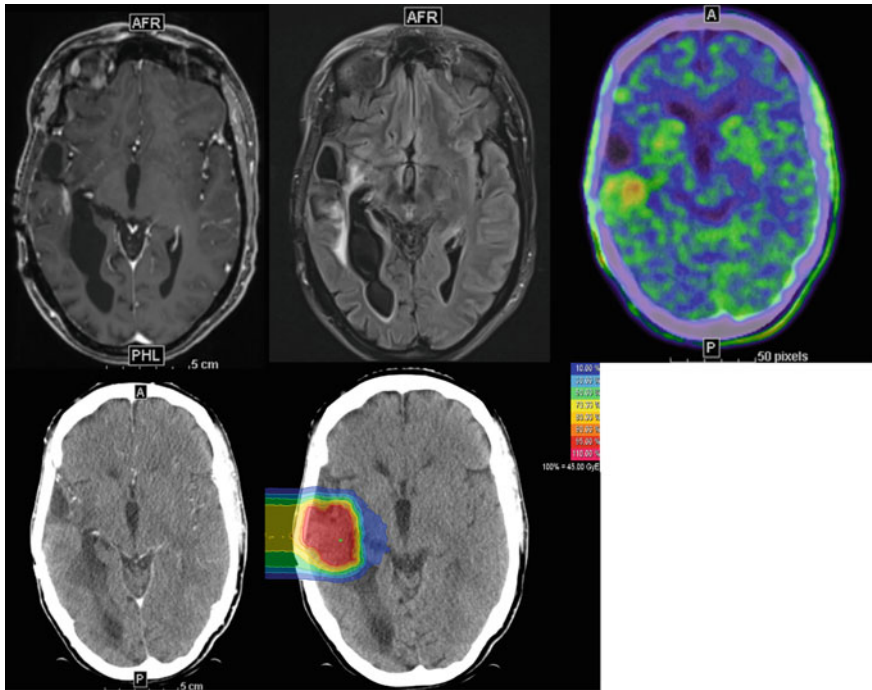


Fig. 28.2 Combining morphological and functional imaging for particle treatment planning: 38-year-old female patient with a history of astrocytoma WHO ^\circ II of 9 years. As the patient was pretreated by surgery and photon radiotherapy, different modalities were used to identify vital tumor and differentiate from treatment-associated changes: (upper row, from left to right) CM-enhanced T1-MPRAGE MRI sequence, T2-FLAIR MRI sequence, FET-PET/CT, and (lower row, left) CM-enhanced CT. Dose distribution of the according treatment plan (lower row, right), re-irradiation was performed with carbon ions, total dose 51 Gy (RBE), single dose 3 Gy(RBE), 17 fractions

process of fragmentation, carbon ion isotopes, ^{11}C and ^{10}C , are created which are positron emitters with a half-life of approx. 20 min and 19 s, respectively. With PET it is possible to detect this decay and monitor the range of the carbon ion beam in situ, which has been routinely done at the Gesellschaft für Schwerionenforschung (GSI) by the pioneers of carbon ion radiotherapy in Germany. A comparison with the expected dose distribution from the treatment plan can be calculated and mispositioning or shifts in dose distribution of approx. 2 mm can be detected and corrected, if necessary [1].

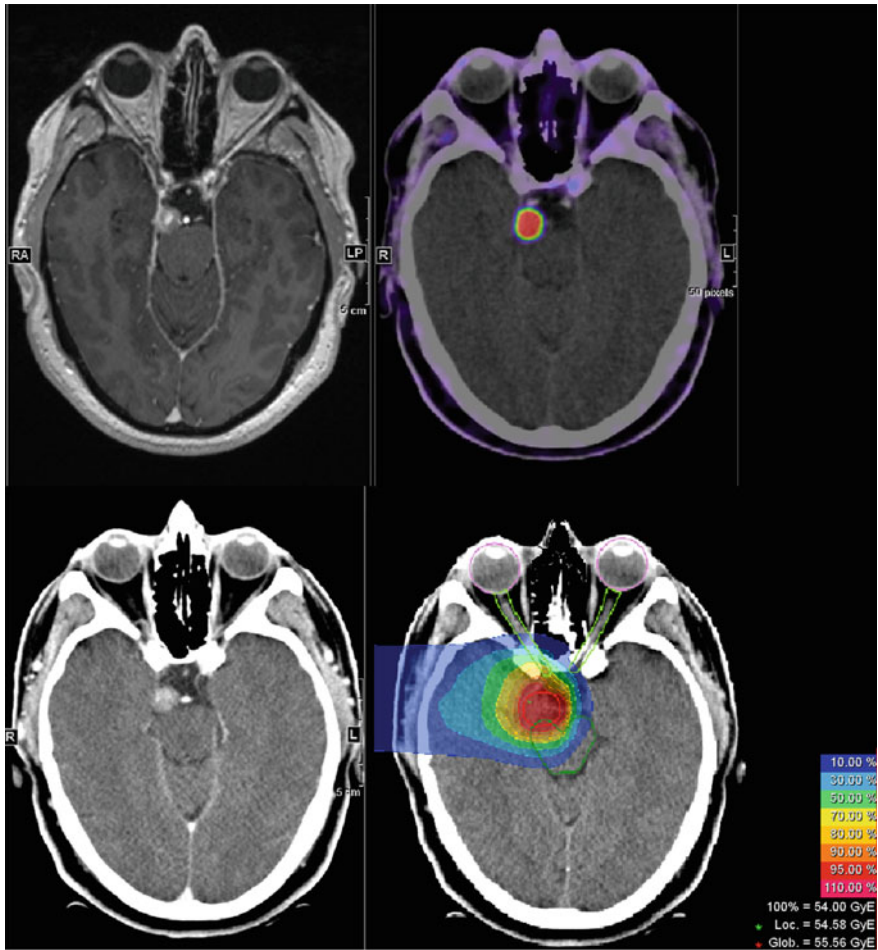


Fig. 28.3 DOTATOC PET for diagnosis and target volume definition of meningioma: 58-year-old patient with a 10-year history of meningioma without histopathological confirmation, treatment was initiated as a progression was seen on MRI on the long term and the patient developed mild symptoms. Treatment planning was based on CM-enhanced T1-MPRAGE MRI sequence (upper row left), DOTATOC PET/CM (upper row right), CM-enhanced CT (lower row left). The figure in the lower row right shows the according proton plan, total dose 54 Gy (RBE), single dose 2 Gy (RBE), 27 fractions

28.3 Metabolic Activity: Imaging of Glucose Metabolism in Oncology

2-Fluor-2-deoxy-D-glucose (FDG) is by far the longest known and most used PET tracer. Its uptake reflects the upregulation of glucose transporters and enhanced glucose metabolism of tumor cells, thus FDG is not tumor specific. FDG is a useful and reliable diagnostic tool for mainly three issues in oncology: differentiating between benign and malignant processes, detecting affected lymph nodes and distant metastases as well as assessing the extent of the primary tumor and differentiating between vital tumor and scar tissue. It is useful for many malignancies such as head and neck, rectal and esophageal cancer as well as lymphoma. Particularly for non-small cell lung cancer (NSCLC), FDG-PET/CT has become the standard of care baseline staging.

However, FDG-PET/CT is prone to pitfalls and incidental findings. False positive results might be thymus, brown fatty tissue, bone marrow, or infection/inflammation among others. A high physiologic uptake of the normal tissue as brain can disguise tumor processes [2].

Research implementing FDG-PET into radiation oncology mainly focuses on maximizing survival and minimizing morbidity by biological characterization of the tumor and individualized adaptation of the treatment. Not only the target volume definition can be supported by FDG-PET but also treatment guidance/decision-making can be based on residual FDG uptake after foregoing treatment, which will be explained below for lymphoma as an example.

A growing area of research employs FDG-PET/CT during radiotherapy in order to facilitate treatment escalation or de-escalation strategies based on the metabolic evolution of the tumor as a surrogate of the speed and quality of response to the ongoing treatment [3].

But also the field of response prediction after completed treatment is evolving [4]. As an example, a multicenter study performed in the United Kingdom demonstrated that PET/CT-guided surveillance of head and neck squamous cell carcinoma patients with advanced nodal disease (stage N2 or N3) 12 weeks after RT spares patients planned neck dissections without compromising survival [5]. Assessing response to treatment of head and neck tumors with squamous cell histology might be particularly interesting following carbon ion re-irradiation [6], as morphological imaging hits its limits due to equivocal results after several previous treatments.

Pediatric patients are preferably treated by protons for several reasons. Due to the smaller size of the body and the organs, the integral dose to the neighboring organs at risk is significantly higher compared to adults. As they have not finished growth and development, a different scope of side effects such as growth abnormalities which can lead to scoliosis or facial asymmetry has to be considered. Hormonal deficiency after radiotherapy of brain tumors leads to more severe side effects due to the ongoing development [7, 8]. The prognosis of children with cancer has significantly increased over the last decades: for many malignancies,

overall survival rates of more than 70% percent after 5 years can be achieved [9]. Thus, reducing the risk of secondary malignancies or other severe treatment-related late sequelae by reducing the absorbed dose to non-target tissues is crucial. In pediatric malignancies, FDG-PET is primarily used for staging. The typical indications are neuroblastoma (MIBG negative), osteosarcoma, Ewing sarcoma, rhabdomyosarcoma, and MPNST [10].

Hodgkin's lymphoma is the third commonest pediatric malignancy after leukemia and central nervous system tumors. FDG-PET/CT is routinely used for staging of pediatric and adult patients. Besides staging, assessment of treatment response and adaptation of treatment procedures are based on FDG-PET/CT. Current treatment regimens are of increasing efficacy, and therefore reducing the risk of secondary malignancy and cardiovascular disease due to consolidation radiotherapy becomes of higher importance. Current efforts are focused on reducing the number of patients receiving consolidation radiotherapy without compromising the excellent survival rates (EuroNet PHL-C1/C2) [10]. The risk for women to develop breast cancer after chest radiotherapy in the childhood is among the highest described for any population [11]. For coronary heart disease, a linear dose–response relationship was identified for Hodgkin lymphoma survivors [12]. The HD-15 study for adult patient with advanced Hodgkin's lymphoma has identified treatment with six cycles of chemotherapy with BEACOPP^{escalated} followed by PET-guided radiotherapy superior to eight cycles of the chemotherapy alone [13]. The same rationale was applied in the HD 16 study for early-stage Hodgkin's lymphoma. Here PET staging was performed after two cycles of chemotherapy by ABVD. In the standard arm, all patients received involved field radiotherapy with 20 Gy, and in the experimental arm only the PET positive patients received radiotherapy but not the PET negative. In those cases where radiotherapy cannot be omitted safely, proton therapy can significantly reduce the dose to the heart as well as to the breast tissue due to its steep dose gradients (Fig. 28.1). Chung et al. showed in a matched pair analysis of 558 patients treated with protons and photons a reduced risk of secondary malignancies for proton-treated patients of 5.2 versus 7.5% [14]. Nowadays, most pediatric and young patients are still treated with photons worldwide due to the limited accessibility of proton therapy. With decreasing costs for proton facilities this will hopefully change in future.

28.4 The New Tracer FAPI

Most recently, a new tracer has been developed as an alternative to FDG-PET. It utilizes the fact that cancer-associated fibroblasts (CAF) of the tumor microenvironment of several tumors (breast cancer, pancreatic cancer, or colon cancer) overexpress fibroblast activation protein (FAP). A strong desmoplastic reaction of those tumors causes that up to 90% of the tumor mass can consist of stromal cells. In contrast to fibroblasts that are found ubiquitous in the body, the expression of FAP is found selectively in CAFs and in contrast to tumor cells they are more stable

from genetic alterations, which makes FAP a promising target for a theranostic (therapeutic and diagnostic) approach. The first published results show that PET tracers with FAP targeting inhibitors as FAPI-2 and FAPI-4 are a promising alternative to FDG-PET. It shows a lower background uptake in brain, liver, or oral–laryngeal mucosa. And complimentary to FDG it performs well in pancreatic or liver cancer. FAPI is more convenient for patients compared to FDG as no starvation time before the examination is necessary. However, as FAPI also accumulates in inflammation it is generally not considered more specific than FDG. In future, it might be a helpful tool for target volume definition of tumors that tend to be poorly marginated and that are, therefore, difficult to delineate [15–17].

Pancreatic cancer belongs to the most lethal malignant neoplasms worldwide with an overall survival rate of approximately 6% in 5 years and negligible changes in survival over the last decades. It is difficult to diagnose and most patients are diagnosed at an advanced, inoperable stage as there is no workable modality for screening and early diagnosis [18]. Carbon ion radiotherapy has been introduced to the treatment of pancreatic cancer in the recent years; due to the high precision of the treatment as well as a higher biological effectivity, it is promising in the treatment of radioresistant malignancies. The recently published experience for carbon ion radiotherapy with concomitant chemotherapy by gemcitabine from the Japan Carbon-Ion Radiation Oncology Study Group (J-CROS) for pathologically confirmed invasive ductal adenocarcinoma of the pancreas is promising and shows overall survival rates of 46% (95% CI, 31%–61%) at 2 years with a median OS of 21.5 months (95% CI, 11.8–31.2 months) [19, 20]. In those studies, target volume delineation was performed by CT, MRI, and FDG-PET and the evaluation of treatment response was done with CT and FDG-PET. With the current imaging modalities, it is, nowadays, still difficult to stage and assess treatment response and a discrepancy between the different techniques is commonly seen. FDG-PET is described to have only a moderate sensibility for pancreatic cancer and to be poor especially in nodal staging [21]. As pancreatic cancer is described to have a high desmoplastic activity, FAPI-PET/CT might be a useful tool in patient selection, development of treatment strategies, and response assessment to carbon ion radiotherapy in future.

28.5 Tumor-Specific Tracers: PSMA

Prostate-specific membrane antigen (PSMA) PET/CT has been introduced into the diagnostics of prostate cancer patients in the last years. Clinical management of prostate cancer patients in radiation oncology is highly influenced by the introduction of PSMA-PET/CT. Oligometastatic disease can be treated in a curative intent by radiotherapy after clear identification of the metastatic sites. Salvage radiotherapy in biochemical failure after surgery can be supported by the identification of the recurrence site in the prostatic fossa. Increased dose as an integrated boost to lymph node metastasis that are morphologically not suspicious but PET

positive can be administered to account for macroscopic tumor spread. It is described that information from PSMA-PET/CT can account for over 50% of changes in disease management [22]. Yet, treatment guidelines for the management of information from PSMA-PET/CT scans have to be developed in future not only for photon but also for particle therapy, which has been steadily implemented into the treatment of prostate cancer over the recent years and offers different treatment options. Hypofractionated proton therapy can be performed as a definitive, adjuvant, or salvage radiotherapy. Furthermore, a proton boost can be administered with a photon base plan combining the advantages of both techniques and allowing dose escalation [23].

28.6 Metabolic Activity: Amino Acid Metabolism in Brain Tumors

Particle irradiation with protons is currently performed worldwide for low-grade glioma (LGG) especially in children and young patients, in order to spare the healthy brain tissue from medium and low dose and reduce the risk of acute and especially late side effects, like cognitive disturbance, concentration impairment, or secondary malignancy. For high-grade glioma (HGG) in the primary situation, it is possible to combine a proton boost and a photon base plan [24] and in case of recurrence small volume re-irradiation can be performed with carbon ions, e.g., with 45 Gy (RBE) in 15 fractions (56.2 Gy EQD2, $\alpha/\beta = 2$) [25, 26] (unpublished clinical experience from Heidelberg Ion-Beam Therapy Center) safely and efficiently. One has to be aware that due to the characteristic steep depth-dose profile of particles, uncertainties or inaccuracies in tumor delineation can lead to a differing therapeutical dose coverage and thus compromise the local control. Confident and consistent definition of the target volume is crucial. Especially in high-grade glioma recurrence, accurate spatial allocation is difficult due to the infiltrative nature and heterogeneous tumor structures. Additionally, gliosis, necrosis, and edema from forgoing treatments as operation and radiotherapy can make differentiation from vital tumor difficult. This emphasizes the need for novel imaging modalities in the time of high precision therapy.

Amino acid tracers tend to accumulate in brain tumors due to increased expression of amino acid transporters by tumor cells. ^{18}F -fluoroethyltyrosine (FET) PET/CT is widely considered as a useful tool for target volume definition of malignant and especially recurrent glioma, although the details of implementation into the daily clinical routine are currently discussed (Fig. 28.2). Especially the optimal strategy for the segmentation of the PET active volume is not properly defined yet. Manual segmentation, on the one hand, has high inter- and intra-rater variations due to the applied window level and the physicians' experience. Semi-automatic segmentation (region-growing or thresholding) depends on the definition of thresholds and seed points of different users. The application of a fixed threshold on the standardized uptake value (SUV) is hampered by a great variability between patients. Finally,

using percentage thresholds on the maximum SUV (isocontours) seems promising, but the optimal value varies greatly in literature [27].

FET and l-[methyl-11C] methionine (MET) are the two most commonly used amino acid tracers. MET has been available at many centers worldwide since 1980s while FET emerged in 1990s and shows a more favorable half-life time for routine clinical application of 110 min compared to the half-life of 20 min of MET. FET is reported to be more specific than MET in differentiating tumor tissue and inflammation [28].

It has been shown in several publications that integrating FET-PET signaling yields larger target volumes (GTV) in comparison to MRI T1-weighted (T1w) gadolinium enhancement based GTV definition [27, 29, 30]. Furthermore, the congruence of MRI and FET signals is poor leading to a mismatch of the GTV's based on MRI and PET. This is different when the GTV is defined by the T2-FLAIR signal, e.g., in patients with LGG, and here the hyperintensity covers approximately 80% of the PET positive volume [31].

It is worth noting that increased standardized uptake ratios ($SUR > 2.92$) were correlated significantly to a poor median overall survival in high-grade glioma [27] and FET-PET has been attributed prognostic value in the treatment of glioblastoma by further publications [32, 33]. Addition of FET-PET to MRI enhances the specificity for the detection of tumor tissue by biopsy in patients with suspected glioma from 53% to 94% [34].

Especially for LGG and re-irradiation of HGG PET with amino acid tracers might be quite useful, but more studies are needed for the evaluation of the potential benefits.

28.7 Tumor-Specific Markers: DOTATOC

Skull base meningioma arises at the sphenoidal wing, the petroclival region, or the cavernous sinus and in more than 90% they are of benign origin. Due to the complex anatomy of the skull base, involvement of vital structures such as cranial nerves, blood vessels, and the cavernous sinus is common and makes them particularly difficult to treat. For a long time, surgical resection was the treatment of choice but in many cases total resection is not feasible as it bears the risk of intolerable morbidity. Incomplete resection cannot reach high long-term control and overall survival rates. Additional radiation therapy can reduce the risk of local recurrence [35]. Thus, irradiation with protons among other techniques is an important treatment alternative which shows excellent local control and overall survival rates [36]. Compared to IMRT proton therapy has a significantly reduced low dose deposition in the surrounding healthy tissue, which is associated with a lower risk of secondary malignancies [37]. Whether protons are superior to photons with regard to other relevant clinical parameters like neurocognitive performance or endocrine dysfunction still remains to be answered. Many meningiomas are discovered incidentally and show no tendency to grow over a long period of time due

to a low proliferation index, and in such cases an observation strategy is reasonable. Initiation of treatment is indicated in case of neurological symptoms or detection of tumor growth by high-resolution imaging with MRI. In approximately 38% of cases, no pathological confirmation of the diagnosis is available [36]. In those cases, biopsy might be limited or declined by the patient and ^{68}Ga -DOTATOC PET/CT is used to confirm the diagnosis. It is worth noting that DOTATOC PET/CT has a higher sensitivity than contrast-enhanced MRI, particularly when tumors are adjacent to the falx cerebri or at the skull base [38].

Commonly, morphological imaging is used for target volume definition. Though it has limitations in distinguishing between vital meningioma tissue, postoperative scar tissue, and other neighboring anatomical structures of the skull base. The high expression of somatostatin type 2 receptor as well as an excellent tumor-to-background ratio makes imaging with somatostatin receptor ligands as DOTATOC a very useful and well-established tool not only for the diagnosis but particularly for the target volume definition of meningiomas with equivocal presentation on MRI. For benign meningioma, the gross target volume equals the clinical target volume, and thus accurate definition of the tumor's margins is crucial, considering the steep dose gradients of protons (Fig. 28.3). It is worth noting that combining a carbon ion boost with a photon base plan is currently investigated for atypical meningioma utilizing the superior physical and biological characteristics of carbon ions in order to improve local control rates [39].

28.8 Future Directions: Individualized Adaptive Treatment Planning Based on Functional and Biological Characteristics

It is well known that hypoxic tumors can overcome the effects of conventional radiotherapy and hypoxia is one key point mechanism of radioresistance. The high linear energy transfer (LET) of carbon ions leads to a different pattern of DNA damage in tumor cells with a higher rate of complex, irreparable DNA damage (e.g., double-strand breaks) and less dependence on the re-oxygenation of the tumor. Thus, carbon ion radiotherapy is especially effective in hypoxic tumors [1, 40]. As a consequence, measuring tumor hypoxia might be a potential future marker for adaptation of radiotherapy in an individualized treatment. Besides favoring heavy ion treatment when feasible and available, dose escalation might be a reasonable approach. Radiolabeled tracers such as ^{18}F -FMISO, ^{18}F -FAZA, ^{18}F -HX4 allow detection of hypoxia by PET/CT, and high levels of uptake are not only hypothetically interesting but also of relevance for the patient's outcome. A number of studies have shown that high uptake of ^{18}F -FMISO or ^{18}F -FAZA correlates with poor treatment response [41]. Quantification of hypoxia and thus comparability of the PET result for large multicenter studies will make further investigation of this approach in personalized medicine possible [42].

Besides hypoxia and metabolism, tumor cell proliferation is one molecular parameter which can predict the response to treatment. Fluorothymidine (^{18}F -FLT) is a tracer which highly correlates to the proliferation marker Ki-67 and enables to visualize proliferation in vivo [43, 44, 45]. Thus, it might also be an interesting tool for treatment planning in future.

Further functional parameters that can be integrated into molecular PET information are perfusion and diffusion measured by MRI. Dynamic-enhanced MRI measures surrogates of tissue perfusion. Diffusion-weighted MRI can determine regions with abnormal extracellular space and thus estimate tumor cell density. As an example, it was shown that combining ADC (apparent diffusion coefficient) and ^{18}F -FDG SUV predicted disease progression better than each modality alone in NSCLC [46]. Hybrid imaging technology combining PET signaling as well as anatomical and functional data from MRI (PET/MRI) will provide data for multi-parameter functional imaging and is investigated currently with great interest [47]. In future, more complex methods in treatment planning based on different modalities including functional and molecular imaging might make high-quality individualized treatment possible [42, 48].

Over the last decades, the treatment techniques have reached a grade of sub-millimeter precision. Implementing the superior dose distribution of particle therapy requires enhanced diligence. High-precision radiation therapy based upon equivocal morphological images and inaccurate tumor mass delineation forms a paradox situation which should be considered with great care by the treating radiation oncologist. High-quality imaging modalities are a key prerequisite in order to utilize the full potential of this accuracy. Personalized treatment could be reached by prescribing a non-uniform dose to the target volume to cover, e.g., regions of high risk for local relapse based on information from functional and molecular imaging (dose-painting) [48] and by adaptive treatment planning based on repeated imaging during the course of fractionated radiotherapy.

Conceptual designs for a combination of a PET scanner and a LINAC are currently in development. Online PET imaging with tracers such as FDG would not only allow target volume identification before treatment but tracking of the target by the PET signal and adaptation of the target volume by the integration of molecular imaging information. Guidance of particles by PET might become an interesting topic in the future.

References

1. Weber U, Kraft G (2009) Comparison of Carbon Ions versus protons 15 325–332
2. Corrigan AJG, Schleyer PJ, Cook GJ (2015) Pitfalls and artifacts in the use of PET/CT in oncology imaging. *Semin Nucl Med* 45(6):481–499
3. Farina E et al (2017) ^{18}F -Fdg-PET-guided planning and re-planning (adaptive) radiotherapy in head and neck cancer: current state of art. *Anticancer Res* 37(12): 6523–6532

4. Cliffe H et al (2017) Radiotherapy response evaluation using FDG PET-CT-established and emerging applications. *Br J Radiol* 90(1071):20160764
5. Mehanna H et al (2016) PET-CT surveillance versus neck dissection in advanced head and neck cancer. *N Engl J Med* 374(15):1444–1454
6. Jensen AD et al (2011) Re-irradiation with scanned charged particle beams in recurrent tumours of the head and neck: acute toxicity and feasibility. *Radiother Oncol* 101(3):383–387
7. Vatner RE et al (2018) endocrine deficiency as a function of radiation dose to the hypothalamus and pituitary in pediatric and young adult patients with brain tumors. *J Clin Oncol* 36(28):2854–2862
8. Merchant TE et al (2011) Growth hormone secretion after conformal radiation therapy in pediatric patients with localized brain tumors. *J Clin Oncol* 29(36):4776–4780
9. Gatta G et al (2014) Childhood cancer survival in Europe 1999–2007: results of EUROCORE-5—a population-based study. *Lancet Oncol* 15(1):35–47
10. Chambers G et al (2018) 18F-FDG PET-CT in paediatric oncology: established and emerging applications. *British J Radiol*
11. Moskowitz CS et al (2014) Breast cancer after chest radiation therapy for childhood cancer. *J Clin Oncol* 32(21):2217–2223
12. van Nimwegen FA et al (2016) Radiation dose-response relationship for risk of coronary heart disease in survivors of hodgkin lymphoma. *J Clin Oncol* 34(3):235–243
13. Engert A et al (2012) Reduced-intensity chemotherapy and PET-guided radiotherapy in patients with advanced stage Hodgkin’s lymphoma (HD15 trial): a randomised, open-label, phase 3 non-inferiority trial. *The Lancet* 379(9828):1791–1799
14. Chung CS et al (2013) Incidence of second malignancies among patients treated with proton versus photon radiation. *Int J Radiat Oncol Biol Phys* 87(1):46–52
15. Giesel F et al (2018) FAPI-PET/CT: biodistribution and preliminary dosimetry estimate of two DOTA-containing FAP-targeting agents in patients with various cancers. *J Nucl Med*
16. Lindner T et al (2018) Development of quinoline-based theranostic ligands for the targeting of fibroblast activation protein. *J Nucl Med* 59(9):1415–1422
17. Loktev A et al (2018) A tumor-imaging method targeting cancer-associated fibroblasts. *J Nucl Med* 59(9):1423–1429
18. Ilic M, Ilic I (2016) Epidemiology of pancreatic cancer. *World J Gastroenterology*, 22(44)
19. Kawashiro S et al (2018) Multi-institutional Study of Carbon-ion Radiotherapy for Locally Advanced Pancreatic Cancer: Japan Carbon-ion Radiation Oncology Study Group (J-CROS) Study 1403 Pancreas. *Int J Radiation Oncology*Biophysics* 101(5):1212–1221
20. Shinoto M et al (2016) Carbon Ion Radiation Therapy With Concurrent Gemcitabine for Patients With Locally Advanced Pancreatic Cancer. *Int J Radiation Oncology Biology Physics*, 95(1):498–504
21. Wang Z et al (2013) FDG-PET in diagnosis, staging and prognosis of pancreatic carcinoma: a meta-analysis. *World J Gastroenterol* 19(29):4808–4817
22. Han S et al (2018) Impact of (68)Ga-PSMA PET on the Management of Patients with Prostate Cancer: A Systematic Review and Meta-analysis. *Eur Urol* 74(2):179–190
23. Zietman AL et al (2010) Randomized trial comparing conventional-dose with high-dose conformal radiation therapy in early-stage adenocarcinoma of the prostate: long-term results from proton radiation oncology group/american college of radiology 95-09. *J Clin Oncol* 28(7):1106–1111
24. Adeberg S et al (2017) Sequential proton boost after standard chemoradiation for high-grade glioma. *Radiother Oncol* 125(2):266–272
25. Rieken S et al (2012) Proton and carbon ion radiotherapy for primary brain tumors delivered with active raster scanning at the Heidelberg Ion Therapy Center (HIT): early treatment results and study concepts. *Radiat Oncol* 7:41

26. Combs SE et al (2010) Randomised phase I/II study to evaluate carbon ion radiotherapy versus fractionated stereotactic radiotherapy in patients with recurrent or progressive gliomas: The CINDERELLA trial. *BMC Cancer* 10(1):533
27. Debus C et al (2018) Impact of 18F-FET PET on Target Volume Definition and Tumor Progression of Recurrent High Grade Glioma Treated with Carbon-Ion Radiotherapy. *Scientific Reports* 8(1):7201
28. Juhász C et al. (2014) Comparison of amino acid positron emission tomographic radiotracers for molecular imaging of primary and metastatic brain tumors. *Molecular imaging*, 13: <https://doi.org/10.2310/7290.2014.00015>
29. Niyazi M et al (2011) FET-PET for malignant glioma treatment planning. *Radiother Oncol* 99(1):44–48
30. Piroth MD et al (2012) Integrated boost IMRT with FET-PET-adapted local dose escalation in glioblastomas. *Strahlenther Onkol* 188(4):334–339
31. Rieken S et al (2013) Analysis of FET-PET imaging for target volume definition in patients with gliomas treated with conformal radiotherapy. *Radiother Oncol* 109(3):487–492
32. Piroth MD et al (2011) Prognostic impact of postoperative, pre-irradiation 18F-fluoroethyl-L-tyrosine uptake in glioblastoma patients treated with radiochemotherapy. *Radiother Oncol* 99(2):218–224
33. Piroth MD et al. (2011) Prognostic Value of Early [18F]Fluoroethyltyrosine Positron Emission Tomography After Radiochemotherapy in Glioblastoma Multiforme. *Int J Radiat Oncology*Biolog*Physics* 80(1):176–184
34. Pauleit D et al (2005) O-(2-[18F]fluoroethyl)-L-tyrosine PET combined with MRI improves the diagnostic assessment of cerebral gliomas. *Brain* 128(Pt 3):678–687
35. Combs SE et al (2012) State-of-the-art treatment alternatives for base of skull meningiomas: complementing and controversial indications for neurosurgery, stereotactic and robotic based radiosurgery or modern fractionated radiation techniques. *Radiat Oncol* 7(1):226
36. El Shafie RA et al (2018) Clinical outcome after particle therapy for meningiomas of the skull base: toxicity and local control in patients treated with active raster-scanning. *Radiat Oncol* 13(1):54
37. Arvold ND et al (2012) Projected second tumor risk and dose to neurocognitive structures after proton versus photon radiotherapy for benign meningioma. *Int J Radiat Oncol Biol Phys* 83(4):e495–e500
38. Afshar-Oromieh A et al (2012) Detection of cranial meningiomas: comparison of (68) Ga-DOTATOC PET/CT and contrast-enhanced MRI. *Eur J Nucl Med Mol Imaging* 39(9):1409–1415
39. Combs SE et al (2010) Treatment of patients with atypical meningiomas Simpson grade 4 and 5 with a carbon ion boost in combination with postoperative photon radiotherapy: The MARCIE Trial. *BMC Cancer* 10(1)
40. Schardt D, Elsässer T, Schulz-Ertner D (2010) Heavy-ion tumor therapy: Physical and radiobiological benefits. *Rev Mod Phys* 82(1):383–425
41. Lee ST, Scott AM (2007) Hypoxia positron emission tomography imaging with 18F-fluoromisonidazole. *Semin Nucl Med* 37(6):451–461
42. Thorwarth D (2015) Functional imaging for radiotherapy treatment planning: current status and future directions—a review. *Br J Radiol* 88(1051):20150056
43. Woolf DK et al (2014) Evaluation of FLT-PET-CT as an imaging biomarker of proliferation in primary breast cancer. *Br J Cancer* 110(12):2847–2854
44. Wagner M et al (2003) 3'-[18F]fluoro-3'-deoxythymidine ([18F]-FLT) as positron emission tomography tracer for imaging proliferation in a murine B-Cell lymphoma model and in the human disease. *Cancer Res* 63(10):2681–2687
45. Chalkidou A et al (2012) Correlation between Ki-67 immunohistochemistry and 18F-Fluorothymidine uptake in patients with cancer: A systematic review and meta-analysis. *Eur J Cancer* 48(18):3499–3513

-
46. Iizuka Y et al (2014) Prediction of clinical outcome after stereotactic body radiotherapy for non-small cell lung cancer using diffusion-weighted MRI and (18)F-FDG PET. *Eur J Radiol* 83(11):2087–2092
 47. Ehman EC et al (2017) PET/MRI: Where might it replace PET/CT?. *J Magn Reson Imaging* 46(5):1247–1262
 48. Bentzen SM, Gregoire V (2011) Molecular imaging-based dose painting: a novel paradigm for radiation therapy prescription. *Semin Radiat Oncol* 21(2):101–110



Internal Radiation Therapy

29

Uwe Haberkorn, Clemens Kratochwil, and Frederik Giesel

Contents

29.1	Non-specific Therapy	882
29.1.1	Selective Internal Radiotherapy (SIRT)	882
29.1.2	Radiopharmaceuticals with Accumulation in Areas of Bone Remodeling	884
29.1.3	Specific Procedures	885
29.1.4	Peptide Receptor Radionuclide Therapy (PRRT)	885
29.1.5	Somatostatin Receptor Ligands	885
29.1.6	Cholecystokinin (CCK) Receptor Ligands	890
29.1.7	Vasoactive Intestinal Peptide (VIP) Receptor Ligands	891
29.1.8	Bombesin (BN) Receptor Ligands	891
29.1.9	Glucagon-like Peptide 1 (GLP1) Receptor Ligands	892
29.1.10	Neurotensin (NT) Receptor Ligands	892
29.1.11	Other Targets	893
29.1.12	Prostate-Specific Membrane Antigen	893
29.1.13	Endoradiotherapy with Antibodies and Small Molecules	894
	References	897

Internal radiation therapy or endoradiotherapy of tumors refers to a localized introduction of radioactively labeled particles or molecules with therapeutically usable radiation. This can be done either by invasive methods in which radiolabeled non-tumor-affine particles are brought directly to the tissue to be treated (non-specific

U. Haberkorn (✉) · C. Kratochwil · F. Giesel
Department of Nuclear Medicine, University Hospital Heidelberg,
Im Neuenheimer Feld 400, 69120 Heidelberg, Germany
e-mail: uwe.haberkorn@med.uni-heidelberg.de

U. Haberkorn
Clinical Cooperation Unit Nuclear Medicine,
German Cancer Research Center (DKFZ), Heidelberg, Germany

Translational Lung Research Center Heidelberg (TLRC),
German Center for Lung Research (DZL), Heidelberg, Germany

method) or by the administration of tumor affinity molecules that selectively accumulate in the tumor after intravenous administration (specific method). An advantage of endoradiotherapy with specific ligands over traditional therapies or immunotherapy is the cross-fire effect induced by the β -particles emanating from the binding site. These particles lead to the destruction of multiple cells in the vicinity of the receptor-positive cell and can, therefore, partially compensate for heretogenic expression of the target structure in the tumor. This cannot be achieved with non-radioactive methods, because only those cells are destroyed which bind the molecule used therapeutically. A further increase in the therapeutic effect is achieved by the radiation-induced bystander effect (RIBE). RIBE describes the situation in which cells that are not directly exposed to ionizing radiation behave like exposed cells: these cells die or show chromosomal instabilities. Although the exact mechanism of RIBE is not yet fully understood, there is evidence that chemical signaling leads to deleterious information from exposed cells to adjacent cells.

29.1 Non-specific Therapy

29.1.1 Selective Internal Radiotherapy (SIRT)

The SIRT radionuclides are introduced into the tumor or metastases via the blood supplying arterial vessels after coupling to glass or resin beads (microspheres). The isotopes used for SIRT are ^{90}Y , ^{131}I , and ^{188}Re , with the current focus on the commercially available ^{90}Y microspheres. TheraSpheres[®] are non-degradable glass microspheres incorporating ^{89}Y , which is converted to ^{90}Y by neutron bombardment in a reactor. The SIR-Spheres[®] are synthetic resin particles with the radionuclide bound on their surface. TheraSphere[®] has a significantly higher activity per particle than the SIR-Spheres[®]. Therefore, SIR-Spheres requires significantly more particles than TheraSpheres. The increased number of particles and the larger diameter of the SIR-Spheres[®] usually result in embolization of the tumor and its afferent vessels. ^{90}Y emits β particles with an energy of 2.24 MeV and has a half-life of 64 h. The β particles have an average range of 2.5–3.5 mm in the tissue. The SIRT therapy is used either for the treatment of liver metastases or hepatocellular carcinoma (HCC). Therapy of HCC with ^{90}Y microspheres is based on the strong arterial hypervascularization of these tumors. Since the arterially injected microspheres are deposited in proportion to the perfusion and the tumors usually are highly perfused this leads to a higher concentration as compared to the liver and thus a higher radiation dose in the tumor. Important prerequisites in addition to the proof of hypervascularization are verified tumor diagnosis, adequate liver function, missing extrahepatic metastases, no or correctable visceral shunt, a shunt-related lung dose below 30 Gy, no other vascular anatomic contraindications, and a missing portal vein thrombosis (only SIR-Spheres) ([29] and Table 29.1).

So far, only non-randomized studies are available for HCC and liver metastases. However, despite their heterogeneity in patient populations and tumor stage, many

Table 29.1 Contraindications for SIRT (according to [29])

<i>Absolute contraindications</i>
Not correctable gastrointestinal shunt
Lung dose > 30 Gy
Contraindications against angiography of the liver artery
Severe liver and lung dysfunction
<i>Relative contraindications</i>
Thrombosis of the portal vein (only SIR-Spheres®)
Bilirubin > 2 mg/dl
Infiltrative tumor growth
Tumor volume > 70% of the target volume
Transaminases > 5 ULN
Extrahepatic metastases
Situation after papillotomy of the Papilla Vater and/or biliary stent insertion

open-label Phase 2 studies have demonstrated a positive effect on survival and quality of life. Similarly, these studies demonstrate that the toxicity of therapy can be minimized with optimal preparation of the patient [13, 21, 61]. A multivariate analysis of prognostic factors revealed that a dose of >104 Gy, a tumor in Okuda stage I, and a tumor-to-liver ratio of >2 correlated significantly with improved survival in terms of microsphere distribution [13]. Median survival is reported in several larger studies for Okuda I patients with 628–649 days and Okuda II patients with 302–324 days, which are significantly better than the 244- and 64-day historical control. A comparison with chemoembolization with respect to postembolization (PES) effects such as fever, nausea, and abdominal pain showed a better radiological tumor response after SIRT and that the PES occurred after treatment with ^{90}Y microspheres about four times less often than after chemoembolization [11, 19]. Several studies addressed treatment of liver metastases showing also positive results [27, 40]. In a large recent study, Sato et al. performed 225 therapeutic treatments in 137 patients. The primary tumors in these patients were colon, breast, neuroendocrine tumors, pancreas, lung, cholangiocarcinoma, melanoma, kidney, esophagus, ovary, adenocarcinoma of unknown origin, lymphoma, stomach, duodenum, bladder, angiosarcoma, thyroid, adrenal, and parotid. The mean number of therapies was 1.6 and the mean activity and dose were 1.83 GBq and 112.8 Gy. Side effects included fatigue (56%), abdominal pain (26%), and nausea (23%). Further follow-up showed a response in 42.8% of the patients (2.1% complete, 40.7% partial). The median survival in all patients was 300 days (1-year survival 47.8%, 2-year survival 30.9%). In patients with colorectal tumors, median survival was 457 days, in patients with neuroendocrine tumors even 776 days [63].

29.1.2 Radiopharmaceuticals with Accumulation in Areas of Bone Remodeling

Patients in late stages of their disease often have bone metastases with severe pain. In these patients, radionuclide therapy with bone-searching molecules has great potential. The procedure is used when multiple lesions with associated pain symptoms are shown in the bone scintigraphy. The anionic bone-seeking substances, mostly based on organic phosphates, are incorporated into the bone matrix. Rhenium and samarium phosphonates accumulate specifically at the site of the osseous conversion zones. In this case, the γ -portion of the radiation allows a post-therapeutic imaging or the follow-up when several cycles are given. Initially, this therapy was more likely to be used in late stages. However, it is now believed that earlier use could also lead to an increase in survival. Absolute contraindications are pregnancy and breastfeeding, relative contraindications are low hematological parameters, i.e., values for platelets $< 1 \times 10^5/\mu\text{l}$, leukocytes $< 3 \times 10^3/\mu\text{l}$, red blood cells $< 3 \times 10^6/\mu\text{l}$, hemoglobin $< 12 \text{ g/l}$, or hematocrit < 30 . Some randomized studies showed a significant improvement in the pain symptoms for rhenium and samarium versus placebo with pain reduction in over 80%. In 30–60%, there was a complete disappearance of the pain. A short-term increase of pain known as flare phenomenon can be observed in less than 10% of cases, which usually occurs on day 2 or 3 and disappears after 1 week. The reduction in pain can last up to a year. Furthermore, it can lead to a stabilization or even regression of the lesions. Decrease of tumor markers and prolonged survival up to 1 year have been described as further effects, especially in case of early use.

The hematological toxicity is usually low and only transient with a normalization within 3 months. The nadir with a drop of 25–30% is reached after about 2–6 weeks. Factors that influence the extent and duration of toxicity are dose and concomitant chemo or radiotherapy. Even repeated treatment with $^{153}\text{Sm-EDTMP}$ in patients with metastatic prostate cancer did not lead to pronounced and long-lasting hematological effects. Radionuclide therapy with rhenium or samarium has so far only been used to a limited extent by oncological colleagues, despite its known effect and low side effects. All the more surprising is the acceptance of radium-223 chloride (Xofigo). Radium-223 is an alpha emitter with a half-life of 11.4 days and a penetration distance of 80–90 microns. A multinational Phase III study (ALSYMPCA trial) evaluated the efficacy and side effects of Xofigo in patients with metastatic, castration-resistant prostate cancer versus a placebo group [31, 49, 60, 62]. Therapy with Ra-223 prolonged the median survival by about 3 months with minor hematological and non-hematological (diarrhea) side effects. There was also a delay of osseous complications and pain reduction in at least 50% of patients. A controlled study investigating the therapeutic potential of rhenium or samarium compounds over radium ^{223}Ra would be desirable.

29.1.3 Specific Procedures

Specific methods use transport molecules that specifically bind to target structures. These transport molecules can be coupled with chemotherapeutic agents or radioactive isotopes. In most cases, antibodies are used against tumor antigens or peptides that bind to overexpressed receptors.

29.1.4 Peptide Receptor Radionuclide Therapy (PRRT)

Peptides are useful molecules for the targeted delivery of radionuclides to the desired localization in an organism. If the corresponding receptor is overexpressed in a tumor, therapeutically relevant doses can be achieved in tumor lesions with low or moderate side effects. Depending on the isotopes used, radioactively labeled peptides additionally allow imaging. The attractive feature here is that first the peptide can be labeled with a γ or positron emitter and used to identify those patients who can benefit from a PRRT, i.e., those patients showing a high accumulation in tumor lesions. Then the same molecule can be labeled with an α or β emitter and used for therapy.

29.1.5 Somatostatin Receptor Ligands

Imaging and therapy with somatostatin receptor ligands can be seen as a paradigm for a whole range of possible methods based on the use of peptides. The high affinity of the peptides for the receptor as well as the internalization of the receptor-peptide complex facilitates the retention of the radiation source in receptor-positive tumors, while the relatively small size enables a quick clearance from the blood. Somatostatin receptors are overexpressed by a variety of tumors such as neuroendocrine tumors of the pancreas and intestine, pituitary adenoma, pheochromocytoma, paraganglioma, small cell lung carcinoma, neuroblastoma, medullary thyroid carcinoma, and meningioma (Table 29.2). Due to their high receptor density, gastroenteropancreatic neuroendocrine tumors, pheochromocytomas, paragangliomas, and bronchial carcinoids are promising candidates for PRRT. In some cases, small cell lung and medullary thyroid carcinomas or a small proportion of non-operable meningiomas, neuroblastomas, thyroid carcinomas, renal cell carcinomas, or breast cancers can be treated. Various peptides have already been labeled for therapeutic use with the following radionuclides: ^{111}In , ^{90}Y , and ^{177}Lu . The physical properties of isotopes that may possibly be used for endoradiotherapy are shown in Table 29.3. Due to the high particle energy and relatively short half-life, ^{90}Y -labeled molecules result in a higher tumor cell dose per peptide and a better cross-fire effect. This feature is particularly needed for the treatment of larger tumors and tumors with heterogeneous receptor expression. In contrast, the lower energy and smaller particle range of ^{177}Lu lead to better absorption in smaller tumors. Furthermore, the γ radiation of ^{177}Lu can be used in addition to therapy for

Table 29.2 Peptide receptor expression in different tumors (modified according to [23])

Tumor	Receptors
Carcinoid (intestine)	SSTR2 > SSTR1, SSTR5, VIP, GRP/Bombesin (NMB-R), CCK (CCK1)
Gastrinoma	SSTR2, VIP, GRP-R
Insulinoma	SSTR, VIP, CCK (CCK2)
Paraganglioma	SSTR2, VIP (PAC1), CRF1
Pheochromocytoma	SSTR2, VIP(PAC1)
C-cell carcinoma	SSTR, NTR1, CCK (CCK2), NK1
SCLC	SSTR2, VIP, GRP/Bombesin (BB3), CCK (CCK2), NK1
NSCLC	VIP (VPAC1)
Meningioma	SSTR2, VIP, NTR1, CCK (CCK1)
Neuroblastoma	SSTR2, VIP (PAC1), CCK (CCK1)
Medulloblastoma	SSTR2, VIP, NTR1
Astrocytoma	SSTR, VIP (PAC1), NTR1, CCK (CCK2), NK1
Glioblastoma	VIP (PAC1), NK1
Exocrine pancreatic cancer	VIP (VPAC1), NTR1
Colorectal carcinoma	VIP (VPAC1)
Gastric cancer	SSTR, VIP (VPAC1)
Hepatocellular carcinoma	SSTR, VIP (VPAC1)
Esophageal carcinoma	VIP (VPAC1)
Renal cell carcinoma	SSTR, VIP (VPAC1), GRP/Bombesin
Prostate carcinoma	SSTR1, VIP (VPAC1), GRP/Bombesin
Bladder cancer	VIP (VPAC1)
Breast cancer	SSTR, VIP (VPAC1), GRP/Bombesin (GRP-R), NK1, NPY-R (Y1)
Ovarian cancer	SSTR, VIP (VPAC1)
Lymphoma	SSTR, VIP
Ewing sarcoma	NTR1
Leiomyoma	SSTR, VIP (VPAC2)
GIST	BB2, CCK2, VIP2

BB2 and BB3: Bombesin receptor subtype 2 and 3

CCK1 and CCK2: Cholecystokinin receptor subtype 1 and 2

CRF1 and CRF2: Corticotropin-releasing factor 1 and 2

GRP: gastrin-releasing peptide

NK1: Neurokinin receptor subtype 1

NPY: Neuropeptide Y

NTR1: Neurotensin receptor subtype 1

PAC1: PACAP receptor subtype 1

SSTR1, SSTR2, and SSTR5: Somatostatin receptor subtype 1, 2, and 5

VIP: vasoactive intestinal peptide

VPAC1 and VPAC2: VIP receptor subtype 1 and 2

Y1: NPY receptor subtype 1

Table 29.3 Physical properties of isotopes with possible application for radionuclide therapy (modified according to [23])

Isotope	Emission	Half-life (<i>d</i>)	Max β energy (keV)	Max distance (mm)
^{90}Y	β^-	2.7	2,270	12
^{177}Lu	γ, β^-	6.7	497	2.1
^{131}I	γ, β^-	8	606	2.4
^{64}Cu	β^-, β^+	0.5	570	2.5
^{67}Cu	γ, β^-	2.5	40; 480; 580	0.4
^{166}Ho	β^-	1.1	711; 1,850	8.7
^{188}Re	β^-	0.7	1,960; 2,120	11
^{211}At	α	7.2 h	5.867; 7.450	<0.1
^{213}Bi	α	45 min	8.380	<0.1

imaging and dosimetry. Preclinical studies on tumor-bearing animals confirmed these properties by showing excellent antitumor effects and the expected influence of tumor size. Therefore, a combination of both radionuclides has been proposed for the treatment of tumors of different sizes and inhomogeneous distribution of receptor expression [16].

Many of the available reports suffer somewhat from the heterogeneity of patient populations and the use of different isotopes, peptides, and non-standardized doses. In contrast to antibodies in radioimmunotherapies, no evidence of immunogenicity of the peptides was found. Initial studies with high doses (cumulative doses between 20 and >100 GBq) of the Auger electron-emitting ^{111}In -DTPA0 octreotide in patients with metastatic neuroendocrine tumors and in poor clinical condition have shown positive symptom-related effects, but few partial remissions [70]. Toxicity was mainly observed in the form of bone marrow suppression. ^{90}Y -DOTA0, Tyr3 octreotide (DOTATOC) binds to the somatostatin receptor subtype 2 with an approximately 10-fold higher affinity than ^{111}In -DTPA0 octreotide. Therefore, some Phase 1 and Phase 2 PRRT studies were performed with this molecule. Initial therapies with doses of 6 and 7.4 GBq given over four cycles showed a general response rate of 24 or 33% with administration of 7.4 GBq in two cycles [73]. A dose escalation of up to 5.6 GBq/cycle did not result in severe acute reactions and in reversible grade 3 hematologic toxicity in 43% of patients after administration of 5.2 GBq. This dose was then defined as the maximum tolerated dose per cycle. The proportion of partial (PR) and complete remissions (CR) was 28% in 87 patients [12]. Other studies report similar results with a median interval to clinical progression of 33 months [9]. In summary, despite differences in protocols, CRs and PRs were at 10–30% with ^{90}Y -DOTA0, Tyr3 octreotide in most of these studies, higher than those obtained with ^{111}In -DTPA0 octreotide.

Replacement of the C-terminal threoninol by threonine at the C-terminus of DOTATOC results in DOTA0, Tyr3 octreotate (DOTATATE), which results in a further increase (9-fold) in affinity to DOTATOC [55]. The ^{177}Lu DOTATATE complexes showed a higher affinity than the ^{90}Y complexes. Preclinical studies with

tumor-bearing rats revealed improved tumor regression and survival of the animals with the ^{177}Lu compound. ^{177}Lu -DOTATATE was comparable to ^{111}In -DTPA0 octreotide in terms of its accumulation in kidney, spleen, and liver, but showed a 3–4-fold higher accumulation in tumors [38]. Therefore, ^{177}Lu -DOTA0, Tyr3 octreotate represents an interesting development as it results in higher absorbed tumor doses at comparable doses for potentially dose-limiting organs. Therapy of patients with gastroenteropancreatic neuroendocrine tumors with ^{177}Lu -DOTA0, Tyr3 octreotate resulted in complete or partial remissions in 30%, metabolic response in 12%, stable disease in 40%, and progression in 18% of 76 patients. Figure 29.1 shows an example of a patient with metastasized NET receiving four doses of ^{177}Lu -labeled DOTATOC. The tumor regression was positively correlated to a higher uptake observed in OctreoScan[®] scintigraphy, a limited hepatic tumor mass, and a high Karnofsky index. Adverse events were rare and transient, mainly as low-to-moderate bone marrow suppression. In summary, improvements in symptoms after therapy with somatostatin analogs have been observed, with better results for tumor regression after therapy with ^{90}Y -DOTA0, Tyr3 octreotide and ^{177}Lu -DOTA0, Tyr3 octreotate. Renal toxicity could be reduced by the simultaneous infusion of lysine and arginine solutions. Further side effects of this therapy were only mild. The duration of therapy response was more than 2 years for both radiopharmaceuticals. Differences in therapeutic efficacy are most likely caused by the already mentioned variations in doses, regimens of therapy (dose-escalating versus fixed dose) and patient populations. A critical point here is the proper selection of patients who can benefit from treatment. Criteria for successful application are the level of uptake in pretherapeutic imaging (i.e., receptor density), total tumor burden, and the extent of liver and kidney accumulation.

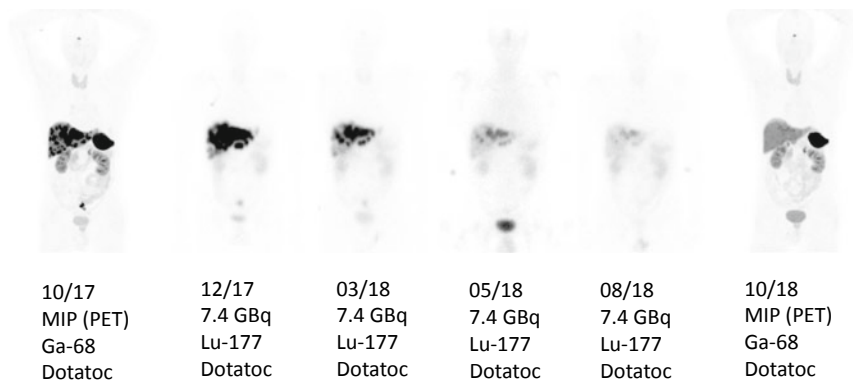


Fig. 29.1 Patient with metastasized NET with multiple lesions in the liver and one lesion in the lower abdomen as shown in the DOTATOC-PET/CT from 10/2017 (MIP). The patient got four doses of 7.4 GBq ^{177}Lu -DOTATOC until 8/2018. The corresponding scintigraphic images (images 2–5 from the left) during therapy demonstrated a decline in number and intensity of the lesions. Finally, the DOTATOC-PET taken in 10/2018 revealed only a few remaining metastases in the liver

Recently, the NETTER trial, a randomized multicenter study evaluating ^{177}Lu -DOTATATE therapy in 229 patients with advanced progressive, somatostatin-receptor-positive midgut neuroendocrine tumors was published. In this study, the patients were randomized to receive either four doses of 7.4 GBq ^{177}Lu -DOTATATE every 8 weeks and best supportive care including i.m. 30 mg octreotide long-acting repeatable (LAR) or 60 mg octreotide LAR alone every 4 weeks (control group).

The estimated rate of progression-free survival at month 20 was 65.2% in the ^{177}Lu -DOTATATE group and 10.8% in the control group. In addition, the response rate was 18% in the ^{177}Lu -DOTATATE group versus 3% in the control group ($P < 0.001$). During that period 14 deaths occurred in the ^{177}Lu -DOTATATE group and 26 in the control group ($P = 0.004$). Grade 3 or 4 neutropenia, thrombocytopenia, and lymphopenia occurred in 1%, 2%, and 9%, respectively, of patients in the ^{177}Lu -Dotatate group as compared with no patients in the control group. No evidence of renal toxicity was seen [67]. A second evaluation determined the impact of ^{177}Lu -DOTATATE treatment on time to deterioration in health-related quality of life. Patients completed the European Organisation for Research and Treatment of Cancer quality-of-life questionnaires QLQ C-30 and G.I.NET-21 at baseline and every 12 weeks until tumor progression. The analysis showed that the time to quality-of-life deterioration (TTD) was significantly longer in the ^{177}Lu -DOTATATE group versus the control group with respect to global health status (hazard ratio [HR], 0.406), physical functioning (HR, 0.518), role functioning (HR, 0.580), fatigue (HR, 0.621), pain (HR, 0.566), diarrhea (HR, 0.473), disease-related worries (HR, 0.572), and body image (HR, 0.425). Differences in median TTD were clinically significant with 28.8 months versus 6.1 months for global health status and 25.2 months versus 11.5 months for physical functioning [68].

Improvement of therapeutic efficacy can be obtained by changing the administration route of the tracer. This was first evaluated in 15 patients with gastroenteropancreatic neuroendocrine tumors where intravenous and intraarterial administration of ^{68}Ga -DOTATOC was compared and quantified using PET [33]. Compared with i.v. infusion, the i.a. infusion resulted in an increased SUV in 117 of 122 (96%) liver metastases. The average increase in SUV was 3.75-fold higher for the i.a. administration. The increase in uptake of primary tumors was dependent on the selectivity of the catheter placement with increases in SUV after i.a. injection which were between 1.44- and 7.8-fold higher. Consequently, the therapeutic effectiveness of arterial administered DOTATOC, labeled with ^{90}Y and ^{177}Lu , was evaluated in 15 patients with liver metastases from GEP-NETs [34]. Response was assessed using DOTATOC-PET, multiphase contrast-enhanced computed tomography, magnetic resonance imaging, and chromogranin A values. Complete remission was obtained in one (7%) patient and partial remission in eight (53%) patients, and six patients were classified as stable (40%). Furthermore, there was a correspondence of the decrease of chromogranin A and the radiologic response. The median time to progression was not reached within a mean follow-up period of 20 months. Receptor saturation and redistribution effects were identified as limiting factors for i.a. DOTATOC therapy. The high rate of objective radiologic response

in these NET patients treated with arterial infusion of ^{90}Y -/ ^{177}Lu -DOTATOC compared favorably with systemic chemotherapy and intravenous radiolabeled peptide therapy.

Another interesting group of radioactively labeled peptides is somatostatin receptor antagonists. DOTA coupled to [NH₂-CO-c (DCys-Phe-Tyr-DAGl8 (Me, 2-naphthoyl)-Lys-Thr-Phe-Cys)-OH (DOTA-sst3-ODN-8) and [4-NO₂-Phe-c (DCys-Tyr-DTrp-Lys-Thr-Cys)-DTyr-NH₂] (DOTA-sst2-ANT)] showed high sst3 and sst2 binding affinity after complexing with ^{111}In [20]. The uptake and persistence of both peptides in ST3- or sst2-receptor-transfected HEK293 cells and tumor transplants were surprisingly high. This effect was explained by more than 10-fold higher number of binding sites on the receptor compared to the agonist. Whether these promising properties can also be used on human tumors and within the framework of a PRRT remains to be clarified. In addition to combinations of peptide analogs labeled with different radionuclides, future activities could use several strategies: upregulation of somatostatin receptor expression of tumors, early diagnosis with PET tracers could identify patients with a low tumor burden and higher chance of response, peptides with binding to multiple receptors or receptor subtypes and combination with radiosensitizers, surgery, chemotherapy, immunotherapy, and radiotherapy.

29.1.6 Cholecystinin (CCK) Receptor Ligands

These receptors show increased expression in medullary thyroid carcinomas, gastroenteropancreatic neuroendocrine tumors, SCLC, ovarian carcinomas, and also in gastrointestinal stromal tumors. Therefore, various cholecystinin (CCK)-A and CCK-B/gastrin-related peptides have been developed and evaluated in preclinical studies [14]. The human heptadecapeptide gastrin-I and ^{111}In -DOTA/DTPA-CCK-B analogs [54] showed biological half-lives of several hours, a predominantly renal excretion and a specific uptake both in CCK-B-expressing organs and in medullary thyroid carcinomas with values up to 9% ID/g 1 hour after administration of the tracer. Since medullary thyroid carcinomas express CCK2 receptors in almost all cases, a first clinical study was performed in patients with these tumors. A DTPA-D-Glu-modified minigastrin labeled with ^{90}Y was used. Unfortunately, this first attempt had to be stopped because of kidney and hematotoxicity [6]. The situation changed with the development of new CCK analogs with lower renal uptake and improved affinity for the target structure. These new ligands were obtained by removing four glutamic acid residues from a minigastrin analog and showed a 5-fold higher binding affinity for the CCK2 receptor (0.2 nM) and a 25-fold lower renal uptake [6]. In a European collaboration as part of a COST action, the in vitro stability of a series of peptides binding to the CCK2 receptor was compared [48]. Twelve different 1,4,7,10-tetraazacyclododecane-N,N',N'',N'''-tetraacetic acid (DOTA)-minigastrin/CCK conjugates were radiolabeled with ^{177}Lu and the in vitro stability was tested in fresh human serum. In these compounds, a variable stability in human serum was found with half-lives between 4.5 ± 0.1 and 198 ± 0.1 h. In urine of

normal mice, only metabolized peptide fragments were detected even at short times after injection for all peptides. MALDI-TOF MS revealed a major cleavage site of all minigastrin derivatives between Asp and Phe-NH(2) at the C-terminal end.

29.1.7 Vasoactive Intestinal Peptide (VIP) Receptor Ligands

Since VIP receptors are overexpressed in a variety of tumors including gastrointestinal adenocarcinomas and carcinoids, studies to develop diagnostic tracers were first performed by labeling VIP with ^{123}I [51] or its TP-3654 analogs with $^{99\text{m}}\text{Tc}$ [69]. Unfortunately, these compounds showed a rapid degradation in the blood. Furthermore, VIP is pharmacologically highly potent with the potential for toxic effects at submicrogram doses, requiring preparations with high specific activity. These disadvantages limited the clinical application of VIP-derived tracers to a few studies reporting imaging in selected patients [28, 72]. In these studies, ^{123}I -VIP was used as a non-specific molecule for the receptor subtypes VIP-pituitary adenylate cyclase-activating polypeptide 1 and 2 (VPAC1 and 2). Targeting of subtype 1, despite its expression in many tumors, does not appear promising because the receptor is ubiquitously expressed. In contrast, VPAC2 shows low expression in normal tissues and could be used as a target in patients with VPAC2-expressing tumors such as GIST.

29.1.8 Bombesin (BN) Receptor Ligands

Bombesin receptors belong to the group of G-protein-coupled receptors and are overexpressed in common tumors such as prostate and breast cancers [43]. Therefore, some bombesin-based radioligands have been developed and evaluated in preclinical and clinical studies [10, 65]. One of the first molecules, $^{99\text{m}}\text{Tc}$ -BN (7-14), showed a high specific binding to rat cortex membranes in the nanomolar range (IC₅₀ 0.8 nM) [3]. Preliminary clinical results showed good tumor demarcation in prostate cancer patients. Some of these new bombesin-based radiopeptides were conjugated to DOTA and labeled with ^{68}Ga , ^{67}Ga or ^{68}Ga -DOTA-PEG2-[D-Tyr6, βAla11, Thi13, Nle14] bombesin (6-14) showed in a pancreatic carcinoma model (AR42J) high affinity and rapid internalization in vitro with more than 85% internalized activity after 1 h. The tumor uptake in vivo at 1 h p.i. was between 5.5 and 11% ID/g depending on the amount of injected peptide and with a biological half-life of 15 h. Scintigraphic images after 1 h p.i. showed a high specific accumulation in the tumor, kidneys, intestine, and pancreas [64], which was confirmed by biodistribution and competition studies. Since internalization has been described for the DTPA-coupled BN agonists, these molecules are of interest not only for diagnostic but also for PRRT, as the chelator also allows labeling with ^{90}Y or ^{177}Lu . Nevertheless, the pharmacological activity of the BN derivative could limit therapeutic application of these peptides.

The gastrin-releasing peptide (GRP) receptor is overexpressed in a variety of tumors such as carcinoma of the lung, breast, prostate, and pancreas. GRP receptor heterogeneity often occurs in breast cancer and may be a problem for GRP receptor radiotherapy. On the other hand, GISTs are exceptionally well suited for a PRRT because of their extremely high GRP receptor density [57]. Prostate carcinomas represent another interesting field of application, especially because overexpression of GRP receptors is seen in invasive or advanced tumors. Although the 14 amino acid neuropeptide bombesin (BN) has a high binding affinity for GRP receptors, various derivatives of this molecule showed suboptimal hepatobiliary clearance with a correspondingly difficult interpretation of the abdomen due to high background activity. However, a BN derivative with low liver and intestinal uptake has been synthesized [42].

In addition to agonists, also antagonists have been developed [18, 22, 44, 50, 66]. These have been used for mono- or combined therapy with rapamycin of prostate cancer. The antagonist ^{177}Lu -RM2 was applied alone and in combination with rapamycin in tumor cells and tumor-bearing animals. Monotherapy with ^{177}Lu -RM2 was effective at doses of 72 and 144 MBq with complete tumor remission in 60% of the treated mice. However, combination therapy with 37 MBq ^{177}Lu -RM2 and rapamycin resulted in a significantly longer survival than with either agent alone without treatment-related toxicity [18]. Since the gastrin-releasing peptide receptor (GRPR) is also overexpressed in breast cancer, ^{68}Ga -labeled RM2 was used for an imaging study in 15 patients with breast cancer [66]. In 13 of 15 tumors a high tracer uptake was found, whereas normal breast tissue showed inter- and intraindividually variable and moderate tracer accumulation. The uptake in other organs was considerably less except in the pancreas. The implication of these findings for radiopeptide therapy of breast cancer has to be determined.

29.1.9 Glucagon-like Peptide 1 (GLP1) Receptor Ligands

A high density of GLP1 receptors has been reported in insulinomas and gastrinomas, suggesting the use of GLP1 analogs for the PRRT of these tumors [23]. A GLP1 analog [Lys40 (Ahx-DTPA- ^{111}In) NH₂] exendin-4 was presented in 2006 [75] which is now in clinical use for imaging. The molecule showed a high binding affinity ($\text{IC}_{50} = 2.1 \text{ nM}$) and specific tumor targeting in biodistribution experiments (up to 290% ID/g). Furthermore, an exclusively renal metabolism and a short plasma half-life were observed, with a simultaneous long retention in transgenic Rip1Tag2 mice developing tumors originating from pancreatic β -cells. The high uptake and the long tumor retention are good prerequisites for a PRRT.

29.1.10 Neurotensin (NT) Receptor Ligands

A subgroup of ductal pancreatic tumors is considered to be good candidates for a PRRT as they have a high density of NT receptors. Various $^{99\text{m}}\text{Tc}$ and ^{111}In -DTPA/

DOTA-labeled neurotensin derivatives were, therefore, evaluated in preclinical and clinical studies, unfortunately with the result of rapid degradation *in vivo* [23]. Nevertheless, several ^{111}In -labeled NT analogs with better serum stability and rapid internalization after binding to the NT receptor could be found and recently promising new tracers have been developed [46]. Biodistribution experiments revealed evidence of high potential for efficient tumor targeting [15]. Other tumors with NT receptor expression are meningiomas and Ewing sarcomas.

29.1.11 Other Targets

Other possible target structures are located on the membranes of endothelial cells, such as z-B. $\alpha\nu$ integrins ($\alpha\nu\beta 3$, $\alpha\nu\beta 5$), vascular endothelial growth factor (VEGF) receptors, and fibroblast growth factor (FGF) receptors. ^{123}I -labeled VEGF165 and VEGF121 have been used in animal experiments, as well as in initial clinical trials, and demonstrated binding to a variety of human tumor cells or tissues and a 58% detection rate in a study of 40 patients with gastrointestinal tumors [41]. Furthermore, some other peptides are considered, e.g., for CXCR4 [39, 74], melanocortin receptors [45, 59, 77], endoglin (CD105), epidermal growth factor (EGF), or $\alpha\nu\beta 6$ ligands [2, 58].

Future developments of PRRT are the transfer of this therapeutic approach from somatostatin receptors to other target structures, as many tumors, including mammary, prostate, colon, pancreatic, and brain tumors overexpress various other peptide receptors (see above and Table 29.2). Since tumors can simultaneously express multiple peptide receptors, combinations of two or more peptides represent a promising option. This approach should result in a higher tumor dose and a more homogeneous distribution of the radioactivity in the tumors. Tumors that are good targets for multi-receptor targeting are breast cancers (GRP and NPY receptors) and GISTs (GRP, CCK2, and VPAC2 receptors) [56, 57].

29.1.12 Prostate-Specific Membrane Antigen

The prostate-specific membrane antigen (PSMA) is an ideal membrane-bound structure for imaging and targeted therapy of prostate cancer: as a transmembrane protein with glutamate-carboxypeptidase activity and its active site located extracellularly it can be addressed by rational design of inhibitors mimicking the binding of the natural substrates, for example, the peptidic neurotransmitter NAAG. Furthermore, after binding of a ligand internalization occurs via clathrin-coated pits and subsequent endocytosis. This results in enhanced uptake and retention in the tumor, which are prerequisites for a high contrast in imaging and a high local dose deposit obtained in therapeutic applications. Finally, the protein shows high expression in most tumors and low expression in normal tissues. Possible ligands for PSMA are antibodies like J591 and small molecule inhibitors. Both have been used for imaging as well as for therapy and, therefore, are candidates for *in vivo*

theranostics. With respect to the influence of PSMA ligand imaging on the planning of therapies other than endoradiotherapy, several studies showed changes in up to 63% of the cases in the setting of biochemical relapse and approximately in 25% in the primary situation [24, 25, 35, 36]. On the other hand, the attractive feature of endoradiotherapy is that patients may first be identified as possible candidates for this treatment after labeling of the carrier molecule with a beta or positron emitter. Upon positive findings, the same molecule can be used for therapy by labeling with an α - or β -emitting isotope. In addition, a pretherapeutic dosimetry is possible.

29.1.13 Endoradiotherapy with Antibodies and Small Molecules

Although phase I and II studies with ^{90}Y - or ^{177}Lu -labeled J591 revealed benefits with respect to survival and stabilization of PSA and manageable side effects [4, 47, 71], small molecule radiopharmaceuticals have some advantages over antibodies such as better tumor penetration, fast blood clearance, and low background activity. This should result in a lower dose for normal organs. Dosimetry with the compound ^{124}I -MIP-1095 revealed that the organs receiving the highest absorbed doses after administration of ^{131}I -MIP-1095 are the salivary glands (mean dose 4.6 mGy/MBq), the liver (1.5 mGy/MBq), and the kidneys (1.5 mGy/MBq). The mean total whole body absorbed dose was 0.38 mGy/MBq resulting in 0.76 to 2.7 Gy based on the injected activities. Due to faster kinetics, the PSMA-targeted small molecule ^{131}I -MIP-1095 showed a better therapeutic range in comparison to J591 with PSA responses after one therapeutic dose (mean activity 4.8 GBq) in 17/28 patients [76].

Since ^{177}Lu has a better beta-to-gamma ratio as compared to ^{131}I PSMA, ligands coupled to more universal chelates were developed such as PSMA617 [7, 8]. Doses obtained with ^{177}Lu -PSMA-617 were even lower with 1.4 mGy/MBq for the salivary glands, 0.1 mGy/MBq for the liver, 0.75 mGy/MBq for the kidneys, and 0.03 mGy/MBq for the red marrow. These dosimetric data were found independently by four centers [17, 30, 32, 35, 36]. Consequently, side effects with respect to bone marrow were mild to moderate. Diffuse bone marrow involvement was a risk factor for higher grade myelosuppression but could be identified by PSMA imaging in advance. A therapy response as measured by a decrease in PSA as well as lesion number and size was seen in approximately 70% for both ^{131}I -MIP1095 and ^{177}Lu -PSMA-617 [35, 36, 76]. Furthermore, pain relief was obtained in almost all patients. Another chelator-coupled tracer, ^{177}Lu -DOTAGA-(I-y)fk(Sub-KuE), resulted in high absorbed tumor doses (median 3.3 Gy/GBq) as compared to normal organs of 0.8 Gy/GBq for kidneys or 1.3 Gy/GBq for salivary glands. Furthermore, a high rate of overall PSA responders without presence of severe acute toxicity was seen [5]. However, the first reports suffered from variations of dose and schedule as well as from heterogeneity of the patient population.

Ahmadzadehfar et al. [1] reported therapeutic effects in 24 patients receiving two doses ^{177}Lu -PSMA-617 (mean dose 6 GBq per cycle). Although the PSA response after the first dose was approximately 80%, some patients presented with early

relapse and in only 70% of the patients the PSA response lasted until 8–10 weeks after the first dose. Kratochwil et al. [35, 36] found in 30 patients receiving up to 3 doses ^{177}Lu -PSMA-617 given bimonthly at a dose of 6 GBq a PSA response (any decline of PSA at week-8) in 70% of the patients after the first dose. Figures 29.2 and 29.3 show examples of a varying response after treatment with multiple doses of ^{177}Lu -PSMA-617. However, the duration of response was also limited and only 40% of the patients presented with ongoing response until 6 months after initiation of treatment. In both analyses, few patients died early after therapy by tumor progression, and only grade-1/2 hematologic toxicities were seen as well as sporadically mild xerostomia and fatigue.

Furthermore, the >50% PSA decline rate at week-8 was similar with 41.6% [1] and 43.3% [35, 36]. Another analysis in patients treated with 7.4 GBq ^{177}Lu -PSMA-I&T reported a >50% PSA response rate of 33% at 8 weeks after therapy [26]. In summary, independent of the PSMA ligand applied all centers reported that the treatment was well tolerated with no or only few grade-3/4 toxicities. However, a further common finding was that 20–40% of the patients were refractory to treatment with ^{177}Lu -PSMA ligands despite a high tracer uptake in the pretherapeutic PSMA ligand PET/CT. Patients with a diffuse infiltration of the red marrow have to be considered as patients at risk for the development of higher grade hematotoxicity [35, 36].

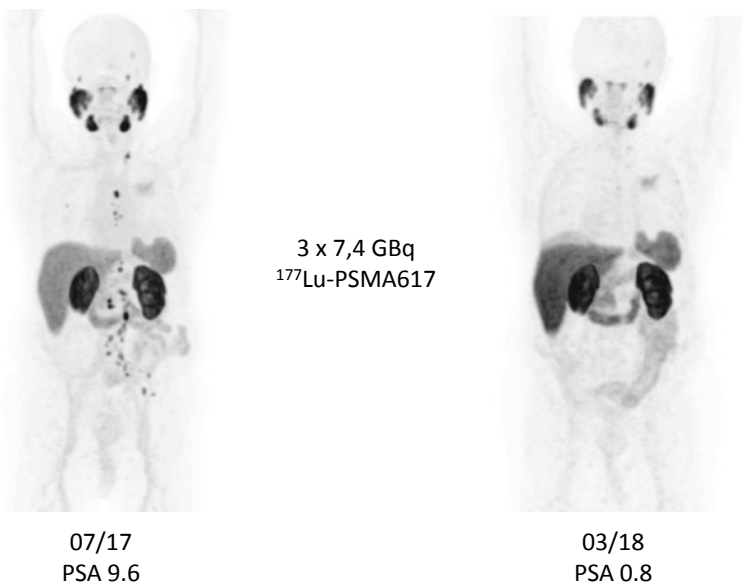


Fig. 29.2 PSMA ligand PET/CT (MIP) of a patient with metastasized prostate cancer prior (left) and after (right) three doses of 7.4 GBq ^{177}Lu -PSMA-617. The PSA value decreased from 9.6 to 0.8 indicating a partial response. Imaging revealed a substantial decrease in the number of lesions

A multicenter retrospective analysis in Germany was performed for 145 patients with mCRPC receiving 1–4 therapy cycles with 2–8 GBq ^{177}Lu -PSMA-617. Nineteen patients died during the observation period. Grade 3–4 hematotoxicity occurred in 18 patients: 10%, 4%, and 3% of the patients experienced anemia, thrombocytopenia, and leukopenia, respectively. Xerostomia occurred in 8%. The overall biochemical response rate was 45% after all therapy cycles, whereas 40% of patients already responded after a single cycle [52].

Replacement of beta emitters by alpha emitters such as ^{225}Ac is one option to address resistance to beta irradiation as well as diffuse involvement of the bone marrow. In a first approach, a dosimetry estimate was calculated on the basis of time-activity curves derived from serially obtained ^{177}Lu -PSMA-617 scans extrapolated to the physical half-life of ^{225}Ac , assuming instant decay of unstable daughter nuclides. This revealed mean doses of 2.3 Sv for salivary glands, 0.7 Sv for kidneys, and 0.05 Sv for red marrow. Thereafter, therapy was initiated in final stage patients with 50, 100, 150, and 200 kBq/kg of ^{225}Ac -PSMA-617. Severe xerostomia was identified as the dose-limiting toxicity for therapeutic doses greater than 100 kBq/kg per dose. With 100 kBq/kg, the duration of a decrease in PSA was less than 4 months. However, repeated bimonthly administration resulted in additive antitumor effects. Significant antitumor activity measured as radiologic response and/or decrease of PSA was seen in 9 of 11 patients [37]. A further analysis was done in 40 patients after treatment with three 100 kBq/kg doses of ^{225}Ac -PSMA-617 at 2-mo intervals [53]. The median duration of tumor control after ^{225}Ac -PSMA-617 last-line therapy was 9 months; 5 patients had a long-lasting response of more than 2 years. Since all patients were final stage patients, this compares favorably with the tumor control rates

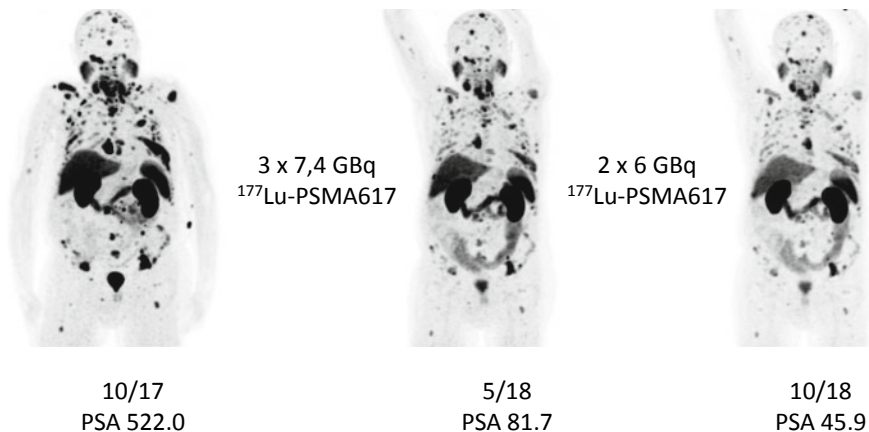


Fig. 29.3 PSMA ligand PET/CT (MIP) of a patient with metastasized prostate cancer prior (left) and three doses of 7.4 GBq ^{177}Lu -PSMA-617 (middle) and after two additional doses of 6 GBq ^{177}Lu -PSMA-617 (right). The PSA value decreased from 522 to 81.7 and 45.9 after three doses and five doses of ^{177}Lu -PSMA-617, respectively. Imaging showed a corresponding decrease in number and intensity of the tumor lesions

associated with medications given at earlier stages of the disease such as abiraterone (10 months), docetaxel (6.5 months), enzalutamide (6.5 months), and cabazitaxel (6 months), respectively. Xerostomia was the main reason for discontinuation of therapy and was in the same dimension as nonresponse. According to these preliminary experiences, there is a clear benefit of ^{225}Ac over ^{177}Lu in prostate cancer patients with disseminated late-stage disease in the bone marrow. This relates to antitumor effects as well as to hematologic side effects. However, effects as well as side effects are a matter of radionuclide, dose, and time. Although more efficient with respect to tumor cell killing α emitters will destroy the salivary glands with a reduction of quality of life. For this reason, strategies need to be developed which reduce the tracer accumulation in these organs.

Another aspect to be considered is the obvious heterogeneity of PSMA expression in primary tumors and metastases. This heterogeneity may lead to the selection of clones with low or even no PSMA expression and, therefore, to resistance to endoradiotherapy with PSMA ligands. In the latter case, new biological targets and new radiopharmaceuticals have to be identified and developed for clinical application.

References

1. Ahmadzadehfar H, Eppard E, Kürpig S, Fimmers R, Yordanova A, Schlenkhoff CD, Gärtner F, Rogenhofer S, Essler M (2016) Therapeutic response and side effects of repeated radioligand therapy with ^{177}Lu -PSMA-DKFZ-617 of castrate-resistant metastatic prostate cancer. *Oncotarget* 7:12477–12488
2. Altmann A, Sauter M, Roesch S, Mier W, Warta R, Debus J, Dyckhoff G, Herold-Mende C, Haberkorn U (2017) Identification of a novel ITG α v β 6-binding peptide using protein separation and phage display. *Clin Cancer Res* 23:4170–4180
3. Baidoo KE, Lin KS, Zhan Y, Finley P, Sheffel U, Wagner HN Jr (1998) Design, synthesis, and initial evaluation of high-affinity technetium bombesin analogues. *Bioconjug Chem* 9:218–225
4. Bander NH, Milowsky MI, Nanus DM, Kostakoglu L, Vallabhajosula S, Goldsmith SJ (2005) Phase I trial of ^{177}Lu -labeled j591, a monoclonal antibody to prostate-specific membrane antigen, in patients with androgen-independent prostate cancer. *J Clin Oncol* 23:4591–4601
5. Baum RP, Kulkarni HR, Schuchardt C, Singh A, Wirtz M, Wiessalla S, Schottelius M, Mueller D, Klette I, Wester HJ (2016) Lutetium-177 PSMA radioligand therapy of metastatic castration-resistant prostate cancer: safety and efficacy. *J Nucl Med* 2016(57):1006–1013
6. Behr TM, Béhé M (2002) Cholecystokinin-B/gastrin receptor-targeting peptides for staging and therapy of medullary thyroid cancer and other cholecystokinin-B receptor-expressing malignancies. *Semin Nucl Med* 32:97–107
7. Benešová M, Schäfer M, Bauder-Wüst U, Afshar-Oromieh A, Kratochwil C, Mier W et al (2015) Preclinical evaluation of a tailor-made DOTA-conjugated PSMA inhibitor with optimized linker moiety for imaging and endoradiotherapy of prostate cancer. *J Nucl Med* 56:914–920
8. Benešová M, Bauder-Wüst U, Schäfer M et al (2016) Linker modification strategies to control the prostate-specific membrane antigen (PSMA)-targeting and pharmacokinetic properties of DOTA-conjugated PSMA inhibitors. *J Med Chem* 59:1761–1775

9. Bodei L, Cremonesi M, Zoboli S, Grana C, Mazzetta C, Rocca P, Caracciolo M, Mäcke HR, Chinol M, Paganelli G (2003) Receptor-mediated radionuclide therapy with ^{90}Y -DOTATOC in association with amino acid infusion: a phase I study. *Eur J Nucl Med Mol Imaging* 30:207–216
10. Breeman WA, de Jong M, Erion JL, Bugaj JE, Srinivasan A, Bernard BF, Kwekkeboom DJ, Visser TJ, Krenning E (2002) Preclinical comparison of (^{111}In) -labeled DTPA- or DOTA-bombesin analogs for receptor-targeted scintigraphy and radionuclide therapy. *J Nucl Med* 43:1650–1656
11. Carr BI (2004) Hepatic arterial ^{90}Y trium glass microspheres (Therasphere) for unresectable hepatocellular carcinoma: interim safety and survival data on 65 patients. *Liver Transpl* 10: S107–S110
12. Chinol M, Bodei L, Cremonesi M, Paganelli G (2002) Receptor-mediated radiotherapy with Y-DOTA-DPhe-Tyr-octreotide: the experience of the European Institute of Oncology Group. *Semin Nucl Med* 32:141–147
13. Dancey JE, Shepherd FA, Paul K, Sniderman KW, Houle S, Gabrys J et al (2000) Treatment of nonresectable hepatocellular carcinoma with intrahepatic ^{90}Y -microspheres. *J Nucl Med* 41:1673–1681
14. de Jong M, Bakker WH, Bernard BF, Valkema R, Kwekkeboom DJ, Reubi JC et al (1999) Preclinical and initial clinical evaluation of ^{111}In -labeled nonsulfated CCK8 analog: a peptide for CCK-B receptor-targeted scintigraphy and radionuclide therapy. *J Nucl Med* 40:2081–2087
15. de Visser M, Janssen PJJM, Srinivasan A, Reubi JC, Waser B, Erion JL, Schmidt MA, Krenning EP, de Jong M (2003) Stabilised ^{111}In -labelled DTPA- and DOTA-conjugated neurotensin analogues for imaging and therapy of exocrine pancreatic cancer. *Eur J Nucl Med* 30:1134–1139
16. Dejong M, Breeman WAP, Valkema R, Bernard BF, Krenning EP (2005) Combination radionuclide therapy using ^{177}Lu - and ^{90}Y -labeled somatostatin analogs. *J Nucl Med* 46:13S–17S
17. Delker A, Fendler WP, Kratochwil C et al (2016) Dosimetry for ^{177}Lu -DKFZ-PSMA-617: a new radiopharmaceutical for the treatment of metastatic prostate cancer. *Eur J Nucl Med Mol Imaging* 43:42–51
18. Dumont RA, Tamma M, Braun F et al (2013) Targeted radiotherapy of prostate cancer with a gastrin-releasing peptide receptor antagonist is effective as monotherapy and in combination with rapamycin. *J Nucl Med* 54:762–769
19. Geschwind JF, Salem R, Carr BI, Soulen MC, Thurston KG, Goin KA et al (2004) Yttrium-90 microspheres for the treatment of hepatocellular carcinoma. *Gastroenterology* 127 (5 Suppl 1):S194–S205
20. Ginj M, Zhang H, Waser B, Cescato R, Wild D, Wang X, Ercegyi J, Rivier J, Maecke HR, Reubi JC (2006) Radiolabeled somatostatin receptor antagonists are preferable to agonists for in vivo peptide receptor targeting of tumors. *Proc Natl Acad Sci USA* 103:16436–16441
21. Goin JE, Salem R, Carr BI, Dancey JE, Soulen MC, Geschwind JF et al (2005) Treatment of unresectable hepatocellular carcinoma with intrahepatic yttrium 90 microspheres: factors associated with liver toxicities. *J Vasc Interv Radiol* 16:205–213
22. Gourni E, Mansi R, Jamous M et al (2014) N-terminal modifications improve the receptor affinity and pharmacokinetics of radiolabeled peptidic gastrin-releasing peptide receptor antagonists: examples of ^{68}Ga - and ^{64}Cu -labeled peptides for PET imaging. *J Nucl Med* 55:1719–1725
23. Haberkorn U, Eisenhut M, Altmann A, Mier W (2008) Endoradiotherapy with peptides—status and future development. *Curr Med Chem* 15:219–234
24. Haberkorn U, Eder M, Kopka K, Babich JW, Eisenhut M (2016) New Strategies in prostate cancer: prostate-specific membrane antigen (PSMA) ligands for diagnosis and therapy. *Clin Cancer Res* 22:9–15

25. Haberkorn U, Kopka K, Giesel F, Kratochwil C (2016) Future trends in prostate cancer theranostics with PSMA ligands. *Clin Transl Imaging* 4:487–489
26. Heck MM, Retz M, D Alessandria C, Rauscher I, Scheidhauer K, Maurer T, Storz E, Janssen F, Schottelius M, Wester HJ, Gschwend JE, Schwaiger M, Tauber R, Eiber M (2016) Systemic radioligand therapy with ^{177}Lu -PSMA-I&T in patients with metastatic castration-resistant prostate cancer. *J Urol* 196:382–391
27. Herba MJ, Thirlwell MP (2002) Radioembolization for hepatic metastases. *Semin Oncol* 29:152–159
28. Hesse C, Bäder M, Meinhold H, Bohmig M, Faiss S, Reubi JC, Wiedenmann B (2000) Vasoactive intestinal peptide receptor scintigraphy in patients with pancreatic adenocarcinomas or neuroendocrine tumours. *Eur J Nucl Med* 27:1684–1693
29. Hilgard P, Müller S, Hamami M, Sauerwein WS, Haberkorn U, Gerken G, Antoch G (2009) Selektive interne Radiotherapie (Radioembolisation) und Strahlentherapie beim HCC - Stand und Perspektiven. *Z Gastroenterol* 47:37–54
30. Hohberg M, Eschner W, Schmidt M et al (2016) Lacrimal glands may represent organs at risk for radionuclide therapy of prostate cancer with ^{177}Lu DKFZ-PSMA-617. *Mol Imaging Biol* 18(3):437–445
31. Hoskin P, Sartor O, O'Sullivan JM et al (2014) Efficacy and safety of radium-223 dichloride in patients with castration-resistant prostate cancer and symptomatic bone metastases, with or without previous docetaxel use: a prespecified subgroup analysis from the randomised, double-blind, phase 3 ALSYMPCA trial. *Lancet Oncol* 15:1397–1406
32. Kabasakal L, AbuQbeith M, Aygün A et al (2015) Pre-therapeutic dosimetry of normal organs and tissues of ^{177}Lu -PSMA-617 prostate-specific membrane antigen (PSMA) inhibitor in patients with castration-resistant prostate cancer. *Eur J Nucl Med Mol Imaging* 42:1976–1983
33. Kratochwil C, Giesel FL, López-Benítez R et al (2010) Intraindividual comparison of selective arterial versus venous ^{68}Ga -DOTATOC PET/CT in patients with gastroenteropancreatic neuroendocrine tumors. *Clin Cancer Res* 16:2899–2905
34. Kratochwil C, Lopez-Benitez R, Mier W et al (2011) Hepatic arterial infusion enhances DOTATOC radiopeptide therapy in patients with neuroendocrine liver metastases. *Endocr Relat Cancer* 18:595–602
35. Kratochwil C, Afshar-Oromieh A, Kopka K et al (2016) Current status of prostate-specific membrane antigen targeting in nuclear medicine: clinical translation of chelator containing prostate-specific membrane antigen ligands into diagnostics and therapy for prostate cancer. *Semin Nucl Med* 46:405–418
36. Kratochwil C, Giesel FL, Stefanova M, Benešová M, Bronzel M, Afshar-Oromieh A, Mier W, Eder M, Kopka K, Haberkorn U (2016) PSMA-targeted radionuclide therapy of metastatic castration-resistant prostate cancer with Lu-177 labeled PSMA-617. *J Nucl Med* 57:1170–1176
37. Kratochwil C, Bruchertseifer F, Rathke H et al (2017) Targeted α -therapy of metastatic castration-resistant prostate cancer with ^{225}Ac -PSMA-617: dosimetry estimate and empiric dose finding. *J Nucl Med* 58:1624–1631
38. Kwekkeboom DJ, Bakker WH, Kooij PP, Konijnenberg MW, Srinivasan A et al (2001) [^{177}Lu -DOTAOTyr3]octreotate: comparison with [^{111}In -DTPAO]octreotide in patients. *Eur J Nucl Med* 28:1319–1325
39. Lapa C, Herrmann K, Schirbel A et al (2017) CXCR4-directed endoradiotherapy induces high response rates in extramedullary relapsed multiple myeloma. *Theranostics* 7:1589–1597
40. Lewandowski RJ, Thurston KG, Goin JE et al (2005) ^{90}Y microspheres (TheraSphere) treatment for unresectable colorectal cancer metastases of the liver: response to treatment at targeted doses of 135–150 Gy as measured by [^{18}F] fluorodeoxyglucose positron emission tomography and computed tomographic imaging. *J Vasc Interv Radiol* 16:1641–1651

41. Li S, Peck-Radosavljevic M, Kienast O, Preitfellner J, Hamilton G, Kurtaran A, Pirich C, Angelberger P, Dudczak R (2003) Imaging gastrointestinal tumours using vascular endothelial growth factor-165 (VEGF165) receptor scintigraphy. *Ann Oncol* 14:1274–1277
42. Lin KS, Luu A, Baidoo KE, Hashemzadeh-Gargari H, Chen MK, Brennehan K et al (2005) A new high affinity technetium-99 m-bombesin analogue with low abdominal accumulation. *Bioconjug Chem* 16:43–50
43. Maecke HR, Hofmann M, Haberkorn U (2005) Gallium-68 labeled peptides in tumor imaging. *J Nucl Med* 46:172–178
44. Mansi R, Abiraj K, Wang X et al (2015) Evaluation of three different families of bombesin receptor radioantagonists for targeted imaging and therapy of gastrin releasing peptide receptor (GRP-R) positive tumors. *J Med Chem* 58:682–691
45. Martin ME, Sue O'Dorisio M, Leverich WM, Kloeping KC, Walsh SA, Schultz MK (2013) "Click"-cyclized (68)Ga-labeled peptides for molecular imaging and therapy: synthesis and preliminary in vitro and in vivo evaluation in a melanoma model system. *Recent Results Cancer Res* 194:149–175
46. Maschauer S, Prante O (2018) Radiopharmaceuticals for imaging and endoradiotherapy of neurotensin receptor-positive tumors. *J Label Compd Radiopharm* 61:309–325
47. Milowsky MI, Nanus DM, Kostakoglu L et al (2007) Vascular targeted therapy with anti-prostate-specific membrane antigen monoclonal antibody J591 in advanced solid tumors. *J Clin Oncol* 25:540–547
48. Ocak M, Helbok A, Rangger C et al (2011) Comparison of biological stability and metabolism of CCK2 receptor targeting peptides, a collaborative project under COST BM0607. *Eur J Nucl Med Mol Imaging* 38:1426–1435
49. Parker CC, Coleman RE, Sartor O, et al (2017) Three-year safety of radium-223 dichloride in patients with castration-resistant prostate cancer and symptomatic bone metastases from phase 3 randomized alpharadin in symptomatic prostate cancer trial. *Eur Urol pii:S0302-2838(17)30516-X*. <https://doi.org/10.1016/j.eururo.2017.06.021>
50. Popp I, Del Pozzo L, Waser B et al (2017) Approaches to improve metabolic stability of a statine-based GRP receptor antagonist. *Nucl Med Biol* 45:22–29
51. Raderer M, Kurtaran A, Leimer M, Angelberger P, Niederle B, Vierhapper H, Vorbeck F, Hejna MH, Scheithauer W, Pidlich J, Virgolini I (2000) Value of peptide receptor scintigraphy using (123)I-vasoactive intestinal peptide and (111)In-DTPA-D-Phe1-octreotide in 194 carcinoid patients: Vienna University Experience, 1993 to 1998. *J Clin Oncol* 18:1331–1336
52. Rahbar K, Ahmadzadehfar H, Kratochwil C et al (2017) German multicenter study investigating ¹⁷⁷Lu-PSMA-617 radioligand therapy in advanced prostate cancer patients. *J Nucl Med* 58:85–90
53. Kratochwil C, Bruchertseifer F, Rathke H et al (2018) Targeted a-therapy of metastatic castration-resistant prostate cancer with ²²⁵Ac-PSMA-617: swimmer-plot analysis suggests efficacy regarding duration of tumor control. *J Nucl Med* 59:795–802
54. Reubi JC, Waser B, Schaer JC, Laederach U, Erion J, Srinivasan A, Schmidt MA, Bugai JE (1998) Unsulfated DTPA- and DOTA-CCK analogs as specific high-affinity ligands for CCK-B receptor-expressing human and rat tissues in vitro and in vivo. *Eur J Nucl Med* 25:481–490
55. Reubi JC, Schar JC, Waser B, Wenger S, Heppeler A, Schmitt JS, Mäcke HR (2000) Affinity profiles for human somatostatin receptor subtypes SST1-SST5 of somatostatin radiotracers selected for scintigraphic and radiotherapeutic use. *Eur J Nucl Med* 27:273–282
56. Reubi JC, Gugger M, Waser B (2002) Co-expressed peptide receptors in breast cancer as a molecular basis for in vivo multireceptor tumour targeting. *Eur J Nucl Med* 29:855–862
57. Reubi JC, Korner M, Waser B, Mazzucchelli L, Guillou L (2004) High expression of peptide receptors as a novel target in gastrointestinal stromal tumours. *Eur J Nucl Med Mol Imaging* 31:803–810

58. Roesch S, Lindner T, Sauter M, Loktev A, Flechsig P, Müller M, Mier W, Warta R, Dyckhoff G, Herold-Mende C, Haberkorn U, Altmann A (2018) Comparative study of the novel RGD motif-containing $\alpha v \beta 6$ integrin binding peptides SFLAP3 and SFITGv6 for diagnostic application in HNSCC. *J Nucl Med* pii: jnumed.118.210013. <https://doi.org/10.2967/jnumed.118.210013>
59. Rosenkranz A, Slastnikova TA, Durymanov MO, Sobolev AS (2013) Malignant melanoma and melanocortin 1 receptor A. *Biochem (Mosc)* 7:1228–1237
60. Saad F, Carles J, Gillessen S et al (2016) Radium-223 and concomitant therapies in patients with metastatic castration-resistant prostate cancer: an international, early access, open-label, single-arm phase 3b trial. *Lancet Oncol* 17:1306–1316
61. Salem R, Thurston KG, Carr BI, Goin JE, Geschwind JF (2002) Yttrium-90 microspheres: radiation therapy for unresectable liver cancer. *J Vasc Interv Radiol* 13:S223–S229
62. Sartor O, Coleman R, Nilsson S et al (2014) Effect of radium-223 dichloride on symptomatic skeletal events in patients with castration-resistant prostate cancer and bone metastases: results from a phase 3, double-blind, randomised trial. *Lancet Oncol* 15:738–746
63. Sato KT, Lewandowski RJ, Mulcahy MF, Atassi B, Ryu RK, Gates VL, Nemcek A, Barakat O, Benson A III, Mandal R, Talamonti M, Wong CY, Miller FH, Newman SB, Shaw JM, Thurston KG, Omary KA, Salem R (2008) Unresectable chemorefractory liver metastases: radioembolization with ^{90}Y microspheres—safety, efficacy, and survival. *Radiology* 247:507–515
64. Schuhmacher J, Zhang H, Doll J, Mäcke HR, Matys R, Hauser H, Henze M, Haberkorn U, Eisenhut M (2005) GRP receptor-targeted PET of a rat pancreas carcinoma xenograft in nude mice with a ^{68}Ga labeled bombesin (6-14) analog. *J Nucl Med* 46:691–699
65. Scopinaro F, De Vincentis G, Varvarigou AD, Laurenti C, Iori F, Remediani S, Chiarini S, Stella S (2003) $^{99\text{m}}\text{Tc}$ -bombesin detects prostate cancer and invasion of pelvic lymph nodes. *Eur J Nucl Med Mol Imaging* 30:1378–1382
66. Stoykow C, Erbes T, Maecke HR et al (2016) Gastrin-releasing peptide receptor imaging in breast cancer using the receptor antagonist (68)Ga-RM2 and PET. *Theranostics* 6:1641–1650
67. Strosberg J, El-Haddad G, Wolin E, the NETTER-1 Trial Investigators (2017) Phase 3 trial of ^{177}Lu dotatate for midgut neuroendocrine tumors. *N Engl J Med* 376:125–135
68. Strosberg J, Wolin E, Chasen B, the NETTER-1 Study Group (2018) Health-related quality of life in patients with progressive midgut neuroendocrine tumors treated with ^{177}Lu -dotatate in the phase III NETTER-1 trial. *J Clin Oncol* 36:2578–2584
69. Thakur ML, Marcus CS, Saeed S, Palella V, Minami C, Diggles L, Le Pham H, Ahdoot R, Kalinowski EA (2000) $^{99\text{m}}\text{Tc}$ -labeled vasoactive intestinal peptide analog for rapid localization of tumors in humans. *J Nucl Med* 41:107–110
70. Valkema R, de Jong M, Bakker WH, Breeman WA, Kooij PP, Lugtenburg PJ, DeJong FH, Christiansen A, Kam BL, DeHerder WW, Stridsberg M, Lindemans J, Ensing G, Krenning EP (2002) Phase I study of peptide receptor radionuclide therapy with [^{111}In -DTPA]octreotide: the Rotterdam experience. *Semin Nucl Med* 32:110–122
71. Vallabhajosula S, Nikolopoulou A, Jhanwar YS et al (2016) Radioimmunotherapy of metastatic prostate cancer with ^{177}Lu -DOTAhuJ591 anti prostate specific membrane antigen specific monoclonal antibody. *Curr Radiopharm* 9:44–53
72. Virgolini I, Raderer M, Kurtaran A, Angelberger P, Yang Q, Radosavljevic M et al (1996) ^{123}I -vasoactive intestinal peptide (VIP) receptor scanning: update of imaging results in patients with adenocarcinomas and endocrine tumors of the gastrointestinal tract. *Nucl Med Biol* 23:685–692
73. Waldherr C, Pless M, Maecke HR, Haldemann A, Mueller-Brand J (2001) The clinical value of [^{90}Y -DOTA]-D-Phe1-Tyr3-octreotide (90Y-DOTATOC) in the treatment of neuroendocrine tumours: a clinical phase II study. *Ann Oncol* 12:941–945
74. Walenkamp AME, Lapa C, Herrmann K, Wester HJ (2017) CXCR4 ligands: the next big hit? *J Nucl Med* 58:77S–82S

75. Wild D, Béhé M, Wicki A, Storch D, Waser B, Gotthardt M, Keil B, Christofori G, Reubi JC, Mäcke HR (2006) Lys40(Ahx-DTPA-111In)NH₂]exendin-4, a very promising ligand for glucagon-like peptide-1 (GLP-1) receptor targeting. *J Nucl Med* 47:2025–2033
76. Zechmann CM, Afshar-Oromieh A, Armor T et al (2014) Radiation dosimetry and first therapy results with a ¹²⁴I/¹³¹I-labeled small molecule (MIP-1095) targeting PSMA for prostate cancer therapy. *Eur J Nucl Med Mol Imaging* 41:1280–1292
77. Zhang C, Zhang Z, Lin KS, Lau J, Zeisler J, Colpo N, Perrin DM, Bénard F (2018) Melanoma imaging using ¹⁸F-labeled α -melanocyte-stimulating hormone derivatives with positron emission tomography. *Mol Pharm* 15:2116–2122

Part V
Future Challenges



Future Challenges of Multimodality Imaging

30

Diego Alfonso López-Mora, Luis Alarcón Lagos, Montserrat Estorch, and Ignasi Carrio

Contents

30.1 Introduction.....	905
30.2 Technology and Probe Design.....	906
30.2.1 SPECT/CT.....	906
30.2.2 PET/CT.....	907
30.2.3 SPECT/MRI and PET/MRI.....	908
30.3 Tracers.....	910
30.4 Future and Conclusions.....	914
References.....	915

30.1 Introduction

To understand genetics of cancer and its proliferative nature remains the main objective of current cancer research. Improved knowledge of cancer pathogenesis results in an array of biomarkers to be used for diagnosis and treatment of the disease. Molecular imaging is the visualization, characterization, and measurement of biological processes at the molecular and cellular levels in a living system. Molecular imaging techniques using radiotracers allow the demonstration of functional or phenotypic changes associated with pathology in vivo, and the characterization of both genotypic and phenotypic tumoral signatures.

D. A. López-Mora · M. Estorch · I. Carrio (✉)
Nuclear Medicine Department, Hospital de la Santa Creu i Sant Pau, Barcelona, Spain
e-mail: i.carrio@santpau.cat

L. A. Lagos
Nuclear Medicine Department, Hospital Dr. Gustavo Fricke, Viña del Mar, Valparaíso, Chile

Positron emission tomography/computed tomography (PET/CT) and single-photon emission computed tomography/computed tomography (SPECT/CT) have procured advances in research and clinical application of fusion imaging unthinkable before, due to its simultaneous developments of new technologies, acquisition and reconstruction parameters, and advanced quantitative methods to measure absolute concentration of radiotracers related to the severity and/or progression of cancer.

The introduction of new hybrid imaging systems such as the digital PET/CT and PET/MRI opened horizons for multimodality molecular imaging, more precise, with simultaneous morphologic, functional, and molecular information of a living system. Moreover, the combinations of anatomic and functional imaging modalities hold further promise in basic medical research or in clinical medicine, especially in the field of staging/restaging and follow-up of oncological diseases. These developments are paralleled by advances of biomolecules and particles that will provide new agents useful for more than one imaging modality and will facilitate the study of the same target by different imaging devices.

30.2 Technology and Probe Design

After the introduction of multimodality systems combining CT with SPECT and PET that changed significantly the capabilities of stand-alone SPECT and PET, fused functional and anatomic images have gained wide acceptance, becoming a powerful clinical tool especially in oncology. With multimodality imaging the research efforts were mostly focused on the integration of MRI with PET and SPECT [46]. The recent introduction of digital detectors in PET/CT systems may change the paradigm in hybrid imaging and may improve the diagnostic performance in oncological and non-oncological diseases, such as neurodegenerative and inflammatory processes [23, 40, 45].

30.2.1 SPECT/CT

New technologies have improved the performance of SPECT and SPECT/CT beyond the technology invented by Hal Anger in 1957 [1]. The initial primary goal of simultaneous SPECT and CT studies was to improve sensitivity and specificity by the combination of coregistered anatomical and functional images and to facilitate lesion localization and attenuation correction [39]. With the incorporation of diagnostic CT, the clinical information from SPECT/CT has been significantly improved. In consequence, guidelines of clinical practice and a number of clinical protocols in cancer, especially in neuroendocrine and thyroid tumors, incorporate SPECT/CT to facilitate precise diagnosis.

Involuntary motions because of cardiac contraction, respiration, or bowel movement are common technical problems encountered in SPECT/CT. Respiratory

motion results in inaccuracy of attenuation correction for lung tumors because of eventual misregistration between emission and transmission data. Research efforts developed methods for correction of respiratory motion effects, such as external or internal devices that make possible to estimate respiratory motion gating emission data and the adequate matching to CT cine data, or the use of modeling motion and matching of CT data from a single CT and a respiratory-gated emission study. Additionally, the development of new technologies such as dose modulation and iterative reconstruction methods can help to reduce radiation dose [39].

The adoption of cadmium zinc telluride (CZT) detectors has impacted the design of new SPECT/CT technologies, such as the adoption of solid-state reading systems. This includes pin diodes (PD), avalanche photodiodes (APD) including position-sensitive devices (PSAPD), silicon photomultipliers (SiPM), and silicon drift detectors (SDD) [31]. The collimator continues to be the main barrier to SPECT/CT progress. Multipinhole collimators in combination with high intrinsic resolution have demonstrated greater potential [31].

30.2.2 PET/CT

The introduction of combined PET/CT in 2001 opened a new era in the field of nuclear and molecular imaging, improving the sensitivity and specificity of clinical PET, and facilitating clinical acceptance and implementation of multimodality imaging [6]. The combination of PET and CT into a single gantry has provided the paradigm for multimodality imaging and has improved and simplified clinical management of patients. Currently, PET/CT is a critical component in the diagnosis and treatment management of oncologic and non-oncological diseases, being a well-known useful in vivo noninvasive imaging tool to measure disease burden [43, 55, 75].

Continuing advances in PET technology include detectors with improved spatial resolution, increased axial field of view (aFOV) with subsequent improvement of sensitivity, faster and more efficient iterative reconstruction algorithms, and improved signal-to-noise ratio by incorporating time-of-flight (TOF) information. Additionally, on the CT field, the development of faster scanner multislice detectors allows the implementation of new acquisition protocols. These evolution advances also include significant changes in reconstruction softwares, integrating resolution recovery with advance iterative techniques [62].

Recently, the introduction of the new generation of PET/CT based on the use of digital detectors may improve detectability and result in enhanced diagnostic performance. The higher detectability of the digital system lies in the different scintillator element coupling technology. Until now, the conventional (analog) PET/CT scanners have been mainly based on multiple scintillation crystals coupled to multiple detectors, while in the digital PET/CT scanners each scintillation crystal is coupled to a single detector. This 1:1 counting coupling of the digital systems provides an enhanced time of flight (TOF) and lower dead time, as well as higher timing and spatial resolution [17, 22, 47, 62]. These advantages of the digital

system improve localization of the annihilation events, significantly influence image quality, diagnostic confidence, and detection/characterization of small lesions (subcentimeter) [23, 40]. Additionally, the smaller volume definition and the improved lesion conspicuity and sharpness of digital system allow more accurate tumor rendering over the analog PET/CT, facilitating radiotherapy planning, prognostication, and treatment monitoring [45]. Therefore, clinical implementation of digital PET/CT opens new perspectives in the assessment of tumor quantification and characterization [40, 55].

In this scenario, digital PET/CT may bring new opportunities for personalized nuclear medicine, as enhanced image quality can be used to optimize administered radioactivity and/or scan duration. In clinical practice, such factors should be considered especially in pediatric (low-dose radiation) or unstable patients (from intensive care units) who cannot sustain long scanning periods [35, 42, 59]. Further developments may include advances in timing resolution and the construction of the first total-body PET/CT with an increase of the geometric coverage to encompass the whole body, which may increase sensitivity by a factor of about 40 for entire body and a factor of about 4–5 for a single organ [16, 55].

As it happens in SPECT/CT, motion between or during PET/CT studies poses technical problems, with remaining uncertainties in the registration process. The correction of respiratory motion effects, which may result in inaccuracy in attenuation correction for lung tumors, represents a challenge for PET/CT. Methods to reduce the effect of respiratory motion include breath-hold during treatment, “gating” in which the beam is turned on or off in synchrony with the respiratory cycle and “tracking” in which the beam follows the tumor based on imaging technology [7, 12, 14]. It has been shown that respiratory gating PET/CT is a valid approach not only to improve quantification, detectability, and definition of radiotherapy of moving lesions and organs, but to be applied routinely in most PET/CT scans [26].

Accurate definition of the boundaries of active disease is of clinical relevance in guiding biopsy sites and in planning surgery and radiotherapy fields. PET/CT studies facilitate the correct anatomical delineation of 18F-FDG uptake optimizing biopsy and improving the planning of surgical procedures [2, 25]. The better delineation of tumor tissue by PET/CT has supported the implementation of this multimodality system in radiation therapy planning of various tumors as non-small cell lung carcinomas, head and neck tumors, and lymphoma [20, 27, 64].

30.2.3 SPECT/MRI and PET/MRI

Over the years, numerous working prototypes of PET/MRI systems have been described and introduced [8, 33, 56, 62]. The combination of SPECT and PET with MRI can be important in areas where this technique is the preferred anatomic imaging modality. There are clear synergies between these modalities in areas where, beyond anatomic landmarking, MRI can detect organ-specific abnormalities and pathologies by spectroscopic quantification of concentrations of molecules.

Moreover, the expected radiation dose for SPECT and PET/MRI is significantly less than that for SPECT and PET/CT, which may be of importance in oncologic patients that are followed with multiple studies to monitor disease progression and response to therapy.

A potential limitation of MRI in multimodality imaging systems is that this technique does not provide adequate information for attenuation correction of emission studies, being a challenge to separate air and bone, and to measure the variations of density in the lung. Attenuation correction based on MRI is an active area of research, and its developments will be key for future clinical applications of PET/MRI [30, 41, 44, 76].

To integrate SPECT and PET with MRI is a technical challenge because these systems can interfere each other. Several prototypes have been designed and are at various stages of development [48, 74]. Even if to merge the hardware of SPECT or PET and MRI into a single device is limited by space, the principal challenge derives from conventional PET detectors based on photomultiplier tubes (PMTs), which do not operate properly in presence of the magnetic field of MRI. The consequent mutual interference between both image modalities needs to be reduced at maximum to provide high-quality studies, as much PET as MRI. PET systems can interfere with MRI systems degrading the homogeneity of magnetic and radiofrequency fields resulting in a loss of image quality with presence of artifacts. On the other hand, the strong external magnetic field of MRI systems can interfere with PET systems deflecting the normal trajectory of electrons into the PMTs, and the radiofrequency field and the gradient system pulses can affect the electronic of PET producing artifacts on image. To solve mutual interference between PET and MRI, light fibers coupled to the scintillation crystals of PET detectors have been used, with only the MRI elements remaining in the magnetic field and directing the scintillations out of this field through light fibers. Scintillation crystals produce several distortion and artifacts on MRI image, due to their different magnetic susceptibilities compared with human tissue. The replacement of photomultiplier tubes by solid-state scintillation detectors has been proposed and developed [71]. These detectors, based on avalanche photodiodes, have the advantage of being insensitive to magnetic fields and can be directly connected to the scintillation crystal block within the magnetic field using a short 1–2 mm light guide. In this way, light loss is minimized and the conversion of light to electronic signals takes place inside the MRI system, avoiding the use of optical fibers. Another advantage of avalanche photodiodes is that these are smaller than PMTs allowing a design with a fully integrated PET. This design has the advantages that no metallic components are placed directly in the MRI field of view and that the short light guides lossless light. The design of compact systems using solid-state light detectors and based on superconducting magnet (split magnet) or on field cycling MRI is a challenging task [15, 61].

The integration of PET with MRI is a promising hybrid imaging tool in many aspects (including decreased radiation dose, improved motion correction, and the convenience of a combined exam), but there are many obstacles that prevent PET/MRI widespread worldwide (access, cost, speed, and familiarity). In this

scenario, clinical PET/MRI systems are still relatively rare and therefore the precise clinical patient's benefit remains unclear. However, PET/MRI seems to be promising in characterization of primary bronchogenic tumors, it fails to detect small pulmonary nodules [29, 52, 53] as well as the determination of their extent and metastases [52, 53, 57]. In the same line, PET/MRI seems also to be promising in non-traumatic neurological disease (dysplasias, tuberous sclerosis, and temporal lobe epilepsy) [9, 13, 50], detection and characterization of hepatic lesions [34], and head and neck tumors [49]. Overall, PET/CT scanners are unlikely to be replaced by PET/MRI in a short-term period [19].

30.3 Tracers

The clinical use of PET for diagnosis, staging, and characterization of tumors is based on the assessment of increased metabolism as an important hallmark of cancer. As most tumors display considerably increased glycolytic activity, uptake and accumulation of 18F-FDG have been widely employed for tumor localization and characterization and have been approved for clinical use in suspected or existing cancers by most international health care regulatory agencies [73].

However, 18F-FDG has some disadvantages and limitations. Increased glycolytic activity is a relatively nonspecific and sometimes imprecise indicator of malignancy mainly because increased 18F-FDG uptake is also observed in inflammatory disorders and infections. 18F-FDG PET is less suitable for brain tumors because of the high background in normal brain tissues. Relatively indolent tumors, such as prostate cancer, low-grade lung adenocarcinomas, renal cell cancers, and mucinous neoplasms, are known to have generally low 18F-FDG uptake [21]. Another tumor type with generally low uptake of 18F-FDG is the group of neuroendocrine tumors [67]. Therefore, additional PET imaging tracers have been developed, such as 68 Ga-labeled somatostatin analogs (68 Ga-SSA). Other new tracers are in development, labeled with various isotopes such as 124I. 124I is a PET isotope with a favorable half-life of 4.2 days. It offers superior imaging characteristics with enhanced spatial resolution and image sensitivity, and permits the evaluation of *in vivo* iodine kinetics. Therefore, 124I made it possible to detect and scan thyroid cancer lesions with high sensitivity [36, 51].

68 Ga-SSA include several tracers sharing a similar structure (68 Ga-DOTA-TOC, 68 Ga-DOTA-NOC, 68 Ga-DOTA-TATE) and bind, with specific affinity, to somatotropin receptors which are frequently overexpressed in neuroendocrine tumors (NETs) [5]. Other tracers available for PET/CT included choline labeled with 11C or 18F and PSMA labeled with 68 Ga or 18F for prostate cancer. Choline is a water-soluble nutrient that is incorporated into cell membranes as phosphatidylcholine. Radiolabeled choline is found in proliferating cells, such as cancer and inflammation, and therefore may be less specific demonstrating modest sensitivity [63]. PSMA is a transmembrane protein that is highly overexpressed in prostate cancer cells. The recent development of small-molecule inhibitors (i.e.,

68 Ga-PSMA-11 and 18F-labeled PSMA agents) that target the active substrate recognition site of PSMA has demonstrated superior sensitivity even at very low PSA levels with high background-to-tumor ratios [63].

PET compounds available for multimodality imaging also include those capable to target specific key biologic processes in oncogenesis, such as proliferation (18F-3-fluoro-3-deoxy-L-thymidine [18F-FLT]), hypoxia (18F-fluoromisonidazole [18F-FMISO] and 18F-fluoroazomycin arabinoside [18F-FAZA]), angiogenesis (18F-galacto-arginine-glycine-aspartic acid [18F-galacto-RGD]), and apoptosis (124I- or 64Cu-Annexin V). Imaging of these biologic targets is expected to provide meaningful information for the selection and monitoring of targeted therapy in individual cancer patients, facilitating personalized treatment of the disease.

18F-FMISO is a highly stable radiopharmaceutical directly derived from misonidazole and has been extensively studied for regional mapping of hypoxia. 18F-FMISO shows high accumulation in hypoxic tissue which is proportional to the hypoxic fraction of the tumor and allows identification of patients who may benefit from changes in their therapeutic regimen as hypoxia has been identified as a major adverse prognostic factor for tumor progression and for resistance to treatment. In addition, such mapping of hypoxia can be used to guide intensity-modulated radiotherapy [32, 65]. Clinical trials are being developed to further investigate the feasibility and safety of individualized, hypoxia-adapted, radiotherapy.

The thymidine analog 18F-FLT, derived from the cytostatic drug azidovudine, has been suggested for noninvasive assessment of cell proliferation. Hence, it should provide valuable information for response assessment to tumor therapies, and more could offer more specific tumor imaging than 18F-FDG. 18F-FLT is taken up by cell by the same mechanisms as the nucleoside thymidine. This transport step is facilitated by nucleoside transporters, especially by the human nucleoside transporter 1 (hENT1). Once within the cell, 18F-FLT is phosphorylated by the enzyme thymidine kinase 1 (TK1), which results in the intracellular accumulation of the tracer. 18F-FLT PET has still seldom been used for tumor therapy follow-up in clinical trials, in part due to limited knowledge of the factors determining 18F-FLT uptake and therapy-induced changes of its retention [54]. Labeled amino acids have been used for the diagnosis of brain tumors, like 18F-labeled fluoroethyltyrosine or 18F-fluorodihydroxyphenylalanine (DOPA) as well as 11C-methionine. 18F-fluoroestradiol has been used for the assessment of the estrogen receptor status in breast cancer [18].

One of the primary goals in cancer research is to increase knowledge on genetics of the disease and its proliferative nature. High-throughput gene-sequencing techniques of the primary tumor or its metastases will allow genetic analysis of the tumor on an individual basis. The integration of molecular imaging into clinical routine and the combination with gene-sequencing techniques should be the goal for the near future to provide a personalized medicine for most oncological patients and not only for scientific purposes [18]. Along this line, non-somatostatin receptor biomarkers overexpressed on the surface of malignant cell have been explored. These are VPAC receptors, a family of 3G protein-coupled receptors located on the plasma membrane of tumor cells that mediate the biological action of vasoactive

intestinal peptide (VIP) and pituitary adenylate cyclase-activating polypeptide (PACAP). These receptors are present on several common tumors, such as breast, prostate, bladder, and colon, and VIP and PACAP can be labeled with ^{99m}Tc , ^{64}Cu , and ^{68}Ga , with opportunities to image these oncologic diseases early and specifically in the future [24, 37, 58].

Another exciting and challenging goal in cancer research is the possibility to target intracellular biomarkers for diagnostic application. It has been demonstrated that oncogene expression of tumoral cells is different from their normal cohorts. Targeting specific oncogene mRNA copies with ^{99m}Tc , ^{64}Cu , and ^{68}Ga for SPECT or PET in dividing cells may permit imaging of oncogene expression in several tumors. This technique could be also useful to monitor effectiveness of therapy, with assessment of the upregulation or downregulation of oncogene mRNA copies and of proliferative tumoral status after treatment [10, 11, 38, 68–70, 72]. Other studies have examined the possibility to assess tumor suppressor gene p53 transcription in a cell or to determine the expression of Ki-67 protein as proliferative index of tumoral cells [60, 66]. Currently, therapeutic approaches are focused to block the division of cells, even if these approaches do not discriminate between normal and cancerous cells. To increase cell specificity, antisense technology has emerged. It is based on the sequence-specific binding of an antisense oligonucleotide to target RNA, preventing the oncogene mRNA translation and modulating the oncogene expression involved in the pathogenesis of oncologic diseases [28, 38]. Challenges to be resolved include *in vivo* stability, sequence length, and poor uptake in malignant cells. For new targeted therapy approaches, the identification of the correct concentration of therapeutic agent and its dose schedule has to be investigated [3, 4].

Molecular PET imaging provides diverse structural and functional information of drug development: drug distribution and concentration can be assessed using the radiolabeled compound, thereby demonstrating that the compound reaches the target and does not accumulate at sites of potential toxicities. The development of new therapeutic antibodies which have been approved for the treatment of hematologic malignancies and for solid tumors with good therapeutic results led to new attempts of radiolabeling these promising therapeutic antibodies. Such a newly developed tracer is ^{64}Cu -DOTA-trastuzumab, which is a humanized monoclonal antibody against HER2 that is widely used for treatment of HER2-positive breast carcinomas. Another interesting newly developed tracer is Zr-89-bevacizumab, which is a recombinant humanized monoclonal antibody that blocks angiogenesis by inhibiting the VEGF-A. This approach may allow a noninvasive evaluation of the antiangiogenic therapeutic result in patients with, for example, colorectal cancer or breast cancer [18, 73].

The new technological achievements in both genomics and proteomics as well as in the bioinformatics will allow a better understanding of the molecular mechanisms of a cancer disease and will help to identify specific biomarkers for both diagnostic and therapeutic purposes. The clinical use of the new hybrid scanners together with the application of cancer-specific biomarkers will revolutionize treatment and open new ways of individual treatment.

Main existing PET tracers of ^{18}F and of other positron-emitting radionuclides available for multimodality molecular imaging and their biochemical process, mechanism of uptake, and localization are, respectively, shown in Tables 30.1 and 30.2.

Table 30.1 PET tracers of ^{18}F : biochemical process, mechanisms of uptake and localization

Radiotracer	Biochemical process	Mechanism of uptake and localization
^{18}F -FDG	Glucose	Facilitate diffusion via glucose transporters
	Metabolism	Substrate for hexokinase in glucose metabolism
^{18}F -Fluoride	Bone metabolism	Incorporation in the hydroxyapatite crystals in bone
^{18}F -Fluorocholine	Membrane	Substrate for choline kinase in choline metabolism
	Synthesis	
^{18}F -Fluoroacetate	Lipid synthesis	Acetate is activated to acetyl-CoA in both the cytosol and mitochondria by acetyl-CoA synthetase
^{18}F -Fluorothymidine	DNA synthesis	Substrate for thymidine kinase in DNA synthesis and reflects tumor cell proliferation rate
^{18}F -FMISO	Hypoxia	Intracellular reduction and binding
^{18}F -FES	Receptor binding	Specific binding to estrogen receptors in breast cancer
^{18}F -FDOPA	AA transport and	Precursor for the synthesis of dopamine
^{18}F -FMT	Protein synthesis	Transport into the cells involves amino acid carrier protein
^{18}F -FCCA		Intracellular trapping involves protein synthesis or transmethylation
^{18}F -FB-	Angiogenesis	Integrin receptors on endothelial cells of
E[c(RGDyK)]2		Neovasculature
^{18}F -Oligonucleotide	Gene expression	In vivo hybridization with mRNA Substrate to herpes virus thymidine kinase
^{18}F -FHBG		
^{18}F -labeled PSMA	Membrane antigen	Binding sites for PSMA ligands

Table 30.2 PET tracers of positron-emitting radionuclides non- ^{18}F : biochemical process, mechanisms of uptake and localization

Radiotracer	Biochemical process	Mechanism of uptake and localization
^{15}O -Water	Blood flow/perfusion	Freely diffusible across membranes
^{11}C -Choline	Membrane synthesis	Substrate for choline kinase in choline metabolism
^{11}C -Thymidine	DNA synthesis	Substrate for thymidine kinase in DNA synthesis and reflects tumor cell proliferation rate

(continued)

Table 30.2 (continued)

Radiotracer	Biochemical process	Mechanism of uptake and localization
⁶⁸ Ga-DOTATOC ⁶⁸ Ga-DOTANOC ⁶⁸ Ga-DOTATATE	Receptor binding	Specific binding to somatostatin receptor (SSTR-II) Specific binding to somatostatin receptor (SSTR-II, III, V) Specific binding to somatostatin receptor (SSTR-II)
¹¹ C-L-methionine	AA transport and protein synthesis	Transport into the cells involves amino acid carrier protein Intracellular trapping involves protein synthesis or transmethylation
¹²⁴ I- ⁶⁴ Cu- ⁸⁸ Y-Labeled Antibodies	Binding to tumor antigens	Specific binding to tumor-associated antigenic binding sites
¹²⁴ I- ⁶⁴ Cu-Annexin V	Apoptosis	Specific binding to phosphatidylserine On cell membrane
⁶⁸ Ga-PSMA-11	Membrane antigen	Binding sites for PSMA ligands

30.4 Future and Conclusions

Molecular imaging employing multimodality systems will strongly influence the practice of medicine in the next generations. Specific imaging biomarkers will be developed to enable physicians to ensure better strategies of patient management, to stratify cancer, and to perform personalized medicine. Smarter devices, coupling different imaging modalities, with higher spatial resolution and greater sensitivity will be developed, allowing the visualization of a cluster of cells *in vivo*. These smart devices will use smart probes to target specific biologic phenomena that will provide a true early diagnosis and will drive the design of therapy and the assessment of its effectiveness. Even if PET/CT will ultimately replace SPECT/CT, advances in instrumentation, CT technology, and development of radiotracers have the potential to advance beyond its current level of performance. The horizon for hybrid imaging lies in the development of new tumor-specific agents that can improve oncologic clinical diagnostic and therapeutic applications.

In the near future, digital PET/CT may emerge as a powerful multimodality technique in clinical oncology, offering considerable potential for imaging applications beyond simple correlation of functional and anatomic images. Future developments should include the simultaneous acquisition of multifunctional data with quantification of PET tracer accumulation. Finally, the use of imaging as a surrogate endpoint requires demonstration of a significant relationship between imaging results and clinical outcome. Cooperation with the pharmaceutical and the instrumentation industry is needed to foster prospective randomized multicenter trials that are mandatory to demonstrate the relationship between appropriate use of multimodality imaging and better patient outcomes.

References

1. Anger HO (1957) Scintillation camera. *Rev Sci Instrum* 29:27–33
2. Acuff SN, Jackson AS, Subramanian RM, Osborne D (2018) Practical considerations for integrating PET/CT into radiation therapy planning. *J Nucl Med Technol* 46(4):343–348
3. Bennett CF, Swayze EE (2010) RNA targeting therapeutics: molecular mechanisms of antisense oligonucleotides as a therapeutic platform. *Annu Rev Pharmacol Toxicol* 50:259–293
4. Bennett CF, Baker BF, Pham N et al (2017) Pharmacology of antisense drugs. *Annu Rev Pharmacol Toxicol* 57:81–105
5. Bergeret S, Charbit J, Ansquer C et al (2019) Novel PET tracers: added value for endocrine disorders. *Endocrine* 64(1):14–30
6. Beyer T, Townsend DW, Brun T et al (2000) A combined PET/CT scanner for clinical oncology. *J Nucl Med* 41:1369–1379
7. Bundschuh R, Martínez-Möller A, Essler M et al (2008) Local motion correction for lung tumours in PET/CT—First results. *Eur J Nucl Med Mol Imaging* 35:1981–1988
8. Catana C, Procissi D, Wu YB et al (2008) Simultaneous in vivo positron emission tomography and magnetic resonance imaging. *Proc Natl Acad Sci USA* 105:3705–3710
9. Carne R, O'Brien T, Kilpatrick C et al (2004) MRI-negative PET-positive temporal lobe epilepsy: a distinct surgically remediable syndrome. *Brain* 127:2276–2285
10. Chakrabarti A, Aruva MR, Sajankila SP (2005) Synthesis of novel peptide nucleic acid-peptide chimera for non-invasive imaging of cancer. *Nucleosides Nucleotides Nucleic Acids* 24:409–414
11. Chakrabarti A, Zhang K, Aruva MR et al (2007) Radiohybridization PET imaging of KRAS G12D mRNA expression in human pancreas cancer xenografts with [64Cu]DO3A-peptide nucleic acid-peptide nanoparticles. *Cancer Biol Ther* 6:948–956
12. Chang G, Chang T, Pan T, Clark JW Jr, Mawlawi OR (2010) Implementation of an automated respiratory amplitude gating technique for PET/CT: clinical evaluation. *J Nucl Med* 51:16–24
13. Chandra PS, Salamon N, Huang J et al (2006) FDG-PET/MRI Coregistration and diffusion-tensor imaging distinguish epileptogenic tubers and cortex in patients with tuberous sclerosis complex: a preliminary report. *Epilepsia* 47:1543–1549
14. Cheng NM, Yu CT, Ho KC, Wu YC, Liu YC, Wang CW, Yen TC (2009) Respiration-averaged CT for attenuation correction in non-small-cell lung cancer. *Eur J Nucl Med Mol Imaging* 36:607–615
15. Cherry SR, Louie AY, Jacobs RE (2008) The integration of positron emission tomography with magnetic resonance imaging. *Proc IEEE* 96:416–438
16. Cherry SR, Jones T, Karp JS et al (2018) Totalbody PET: maximizing sensitivity to create new opportunities for clinical research and patient care. *J Nucl Med* 59:3–12
17. Degenhardt C, Prescher G, Frach T et al (2009) The digital silicon photomultiplier: a novel sensor for the detection of scintillation light. In: *IEEE Nuclear Science Conference Record* 2383–2386
18. Dimitrakopoulou-Strauss A (2015) PET-based molecular imaging in personalized oncology: potential of the assessment of therapeutic outcome. *Future Oncol* 11(7):1083–1091
19. Ehman E, Johnson G, Villanueva-Meyer J et al (2017) PET/MRI: where might it replace PET/CT? *J Magn Reson Imaging* 46(5):1247–1262
20. Faria SL, Menard S, Devic S, Sirois C, Souhami L, Lisbona R, Freeman CR (2008) Impact of FDG-PET/CT on radiotherapy volume delineation in non-small-cell lung cancer and correlation of imaging stage with pathologic findings. *Int J Radiat Oncol Biol Phys* 70:1035–1038
21. Flavell R, Naeger D, Aparici C et al (2016) Malignancies with low fluorodeoxyglucose uptake at PET/CT: pitfalls and prognostic importance: resident and fellow education feature. *RadioGraphics* 36:293–294

22. Frach T, Prescher G, Degenhardt C et al (2009) The digital silicon photomultiplier: principle of operation and intrinsic detector performance. In: *IEEE Nuclear Science Conference Record 1959–1965*
23. Fuentes-Ocampo F, López-Mora DA, Flotats A et al (2019) Digital versus analog PET/CT: intra-subject comparison of the SUVmax in target lesions and reference regions. *Eur J Nucl Med Mol Imaging*. In press
24. Germano PM, Le SV, Oh DS et al (2004) Differential coupling of PAC1 SV1 splice variant of human colonic tumors to the activation of intracellular cAMP but not intracellular Ca^{2+} does not activate tumor proliferation. *J Mol Neurosci* 22:83–92
25. Goerres GW, Stupp R, Barghouth G et al (2005) The value of PET, CT and in-line PET/CT in patients with gastrointestinal stromal tumours: long-term outcome of treatment with imatinib mesylate. *Eur J Nucl Med Mol Imaging* 32:153–162
26. Guerra L, Ponti E, Morzenti S et al (2017) Respiratory motion management in PET/CT: applications and clinical usefulness. *Curr Radiopharm* 10(2):85–92
27. Guido A, Fuccio L, Rombi B, Castellucci P, Ceconi A, Bunkheila F, Fuccio C, Spezi E, Angelini AL, Barbieri E (2009) Combined 18F-FDG-PET/CT imaging in radiotherapy target delineation for head-and-neck cancer. *Int J Radiat Oncol Biol Phys* 73:759–763
28. Hersey P, Bastholt L, Chiarion-Sileni V, Cinat G, Dummer R, Eggermont AM, Espinosa E, Hauschild A, Quirt I, Robert C, Schadendorf D (2009) Small molecules and targeted therapies in distant metastatic disease. *Ann Oncol* 20(Suppl6):vi35–vi40
29. Heusch P, Buchbender C, Kohler J et al (2013) Correlation of the apparent diffusion coefficient (ADC) with the standardized uptake value (SUV) in hybrid 18F-FDG PET/MRI in non-small cell lung cancer (NSCLC) lesions: initial results RoFo 185:1056–1062
30. Hofmann M, Steinke F, Scheel V et al (2008) MRI-based attenuation correction for PET/MRI: a novel approach combining pattern recognition and atlas registration. *J Nucl Med* 49:1875–1883
31. Hutton BF (2014) The origin of SPECT and SPECT/CT. *Eur J Nucl Med Mol Imaging* 41 (Suppl 1):S3–S16
32. Inobushi M, Tatsumi M, Yamamoto Y et al (2018) European research trends in nuclear medicine. *Ann Nucl Med* 32:579–582
33. Judenhofer MS, Wehrl HF, Newport DF et al (2008) Simultaneous PET-MRI: a new approach for functional and morphological imaging. *Nat Med* 14:459–465
34. Kang B, Lee JM, Song YS et al (2016) Added value of integrated whole-body PET/MRI for evaluation of colorectal cancer: comparison with contrast-enhanced MDCT. *AJR Am J Roentgenol* 206:W10–W20
35. Koopman D, Groot Koerkamp M, Jager PL et al (2017) Digital PET compliance to EARL accreditation specifications. *EJNMMI Phys* 4:9. <https://doi.org/10.1186/s40658-017-0176-5>
36. Kuker R, Szejnberg M, Gulec S (2017) I-124 imaging and dosimetry. *Mol Imaging Radionucl Ther* 26(suppl 1):66–73
37. Kumar P, Tripathi SK, Chen CP et al (2019) Evaluating Ga-68 peptide conjugates for targeting VPAC receptors: stability and pharmacokinetics. *Mol Imaging Biol* 21(1):130–139
38. Lendvai G, Estrada S, Bergström M (2009) Radiolabelled oligonucleotides for imaging of gene expression with PET. *Curr Med Chem* 16:4445–4461
39. Ljungberg M, Preterius H (2018) SPET/CT: an update on technological developments and clinical applications. *Br J Radiol* 90:20160402
40. Lopez-Mora DA, Flotats A, Fuentes-Ocampo F et al (2019) Comparison of image quality and lesion detection between digital and analog PET/CT. *Eur J Nucl Med Mol Imaging* 46 (6):1383–1390
41. Mehranian A, Arabi H, Zaidi H (2016) Vision 20/20: magnetic resonance imaging-guided attenuation correction in PET/MRI: challenges, solutions, and opportunities. *Med Phys* 43 (3):1130–1155. <https://doi.org/10.1118/1.4941014>
42. Messerli M, Stolzmann P, Egger-Sigg M et al (2018) Impact of a Bayesian penalized likelihood reconstruction algorithm on image quality in novel digital PET/CT: clinical

- implications for the assessment of lung tumors. *EJNMMI Phys* 5:27. <https://doi.org/10.1186/s40658-018-0223-x>
43. Mitra E, Quon A (2009) Positron emission tomography/computed tomography: the current technology and applications. *Radiol Clin N Am* 47:147–160
 44. Mollet P, Keereman Vincent, Bini J et al (2014) Improvement of attenuation correction in time-of-flight PET/MR imaging with a positron-emitting source. *J Nucl Med* 55(2):329–336
 45. Nguyen N, Vercher-Conejero JL, Sattar A et al (2015) Image quality and diagnostic performance of a digital PET prototype in patients with oncologic diseases: initial experience and comparison with analog PET. *J Nucl Med* 56:1378–1385
 46. Patton JA, Townsend DW, Hutton BF (2009) Hybrid imaging technology: from dreams and vision to clinical devices. *Semin Nucl Med* 39:247–263
 47. Rausch I, Ruiz A, Valverde-Pascual I et al (2018) Performance evaluation of the Philips Vereos PET/CT system according to the NEMA NU2-2012 standard. *J Nucl Med* 60(4):561–567
 48. Raylman RR, Majewski S, Lemieux SK et al (2006) Simultaneous MRI and PET imaging of a rat brain. *Phys Med Biol* 51:6371–6379
 49. Ruhlmann V, Ruhlmann M, Bellendorf A et al (2016) Hybrid imaging for detection of carcinoma of unknown primary: a preliminary comparison trial of whole-body PET/MRI versus PET/CT. *Eur J Radiol* 85:1941–1947
 50. Salamon N, Kung J, Shaw S et al (2008) FDG-PET/MRI coregistration improves detection of cortical dysplasia in patients with epilepsy. *Neurology* 71:1594–1601
 51. Santhanam P, Taieb D, Solnes L et al (2017) Utility of I-124 PET/CT in identifying radioiodine avid lesions in differentiated thyroid cancer: a systematic review and meta-analysis. *Clin Endocrinol (Oxf)* 86(5):645–651
 52. Sawicki LM, Grueneisen J, Buchbender C et al (2016) Evaluation of the outcome of lung nodules missed on 18F-FDG PET/MRI compared with 18F-FDG PET/CT in patients with known malignancies. *J Nucl Med* 57:15–20
 53. Sawicki LM, Grueneisen J, Buchbender C et al (2016) Comparative performance of 18F-FDG PET/MRI and 18F-FDG PET/CT in detection and characterization of pulmonary lesions in 121 oncologic patients. *J Nucl Med* 57:582–586
 54. Schelhaas S, Heinzmann K, Bollineni VR (2017) Preclinical applications of 3'-deoxy-3'-[18F] fluoro-thymidine in oncology-A systematic review. *Theranostics* 7(1):40–50
 55. Schillaci O, Urbano N (2019) Digital PET/CT: a new intriguing chance for clinical nuclear medicine and personalized molecular imaging. *Eur J Nucl Med Mol Imaging* 46(6):1222–1225
 56. Schlemmer HPW, Pichler BJ, Schmand M et al (2008) Simultaneous MR/PET imaging of the human brain: feasibility study. *Radiology* 248:1028–1035
 57. Schmidt H, Brendle C, Schraml C et al (2013) Correlation of simultaneously acquired diffusion-weighted imaging and 2-deoxy-[18F] fluoro-2-D-glucose positron emission tomography of pulmonary lesions in a dedicated whole-body magnetic resonance/positron emission tomography system. *Invest Radiol* 48:247–255
 58. Schulz S, Rocken C, Mawrin C et al (2004) Immunocytochemical identification of VPAC1, VPAC2 and PAC1 receptors in normal and neoplastic human tissues with subtype specific antibodies. *Clin Cancer Res* 10:8234–8242
 59. Sekine T, Delso G, Zeimpekis KG et al (2018) Reduction of (18)F-FDG dose in clinical PET/MR imaging by using silicon photomultiplier detectors. *Radiology* 286:249–259
 60. Shah C, Miller TW, Wyatt SK, McKinley ET, Olivares MG, Sanchez V, Nolting DD, Buck JR, Zhao P, Ansari MS, Baldwin RM, Gore JC, Schiff R, Arteaga CL, Manning HC (2009) Imaging biomarkers predict response to anti-HER2 (ErbB2) therapy in preclinical models of breast cancer. *Clin Cancer Res* 15:4712–4721
 61. Sikkandhar M, Krishna KG, Sachin M et al (2017) PET/MRI: a frontier in era of complementary hybrid imaging. *Eur J Hybrid Imaging* 2018; 2(1):12

62. Slomka PJ, Pan T, Germano G (2016) Recent advances and future progress in PET instrumentation. *Semin Nucl Med* 46(1):5–19
63. Smith CP, Laucis A, Harmon S et al (2019) Novel imaging in detection of metastatic prostate cancer. *Curr Oncol Rep* 21(4):31
64. Specht L, Berthelsen AK (2018) PET/CT in radiation therapy planning. *Semin Nucl Med* 48(1):67–75
65. Stieb S, Eleftheriou A, Warnock G et al (2018) Longitudinal PET imaging for tumor hypoxia during the course of radiotherapy. *Eur J Nucl Med Mol Imaging* 45(12):2201–2217
66. Tan PH, Bay BH, Yip G et al (2005) Immunohistochemical detection of Ki67 in breast cancer correlates with transcriptional regulation of genes related to apoptosis and cell death. *Mod Pathol* 18:374–381
67. Tang C, Nie D, Tang G et al (2017) Radiosynthesis and biological evaluation of N-(2-[18F] fluoropropionyl)-3,4-dihydroxy-L-phenylalanine as a PET tracer for oncologic imaging. *Nucl Med Biol* 50:39–46
68. Tian X, Aruva MR, Qin W et al (2004) External imaging of CCND1 cancer gene activity in experimental human breast cancer xenografts with ^{99m}Tc-peptide–peptide nucleic acid-peptide chimeras. *J Nucl Med* 45:2070–2082
69. Tian X, Aruva MR, Wolfe HR et al (2005) Tumor-targeting peptide-PNA peptide chimeras for imaging overexpressed oncogene mRNAs. *Nucleosides Nucleotides Nucleic Acids* 24:1085–1091
70. Tian X, Aruva MR, Zhang K et al (2007) PET imaging of CCND1 mRNA in human MCF7 estrogen receptor positive breast cancer xenografts with oncogene-specific [⁶⁴Cu] chelator-peptide nucleic acid-IGF1 analog radiohybridization probes. *J Nucl Med* 48:1699–1707
71. Townsend DW (2008) Multimodality imaging of structure and function. *Phys Med Biol* 53:R1–R39
72. Velikyan I (2014) Prospective of ⁶⁸Ga-radiopharmaceutical development. *Theranostics* 4(1):47–80
73. Voigt W (2017) Advanced PET imaging in oncology: status and developments with current and future relevance to lung cancer care. *Curr Opin Oncol* 30(2):77–83
74. Woody C, Schlyer D, Vaska P et al (2007) Preliminary studies of a simultaneous PET/MRI scanner based on the RatCAP small animal tomograph. *Nucl Instrum Methods A* 571:102–105
75. Wright C, Binzel K, Zhang J et al (2017) Advanced functional tumor imaging and precision nuclear medicine enabled by digital PET technologies. *Contrast Media Mol I*. <https://doi.org/10.1155/2017/5260305>
76. Zaidi H (2007) Is MR-guided attenuation correction a viable option for dual modality PET/MR imaging? *Radiology* 244:639–642